NUCLEAR PHYSICS

JOURNAL DEVOTED TO THE EXPERIMENTAL AND THEORETICAL STUDY OF THE FUNDAMENTAL CONSTITUENTS OF MATTER AND THEIR INTERACTIONS

EDITOR: L. ROSENFELD - COPENHAGEN
ASSOCIATE EDITOR: O. NATHAN - COPENHAGEN

VOLUME XVI

NORTH-HOLLAND PUBLISHING COMPANY - AMSTERDAM

NUCLEAR PHYSICS

EDTIORIAL BOARD

AUSTRALIA & NEW ZEALAND:	H. Messel (Sydney), M. L. Oliphant (Canberra)
AUSTRIA:	B. Karlik, (Vienna), H. Thirring (Vienna)
BELGIUM:	M. de Hemptinne (Louvain), J. Verhaeghe (Ghent)
CANADA:	G. Volkoff (Vancouver)
DENMARK:	C. Møller (Copenhagen), S. Rozental (Copenhagen)
FINLAND:	L. Simons (Helsinki)
FRANCE:	A. Berthelot (Saclay), S. Gorodetzky (Strasbourg)
GERMANY (DEM. REP.):	G. Hertz (Leipzig)
GERMANY (FED. REP.):	W. Gentner (Freiburg i. B.), J. H. D. Jensen (Heidelberg)
GREAT BRITAIN:	S. Devons (Manchester), T. H. R. Skyrme (Harwell)
HUNGARY:	L. Janossy (Budapest)
INDIA:	H. Bhabha (Bombay), R. Ramanna (Trombay)
IRISH REPUBLIC:	J. McConnell (Maynooth)
ISRAEL:	G. Racah (Jerusalem)
ITALY:	E. Amaldi (Rome)
JAPAN:	S. Kikuchi (Tokyo), S. Tomonaga (Tokyo)
MEXICO:	M. Moshinsky (Mexico)
NETHERLANDS:	H. Brinkman (Groningen), S. R. de Groot (Leiden)
NORWAY:	E. Hylleraas (Oslo), A. Lundby (Oslo), H. Wergeland (Trondheim)
POLAND:	L. Infeld (Warsaw)
PORTUGAL:	J. M. Araújo (Porto), J. R. de Almeida Santos (Coimbra)
SOUTH AMERICA:	G. Beck (Saõ Paulo), J. Leite Lopes (Rio de Janeiro)
SPAIN:	J. M. Otero (Madrid), C. Sanchez del Rio (Madrid)
SWEDEN:	O. Klein (Stockholm), K. Siegbahn (Uppsala), I. Waller (Uppsala)
SWITZERLAND:	P. Huber (Basel), P. Scherrer (Zürich)
U.A.R. & ARAB COUNTRIES:	F. El Bedewi (Alexandria), M. G. Nooh (Cairo)
U.S.A.	H. H. Barschall (Madison, Wisconsin), V. Weisskopf (Cambridge, Mass.)
U.S.S.R.:	M. A. Markov (Moscow), I. S. Shapiro (Moscow), D. V. Skobeltzyn (Moscow)
YUGOSLAVIA:	I. Supek (Zagreb)

NUCLEAR PHYSICS

JOURNAL DEVOTED TO THE EXPERIMENTAL AND THEORETICAL STUDY OF THE FUNDAMENTAL CONSTITUENTS OF MATTER AND THEIR INTERACTIONS

EDITOR: L. ROSENFELD - COPENHAGEN

VOLUME XVI

APRIL 1960—JUNE 1960

NORTH-HOLLAND PUBLISHING COMPANY-AMSTERDAM

PRINTED IN THE NETHERLANDS

1.D.2:
1.E.1:
3.B

Nuclear Physics **16** (1960) 1—26; © *North-Holland Publishing Co., Amsterdam*
Not to be reproduced by photoprint or microfilm without written permission from the publisher

CONVERSION ELECTRON SPECTRUM FROM Ce^{144} DECAY

J. S. GEIGER, R. L. GRAHAM and G. T. EWAN
Atomic Energy of Canada Limited, Chalk River, Canada

Received 26 November 1959

Abstract: The internal conversion electron spectrum following the β decay of Ce^{144} has been studied in the Chalk River iron-free $\pi\sqrt{2}$ β spectrometer at a momentum resolution of ≈ 0.1 %. The 33 conversion lines observed are identified with 7 transitions of energies (in keV) and multipolarities 33.57 ± 0.03, M1; 40.93 ± 0.03, M1; 53.41 ± 0.03, M1; 59.03 ± 0.03, M3; 80.12 ± 0.03, M1; 99.95 ± 0.03, E2; and 133.53 ± 0.03, M1. The multipolarity assignment for each transition was obtained by comparing the observed conversion line intensity ratios with the theoretical line intensity ratios of Sliv. The intensity of the K conversion line of the 133.53 keV transition has been measured relative to the total intensity of the Pr^{144} β spectrum; $I_{K\,133}/I_{Pr\,\beta\,sp.} = 0.053\pm0.002$. The momentum ratio of the Ce^{144} K 133.53 and Cs^{137} K 661.6 lines, corrected for electron energy loss in the Ce course, is $B\rho_{K\,133}/B\rho_{K\,661} = 0.31495\pm0.00003$. Intensity limits are placed on all previously reported Ce^{144} conversion lines not presently observed. Relative quantum intensities and total transition intensities are deduced from the conversion line data. A decay scheme for Ce^{144} is given which satisfactorily accounts for all the results of this investigation and is compatible with the results of earlier workers when some line reassignments are made. Interpretations of the Pr^{144} levels, established in this work, are discussed in terms of both the shell model and the unified model. With $\delta \approx +0.07$, the unified model accounts for the experimental evidence in a simple but convincing fashion.

1. Introduction

Ce^{144} is one of the few readily available β emitters which feed levels in an odd-odd nucleus and which can be conveniently studied by magnetic spectrometer techniques. Numerous studies have been made of the Ce^{144} decay and all experimenters have agreed on the existence of two strong γ transitions which de-excite states in Pr^{144} at 80 and 133 keV. Because of the low energies of the Pr^{144} γ transitions, conversion electron studies have provided most of the present knowledge about them. In most of the investigations to date the momentum resolutions have been insufficient to resolve the L and higher subshell line-components. In some of the studies photographic recording was used and in these cases it was difficult to deduce reliable conversion-line intensity-ratios. In consequence several uncertain transition-assignments have been made and the multipolarities assigned to all but the 133 keV transition have been speculative.

In the present work the Ce^{144} conversion electron spectrum was studied at a momentum resolution of 0.1 % which was adequate to resolve all L and most M subshell lines. The energies of the seven transitions observed have been determined with an absolute uncertainty of < 50 eV. The transition multipolarities

have been established unambiguously by comparing the measured intensities of the L and M subshell conversion lines with the theoretical conversion coefficients of Sliv and of Rose. A decay scheme is proposed on the basis of the deduced transition energies, multipolarities and intensities which neatly accounts for all of our experimental results. Careful searches were made for conversion lines from all transitions which had been reported by earlier workers.

2. Source Preparation

The fission product Cerium used in this investigation was obtained from the Radiochemical Centre, Amersham, and had a specific activity of $\approx 7\ \mu c/\mu g$. "Line" sources 1cm × 2 mm wide were prepared by subliming in vacuo the activity from a tantalum filament at 2000°C through a 2 mm wide slit onto 800 $\mu g/cm^2$ Al foil backing. This source backing was supported by a $1\frac{3}{16}$" O.D. by $1\frac{1}{16}$" I.D. by $\frac{1}{16}$" thick brass ring. The two sources used had initial strengths of $\approx 30\ \mu c$ and $\approx 200\ \mu c$ and respective surface densities of ≈ 15 and 100 $\mu g/cm^2$. As will be discussed below the surface density of the stronger source was large enough to give rise to straggling in the source which broadened the conversion lines noticeably. The specific activity of the fission product Cerium therefore limited the usable spectrometer resolution in this investigation to $\approx 0.1\ \%$.

3. Experimental Apparatus and Procedure

This study of the Ce^{144} conversion electron spectrum was carried out using the Chalk River precision, air-cored, $\pi\sqrt{2}\beta$ spectrometer. Brief descriptions of this 1 meter radius spectrometer have already been given [1,2,3] and a complete account is in preparation [4]). The shaped magnetic field is created by three pairs of coils following the theoretical design of Lee-Whiting [5]). This instrument is designed to have a resolution of from 0.01 % to 1 % full line width at half maximum depending on the transmission aperture which can be adjusted from 0.1 % to 1.0 % of 4π steradians. For most of the investigations described here a transmission of $\approx 0.3\ \%$ was used which, together with a 2 mm wide source and a 3 mm wide counter defining slit, gave a resolution of $\approx 0.09\ \%$ in momentum. In a few of the later studies the transmission was increased to $\approx 0.5\ \%$ and the counter slit to 5 mm to give higher counting rates on the β continuum. Under these conditions the momentum resolution was $\approx 0.2\ \%$. It was not practical to operate at better than $\approx 0.09\ \%$ resolution because of the specific activity of the source material; fortunately improved resolution was not required to resolve any closely spaced line groups.

The detector used in these experiments was a continuous flow proportional counter which had a plateau of ≈ 500 volts with a slope of $\approx 0.4\ \%$ per 100 volts. This counter, A.E.C.L. type FB-2, was designed by I. L. Fowler of

the counter development group and was adapted by him for use with the $\pi\sqrt{2}$ spectrometer. The β-rays entered it through a 1" dia. end window of ≈ 1 mg/cm² Mylar film which was coated on its inner surface with a thin layer of "Aquadag" colloidal graphite to prevent charging. A simple grid of four stiff wires helped support the window against the atmospheric pressure of the methane filling.

In order to determine the counter window absorption correction, the continuous spectrum of a ≈ 1 mc source of Au^{198} plus Au^{199} was studied. The departure of the Fermi plot from the expected shape at low energies was used to estimate the transmission from cut off $T = 0$ % at ≈ 20 keV to $T \approx 40$ % at 26 keV. The method of estimating the absorption loss depends critically on the

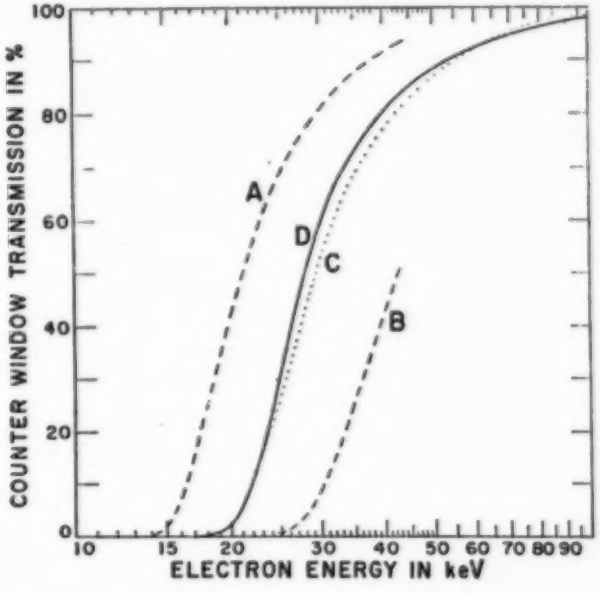

Fig. 1. The solid curve D gives the counter window electron transmission used in deducing the conversion line intensities listed in tables 1 and 2. This curve, for the 1.07 mg/cm² Mylar window, was obtained in part by an extrapolation of the plastic film data of Lane and Zaffarano as described in the text. Dashed lines A and B are Lane and Zaffarano's experimental transmissions for a 0.63 mg/cm² aluminized Formvar film and a 1.57 mg/cm² aluminium foil respectively. The dotted curve C gives the window transmission assumed in an earlier publication from this laboratory. It is essentially an interpolation between the dashed curves A and B. The reasons for using curve D are discussed in the text.

particular extrapolated shape assumed in the Fermi plot. It becomes increasingly difficult to assess absorption losses at higher energies where $T \to 100$ % since the Au spectrum shape is complex. For this reason we have computed the shape of the transmission curve for $T > 40$ % using the experimental data of Lane and Zaffarano [6]) for electron absorption in aluminium coated Formvar films of 0.1 mg/cm², 0.39 mg/cm², and 0.63 mg/cm². Log log plots were made of electron energy vs film surface density for various transmission efficiencies, e.g. $T = 20$ %, 30 %, etc. The points for constant T lie on straight lines with

slopes similar to that of the electron range energy curve ($T = 0$) in aluminium [7]). These lines were extrapolated to 1.07 mg/cm^2 where they match the results deduced from the $Au^{198-199}$ Fermi plot for $T \leqq 40$ %. The intercepts for $T > 40\%$ were used to construct the remainder of the curve shown in fig. 1. This correction curve when applied to the $Au^{198-199}$ spectrum gives a Fermi plot which is consistent with that expected for constant counter efficiency. In an earlier work [3]) a transmission curve (curve C in fig. 1) was deduced by interpolating between Lane and Zaffarano's results for the 0.63 mg/cm^2 plastic window and a 1.57 mg/cm^2 Al window. Since the extrapolated ranges of electrons in plastic and aluminium are different we feel that the curve of fig. 1 used here gives a more accurate estimate of the true window transmission efficiency; nevertheless it is a computed curve whose validity is not known with high accuracy.

The focussed electrons entering the counter passed between rectangular edged 1 mm thick brass plates which defined the counter aperture. The slit was 25 mm high × 3.0 mm wide for the experiments at 0.09 % resolution and 25 mm high × 5.0 mm wide for the later experiments at 0.2 % resolution. During these experiments in which the conversion line intensities were normalized to the energetic ($E_0 = 3$ MeV)Pr^{144} β spectrum, penetration of the 1 mm thick slit edges became apparent for electron energies above ≈ 2 MeV. The thickness was then increased to 3 mm and the edges shaped to minimize penetration through the sharp corners. Comparison of the Pr^{144} β spectrum shape obtained after this modification with that obtained in a different instrument in this laboratory [8]) and in other laboratories [9]) shows that intensity errors due to edge penetration were then negligible for energetic β rays.

Some difficulty has been experienced in determining the background counting rate to be subtracted from the experimental data despite the 2" Pb shielding around the counter. A fluctuating contribution to the counter background arises from the penetrating 1.4 MeV γ rays of A^{41} which is created by neutron activation of the cooling air which flows through the NRX and NRU reactors and is ventilated to the atmosphere. The effect of A^{41} γ rays on the counter background counting rate depends upon atmospheric conditions. As a result the A^{41} γ ray contribution to the detector counting rate is sometimes appreciable for periods of hours and quite erratic. The total counting rate on the β continuum was typically 100 counts per minute including the normal counter background rate of ≈ 30 counts per minute. In some runs the additional A^{41} background, varying from 0 to ≈ 40 c.p.min., was the most important factor to be considered in assigning line intensity errors. To aid in the selection of reliable data a Geiger counter was placed near the detector to monitor the γ ray background and the resulting counting-rate-meter signal was applied to a pen recorder with a time calibrated chart.

The spectrometer current stabilizer maintains any preselected current with a long term precision of ≈ 1 part in 10^5. The spectrometer coils are all connected

in series and the current is derived from a 600 Volt 50 Ampere D.C. generator. The coil current passes through one of a set of precision resistors and a bank of series tubes which provides the high frequency control of the current in the regulator system. The current regulator control signal is derived from a high gain D.C. chopper amplifier which compares the RI drop across the standard resistor with a reference potential. The output signal is applied both to the series tubes and a generator field control and seeks to make the input signals equal. The preselected reference potentials for these experiments were created by a stepping potentiometer which could be programmed to give up to 1000 equally spaced reference voltages in sequence. The minimum or starting voltage and the size of the voltage increments could be adjusted independently to any desired values in the range 0—1 Volt and 0—1 milli Volt respectively. With this stepping reference potentiometer in operation the current settings were checked before and after each run by measuring the RI drop across the standard resistor using an independent potentiometer and galvanometer. In the initial work a Leeds and Northrup type K2 potentiometer was used. Since the accuracy desired in these measurements was near the limit of linearity claimed by the manufacturer for this potentiometer, the linearity of its slidewire was in turn checked using a Rubicon potentiometer and found to be within the manufacturer's specifications. A much more accurate potentiometer, a Tinsley type 6343D, became available during the later stages of this investigation and was used in the final precision comparison of the momenta of a few of the intense Ce^{144} conversion lines with that of the K line of the 661.6 keV transition in Ba^{137}.

All the data for this paper were obtained using automatic operation of the spectrometer, usually on a 24-hour day, 7-day week basis. At the end of each counting period, usually one minute, the index number of the stepping reference potentiometer was typed out followed by the counts accumulated in the detector scaler (up to 10^6). The stepping potentiometer was then advanced to the next setting, the scaler cleared and counting restarted; the read-out cycle required about 2 seconds. The stepping potentiometer could be programmed to recommence the sequence of current settings after any desired decade of increments, e.g. at position 80, 90, 100, 110, etc.; this feature proved valuable in searching for weak lines when it was important to accumulate counts for good statistics and also check for any possible inconsistencies between successive runs which might have led to false line assignments.

The accuracy of electron momentum measurements depends critically on the accuracy with which the earth's field can be compensated. For this reason the spectrometer is located in its own specially constructed building. Two large sets of degaussing coils are used to cancel the vertical and the north-south components of the earth's field. The currents for these two systems were each electronically regulated to preset values within 1 part in 10^4. These values were readjusted

periodically to give cancellation of the earth's magnetic field at one point on the spectrometer orbit to $< 2\times10^{-4}$ G. A Serson type fluxgate magnetometer[10]) was used as the null detector in making these adjustments. The normal short term fluctuations in the earth's magnetic field introduce a typical uncertainty of $\pm 50\times10^{-5}$ G in the spectrometer field. A subsequent examination of the magnetic records from the Dominion Observatory Agincourt magnetometer station revealed that the data reported in this paper were accumulated during periods which were free from magnetic storms.

This Ce^{144} study was initiated with a survey scan of the conversion electron spectrum in the energy range 20—150 keV. The source strength, momentum resolution, and counting interval used in this preliminary survey were 30 μc, 0.09 % and 1 minute respectively. This was followed up with repetitive detailed scans of 1) the various line groups observed in the survey, 2) line groups previously reported and 3) line groups predicted by our proposed decay scheme. In some of these latter studies improved counting statistics were obtained through the use of the 200 μc source.

4. Treatment of the Data

4.1. LINE INTENSITIES

A typical sample of the data taken during this investigation is displayed in fig. 2. Both parts of this figure were taken with the thin 30 μc source. The upper part displays the conversion lines from the intense 133.53 keV transition. The left group in the lower section show the three L lines of the 59.03 keV transition.

The intensities deduced for the conversion lines are their areas on an N/p vs p plot where N is the counting rate. For lines which had no near neighbours the area was determined by summing the total counts, which were taken at equally spaced momentum intervals, over the region of the conversion line in question. From this was subtracted the contribution due to background and β continuum which was calculated by interpolating between the counts observed above and below the region of the line. The net difference multiplied by the momentum increment used in the scan and divided by the momentum assigned to the line gives the required "area" figure together with a statistical error. It was found that when the intense K 133.53 line was scanned on different dates the decay corrected "line area" values showed a scatter of up to 2 % even though the statistically deduced error was $\approx$ 0.5 %. An unpredictable source of error arose from background fluctuations, at certain periods, due to the A^{41} γ rays discussed in the preceding section.

In deducing the areas of partially resolved lines we have found it convenient to subtract the background and β continuum rates and plot the log of the net "line" counts vs momentum as described elsewhere [3]). Line shapes determined

from clearly resolved lines of comparable energy and appropriate to the conversion shells in question are fitted to the data in this form. All closely spaced lines, except K lines, were assumed to have the same shape. This shape narrows quite gradually with increasing momentum; the contribution from energy degradation being less serious at high energies. The total area of the partially resolved line groups was apportioned according to the relative intensities deduced in this semi-log-plot analysis procedure. Since this procedure is necessarily a somewhat subjective one we have made allowance in the assigned intensity errors for the possibility of assuming incorrect low energy tail shapes. As a check for arithmetical errors in our line area determinations we made a

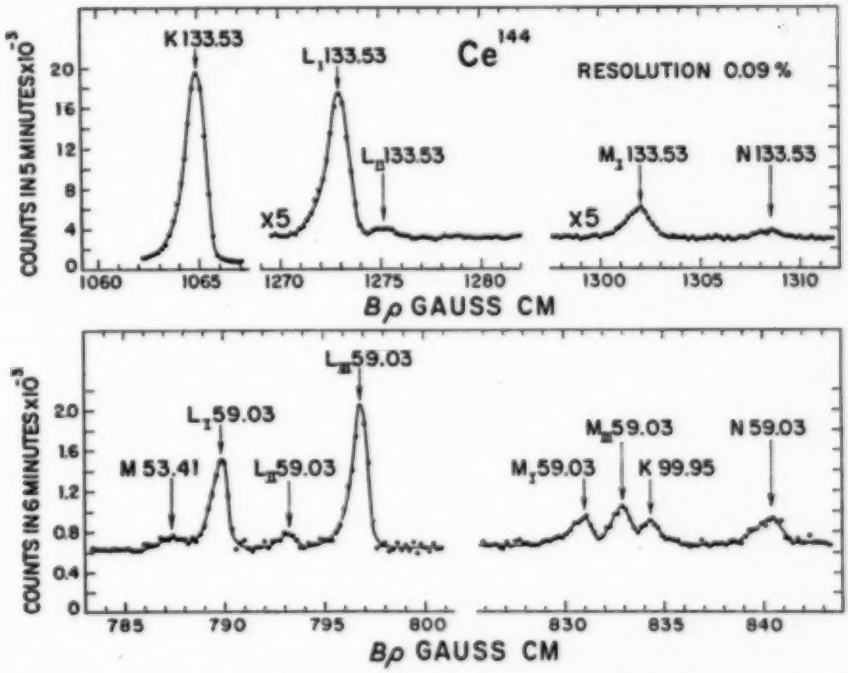

Fig. 2. The upper portion of the figure shows the K, L_I, L_{II}, M_I and N conversion lines of the 133.53 keV M1 transition. The lower half of this figure shows the L_I, L_{II}, L_{III}, M_I, M_{III} and N conversion lines of the 59.03 keV M3 transition, the M line of the 53.41 keV transition and the K line of the 99.95 keV E2 transition. Conversion of the 59.03 keV transition in the M_{IV} and M_V shells accounts for $\approx$ 10 % of the intensity of this latter peak. The $L_I : L_{II} : L_{III}$ ratio for the 59.03 keV transition is characteristic of its M3 multipolarity. The data presented in this figure were obtained with the 30 μc 1 cm $\times$ 2 mm Ce^{144} source and a counter slit width of 3 mm.

plot of the conversion line peak height to line area ratio as a function of energy, the ratio being a sentitive function of line broadening. A smooth rising curve can be passed through all the points except those for the three K lines which lie 5 to 20 % low because of their greater natural width.

The line intensities deduced in this work are summarized in table 1. The intensity errors assigned may be considered to represent standard deviations. They were calculated by combining in quadrature the standard deviations resulting from arithmetic procedures multiplied by a factor of 1.5 to take ac-

TABLE 1

Conversion Lines in Pr^{144}

Present Work				Earlier Work								
E (keV)	Intensity †	Assignment		(a) E	(b) E	(c) E	(d) E	(e) E	(e) Int †	(f) E	(g) Int †	(h)
–	–	K	53.41		11.7							
–	–	K	59.03		17.3		16.7	16.8	4			
26.73	14.8 ±1.2	L_I	33.57	26.8	27.2		26.9	27.0	11	26.6	23 ±9	Line
27.12	0.94±0.72	L_{II}	33.57									
–	<0.7	L_{III}	33.57									
32.06	2.70±0.22	M_I	33.57		32.5		32.0	32.5	4	31.7	<4.4	Line
33.26	0.5 ±0.5	N	33.57									
34.10	12.9 ±1.5	L_I	40.93	34.2	34.5			34.2	11	34.0	28 ±9	Line
34.48	1.1 ±0.4	L_{II}	40.93									
–	<0.5	L_{III}	40.93									
38.12	62.9 ±1.9	K	80.12	38.2	38.8	37.5	38.7	38.5	49	38.1	57 ±4	Line
39.41	2.73±0.38	M_I	40.93		40.0			39.6	≈1	39.3		Line
39.58	0.4 ±0.4	M_{II}	40.93									
40.63	0.56±0.28	N	40.93									
46.57	1.90±0.19	L_I	53.41	46.1	47.0	48.3	46.6	46.6	3	46.4	0.9±0.4	Line
46.93	0.15±0.10	L_{II}	53.41									
–	<0.1	L_{III}	53.41									
51.89	0.46±0.18	M_I	53.41									
52.19	4.16±0.26	L_I	59.03	52.8††	53.0††		53.1	52.7††	7	52.2		
52.59	0.73±0.18	L_{II}	59.03									
53.06	6.42±0.28	L_{III}	59.03		53.8			53.3	4	53.0††	9.3±1.6	Line
57.51	1.21±0.10	M_I	59.03									
57.77	1.74±0.13	M_{III}	59.03									
57.95	1.09±0.10	K	99.95	57.6	58.5		58.0			57.6	4.4±0.8	Line
–		$M_{IV, V}$	59.03									

—	<0.07	$L_{II, III}$	74.50									
73.30	7.81±0.32	L_I	80.12	73.5	74.1	72.8	74.1	74.0	9	73.1	10 ±0.8	Line
73.68	0.52±0.21	L_{II}	80.12							73.9		
—	<0.2	L_{III}	80.12									
78.59	1.73±0.64	M_I	80.12	78.8	79.4		79.2	79.2	≈1	78.4	0.9±0.3	Line
79.81	0.56±0.19	N	80.12		80.6							
—	<0.25	L	95							88.2		
91.53	100 ±2	K	133.53	92.0	92.4	92.1	92.2	92.2	100	91.6	100 ±4.4	Line
93.11	0.12±0.05	L_I	99.95									
93.48	0.22±0.05	L_{II}	99.95				93.8					
94.00	0.23±0.05	L_{III}	99.95									
—	<0.4	M	99.95				98.6	99.0	1			
—	<0.1	K	145.2							103.2		
126.69	12.8 ±0.4	L_I	133.53	127.1	127.8	127.1	127.3	127.8	12	126.7	14 ±2	Line
127.09	0.95±0.05	L_{II}	133.53									
127.58	0.23±0.06	L_{III}	133.53									
132.02	2.94±0.20	M_I	133.53	132.5	133.0		133.0	133.1	≦3	131.9	4 ±0.8	Line
133.21	0.62±0.13	N	133.53		134.1							
—	<1.0	L	145.4							138.6	<0.2	
—	<1.0	M	145.3							143.7	<0.2	
—	<0.06	K	230			188.0						
—	<0.09	L	230			233						

† Normalized to $I_{K\,133.53} \equiv 100$. The assumed counter window correction for present work is shown in fig.1.

†† Identified as K 95, see text

(a) Emmerich, John and Kurbatov, Phys. Rev. **82** (1951) 968
(b) Keller and Cork, Phys. Rev. **84** (1951) 1079
(c) Lin-Shing, John and Kurbatov, Phys. Rev. **85** (1952) 487
(d) Porter and Cook, Phys. Rev. **87** (1952) 464
(e) Emmerich, Auth and Kurbatov, Phys. Rev. **94** (1954) 110
(f) Cork, Brice and Schmid, Phys. Rev. **96** (1954) 1295
(g) Pullman and Axel, Phys. Rev. **102** (1956) 1366
(h) Parfanova, Forafontov and Slipinel, Izvestiia Akademii Nauk. S.S.S.R. **21** (1957) 1601

count of the non-statistical background uncertainty, together with the fixed figure of 2% which takes into account lack of reproducibility. The small errors assigned to some of the weak lines result from an intensive study of this particular portion of the spectrum with the stronger source. The intensity figure deduced from each observed line area has been corrected for counter window absorption before listing it in table 1. The intensity errors have not been increased to allow for any uncertainty in window absorption. This additional uncertainty is not important for the relative values of closely grouped lines but should be taken into account when comparing low and high energy line intensities.

4.2. LINE MOMENTA

The line shape we observe is asymmetrical with a low energy tail partly because of the focussing properties of the spectrometer and partly because of energy degradation in the finite surface density of the source deposit. The former is a constant of the instrument and independent of the electron momentum. The most obvious effect of energy degradation in the source in these studies was an increase in and an extension of the low energy tails of the lines. While natural width broadening [11, 1]) of the L and M subshell conversion lines was too small to be detected in these studies, the K lines showed a greater breadth consistent with a natural width of ≈ 21 eV for the K shell vacancy.

The momentum setting for each conversion line has been deduced from the centre of the top of the peak rather than from the peak centroid or from a linear extrapolation of the high energy side of the peak down to the continuum. This empirical procedure for determining line peak positions is nearly independent of natural width effects and appears to be relatively insensitive to energy degradation in the source. The mid-point of the line is determined at several heights and a line passing through these mid-points is extrapolated up to the top of the line and this point of intersection is taken as the momentum setting assigned to the line. The difference in the top-line-centre positions of the 91.53 keV K conversion lines from the thick and thin Ce^{144} sources, taken under identical experimental conditions is ≈ 30 eV while the difference in the centroid positions of these same two lines is ≈ 80 eV.

5. Spectrometer Calibration

The momentum calibration of the spectrometer for the baffle and counter slit settings used in the initial experiments [15]) was done by removing the Ce^{144} source and substituting a similar source of Cs^{137}. The conversion line used was Cs^{137} K 661.6 with $B\rho = 3381.09 \pm 0.20$ G · cm †. This calibration, applied to

† This momentum value was obtained by comparing the K 661.6 line in Ba^{137} with seven conversion lines of γ 411.770±0.036 in Hg^{198} at a resolution of 0.015 % with the Chalk River precision beta-ray spectrometer. It is in good agreement with the value of 3381.11±0.5 G · cm deduced from the curved crystal γ energy measurement of Muller *et al.* [13]) of 661.60±0.14 keV and the Ba K binding energy of 37.432 keV due to Cauchois [12]). It is to be compared with the value of 3381.3±0.4 G · cm cited by Wapstra *et al.* [14]).

both the thick and thin source data, led directly to the transition energies given in the preliminary report of this work [15]). The "top-line-centre" method used in determining the "peak positions" is discussed above in section 4.2. One source of uncertainty in the calibration procedure used here results from the limited accuracy with which sources can be positioned. They were aligned visually with respect to millimeter scales on a dowelled plastic positioning plate, with an estimated reproducibility of $\leqq 0.5$ mm depending on the visibility of the source deposit. This amount of misalignment gives rise to a momentum calibration error of $\leqq 1$ part in 8000. In addition there is a typical $B\rho$ uncertainty of $\lesssim 0.05$ G · cm due to fluctuations of the earth's field between null adjustments of the degaussing system.

A subsequent comparison of the experimental K-L energy differences (determined from the K and L conversion lines of the 80.12, 99.95 and 133.53 keV transitions) with the Pr $K\alpha_1$ and $K\alpha_2$ X-ray energies recently measured by Bergvall [16]) revealed discrepancies of up to 40 eV. Reexamination of both thick and thin source data revealed discrepancies which could be attributed to energy degradation in the thick source. In view of these inconsistencies in our early analysis we carried out a further more elaborate calibration procedure. Since the thin 30 μc Ce source was barely visible and since the activity is not necessarily uniformly distributed over the visible region of either source we decided against further attempts at positioning the sources with respect to the scales on the positioning plate. Instead, the source mount plate was fixed in position. The 1.085" O.D. source rings fit into it with a diametral clearance of 0.006". The K 133.53 keV line from both thick and thin Ce^{144} sources and the Cs K 661.6 keV line were scanned with the 1 cm $\times$ 2 mm wide sources first "up" and then with the sources "down" (the source ring rotated through 180°). The peak position for each line was taken as the average of that observed for the source "up" and the source "down", the two differing typically by 0.11 G · cm. During these scans the RI drop across the standard resistor was monitored manually to the nearest microvolt, i.e. < 2 parts per million, at each momentum setting near the line peak, the voltage increments being 100 μV. As a further precautionary measure a magnetometer probe situated in a small field free region at the centre of the spectrometer † continuously recorded variations in the vertical component of the earth's magnetic field during these runs. Variations in this degaussed vertical component did not exceed 2×10^{-4} G during these runs.

We at present lack a detailed knowledge of the residual earth's field at each point on the spectrometer orbit. The point chosen for setting the field null is for

† Cancellation of the spectrometer field at its centre is achieved through a modification of the original three coil pair design [5]). A fourth pair of "tiny" coils (diameter 11 inches) is connected in series with the three pairs of coils providing the electron focussing field and cancels their field over a spherical volume of ≈ 8 cubic inches.

practical reasons outside the vacuum chamber. A preliminary survey along the top of the vacuum chamber indicates that residual fields do not exceed 5×10^{-4} G along the electron orbits.

The observed momentum ratios for the Ce K 133.53 and the Cs K 661.6 keV lines are for the thin source $B\rho_{K\,133}/B\rho_{K\,661} = 0.31494\pm0.00003$ and for the thick source $B\rho_{K\,133}/B\rho_{K\,661} = 0.31488\pm0.00003$. Here we have taken the top-line-centre values as defining the line momentum (see discussion in section 4.2). The error assigned to these momentum ratios makes allowance for the uncertainty in the top-line-centre position, a 0.005 inch uncertainty in source position, and an uncertainty in the degaussing of the vertical component of the earth's field.

The difference in the above momentum ratios for the thick and thin sources indicates top-line-centre shift due to an excess energy loss in the thick source of 32 eV. A similar comparison of the Ce^{144} K 80.12 line from the two sources showed a top-line-centre shift of 27 eV. A comparison of the thin source Ce K line shape with that of the appropriately scaled Cs K line indicates that the momentum shift of the Cs K line due to energy loss in the source is considerably smaller than that for the Ce lines. In view of the nearly constant energy shift of the Ce lines arising from source thickness and since the source strengths, and presumably also the source thickness, are in the ratio 6.5 : 1 we have added 5 eV to all our thin source line energies. The corrected momentum ratio for the Ce K 133.53 and the Cs K 661.6 keV lines is

$$\frac{B\rho_{K\,133.53}}{B\rho_{K\,661.6}} = 0.31495\pm0.00003.$$

In order to correct our earlier data as dictated by this more accurate calibration, the momenta of the L_I 33.57, L_I 40.93, L_I 59.03, L_{III} 59.03, K 80.12 and the L 133.53 lines were determined relative to that of the K 133.53 line for the "up" position of the thin source under the well monitored conditions described above. Our earlier data were then used to provide the momentum differences within the various line groups.

6. Experimental Results

The energies, intensities and assignments of the conversion lines observed in this work are summarized in table 1. The energies of the recalibrated L_I 33.57, L_I 40.93, L_{III} 59.03, K 80.12, K 133.53 and L_I 133.53 lines are believed to have absolute uncertainties of $\leqq$ 30 eV; this uncertainty resulting from 1) a possible calibration error of 1 part in 10^4 in momentum (5—15 eV) arising from source position and degaussing uncertainties (see section 5), 2) uncertainty in top-line-centre position for these lines corresponding to $\approx$ 10 eV, and 3) a possible error in the source thickness correction of $\approx$ 5 eV (see section 5). The energies of all other lines are believed to be accurate to within 50 eV.

The sources of intensity errors are fully discussed in section 4.1. Again it should be emphasized that these do not include allowance for an uncertainty in the counter window correction. Only the 57.95 keV line has a double assignment. The small contribution expected from the M_{IV} and M_V lines of γ 59.03 has been estimated after multipolarity assignment using Rose's tabulated M shell conversion coefficients [17]) to give relative M3, M shell intensities. This leaves $\approx$ 90 % of the observed intensity attributable to K 99.95.

The intensity scale in column 2 has been arbitrarily normalized to K 133.53 $\equiv$ 100, since relative line intensities can be determined more accurately than absolute intensities. To establish the absolute scale, the K 133.53 line and the high energy β spectrum of the daughter nucleide Pr^{144} which is in equilibrium with the Ce^{144} decay were scanned at 0.2 % resolution using the stronger source in order to improve the counting statistics. After the modification to the counter slits discussed above in section 3 we obtained a ratio of K 133.53/Pr^{144} β spectrum = 0.053 ± 0.002 which is in agreement with the earlier experimental value of 0.052 made in this laboratory using a double lens spectrometer at 2 % resolution [8]) and also with the ratio of 0.053 deduced from the results of Porter and Cook [18]).

The transition energies and atomic shell assignments for the 33 observed conversion lines were deduced using the tabulated binding energies of Cauchois [13]). The seven transition energies so deduced together with their total intensities led to the level scheme shown in fig. 4 and discussed in the next section.

The transition energies presented here are higher than the preliminary values [15]) by 40 to 90 eV. The present values are the result of more elaborate calibration procedures (section 5) and include allowance for source thickness effects (see section 4). We have not listed the Auger lines identified in this investigation.

In columns (a) to (h) in table 1 we summarize the results of other experimenters for comparison with our data. The L line group of the 59.03 keV transition at $\approx$ 52 keV was taken as evidence for a K 95 line by some earlier workers. The limit set in the present work on the L 95 lines rules out this possibility even though Cork *et al.* [19]) report evidence for it. No evidence was found in the present work for the K, L and M lines of a 145.3 keV transition reported by Cork *et al.* [19]) and it may be concluded that these lines arose from 32d Ce^{141} impurity in their source for which a 145 keV γ-ray transition has been reported [20]). There is no evidence for the transition of $\approx$ 231 keV reported by Lin-Shing *et al.* [21]).

7. Discussion

7.1. MULTIPOLARITIES

For convenience in analysing for transition multipolarities we have reorganized our experimental conversion line intensity values in table 2. The multi-

TABLE 2

Relative Transition Intensities in Pr^{144}

E_γ (keV)	K	L_I	L_{II}	L_{III}	M_I	M_{II}	M_{III}	N	Quanta †	Total †	Multipolarity
33.57	–	14.8	0.9	<0.7	2.7	–	–	0.5	4.3	23.3	M1
40.93	–	12.9	1.1	<0.5	2.7	0.4	–	0.6	6.7	24.4	M1
53.41	(14.9) †	1.9	0.15	<0.1	0.5	–	–	–	2.4	19.9	M1
59.03	(8.3) †	4.2	0.7	6.4	1.2	–	1.7	0.7	0.02	23.2	M3
80.12	62.9	7.8	0.5	<0.2	1.7	–	–	0.6	30	103.5	M1
99.95	0.98	0.12	0.22	0.23	–	–	–	–	0.79	2.4	E2
133.53	100	12.8	0.95	0.23	2.9	–	–	0.6	204	322	M1

† Intensity values deduced assuming multipolarities listed and using theoretical coefficients of Sliv [22]).

polarity assignments have been deduced mainly by comparing the experimental L subshell ratios with the theoretical $Z = 59$ ratios deduced from Sliv's tabulations [22]). One set of comparisons, i.e. the L_I/L_{III} ratios, are shown graphically in fig. 3. This ratio provides a sensitive monitor for an E2 admixture in an M1 transition and fig. 3 shows clearly that five of the transitions are pure M1 with less than 1 % E2 admixture. The other conversion ratios for these transitions, e.g. K/L, are also consistent with pure M1. One transition, that at 59.03 keV has an L_I/L_{III} ratio characteristic of a pure M3 transition. The ratio which clearly identifies its multipolarity is the experimental L_{II}/L_{III} ratio of

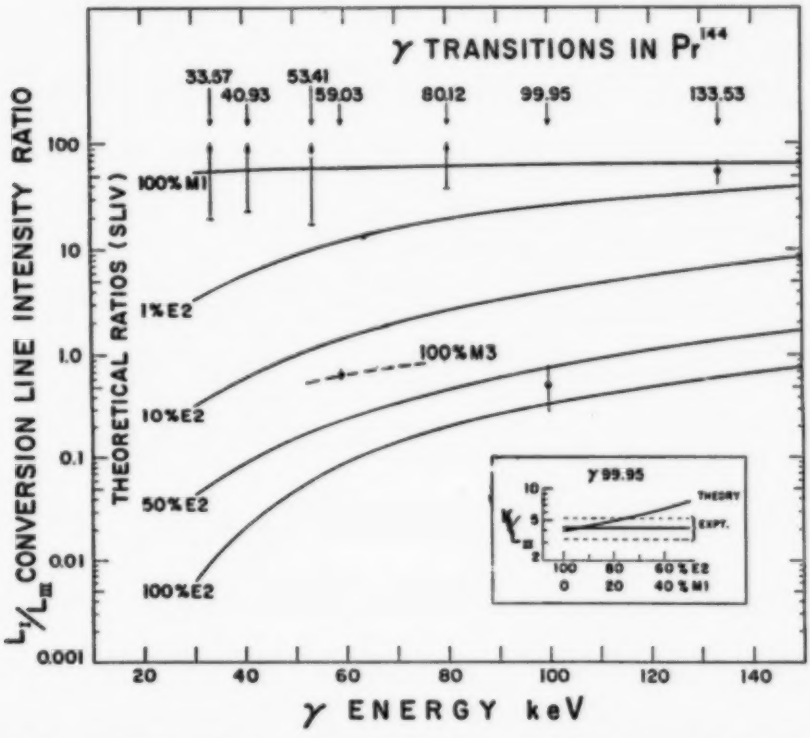

Fig. 3. The L_I/L_{III} conversion-electron line intensity ratio provides a sensitive measure of the E2 admixture in predominantly M1 transitions. It is clear from this figure that the 33.57, 40.93, 53.41, 80.12 and 133.53 keV transitions are > 99 % M1. The experimental L_I/L_{III} line intensity for the 59.03 keV transition is in good agreement with the theoretical prediction of Sliv for this M3 transition. The L_I/L_{III} ratio for the 99.95 keV transition admits the possibility of appreciable M1 admixtures. These L lines are very weak and are not entirely clear of an increased background contribution from the nearby very intense K line of the 133.53 keV transition. The K/L_{III} ratio for this transition plotted in the inset shows that this transition is $\gtrsim$ 75 % E2. Both the L_I/L_{III} and K/L_{III} ratios are entirely consistent with the pure E2 character required by the decay scheme of fig. 4.

0.11 ± 0.03 which is inconsistent with any possible M1 and E2 admixture (theoretical ratios of 4.9 to 0.8) but in excellent agreement with the theoretical M3 ratio of 0.10. Further evidence favouring the M3 assignment is the prominent M_{III} conversion line shown in fig. 2. It is interesting to note that the prominence of the L_{III} 59.03 line led some experimenters to identify it as a K

line of a 95 keV transition. An E2 character for the 99.95 keV γ transition is indicated by its L_I/L_{III} and K/L_{III} intensity ratios. The L conversion lines of this transition are very weak and their proximity to the intense K line of the 133.53 keV transition results in a large background uncertainty. While the observations are consistent with a pure E2 character for this transition it is not possible to exclude an M1 admixture of up to ≈ 25 %.

7.2. TRANSITION INTENSITIES

The quantum intensities listed in table 2 and those of the two K conversion lines not observed in this work have been deduced assuming the pure multipolarity assignments listed and the theoretical conversion coefficients of Sliv[22]). The value so obtained for the K 59.03 line is higher than that reported by Emmerich *et al.* [23]), see column (e) of table 1. The discrepancy is probably due to the inherent inaccuracy of densitometer techniques used by these workers to determine relative line intensities; their low energy lines are consistently less intense than the corresponding counter results of the present work. The latter do, however, have an uncertainty due to the counter window absorption. The most sensitive test we can make here on the validity of the curve used in this connection, see fig. 1, is to compare the experimental K/L_I ratios for pure M1 transitions with the theoretically expected ratio of 7.83 from Sliv's conversion coefficients which is energy independent. For the 80.12 keV transition we obtain $K/L_I = 8.05 \pm 0.40$ and for the 133.53 transition $K/L_I = 7.74 \pm 0.29$. The total transition intensities are also listed in table 2 and must be multiplied by the experimental ratio of 0.053 ± 0.002 (cf. section 6) to obtain absolute percentages per disintegration.

7.3. Pr^{144} LEVEL SCHEME

Fig. 4 shows the level scheme for Pr^{144} which accounts for all the experimental results of this investigation. One compelling feature resulting from the precision of the present work was the number of "coincidences" between sums and differences of transition energies. This led to the sequence shown in fig. 4. These "coincidences" together with the multipolarity determinations and intensities establish the sequence of levels in a most convincing fashion. In creating the level scheme shown in fig. 4 the ground state of Pr^{144} was assumed to be 0—. Strong evidence for this assignment comes from the β—γ angular correlation and coincidence β spectrum shape studies [8, 9]) of the Pr^{144} β decay and from the nuclear alignment studies of Grace *et al.* [24]). The assumption of a ground state of 0—, as shown in fig. 4, requires that the four transitions feeding the ground state be pure multipoles. The 99.95 keV E2 transition is the only one whose purity seems at all questionable; as noted above an admixture of up to 25 % M1 is consistent with the observed conversion line ratios.

The only possible alternative ground state spin and parity assignment for Pr^{144} is 1− [8]). The Pr^{144} conversion line measurements presented in this paper provide a further powerful argument for excluding this 1− possibility †. A number of Pr^{144} level sequences, based on a 1− ground state, can be proposed in which the spin differences account for the observed transition multipolarities. The large intensities of the 133.53 and 80.12 keV transitions require that these feed the ground state. Furthermore application of the Ritz combination principle, i.e. energy sum "coincidences", indicates that the following deexcitation paths are parallel: γ 99.95+γ 33.57 = γ133.53, γ 59.03+γ 40.93 = γ 99.95, and γ 80.12+γ 53.41 = γ 133.53. These restrictions limit one to four choices of level sequence. Two of these require that the 59.03 keV M3 transition compete favourably with an E2 transition of higher energy; a third requires that this M3 transition competes favourably with three M1 γ transitions including the intense γ 133.53. In each of these three cases the lower multipolarity transitions must be inhibited by a factor of $\approx 10^8$ and they are dismissed on this basis. The remaining possibility for the level sequence is that shown in fig. 4 with altered level spins, e.g. ground state 1−. A 3− assignment for the 59.03 level is rejected since one would then have an E2 M3 admixture in which the E2 contribution is hindered by a factor of $\approx 10^8$. The only plausible spin for the 59.03 keV level is 4−. From this it follows that the spin and parity of the 133.53 keV level are then 2− and hence that the β component feeding this level is first forbidden unique (0+ → 2−). All experimental evidence shows that this component has a log $f_0t \approx 7.2$. The value of log f_1t appropriate to this transition, including the statistical factor would then be ≈ 6.2. The minimum possible value for log f_1t may be estimated using the expression of Marshak [25]) for the lifetimes of forbidden unique β transitions. One may take the log f_0t for He^6 decay, log $f_0t \approx 3.3$, as a minimum for allowed GT transitions, i.e. maximum possible nuclear matrix element. Assuming an equal magnitude for the forbidden matrix element one obtains the limit log $f_1t \geqq 7.7$. Experimental values for log f_1t are grouped closely about 8.3, the smallest (Pr^{142}) being ≈ 7.8. We conclude therefore that the β component feeding the 133.53 keV level in Pr^{144}, (log $f_1t \approx 6.2$) cannot be a first forbidden unique transition, 0+ → 2−, and therefore that the ground state spin of Pr^{144} cannot be 1−. This new evidence when taken together with the earlier evidence [8, 9, 24]) provides a most convincing case for a 0− ground state assignment for Pr^{144}.

We note from fig. 4 that three M1 transitions de-excite the 1− level at 133.53 keV. Their relative reduced quantum transition probabilities, as deduced from table 2, are in the ratio γ 33.57 : γ 53.41 : γ 133.53 = 7 : 1 : 7. We have at present no information regarding absolute transition probabilities but attempt to account for the sevenfold relative hindrance of γ 53.41 in the following section.

† The authors wish to thank Dr. L. G. Elliott for bringing this argument to their attention.

Three additional γ transitions may be predicted from the proposed level scheme. Two of these at 19.83 and 21.09 keV were too low in energy to have been detected in this investigation. A search was made for the L conversion lines of a 74.50 keV E2 transition which would be expected to de-excite the 133.53 level in competition with the 133.53 keV M1 transition. The experimental limit of 0.07 units, see table 1, is consistent with the predicted intensity of $\approx$ 0.01 units deduced assuming γ 74.50 has a single particle E2 lifetime and that γ 133.53 is a single particle M1 transition with a typical hindrance factor of 50. The intensity limit does, however, suggest there is no marked enhancement of the E2 transition probability in this case.

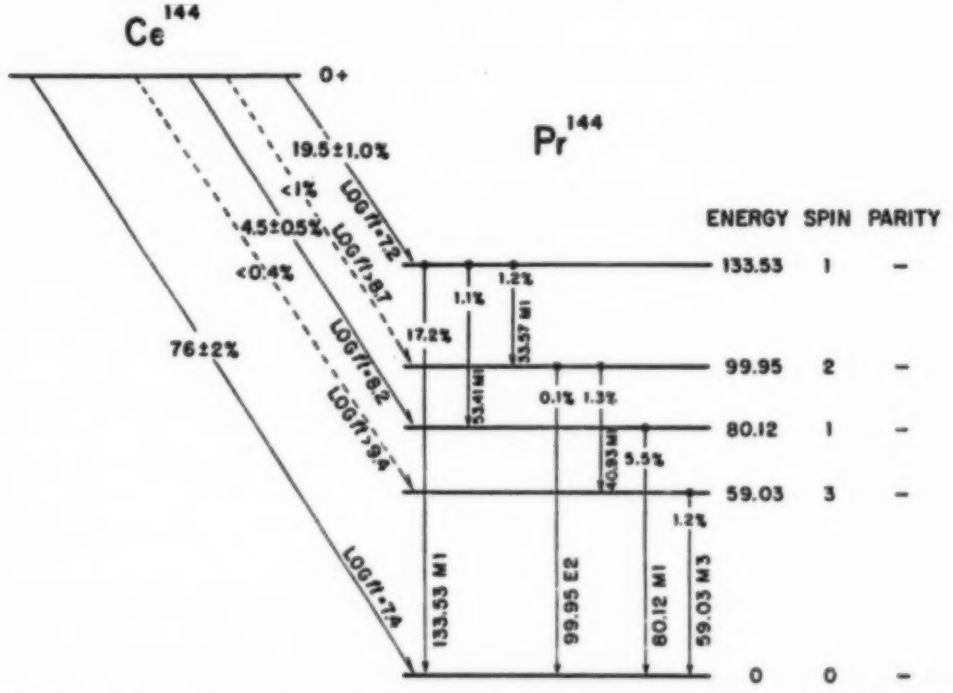

Fig. 4. This Pr^{144} level scheme accounts for all results obtained in this experimental investigation. The level sequence is based on "coincidences" between sums and differences of the precisely measured transition energies and on their multipolarities as established from line intensity ratios. These transition multipolarities together with the log $f_0 t$ of $\approx$ 7.2 for the β feed to the 133.53 keV level require that the ground state spin be 0− in agreement with the results of studies of the Pr^{144} decay scheme. The absolute transition intensities are obtained by combining the relative transition intensities of table 2 with a measure of the intensity of the K line of the 133.53 keV transition relative to that of the total β spectrum of Pr^{144}, the Ce^{144} and Pr^{144} decays being in equilibrium. The β feeds listed are those required by the Pr^{144} level scheme and are in reasonable agreement with the published experimental values.

The results of Ce^{144}-Pr^{144} β spectrum studies to date [20]) provide good evidence for the three spectrum components required on our proposed decay scheme. The most recent of these studies [26]) gives intensity figures of 61±9 %, 6±1 % and 26±4 % for the feeds to the ground state, the 80.12 keV state and the 133.53 keV state, respectively. Earlier workers [20]) favour a higher intensity for

the ground state component. Some authors suggest an additional low energy component ($E_{max} \approx 100$ keV), but qualify their claims by remarks on the back-scattering problem. Back-scattering is difficult to avoid because of the presence of the equally intense 3 MeV Pr^{144} β spectrum in equilibrium with the Ce^{144} decay. An analysis of the Ce^{144} β spectrum observed with the sources used in this work also shows components whose endpoints and relative intensities are in qualitative agreement with the intensities required by fig. 4. The effect of scattering in the spectrometer source region has yet to be investigated fully and we hope to report on this in a later publication.

8. Interpretation of Pr^{144} Level Spectrum

8.1. ON THE SHELL MODEL

The interpretation of the level spins and parities determined in this investigation provides an interesting test of the applicability of presently available nuclear models. Pr^{144} is an odd-odd nucleus with 59 protons and 85 neutrons. Since its neutron number is so close to the magic number 82 one would expect it to be a nearly spherical nucleus and that the shell model would account for at least the ground state spin and parity. The evidence from neighbouring odd-neutron nuclei is unambiguous in assigning the 85th neutron to an $f_{\frac{7}{2}}$ orbit. A shell model interpretation of the spins and parities of neighbouring odd-proton nuclei places the 59th proton in a $d_{\frac{5}{2}}$ orbit. The minimum spin for Pr^{144} on the single particle shell model is then 1−, whereas experiment indicates a 0− ground state spin and parity. A reassignment of the 59th proton to the $g_{\frac{7}{2}}$ orbital, as suggested by indirect evidence [27]) for a ground state spin of $\frac{7}{2}$ for Pr^{145}, leads to a 0− ground state spin. Such an assignment is inconsistent with the measured spin of $\frac{5}{2}$ for Pr^{141} and the deduced spins of $\frac{5}{2}$ for Pr^{139} and Pr^{143} ref. [27]). These do not indicate a departure from the accepted order of level filling. We conclude therefore that the single particle shell model fails to predict correctly the Pr^{144} ground state spin of 0 although a consistent interpretation is perhaps possible.

In a more comprehensive shell model interpretation of the Pr^{144} levels we consider the coupling of the one proton in the $d_{\frac{5}{2}}$ shell to the permitted configurations of the three neutrons in the $f_{\frac{7}{2}}$ shell rather than simply to a single unpaired $f_{\frac{7}{2}}$ neutron. The six configurations permitted for the three $f_{\frac{7}{2}}$ neutrons on the j-j coupling scheme are characterized by total spins $J_n = \frac{3}{2}, \frac{5}{2}, \frac{7}{2}, \frac{9}{2}, \frac{11}{2}$ and $\frac{15}{2}$ [28]). Theoretically, the assumption of short range nuclear forces between the three neutrons leads to a unique ground state neutron configuration with $J_n = j_n = \frac{7}{2}$. The assumption of longer range nuclear forces leads to a ground state configuration having $J_n < j_n$ [29]). Goldhaber and Sunyar [30]) cite Na^{23} and Mn^{55} as examples of three particle (hole) configurations for which the experimental $J < j_p$. Another pertinent example is $_{60}Nd^{147}$ with $N = 87$, which has

three holes in the $f_{\frac{7}{2}}$ shell and a measured ground state spin of $\frac{5}{2}$. In the case of Pr^{144}, if we accept the considerable experimental evidence for $j_p = \frac{5}{2}$, we clearly require $J_n = \frac{5}{2}$ as the ground state neutron configuration in order to account for the Pr^{144} 0− ground state. Other spin states resulting from the coupling of the $j = \frac{5}{2}$ proton with this $J_n = \frac{5}{2}$ neutron configuration are 1, 2, 3, 4 and 5. While the first three of these spins could account for three of the four excited levels in Pr^{144} there are several plausible alternative explanations of the spins of these excited levels. The systematics of neighbouring odd-mass nuclei suggest a low lying proton configuration with $J_p = \frac{7}{2}$ and a low lying neutron configuration with $J_n = \frac{7}{2}$. The three additional configuration pairs $j_p = \frac{5}{2}$, $J_n = \frac{7}{2}$; $J_p = \frac{7}{2}$, $J_n = \frac{5}{2}$ and $J_p = \frac{7}{2}$, $J_n = \frac{7}{2}$ give rise to levels with spins 0, 1, 2, 3 .... There is thus a multiplicity of theoretical configurations available for each of the observed Pr^{144} levels. There appears to be no easy method of removing this theoretical ambiguity without detailed calculations. Since the experimental work of this paper clearly establishes the assignments of the Pr^{144} levels it would be interesting to learn if a detailed many particle shell model calculation could provide a unique description.

8.2. ON THE UNIFIED MODEL

The unified model provides an alternative nuclear description which has proved highly successful in explaining the properties of odd-mass nuclei with large distortions ($\delta > 0.16$). Gallagher and Moszkowski [31]) have interpreted the measured spins of odd-odd nuclei throughout the periodic table in terms of this model, including nuclei in the regions of small deformation, $|\delta| < 0.16$. The spins and parities of the excited states of Pr^{144} established in the present investigation permit a more detailed test of the applicability of the unified model to an odd-odd nucleus which is nearly spherical.

For the spheroidal nuclear potential of the unified model the component Ω of particle angular momentum along the nuclear symmetry axis replaces the total particle angular momentum j as the constant of the motion characterizing particle angular momentum. The ground state spin of odd-odd nuclei is given by one of $I = |\Omega_p \pm \Omega_n|$ with the alternate spin state expected to occur at a low excitation energy [32]). We take at face value the spheroidal orbital sequence in the single particle level diagrams of Mottelson and Nilsson [33]). The orbital assignments for the 59th proton and the 85th neutron for nuclear eccentricities in the range $-0.3 < \delta < +0.3$ are summarized in table 3 together with the resultant ground state spins and parities. For convenience in identifying the orbitals on these diagrams we have included in parenthesis the shell model description for each orbital at $\delta = 0$. There are only two regions of deformation in table 3 which predict the ground state spin and parity (0−) correctly, namely $-0.027 < \delta < 0$ and $+0.03 < \delta < +0.08$. These small nuclear eccentricities are consistent with the observed electric quadrupole moments of neighbouring

nuclei [34]). Spectroscopic studies of the isotope shift [35]) provide some evidence favouring positive distortions, $\delta > 0$, for all nuclei having $82 < N < 95$.

We consider therefore the deformation region $+0.03 < \delta < +0.08$ to see if we can reasonably account for the observed spins and parities of the states in Pr^{144} in terms of the spheroidal orbitals of Mottelson and Nilsson [32, 33]). Both 0— and 3— assignments are predicted and may be assigned to the ground and first excited states respectively. We expect to account for the other observed states by a change in neutron or proton orbital or possibly both. The proton

TABLE 3

Ground State Spin and Parity Assignments for 59th Proton and 85th Neutron

Nuclear deformation δ	Proton Ω_p ††	Neutron Ω_n ††	$\Omega_p+\Omega_n$	$\lvert\Omega_p-\Omega_n\rvert$
$-0.3 \rightarrow -0.275$	$(h_{\frac{11}{2}})\ \frac{9}{2}-$	$(h_{\frac{9}{2}})\ \frac{9}{2}-$	$9+$	$0+$ †
$-0.275 \rightarrow -0.250$	$(h_{\frac{11}{2}})\ \frac{9}{2}-$	$(i_{\frac{13}{2}})\ \frac{13}{2}+$	$11-$ †	$2-$
$-0.250 \rightarrow -0.242$	$(g_{\frac{7}{2}})\ \frac{1}{2}+$	$(i_{\frac{13}{2}})\ \frac{13}{2}+$	$7+$ †	$6+$
$-0.242 \rightarrow -0.225$	$(g_{\frac{7}{2}})\ \frac{1}{2}+$	$(f_{\frac{7}{2}})\ \frac{7}{2}-$	$4-$ †	$3-$
$-0.225 \rightarrow -0.192$	$(g_{\frac{7}{2}})\ \frac{1}{2}+$	$(h_{\frac{9}{2}})\ \frac{9}{2}-$	$5-$	$4-$ †
$-0.192 \rightarrow -0.160$	$(d_{\frac{5}{2}})\ \frac{5}{2}+$	$(h_{\frac{9}{2}})\ \frac{9}{2}-$	$7-$	$2-$ †
$-0.160 \rightarrow -0.092$	$(g_{\frac{7}{2}})\ \frac{3}{2}+$	$(h_{\frac{9}{2}})\ \frac{9}{2}-$	$6-$ †	$3-$
$-0.092 \rightarrow -0.080$	$(h_{\frac{11}{2}})\ \frac{11}{2}-$	$(h_{\frac{9}{2}})\ \frac{9}{2}-$	$10+$	$1+$ †
$-0.080 \rightarrow -0.037$	$(g_{\frac{7}{2}})\ \frac{1}{2}+$	$(h_{\frac{9}{2}})\ \frac{9}{2}-$	$5-$	$4-$ †
$-0.037 \rightarrow -0.027$	$(d_{\frac{5}{2}})\ \frac{5}{2}+$	$(h_{\frac{9}{2}})\ \frac{9}{2}-$	$7-$	$2-$ †
$-0.027 \rightarrow 0.00$	$(d_{\frac{5}{2}})\ \frac{5}{2}+$	$(f_{\frac{7}{2}})\ \frac{5}{2}-$	$5-$ †	$0-$
$\equiv 0$	$d_{\frac{5}{2}}$	$f_{\frac{7}{2}}$	$6-$ †	$1-$
$0.00 \rightarrow 0.02$	$(d_{\frac{5}{2}})\ \frac{1}{2}+$	$(f_{\frac{7}{2}})\ \frac{3}{2}-$	$2-$ †	$1-$
$0.02 \rightarrow 0.03$	$(g_{\frac{7}{2}})\ \frac{7}{2}+$	$(f_{\frac{7}{2}})\ \frac{3}{2}-$	$5-$	$2-$ †
$0.03 \rightarrow 0.08$	$(d_{\frac{5}{2}})\ \frac{3}{2}+$	$(f_{\frac{7}{2}})\ \frac{3}{2}-$	$3-$ †	$0-$
$0.08 \rightarrow 0.107$	$(d_{\frac{5}{2}})\ \frac{3}{2}+$	$(h_{\frac{9}{2}})\ \frac{1}{2}-$	$2-$	$1-$ †
$0.107 \rightarrow 0.120$	$(h_{\frac{11}{2}})\ \frac{1}{2}-$	$(h_{\frac{9}{2}})\ \frac{1}{2}-$	$1+$	$0+$ †
$0.120 \rightarrow 0.145$	$(g_{\frac{7}{2}})\ \frac{5}{2}+$	$(h_{\frac{9}{2}})\ \frac{1}{2}-$	$3-$ †	$2-$
$0.145 \rightarrow 0.170$	$(h_{\frac{11}{2}})\ \frac{3}{2}-$	$(h_{\frac{9}{2}})\ \frac{1}{2}-$	$2+$	$1+$ †
$0.170 \rightarrow 0.177$	$(h_{\frac{11}{2}})\ \frac{3}{2}-$	$(h_{\frac{11}{2}})\ \frac{11}{2}-$	$7+$ †	$4+$
$0.177 \rightarrow 0.270$	$(h_{\frac{11}{2}})\ \frac{3}{2}-$	$(f_{\frac{7}{2}})\ \frac{3}{2}-$	$3+$	$0+$ †
$0.270 \rightarrow 0.332$	$(g_{\frac{9}{2}})\ \frac{9}{2}+$	$(f_{\frac{7}{2}})\ \frac{3}{2}-$	$6-$	$3-$ †
>0.332	$(h_{\frac{11}{2}})\ \frac{1}{2}-$	$(f_{\frac{7}{2}})\ \frac{3}{2}-$	$4+$	$1+$ †

† Preferred ground state spin according to the coupling rules proposed by Gallagher and Moskowski [31]).

†† The shell model nomenclature of the orbital at $\delta = 0$ is included for convenience in identifying them on the single particle level diagrams of Mottelson and Nilsson [32, 33]).

could be promoted from $(d_{\frac{5}{2}})\frac{3}{2}+$ to $(g_{\frac{7}{2}})\frac{7}{2}+$ or alternatively one of the proton pair in the $(g_{\frac{7}{2}})\frac{5}{2}+$ level could be promoted to $(d_{\frac{5}{2}})\frac{3}{2}+$ leaving the unpaired proton in an $\Omega = \frac{5}{2}+$ state. In the same way we should consider a change in neutron orbital from $(f_{\frac{7}{2}})\frac{3}{2}-$ to either $(h_{\frac{9}{2}})\frac{1}{2}-$ or $(f_{\frac{7}{2}})\frac{1}{2}-$. These possibilities make available sixteen states in addition to the 0— and 3— states already mentioned. Since the levels in question are all at low energies it seems reasonable

to exclude those possibilities which involve simultaneous neutron and proton excitation. It also seems probable that only one neutron (or proton) orbital excitation is available at low energy. We seek, therefore, to account for the experimental level sequence in terms of only one alteration in neutron (or proton) orbital. In addition to these tentative restrictions in choice we also wish to account for the relative hindrance of the 53.41 keV M1 transition mentioned above in section 7.3. We present in table 4 the two possible interpretations of the Pr^{144} level sequence which meet these qualifications. The 53.41 keV M1 transition requires a change of both proton and neutron orbital thus accounting for its hindrance relative to the two competing M1 transitions. One of these, the 33.57 keV transition, is interpreted as a flipping over of Ω_n and the other, the 133.53 keV transition, involves a change in Ω_n. The Nilsson orbital assignments shown in table 4 suggest that there should be a low lying 4— level. Because of the spin changes involved we would not expect this level to be fed in the β decay

TABLE 4

Nilsson orbital assignments for $_{59}Pr_{85}^{144}$ levels; $+0.03 < \delta < +0.07$

Energy (keV)	I, π	Ω_p †	Ω_n †
133.53	1−	$(d_{\frac{5}{2}})\ \frac{3}{2}+$	$(f_{\frac{7}{2}})\ \frac{1}{2}-$ or $(h_{\frac{9}{2}})\ \frac{1}{2}-$
99.95	2−		
—	4−	$(d_{\frac{5}{2}})\ \frac{5}{2}+$	$(f_{\frac{7}{2}})\ \frac{3}{2}-$
80.12	1−		
59.03	3−	$(d_{\frac{5}{2}})\ \frac{3}{2}+$	$(f_{\frac{7}{2}})\ \frac{5}{2}-$
0	0−		

† For ease in identifying the orbitals on the single particle level diagrams of Mottelson and Nilsson [33]) we show here the corresponding shell model description at $\delta = 0$.

of Ce^{144} and indeed there is no evidence for such a level. We noted above in section 7.3 that an E2 transition of 74.50 keV is predicted by the level diagram, fig. 4. The experimental intensity limit was shown to be consistent with crude single particle theoretical estimates, barring a high degree of E2 enhancement. The assignments of table 4 make this a single particle transition and are therefore consistent with the experimental ratio.

Gallagher and Moskowski [31]) have proposed rules for the coupling of the angular momenta of the odd neutron and odd proton particle states in odd-odd nuclei which are analogous to Nordheim's rules for spherical (shell model) nuclei. From a comparison of the spins and parities of odd-odd nuclei with those predicted on their coupling rules they conclude that these rules have some validity. The Nilsson orbital interpretation of Pr^{144} proposed here differs from that of Gallagher and Moskowski who assigned as neutron orbital that appropriate to the 87th rather than the 85th neutron and who assumed an oblate rather than prolate distortion. We have therefore applied their coupling rules

to our Nilsson orbital assignments, using the tabulated coefficients $A_{N\Lambda\Sigma}$ [32]) to see what Σ components are dominant in the region of interest, i.e. $+0.03 < \delta < 0.08$. The coupling rules predict that, of the lowest energy pair of levels in table 4, 3— is the preferred ground state choice. There is no clear cut choice for the highest energy pair. The proposed coupling rules therefore fail for Pr^{144}. The Pr^{144} ground state spin assignment is one of a number of violations of these coupling rules which indicate a tendency for Ω_p and Ω_n to couple antiparallel in the ground state.

It is also possible to account for the observed Pr^{144} level sequence for the negative distortion region $-0.027 < \delta < 0$. On the simplest interpretation the existence of two 1— levels requires that there be two different excited neutron orbitals, both available at low energies, as well as one excited proton orbital. Alternatively there could be two excited proton and one excited neutron orbitals. In view of the simpler explanation permitted for the prolate distortion favoured by isotope shift data, a detailed consideration of this negative δ region is not presented here.

8.3. CONCLUDING REMARKS

The single particle shell model fails to predict the ground state spin for Pr^{144} When configurations of the 4 nucleons outside the closed $g_{\frac{7}{2}}$ proton and $h_{\frac{11}{2}}$ neutron shells are considered there is a plausible interpretation for the 0— ground state. Several configuration choices are possible for each of the excited states observed. Systematic evidence from nearby odd-mass nuclei and qualitative theoretical arguments do not provide an obvious basis for choice among the many possible interpretations. Thus we can say no more than that a many-particle shell model description is consistent with the present experimental information on Pr^{144}.

We have seen that it is possible to describe the known level sequence in Pr^{144} very simply as combinations of the intrinsic odd nucleon orbitals of Mottelson and Nilsson [32, 33]). Their coupling scheme implies that there is an axis of symmetry and that the resultant observable spin I is the sum or difference of the individual nucleonic components along this symmetry axis i.e. $I = |\Omega_p \pm \Omega_n|$. While the unified model has proved most successful in accounting for the spins and parities of highly distorted odd-mass nuclei, the experimentally observed spins and parities of odd-mass nuclei with $82 \leqq N < 90$, where $\delta < 0.16$, are almost without exception those appropriate to the shell model sequence. In other words the experimentally observable spin appears to be j_p or j_n, not Ω_p or Ω_n. Why does the unified model account so simply for the levels in the odd-odd nucleus Pr^{144}? One possibility is that this nucleus has a somewhat larger deformation than our analysis, so far, would indicate i.e. $\delta > +0.08$. A slight change in the parameters used by Nilsson [32]) in constructing the single particle level diagrams [33]) could be made which would alter the level spacings sufficient-

ly to allow the description of table 4 to be valid for somewhat larger values of δ without simultaneously disturbing the well established agreement with the level sequences in the rare earth odd-mass nuclei. It seems unlikely, however, that a change of this type could be pushed to give $\delta > 0.16$ i.e. large enough to support rotational patterns. There is no evidence that any of the observed states in Pr^{144} have rotational properties. The most likely candidate is the 2— state at 99.95 keV which might possibly be the first rotational level based on the ground state 0—. However, the 99.95 keV E2 transition de-exciting this level to the ground state competes unfavourably with the 40.93 M1 transition to the 3— state. The latter is almost certainly a particle transition, indicating that this low energy E2 transition does not have the high degree of enhancement expected for a rotational transition. The ratio of quantum intensities γ 40.93/γ 99.95 is ≈ 8, a value consistent with that espected for a typical M1 hindrance factor of ≈ 50 and a small E2 enhancement factor of ≈ 4.

While the interpretation of the Pr^{144} level scheme shown in table 4 accounts for all the presently available evidence in a convincing fashion there remains the possibility that this agreement is fortuitous. Experimental evidence for a low lying 4— level which could be identified with the predicted 4— level would provide further support for this interpretation. Another test which would prove helpful is an experimental determination of the lifetime of the 3— level. The single proton estimate for the de-exciting M3 transition including conversion correction, is about 3 sec. Experimental data on M3 transitions is scarce but does indicate retardation factors of up to 10^3. Thus, if the measured lifetime turns out to be close to 3 sec it would lend support to the simple explanation proposed in table 4, namely that this transition is due to flipping over Ω_p or Ω_n. Measurement of other absolute transition probabilities would also aid in the assessment of this interpretation. As level spectrum information becomes available for other odd-odd nuclei it will be interesting to see how successful the unified model approach, as applied here, is in accounting for all measured properties, particularly for those nuclei which have too small a deformation to support rotational structure.

9. Summary

The conversion line spectrum following β-decay of Ce^{144} has been investigated using the Chalk River air-cored $\pi\sqrt{2}$ spectrometer at 0.1 % resolution. All conversion lines identified have been assigned to seven γ transitions in Pr^{144}; the multipolarities are clearly established from the line intensity ratios. The precision and lack of ambiguity in these energies and multipolarities lead to a unique sequence of levels in Pr^{144}. The branching ratios of the β components from Ce^{144} taken together with this level sequence lead to unique spin and parity assignments for the Pr^{144} levels and confirm the earlier evidence favouring 0— for the Pr^{144} ground state.

The Pr^{144} level scheme is compared with the predictions of the shell model and the unified model. The single particle shell model fails to account for the 0— ground state. A many-particle approach accounts satisfactorily for the 0— ground state but permits several possible interpretations for each of the excited levels. A unified model interpretation is proposed, in terms of the intrinsic odd nucleon level assignments of Mottelson and Nilsson assuming a prolate deformation, $\delta \approx +0.07$. With qualitative restrictions on the possible odd neutron and odd proton level combinations a unique selection of six level assignments emerges. Five of these correspond with the five established states in Pr^{144}; one would not expect the sixth predicted state, 4—, to be fed by beta decay from Ce^{144}.

It is a pleasure to thank Dr. D. R. MacKenzie and Mrs. J. Merritt for their assistance in source preparation and Mr. R. B. Walker for his continued help in the technical aspects of spectrometer design and operation. We are indebted to Drs. H. McManus and T. D. Newton for helpful discussions on theoretical aspects. We are grateful to Dr. L. G. Elliott for his advice and assistance and for his critical review of this manuscript.

References

1) G. T. Ewan, J. S. Geiger, R. L. Graham and D. R. MacKenzie, Can. J. Phys. **37** (1959) 174
2) R. L. Graham, G. T. Ewan and J. S. Geiger, Bull. Am. Phys. Soc. **4** (1959) 64
3) G. T. Ewan, J. S. Geiger, R. L. Graham and D. R. MacKenzie, Phys. Rev. **116** (1959) 950
4) R. L. Graham, G. T. Ewan and J. S. Geiger, to be published in Nuclear Instruments and Methods
5) G. E. Lee-Whiting and E. A. Taylor, Can. J. Phys. **35** (1957) 1;
G. E. Lee-Whiting, Atomic Energy of Canada Ltd., no. 419 (1957)
6) R. O. Lane and D. J. Zaffarano, Iowa State Report I.S.C.-439 (1953) and Phys. Rev. **94** (1954) 960
7) R. D. Evans, The Atomic Nucleus (McGraw Hill Book Company, Inc., New York, 1955) 624
8) R. L. Graham, J. S. Geiger and T. A. Eastwood, Can. J. Phys. **36** (1958) 1084
9) F. T. Porter and P. A. Day, Phys. Rev. **114** (1959) 1286
J. H. Hamilton and L. M. Langer, Bull. Am. Phys. Soc. **3** (1958) 208;
N. J. Freeman, Proc. Phys. Soc. A **73** (1959) 600
10) P. H. Serson, Can. J. Phys. **35** (1957) 1387
11) See e.g. K. Siegbahn, Beta- and Gamma-Ray Spectroscopy (North Holland Publishing Co., Amsterdam 1955) p. 95
12) D. E. Muller, H. C. Hoyt, D. J. Klein and J. W. M. DuMond, Phys. Rev. **88** (1952) 775
13) Y. Cauchois, J. de Physique et le Radium **16** (1955) 253
14) A. H. Wapstra, G. J. Nijgh and R. van Lieshout, Nuclear Spectroscopy Tables (North Holland Publishing Co., Amsterdam 1959)
15) J. S. Geiger, R. L. Graham and G. T. Ewan, Bull. Am. Phys. Soc. **4** (1959) 57
16) P. Bergvall, Ark. J. Fysik **16** (1959) 57
17) M. E. Rose, Internal Conversion Coefficients (North-Holland Publishing Company, Amsterdam, 1958)
18) F. T. Porter and C. S. Cook, Phys. Rev. **87** (1952) 464
19) J. M. Cork, M. K. Brice and L. C. Schmid, Phys. Rev. **96** (1954) 1295
20) D. Strominger, J. M. Hollander and G. T. Seaborg, Revs. Mod. Phys. **30** (1958) 585
21) Lin-Shing, G. John and J. D. Kurbatov, Phys. Rev. **85** (1952) 487

22) L. A. Sliv and I. M. Band, Coefficients of Internal Conversion of γ-Radiation (1957). The K conversion coefficients have been issued as Report 57 I.C.C. K.1 University of Illinois, the L conversion coefficients circulated privately
23) W. S. Emmerich, G. John and J. D. Kurbatov, Phys. Rev. **82** (1951) 968
24) M. A. Grace, C. E. Johnson, R. G. Scurlock and R. T. Taylor, unpublished data (1957) referred to by Strominger *et al.* [20])
25) R. E. Marshak, Phys. Rev. **61** (1942) 431
26) V. P. Parfenova, N.V. Forafontov and V. S. Shipinel, Izvestiia Akademii Nauk. S.S.S.R. **21** (1957) 1601
27) K. Way *et al.*, Nuclear Data Sheets, National Academy of Sciences — National Research Council, Washington 1958 *et seq.*
28) J. P. Elliott and A. M. Lane, Handbuch der Physik, Vol. 39 (Springer-Verlag, Berlin, 1957) 289
29) I. Talmi, Phys. Rev. **82** (1951) 101
30) M. Goldhaber and A. W. Sunyar, Phys. Rev. **83** (1951) 906
31) C. J. Gallagher Jr., and S. A. Moszkowski, Phys. Rev. **111** (1958) 1232
32) S. G. Nilsson, Dan. Mat. Fys. Medd. **29**, No. 16 (1955)
33) B. R. Mottelson and S. G. Nilsson, Mat. Fys. Skr. Dan. Vid. Selsk **1**, No. 8 (1959)
34) K. Okamoto, Phys. Rev. **110** (1958) 143
35) D. L. Hill, Handbuch der Physik, Vol. 39 (Springer-Verlag, Berlin, 1957) 221

2.A.1

Nuclear Physics **16** (1960) 27—37; © *North-Holland Publishing Co., Amsterdam*

Not to be reproduced by photoprint or microfilm without written permission from the publisher

MULTIPLICITY OF RESONANCE NEUTRON CAPTURE GAMMA RAYS

J. E. DRAPER and T. E. SPRINGER †

Yale University, New Haven, Connecticut ††

Received 23 November 1959

Abstract: Measurements of the multiplicity of resonance neutron capture gamma rays are reported for 23 resonances of 15 nucleides in the range $A = 110$ to 198 by comparison with the known multiplicity for $B^{10}(n, \gamma)$ Multiplicities of two resonances forming Eu^{153}, two resonances forming Er^{168}, three resonances forming Lu^{177} and two resonances forming Hf^{178} were not dependent on resonance energy within the limits of experimental uncertainty. Significant variations were found among the multiplicities of three resonances forming In^{116} and two resonances forming Sm^{150}. There is some evidence that $J = 3$ for the 3.9-eV resonance forming Ho^{166}. Direct measurements of the resonance J values are not yet available for comparison.

1. Introduction

The average number of gamma rays emitted following resonance neutron capture is of interest for several reasons. One is the question whether there are variations in this multiplicity among neutron resonances of a given nucleide and whether such variations can be related to the spin of the capturing state. The initial high energy gamma-ray transitions from the capturing state are perhaps dominantly dipole for which the magnitude of spin change is 0 or 1. If this dipole dominance persists for several successive transitions in the cascade, there arises the question whether a lower multiplicity is associated with resonances whose J value is nearer that of the final state. In a related situation such a correlation appears as the "isomeric ratio rule" recently confirmed by der Mateosian and Goldhaber [2]). This rule states that in slow neutron capture when two isomeric states are produced the one with spin nearer to that of the capturing state is more abundant. For isomers with their large spin difference the rule is strong, while for the present situation where the two possible spins differ by only one unit the effect is presumably weak. However, the paucity of available resonance J values and the general difficulty of their measurement motivates an interest in the relation of the multiplicity of resonance neutron capture gamma rays to the resonance J value.

† Present address: Los Alamos Scientific Laboratory, Los Alamos, New Mexico.

†† Derived in part from a thesis submitted by T. S. in partial fulfilment of the requirements for the Degree of Doctor of Philosophy at Yale University.

Supported in part by the U. S. Atomic Energy Commission. Preliminary account of this work has appeared. [1])

The variation of multiplicity among resonances of a given nucleide is also of interest because the counting rate from a capture gamma-ray detector is often used as a measure of the relative number of neutrons captured in various resonances of a nucleide. Such is the case in measurements of resonance parameters for radiative capture and in measurements of partial radiation widths of resonances. There is also interest in making multiplicity measurements for resonances with their well-defined spin, parity and isotopic assignment as contrasted with thermal measurements.

The multiplicity is here defined as the average number of gamma rays emitted in cascade following neutron capture. Multiplicity measurements were first made by Aoki [3]) and by Fleischmann [4]). Muehlhause [5]) has measured the average number of gamma rays following thermal neutron capture using a coincidence method. For energy-independent detectors, the counting rate in one detector of such a coincidence system would be proportional to the multiplicity M, while the coincident counting rate would be proportional to $M(M-1)$ if the same number of photons is emitted in every neutron capture. However, because this method averages the square of the number of photons emitted, it will yield a result higher than the true multiplicity. For example, if neutron capture results in equal probability of emission of three, four, and five photons the measured multiplicity will be 4.2 rather than 4.0. The result is further complicated by energy dependence of the detectors. In addition, the coincidence method misses single transitions to the ground state, thereby biassing the results slightly.

More recently Groshev *et al.* [6]) have measured the spectra of thermal neutron capture gamma rays in many elements, and the integral of such a spectrum is the multiplicity.

The present experiment employs a single thick NaI(Tl) detector. The 4-in. thickness of the NaI(Tl) scintillator affords a detection efficiency of more than 0.7 for gamma rays of energies $\gtrsim$ 15 MeV. The relatively large efficiency of this detector has enabled us to measure the multiplicity for capture in individual resonances as contrasted with the previously available thermal capture results.

2. Experimental Method

The experimental arrangement is shown in fig. 1. The linear electron accelerator provided a source of neutrons pulsed at a repetititon rate of 112 pulses per second. The neutrons, after being moderated, traversed a 3.43-m flight path through a three-inch hole in an eight foot wall of earth and concrete. The detector was a 4-in. thick by 5-in. diam NaI(Tl) scintillation crystal in a lead shield. The gamma-ray bias was 30 keV. The lead, boral, borax, and Li^6 shielding eliminated most of the background from gamma rays and neutrons.

The neutron yield was monitored by means of a BF_3 counter located in the accelerator room.

The multiplicity was obtained by comparing the counting rate of neutron capture gamma rays within a chosen neutron energy region to that of the 480-keV gamma ray emitted from a black B^{10} sample in the same neutron energy region. The multiplicity of B^{10} is known to be 0.935 from measurements of DeJuren and Rosenwasser [7]). It was also necessary to determine the fraction of neutrons captured in the chosen energy region. This fractional capture was

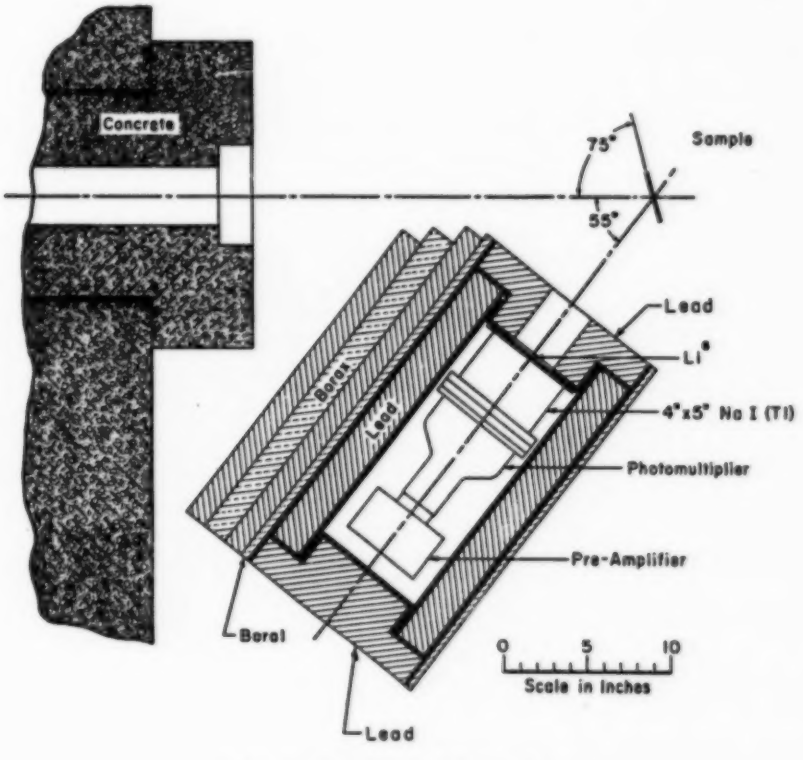

Fig. 1. Experimental geometry.

obtained by a transmission measurement with calculated corrections for neutron scattering, or it was obtained by direct calculation from resonance parameters and sample thickness. In either case the effects of capture in the sample preceded by scattering were included [8]).

For the transmission measurement 480-keV gamma rays emitted from a small B^{10} sample were detected in the NaI crystal. The resulting pulses were gated into the pulse height analyzer only during the time interval selected for the resonance. The area under the 480-keV photopeak was then measured with and without the sample to determine the sample transmission. Direct use of the photopeak made the measurement insensitive to background.

In figs. 2 and 3 the spectra of B^{10} and samarium are shown as examples of

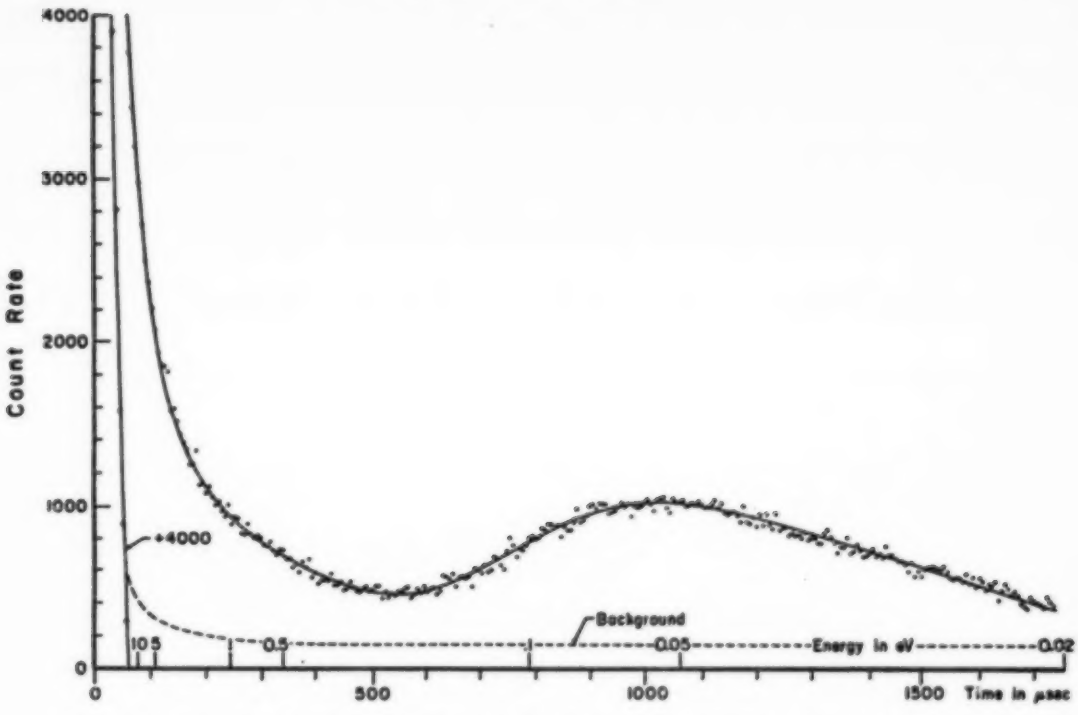

Fig. 2. Neutron capture counting rate with a thick B^{10} sample ($N\sigma_\gamma = 1$ at 800 eV).

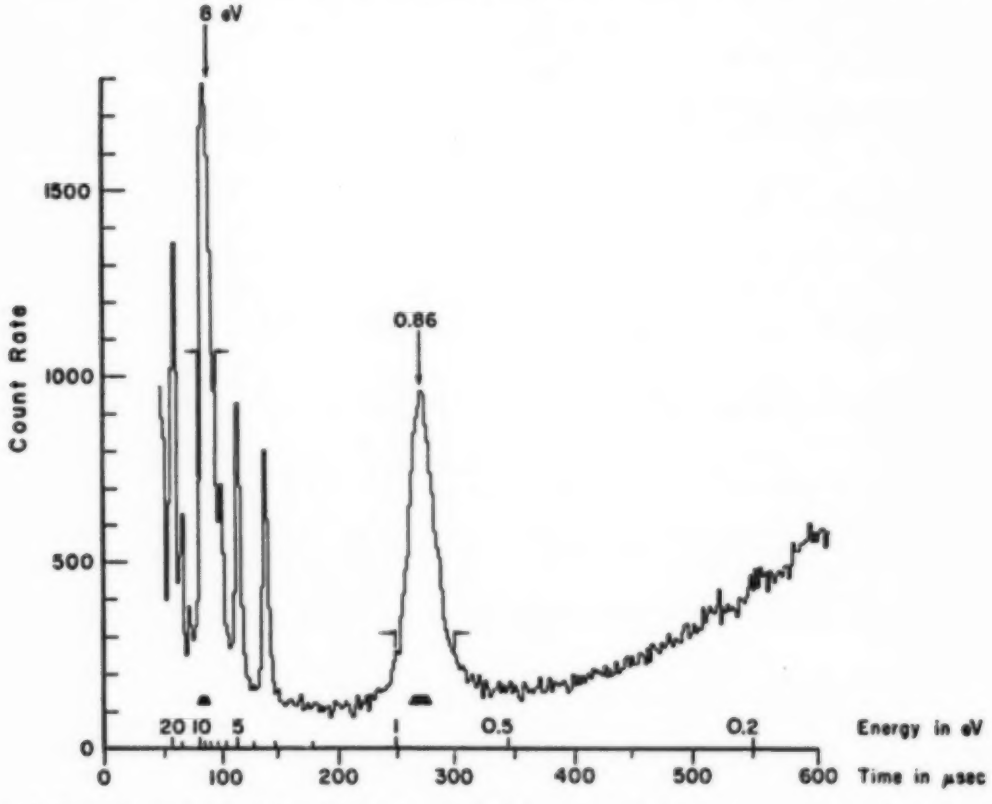

Fig. 3. Counting rate vs. delay for 0.5 g · cm^{-3} of Sm_2O_3. This is representative of the data from which multiplicities were obtained.

the data. The enriched B^{10} sample was of such thickness that its transmission was e^{-1} at 800 eV. Experimental runs were repeated from two to five times to determine the sample transmission and the area under a resonance as in fig. 3. The RMS deviation from the mean for all of the resonances was 3.5 % which was composed of a statistical uncertainty of 2.6 % and an average contribution of 2.3 % from systematic errors.

3. Measurement of Background

Following a series of runs with a group of elements, a background run was made with an empty aluminium sample frame. The resulting background was subtracted from the neutron capture rate spectrum of the sample in question and from the B^{10} capture rate spectrum. This background may be seen dotted on the B^{10} spectrum of fig. 2. The intensity of the neutron beam was held approximately constant during all the runs to keep constant the ratio of accelerator-associated to non-accelerator-associated background.

The amount of background from delayed gamma rays in the beam which were scattered from the sample into the detector was measured by placing a lead foil in the sample position. Neutron capture in the lead was negligible, but the photon scattering was equivalent to the average scattering of the samples. The accelerator-associated background counting rate increased about 10 % with the addition of the lead foil and sample holder as compared to the rate with nothing at the sample position. The effect of photon scattering from the samples of heavier elements was calculated to be less than 1 % of foreground (at a resonance peak).

Possible background caused by resonance scattering of neutrons from the sample into the detector was minimized by the disk of enriched Li^6 (with transmission e^{-1} at 6.8 eV) placed in front of the scintillator. In all but four of the resonances examined, the scattering cross section was less than 5 % of the capture cross section. Of the neutrons scattered, 60 to 100 % were captured in the Li^6. Before comparing this type of background with foreground, the number of neutrons entering the crystal must be divided by the multiplicity of the capture radiation. It was concluded that the uncertainty from this background was negligible in all cases.

Background from neutrons penetrating the detector shielding was assessed by the background measurement in which the sample was removed.

4. Analysis

Let C be the measured fraction of neutrons that is captured by the sample during the time gate. Let M be the average multiplicity of gamma rays for the resonance in question. Let R_x and R_B be the photon counting rate within the selected time gate for the sample x and for the B_{10} sample, respectively.

Then the multiplicity is obtained from the data as

$$M = \frac{0.935}{C} \frac{R_x}{R_B} (1+\alpha). \tag{1}$$

There are four effects which contribute to α: (1) The crystal does not absorb all incident photons. (2) The transmission of the lead collimator has some dependence on photon energy. (3) The detector bias was 30 keV thus rejecting a small fraction of the detector pulses. (4) The samples were relatively thin, but they absorbed some of the lowest energy photons. It was found that the average value of α is 0.06 and that the variation of $(1+\alpha)$ among all the resonances reported here is $\pm 2.5\,\%$. The solid angle subtended by the detector was sufficiently small that summing of coincident photons had negligible effect.

5. Evaluation of the Correction Term α

Let $P_x(E)$ be the probability density for the emission of a photon of energy E, so $P_x(E)$ represents the capture gamma-ray spectrum of sample x for the resonance under investigation. Let $Q(h, E)$ be the detector response function, *i.e.*, the spectrum of pulses of height h produced by a photon of energy E. Let $a(E)$ be the fraction of photons absorbed in the sample. Define Ω_0 as the fractional solid angle subtended by the rear opening of the 3-in. lead collimator in fig. 1. Define $\Omega_0(1+f(E))$ as the effective solid angle of the collimator, where $f(E)$ contains the effect of oblique penetration through the edges of the collimator, penetration through the front 4-in. lead wall of the collimator and scattering of photons by the edges of the collimator followed by detection of the scattered photon.

Define $\varepsilon_0 = 0.82$ as the average efficiency of 4 inches of NaI(Tl) and $\varepsilon_0(1+\delta(E))$ as the energy dependence of the photon efficiency of the detector. The quantity $\delta(E)$ is shown in fig. 4 as calculated for normal incidence on 4 in. of NaI(Tl) using the results of White [9]). The increase of efficiency for a photon entering as obliquely as is permitted by the geometry of fig. 1 is only 0.5 %.

It follows directly from eq. (1) and the above definitions that

$$1+\alpha = \frac{[(1+f)(1+\delta)(1-a)]_{480\text{ keV}} \int_{30\text{ keV}}^{\infty} dh\, Q(h, 480\text{ keV})}{\left[\int_0^{\infty} dE (1+f)(1+\delta)(1-a) P_x(E) \int_{30\text{ keV}}^{\infty} dh\, Q(h, E)\right] \Big/ \int_0^{\infty} dE P_x(E)}. \tag{2}$$

It is apparent in eq. (2) that if f, δ and a vanished, and if the pulse height bias were zero rather than equivalent to 30 keV, then α would vanish. The only approximation in eq. (2) is that the photons which reach the detector after penetrating the collimator retain the initial value for the integral of Q. This assumption has negligible effect on $(1+\alpha)$.

Also shown in fig. 4 is $f(E)$, the energy variation of the solid angle due to

collimator effects. The method of calculating $f(E)$ and a series of experiments to measure $f(E)$ and $\varepsilon_0(1+\delta(E))$ at several photon energies are discussed elsewhere [10]). The sample absorption correction $a(E)$ was calculated by the methods described in ref. [11]).

It remains to insert the spectral shape $P_\gamma(E)$ in eq. (2) to obtain α. The spectra are not known for resonance capture, and if they were available they could already provide the average multiplicity directly by integration. However, for evaluation of the small correction term α it is sufficient to use the thermal neutron capture spectra when available. For this purpose the results of Groshev *et al.* [12]) were used since their Compton spectrometer has provided data down to photon energies below 0.5 MeV. Their results for Cd, Sm, Gd,

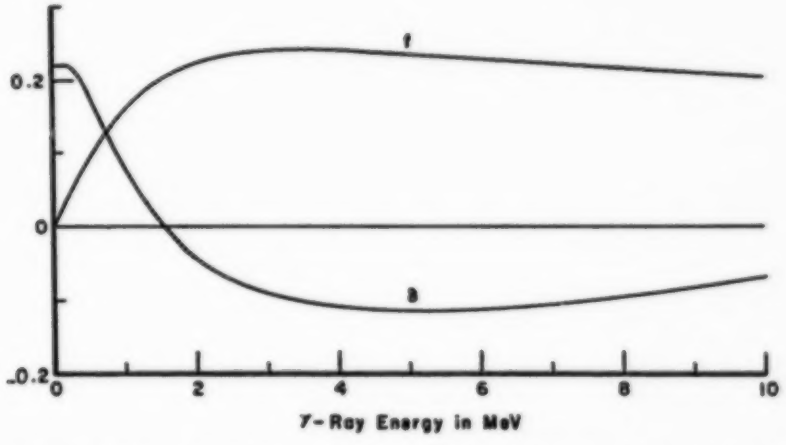

Fig. 4. Detector efficiency correction δ and solid angle correction f contained in eq. (2).

Dy, Er and Hf, given as $\nu(E)H\rho$, were replotted as $\nu(E)$ and used to approximate the resonance $P_\gamma(E)$ in eq. (2). Below 550 keV our previous results with a NaI(Tl) spectrometer [13]) were used. Photons at 511 keV were arbitrarily assumed to be annihilation radiation and were excluded. For the six elements mentioned above, the contribution to $(1+\alpha)$ from photons of energy greater than 550 keV varied by less than ± 2 %. Consequently, the average value of this part of $(1+\alpha)$ was used for the remaining elements. The contribution to $(1+\alpha)$ from photons of energy less than 550 keV was evaluated as described above for each element. The integral of $Q(h, E)$ is nearly unity, and the departures therefrom were estimated from spectra obtained with monoenergetic sources and from the resonance spectra.

6. Experimental Results

In table 1 are listed the experimentally determined average resonance multiplicities as well as those of Muehlhause [5]) and Groshev *et al.* [6]) for thermal capture. For six of the isotopes, the multiplicity was measured for more than

one resonance of an isotope. These product nucleides were In^{116}, Sm^{150}, Eu^{152}, Er^{168}, Lu^{177} and Hf^{178}. The isotopic assignments were obtained from the compilation of Hughes and Schwartz [15]), and from the Nuclear Data Sheets [16]).

TABLE 1

Multiplicities of resonance neutron capture gamma rays

Product nucleide [a]	Resonance energy [a] (eV)	Multiplicity		
		This work	Muehlhause [b] (thermal)	Groshev [c] (thermal)
Ag^{110}	5.2	5.0 ±0.3	2.9 [d]	4.0 [d]
Cd^{114}	0.18	4.1 ±0.3	4.1	4.0
In^{116}	1.5	4.4 ±0.2	3.3	4.4
	3.9	5.6 ±0.4		
	9.1	4.2 ±0.4		
Sm^{150}	0.10	6.2 ±0.3	5.6	4.7
	0.88	5.0 ±0.4		
Sm^{153}	8.0	4.1 ±0.5		
Eu^{152}	0.46	4.4 ±0.3	3.8	3.5
	1.0	3.4 ±0.7		
Gd^{158}	0.03	4.6 ±0.2 [d]	3.9 [d]	4.3 [d]
Gd^{156}	2.6	3.9 ±0.4		4.5
Dy^{165}	neg.	3.1 ±0.2	3.7	3.9
Ho^{166}	3.9	3.0 ±0.3		
Er^{168}	0.47	4.7 ±0.3		5.6
	6.0	4.2 ±0.3		
Tm^{170}	3.9	3.7 ±0.3		
Lu^{177}	0.14	4.35±0.25		
	1.6	4.0 ±0.3		
	2.6	4.4 ±0.3		
Hf^{178}	1.1	4.2 ±0.2	3.8 [d] 4.1 ±0.2 [e]	4.7
	2.4	4.3 ±0.2		
Au^{198}	4.9	3.8 ±0.3	3.5	3.9

[a] See ref. [15]) and [16]).
[b] See ref. [5]).
[c] See ref. [6]).
[d] Less than 90 % of neutrons captured in one isotope.
[e] See ref. [14]).

For In^{116} the multiplicity of the 3.9-eV resonance is larger than that of the 1.5-eV resonance by three standard deviations. The 1.5- and 9.1-eV resonances have the same multiplicity within the limits of uncertainty. The relative intensities of low energy gamma rays in In^{116} have been observed by Draper, Fenstermacher and Schultz [11]), to vary in these three resonances. The radiation widths of the 1.5- and 3.9-eV resonances, measured by Landon and Sailor [17]) were found to differ beyond experimental error. The isomeric activity of In^{116} following capture in these two resonances also differed [18]). The multiplicity variation is further evidence that the In^{116} decay scheme is different for these

two resonances. The spin of the 1.5-eV resonance is known to be 5 from polarization experiments [19]).

In the compound nucleus Sm^{150}, the multiplicities of the 0.10-eV and the 0.88-eV resonances differ by three standard deviations. The product spin of the 0.10-eV resonance is known to be 4 from polarization experiments [19]), while the other possible spin is 3. Marshak and Sailor [20]) have recently measured

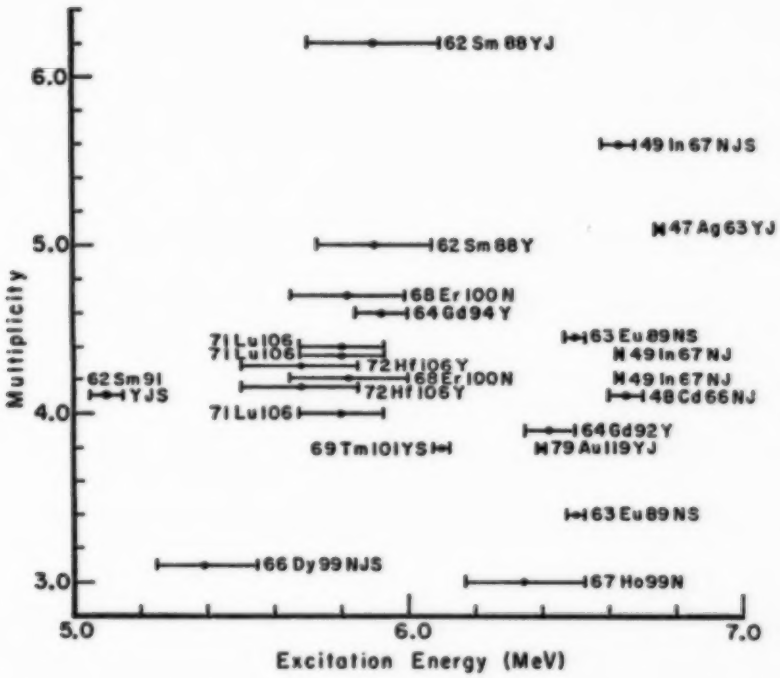

Fig. 5. Multiplicity vs. excitation energy and spin change. The symbols represent, respectively, proton number, element, neutron number and parity change between capturing state and final state (Y for yes, N for no). The symbol J signifies that the resonance spin has already been measured, and the symbol S signifies that the final spin is larger than the resonance spin. The length of each horizontal span is proportional to the magnitude of the spin difference between the capturing state and the final state.

Note: After completion of this manuscript for publication a preprint was received from A. Stolovy concerning polarization measurements on In which showed that the 1.5-, 3.9- and 9.1-eV resonances have $J = 5$, 4 and 5, respectively.

the radiation width of four of the low energy resonances in Sm^{149} and found the 0.88-eV resonance to have a radiation width approximately 7 % lower than that of the other resonances. If the spins of the 0.10-eV and 0.88-eV resonances should later be found to differ, the resonance with lower spin difference between compound and final state would also have lower multiplicity.

The multiplicites of the 0.46- and 1.0-eV resonances producing the compound nucleus Eu^{152} differ by only 1.4 standard deviations. The large uncertainty for the 1.0-eV resonance arises because the fraction of neutrons captured in the

sample was not measured but was calculated from the resonance parameters [15]).

The 1.1- and 2.4-eV resonances in Hf yielded approximately the same multiplicity. However, Igo and Landon [21]) have found these radiation widths to differ, and othter measurements in our laboratory have shown that the absolute intensities [22]) of the 220 keV and 330 keV gamma ray lines differ in these resonances.

The multiplicities of the various resonances are plotted in fig. 5 as a function of the spin difference between compound state and final state and as a function of the excitation energy †. If an isomeric level near the ground state is highly populated after the cascade, it may be considered as the effective ground state. Beside each entry are listed proton number, element, neutron number and parity change between capturing state and final state (*i.e.* Y for yes and N for no), respectively. These are followed by a symbol J if the resonance spin is known from previous measurements and by the symbol S if the spin of the final state is larger than that of the capturing state. The length of the horizontal span at each point is proportional to the spin difference between the capturing state and the final state and represents the average of the two possibilities wherever no measurements of the resonance J are available. The final state spin and parity represented in the figure are those for the state with the largest population by thermal capture [15, 16]).

The general features of fig. 5 can be summarized as follows. For different nucleides there is little correlation between the multiplicity and either the spin change or the excitation energy. There is, however, some indication, as noted above, of a tendency for larger multiplicity to go with larger spin change for resonances of the same nucleide. There is no instance of a multiplicity smaller than the spin change unless the 3.9-eV resonance forming Ho^{166} should have $J = 4$. Thus $J = 3$ is suggested for this resonance. The average multiplicity of the even product nucleides in table 1 is approximately 0.5 unit (or 10 %) larger than that of the other nucleides.

To summarize, the multiplicities of resonances in these different nucleides appear to have little correlation with such properties as excitation energy, spin change (except possibly for holmium) or mass number. On the other hand, for resonances of the same nucleide there are variations of as much as 25 %, and there is some evidence that, when relatively large, they can be correlated with the spin difference between the capturing state and the final state.

More independent measurements of the resonance values of J will be needed to determine the implication of relatively small differences in multiplicity for resonances of a given nucleide.

† The excitation energy is the neutron binding energy less the pairing energy. The pairing energy is taken as $(1.68-0.0042A)$ MeV for odd-mass nucleides and twice as large for even nucleides.

References

1) T. Springer and J. E. Draper, Bull. Am. Phys. Soc. **4** (1959) 35
2) E. der Mateosian and M. Goldhaber, Phys. Rev. **108** (1958) 766
3) H. Aoki, Proc. Phys. Math. Soc. Japan **19** (1937) 799
4) R. Fleischmann, Zeit. f. Phys. **111** (1938) 281
5) C. O. Muehlhause, Phys. Rev. **79** (1950) 277
6) Groshev, Demidov, Lutsenko and Pelekhov, Second Geneva Conference, A/CONF. 15/P/2029, USSR (24 July 1958)
7) J. De Juren and H. Rosenwasser, Phys. Rev. **93** (1954) 831
8) J. E. Draper, Nucl. Sci. and Eng. **1** (1956) 522
9) P. R. Bell in Beta- and Gamma-Ray Spectroscopy, ed. by K. Siegbahn (North-Holland Publ. Co., Amsterdam, 1955);
G. R. White, National Bureau of Standards Report 1003 (1952)
10) T. E. Springer and J. E. Draper, to be published
11) Draper, Fenstermacher and Schultz, Phys. Rev. **111** (1958) 906
12) Recently summarized by Groshev, Demidov, Lutsenko and Pelekhov, Atlas of Spectra of Thermal Neutron Capture Gamma Rays (Moscow, 1958)
13) J. E. Draper, Phys. Rev. **114** (1959) 268
14) Bollinger, Harris, Hibdon and Muehlhause, Phys. Rev. **92** (1953) 1527
15) D. J. Hughes and R. B. Schwartz, Neutron Cross Sections, Brookhaven National Laboratory Report BNL-325, second edition (Superintendent of Documents, U. S. Government Printing Office, Washington, D. C., 1958)
16) K. Way *et al.*, Nuclear Data Sheets (National Academy of Sciences — National Research Council, Washington, D. C., 1959)
17) H. Landon and V. L. Sailor, Phys. Rev. **98** (1955) 1267
18) V. L. Sailor, private communication
19) Roberts, Bernstein, Dabbs and Stanford, Phys. Rev. **95** (1954) 105;
J. A. Moore, Phys. Rev. **109** (1958) 417
20) H. Marshak and V. Sailor, Phys. Rev. **109** (1958) 1219
21) G. Igo and H. Landon, Phys. Rev. **101** (1956) 726
22) Fenstermacher, Draper and Bockelman, Nuclear Physics **10** (1959) 386

1.D.2:
1.E.4;
3.A

Nuclear Physics **16** (1960) 38—51; © *North-Holland Publishing Co., Amsterdam*
Not to be reproduced by photoprint or microfilm without written permission from the publisher

GAMMA RAYS FROM THE 4.24 MeV STATE IN MAGNESIUM-24

R. BATCHELOR †, A. J. FERGUSON, H. E. GOVE and A. E. LITHERLAND
Chalk River Laboratories, Chalk River, Ontario, Canada

Received 4 December 1959

Abstract: The $Mg^{24}(p, p'\gamma)Mg^{24}$ reaction has been studied in the proton energy range from 5 MeV to 6 MeV. The yield of 4.24 MeV γ-rays shows two resonances, at 5.24 MeV and 5.72 MeV, corresponding to states in Al^{25} at 7.30 MeV and 7.77 MeV. The total widths of these resonances are 100 ± 20 keV and 340 ± 50 keV. Angular distributions and correlations of the γ-rays from the 4.24 MeV state of Mg^{24} measured at the 5.72 MeV resonance show that the 4.24 MeV state has spin 2. Spins of 1 and 3 are eliminated by the measurements. The spin of the 7.77 MeV state of Al^{25} is most probably $\frac{3}{2}$. The measured branching ratio of the γ-rays from the 4.24 MeV state to the ground and 1.37 MeV states is $(2.9\pm0.5) : 1$ and the E2/M1 amplitude ratio for the 2.87 MeV transition is $+23\pm9$. These data give qualitative support to the collective model but there are quantitative disagreements with the detailed predictions for both axially symmetric and asymmetric nuclei.

1. Introduction

The nucleus Mg^{24} is of considerable interest since the available information on its low-lying level structure [1,2]) suggests that it has a spheroidal shape. The level scheme is shown in fig. 1. Extensive use has been made of the β-decay of Na^{24} to Mg^{24} to study the first two excited states and the properties of these are now well established [3]). There are, however, very few measurements pertaining to the 4.24 MeV and higher levels. Newton [4]) observed the capture γ-radiation from the bombardment of Na^{23} by protons and showed that the 4.24 MeV level decayed both to the ground state and the 1.37 MeV level. From angular distribution and correlation measurements its spin was deduced to be 2. An even parity was assigned from the fact that the β-transition to the state was second or higher forbidden [5]), and this is confirmed by observed $l = 2$, $l = 0$, transitions to the unresolved levels at 4.12 and 4.24 MeV in the $Na^{23}(d, n)Mg^{24}$ reaction [6,7]). Newton's letter, however, gave very few experimental details.

As can be seen, the level scheme is in good qualitative accord with the collective model [8]). The first three levels can be interpreted as constituting the first three members of a $K = 0$ rotational band and the 4.24 MeV level could be the first member of a $K = 2$ band. The spin 3 level at 5.24 MeV could be the second

† Seconded from the United Kingdom Atomic Energy Authority, Atomic Weapons Research Establishment, Aldermaston.

member of the $K = 2$ band, if its parity is even, but at present its parity is assigned a doubtful negative [9]). The branching ratio of the de-excitation γ-rays of the 4.24 MeV level to the ground state and 1.37 MeV level, as measured by Newton, agrees exactly with the predicted value of 5, assuming that the 2.87 MeV radiation is pure quadrupole.

The level scheme can also be considered in terms of collective excitations with violation of axial symmetry. Davydov and Filippov [10]) show that, in the case of an even nucleus, the rotational spectrum is only slightly affected by the axial asymmetry, but new rotational states with angular momentum 2, 3, 4 etc. appear. Van Patter [11]) has recently surveyed the experimental data regarding E2 transitions from the second 2+ levels in even nuclei, showing that the predictions of this model are quite well borne out. For Mg^{24}, however, the pre-

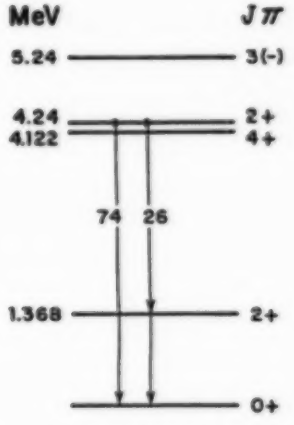

Fig. 1. Level scheme of Mg^{24}. (The branching ratio of the 4.24 MeV level is the result of the present experiment.)

dicted value of the branching ratio from the 4.24 MeV level is 0.88 which is definitely not in agreement with that measured by Newton.

In the present experiment the γ-rays from the 4.24 MeV level have been studied through the inelastic scattering of protons by Mg^{24}. At the bombarding energies used, between 5 and 6 MeV, inelastic scattering to the 1.37 MeV and 4.24 MeV levels are the predominant reaction channels.

Angular distributions of the 4.24 MeV and the 2.87 MeV γ-rays with respect to the proton beam and also the correlations of the 2.87 MeV and 1.37 MeV γ-rays, all with the intermediate proton radiation unobserved, have been measured. The results have been analyzed, by a method first suggested by Warburton and Rose [12]) and later developed by Litherland and Ferguson [13]), to check the spin assignment 2 for the 4.24 MeV state. In this analysis, which is described in detail in ref. [13]), the correlations are expressed as an incoherent sum over the correlations from the different substates of the first gamma-ray emitting state of the residual nucleus. Consequently the considerations of the details of

the formation and decay of the compound nucleus are simplified. The present experiment, in which the analysis is simplified further by the target nucleus having zero spin, is the first of a series on various light nuclei to which this analysis will be applied.

2. Experimental Procedure

The measurements reported here were made with the Chalk River Tandem Accelerator. The proton beam was focussed down to about $\frac{1}{8}$ inch diameter at the target by magnetic quadrupole lenses situated approximately equidistant from the analyzer magnet and the target. The proton energy was known from a previous calibration of the analyzer magnet using known (p, n) thresholds [14]). The gamma rays were observed by two NaI(Tl) scintillators, one 5-inch diameter by 6-inch long and the other 5-inch diameter by 4-inch long, each placed with its front face 6.5-inch from the centre of the target. Each crystal had a $\frac{1}{8}$-inch thick lead absorber placed in front to cut down the counting rate from the coulomb excitation of the gold backing. For angular distribution measurements the former was rotated and the latter acted as a monitor fixed at 90° to the direction of the incident proton beam. For the angular correlation measurements, the 5-inch by 4-inch crystal was again fixed at 90°. In the so-called geometry A a channel was placed on the total absorption peak of the 1.37 MeV gamma-ray in the pulse-height spectrum from the 5-inch by 4-inch crystal and in geometry B the channel was placed on the total absorption peak of the 2.87 MeV gamma ray. These geometrical arrangements of the counters are shown in fig. 5. After amplification, each pulse-height spectrum was displayed on a 100-channel transistorized pulse-height analyzer. A conventional fast-slow coincidence circuit [15]), with a resolving time 2τ of about 50 ns was used for the correlation measurements.

Most of the measurements were made with a natural magnesium target, of thickness approximately 2.5 mg/cm^2, on a gold backing; a few, however, were made with separated Mg^{24}, of thickness about 100 μg/cm^2, on a tantalum backing and supplied by the Electromagnetic Separator Group, Atomic Energy Research Establishment, Harwell, England.

Preliminary experiments were first made to establish that the radiations observed came mainly from the de-excitation of the 4.24 MeV level and not the 4.12 MeV and 5.24 MeV levels. Fig. 2 shows the pulse-height distributions obtained at 5.72 MeV proton bombarding energy from the 5-inch by 6-inch crystal for the natural magnesium (curve a) and separated Mg^{24} (curve b) targets. These measurements were made with the detector at 90° to the incident beam direction. The energy scale was established with various radioactive sources including a Na^{24} source, the pulse-height distribution from which is also shown in fig. 2 (curve c). Negative β-emission from Na^{24} predominantly

feeds the 4.12 MeV level of Mg^{24} which then decays through the 1.37 MeV level. Comparison of the relative positions of the 2.75 MeV peak in curve (c) and the peak labelled (2) in curve (a) shows quite conclusively that the latter is at 2.87 MeV, and hence is from the decay of the 4.24 MeV level. Moreover, the peaks (1) and (2) are not wider than those from single energy groups. (The full width at half height of the 2.61 MeV total absorption peak from a ThC″ source for the 5-inch by 6-inch crystal has been measured to be 5.5 %). This implies

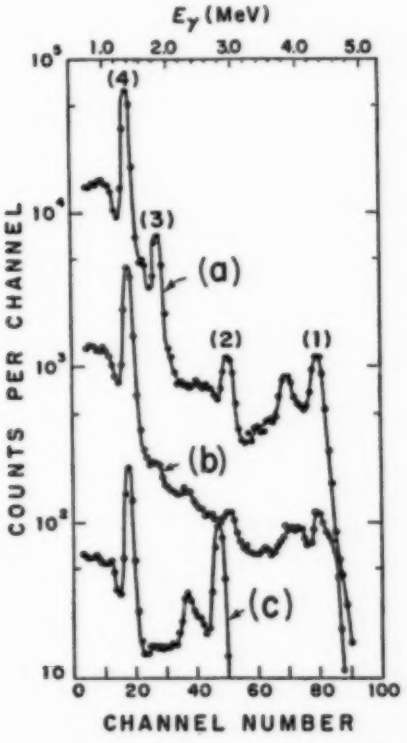

Fig. 2. Pulse height distributions from 5-inch by 6-inch crystal at $E_p = 5.72$ MeV and at 90° to the beam direction for natural magnesium target (curve a) and separated Mg^{24} target (curve b). Curve c is the distribution obtained with a Na^{24} source.

that inelastic scattering at this bombarding energy does not noticeably excite the 4.12 MeV level. There is also no suggestion of a peak at 3.87 MeV which would arise from the decay of the 5.24 MeV level through the 1.37 MeV level.

The peak labelled (3) at 1.83 MeV in curve (a) does not appear in curve (b), and is most likely due to radiation from the first excited state of Mg^{26}. The broadening of the 4.14 MeV peak in curve (b) is due to 4.43 MeV radiation from inelastic scattering by carbon, which contaminates the target. This effect is not noticeable in curve (a) because the target used is much thicker, and hence has a greater ratio of magnesium to carbon.

The yield of 4.24 MeV γ-rays was measured as a function of proton energy,

using the separated target. As seen in fig. 3, two resonances at 5.24 MeV and 5.72 MeV are seen. Strong resonances at these energies were not observed by Seward [16]) in the yield of the $Mg^{24}(p, p')Mg^{24*}$ reaction, leaving Mg^{24} in the 1.37 MeV state, although there was perhaps a slight resonance at about 5.2 MeV.

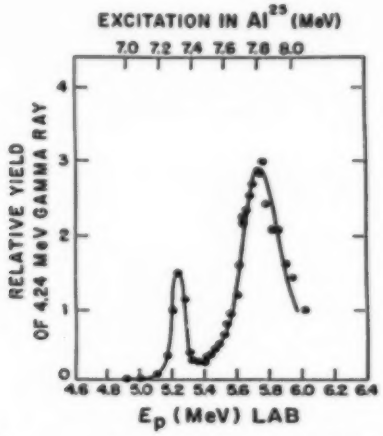

Fig. 3. The 90° yield of 4.24 MeV γ-rays obtained with separated Mg^{24} target, thickness $\approx$ 5 keV.

Angular distributions were taken on both resonances using the natural magnesium target; angular correlations of the gamma rays measured in coincidence in geometry A and B were taken at 5.72 MeV only.

3. Results

Fig. 4 shows a linear plot of the pulse-height distribution from the 5-inch by 6-inch crystal, at 90° to the incident beam direction, and at 5.72 MeV bombarding energy using the natural magnesium target. A similar curve was obtained

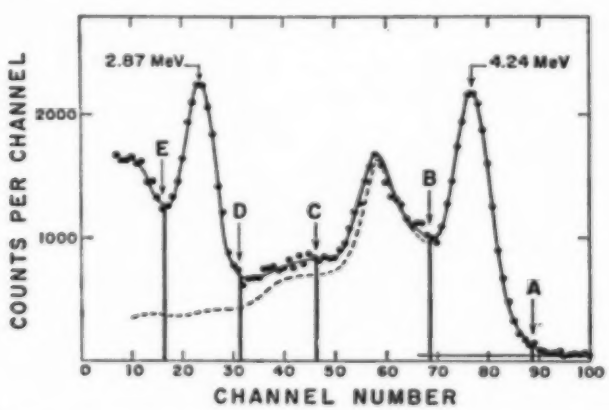

Fig. 4. Pulse height distribution from 5-inch by 6-inch crystal at $E_p = 5.72$ MeV, $\theta = 90°$. The dotted curve is the fitted line shape of the 4.24 MeV γ-ray.

with the 5-inch by 4-inch crystal. Typical coincidence spectra obtained in geometries A and B are shown in figs. 5(a) and (b). In geometry A, peaks in addition to, and at energies lower than, the 2.87 MeV peak are observed since the window around the 1.37 MeV peak in the 5-inch by 6-inch crystal includes the tails of spectra from γ-rays greater than 1.37 MeV. The peaks at 1.14 MeV and 1.83 MeV are due to cascade radiations from the second level in Mg^{26} at 2.97 MeV. In agreement with the deductions made from fig. 2 concerning the possible excitation of the 4.12 MeV level this curve shows no positive indication of a 2.76 MeV γ-ray. By comparing the peak to valley ratio of the 2.87 MeV peak in fig. 5(a) with that for a 2.61 MeV peak (obtained with a ThC'' source) we estimate an upper limit of 0.1 for the ratio of the intensities of the 2.75 MeV and 2.87 MeV γ-rays. For geometry B there is a small but significant counting rate

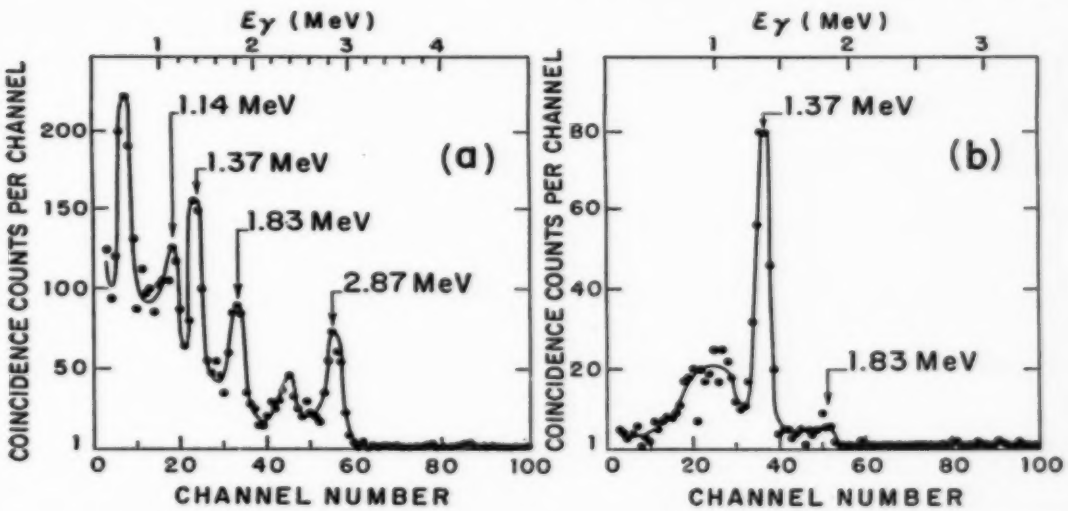

Fig. 5. Coincidence spectra at $E_p = 5.72$ MeV. (a) Geometry A. (b) Geometry B.

above background just below 2 MeV which is probably due to cascade radiation from high energy states in magnesium-26.

The angular distributions and correlations of the cascade γ-rays from the 4.24 MeV level were computed from the number of counts in the appropriate total absorption peaks in the observed spectra. In general this was relatively straightforward. For example the number of counts in the 4.24 MeV peak in the curve of fig. 4 was obtained by extrapolating the background observed beyond the peak, summing the total and background counts between the vertical lines A and B, and taking the difference. Estimation of the counts in the 2.87 MeV peak is however, much less certain, since the background to be subtracted is relatively large and cannot be measured directly. This background is made up of two contributions, that from the tail of the 4.24 MeV peak, and that from

other radiations, such as neutrons from (p, n) reactions with the target nuclei (Mg^{25}, Mg^{26} and gold), and low intensity γ-rays which are not sufficiently strong to show definite peaks (for example a 3.87 MeV γ-ray from the decay of the 5.24 MeV level).

A lower limit to the background was estimated from a measurement of the spectral line shape of a 4.43 MeV γ-ray, which is very close in energy to 4.24 MeV, and normalizing this to fit the 4.24 MeV total absorption peak. The measurement was made by bombarding a $Cu(NO_3)_2$ target, with the nitrogen enriched in N^{15}, with 3 MeV protons and observing the 4.43 MeV γ-rays emitted in the reaction $N^{15}(p, \alpha\gamma)C^{12}$. No other prominent γ-rays are produced in the reactions of protons with N^{15} at this bombarding energy. The fitted line shape is shown as the dotted curve in fig. 4.

An upper limit to the background was taken to be the sum of the counts under the full curve in fig. 4 between the vertical lines C and D, the distance between which is equal to the distance between the lines D and E encompassing the 2.87 MeV peak.

The angular distributions of the 2.87 MeV γ-rays were computed using both these background assumptions. The polynomial coefficients obtained agreed within the statistical errors and hence mean values were taken to obtain the final answers. All the experimental data pertaining to the various angular distributions and correlations, not corrected for the finite angle subtended by the detector, are presented in figs. 6 and 7 and tables 1 and 2. The experimental correlation coefficients shown in the tables were obtained by least squares fitting of the data, for even terms up to P_4, by the Chalk River Datatron computer. The errors given in tables 1 and 2 do not include (a) the effects of the small, but finite, contributions from the other magnesium isotopes and (b) the effect of the small $< 10\,\%$ contribution from the cascading gamma rays from the 4.14 MeV excited state in Mg^{24}.

Upper and lower limits for the branching ratio $I_{4.24}/I_{2.87}$ of the 4.24 MeV level have been calculated using the two background assumptions for the 2.87 MeV peak discussed above. The calculation proceeded with an area analysis of the 90° spectra recorded by the 5-inch by 4-inch crystal, the efficiency of which has been previously measured by Gove [17]), and then integration over 4π using the measured angular distribution coefficients. The correction for the difference in the attenuation of the two γ-rays by the lead shield was negligible. The values obtained are

$$\text{at } E_p = 5.72 \text{ MeV}, \quad 2.6 < \frac{I_{4.24}}{I_{2.87}} < 3.6;$$

$$\text{at } E_p = 5.24 \text{ MeV}, \quad 2.3 < \frac{I_{4.24}}{I_{2.87}} < 3.1.$$

The average value of the ratio is taken to be 2.9 ± 0.5.

4. Theoretical Analysis of the Angular Distributions and Correlations

Although a detailed theoretical treatment of the angular correlation analysis is to be found in ref. [13]), the general outline of the procedure will be discussed here.

Let J_1, J_2 and I denote the spins of the 4.24 MeV, 1.37 MeV and ground states of Mg^{24}, and let 2^{L_1}, 2^{L_2} and $2^{L_{12}}$ be the multipolarities of the 4.24 MeV, 1.37 MeV and 2.87 MeV γ-rays. Since the inelastic protons are not observed, the state J_1 is formed in an axially symmetric way. The angular distribution of the 4.24 MeV is then given by

$$W(\theta_1) = \sum_m \sum_k (-1)^{I-m+L_1+L'_1+\frac{1}{2}k} Q_k P(m) \cdot (J_1 J_1 m - m|k0) Z_1(L_1 J_1 L'_1 J_1, Ik) P_k(\cos\theta_1), \quad (1)$$

where

Q_k is an attenuation factor representing the correction to the Legendre polynomial coefficient for the finite angle subtended by the detector [18]),
$P(m)$ is the relative population of the substate m of the state J_1, and is equal to $P(-m)$,
$(J_1 J_1 m - m|k0)$ is a Clebsch-Gordan coefficient,
$Z_1(L_1 J_1 L'_1 J_1, Ik)$ is a coefficient defined and tabulated by Sharp *et al.* [19]).

The angular distribution of the 2.87 MeV γ-rays is given by an expression similar to (1) with θ_1, I and L_1 replaced by θ_{12}, J_2 and L_{12}, respectively.

The general form of an angular correlation of the γ-rays from the axially symmetric state J_1 is

$$W_{tt'}(\theta_{12}, \theta_2, \phi) = \sum_{KMN} \sum_s (-1)^{L_2+L'_2} Q_K Q_M T(s) D^N_{KM}(tt') X^N_{KM}(\theta_{12}, \theta_2, \phi). \quad (2)$$

The quantities $T(s)$ specify the alignment of the state J_1, and are related to the populations $P(m)$ by the equation

$$P(m) = \sum_s T(s)(sJ_1 m - m|l0)^2,$$

where the quantum numbers † satisfy the relation

$$\mathbf{s}+\mathbf{l} = \mathbf{J}_1.$$

The angle ϕ is the aximuthal angle of the 2.87 MeV γ-ray relative to the plane containing the beam and the 1.37 MeV γ-ray. Corrections for the finite angles subtended by the two detectors are introduced through the factors Q_K and Q_M. The coefficients $D^N_{KM}(tt')$ and $X^N_{KM}(\theta_{12}, \theta_2, \phi)$ have previously been defined by Ferguson and Rutledge [20]).

† The angular momentum quantum number l is chosen so that the $D^N_{KM}(tt')$ coefficients can be obtained from the tables of Ferguson and Rutledge [20]). For the calculations discussed in this paper it was found convenient to choose $l = J_1$.

In the correlations measured here one of the counters was fixed at 90° to the beam direction and the other moved in the plane of the beam and first counter. Hence eq. (2) can be simplified to

$$W_{tt'}(\theta) = \sum_{r}\sum_{s} T(s) A_r P_r(\cos\theta), \tag{4}$$

where

$$A_r = \sum_{KMN} \alpha^N_{rKM} Q_K Q_M D^N_{KM}(tt').$$

The coefficients α^N_{rKM} and $D^N_{KM}(tt')$ have been tabulated by Ferguson and Rutledge [20]).

In the present analysis the attenuation factors Q have been taken from calculations by Gove and Rutledge [21]) for a 5-inch by 4-inch crystal and by Rutledge [22]) for a 5-inch by 6-inch crystal. In these calculations it was assumed that all pulses produced by the γ-ray interactions in the crystal are included in the analysis of the experimental data. In the present experiments only the pulses in the total absorption peaks are computed and hence the attenuation factors used are over-estimates of the actual values. However, the overall errors introduced are small since the uncertainties in the attenuation factors represent errors in applied corrections.

Taking the spins of the 1.37 MeV and ground states of Mg^{24} as 2 and 0, respectively, we see that the unknown quantities in eqs. (1) and (4) are J_1, the multipole mixture of the 2.87 MeV transition and the quantities $T(s)$. The measured angular distribution and correlation coefficients provide sufficient data to solve for these unknowns. The analysis, in fact, proceeded by assuming a value of $J_1 = 2$ and then seeking a consistent set of theoretical fits to all the data. The observations provided 12 polynomial coefficients, and seven parameters had to be fitted. These parameters are the ratios $T(1)/T(0)$ and $T(2)/T(0)$, the quadrupole/dipole mixture of the 2.87 MeV transition, and four normalization factors, one for each correlation. The parameters occur non-linearly and the fits were effected with the assistance of the non-linear least squares sub-routine of the Chalk River Datatron.

The analysis was performed with and without the attenuation corrections Q applied and the fitted curves are shown in figs. 6 and 7. The fits using the attenuation factors appropriate to this experiment would lie between the solid (with attenuation corrections) and dashed (without attenuation corrections) curves. The theoretical polynomial coefficients (with attenuation corrections) are compared with the experimental coefficients in tables 1 and 2. For these fits the ratios $T(1)/T(0)$ and $T(2)/T(0)$ are 1.64 ± 0.06 and 0.30 ± 0.07, respectively, and the quadrupole/dipole amplitude ratio of the 2.87 MeV transition is $+23 \pm 9$. From eq. (3) the ratios $P(1)/P(0)$ and $P(2)/P(0)$ are 0.77 ± 0.06 and 0.09 ± 0.03, respectively.

Figs. 6 and 7 show that the experimental data can be fitted well with $J_1 = 2$. It is now necessary to consider if the data are consistent with other values of J_1.

Values of $J_1 = 1$ and 3 only need be considered since $J_1 = 0$ is ruled out by the observation that the state decays to the ground state, and with $J_1 > 3$, the high multipole transition to the ground state is very improbable †. To check the

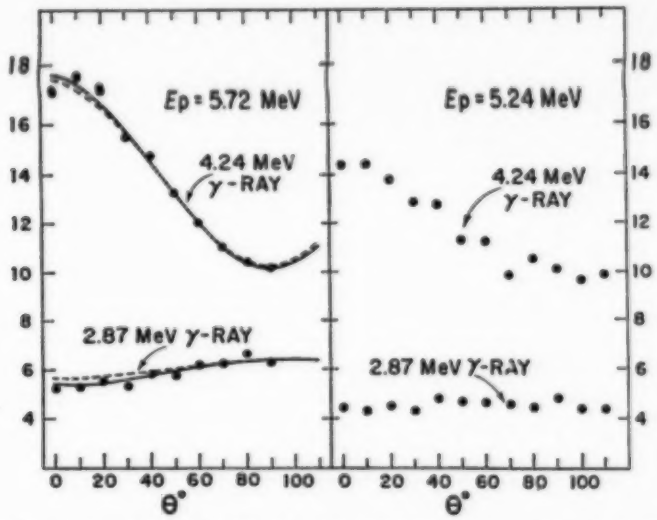

Fig. 6. Angular distributions of the 4.24 MeV and 2.87 MeV γ-rays at $E_p = 5.72$ MeV and 5.24 MeV. The solid curves are the theoretical fits for $J_1 = 2$ with corrections for finite solid angle. The dashed curves are the theoretical fits for $J_1 = 2$ without corrections for finite solid angle.

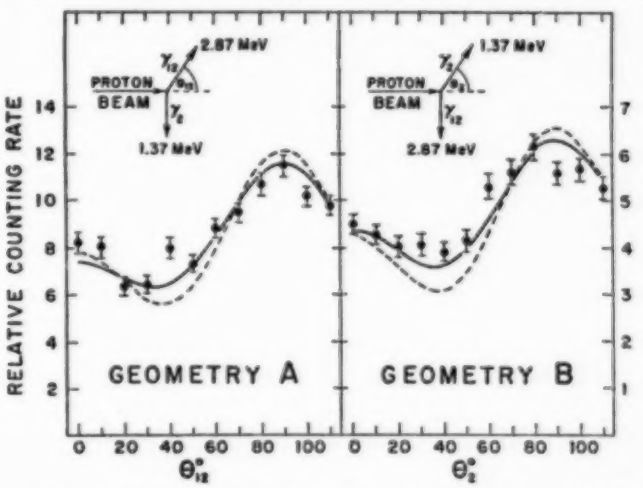

Fig. 7. Angular correlations at $E_p = 5.72$ MeV. Key for curves is similar to that for fig. 6.

consistency of the data with $J_1 = 1$ or 3, the analysis proceeded by first calculating the parameters $P(m)$ and the multipole mixture of the 2.87 MeV transition required to fit the two measured angular distribution coefficients. These calculated parameters were then substituted in eq. (4), with no attenuation corrections applied, to predict the two angular correlations. Since the multipole mixture is two valued, two sets of correlations for each value of J_1 are predicted.

† Calculations of the gamma-ray correlations from an aligned nucleus for the case $J_1 = 4$, $J_2 = 2$, $I = 0$ have been published by Cox and Tolhoek [23]).

TABLE 1
Angular distribution coefficients

E_p (MeV)	E_γ (MeV)	a_2/a_0	a_4/a_0
5.72	4.24	Expt. $+0.398\pm0.014$ Theory ($J_1 = 2$) $+0.393$	-0.013 ± 0.017 -0.002
5.72	2.87	Expt. -0.147 ± 0.015 Theory ($J_1 = 2$) -0.119	$+0.010\pm0.010$ 0
5.24	4.24	Expt. $+0.251\pm0.009$	$+0.034\pm0.018$
5.24	2.87	Expt. -0.050 ± 0.030	$+0.010\pm0.050$

TABLE 2
Angular correlation coefficients at $E_p = 5.72$ MeV

	a_2/a_0	a_4/a_0
Geometry A	Expt. -0.373 ± 0.035 Theory ($J_1 = 2$) -0.442	$+0.278\pm0.047$ $+0.292$
Geometry B	Expt. -0.285 ± 0.07 Theory ($J_1 = 2$) -0.401	$+0.169\pm0.09$ $+0.318$

TABLE 3
Predicted angular correlation coefficients for $J_1 = 1$ and 3

Geom.	J_1	E2/M1	a_2/a_0	a_4/a_0
A	1	1.31	-0.610	-0.389
B	1	1.31	-0.407	$+0.012$
A	1	0.38	-0.530	-0.082
B	1	0.38	-0.569	$+0.549$
A	3	2.33	$+0.432$	-0.200
B	3	2.33	$+0.764$	-0.239
A	3	-0.01	-0.097	0
B	3	-0.01	$+0.338$	-0.014
A (expt)			-0.373	$+0.278$
B (expt)			-0.285	$+0.169$

These are shown in table 3 and, for comparison, the experimental values are also included. Although these predicted values have been obtained without applying the attenuation corrections and also do not represent least squares fitting of the data, as in the case of $J_1 = 2$, they are sufficient to show that the data is not consistent with $J_1 = 1$ or 3. The best fits in table 3 are for $J_1 = 1$ but these have the wrong sign of the P_4 coefficient for geometry A.

5. Discussion

The results of this experiment, combined with the results of previous work (see Introduction) confirm the assignments 2+, 2+ and 0+ for the 4.24 MeV, 1.37 MeV and ground states of Mg^{24}. The feasibility of the relatively simple approach to the interpretations of triple correlations, as developed by Litherland and Ferguson, has also been demonstrated.

An interesting outcome of the theoretical analysis arises from the similarity of the angular correlations in geometry A and B. It can be shown that if $J_2 = L_2 = L_{12}$ and if $I = 0$, then the two coefficients D^N_{KM} and D^N_{MK} are equal and hence geometry A and B correlations should be identical. This was observed to be approximately the case, implying that the L_{12} radiation is predominantly E2.

The two resonances found in the yield of the 4.24 MeV γ-rays correspond to levels in Al^{25} at 7.30 ± 0.03 and 7.77 ± 0.04 MeV, respectively, taking the binding energy of the proton as 2.28 MeV. The thickness of the separated Mg^{24} target, approximately 5 keV at the bombarding energies used, is much less than the experimentally observed widths, which are 100 ± 20 keV and 340 ± 50 keV, respectively.

The tensor parameters ρ_{k0} (see for example Devons and Goldfarb[24])) describing the 4.24 MeV state can be obtained from the population of the magnetic substates from the formula

$$\rho_{k0} = \sum_m (-1)^{J_1 - m} (J_1 J_1 m - m | k0) P(m). \tag{5}$$

Using the values of $P(m)$ quoted in section 4, we find that $\rho_{20}/\rho_{00} = -0.71 \pm 0.03$ and $\rho_{40}/\rho_{00} = 0.00 \pm 0.03$.

The following argument suggests that the spin of the 7.77 MeV level of Al^{25} is most probably $\frac{3}{2}$. The tensor parameters ρ_{k0} can be derived on the assumption that the reaction proceeds through the formation of a well defined state of the compound nucleus. It can readily be shown [24]) that the expression for ρ_{k0} then contains Racah coefficients $W(l_j l_j, \frac{1}{2}k)$, where l and j are the angular momenta of the incoming proton wave and the compound state. Since only the values of ρ_{00} and ρ_{20} are significant and k is even and $\leqq 2j$, it follows that j most probably has a value $\frac{3}{2}$.

Qualitatively the data obtained in this experiment are in agreement with the collective model. If the 4.24 MeV state is assigned to be the first state of a new band with $K = 2$, magnetic dipole transitions to the $K = 0$ band should be strongly inhibited, which is in accord with experiment. However, the observed branching ratio of the 4.24 MeV state — which differs from that previously reported by Newton — is much lower than the value of 5, predicted on the collective model. It is also of interest to note that the energies of the ground state band do not accurately follow a $J(J+1)$ sequence, but this can be attributed to a vibration-rotation interaction term [2]).

The energy sequence of the ground state band can also be explained if the equilibrium shape of the nucleus is assumed to be a triaxial ellipsoid. From the ratio of the energies of the second and first 2+ states the value of γ for magnesium-24, the parameter which determines the deviation of the shape of the nucleus from axial symmetry, is calculated to be 21.9°. Using the detailed calculations of Davydov and Rostovsky [25]) the predicted value of the ratio of the energies of the 4+ and 2+ levels is 3, and this agrees very closely with the observed value.

According to Davydov and Filippov [10]) the predicted branching ratio of the E2 transitions from the 4.24 MeV state and the E2/M1 amplitude ratio of the 2.87 MeV radiation on the ellipsoidal model, are given by the following formulae:

$$\text{Branching ratio } \frac{I(4.24)}{I(2.87)} = \frac{(4.24)^5}{(2.87)^5}\,\frac{7}{20}\left[1-\frac{3-2\sin^2(3\gamma)}{\sqrt{(9-8\sin^2(3\gamma))}}\right]\left[\frac{9-8\sin^2(3\gamma)}{\sin^2(3\gamma)}\right]. \quad (6)$$

$$\text{E2/M1 amplitude ratio} = \sqrt{\frac{0.21}{80}}\,\frac{E_\gamma e Z R_0^2}{\hbar c \mu_0 g_R} \quad (7)$$

where R_0 = radius of the nucleus, μ_0 = nuclear magneton, and g_R = gyromagnetic ratio corresponding to collective motion of the nucleons in the nucleus.

From eq. (6) the calculated branching ratio is 0.88, which is lower than the observed value. From eq. (7), taking $R_0 = 1.2\,A^{\frac{1}{3}} \times 10^{-13}$ cm and $g_R = Z/A = 0.5$, the amplitude ratio is 2. Comparing this with the experimental value of 23, we see that the M1 radiation is more strongly inhibited than is suggested by the model.

To summarize, we see that although the levels of Mg^{24} are in reasonable qualitative accord with a collective model, there are serious quantitative disagreements. From the present work, it is not possible to distinguish between the axially symmetric and asymmetric models. Further information on the higher states will be of considerable interest.

The cooperation of Mr. P. G. Ashbaugh and the operating crew of the tandem accelerator is gratefully acknowledged.

Note added in proof: It has been pointed out to us by B. R. Mottelson that if one wishes to interpret the branching ratio $I(4.24/I(2.87)$ in terms of a classification based on rotational bands, one should take into account the mixing between the $K = 0$ and $K = 2$ bands. If the admixture of $K = 0$ into the $K = 2$ band were only 0.1 % in intensity the observed branching ratio of the 4.24 MeV level can be explained on the reasonable assumption that the B(E2) for a rotational transition $K = 0, I = 2$ to $K = 0, I = 0$ is about ten times that for the possibly vibrational transition $K = 2, I = 2$ to $K = 0, I = 0$. A similar situation occurs in certain rare earth nuclei [26]), in which case general expressions

for such corrections to E2 branching ratios are given. Mottelson also points out that eq. (7) is incorrect. The model of Davydov and Filippov [10]) assumes a single g-factor g_R to describe all the degrees of freedom of the nucleus and hence **u** must point in the same direction as **I**. This requires that $B(M1) = 0$ in eq. (7). However, the K-admixtures permit finite values for $B(M1)$ since the small admixing of a $K = 2, I = 2$ state into the 1.37 MeV level gives values of $B(M1; K = 2, I = 2' \rightarrow K = 2, I = 2)$ which are not K-forbidden. M1 transitions of the type $K = 0, I = 2'$ to $K = 0, I = 2$ of course do not occur. Using the measured E2/M1 amplitude, the above 0.1 % intensity for band mixing and an intrinsic quadrupole moment of 0.5×10^{-24} cm^2 he obtains $|g_K - g_R| = 0.13$ where g_K is the g-factor for the intrinsic motion of the $K = 2$ band. This interpretation of the observed branching and E2/M1 mixtures for gamma decay of the 4.24 MeV level in Mg^{24} could be checked by similar measurements on higher levels in Mg^{24} belonging to the $K = 2$ band.

References

1) P. M. Endt and C. M. Braams, Revs. Mod. Phys. **29** (1957) 683
2) A. E. Litherland, H. McManus, E. B. Paul, D. A. Bromley and H. E. Gove, Can. J. Phys. **36** (1958) 378
3) P. M. Endt and J. C. Kluyver, Revs. Mod. Phys. **26** (1954) 95
4) J. O. Newton, Phys. Rev. **96** (1954) 241 (L);
   L. Simons, Societ. Scient. Fennicae Commentationes Physico-Mathematicae **13**, no. 2 and no. 3 (1959)
5) L. E. Beghian, G. R. Bishop and H. Halban, Phys. Rev. **83** (1951) 186 (L)
6) J. M. Calvert, A. A. Jaffe, A. E. Litherland and E. E. Maslin, Proc. Phys. Soc. A **68** (1955)1008
7) M. El-Wahab, thesis, Alexandria University, Egypt (1956)
8) A. Bohr and B. R. Mottelson, Phys. Rev. **89** (1953) 316
9) P. J. Grant, J. G. Rutherglen, F. C. Flack and G. W. Hutchinson, Proc. Phys. Soc. A **68** (1955) 369
10) A. S. Davydov and G. F. Filippov, Nuclear Physics **8** (1958) 237
11) D. M. van Patter, Bull. Am. Phys. Soc. **4** (1959) 233
12) E. K. Warburton and H. J. Rose, Phys. Rev. **109** (1958) 1199
13) A. E. Litherland and A. J. Ferguson, to be published
14) D. A. Bromley, A. J. Ferguson, H. E. Gove, J. A. Kuehner, A. E. Litherland, E. Almqvist and R. Batchelor, to be published in Can. J. Phys.
15) R. E. Bell, R. Graham and H. E. Petch, Can. J. Phys. **30** (1952) 35
16) F. D. Seward, Phys. Rev. **114** (1959) 514
17) H. E. Gove and A. E. Litherland, Phys. Rev. **113** (1959) 1078
18) M. E. Rose, Phys. Rev. **91** (1953) 610
19) W. T. Sharp, J. M. Kennedy, B. J. Sears and M. G. Hoyle, Chalk River Report No. CRT-556 (1957), Chalk River, Ontario, Canada
20) A. J. Ferguson and A. R. Rutledge, Chalk River Report No. CRP-615 (1957), Chalk River, Ontario, Canada
21) H. E. Gove and A. R. Rutledge, Chalk River Report No. CRP-755 (1958), Chalk River, Ontario, Canada
22) A. R. Rutledge, Chalk River Report No. CRP-851 (1959), Chalk River, Ontario, Canada
23) J. A. M. Cox and H. A. Tolhoek, Physica **19** (1953) 1178
24) S. Devons and L. J. B. Goldfarb, Handbuch der Physik, Vol. **42** (Springer-Verlag 1957) p. 384
25) A. S. Davydov and V. S. Rostovsky, Nuclear Physics **12** (1959) 58
26) Gregers-Hansen, Nielsen and Sheline, Nuclear Physics **12** (1959) 389

2.E:2.L

Nuclear Physics **16** (1960) 52—58; © *North-Holland Publishing Co., Amsterdam*

Not to be reproduced by photoprint or microfilm without written permission from the publisher

THE ELASTIC SCATTERING OF 19 MeV DEUTERONS BY KRYPTON AND XENON

J. B. A. ENGLAND † and R. McKEAGUE ††

Physics Department, Queen's University, Belfast

and

P. E. HODGSON

Clarendon Laboratory, Oxford

Received 11 December 1959

Abstract: Experimental measurements of the elastic differential cross-sections for the scattering of 19 MeV and 19.5 MeV deuterons from krypton and xenon have been made using a nuclear emulsion plate camera. The results are compared with calculations using the optical model of the nucleus. The values of the parameters giving the best fit to the experimental results and the sensitivities of the calculated reaction cross-sections to these parameters are discussed.

1. Introduction

In earlier papers, by Gibson, Prowse and Rotblat [1]), Freemantle, Gibson, Prowse and Rotblat [2]), and Aguilar *et al.* [3]), the scattering of 9.5 MeV protons, 19 MeV deuterons and 38.5 MeV alpha-particles from the nuclei of various gaseous elements has been studied. The results of the proton and alpha-particle scattering, together with those of other workers, are most easily interpreted by the optical model and help to define the parameters of that model. More recently, the optical model has been successfully applied to deuteron scattering, by Melkanoff [4]), Slaus and Alford [5]), and Tobocman [6]).

The present work is a study of the scattering of deuterons by krypton and xenon, together with an attempt to fit the results by a simple optical model.

2. Experimental Method

The experimental technique used is that described by McKeague [7]) and by Gibson *et al.* [1]). A beam of deuterons accelerated to an energy of 20 MeV in the Nuffield cyclotron of the University of Birmingham was passed into a nuclear emulsion camera filled to a suitable pressure with the gas under study. Particles scattered from a well-defined region of the chamber were detected with Ilford C2 plates. The gas pressures used, the total beam charge collected during

† Now at Physics Department, University of Birmingham.

†† Now at Chapel Cross Works, Production Group, U.K.A.E.A..

each exposure by a Faraday cup and the mean beam energy at the scattering element are given in table 1.

TABLE 1

Energy of the incident beam, pressure of the target gas and total collected beam charge for each experiment

Target gas	Beam energy (MeV)	Pressure (cm Hg)	Total charge (μC)
Spectroscopically pure krypton	19.05±0.10	5.27	2.39
Spectroscopically pure krypton	19.59±0.15	4.63	2.20
Spectroscopically pure xenon	19.59±0.05	5.78	2.71

After processing, the plates were examined by the method described by McKeague [7]) and Gibson *et al.* [1]), and the range distributions of the observed tracks were obtained at laboratory angles between $12\frac{1}{2}°$ and 70°. Fig. 1 shows a typical range distribution histogram obtained in this way for krypton. Although it was possible to distinguish clearly between elastically and inelastically scattered particles, the number arising from inelastic processes was rather low and the statistical accuracy poor. Because of this and also because of the difficulty in assigning particles to a particular inelastic reaction, owing to the presence of a number of isotopes in each gas, no cross-sections for inelastic processes were calculated.

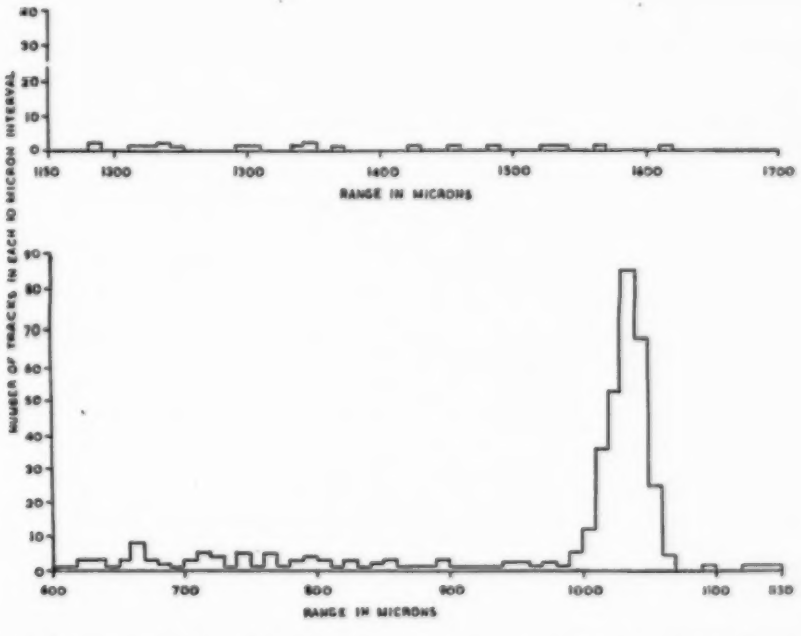

Fig. 1. Range distribution of tracks observed at a laboratory angle of 30° for the scattering of 19.5 MeV deuterons in krypton. The single group is due to elastically scattered deuterons. Other tracks are due to inelastic processes. The ranges plotted are not corrected for dip in the emulsion.

Elastic differential cross-sections were calculated from the number of tracks observed, the pressure of the gas and the total collected beam charge. Corrections were applied for background tracks originating either from inelastic (d, p) reactions or from regions of the chamber other than the scattering gap. The calibration of the current integrator described by Gibson *et al.* [1]) was checked by an independent measurement of the He^4—He^4 elastic scattering cross-section at 38.5 MeV, which was compared with the results of Burcham *et al.* [8]). A second check was provided by comparing the small angle elastic scattering cross-sections for krypton and xenon with the Rutherford cross-sections. The systematic errors in the cross-section are believed to be less than 5 %.

In each exposure the energy at the scattering gap was found from the ranges of the scattered deuterons in the emulsion. This energy is slightly less than the cyclotron energy because of the energy lost in the gas in the beam collimator and in the mica window separating the camera from the main cyclotron vacuum. Range-energy tables derived from the proton data of Gibson, Prowse and Rotblat [9]) were used, afterwards correcting for loss of energy in the gas between the scattering gap and the plates. This correction was made using absolute values of the stopping powers of the gases derived from the air curve of Livingston and Bethe [10]), which is in excellent agreement with the experimental values of Brolley and Ribe [11]).

3. Experimental Results

The experimental elastic differential cross-sections for deuterons of 19 MeV and 19.5 MeV on krypton and of 19.5 MeV on xenon are shown in figs. 2 and 3. The different energies were not chosen deliberately but were the result of using different thicknesses of mica in the camera window in two sets of experiments. The results are compared with the angular distributions obtained from an optical model analysis described in the next section.

The results show diffraction maxima and minima but these are not so pronounced as those obtained for 19 MeV deuterons on oxygen by Freemantle *et al.* [2]) and for protons of the same velocity by Gibson *et al.* [1]). Similar diffraction patterns have been found by Yntema [12, 13]) using 21.6 MeV deuterons and by Fischer *et al.* [14]) using 21 MeV deuterons.

The experimental cross-sections for krypton at 19 MeV and 19.5 MeV are generally quite similar but differ from each other in detail more than the corresponding theoretical curves in which all the parameters except the energy are kept the same. This may be due to a strong energy dependence of the cross-section such as has been found for carbon with protons of 9.5 MeV by Gibson *et al.* [1]). A careful check of experimental measurements revealed no additional errors which would have produced this effect.

No strong variation with energy was observed for xenon. The results of a preliminary experiment at 19 MeV show no significant differences from the results at 19.5 MeV and are not quoted here.

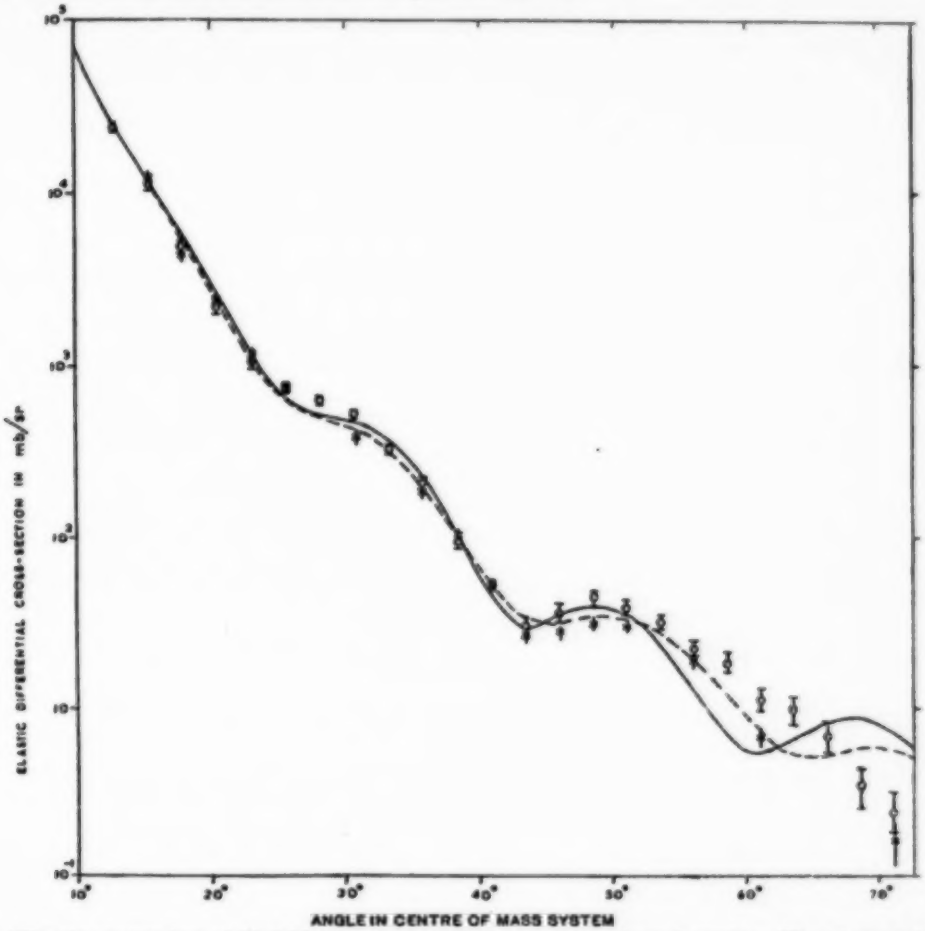

Fig. 2. Elastic scattering of 19.0 MeV and 19.5 MeV deuterons from krypton. The observed cross-sections for the centre of mass system are plotted as functions of the centre of mass angle. The experimental results are compared with calculations based on the optical model using the values of the parameters shown in table 2.

19.0 MeV: ⊼ experimental (McKeague), ——— theoretical (Hodgson); total theoretical reaction cross-section 1.698b.

19.5 MeV: ⊙ experimental (England), – – – theoretical (Hodgson); total theoretical reaction cross-section 1.711 b.

4. Optical Model Analysis

The scattering process may be calculated on the optical model if the nuclear interaction is represented by a complex potential with both absorbing and refracting parts $V(r) = U(r)+iW(r)$. Each part may be conveniently written as the product of a potential depth and a radial variation of the Saxon-Woods form with a nuclear radius $R = r_0 A^{\frac{1}{3}}$ and a parameter a determining the diffuseness of the nuclear surface. The same radial variation was used for the absorbing part $W(r)$. No account was taken of the deuteron spin.

For an assumed potential, the differential and reaction cross-sections can be found from a numerical solution of the Schrödinger wave equation. The radial wave equation was integrated outwards for each partial wave by the

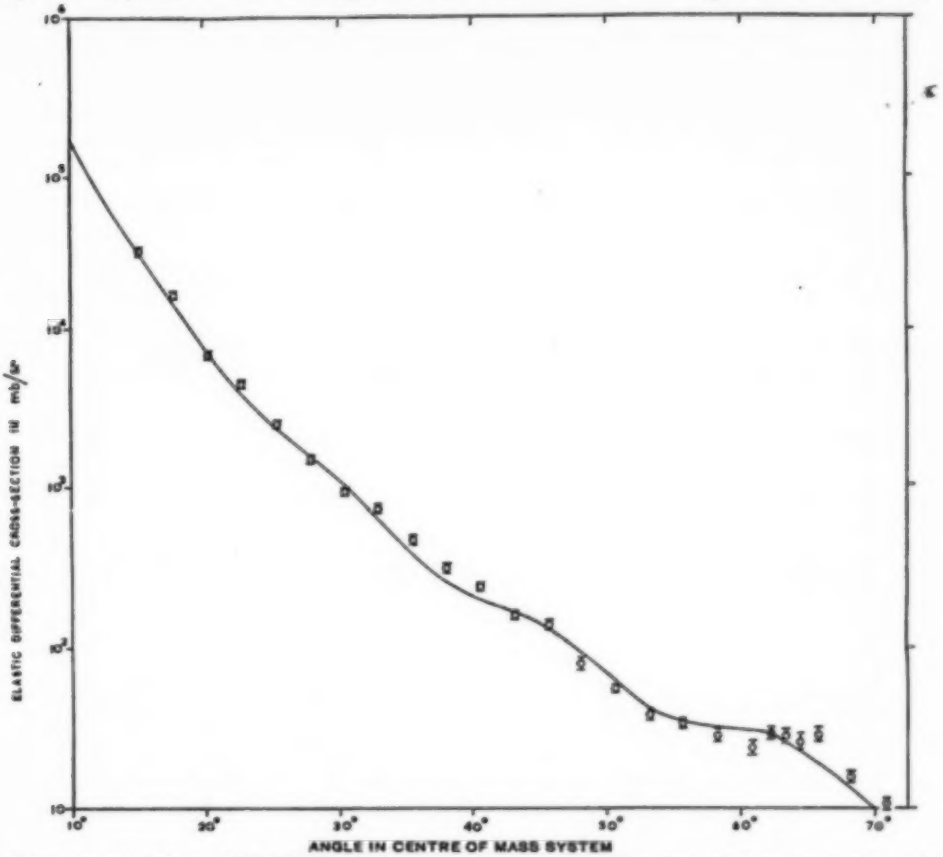

Fig. 3. Elastic scattering of 19.5 MeV deuterons from xenon. The observed cross-sections for the centre of mass system are plotted as functions of the centre of mass angle. The experimental results are compared with calculations based on the optical model using the values of the parameters shown in table 2.

$\overline{\underline{\phi}}$ experimental (England), ——— theoretical (Hodgson); total theoretical reaction cross-section 2.043b.

Runge-Kutta method until the nuclear field became negligible. The internal wave functions found in this way were smoothly joined to the external Coulomb wave functions by the method of Jones [15]). This gives the complex element of the scattering matrix for each partial wave.

The total reaction cross-sections, the differential cross-section, the real and imaginary parts of the scattering matrix and the absorption cross-section for each partial wave were obtained for each set of parameters. The whole calculation was carried out on the Oxford Ferranti Mercury Computer.

The fits were obtained by calculating the cross-section for a trial set of parameters, and then varying them systematically until a reasonable fit was

obtained. Better fits than those shown could certainly be obtained by a more thorough exploration of the six-parameter space, but this was not considered worthwhile until the effects of deuteron spin are taken into account and more is known about the cross-section at higher angles.

5. Discussion

The parameters for the best fits are given in table 2. The values of U are rather lower than would be expected from the results of Melkanoff [4]) and Slaus *et al.* [5]) for other nuclei. Unsuccessful attempts were made to obtain a reasonable fit for higher values of U. The rather large values of r_0, in agreement with those of Melkanoff and Slaus, take account of the diffuseness of the loosely bound

TABLE 2

Best fit optical model parameters for the elastic scattering of deuterons

Element	Energy	U	W	r_0	a	l_{max}
Kr	19.0	−35	−15	1.50	0.6	13
Kr	19.5	−35	−15	1.50	0.6	13
Xe	19.5	−40	−13	1.55	0.6	14

All energies are in MeV and lengths in 10^{-13} cm, l_{max} is the highest l-value considered.

deuteron compared with the compact proton and alpha-particle. The calculated cross-sections are very insensitive to the optical model parameters for small scattering angles, where the Coulomb field predominates. The good agreement with experiment in this region is thus a confirmation of the absolute calibration of the experimental results.

TABLE 3

Dependence of the reaction cross-section σ_R on r_0 for krypton. $W = -15$ MeV, $a = 0.6 \times 10^{-13}$ cm

U	r_0	σ_R	σ_R/r_0^2
−35	1.60	1915.6	749
−37.5	1.55	1819.9	758
−40	1.50	1724.6	767

It is likely that measurements will soon be made of the reaction cross-sections in deuteron scattering, using the technique of Eisberg and Gooding [16]). This makes it useful to study the sensitivity of the reaction cross-section to the optical model parameters. A point of particular interest is whether it could resolve the Ur_0^2 ambiguity. Several calculations were made for krypton with the same value of Ur_0^2 and, as shown in table 3, the reaction cross-section is roughly proportional to r_0^2, as might have been expected, showing that a

measurement of the reaction cross-section can determine r_0 alone and hence resolve the ambiguity. The variation of the reaction cross-section with each parameter in turn is given in table 4. This shows that it is relatively insensitive to U and W but depends strongly on r_0 and a.

TABLE 4

Sensitivity of the reaction cross-section σ_R to small variations in the optical model parameters.

Element	$\delta\sigma_R/\delta U$ (mb · MeV^{-1})	$\delta\sigma_R/\delta W$ (mb · MeV^{-1})	$\delta\sigma_R/\delta r_0$ (mb · 10^{13} cm^{-1})	$\delta\sigma_R/\delta a$ (mb · 10^{13} cm^{-1})
Kr	−2	−5	2200	1750
Xe	−5	−3	2400	1950

We would like to express our thanks to Professor G. E. Brown, Professor W. E. Burcham, F.R.S., and Professor D. H. Wilkinson, F.R.S., for valuable discussions, to Dr. L. Fox, Director of the Oxford University Computing Laboratory, for permitting us to use the Mercury computer, to Dr. W. M. Gibson and Dr. D. J. Prowse for assistance in the experimental work, to Mrs. D. E. Anderson, Mrs. S. E. Baker, Miss M. Crozier, Mrs. K. W. Foster and Mrs. B. R. Stephens for the microscope work and to Miss N. Reynolds, Miss S. Tilley and the staff of the Computing Laboratory for constant assistance.

References

1) W. M. Gibson, D. J. Prowse and J. Rotblat, Proc. Roy. Soc. **243** (1957) 237
2) R. G. Freemantle, W. M. Gibson and D. J. Prowse, Phys. Rev. **92** (1953) 1268
3) J. Aguilar, W. E. Burcham, J. Catala, J. B. A. England, J. S. C. McKee and J. Rotblat, Proc. Roy. Soc. (1960) (in print)
4) M. A. Melkanoff. Proc. Florida Optical Model Conference (1959) p. 207
5) I. Slaus and W. P. Alford, Phys. Rev. **114** (1959) 1054
6) W. Tobocman, Proc. Florida Optical Model Conference, p. 123 (1959)
7) R. McKeague, Ph. D. thesis, Queen's University, Belfast (1956)
8) W. E. Burcham, W. M. Gibson, D. J. Prowse and J. Rotblat, Nuclear Physics **3** (1957) 217
9) W. M. Gibson, D. J. Prowse and J. Rotblat, Nature **173** (1954) 1180
10) M. S. Livingston and H. A. Bethe, Revs. Mod. Phys. **9** (1937) 265
11) J. E. Brolley and F. L. Ribe, Phys. Rev. **98** (1955) 1112
12) J. L. Yntema, Phys. Rev. **113** (1959) 261
13) J. L. Yntema, Phys. Rev. **114** (1959) 820
14) G. E. Fischer and U. K. Fischer, Phys. Rev. **114** (1959) 533
15) P. B. Jones, private communication (1958)
16) R. M. Eisberg and T. J. Gooding Phys. Rev. **105** (1957) 357

1.B:8.B

Nuclear Physics **16** (1960) 59—71; © *North-Holland Publishing Co., Amsterdam*

Not to be reproduced by photoprint or microfilm without written permission from the publisher

MESON CAPTURE IN He^3

CARL WERNTZ

Institut für theoretische Physik, Heidelberg, Germany †

Received 3 August 1959

Abstract: The effective Hamiltonian of Fujii and Primakoff [1,2]) is used to calculate the capture rate $w^{(s)}$ of μ^- mesons by He^3 leading to the bound state of H^3. The ground state of the three-body nucleus is taken to be a state with total angular momentum $\frac{1}{2}$ and isobaric spin $\frac{1}{2}$ with a small D-state admixture to the predominant S-state. The dependence of the capture rate on the percentage of D-state admixture and on the r.m.s. radius of the nucleus is found. A calculation of the r.m.s. radius using S-state wave functions derived from hard core potentials leads to values of $w^{(s)}$ 7 % to 10 % higher than that calculated by Fujü and Primakoff.

1. Introduction

The determination of the V—A character of both μ decay and β decay during the past two years has renewed interest in the universal Fermi interaction [3–6]). Undoubtedly, the least well known special case of this interaction has been the process of μ capture. Tiomno and Wheeler [7]) were the first to show that with the assumption of a β-decay type interaction the coupling constants are of the same order of magnitude as the β-decay constants. Two difficulties hindering a precise determination of the coupling constants are (1) the presence of very large nuclear finite size effects and (2) the fact that the large rest mass of the meson permits the final nuclear state to be any one of a large number of excited states in addition to the ground state. Owing to the latter circumstance, it is difficult experimentally to measure the transition rate for a single pair of initial and final states, while a much better theoretical estimate can be made of this quantity than of the total rate to all energetically possible final states. However, Tolhoek [8]) has used shell model wave functions to analyze the μ capture data for medium weight nuclei and finds that the absolute capture rates and the ratios of capture rates indicate a Gamow-Teller coupling constant for μ capture somewhat larger than that for β-decay, but approximately equal values of the Fermi constants.

Similar results have been obtained by an analysis of a repetition [9]) of Godfrey's experiment [10]) on the rate ratio $(C^{12}+\mu^-\rightarrow B^{12}+\nu)/(B^{12}\rightarrow C^{12}+e^-+\bar{\nu})$. Aside from nuclear size effects the nuclear matrix elements are the same in both reactions so that the rate ratio provides a good opportunity to calculate

† Present address: School of Physics, University of Minnesota, Minneapolis, Minnesota, U.S.A.

$[g_A(\mu\text{-capture})/g_A(\beta\text{-decay})]^2$. The authors give the value of 1.37 ± 0.08 for this ratio.

A direct measurement of the fundamental process could be made by observing the capture of μ^- in hydrogen [11]). However, the capture rate is extremely small and the final neutrons hard to observe so that the experiment is at present not possible. The capture rate in He^3 is higher, the final H^3 nucleus has no excited states, and H^3 could be detected by means of its β-decay activity †. What is involved theoretically is the evaluation of the Fermi and Gamow-Teller matrix elements for a transition between ground states of two relatively simple nuclei. The chief purpose of this paper is to evaluate the dependence of the nuclear matrix elements on the percentage of D-state admixture and on the r.m.s. radius of the three-body system.

2. Interaction Hamiltonian

The interaction Hamiltonian is taken to be the effective Hamiltonian

$$H_{\text{eff}} = \tfrac{1}{2}(1-\boldsymbol{\sigma}\cdot\boldsymbol{\nu}_1)\sum_{i=1}^{A}\tau_i^{(-)}\{G_V^{(\mu)}\mathbf{1}\cdot\mathbf{1}_i+G_A^{(\mu)}\boldsymbol{\sigma}\cdot\boldsymbol{\sigma}_i-G_P^{(\mu)}\boldsymbol{\sigma}\cdot\boldsymbol{\nu}_1\boldsymbol{\sigma}_i\cdot\boldsymbol{\nu}_1\}\delta(\mathbf{r}-\mathbf{r}_i), \quad (1)$$

discussed and used by Fujii and Primakoff [1]) and by Primakoff [2]) in their extensive calculations on the μ capture problem. This effective Hamiltonian corresponds, in a non-relativistic approximation for the meson and the nucleons, to a general transition matrix for the process $\mu^-+p\rightarrow n+\nu$ derived from certain invariance principles [3, 4]) and with the restrictions that the lepton-bare nucleus interaction be V and A and that the neutrinos be emitted with negative helicity. The numerical relationships between the vector coupling constant $G_V^{(\mu)}$, the axial vector coupling constant $G_A^{(\mu)}$, and the pseudoscalar coupling constant $G_P^{(\mu)}$, and the renormalized β-decay coupling constants $g_V^{(\beta)}$ and $g_A^{(\beta)}$ have been taken over from the work of several authors [4, 5, 6]) on the effects of the strong interactions on the universal Fermi interaction. The other symbols in the definition (1) are as follows: $\hbar\boldsymbol{\nu}=\hbar\nu\boldsymbol{\nu}_1$ is the neutrino momentum; $\mathbf{1}$, $\mathbf{1}_i$ and $\boldsymbol{\sigma}$, $\boldsymbol{\sigma}_i$ are 2×2 matrix unit and spin operators for the lepton and the ith nucleon; $\mathbf{r}$ and $\mathbf{r}_i$ are the spatial coordinates of the lepton and the ith nucleon; $\tau_i^{(-)}$ is an isobaric spin operator for the ith nucleon which yields zero when acting upon the wave function of a neutron and changes a proton function into a neutron function.

With this Hamiltonian, the transition probability for the capture of a bound S-state μ^- and the emission of a neutrino with wave vector $\boldsymbol{\nu}$ is

† In a private communication to J. H. D. Jensen, G. Goldhaber states that there is a possibility that the experiment can be performed and that the theoretical treatment should be on a much firmer basis than for heavier nuclei.

$$dw^{(\mu)} = \tfrac{1}{2}\pi^2 (G_V^{(\mu)})^2 (\tfrac{1}{137} ZM'_\mu) \times 1/\hbar^7 E_\nu^2 (1 - E_\nu/Mc^2)$$
$$\{\tfrac{1}{2} \sum_{m,m'=-\frac{1}{2}}^{+\frac{1}{2}} [| \sum_{j=1}^{3} \langle \Psi^{m,-\frac{1}{2}} | \varphi(\mathbf{r}_j) \exp -i\boldsymbol{\nu} \cdot \mathbf{r}_j \tau_j^{(-)} | \Psi^{m,+\frac{1}{2}} \rangle|^2 \qquad (2)$$
$$+ (\Gamma^{(\mu)})^2 | \sum_{j=1}^{3} \langle \Psi^{m;-\frac{1}{2}} | \varphi(\mathbf{r}_j) \exp -i\boldsymbol{\nu} \cdot \mathbf{r}_j \tau_j^{(-)} \sigma_j | \Psi^{m,+\frac{1}{2}} \rangle|^2]\}$$

The ratio $\Gamma^{(\mu)}$ of the effective Gamow-Teller coupling constant to the effective Fermi coupling constant is given in terms of the G's by

$$(\Gamma^{(\mu)})^2 = \frac{(\Gamma_A^{(\mu)})^2}{(G_V^{(\mu)})^2} = \frac{(G_A^{(\mu)})^2 + \frac{1}{3}((G_P^{(\mu)})^2 - 2(G_A^{(\mu)})(G_P^{(\mu)}))}{(G_V^{(\mu)})^2}.$$

In addition, M is the mass of the final nucleus H^3; $M'_\mu = M_\mu/[1+(M_\mu/M)]$ is the reduced mass of the meson; E_ν is the energy of the neutrino in the laboratory system; $\varphi(\mathbf{r})$ is the wave function of the S-state meson, which for small distances takes the form $\varphi(r) \approx \exp -r/D$, with $D = \hbar/ZM'_\mu e^2$; $\Psi^{m;\pm\frac{1}{2}}$ is the nuclear wave function with z-component of angular momentum m' and z-component of isobaric spin $\pm\frac{1}{2}$. It is important to mention that both eq. (1) and eq. (2) take account of first order nucleon recoil, that is, terms of the order $E/m_p c^2$ are included.

3. D-State Effect

The problem at hand is to evaluate the nuclear matrix elements. Since $J = \frac{1}{2}$, the ground state of the three body system is expected to be a mixture of S, P, and D-states with symmetric S-state predominating. Variational calculations [12]) in the past have shown that good values of the binding energies may be obtained by using only combinations of the S- and D-states. Therefore, only S- and D-states are taken into account here and, explicitly, the two S-states, $\psi_{1,2}^{m,t}$, and three D-states $\psi_{6,7,8}^{m,t}$ which are listed in Sachs [13]):

$$\Psi^{m,t} = \sum_{i=1}^{2} S_i \psi_i^{m,t} + \sum_{i=6}^{8} D_i \psi_i^{m,t}. \qquad (3)$$

There should be no other S- or D-state functions which are linearly independent of the above sets of functions. It was convenient to use the functions given by Sachs since they contain isobaric spin variables and are completely anti-symmetric in the exchange of any two nucleons.

The exponential function of the neutrino is most easily handled by using Bauer's formula to expand it in terms of spherical Bessel functions. Because of the complete anti-symmetry of the wave functions of the initial and final nuclei it is possible to eliminate the sum over j in eq. (2) and replace it by a single term, $j = 3$. The factor in (2) which is enclosed in parentheses becomes

$$\begin{aligned}\tfrac{9}{2}(4\pi)^2 \sum_{m,m=-\frac{1}{2}}^{+\frac{1}{2}} \sum_{L,L'} \sum_{M,M'} i^{(L-L')}\, Y_{L'}^{*M'}(\theta_\nu\varphi_\nu) \\ \times Y_L{}^{M}(\theta_\nu\varphi_\nu)\{\langle\Psi^{m,-\frac{1}{2}}|j_L{}^{*}(\nu r_3)\exp(-r_3/D)Y_L{}^{*M}(\theta_3\varphi_3)\tau_3{}^{(-)}|\Psi^{m,+\frac{1}{2}}\rangle \\ \times\langle\Psi^{m,+\frac{1}{2}}|j_{L'}(\nu r_3)\exp(-r_3/D)Y_{L'}^{M'}(\theta_3\varphi_3)\tau_3{}^{(-)}|\Psi^{m,-\frac{1}{2}}\rangle \\ +(\Gamma^{(\mu)})^2\langle\Psi^{m,-\frac{1}{2}}|j_L{}^{*}(\nu r_3)\exp(-r_3/D)Y_L{}^{M*}(\theta_3\varphi_3)\tau_3{}^{(-)}\sigma_3\cdot|\Psi^{m,+\frac{1}{2}}\rangle \\ \times\langle\Psi^{m,+\frac{1}{2}}|j_{L'}(\nu r_3)\exp(-r_3/D)Y_{L'}^{M'}(\theta_3\varphi_3)\tau_3{}^{(-)}\sigma_3|\Psi^{m,-\frac{1}{2}}\rangle\};\end{aligned} \tag{4}$$

θ_ν and φ_ν specify the direction of ν and the factor 9 comes from replacing the sum over j by one term.

In the sum over L and L' all cross terms yield zero upon averaging over the directions of the neutrino. Because of the even parity of the S and D-states the lowest order terms which appear are $L = L' = 0$ and $L = L' = 2$. In the latter, the coefficients of the D-state, the D_i's, appear to the fourth power. In addition, the leading term in $j_2(\nu r_3)$ contains a factor $\frac{1}{15}$ so that the $L = L' = 2$ term is considerably less than 1 % of the $L = L' = 0$ term and may safely be neglected. Upon averaging over all neutrino directions and substituting eq. (3) into (4), the nuclear factor becomes

$$\begin{aligned}\tfrac{9}{2}\sum_{m,m=-\frac{1}{2}}^{+\frac{1}{2}}\{|\sum_{i=1}^{2} S_i{}^2\langle\psi_i{}^{m,-\frac{1}{2}}|j_0(\nu r_3)\exp(-r_3/D)\tau_3{}^{(-)}|\psi_i{}^{m,+\frac{1}{2}}\rangle \\ +\sum_{i=6}^{8} D_i{}^2\langle\psi_i{}^{m;-\frac{1}{2}}|j_0(\nu r_3)\exp(-r_3/D)\tau_3{}^{(-)}|\psi^{m,+\frac{1}{2}}\rangle|^2 \\ +(\Gamma^{(\mu)})^2|\sum_{i=1}^{2} S_i{}^2\langle\psi_i{}^{m;-\frac{1}{2}}|j_0(\nu r_3)\exp(-r_3/D)\tau_3{}^{(-)}\sigma_3|\psi_i{}^{m,+\frac{1}{2}}\rangle \\ +\sum_{i=6}^{8} D_i{}^2\langle\psi_i{}^{m;-\frac{1}{2}}|j_0(\nu r_3)\exp(-r_3/D)\tau_3{}^{(-)}\sigma_3|\psi_i{}^{m,+\frac{1}{2}}\rangle|^2\}.\end{aligned} \tag{5}$$

The expectation values of $j_0(\nu r_3)\tau_3{}^{(-)}$ and $j_0(\nu r_3)\tau_3{}^{(-)}\sigma_3$ can be evaluated very simply (see Appendix A) and the result is

$$\begin{aligned}\{1|\langle\Psi|j_0(\nu r_3)\exp-(r_3/D)|\Psi\rangle|^2+3(\Gamma^{(\mu)})^2|\langle\Psi|j_0(\nu r_3)\exp(-r_3/D)|\Psi\rangle \\ -\tfrac{2}{3}\sum_{i=6}^{8} D_i{}^2\langle\psi_i|j_0(\nu r_3)\exp(-r_3/D)|\psi_i\rangle|^2\}.\end{aligned} \tag{6}$$

On account of the very small value of all the $D_i{}^2$ the above expression can be very nearly approximated by

$$\begin{aligned}[1+3(\Gamma^{(\mu)})^2]|\langle\Psi|j_0(\nu r_3)\exp(-r_3/D)|\Psi\rangle|^2 \\ \times\left[1-\frac{4(\Gamma^{(\mu)})^2}{1+3(\Gamma^{(\mu)})^2}\sum_{i=6}^{8}\frac{D_i{}^2\langle\psi_i|j_0(\nu r_3)\exp(-r_3/D)|\psi_i\rangle}{\langle\psi|j_0(\nu r_3)\exp(-r_3/D)|\psi\rangle}\right].\end{aligned} \tag{7}$$

The ratio $\langle\psi_i|j_0(\nu r_3)\exp(-r/D|\psi_i\rangle/\langle\Psi|j_0(\nu r_3)\exp(-r/D|\Psi\rangle$ should be within 5 % of unity, and therefore expression (7) can be further simplified to

$$[1+3(\Gamma^{(\mu)2}][|\langle\psi|j_0(\nu r_3)\exp(-r_3/D)|\psi\rangle|^2]\times\left[1-\frac{4(\Gamma^{(\mu)})^2}{1+3(\Gamma^{(\mu)})^2}\sum_{i=6}^{8} D_i{}^2\right]. \tag{8}$$

The latter sum is the total D-state admixture to the ground state.

Retaining the first three terms of $j_0(\nu r_3)$ and the first two terms in $\exp(-r_3/D)$ the expectation value of $j_0(\nu r_3)\exp(-r_3/D)$ is

$$\langle\Psi|j_0(\nu r_3)\exp(-r_3/D)|\Psi\rangle = 1-\tfrac{1}{6}\nu^2\overline{r_3^2}+\tfrac{1}{120}\gamma_4\nu^4(\overline{r_3^2})^2-(1/D)[\gamma_1(\overline{r_3^2})^{\frac{1}{2}}-\tfrac{1}{6}\gamma_3\nu^2(\overline{r_3^2})^{\frac{3}{2}}]. \quad (9)$$

The γ_n's are defined the same way as in Fujii and Primakoff [1]):

$$\overline{r_3^n} = \gamma_n[\overline{r_3^2}]^{\frac{1}{2}n}. \quad (10)$$

They were approximated by defining $\overline{r_3^n}$ as

$$\overline{r_3^n} = \frac{\int \exp(-\alpha r_3) r_3^{n+2}\mathrm{d}r}{\int \exp(-\alpha r_3) r_3^2\mathrm{d}r} \quad (11)$$

and adjusting α so that $\overline{r_3^2}$, the square of the r.m.s. radius of the nucleus, had the desired value.

According to eqs. (8) and (9), the nuclear matrix elements can be calculated to about 1 % accuracy from a knowledge of the r.m.s. radius of the three-body nucleus and the percentage of D-state present. Electron scattering experiments on He^3 have not yet been performed, and estimates of the r.m.s. radius must therefore be derived from wave functions obtained in calculations of the binding energy of H^3 made with reasonable potentials. Two sets of wave functions derived from hard core potentials have been used to estimate the r.m.s. radius and the results are discussed in the next section. Since tensor forces were neglected, these wave functions consist of S-state functions alone, so that values of D_i^2 could not be inserted.

4. Numerical Results

Restricting ourselves to S-state wave functions, eqs. (2) and (7) may be combined to give

$$w(\mu) = C(1+3(\Gamma^{(\mu)})^2)|\langle\Psi|j_0(\nu r_3)\mathrm{e}^{-r_3/D}|\Psi\rangle|^2,$$
$$C = \tfrac{1}{2}\pi^2(G_\nu^{(\mu)})^2(\tfrac{1}{137}ZM_\mu)^3\times(1/\hbar^7)E_\nu^2(1-E_\nu/Mc^2). \quad (12)$$

The neutrino energy E_ν is given by

$$E_\nu = \{[M_p-M_n+M_\mu]c^2+\Delta\ \text{b.e.}\}\times[1-M_\mu/2(M_\mu+M)] = 103.2\ \text{MeV}. \quad (13)$$

In the above equation, obtained from energy and momentum conservation, the difference between the binding energies of H^3 and He^3, $\Delta_{\text{b.e.}}$, as well as the binding energies themselves have been neglected in the recoil correction term, $[1-M_\mu/2(M_\mu+M)]$. The binding energy of the meson has been neglected in

the first factor. Taking the same values for the constants as Fujii and Primakoff,

$$[G_V^{(\beta)}/g_V^{(\beta)}] = 1.04, \qquad [\Gamma_A^{(\beta)}/G_V^{(\beta)}]^2 = 1.04,$$
$$g_V^{(\beta)} = 1.40\times 10^{-49}\ \text{erg}\cdot\text{cm}^3, \qquad [g_A^{(\beta)}/g_V^{(\beta)}] = -1.21, \tag{14}$$

one finds

$$C[1+3(\Gamma^{(\beta)})^2] = 1.96\times 10^3\ \text{sec}^{-1}.$$

It is generally convenient to have $j_0(\nu r_3)$ expressed as a function of relative coordinates. To this end relative and centre of mass coordinates are introduced:

$$\mathbf{R} = \tfrac{1}{3}(\mathbf{r}_1+\mathbf{r}_2+\mathbf{r}_3), \qquad \mathbf{r}_{ij} = \mathbf{r}_i-\mathbf{r}_j, \qquad \mathbf{r}_3 = \mathbf{R}-\tfrac{1}{3}(\mathbf{r}_{13}+\mathbf{r}_{23}). \tag{15}$$

The $\mathbf{r}_3$ appearing hithertofore in our equations has been implicitly assumed to have the centre of mass of the nucleus as its origin. For shell model wave functions the centre of mass is not generally the origin of the coordinates, so that $\mathbf{r}_3$ should everywhere be replaced by $\mathbf{r}_3-\mathbf{R}$. Owing to the antisymmetry of the wave functions it is easy to show that

$$\overline{r_3^2} \to \overline{(\mathbf{r}_3-\mathbf{R})^2} = r_{\text{r.m.s.}}^2 = \tfrac{1}{3}\overline{r_{12}^2}. \tag{16}$$

The first wave function used in evaluating $r_{\text{r.m.s.}}^2 \equiv \frac{1}{3}\overline{r_{12}^2}$ is that obtained by Kikuta, Morita and Yamada [14]). Their potential had the form

$$V_{ij} = \tfrac{1}{4}(3+\sigma_i\cdot\sigma_j)V_t(r_{ij})+\tfrac{1}{4}(1-\sigma_i\cdot\sigma_j)V_s(r_{ij}) \quad \text{for} \quad r_{ij} \geqq d,$$
$$V_{ij} = +\infty \quad \text{for} \quad r_{ij} < d; \tag{17}$$
$$V_{t,s}(r_{ij}) = -A_{t,s}\exp(-\alpha_{t,s}r_{ij}) \quad (r_{ij} \geqq d).$$

The parameters in the potential were obtained from the binding energy of the deuteron and n–p low energy scattering data. Because of uncertainties in the singlet n–p effective range r_{0s}, two different values were chosen as reasonable which led to two slightly different potentials. In addition, the parameter d was given a number of different values, the other parameters being adjusted accordingly. With a trial wave function of the spatial form

$$\varphi(123) = N\prod_{i<j=1}^{3}[\exp[-\mu(r_{ij}-d)]-\exp[-\nu(r_{ij}-d)] \quad \text{for} \quad \text{all } r_{ij} \geqq d$$
$$= 0 \text{ otherwise}, \tag{18}$$

the minimum energy was calculated as a function of μ and ν. The best results were obtained for $d = 0.4\times 10^{-13}$ cm and the energies and minimizing parameters are listed in table 1.

The two sets of minimizing parameters were used to calculate $\overline{r_{12}^2}$ (see Appendix B) and through eqs. (9) and (12) the capture rate (table 2).

TABLE 1

The two best solutions

$r_{ss}(10^{-13}$ cm)	$\mu(10^{13}$ cm$^{-1})$	$\nu(10^{13}$ cm$^{-1})$	b.e. H^3 (MeV)	Δb.e.(H^3-He^3) (MeV)
2.7	0.4415	4.100	6.49	0.729
2.4	0.4811	4.230	7.65	0.777
		Experimental	8.49	0.764

TABLE 2

Capture rates

$\mu(10^{13}$ cm$^{-1})$	$\nu(10^{13}$ cm$^{-1})$	$r_{\text{r.m.s.}}(10^{-13}$cm)	Capture rate (sec^{-1})
0.4415	4.100	1.55	1.56×10^{-3}
0.4811	4.230	1.45	1.60×10^{-3}

Mang and Wild [15]) have obtained wave functions and energies of the three and four body nuclear systems by adapting to the three and four body problems a method due to Brenig [16]) of treating the many body problem. Essentially, they have obtained approximations to the one and two particle projections of the actual wave function of H^3 onto a set of appropriately chosen single particle oscillator functions. The potential they used was a square well, hard core, central potential with the singlet and triplet forces chosen to be equal.

In the independent particle approximation the special wave functions of the ground state of He^3 can be represented by

$$\Psi \approx \varphi(\mathbf{r}_1)\varphi(\mathbf{r}_2)\varphi(\mathbf{r}_3). \tag{20}$$

The φ's are of the form $\exp(-\alpha r_i^2)$ and from the value of α given by the authors $r^2_{\text{r.m.s.}}$ was calculated.

In the independent pair approximation the spatial part of the wave function is given by

$$\Psi \approx \frac{\psi(\mathbf{r}_1, \mathbf{r}_2)\psi(\mathbf{r}_2, \mathbf{r}_3)\psi(\mathbf{r}_3, \mathbf{r}_1)}{\varphi(\mathbf{r}_1)\varphi(\mathbf{r}_2)\varphi(\mathbf{r}_3)}. \tag{21}$$

However, the functional form of $\psi(r_i, r_j)$ is such as to preclude the evaluation of $r^2_{\text{r.m.s.}}$ with Ψ as the wave function. Instead, a value of $r^2_{\text{r.m.s.}}$ was obtained by using the expression

$$r^2_{\text{r.m.s.}} = \tfrac{1}{3}\iint \bar{\varphi}^*(\mathbf{r}_1)\bar{\varphi}^*(\mathbf{r}_2)r_{12}^2\psi(\mathbf{r}_1, \mathbf{r}_2)\mathrm{d}^3r_1\mathrm{d}^3r_2 \tag{22}$$

which, except for a constant factor, is J_0^s of ref. [15]).

The results for the two different determinations of $r^2_{\text{r.m.s.}}$ are shown in table 3.

TABLE 3
Capture rates

Approximation to $r^2_{\text{r.m.s.}}$	$r_{\text{r.m.s.}}$ (10^{-13} cm)	Δb.e. (H^3-He^3) (MeV)	Capture rate (sec^{-1})
$\frac{1}{4}\iiint \varphi^2(r_1)\varphi^2(r_2)\varphi^2(r_3)\times r_{12}^2$	1.56	0.753	1.56×10^{-3}
$\frac{1}{4}\iint \bar{\varphi}^2(r_1)\bar{\varphi}^2(r_2)\psi(r_1, r_2)\times r_{12}^2$	1.56	0.718	1.56×10^{-3}

It should be pointed out that there is no rigorous reason why eq.(22) should give a better estimate of the r.m.s. radius than the one obtained from the independent particle wave function. The fact that the two values of the radii are the same is fortuitous and comes about by virtue of the fact that at the interparticle distances important in determining the r.m.s. radius the two particle wave function and the product of two single particle wave functions are nearly equal. In other words, the r.m.s. radius is determined by values of the wave function outside of the "healing distance".

5. Discussion

The capture rates listed in tables 2 and 3 are from 7 % to 10 % higher than the one obtained by Fujii and Primakoff, $w^{(s)} = 1.46\times10^3$ sec^{-1}, due to smaller r.m.s. radii. ($\approx 1.56\times10^{-13}$ cm as against 1.78×10^{-13} cm). This seems to be due to the fact that while the hard core potentials used here exclude close approaches they also make the wave function for large nucleon separations fall off more rapidly than do potentials without hard cores. P. Goldhammer [17]) has developed a "soft core" central and tensor potential which fits the low energy two-body data and has used it in making a perturbation calculation on the three and four body systems. He finds a value of 1.60×10^{-13} cm for the r.m.s. radius, which is close to the values used in this paper. If one were to believe that the energy difference between H^3 and He^3 should be given very nearly by the expectation value of the Coulomb potential, $+e/r$, it is clear that potentials which bar close approaches of the nucleons must also cause the wave function to drop off more sharply for large separations in order to keep the Coulomb energy sufficiently large. Therefore, if potentials with large or infinite positive core are accepted as giving a better description than other potentials of low energy phenomena, the smaller values of the r.m.s. radius are likely to be the more realistic ones. Clearly, it would be very useful to have data from electron scattering experiments on He^3 to turn to in order to get further estimates of the r.m.s. radius.

The presence of D-state admixture lowers the capture rate for a given r.m.s. radius. An estimate of the percentage of D-state in the three-body ground

state can be made from a comparison of the ft values of the neutron and the $H^1\beta$ decay. This ratio is given by

$$\frac{ft\frac{1}{2}(n \to p)}{ft\frac{1}{2}(H^3 \to He^3)} = \frac{1+3\lambda^2}{(1+3\lambda^2)\left(1-\frac{4\lambda^2 \sum_i D_i^2}{1+3\lambda^2}\right)}$$

$$\approx 1+\frac{4\lambda^2}{1+3\lambda^2}\sum_{i=1}^{6} D_i^2, \qquad \lambda = \left[\frac{g_A^{(\beta)}}{g_V^{(\beta)}}\right]^2.$$

Using a value of 1180 ± 35 for the neutron [18]) decay and 1132 ± 40 for H^3 [19]) the ratio is 0.959 ± 0.064. The uppermost value gives $\sum D_i^2 \approx 0.02$. Pease and Feshback [12]) obtained a 3 % D-state admixture in agreement with this result. Thus, the correction due to D-state admixture is of the order of 3 % and is small compared to the finite size correction of 20 %. The ratio $-g_A^{(\beta)}/g_V^{(\beta)}$ has been found experimentally [20]) to be between 1.18 and 1.27 so that there is a possible error of about 7 % in the values of the capture rates quite apart from uncertainties as to nuclear size and D-state admixture.

I want to thank Professor J. H. D. Jensen for his suggesting this problem as well as for this helpful discussions and comments. The assistance Dr. W. Wild gave to me in connection with his He^3 wave functions was very helpful. To Professor Jensen again go thanks for his kindness in extending to me the use of the facilities of the Institute of Theoretical Physics in Heidelberg.

Appendix A

The nuclear matrix element factor to be evaluated is

$$\begin{aligned}
&\tfrac{9}{2}\sum_{m',m=-\frac{1}{2}}^{+\frac{1}{2}}\{|\sum_{i=1}^{2} S_i^2\langle\psi_i^{m',-\frac{1}{2}}|j_0(\nu r_3)\exp(-r_3/D)\tau_3^{(-)}|\psi_i^{m,+\frac{1}{2}}\rangle \\
&\quad+\sum_{i=6}^{8} D_i^2\langle\psi_i^{m',-\frac{1}{2}}|j_0(\nu r_3)\exp(-r_3/D)\tau_3^{(-)}|\psi_i^{m,+\frac{1}{2}}\rangle|^2 \\
&\quad+(\Gamma^{(\rho)})^2|\sum_{i=1}^{2} S_i^2\langle\psi_i^{m;-\frac{1}{2}}|j_0(\nu r_3)\exp(-r_3/D)\tau_3^{(-)}\sigma_3|\psi_i^{m,+\frac{1}{2}}\rangle \\
&\quad+\sum_{i=6}^{8} D_i^2\langle\psi_i^{m;-\frac{1}{2}}|j_0(\nu r_3)\exp(-r_3/D)\tau_3^{(-)}\sigma_3|\psi_i^{m,+\frac{1}{2}}\rangle|^2\}.
\end{aligned} \tag{A—1}$$

Following the notation of Sachs, ψ_i can be written

$$\psi_i^{m,t} = N[F_i^m\bar{\eta}^t - \bar{F}_i^m\eta^t]; \tag{A—2}$$

N is a normalization constant; η^t and $\bar{\eta}^t$ are isobaric spin functions with $T=\frac{1}{2}$, $T_z=t$; and F_i^m and $\bar{F}_i^m$ are functions of the spin and the coordinates with

$J = \frac{1}{2}$ and $J_z = m$. The normalization relations between the functions are the following:

$$\begin{aligned}
&\langle \eta^t | \eta^{t'} \rangle = \delta_{t,t'}, \quad \langle \bar{\eta}^t | \bar{\eta}^{t'} \rangle = 12\delta_{t,t'}, \\
&\langle \eta^t | \bar{\eta}^t \rangle = 0, \quad 12\langle F_i^m | F_i^m \rangle = \langle \bar{F}_i^m | \bar{F}_i^m \rangle, \\
&\frac{\langle F_i^{m'} | F_i^m \rangle}{\langle F_i | F_i \rangle} = \frac{\langle \bar{F}_i^{m'} | \bar{F}_i^m \rangle}{\langle \bar{F}_i | \bar{F}_i \rangle} = \delta_{m',m}, \quad \langle \bar{F}_i^{m'} | F_i^m \rangle = 0.
\end{aligned} \tag{A—3}$$

As a result of the above,

$$N^2 = [12\langle F_i | F_i \rangle + \langle \bar{F}_i | \bar{F}_i \rangle]^{-1} = [24\langle F_i | F_i \rangle]^{-1} = [2\langle \bar{F}_i | \bar{F}_i \rangle]^{-1}. \tag{A—4}$$

(In writing down diagonal matrix elements, whose values are independent of certain quantum numbers, these numbers will be omitted.)

The expectation values of the operator $\tau_3^{(-)}$ are

$$\langle \eta^{t'} | \tau_3^{(-)} | \eta^t \rangle = \delta_{1,\, t-t'}, \qquad \langle \bar{\eta}^{t'} | \tau_3^{(-)} | \bar{\eta}^t \rangle = -4\delta_{1,\, t-t'}. \tag{A—5}$$

Hence, for any of the ψ_i's,

$$\begin{aligned}
&\langle \psi_i^{m',\, -\frac{1}{2}} | j_0(\nu r_3) \exp(-r_3/D) \tau_3^{(-)} | \psi_i^{m,\, +\frac{1}{2}} \rangle \\
&\qquad = \delta_{m',m} \frac{[-4\langle F_i | j_0(\nu r_3) \exp(-r_3/D) | F_i \rangle + \langle \bar{F}_i | j_0(\nu r_3) \exp(-r_3/D) | \bar{F}_i \rangle]}{12\langle F_i | F_i \rangle + \langle \bar{F}_i | \bar{F}_i \rangle}.
\end{aligned}$$

In the special case of $\psi_1^{m,\, t}$, the symmetric S-state, $F_i^m = \varphi^m f_1$ and $\bar{F}_i^m = \bar{\varphi}^m f_1$: φ^m and $\bar{\varphi}^m$ are spin functions analogous to the η's and f_1 is a scalar function of the spatial coordinates. For $\psi_1^{m,\, t}$ eq. (A—6) simplifies to

$$\langle \psi_1^{m',\, -\frac{1}{2}} | j_0(\nu r_3) \exp(-r_3/D) | \psi_1^{m,\, +\frac{1}{2}} \rangle = \tfrac{1}{3} \langle \psi_1 | j_0(\nu r_3) \exp(-r_3/D) | \psi_1 \rangle. \tag{A—1}$$

The other S-state and the D-states are not quite so easy to handle because the F's do not factor into two parts. It is convenient to define the quantities $\underline{\Delta}_i$ and $\underline{\bar{\Delta}}_i$ by the equations

$$\begin{aligned}
\frac{\langle F_i^m | j_0(\nu r_3) \exp(-r_3/D) | F_i^m \rangle}{\langle F_i | F_i \rangle} &= \langle \psi_i | j_0(\nu r_3) \exp(-r_3/D) | \psi_i \rangle + \Delta_i, \\
\frac{\langle \bar{F}_i^m | j_0(\nu r_3) \exp(-r_3/D) | \bar{F}_i^m \rangle}{\langle \bar{F}_i | \bar{F}_i \rangle} &= \langle \psi_i | j_0(\nu r_3) \exp(-r_3/D) | \psi_i \rangle + \bar{\Delta}_i.
\end{aligned} \tag{A—8}$$

Adding the two equations, the relation $\Delta_i + \bar{\Delta}_i = 0$ is obtained.

Eq. (A—6) can now be written

$$\begin{aligned}
&\langle \psi_i^{m;\, -\frac{1}{2}} | j_0(\nu r_3) \exp(-r_3/D) \tau_3^{(-)} | \psi_i^{m,\, +\frac{1}{2}} \rangle \\
&\qquad = \tfrac{1}{3}\delta_{m,m} [\langle \Psi | j_0(\nu r_3) \exp(-r_3/D) | \Psi \rangle - 2\Delta_i].
\end{aligned} \tag{A—9}$$

The Fermi transition part of expression (A—1) is then

$$|\sum_{i=1}^{2} S_i^2\langle\psi_i|j_0(\nu r_3)\exp(-r_3/D)|\psi_i\rangle + \sum_{i=6}^{8} D_i^2\langle\psi_i|j_0(\nu r_3)\exp(-r_3/D)|\psi_i\rangle - 2[S_2^2\Delta_2+\sum_{i=6}^{8} D_i^2\Delta_i]|^2 \quad \text{(A—10)}$$
$$= |\langle\Psi|j_0(\nu r_3)\exp(-r_3/D)|\Psi\rangle - 2[S_2^2\Delta_2+\sum_{i=6}^{8} D_i^2\Delta_i]|^2.$$

The expectation value of $j_0(\nu r_3)\tau_3^{(-)}\sigma_3$ with respect to any of the ψ_i's is, in analogy to eq. (A—6),

$$\langle\psi_i^{m',-\frac{1}{2}}|j_0(\nu r_3)\exp(-r_3/D)\tau_3^{(-)}\sigma_3|\psi_i^{m,+\frac{1}{2}}\rangle = \frac{[-4\langle F_i^{m'}|j_0(\nu r_3)\exp(-r_3/D)\sigma_3|F_i^{m}\rangle + \langle\bar{F}_i^{m'}|j_0(\nu r_3)\exp(-r_3/D)\sigma_3|F_i^{m}\rangle]}{12\langle F_i^{m}|F_i^{m}\rangle+\langle\bar{F}_i^{m}|\bar{F}_i^{m}\rangle}.$$

For the $\psi_1^{m,t}$ state, this immediately simplifies to

$$\tfrac{1}{3}\langle\psi_1^{m',t}|j_0(\nu r_3)\exp(-r_3/D)|\psi_1^{m,t}\rangle\langle\varphi^{m'}|\sigma_3|\varphi^{m}\rangle. \quad \text{(A—12)}$$

But $\varphi^{m'}$ and φ^{m} are eigenfunctions of σ_3^2 and σ_{3z} so that by expressing σ_3 in terms of its spherical components [21]) expression (A—12) becomes

$$\tfrac{1}{3}\langle\psi_1|j_0(\nu r_3)\exp(-r_3/D)|\psi_1\rangle\mathbf{S}(m',m) \quad \text{(A—13)}$$

where

$$\mathbf{S}(m',m) = [\hat{\mathbf{i}}+i\hat{\mathbf{j}}]\delta_{m',m-1}+[\hat{\mathbf{i}}-i\hat{\mathbf{j}}]\delta_{m',m+1}+2m\hat{\mathbf{k}}\delta_{m',m}.$$

For the D-states, all of which are totally symmetric in the spins,

$$\langle F_i^{m'}|j_0(\nu r_3)\exp(-r_3/D)\sigma_3|F_i^{m}\rangle = \tfrac{2}{3}\langle F_i^{m'}|j_0(\nu r_3)\exp(-r_3/D)\mathbf{S}|F_i^{m}\rangle = \frac{2}{3J(J+1)}\langle F_i^{m'}|j_0(\nu r_3)\exp(-r_3/D)(\mathbf{J}\cdot\mathbf{S})\mathbf{J}|F_i^{m}\rangle, \quad \text{(A—14)}$$
$$\langle\bar{F}_i^{m'}|j_0(\nu r_3)\exp(-r_3/D)|\bar{F}_i^{m}\rangle = \frac{2}{3J(J+1)}\langle\bar{F}_i^{m'}|j_0(\nu r_3)\exp(-r_3/D)(\mathbf{J}\cdot\mathbf{S})\mathbf{J}|\bar{F}_i^{m}\rangle.$$

Since the F_i's are eigenfunctions of J, L and S with values of $\frac{1}{2}$, 2 and $\frac{3}{2}$ respectively, eq. (A—14) is equivalent to

$$\langle F_i^{m'}|j_0(\nu r_3)\exp(-r_3/D)\sigma_3|F_i^{m}\rangle = \tfrac{2}{3}\langle F_i^{m'}|j_0(\nu r_3)\exp(-r_3/D)\mathbf{J}|F_i^{m}\rangle = \tfrac{1}{3}\langle F_i|j_0(\nu r_3)\exp(-r_3/D)|F_i\rangle\mathbf{S}(m',m),$$
$$\langle\bar{F}_i^{m'}|j_0(\nu r_3)\exp(-r_3/D)\sigma_3|\bar{F}^{m}\rangle = \tfrac{1}{3}\langle\bar{F}_i|j_0(\nu r_3)\exp(-r_3/D)|\bar{F}_i\rangle\mathbf{S}(m',m). \quad \text{(A—15)}$$

With the above, eq. (A—11) can be written as

$$\langle \Psi_i^{m;-\frac{1}{2}} | j_0(\nu r_3) \exp(-r_3/D) \tau_3^{(-)} \sigma_3 | \Psi^{m,+\frac{1}{2}} \rangle = \tfrac{1}{6}[\langle \psi_i | j_0(\nu r_3) \exp(-r_3/D) | \psi_i \rangle - 2\Delta_i].$$

The result for the second S-state is the same as for $\psi_1^{m,t}$ except for the addition of a term $-2\Delta_2$. The sum $\frac{1}{2}\sum_{m;\,m-\frac{1}{2}}^{+\frac{1}{2}} |S(m;m)|^2 = 3$ so that the Gamow-Teller part of expression (A—1) is

$$\begin{aligned} &3(\Gamma^{(\mu)})^2 | \sum_{i=1}^{2} S_i^2 \langle \psi_i | j_0(\nu r_3) \exp(-r_3/D) | \psi_i \rangle - 2S_2^2 \Delta_2 \\ &+\tfrac{1}{3}\sum_{i=6}^{8} D_i^2 [\langle \psi_i | j_0(\nu r_3) \exp(-r_3/D) | \psi_i \rangle - 2\Delta_i]|^2 \\ &= 3(\Gamma^{(\mu)})^2 | \langle \Psi | j_0(\nu r_3) \exp(-r_3/D) | \Psi \rangle - 2S_2^2 \Delta_2 \\ &-\tfrac{2}{3}\sum_{i=6}^{8} D_i^2 [\langle \psi_i | j_0(\nu r_3) \exp(-r_3/D) | \psi_i \rangle + \Delta_i]|^2. \end{aligned} \tag{A—16}$$

This expression, as well as eq. (A—10), still differs from eq. (6) in the text because of the presence of Δ_i's. To estimate their size a trial calculation was carried out for Δ_1 which indicated that its value was only $\frac{1}{200}$th of $\frac{1}{6}\nu^2 r^2_{\text{r.m.s.}}$, the second term in $\Psi\langle | j_0(\nu r_3) \exp(-r_3/D | \Psi \rangle$. On the basis of this result all the Δ_i's were ignored.

Appendix B

The expectation value of r_{12}^2, using the same integration scheme as Kikuta, Morita and Yamada [14]), is given by

$$\begin{aligned} \langle \varphi | r_{12}^2 | \varphi \rangle = N^2 \Big\{ &\int_d^\infty dr_{12} \int_d^\infty dr_{23} \int_d^\infty dr_{13} \varphi^2 r_{12}^2 r_{23} r_{13} \\ &-2\int_d^\infty dr_{12} \int_d^\infty dr_{23} \int_0^\infty dw\, \varphi^2 r_{13}^2 r_{23} (w + r_{12} + r_{23}) \\ &-1\int_d^\infty dr_{23} \int_d^\infty dr_{13} \int_0^\infty d\mu\, \varphi^2 (\mu + r_{23} + r_{13})^2 r_{23} r_{13} \Big\} \\ = N^2 &\{I_1 - 2I_2 - I_3\}, \end{aligned}$$

with

$$w = +r_{13} - r_{12} - r_{23}, \quad \mu = +r_{12} - r_{23} - r_{13}.$$

Straightforward integration yields

$$\begin{aligned} I_1 &= [dA_1(0) + A_2(0)]^2 [d^3 A_1(0) + 3d^2 A_2(0) + 6dA_3(0) + A_4(0)], \\ I_2 &= M'(2\mu) - 2M'(\mu+\nu) + M'(2\nu), \\ I_3 &= P'(2\mu) - 2P'(\mu+\nu) + P'(2\nu). \end{aligned}$$

The A's, M''s and P''s are given by

$$A_n(x) = \frac{1}{(2\mu+x]^n} - \frac{2}{[\mu+\nu+x]^n} + \frac{1}{[2\nu+x]^n},$$

$$M'(x) = \frac{\exp(-xd)}{x}\{[dA_1(x)+A_2(x)] \cdot [36A_5(x)+36dA_4(x)+18d^2A_3(x)+6d^3A_2(x)+d^4A_1(x)] \quad \text{(A-3)}$$
$$+[d^2A_1(x)+2dA_2(x)+2A_3(x)]\,[6A_4(x)+6dA_3(x)+3d^2A_2(x)+d^3A_1(x)]\}.$$

$$P'(x)=\frac{\exp(-dx)}{x}\Bigg\{[dA_1(x)+A_2(x)]\Bigg[48A_5(x)+\left(48d+\frac{36}{x}\right)A_4(x)+\left(24d^2+\frac{36d}{x}\right)$$
$$+\frac{24}{x^2}A_3(x)+\left(8d^3+\frac{18d^2}{x}+\frac{24d}{x^2}+\frac{6}{x^3}\right)A_2(x)+\left(2d^4+\frac{6d^3}{x}+\frac{12d^2}{x^2}+\frac{6d}{x^3}\right)A_1(x)\Bigg]$$
$$+[d^2A_1(x)+2dA_2(x)+2A_3(x)]\left[36A_4(x)+\left(36d+\frac{12}{x}\right)A_3(x)\right.$$
$$\left.+\left(18d^2+\frac{12d}{x}\right)A_2(x)+\left(6d^3+\frac{6d^2}{x}\right)A_1(x)\right]\Bigg\}.$$

The formula for N^2 is given in ref. [14]).

References

1) A. Fujii and H. Primakoff, Nuovo Cimento **12** (1959) 327
2) H. Primakoff, Rev. Mod. Phys. **31** (1959) 802
3) S. Weinberg, Phys. Rev. **112** (1958) 1375
4) M. L. Goldberger and S. B. Treiman, Phys. Rev. **111** (1958) 355
5) T. Wolfenstein, Nuovo Cimento **8** (1958) 882
6) R. P. Feynman and M. Gell-Mann, Phys. Rev. **109** (1958) 193;
   M. Gell-Mann, Phys. Rev. **111** (1958) 362;
   J. Bernstein and R. R. Lewis, Phys. Rev. **112** (1958) 232
7) J. Tiomno and John A. Wheeler, Revs. Mod. Phys. **21** (1949) 153
8) H. A. Tolhoek and J. R. Luyten, Nuclear Physics **3** (1957) 679
9) J. O. Burgman, J. Fischer, B. Leontic, A. Lundby, R. Meunier, J. P. Stroot and J. O. Teja, Phys. Rev. Letters **1** (1958) 469
10) T. N. Godfrey, Phys. Rev. **92** (1953) 512
11) K. Huang, C. N. Yang and T. D. Lee, Phys. Rev. **108** (1957) 1340
12) Pease and Feshbach, Phys. Rev. **88** (1952) 945;
    Hu and Hsu, Proc. Roy. Soc. A **204** (1950) 476
13) R. Sachs, Nuclear Theory (Addison-Wesley Publishing Company, Cambridge, Mass. 1953) p. 336
14) Kikuta, Morita and Yamada, Progress of Theoretical Physics **15** (1956) 222
15) H. J. Mang and W. Wild, Zeitschrift für Physik **154** (1959) 182
16) J. Brenig, Nuclear Physics **4** (1957) 363
17) P. Goldhammer, preprint
18) Sosnovskij, Spivak, Prokofiev, Kutikov and Dobrynin, JETP **35** (1958) 1059
19) Kistner and Rustad, Proceedings 1958 Annual Conference on High Energy Physics at Cern, pp. 237, 238.
20) C. S. Wu, Revs. Mod. Phys. **31** (1959) 783
21) M. E. Rose, Multipole Fields (John Wiley and Sons, New York, 1955) p. 22

8.B

Nuclear Physics **16** (1960) 72—80; © *North-Holland Publishing Co., Amsterdam*

Not to be reproduced by photoprint or microfilm without written permission from the publisher

ON THE DECAY INTERACTION OF STRANGE PARTICLES

B. SAKITA

Department of Physics, University of Wisconsin, Madison, Wisconsin

and

S. ONEDA †

Department of Physics, University of Maryland, College Park, Maryland ††

Received 26 October 1959

Abstract: It is proposed that the strength of the coupling constants is different for the strangeness non-conserving and strangeness conserving currents in the scheme of Fermi interactions of an ordinary charged current-current type.

First, the consistency with experimental results is analyzed by introducing phenomenologically the direct $\bar{\Lambda}$n interaction. Then, the possibility of the derivation of this interaction as the effective interaction of the primary Fermi interactions is discussed.

1. Introduction

There are several theoretical attempts to explain the striking difference between the rates of $K^+ \to \pi^+ + \pi^0$ and $K_1^0 \to \pi + \pi$ decay †††. The simplest explanation would be to impose the so called $|\Delta I| = \frac{1}{2}$ selection rule for the non-leptonic decay processes. Presently available experiments [2]) on the hyperon decay and the K-meson decays into pions seem to be consistent with this selection rule. Of course, this rule cannot be strict since the $K^+ \to \pi^+ + \pi^0$ decay, though slow, does take place. It is also usually believed that the electromagnetic interactions are too small to be responsible for the violation of $|\Delta I| = \frac{1}{2}$ rule.

If we wish to explain all the weak processes in terms of the universal Fermi interaction (U. F. I.), we must construct the U.F.I. in such a fashion that the $|\Delta I| = \frac{3}{2}$ part of the matrix elements of K-decay is suppressed about 20 times compared with the $|\Delta I| = \frac{1}{2}$ part. This does not seem to be an easy problem, especially if we wish to restrict the form of the U.F.I. to the charge-exchange type in order to forbid many unwanted reactions involving leptons. Another difficulty of the U.F.I. arises from the recently established slow rate of hyperon decays into leptons [3]). Present experiments on the $\Lambda^0 \to p + e^- + \bar{\nu}$ and

† On leave of absence from Kanazawa University, Japan.

†† Supported in part by the U. S. Atomic Energy Commission, under Contract No. AT(11-1)-30 and in part by the United States Air Force through the Air Force Office of Scientific Research and Development Command.

††† Okubo and Marshak [1]) have tried to explain this difference of decay rates by taking into account the final state interaction in $T = 0$ and $T = 2$ states. It is, however, concluded by Chew and Mandelstam [1]) that there are no low energy resonances in the S-state in $\pi - \pi$ interaction

$\Sigma^{\pm} \to n+e^{\pm}+\nu$ decays have shown that the rates of these decays are, at least, about ten times smaller than those expected from the U.F.I. We have, as a matter of fact, conjectured this result from the related experimentally better known processes, viz. the leptonic decay modes of the K-meson. That is, a dispersion calculation of the $K \to \mu+\nu$ decay rate and the comparison of the rate [4]) of $K_1^0 \to \pi^+ + \pi^-$ to that of $K^0 \to e(\mu)+\nu+\pi$ decay also suggest that both the A- and V-part of the strangeness non-conserving baryon-lepton interactions have weaker coupling constants than the usual Fermi coupling constant.

Under these circumstances, we feel that we should now try to reconstruct a theory based on the above mentioned facts. In this paper, we would like to propose an improved scheme of Fermi interaction in which the values of the coupling constants depend upon whether the strangeness is conserved or not. Although the situation may certainly not be ideal from the standpoint of universality, it may be compared to the similar situation in strong interactions; that is, the coupling constants for the strong pion and K-meson interactions seem to be different and also the highest possible symmetry of the interactions seems to be violated.

2. Phenomenological Analysis

As discussed above, we shall assume that the coupling of strangeness non-conserving current is weaker than that of the strangeness conserving current ($f \gg f'$).

The Lagrangian density of this interaction is

$$\frac{f}{\sqrt{2}}\left(j_\lambda + J_\lambda + \frac{f'}{f}\mathcal{J}_\lambda\right)^* \left(j_\lambda + J_\lambda + \frac{f'}{f}\mathcal{J}_\lambda\right) \qquad \text{(A)}$$

where j_λ, J_λ and $\mathcal{J}_\lambda$ are leptonic, strangeness conserving baryonic and strangeness non-conserving baryonic currents:

$$\begin{aligned} j_\lambda &= \bar{\nu}\gamma_\lambda(1+\gamma_5)(\mu+e), \\ J_\lambda &= \bar{p}\gamma_\lambda(1+\gamma_5)n, \\ \mathcal{J}_\lambda &= \bar{p}\gamma_\lambda(1+\gamma_5)\Lambda. \end{aligned}$$

For simplicity, we have in this paper adopted the Sakata model [5]), in which the Λ-particle is the only fundamental hyperon and all other strange particles are regarded as the appropriate compound states of the nucleons and the Λ-particle. Then the choice of the above primary interaction will be unique as long as we insist on limiting the interaction to charged currents. (For another model see the remark in the end of section 3). It should be noted that the non-leptonic part of the interaction (A) contains an appreciable fraction of the $|\Delta I| = \frac{3}{2}$ part as well as the $|\Delta I| = \frac{1}{2}$ part.

In order to explain the idea in a simpler way, let us, for the moment, introduce

the following phenomenological interaction (B) in addition to the interaction (A):

$$\rho m\bar{n}(1+\gamma_5)\Lambda+\text{h.c.}, \tag{B}$$

where ρ is a parameter to be determined and m denotes the neutron mass. In this interaction scheme (A) and (B), since the interaction (B) behaves as an isospinor, the slowness of the hyperon leptonic decays as well as the $|\Delta \mathbf{I}| = \frac{1}{2}$ selection rule for the non-leptonic decay processes could be explained, provided $f \gg f'$ and the value of parameter ρ is large enough so that for the non-leptonic processes the contribution from the interaction (B) exceeds that from the non-leptonic part of the interaction (A). We will examine this statement by choosing values of the constants ρ and f' to be, for example,

$$\rho = 3\times 10^{-8}, \quad f' = \tfrac{1}{5}f, \quad f = 1\times 10^{-5}/m^2, \tag{C}$$

where f is the usual value of the Fermi coupling constant.

2.1. Λ-DECAY

For the non-leptonic decays of Λ there are two types of decay scheme as shown in fig. 1: one is through (A), the other through (B). The ratio of the

Fig. 1. Feynman diagrams of Λ^0-decay.

matrix elements of diagram (a) to (b) is given by

$$f' F : \frac{\rho m g_\pi}{m_\Lambda{}^2 - m^2}, \tag{1}$$

where F represents the whole contribution from the black bubble in fig. 1(a) and g_π denotes the pion-nucleon coupling constant. Goldberger and Treiman [6]) have calculated F by dispersion relation techniques to give

$$F \approx \frac{m}{g_\pi}, \tag{2}$$

which is in an excellent agreement with the experimental rate of the π-meson. Using the numbers given in (C), the value of the ratio (1) turns out to be

$$1 : \sqrt{8}. \tag{1'}$$

The above choice of the value of ρ gives the correct decay rate of the Λ-particle.

The form of the matrix elements (a) and (b) is exactly the same so that the asymmetry parameter α is the same as that given by the effective interaction

$$\bar{\Lambda}\gamma_\lambda(1+\gamma_5)\mathrm{p}\partial_\lambda\phi_\pi. \tag{3}$$

Of course, $W(\Lambda^0 \to \mathrm{p}+\pi^-)/W(\Lambda^0 \to \mathrm{n}+\pi^0) = 2$ for the diagram (b).

For the β-decay of Λ, the numerical value of f' in (C) gives

$$\frac{W(\Lambda^0 \to \mathrm{p}+\mathrm{e}+\bar{\nu})}{W(\Lambda^0 \to \mathrm{n}+\pi^0)+W(\Lambda^0 \to \mathrm{p}+\pi^-)} \approx 0.07\ \%, \tag{4}$$

which is slightly smaller than, but not inconsistent with, the present experimental value.

We have chosen the fig. 1(a) as one of the typical diagrams through (A). However, it contains an appreciable amount of $|\Delta\mathbf{I}| = \frac{3}{2}$ in addition to $|\Delta\mathbf{I}| = \frac{1}{2}$ transitions. Therefore, though fig. 1(b), which satisfies the strict $|\Delta\mathbf{I}| = \frac{1}{2}$ rule, is more important than fig. 1(a), we have to suppress the $|\Delta\mathbf{I}| = \frac{3}{2}$ part of such diagrams as fig. 1(a) to some extent (possibly by higher order corrections) in order to explain the approximate validity of the $|\Delta\mathbf{I}| = \frac{1}{2}$ rule for the branching ratio of the Λ-decay.

2.2. K-MESON DECAY INTO PIONS

For the $\mathrm{K} \to \pi+\pi$ decay, the Feynman diagrams through the interaction (A) (diagrams (a) and (b)) and through (B) (diagram (c)) are shown in fig. 2. Let

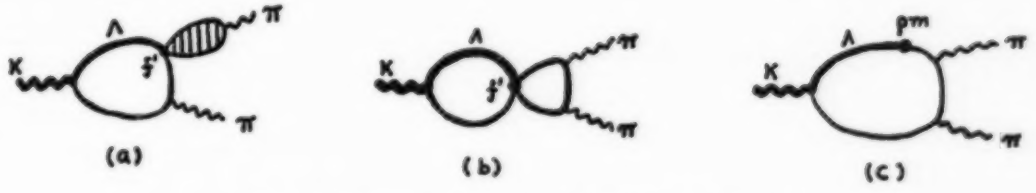

Fig. 2. Feynman diagrams of $\mathrm{K} \to \pi+\pi$ decay.

us compare the matrix element of the diagram (a) with that of the diagram (c). By a perturbation calculation, both of them are logarithmically divergent but their ratio is finite and is given by

$$f' F \frac{m_K{}^2+m_\pi{}^2}{2} : \rho m g_\pi, \tag{5}$$

where F again represents the black bubble of fig. 2a. Using the values (C), this ratio turns out to be

$$1 : 20. \tag{5'}$$

The diagram (b) does not contribute to both the $\mathrm{K}^+ \to \pi^+ + \pi^0$ and the $\mathrm{K}_1{}^0 \to \pi+\pi$ decay. However, if we allow for the radiative corrections between

the two bubbles, the diagrams of this type may no longer be unimportant. The contributions of such diagrams however, are not likely to surpass that of the diagrams of the type (a). For the $K^+ \to \pi^+ + \pi^0$ decay, the diagram (c) does not contribute and, therefore, if we discard the diagram (b) for the moment, the ratio of the decay rate of $K_1^0 \to \pi^+ + \pi^-$ to $K^+ \to \pi^+ + \pi^0$ in the present scheme will be approximately derived from the ratio (5'). We obtain

$$\frac{W(K_1^0 \to \pi^+ + \pi^-)}{W(K^+ \to \pi^+ + \pi^0)} \approx 400,$$

agreeing well with the experimental ratio. As mentioned above, even if we include the diagram (b) the qualitative feature will not be changed drastically. The charge branching ratio of the K_1^0-decay is, of course, compatible with the $|\Delta I| = \frac{1}{2}$ selection rule. In the same way, for the $K \to 3\pi$ processes the $|\Delta I| = \frac{1}{2}$ part due to the interaction (B) will play a dominant role. Note that in the present model there is no trouble of looking for the component $|\Delta I| = \frac{3}{2}$.

2.3. OTHER PROCESSES

It will now be worthwhile to see in the present scheme what processes are expected to be different from U.F.I. (by this we mean the scheme with $f = f'$ and $\rho = 0$) and what processes remain unchanged.

i) It is obvious that strangeness conserving processes such as μ-decay, π-decay, nuclear β-decay, etc., are the same as in U.F.I.

ii) As to the leptonic decay of the K-meson, dispersion relation calculation of the $K \to \mu + \nu$ decay is now consistent with experiment since $f' \approx \frac{1}{5} f$. The ratio $W(K^+ \to e(\mu) + \nu + \pi^0)/W(K^+ \to \pi^+ + \pi^0)$ is the same as U.F.I. If we compare the processes $K^+ \to \mu(e) + \nu + \pi^0$ with the $K^+ \to \pi^+ + \pi^0$ decay due to fig. (2a) we get the following estimate. We write the matrix-elements of $K^+ \to \pi^0 + \mu(e) + \nu$ decay in the form [4])

$$\frac{f'}{\sqrt{2}} \phi_K(k) \phi_\pi^*(k-p)(k_\alpha M + p_\alpha N) \bar{\mu} \gamma_\alpha (1+\gamma_5) \nu,$$

where k_α and $(k-p)_\alpha$ denote the four momenta of the K-meson and the π^0-meson respectively and M and N are the form factors which will probably be approximately constant. We get

$$\frac{W(K^+ \to \pi^0 + \mu^+ + \nu)}{W(K^+ \to \pi^0 + e^+ + \nu)} = 0.80 + 0.33 \left(\frac{N}{M}\right) + 0.077 \left(\frac{N}{M}\right)^2$$

and

$$\frac{W(K^+ \to \pi^0 + e^+ + \nu)}{W(K^+ \to \pi^+ + \pi^0)} = 0.4 \frac{M^2}{(6.3M + N)^2}.$$

The experimental ratio $W(K^+ \to \pi^0 + \mu^+ + \nu) \approx W(K^+ \to \pi^0 + e^+ + \nu)$ is obtained

for the value $|N/M| \approx 1$. In fact, the lowest order calculation with cut off momentum $\approx m$ (nucleon mass) gives $N \approx -M$, which implies

$$\frac{W(K^+ \to \pi^0+e^++\nu)}{W(K^+ \to \pi^++\pi^0)} \approx \frac{1}{50}. \tag{6}$$

As noted at the end of sect. 2.1, we have to suppress the $|\Delta I| = \frac{3}{2}$ part of fig. 1(a) to some extent. This suppression tends to decrease the rate of $K^+ \to \pi^++\pi^0$ decay. On the other hand, we have used the value $g_\pi^2/4\pi \approx 15$ for the vertex in which a pion is emitted from a nucleon and anti-nucleon loop. However, we should probably expect a damping effect as indicated by the calculation of the $\pi \to \mu+\nu$ decay [6]). In fact, the branching ratio of $K^+ \to \pi^0+e+\nu$ to $K^+ \to \mu^++\nu$ decay seems also to indicate a damping of the pion vertex by a factor ≈ 3 (i.e., $g_\pi^2/4\pi \approx 5$). The above two effects are consistent with keeping the value of (5′) unchanged and also with changing the value of the ratio (6) obtained above to one which is close to the experimental value. (Detailed discussion of various K-meson decay modes will be published in a forthcoming paper of this journal.) In the present model we have, of course, the relation (taking into account the mass difference of pions)

$$W(K_1^0 \to e^\pm(\mu^\pm)+\nu+\pi^\mp) = W(K_2^0 \to e^\pm(\mu^\pm)+\nu+\pi^\mp) = 0.85 \times 2W(K^+ \to e(\mu)+\nu+\pi^0).$$

Now since the rate of $K_1^0 \to \pi+\pi$ is enhanced by the existence of the interaction (B), the discrepancy between the rates of $K_1^0 \to \pi+\pi$ and $K \to \pi+e(\mu)+\nu$ as previously pointed out [4]) becomes unimportant.

iii) We cannot say much about the Σ-decay in this scheme, just as in the U.F.I. †

iv) As to the non-mesonic decay of hyperfragment, Treiman [8]) pointed out that if we adopt the U.F.I. the direct four baryon interaction is important as well as the pion exchange term. In our scheme, however, the former (fig. 3a) is

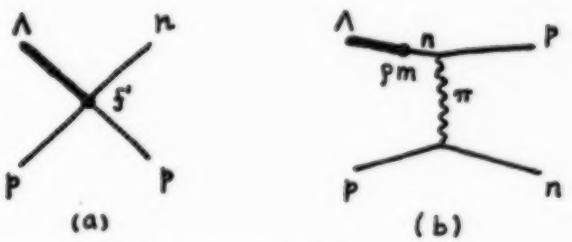

Fig. 3. Feynman diagrams of non-mesonic decay of the hyperfragment.

† H. Obayashi calculated asymmetry parameters of Λ and Σ-decay by taking the interaction (B) as a primary interaction. According to his results, these parameters depend sensitively on the cut off momentum. Therefore, we cannot say much about Σ-decays.

less important than the latter (fig. 3b) due to the interaction (B). This problem might be very important to distinguish the present scheme from the U.F.I. provided a quantitative discussion is feasible.

We have introduced a rather unfamiliar interaction (B), which breaks down the fine symmetry of the weak interaction (A). It would therefore be very desirable, from the symmetry point of view, that the interaction (B) could be considered as a kind of effective interaction which is derived from the interaction (A) by the radiative corrections due to the strong interactions. Then we may attribute the difference of the coupling constants f and f' to the qualitative difference of the strangeness conserving and non-conserving currents. Therefore, we shall examine the possibility of this statement in the next section †.

3. On the Possibility of the Interaction (B) as the Effective Interaction of (A)

There are two points of view in looking at this interaction (B): one is that it is a counter term arising from the renormalization effects including weak interactions ††, the other that it is due to the radiative corrections mentioned above. From the former point of view, not only this counter term, but also the π-meson and K-meson decay matrixelements themselves, should be taken as renormalization parameters to be determined from experiments. The latter point of view is that the renormalization effect produced by the strong interaction itself could be calculated by the theory. A typical example of this is the calculation of the n—p mass difference done by Feynman and Speisman [12]).

Let us take the latter point of view and estimate the numerical value of ρ by assuming that (B) is an effect of the interaction (A) caused by the strongly interacting meson cloud. The simplest diagram is shown in fig. 4. The diagram

Fig. 4. Feynman diagram of effective Λn interaction due to the Fermi interaction.

† The possibility that the effective Λn interaction of the form (B) will be derived in some model was also mentioned by M. Gell-Mann [9]). In fact, Oneda and Tanikawa [10]) have actually used this effective Λn interaction (derived from the intermediate boson) for the non-leptonic processes. The possibility that $f \gg f'$ is also considered there. However, this model leads to the prediction of the occurrence of the $K^+ \to \pi^+ + \nu + \bar{\nu}$ decay, which does not seem to be confirmed by experiments. After we had written this paper, one of us (S. O.) had a chance to see the lecture notes by Feynman at Cornell University and found that apparently Feynman was aware of the possibility discussed in this paper. He thanks Dr. J. Sucher for showing him the lecture notes.

†† We use here the word "renormalization" for the renormalization due to strong interactions in the lowest order perturbation of the weak interactions (cf. ref. [11])).

without the pion line in fig. 4 gives no contribution. However, with the pion lines this type of diagram will not vanish and seems to give an important contribution to the non-leptonic processes. Using the value (2) for the black bubble and taking the cut off momentum to be of the order of nucleon mass we obtain $\rho \approx 10^{-8}$. The asymmetry parameter of the Λ^0-decay due to this diagram is not inconsistent with the present experimental value although calculations including higher order corrections are desired. The above calculation seems to show that a class of effective interactions of the type shown in fig. 4 could easily be induced, which may play an important role in the interaction (B) introduced in the previous section. As an another way of obtaining a rough order of estimate let us assume that the Fermi interaction (A) is intermediated by a charged vector meson. Then an effective interaction of the form (B) could be derived by the mechanism shown in fig. 5, where the black box represents all

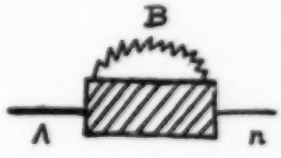

Fig. 5. Feynman diagram of effective $\bar{\Lambda}$n interaction due to the intermediate Boson.

the possible intermediate states. This is similar to the electromagnetic mass shift of the nucleon which is known to be of the order of 1 MeV. Using this analogy and putting the mass of intermediate boson equal to the nucleon mass, we may estimate

$$\rho e^2 / f' m \approx 1 \text{ MeV}.$$

From this, we again obtain $\rho \approx 10^{-8}$. We have, in fact, also made an explicit lowest order calculation on this model. Using a Feynmann cut off $(-\lambda^2/k^2-\lambda^2)^2$ with $\lambda \approx m$, which yields a correct value for F given by (2), we have obtained the value $\rho \approx 10^{-8}$ assuming that the charged vector meson has a mass of approximately the nucleon mass†. That is, we have got a value $1 : \sqrt{10}$ for the ratio (1′) in this model. These estimates seem to support the idea that only the interaction (A) could be a primary weak interaction although these rough order of magnitude estimates must be replaced by more accurate calculations.

Finally we would add a comment in the case when we adopt a model other than the Sakata model. In general, we must expect that not only the effective $\bar{\Lambda}$n interaction but also such effective interactions as $\bar{\Sigma}^+$p, $\bar{\Sigma}_0$n and $\bar{\Xi}\Sigma^-$ etc. can be induced and may play a predominant role in the non-leptonic processes. Therefore, we must guarantee that these induced effective interactions satisfy $|\Delta I| = \frac{1}{2}$ rule. The simplest and probably the safest way to do this is to require

† As regards the asymmetry parameter, the lowest order perturbation theory gives a wrong sign if we take a conventional model of charged vector meson. We have recently investigated the possibility pointed out in this section in more detail (see forthcoming paper in the Physical Review).

that the Lagrangian of weak interactions should behave as an isospinor, at least for the most important weak interactions, and then try to invoke the $|\Delta I| = \frac{3}{2}$ part as the weaker interactions.

One of the authors (B. S.) thanks Professor M. E. Ebel for discussions. One of us (S. O.) wishes to express his thanks to Professor John S. Toll and also to the high energy group of the University of Maryland for their hospitality and encouragements.

References

1) S. Okuobo and R. E. Marshak, Phys. Rev. **100** (1955) 1809;
G. F. Chew and S. Mandelstam, UCRL 8728
2) Crawford *et al.*, Phys. Rev. Lett. **2** (1958) 266;
Cool, Cork, Cronin and Wentzel, Phys. Rev. **114** (1959) 912; earlier references will be found in these papers
3) Crawford *et al.*, Phys. Rev. Lett. **1** (1958) 377;
Nordin *et al.*, Phys. Rev. Lett. **1** (1958) 380;
Leitner *et al.*, Phys. Rev. Lett. **3** (1959) 186
4) C. H. Albright, Phys. Rev. **114** (1959) 1648;
B. Sakita, Phys. Rev. **114** (1959) 1650;
S. Oneda, Nuclear Physics **9** (1958) 476
5) S. Sakata, Prog. Theor. Phys. **16** (1956) 686
6) M. L. Goldberger and S. B. Treiman, Phys. Rev. **111** (1958) 354
7) H. Obayashi, Soryushiron Kenkyu **19** (1959) 142 (in Japanese), to be published in Prog. Theor. Phys.
8) S. B. Treiman, Proceedings of the 1958 Annual International High Energy Conference at CERN (CERN, Geneva, 1958)
9) M. Gell-Mann, Discussions in 1958 Annual International Conference on High Energy Physics at CERN, Geneva
10) S. Oneda and Y. Tanikawa, Phys. Rev. **113** (1959) 1354
11) S. Weinberg, Phys. Rev. **106** (1957) 1301
12) Feynman and Speisman, Phys. Rev. **94** (1954) 500

1.D.2:
1.E.4:
3.C

Nuclear Physics **16** (1960) 81—89; © *North-Holland Publishing Co., Amsterdam*
Not to be reproduced by photoprint or microfilm without written permission from the publisher

NUCLEAR RESONANCE FLUORESCENCE WITH THE 105-keV E1 TRANSITION OF Gd^{155} USING AN ULTRACENTRIFUGE

B. I. DEUTCH, F. R. METZGER and F. J. WILHELM †

Bartol Research Foundation of the Franklin Institute, Swarthmore, Pennsylvania ††

Received 14 December 1959

Abstract: Resonance fluorescence from the 105-keV level in Gd^{155} was studied with the centrifuge method. Assuming a branching ratio $\Gamma_0/\Gamma = 0.69$ for this E1 transition to the ground state, a mean life $\tau_\gamma = 6.0^{+6}_{-3} \times 10^{-10}$ sec was calculated from the measured resonance scattering at different source velocities. This lifetime and τ_γ of the 87-keV level measured by Vergnes are consistent with the E1 lifetime predictions of the Nilsson model if the 87-keV orbital is [651$\frac{3}{2}$] and the 105-keV orbital is [643$\frac{3}{2}$] at a nuclear deformation $\delta \approx 0.26$.

1. Introduction

A simplified version of the decay scheme given by Boehm and Hatch [1]) for 1.7-year Eu^{155} is reproduced in fig. 1. According to it the 87- and 105-keV gamma rays are E1 transitions. Using delayed coincidences, Vergnes [2]) measured the lifetime of the 87-keV level and established an upper limit for the mean life of the 105-keV state. Taking into account the branching from these levels [1]) and using theoretical conversion coefficients [3]), one calculates from Vergnes'

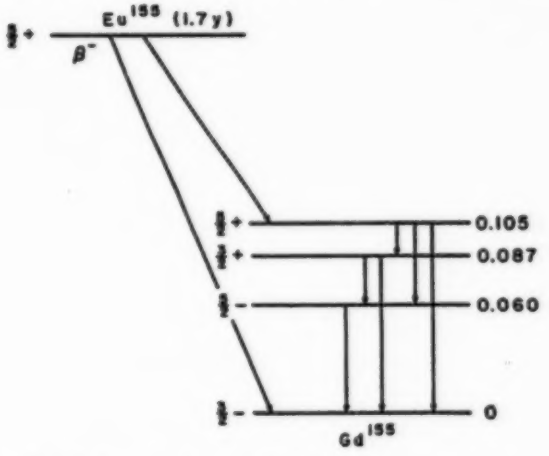

Fig. 1. Simplified decay scheme of Eu^{155}. Energies are given in MeV.

results partial gamma ray mean lives of $\tau_\gamma(87) = 1.1 \times 10^{-8}$ sec and $\tau_\gamma(105) \leqq 2.3 \times 10^{-9}$ sec. Vergnes indicated that, in line with the experience in other

† Now with the Franklin Institute Research Laboratories, Philadelphia, Pennsylvania.

†† Supported by a grant from the National Science Foundation.

strongly deformed nuclei [4]), the lifetime of the hindered 87-keV E1 transition agreed within one order of magnitude with the prediction of the Nilsson model[5]). Since there existed some ambiguity in the assignment of the proper orbitals to the two levels, and since it appeared to be of interest to test the Nilsson model for two hindered E1 transitions in the same nucleus, it was decided to measure the actual lifetime of the 105-keV level in Gd^{155}.

Of the available resonance fluorescence techniques [6]) the centrifuge method [7]) was chosen because it allows one to change the resonance scattering in a well understood manner and thus enables one to separate it from the background radiation. It should be pointed out here that with a gadolinium scatterer and a Eu^{155} source at rest a resonance fluorescence effect already exists at room temperature. It would, however, be difficult to establish the existence of this effect because it would involve the precise matching of two scatterers for all non-resonant scattering processes.

2. Source Preparation

The source was prepared by irradiating 99.07 % enriched Sm^{154} in the form of Sm_2O_3 † in the Oak Ridge Laboratory Low Intensity Testing Reactor. 1.7-year Eu^{155} was formed from the 23-minute decay of Sm^{155} produced by the reaction $Sm^{154}(n, \gamma)Sm^{155}$. The Eu^{155} had to be separated from the Sm because the maximum capacity of the centrifuge tubes was about 25 milligrams of material. For this separation, an ion exchange column [8–10]) with Dowex 50—X12, 200—400 mesh cation exchange resin and with α-hydroxy-iso-butyric acid as the eluant was used. The Sm_2O_3 was dissolved in 1*M* HCl and added to the resin column which had been ammoniated with 0.25*M* ammonium α-hydroxy-iso-butyric acid. After the elution, the activity was dried, ashed, and added to the small centrifuge tube in a rubber matrix.

After the decay of the 14-day Eu^{156} formed in a second order reaction, the main remaining radioactive contaminants were the long lived isotopes Eu^{152} and Eu^{154} which represented approximately 1 percent of the total activity.

3. Experimental Procedures

A cut-out view of the experimental apparatus is shown in fig. 2. The 5 in. diameter Al rotor of the ultracentrifuge was shaped for minimum gamma ray absorption and allowed the use of sources with up to 0.01 ml volume. Gd_2O_3 and Sm_2O_3 scatterers of $1\frac{1}{2}$ in. diameter and 0.080 in. thickness were used at a position 15 cm from the mean position of the source. The detector, a 6 mm thick NaI(Tl) crystal mounted on an RCA 6342 photomultiplier tube, was located 9 cm from the mean position of the scatterer. A $\frac{1}{16}$ in. copper absorber

† Obtained from the Stable Isotopes Division of the U. S. Atomic Energy Commission.

in front of the crystal preferentially attenuated the low energy portion of the scattered radiation. Gold and lead shielding, placed between source and crystal in the manner indicated, absorbed the high energy gamma rays from the $Eu^{152,154}$ contaminant. Both the vacuum vessel of the centrifuge and the detector were in addition encased in lead to reduce the background counting rate. Since, for an angular distribution of the form $W(\theta) = 1+a_2 \cos^2\theta$, the differential cross section at a scattering angle of 125 degrees is equal to $1/4\pi$ times the total cross section, independent of the value of a_2, this angle was chosen for the experiment.

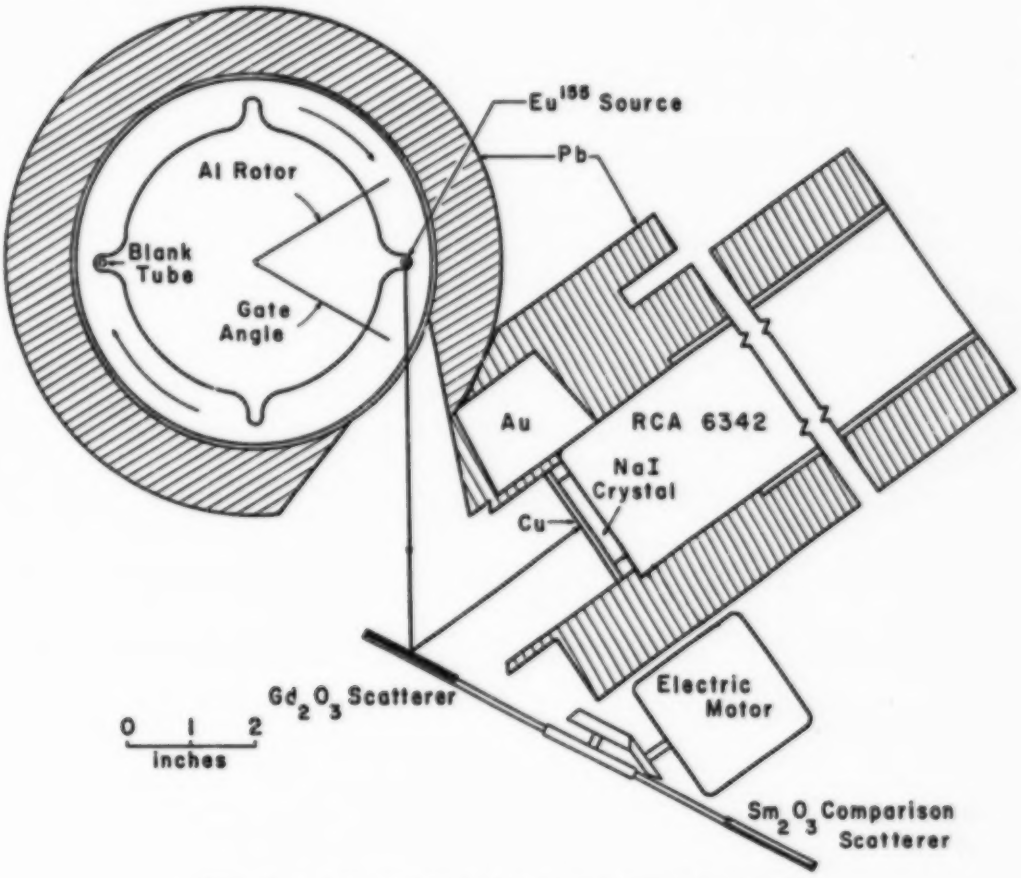

Fig. 2. A cut-out view of the experimental apparatus.

A 10 HP compressor provided the air pressure for the driving as well as the lifting systems of the centrifuge which had been built according to a design by Beams *et al.* [11]). Once the source in the tip of the rotor had reached the desired speed, a simple reducing valve kept the air flow constant enough to maintain the source velocity to better than ± 1 %. The angular velocity of the rotor was measured by observing with a frequency meter the signal from a pick-up coil surrounding a small magnet attached to the rotor shaft.

In order to improve the signal-to-noise ratio of the scattering experiment,

the detection equipment was gated so that counts were accepted only when the gamma rays striking the scatterer were emitted essentially in a tangential direction to the path of the source. The gate was operated by light signals reflected from a polished surface of the magnet mentioned above. The gate width corresponded to a 60 degree rotation; the duty cycle ($\frac{1}{6}$) was checked with a stationary source of Cs^{137} by comparing the "gated" counting rate with the counting rate unrestricted by a gate. The correct angular position of the gate was assured by visually aligning the source and the light beam that provided the initiating gate signal.

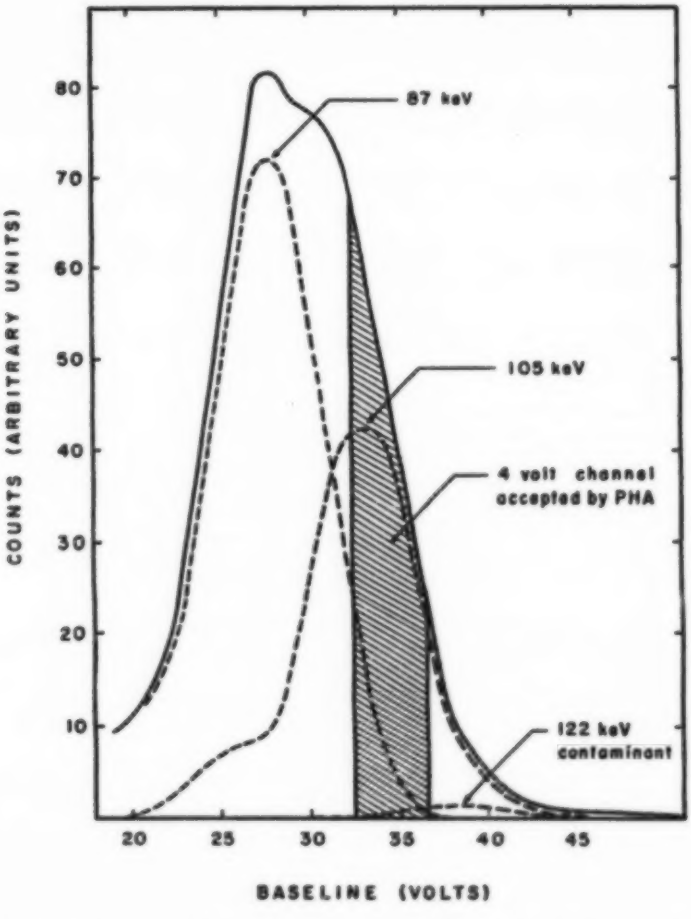

Fig. 3. The pulse height spectrum of the direct radiation from a Eu^{155} source. The decomposition into the main gamma lines is indicated by the dashed curves.

The pulse height spectrum of the direct Eu^{155} radiation is shown in fig. 3. The decomposition of this spectrum into 87-, 105-, and 122-keV lines is indicated by dashed lines. The 122-keV gamma ray is the main radiation from the Eu^{152} contaminant. The shapes of the lines and their positions were derived from the pulse height distributions observed for the 97- and 279-keV gamma rays emitted by Cd^{107} and Hg^{203}, respectively. The shaded area represents the

channel accepted by the single channel analyzer in the scattering experiment. The 105-keV radiation is responsible for (77±7) % of the direct beam counting rate in this channel.

Measurements were carried out with the Eu^{155} source moving towards the scatterer at a velocity of 230 m/sec ("forward velocity"), with the source at rest, and finally with the source moving away from the scatterer at a velocity of 294 m/sec ("reverse velocity"). When the source is moving towards the scatterer, the emission line is Doppler shifted so that it overlaps the absorption line completely, thus giving rise to the maximum resonance scattering effect. With the source moving away from the scatterer, the effect of the Doppler shift is to separate the two lines and to reduce the resonance effect practically to zero. With the source at rest, the intermediate situation of partial overlap exists.

4. Results

The average values of the differences between the counting rates with the Gd_2O_3 scatterer and the Sm_2O_3 comparison scatterer for the three experimental source velocities are given in table 1.

TABLE 1

The experimental values for the difference $N(v)$ between the counting rate N_{Gd} with the Gd_2O_3 scatterer and the counting rate N_{Sm} with the Sm_2O_3 comparison scatterer for the three velocities v used in the Gd^{155} study.

Velocity v (m/sec)	Counting rate difference $N(v) = N_{Gd} - N_{Sm}$ in counts/minute
+230 (forward)	0.60±0.12
0	0.40±0.06
−294 (reverse)	0.23±0.12

The errors given are purely statistical; they are large because the resonance scattering effect represented only a small fraction of the total counting rate. With the gate in operation, typical counting rates were of the order of 17 counts per minute.

The results shown in table 1 were obtained in three independent runs. The data of a fourth run were not included in the average because an unexplained increase in the background counting rate occurred during this run; inclusion of this fourth run in the average would have resulted in a 30 per cent increase of the value for τ_γ.

Since the residual resonance effect for the reverse velocity (−294 m/sec) was expected to amount to less than two percent of the maximum resonance scatter-

ing effect (see eq. (1)), the counting rate difference with the reverse velocity represented essentially the mismatch of the scatterers for all non-resonant effects. In plotting the experimental points in fig. 4, 0.22 counts/minute were subtracted from the counting rates given in table 1.

5. Evaluation

For the centrifuge experiment the effective resonance scattering cross section may be written in the form

$$\sigma_R = \frac{2J_1+1}{2J_0+1}\,\frac{\lambda^2}{4\sqrt{\pi}}\,\frac{\Gamma_0^2}{\Gamma}\,\frac{1}{E_\gamma}\sqrt{\frac{Mc^2}{2k(T_s+T_{sc})}}\,e^{-\frac{M(E_\gamma/Mc-v)^2}{2k(T_s+T_{sc})}}, \qquad (1)$$

where J_1 and J_0 are the total angular momenta of the excited state and the ground state, respectively, E_γ is the energy of the gamma ray and λ the corresponding wavelength; Γ_0 is the partial width for the direct gamma ray transition to the ground state, and Γ the total width of the level; M designates the mass of the nucleus, k Boltzmann's constant; T_s and T_{sc} are the effective temperatures [6, 12]) of the source and the scatterer, respectively; v is the relative velocity of source and scatterer, c the velocity of light. For the 105-keV transition in Gd^{155} a value $\Gamma_0/\Gamma = 0.69$ was calculated on the basis of the decay scheme of Boehm and Hatch [1]) and the theoretical conversion coefficients of Rose [3]). A Debye temperature of 250° was assumed in the calculation of the effective temperatures $T_s = T_{sc} = 308°$.

Using eq. (1), the counting rates expected for different relative velocities v and different values of Γ_0 were calculated for the geometry of fig. 2. For this purpose the contributions of different sections of the scatterer for the subdivisions of the source path had to be summed. The electronic attenuation of the incoming and outgoing radiation was taken into account using a total cross section [13]) $\sigma_t = 8.4\times10^{-22}$ cm² per Gd atom. The counting rate versus velocity curves expected for mean lives $\tau_\gamma = \hbar/\Gamma_0$ of 4, 6, and 12×10^{-10} sec, are compared in fig. 4 with the experimental results. The curve calculated for $\tau_\gamma = 6\times10^{-10}$ sec agrees well with the experimental points. Taking into account the statistical errors, our final value for the mean gamma lifetime is

$$\tau_\gamma = (6^{+6}_{-2})\times10^{-10}\ \text{sec}.$$

The dashed curves in fig. 4 are those calculated for the upper and lower limits of the lifetime.

It might be mentioned that the assumption of a Debye temperature of 250° was checked in a separate experiment. In this experiment, with the source at rest, the resonance scattering with source and scatterer at liquid nitrogen temperature was compared with the scattering at room temperature. From the

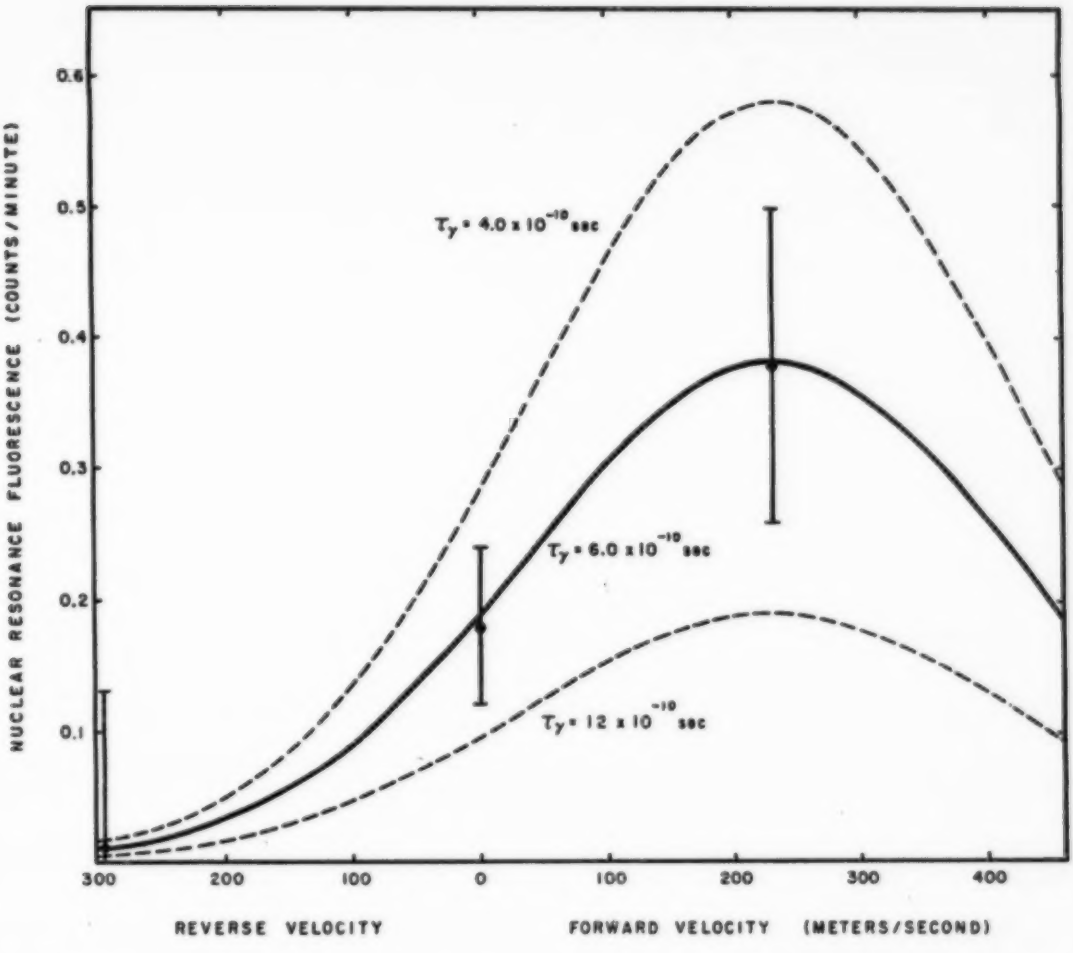

Fig. 4. The resonance scattering effect as a function of the velocity of the source. The heavy line represents the theoretical counting rate for $\tau_\gamma = 6 \times 10^{-10}$ sec for the geometry used. The dashed curves are the theoretical counting rates for the upper and lower experimental lifetime limits. The experimental points are shown for comparison purposes.

absence of a marked effect of the crystalline binding [12, 14]) it can be concluded that the "Debye" temperature of our source-scatterer combination must be smaller than 255°.

6. Discussion

For the comparison of the experimental lifetimes with the predictions of the Nilsson model the theoretical lifetimes were calculated as a function of the nuclear deformation δ for the two ways in which the orbitals $[651\frac{3}{2}]$ and $[642\frac{5}{2}]$ can be assigned to the 87- and 105-keV levels. The wave-functions of Nilsson [5]) were used. The results of these calculations are shown in fig. 5 where the experimental ranges of lifetimes as reported in this paper (105 keV) and by Vergnes [2])

(87 keV) are also indicated †. If the calculated curves are taken at face value, the experimental lifetimes unambiguously assign the 87-keV level to the $[651\frac{3}{2}]$ orbital and the 105-keV level to the $[642\frac{5}{2}]$ orbital. It is gratifying that for these two levels the agreement of experiment and theory occurs for the

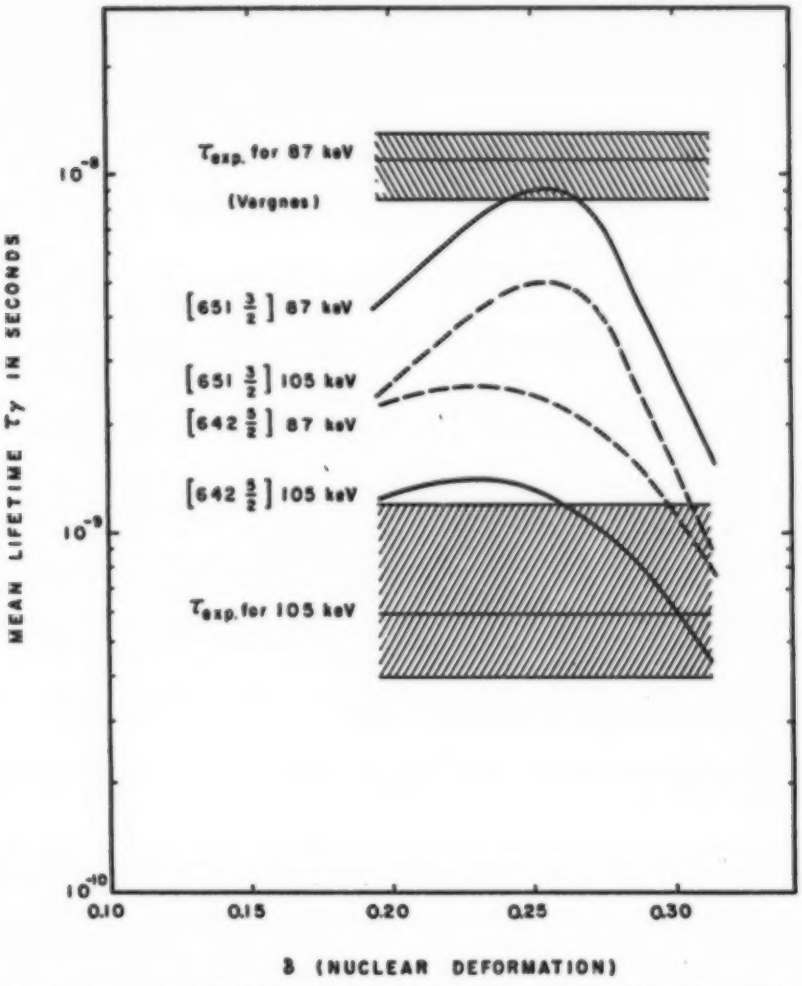

Fig. 5. The mean gamma ray lifetimes for the 87- and 105-keV transitions in Gd^{155} as a function of the nuclear deformation δ. The solid curves represent the theoretical predictions of the Nilsson model for the most probable assignments of orbitals to the 87- and 105-keV levels. The dashed curves correspond to the opposite assignment of orbitals. The experimental τ_γ for the 105-keV level has to be reduced by a factor of 1.5 if the 105-keV orbital is $[651\frac{1}{2}]$.

same nuclear deformation $\delta \approx 0.26$, and that the assignment $[521\frac{3}{2}]$ for the ground state is consistent with such a deformation.

The agreement between the experimental lifetimes and the predictions of the Nilsson model is impressive when one realizes that the ratio of the experimental

† The lifetime for the 105-keV transition indicated in fig. 5 is that calculated with $J_1 = \frac{1}{2}$. For $J_1 = \frac{3}{2}$ the shaded area would have to be moved downwards, i.e. the lifetime would be shorter by a factor of 1.5.

lifetimes to the Weisskopf single particle values [15]) for a nuclear radius $R = 1.2\times10^{-13}A^{\frac{1}{3}}$ cm are $\approx 2\times10^{3}$ for the 105-keV transition and $\approx 2\times10^{4}$ for the 87-keV transition.

We wish to thank Dr. S. Fallieros for helping us with the calculations using the Nilsson model, and for informative discussions. The generous advice of Prof. J. W. Beams and Mr. F. Linke of the University of Virginia concerning the design of the ultracentrifuge is gratefully acknowledged.

References

1) F. Boehm and E. N. Hatch, Z. Physik **155** (1959) 609
2) M. Vergnes, Comptes Rendus **248** (1959) 1158
3) M. E. Rose, Internal Conversion Coefficients (North-Holland Publishing Co., Amsterdam, 1958)
4) M. E. Voikhanskii, JETP **33** (1958) 771
5) S. G. Nilsson, Mat. Fys. Medd. Dan. Vid. Selsk. **29**, No. 16 (1955)
6) See, for instance, F. R. Metzger in Progress in Nuclear Physics, Vol. 7 (O. R. Frisch, editor) (Pergamon Press, New York, 1959)
7) P. B. Moon, Proc. Soc. A **64** (1951) 76
8) J. R. Grover (Brookhaven National Laboratory), private communication
9) R. K. Sheline (Florida State University), private communication
10) G. R. Choppin and R. J. Silva, Journ. Inorg. and Nucl. Chem. **3** (1956) 153
11) Beams, Linke and Sommer, Rev. Sci. Instr. **9** (1938) 248
12) W. E. Lamb, Phys. Rev. **55** (1939) 190
13) C. M. Davisson and R. D. Evans, Revs. Mod. Phys. **24** (1952) 79
14) R. Mössbauer, Z. Physik **151** (1958) 124
15) See, for instance, J. M. Blatt and V. F. Weisskopf, Theoretical Nuclear Physics (John Wiley and Sons, Inc., New York, 1952) Chap. XII

2.I

Nuclear Physics **16** (1960) 90—91; © *North-Holland Publishing Co., Amsterdam*

Not to be reproduced by photoprint or microfilm without written permission from the publisher

THE PHOTONUCLEAR REACTIONS (γ, d) AND (γ, np) ON K^{39}

P. HORVAT, J. PAHOR and M. VAKSELJ

Institute "Jožef Stefan", Ljubljana, Yugoslavia

Received 19 January 1960

Abstract: Argon 37 has been identified as the product of (γ, d) and (γ, np) reactions on potassium 39. The combined yield curve of these reactions has been measured for X-rays of 20 to 25 MeV maximum energy. A proportional counter technique for gaseous sources has been used for spectrum identification and for yield curve measurements.

The photonuclear reactions (γ, d) and (γ, np) on K^{39} have not been reported before, probably because the reaction product A^{37} has a relatively long half life (34 days), and decays by pure electron capture, emitting only K and L X-rays of 2.8 and 0.25 keV, respectively. Because of the low energy of these X-rays, it appeared necessary to use for their identification a proportional counter.

In our experiments, samples each containing about 10 g of metallic potassium have been prepared under vacuum in a glass vessel with a diameter of 2.5 cm. During irradiation the sample has been placed in the axis of the betatron X-ray beam, 62 cm from the target.

The X-ray doses have been monitored with a thin transmission ionization chamber located between the sample and the betatron target. A Victoreen thimble inserted in the centre of an 8 cm lucite cube at the site of the sample, has been used for the calibration of the monitor, in a similar way as has been done by H. E. Johns *et al.* [1]).

After irradiation by a dose between 5 and 50 kiloroentgens the sample has been melted and stirred for 10 minutes. The previously evacuated proportional counter was then filled up to 1 atmosphere by a gas mixture (90% argon + 10% methane) flowing over the stirred liquid potassium. Thus any active gas was practically completely extracted from the potassium, as shown by a repetition of the extracting process.

The spectrum of the activity being investigated showed peaks at 2.8 and 0.25 keV with the intensity ratio 10 : 1. Within the limit of experimental error this spectrum, as well as the half life, proved to be identical with the spectrum and half life of A^{37}. So it was confirmed that A^{37} appears as a product of photonuclear reactions on potassium.

Absolute activities have been determined by means of an end-corrected

counter. The resulting yield curve is given on the figure below. Taking into account the abundance of potassium isotopes and the threshold values for the various possible photonuclear reactions on potassium, we see that $K^{39}(\gamma, d)$ and $K^{39}(\gamma, np)$ are practically the only ways leading to A^{37}, if the photon energies are below 25 MeV. In this energy region therefore the mentioned curve shows the combined yield of those two processes. A discrimination between both reactions has so far not been achieved. Owing to the small yield between the two thresholds it has not been possible to identify the (γ, d) process in this region. The reaction $K^{40}(\gamma, t)A^{37}$ (with the threshold at 17.5 MeV) can be neglected due to the small abundance of K^{40}.

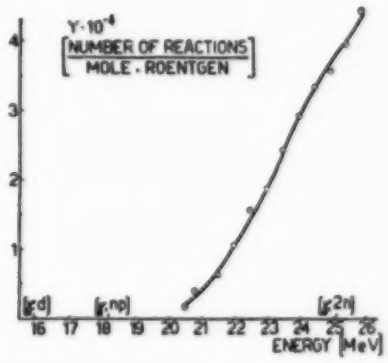

Above 25 MeV the $K^{39}(\gamma, 2n)K^{37}$ reaction also leads indirectly to A^{37} through positon decay of K^{37} (half life 1.2 sec). In this energy region, the A^{37} activity measures the sum of (γ, d), (γ, np) and $(\gamma, 2n)$ photonuclear processes on K^{39}.

The yield curve shows that an activity of 2.3×10^{-7} microcuries of A^{37} per roentgen and per mole of natural potassium can be produced at 25 MeV maximum photon energy. About twice as much can be obtained at 30 MeV. The mentioned photonuclear reactions seem to be a convenient way for the production of A^{37}.

We thank Mr. B. Obersnel and Mr. J. Šnajder for their help during the experimental work.

Reference

1) H. E. Johns, L. Katz, R. A. Douglas and R. N. H. Haslam, Phys. Rev. 80 (1950) 1062

2.H

Nuclear Physics 16 (1960) 92—98; © *North-Holland Publishing Co., Amsterdam*

Not to be reproduced by photoprint or microfilm written without permission from the publisher

COULOMB EXCITATION OF Li^7, F^{19} AND Na^{23} BY Ne^{20} IONS

P. H. STELSON and F. K. McGOWAN

Oak Ridge National Laboratory, Oak Ridge, Tennessee

Received 1 December 1959

Abstract: Ne^{20} ions of 9 to 11 MeV obtained by the acceleration of doubly charged ions in the ORNL 5.5 MV Van de Graaff have been used to study Coulomb excitation in light nuclei. Excitation of the following states has been observed: Li^7, 478 keV; F^{19}, 110 and 197 keV; Na^{23}, 440 keV. Absolute values for the reduced electromagnetic transition rates have been obtained with an accuracy of ± 20 %.

To study the Coulomb excitation of light nuclei it is advantageous to use heavy ions in order to minimize complications resulting from reactions directly involving nuclear forces. Coulomb excitation work has been reported with heavy ions of energies 15 to 120 MeV produced by cyclotrons and linear accelerators [1, 2]). In this note we wish to point out that heavy ions with somewhat lower energies which can be produced by acceleration in electrostatic generators are also valuable for the study of Coulomb excitation in light nuclei.

Neon gas was fed into the conventional R.F. ion source of the 5.5 MV ORNL electrostatic accelerator. Approximately 0.5 μA of accelerated $(Ne^{20})^{++}$ was obtained and hence Ne^{20} ions with energy variable up to 11 MeV were available. Because of the low charge to mass ratio of the $(Ne^{20})^{++}$ ions, it was not possible to bend these ions through the required angle with the analyzing magnet. Therefore, before entering the magnet, the ions were passed through a gas stripper tube fed with argon gas. About 25 % of the $(Ne^{20})^{++}$ was converted to $(Ne^{20})^{+++}$ which could be analyzed by the magnet.

Figures 1, 2, and 3 are representative γ-ray scintillation spectrometer spectra showing excitation of low-lying states of F^{19}, Na^{23} and Li^7, respectively. Thick targets of CaF_2, NaCl, and Li_2CO_3 were used. Because of the rapid decrease of the Coulomb excitation cross section both with increasing energy of the excited state and with increasing target Z, the elements Ca, Cl, C and O_2 are not appreciably excited. The Coulomb excitation of the two states in F^{19} at 110 keV and 197 keV is especially strong and clean with these energy Ne^{20} ions. Evidence for the Coulomb excitation of the first excited state of Li^7 has not previously been reported.

The variation of the gamma-ray intensities has been measured for Ne^{20} energies of 9, 10 and 11 MeV. These γ-ray intensities are given in column 3 of table 1. In general, the intensity measurements have an absolute accuracy of

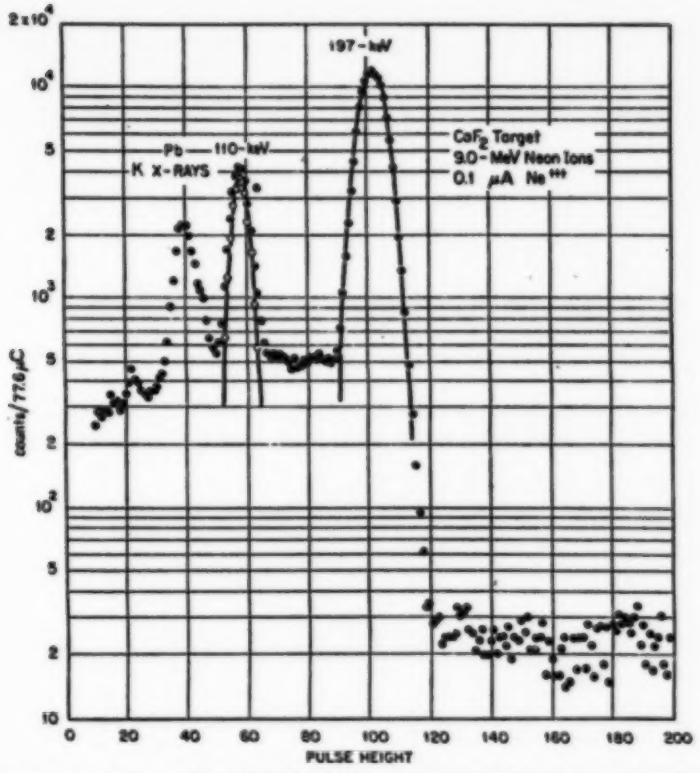

Fig. 1. Gamma-ray spectrum with 3″×3″ NaI crystal resulting from bombardment of CaF_2 target with 9.0-MeV Ne^{20} ions. The lead K X-rays result from the fact that the crystal was surrounded by a lead shield to reduce room background. About 15 % of the intensity of the 110-keV peak (indicated by the open circles) is attributed to the backscatter peak of the intense 197-keV γ-ray.

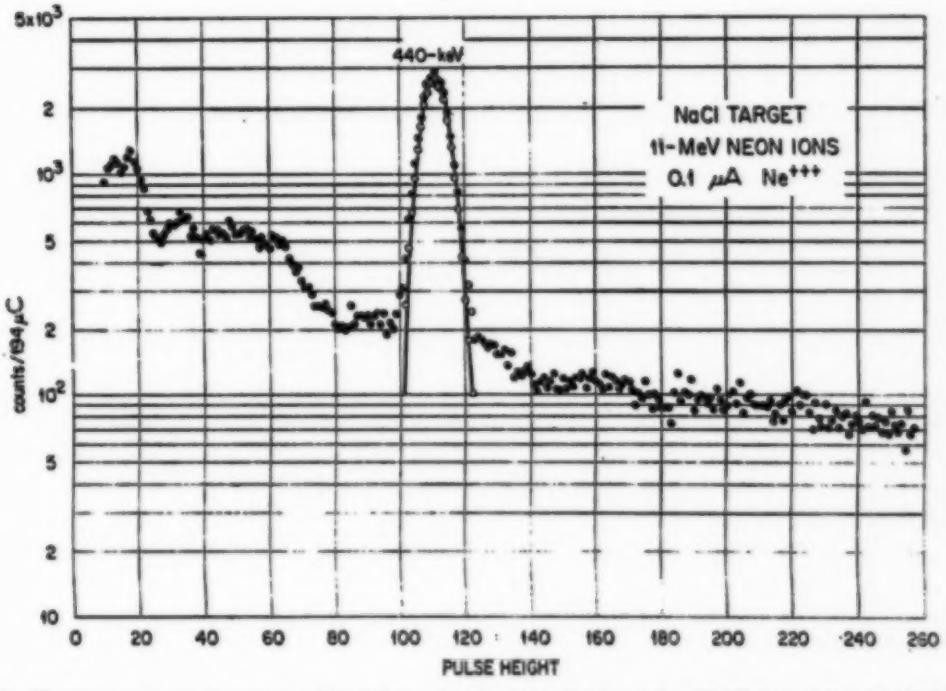

Fig. 2. Gamma-ray spectrum resulting from the bombardment of a NaCl target by 11-MeV Ne^{20} ions.

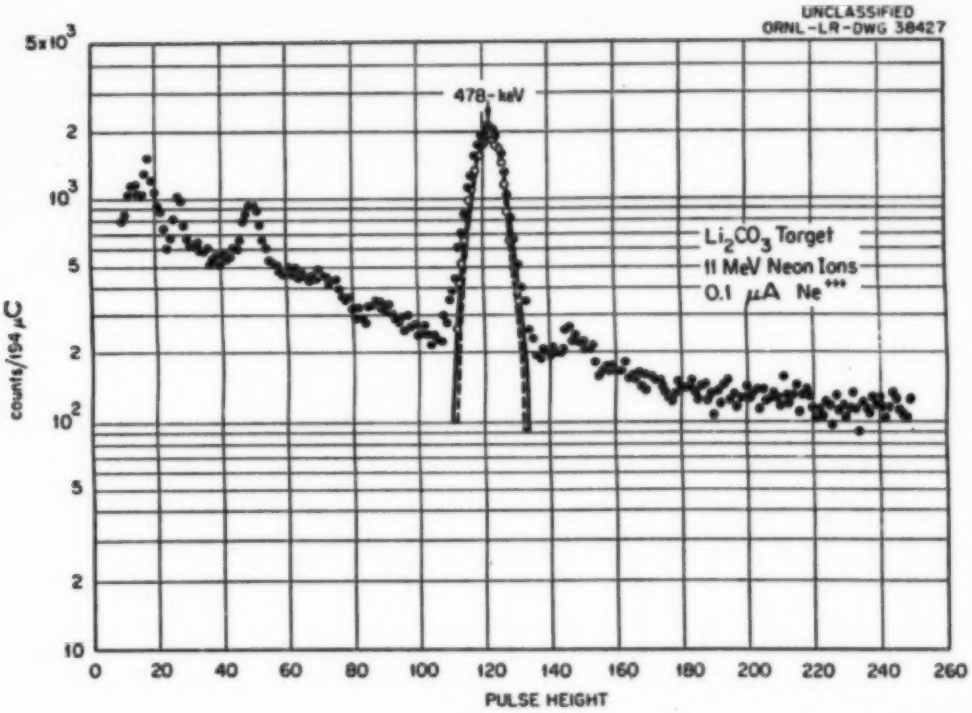

Fig. 3. Gamma-ray spectrum resulting from the bombardment of Li_2CO_3 target by 11-MeV Ne^{20} ions. The observed width of the 478-keV peak is about 12 % larger than one expects for a monoenergetic γ-ray. It is reasonable to attribute the larger width to the Doppler broadening of the 478-keV γ-ray which results from the large translational energies of the Li^7 nuclei when bombarded by Ne^{20}.

TABLE 1

Coulomb excitation by Ne^{20} ions

The first column lists the energy of the Ne^{20} ions in MeV. The second column lists the target nucleus, the observed γ-ray energy in keV and the target material. The third column lists the observed thick target γ-ray yield in units of γ-rays per incident particle. The fourth column lists the theoretical thick target Coulomb excitation integral. The final column lists the reduced electromagnetic transition probability.

$E_{Ne^{20}}$ (MeV)	Nucleus and State	Yield $\left(\frac{\gamma\text{'s}}{\text{incident particle}}\right)$	Y (keV · mg · cm^{-2})	$B(E2)_{ex}$ (cm^4)
9	F^{19}	1.32×10^{-9}	0.487 †	7.1×10^{-50} †
10	110-keV	1.71×10^{-9}	0.701 †	6.3×10^{-50} †
11	CaF_2	2.21×10^{-9}	0.933 †	7.1×10^{-50} †
9	F^{19}	8.80×10^{-9}	121	5.0×10^{-51}
10	197-keV	1.57×10^{-9}	218	5.0×10^{-51}
11	CaF_2	2.44×10^{-8}	348	4.9×10^{-51}
9	Na^{23}	1.07×10^{-10}	1.80	0.92×10^{-50}
10	440-keV	5.22×10^{-10}	6.87	1.16×10^{-50}
11	NaCl	1.41×10^{-9}	19.7	1.11×10^{-50}
9	Li^7	2.84×10^{-10}	2.57	8.3×10^{-52}
10	478-keV	6.78×10^{-10}	7.25	7.2×10^{-52}
11	Li_2CO_3	1.40×10^{-9}	16.5	6.5×10^{-52}

† Excitation of the 110-keV state in F^{19} is an E1 excitation. Hence the quantity in the last column is $B(E1)_{ex}$(cm^2) and the quantity Y is given in MeV^{-1} · mg · cm^{-2}.

10 %. The intensity of the 110 keV γ-ray of F^{19} is less accurate (± 15 %) because the backscatter peak of the strong 197-keV γ-ray occurs at approximately 110 keV. An estimate of the intensity of the backscatter γ-rays was made by measuring other γ-ray spectra under the same experimental conditions. Additional information on this point was obtained by measuring the spectrum of the 197-keV γ-ray at the 870-keV resonance in the $F^{19}(p, p'\gamma)$ reaction where the yield of the 110-keV γ-ray is quite low [3]). Column 4 lists the theoretical thick target integral [4]). The last column lists the corresponding reduced electromagnetic transition probability [$B(E2)_{ex}$ or $B(E1)_{ex}$]. In all cases these quantities are essentially constant for the different Ne^{20} energies and this indicates that the yields vary correctly for Coulomb excitation.

The largest source of error in the absolute values for the reduced electromagnetic transition probabilities results from the lack of knowledge of the stopping powers of Ne^{20} ions in the target materials. These stopping powers enter directly into the integrals listed in column 4 of table 1. The estimated accuracy of these integrals is 15 to 20 %. The energy losses of the Ne^{20} ions in the different target materials were obtained following the method of Papineau [5]) which relates the energy loss for Ne^{20} to the average charge of the Ne ions and the energy loss for protons. The required energy loss values for protons were obtained from the work of Bader *et al.* [6]). The values for the energy loss of Ne^{20} ions as a function of energy for the three target materials † are listed in table 2.

TABLE 2

Values taken for the energy loss of Ne^{20} ions in MeV · $(mg/cm^2)^{-1}$ for the three target materials NaCl, CaF_2, and Li_2CO_3

E_{Ne} (MeV)	$(dE/d\rho x)$NaCl	$(dE/d\rho x)CaF_2$	$(dE/d\rho x)Li_2CO_3$
4.0	6.3	7.4	9.6
6.0	7.1	8.1	10.65
8.0	7.4	8.9	11.1
10.0	8.0	9.6	11.25
12.0	8.5	10.1	11.4

The best values for the reduced electromagnetic transition probabilities are as follows: 110-keV state of F^{19}, $B(E1)_{ex} = 6.3 \times 10^{-30} \pm 25$ % (cm^2); 197-keV state of F^{19}, $B(E2)_{ex} = 5.0 \times 10^{-51} \pm 20$ % (cm^4); 440-keV state of Na^{23}, $B(E2)_{ex} = 1.1 \times 10^{-50} \pm 20$ % (cm^4); 478-keV state of Li^7, $B(E2)_{ex} = 7.3 \times 10^{-52} \pm 20$ % (cm^4).

Temmer and Heydenburg [7]), who used α-particle excitation, have given a value of 1.60×10^{-50}(cm^4) for the $B(E2)_{ex}$ of the 440-keV state in Na^{23}.

The above $B(E2)_{ex}$ value for the 197-keV state in F^{19} leads to a half-life of

† We wish to thank Dr. A. Zucker for helpful discussion of the stopping power for heavy ions.

$(114\pm25)\times10^{-9}$ sec. A previous Coulomb excitation value obtained by α-particle excitation is 150×10^{-9} sec with an uncertainty of a factor 2 [8]). Two direct measurements of the half-life of this state have been made: 56×10^{-9} sec (within a factor 2) [9]) and $(84\pm5)\times10^{-9}$ sec [10]). Similarly, the $B(E1)_{ex}$ given above for the 110-keV state leads to a half-life of $(5.2\pm1.3)\times10^{-10}$ sec. (The 110-keV state is taken as $\frac{1}{2}^-$.) A previous Coulomb excitation value obtained by α-particle excitation is 10×10^{-10} sec (within a factor 2) [8]). A direct half-life measurement of $(6.9\pm1.7)\times10^{-10}$ sec has been reported [9]). The comparison of these values and the quoted errors indicates that there is good agreement among the different determinations of the half-lives for these two states of F^{19}.

Elliott and Bell [11]) first measured the half-life of the 478-keV state in Li^7; they found a value of 5×10^{-14} sec. A recent accurate measurement has been made by Swann, Rasmussen and Metzger [12]) who found $(8\pm1)\times10^{-14}$ sec. This short half-life indicates that the 478-keV γ-ray is predominantly an M1 transition. The above value for the $B(E2)_{ex}$ gives the result that the partial half-life for the E2 decay of the 478-keV transition is 1.5×10^{-9} sec. (The spin of the 478-keV state is taken to be $\frac{1}{2}$.) Consequently, one obtains the very small value of 5×10^{-5} for the ratio E2/M1.

The M1 matrix element for the 478-keV transition is relatively large and one might think it conceivable that the observed excitation results from M1 Coulomb excitation rather than from E2 excitation. However, a calculation of the expected cross section for M1 excitation shows that it is much too small to account for the observed cross section.

Compound nucleus inelastic scattering is a possible alternative mechanism for the production of 478-keV γ-rays by bombardment of Li^7 by Ne^{20}. However, there are reasons for believing that this contribution to the observed yield is not significant. The observed variation in γ-ray yield is correctly predicted by the Coulomb excitation theory. The possible variation in yield for compound nucleus inelastic scattering is not now known, but it is unlikely that it varies in just the same way as that for Coulomb excitation. To gain further evidence on this point, it would be desirable to extend the yield measurements over a larger range of bombarding energies. One can make a rough estimate of the expected cross section for compound nucleus formation when Ne^{20} bombards Li^7. At 11-MeV Ne^{20} energy, only 2.85 MeV is available in the centre-of-mass system. Hence, the collision energy is about 0.4 of the barrier height. Using Coulomb penetrabilities, one finds that the cross section for compound nucleus formation is a few microbarns. On the other hand, the observed cross section at 11 MeV is approximately 1 millibarn.

An intermediate-coupling shell model calculation of the M1 half-life for the 478-keV transition in Li^7 has been made by Lane [13]). In Lane's notation and units, the maximum transition strength A expected theoretically is 19. The recent experimental result of Swann *et al.* [12]) agrees well with this prediction.

It would be of interest to have a similar prediction for the E2 component of this transition. The observed E2 decay rate is about 7 times larger than the single particle estimate used by Wilkinson [14]). However, this estimate takes the case of a transition between states with the spin of the initial state larger than that of the final state. The opposite situation exists for the transition in Li^7. Using the statistical factor worked out by Moszkowski [15]), one concludes that for the Li^7 case, the Wilkinson estimate should be multiplied by 2, thus bringing the estimate to 3.5 times less than the observed value.

On the other hand, Lane and Radicati [16]) have given a single particle estimate which is very close to the observed E2 transition rate. Probably this difference in the two single-particle estimates is caused by the sensitive dependence of the E2 transition rate on the somewhat uncertain radial integral of the wave functions. The Wilkinson estimate assumes good overlap of initial and final states with radii given by $1.5\times10^{-13}A^{\frac{1}{3}}$ cm. Lane and Radicati obtain this radial integral by fitting certain properties of the N^{13} nucleus with shell model calculations. They then state that this value for the integral might be expected to be roughly correct throughout the 1p-shell. A recent analysis of electron scattering information shows that the rms radius of the charge distribution remains rather constant throughout the 1p-shell and this tends to support the use of a constant value for the radial integral in the 1p-shell [17]).

Although not explicitly given by Lane and Radicati for the case of the E2 transition in Li^7, a value for A for the limit of pure L-S coupling can be worked out. Here, A is the ratio of the expected transition rate for the shell model in the L-S coupling limit to the single particle estimate. The value † for A is $\frac{9}{25}$. This is lower by a factor of 3 than the observed value of $A \approx 1$.

The above discussion indicates that the observed E2 transition rate for the 478-keV γ-ray in Li^7 is roughly in accord with theoretical estimates. The fact that the theoretical estimates are possibly 2 to 3 times smaller than the observed rate is in line with other observed E2 transitions and suggests the presence of cooperative motion.

† We wish to thank Dr. G. R. Satchler for working out this value. Lane and Radicati list a closely analogous case for an E2 transition in N^{13} which is a $\frac{3}{2}^-$ to $\frac{1}{2}^-$ transition. However, the entry of $^{27}/_{25}$ for A is in error by a factor of 6 and should be $^{9}/_{50}$ (private communication, of A. M. Lane to G. R. Satchler).

References

1) Alkhazov, Andreyev, Greenberg and Lemberg, Nuclear Physics **2** (1956) 65
2) J. O. Newton and F. S. Stephens, Phys. Rev. Letters **1** (1958) 63
3) C. A. Barnes, Phys. Rev. **97** (1955) 1226
4) P. H. Stelson and F. K. McGowan, Phys. Rev. **110** (1958) 489 (See page 492)
5) M. A. Papineau, Comptes Rendus **242** (1956) 2933
6) Bader, Pixley, Moyer and Whaling, Phys. Rev. **103** (1956) 32
7) G. M. Temmer and N. P. Heydenburg, Phys. Rev. **104** (1956) 967

8) Sherr, Li and Christy, Phys. Rev. **94** (1954) 1076
9) Thirion, Barnes and Lauritsen, Phys. Rev. **94** (1954) 1076
10) Lehman, Leveque and Pick, Phys. Rev. **104** (1956) 411
11) L. G. Elliot and R. E. Bell, Phys. Rev. **74** (1948) 1869; and Phys. Rev. **76** (1949) 168
12) Swann, Rasmussen and Metzger, Phys. Rev. **114** (1959) 862
13) A. M. Lane, Proc. Phys. Soc. A **68** (1955) 189
14) D. H. Wilkinson, Phil. Mag. **1** (1956) 127
15) S. A. Moszkowski, Phys. Rev. **89** (1953) 474
16) A. M. Lane and L. A. Radicati, Proc. Phys. Soc. A **67** (1954) 167
17) Meyer-Berkhout, Ford and Green, Annals of Physics **8** (1959) 119

1.E.5

Nuclear Physics **16** (1960) 99—104; © *North-Holland Publishing Co., Amsterdam*

Not to be reproduced by photoprint or microfilm without written permission from the publisher

ISOTOPE SHIFT AND NUCLEAR DEFORMATIONS

A. S. MELIGY, S. TADROS and M. A. EL-WAHAB

Faculty of Science, University of Alexandria, Egypt

Received 25 November 1959

Abstract: The expression for the isotope shift obtained in a previous paper by considering the nucleus as a sphere in which the charge distribution has the trapezoidal shape is refined and then used to calculate the isotope shift constants for isotopic pairs for which experimental results are available. The isotope shift constants due to nuclear deformation have also been computed taking the deformations from the measured $B(E2)$ transition probabilities. The calculated and experimental results of the isotope shifts of various elements are found to be in agreement within experimental uncertainties. On this evidence, the deformations of a number of nuclei have been deduced from the isotope shift data.

1. Introduction

In a previous paper [1]) it was shown that agreement between the average magnitudes of the observed isotope shifts and the predicted values can be obtained by considering the nucleus as a sphere in which the charge distribution has the trapezoidal shape determined by the electron-nucleus scattering experiments. The observed isotope shifts of some elements, however, show large variations from the shifts predicted by spherical nuclei. Such variations arise from a difference in nuclear quadrupole deformation of two isotopes, as has been pointed out by Brix and Kopfermann [2]). The effect of nuclear deformation on the isotope shift has been calculated by Wilets, Hill and Ford [3]), and independently and more accurately by Bodmer [4]). They showed that the general trend of the observed variations can be explained by the deformation effect. With the theory of the isotope shift developed in the previous paper and with Bodmer's formula for the deformation dependent effect together with the recent measurements of nuclear deformations our aim in the present paper is to obtain quantitative agreement with the experimental results of isotope shifts.

2. The Isotope Shift Formula

From eq. (21) of ref. [1]), the energy displacement for an s electron due to the finite size of the nucleus is sufficiently accurately given by

$$\Delta E = \frac{RZ^2 y_0^{2\sigma}\left(\varepsilon+(1+\sigma)K\right)}{\sigma\Gamma^2(2\sigma)n^3\left(\varepsilon+(1-\sigma)K\right)}\ \mathrm{cm}^{-1}, \qquad (1)$$

where

$$y_0 = \frac{2Z}{a_H}(c+z), \quad \varepsilon = Z\alpha, \quad \sigma = \sqrt{1-\varepsilon^2}, \tag{2}$$

Ze is the nuclear charge, a_H is the Bohr radius for hydrogen, n is the principal quantum number, α is the fine structure constant, R is Rydberg's constant, c and z are the radial parameters of the nuclear charge distribution and

$$K = f^{(2)}(c+z)/g^{(2)}(c+z) \tag{3}$$

is the ratio, at $r = c+z$, of the small and large components of the radial wave function in the nuclear domain. In ref. [1]), the expression for K given by eq. (11) does not include the terms in ε^2 and higher powers. When ε^2 is retained the following more accurate expression is obtained:

$$K = -\frac{2}{5}\varepsilon\left[\left(1+\frac{z^2}{c^2}\right)^{-1}\left(1+\frac{z}{c}\right)^{-1}\left\{1+\frac{3}{2}\frac{z}{c}+\frac{1}{6}\frac{z^2}{c^2}+\frac{z^3}{c^3}\left(\frac{7}{3}+\frac{z}{c}\right)\left(1+\frac{z}{c}\right)^{-1}\right\}\right.$$
$$\left.+\frac{368}{3465}\varepsilon^2\left(1+\frac{325}{184}\frac{z}{c}-\frac{2827}{1104}\frac{z^2}{c^2}+\cdots\right)\right]. \tag{4}$$

The analysis leading to (4) is omitted, since it follows the same lines as in ref. [1]). Substituting (4) in (1) we obtain

$$\Delta E = \frac{RZ^2 y_0^{2\sigma}(3-2\sigma-(1+\sigma)\phi)}{\sigma\Gamma^2(2\sigma)n^3(3+2\sigma-(1-\sigma)\phi)}, \tag{5}$$

where

$$\phi = \frac{z}{c}\left(1+\frac{z^2}{c^2}\right)^{-1}\left(1+\frac{z}{c}\right)^{-2}\left(1-\frac{2}{3}\frac{z}{c}+\frac{z^2}{c^2}\right)$$
$$+\frac{736}{3465}\varepsilon^2\left(1+\frac{325}{184}\frac{z}{c}-\frac{2827}{1104}\frac{z^2}{c^2}\right). \tag{6}$$

The isotope shift due to the normal volume effect is the differential of ΔE with respect to c and is given from eq. (5) as

$$(\delta\Delta E)_v = 2\sigma(\Delta E)\frac{\delta c}{c}\left(1+\frac{z}{c}\right)^{-1}$$
$$\times[1+\psi(3-2\sigma-(1+\sigma)\phi)^{-1}(3+2\sigma-(1-\sigma)\phi)^{-1}], \tag{7}$$

where

$$\psi = 5\frac{z}{c}\left(1+\frac{z^2}{c^2}\right)^{-2}\left(1+\frac{z}{c}\right)^{-2}\left(1-\frac{z}{c}\right)^{3}\left(1+\frac{2}{3}\frac{z}{c}+\frac{z^2}{c^2}\right)$$
$$+\frac{1300}{693}\frac{z}{c}\varepsilon^2\left(1-\frac{1852}{975}\frac{z}{c}\right). \tag{8}$$

The isotope shift due to differing nuclear deformations e_1 and e_2 of the lighter

and heavier isotopes respectively, as given by Bodmer [4]), is

$$(\delta\Delta E)_s = \frac{2}{3}\frac{A}{\delta A}(e_2^2 - e_1^2)(\delta\Delta E)_v, \tag{9}$$

where A is the mass number of the lighter isotope and

$$e = (a-b)/r_0; \tag{10}$$

a and b being the major and minor radii respectively of the nuclear spheroid and r_0 is the radius of a sphere of the same volume.

For each pair of isotopes it is convenient to define a volume dependent isotope shift constant C_v and a deformation dependent isotope shift constant C_s as

$$C_v = (\delta\Delta E)_v(n^3/Z^2) \quad \text{and} \quad C_s = (\delta\Delta E)_s(n^3/Z^2). \tag{11}$$

It follows from eqs. (5), (7) and (9) that

$$C_v = \frac{2Ry_0^{2\sigma}(3-2\sigma-(1+\sigma)\phi)}{\Gamma^2(2\sigma)(3+2\sigma-(1-\sigma)\phi)}\left(1+\frac{z}{c}\right)^{-1}\frac{\delta c}{c} \times [1+\psi(3-2\sigma-(1+\sigma)\phi)^{-1}(3+2\sigma-(1-\sigma)\phi)^{-1}], \tag{12}$$

and

$$C_s = \frac{2}{3}\frac{A}{\delta A}(e_2^2 - e_1^2)C_v. \tag{13}$$

The formula for the theoretical isotope shift constant is

$$C_{th} = C_v + C_s. \tag{14}$$

3. Nuclear Deformations

The calculation of the isotope shift constants C_s due to deformation requires a knowledge of the magnitudes of nuclear deformations. The most accurate values of nuclear deformations available at present are obtained from electric quadrupole transition probability measurements. The deformation e is related to the intrinsic quadrupole moment Q_0 by

$$e(1+0.17\,e+\cdots) = \frac{5Q_0}{4Zr_0^2}. \tag{15}$$

In computing e from (15) we shall take $r_0 = (1.5)^{\frac{1}{2}} \times 10^{-13} A^{\frac{1}{3}}$ cm and use Q_0 values obtained from the measured transition probabilities for going from the ground state spin I_0 to the rotational states I_0+1 and I_0+2 by means of the equations [5])

$$\begin{aligned} B(\mathrm{E2}; I_0 \to I_0+1) &= \frac{15 I_0 e^2 Q_0^2}{16\pi(I_0+1)(I_0+2)}, \\ B(\mathrm{E2}; I_0 \to I_0+2) &= \frac{15 e^2 Q_0^2}{8\pi(2I_0+3)(I_0+2)}. \end{aligned} \tag{16}$$

The results available at present for nuclei whose angular shape is of interest to the isotope shift are given in table 1. The deformation is taken [6, 7]) as zero at the magic neutron numbers $N = 82$ and 126.

TABLE 1

Intrinsic quadrupole moments and deformations obtained from transition probabilities

Nucleus	Q_0 (10^{-24} cm^2)	e	ref.	Nucleus	Q_0 (10^{-24} cm^2)	e	ref.
$_{46}Pd^{108}$	3.27	0.251	[8])	$_{64}Gd^{156}$	6.75	0.287	[13, 14])
$_{46}Pd^{110}$	3.11	0.236	[8])	$_{72}Hf^{178}$	7.7	0.270	[15])
$_{47}Ag^{107}$	2.38	0.187	[8])	$_{72}Hf^{180}$	7.2	0.251	[15])
$_{47}Ag^{109}$	2.38	0.185	[8])	$_{74}W^{182}$	7.1	0.239	[16])
$_{48}Cd^{110}$	2.60	0.190	[9])	$_{74}W^{184}$	6.5	0.218	[16])
$_{48}Cd^{112}$	2.60	0.188	[9])	$_{75}Re^{185}$	5.5	0.188	[16, 17])
$_{54}Xe^{128}$	0	0	[7])	$_{75}Re^{187}$	5.2	0.172	[16, 17])
$_{56}Ba^{138}$	0	0	[7])	$_{76}Os^{186}$	5.5	0.179	[16])
$_{58}Ce^{140}$	0	0	[7])	$_{76}Os^{188}$	5.1	0.165	[16])
$_{60}Nd^{146}$	1.58	0.078	[10])	$_{76}Os^{190}$	4.2	0.136	[18])
$_{60}Nd^{148}$	2.63	0.128	[10])	$_{77}Ir^{191}$	4.39	0.140	[19])
$_{60}Nd^{150}$	4.80	0.227	[10])	$_{77}Ir^{193}$	3.40	0.108	[19, 20])
$_{62}Sm^{148}$	2.24	0.108	[10])	$_{78}Pt^{194}$	4.19	0.131	[8, 21])
$_{62}Sm^{150}$	3.13	0.149	[10])	$_{78}Pt^{196}$	2.97	0.093	[8, 21])
$_{62}Sm^{152}$	5.57	0.263	[10])	$_{80}Hg^{198}$	3.36	0.101	[22])
$_{63}Eu^{151}$	2.90	0.132	[11, 12])	$_{80}Hg^{200}$	2.92	0.088	[22])
$_{63}Eu^{153}$	5.80	0.257	[11, 12])	$_{80}Hg^{202}$	2.43	0.073	[22])
$_{64}Gd^{154}$	6.64	0.287	[13, 14])	$_{82}Pb^{206}$	1.02	0.030	[8])
$_{64}Gd^{156}$	6.71	0.287	[14])	$_{82}Pb^{208}$	0	0	[6])

4. Theoretical and Experimental Isotope Shift Constants and Deformations from Isotope Shifts

The theoretical and experimental results on isotope shifts are given in table 2. Column 5 lists the volume dependent isotope shift constants C_v as computed from eq. (12) with

$$c = 1.05 \times 10^{-13} A^{\frac{1}{3}} \text{ cm}, \quad z = 1.53 \times 10^{-13} \text{ cm}. \tag{17}$$

Column 6 lists the deformation dependent isotope shift constants C_e as computed from eq. (13) using the values of e in table 1. Column 7 lists the theoretical isotope shift constants C_{th} given by eq. (14) and column 8 lists the experimental constants C_{exp} taken from the up-to-date table of Brix and Kofpermann [23]). It should be noted that C_{exp} involves an error of the order of $\pm 20\,\%$ of its value and that C_{th} involves also an error due to the error in the measured deformation e which appears in eq. (13) and to the error in the values of the parameters z and c which appear in eq. (12). It is seen from table 2 that the C_{th} and C_{exp} values are in good agreement within the errors involved. This indicates that the isotope shift is correctly given by eqs. (12), (13) and (14)

TABLE 2

Isotope shift constants

1 Element	2 Z	3 A_1—A_2	4 N	5 C_e (cm^{-1})	6 C_s (cm^{-1})	7 C_{th} (cm^{-1})	8 C_{exp} (cm^{-1})
Ru	44	96— 98	54	0.038			
		98—100	56	0.038	≈0	0.038	0.034±0.009
		100—102	58	0.038			average
		102—104	60	0.037			
Pd	46	106—108	62	0.043			0.042±0.009
		108—110	64	0.043	−0.011	0.032	0.036±0.005
Ag	47	107—109	62	0.046	−0.001	0.045	0.038±0.006
Cd	48	110—112	64	0.049	−0.001	0.048	0.032±0.004
Sn	50	112—114	64	0.056			0.040±0.010
		114—116	66	0.056			0.040±0.010
Xe	54	132—134	80	0.070			0.018±0.004
		134—136	82	0.069			0.025±0.006
Ba	56	134—136	80	0.080			0.012±0.005
		136—138	82	0.080			0.015±0.005
Ce	58	136—138	80	0.091			0.006±0.001
		138—140	82	0.091			0.006±0.001
		140—142	84	0.090			0.147±0.030
Nd	60	146—148	88	0.102	0.051	0.153	0.202±0.038
		148—150	90	0.102	0.177	0.279	0.286±0.054
Sm	62	148—150	88	0.117	0.061	0.178	0.217±0.046
		150—152	90	0.117	0.274	0.391	0.317±0.067
Eu	63	151—153	90	0.125	0.306	0.457	0.450±0.050
Gd	64	152—154	90	0.134			0.375±0.060
		154—156	92	0.133	0	0.133	0.162±0.026
		156—158	94	0.132	0	0.132	0.121±0.019
Hf	72	178—180	108	0.221	−0.130	0.091	0.114±0.013
W	74	180—182	108	0.253			0.080±0.020
		182—184	110	0.252	−0.147	0.105	0.117±0.030
Re	75	185—187	112	0.270	−0.096	0.174	0.157±0.040
Os	76	186—188	112	0.289	−0.086	0.203	0.175±0.027
		188—190	114	0.287	−0.157	0.130	0.150±0.023
		190—192	116	0.286			0.130±0.020
Ir	77	191—193	116	0.307	−0.155	0.152	0.130±0.030
Pt	78	194—196	118	0.328	−0.181	0.147	0.135±0.025
Hg	80	198—200	120	0.376	−0.061	0.315	0.243±0.027
		200—202	122	0.374	−0.057	0.317	0.270±0.030
		202—204	124	0.373			0.267±0.030
Pb	82	204—206	124	0.429			0.280±0.031
		206—208	126	0.427	−0.027	0.400	0.315±0.035
		208—210	128	0.425			0.548±0.061

with deformations obtained from transition probabilities by the theory of Bohr and Mottelson. Thus the isotope shift is consistent with the present ideas of charge distribution and shapes of nuclei.

The agreement of calculated and observed isotope shifts here established indicates that there are no important effects other than those due to the

volume and deformation entering the explanation of the phenomenon of the isotope shift. On this basis, a deduction can be made of nuclear deformations from isotope shifts. Eqs. (13) and (14) with C_{th} replaced by C_{exp}, give

$$e_2^2 - e_1^2 = \frac{3}{2}\frac{\delta A}{A}\left(\frac{C_{exp}}{C_v} - 1\right). \tag{18}$$

Now, if the deformation of one isotope is known, the deformations of other isotopes of the element can be deduced from this equation. Intrinsic quadrupole moments and deformations based on the data of table 1 have been deduced from the values of C_{exp} and C_v in table 2 by means of eqs. (15) and (18) as shown in table 3. Thus the isotope shift provides a valuable source of information on the shapes of nuclei.

TABLE 3

Intrinsic quadrupole moments and deformations obtained from isotope shifts

Nucleus	Q_0 (10^{-24} cm^2)	e	Nucleus	Q_0 (10^{-24} cm^2)	e
$_{46}Pd^{106}$	3.25	0.252	$_{58}Ce^{142}$	2.23	0.116
$_{54}Xe^{132}$	3.06	0.177	$_{64}Gd^{152}$	4.90	0.216
$_{54}Xe^{134}$	2.07	0.120	$_{74}W^{180}$	7.76	0.262
$_{56}Ba^{134}$	3.50	0.193	$_{76}Os^{192}$	3.06	0.099
$_{56}Ba^{138}$	2.43	0.134	$_{80}Hg^{204}$	1.10	0.033
$_{58}Ce^{136}$	3.85	0.202	$_{82}Pb^{204}$	2.66	0.077
$_{58}Ce^{138}$	2.71	0.142	$_{82}Pb^{210}$	2.29	0.065

References

1) A. S. Meligy, Nuclear Physics **14** (1959) 248
2) P. Brix and H. Kopfermann, Z. Physik **126** (1949) 344
3) L. Wilets, D. L. Hill and K. W. Ford, Phys. Rev. **91** (1953) 1488
4) A. R. Bodmer, Proc. Phys. Soc. A **67** (1954) 622
5) A. Bohr and B. R. Mottelson, Mat. Fys. Medd. Dan. Vid. Selsk. **27**, No. 16 (1953)
6) K. W. Ford, Phys. Rev. **90** (1953) 29
7) K. W. Ford, Phys. Rev. **95** (1954) 1250
8) P. H. Stelson and F. K. McGowan, Phys. Rev. **99** (1955) 112
9) G. M. Temmer and N. P. Heydenburg, Phys. Rev. **98** (1955) 1308
10) K. Alder, A. Bohr, T. Huus, B. Mottelson and A. Winther, Revs. Mod. Phys. **28** (1956) 432
11) T. Huus, J. H. Bjerregaard and B. Elbek, Mat. Fys. Medd. Dan. Vid. Selsk. **30**, No. 17 (1956)
12) C. M. Class and U. Meyer-Berkhout, Nuclear Physics **3** (1957) 656
13) N. P. Heydenburg and G. M. Temmer, Phys. Rev. **104** (1956) 981
14) O. Nathan, Nuclear Physics **5** (1958) 401
15) A. Bohr and B. R. Mottelson, Mat. Fys. Medd. Dan. Vid. Selsk. **30**, No. 1 (1955)
16) E. A. Wolicki, L. W. Fagg and E. H. Geer, Phys. Rev. **105** (1957) 238
17) S. L. Segel and R. G. Barnes, Phys. Rev. **107** (1957) 638
18) E. Ye. Berlovich, K. Grotovski, M. Bonitz, V. I. Breslav and B. K. Preobrazhensky, Nuclear Physics **6** (1958) 672
19) B. R. Mottelson and S. G. Nilsson, Mat. Fys. Skr. Dan. Vid. Selsk. **1**, No. 8 (1959)
20) R. H. Davis, A. S. Divatia, D. A. Lind and R. D. Moffat, Phys. Rev. **103** (1956) 1801
21) C. McClelland, H. Mark and C. Goodman, Phys. Rev. **97** (1955) 1191
22) R. Barloutaud, T. Grjebine and M. Riou, C. R. Acad. Sci. **242** (1956) 1284
23) P. Brix and H. Kopfermann, Revs. Mod. Phys. **30** (1958) 517

1.D.2

Nuclear Physics **16** (1960) 105—112; © *North-Holland Publishing Co., Amsterdam*

Not to be reproduced by photoprint or microfilm without written permission from the publisher

COMPARISON OF ASYMMETRIC QUADRUPOLE ROTOR ENERGY LEVEL PREDICTIONS FOR EVEN NUCLEI WITH EXPERIMENTAL RESULTS

C. A. MALLMANN and A. K. KERMAN

Argonne National Laboratory, Lemont, Illinois †

Received 1 October 1959

Abstract: The asymmetric quadrupole rotor energy predictions, taking into account the interactions of the rotations with the beta vibrations, are compared with experimental results. The agreement between experiment and theory is good for nuclei with $R_e(^14+) = [E_e(^14+)/E_e(^12+)] \geqq \frac{3}{2}$. Even parity energy levels of nuclei with $R_e(^14+) < \frac{3}{2}$ are not explained adequately.

As is well known the low lying even-parity states in even nuclei far away from closed shells have spectra characteristic of the axially symmetric rotor including a small rotation-vibration interaction. Recently [1]) it has been shown that the energies of low lying levels in even nuclei outside the well known rotational regions have a systematic dependence on the ratio of the energy of the first 4+ state to the energy of the first 2+ state. In the following we show that the energy levels characteristic of an asymmetric quadrupole rotor taking into account the rotation-vibration interaction agree with experimental data over a wider range of nuclei than those characteristic of the axially symmetric rotor theory, taking into account the same interaction. The energy level predictions are in disagreement with systematics [1]) for nuclei close to closed shells, although the gamma ray transition probabilities predicted for the second 2+ state ($^22+$) appear to agree with experimental results, as pointed out by Van Patter[3]).

For the asymmetric quadrupole rotor [2]) the energy of the n^{th} spin I level is given by

$$E_0(^nI, \gamma, \beta) = A(\beta)\, \varepsilon\, (^nI, \gamma), \tag{1}$$

where $A(\beta)$ is a constant for a given nucleus and depends only on the deformation β. The zero indicates that the rotation-vibration interaction has not been taken into account. As a result of this relation the ratio of energies of two states is independent of $A(\beta)$, and depends only on the parameter γ which measures the deviation from axial symmetry. In order to determine A and γ, the two parameters of the theory, we need to know two energy levels. The experimental ratio $R_e(^22+)$ between the energy of the $^22+$ and the energy of the $^12+$ state is used [2]) to determine γ and the energy of the $^12+$ state to determine A.

† Based on work performed under the auspices of the U. S. Atomic Energy Commission.

These levels are used because $R_0(^22+) = \varepsilon(^22+, \gamma)/\varepsilon(^12+, \gamma)$ is a very sensitive function of γ and because there are many nuclei in which these two levels are known. For reasons of simplicity $R_0(^22+)$ is used directly instead of the parameter γ. The γ value can be obtained from table 1, where $R_0(^22+)$ is given as a function of γ. In the following we shall speak only of the ratio $R(^nI)$ of the energy of the level ^nI to that of the level $^12+$ because we are interested in seeing if the energy ratios are correct no matter what the scale factor A is.

Following Davydov and Filippov it can be shown that these relations hold †:

$$\begin{aligned} R_0(^13+) &= 1+R_0(^22+), \\ R_0(^15+) &= 4+R_0(^22+), \\ R_0(^25+) &= 1+4R_0(^22+). \end{aligned} \tag{2}$$

For the $^14+$; $^24+$; $^34+$; $^16+$ and $^18+$ there is no simple relation between $R_0(^nI)$ and $R_0(^22+)$, therefore we give the numerical value as a function of $R_0(^22+)$ in table 1. We also give $\varepsilon(^12+, \gamma)$ as a function of $R_0(^22+)$, because this is needed to determine $A(\beta)$ from the energy of the $^12+$ state (see eq. (1)). Fig. 1 (full lines) is a plot of $R_0(^nI)$ as a function of $R_0(^22+)$.

TABLE 1

Theoretical asymmetric quadrupole rotor predictions for the ratios $R_0(^nI)$ of the energy of the n^{th} spin I level to the energy of the $^12+$ level, for γ, and for the energy of the $^12+$ state in units of A as a function of $R_0(^22+)$.

$R_0(^22+)$	∞	25.16	15.94	9.254	6.854	3.732	2.408	2.000
γ (°)	0	8	10	13	15	20	25	30
ε ($^12+$)	4.000	4.159	4.251	4.432	4.584	5.072	5.661	6.000
$R_0(^14+)$	3.333	3.329	3.324	3.301	3.272	3.117	2.836	2.666
$R_0(^34+)$	∞	27.50	18.30	11.63	9.268	6.361	5.514	5.666
$R_0(^34+)$	∞	–	–	36.34	26.73	14.18	8.690	6.666
$R_0(^16+)$	7.000	6.978	6.943	6.829	6.695	6.069	5.372	5.000
$R_0(^18+)$	12.00	11.93	11.82	11.48	11.10	9.844	8.602	8.000

In order to compare these predictions with experiment, a survey of the experimental results has been made. For $40 \leqq A \leqq 154$ and $180 \leqq A \leqq 226$ the data are given in ref. [4]) with the exceptions of Ru^{98}, Te^{124} and Nd^{144} which are taken from refs. [5, 6]) and [7]) respectively. The 6+ levels were taken from ref. [1]). For $154 \leqq A \leqq 180$ and $A \geqq 226$ we give $E_0(^12+)$ and $R_0(^nI)$ with their errors in table 2††. In case the error of an energy measurement has not been published an estimate has been made taking into account the type of instrument used and its resolution.

† The relations (2) are independent of the particular assumptions made by Davydov and Filippov about the dependence of the three moments of inertia on γ. They hold for the even parity states of *any* rotor

†† We would like to express our gratitude to W. Scheuer for making available to us his up-to-date compilation for these A values.

TABLE 2

The experimental ratios $R_e(^nI)$ of the energy of the n^{th} spin I level to the energy of the $^12+$ level, the energy of the $^12+$ sate, the b, $R_e(^32+)$ and $\hbar\omega_\beta$ values determined from them and the energy of the $^30+$ β-vibrational state

Nucleus	$E_e(^12+)$ (keV)	$R_e(^32+)$	$R_e(^13+)$	$R_e(^14+)$	$R_e(^34+)$	$R_e(^15+)$	$R_e(^16+)$	$R_e(^18+)$	$b\times10^4$	$R_e(^32+)$	$\hbar\omega_\beta$ (keV)	$E_e(^30+)$ (keV)
Os^{192}	205.75 20	2.377 1	3.356 7	2.821 6					6.9 50	2.38 1	3.900 900	
Os^{190}	186.70 10	2.989 18	4.039 40	2.935 18	5.121 40?		5.613 18	8.902 24	6.7 13	3.00 1	3 800 300	
Os^{188}	155.00 10	4.085 21		3.084 18					23 6	4.09 1	1 800 200	
Os^{186}	137.22 2	5.598 6		3.164 3			6.332 6		?	?		
Gd^{154}	123.07 4	8.109 16	9.182 18	3.016 2					?	?		700
W^{184}	111.13 6	8.136 1	9.053 13	3.275 7					?	?		
Sm^{152}	122.31 4	8.928 27	10.138 30	3.008 1					?	?		685
Er^{166}	80.57 2	9.770 40	10.686 60	3.294 6	11.889 50	13.43 20	6.774 30		7.4 34	10.1 1	1 900 400	1 450
Er^{168}	79.90 40	10.29 10	11.22 11	3.309 30	12.47 13		6.872 70		5 6	10.5 2	2 300 700	
Dy^{160}	87.00 13	11.138 18	12.093 29	3.271 6					12 4	12.0 2	1 600 200	
W^{182}	100.09 2	12.209 12	13.305 15	3.291 2					?	?	—	
Gd^{156}	88.97 1	12.746 12		3.239 1					27 2	15.1 2	1 100 100	
Gd^{158}	79.56 3	14.860 30	15.800 40	3.292 3			6.774 6	11.29 2	9.5 5	15.8 1	1 700 50	
Th^{232}	51 1	15.49 10		3.235 62					22 4	18.7 10	730 60	
Hf^{178}	93.15 10	15.89 18		3.294 14			6.792 18	11.38 12	8.7 17	17.0 3	2 100 200	
Th^{228}	57.48 5	16.81 10	17.71 10	3.238 5					15 2	20 4	1 000 60	
U^{232}	47.20 20	18.39 12	19.98 12?	3.311 22			6.801 50		8.0 25	19.5 4	1 100 150	
Pu^{238}	44.03 5	23.390 70	24.32 8	3.316 6			6.898 14	11.67 3	4.5 18	24.5 4	1 400 200	940
Cf^{250}	42.20 50	24.50 40	25.5 5	3.327 66					0 20	24.5 5		

Question marks indicate disagreement with theoretical predictions (see the text). Errors are indicated in the following way: 3.253 40 means 3.253 ± 0.040.

The experimental values are shown in fig. 1. One can see that for nuclei close to closed shells, which are given in the insert, the points are far away from the asymmetric rotor predictions. For nuclei far away from closed shells the theoretical predictions are a few per cent too high.

In order to try to explain this discrepancy of a few per cent we investigated the effect of the interactions of the rotations with the β vibrations. One can show that in first order approximation the energy of the rotational states is given by

$$E_b({}^nI, \gamma, \beta) = A(\beta)\, \varepsilon\, ({}^nI, \gamma) - bA(\beta)\{\varepsilon({}^nI, \gamma)\}^2 \tag{3}$$

where b is a constant. With the additional assumption of irrotational flow one can show that

$$b = \frac{8}{\left(\frac{\hbar\omega_\beta}{A(\beta)}\right)^2} \tag{3a}$$

where $\hbar\omega_\beta$ is the one-phonon vibrational energy. This additional assumption seems to be unrealistic so that one expects that eq. (3) gives us only a very rough estimate of b. The ratios $R_b({}^nI) = E_b({}^nI, \gamma, \beta)/E_b({}^12, \gamma, \beta)$ are now functions of two variables b and γ. They are shown in fig. 1 (dashed curves) for $b = 10^{-3}$. In the expanded view of the region $0 \leqq R({}^32+) \leqq 5$ the dashed curves have $b = 10^{-2}$.

In order to determine the three parameters (A, γ, b) three energy levels are necessary, the ${}^12+$, ${}^22+$ and any other one. We can then write down three equations

$$R_e({}^22+) = R_b({}^22+, \gamma), \quad R_e({}^nI) = R_b({}^nI, \gamma),$$
$$R_e({}^12+) = A(\beta)[\varepsilon({}^12+, \gamma) - b\{\varepsilon({}^12+, \gamma)\}^2]$$

which, when solved, give the desired values of b, γ and A. This is very impractical because the functions involved are very complicated. There is a simple graphical method to obtain b and $R_0({}^22+)$ for values of $b \leqq 10^{-3}$. One may expand $R_b({}^nI)$ in powers of b and neglect terms in second and higher powers of b. One thus obtains

$$R_b({}^nI) = R_0({}^nI) + b\, \varepsilon\, ({}^nI, \gamma)[1 - R_0({}^nI)]. \tag{4}$$

This implies that for a given $R_0({}^22+)$ (γ value) and different b values we move on a straight line (dotted lines) in fig. 1. The distance from the $R_0({}^nI)$ curve along these straight lines is proportional to b. These properties allow us to obtain b and $R_0({}^22+)$ by a simple linear interpolation for nuclei with $b \leqq 10^{-3}$.

The theory is said to be in agreement with experiment if the values of b and $R_0({}^22+)$ determined by this procedure for different levels of the same nucleus (${}^14+$, ${}^16+$, ${}^18+$, ${}^13+$, ${}^24+$, ${}^15+$, etc.) are the same within their errors, i.e., if

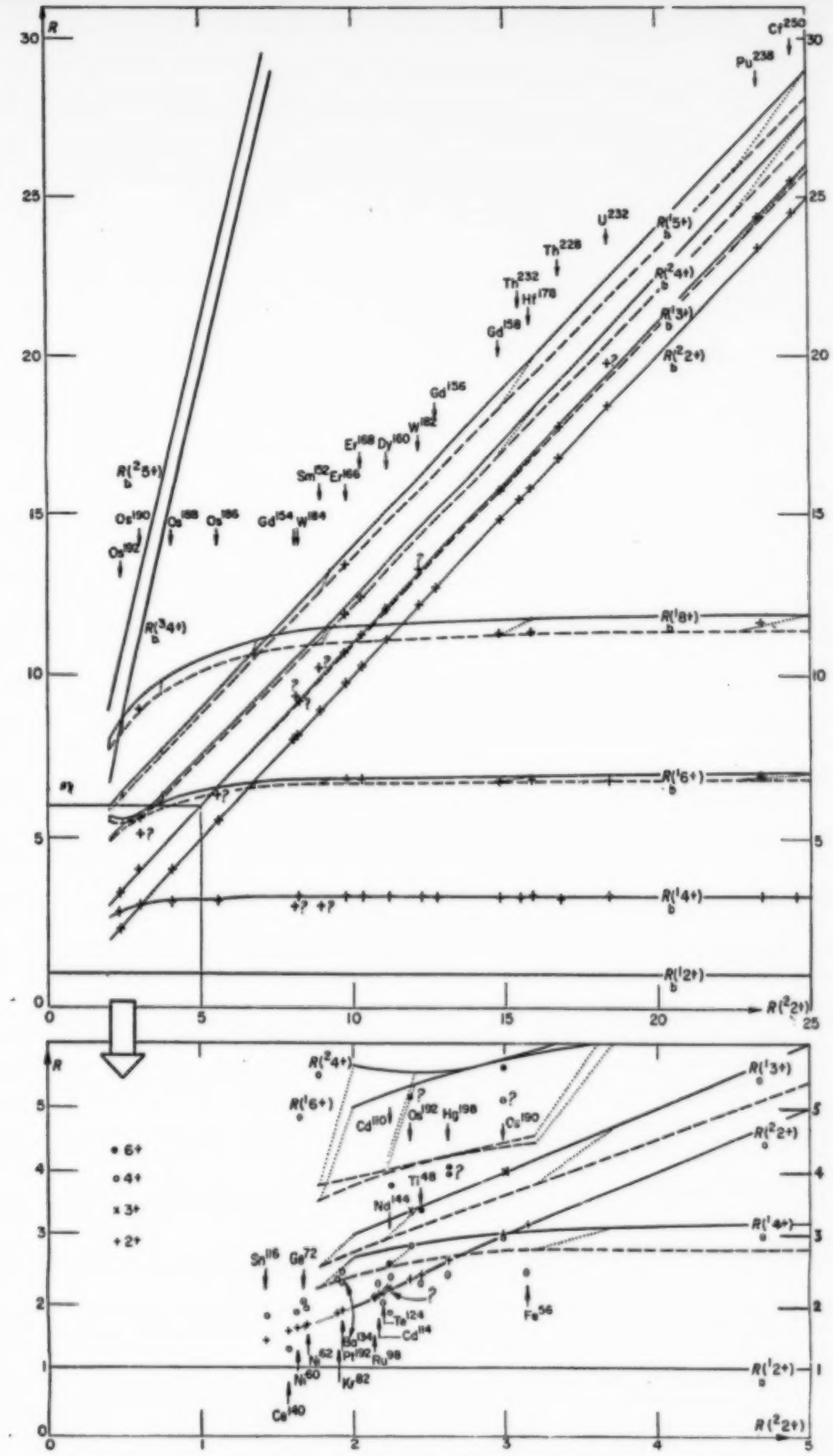

Fig. 1. The full curves are the ratios $R_a(^nI)$ of the energy $E_a(^nI)$ of the n^{th} spin I level to the energy $E_a(^12+)$ of the first excited 2+ level as given by the asymmetric rotor theory. The dashed curves are the ratios $R_b(^nI)$ of the energies of the same excited states taking into account the vibrational rotational interactions. The value of b used is 10^{-3}. In the expanded view of the region $0 \leqq R(^22+) \leqq 5$ the b value is 10^{-2}. The experimental values $[R_e(^nI); R_e(^22+)]$ are also shown. The question marks indicate that the energy of the level is not predicted correctly by theory. In the expanded view of the region $0 \leqq R(^22+) \leqq 5$ the question marks indicate that the spin assignment of the level is not certain.

there is one value of b and $R_0(^22+)$ which explains all the known levels of the ground state asymmetric rotor band. When this can be done we give the values of $R_0(^22+)$, b and $\hbar\omega_\beta$ in table 2. When one out of three or more levels gives a different value of b and of $R_0(^22+)$ than the others we put a question mark beside the $R_e(^nI)$ value of this level in table 2. The question marks in columns b and $R_0(^22+)$ in table 2 indicate that one cannnot find a value of b and of $R_0(^22+)$ which give agreement with experiment. The last column in table 2 gives the energy of the known $^20+$ β-vibrational states.

TABLE 3

Comparison of symmetric rotor theory and asymmetric rotor theory with experimental results in Os^{190}

Os^{190}	R_b (asymmetric)	R_e	R_b (symmetric)
$^22+$	2.98	$2.99\frac{2}{}$	—
$^14+$	2.96	$2.94\frac{2}{}$	3.05
$^16+$	5.60	$5.61\frac{2}{}$	5.44
$^18+$	8.89	$8.90\frac{2}{}$	7.11

R_b are the predictions for the ratios of the energy of the ^nI level to the energy of the $^12+$ level using the best-fit value for b, the parameter of the vibrational-rotational interaction. R_e are the experimental ratios.

For all nuclei with $R_e(^14+) \geqq 3.27$ the theory is in agreement with experiment with the exception of W^{182}, W^{184} and the $^13+$ level in U^{232}. Also $\hbar\omega_\beta$ is in reasonable agreement with the position of the $^20+$ β-vibrational level. At this point it is important to say that the same agreement is obtained for these nuclei assuming rotations of an axially symmetric deformed nucleus. As is well known the $^12+$, $^14+$, $^16+$, $^18+$ levels are then interpreted as rotations and the $^22+$, $^13+$, $^24+$, $^15+$ are explained as a rotational band based on the $^22+$ γ-vibrational state. The energy of the rotational states is given by

$$E_b(I) = A(\beta)\tfrac{2}{3}I(I+1) - bA(\beta)[\tfrac{2}{3}I(I+1)]^2. \qquad (5)$$

Transition probabilities [3]) from the $^22+$ level to other states for these nuclei favour the asymmetric rotor theory.

Nuclei with $\frac{8}{3} \leqq R_e(^14+) < 3.27$ are not explained [1]) by the axially symmetric rotor theory. For these nuclei the situation with respect to the asymmetric rotor theory is as follows:

Sm^{152} is in disagreement. The theoretical $^13+$ level seems to be low and the b value for the $^14+$ level large. The latter fact ties in with the existence of a low lying $^20+$ β-vibrational level.

Gd^{154} is in disagreement. The same comment as about Sm^{152} applies here.

Gd^{156} Only three states of the ground state band are known and therefore nothing can be said.

Os^{186} is in disagreement, although there does not seem to be enough experimental evidence [8, 9]) for the spin assignments of these levels.

Os^{188} Only three states of the ground state band are known and therefore nothing can be said.

Os^{190} is in agreement. The level assigned $^24+$ by O. B. Nielsen *et al.* [10]) because of symmetric rotor energy considerations does not seem to correspond to the $^24+$ asymmetric rotor state. In table 3 we give the predictions for the symmetric rotor, the asymmetric rotor, and the experimental values. The interaction with vibrations has been taken into account.

Os^{192} is in agreement.

Th^{228} is in agreement.

Th^{232} is in agreement.

Thus, for the nuclei around $A = 190$ and $A = 230$ the asymmetric rotor theory is satisfactory. For nuclei around $A = 154$ it seems to fail although more experimental information is necessary. The transition probabilities [3]) of the $^22+$ level for these nuclei are in quite good agreement with the asymmetric rotor predictions.

Nuclei with $R_e(^14+) < 2.67$ are shown in the expanded part of fig. 1, together with Os^{192} and Os^{190}. One can see that all of them require values of b approximately ten times larger than those used in the previous groups of nuclei. The few cases in which one knows more than three members of the ground state asymmetric rotor band (Cd^{110}, Hg^{198}?; Ti^{48}? and Nd^{144}?) show that the b and $R_0(^22+)$ values obtained for the various levels are different by an amount larger than their errors. Although the energy levels are not predicted correctly the general trend of the experimental transition probabilities from the $^22+$ level is again predicted correctly [3]).

In conclusion it can be said that the asymmetric rotor theory is in agreement with experiment over a wider range of nuclei than the symmetric rotor theory. It does not, in its present stage, explain adequately the energy of the low lying even parity states of nuclei with $R_e(^14+) < 2.67$.

The authors are indebted to D. Kurath and J. E. Monahan for many enlightening discussions and to F. T. Porter for his valuable criticisms and constant help.

Note added in proof: The authors are pleased to note that A. S. Davydov and V. S. Rostovsky (Nuclear Physics **12** (1959) 58) and G. R. De Mille, T. M. Kavanagh, R. B. Moore, R. S. Weaver and W. White (Canadian Journal of Physics **37** (1959) 1036) have also made a comparison of the asymmetric quadrupole rotor energy predictions with experiment.

References

1) C. A. Mallmann, Phys. Rev. Lett. **2** (1959) 507
2) A. S. Davydov and G. F. Filippov, Nuclear Physics **8** (1958) 237
3) D. M. Van Patter, Bull. Am. Phys. Soc. **4** (1959) 233; and private communication
4) C. A. Mallmann, Proceedings of the Second United Nations International Conference on the Peaceful Uses of Atomic Energy, Geneva, 1958 (United Nations, Geneva, 1959), paper A/Conf. P/1971
5) F. K. McGowan and P. H. Stelson, Bull. Am. Phys. Soc. **4** (1959) 232
6) B. S. Dzelepow and N. H. Zhukovsky, Nuclear Physics **6** (1958) 653
7) P. J. Campion, J. W. Knowles and G. A. Bartholomew, Bull. Am. Phys. Soc. **4** (1959) 247
8) G. Scharff-Goldhaber, Proceedings of the University of Pittsburgh Conference on Nuclear Structure (1958) 447
9) R. M. Diamond and J. M. Hollander, Nuclear Physics **8** (1958) 143
10) O. B. Nielsen, N. O. Roy Poulsen, R. K. Sheline and B. Skytte Jensen, Nuclear Physics **10** (1959) 475

1.E.1:
3.A

Nuclear Physics **16** (1960) 113—118; © *North-Holland Publishing Co., Amsterdam*
Not to be reproduced by photoprint or microfilm without written permission from the publisher

ANGULAR CORRELATION OF THE 1.07—1.24 MeV GAMMA CASCADE IN THE DECAY OF Ga^{68}

M. K. RAMASWAMY and P. S. JASTRAM

Department of Physics, Ohio State University, Columbus 10, *Ohio* †

Received 4 January 1960

Abstract: We have measured the angular correlation of the 1.07—1.24 MeV gamma-ray cascade in Zn^{68} following the decay of 68-min Ga^{68}. The Legendre polynomial expansion coefficients were determined to be $A_2 = 0.31 \pm 0.03$ and $A_4 = 0.23 \pm 0.07$. The measured correlation establishes the spin sequence to be 2-2-0, with a quadrupole-dipole mixing ratio δ of $+1.8 \pm 0.2$ for the 1.24-MeV gamma-ray. The result of the angular correlation work together with the allowed nature (log $ft = 5.7$) of the electron-capture decay to the 2.3-MeV level fixes the spin and parity of this level to be 2^+. The results are consistent with the near-harmonic model of Scharff-Goldhaber and Weneser for even nuclei.

1. Introduction

The decay of 68-min Ga^{68} has been recently reinvestigated by Horen [1]) who found evidence for levels in Zn^{68} at 1.07, 1.88 and 2.3 MeV. The decay scheme is shown in fig. 1. On the basis of his angular correlation results (with rather large errors) and the allowed nature (log $ft = 5.7$) for electron-capture

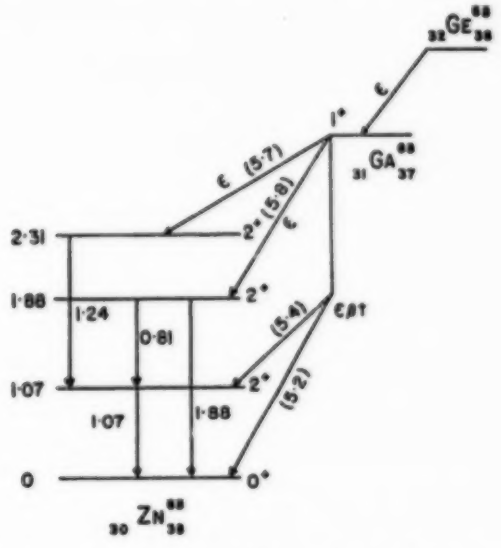

Fig. 1. Decay scheme of Ga^{68} as given by Horen [1]). The log ft values shown are taken from Horen.

† Supported by the U. S. Atomic Energy Commission.

decays from Ga^{68} (measured spin 1^+ [2]) Horen made spin and parity assignments of 2^+ for the 2.3-MeV level and a choice between 1^+ and 2^+ for the 1.88-MeV level. However, the absence of a cross-over gamma-ray transition from the 2.3-MeV level to the 0^+ ground state suggested to one of us [3]) that an alternative assignment of 0^+ might be likely for this state. In fact, the near-harmonic model of Scharff-Goldhaber and Weneser [4]) for even nuclei predicts the existence of such 0^+ levels at approximately twice the energy of the first excited state. Accordingly, a search was made [3]) for E0 conversion electrons from the 2.3-MeV level, using a plastic scintillator and a shielded anti-coincidence arrangement. The results, although not conclusive, appeared to disfavour the 0^+ assignment. In view of the striking difference between the 0-2-0 and 2-2-0 correlations, it seemed desirable to remeasure the angular correlation of the 1.07—1.24 MeV gamma cascade in order to decide the spin of the 2.3-MeV level, as well as to determine the mixing ratio. The present availability of commercially produced sources of Ga^{68} in equilibrium with long-lived Ge^{68} has made such a study feasible.

2. Source Preparation

The germanium-gallium equilibrium source used in the present study was obtained from the Nuclear Science and Engineering Corporation, Pittsburgh, in the form of $GeCl_4$ in 4*N*HCl. The Germanium tetrachloride was converted into GeS_2 by saturating with H_2S. The source employed consisted of solid GeS_2 mounted on Scotch tape. In view of the short lifetime † of the intermediate (1.07-MeV) level, the use of a solid source was not expected to introduce any appreciable attenuation of the angular correlation. The strength of a typical source was approximately 150 microcuries.

3. Experimental Procedure

The angular correlation equipment used here is the same as employed in recent angular correlation studies [5]) in this laboratory. It consists of a system of four counters with one fixed and the other three permuted at angular positions of 90°, 135° and 180° with respect to the fixed counter. The gamma counters were all $1'' \times 2''$ NaI(Tl) crystals mounted on EMI 9536B photomultiplier tubes. The counters had resolutions of 8 to 11 %. A resolving time of 16 ns was employed in the coincidence work. Singles and coincidences could be simultaneously recorded in turn for each of the three permutations of the movable

† Although no direct measurement of the lifetime of the 1.07-MeV level has been made, comparison with lifetimes measured for neighbouring even zinc isotopes by Coulomb excitation indicates a lifetime of $< 10^{-11}$ sec.

counters. With this procedure, the efficiences, solid angles and inequalities in the fast coincidence circuit efficiencies can be shown to cancel out [6]).

Before measuring the angular correlation, the gamma spectrum of a Ge^{68}—Ga^{68} equilibrium source was measured in each of the counters. Fig. 2 shows a typical gamma spectrum. In addition to the annihilation radiation peak, gamma-rays were found to be present at 1.07, 1.24 and 1.88 MeV (not shown). No gamma-rays are emitted in the immediate Ge^{68} decay [7]). No attempt was made to include the 0.810-MeV gamma-ray found by Horen in the

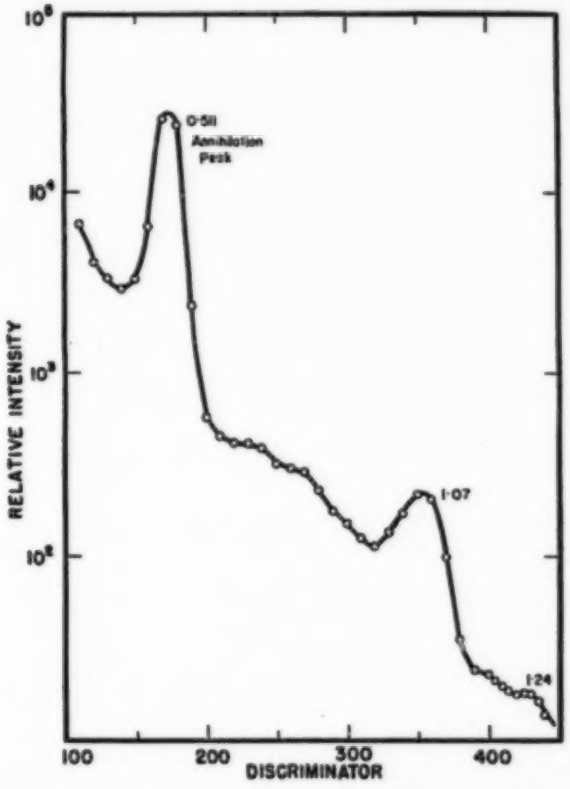

Fig. 2. Gamma-ray spectrum of Ge^{68}—Ga^{68} measured in a 1″×2″ NaI(Tl) scintillation spectrometer. Only the gamma-rays at 1.07 and 1.24 MeV are shown.

present measurements. From the present work, an upper limit of 3.6 % can be set on the intensity of any possible 2.3-MeV cross-over gamma-ray relative to that of the 1.24-MeV gamma-ray. Coincidence experiments confirmed that the 1.07 and 1.24 MeV gamma-rays are, indeed, in cascade.

For the angular correlation work, advantage was taken of the fact that the 1.07-MeV gamma-ray is in coincidence only with the 1.24-MeV gamma-ray and with no higher energy photon (see fig. 1). The fixed counter and the movable-counter descriminators were adjusted to accept all energies from 0.95 MeV to 1.45 MeV †.

† The presence of the Compton background due to the 1.88-MeV gamma-ray does not introduce any corrections, since it is non-coincident.

4. Results and Discussion

Two independent runs yielded the following values for the Legendre polynomial expansion coefficients after correcting for finite solid angle:

$$A_2 = 0.31 \pm 0.03, \quad A_4 = 0.23 \pm 0.07.$$

Fig. 3 shows a parametric plot of A_2, A_4 as a function of the mixing ratio δ for

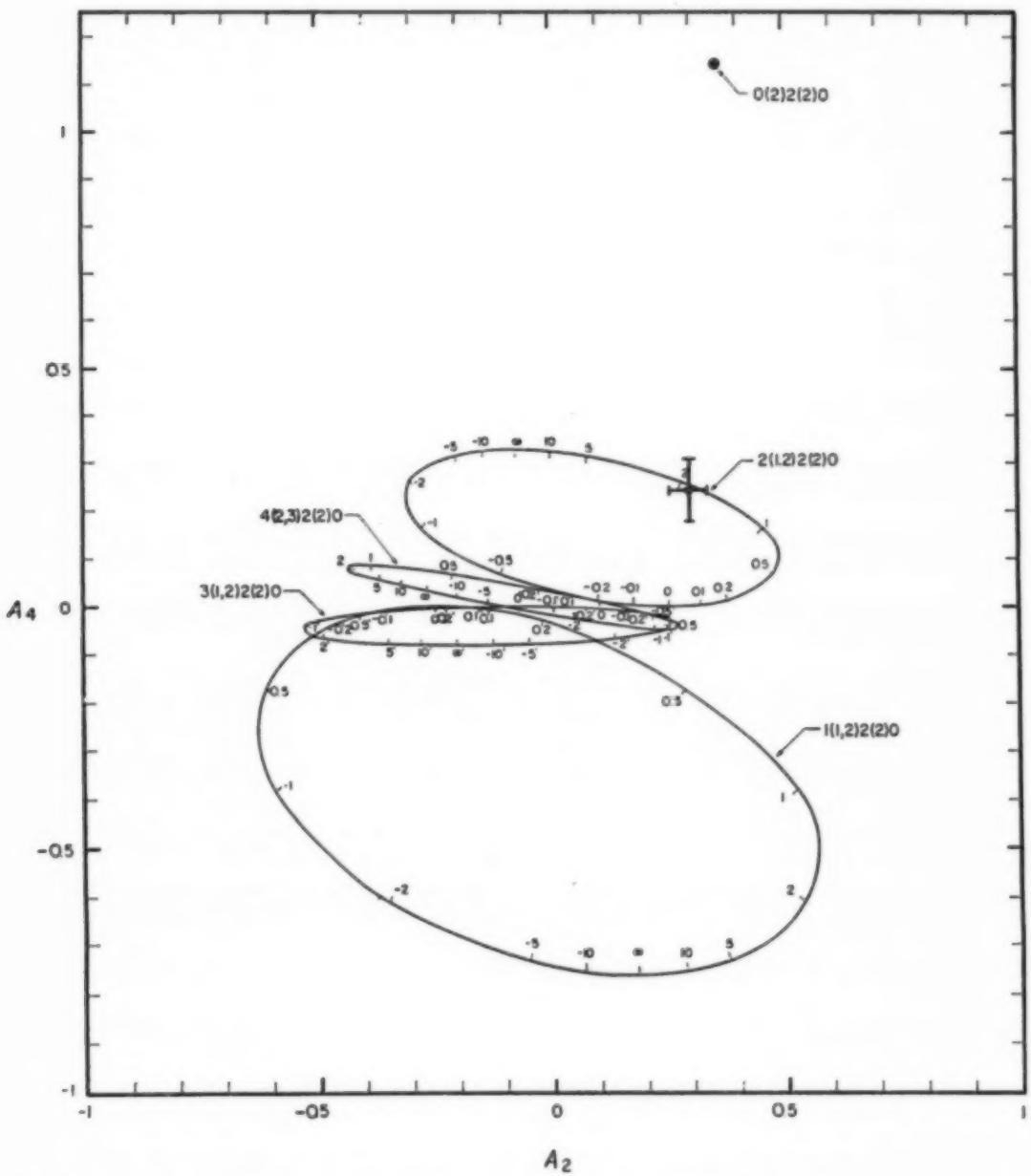

Fig. 3. Parametric plot of A_2 *vs* A_4 as a function of the mixing ratio δ for various sequences. The experimental point is shown with the statistical errors.

the various possible sequences taken from Jastram, Hurley and Wood [8]). The experimental values for A_2 and A_4 are seen to require a 2-2-0 spin sequence, with a quadrupole-dipole mixing ratio $\delta = +1.8 \pm 0.2$. The assignment of 0^+ for the 2.3-MeV level is thus completely ruled out. Even parity is indicated by the allowed nature ($\log ft = 5.7$) of the electron-capture decay to this level. A rather interesting feature of the Zn^{68} level structure is the appearance of three successive 2^+ levels (recent inelastic neutron scattering experiments of Nath *et al.* [9]) have established that the spin of the 1.88-MeV level is 2^+).

The mixing ratio affords a comparatively sensitive test of the applicable nuclear models. The single-particle model [10]) predicts a value of $\delta < \frac{1}{23}$, which is a factor of 50 less than the observed value. If we assume that the transition is due to a proton going from a $p_{\frac{3}{2}}$ level to an $f_{\frac{5}{2}}$ level, then an orbital change $\Delta l = 2$ is required. The inhibiting effect of the attendant l-forbiddenness amounts to about a factor of 100 in the M1 part of the transition with a resulting δ of approximately 4. Although this result might appear to be in agreement with the experimental value the observed intensity of the 2.3-MeV gamma-ray relative to the 1.24-MeV gamma-ray is at least a factor of 12 less than that computed on the basis of the single particle model.

On the other hand, the model proposed by Scharff-Goldhaber and Weneser [4]) may be expected to apply in this case. According to this "near harmonic" model for even nuclei, the excited levels are vibrational in character, the first excited state being 2^+ and the second excited state a triplet consisting of 0^+, 2^+ and 4^+ levels at about twice the energy of the first excited state. If one identifies the 2.3-MeV level with the second excited vibrational level, this model would predict an energy ratio E_2/E_1 of ≈ 2.2, in good agreement with the actual value of 2.1. The enhanced E2 character of the 1.24-MeV transition with an E2/M1 intensity ratio of about 4 is also compatible with this model. The observed low intensity of the 2.3-MeV cross-over ($2' \rightarrow 0$) transition relative to that of the 1.24-MeV cascade ($2' \rightarrow 2$) gamma-ray is not unusual, in spite of the higher energy available for the ground-state transition. For instance, Alburger [11]) found a value of 0.005 for the cross-over/cascade E2 ratio in Pt^{196}, compared with a ratio of < 0.04 in our case.

The observed features of the 1.07—1.24 MeV angular correlation appear to be consistent with the near-harmonic model; in addition, the mixing ratio, the cross-over/cascade E2 intensity ratio, and the energy ratio of the corresponding levels are in excellent agreement with it.

References

1) D. J. Horen, Phys. Rev. **113** (1959) 572; and private communication (June 1958)
2) Hubbs, Marrus and Worcester, Phys. Rev. **110** (1958) 534
3) M. K. Ramaswamy, Ph. D. Dissertation, Johns Hopkins University (1959) unpublished; and to be published

4) G. Scharff-Goldhaber and J. Weneser, Phys. Rev. **98** (1955) 212
5) M. K. Ramaswamy, D. L. Hutchins and P. S. Jastram, Bull. Am. Phys. Soc. **5** (1960) 20
6) P. S. Jastram, U.S.A.E.C. Contract AT(11-1)-605 Annual Progress Report No. 1, Ohio State University (1959)
7) M. K. Ramaswamy, Nuclear Physics **10** (1959) 205
8) P. S. Jastram, J. P. Hurley and G. T. Wood (in preparation)
9) Nath, Malik, Rothman and Van Patter, Bull. Am. Phys. Soc. **4** (1959) 258
10) S. A. Moszkowski, in Beta and Gamma-ray Spectroscopy (North-Holland Publishing Co., 1955) Ch. 13
11) D. E. Alburger, Proceedings of Rehovoth Conference on Nuclear Structure (North-Holland Publishing Co., 1958) p. 107

1.E.1:
1.E.2

Nuclear Physics **16** (1960) 119—137; © *North-Holland Publishing Co., Amsterdam*
Not to be reproduced by photoprint or microfilm without written permission from the publisher

STUDY OF HEAVY ODD-MASS INDIUM ISOTOPES FROM THE (γ, p) REACTION ON TIN

H. YUTA and H. MORINAGA

Department of Physics, Tôhoku University, Sendai, Japan

Received 28 December 1959

Abstract: A series of bombardments using the 25-MeV bremsstrahlung on enriched isotopes $Sn^{120}O_2$, $Sn^{122}O_2$, $Sn^{124}O_2$, and natural tin have resulted in the discovery of new isotopes In^{121}, In^{123}, and their isomers. The previously reported activity of In^{119} is assigned to In^{119g}. The results are as follows:

	half-lives	energies of β rays (MeV)	energies of γ rays (MeV)
In^{119g}	2.3 min	1.6	0.77
In^{121g}	30 sec		0.94
In^{123g}	10 sec		1.10
In^{121m}	3.1 min	3.7	
In^{123m}	36 sec	4.6	

Decay schemes and level assignments are proposed. All the decay characteristics beautifully fit into shell model systematics, allowing us systematical studies on pertinent nuclear properties. Relative yields of photoreaction on tin are also derived on the basis of these decay schemes.

1. Introduction

From the early stage of nuclear physics, the element tin drew particular attention because of having very many stable isotopes. This fact contributed to the discovery of the nuclear shell model and was explained as caused by the proton magic number 50.

This "length" of isotopes (ten stable isotopes) makes tin a very suitable element to study the systematic change of nuclear properties according to the change of the neutron number. Also the fact that the protons are in a frozen state makes it easier to make an analysis of the nuclear states.

The medium weight, or even light weight, tin isotopes are rather well studied from the decay of the unstable indium or antimony isotopes. Quite a few corresponding states of the $s_{\frac{1}{2}}$, $d_{\frac{3}{2}}$, and $h_{\frac{11}{2}}$ configurations have been identified with a systematic variation in energies in the odd-mass tin isotopes. For studying these states, the decay of indium isotopes should give good information,

since the odd-mass indium isotopes have a $p_{\frac{1}{2}}$, isomeric state right above the $g_{\frac{9}{2}}$ ground state, both of which independently decay to the lower- and higher-spin states of the tin isotopes.

However, the heavy tin isotopes to which indium isotopes decay have not been studied extensively, since the heavy indium isotopes are scarcely known. The heaviest odd-mass indium isotope about which we have good information is the probably isomeric state of In^{119}. This decays to the low states of Sn^{119} with a half-life of 17.5 min [1]). Only very recently, an indication of the ground $g_{\frac{9}{2}}$ state in In^{119} was reported [2]). Of In^{121}, two half-lives, 12 min and 32 min, have been reported [3]), but from the systematics of the decay of the odd-mass indium isotopes, these values are quite doubtful. Of In^{123} nothing has been reported so far.

For the purpose of extending the systematic knowledge about nuclear properties along the $Z = 50$ line, we wished to look for and study the decay properties of In^{119}, In^{121} and In^{123}, and their expected isomeric states.

Also we have aimed at using these nucleides for obtaining some information on the mechanism of photonuclear reactions, since little work has been done to study the reactions from different isotopes of an element. Tin is again one of the most suitable elements to perform this kind of investigation because of the long chain of stable isotopes.

2. Experimental Procedure

In^{121} and In^{123} are practically produced only from the (γ, p) reaction on Sn^{122} and Sn^{124}. They are both expected to have isomers, which probably decay by independent beta decay. The ground state of In^{119} can also be produced from the (γ, p) reaction on Sn^{120}. All these activities have, or are expected to have, rather short half-lives of comparable order. Moreover, since the (γ, p) cross section is two orders of magnitude smaller than the (γ, n) cross section and since tin has so many isotopes, we decided to use enriched isotopes of Sn^{120}, Sn^{122} and Sn^{124}, in addition to 99.99 percent tin metal, in order to get clean data. The latter helped us in getting the general aspects of activities from tin and of their yields. The enriched isotopes were in the form of SnO_2 and were purchased from Oak Ridge. The enrichment of these samples is given in table 1, with the abundance of the natural tin.

The 25-MeV betatron at Tohoku University was used for the irradiation of the samples by bremsstrahlung. The internal bombarding technique which has been developed in our laboratory has proved to be extremely useful in the case of the bombardment of those enriched isotopes and in the study of the beta and gamma ray spectra of short half-lived isotopes [4]). The samples, which are 50 mg SnO_2 powder in most cases, were wrapped in thin aluminium foils and placed at the bombarding position of the internal target during the irradiations.

The counting was made with the aluminium foil. This did not disturb our measurements.

TABLE 1

Atomic percent for enriched isotopes of tin and natural tin

Isotope	Sn	Sn^{120}	Sn^{122}	Sn^{124}
112	0.95	—	<0.2	<0.1
114	0.65	—	<0.2	0.7
115	0.34	—	<0.1	<0.1
116	14.24	0.5	1.4	3.0
117	7.57	0.4	0.8	3.4
118	24.01	1.9	2.1	5.3
119	8.58	4.2	1.4	3.8
120	32.97	90.4	18.3	10.8
122	4.71	2.0	68.5	2.1
124	5.98	0.5	7.5	71.0

For the measurement of the radiations, a scintillation spectrometer was used. For the measurement of low energy gamma rays, a $1\frac{1}{2}'' \times 1\frac{1}{2}''$ NaI(Tl) crystal mounted on a DuMont 6292 photomultiplier tube was used. For high energy gamma rays a $4'' \times 4''$ NaI(Tl) crystal was used for improving the counting efficiency. The spectra were displayed on the oscilloscope screen of a 100 channel analyzer and photographs of the screen were taken when necessary.

The energy resolution of the small NaI crystal was 9 percent at the 0.661-MeV Cs^{137} line and the resolution of the large crystal was 13 percent at 0.661-MeV line of Cs^{137}. The energy calibrations were done using all or some of the following gamma ray sources: In^{114} (0.192, 0.556 and 0.722 MeV), Hg^{203} (0.279 MeV), Cs^{137}(0.661 MeV), Zn^{65} (1.11 MeV) and Co^{60} (1.17 and 1.33 MeV).

Beta spectra were measured with a plastic phosphor, 2″ in diameter and 1″ in thickness, mounted on DuMont 6292 photomultiplier tube. The energy resolution of this phosphor was about 15 percent at the 0.635-MeV conversion line of Cs^{137}. Energy calibration was made by several negaton sources of P^{32} (1.70 MeV), Au^{198}(0.96 MeV), In^{114}(1.98 MeV) and Ag^{112}(4.05 MeV), all of which have allowed spectral shapes. Because of the lack of appropriate high energy negaton sources, Cl^{34}, which has high energy positons, was sometimes used for high energy calibration. The Kurie plot was made each time without the correction of the resolution of the phosphor for the construction of the calibration curve and the determination of the beta decay end point.

A calculation showed that the Kurie plot should become practically linear except for the very highest end of the spectra, even for the pulse-height spectra with finite resolution of the phosphor. The intersection of a tangent along the linear part of the Kurie plot with the abscissa was found to agree with the end point of the beta rays.

Spectra of gamma-gamma and beta-gamma coincidence were studied with a fast-slow coincidence circuit whose resolving time was 40 ns.

3. Results

3.1. NATURAL TIN

One of the gamma ray spectra obtained from natural tin after a two-minute irradiation with 25-MeV bremsstrahlung is shown in fig. 1. This spectrum was

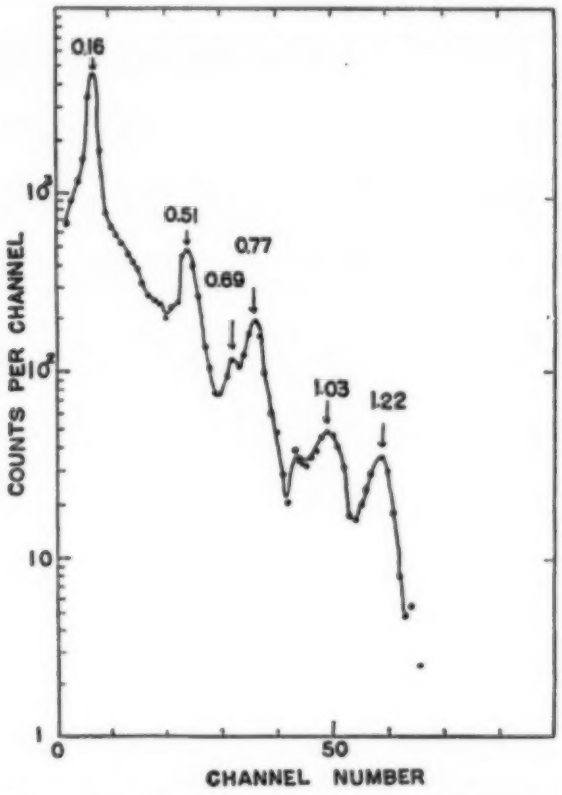

Fig. 1. Gamma ray spectrum obtained from the photo-disintegration of natural tin.

taken for 1 minute from 3 min after the irradiation. As shown in fig. 1, there are six outstanding peaks at 0.16, 0.51, 0.69, 0.77, 1.03 and 1.22 MeV. Following the decays of these peaks, the peak at 0.16 MeV was identified as a superposition of two peaks of 0.153 MeV and 0.161 MeV, which are due to Sn^{123} and In^{117}, respectively. The peak at 0.5 MeV contained the gamma rays from Sn^{111} and In^{117} which have 0.51 and 0.56 MeV energy, respectively. The peaks of 1.22 and 1.03 MeV were assigned to In^{116} and In^{118}, respectively.

Peaks at 0.69 and 0.77 MeV have not been reported previously. These gamma rays decayed with half-lives of about 4 min and 2.4 min respectively.

The 0.69-MeV gamma ray was found to be in coincidence with the 1.22-MeV gamma ray as a consequence of the coincidence measurement. This indicated

that the 0.69-MeV gamma ray belongs to In^{118}, which has two half-lives, 5 sec and 4.5 min. Since the 5 sec activity is probably from the 1^- state of In^{118}, the 4.5 min state has a rather high spin, probably 5^-, and it is natural that the 1.22-MeV gamma ray in In^{118} is in coincidence with other gamma rays. The 0.69-MeV gamma ray must be one of such gamma rays.

The 2.5-min, 0.77-MeV gamma ray was suspected to belong to the In^{119} ground state.

Longer bombardments and measurements were also performed on natural tin. All the observed peaks were assigned to some known transitions in isotopes produced by the (γ, p) or (γ, n) reactions on some stable isotopes of tin.

3.2. Sn^{120}

Fig. 2 shows the gamma ray spectrum of $Sn^{120}O_2$ after a 15-minute irradiation. The measurement was done from 1.25 minutes after the termination of the

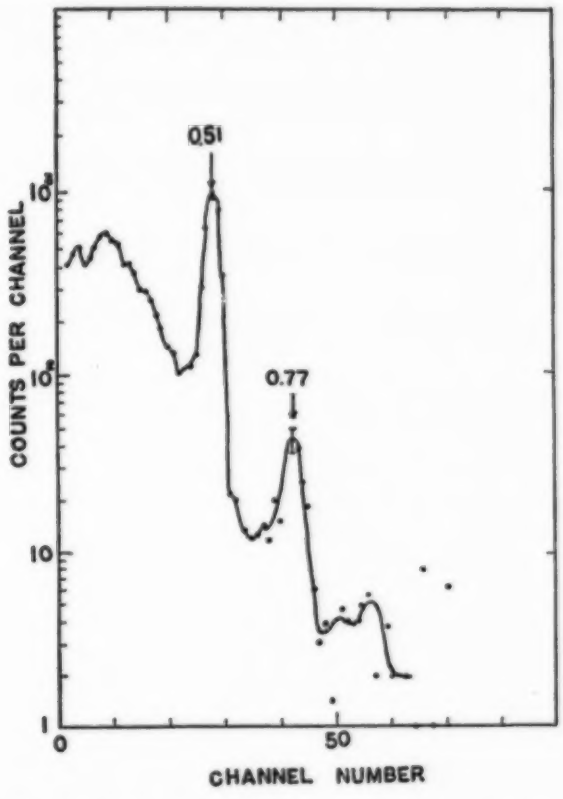

Fig. 2. Gamma ray spectrum obtained from the photo-disintegration of enriched isotope $Sn^{120}O_2$.

bombardment for 2 minutes. The decay of each peak was studied by taking the spectrum many times subsequently. The peak at 0.15-MeV decayed with a half-life of 40 min. This was identified as Sn^{123} produced from the (γ, n) reaction on Sn^{124} which presents in the sample by 0.5 percent. The peak at

0.51-MeV is due to the positons from O^{15} and Sn^{111}. They are produced by the (γ, n) reactions on O^{16} and Sn^{112}, respectively.

The 0.77-MeV peak which was seen in the spectrum from natural tin is seen more clearly in this case. The decay of this peak was followed by taking the area of each spectrum in this series of measurements. The result is shown in fig. 3. The half-life is 2.3 ± 0.3 min. The yields of this 0.77-MeV gamma ray from the natural tin and the Sn^{120} sample were obtained from the area of the peak under various bombarding conditions and they were found to be almost proportional to the abundances of Sn^{120} in the two samples. Therefore, this gamma ray must belong to a photonuclear product from Sn^{120}.

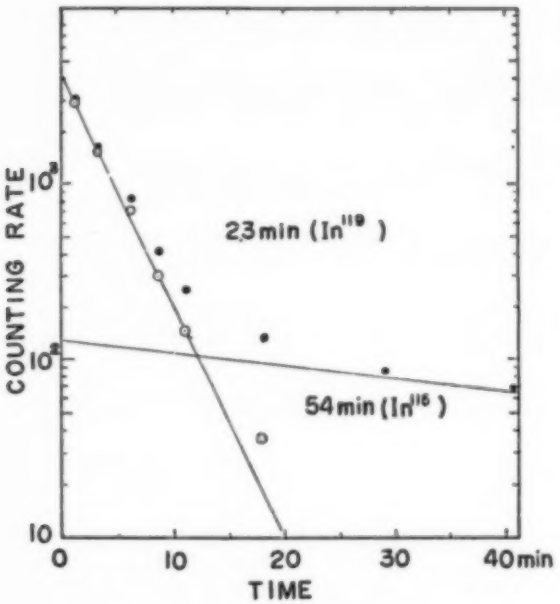

Fig. 3. Decay curve following the 0.77-MeV gamma ray.

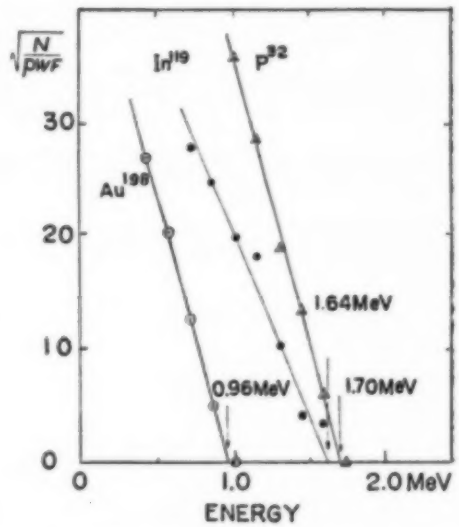

Fig. 4. Kurie plot of the beta ray spectrum coincident with the 0.77-MeV gamma ray.

The beta-ray spectrum in coincidence with this gamma ray was obtained and is shown in fig. 4. The Kurie plot shows that the end point of this beta decay is 1.6 MeV. The fact that this beta ray is in coincidence with the gamma ray excludes the possibility that this belongs to an isomer of Sn^{119} or Sn^{118}. Therefore, this gamma ray must be emitted in the decay of In^{119}. Since it is well known that In^{119} has 17.5-min beta decay with scarce gamma rays. this 2.3-min decay must be an independent decay of a state in In^{119}. Such an In^{119} activity with a half-life of 2 min has been reported. The sum of the gamma ray energy and beta decay-end point is about 2.4 MeV, which is 0.3 MeV lower than the decay energy of 17.5-min In^{119}. These facts are in agreement with an assignment of the $p_{\frac{1}{2}}$ state to the 17.5-min component and the $g_{\frac{9}{2}}$ state to the 2.3-min activity (cf. section 4). A gamma ray and a conversion electron which

may decay with 17.5-min half-life was looked for carefully in the region of 0.2 to 0.4 MeV in order to detect a possible M4 transition to the lower state. No indication was found in our measurements.

3.3. Sn^{122}

The gamma ray spectrum of the $Sn^{122}O_2$ sample irradiated with the 25-MeV bremsstrahlung is shown in fig. 5. The spectrum was taken with a 4″×4″ NaI crystal for one minute starting from 20 seconds after one minute bombardment.

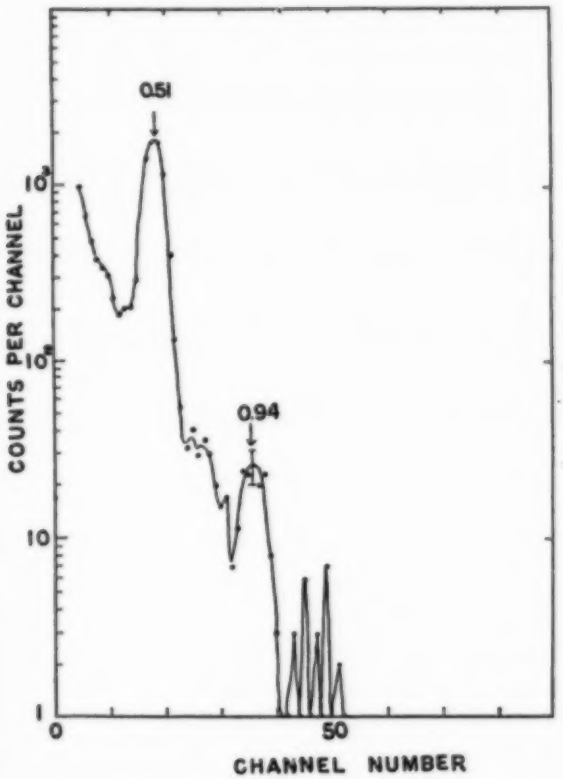

Fig. 5. Gamma ray spectrum obtained from the photo-disintegration of enriched isotope $Sn^{122}O_2$.

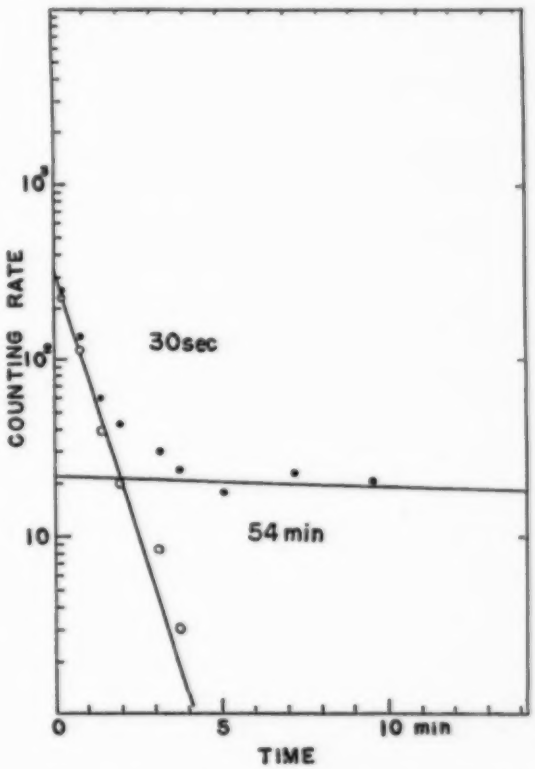

Fig. 6. Decay curve following the 0.94-MeV gamma ray.

The change of the spectrum was followed by taking photographs. Here, a new peak at 0.94 MeV is clearly seen. This peak decayed with a half-life of 30 ± 3 sec. (fig. 6). Since this peak was not seen in the spectrum of natural tin or $Sn^{120}O_2$, or $Sn^{124}O_2$ which is discussed later, it is attributed to a photonuclear product of Sn^{122}. Actually, it is assigned to the $g_{\frac{9}{2}}$ state of In^{121}. The gamma ray corresponds to the 0.77-MeV gamma ray in In^{119} and to the 0.565-MeV gamma ray in In^{117}, respectively. Because of the low intensity and short half-life of this gamma ray no coincidence measurement was performed. But from various systematics there cannot be any doubt about this assignment.

The beta ray measurements of this sample indicated that there is a beta decay with a half-life of 3.1 ± 0.3 min and an end-point energy of 3.7 MeV (fig. 11). Since O^{15} has a half-life of 2.1 min the decay was followed by taking the part of spectrum higher than 2 MeV (fig. 7), Since this is the characteristic beta decay of this sample, it is assigned to In^{121}. From systematics it is assigned to the $p_{\frac{1}{2}}$ state of In^{121}.

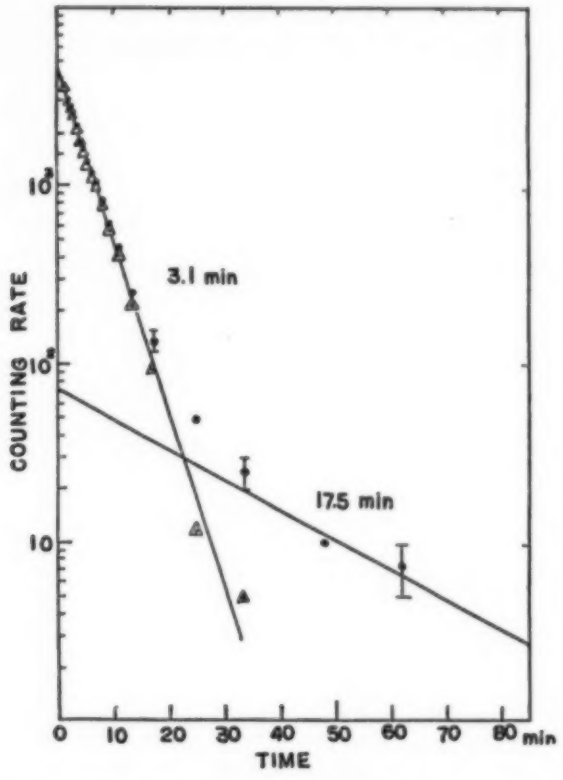

Fig. 7. Decay curve following the beta rays above 2 MeV, when the enriched isotope $Sn^{123}O_2$ was bombarded.

There should be another component of beta decay which belongs to the $g_{\frac{7}{2}}$ state of In^{121} but since this should have an energy as low as 2.5 MeV and the cross section to produce this state is quite low (cf. subsection 3.5) the activity is quite badly masked by the O^{15} activity. The isomeric transition between the $p_{\frac{1}{2}}$ and $g_{\frac{7}{2}}$ states was not looked for either, since from systematics the partial half-life of such an M4 transition should have an order of hours, which makes the branching of such a transition very weak.

3.4. Sn^{124}

The gamma ray spectrum of In^{123} produced from the bombardment of the enriched isotope Sn^{124} is shown in fig. 8. A peak at 1.10 MeV appears here and has a half-life of 10 sec. It is assigned to the $g_{\frac{7}{2}}$ state of In^{123} as in the cases of

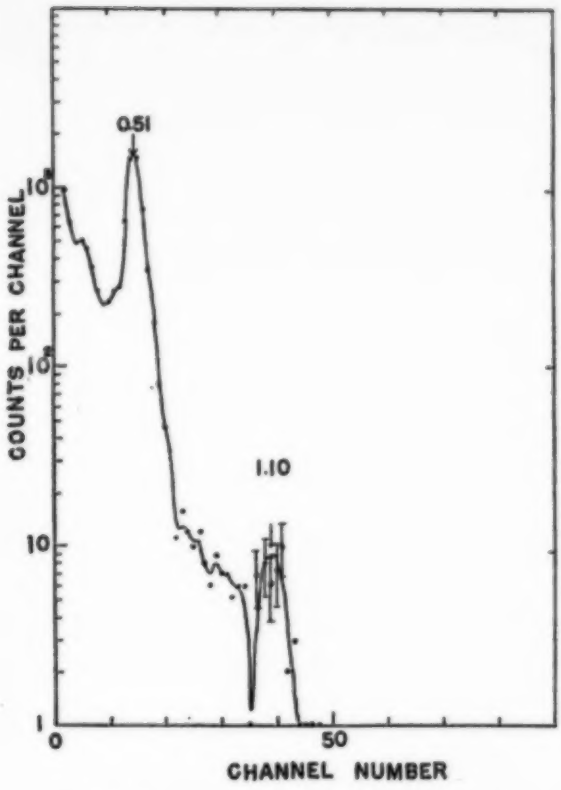

Fig. 8. Gamma ray spectrum obtained from the photo-disintegration of enriched isotope $Sn^{124}O_2$. The spectrum was measured for 15 sec starting from 5 sec after a 15 sec bombardment.

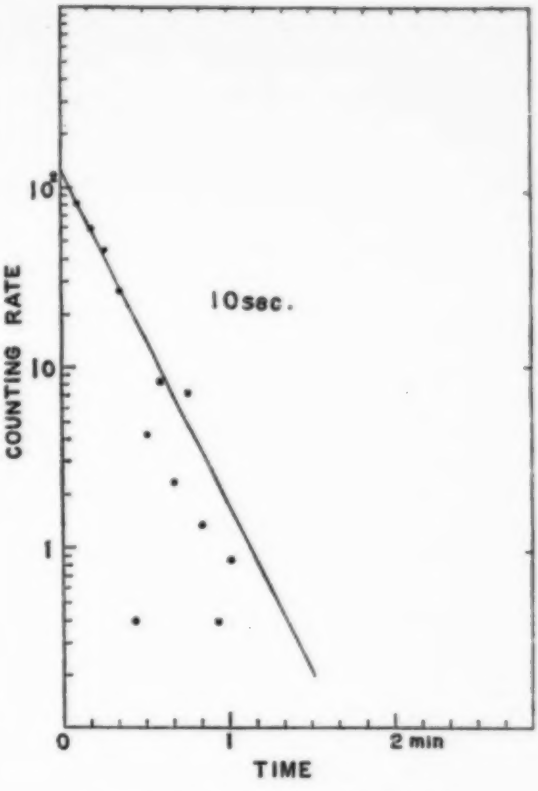

Fig. 9. Decay curve following the 1.10-MeV gamma ray.

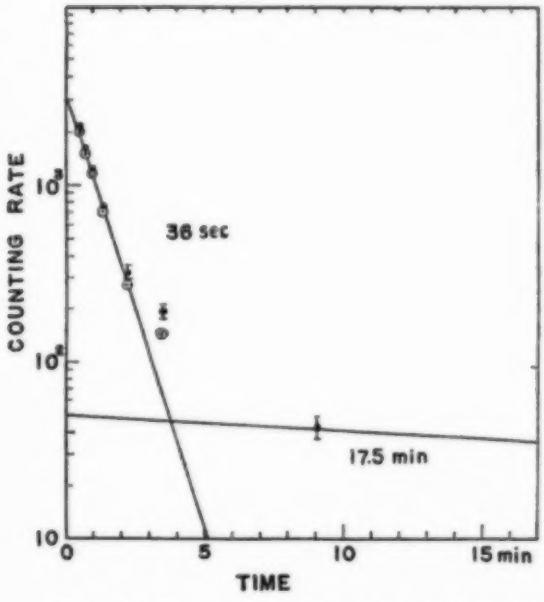

Fig. 10. Decay curve following the beta ray above 2 MeV, when the enriched isotope $Sn^{124}O_2$ was bombarded.

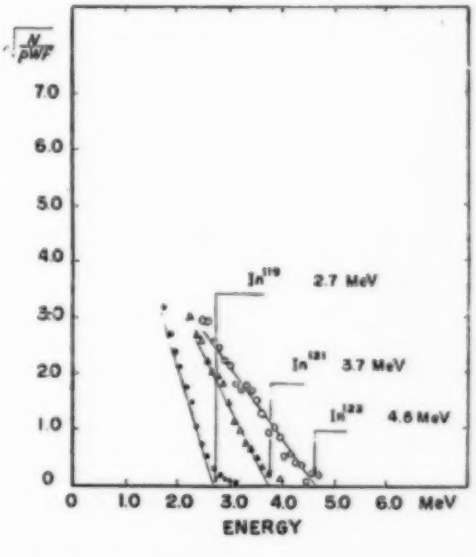

Fig. 11. Kurie plots for the beta spectra, when the enriched isotopes $Sn^{120}O_2$, $Sn^{122}O_2$ and $Sn^{124}O_2$ were bombarded.

Sn^{120} and Sn^{122}. The half-life of this gamma ray is measured to be 10 ± 2 sec (fig. 9). From the measurement with the plastic scintillator (figs. 10 and 11), a beta ray having a maximum energy of 4.6 MeV and a half-life of 36 ± 3 sec was found. This beta ray is assigned to $p_{\frac{1}{2}}$ state of In^{123} by a similar argument to that made in former subsections. The results of the measurements of the new radiations are summarized in table 3.

3.5. RELATIVE YIELDS

Relative yields of the (γ, p) product activities, i.e., those of $In^{119m,g}$, $In^{121m,g}$ and $In^{123m,g}$ to the (γ, n) yields of the two Sn^{123} activities from Sn^{124} were measured under our experimental conditions. The yield of the $d_{\frac{3}{2}}$ state of Sn^{121} from the $Sn^{122}(\gamma, n)$ Sn^{123} was also measured for comparison. Throughout these comparisons the energy of the betatron was set at 25 MeV. The shape of the bremsstrahlung is not expected to be any simple one, since our internal target is essentially a thick target of a very complicated nature.

For determining the relative yield of the 17.5-min isomeric state to that of the 2.3-min ground state, a simultaneous counting of the 0.77-MeV gamma ray by a NaI scintillation spectrometer with a multichannel pulse height analyzer and beta ray counting with a Geiger-Müller counter was performed. The $Sn^{120}O_2$ sample was employed. The relative counting efficiency of this simultaneous counting system was calibrated with the aid of well known samples with both beta and gamma rays.

In the case of In^{121}, the beta counting with a Geiger-Müller counter was badly disturbed by the 2.1-min O^{15} produced in $Sn^{122}O_2$. Therefore, the beta ray spectrum was used for decomposing the beta activity into the O^{15} activity

TABLE 2

Relative yields of photoreactions on tin

	Experimental yields				Calculated yields
	$Y(p_{\frac{1}{2}})$ $(\times10^{-3})$	$Y(g_{\frac{7}{2}})$ $(\times10^{-3})$	Y_{total} $(\times10^{-3})$	$Y(g_{\frac{7}{2}})/Y(p_{\frac{1}{2}})$	$(\times10^{-4})$
$Sn^{120}(\gamma, p)In^{119}$	4.6 ± 0.8	1.4 ± 0.3	6.0 ± 1.1	$0.32\ \pm0.10$	11.1
$Sn^{122}(\gamma, p)In^{121}$	3.9 ± 0.7	0.7 ± 0.1	4.6 ± 0.8	$0.17\ \pm0.06$	1.8
$Sn^{124}(\gamma, p)In^{123}$	3.1 ± 0.7	0.24 ± 0.0	3.3 ± 0.8	0.075 ± 0.04	0.39
	Experimental yields				
	$Y(d_{\frac{3}{2}})$	$Y(h_{\frac{11}{2}})$	Y_{total}	$Y(d_{\frac{3}{2}})/Y(h_{\frac{11}{2}})$	
$Sn^{122}(\gamma, n)Sn^{121}$	0.4 ± 0.1				
$Sn^{124}(\gamma, n)Sn^{123}$	0.6 ± 0.1	0.4 ± 0.1	1.0 ± 0.2	1.5 ± 0.4	

Calculation was made on the assumption of the statistical theory.
Total yield of Sn^{123} was taken as a unit.

and the In^{121m} activity. This result was cross-checked by another measurement described below.

The relative yields of In^{119m}, In^{121m}, and In^{123m} were obtained from bombardments of natural tin. The change of beta spectrum with time was used for obtaining these ratios.

The relative yields of In^{119g}, In^{121g}, and In^{123g} were obtained from the relative intensity measurement of 0.77-, 0.94-, and 1.10-MeV gamma rays to the intensity of 0.51-MeV annihilation radiation from the O^{15} activity. The In^{121g} to In^{121m} ratio is also obtained from these measurements and the result turned out to be in good agreement with the former measurement described above.

For determining the (γ, p) to (γ, n) yield ratio we compared the 0.77-MeV radiation in In^{119g} with the 0.153-MeV gamma ray of the $d_{\frac{3}{2}}$ state in Sn^{123}. The yield ratio of the $h_{\frac{11}{2}}$ state of Sn^{123} to the $d_{\frac{3}{2}}$ state was determined comparing the 40-min activity of the $d_{\frac{3}{2}}$ state to the 136-d activity of the $h_{\frac{11}{2}}$ state with a Geiger-Müller counter. In the same measurement the yield of the 27-h $d_{\frac{3}{2}}$ state of Sn^{121} was obtained. The results are summarized in table 2.

4. Discussion

4.1. DECAY SCHEMES

The $p_{\frac{1}{2}}-g_{\frac{9}{2}}$ energy differences or the isomeric transition energies of indium isotopes decrease smoothly with increasing mass number as shown in fig. 12.

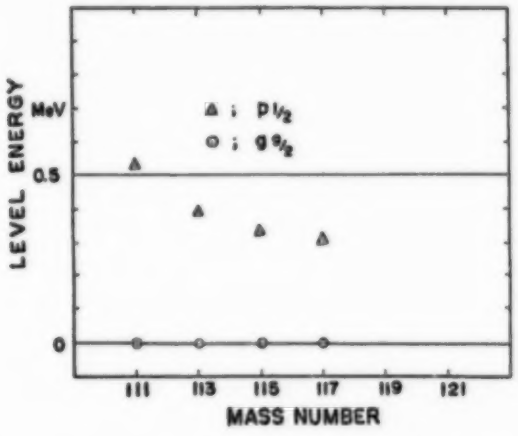

Fig. 12. Energy differences between the $p_{\frac{1}{2}}$ isomeric states and the $g_{\frac{9}{2}}$ ground states of odd-mass indium isotopes as a function of mass number.

Since there is no reason why this smooth dependence should be interrupted, we may suspect that in In^{119} this difference is approximately 300 keV. More precisely, it is expected to be found between 200 and 400 keV. Since the 17.5-min decay of In^{119} is attributed to the decay of the $p_{\frac{1}{2}}$ state from its log *ft* value and the absence of any appreciable high energy gamma rays (of the order of several hundred keV), there must be some branching of such an isomeric

transition in this decay. No gamma ray was detected between 0.2 and 0.4 MeV in our measurements. We could have found such a transition if the energy were more than 0.3 MeV. Because of the sharp decrease of expected branching of such M4 transitions, it could have easily been missed if the energy were less than 0.3 MeV. Therefore, we may set the upper limit of the energy of the isomeric state at 0.3 MeV.

Our experimental results on the 2.3-min activity of In^{119} are consistent with the assignment of this activity to the $g_{\frac{9}{2}}$ ground state. In In^{119} the $g_{\frac{9}{2}}$ ground state is found to decay to a probable $g_{\frac{7}{2}}$ state in Sn^{117} which decays to the lower $d_{\frac{5}{2}}$ state by the 0.565-MeV radiation [5]). The 0.77-MeV gamma ray in 2.3-min In^{119} is considered to be the corresponding radiation.

The 3.1-min activity with a beta-ray end point of 3.7 MeV and without any appreciable gamma ray is considered to be the independent decay of the $p_{\frac{1}{2}}$ state of $In^{121}(In^{121m})$. This corresponds to the 17.5-min decay of In^{119m}. The 0.94 MeV-gamma ray which decays with a half-life of 30 sec is assigned to the ground state decay of In^{121}.

TABLE 3

Spectroscopical data summarized for heavy odd-mass indium isotopes

	E_β (MeV)	E_γ (MeV)	$T_{\frac{1}{2}}$	log ft	Classification of beta decay
In^{115m} a)	0.83		4.5 h	6.6	$p_{\frac{1}{2}} \rightarrow s_{\frac{1}{2}}$
In^{117m} b)	1.62		1.9 h	6.7	$p_{\frac{1}{2}} \rightarrow d_{\frac{3}{2}}$
	1.77			6.5	$p_{\frac{1}{2}} \rightarrow s_{\frac{1}{2}}$
In^{119m} c)	2.7		1.75 m	6.2	$p_{\frac{1}{2}} \rightarrow d_{\frac{3}{2}} s_{\frac{1}{2}}$
In^{121m}	3.7		3.1 m	6.1	$p_{\frac{1}{2}} \rightarrow d_{\frac{3}{2}} s_{\frac{1}{2}}$
In^{123m}	4.6		36 s	5.9	$p_{\frac{1}{2}} \rightarrow d_{\frac{3}{2}} s_{\frac{1}{2}}$
In^{115g} a)	0.50	no	6×10^{14} y	22.7	$g_{\frac{9}{2}} \rightarrow s_{\frac{1}{2}}$
In^{117g} b)	0.74	0.565	1.1 h	4.5	$g_{\frac{9}{2}} \rightarrow g_{\frac{7}{2}}$
In^{119g}	1.6	0.77	2.3 m	4.5	$g_{\frac{9}{2}} \rightarrow g_{\frac{7}{2}}$
In^{121g}	($\approx$2.5)	0.94	30 s	4.5	$g_{\frac{9}{2}} \rightarrow g_{\frac{7}{2}}$
In^{123g}	($\approx$3.2)	1.10	10 s	4.5	$g_{\frac{9}{2}} \rightarrow g_{\frac{7}{2}}$

These experimental values were taken from refs. [10]) and [11]) for (a), [5]) for (b), and [1]) for (c).

In In^{123} a very similar result has been obtained, that is, the 36-sec activity with the end point of 4.6 MeV is assigned to the $p_{\frac{1}{2}}$ isomer and the 10-sec 1.10-MeV gamma ray is assigned to the decay of $g_{\frac{9}{2}}$ ground state of In^{123}.

The absence of any other appreciable gamma ray of considerable intensity than that of the $g_{\frac{9}{2}}$ state decay in the latter two cases indicates that the decay schemes of both $p_{\frac{1}{2}}$ and $g_{\frac{9}{2}}$ state in In^{121} and In^{123} are quite similar to those of In^{119}, in spite of the higher decay energies of the former two cases.

The isomeric transitions between the $p_{\frac{1}{2}}$ and $g_{\frac{9}{2}}$ states are probably negligible in both cases since the half-lives of the $p_{\frac{1}{2}}$ states are shorter and the energies of

the isomeric transitions are expected to be less than the case of In^{117} and In^{119}.

On this basis we may propose the decay schemes of heavy odd-mass indium isotopes as in fig. 13. The decay characteristics are also summarized in table 3.

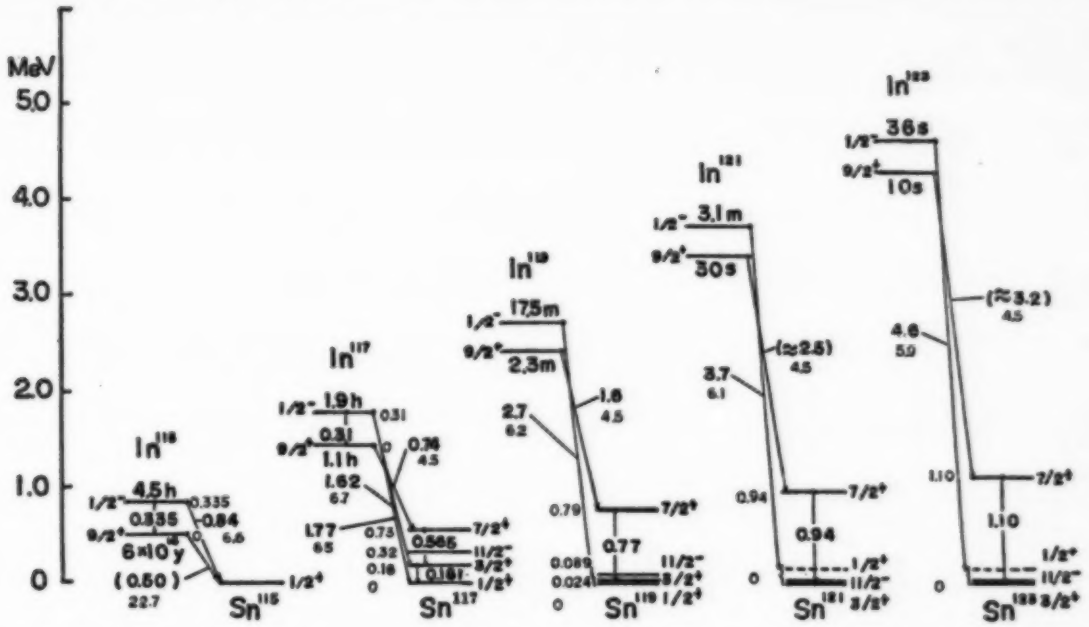

Fig. 13. Proposed decay schemes for In^{119}, In^{121} and In^{123} together with the decay schemes of In^{115} and In^{117}.

4.2. SYSTEMATICS OF THE DECAY PROPERTIES

4.2.1. Beta decay energies

Fig. 14 shows the variation of the beta-decay energies as a function of the mass number. The points fall on straight lines quite well. This is one of the features supporting the assignments of the activities.

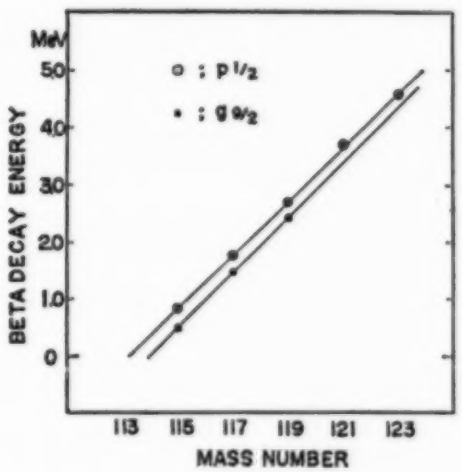

Fig. 14. Beta decay energy systematics for the decay from indium to tin.

4.2.2. Lower excited states of odd-mass tin isotopes

The energies of the lower states of odd-mass tin isotopes so far known are summarized with our new data in fig. 15. Here, the level energies are given taking the $d_{\frac{3}{2}}$ states as the origin on the ordinates. The points given by ⊙, +, and △ are assigned to $d_{\frac{3}{2}}$, $h_{\frac{11}{2}}$ and $s_{\frac{1}{2}}$, respectively [6,7,8]). The points enclosed by a little square □ are those corresponding to the states attained by the beta decay of the $g_{\frac{9}{2}}$ ground states of heavy indium isotopes. In the case of In^{117} it has been assigned to $g_{\frac{7}{2}}$ [5]).

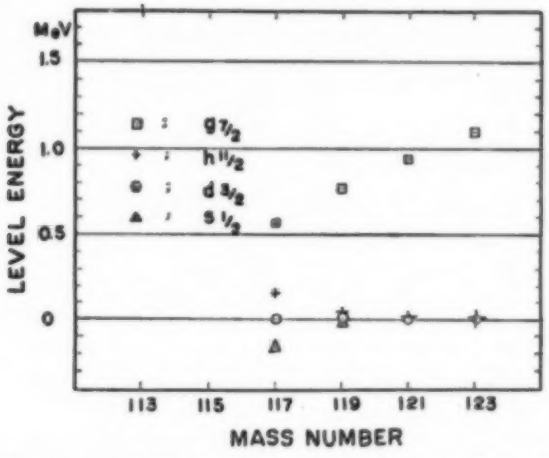

Fig. 15. Level energy difference for Sn^{117}, Sn^{119}, Sn^{121} and Sn^{123}. Each $d_{\frac{3}{2}}$ state was taken as a base of energy.

The characteristic features of these points are that the log *ft* values of the decays from $g_{\frac{9}{2}}$ states are very low ($\approx$ 4.5) and also that the energies increase rapidly with the mass number. The former fact argues for the single particle (or hole) $g_{\frac{7}{2}}$ assignments of this sequence of states. The latter fact also seems to support the $g_{\frac{7}{2}}$ assignments, since if these states were associated with vibrational motion of the lower states or more complicated excitation, there should not be such a large dependence of energies on mass number. In fact, the energies of the first 2^+-states in even-mass tin isotopes do not change much with the mass number [9]).

4.2.3. Beta decay transition rates

The comparative half-lives of the beta transitions involved are tabulated in table 3. For calculating the log *ft* values of the $g_{\frac{9}{2}} \rightarrow g_{\frac{7}{2}}$ decays it is necessary to know the energies of the transitions. For the decays of In^{121} and In^{123} they were not measured experimentally. Therefore, we estimated the beta decay energy assuming that the measured decay energies of In^{121m} and In^{123m} practically correspond to the $p_{\frac{1}{2}} \rightarrow d_{\frac{3}{2}}$ transitions and that the $p_{\frac{1}{2}}-g_{\frac{9}{2}}$ differences in In^{121} and In^{123} may be found by linearly extrapolating the values from In^{115}, In^{117} and In^{119} (see fig. 12).

Then we get the beta-decay energies of $g_{\frac{9}{2}} \rightarrow g_{\frac{7}{2}}$ transitions in $In^{121} \rightarrow Sn^{121}$ and $In^{123} \rightarrow Sn^{123}$ as 2.5 MeV and 3.2 MeV. Then we get log $ft = 4.5$ for all the three transitions we measured. The transition in $In^{117} \rightarrow Sn^{117}$ is already measured to have a log ft value of 4.5.

This striking resemblance of the transition rates reveals the simplicity of the situation. It is considered that the $g_{\frac{9}{2}}$ states are represented very well by a single hole in the $g_{\frac{9}{2}}$ shell in the $Z = 50$ core, and the transition corresponds to that of a neutron from the well filled $g_{\frac{7}{2}}$ shell into this hole. Outer $d_{\frac{5}{2}}$, $s_{\frac{1}{2}}$ and $h_{\frac{11}{2}}$ neutrons, whose number changes with A, do not seem to effect such well-defined transitions appreciably.

On the contrary, the log ft values of $p_{\frac{1}{2}} \rightarrow d_{\frac{5}{2}}$, $s_{\frac{1}{2}}$ decay differ from each other. In In^{119m}, In^{121m} and In^{123m}, it is experimentally impossible to resolve the decay into $p_{\frac{1}{2}} \rightarrow d_{\frac{5}{2}}$ and $p_{\frac{1}{2}} \rightarrow s_{\frac{1}{2}}$ decays. Therefore, the values listed in table 3 are "effective" log ft values, that is, total log ft values for the two transitions which have almost equal energies. (The $s_{\frac{1}{2}}$ and $d_{\frac{5}{2}}$ states in those nuclei are, or are expected to be, very close to each other.) In In^{117} this effective log ft value is 6.3. Then there seems to be a smooth decrease of the log ft value with the mass number.

The following circumstances may be considered to be responsible for these effects: (1) poor calibration of the beta-ray spectrometer, (2) neglect of branching, (3) the effect of non-linearity of the Kurie plot, and (4) a nuclear effect. The first two, however, do not seem to be sufficient for explaining such a large change in log ft value under our experimental conditions. The third effect may come in, since the energy of the beta decay is quite high, namely, for In^{123}, of the order $Z\alpha/2\rho$. Under these conditions the Kurie plot of the non-unique first forbidden transition is not assured to be linear. This should affect the log ft values. This effect, however, can be estimated fairly safely and it proves to be small (cf. Appendix).

It seems, therefore, that it is afterall the nuclear effect which is solely responsible for this change in log ft value. The transitions are caused by the dropping in of the $s_{\frac{1}{2}}$ or $d_{\frac{5}{2}}$ neutron into the $p_{\frac{1}{2}}$ proton hole as the former changes itself into a proton by the beta-decay. It is natural, therefore, that the decay rate should be affected by the occupation numbers of the $s_{\frac{1}{2}}$ and $d_{\frac{5}{2}}$ neutrons. The tendency that the log ft value decreases as the neutron number increases is natural. It is interesting, however, to see that the log ft value is still decreasing from 121 to 123. If the $d_{\frac{5}{2}}$ and $s_{\frac{1}{2}}$ states start to fill up after the 64 submagic shell is filled with the $g_{\frac{7}{2}}$ and $d_{\frac{5}{2}}$ neutrons, without letting the $h_{\frac{11}{2}}$ shell or other perturbations come in, this filling should end at $N = 70$ ($A = 120$). In such an over-simplified model the log ft value should not change from 121 to 123. And if the $h_{\frac{11}{2}}$ shell filled up before the $d_{\frac{5}{2}}$ and $s_{\frac{1}{2}}$ states, which is not so realistic an assumption, the log ft would not change as much as observed. From this discussion we may conclude that the situation with such "surface" nucleons is

not so simple, even for such half-magic nucleides as the tin isotopes, whose other properties are expained quite well from simple shell theory.

4.3. RELATIVE YIELDS OF PHOTOREACTIONS

The (γ, p) yields of the In^{119g}, In^{121g}, In^{123g} and their isomers measured under our experimental conditions (see table 2 and fig. 16) show the following characteristics:

1) They are about 1 % of the (γ, n) yield on Sn^{124}.

2) The yields of isomers are higher than that of the ground state by a factor 3 for $A = 119$, and this factor increases with A.

3) The yield of isomers decreases slowly and smoothly with A.

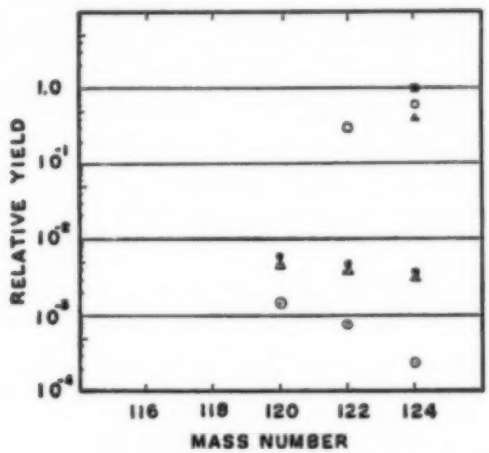

Fig. 16. Relative yields of photoreaction on tin.

■ Total (γ, n) yield ○ (γ, n) yield of $d_{\frac{1}{2}}$ state △ (γ, n) yield of $h_{\frac{11}{2}}$ state

● Total (γ, p) yield ▲ (γ, p) yield of $p_{\frac{1}{2}}$ state ⊙ (γ, p) yield of $g_{\frac{9}{2}}$ state

Since we do not know the detail of the X-ray spectra and the shapes of the cross sections, no detailed analysis can be made. However, some qualitative discussion may be based on these data.

From the statistical theory, the features 2) and 3) may be qualitatively explained. The result of a very rough calculation is given in table 2. The result is not in good agreement with observation; especially the total yields are much smaller than the observed values. Therefore, the previous finding [12]) that the photoproton emissions from nuclei around this region are accounted for by the statistical theory seems to be rather accidental; the statistical theory seems to be good for explaining the photoproton yield only in the neutron-deficient region but not for the neutron excess isotopes.

The single particle excitation theory for the giant resonance, on the contrary, seems to give a better result for the explanation of the present data. Wilkinson calculates the (γ, p) yield of tin, using such a model [13]). According to this calculation, the ratio of the yield for proton emission to that for neutron emis-

sion under 23-MeV bremsstrahlung is 10^{-2}, which is in farily good agreement with the present data. Furthermore, the (γ, p) yield ratio of $g_{\frac{9}{2}}$ state to $p_{\frac{1}{2}}$ state becomes 0.24, if we assume that the $g_{\frac{9}{2}}$ and $f_{\frac{7}{2}}$ hole states of indium result in the $g_{\frac{9}{2}}$ ground state, and the $f_{\frac{5}{2}}$, $p_{\frac{3}{2}}$ and $p_{\frac{1}{2}}$ hole states result in the $p_{\frac{1}{2}}$ isomeric state.

The decrease of the yield of the $g_{\frac{9}{2}}$ state is explicable, since the (γ, p) threshold goes up with A and the yield of $g_{\frac{9}{2}}$ state should be more affected by the Coulomb barrier. Quantitative estimation, however, is difficult since the yield is sensitive to the exact positions of the single particle states.

Appendix

Since the decay energy becomes the order of Coulomb energy for the first forbidden beta transitions which appear in heavy odd-mass tin isotopes, $(\alpha Z/2\rho \approx W)$ there can occur a deviation of the Kurie plot from linearity. This may have an effect on the comparative half-life. Here, we calculate such a deviation using V—A interaction and the single particle wave functions as employed by Brysk for the estimation of the matrix element.

The comparative half-life for the first forbidden transition $(ft)_1$ is given by

$$(ft)_1 = \frac{2\pi \ln 2}{g^2} \langle C_{1\mathrm{VA}} \rangle^{-1}, \tag{1}$$

where

$$\langle C_{1\mathrm{VA}} \rangle = \frac{1}{f} \int_1^{W_0} \mathrm{d}W F_0 pW (W_0 - W)^2 C_{1\mathrm{VA}} \tag{2}$$

and

$$f = \int_1^{W_0} \mathrm{d}W F_0 pW (W_0 - W)^2; \tag{3}$$

F_0 is the Fermi function, g the coupling constant, p the electron momentum in units of mc, W the electron energy in units of mc^2, W_0 the energy available in the decay; $C_{1\mathrm{VA}}$ is the correction factor for the beta spectrum on the assumption that the beta-interaction is V—A and time-invariant. It can be expressed as follows [14]):

$$C_{1\mathrm{VA}} = \left| C_{\mathrm{A}} \int \boldsymbol{\sigma} \cdot \mathbf{r} \right|^2 \left\{ |x_1^{(0)}|^2 + \tfrac{2}{3} \left(q + \frac{p^2}{W} \right) \mathrm{Re}\, (x_1^{(0)}) + \tfrac{1}{9} \left(q^2 + p^2 + \frac{2qp^2}{W} \right) \right\}$$

$$\left| C_{\mathrm{A}} \int \boldsymbol{\sigma} \times \mathbf{r} \right|^2 \left\{ |x_1^{(1)}|^2 - \tfrac{2}{3} \left(q + \frac{p^2}{W} \right) \mathrm{Re}\, (x_1^{(1)*} y_1^{(1)}) + \tfrac{2}{3} \left(q - \frac{p^2}{W} \right) \mathrm{Re}\, (x_1^{(1)}) \right.$$

$$\left. + \tfrac{1}{3} \left(q^2 + p^2 + \frac{2qp^2}{3W} \right) |y_1^{(1)}|^2 + \tfrac{1}{6}(q^2 + p^2) - \frac{2qp^2}{9W} + \frac{2p^2}{9} [\mathrm{Re}(y_1^{(1)}) - \mathrm{Re}(y_1^{(1)*})] \right\}$$

$$+ \sum_{ij} \left| C_{\mathrm{A}} \int B_{ij} \right|^2 \tfrac{1}{12}(q^2 + p^2), \tag{4}$$

$$x_1^{(0)} = \frac{\alpha Z}{2\rho} + i\frac{\int \gamma_5}{\int \boldsymbol{\sigma}\cdot\mathbf{r}},$$

$$x_1^{(1)} = \frac{C_V\int \boldsymbol{\alpha} - (\alpha Z/2\rho)C_A\int \boldsymbol{\sigma}\times\mathbf{r} - i(\alpha Z/2\rho)C_V\int \mathbf{r}}{C_A\int \boldsymbol{\sigma}\times\mathbf{r}},$$

$$y_1^{(1)} = \frac{iC_V\int \mathbf{r}}{C_A\int \boldsymbol{\sigma}\times\mathbf{r}},$$

where q is the neutrino momentum in units of mc, ρ is the nuclear radius in units of the electron Compton wave length, and α is the fine structure constant. C_A and C_V are the interaction constants and these values are given by [15])

$$C_A = -(1.25\pm 0.04)C_V.$$

To see the deviation from the allowed shape and the variation of $(ft)_1$ according to W_0, one must estimate the nuclear matrix elements $\int \boldsymbol{\sigma}\cdot\mathbf{r}$, etc. . . . Brysk [16]) formulated the nuclear matrix elements using the wave function of a Dirac particle in a square-well potential. For the case of the $p_{\frac{1}{2}} \rightarrow s_{\frac{1}{2}}$ transition, the nuclear matrix elements were estimated as follows:

$$\lambda^{-1}\left|\int \boldsymbol{\sigma}\cdot\mathbf{r}\right| = 0.0041, \quad \lambda^{-1}\left|\int \mathbf{r}\right| = 0.0024, \quad \lambda^{-1}\left|\int \boldsymbol{\sigma}\times\mathbf{r}\right| = 0.0047,$$

$$\left|\int \gamma_5\right| = 0.15, \quad \left|\int \boldsymbol{\alpha}\right| = 0.060, \quad \left|\int B_{ij}\right| = 0.$$

In this case the dominant effects in V_{1VA} come from the energy-independent terms of $|\int\gamma_5|$, $|\int\boldsymbol{\alpha}|$, and $\alpha Z/2\rho$. Therefore, the deviations from the allowed shape are expected to be small. Actually, the calculation showed that the deviations from the allowed shape are within 10 percent.

The values of C_{1VA} numerically estimated for our cases are

$$\begin{aligned} &\mathrm{In}^{119}\text{: } C_{1VA} = 1.0\,C_0, \quad W_0 = 6.4;\\ &\mathrm{In}^{121}\text{: } C_{1VA} = 1.0\,C_0, \quad W_0 = 8.4;\\ &\mathrm{In}^{123}\text{: } C_{1VA} = 1.0\,C_0, \quad W_0 = 10.2. \end{aligned}$$

where C_0 is a constant. Therefore, the comparative half-lives are almost constant with respect to the neutron number. It is safely guessed that the variation of log ft values in the case of the $p_{\frac{1}{2}} \rightarrow d_{\frac{3}{2}}$ transition is of the same order of magnitude.

References

1) R. B. Duffield and J. D. Knight, Phys. Rev. **75** (1949) 1967
2) C. E. Gleit, M. I. T. LNS Progr. Report **30** (1957) 8

3) N. Nussis, J. Pahissa and E. Ricci, Z. Naturforsch. **12a** (1957) 520
4) H. Morinaga and T. Kuroyanagi, Nuclear Instruments **6** (1959) 66
5) Carl L. McGinnis, Phys. Rev. **97** (1955) 93
6) G. Scharff-Goldhaber, E. der Mateosian, M. Goldhaber, G. W. Johnson and M. Mckeown, Phys. Rev. **83** (1951) 480
7) C. M. Nelson, B. H. Ketelle, and G. E. Boyd, Oak Ridge National Laboratory Report, ORNL-828 (Nov. 1950)
8) R. B. Duffield and L. M. Langer, Phys. Rev. **76** (1949) 1272
9) P. H. Stelson and F. K. McGowan, Bull. Am. Phys. Soc. **2** (1957) 69
10) L. M. Langer, R. D. Moffat and G. A. Graves, Phys. Rev. **86** (1952) 632A
11) R. W. King, Revs. Mod. Phys. **26** (1954) 327
12) B. C. Diven and G. M. Almy, Phys. Rev. **80** (1950) 408
13) D. H. Wilkinson, Physica **22** (1956) 1039
14) Zyun-itiro Matumoto and Masami Yamada, Progr. Theo. Phys. **19** (1958) 285
15) 1958 Annual International Conference on High Energy Physics at CERN
16) Henry Brysk, Phys. Rev. **86** (1953) 996

1.E.1:
4.E

Nuclear Physics **16** (1960) 138—152; © *North-Holland Publishing Co., Amsterdam*
Not to be reproduced by photoprint or microfilm without written permission from the publisher

ON THE DECAY OF ^{106}Rh

O. J. SEGAERT and J. DEMUYNCK
Natuurkundig Laboratorium, Rijksuniversiteit Gent, Ghent, Belgium
and
A. M. HOOGENBOOM † and H. VAN DEN BOLD
Fysisch Laboratorium der Rijksuniversiteit, Utrecht, The Netherlands

Received 5 October 1959

Abstract: The beta and gamma radiation following the 30 sec decay of ^{106}Rh has been investigated with a double-focusing beta-ray spectrometer, single-crystal, coincidence and sum-coincidence gamma-ray spectrometers. Gamma rays of 0.513, 0.624, 0.87, 0.89, 1.045, 1.14, 1.31, 1.51, 1.55, 1.76, 1.93, 2.13, 2.30, 2.37, 2.44, 2.63 and 2.88 MeV have been found in the decay of ^{106}Pd. Relative intensities of beta and gamma rays are reported (table 1, table 3) and a level scheme for ^{106}Pd is proposed. Two new levels at 2.02 and 2.88 MeV are added. The intensity measurement of the K and L lines of the 0.513 MeV transition yields a K/LM ratio of 6.15 ± 0.62.

1. Introduction

Shortly after the discovery of ^{106}Ru, Grummit and Wilkinson [1]) reported half lives of 290 days and 30 sec for ^{106}Ru and ^{106}Rh, respectively, and a maximum beta-ray energy of 3.3 MeV for the latter. Peacock [2]) proposed a decay scheme of ^{106}Rh consisting of two beta branches with endpoints at 3.55 and 2.30 MeV, the latter followed by two gamma rays of 0.51 and 0.73 MeV in cascade with a weak cross-over. Gamma-gamma angular distribution correlation and directional-polarisation correlation experiments done by Brady and Deutsch [3]), and by Deutsch and Metzger [4]), respectively, exhibited a strong anisotropy. Ling and Falkoff [5]), and at nearly the same time, Spiers [6]), and Williams and Wiedenbeck [7]) examined the correlation results. Greater complexity of the ^{106}Rh decay scheme was suggested together with possible spin values for the first and higher excited states (2^+, 0^+, 1^+, 1^-, or 3^+). Similar experimental evidence was obtained by Goldhaber and der Mateosian [8]), and gamma rays above 2.23 MeV were reported. Since the angular correlation of the gamma rays in ^{106}Pd constituted a puzzling discrepancy between experiment and theory, the angular correlation measurements were also repeated by Arfken, Klema and McGowan [9]). Alburger [10]) reinvestigated the decay scheme with a lens spectrometer, and observed beta rays with endpoints of 3.53, 3.1, 2.44, and 2.0 MeV together with internal conversion lines of 0.513 MeV ($K/L = 7.8 \pm 1.0$ indicating an E2 transition) and 0.624 MeV. His lens and

† Now at Massachusetts Institute of Technology, Cambridge, Massachusetts.

scintillation spectrometer measurements showed that the gamma-ray spectrum consists of lines of 0.511, 0.621, 0.87, 1.045, 1.55 and 2.41 MeV, and that beta decay takes place to states at $0(0^+)$, $0.513(2^+)$, $1.137(0^+)$, $1.55(2^+)$ and $2.42(2^+)$ MeV. Klema and McGowan [11]) finally found the correlation function of the 0.624—0.513 MeV cascade and the 1.045—0.513 MeV cascade. Kahn and Lyon [12]) proposed an additional level at 2.28 MeV finding new gamma rays of 1.14, 1.76, and 2.28 MeV. In 1955 Alburger [13]) and Toppel measured gamma rays of 1.96, 2.10, and 2.66 MeV in addition to the lines previously known. Three new weakly excited levels at 1.85, 2.27, and 2.66 MeV were postulated. Coulomb-excitation measurements done by McGowan and Stelson [14]) have located a 2^+ state at 1120 ± 8 keV very close to the 0^+ state at 1137 keV.

The present study was initiated to obtain further information regarding possible high-energy levels and their decay, applying large scintillation crystals and coincidence techniques. Especially the sum-coincidence method was thought to be useful for establishing the energy levels above 1 MeV. In view of the complex decay scheme proposed by Alburger and Toppel, the spectrum was subdivided into a number of possible cascades. During the reexamination it was tried to find confirmation of the existence of the 1.12 MeV level. The results are summarized in a disintegration scheme for ^{106}Pd to which 1.12 MeV, 2.02 MeV, and 2.88 MeV levels are added.

2. Sources and Apparatus

The ^{106}Ru, as nytrosyl ruthenium trinitrate in nitric acid, having radiochemical purity better than 99 %, was prepared in December 1957. The experiments reported here were started December 1958 so that all activities except ^{106}Ru and ^{106}Rh had decayed. A beta spectrometer source was prepared by electrodeposition of the ruthenium on a narrow strip of Al, thickness 5 micron, previously covered by a thin layer of evaporated copper. The source was supported by a thin aluminium sheet of equal thickness. Gamma-gamma angular correlations were measured with liquid samples in glass tubes of approximately 1 mm diameter.

The ^{106}Rh spectrum was examined with gamma-ray spectrometers used for individual, coincidence and sum-coincidence counting. NaI crystals 2″ long and $1\frac{5}{8}$″ diameter, and 4″ by 4″ cylindrical crystals were mounted on Dumont photomultipliers. The sources were centered 4.5 cm above the top surface of the detectors. To eliminate the β^--background it was necessary to place a 11.5 mm thick Al or 3 mm thick Cu absorber between the sample and the crystal. The spectra were recorded with a hundred channel Hutchinson Scarott analyser.

3. Single-Crystal and Beta-ray Spectrometer Results

The spectrum obtained with the 2″ crystal, corrected for background, covering energies between 100 and 1800 keV, is shown in fig. 1. The number of

counts has been normalized to that obtained during a 10 min or a 1 hour measuring period, although a 13 hours run was necessary to obtain good statistics in the higher energy part of the spectrum.

Figure 2 represents the spectrum obtained with the 4″ crystal, originally measured for 6 hours and corrected for background, it covers energies from 100 to 2900 keV. Although a complete analysis was performed to obtain the full

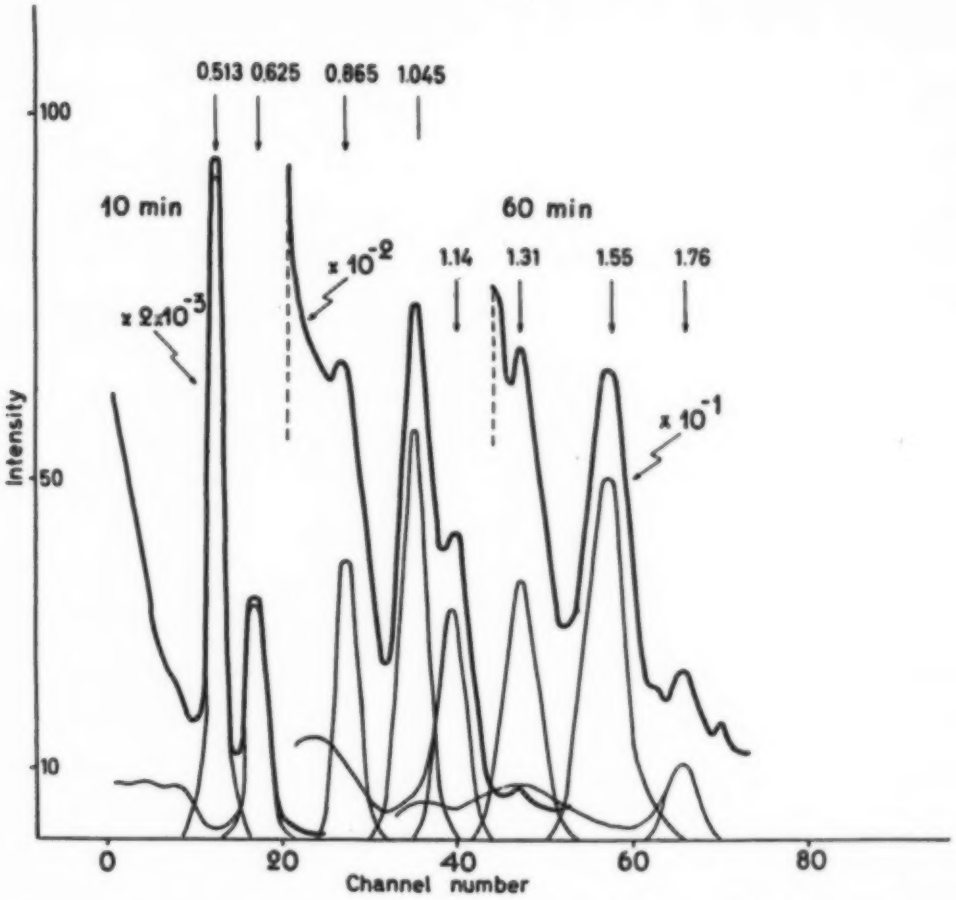

Fig. 1. Gamma-ray spectrum of ^{106}Pd in the energy region of 100 to 1800 keV (2″ NaI crystal).

energy peaks, only the 2.33 and 0.624 MeV gamma rays have their complete pulse height distribution shown. The shapes for Compton and pair peaks are obtained from the pulse distributions of various single gamma-ray sources, run under conditions similar to this experiment. The absolute intensities were obtained from the number of counts in the photopeak corrected for the attenuation in the β^--absorber and divided by the photoefficiency. The highest peak in the 4″ spectrum which has a height of about 200 pulses in the 6 hour run is interpreted as the photoline of a 2.88 ± 0.03 MeV gamma ray. This information, which indicates the existence of a level above 2.66 MeV, previously

reported and added to the decay scheme by Alburger and Toppel [13]), is used to extend the sum-coincidence measurements to energies above 2.66 MeV.

The decomposition of the beta spectrum leads to the identification of two strong components. The endpoint energies in the Kurie plot are 3.55 ± 0.02 MeV

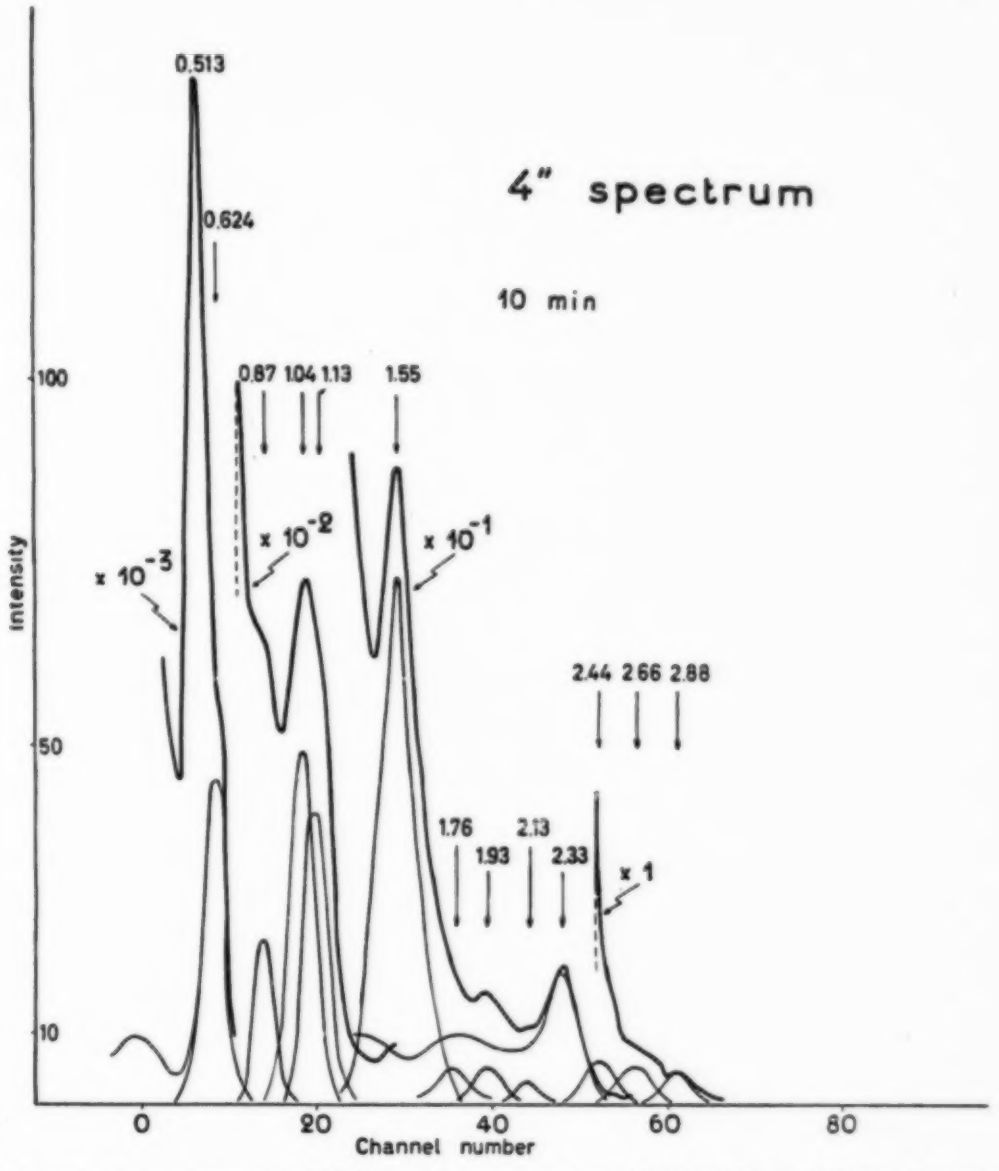

Fig. 2. Gamma-ray spectrum of ^{106}Pd in the energy region of 100 to 3000 keV (4" NaI crystal).

and 3.05 ± 0.02 MeV. Because of the low activity of the beta source giving rise to considerable statistical errors, the separation of the weak lower energy components has not been attempted. The relative intensities of the two groups mentioned before are 70 and 12 %, lower components $\leqq 18$ %. Internal conversion lines are found superimposed on the ^{106}Rh beta-decay spectrum.

The energies of the transitions are 512.84±0.62 keV and 623.65±0.65 keV. The intensity measurement of the separated K and L lines of the 513 keV transition yields a K/LM ratio of 6.15±0.62.

Relative intensities and energies of the ^{106}Rh gamma rays from the single-crystal, coincidence, and sum-coincidence measurements are included in table 1,

TABLE 1

Energies and relative intensities of the gamma rays following the decay of ^{106}Pd.

Alburger and Toppel [13])		Present investigation	
E_γ (MeV)	Relative Intensity	E_γ (MeV)	Relative Intensity
0.513	100	0.513±0.003	100
0.624	53	0.624±0.004 [1])	53 ±2
0.87	3	0.865±0.005 [2])	3.5 ±0.5
1.045	8	1.045±0.007 [3])	9 ±1
1.13	≦0.8	1.14 ±0.01	6.5 ±1.0
—	—	1.31 ±0.01	0.8 ±0.3
1.55	2.5	1.55 ±0.01 [4])	1.5 ±0.3
1.77	1.0	1.76 ±0.02	0.20 ±0.07
1.96	0.6	1.93 ±0.02	0.18 ±0.06
2.13	0.5	2.13 ±0.02	0.3 ±0.1
—	—	2.30 ±0.02	0.6 ±0.1
—	—	2.37 ±0.02	
2.41	1.0	2.44 ±0.02	0.03 ±0.01
2.66	0.2	2.63 ±0.03	0.03 ±0.01
—	—	2.88 ±0.03	0.020±0.007

1) In the analysis it is proved that this is a doublet with a strong component of 0.624 MeV and a weak component of 0.607 MeV.
2) a doublet with components: 0.87 MeV, and 0.89 MeV.
3) a doublet with components: 1.045 MeV, and 1.07 MeV.
4) a doublet with components: 1.51 MeV, and 1.56 MeV.

together with previous results reported by Alburger and Toppel [13]). Because of the finite distance from source to crystal, in some cases the intensities had to be corrected for sum effects due to strong cascades.

4. Gamma-Gamma Coincidence and Sum-Coincidence Spectra

Sum-coincidence spectra were measured with the apparatus described by Hoogenboom [15]). In order to increase the counting efficiency the gamma-gamma coincidence spectrometer has been provided with two 4″ crystals in parallel, their pulses measured in coincidence with the signals from a 2″ crystal. A schematic diagram is shown in fig. 3. The pulses from the 4″ detectors D1 and D2 were fed into a linear network through the cathode followers CF1 and CF2. Both scintillation counters must have the same energy calibra-

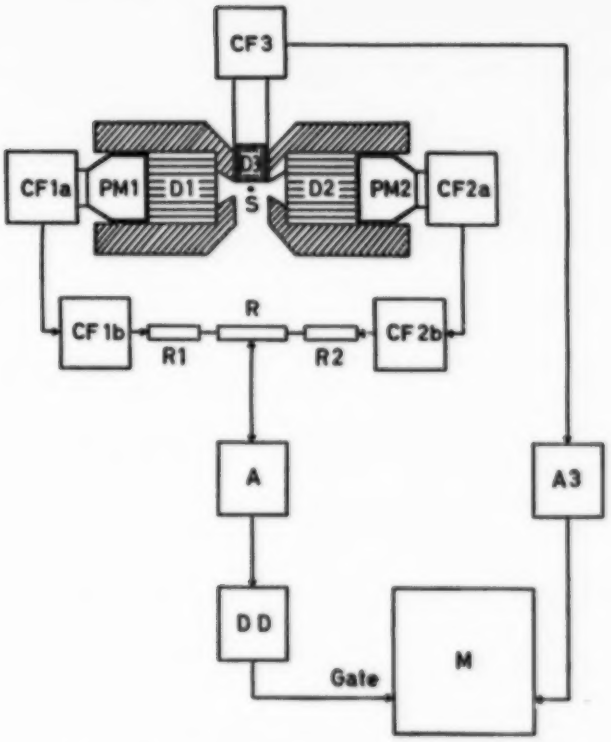

Fig. 3. Schematic diagram of the coincidence spectrometer.

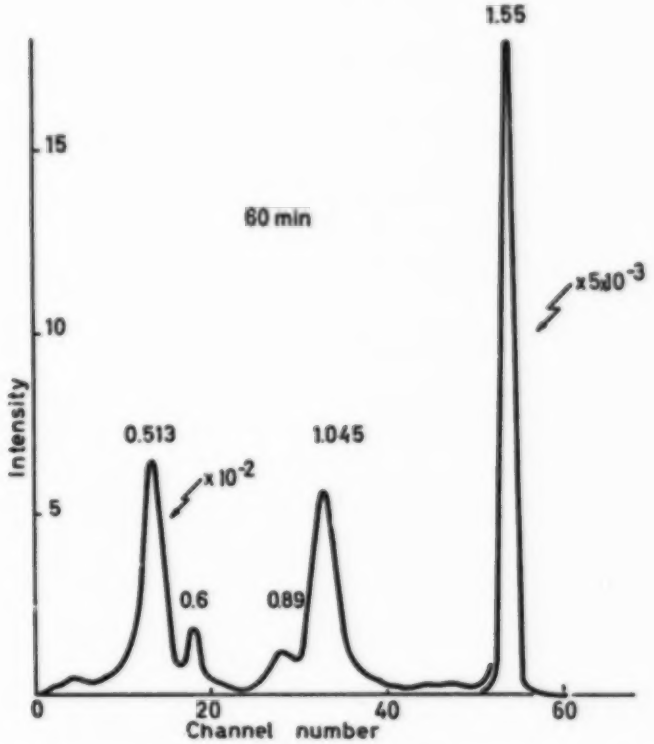

Fig. 4. Sum-coincidence spectrum obtained with the sum channel set at 1.55 MeV.

tion. After amplification, a specific gamma-ray photopeak is selected by the differential discriminator (D.D). The multichannel analyser (M) measuring the spectrum of the 2″ crystal (D3) is gated with these selected pulses. The use of the 2″ crystal for the coincidence spectra allowed better resolution.

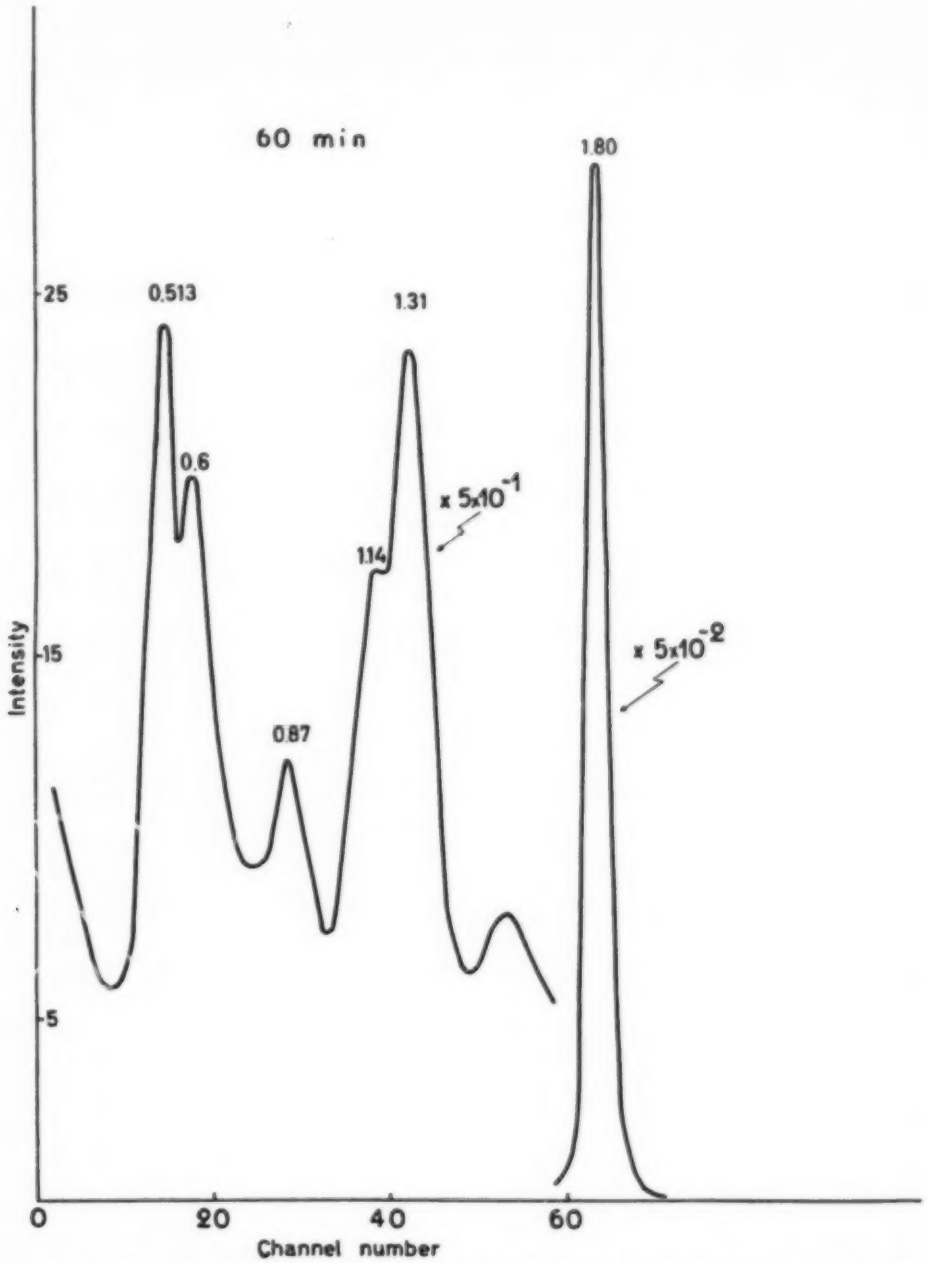

Fig. 5. Sum-coincidence spectrum obtained with the sum channel set at 1.80 MeV.

The 0.513 MeV coincidence spectrum showed that 0.513 MeV gamma rays are coincident with 0.624, 0.87, 0.89, 1.04 (1.07), 1.14, 1.31, 1.51, 1.76, 1.91, 2.1, and 2.37 MeV gamma rays. In order to select the direct transitions to the

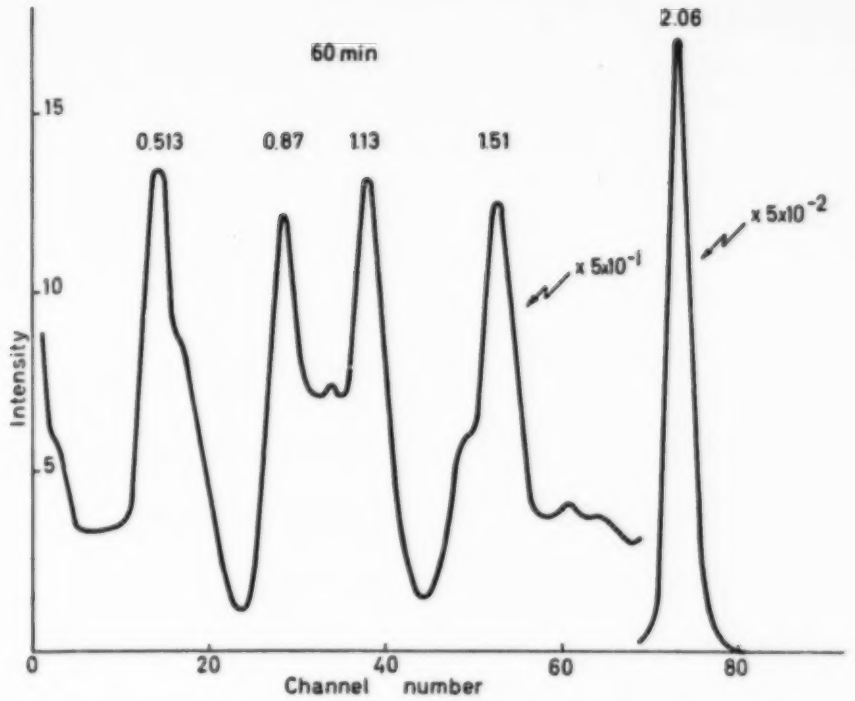

Fig. 6. Sum-coincidence spectrum obtained with the sum channel set at 2.06 MeV.

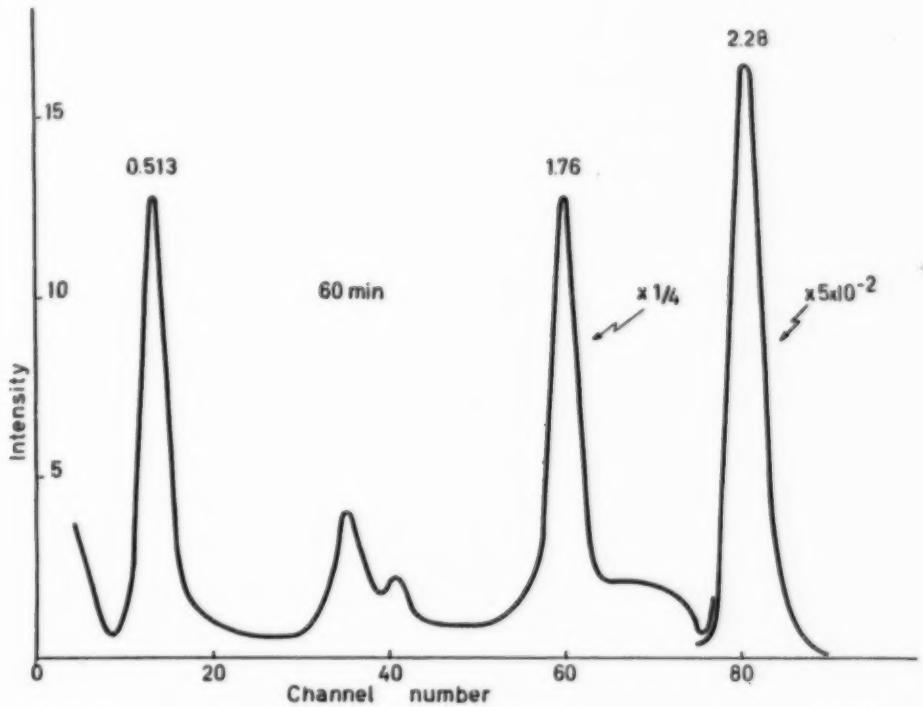

Fig. 7. Sum-coincidence spectrum obtained with the sum channel set at 2.28 MeV.

0.513 MeV level the 0.624, 1.04, and 1.10 MeV coincidence spectra were measured. The 0.624 MeV coincidence spectrum showed a very intense peak at 0.513 MeV together with peaks at 0.89, 1.12, 1.31 and 1.51 MeV. The presence of a peak at 1.04 MeV could be explained by the fraction of 0.513 MeV gamma-ray pulses entering the channel centered at 0.624 MeV. Peaks at 0.513, 0.87 and 1.07 MeV occurred in the 1.04 MeV coincidence spectrum. The appearance of a

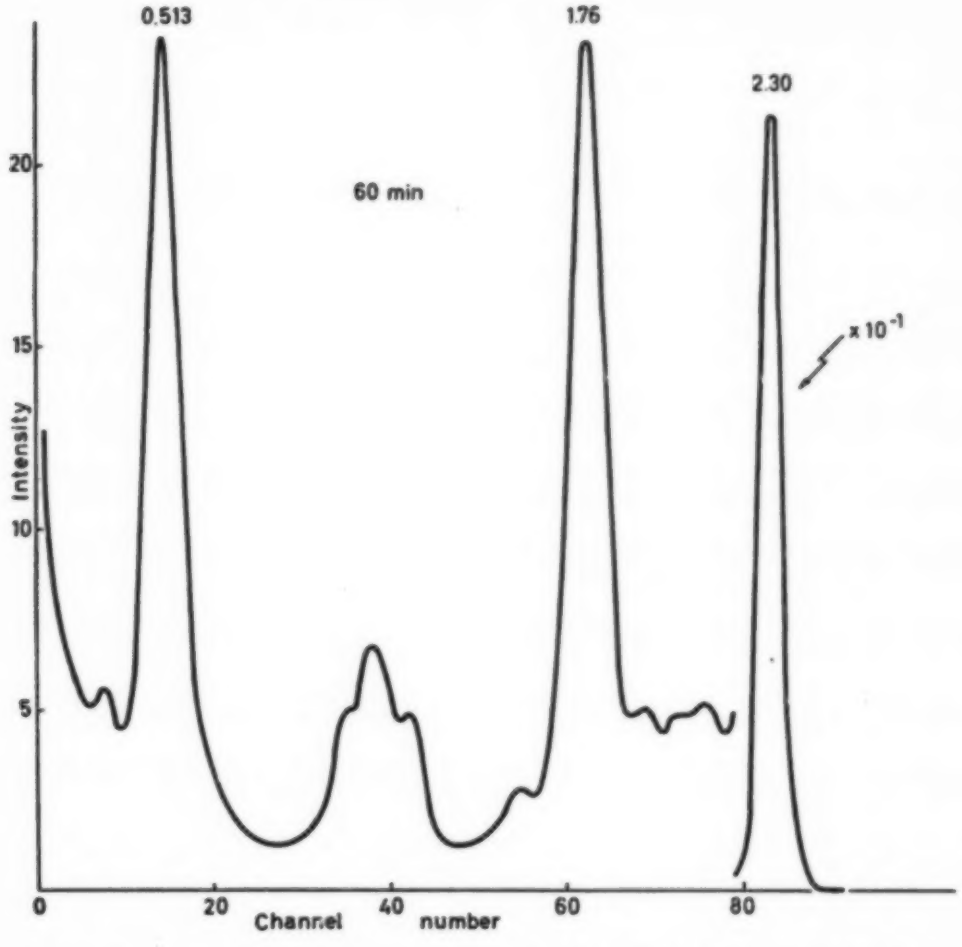

Fig. 8. Sum-coincidence spectrum obtained with the sum channel set at 2.30 MeV.

small 0.6 MeV peak is due to pulses from the 1.14 MeV gamma-ray. The 1.10 MeV coincidence spectrum showed peaks at 0.513, 0.624, 0.89, 1.13 and 1.31 MeV (very weak).

The coincidence spectra were analysed in detail in order to obtain the relative intensities of the coincident gamma rays. Table 2 shows the results of this analysis. The intensities are corrected for random coincidences, for channel width, for angular anisotropy (in table 2 indicated by a)) and for contribution from Compton background b) or fractions of photopeaks c) due to higher

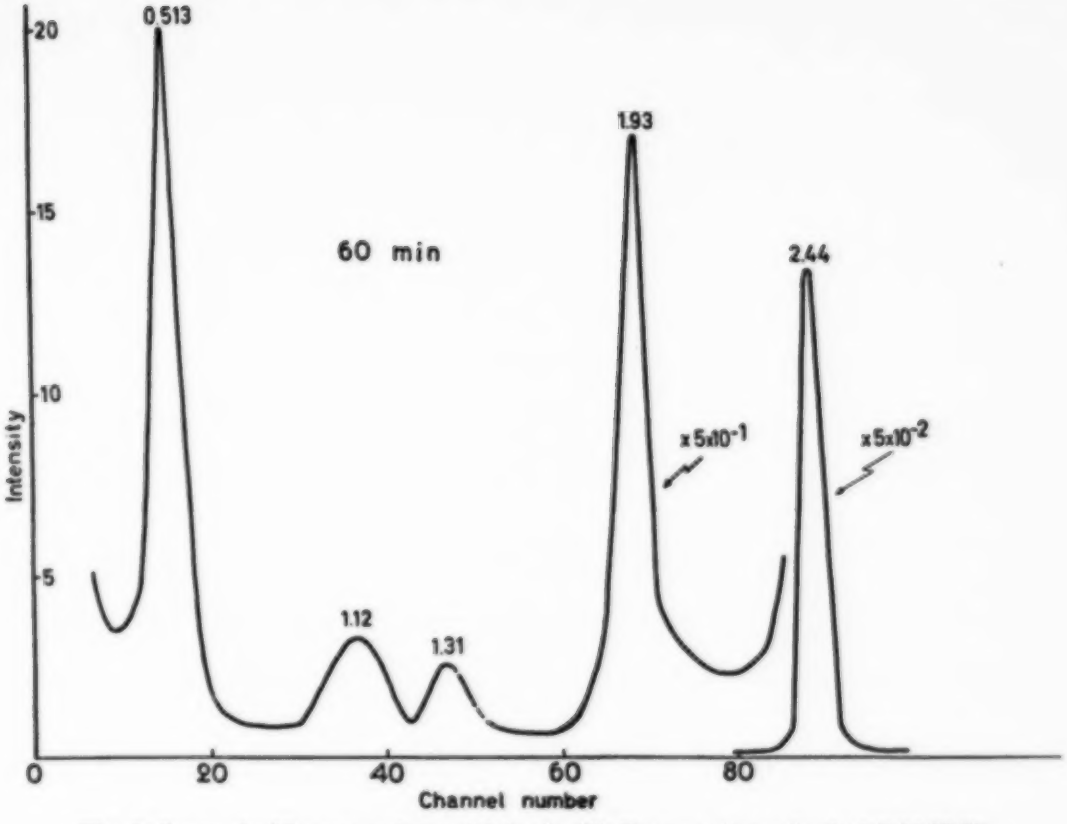

Fig. 9. Sum-coincidence spectrum obtained with the sum channel set at 2.44 MeV.

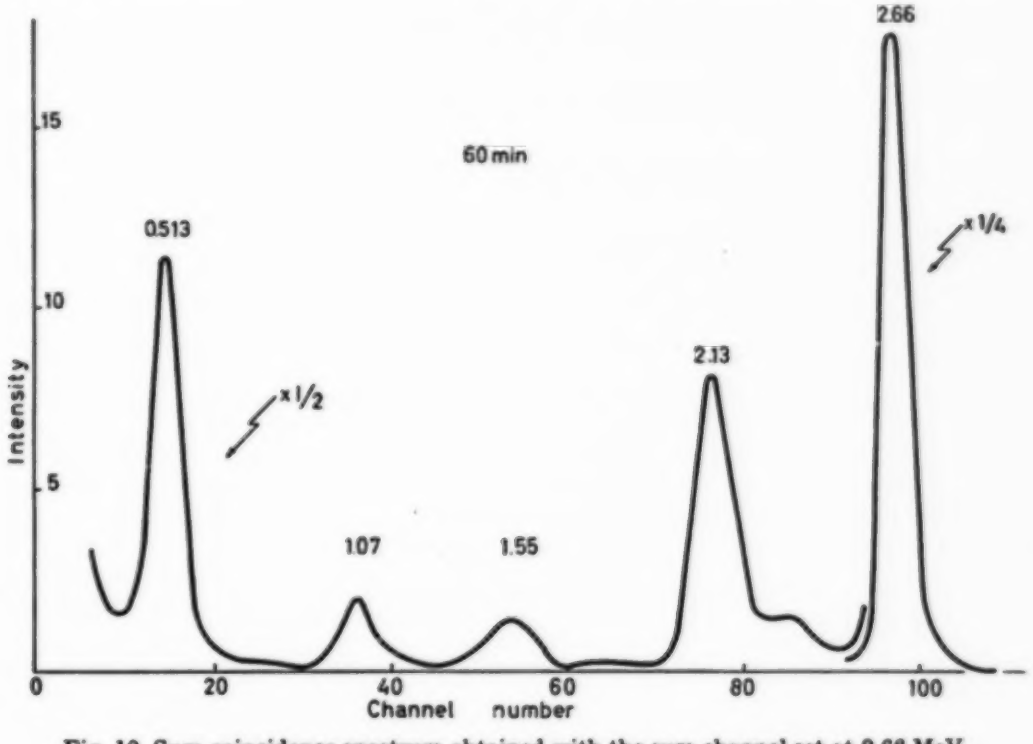

Fig. 10. Sum-coincidence spectrum obtained with the sum channel set at 2.66 MeV.

energy gamma rays in the discriminating channel. Of the various possible gamma-ray cascades in the decay of ^{106}Pd a selection was made based on the level scheme proposed by Alburger and Toppel and on the principal observations from the coincidence measurements. In the sum-coincidence measure-

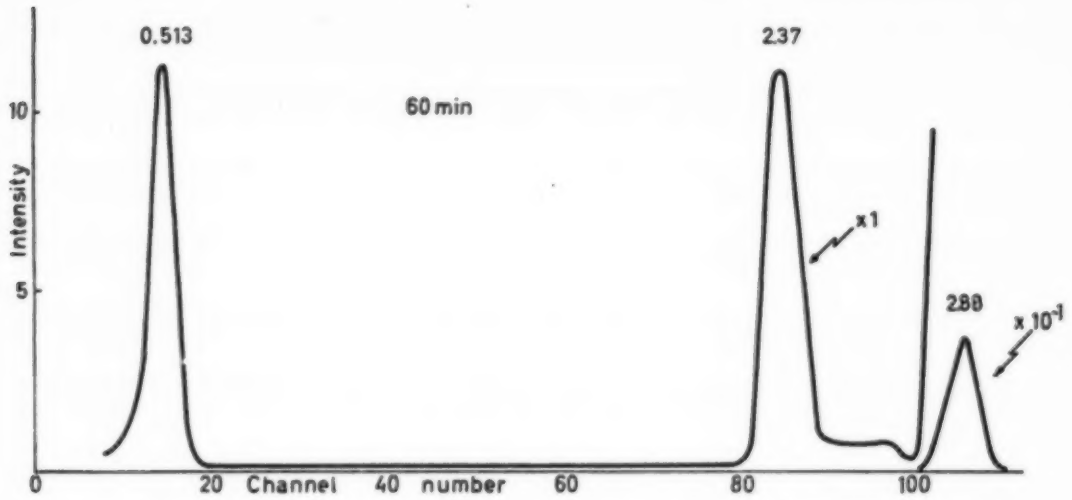

Fig. 11. Sum-coincidence spectrum obtained with the sum channel set at 2.88 MeV.

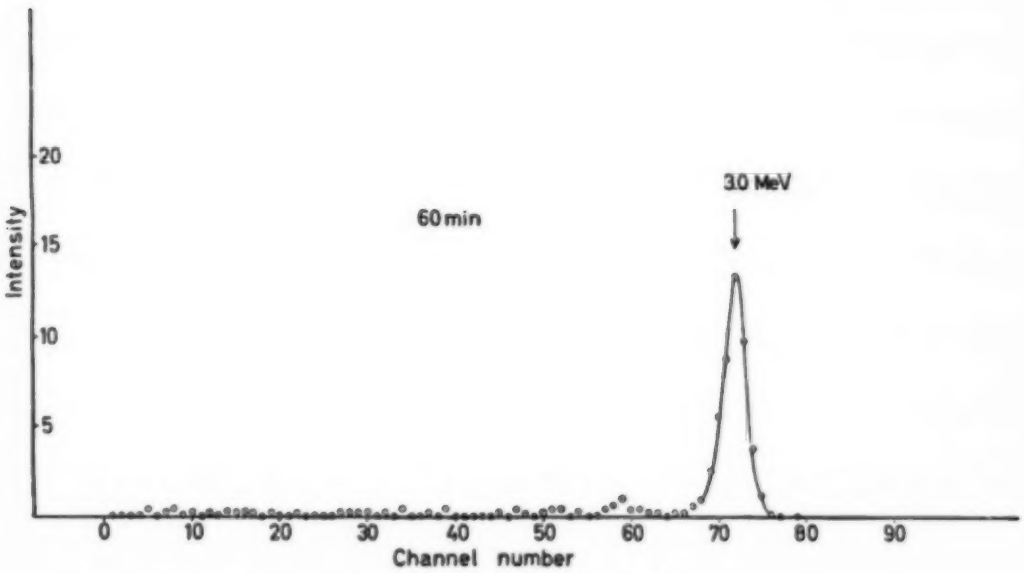

Fig. 12. Sum-coincidence spectrum with sum channel at 3.0 MeV (the spectrum has an absolute channel width different from the previous sum-coincidence spectra).

ments the sum channel was set at 1.14, 1.55, 1.77, 1.80, 1.85, 2.06, 2.28, 2.30, 2.44, 2.66, 2.88 and 3.0 MeV, respectively. Figures 4 to 12 show some of the experimental results normalised to 60 min. The 3.0 MeV sum spectrum has an absolute channel width different from the others. The 1.55 MeV sum spectrum shows two peaks corresponding to energies of 0.513 MeV and 1.045 MeV and two

peaks (approximately at 0.63 MeV and at 0.9 MeV) due to gamma rays in cascade, whose energy sum is smaller than 1.55 MeV. This causes a shift and therefore the actual energy of the corresponding gamma rays is somewhat lower than the measured values. From figs. 5 and 6, the existence of, respectively, 0.513—1.3 MeV and 0.607—1.14 MeV cascades, and 0.513—1.51 MeV, 0.607—1.31 MeV and 0.87—1.12 MeV cascades can be concluded. The 2.28, 2.30, 2.44, and 2.66 MeV sum spectra prove the occurence of 0.513—1.76 MeV, 1.12—1.14 MeV, 0.513—1.93 MeV, 1.12—1.32 MeV, 0.513—2.13 MeV, and 1.07—1.55 MeV cascades. The 2.88 MeV coincidence spectrum reveals the existence of a 2.88 MeV level decaying by a 0.513—2.37 MeV cascade. The absence of higher levels decaying through double cascades is shown by means of the measurement at 3.0 MeV.

TABLE 2

The ratio of the number of coincidences to the absolute intensity for each gamma-ray in coincidence with the discriminating gamma-transition

Coincid. spectrum MeV \ Coincidence channel MeV	From 0.478 to 0.548	From 0.585 to 0.655	From 1.00 to 1.10	From 1.10 to 1.20
0.513	– [b]	0.49 ±0.03 [a] [c]	0.092±0.009 [b]	0.006±0.002 [b] [c]
0.607 0.624	1 [a]	–	– [b]	0.006±0.001
0.87	0.17 ±0.04	– [c]	0.17 ±0.04 [b]	–
0.89	0.44 ±0.06 [b]	0.44 ±0.06 [c]	–	0.26 ±0.04 [c]
1.045 1.07	0.92 ±0.08	– [c]	– 0.016±0.009 [b]	–
1.12 1.14	0.085±0.013 [b]	0.05 ±0.01 [c]	–	0.016±0.004 [c]
1.31	0.3 ±0.1 [b]	0.17 ±0.07 [c]	0.1 ±0.1 [b]	0.16 ±0.04 [c]
1.51	0.23 ±0.04 [b]	0.06 ±0.06 [c]	–	–
1.76	1	–	–	–
1.91	1	–	–	–
2.1	1	–	–	–
2.37	1	–	–	–

Intensity corrected for: [a]) angular anisotropy.
[b]) Compton pulses in discriminating channel.
[c]) fraction of unwanted photopeak in discriminating channel.

The relative intensities of the coincident gamma rays were also determined from the analysis of the sum-coincidence spectra. The results were in good agreement with the coincidence data. The errors in table 2 are calculated from both sets of experimental data.

Some of the unresolved complex peaks in the single and coincidence spectra could be interpreted as the result of gamma rays of nearly the same energy. This explains the subdivisions included in table 2. (A further discussion is given in the next section).

5. Conclusions

The complexity of the ^{106}Pd gamma ray spectrum makes definite conclusions about the level scheme of ^{106}Pd difficult. Therefore the level scheme proposed in ref. [13]) has been adopted as a starting point. New levels are proposed at 2.02 ± 0.04 and 2.88 ± 0.03 MeV. The interpretation of our results does not require the existence of a 1.77 MeV level. The proposed decay scheme is shown in fig. 13. Many other combinations of levels have been tried on the basis of energy matching. Most of these were rejected on the basis of arguments concerning the relative intensities, the coincidence and sum-coincidence results.

The level at 2.88 MeV shows branching to the groundstate and to the first excited state. Possible decays by 0.61 MeV and 0.86 MeV gamma-ray transitions between the 2.88 MeV level and the 2.27 MeV, and 2.02 MeV levels are contradicted by the sum-coincidence measurement. Evidence is found for the level structure between 2 and 3 MeV. The levels at 2.63 ± 0.03 MeV, 2.44 ± 0.02, and 2.27 ± 0.02 MeV are not populated by gamma decay. Gamma-ray transitions of approximately 0.22, 0.44 MeV were not observed in the low energy spectrum. Our results indicate that, besides the groundstate transition, the 2.13 and 1.07 MeV transitions originate at the 2.63 MeV state; the 0.87, 1.31, and 1.93 MeV gamma rays decay from the 2.44 MeV level. The decay of the 2.27 MeV state by 1.14 and 1.12 MeV gamma rays in cascade, together with the 1.14—0.513 MeV and 1.14—0.6 MeV coincidence results, confirm the existence of a 1.12 MeV level. This is in agreement with the location of the second 2^+ state at 1.12 MeV established by Stelson and McGowan [14]). This 2^+ state is very close to the well known 0^+ state at 1.137 MeV which cannot decay by direct transition to the groundstate. The existence of the 2.02 MeV level is proposed from both coincidence and sum-coincidence measurements, together with intensity considerations. Channeling on 1.77 MeV, the sum-coincidence measurements indicated that no 1.77 MeV level decayed by a double cascade. Apart from Compton contributions and summing of Compton pulses, the number of pulses in the 1.77 MeV sum peak could be ascribed to 1.76 MeV gamma rays which in other measurements appeared to be coincident with the 0.513 MeV gamma-ray. This may explain the discrepancy in the decay of this state as obtained by Alburger and Toppel [13]).

The new level scheme indicates beta components with energies and intensities presented in table 3. The intensities have been obtained from measurements of the beta transitions to the groundstate and the first excited state. The branching of the remaining components can be calculated from the proposed decay scheme

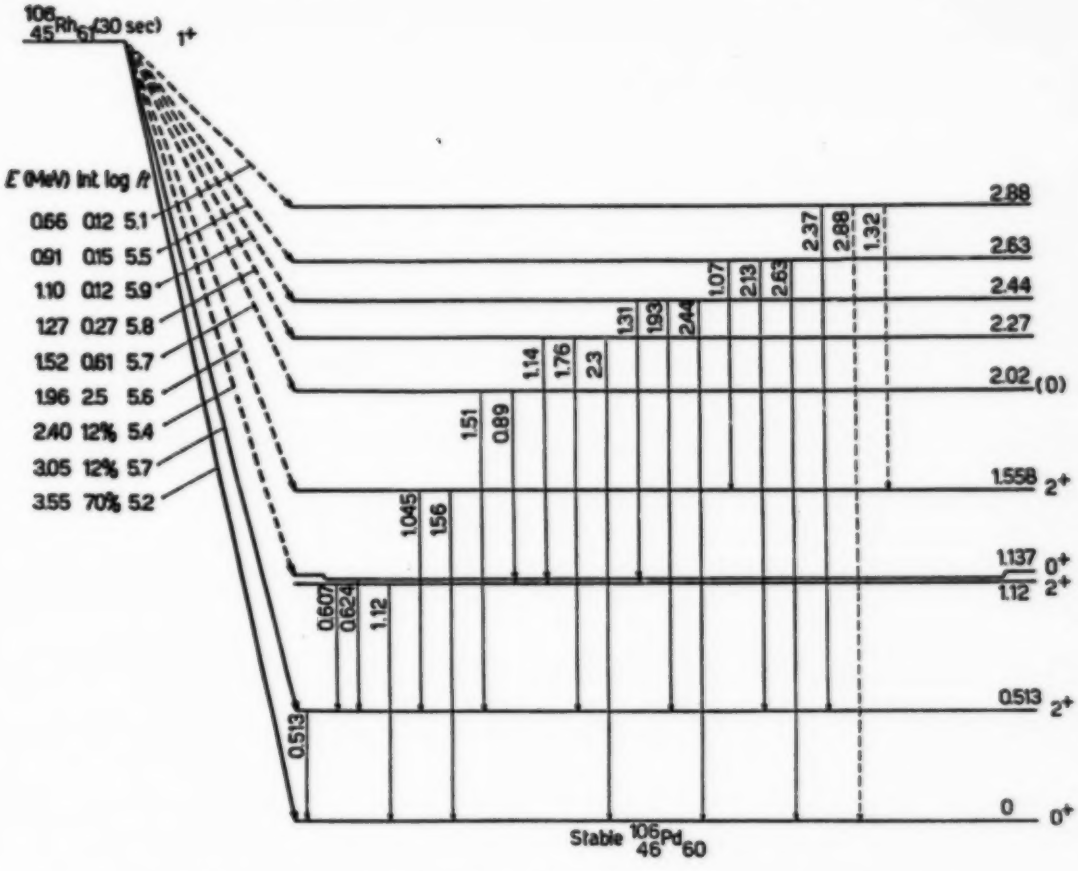

Fig. 13. Level scheme of ^{106}Rh as deduced from present investigation.

TABLE 3

Intensities and log *ft*-values of the various beta branches in ^{106}Pd

Level (MeV)	Assumed E_e (MeV)	% Population	Log *ft*
2.88	0.66±0.06	≦0.12	≦5.1
2.63	0.91±0.06	0.15	≦5.5
2.44	1.10±0.06	0.12	≦5.9
2.27	1.27±0.05	0.27	5.8±0.2
2.02	1.52±0.05	0.61	5.7±0.2
1.558	1.96±0.04	2.5	5.6±0.2
1.137	2.40±0.06	12	5.4±0.2
1.12			
0.513	3.05±0.02	12	5.7±0.2
0	3.55±0.02	70	5.2±0.2

and the relative intensities of the different gamma rays. One may also calculate the corresponding *ft* values. Since all transitions seem to be allowed, the 30 sec level of ^{106}Rh should have even parity and spin 1.

The measured angular correlation of the 0.89—1.12 MeV cascade is given by

$$W(\theta) = 1-(2.4\pm0.3)\cos^2\theta+(3.3\pm0.4)\cos^4\theta.$$

The window of the differential analyser of the fixed detector was set on the high-energy side of the full-energy peak of the 0.89 MeV gamma-ray. The corrections due to correlation effects of higher energy gamma rays in cascade with the 1.12 MeV transition result in a reduction of anisotropy of about 20 %. The correlation can be explained theoretically on the assumption of a 0-2-0 spin sequence. None of the spin sequences 0-1-0, 0-2-1, 0-2-2 is consistent with the observed $W(\theta)$. This proves the existence of a 2^+ level at 1.12 MeV and is in agreement with the absence of a 2.02 MeV groundstate transition (0^+-0^+).

The proposed decay scheme of fig. 13 can be deduced from and is consistent with the various measurements described above within their respective errors. Some of the ambiguities in the above interpretation can be resolved by beta-gamma coincidences which will be undertaken in the near future.

The authors would like to thank Prof. Dr. P. M. Endt and Prof. Dr. J. L. Verhaeghe for their interest in this work. This work was performed as part of the research program of the "Interuniversitair Instituut voor Kernwetenschappen-Belgium". One of the authors (O. J. S.) is indebted to Prof. Dr. P. M. Endt for extending to him the facilities of the Fysisch Laboratorium Utrecht University, the Netherlands.

References

1) W. E. Grummit and G. Wilkinson, Nature **158** (1946) 163
2) W. C. Peacock, Phys. Rev. **72** (1947) 1049
3) E. Brady and M. Deutsch, Phys. Rev. **78** (1950) 558
4) M. Deutsch and F. Metzger, Phys. Rev. **74** (1948) 1542
5) D. Ling and D. Falkoff, Phys. Rev. **76** (1949) 431, 1639
6) J. Spiers, Phys. Rev. **78** (1950) 75
7) A. Williams and M. Wiedenbeck, Phys. Rev. **78** (1950) 822
8) M. Goldhaber and E. der Mateosian, Brookhaven National Laboratory Report BNL 51 (S-5) (unpublished)
9) G. Arfken, E. Klema and F.McGowan, Phys. Rev. **86** (1952) 413
10) D. Alburger, Phys. Rev. **85** (1952) 734; Phys. Rev. **88** (1952) 339
11) E. Klema and F. McGowan, Phys. Rev. **92** (1953) 1469
12) B. Kahn and W. Lyon, Phys. Rev. **92** (1953) 902
13) D. Alburger and B. Toppel, Phys. Rev. **100** (1955) 1357
14) F. McGowan and P. Stelson, Bulletin of the American Physical Society (1957) 267
15) A. M. Hoogenboom, Nuclear Instruments **3** (1958) 56

1.C:
1.D.1

Nuclear Physics **16** (1960) 153—157; © *North-Holland Publishing Co., Amsterdam*
Not to be reproduced by photoprint or microfilm without written permission from the publisher

SYMPLECTIC INVARIANCE AND THE PAIRING PROPERTY OF NUCLEAR INTERACTIONS

IGAL TALMI

Department of Physics, The Weizmann Institute of Science, Rehovoth, Israel

Received 28 December 1959

Abstract: The condition of symplectic invariance of a general two-body interaction in the j^n configuration is derived for all values of T without the explicit use of group theory. The relation of symplectic invariance to the pairing property is also discussed.

In a recent paper [1]) the condition for the symplectic invariance of an ordinary two-body potential interaction was investigated in the case of the j^n configurations with maximum isospin. The result that the interaction must be a certain linear combination of scalar products of *even* tensor operators, seems to be different from earlier results on interactions possessing the pairing property [2]). It was shown [2]) that interactions which have the pairing property can be written in terms of scalar products of *odd* tensor operators. The author of ref. [1]) correctly points out that symplectic invariance is different from the pairing property. However, we shall show that the condition of symplectic invariance can be written as simply in terms of odd tensors. Therefore the symplectic invariance of an interaction implies that it has, with a trivial modification, also the pairing property.

We consider the matrix of the interaction Hamiltonian, defined by all the states of a certain configuration j^n. It is sufficient to consider the two particle configuration since the interaction in the n-particle configuration is a linear combination of two particle interactions. If each of the two particle interactions is symplectic invariant so also is their sum. Symplectic invariance means that the interaction matrix in the j^2 configuration is invariant under linear transformations of the wave functions induced by the symplectic group in $2j+1$ dimensions. A necessary and sufficient condition that a matrix will be invariant under all transformations of a group is that a scheme of wave functions which are bases of the irreducible representations of the group can be found in which the matrix is diagonal and that all diagonal elements are then equal in a submatrix, defined by wave functions which transform irreducibly among themselves (Schur's lemma).

In the case of identical particles this means that the interaction matrix must first be diagonal in the seniority scheme. Furthermore its eigenvalues for all

states with the same seniority v must be equal. In the j^2 configuration the state with $v = 0$ has $J = 0$. The other states have $v = 2$ and $J = 2, 4, \ldots, 2j-1$. Let E_J denote the eigenvalues of the j^2 interaction matrix. The necessary and sufficient condition for an interaction to be symplectic invariant is that it will satisfy

$$E_J = E_2 \quad \text{for } J > 0 \text{ even.} \tag{1}$$

An immediate conclusion is that the δ-potential interaction is not symplectic invariant. The energies of the j^2 configuration in this case are well known [3]) and do not satisfy (1).

The condition (1) is equivalent to requiring that the interaction can be expressed as

$$V_{12} = a + bq_{12} \tag{2}$$

where q is the seniority operator [2]). Every two-particle interaction, invariant under rotations, can be expressed as a linear combination of scalar products of irreducible tensor operators. Let the expansion of an arbitrary interaction, in the j^2 configuration after the radial intergrations have been carried out, be

$$V_{12} = \sum_{k=0}^{2j} A_k \mathbf{u}_1^{(k)} \cdot \mathbf{u}_2^{(k)}. \tag{3}$$

In (3) $\mathbf{u}^{(k)}$ is the unit irreducible tensor operator of degree k defined by [4]) $(j||u^{(k)}||j) = 1$. If V_{12} is an ordinary potential (Wigner force) the only terms which appear in (3) have even values of k. In this case the A_k are given in terms of the Slater radial integrals by $A_k = F^k(j||C_k||j)^2$. In the case of exchange forces or tensor forces, (3) contains terms with odd as well as even values of k. The expansion (3) of the special interaction (2) is quite simple. The operator q_{12} is given for jj-coupling by the same expression as in LS-coupling [5]):

$$q_{12} = \sum_{k=0}^{2j} (-1)^k (2k+1)\, \mathbf{u}_1^{(k)} \cdot \mathbf{u}_2^{(k)}. \tag{4}$$

Therefore the necessary and sufficient condition for an interaction to be symplectic invariant is that it can be expressed as

$$V_{12} = a + (2j+1)^{-1} b + b \sum_{k=1}^{2j} (-1)^k (2k+1)\, \mathbf{u}_1^{(k)} \cdot \mathbf{u}_2^{(k)}. \tag{5}$$

In this expansion $A_0 = (2j+1)a + b$ and $A_k = b(-1)^k(2k+1)$ for $k = 1, 2, \ldots, 2j$.

Although the expansion (5) of an interaction is necessary and sufficient for its symplectic invariance it is not unique in the case of identical particles. In this case the matrices of $(\mathbf{u}_1^{(k)} \cdot \mathbf{u}_2^{(k)})$ are not linearly independent since there are $2j+1$ of them but only $j+\frac{1}{2}$ states with even J. We shall make use here of one of the many relations between these matrices. This relation is derived from an identity of the Racah co-efficients [6])

$$(-1)^{2j-J} = \sum_{k=0}^{2j} (2k+1)\langle j^2 JM|\mathbf{u}_1^{(k)} \cdot \mathbf{u}_2^{(k)}|j^2 JM\rangle. \tag{6}$$

In the j^2 configuration of identical particles only states with even J occur. Therefore, in this case the following relation holds:

$$-1 = \sum_{k=0}^{2j} (2k+1)\, \mathbf{u}_1^{(k)} \cdot \mathbf{u}_2^{(k)} = (2j+1)^{-1} + \sum_{k=1}^{2j} \mathbf{u}_1^{(k)} \cdot \mathbf{u}_2^{(k)}. \tag{7}$$

Multiplying (7) by b and adding it to (5) gives for a symplectic invariant interaction the form

$$V_{12} = a + \frac{2j+3}{2j+1} b + 2b \sum_{k=2,\,\text{even}}^{2j-1} (2k+1)\mathbf{u}_1^{(k)} \cdot \mathbf{u}_2^{(k)}. \tag{8}$$

The condition (8) implies $A_k = 2b(2k+1)$ for $k > 0$ and is the same as that given in ref. [1]). Since the $(\mathbf{u}_1^{(k)} \cdot \mathbf{u}_2^{(k)})$ for even k are linearly independent, (8) means that *if* the expansion of an interaction contains only *even* tensors, the A_k for $k > 0$ should be proportional to $(2k+1)$. In this case the expansion (8) of the interaction is unique. On the other hand we can multiply (7) by b and subtract it from (5). The condition of symplectic invariance becomes that V_{12} must be equal to

$$V_{12} = a - b - 2b \sum_{k=1,\,\text{odd}}^{2j} (2k+1)\mathbf{u}_1^{(k)} \cdot \mathbf{u}_2^{(k)}. \tag{9}$$

Thus, an interaction V_{12} which is symplectic invariant is equal to the sum of a constant $(a-b)$ (which gives rise to a term $(a-b)\frac{1}{2}n(n-1)$ in the j^n configuration), and an interaction with odd tensors only, which has therefore the pairing property [2]). Other equivalent conditions, "intermediate" between (8) and (9), can also be obtained by using (7).

The situation is greatly simplified when we consider the general case of symplectic invariance in the j^n configuration of protons and neutrons. In addition to the seniority v the states are characterized in the seniority scheme by the reduced isospin t [7]). Also in this case it is sufficient to consider the j^2 configuration. The state with $v = 0$ has $J = 0$, $T = 1$, and $t = 0$. The states with $v = 2$ belong to two irreducible representations of the symplectic group $\mathrm{Sp}(2j+1)$. The states with $J(> 0)$ even have $t = T = 1$ and the states with odd J have $t = T = 0$. The necessary and sufficient condition for symplectic invariance in this case is therefore

$$E_J = E_2 \quad \text{for} \quad J(>0) \quad \text{even} \qquad \text{and} \quad E_J = E_1 \quad \text{for } J \text{ odd}. \tag{10}$$

The condition (10) implies that the interaction can be expressed in the form

$$V_{12} = a + bq_{12} + 2c\mathbf{t}_1 \cdot \mathbf{t}_2. \tag{11}$$

Since $P_T = \frac{1}{2}[1+4\mathbf{t}_1 \cdot \mathbf{t}_2] = -(-1)^T$ we can replace $2\mathbf{t}_1 \cdot \mathbf{t}_2$ by $-\frac{1}{2}-(-1)^T$

in the j^2 configuration. Since in this case $(-1)^{T+J} = -1$ we obtain $-\frac{1}{2}-(-1)^T = -\frac{1}{2}+(-1)^J$ which can be expressed by tensor operators (in ordinary and spin space) according to (6). Inserting in (11) the expressions from (4) and (6) we obtain for a symplectic invariant V_{12} the form

$$V_{12} = a+b\sum_{k=0}^{2j}(-1)^k(2k+1)\mathbf{u}_1^{(k)}\cdot\mathbf{u}_2^{(k)}-\tfrac{1}{2}c-c\sum_{k=0}^{2j}(2k+1)\mathbf{u}_1^{(k)}\cdot\mathbf{u}_2^{(k)}. \quad (12)$$

Separating the terms with $k = 0$, $k(>0)$ even and k odd we can rewrite (12) as

$$V_{12} = a+(2j+1)^{-1}\{b-(j+\tfrac{3}{2})c\}+(b-c)\sum_{k=2,\,\text{even}}^{2j-1}(2k+1)\mathbf{u}_1^{(k)}\cdot\mathbf{u}_2^{(k)} - (b+c)\sum_{k=1,\,\text{odd}}^{2j}(2k+1)\mathbf{u}_1^{(k)}\cdot\mathbf{u}_2^{(k)}. \quad (13)$$

The matrices $\langle j^2TJ|\mathbf{u}_1^{(k)}\cdot\mathbf{u}_2^{(k)}|j^2TJ\rangle$ are linearly independent in this general case. Therefore the expansion (13) is uniquely determined by the interaction (11) which in turn is uniquely determined by the values of E_0, E_1 and E_2. There is in this case only one form of the necessary and sufficient condition for symplectic invariance of a two-body interaction. This condition is that the A_k for the $k(>0)$ even will be equal to a constant multiplied by $2k+1$ and that the A_k for k odd will be equal to another constant multiplied by $2k+1$.

The interaction (11) can also be written in terms of odd tensors only if we make use also of $\mathbf{t}_1\cdot\mathbf{t}_2$ in addition to tensors in ordinary and spin spaces. The even tensors in the expansion of q_{12} can be eliminated by subtracting from (11) the expansion (6) of $-(-1)^J = (-1)^T = -\frac{1}{2}-2\mathbf{t}_1\cdot\mathbf{t}_2$ multiplied by b. We thus obtain for (11) the form

$$V_{12} = a-\tfrac{1}{2}b+(c-b)2\mathbf{t}_1\cdot\mathbf{t}_2-2b\sum_{k=1,\,\text{odd}}^{2j}(2k+1)\mathbf{u}_1^{(k)}\cdot\mathbf{u}_2^{(k)}. \quad (14)$$

This means that a symplectic invariant interaction (14) has a constant term (with $k = 0$) which in the j^n configuration gives rise to a term $(a-\frac{1}{2}b)\frac{1}{2}n(n-1)$, a term proportional to $2\mathbf{t}_1\cdot\mathbf{t}_2$ which gives rise to $(c-b)[T(T+1)-\frac{3}{4}n]$ and a sum of scalar products of odd tensors. This last term has also the pairing property. In this case an interaction with the pairing property satisfies

$$\langle j^n vtTJ|\sum_{i<k}^{n}V_{ik}|j^n vtTJ\rangle$$
$$=\langle j^v vt,\,T=t,\,J|\sum_{i<k}^{v}V_{12}|j^v vt,\,T=t,\,J\rangle+\tfrac{1}{2}(n-v)\langle j^2,\,J=0|V_{12}|j^2,\,J=0\rangle. \quad (15)$$

A condition for the invariance of the interaction Hamiltonian in the case of the l^n configuration (in LS-coupling) of identical particles can analogously be found. The invariance in this case is with respect to the group of rotations

$R(2l+1)$ in the $2l+1$ dimensional space of the single particle wave functions ψ_{lm}. In this case we use a two-body interaction with $\mathbf{s}_1 \cdot \mathbf{s}_2$ instead of $\mathbf{t}_1 \cdot \mathbf{t}_2$. We make use of $(-1)^{L+S} = 1$ to eliminate expressions with spin operators by using instead of $(-1)^S$ the $(-1)^L$ which in turn can be expanded in the form (6). The result is that an interaction Hamiltonian invariant under $R(2l+1)$ can always be uniquely expanded in the form (3) with only three independent coefficients α, β, γ, where $A_0 = \alpha$, $A_k = (2k+1)\beta$ for $k(>0)$ even, and $A_k = (2k+1)\gamma$ for k odd. If the interaction is an ordinary potential, γ is obviously zero. In this last case the condition of invariance under $R(2l+1)$ was already given by Racah [8]).

References

1) K. Helmers, Nuclear Physics **12** (1959) 647
2) G. Racah and I. Talmi, Physica **18** (1952) 1097
3) I. Talmi, Phys. Rev. **90** (1953) 1001
4) G. Racah, Phys. Rev. **62** (1942) 438
5) G. Racah, Phys. Rev. **63** (1943) 367, eq. (37)
6) Eq. (43) of ref. [4])
7) A. R. Edmonds and B. H. Flowers, Proc. Roy. Soc. A **214** (1952) 515
8) Eq. (55) of ref. [5])

2.L

Nuclear Physics **16** (1960) 158—167; © *North-Holland Publishing Co., Amsterdam*

Not to be reproduced by photoprint or microfilm without written permission from the publisher

NITROGEN-ALUMINIUM ELASTIC SCATTERING

M. L. HALBERT and A. ZUCKER

Oak Ridge National Laboratory, Oak Ridge, Tennessee †

Received 4 January 1960

Abstract: The differential cross section for elastic scattering of 27.3-MeV nitrogen ions from aluminium was measured from 36° to 134° in the centre-of-mass system. A coincidence system detecting both the nitrogen and the aluminium ions was used to identify the elastic events. The angular resolution was about ±1 degree. The ratio of the elastic cross section to the Coulomb cross section exhibits a small rise above unity near 50° (c.m.), then drops almost exponentially from 60° to 134° (c.m.), where it has a value of 0.0265. The results of the experiment are compared with the predictions of a sharp cutoff calculation. Reasonably good agreement is obtained from 36° to 96° (c.m.) with an interaction radius $R = 9.07 \times 10^{-13}$ cm. If we define $R = r_0(A_1^{\frac{1}{3}} + A_2^{\frac{1}{3}})$, the value of r_0 is 1.68×10^{-13} cm. Beyond 96° (c.m.) the sharp cutoff calculation displays increasing oscillations and no longer fits the data. The results of a semi-classical scattering theory due to Ford and Wheeler are also compared with the experimental data. The best fit is obtained for a rainbow angle $\theta_r = 94°$, corresponding to $r_0 = 1.59 \times 10^{-13}$ cm, and a surface thickness parameter $\Delta R = 0.83 \times 10^{-13}$ cm. Quite good agreement between this theory and experiment is obtained from about 94° to 134° (c.m.).

1. Introduction

This paper is one in a series concerning the measurement of the elastic scattering of 27.3-MeV nitrogen ions from light elements. Previously beryllium[1]) and carbon [2]) were used as scatterers while in this experiment we investigate a target of higher atomic number, namely aluminium. A coincidence technique in which both the scattered nucleus and the recoiling target atom are detected enables us to investigate the elastic scattering process to larger angles than has been done by methods in which only the scattered particle is observed. Putting it another way, the coincidence scheme enables one to measure lower elastic cross sections and distinguish elastic events from confusing reactions such as transfer reactions or inelastic scattering. As a matter of fact, even with good energy resolution in the detector the elastic scattering peak becomes comparable with the welter of other reaction products soon after the elastic cross section dips below the Coulomb cross section.

Nitrogen-aluminium elastic scattering may reasonably be interpreted by a semi-classical scattering theory. The relevant parameter $n = Z_1 Z_2 e^2/\hbar v$ is 10.3 in this case. The data are therefore compared with a sharp cutoff model due to Blair [3]), and with the rainbow scattering theory recently proposed by Ford and Wheeler [4]).

† Operated for USAEC by Union Carbide Corporation.

2. Experimental Procedure

An aluminium foil 0.20 mg/cm^2 thick was bombarded with an N^{14}-ion beam whose energy was measured to be 27.8 MeV [5]). The beam lost about 1 MeV in the target and henceforth we consider the beam to have a mean energy of 27.3 MeV. The spread in the incident energy is less than 600 keV full width at half maximum. The beam passed through the target and was stopped in a Faraday cup as shown in fig. 1.

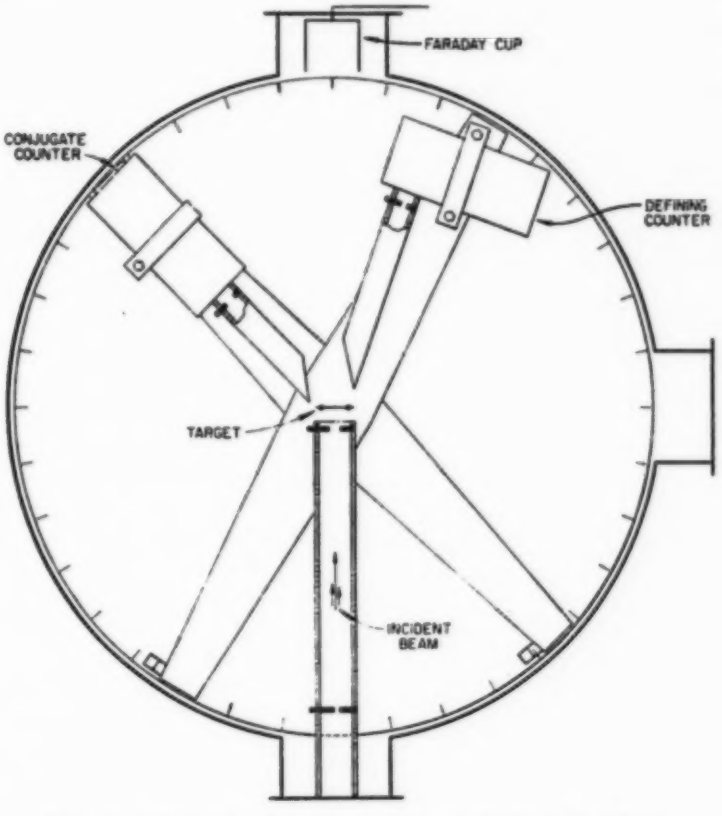

Fig. 1. Schematic drawing of the scattering chamber.

The scattered nitrogen nuclei as well as the recoil aluminium nuclei were detected with 0.005-in CsI(Tl) crystals mounted on Dumont 6291 photomultiplier tubes. All of the apparatus was in a 2-ft diameter scattering chamber connected directly to the cyclotron vacuum. The beam was collimated by a $\frac{1}{8}$-in. circular aperture at the entrance to the chamber.

The defining counter had a circular aperture with an acceptance cone of about 0°.25 half-angle in the laboratory system and defined the solid angle for scattering events at all angles. The conjugate counter had an aperture sufficiently large to detect all the coincident particles, taking into account multiple scattering and the solid angle in the centre-of-mass system. Both counters could be moved independently inside the chamber without breaking the

vacuum. The target itself was mounted on a frame so that the angle between the beam and the plane of the target could be set, as conditions demanded, anywhere from 90 to 45 degrees. The angular position of either counter could be reproduced to $\pm 0°.1$ (lab.).

The beam direction was determined in three ways: (1) a spot was burned on a piece of tape affixed to the defining counter, (2) in the region from 72° to 96° (c.m.) the cross section was measured by counting both nitrogen and aluminium particles in the defining counter, and (3) scattered nitrogen and recoil aluminium singles were counted over a 30° (lab.) region on either side of the beam direction. All three methods gave the same result for the direction of the incident beam. Considering the errors of these determinations we conclude that we measure true laboratory angles with a standard deviation of $\pm 0°.2$.

Pulses from the defining counter were amplified and fed to a 256 channel pulse height analyzer [6]). The analyzer was gated by pulses from an integral discriminator at the output of the conjugate-counter amplifier. In this way pulse height information was obtained for particles entering the conjugate counter. The resolving time of the gating circuit was about 0.6 μsec. The gated spectra were uniformly clean and easily interpreted.

The coincidence method was used from 50° to 134° (c.m.). At the smaller angles the scattered nitrogen was detected in the defining counter since it had the higher pulse height. At larger angles, because of its higher energy, the aluminium recoil was detected in the defining counter. Both kinds of particles impinge on the defining counter, but the position of the conjugate counter was set so that only the desired kind of particle produced coincidences. Reasons for switching from the scattered to the recoil particle, as well as the many experimental checks to insure against losing coincidences are given in considerable detail in the paper on N-Be scattering [1]), to which we refer the reader who is interested in the detailed design of this kind of experiment.

At angles between 36° and 50° (c.m.) it was found that the recoil aluminium ions did not have enough energy to operate the gating circuit reliably. The pulse height of the aluminium was so low that the signal-to-noise ratio became too small. Multiple scattering was also a serious problem. In this region elastic scattering has a far larger cross section than any competing process, and it was readily identified by pulse-height analysis alone. Therefore, the cross section at small angles was determined by counting nitrogen singles. This method is good to about 76° (c.m.) providing considerable overlap with the coincidence method. The complete data then consist of the following experimental measurements: (1) nitrogen singles from 36° to 76° (c.m.), (2) nitrogen coincidences from 50° to 96° (c.m.), and (3) aluminium coincidences from 72° to 134° (c.m.). In the overlapping regions the different methods give identical results within the experimental errors.

The coincidence technique was adequate to resolve elastic events from transfer reactions and scattering from target impurities. However, inelastic scattering presented a more serious problem. Inelastic scattering from the third excited state † of Al^{27} at 2.23 MeV requires that the conjugate-counter position be shifted 6° (lab) at small angles or 3° (lab) at the largest angles to produce coincidences. The angular acceptance of the conjugate counter was such that inelastic scattering from this state contributed less than about 30 % of its cross section. The cross sections for inelastic processes to states of similar excitation have, in N—Be and N—C scattering [1, 2]), been found to be at least 20 times smaller than the cross sections for elastic scattering. If the same is true of N—Al scattering, we estimate that at small angles at most one or two percent of the measured cross section could be due to these inelastic events, and at angles larger than 100° (c.m.) this might go as high as 4 %. The shift in counter angle for inelastic events from states higher than 2.23 MeV, and this includes all excited states in N^{14}, should be larger, so that their contribution to the measured cross section is negligible.

There remain two excited states in Al^{27}, at 0.843 and 1.01 MeV. The kinematics are such that at small angles the difference in conjugate counter position is 2° (lab), decreasing with angle until at 130° (c.m.) the difference is only 1° (lab). The plateaus in the angular position of the conjugate counter were about 4° (lab) full width. A difference of 2° would lower the counting rate only slightly. Our experience concerning yields in Be and C targets may not be applicable to the present situation since the Al^{27} levels are much closer to the ground state than any which were previously observed. We must conclude that the measured cross section includes all inelastic scattering from the first two states in Al^{27} for angles larger than 70° (c.m.). At smaller angles we would have seen an effect in the shape of the elastic peak in the defining counter. The energy of the inelastic events is 5 % lower and if any appreciable inelastic scattering had taken place there it should have resulted in an asymmetric peak. No such asymmetry was observed which indicated that at small angles the contribution is probably smaller than 20 %. Anticipating our results we note that at 36° and 70° (c.m.) the cross section is 3400 and 200 mb/sr, respectively; certainly one would not expect to find inelastic scattering with anything like this cross section.

We conclude that the measured values of the scattering cross section probably include elastic scattering events only, but we cannot rule out inelastic scattering from the first two states in Al^{27} as contributing to the cross section beyond 70° (c.m.). Better energy resolution in the defining counter is required to eliminate the contributions from inelastic scattering.

† Energy levels were taken from ref. [7]).

3. Results

The results of this experiment are shown graphically in fig. 2. The experimental cross section was calculated from the solid angle, target thickness, etc. It agrees with the Rutherford cross section at small angles; the two have not been normalized in any way.

The errors shown on the graph are standard deviations and include (1) uncertainties in the counting statistics, (2) uncertainty in beam integration (± 3 %), and (3) errors in background subtraction, if any. The uncertainty in setting counter angles amounts to about ± 0.15 % error in the cross section over the steepest portions of the angular distribution.

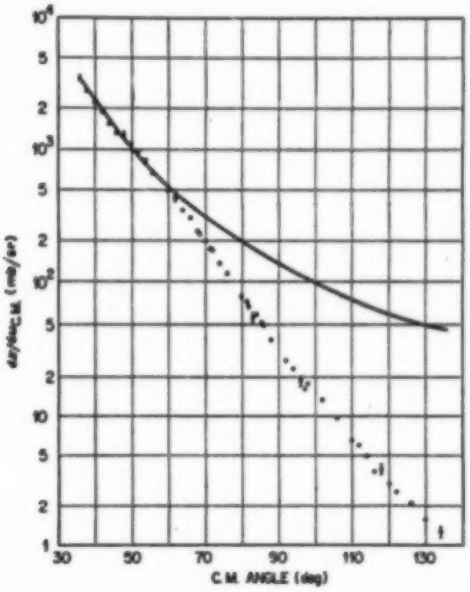

Fig. 2. The differential cross section of N^{14}—Al^{27} elastic scattering as a function of the nitrogen c.m. angle. The dots are the experimental results, and the smooth curve is the cross section for Coulomb scattering.

Probably the most serious source of random errors is associated with the energy variation of the cyclotron beam. No energy regulation of the incident beam is available on the cyclotron, and changes of the order of 300 keV could not be detected in the course of this experiment. At small angles where the cross section is that of Coulomb scattering it varies only as E^{-2} and the error due to energy variation is small. The dependence of the cross section on energy was measured at 54°, 71°.4, 94° and 110° (c.m.) by inserting absorbers in the incident beam to obtain 26.4-MeV and 23.5-MeV mean energy in the target. At 54° the cross section displayed approximately an E^{-2} dependence on energy. The results of the measurements at the other angles are given in table 1. It can be seen that at 110°$d\sigma/\sigma$ is 0.43 MeV^{-1} so that a variation of 300 keV in beam energy would produce a change of about 13 % in the cross

section. We therefore include the error estimated on a ±300-keV shift in the energy in the random errors shown in fig. 2.

TABLE 1

Ratio of the cross section for 26.4 and 23.5 MeV mean energy in the target to the cross section at 27.3 MeV at four c.m. angles

	54°	71.4°	94°	110°
26.4 MeV	1.07	1.28	1.42	1.48
23.5 MeV	1.16	2.14	4.15	5.30

There are systematic sources of error which do not change the shape of the curve but do affect the absolute magnitude of the ordinate. First is the uncertainty of the target thickness. The thickness was determined by weighing the foil and measuring it area; the uniformity of the foil was ascertained by scattering from different portions of the target and also by cutting it up into smaller portions and measuring the thickness of each piece. On this basis we estimate the standard deviation of the foil thickness measurements and its uniformity to be ±3 %. Uncertainties in the solid angle subtended by the defining aperture, absolute calibration of the beam integrator, and the average charge of the ion after passing through the targets were each of the order of a few percent. As a check, the cross section for elastic scattering of nitrogen from nickel was measured. The available nitrogen energy is well below the Coulomb barrier for nickel so that the cross section may be reliably calculated. The nickel measurement agreed with the calculations based on the measured solid angle, beam integrator calibration, and estimate of the average charge to within ±2 %. The estimated error in the nickel thickness measurement on which this comparison is based is ±3 %.

At small angles where only singles were counted the presence of impurities could introduce errors. Pulse-height analysis of the scattered nitrogen eliminates the contribution from heavy impurities. Scattering from oxygen could be only partly resolved. Chemical analysis showed that less than 1 % of the target is oxygen, and the Z^2 dependence of the scattering cross section at small angles makes its contribution entirely negligible. The same argument holds for scattering from carbon originating in the pump oil which may be deposited on the target in the course of the experiment.

We estimate that the standard deviation of all systematic errors is ±5 %.

4. Discussion

Semi-classical scattering theories ought to be applicable to nitrogen-aluminium scattering at this energy. The parameter $n = Z_1 Z_2 e^2/\hbar v$ is 10.3, which is large compared to unity. The data are first compared with the results of a

sharp cutoff model due to Blair [3]), which predicts the ratio of the elastic cross section to the Coulomb cross section as

$$\frac{\mathrm{d}\sigma}{\mathrm{d}\sigma_{\mathrm{c}}} = \left| \frac{-in}{\sin^2 \frac{1}{2}\theta} \mathrm{e}^{-in \log \sin^2 \frac{1}{2}\theta + 2i\delta_0} - \sum_{l=0}^{l'} (2l+1) \mathrm{e}^{2i\delta_l} P_l(\cos\theta) \right|^2 \frac{\sin^4 \frac{1}{2}\theta}{n^2}. \quad (1)$$

The choice of l', the cutoff l-value, was made empirically by fitting the data. It was found that $l' = 11$ fits the data better than any other single l'. However, the fact that the target is 1 MeV thick must be considered at this point. This has a twofold effect: (1) the energy dependence on the Blair calculation for a given l' must be examined, and (2) different values of l' will be applicable to different parts of the target, since l' is calculated from the semi-classical relation

$$l'(l'+1) = 2\mu\hbar^{-2} R^2 (E - E_{\mathrm{B}}). \quad (2)$$

The energy dependence of the Blair formula for constant l' was determined by making calculations at 26.8, 27.3 and 27.8 MeV. The magnitude of the cross section was only slightly energy dependent, a few percent at most, and the oscillations did not damp out. Therefore, it was considered sufficient to use $E = 27.3$ MeV for all calculations. On the other hand admixtures of different l' had a considerable effect on the cross section. In fact, a mixture of 50 % $l' = 11$, 25 % $l' = 10$, and 25 % $l' = 12$ reproduces the data excellently out to 100°. Such a mixture is an artificial one, however, and amounts essentially to an optimization by a 3-parameter fit.

If we make use of the fact that $l' = 11$ gives a better fit than any other single l', we arrive at a value for the interaction distance $R = 9.10 \times 10^{-13}$ cm. Using this result in eq. (2), for a 1-MeV thick target 85 % of the target thickness lies in the region of $l' = 11$, and 15 % in the region of $l' = 10$. The final calculation then was made such that

$$\mathrm{d}\sigma/\mathrm{d}\sigma_{\mathrm{Coul}} = 0.85(\mathrm{d}\sigma/\mathrm{d}\sigma_{\mathrm{Coul}})_{l'=11} + 0.15(\mathrm{d}\sigma/\mathrm{d}\sigma_{\mathrm{Coul}})_{l'=10}.$$

The result of this calculation is compared with the experimental points in fig. 3. It is to be noted that we are adding cross sections and not amplitudes for different l'. In other words the scattering for most of the foil behaves as if $l' = 11$, and only in the last 15 % of the target is the energy degraded to such an extent that $l' = 10$. The weighted average of R thus obtained is 9.07×10^{-13} cm, or $r_0 = R/(A_1^{\frac{1}{3}} + A_2^{\frac{1}{3}}) = 1.68 \times 10^{-13}$ cm. This procedure does not alter the shape of the potential, it merely corrects for a thick target. It is not equivalent to the rounded Blair potential used by Wall, Rees and Ford [8]).

Recently a semi-classical scattering theory was developed by Ford and Wheeler [1]) which they applied to the scattering of α-particles by heavy nuclei. We now compare its results with the scattering of nitrogen by aluminium.

The quantal expression for scattering is

$$\sigma(\theta) = |f(\theta)|^2,$$

where the amplitude $f(\theta)$ is

$$f(\theta) = \frac{1}{2ik}\sum_{l=0}^{\infty}(2l+1)[(\exp 2i\eta_l)-1]P_l(\cos\theta).$$

The following approximations valid for large l are then made: the sum is replaced by an integral and the Legendre polynomial is replaced by its asymptotic form. The phase shifts η_l are evaluated by the JWKB method. The classical angle of deflection as a function of l is defined as the deflection function Θ.

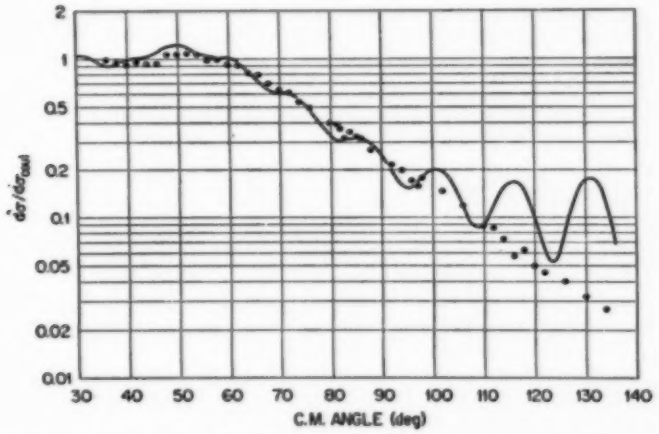

Fig. 3. The ratio of the elastic to the Coulomb scattering cross section. The dots are experimental data and the solid line is the result of a Blair model calculation with 85 % $l' = 11$, and 15 % $l' = 10$

The angle of observation is θ. In the JWKB approximation Θ obeys the relation $\Theta(l) = 2\mathrm{d}\eta_l/\mathrm{d}l$. The classical scattering cross section can be written in terms of the deflection function as

$$\sigma_{\mathrm{cl}} = \frac{\lambda^2(l+\frac{1}{2})}{\sin\theta\left|\frac{\mathrm{d}\Theta}{\mathrm{d}l}\right|_{\Theta=\theta}}$$

where θ is the angle of observation. This cross section has a singularity when $\mathrm{d}\Theta/\mathrm{d}l = 0$. In classical optics the appearance of rainbows is caused by such singularities.

Scattering by a potential which is repulsive at large distances and changes smoothly to an attractive potential at small distances will give rise to a maximum in Θ, which corresponds to a rainbow angle θ_r. In the case of scattering by a nucleus with a non-absorbing surface and a strongly absorbing interior, the largest angle of scattering θ_r is due to grazing collisions. Thus rainbow scattering, contrary to the Blair model, is applicable to a nucleus which has a

diffuse surface with no absorption. Its predictions are limited to the dark side of the rainbow (angles larger than θ_r), and it will necessarily involve two parameters: an internuclear distance related to θ_r and a nuclear surface thickness parameter.

Near the rainbouw angle the deflection function is expanded in the form

$$\Theta(l) = \theta_r - q(l-l_r)^2.$$

Using the three approximations outlined above, the amplitude for rainbow scattering becomes

$$f(\theta) = \lambda[2\pi(l_r+\tfrac{1}{2})/\sin\theta_r]^{\frac{1}{2}} q^{-\frac{1}{3}} e^{i\delta} \mathrm{Ai}(x),$$

where Ai is the Airy integral and $x = q^{-\frac{1}{3}}(\theta-\theta_r)$. If there is no significant interference of the rainbow amplitude with amplitudes from other branches of the deflection function the cross section is

$$\sigma(\theta) = \lambda^2(l_r+\tfrac{1}{2})(2\pi/\sin\theta_r) q^{-\frac{2}{3}} \mathrm{Ai}^2(x).$$

If this expression is divided by the cross section for Coulomb scattering at angle θ_r, the result is

$$\frac{\sigma}{\sigma_c} = \frac{2\sin^2\tfrac{1}{2}\theta_r}{nq^{\frac{2}{3}}} 2\pi \mathrm{Ai}^2(x).$$

The experimentally observed ratio $\sigma/\sigma_{\mathrm{Coul}}$ is compared with the result of the rainbow scattering theory in fig. 4. The best fit is obtained with $\theta_r = 94°$, and

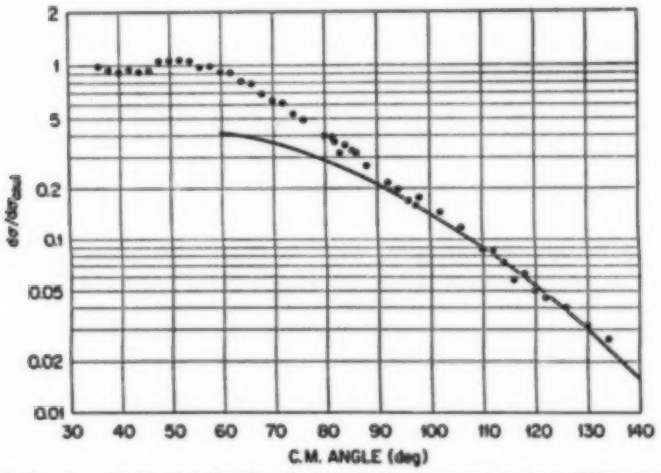

Fig. 4. The ratio of the elastic to the Coulomb scattering cross section. The dots are experimental data and the solid line is the result of a rainbow scattering calculation with $\theta_r = 94°$, and $q = 0.30$

$q = 0.30$. The optimum values of the two parameters are probably good to $\pm 1°$ for θ_r and ± 0.02 for q. The fit does not change appreciably within these limits but so far as we know can not be obtained with any other combination of θ_r and q.

We now examine, a posteriori, whether the approximations made in the theory are in fact valid in this case. Two conditions must be met: (a) l must be large compared to unity, and (b) through the surface region more than one l-value should contribute ($\Delta l > 1$), and the phase shift η_l should also change by more than one radian. Condition (a) is satisfied since we get $l_r = 8.9$ from $l_r + \frac{1}{2} = n \cot \frac{1}{2}\theta_r$, which is the classical relation for a Coulomb orbit. So far as condition (b) is concerned we make use of $\Delta l = \sqrt{(\theta_r/q)} = 2.3$, which is greater than unity as required. However, $\Delta\eta_l = \frac{1}{2}\theta_r \Delta l - \frac{1}{2}\theta_r = 1.1$, which only marginally satisfies the requirement. Nevertheless the agreement between theory and experiment is quite satisfactory over a 40° angular region.

As has been pointed out, the rainbow theory contains a parameter which is related to the nuclear surface thickness ΔR. Using $q = \theta_r/(k\Delta R)^2$, we obtain $\Delta R = 0.83 \times 10^{-13}$ cm, a value somewhat smaller than $\Delta R = 0.93 \times 10^{-13}$ cm obtained by Ford and Wheeler for the scattering of 22-MeV α-particles on silver.

One may obtain a distance of closest approach R by assuming a Coulomb orbit for the particles scattered at the rainbow angle:

$$R = n\lambda(1 + \csc \tfrac{1}{2}\theta_r).$$

For $\theta_r = 94°$, $R = 8.62 \times 10^{-13}$ cm, and $r_0 = R/(A_1^{\frac{1}{3}} + A_2^{\frac{1}{3}}) = 1.59 \times 10^{-13}$ cm. This value of r_0 from the rainbow scattering theory is close to $r_0 = 1.68 \times 10^{-13}$ cm from the Blair model calculation. This similarity is remarkable considering the differences between the theories and the fact that completely different portions of the experimental data are used to calculate the distance r_0.

The authors wish to thank R. H. Bassel for some illuminating discussions. Our thanks also go to A. W. Riikola and H. L. Dickerson for the operation of the cyclotron, to G. A. Palmer for his invaluable help in taking data, and to J. G. Harris for the construction of the apparatus.

References

1) M. L. Halbert and A. Zucker, Phys. Rev. **115** (1959) 1635
2) Halbert, Hunting and Zucker, Phys. Rev. (in press)
3) J. S. Blair, Phys. Rev. **95** (1954) 1218
4) K. W. Ford and J. A. Wheeler, Annals of Physics **7** (1959) 259
5) Reynolds, Scott and Zucker, Phys. Rev. **102** (1956) 237
6) Radiation Instrument Development Laboratory, Model 3301
7) F. Ajzenberg-Selove and T. Lauritsen, Nuclear Physics **11** (1959) 1
8) Wall, Rees and Ford, Phys. Rev. **97** (1955) 726

1.E.1:
3.A

Nuclear Physics **16** (1960) 168—174; © *North-Holland Publishing Co., Amsterdam*
Not to be reproduced by photoprint or microfilm without written permission from the publisher

LOW-LYING ENERGY LEVELS OF Cs^{134}

I. V. ESTULIN, A. S. MELIORANSKY and L. F. KALINKIN
Research Institute of Nuclear Physics, Moscow State University, Moscow

Received 2 October 1959

Abstract: A study is made of the cascade γ-transitions following thermal neutron capture in cesium nuclei. Energy and quantum characteristics of low-lying excited states of Cs^{134} with excitation energy up to 320 keV are determined.

1. Introduction

The character of energy levels of odd nuclei may yield data on interaction of an odd proton with an odd neutron or of these nucleons with an even nucleus core. The odd nuclei are for the most part radioactive. Energy states of such nuclei can be studied through some nuclear reactions and, particularly, through γ-radiation emitted by nuclei in the capture of neutrons [1]). In earlier work [2, 3]) we studied soft γ-radiation resulting from the radiative capture of thermal neutrons. The positions of energy levels and their quantum characteristics could not then be determined uniquely. More complete data can be obtained by measuring cascade γ-quanta, as was shown in a number of papers [4, 5, 6]).

The present work reports the results of investigating cascade γ-radiation emitted by cesium nuclei following the radiative capture of thermal neutrons. Apart from this, the characteristic X-radiation was registered, which made it possible to determine the K-shell internal conversion coefficients of γ-quanta. A scheme for low-lying energy levels of the odd Cs^{134} nucleus is discussed.

2. Method of Measurement

A luminescent coincidence spectrometer worked out by one of the authors of the present paper [7]) was used for measuring cascade γ-quanta. The spectrometer consists of the governing and the main channels with NaI(Tl) crystals and a photomultiplier as γ-rays directors. The apparatus allows one to measure the spectrum of pulses in the main channel which are in coincidence with the chosen energy interval in the governing channel (the resolving time of coincidence selection is 8×10^{-8} sec). In order to measure the pulse spectrum of accidental coincidences the pulses in the main channel were delayed.

The CsF target (a disc 20 mm in diameter, 0.25 g in weight) was placed in the neutron beam deflected from the shield of the heavy water physical reactor of

the Academy of Sciences of the USSR [8]). Luminescent counters in Pb and B_4C shield were placed at an angle of 90° to each other in the plane perpendicular to the neutron beam. Without the target the number of coincidences was negligibly small as compared with that in the presence of the target. With the CsF target the total number of coincidences constituted 20—60 c.p.s. the counting rate in channels being $2—5 \times 10^4$ c.p.s. Approximately 50% of the total number of coincidences were accidental. The pulse spectrum of accidental coincidences was similar to the pulse spectrum in the channels. Each measurement of the total coincidence spectrum was accompanied by measuring the spectrum of accidentals, the spectrum of real coincidences being obtained by a subtraction operation with these successively measured spectra.

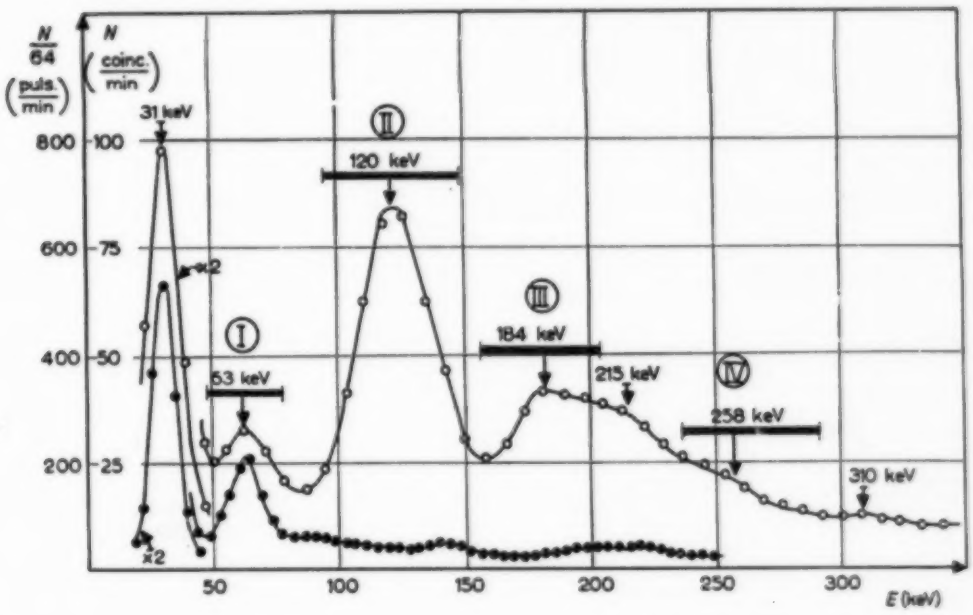

Fig. 1. Pulse height spectra of gamma-rays from the $Cs^{133}(n, \gamma)Cs^{134}$ reaction. Upper curve is the governing channel (radiation absorbed in 2 mm of Pb). Lower curve is the spectrum of coincidence with 120 keV γ-line.

In the investigated spectra the photopeaks from the soft γ-rays appear to be on a considerable "pedestal" resulting from Compton distribution of harder γ-rays. It was earlier shown [2]) that this "pedestal" can be substantially reduced by measuring spectra of γ-rays absorbed in Pb or Sn filters. A similar procedure for discerning "pedestal" coincidences was applied in the present work when measurements were carried out of coincidence spectra "with" and "without" a filter in the γ-ray collimator of the governing channel. As a result coincidence spectra only for soft γ-rays absorbed in filters have been obtained. The upper curve in fig. 1 shows the pulse spectrum in the governing channel (radiation absorbed by 2 mm of Pb). The lower curve presents the results of one of the experiments which selected the coincidences with photopeaks from 120 keV

γ-quanta (slit II on the upper curve). The method of measurements is treated in greater detail in ref. [9]).

Besides the photopeaks from γ-lines the coincidence spectra distinctly revealed a 31 ± 2 keV peak whose energy was equal to the energy of X-radiation from Cs atom. This radiation can be explained mainly by the internal K-conversion of γ-quanta and partly by the photoeffect of the γ-quanta self-absorption in the target. For a thin CsF target employed in experiments, an account was taken of the selfabsorption effect which was not great. The K-shell internal conversion coefficient (α_K) of γ-quanta was determined by way of comparing the area of the peak from X-radiation with the area of the photopeak. The luminescent counter efficiency and radiation absorption were at the same time taken into account [2, 3]). The experimental values of α_K were compared with the theoretical ones [10]) in order to determine the multipolarity of the respective radiative transition. A control experiment with Cs^{134m}($T_{\frac{1}{2}} = 3.1$ h), whose radiation was studied by other workers [11]) was carried out to provide a check on the accuracy of the α_K determination. In the present experiment an isomer was obtained after a sufficiently long exposure of the CsF target to the neutron beam. The spectrum resulting from the induced activity was measured after switching off the beam with the same target and in the same geometry as was employed when measuring γ-rays from (n, γ)-reaction. The coincidence spectrometer was used in these experiments as a single crystal luminescent spectrometer. Comparison of the areas of peaks from 127 keV γ-quanta and from X-radiation yielded a value of $\alpha_K = 2.8 \pm 0.3$ for the isomeric transition which is in good agreement with the value obtained in ref. [11]) and with theoretical value $\alpha_{theor} = 2.82$ for the transition of E3 type.

3. Neutron Capture Gamma-Rays from Cs

Investigation of the cascade γ-transitions following the radiative capture of neutrons in Cs was carried out in four sets of experiments which differed by energy intervals in the governing channel (fig. 1). These experiments were supplemented by measurements performed with a single crystal spectrometer. As a result the data of ref. [3]) on energy and intensity of γ-quanta from the Cs^{133}(n, γ)Cs^{134} reaction were rendered more specific, a number of new γ-lines was detected and the coincidence between them was checked. The data are summarized in table 1.

In the additional experiment the luminescent counter of the governing channel selected the pulses corresponding to γ-quanta of the energy close to the binding energy of the last neutron in Cs^{134} nucleus $E_n = 6.8$ MeV (the slit width is 2 MeV). The γ-lines detected in this experiment are marked with number V in the last column of table 1. The excited states revealed in coincidence measurements have a lifetime of less than 4×10^{-8} sec, which is proved

by the lifetime estimation made with the help of the delayed coincidence method. Thus, the investigated γ-transitions belong to E1, M1 or E2 types. M2 transitions or transitions with greater multipolarity would have had much larger lifetimes.

TABLE 1

No. γ-lines	Energy (keV)	Number of γ-quanta per captured neutron (%)	Coincidences
	31± 2	50±8	I, II, III, V
1	63± 2	9±2	II, V
2	75± 5	1.5	III, does not contradict I and II
3	120± 3	18±3	I, V
4	138± 4	2±1	III, V, does not contradict II
5	184± 4	9+2	V
6	195–260	3±2	I
7	215± 4	7±2	V
8	258± 4	5±1	V
9	310± 5	4±1	V

In the IVth set of experiments measurements were carried out of the coincidence spectrum with a photopeak from 258 keV γ-quanta. No coincidence of this γ-line with any other soft γ-quanta was discovered.

In the IIIrd set coincidences in the area of the photopeak from 184 keV γ-quanta were selected. The spectrum revealed photopeaks from two low-intensity lines of 75 and 138 keV and X-radiation whose intensity n_X exceeds the intensity of the 138 keV γ-quanta approximately by a factor 3. In order to explain the observed intensity n_X one should take into account the conversion of the two aforementioned γ-lines in the K-shell. The intensity of the 75 keV γ-quanta then proves to be $\approx 1.5\%$ per captured neutron, which does not contradict the intensity estimations obtained in other experiments. The 75 keV transition may be either E2 or a mixture of M1 and E2. In the chosen transition scheme preference is given to the latter.

In the IInd set of experiments the spectrum in coincidence with the 120 keV γ-quanta was measured (lower curve in fig. 1). Distinct peaks from X-radiation and from 63 keV γ-quanta are seen in fig. 1. In the control experiment of this set unresolved γ-lines were discerned in the 195—260 keV energy range. The intensity of X-radiation with respect to the number of 63 keV γ-quanta was found to be $n_X/n_{63} = 4.9 \pm 0.6$. The internal converson coefficient of the 63 keV γ-quanta was obtained with account of the possible conversion of the low-intensity γ-lines revealed in the measurements. Comparison with the theoretical values of α_K favours the conclusion that the 63 keV transition is an electric quadrupole one.

In the Ist set of experiments the spectrum in coincidence with the 63 keV γ-line was measured. Peaks from 120 keV γ-quanta and from X-radiation were detected. The relative intensity of X-radiation was found to be $n_X/n_{120} = 0.81 \pm 0.20$. The internal conversion coefficient of 120 keV γ-quanta in the

TABLE 2

Values of coefficients of internal conversion in the K-shell of Cs

Transition energy (keV)	Theoretical value		Experimental value
	M1	E2	
63	2.82	4.47	4.3 ± 0.6
120	0.46	0.685	0.6 ± 0.25

K-shell can be obtained hence by introducing a correction for a possible conversion of 75 and 138 keV γ-quanta. Table 2 shows that one cannot make a unique choice between the transitions of M1 and E2 types. In the most plausible transition scheme the 120 keV γ-quanta are to be considered as dipole ones.

4. Scheme of Cs^{134} levels

The proposed scheme of the excited Cs^{134} levels and of transitions between them is plotted in fig. 2. In constructing this scheme coincidences and anti-coincidences of separate γ-transitions revealed in the experiments (see table 1)

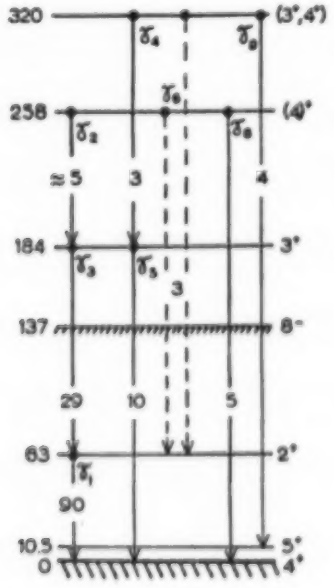

Fig. 2. Scheme of Cs^{134} levels.

were taken into account. Account was also taken of the values of energies and of transition intensities, of lifetimes, spins and parity of levels (both known before and newly prescribed). Apart from the levels whose existence was established in the present work the scheme includes also the 10.5 and 137 keV levels known from the decay of the Cs^{134} isomeric state [11]). The numbering of transitions in fig. 2 corresponds to that of table 1. Figures within the arrows in fig. 2 indicate total probabilities of transitions including γ-transition intensity and the internal K- and L-conversions. The accuracy of these data is determined by the accuracy of the intensity measurements of γ-lines (table 1).

The scheme was constructed on the basis of the most intense 63—120 keV cascade. It follows from the intensity ratio that the 120 keV transition precedes the 63 keV transition. A greater value of the absolute intensity of the latter induces to place it near the ground state. The assumption that it terminates at the 10.5 keV level leads to a worse agreement between the energies of the cascade and direct transitions. In this case some complications also arise in the spin assignment to the level from which the 63 keV transition occurs. The 63—120 keV cascade is not separated by intermediate levels because there is a direct 184 keV transition which is in anticoincidence with the cascade under consideration.

The scheme includes the levels whose energies (258 and 320 keV) are respectively equal to the sums of γ-lines energies—184 and 75 keV and 184 and 138 keV. With respect to the direct 258 and 310 keV transitions there are no sufficiently sound arguments supporting the inference that they terminate at the ground or the first excited states or perhaps even at the both.

In the proposed scheme the character of the 63 keV level is determined from the experimental multipolarity of the transition (see table 2) with due account of the character of the isomeric and ground states. The 3^+ character of the 184 keV level follows from the value of the measured α_K (120), the comparable intensities from this level and the absence of 174 keV γ-quanta in the spectrum. On the basis of similar considerations, though less uniquely, a moment assignment is made for the level with the excitation energy of 258 keV. The positive parity of this level follows from the fact that the 75 keV transition does not change parity. The presence of the competing transitions from the 320 keV level and their intensity ratio allow us to assume that the most suitable character of this level is 3^+ or 4^+.

The hard γ-quanta from the $Cs^{133}(n, \gamma)$ Cs^{134} reaction, which have been reported recently [12]), confirm the existence of the 184 keV and 320 keV levels in Cs^{134}. The transition from the capturing state to the 63 keV level, however, has not been observed. Therefore, the capturing state has probably the characteristics 4^+ and not 3^+.

The transition scheme shows that there are many excited levels near the Cs^{134} ground state, which is characteristic of odd nuclei. Let us compare these

levels with the levels of the neighbouring odd-neutron and odd-proton nuclei. The configuration $(g_{\frac{7}{2}}, d_{\frac{5}{2}})$ (in which the indicated shells are those of the odd proton and odd neutron) corresponds to the Cs^{134} ground state 4^+. The $(g_{\frac{7}{2}}, d_{\frac{5}{2}})$ configuration admits the 5^+, 4^+, 3^+ and 2^+ states. It is to this configuration that the level with the excitation energy of 10.5 keV (5^+) was assigned [11]). To the same configuration one should probably assign the 63 keV excitation level. Here we are faced with the multiplet structure of nuclear levels [13]). But the E2 transition from the 63 keV level is 200 times more probable than a one-particle transition.

Like the isomeric levels of the neighbouring odd-nuclei, the Cs^{134} isomeric level (137 keV) is to be interpreted as a first excited level of the neutron. The $(g_{\frac{7}{2}}, h_{\frac{11}{2}})$ configuration is usually ascribed to the isomeric level. However, the energy of this level notably differs from the energy of isomeric transitions in the neighbouring odd-neutron nuclei with neutron number $N = 79$, the same as for the Cs^{134} nucleus (232 keV in $_{54}Xe^{133}$, 268 keV in $_{56}Ba^{135}$). This is probably the result of the odd nucleus interaction.

For odd-proton isotopes of Cs, the energy of the first excited level of an odd proton in the $d_{\frac{5}{2}}$ state is equal to 82 keV (Cs^{133}) and 250 keV (Cs^{135}). In this excitation energy range one may expect a multiplet structure corresponding to the $(d_{\frac{5}{2}}, d_{\frac{5}{2}})$ configuration of 4^+, 3^+, 2^+ and 1^+ characters. It is possible that the Cs^{134} levels with the 184 and 258 keV excitation energy belong to the same configuration. Unfortunately, there are no theoretical values with which one might compare the disintegration of multiplet nuclear levels.

In conclusion the authors wish to thank the physical reactor crew and to acknowledge the help of student B. S. Kudinov in carrying out the experiment.

References

1) L. V. Groshev, A. M. Demidov, V. N. Lutsenko and V. I. Pelekhov, Atlas of γ-ray spectra from radiative capture of thermal neutrons (Moscow, 1958)
2) I. V. Estulin, L. F. Kalinkin and A. S. Melioransky, Nuclear Physics **4** (1957) 91
3) L. F. Kalinkin, A. S. Melioransky and I. V. Estulin, JETP **35** (1958) 592
4) R. E. Segel, Phys. Rev. **113** (1959) 844
5) G. A. Bartholomew, P. J. Campion, J. W. Knowles and G. Manning, Nuclear Physics **10** (1959) 590
6) V. G. Burmistrov, Izv. Akad. Nauk SSSR, Ser. Fiz. **23** (1959) 898
7) A. S. Melioransky (to be published)
8) Atomnaya Energiya **3** (1957) 376
9) A. S. Melioransky, I. V. Estulin, L. F. Kalinkin and B. S. Kudinov, JETP (in press)
10) L. A. Sliv and N. M. Band, Tables of Internal Conversion Coefficients of Gamma Rays (1956)
11) A. W. Sunyar, J. W. Mihelich and M. Goldhaber, Phys. Rev. **95** (1954) 570
12) R. Balzer, H. Knoeppel, Y. Yong, P. Stoll and W. Wölfli, Helv. Phys. Acta **32** (1959) 764
13) L. V. Groshev and A. M. Demidov, Atomnaya Energiya **3** (1957) 91

1.D.2:
1.E.4:
3.A

Nuclear Physics **16** (1960) 175—187; © *North-Holland Publishing Co., Amsterdam*
Not to be reproduced by photoprint or microfilm without written permission from the publisher

DETERMINATION OF A 7×10^{-11} SEC HALFLIFE FOR THE FIRST EXCITED STATE IN THALLIUM 201

J. LINDSKOG, E. BASHANDY † and T. R. GERHOLM

Institute of Physics, University of Uppsala, Sweden

Received 3 December 1959

Abstract: A halflife $T_{\frac{1}{2}} = (7 \pm 2) \times 10^{-11}$ sec has been found for the first excited 330-keV state in Tl^{201}. The measurements have been performed in an electron-electron coincidence spectrometer by means of delayed coincidence technique. A new method to reduce the influence of energy dependent instrumental timedelays has been developed.

The K/L_I+L_{II} and L_I+L_{II}/L_{III} ratios for the 330 keV transition have been measured by means of an iron yoke double focusing spectrometer. From these measurements the mixing ratio E2/M1 was found to be 2.2 ± 0.4.

The transition matrix elements have been calculated and are compared with the corresponding matrix elements in Tl^{203}.

1. Introduction

The odd mass thallium isotopes are only one proton-hole away from a closed shell and also the neutron cores are nearly closed shells. These isotopes therefore give an opportunity to check the validity of the shell model. The decay schemes of the odd thallium isotopes are almost identical, at least as far as the low lying levels are concerned. The assignments $s_{\frac{1}{2}}+$, $d_{\frac{3}{2}}+$ and $d_{\frac{5}{2}}+$ for the ground state, first excited and second excited state have been proposed. The cascade to the ground state thus consists of two mixed E2+M1 transitions. The $d_{\frac{3}{2}} \rightarrow d_{\frac{5}{2}}$ transition is almost pure M1 while the $d_{\frac{3}{2}} \rightarrow s_{\frac{1}{2}}$ transition consits of comparable amounts of M1 and E2. This is in accordance with the single particle model. In the $d_{\frac{3}{2}} \rightarrow s_{\frac{1}{2}}$ transition the E2 part can compete with the M1 part since the latter is l-forbidden ($l = 2$) according to the single particle model. The upper transition, however, is l-allowed and one should therefore expect an almost pure M1 transition.

From the lifetimes of the excited levels and the mixing ratio of the deexciting gamma ray the partial transition rates can be calculated. These transition rates which are very sensitive to nuclear effects can be compared with single particle estimates. Such a comparison has been made by Gerholm

† On leave from the Egyptian Atomic Energy Commission.

and Bosch [1]) in a review article on Tl^{203}. They find for the transition from the first excited state to the ground state that the E2 multipole is enhanced about a factor of ten over the single particle estimate. This enhancement may be accounted for in terms of the weak coupling model [2, 3]). The *l*-forbidden M1 transition on the other hand is retarded by a factor of about 900. Thus the *l*-selection rule of the single particle model does reduce the M1 matrix element considerably but it still has a finite value. The collective admixture that may explain the E2 enhancement probably cannot account for the finite M1 matrix element. Various attempts have been made to explain this *l*-forbidden M1 transition, some of which are based on exchange current effects [4]) and others on configurational mixing [5]).

Recently Arima, Horie and Sano [6]) have developed a theory based on configurational mixing which accounts very successfully for the static magnetic dipole moments or more precisely the deviation from the Schmidt lines. This theory has also been applied to the *l*-forbidden M1 transitions. The agreement is less impressive but there is a considerable improvement over the single particle model. According to Arima, Horie and Sano [7]), for an odd proton isotope the configurational mixing that accounts for the *l*-forbidden M1 transition is mainly due to proton-proton interaction. One should therefore expect the same matrix element in Tl^{203} and Tl^{201}. However, there is also a minor correction due to proton-neutron interaction. It would be of interest to study the M1 matrix-element for a sequence of thallium isotopes of odd mass. In the present work we report experimental matrix elements for Tl^{201}.

Pb^{201} decays by electron capture and positon emission to Tl^{201}. The positon spectrum has been investigated by G. Andersson *et al.* [8]). Conversion electron measurements have been performed by Wapstra *et al.* [9]) and K. E. Bergkvist *et al.* [10]). The halflife of Pb^{201} was found by Bergkvist *et al.* to be 9.4 ± 0.2 h. They also report 15 gamma transitions most of which could be given multipolarity assignments from K/L ratios. The two strongest gamma transitions have the energies 330.3 and 361.2 keV. These were shown by electron-electron coincidence measurements to be strongly in coincidence [11]). From intensity considerations the 330 keV transition could be shown to take place between the first excited state and the ground state, while the 362 keV transition takes place between the second and the first excited states. The K/L+M ratio for the 330 keV transition has been measured by Wapstra *et al.* [9]); they report 5.5 ± 1.5. Bergkvist *et al.* [10]) found K/L = 4.7. Bergkvist has remeasured his value and has privately reported (12) $K/L_I+L_{II} = 4.55$ and $L_I+L_{II}/L_{III} = 7.4$. This indicates a mixed M1 and E2 transition. The 362 keV transition is thought to be almost pure M1 [10]). From level systematics the single particle assignments $s_{\frac{1}{2}+}$, $d_{\frac{3}{2}+}$, $d_{\frac{5}{2}+}$ have been confirmed for the ground state, the first excited and second excited states [13]). The ground state spin assignment has been confirmed by atomic beam resonance measurements [14, 15]).

2. The Lifetime Measurements

Natural thallium was bombarded with 65 MeV protons in the synchrocyclotron at the Werner institute at Uppsala. After chemical separation the lead activity was evaporated in vacuum onto a backing of 1.6—2.0 mg/cm² of aluminium. The diameter of the sources was 3—4 mm.

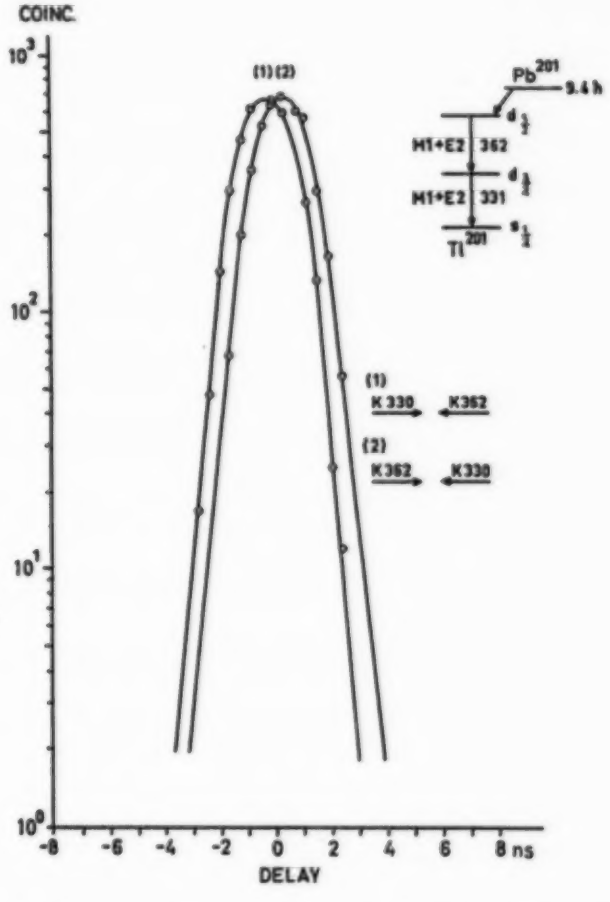

Fig. 1. Representative self-comparison plot. The random coincidence background is subtracted.

The decrease with time of the coincidence counting rate between the 330 keV and 362 keV transitions was measured. This measurement gave a halflife of 10.0 ± 0.8 h in good agreement with the 9.4 ± 0.2 h halflive previously reported for Tl^{201} [10]. This shows that interference of the other isotopes that are present in the source gives a negligible contribution to the coincidence measurements.

The lifetime measurements were performed with delayed coincidence technique. The coincidence unit is of the type described by R. E. Bell *et al.* [16]. In this investigation resolving times between 2.1 and 2.7 ns were used.

As the energy difference between the two transitions is only about 10 % it is necessary to use a magnetic spectrometer to be able to resolve the lines. For

this purpose an electron-electron coincidence spectrometer [17]) with a momentum resolution of 3 % and a transmission of 3 % was used.

The measurements were performed according to the self comparison method [16]). Two time resolution curves were measured. One curve was taken with the 330 keV transition focused in spectrometer I and the 362 keV transition focused in spectrometer II. The second curve was measured with the conversion lines shifted in the spectrometers to get the inverse combination (fig. 1). According to Newton [18]) and Bay [19]) the centroid shift between the two curves is equal to twice the meanlife of the intermediate level. This is correct, however, only if the instrumental time delays for the two curves can be neglected. As will be shown below, certain time delays are energy dependent. Since the two time resolution curves correspond to slightly different energy settings of the coincidence spectrometer a systematic error is introduced. For lifetimes of nuclear levels of the order of magnitude which is of interest here ($\approx 10^{-10}$ sec) this systematic error is comparable to or even larger than the effect due to the lifetime itself. It is therefore necessary to find a method to eliminate or greatly reduce the influence of these energy dependent instrumental time delays. In our case we have to consider three types of instrumental time delays, namely: i) the instrumental shift due to the difference in transit time of the electrons through the spectrometer, ii) the difference in response time of the scintillation detector for different electron energies, and iii) possible influence of the magnetic field on the transit time of the electrons through the photomultipliers.

In order to check point iii) the following experiment was undertaken. The scintillators and light-collectors were replaced by a rod of lucite with an anthracene scintillator in the middle. This rod formed a long light guide between the two photomultipliers in the spectrometer. A Co^{60} source was placed close to the scintillator and two time resolution curves were measured corresponding to the different current settings used in the self-comparison measurement described above. The observed shift was less than the statistical error which was equal to 2×10^{-11} sec. This implies that the influence of the magnetic field is negligible.

The other two instrumental time delays had to be corrected for in the following way. According to Post and Schiff [20]) the average time $\bar{t}$ between the absorption of the conversion electron in the scintillator and the appearence of the first photoelectron at the photocathode is

$$\bar{t} = \frac{Q}{R\lambda}\left[1 + \frac{Q+1}{2R} + \ldots\right] \tag{1}$$

where Q is the number of photo-electrons necessary to trigger the fast coincidence circuit, R is the average total number of photo-electrons per scintillation and thus proportional to the energy of the conversion electron, and λ is the

decay constant of the scintillator. To a very good approximation this instrumental time delay is inversely proportional to the energy:

$$l = \frac{K}{E}. \tag{2}$$

An expansion in Taylor series to second order in ΔE gives the difference in response time for the energies $E+\Delta E$ and E:

$$t_K(E+\Delta E)-t_K(E) = -\frac{\Delta E}{E}\frac{K}{E} + \left(\frac{\Delta E}{E}\right)^2 \frac{K}{E}. \tag{3}$$

The transit time of the electrons through the spectrometer can be written

$$t_l(E) = \frac{l}{v} = \frac{l}{c}\frac{E_0+E}{\sqrt{E_2+2E_0E}}; \tag{4}$$

l is the length of the electron trajectory, v and E are the velocity and energy of the electrons, c is the velocity of light and E_0 is the electron rest mass expressed in keV. Expanding again in Taylor series to second order in ΔE we find for the difference in transit time

$$t_l(E+\Delta E)-t_l(E) = -\Delta E\frac{l}{c}\frac{E_0^2}{(E^2+2E_0E)^{\frac{3}{2}}} + \frac{1}{2}(\Delta E)^2\frac{3E_0^2}{(E^2+2E_0E)^2}t_l(E). \tag{5}$$

To reduce the influence of the instrumental shifts the lifetime was measured by means of an interpolation method, which may be described as follows. Let A and B be the two cascading transitions. One line (e.g. the K-line) from transition A and two lines (e.g. the K- and L-lines) from transition B are utilized. These last two lines are called B_1 and B_2. According to the self-comparison method described above, two time resolution curves are measured between line A and each of the lines B_1 and B_2. We use a delay line scaled from negative to positive values and call the spectrometer connected to the negative side of the delay line spectrometer I, the spectrometer connected to the positive side of the delay line spectrometer II. If we focus line A in spectrometer I and line B_1 in spectrometer II we obtain C_1 for the position on the delay line of the centroid of the time resolution curve, and correspondingly for the other combinations as illustrated below:

	Conversion line
Spectrometer I	A B_1 A B_2
Spectrometer II	B_1 A B_2 A
Centroid position	C_1 C_1^* C_2 C_2^*

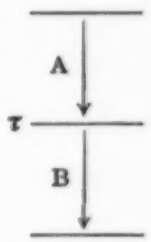

The quantity $\frac{1}{2}(C_1-C_1^*)$ is the time difference between the pulses, caused by the conversion electrons from transition A and those signals that are caused by coincident electrons from transition B_1. This time difference is due to the life-time of the intermediate level and to the difference in the instrumental time delays for the two signals. Thus we find from equations (3) and (5), where E is the electron energy of the conversion line A,

$$\begin{aligned} C_1-C_1^* &= 2\tau-2\Delta E_1 P+2(\Delta E_1)^2 Q, \\ C_2-C_2^* &= 2\tau-2\Delta E_2 P+2(\Delta E_2)^2 Q, \end{aligned} \tag{6}$$

where

$$P=\frac{l}{c}\frac{E_0^2}{(E^2+2E_0E)^{\frac{1}{2}}}+\frac{K}{E^2}, \quad Q=\frac{3E_0^2}{2(E^2+2E_0E)^2}t_1(E)+\frac{K}{E^3} \quad K=\tfrac{1}{2}(K_1+K_2),$$

(K_1 and K_2 are the constants for each spectrometer).
Eliminating P gives

$$\tau=\frac{\Delta E_2(C_1-C_1^*)-\Delta E_1(C_2-C_2^*)}{2(\Delta E_2-\Delta E_1)}+\Delta E_1\Delta E_2 Q. \tag{7}$$

In this formula,

$$\Delta E_1 = \text{electron energy of } B_1 - \text{electron energy of A}$$
$$\Delta E_2 = \text{electron energy of } B_2 - \text{electron energy of A,}$$

and C, C^* and the ΔE's are to be introduced with their signs. In eq. (7) the first term corresponds to a linear interpolation between $C_1-C_1^*$ and $C_2-C_2^*$, as seen in fig. 2. To account for the curvature of the exact curve in fig. 2 the second order term in eq. (7) has to be considered. The value of τ calculated in this way can be positive or negative. A positive value of τ means that A is the upper transition and B the lower transition in the cascade. A negative τ corresponds to the reverse situation.

In the present investigation K362 was used for A, and K330 and L330 for B_1 and B_2 respectively.

It may be pointed out that the formulae presented above are quite general and apply for both extrapolation and interpolation. Similar formulae can also be evaluated when comparison is made between two different sources: for instance, between one nucleus with a level which has a prompt decay and another nucleus with a level of measurable lifetime.

In order to apply the second order correction one has to make an estimate of the two constants l and K. Rough estimates of the constants are sufficient as the correction usually is very small.

The length of the electron path, l, has been determined by photographic ray

tracing in a plane through the axis of the spectrometer and measurements of the rotation of the electron trajectories around the axis of the spectrometer. The value found in this way was 30 cm. This value of l can be put in eq. (6), which then can be used to determine both τ and K. In this way we obtain $K = 4100\times 10^{-10}$ keV · sec.

The constant K has also been determined directly in two different ways. According to Bell[21]), l can be found from the slope of the prompt time resolution curve. On the flanks the coincidence counting rate decays to half its value in 0.693 l sec, This method gave $K = 1200\times10^{-10}$ keV · sec.

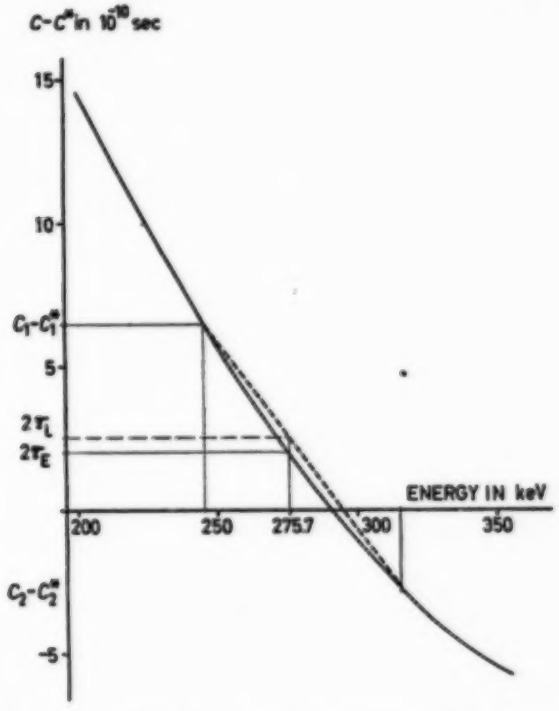

Fig. 2. Diagram showing $C-C^*$ as a function of the energy setting in one spectrometer with the other spectrometer set at the energy 275.7 keV. τ_L is the mean life calculated from linear interpolation between $C_1-C_1^*$ and $C_2-C_2^*$. τ_E is the meanlife taking the second order correction into consideration.

The other experiment was performed in the following way. The two detectors were taken out of the spectrometer and adjusted to register coincidences between the 1.17 keV and 1.33 keV transitions in Co^{60}. The discriminators were set to accept different parts of the Compton distribution, thus pulses corresponding to different energies absorbed by the scintillator were selected. Now, the centroids of the delay curves were measured for different settings of the discriminators. From the energies corresponding to the settings of the discriminators and the centroid shifts the value of K was calculated and found to be $3\,000\times10^{-10}$ keV · sec.

One should not expect good agreement between the values of K determined with these methods. As we only need a rough estimate of K the mean value 2800×10^{-10} keV · sec is good enough for our purpose.

The dominating contribution to the second order correction (7) stems from the second term in Q which is the correction due to the response time of the scintillator. The first term, the correction due to the transit time of the electrons through the spectrometer, is only about one fifth of this. Work is now in progress to try to reduce the K-value. By paying special attention to the light collection and to the focussing of the photoelectrons from the catode of the photomultiplier we have found that one can easily reach a K-value of 840×10^{-10} keV · sec which will reduce the second order correction considerably [22]).

In calculating the error of the lifetime we have considered the contribution from the error in $(C_1 - C_1^*)_{Av}$ and $(C_2 - C_2^*)_{Av}$ together with the uncertainty in $\Delta\tau$ due to the poor knowledge of the constant K. This last contribution is only a fraction of the first so that the error is mainly statistical. Thus we have determined the meanlife with an accuracy of 2×10^{-11} sec. To account for other possible contributions we have arbitrarily increased this error to 3×10^{-11} sec.

From five measurements of $C_1 - C_1^*$ and $C_2 - C_2^*$, with four different sources (table 1) we found the meanlife $\tau = (1.0 \pm 0.2) \times 10^{-10}$ sec, applying a second

TABLE 1

Combination	$C - C^*$ (ns)	$C - C^*$ average (ns)
K 330 – K 360	0.679 ± 0.045 0.549 ± 0.059 0.652 ± 0.031 0.731 ± 0.028 0.621 ± 0.027	$+0.646 \pm 0.040$
K 360 – L 330	-0.346 ± 0.029 -0.312 ± 0.030 -0.270 ± 0.034 -0.254 ± 0.031 -0.280 ± 0.033	-0.292 ± 0.022

The errors given for the values of $C - C^*$ are the statistical errors The error for the average value of $C - C^*$ has been estimated from the spread of the values for $C - C^*$.

order correction of -0.2×10^{-10} sec. This corresponds to $T_{\frac{1}{2}} = (7 \pm 2) \times 10^{-11}$ sec.

The order of the two lines in the cascade proposed from intensity considerations (10) was confirmed.

3. The Mixing Ratio of the 330 keV Transition

In order to be able to calculate the partial transition rates it is necessary to know the mixing ratio of the 330 keV transition accurately. It is not possible in this particular case to determine the mixing ratio by gamma-gamma or electron-gamma angular correlation without additional information. As we have a cascade of mixed-mixed transitions gamma-gamma angular correlation will only give a relation between the mixing ratios for the upper and lower transitions. Electron-gamma angular correlation on the other hand requires a knowledge of the values for the conversion coefficients as well as the particle parameters. In the case of the *l*-forbidden M1 transitions these depend on the nuclear structure [23]) and are therefore not known with sufficient accuracy.

Measurements of the relative intensities of the conversion lines of the 330 keV transition have earlier been performed by Wapstra [9]) and Bergkvist [10]). Since their values were given with rather large errors we decided to repeat the measurements.

The conversion lines were measured with an iron yoke double focusing beta spectrometer [24]) ($\rho = 50$ cm) at a resolution of about 0.2 percent. The sources were prepared in the way described above. The measurements were performed with two different sources. Altogether the K/L_I+L_{II} ratio was measured seven times and the L_I+L_{II}/L_{III} ratio six times. The intensities were determined from the areas under the curves.

For the energy of the 400 keV transition on Tl^{203} Bergkvist [12]) found 400.4 ± 0.4 keV and Ong Ping Hok [25]) 403.8 ± 0.3 keV. If the first energy value is correct K 400 would be hidden under the L_I+L_{II} group of the 330 keV transition in Tl^{201} which might influence the experimental L_I+L_{II} intensity.

In order to determine wheather K 400 in Tl^{203} interferes with the intensity measurement of (L_I+L_{II}) 330 or not, the energies of the 400- and 330 keV transitions were carefully determined. The 411.77 keV transition in Hg^{198} [26]) and the 279.12 keV transition in Tl^{203} [27]) were used as reference lines. The Tl^{203} source was prepared by bombarding natural thallium in the synchrocyclotron at Uppsala with 35 MeV protons. After about 90 hours the chemical separation was made and the source was evaporated. The contamination of Tl^{201} was checked by measuring the K 330 line which is the strongest conversion line in Tl^{201}. No trace of K 330 could be seen.

We found 401.3 ± 0.2 keV for the transition in Tl^{203} and 331.1 ± 0.3 keV for the transition in Tl^{201}. These values are slightly higher than those reported by Bergkvist [12]) but K 400 is still lying under $(L_I+L_{II})330$.

In order to correct the intensity of the L_I+L_{II} group of the 330 keV transition for the admixture of K 400 we measured the intensity of K 279 in Tl^{203}. From this intensity and the known intensity ratio K 279/K 400(28) the intensity of K 400 was calculated.

The admixture of K 400 in $(L_I+L_{II})330$ varied during the measurement from 3.1 to 18.7 percent.

From these measurements we found $K/L_I+L_{II} = 4.2\pm0.2$ and L_I+L_{II}/L_{III} 6.5 ± 0.5. Our results are in resonable agreement with values privately communicated by K. E. Bergkvist, who got $K/L_I+L_{II} = 4.55$ and $L_I+L_{II}/L_{III} = 7.4$ [12]).

The mixing ratio E2/M1 was calculated using the conversion coefficient of both Rose [29]) and Sliv and Band [30]). From table 2 it is seen that there is

TABLE 2

Comparison between mixing ratios in Tl^{203} and Tl^{201}

	Tl^{203} 279 keV transition			Tl^{201} 330 keV transition		
Shell	Ratio	Mixing ratio		Ratio	Mixing ratio	
		Rose	Sliv		Rose	Sliv
K/L_I+L_{II}	3.9 ± 0.1	2.6 ± 0.5	2.0 ± 0.4	4.2 ± 0.2	2.9 ± 0.6	2.1 ± 0.6
L_I+L_{II}/L_{III}	4.8 ± 0.1	2.3 ± 0.2	2.5 ± 0.3	6.5 ± 0.5	2.2 ± 0.3	2.3 ± 0.4
Stelson and Mc Gowan		2.25 ± 0.25				

some variation in the mixing ratios due to differences in the theoretical conversion coefficients. In order to derive a more precise figure for the mixing ratio we have compared these mixing ratios for the 330 keV transition in Tl^{201} with the same ratios for the corresponding transitions in Tl^{203}. Since these two transitions take place between the same levels in two very similar nuclei one should expect the same situation in both cases. The K/L_I+L_{II} and L_I+L_{II}/L_{III} ratios of the 279 keV transition in Tl^{203} was calculated using the absolute values of the conversion coefficients given by C. Nordling *et al.* [31]). Furthermore, in Tl^{203} the mixing ratio has been determined by Stelson and McGowan [32]) from the polarization direction distribution of gamma rays following Coulomb excitation. This value of the mixing ratio is independent of the theoretical conversion coefficients and is therefore thought to be the most accurate one. From table 2 it is seen that the situation in Tl^{201} and Tl^{203} indeed is similar. From a comparison between the two nuclei we found E2/M1 for the 330 keV transition in Tl^{201} equal to 2.2 ± 0.4.

4. The partial transition rates

The experimental partial transition rates were calculated according to the following formulae:

$$\{\lambda_\gamma(\mathrm{M1})\}^{-1} = \tau(1+\delta^2+\delta^2\alpha_2{}^{\mathrm{tot}}+\beta_1{}^{\mathrm{tot}}) \tag{8}$$

where

$$\delta^2 = \frac{\lambda_\gamma(\mathrm{E2})}{\lambda_\gamma(\mathrm{M1})}.$$

The experimental values thus obtained were then compared with the theoretical estimates based on the single particle model [33]):

$$\lambda_\gamma(\mathrm{M1}) = 2.8\times10^{13}E_\gamma{}^3S, \tag{9}$$

$$\lambda_\gamma(\mathrm{E2}) = 7.4\times10^{7}E_\gamma{}^5A^{\frac{1}{3}}S, \tag{10}$$

where E_γ is given in MeV.

(The nuclear radius was taken to be $R_0 = 1.2\times10^{-13}A^{\frac{1}{3}}$. The statistical factor S is equal to unity in both cases.)

The matrix element for the M1 transition was calculated from the expression given by Arima, Horie and Sano [7]):

$$m^2 = \frac{2j+1}{0.419\times10^{13}E_\gamma^3\tau_\gamma(\mathrm{M1})}; \tag{11}$$

j is the spin of the excited level, m^2 is expressed in nuclear magnetons; E_γ is measured in MeV.

The l-forbiddenness of the M1 transition shows up clearly in the large retardation factor as seen in table 3.

TABLE 3

Transition probabilities for the $d_{\frac{1}{2}}-S_{\frac{1}{2}}$ transitions in Tl^{201} and Tl^{203}

Isotope	Experimental matrix element for M1 (n.m.)	SPM matrix element for an allowed M1 transition (n.m.)	Retardation factor	Arima *et al*'s matrix element for an l-forbidden M1 transition (n.m.)
Tl^{201}	0.071 ± 0.021	26.8	$380\ \pm110$	0.267
Tl^{203}	0.026 ± 0.003	26.8	$1000\ \pm110$	0.267
	$B(\mathrm{E2})_{\mathrm{exp}}$ $(10^{-48}\ e^2\ \mathrm{cm}^4)$	$B(\mathrm{E2})_{\mathrm{SPM}}$ $(10^{-48}\ e^2\ \mathrm{cm}^4)$	Enhancement factor	Surface tension according to weak coupling model (MeV)
Tl^{201}	0.122 ± 0.044	0.0071	$17.4\pm\ 6.3$	$410\ \pm140$
Tl^{203}	0.065 ± 0.011	0.0071	$9.2\pm\ 1.5$	$640\ \pm110$

Arima, Horie and Sano [7]) have calculated the matrix element from configurational mixing of excited states. The experimentally determined M1 matrix element is about 4 times smaller than its theoretical value.

The reduced transition probability for the E2 transition was calculated from the formula [2])

$$B(\mathrm{E2}) = 81.4 \times (\Delta E)^{-5} \lambda_\gamma(\mathrm{E2}), \tag{12}$$

where $B(\mathrm{E2})$ is expressed in units of $10^{-48} e^2$ cm^4 and ΔE in keV. For the E2 transition we find an enhancement factor of 17.4 compared to the single particle estimate. This enhancement may be accounted for, in terms of weak surface coupling [2,3]).

In the weak coupling model an effective proton charge is introduced

$$\frac{e_{\mathrm{eff}}}{e} = 1 + \frac{5Zk}{4\pi C}, \tag{13}$$

where k is a constant ($= 40$ MeV), and C is the surface tension of the core coupled to the odd proton. This may be adjusted to fit the experimental enhancement factor. In this way we find a surface tension of 410 ± 140 MeV. This value should be compared with the values given for Pb^{206} [3]): 1140 MeV, for Hg^{202}: 170 MeV, and for Hg^{200}: 120 MeV [34]). In fact one should expect the value of the surface tension in Tl^{201} to lie between the values for the surface tensions in the Hg and Pb isotopes.

In table 3 we have compared the two very similar isotopes Tl^{201} and Tl^{203}. In Tl^{203} we have used $\tau = (4.2 \pm 0.3) \times 10^{-10}$ sec for the meanlife of the first excited state [35]).

It is seen that there is a clear difference between the corresponding quantities in the two isotopes which in the case of the M1-transitions definitely is significant. It is interesting to note that both the M1 and E2 transitions are enhanced by about the same factor compared to Tl^{203}. We are planning to extend this investigation to other odd mass thallium isotopes.

The authors thank Professor K. Siegbahn for his kind interest in this work. We are indebted to the cyclotron group of the Gustav Werner Institute, Uppsala, for several irradiations. The valuable work of Mr. W. C. Parker in making some of the sources and correcting the English is gratefully acknowledged. One of us, E. B., should like to express her gratitude to Professor K. Siegbahn for his kind hospitality during her stay at this institute.

References

1) T. R. Gerholm and Horacio E. Bosch, Publicationes de la Comision Nacional de Energia Atómica, Argentina (Serie Fisica), in course of publication
2) A. Bohr and B. R. Mottelson, Mat. Fys. Medd. Dan. Vid. Selsk. **27**, No. 16 (1953)
3) W. W. True and K. W. Ford, Phys. Rev. **109** (1958) 1675
4) R. G. Sachs and M. Ross, Phys. Rev. **84** (1951) 379

5) A. B. Volkov, Phys. Rev. **94** (1954) 1664
6) A. Arima and H. Horie, Prog. Theor. Phys. **12** (1954) 623
7) A. Arima, H. Horie and M. Sano, Prog. Theor. Phys. **17** (1957) 567
8) G. Andersson, E. Arbman and B. Jung, Ark. Fys. **11** (1957) 297
9) A. H. Wapstra *et al.*, Physica **20** (1954) 169
10) K. E. Bergkvist *et al.*, Phil. Mag. **46** (1955) 65
11) T. R. Gerholm, unpublished
12) K. E. Bergkvist, private communication
13) I. Bergström and G. Andersson, Ark. Fys. **12** (1957) 415
14) I. Lindgren, C. M. Johansson and S. Axensten, Phys. Rev. Letters **1** (1958) 473
15) L. L. Marino *et al.*, Bull. Am. Phys. Soc. **3** (1958) 186
16) R. E. Bell, R. L. Graham and H. E. Petch, Can. J. Phys. **30** (1952) 35
17) T. R. Gerholm, Rev. Sci. Instr. **26** (1955) 1069
18) T. D. Newton, Phys. Rev. **78** (1950) 490
19) Z. Bay, Phys. Rev. **77** (1950) 419
20) R. F. Post and L. I. Schiff, Phys. Rev. **80** (1950) 1113
21) R. E. Bell, Beta and Gamma Ray Spectroscopy, ed. Kai Siegbahn (North-Holland Publishing Company, 1955)
22) E. Bashandy, Nucl. Instr. (in course of publication)
23) E. L. Church, J. Weneser, Phys. Rev. **104** (1956) 1382
24) A. Hedgran, K. Siegbahn and N. Svartholm, Proc. Phys. Soc. A **63** (1950) 960
25) Ong Ping Hok, P. Kramer and G. Mayer, Private communication G. J. Nijgh *et al.*, Nuclear Physics **9** (1959) 528
26) D. E. Muller and H. C. Hoyt, D. J. Klein and J. W. M. DuMond, Phys. Rev. **88** (1952) 775
27) K. Edvarson, K. Siegbahn and A. H. Wapstra, private communication to G. J. Nijgh *et al.*, Nuclear Physics **9** (1959) 528
28) J. R. Prescott, Proc. Phys. Soc. A **67** (1954) 254
29) M. E. Rose, Internal Conversion Coefficients (North-Holland Publishing Company, 1958)
30) L. A. Sliv and I. M. Band, Coefficients of the Internal Conversion of Gamma Radiation, Part I and II (Academy of Sciences of the USSR, Moscow, Leningrad, 1956)
31) C. Nordling *et al.*, Nuclear Physics **1** (1956) 326
32) P. H. Stelson and F. K. McGowan, Phys. Rev. **99** (1955) 112
33) S. A. Moszkowski, Beta and Gamma Ray Spectroscopy, ed. Kai Siegbahn (North-Holland Publishing Company, 1955)
34) K. Alder *et al.*, Revs. Mod. Phys. **28** (1956) 432
35) E. Bashandy, T. R. Gerholm and J. Lindskog, Ark. Fys. (in course of publication)

10.A *Nuclear Physics* **16** (1960) 188—189; © *North-Holland Publishing Co., Amsterdam*

BOOK REVIEWS

L. KOWARSKI (Editor), *Procceedings of the International Conference on high-energy accelerators and instrumentation* — CERN 1959 (CERN, Genève, 1959. xvi—705 p. 50 fr. suisses)

This volume follows the by now familiar pattern of the CERN conference proceedings, and achieves the usual excellence in typography, illustration and outward appearance. For the kind of material presented here, speed of publication is especially important, and what the devoted CERN staff have again achieved in this respect is truly remarkable. The interest of the contents entirely justifies the effort: we have an up-to-date survey of the construction projects of the largest accelerators all over the world, with full technical descriptions and discussions of the theoretical problems involved; and in the second half of the book a similarly detailed treatment of the various kinds of ancillary instrumentation. The staggering scale which all this apparatus is reaching has induced some soul-searching among the protagonists: the conference opened on the theme of the "need for new particle accelerators", and Panofsky's brilliant report on the future prospects of this adventurous domain, as well as the other communications and discussions of this session, form one of the most interesting contributions of this conference to the more scientific aspect of the question. Even when, for practical purposes, the contents of the book will have been superseded by further developments, it will remain a record of lasting historical value about a decisive stage in the breath-taking expansion and transformation of scientific research which we are witnessing.

L. R.

H. KOPFERMANN, *Nuclear moments* (Academic Press, New York 1958. xiii—505 p. 95s.)

The original German edition of this fundamental treatise was reviewed in this journal (**3** (1957) 624). In order to have an expert assessment of the book I had asked Professor Ebbe Rasmussen to review the English translation, but his fatal illness prevented our regretted colleague from fulfilling this task. I can therefore only refer the reader to the previous review.

L. R.

ULRICH SCHINDEWOLF, *Physikalische Kernchemie* (Friedr. Vieweg & Sohn, Braunschweig 1959. viii—191 p. DM 29.50)

"Nuclear chemistry" is as old a term as nuclear physics itself and a very considerable part of our knowledge of the atomic nucleus is due to contributions from chemists involved in nuclear research. However, not many introductory textbooks in nuclear physics are available which are especially adapted for students of chemistry, and the present book by Schindewolf will no doubt be very welcome at Universities where nuclear chemistry is regularly taught. The first seven chapters deal with nuclear physics on a phenomenological basis in a presentation which should be suitable for a student of chemistry who has passed an elementary course in atomic physics. The remaining seven chapters are mainly concerned with subjects in the nuclear field which are particularly interesting to the chemist, such as e.g. tracer chemistry, the cosmological synthesis of the elements, isotope separation and nuclear geochemistry.

To press this variety of subjects into a volume of less than 200 pages presents a serious problem which the author has solved remarkably well. Detailed discussions of instruments and techniques have been avoided throughout, but ample space is given to illustrate theoretical results by examples and figures, and formulas are rarely quoted without stating the basic physical ideas involved.

The order of the material is logical and the selection seems quite adequate for the purpose, with one possible exception: the chapter on the interaction of radiation with matter appears very late in the book, and the treatment is rather hurried for such an important subject. An extensive list of references and a large chart of nuclei complete the book.

Ove Nathan

J. McCONNELL, *Quantum particle dynamics*, 2nd revised edition (North-Holland Publishing Co., Amsterdam 1960. xi—266 p. fl. 20)

The success of this book, whose first edition was sold out in a few months, is the most convincing proof that it is well adapted to a widespread demand. One may share the first reviewer's concern (cf. this journal **14** (1959/60) 697) at the prospect, suggested by this eager demand, that there must be a large number of nuclear technologists about, whose knowledge of the basic theories is reduced to the bare minimum skilfully condensed in the present textbook. It is a consolation, however, to know that the digest of nuclear physics thus provided to them is of such a high quality.

L. R.

P. ROMÁN, *Theory of elementary particles* (North-Holland Publishing Co., Amsterdam 1960. xii—575 p. fl. 50)

This is the first detailed and up-to-date textbook specially devoted to the theory of the fundamental constituents of matter (improperly called elementary particles) and their interactions. The author has tackled his task very thoroughly and with remarkable pedagogical skill. Although he adopts a rather sophisticated point of view — stressing the basic requirements of covariance and proceeding from them in an abstract, deductive manner — he is so clear and, as it were, so candid that the student is never left with any wrong impression of the scope and meaning of such deductions. In fact, the physical or mathematical arguments are everywhere carefully presented, in simple and straightforward language, with such an explicitness that the *raison d'être* of each step is plainly apparent; this feature is too rare in modern textbooks not to deserve special commendation.

After an extensive treatment of the four-dimensional orthogonal group (91 pages), the author reviews the differential equations describing fields of spin 0 or 1, of spin $\frac{1}{2}$ and of arbitrary spin (74 pages), and discusses the quantization of these fields, including the relation between spin and statistics (39 pages). He is then well armed for the detailed analysis of invariance properties, conservation laws and selection rules, which forms one of the main topics of the book (196 pages). The last chapter is devoted to a detailed consideration of isobaric space, including an account of the theory of Prentki and d'Espagnat, and of the four-dimensional extension of the concept of isospace (147 pages). Even this extended survey is far from exhausting all the schemes of classification of the fundamental constituents which have been proposed; in this, the author has exercised wise restraint, since many of these ingenious, but artifical, constructions will necessarily be of ephemeral interest; likewise, the bibliography offers only a judicious selection from the all-too-abundant literature. In this connexion, the author might usefully have mentioned, even in some detail, the instructive paper by Cerulus (this journal **1** (1956) 557), in which the essential indeterminateness of the classification problem is clearly set out.

Whatever surprises the future study of this rapidly developing subject may have in store for us, the aspects so competently treated by Dr. Román will continue to play an important part in the description and interpretation of the facts. One can therefore safely predict that this book, by its substantial and well-balanced contents, and its outstanding didactic qualities, will long remain unchallenged as an introduction into the domain of fundamental research from which we expect decisive new insight into the properties of matter.

L. R.

OEEC, *Towards a new energy pattern in Europe* (OEEC, Paris, 1960. 125 p. 6 n.f.)

This report by a commission under the chairmanship of Professor A. Robinson of Cambridge University, set up by the OEEC in 1956 to keep energy problems under constant survey, contains an up-to-date reassessment of the prospective energy requirements and supplies of Western Europe from now to 1975. It takes account of the most recent developments, not only in the use of nuclear energy, but also in the exploitation of oil and natural gas resources, and discusses their repercussions in particular on the position of coal industry. The methods by which the various estimates have been computed are presented in detail, and the underlying data collected in a large number of tables, very useful for purposes of reference. The rather unorthodox views and conclusions of this interesting report deserve the closest attention.

L. R.

10.D *Nuclear Physics* **16** (1960) 190—191; © *North-Holland Publishing Co., Amsterdam*

NEWS ITEM

INTERNATIONAL CONFERENCE ON NUCLEAR STRUCTURE

Queen's University, Kingston, Ontario, Canada

August 29 — September 3, 1960

A Conference on Nuclear Structure will be held at Queen's University, Kingston, Ontario from August 29 to September 3, 1960. The Conference is sponsored by the International Union of Pure and Applied Physics, the National Research Council of Canada, Atomic Energy of Canada Limited, and Queen's University.

PRELIMINARY PROGRAM

(Additional speakers will be announced in future circulars.)

1 Monday, August 29 (AM)
Introductory Session
Chairman: W. B. Lewis
Speakers: R. E. Peierls and D. H. Wilkinson

2 Monday, August 29 (PM)
Physical Foundations of Nuclear Models
Chairman: V. F. Weisskopf
Speakers: K. A. Brueckner and A. de-Shalit

3 Tuesday, August 30 (AM)
Gross Properties of Nuclear Matter
Chairman: H. H. Barschall
Speaker: P. C. Gugelot

4 Tuesday, August 30 (PM)
Nuclear Reaction Mechanisms
Chairman: B. B. Kinsey
Speaker: N. Austern

5 & 6 Thursday, September 1 (AM and PM)
Properties of Individual Levels
Chairmen: D. R. Inglis (Session 5)
and A. Bohr (Session 6)
Speakers: J. B. French, H. E. Gove, B. R. Mottelson, E. B. Paul and P. H. Stelson
The division of topics between Sessions 5 and 6 has not yet been settled.

7 Friday, September 2 (AM)
Statistics of Nuclear Levels
Chairman: A. M. Lane
Speakers: L. Katz and J. P. Schiffer

8 Friday, September 2 (PM)
Topics to be selected later
Chairman: B. H. Flowers

9(a) Saturday, September 3 (AM - before coffee)
Fission
Chairman: R. F. Taschek
Speakers: J. J. Griffin and G. C. Hanna

9(b) Saturday, September 3 (AM - after coffee)
Summary and Conclusions

All those named above have agreed to participate.

Wednesday, September 1 is left free for an excursion. Extra sessions may be arranged for Wednesday evening and Saturday afternoon. In addition to the mid-conference excursion a trip to the Chalk River Laboratories of Atomic Energy of Canada Limited will be arranged on the Sunday following the Conference.

ORGANIZATION OF THE SESSIONS

Except in the case of Sessions 1, 8 and 9(b), the invited speakers will act as rapporteurs. The topics of each session will be divided between two, three or four invited speakers. Each invited speaker will introduce his subject and discuss the work of the contributors who have submitted communications on that subject. With the limited time available we believe that a unified presentation of a field by a selected individual is easier to understand and absorb than a collection of original contributions.

It is expected that the talks of the invited speakers will take up rather more than half the session. The remainder of the time will be devoted to discussion. At the discretion of the chairman, contributors may then have an opportunity to correct or amplify the presentation of the invited speaker and show one or two slides. In order to leave ample time for discussion there will be no opportunity for the presentation of formal contributed papers in these sessions. Session 8 and possible extra sessions may be devoted to individual contributions.

COMMUNICATIONS

The success of the Conference depends upon the submission of contributions of recent work. *The deadline for receipt of communications is July 15, 1960.* Communications should not exceed 600 words plus figures. Instructions on their format will be included in the Second Circular. The Conference Committee will distribute them to the appropriate chairmen and speakers. Delegates will receive at the beginning of the Conference a program which will include abstracts of the papers of the invited speakers and a list of all communications received before July 15.

The chairmen and speakers will select from the submitted communications those that are to be published in full in the Conference Proceedings. The Proceedings will contain also the invited papers, a full record of the discussion, and a listing of all communications received.

TOPICS NOT INCLUDED IN THE CONFERENCE

Because of limitations of time it is necessary to exclude from the Conference certain topics that are not at this time primarily relevant to nuclear structure. Examples of such excluded topics are the study of weak interactions, electron and nucleon scattering at energies above about 50 MeV, and those aspects of fission that do not yield direct information about nuclear structure.

The main emphasis will be placed on experimental data and their interpretation. Discussion of techniques, both experimental and theoretical, will be avoided.

REGISTRATION AND OTHER INFORMATION

Since lecture room space is limited, all who wish to attend are requested to obtain a registration form from the Conference Secretary and to submit it as soon as possible.

Queen's University has new student residences with single or double rooms as desired for all delegates and these are recommended by the Committee. Hotel and motel accommodation is also available in and around Kingston.

It is expected that the Second Circular will be mailed around the end of March to those who have returned registration forms. It will outline the topics covered by each session, give further information concerning communications, list additional invited speakers, and give details of social activities.

Inquiries about the Conference and requests for registration forms should be sent to the Conference Secretary: Dr. L. G. Elliott, Atomic Energy of Canada Limited, Chalk River, Ontario, Canada.

CONFERENCE COMMITTEE

President: Dr. W. B. Lewis, Chalk River, Ontario, Canada
Vice-president: Dr. V. F. Weisskopf, Cambridge, Mass., U.S.A.
Secretary: Dr. L. G. Elliott, Atomic Energy of Canada Limited, Chalk River, Ontario, Canada

Organizing committee:
Chairman: H. E. Gove
Members: G. A. Bartholomew, D. A. Bromley, L. G. Elliott, R. L. Graham, B. W. Sargent, W. T. Sharp, E. Vogt.

10.F *Nuclear Physics* **16** (1960) 192; © *North-Holland Publishing Co., Amsterdam*

ERRATUM

R. BALIAN, Densité de niveaux d'un système de Nucléons en interaction dans une couche (Nuclear Physics **13** (1959) 594).

La figure ci-dessous corrige et remplace la figure 5, page 610.

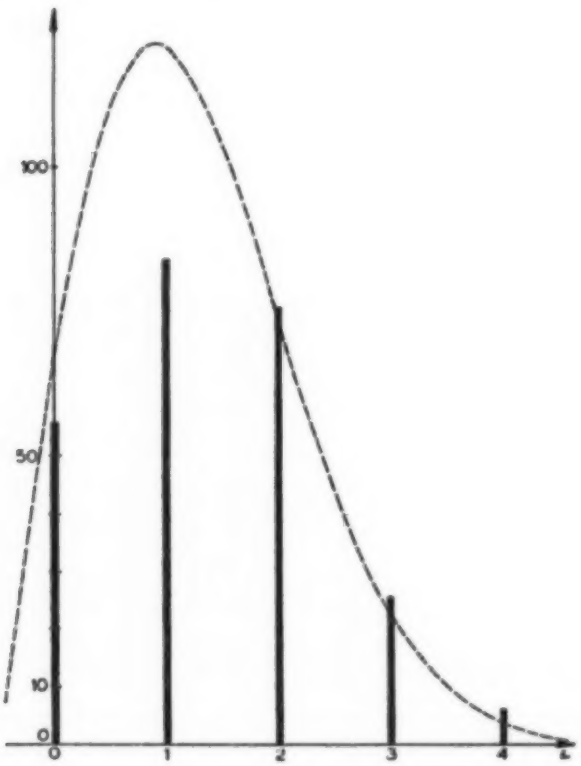

Fig. 5

1.D.1:
1.E.3

Nuclear Physics **16** (1960) 193—205; © *North-Holland Publishing Co., Amsterdam*
Not to be reproduced by photoprint or microfilm without written permission from the publisher

ELECTRIC AND MAGNETIC MOMENTS OF ODD-NEUTRON NUCLEI ON THE SINGLE CONFIGURATION MODEL

HAJIME NARUMI †

Research Institute for Fundamental Physics, Kyoto University, Kyoto

and

HIROYUKI NAGAI ††

Yukawa Laboratory, Institute for Chemical Research, Kyoto

Received 23 November 1959

Abstract: Without taking account of the effect of configuration mixing, we attempt to derive the electric moments as well as magnetic moments of odd-neutron nuclei on the basis of the single configuration model. The quadrupole moments of odd-neutron nuclei may be obtained by the promotion of two protons from the zeroth order proton state of seniority zero to the states of seniority two. These mixing coefficients of the ground state are determined by fitting the wave function to the magnetic moment of the odd-neutron nucleus considered. Thus we find a fairly good agreement between the calculated and observed values except for the nuclei with very large quadrupole moments and for the nuclei in the vicinity of each closed shell.

The quadrupole and hexadecapole moments of the first excited state of ^{111}Cd are also evaluated.

1. Introduction

The extreme single-particle model manifests its most serious deficiency ni accounting for the nuclear quadrupole moments, particularly those of odd-neutron nuclei, although there is a definite correlation between nuclear quadrupole moments and nuclear shell structures. The quadrupole moment of the nucleus with a single proton in an orbit j outside the core is given by

$$Q_j^{(2)} = -\frac{2j-1}{2j+2}\langle r^2\rangle. \tag{1}$$

On the other hand, the single-particle shell model gives almost zero quadrupole moments for odd-neutron nuclei, since the neutrons carry no charge and the quadrupole moment $Q_{\text{recoil}}^{(2)}$ induced by the recoil effect of the core

$$Q_{\text{recoil}}^{(2)} = \frac{Z}{(A-1)^2} Q_j^{(2)} \tag{2}$$

is negligibly small except for extremely light nuclei. But the facts that the

† On leave of absence from Doshisha University, Kyoto, Japan.
†† Now at Kyushu Institute of Technology, Tobata, Japan.

quadrupole moments of odd-neutron nuclei are just as large as those of odd-proton nuclei and that the behaviour of odd-neutron nuclei is similar to some extent to that of odd-proton nuclei which have the same number of nucleons outside their closed shells, seem to indicate that the total angular momentum of odd-neutron nuclei should be shared between the neutrons and the protons. As an explanation of the fact that the odd-neutron nuclei have electric quadrupole moments the following three prescriptions have been proposed by various authors.

Firstly, in the individual particle model the angular momentum of a nucleus is, indeed, shared among all nucleons outside closed shells and therefore the odd-neutron nuclei in which there are loose protons outside closed shells can possess electric quadrupole moments. Flowers [1]) has calculated as a particular example the quadrupole moments of j^3 configurations for which $I = j$, $T = \frac{1}{2}$ and $v = 1$, where I is the total angular momentum of the nucleus, T the total isobaric spin, and v the seniority number. His results are as follows:

$$Q(1n+2p) = \frac{2j+7}{6j+6} Q_j^{(2)} \tag{3}$$

for odd-neutron nuclei and

$$Q(1p+2n) = \frac{4j+5}{6j+6} Q_j^{(2)} \tag{3'}$$

for odd-proton nuclei treated from the same point of view. Then we find that these results are in fairly good agreement with the observed values of several light nuclei. But this kind of effect for heavier nuclei, in which the unfilled neutron shell is different from the unfulled proton shell, cannot be expressed in as simple a form as above.

Secondly, the hydrodynamical model ascribes the quadrupole moments of odd-neutron nuclei to the core deformation induced by an extra-neutron [2]). However, this model gives too large quadrupole moments for light and medium-heavy odd-neutron nuclei, although a recent collective treatment has improved these results [3]).

Finally, the mixing of excited configurations to the ground configuration given by the single-particle shell model can also give quadrupole moments for odd-neutron nuclei [4]). In the configuration mixing approach it is assumed that this admixture is so small that the effects proportional to the square of the mixing coefficients can be neglected. The mixing coefficients α's are given by the perturbation theory in terms of the off-diagonal elements of residual nuclear interactions and the energy differences between the ground configuration and excited configurations. All the excited configurations are taken into account for which the off-diagonal elements of the quadrupole moment operator $Q_{op}^{(2)} = \sum_p r_p^2(3\cos^2\theta_p - 1)$ do not vanish. The quadrupole moments of odd-

neutron nuclei are due to the contributions from the off-diagonal elements of the quadrupole moment operator $Q_{\rm op}^{(2)}$ between the ground and excited configurations. Then the values of the quadrupole moments calculated in configuration mixing are in satisfactory agreement with the observed values [5]).

However, we do not know enough about the nuclear interaction between two free nucleons, and we know even less about the residual nuclear interactions which should be considered in shell model calculations, and it is difficult to determine precisely the energy differences between the ground and excited configurations. And the complete execution of the configuration mixing calculations are considerably laborious. Thus one may consider to restrict the basic set of states in practical calculations, usually taking explicit account of only nucleons outside closed shells and considering only the lowest configuration. In fact, the quadrupole moments of odd-neutron nuclei can be deduced on the assumption that two protons in an unfilled shell are promoted from the zeroth-order proton state of seniority zero to the states of seniority two, which gives rise to a large admixture of these states in the ground state wave function. The mixing coefficients of the ground state are determined by fitting the wave function to the magnetic moment of the odd-neutron nucleus considered.

2. Method of Calculations

First of all we shall explain the essential features of our procedure in the simplest case, i.e. a nucleus with one neutron and two protons outside closed shells. Let us denote the zeroth-order ground state wave function given by the single-particle model by

$$\psi_0(j, j_1^2, v = 0(J_{\rm p} = 0), J = j = M),$$

where j is the total angular momentum of the odd-neutron and j_1 is that of the outmost protons. Then we represent the excited states in which two j_1-protons in the unfilled shell are promoted from the zeroth-order state of seniority zero to the states of seniority two as

$$\psi_{J_{\rm p}}(j, j_1^2, v_1 = 2(J_{\rm p} \neq 0), J = j = M),$$

where $J_{\rm p}$ is even and restricted by the conditions

$$2j_1 - 1 \geqq J_{\rm p} \geqq 2, \quad j + J_{\rm p} \geqq j \geqq |j - J_{\rm p}|.$$

However, it can easily be shown that the off-diagonal elements of $Q_{\rm op}^{(2)}$ between two proton states with $J_{\rm p}$ differing by two are non-vanishing. In the present paper we assume that the ground state wave function is expressed by the following linear combination with a sufficiently good approximation:

$$\Psi(j, j_1^2, J = j = M) = \alpha_0 \psi_0(j, j_1^2, v = 0(J_{\rm p} = 0), J = j = M) + \sum_{J_{\rm p}} \alpha_{J_{\rm p}} \psi_{J_{\rm p}}(j, j_1^2, v_1 = 2(J_{\rm p}), J = j = M). \quad (4)$$

In order to calculate the matrix elements of the quadrupole moment operator $Q^{(2)}_{\rm op}$ we transform the wave functions in eq. (4) as follows:

$$\psi(j, j_1^2(J'), J=j=M) = \sum_{J''} \psi(jj_1(J''), j_1, J=j=M)\langle jj_1(J''), j_1, J=j | j, j_1^2(J'), J=j\rangle$$
$$= \sum_{J''} \sum_{M''m_1} U(jj_1jj_1; J''J')(J''M'', j_1m_1|J=j=M)\psi(jj_1J''M'')\phi(j_1m_1), \quad (5)$$

where U is the modified Racah coefficient defined by Jahn [6]) and $(J''M'', j_1m_1|J=j=M)$ is the Clebsch-Gordan coefficient. By using this expression for the wave function we can easily calculate the diagonal matrix elements of $Q^{(2)}_{\rm op}$:

$$\langle Q^{(2)}\rangle = \langle j, j_1^2(J_p), J=j=M|Q^{(2)}_{\rm op}|j, j_1^2(J_p), J=j=M\rangle$$
$$= 2\sum_{J''}\sum_{M''m_1} U^2(jj_1jj_1; J''J_p)|(J''j, j_1j|M''m_1)|^2(j_1m_1, 20|j_1m_1)\langle j_1||Q^{(2)}||j_1\rangle$$
$$= 2(2j+1)(2j_1+1)^{\frac{1}{2}}\langle j_1||Q^{(2)}||j_1\rangle \sum_{J''}(-1)^{2j}U^2(jj_1jj_1; J''J_p)$$
$$\times W(J''j_1j2; jj_1)V(j2j; j0-j),$$

where W is the Racah coefficient [7]) and V represents the so-called V-function [7]) given by

$$V(j2j; j0-j) = (-1)^{2j}\left[\frac{2j(2j-1)}{(2j+3)(2j+2)(2j+1)}\right]^{\frac{1}{2}}.$$

Besides, the reduced matrix elements in the above formula can be written

$$\langle j_1||Q^{(2)}||j_1\rangle = (2j_1+1)^{-\frac{1}{2}}(j_1||Q^{(2)}||j_1) = \left[\frac{(2j_1+3)(2j_1+2)}{2j_1(2j_1-1)}\right]^{\frac{1}{2}}Q^{(2)}_{j_1}.$$

Then we find

$$\langle Q^{(2)}\rangle = \frac{2(2j+1)!}{(2j_1)!}\left[\frac{(2j_1+3)!(2j_1-2)!}{(2j+3)!(2j-2)!}\right]^{\frac{1}{2}}(2J_p+1)Q^{(2)}_{j_1}\sum_{J''}(2J''+1)W(jj_1jj_1; J''J_p)$$
$$\times W(j_1jj_1j; J''J_p)W(J''j_1j2; jj_1)$$
$$= \frac{2J_p(J_p+1)\{3J_p(J_p+1)-3-4j_1(j_1+1)\}\{3J_p(J_p+1)-3-4j(j+1)\}}{(2J_p+3)(2J_p-1)(2j+3)(2j+2)2j_1(2j_1-1)}Q^{(2)}_{j_1}. \quad (6)$$

Similarly the off-diagonal elements of $Q^{(2)}_{\rm op}$ between $\psi_{J_p}(j, j_1^2(J_p), J=j=M)$ and $\psi_{J'_p}(j, j_1^2(J'_p), J=j=M)$ are easily obtained as follows:

$$\langle j, j_1^2(J_p), J=j=M|Q^{(2)}_{\rm op}|j, j_1^2(J'_p), J=j=M\rangle$$
$$= 2\frac{(2j+1)!}{(2j_1)!}\left[\frac{(2J_p+1)(2J'_p+1)(2j_1+3)!(2j_1-2)!}{(2j+3)!(2j-2)!}\right]^{\frac{1}{2}}W(jj2J_p; J'_pj) \quad (7)$$
$$\times W(j_1j_12J_p; J'_pj_1)Q^{(2)}_{j_1}.$$

By the triangular conditions among the arguments of the Racah coefficients in eq. (7) it can easily be verified that we have non-vanishing elements in the case of $J_p = 0$ and $J'_p = 2$ or $J_p = 2$ and $J'_p = 4$. For the former case the above formula is reduced to

$$\langle j, j_1^2(0), J=j=M|Q_{op}^{(2)}|j, j_1^2(2), J=j=M\rangle = \left[\frac{4}{5}\frac{2j(2j-1)(2j_1+3)(2j_1+2)}{2j_1(2j_1-1)(2j+3)(2j+2)}\right]^{\frac{1}{2}} Q_{j_1}^{(2)}. \quad (8)$$

Now in general let us consider the odd-neutron nuclei with an odd number (say n) of neutrons in the orbit j and an even number (say p) of protons in the orbit j_1 outside closed shells. We can write down the zeroth-order ground state of the odd-neutron nucleus given by the sinle-particle model as

$$\psi_0(j^n, v = 1(J_n = j), j_1^p, v_1 = 0(J_p = 0), J = j = M).$$

Then we represent the states in which two protons in the unfilled j_1-shell are promoted from the zeroth-order state of seniority zero to the states of seniority two as

$$\psi_{J_p}(j^n, v = 1(J_n = j), j_1^p, v_1 = 2(J_p), J = j = M).$$

Also we assume that the ground state wave function is expressed by the following linear combination:

$$\Psi(j^n, j_1^p, J=j=M) = \alpha_0\psi_0(j^n, v=1(J_n=j), j_1^p, v_1=0(J_p=0), J=j=M) + \sum_{J_p}\alpha_{J_p}\psi_{J_p}(j^n, v=1(J_n=j), j_1^p, v_1=2(J_p), J=j=M). \quad (4')$$

In order to calculate the matrix elements we transform the wave functions as follows:

$$\begin{aligned}
&\psi_{J_p}(j^n, v=1(J_n=j), j_1^p, v_1(J_p), J=j=M)\\
&=\sum_{v'J'}\psi(j^n, v=1(J_n=j), [j_1^{p-1}v'(J'), j_1](J_p), J=j=M)(j_1^{p-1}v'J', j_1j_1^pv_1J_p|\}j_1^pv_1J_p)\\
&=\sum_{v'J'}\sum_{J''}\psi([j^n, v=1(J_n=j), j_1^{p-1}v'(J')](J'')j_1, J=j=M)\\
&\qquad\times\langle jJ'(J''), j_1, J=j|j, J'j_1(J_p), J=j\rangle(j_1^{p-1}v'J', j_1^pv_1J_p|\}j_1^pv_1J_p)\\
&=\sum_{v'J'}\sum_{J''}\sum_{M''m_1}\psi(j^n, v=1(J_n=j), j_1^{p-1}v'(J')J''M'')\phi(j_1m_1)(J''M'', j_1m_1|jj)\\
&\qquad\times U(jJ'j_1j_1; J''J_p)(j_1^{p-1}v'J', j_1, j_1^pv_1J_p|\}j_1^pv_1J_p),
\end{aligned}$$

where $(j_1^{p-1}v'J', j_1, j_1^pv_1J_p|\}j_1^pv_1J_p)$ represents the fractional parentage coefficient for the removal of one proton from p j_1-protons vector-coupled to J_p [8]). By making use of this expression for the wave function, we can calculate the matrix elements of $Q_{op}^{(2)}$ in the same way as in the simplest case mentioned

above. The results obtained are as follows:

$$\langle j^n, v=1(J_n=j), j_1{}^p, v_1=2(J_p), J=j=M|Q_{op}^{(2)}|j^n, v=1(J_n=j), j_1{}^p, v_1=2(J'_p), J=j=M\rangle$$
$$=p[(2J_p+1)(2J'_p+1)]^{\frac{1}{2}}\frac{(2j+1)!}{(2j_1)!}\left[\frac{(2j_1+3)!(2j_1-2)!}{(2j+3)!(2j-2)!}\right]\sum_{v'J'}(j_1{}^{p-1}v'J', j_1, j_1{}^pv_1J'_p|\}j_1{}^pv_1J'_p)$$
$$\times(j_1{}^pv_1J_p\{|j_1{}^{p-1}v'J', j_1{}^pv_1J_p)\cdot W(jJ'2J_p; J'_pj_1)W(jj2J_p; J'_pj)Q_{j_1}^{(2)} \quad (9)$$

and in particular

$$\langle j^n, v=1(J_n=j), j_1{}^pv_1=0, J=j=M|Q_{op}^{(2)}|j^n, v=1(J_n=j), j_1{}^pv_1=2(J_p=2), J=j=M\rangle$$
$$=p\left[\frac{2j(2j-1)(2j_1+3)(2j_1+2)}{5(2j+3)(2j+2)2j_1(2j_1-1)}\right]^{\frac{1}{2}}(j_1{}^{p-1}, v=1(J'=j_1)j_1, j_1{}^p, v=2, J_p=2|\}j_1{}^pv_1=2, J_p=2). \quad (10)$$

Finally, in the same way as for the quadrupole moment we can calculate the matrix elements of the electric hexadecapole moment operator

$$Q_{op}^{(4)}=\sum_p r_p{}^4(35\cos^4\theta_p-30\cos^2\theta_p+3)$$

for the nuclei with one neutron and two protons outside different closed shells. The results are

$$\langle Q^{(4)}\rangle=\langle j, j_1{}^2(J_p), J=j=M|Q_{op}^{(4)}|j, j_1{}^2(J_p), J=j=M\rangle$$
$$=2(2J_p+1)\frac{(2j+1)!}{(2j_1)!}\left[\frac{(2j_1+5)!(2j_1-4)!}{(2j+5)!(2j-4)!}\right]^{\frac{1}{2}}W(jj4J_p; J_pj)W(j_1j_14J_p; J_pj_1)Q_{j_1}^{(4)}$$
$$=\frac{(J_p+2)(J_p+1)J_p(J_p-1)\{70J_p{}^2(J_p+1)^2-360J_p(J_p+1)+360-240J_p(J_p+1)j(j+1)+96j^2(j+1)^2+888j(j+1)\}}{8(2J_p+5)(2J_p+3)(2J_p-1)(2J_p-3)(2j+5)(2j+4)(2j+3)(2j+2)} \quad (11)$$
$$\times\frac{70J_p{}^2(J_p+1)^2-360J_p(J_p+1)+360-240J_p(J_p+1)j_1(j_1+1)+96j_1{}^2(j_1+1)^2+888j_1(j_1+1)\}}{2j_1(2j_1-1)(2j_1-2)(2j_1-3)}Q_{j_1}^{(4)}$$

for the diagonal elements (which vanish for $J_p<2$), while the off-diagonal elements are

$$\langle j, j_1{}^2(0), J=j=M|Q_{op}^{(4)}|j, j_1{}^2(J_p), J=j=M\rangle$$
$$=2\frac{(2j+1)!}{(2j_1)!}\left[\frac{(2J_p+1)!(2j_1+5)!(2j_1-4)!}{(2j+5)!(2j-4)!}\right]W(jj4J_p; 0j)W(j_1j_14J_p; 0j_1)Q_{j_1}^{(4)}. \quad (12)$$

Here $Q_{j_1}^{(4)}$ is the hexadecapole moment of the nucleus with a single proton in the

orbit j_1 outside a closed shell, that is

$$Q_{j_1}^{(4)} = \frac{3}{8}\frac{(2j_1-1)(2j_1-3)}{(2j_1+4)(2j_1+2)}\langle r^4\rangle. \tag{13}$$

Again by the triangular conditions among the arguments of the Racah coefficients it can easily be shown that we have non-vanishing elements only in the case of $J_p = 4$. Then we obtain the following result:

$$\langle j, j_1^2(0), J = j = M|Q_{op}^{(4)}|j, j_1^2(4), J = j = M\rangle$$
$$= \frac{2}{3}\left[\frac{2j(2j-1)(2j-2)(2j-3)(2j_1+5)(2j_1+4)(2j_1+3)(2j_1+2)}{2j_1(2j_1-1)(2j_1-2)(2j_1-3)(2j+5)(2j+4)(2j+3)(2j+2)}\right]^{\frac{1}{2}} Q_{j_1}^{(4)}, \tag{12'}$$

where $j, j_1 \geqq \frac{5}{2}$.

3. Comparison with the Observed Values

In order to evaluate the quadrupole and hexadecapole moments of odd-neutron nuclei, we should determine the mixing coefficients of the wave function (4) or (4′). In the configuration mixing approach the mixing coefficients have been given by the perturbation theory in terms of off-diagonal elements of residual nuclear interactions and the energy differences between the ground and excited configurations.

In our single configuration approach, on the contrary, we assume that both electric and magnetic moments can be calculated by using the same wave function for the nuclear state in question, and therefore the mixing coefficients are determined by fitting the wave function to the magnetic moment of the odd-neutron nucleus considered. Large deviations of the magnetic moments of odd-neutron nuclei from the Schmidt lines require a large admixture between the zeroth-order ground state and excited states.

The expectation value of the magnetic moment operator

$$\mu_{op} = g_j \sum_{i=1}^{n} \mathbf{j}_i + g_{j_1} \sum_{k=1}^{p} \mathbf{j}_k$$

for the state (4′) is given by

$$\langle\mu\rangle = \langle j^n(J_n = j), j_1^p(J_p), J = j = M|\mu_z|j^n(J_n = j), j_1^p(J_p), J = j = M\rangle$$
$$= \alpha_0^2 g_j j + \sum_{J_p} \alpha_{J_p}^2 \frac{1}{2(j+1)}\{2g_j j(j+1) + (g_{j_1} - g_j)J_p(J_p+1)\}, \tag{14}$$

where $\alpha_0^2 + \sum_{J_p}\alpha_{J_p}^2 = 1$; g_j and g_{j_1} are the g-factor of a neutron in the orbit j and that of a proton in the orbit j_1, respectively. Even by fitting the value of the theoretical magnetic moment (14) to the observed value we cannot determine the signs of the mixing coefficients α_0 and α_{J_p}. In principle these mixing

TABLE 1

Calculated and observed values of quadrupole moments of odd-neutron nuclei

Nucleus	Assumed $\left\{\begin{matrix}\text{neutron}\\ \text{proton}\end{matrix}\right\}$ configurations	$Q_{\text{h.d.}}$	$Q_{\text{c.m.}}$	$Q_{\text{col.}}$	$Q_{\text{s.c.}}$	$Q_{\text{obs.}}$
$^{73}_{32}$Ge	$\left\{\begin{matrix}g_{\frac{9}{2}}\\ (f_{\frac{5}{2}})^2(p_{\frac{1}{2}})^2\end{matrix}\right\}$	−1.2	−0.27	−0.11	−0.12	−0.21
$^{83}_{36}$Kr	$\left\{\begin{matrix}(g_{\frac{9}{2}})^{-2}\\ (p_{\frac{1}{2}})^{-2}\end{matrix}\right\}$	—	0.24	—	0.14	0.15
$^{85}_{36}$Kr	$\left\{\begin{matrix}(g_{\frac{9}{2}})^{-1}\\ (p_{\frac{1}{2}})^{-2}\end{matrix}\right\}$	—	0.47	—	0.14	0.25
$^{111}_{48}$Cd*	$\left\{\begin{matrix}(d_{\frac{5}{2}})^{-1}\\ (g_{\frac{9}{2}})^{-2}\end{matrix}\right\}$	—	—	—	0.18 (0.19)	≈2
$^{131}_{54}$Xe	$\left\{\begin{matrix}d_{\frac{3}{2}}\\ (g_{\frac{7}{2}})^4\end{matrix}\right\}$	—	−0.15	—	−0.07 (−0.08)	−0.12
$^{201}_{80}$Hg	$\left\{\begin{matrix}p_{\frac{3}{2}}\\ (h_{\frac{11}{2}})^{-2}\end{matrix}\right\}$	—	0.08	—	0.17 (0.16)	0.45

We adopted for the parameter $\langle r^2\rangle$ the value $^3/_5A^{\frac{2}{3}}r_0^2$, where $r_0 = 1.4\times10^{-13}$ cm. The $Q_{\text{h.d.}}$, $Q_{\text{c.m.}}$, $Q_{\text{col.}}$ and $Q_{\text{s.c.}}$ are the values of electric quadrupole moments calculated by hydrodynamical [3]) configuration mixing [4]), collective [2]), and the present single configuration model, respectively. The $Q_{\text{obs.}}$ are taken from a recent article [9]) and all the Q's are expressed in barn.

TABLE 2

Calculated and observed values of quadrupole moments of odd-neutron nuclei (continued)

Nucleus	$Q_{\text{h.d.}}$	$Q_{\text{c.m.}}$	$Q_{\text{col.}}$	$Q_{\text{s.c.}}$	$Q_{\text{obs.}}$
$^{17}_{8}$O	−0.16	−0.04	−0.03	−0.01 †	−0.03
$^{33}_{16}$S	−0.22	−0.09	−0.05	−0.04 −0.04 ††	−0.064
$^{35}_{16}$S	−0.22	0.09	0.04	0.03 0.04 ††	0.035

† Including the recoil effect.

†† The values calculated by the Flowers formula (3).

TABLE 3

Mixing weights of ground and excited states of seniority 2

	α_0^2	α_2^2	α_4^2
^{17}O	0.99	0.01	—
^{33}S	0.38	0.62	—
^{35}S	0.82	0.18	—
^{37}Ge	0.36	0.64	—
^{83}Kr	0.42	0.58	—
^{85}Kr	0.44	0.56	—
^{111}Cd*	0.42 (0.50)	0.58 (0.47)	(0.03)
^{131}Xe	0.19 (0.45)	0.81 (0.44)	(0.11)
^{201}Hg	0.59 (0.64)	0.51 (0.34)	(0.02)

coefficients should be determined by solving the secular determinant equation for the residual interactions between neutrons and protons. But if the residual interactions can usually be considered as attractive, α_0 and α_{J_p} may be assumed to have equal signs for the ground state. Thus we assume that both α_0 and α_{J_p} are positive.

By using these mixing weights given in table 3, under conditions which will be pointed out in the next section, the quadrupole moments were evaluated only for the odd-neutron nuclei with normal coupling, and the values are listed in table 1. We have a fairly good agreement between the calculated and observed values for light and medium-heavy nuclei.

It should be noted here that the unusual assignments for the proton configurations of the Ge and Kr nuclei were assumed, on the basis of Klinkenberg's table 1 [10]) for the shell filling of odd proton nuclei, from the fact that there exist strong competitions between the states of the $p_{\frac{1}{2}}$ and $f_{\frac{5}{2}}$ configurations as well-known in the As, Br, and Rb isotopes [11]). It is true in principle that these strong competitions may require an appropriate combination of these configurations, while from the point of view of the present single configuration model we singled out the effective one by considering the possibility of a particular kind of successive filling, different from the usual single nucleon levels of the shell model, for the nucleon configurations of the even group, resulting from a certain disturbance by an odd group nucleon.

On the other hand, our model cannot be applied in the above mentioned simple form to the nuclei with proton configurations corresponding to closed or sub-closed shells. But, if a pair excitation from these proton cores might be permitted, we should also be able to deal with the moments of the ^{17}O, ^{33}S, and ^{35}S nuclei, for which, concerning the proton pair excitation with seniority two, we assume $(p_{\frac{1}{2}})^{-2}(d_{\frac{5}{2}})^2$ for ^{16}O, $(d_{\frac{5}{2}})^2$ and $(d_{\frac{5}{2}})^{-2}$ for ^{33}S and ^{35}S, respectively. The values thus obtained of the electric quadrupole moments of the above nuclei are listed in table 2. These values will, however, be regarded as only partial contributions δQ to these moments.

In our calculations of the nuclear moments, instead of the conventional isobaric spin formalism in which we treat the proton and the neutron as two states of a nucleon, we have regarded them as different kinds of particles. The corresponding values calculated by the Flowers formula (3) are listed also in table 2.

Recently the electric quadrupole and hexadecapole moments of the first excited state of $^{111}_{48}Cd$ have been measured by angular correlation experiments [12, 13]), although the latter moment has not yet been determined from these experiments [14]). The configuration for this state, which it is impossible to regard as a collective rotational level, is assumed to be $(d_{\frac{5}{2}})^{-1}$ and $(g_{\frac{9}{2}})^{-2}$ for the neutron and the proton, respectively. By using the observed value of -0.78 n.m. for the magnetic moment of the above nuclear state, we obtained the

values of 0.18×10^{-24} e cm^2 and -1.0×10^{-51} e cm^4 for the quadrupole and hexadecapole moments, respectively. The former value is smaller by one order of magnitude than the collective-model value of 1.8 barn calculated by us, which agrees with the experimental or empirically estimated value[12]) of 2×10^{-24} e cm^2, but it does not seem to be unreasonable for the value of a quadrupole moment in the range of these shell configurations as well as in an excited state. Meanwhile the value of the hexadecapole moment of this state by our model is consistent with our value of -3.2×10^{-51} e cm^4 calculated on the basis of the collective model in the case of weak coupling.

4. Discussion

In order to shift the values of the magnetic moments calculated by our procedure from the Schmidt lines in the experimentally required direction, we should assume that an odd neutron whose orbital angular momentum combines in parallel (or anti-parallel) orientation with its ordinary spin excites a pair of outmost protons whose orbital and spin angular momenta couple in parallel (or anti-parallel) orientation. In principle we should consider all the proton states of seniority two. But in the first place, we take only account the state with $J_p = 2$, since in practice this restriction proves to be reasonable.

If the mixing coefficients are determined by fitting the wave function (4) exactly to the observed value of the magnetic moment, large deviations of the magnetic moment from the Schmidt lines give rise to a large admixture between the zeroth-order ground states and excited states, and further the amplitude α_0 of the zeroth-order ground state is sometimes smaller than α_2, that of the zeroth-order excited state, in contradiction to the starting point of our theory. If we relax the severe condition of exact fitting, taking account of the fact that the nuclear magnetic moment involves indefinite terms, such as relativistic effects, exchange effects, and so on, we can avoid this difficulty with results unchanged in practice for the quadrupole moments, because the contribution from the off-diagonal elements of the quadrupole moment operator $Q^{(2)}_{op}$, written in the form of $2\alpha_0\alpha_2\langle J_p = 0|Q^{(2)}_{op}|J_p = 2\rangle$, is dominant.

When the mixing weight α_2^2 of the zeroth-order excited state in the ground state is fifty percent, $2\alpha_0\alpha_2$ amounts to the maximum value of 1.0. If we take 0.20, 0.10 and 0.06 for values of α_2^2, the values of $2\alpha_0\alpha_2$ are given by 0.8, 0.6 and 0.5, respectively. When α_2^2 becomes smaller than six percent, $2\alpha_0\alpha_2$ decreases rapidly with α_2.

Now we would take account of the state with $J_p = 4$ in addition to that with $J_p = 2$. The permissible range of the last parameter α_0 obtained by the conditions of the normalization and the fit of the magnetic moment can be given from the expression for $\langle Q^{(2)}\rangle$ with the state (4) or (4′) as follows:

$$\frac{\mu-\mu_4}{\mu_S-\mu_4} \geqq \alpha_0^2 \geqq \frac{\mu-\mu_2}{\mu_S-\mu_2},$$

$$\alpha_2^2 = \frac{(\mu-\mu_4)-(\mu_S-\mu_4)\alpha_0^2}{\mu_2-\mu_4},$$

$$\alpha_4^2 = -\frac{(\mu-\mu_2)-(\mu_S-\mu_2)\alpha_0^2}{\mu_2-\mu_4},$$

where μ is the experimental value of the magnetic moment, μ_S the Schmidt value, and μ_2, μ_4 are the theoretical values for the states with $J_p = 2$ and 4, respectively. We find that by adding a little amount of the state with $J_p = 4$ we can obtain a reasonable amplitude α_0 larger than α_2. On the basis of the relation of $\alpha_0 > \alpha_2 > \alpha_4$, assumed from energy considerations in the usual particle picture, the maximum values calculated for the quadrupole moments are given in parentheses in table 1. Even the maximum values (differing by at most five percent from the minimum values) obtained by this procedure are hardly different from the values obtained by taking into account only the state with $J_p = 2$. Finally, it can easily be seen that the allowed states with $J_p = 6$ need hardly to be considered because of the very large deviation of these magnetic moments from the experimental values.

If there were no interactions between the proton and neutron shells, we would have no admixture between the zeroth-order ground state and excited states, since each total angular momentum of the proton group or the neutron group is a good quantum number. But in fact since there exist interactions between the proton and neutron groups, the respective angular momenta of the proton and neutron groups are no longer good quantum numbers, and consequently the proton-neutron interaction gives rise to an admixture between zeroth-order states with different total angular momenta of the proton and neutron groups.

In order to explain the observed values for the quadrupole moments of odd-neutron nuclei by our theory, the mixing weight α_2^2 needs to be about thirty percent. Such a large admixture cannot be explained by the first order perturbation theory. On the contrary, the off-diagonal matrix element of the proton-neutron interactions should not be very small as compared with the energy difference between the zeroth-order ground and excited states, but both quantities should be of comparable magnitude. In order to obtain a rough evaluation of α_2^2, we represent the effective neutron-proton interaction by

$$V_{\lambda\mu} = V_0[(1-\xi)+\xi(\boldsymbol{\sigma}_\lambda \cdot \boldsymbol{\sigma}_\mu)]\delta(\mathbf{r}_\lambda-\mathbf{r}_\mu)$$
$$= \tfrac{1}{4}\{V_s[1-(\boldsymbol{\sigma}_\lambda \cdot \boldsymbol{\sigma}_\mu)]+V_t[3+(\boldsymbol{\sigma}_\lambda \cdot \boldsymbol{\sigma}_\mu)]\}\delta(\mathbf{r}_\lambda-\mathbf{r}_\mu), \quad (15)$$

where V_s and V_t are interaction strengths in the singlet and triplet states, respectively, and $V_s = (1-4\xi)V_0$, $V_t = V_0$. In the simplest case, namely, in

the case of odd-mass nuclei with one neutron and two protons outside closed shells the interaction energy matrix elements can be obtained by straightforward calculation as follows:

$$\langle j, j_1^2(0), J=j|\sum_{\lambda=2,3} V_{1\lambda}|j, j_1^2(2), J=j\rangle$$
$$=(-1)^{j_1+j-1}(V_s+3V_t)[\tfrac{1}{5}(2j_1+1)(2j+1)]^{\frac{1}{2}}(j\tfrac{1}{2}, j-\tfrac{1}{2}|20)(j_1\tfrac{1}{2}, j_1\tfrac{1}{2}|20)F^0(ll_1)$$

and

$$\langle j, j_1(2), J=j|\sum_{\lambda=2,3} V_{1\lambda}|j, j_1(2), J=j\rangle$$
$$=(-1)^{j_1+j-1}\tfrac{1}{2}(V_s+3V_t)5(2j_1+1)(2j+1)\sum_k (j\tfrac{1}{2}, j-\tfrac{1}{2}|k0)(j_1\tfrac{1}{2}, j_1-\tfrac{1}{2}|k0)$$
$$\times W(jjk2; 2j)W(j_1j_1k2; 2j_1)F^0(ll_1),$$

where

$$F^0(ll_1)=\tfrac{1}{2}\int_0^\infty R^2(l)R^2(l_1)r^2\mathrm{d}r.$$

The $R(l)$ is the radial wave function for a single nucleon with orbital angular momentum l. The quantity $V_sF^0(ll_1)$ could be estimated at $-25/A$ MeV from the difference of binding energies of odd-mass and even nuclei [15, 16]. Values of ξ between $\frac{1}{6}$ and $\frac{1}{4}$ have been obtained by Schwartz [17] for the sake of explaining Nordheim's empirical rules for the spins of the ground states of odd nuclei. On the basis of the theory developed by de-Shalit [18], on the other hand, Elliott and Lane [19] have derived the condition of $\xi > \frac{1}{10}$ for odd nuclei with one proton and one neutron outside closed shells. Then we take $\frac{1}{6}$ as a value of ξ. If we assume that the level spacing ΔE between the states with $J_p=0$ and $J_p=2$ of the even proton group in odd-neutron nuclei is equal to that of the corresponding even nuclei, we can construct the two-by-two energy matrices with the above neutron-proton interaction and can diagonalize them. Consequently we can determine the mixing coefficients α_0 and α_2.

For example, let us consider the ^{33}S and ^{73}Ge nuclei. Since the ΔE are about 2.4 and 0.6 MeV for ^{33}S and ^{73}Ge, respectively, we have the following results for the mixing weight α_2^2:

$$\alpha_2^2=0.21 \quad \text{for } ^{33}\text{S},$$
$$\alpha_2^2=0.33 \quad \text{for } ^{73}\text{Ge}.$$

On the other hand, if we assume $|V_t|=1.5|V_s|$, i.e. $\xi=\frac{1}{12}$, which agrees with the experimental data of two-nucleon systems at low energies, we have $\alpha_2^2=0.14$ and 0.27 for ^{33}S and ^{73}Ge, respectively. With the effective neutron-proton interaction (15) and with the estimation $V_sF^0=-25/A$ MeV, the admixture between the zeroth-order ground and excited state depends largely on the choice of the value of ξ: α_2^2 increases with ξ (for $\frac{1}{4}>\xi>0$) up to a maximum value of 0.5. In fact, if we regard eq. (15) as the effective neutron-proton interaction,

it can be shown that by an appropriate and reasonable choice of the value of ξ we have a large admixture between states with $J_p = 0$ and $J_p = 2$ of the even proton group in odd-neutron nuclei. Accordingly it seems possible to explain consistently the electric and magnetic moments of these nuclei on the basis of a single configuration.

The nuclear moments of odd-proton nuclei will be treated by the present method in a following paper with some generalizations.

References

1) B. H. Flowers, Phil. Mag. **43** (1952) 1330
2) A. Bohr and B. R. Mottelson, Dan. Vid. Selsk. Mat. Fys. Medd. **27** No. 16 (1953)
3) S. Hayakawa and T. Marumori, Prog. Theor. Phys. **17** (1957) 43
4) H. Horie and A. Arima, Phys. Rev. **99** (1955) 778
5) H. Horie and A. Arima, private communication
6) H. A. Jahn, Proc. Roy. Soc. A **205** (1951) 192
7) G. Racah, Phys. Rev. **62** (1942) 438
8) G. Racah, Phys. Rev. **73** (1953) 367
9) K. F. Smith, Progress in Nuclear Physics **6** (1957) 52
10) P. F. A. Klinkenberg, Revs. Mod. Phys. **24** (1952) 63
11) N. Zeldes, Nuclear Physics **7** (1958) 29
12) H. Albers-Schönberg, E. Heer, T. B. Novey and P. Scherrer, Helv. Phys. Acta **27** (1954) 547
13) E. Heer und R. Rüetshi, Helv. Phys. Acta **28** (1955) 525
14) H. Narumi and S. Matsuo, Nuovo Cimento **6** (1957) 398
15) M. G. Mayer, Phys. Rev. **78** (1950) 16, 22
16) A. Arima and H. Horie, Prog. Theor. Phys. **12** (1954) 623
17) C. Schwartz, Phys. Rev. **94** (1954) 95
18) A. de Shalit, Phys. Rev. **91** (1953) 1479
19) J. P. Elliott and A. M. Lane, Handbuch der Physik **39** (1957) 241

2.C

Nuclear Physics **16** (1960) 206—214; © *North-Holland Publishing Co., Amsterdam*

Not to be reproduced by photoprint or microfilm without written permission from the publisher

RESONANT ABSORPTION OF THE GAMMA RADIATION FROM THE $Ne^{22}(p, \gamma)Na^{23}$ REACTION

W. L. MOUTON and P. B. SMITH

Fysisch Laboratorium der Rijksuniversiteit, Utrecht, the Netherlands

Received 4 January 1960

Abstract: The gamma rays emitted in the reaction $Ne^{22}(p, \gamma)Na^{23}$ at $E_p = 637$ keV have been selectively absorbed in sodium fluoride, using the technique of collision produced Doppler shift. Resonant absorption of the 9.40 MeV gamma rays occurs at 74°.3 with respect to the proton beam direction. The instrumental resolution curve has been determined by observing the resonant absorption of the 12.33 MeV gamma radiation from the reaction $Al^{27}(p, \gamma)Si^{28}$ at $E_p = 771$ keV. The absorption curve for Na^{23} is broader than the measured instrumental curve and therefore it has been possible to determine directly the total width of the resonance level as 460 ± 360 eV. From the absorption integral, together with this value of the total width, the radiation width ($\Gamma_{\gamma 0}$) for transitions to the ground state is found to be 2.7 ± 1.1 eV. This result is in agreement with the value $\Gamma_{\gamma 0} = 2.0 \pm 0.5$ eV, found from a yield measurement. No definite assignment of parity can be made on the basis of the partials widths obtained.

1. Introduction

The resonant absorption of gamma rays from a (p, γ) reaction has been observed in several cases [1–5]). In these experiments a collimator is rotated about the direction of the proton beam (with the target as centre of rotation) and the intensity of the gamma radiation transmitted through the collimator and an absorber to a scintillation detector measured as a function of the angle. Resonant absorption occurs when the absorber is at an angle where the energy loss upon emission and reabsorption is equal to the energy gain from the Doppler shift caused by the motion of the excited nucleus. The effect has now also been observed in sodium fluoride for the gamma rays emitted in the reaction Ne^{22} (p, γ)Na^{23} from the Na^{23} level at 9.40 MeV excitation. The decay of this level has been studied previously [6, 7]) and has been shown to proceed preferentially to the ground state. The isotropic character of the radiation determines the spin of the resonance level as $\frac{1}{2}$, while the parity is still unknown, although a tentative assignment of odd parity has been made [6]).

In the present investigation values for the total width of the excited state and the radiation width for the ground state transition were found. It has, however, not been possible to make an assignment of parity to the level in the light of the present measurements although both the total width and the radiation width favour the negative parity slightly.

In section 2 a description of the measurement follows, in section 3 the calculations of the partial widths are discussed and in section 4 the parity of the level is considered.

2. Measurement

The apparatus has been described previously [3]). A new collimator, 30 cm long, was used in the present investigation, however, instead of the one described in this reference. It consisted essentially of two precisely machined lead blocks, $6\times10\times30$ cm, and was mounted on an angular distribution table in front of the counter. A diagram of the target holder is given in fig. 1. The

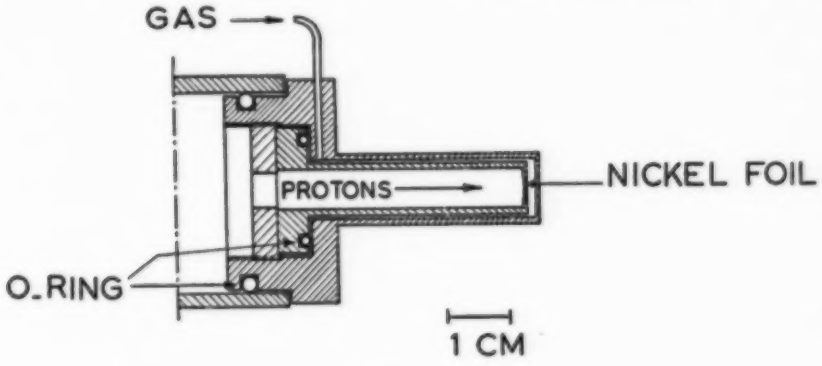

Fig. 1. Target holder.

right cylindrical shape was chosen in order to facilitate the mounting of the nickel foils. The foils were 0.5 μ thick and obtained from the Chromium Corporation of America. Isotopic Ne^{22}, furnished by the Laboratory of Mass Spectroscopy (F.O.M.) at Amsterdam, was used in the experiment. The gas layer (pressure 35 cm Hg) was 1.8 mm thick along the direction of the proton beam.

No measurable absorption was found in a series of preliminary measurements with a collimator opening of 0.4 cm, corresponding to an angular opening of 0°.72. This indicated that the level width was large and therefore the maximum absorption small. The collimator width was then increased to 1.4 cm (angular opening 2°.5) in order to obtain a higher counting rate, and the range of angles over which measurements were made increased proportionally. Despite the high yield of this resonance the counting rates were quite low due to the fact that the maximum beam current which could be used for more than several hours without causing leakage was only about 1.2 μA.

For the absorber, tablets of sodium fluoride of dimensions $3.3\times3.3\times0.4$ cm and $3.3\times3.3\times0.6$ cm were used. The tablets were made in a specially designed form under a pressure of 4 t/cm^2, using sodium fluoride powder of apparent density 0.85 g/cm^3. The specific gravity of the tablets was 2.2 and

the total length of absorber used 40 cm, yielding a sodium absorber thickness of 46.8 g/cm^2.

The absorption curve shown in fig. 2 (curve A), required 90 hours of bombardment at an average current of 1.2 μA, during which time 60 runs were made over the angle of resonance (in this case calculated to be 74°.3). Initially measurements were made from 59°.9 to 88°.7 in steps of 3°.6. To get better

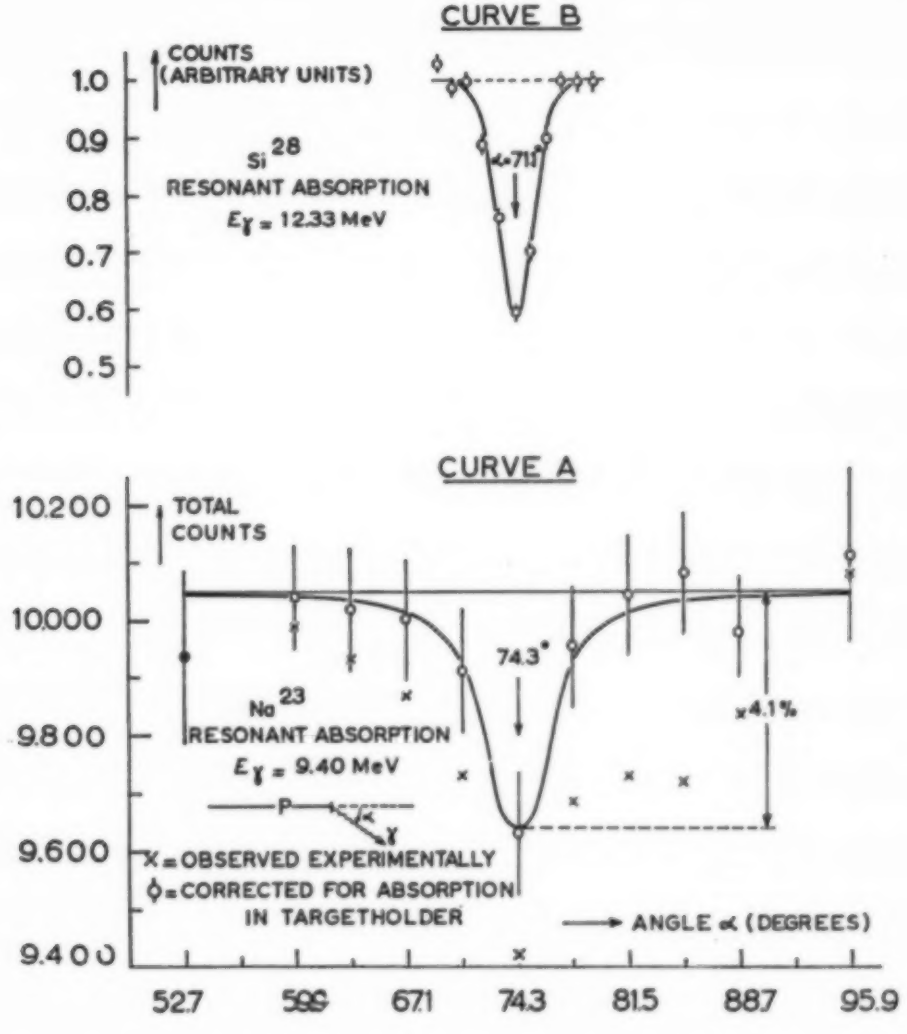

Fig. 2. *Curve A:* Resonant absorption of the 9.40 MeV gamma rays from Na^{23} as a function of angle. The crosses indicate the experimentally observed points and the circles the position of the points after correcting for absorption in the material of the target holder. For comparison the uncorrected experimental points have been moved upward 240 counts. Standard counting errors are indicated. The arrow shows the centroid of the absorption peak, and the indicated angle is that calculated theoretically.

Curve B: The instrumental resolution curve obtained by observing the resonant absorption of the 12.33 MeV gamma rays from Si^{28} as a function of angle. For comparison the curve has been normalized to the same height as the absorption curve for sodium and displaced 3°.2. Standard counting errors are indicated. The arrow shows the centroid of the absorption peak, and the indicated angle is that calculated theoretically.

wing points, readings were then taken at angles 52°.7 and 95°.9 as well as 59°.9 and 88°.7 after completing the first measurements. These reading were then matched to the first set.

The absorption of the gamma rays in the material of the target holder was comparable with the resonant absorption. The absorption was calculated by breaking the gas volume up into a large number (126) of smaller volumes and calculating the absorption of the gamma rays from each for every angle. In fig. 2 (curve A) the points are shown before and after correcting for this absorption. It is rather unfortunate that there are so few points in the region where maximum absorption occurs. Due to the extremely small absorption (maximum 4.1 %), however, the appropriate angular steps could not be determined before the measurement and analysis were done.

To determine the instrumental resolution curve, the resonant absorption curve for the 12.33 MeV gamma rays from the reaction Al^{27} (p, γ)Si^{28} was observed, using the same collimator opening as for the neon experiment. The absorber was silicon powder. The width in this case is almost entirely instrumental and attributed to geometrical factors [4]). The results of the measurement are shown in fig. 2 (curve B). The solid curve, which is seen to fit the points very well, is a Gaussian of full width at half maximum of 2°.7, which is very close to the geometrical collimator opening of 2°.5. In the neon experiment the Doppler broadening is also negligible and since the width of the collimator and distance between target and collimator remained unchanged, and the angles at which resonant absorption occurs in the two cases are nearly the same, the instrumental width for the sodium case can be taken to be the same as that obtained from the resonant absorption curve for silicon.

3. Results

3.1. DETERMINATION OF THE TOTAL WIDTH Γ_t

The observed absorption curve was wider than the known instrumental resolution curve. To find Γ_t the method described by Smith and Endt [4]) was therefore used: several trial Breit-Wigner curves are folded into the known instrumental curve until a best fit, using a least squares criterion, is found. The value of Γ_t is one-half of the width of the appropriate Breit-Wigner curve found in this way.

The fitting procedure was difficult in the present case since neither the position of the base line nor the maximum absorption was known with a high degree of certainty. The error in the alignment procedure is small and therefore the angle where maximum absorption occurred was taken to be 74°.3. For a Breit-Wigner curve of a given width, an absorption curve was calculated, assuming a value for the maximum absorption. The maximum absorption as well as the position of the base line, which was assumed to be horizontal since

the radiation is isotropic, were varied and the minimum value for the sum of the squares of the deviations from the experimental points determined. The width of the Breit-Wigner curve was then changed and the procedure repeated. The width giving the smallest minimum for the sum of the squared deviations was accepted as the width of the required Breit-Wigner curve.

The best fit was obtained with a Breit-Wigner curve of width 920 eV. The fold of the instrumental Gaussian curve and this Breit-Wigner curve is shown in fig. 2 (curve A). The natural line width is therefore 460 eV. The standard error was determined by an analysis which was based on the variation of the sum of the squares of the deviations from the experimental points as the trial width was varied. The value of the width adopted is

$$\underline{\Gamma_t = 460 \pm 360 \text{ eV}.}$$

The large error is mainly due to the lack of points lying high on the flank of the absorption dip, where the deviation is most sensitive to width.

3.2. DETERMINATION OF THE GROUND STATE RADIATION WIDTH $\Gamma_{\gamma 0}$

It has been shown [3]) that the value of the absorption integral is related to Γ_t and $\Gamma_{\gamma 0}$ by

$$A_\alpha = \int_0^\pi A(\alpha)\mathrm{d}\alpha = \tfrac{1}{2}\Gamma_t \pi \left(\frac{\mathrm{d}\alpha}{\mathrm{d}E_\gamma}\right)_r F(n\sigma_0), \tag{1}$$

where $A(\alpha)$ is the measured (resonant) absorption as a function of angle, $(\mathrm{d}\alpha/\mathrm{d}E_\gamma)_r$ is the reciprocal of the rate of change of gamma-ray energy with angle (evaluated at the angle of resonance), n is the number of absorber atoms per unit area, $F(n\sigma_0)$ is given by $n\sigma_0\, \mathrm{e}^{-\frac{1}{2}n\sigma_0}[I_0(\frac{1}{2}n\sigma_0)+I_1(\frac{1}{2}n\sigma_0)]$ (see ref. [3]) for notation), and

$$\sigma_0 = \frac{g\lambda^2}{2\pi}\,\frac{\Gamma_{\gamma 0}}{\Gamma_t}. \tag{2}$$

The statistical factor g is defined as $(2J_r+1)/(2J_g+1)$, where J_r and J_g are the spins of the excited state and the ground state, respectively.

In the present experiment $n\sigma_0 \ll 1$, so that $\mathrm{e}^{-\frac{1}{2}n\sigma_0}[I_0(\frac{1}{2}n\sigma_0)+I_1(\frac{1}{2}n\sigma_0)]$ is almost equal to unity. Without introducing an appreciable error, $F(n\sigma_0)$ can therefore be replaced by $(n\sigma_0)$ in eq. (1). Using eq. (2), the following simplified expression for the absorption integral is then obtained:

$$A_\alpha = \left(\frac{\mathrm{d}\alpha}{\mathrm{d}E_\gamma}\right)_r \frac{ng\lambda^2}{4}\,\Gamma_{\gamma 0}. \tag{3}$$

If the absorption integral and g are known, $\Gamma_{\gamma 0}$ can be calculated from this expression.

The absorption integral can be determined from the absorption points.

The five points from 67°.1 to 81°.5 were used for this purpose and the wing area was calculated on the assumption that the curve is of Breit-Wigner form in this region [8]). The final result for the absorption integral is 0°.287. As mentioned in section 1, the spin of the excited state is known to be $\frac{1}{2}$, and since the ground state has spin $\frac{3}{2}$, g is equal to $\frac{1}{2}$. The calculated value for $(\mathrm{d}\alpha/\mathrm{d}E_\gamma)_\mathrm{r}$ is 3.94×10^{-3} deg · eV^{-1}. Using these values, $\Gamma_{\gamma 0}$ was calculated from eq. (3), and found to be 2.77 eV. Three corrections must, however, be applied to this result: (1) resonant absorption also occurs in the sodium iodide detecting crystal, and the expression for the absorption integral must be

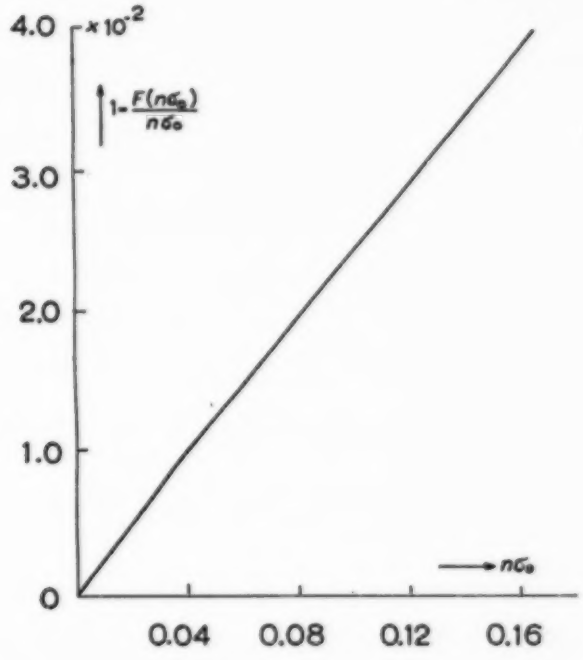

Fig. 3. Graph showing the deviation of the function $F(n\sigma_0)/n\sigma_0$ from unity for small values of $n\sigma_0$.

modified to take into account this effect; (2) a small correction must be applied due to the fact that $F(n\sigma_0)$ is only approximately equal to $n\sigma_0$; (3) the effect of the temperature motion of the absorbing nuclei must be taken into account.

The first correction amounts to 6 % (see appendix for calculation) and reduces the value of $\Gamma_{\gamma 0}$ to 2.60 eV. Assuming this value for the ground state radiation width, $n\sigma_0$ was calculated, and from the graph given in fig. 3, the error introduced by assuming $F(n\sigma_0) = n\sigma_0$ was found to be 2.3 %. This correction increases the value for $\Gamma_{\gamma 0}$ to 2.66 eV. The third correction is negligible in the present case.

The error associated with $\Gamma_{\gamma 0}$ is almost entirely determined by the statistical accuracy of the absorption integral, because the relatively small value of $n\sigma_0$ makes the absorption integral almost independent of Γ_t. The standard error in the determination of the absorption integral is about 40 %, assuming

all points to be effective in determining the position of the base line. The final result for the ground state radiation width is then

$$\underline{\Gamma_{\gamma 0} = 2.7 \pm 1.1 \text{ eV.}}$$

The ground state radiation width was also determined by a yield measurement of the 9.40 MeV gamma rays. It was not possible to perform a thick target yield measurement. The maximum pressure which could be reached in the target was 35 cm Hg, and this was not sufficient to produce the saturation yield. Measurements were therefore made with a gas pressure of 10 cm Hg. For a thin target, the yield integral [9]) is given by

$$A_\gamma = \frac{N\lambda^2}{4} \frac{2J_r+1}{2I+1} \frac{\Gamma_p \Gamma_{\gamma 0}}{\Gamma_p+\Gamma_{\gamma 0}};$$

here N is the number of nuclei/cm^2 in the target, I the spin of the target nucleus, Γ_p the proton width, and $\lambda^2 = \frac{1}{2}\hbar^2/M_p E_r$, where M_p denotes the reduced proton mass and E_r the resonance energy. The conditions [9]) on the validity of this expression are well-fulfilled in our experimental arrangement. From the resonant absorption experiment it is known that $\Gamma_p \gg \Gamma_{\gamma 0}$ for the 9.40 MeV level in Na^{23}, and therefore

$$A_\gamma = \frac{N\lambda^2}{4} \frac{2J_r+1}{2I+1} \Gamma_{\gamma 0}.$$

Taking into account the discriminator setting, the solid angles subtended by the detecting crystal and its efficiency, A_γ was determined from the resonance curve. A value of 7.35×10^{-6} eV was calculated. Assuming $J_r = \frac{1}{2}$, $I = 0$ and the gas to be 93 % pure (according to the suppliers), a value for $\Gamma_{\gamma 0} = 2.02$ eV was obtained. Owing to uncertainty in counter efficiency, beam measurement, and effective solid angle, an error of 25 % is assigned to this value, giving a final result

$$\Gamma_{\gamma 0} = 2.0 \pm 0.5 \text{ eV.}$$

This value is in agreement with the result found from the absorption integral.

4. Conclusions

For the strength in Weisskopf units ($|M|^2$) of 15 E1 and 19 M1 transitions Van der Leun [10]) found average values of 0.0017 and 0.025 respectively, for nuclei with $22 < A < 35$. For the reduced proton width (θ_p) an average values of 0.07 was obtained for this region of the periodic table. Using these valuee one can estimate the radiative and proton widths which would be expected for the 9.40 MeV level in Na^{23}. For a negative parity assignment the results

were $\Gamma_{\gamma 0} = 1.2$ eV and $\Gamma_p = 280$ eV, and for positive parity $\Gamma_{\gamma 0} = 0.45$ eV, $\Gamma_p = 1100$ eV. The spread in the measured values of $|M|^2$ and θ_p is rather large (a factor of 10 for $|M|^2$), so that no definite conclusions with regard to the parity of the level can be made by comparing these values with the present experimental results, but the deviations from both the most probable total width and the radiation width are considerably larger for the positive than for the negative parity assignment, so that the that latter is slightly favoured by these results.

This investigation was partly supported by the joint research programme of the "Stichting voor Fundamenteel Onderzoek der Materie" and the "Nederlandse Organisatie voor Zuiver-Wetenschappelijk Onderzoek".

The authors acknowledge the invaluable help and encouragement received during this experiment from Prof. Dr. P. M. Endt. Our thanks are also due to Dr. M. Suffert for help received in taking data. We extend our grateful appreciation to Prof. Dr. J. Kistemaker for kindly supplying us with the isotopically pure neon. One of the authors (W.L.M.) would like to thank the University of Natal in South Africa for granting leave of absence during the past year and the "Commissie van Advies en Coördinatie ten dienste van de Culturele Betrekkingen tussen Nederland en Zuid-Afrika" as well as the South African Council for Scientific and Industrial Research for financial support.

Appendix

We give here the calculation of the correction which must be applied to the value obtained for $\Gamma_{\gamma 0}$ in section 3.2, due to the resonant absorption of the gamma radiation occurring in the sodium iodide detector. Since $\Gamma_p \gg \Gamma_{\gamma 0}$ for the 9.40 MeV level in Na^{23}, re-emission and re-absorption of the resonantly absorbed quanta in the crystal need not be considered. However, strong (non-resonant) absorption occurs in the detector and therefore the variation in intensity of the gamma rays on passing through the sodium iodide has to be taken into account when calculating the resonant absorption occurring in the detector. The expression for the absorption integral then becomes

$$A_a = \Gamma_{\gamma 0} \frac{g\lambda^2}{4} \left(\frac{\mathrm{d}\alpha}{\mathrm{d}E_\gamma}\right)_r \left\{n + \int_0^{l_1} n_1 \mathrm{e}^{-cx}\,\mathrm{d}x\right\} = \Gamma_{\gamma 0} \frac{g\lambda^2}{4} \left(\frac{\mathrm{d}\alpha}{\mathrm{d}E_\gamma}\right)_r \left\{n + \frac{n_1}{c}(1-\mathrm{e}^{-cl_1})\right\},$$

where n is the number of sodium atoms/cm^2 in the sodium fluoride, n_1 the number of sodium atoms/cm^3 in the sodium iodide, l_1 the length of the sodium iodide crystal and c the total absorption coefficient of sodium iodide.

Taking $l_1 = 10$ cm, $c = 0.138$ cm^{-1} [11]), and using the values for A_a, g and $(\mathrm{d}\alpha/\mathrm{d}E_\gamma)_r$ mentioned before, $\Gamma_{\gamma 0}$ was calculated and found to be 2.60 eV. Thus the value calculated in section 3.2 is reduced by 6 % due to resonant absorption occurring in the detector.

References

1) S. S. Hanna and L. Meyer-Schützmeister, Phys. Rev. **108** (1957) 1644
2) L. Meyer-Schützmeister and S. S. Hanna, Bull. Am. Phys. Soc. **3** (1958) 188
3) P. B. Smith and P. M. Endt, Phys. Rev. **110** (1958) 397
4) P. B. Smith and P. M. Endt, Phys. Rev. **110** (1958) 1442
5) P. B. Smith, Congrès International de Physique Nucléaire, edited by Mme P. Gugenberger (Dunod, Paris 1959) p. 655
6) Thornton, Meads and Collie, Phys. Rev. **109** (1958) 480
7) Singh, Davis and Krone, Phys. Rev. **115** (1959) 170
8) Melkonian, Havens and Rainwater, Phys. Rev. **92** (1953) 702
9) H. E. Gove, in Nuclear Reactions, edited by Endt and Demeur (North-Holland Publ. Co., Amsterdam 1959) p. 293 ff
10) C. van der Leun, thesis Utrecht (1958)
11) P. R. Bell, in Beta- and Gamma-ray Spectroscopy, edited by K. Siegbahn (North-Holland Publ. Co., Amsterdam 1955) p. 153

1.D.2.

Nuclear Physics **16** (1960) 215—230; © *North-Holland Publishing Co., Amsterdam*

Not to be reproduced by photoprint or microfilm without written permission from the publisher

CLASSIFICATION OF BETA- AND GAMMA-RAY TRANSITIONS BETWEEN INTRINSIC STATES IN DEFORMED EVEN-MASS NUCLEI

C. J. GALLAGHER †

Institute for Theoretical Physics, University of Copenhagen, Denmark

Received 22 February 1960

Abstract: The description of intrinsic states of deformed even-mass nuclei by the product wave functions of the strong coupling model, using Nilsson wave functions to describe the intrinsic particle configurations, is shown to lead to selection rules which depend on the coupling between the last two particles. In the case in which the coupling in the final and initial states is the same, the description leads, in the asymptotic limit of the Nilsson wave functions, to selection rules similar to those proposed earlier for odd-mass nuclei. For nuclear states with different relative couplings the selection rules lead most frequently to K-forbiddenness. It is shown that, if the non-transforming particle in the two-particle product wave function is not the same in the final and initial states, the resulting two-particle transition is formally forbidden. The experimental transition rates in even-mass nuclei to which definite configurations can be assigned are observed to fall within well-defined ranges characteristic of the degree of forbiddenness predicted by the selection rules. Furthermore, the data on log ft-values indicate that single-particle transitions occur with essentially the same speed whether the transforming particle is in an odd-mass or an even-mass nucleus.

1. Introduction

Recent years have seen a rapid development of the theoretical understanding of the low energy states of nuclei. Most important in this respect have been the single-particle shell model [1,2]) and the collective model [3,4]), which can be interpreted as representing two extreme cases of nuclear behaviour. Within the framework of these models has come a significant understanding of the physical properties of two of the three symmetry classes of nuclei, even-even and odd-mass. It is chiefly with the third class, odd-odd nuclei whose properties are not so well understood, that this paper is concerned.

The question of the coupling of angular momenta in deformed odd-odd nuclei has recently been discussed by Gallagher and Moszkowski [5]) (hereinafter referred to as GM). They showed that the ground state spins of deformed odd-odd nuclei could be explained very simply by assuming that, for any given isotope, the last odd proton and odd neutron move independently in the Nilsson states [6]) appropriate for that Z and N. Furthermore, they re-emphasized, what had been first pointed out by Bohr and Mottelson [4]), that in these deformed

† National Science Foundation Postdoctoral Fellow, 1959—1960.

nuclei the strong coupling model applies and the two particles are constrained to move with a definite angular momentum along the symmetry axis. Because of this constraint, only two intrinsic states are possible for any neutron-proton configuration, corresponding to the parallel or antiparallel orientation of the total angular momenta of the two particles along the symmetry axis. They further showed that empirical evidence favours the interpretation that of these two the state with lower energy is the one in which the *intrinsic* spins of the particles couple parallel.

The success that the configurations proposed by GM have had in explaining the ground state spins [5]) and magnetic moments [5, 7]) of deformed odd-odd nuclei suggested that a further attempt be made to see whether log *ft*-values and electromagnetic transition probabilities can also be explained by this scheme. The present paper contains the results of such an attempt.

The calculation of beta- and gamma-ray transition probabilities in an odd-odd nucleus, when the particle configurations are described by the Nilsson wave functions, is closely related to the same problem in odd-mass nuclei. Because of the product nature of the strongly coupled two-particle wave function, the matrix element is also a product, consisting of an overlap integral multiplied by an integral which also occurs in the calculation of single- particle transition rates. In subsection 2.1, we shall therefore briefly discuss the general results which have been obtained earlier for strongly coupled systems, and also how they have been applied to odd-mass nuclei. In subsections 2.2, 2.3 and 2.4, the general expressions which result from the use of two-particle product wave functions will be given. In section 3, the available experimental data are presented, and in section 4, a comparison between theory and experiment is made, which is discussed in section 5.

2. Theoretical

2.1. GENERAL RESULTS FOR THE STRONGLY COUPLED SYSTEM

The strong coupling wave function, in the notation of Bohr and Mottelson, is

$$\psi = \sqrt{\frac{2I+1}{16\pi^2}}\{\chi_\Omega \mathscr{D}^I_{MK}(\vartheta_i) + (-)^{I-j}\chi_{-\Omega}\mathscr{D}^I_{M-K}(\vartheta_i)\}\varphi_{00}. \quad (1)$$

The meaning of the quantum numbers j, I, M, K and Ω is illustrated in fig. 1, which is taken from Bohr and Mottelson's paper [4]).

The $\mathscr{D}^I_{MK}(\vartheta_i)$ are the proper functions for the symmetric top normalized to give a unitary transformation from the space fixed to the nuclear coordinate system; φ_{00} is the vibrational wave function for the nuclear ground state, and the $\chi_{\pm\Omega}$ are the intrinsic particle wave functions which we shall consider in more detail later.

According to Bohr and Mottelson, the reduced transition probability is in general

$$G(\lambda, I_1 \to I_f) = \sum_{\mu, M_f} |\langle I_f M_f | \mathcal{M}(\lambda, \mu) | I_1 M_1 \rangle|^2, \tag{2}$$

where

$$G(\lambda, I_1 \to I_f) = B(\lambda, I_1 \to I_f) \tag{3a}$$

for electromagnetic transitions, and

$$G(\lambda, I_1 \to I_f) = D_{GT}(n, I_1 \to I_f) \tag{3b}$$

for unique beta transitions of order n.

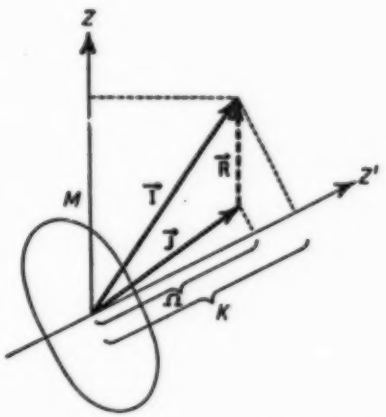

Fig. 1. Coupling scheme for strong particle-surface interaction. In strong coupling the nuclear surface becomes spheroidally deformed, with the axis of symmetry z'. The angular momentum $\mathbf{j}$ of the particle precesses about z' with a constant projection Ω. The total angular momentum $\mathbf{I}$ is the sum of $\mathbf{j}$ and the angular momentum $\mathbf{R}$ of the surface. The coupled system of particle and surface rotates like a symmetric top with quantum numbers I, K (projection of $\mathbf{I}$ on z') and M (projection of $\mathbf{I}$ on the space fixed axis z).

Without a detailed understanding of the intrinsic particle wave functions it is not possible to proceed further with the evaluation of eq. (2) than to carry out the summation over M_f and μ. However, Alaga *et al.*[8]) have shown that, if only the ratio of beta- or gamma-decay to two rotational states of a given intrinsic state is considered, the relative reduced transition probabilities become just the ratio of squares of Clebsch-Gordan coefficients:

$$\frac{G(\lambda, I_1 \to I_f)}{G(\lambda, I_1 \to I'_f)} = \frac{\langle I_1 \lambda K_1 K_f - K_1 | I_1 \lambda I_f K_f \rangle^2}{\langle I_1 \lambda K_1 K_f - K_1 | I_1 \lambda I'_f K_f \rangle^2}. \tag{4}$$

In addition to predicting the branching ratios to rotational states of a definite intrinsic state, this relationship has significance because formally the Clebsch-Gordan coefficients vanish if $L < K_f - K_1$, and transitions between states with $\Delta I \leqq L$ but with $\Delta K > L$ may be forbidden. Alaga *et al.* first

discussed this K-forbiddenness and showed that it explained several otherwise-anomalous beta- and gamma-ray transition rates.

Alaga *et al.* did not attempt to evaluate the dependence of this expression on the intrinsic structure, as such an evaluation depends on a knowledge of the particle wave functions. Nilsson [6]) has since calculated particle wave functions for a harmonic oscillator in a potential well with quadrupole deformation as a function of deformation. If the Nilsson wave functions are inserted into eq. (2), and the resulting expression is reduced, the general expression for $G(\lambda, I_1 \to I_f)$ becomes (cf. ref. [6]), p. 31):

$$G(\lambda, I_1 \to I_f) = |\langle I_1 \lambda K_1 K_f - K_1 | I_1 \lambda I_f K_f \rangle \int \chi^{\dagger}_{\Omega_f} \mathscr{J}(\lambda,\ K_f - K_1) \chi_{\Omega_1} d\tau$$
$$+ \langle I_1 \lambda K_1 - K_f - K_1 | I_1 \lambda I_f - K_f \rangle \int (-)^{I-j} \chi^{\dagger}_{-\Omega_f} \mathscr{J}(\lambda,\ -K_f - K_1) \chi_{\Omega_1} d\tau|^2, \quad (5)$$

where χ_Ω has the meaning $\sum_j c_j \chi_{\Omega^j}$ and $(-)^{I-j}\chi_{-\Omega}$ has the meaning $\sum_j (-)^{I-j} c_j \chi^j_{-\Omega}$. Nilsson has also calculated explicitly the general forms for the integrals corresponding to the meanings of $G(\lambda, I_1 \to I_f)$ listed above. In this expression the integral over the vibrational wave functions has been set equal to unity.

In the limit of infinite quadrupole deformation, the Nilsson wave functions reduce to the wave functions for a harmonic oscillator in a cylindrical coordinate system, in the presence of certain perturbation terms. In this limit the wave functions are still doubly degenerate, but can be characterized by definite "asymptotic limit" quantum numbers. These are the principal quantum number N, the number of nodes along the z-axis n_z; and Λ, the number of nodes in the (x, y)-plane or, from a physical viewpoint, the total angular momentum directed along the symmetry axis. (To Λ is coupled the intrinsic spin Σ to yield Ω, the total angular momentum along the symmetry axis.)

In this limit, the expressions for transition probabilities also reduce to one term which can be evaluated generally in terms of the asymptotic-quantum-number selection rules [9–11]). These rules, for most cases of interest, are to be found in Mottelson and Nilsson's compilation of data on deformed odd-mass nuclei, where the application of the Nilsson wave functions is thoroughly discussed [12]).

2.2. THE TWO-PARTICLE SYSTEM

In order to calculate transition probabilities in the two-particle system, the two-particle wave functions need to be defined. In the representation we employ, the $\chi_{\pm\Omega}$ of eq. (1) are products of two Nilsson single-particle wave functions:

$$\chi_\Omega = \chi_{\Omega_1}\ \chi_{\pm\Omega_2}, \quad (6a)$$

$$\chi_{-\Omega} = \chi_{-\Omega_1} \chi_{\mp\Omega_2}, \quad (6b)$$

where the sign of Ω_2 is determined by the coupling of the particles, and the

subscripts 1 and 2 indicate that this general form applies to neutron-neutron, proton-proton, and proton-neutron configurations.

It is important to note here that Ω and $-\Omega$ specify definite (and opposite) directions along the symmetry axis. Thus, in two-particle systems, the non-transforming particle can be looked upon as defining a polarization axis, and the parallel or antiparallel alignment of the second particle with respect to this axis determines the total spin of the system. In this two-particle system the coupling diagram corresponding to fig. 1 is somewhat more complicated. However, for the purposes of our argument, the quantities in fig. 1 can be considered to represent the quantities resulting from coupling two particles.

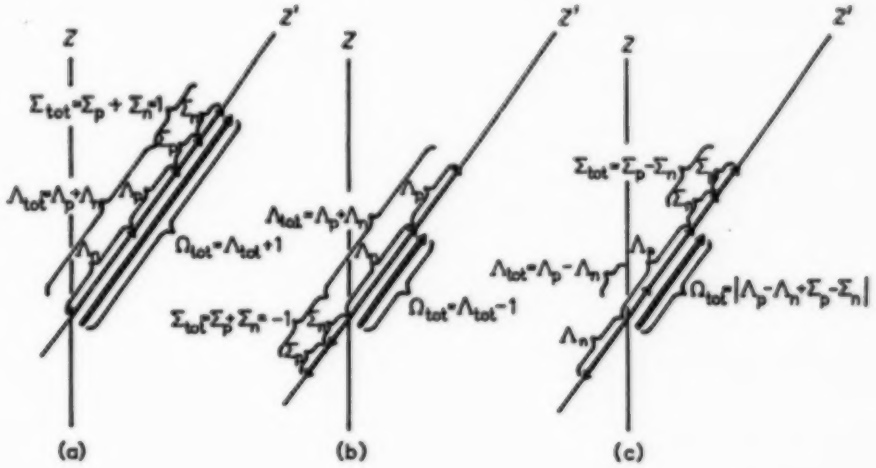

Fig. 2. Decomposition of the Ω_{tot} of the two-particle system into its Λ_{tot} and Σ_{tot} components. According to the Nilsson scheme, the single particle $\Omega=\Lambda+\Sigma$, where Λ is the orbital angular momentum about the nuclear symmetry axis and $\Sigma=\pm\frac{1}{2}$ is the particle intrinsic spin. The three configurations shown represent the 3 configurations possible for the two particles in the ground state of an odd-odd nucleus if the intrinsic spins are assumed to add so that $\Sigma_{tot}=1$. (a) Case in which both particles have $\Omega=\Lambda+\frac{1}{2}$. (b) Case in which both particles have $\Omega=\Lambda-\frac{1}{2}$. (c) Case in which one particle has $\Omega=\Lambda+\frac{1}{2}$ and the other has $\Omega=\Lambda-\frac{1}{2}$.

Thus, Ω in fig. 1 can be considered as representing the total Ω of the even-mass nucleus, which can be made up from the Λ_{tot} and Σ_{tot} of the last two particles in a limited number of ways; these are illustrated in fig. 2 for the case of an odd-odd nucleus in which the particles are coupled in configurations in which the *intrinsic* spins add.

For the ground state of an odd-odd nucleus we define the phase of the wave function by the expression

$$\Psi_{00}=\sqrt{\frac{2I+1}{16\pi^2}}\{\chi^{(1)}_{\Omega_p}\chi^{(2)}_{\pm\Omega_n}\mathcal{D}^I_{MK}(\vartheta_1)+(-)\chi^{I-j_p-j_n}\chi^{(1)}_{-\Omega_p}\chi^{(2)}_{\mp\Omega_n}\mathcal{D}^I_{M-K}(\vartheta_1)\}\varphi'_{00}, \quad (7)$$

where the sign of Ω_n is determined from the coupling rule which is applicable to the case in question.

For a proton pair in an even-even nucleus we write

$$\Psi_{ee} = \sqrt{\frac{2I+1}{16\pi^2}} \{\chi^{(1)}_{\Omega_p}\chi^{(2)}_{-\Omega_p} + (-)^{I-2j_p}\chi^{(1)}_{-\Omega_p}\chi^{(2)}_{\Omega_p}\}\mathcal{D}^I_{M0}(\vartheta_1)\varphi_{00}. \quad (8)$$

If the full symmetry of the even-even nucleus ground state were considered, the correct wave function would be (for a proton pair)

$$\Psi_{ee} = \sqrt{\frac{2I+1}{32\pi^2}} \{(\chi^{(1)}_{\Omega_p}\chi^{(2)}_{-\Omega_p} - \chi^{(1)}_{-\Omega_p}\chi^{(2)}_{\Omega_p}) + (-)^{I-2j_p}(\chi^{(1)}_{-\Omega_p}\chi^{(2)}_{\Omega_p} - \chi^{(1)}_{\Omega_p}\chi^{(2)}_{-\Omega_p})\}\mathcal{D}^I_{M0}\varphi_{00}, \quad (9)$$

where, because the second expression within the curly brackets equals the negative of the first term, the wave function will vanish for states with I odd. However, for the purpose of the present discussion we do not need the full symmetry.

It should perhaps also be noted here that, in the case of an odd-odd nucleus in which the particles couple to total spin zero, $\mathcal{D}^I_{MK}(\vartheta_1) = \mathcal{D}^I_{M-K}(\vartheta_1) = \mathcal{D}^I_{M0}(\vartheta_1)$ and the $\mathcal{D}^I_{M0}(\vartheta_1)$ can again be factored from the two terms of the wave function, i.e.

$$\Psi_{00} = \sqrt{\frac{2I+1}{16\pi^2}} \{\chi^{(1)}_{\Omega_p}\chi^{(2)}_{-\Omega_n} + (-)^{I-j_p-j_n}\chi^{(1)}_{-\Omega_p}\chi^{(2)}_{\Omega_n}\}\mathcal{D}^I_{M0}(\vartheta_1)\varphi'_{00}. \quad (10)$$

In this case, however, the two terms within the curly brackets are not equivalent, and the rotational band will have both odd and even spin states. However, because the sign of the second term will be different when I is odd or even, the energies of the rotational states will not follow the simple $I(I+1)$ rule, but rather will be raised or lowered, somewhat in energy depending on whether I is odd or even. If this energy is great enough, the band may actually separate into two bands, one with odd spins, the other with even spins. An estimate of which band should lie lower would depend on more detailed considerations. In Am^{242}, the odd band apparently lies lower (an $I=1$, $K=0$ state has been observed as the ground state [16, 17]) †.

In order to present a simple discussion, yet obtain some specific results, we consider only the case of the allowed beta decay from the ground state of an odd-odd nucleus to the ground state of an even-even nucleus. It should be noted that these transitions will always be Gamow-Teller (or spin-flipping) transitions if the GM coupling rules hold. The general formulation of the problem is the same for electromagnetic transitions, although, of course, such transitions take place only between either proton or neutron states. In the final expressions we display only the general forms of the integrals because Nilsson has already evaluated them explicitly. Our results indicate that two

† I am indebted to Prof. B. R. Mottelson and Dr. S. G. Nilsson for a discussion of these points.

distinct cases exist, which arise from the two possible relative couplings of the final and initial states; we consider these cases separately in sects. 2.3 and 2.4.

2.3. TRANSITIONS BETWEEN NUCLEAR STATES WITH THE SAME RELATIVE COUPLINGS

The ground state of an even-even nucleus will consist of pairs of nucleons coupled to spin zero. Because only one pair is of interest to us, we will use eq. (8) as the even-even ground state wave function.

The corresponding odd-odd wave function for the case in which the Ω of the nucleus is defined as $\Omega=\Omega_p-\Omega_n$ is then specified because of the coupling rules:

$$\Psi_{\omega} = \sqrt{\frac{2I+1}{16\pi^2}}\{\chi^{(1)}_{\Omega_p}\chi^{(2)}_{-\Omega_n}\mathscr{D}^I_{MK}(\vartheta_1)+(-)^{I-j_p-j_n}\chi^{(1)}_{-\Omega_p}\chi^{(2)}_{\Omega_n}\mathscr{D}^I_{M-K}(\vartheta_1)\}\varphi'_{\omega}. \quad (11)$$

When eqs. (8) and (11) are substituted into eq. (2), and eq. (2) is reduced to the analogue of eq. (5), we obtain finally

$$D_{GT}(n, I_1 \to I_f) = |\langle I_1 n+1 K_1 K_f-K_1|I_1 n+1 I_f K_f\rangle \int \chi^{\dagger(1)}_{\Omega_p}\chi^{(1)}_{\Omega_p}\mathrm{d}\tau_1 \times \int \chi^{\dagger(2)}_{\Omega_p}\mathscr{D}(n+1,\ K_f-K_1)\chi^{(2)}_{\Omega_n}\mathrm{d}\tau_2|^2. \quad (12)$$

For the case in which the ground state $\Omega=\Omega_n-\Omega_p$, it can be shown that the same result is obtained.†

In this expression there are two integrals, an overlap integral and an integral which is that ordinarily encountered in calculating transition probabilities in odd-mass nuclei. For cases of finite deformation the general formulae given by Nilsson can therefore be used directly. In order that the overlap integral does not vanish, however, the non-transforming particle must be the same in the final and initial states. Thus, formally, two partical transitions are forbidden, and give rise to what we shall call non-overlap forbiddenness.

In the asymptotic limit the sum over the particle quantum numbers j in $\chi_\Omega{}^j$ reduces to a single term and the matrix element becomes simply an overlap integral times an integral which can be described generally by the selection rules for asymptotic quantum numbers[9-11]).

2.4. TRANSITIONS BETWEEN NUCLEAR STATES WITH DIFFERENT RELATIVE COUPLINGS

Because the wave function of the even-even ground state has already been specified, we only need to give the form of the wave function for the

† Although the sign of the electric multipole matrix elements is the same in both cases, the magnetic multipole matrix elements have different signs. The $G_{M\lambda}$ corresponding to $\Omega=\Omega_n-\Omega_p$ has the same sign as $G_{M\lambda}$ in ref. [6]).

odd-odd nucleus, which is in this case

$$\Psi_{\omega\omega} = \sqrt{\frac{2I+1}{16\pi^2}}\{\chi^{(1)}_{\Omega_p}\chi^{(2)}_{\Omega_n}\mathscr{D}^I_{MK}(\vartheta_1)+(-)^{I-j_p-j_n}\chi^{(1)}_{-\Omega_p}\chi^{(2)}_{-\Omega_n}\mathscr{D}^I_{M-K}(\vartheta_1)\}\varphi'_{\omega\omega}. \quad (13)$$

When eqs. (8) and (13) are substituted into eq. (2) and the expression is evaluated as in sect. 2.3 above, the expression for the reduced transition probability, analogous to eq. (12), is

$$D_{GT}(n,\ I_1 \to I_f)$$
$$=|\langle I_1 n+1 K_1 K_f - K_1 | I_1 n+1 I_f K_f\rangle \int \chi^{\dagger(1)}_{\Omega_p}\chi^{(1)}_{\Omega_p}d\tau_1 \int \chi^{\dagger(2)}_{-\Omega_p}\mathscr{D}(n+1, K_f-K_1)\chi^{(2)}_{\Omega_n}d\tau_2|^2. \quad (14)$$

The requirements on the overlap integral are as above. In the matrix element the Ω of the transforming particle is directed along the symmetry axis in opposite directions in the final and initial states; hence, in order to conserve angular momentum, the angular momentum L carried off by the transition, must have the value $L \geqq |K_f - K_1|$, or the integral vanishes. In fact, this integral will be non-zero for allowed or first-forbidden beta transitions only when both the odd-proton part and the odd-neutron part of an odd-odd nucleus have $\Lambda_p = \Lambda_n = 0$ and $\Omega_p = \Omega_n = \frac{1}{2}$. In cases ordinarily observed, however, $L=0$ or $L=1$, and $K_1 + K_f > L$, so that transitions between states which do not have the same relative couplings will, in general, be K-forbidden (or, more specifically, Λ-forbidden).

3. Experimental Data

The experimental data and spin assignments are for the most part as quoted in Strominger, Hollander and Seaborg[13]). Parity assignments are based almost entirely on those predicted by the intrinsic configurations assigned by GM, which have been retained except where new experimental data on neighbouring odd-mass nuclei have indicated that they should be changed. Where new data have become available specific references are given.

4. Results

The configurations assigned to the odd-odd nuclei considered in the discussion of beta decay are shown in table 1. In almost all cases the nuclei are assigned spin 1 because they decay to the 0+ and 2+ states of the even-even ground state rotational band. The branching ratios are shown in table 2. In some cases deviations from the theoretically expected ratios are observed, but an investigation of these deviations is outside the scope of this paper.

The results of the application of the beta-decay selection rules to the experimental data of table 1 are shown in table 3(a), (b) and (c). The data on

allowed transitions are shown in (a) and (b) and those on forbidden transitions in (c). Table 4 (a) shows the only clear-cut examples of beta decay to definite excited intrinsic configurations in even-even nuclei. In table 4(b) examples of K-forbidden transitions (cf. Alaga *et al.*, ref. [8])) are shown.

The last columns of table 3 and table 4 contain the log ft-values for the same single-particle transition as observed in the beta decay of an odd-mass nucleus[12]).

The presently available data on electromagnetic transitions are shown in table 5. The configurations shown in table 5 are to be found either in table 1 or in GM.

TABLE 1

Experimental spin assignments for the odd-odd nuclei discussed in this paper. The configuration assignments are based on the proposals of Gallagher and Moszkowski [5])

$_Z X^A$	Spin of state I_0 [a])	Configuration proton neutron	Configuration assignment	Experimental obs. of state [b]) proton neutron
$_{65}Ho^{162}$	(6−)	$523\uparrow+642\uparrow$	[c])	0 0
$_{69}Tm^{170}$	(1−)	$411\downarrow+521\downarrow$	GM	0 0
$_{71}Lu^{176m}$	(1+)	$404\downarrow-624\uparrow$	[d])	0 1
$_{71}Lu^{176}$	7−	$404\downarrow+514\downarrow$	GM [e])	0 0
$_{73}Ta^{178}$	(1+)	$514\uparrow-514\downarrow$	[d])	(1) 0
$_{73}Ta^{178}$	(9−)	$514\uparrow+624\uparrow$	GM	(1) 1
$_{73}Ta^{180m}$	(1+)	$404\downarrow-624\uparrow$	[d])	0 0
$_{75}Re^{186}$	(1−)	$402\uparrow-512\downarrow$	GM	0 0
$_{75}Re^{188}$	(1−)	$402\uparrow-512\downarrow$	GM	0 0 [f])
$_{93}Np^{236}$	(1+)	$523\downarrow-743\uparrow$	GM [e])	1 0
$_{93}Np^{238}$	2(+)	$642\uparrow-631\downarrow$	GM	0 0
$_{95}Am^{242}$	1−	$523\downarrow-622\uparrow$	[g])	0 0

[a]) See Strominger, Hollander and Seaborg [13]) for references to original data.

[b]) See Mottelson and Nilsson [12]) for assignments of odd particle configurations. The zero in this column indicates that the configuration is observed as the ground state configuration for this neutron (or proton) in an odd-neutron (or odd-proton) nucleus. Similarly, a 1 means the state is observed as a first excited state. Parentheses indicate an uncertain assignment.

[c]) Private communication from O. B. Nielsen. I am indebted to him for the permission to use these data in advance of their publication.

[d]) New experimental data [12, 15]) indicate that in Lu and Ta the competition for the ground state configuration is much closer between proton states $514\uparrow$ and $404\downarrow$ than previously thought. The configuration has therefore been reassigned, because proton state $402\uparrow$ apparently occurs at higher excitation energy.

[e]) There has been no change of assignment. The assignment in GM was the result of an error in transcription.

[f]) See Gallagher, Edwards and Manning, Nuclear Physics (to be published).

[g]) Spin as measured by Winocur *et al.* [16]) and configuration as reported by Asaro *et al.* [17]).

TABLE 2

Experimental data on the beta decay of the odd-odd nuclei discussed in this paper, and used in the calculation of log *ft*-values. Beta-branching ratios to the 2+ and 0+ rotational states of the ground state band of adjacent even-even nuclei are compared with the theoretical predictions of Alaga *et al.* [1]) in the last two columns.

Initial nucleus	Spin assignment[a]) $I\pi K$	Final nucleus	Decay fraction[a]) (per cent)		Total decay energy[a]) Q (MeV)	Total half-life[a])	Reduced transition probability ratio	
			0+0	2+0			Theor.	Exp.[a])
Tm^{170}	$1-1$	Yb^{170}	76	24	0.969	129 d	2	1.9 ± 0.2
Lu^{176m}	$1+1$	Hf^{176}	(70)	(30)[b])	1.2	3.71 h	2	
Ta^{178}	$1+1$	Hf^{178}	53	41	1.88	9.3 m	2	≈ 1.4
Ta^{180}	$1+1$	Hf^{180}	(60)	(19)[b])	$1 \leqq Q_{EC} \leqq 2$[c])	8.15 h	2	
Ta^{180}	$1+1$	W^{180}	10	10	0.710	8.15 h	2	≈ 0.5[d])
Re^{186}	$1-1$	W^{186}	6	2	$0.4 \leqq Q_{EC} \leqq 0.8$[c])	89 h	2	≈ 1.4 to 4.0
Re^{186}	$1-1$	Os^{186}	70	22	1.068	89 h	2	2.1
Re^{188}	$1-1$	Os^{188}	79	20	2.12	17 h	2	3.7
Np^{236}	$1+1$	U^{236}	34	9	0.91	22 h	2	3.2
Np^{236}	$1+1$	Pu^{236}	45	12	0.52	22 h	2	3.2
Am^{242}	$1-0$[e])	Pu^{242}	33	49	0.64	16 h	0.5	≈ 0.5
Am^{242}	$1-0$[e])	Cm^{242}	8	12	0.667	16 h	0.5	≈ 0.2
Transitions to excited states								
Ho^{162}	$6-6$	Dy^{162}			$Q_{EC} < 2.5$[f])	68 min[f])		
Ta^{178}	$9-9$	Hf^{178}			$1.6 \leqq Q_{EC} \leqq 2.6$[c])	2.1 h		

[a]) For references to original sources of data see Strominger, Hollander and Seaborg [13]).
[b]) Intensities estimated.
[c]) Energies estimated.
[d]) Although this branching ratio is in better agreement with a $K = 0$, spin 1 state than a $K = 1$, spin 1 state, we prefer the present assignment on the basis of the single-particle states observed for these values of Z and N.
[e]) See refs. [16, 17]).
[f]) See footnote c, table 1.

TABLE 3

Classification of the beta transitions of deformed odd-odd nuclei to the ground states of even-even nuclei in terms of the asymptotic-quantum-number selection-rules

Nuclei	Initial configuration proton neutron	$I\,\pi\,K$	Final configuration	$I\,\pi\,K$	Classification	Log ft observed	Log ft single particle [a])
a) Allowed unhindered							
$Ta^{178} \rightarrow Hf^{178}$	$514\uparrow - 514\downarrow$	$1 + 1$	$514\downarrow - 514\downarrow$	$0 + 0$	au	4.7	4.5
b) Allowed hindered							
$Lu^{176} \rightarrow Hf^{176}$	$404\downarrow - 624\uparrow$	$1 + 1$	$404\downarrow - 404\downarrow$	$0 + 0$	ah	6.5	6.2
$Ta^{180} \rightarrow Hf^{180}$	$404\downarrow - 624\uparrow$	$1 + 1$	$404\downarrow - 404\downarrow$	$0 + 0$	ah	$5.8 \leqq \log ft \leqq 6.4$ [b])	6.2 [c])
$Ta^{180} \rightarrow W^{180}$	$404\downarrow - 624\uparrow$	$1 + 1$	$624\uparrow - 624\uparrow$	$0 + 0$	ah	6.8	6.3
$Np^{236} \rightarrow U^{236}$	$523\downarrow - 743\uparrow$	$1 + 1$	$743\uparrow - 743\uparrow$	$0 + 0$	ah	7.0	not obs.
$Np^{236} \rightarrow Pu^{236}$	$523\downarrow - 743\uparrow$	$1 + 1$	$523\downarrow - 523\downarrow$	$0 + 0$	ah	6.6	not obs.
c) First forbidden, unhindered							
$Re^{186} \rightarrow W^{186}$	$402\uparrow - 512\downarrow$	$1 - 1$	$512\downarrow - 512\downarrow$	$0 + 0$	lu	$7.1 \leqq \log ft \leqq 7.7$ [d])	>6.5 [e])
$Re^{186} \rightarrow Os^{186}$	$402\uparrow - 512\downarrow$	$1 - 1$	$402\uparrow - 402\uparrow$	$0 + 0$	lu	7.7	7.5
$Re^{188} \rightarrow Os^{188}$	$402\uparrow - 512\downarrow$	$1 - 1$	$402\uparrow - 402\uparrow$	$0 + 0$	lu	8.0	7.9
$Am^{242} \rightarrow Pu^{242}$	$523\downarrow - 622\uparrow$	$1 - 0$	$523\downarrow - 523\downarrow$	$0 + 0$	lu	7.3	≈ 5.6 [f])
$Am^{242} \rightarrow Cm^{242}$	$423\downarrow - 622\uparrow$	$1 - 0$	$622\uparrow - 622\uparrow$	$0 + 0$	lu	6.9	≈ 6.2
d) First forbidden, hindered							
$Tm^{170} \rightarrow Yb^{170}$	$411\downarrow + 521\downarrow$	$1 - 1$	$411\downarrow - 411\downarrow$	$0 + 0$	lh	9.0	6.2 [g])

[a]) See Mottelson and Nilsson [12]).
[b]) If $1 \leqq Q_{EC} \leqq 2$ (MeV).
[c]) Observed in beta-decay only.
[d]) If $0.4 \leqq Q_{EC} \leqq 0.8$ (MeV).
[e]) See Thulin *et al.* [18]).
[f]) Mottelson and Nilsson [12]) have pointed out that this anomalously low log ft-value may be due to some small error in the Fermi function for this low energy (21 keV) transition.
[g]) The single particle transition is lu.

TABLE 4

Classification of the beta decay of deformed odd-odd nuclei to excited intrinsic states of even-even nuclei in terms of the asymptotic-quantum-number selection-rules.

Nuclei	Initial configuration proton neutron	$I\,\pi\,K$	Final configuration	$I\,\pi\,K$	Classification	Log ft observed	Log ft single particle [a])
a) Allowed, unhindered							
$Ho^{163} \rightarrow Dy^{163}$	$523\uparrow+642\uparrow$	$6-6$	$523\downarrow+642\uparrow$	$5-5$	au	$\log ft \leqq 5.0$ [b])	4.5
$Ta^{178} \rightarrow Hf^{178}$	$514\uparrow+624\uparrow$	$9-9$	$514\downarrow+624\uparrow$	$8-8$	au	$4.5 \leqq \log ft \leqq 5.4$ [c])	4.5
b) K forbidden transitions [d])							
$Lu^{176} \rightarrow Hf^{176}$	$404\downarrow+514\downarrow$	$7-7$	$404\downarrow-404\downarrow$	$6+0$	K forbidden ($\nu=7$)	18.7	6.4
$Np^{238} \rightarrow Pu^{238}$	$642\uparrow-631\downarrow$	$2+2$	$642\uparrow-642\uparrow$	$2+0$	K forbidden ($\nu=2$)	8.5	not obs.

[a]) See Mottelson and Nilsson [12]).
[b]) If $Q_{EC} \leqq 2.5$ MeV.
[c]) If $1.6 \leqq Q_{EC} \leqq 2.6$ (MeV).
[d]) The decay of most odd-odd nucleides to the ground states of even-even nuclei is K-forbidden. These are included as illustrative examples. The original discussion of K-forbiddenness was given by Alaga *et al.* [8]).

TABLE 5

Classification of the electromagnetic transitions observed between intrinsic states of deformed even-mass nuclei in terms of the asymptotic-quantum number selection rules.

Isotope	Initial configuration	Final configuration	Gamma-ray energy (keV)	Gamma-ray multipolarity	Percent gamma-ray branching [a]	Partial gamma-ray half-life (sec)	Hindrance factor F [b]	ΔI	ΔK	Classification
Eu^{151}	$413\downarrow - 512\uparrow$	$411\uparrow + 521\uparrow$	50	(M3)	$< 2\times10^{-3}$ [c]	$\gtrsim 2\times10^{9}$	$> 5\times10^{6}$	3	3	Non-overlap forbidden
Hf^{179}	$514\downarrow + 624\uparrow$	$514\downarrow - 514\downarrow$ $624\uparrow - 624\uparrow$	88.8	E1	$\geqq 50$ [d]	$\leqq 9.6$	$\leqq 5\times10^{13}$	0	8	K-forbidden ($\nu = 7$)
Hf^{180}	$514\downarrow + 624\uparrow$	$514\downarrow - 514\downarrow$ $624\uparrow - 624\uparrow$	57.6	E1	64 [f]	3.1×10^{4}	4×10^{15}	0	8	K-forbidden ($\nu = 7$)
Hf^{180}	$514\downarrow + 624\uparrow$	$514\downarrow - 514\downarrow$ $624\uparrow - 624\uparrow$	50.1	E3	20 [g]	1×10^{5}	4×10^{9}	0	8	K-forbidden ($\nu = 5$)
Am^{243}	$523\downarrow + 622\uparrow$	$523\downarrow - 622\uparrow$	48.6 [h]	E4	$< 4.0\times10^{-4}$ [i]	$> 8\times10^{13}$	$> 2\times10^{3}$	5	4	K-forbidden ($\nu = 1$)

[a]) Corrected for internal conversion. Experimental data are as quoted in ref. [18]), except where indicated.

[b]) $F = (t_{\frac{1}{2}\,\mathrm{exp}}/t_{\frac{1}{2}\,\mathrm{theor}})$; $t_{\frac{1}{2}\,\mathrm{theor}} = 0.693/\lambda_{sp}$, where λ_{sp} is calculated from the formulae given by Moszkowski [19]).

[c]) Assuming an estimated transition branching of $\leqq 5$ % of beta branching. Only L-shell internal conversion coefficients were considered in estimating the radiative half-life. Sliv and Band's L-shell conversion coefficients [20]) $\alpha_{L_I}+\alpha_{L_{II}}+\alpha_{L_{III}} = 2.3\times10^{3}$ were used. (See ref. [21]) for data).

[d]) Assuming $\alpha_{\mathrm{total}} \leqq 0.5$.

[e]) The degree of forbiddenness ν is defined as $\nu = \Delta K - L = |K_f - K_i| - L$.

[f]) Assuming $\alpha_{\mathrm{total}} = \alpha_L = 0.2$.

[g]) Assuming $\alpha_{\mathrm{total}} \approx 0$.

[h]) Private communication from F. Asaro to F. S. Stephens Jr. I thank Dr. Stephens for this datum.

[i]) Assuming only L-shell internal conversion, where $\alpha_{L\,\mathrm{total}} = \alpha_{L_I}+\alpha_{L_{II}}+\alpha_{L_{III}} = 2.50\times10^{5}$ as determined from the tables of Sliv and Band [20]).

5. Discussion

5.1. Log *ft*-VALUES

Mottelson and Nilsson[12]) have concluded from their extensive review of the log *ft*-values on the beta decay of deformed odd-mass nuclei that the following ranges of log *ft*-values occur for the various degrees of hindrance:

$$4.5 < \log ft < 5.0 \quad \text{(au)},$$
$$6.0 < \log ft < 7.5 \quad \text{(ah)},$$
$$5.5 < \log ft < 7.5 \quad \text{(lu)},$$
$$7.5 < \log ft < 8.5 \quad \text{(lh)}.$$

The log *ft* values in tables 3 and 4 show essentially the same range for hindered and unhindered transitions as do the single-particle transitions in odd-mass nuclei. Particularly striking examples are obtained from the beta decays of the Ta^{178} isomers and Ho^{162}, where the selection rules easily explain the very low log *ft*-values observed. Another good example is Tm^{170} decay, where the large retardation observed in an apparently unhindered transition can be explained by *A*-forbiddenness.

A result predicted by the idea of independent motion of the two odd nucleons is the similarity of the log *ft* values in columns 7 and 8 of table 3. This similarity is evidence that the additional odd nucleon present does not appreciably alter the transition rate of the particle undergoing decay, although the log *ft*-values in column 7 seem to be slightly larger than those in column 8.

The log *ft*-values of 7.7 and 8.0 for the (lu) transitions in Re^{186} and Re^{188} are somewhat larger than is ordinarily observed for this class. However, similar log *ft*-values occur in W^{185} and W^{187}, which are isotones of Re^{186} and Re^{188}. Here, the beta decay is also between neutron state 512↓ and proton state 402↑, and the log *ft*-values are 7.5 and 7.9, respectively. Thus the log *ft*-values of the odd-particle transitions in the odd-mass nuclei support the odd-odd assignments, but the reason for the small transition rate remains undetermined.

5.2. ELECTROMAGNETIC TRANSITIONS

The application of the selection rules to electromagnetic transitions in odd-odd nuclei is limited by the small amount of experimental information available. Theoretically, one of the two significant differences between the spectra of odd-mass and even-mass nuclei to be expected on the basis of the present considerations is that two additional types of isomerism should exist in even-mass nuclei which do not occur in odd-mass nuclei: namely *K*- and "non-overlap"-forbiddenness. *K*-forbiddenness has been known for some time, and several well-established cases are shown in table 5. The observation of a finite transition probability in *K*-forbidden transitions is most certainly due

to a breakdown of the strong coupling description in which off-diagonal terms in the strong-coupling Hamiltonian are present and mix states with different K. K-forbiddenness is observed to result usually in a retardation of $\approx 10^{-2}$ over single-particle rates per unit of K-forbiddenness. (See table 4(b) and table 5). The forbiddenness that results from the vanishing of the overlap integral should probably result in somewhat larger retardations, if the Nilsson wave functions are a good representation of the particle states. In addition, these two particle transitions can also be K-forbidden. A possible example of such a "non-overlap" forbidden transition may exist in Eu^{152}, where two isomers are known to occur with an energy separation of ≈ 50 keV and a spin difference $\Delta I=3$, and no transition is observed between them. It is interesting that the existence of such a new type of isomerism, for which the need was first pointed out by Peker [14])† to explain the Eu^{152} case, follows directly from the product nature of the strong coupling wave function.

The second difference is that both odd-proton and odd-neutron transitions can occur in even-mass nuclei. In odd-odd nuclei, in fact, because of the non-overlap forbiddenness associated with two particle transitions which change both the odd-proton and odd-neutron states simultaneously, the decay of a relatively highly excited state can be expected to occur by a gamma-ray cascade through different neutron states which are coupled to the same proton state, or through different proton states which are coupled to the same neutron state, or, perhaps, by some combination of transitions in which the proton and neutron states change alternately.

An inspection of table 5 indicates clearly, however, that more experimental data on the excited states of odd-odd nuclei are needed.

6. Conclusions

The data shown in tables 3 and 4 indicate that the log ft-values for the beta decay of deformed odd-odd nuclei to intrinsic states of even-even nuclei can

† Although new experimental data now indicate that the previous spin assignment of 1− for Eu^{152m} was incorrect, Peker's conclusion that the isomers must be of a different nature than ordinarily observed still seems valid. Peker's suggestion was that the isomerism is due to different equilibrium shapes rather than different particle configurations, as is suggested here. Moreover, because Eu^{152} with 89 neutrons is just on the edge of the region where strong deformations are known to exist, the strong coupling wave functions and the Nilsson configurations need not necessarily apply. However, the agreement between the value of the experimental magnetic moment and that calculated from Nilsson orbitals [7]) for the 3-ground state indicates that they do, at least for the ground state. The configuration assignment and the prolate deformation assignment of the 0-state are not established. The assignment made by GM is reasonable on the basis of the levels observed in the adjacent odd-mass nuclei, but Peker's interpretation cannot be ruled out, because the present assignment does not explain the greater intensity of beta branching from Eu^{152m} to the Gd^{152} ground state (spherical deformation) relative to that to the Sm^{152} ground state (spheroidal deformation).

be classified according to the selection rules for asymptotic quantum numbers when the odd nucleon configurations are as proposed by GM. Furthermore, the log *ft* values for the odd particle transitions are essentially the same whether the transition takes place in an odd-mass or an odd-odd nucleus. These results, when taken with the previous conclusions of GM on the spins, and those of GM and Hooke[7]) on the magnetic moments of deformed odd-odd nuclei, show clearly that in these nuclei the strong coupling model applies and the odd proton and odd neutron move independently in particle configurations which are well described by the Nilsson wave functions.

I thank Dr. Frank Stephens for several stimulating discussions, and the National Science Foundation for a fellowship held during the time this paper was written. The excellent working conditions provided by Professor Niels Bohr at his institute, and the interest of Professors A. Bohr and B. R. Mottelson in this work, are gratefully acknowledged.

References

1) M. G. Mayer, Phys. Rev. **78** (1950) 16
2) Haxel, Jensen and Suess, Ergeb. Exakt. Naturw. **26** (1950) 244
3) A. Bohr, Mat. Fys. Medd. Dan. Vid. Selsk. **26**, no. 14 (1952)
4) A. Bohr and B. R. Mottelson, Mat. Fys. Medd. Dan. Vid. Selsk. **27**, no. 16 (1953)
5) C. J. Gallagher, Jr. and S. A. Moszkowski, Phys. Rev. **111** (1958) 1782
6) S. G. Nilsson, Mat. Fys. Medd. Dan. Vid. Selsk. **29** (1955) no. 16
7) W. M. Hooke, Phys. Rev. **115** (1959) 453
8) Alaga, Alder, Bohr and Mottelson, Mat. Fys. Medd. Dan. Vid. Selsk. **29**, no. 9 (1955)
9) G. Alaga, Phys. Rev. **100** (1955) 432; Nuclear Physics **4** (1957) 625
10) S. G. Nilsson, dissertation (Berlingska boktryckeriet, Lund, 1955)
11) R. Chasman and J. O. Rasmussen, University of California Radiation Laboratory Report, UCRL-3629 (1956)
12) B. R. Mottelson and S. G. Nilsson, Mat. Fys. Skr. Dan. Vid. Selsk. **1**, no. 8 (1959)
13) Strominger, Hollander and Seaborg, Revs. Mod. Phys. **30** (1958) 585
14) L. K. Peker JETP (USSR) **33** (1957) 191; English translation: Soviet Phys., JETP **6** (1958) 226 (L)
15) A. H. Muir and F. Boehm, Bull. Am. Phys. Soc. **4** (1959) 367
16) Winocur, Marrus and Nierenberg, Bull. Am. Phys. Soc. **4** (1959) 451
17) Asaro, Perlman, Rasmussen and Thompson, Bull. Am. Phys. Soc. **4** (1959) 461
18) Thulin, Rasmussen, Gallagher, Smith and Hollander, Phys. Rev. **104** (1956) 471
19) S. A. Moszkowski in Beta- and Gamma-Ray Spectroscopy, edited by K. Siegbahn (North-Holland Publishing Company, Amsterdam, 1955) Ch. XIII, p. 391
20) L. A. Sliv and I. M. Band, Leningrad Physico-Technical Institute Reports (1956 and 1958); reproduction: Reports ICC 57K1 and ICC 58 LI, issued by Physics Department, University of Illinois (Urbana, Illinois), unpublished
21) Alburger, Ofer and Goldhaber, Phys. Rev. **112** (1958) 1998;
L. Grodzins and A. Sunyar, Phys. Rev. Lett. **2** (1959) 307

1.D.1:
3.A

Nuclear Physics 16 (1960) 231—245; © *North-Holland Publishing Co., Amsterdam*
Not to be reproduced by photoprint or microfilm without written permission from the publisher

ISOMERS IN $N = 81$ NUCLEI

K. KOTAJIMA † and H. MORINAGA †

Department of Physics, Tôhoku University, Sendai, Japan

Received 19 January 1960

Abstract: Two new isomers, Nd^{141m} and Sm^{143m}, were found from the (γ, n) reactions on natural neodymium and samarium. Their energies and half lives as well as those of previously known Ce^{139m} and Xe^{135m} were determined very precisely by careful and repeated measurements. They are

	Energy	Half life
Nd^{141m}	0.755±0.002 MeV	61 ±2 sec
Sm^{143m}	0.748±0.003 MeV	64 ±3 sec
Ce^{139m}	0.746±0.002 MeV	60 ±2 sec
Xe^{135m}	0.528±0.003 MeV	15.65±0.1 min

Systematic variations of the decay characteristics of these four isomers together with those of Te^{133m} and Ba^{137m} are discussed qualitatively.

1. Introduction

It is well known that the matrix elements of M4 transitions take values not far from the Weisskopf's estimate. This is understood as due to the fact that the M4 transitions are, in the majority of the cases, observed between rather well defined single particle levels around the ground states of nuclei. This leads one to the conclusion that a careful study of the M4 transition rates would help one to understand the detailed nature of the shell model wave functions.

One of the investigations done in this spirit is the work of Gupta and Lawson[1]) who calculated the fluctuation of the M4 matrix elements taking into account the effect of the configuration mixing. They conclude that the deviation of the experimental results from the single particle estimate cannot be accounted for by the configuration mixing only and suggest that some other effects, for example meson current in the nuclei, may have to be considered.

Alväger and Oelsner [2]), on the other hand, studied the M4 transition rates between the $h_{\frac{11}{2}}$- and $d_{\frac{3}{2}}$+ neutron states in order to detect any systematic variation of the matrix elements. They attribute the fluctuation only to the radial matrix elements, but no consideration on the effect of the configuration mixing has been taken into account. Their analysis includes nuclei with neutron

† Now at Department of Physics, University of Tôkyô, Bunkyô-ku, Tôkyô, Japan.

numbers ranging from 67 to 81. Therefore, it is not certain that the pertinent states are pure states without configuration mixing.

What we want under such circumstances are more precise data on the purer states. It is usually thought from various evidence that the single-hole states are the purest of all. Accumulation of good data on such purer shell model states, therefore, will help one to understand what is really happening.

At $N = 81$, four M4 transitions from $h_{\frac{11}{2}^-}$ to $d_{\frac{3}{2}^+}$ states have been investigated. They are observed in the decays of ${}_{52}Te_{81}^{133m}$ [3]), ${}_{54}Xe_{81}^{135m}$ [4]), ${}_{56}Ba_{81}^{137m}$ [5]) and ${}_{58}Ce_{81}^{139m}$ [6]). No isomer has been identified yet in ${}_{60}Nd_{81}^{141}$ and ${}_{62}Sm_{81}^{143}$. But it is easy to expect that such isomers may exist.

In the following section we shall describe our investigations on the latter two, previously unknown, isomers. We have also re-measured the energies and half lives of Ce^{139m} and Xe^{135m} with better accuracy. The characteristics of these six isomers will be discussed in the last section.

2. Experimental Procedures and Results

2.1. Nd^{141m}

In order to look for Nd^{141m} which is to be produced from the (γ, n) reaction on Nd^{142}, we irradiated high purity oxide samples (above 99.9 %) of natural neodymium with the 25-MeV bremsstrahlung from the Tôhoku University betatron. Each sample was about 200 mg weight and was placed inside the internal target [7]) for irradiating, where the x-ray flux density was about 10 000 r/min.

From the systematics of the four known isomers with $N = 81$, the half life of Nd^{141m} was expected to be about one minute or so and the energy was expected to be between 0.7 MeV and 0.8 MeV. We observed, therefore, single gamma-ray spectra with a $1\frac{1}{2}'' \times 1\frac{1}{2}''$ NaI(Tl) scintillation spectrometer after one-minute irradiations. An outstanding peak at 0.75 MeV was found to decay with a half life of approximately one minute.

This gamma ray was readily suspected to be due to Nd^{141m} because of the following reasons: Calculating from the abundance ratio of natural neodymium isotopes and the cross section of photoreaction, the intensity of this line was too strong to be assigned to any short-lived praseodymium isotopes produced by the (γ, p) or (γ, np) reaction. One gamma ray having the almost same energy and half life has been found in the decay of Ce^{139} isomeric state which has some possibility to be produced by the $Nd^{143}(\gamma, \alpha)Ce^{139m}$ reaction. But this assignment is also discarded since the (γ, α) cross section cannot be large enough to induce such a strong gamma ray. Neither possible impurity may cause such a strong line.

We attempted very careful series of measurements on the characteristics of this new gamma ray, especially the energy value, since the M4 transition matrix

element is proportional to E_γ^{-9}; the errors in the energy measurement, therefore, will be multiplied by nine in the values of matrix element.

In the single gamma-ray spectra of irradiated Nd_2O_3, the intensity ratio of the 0.75-MeV gamma ray to 0.51-MeV annihilation radiation was approximately one eighth at about 1.5 minutes after the irradiation, and this ratio became rapidly smaller with time. This strong 0.51-MeV gamma ray is almost entirely due to O^{15} produced by the (γ, n) reaction on O^{16}. This gamma ray caused much counting loss of the 0.75-MeV gamma ray when the pulse height spectrum was recorded with a 100-channel analyzer which has a maximum dead time of

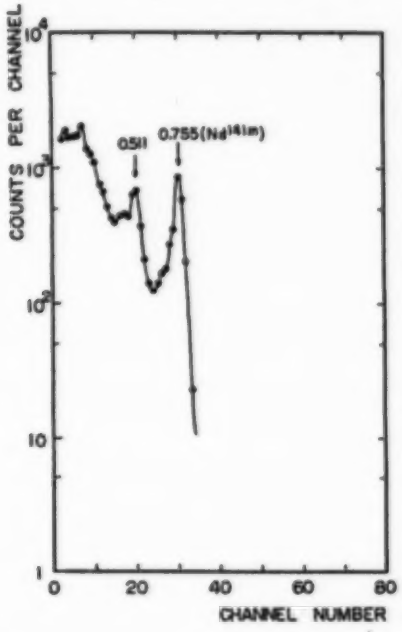

Fig. 1. Gamma-ray spectrum observed from photodisintegration of neodymium at about 2 min after a 1-min irradiation.

1.4 msec. Also, too-high counting rate could cause the shift of the observed spectrum.

In order to remove this disturbing activity, each irradiated sample was dissolved into 0.5 ml of hot 6*N* HCl and was fumed to dryness. The sample was, then, quickly mounted on the face of a NaI(Tl) scintillator. It took only about 2 minutes before starting to count from the termination of the bombardments.

In order to get the best resolution of the system, which is essential for the precise energy determination, we selected the best combination out of three $1\frac{1}{2}'' \times 1\frac{1}{2}''$ NaI(Tl) crystals and five 6292 DuMont photomultipliers. The energy resolution of this combination for 0.662-MeV line of Cs^{137} was 6.8 %.

The linearity of the system was checked in the energy region between 0.192 MeV and 1.277 MeV with seven known lines of In^{114}, Na^{22}, Cs^{137} and Zn^{65}. This calibration was made twice for each running, once before and once after

the energy measurements. Nine good measurements were done and in all cases the both calibration curves agreed within the statistical error which was less than 5 keV. One of the observed spectra is shown in fig. 1.

The weighted mean was calculated from these measurements and the isomeric transition energy was determined as

$$E_\gamma = 0.755 \pm 0.002 \text{ MeV}.$$

For the measurement of the half life of this gamma ray, a $4'' \times 4''$ NaI(Tl) scintillator was used for increasing the statistics. Instead of using the 100-channel analyzer with long dead time, a single channel analyzer which has dead

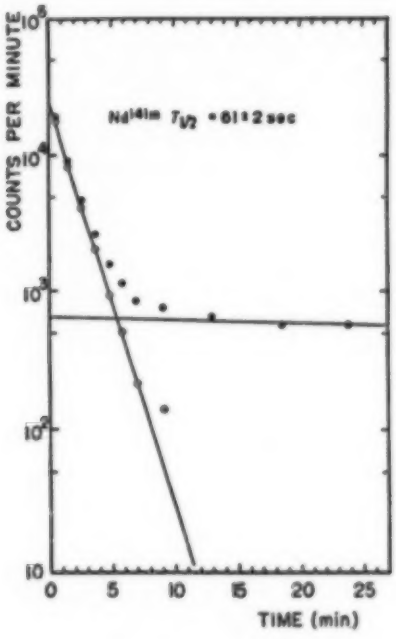

Fig. 2. Decay curve of the 0.755-MeV gamma ray. Long component is due to the 2.42-h Nd^{141s}.

time of $\approx 4\,\mu$sec was employed. The dead time was experimentally checked by the two source method. It is proved that no correction for counting loss is necessary for treating our data. On the other hand, to see the time drift of this system, a narrow window was set at about a half-height point of high energy side of 0.662-MeV photopeak of Cs^{137}, and this counting rate was watched for long time. The energy resolution of this system for 0.662-MeV line of Cs^{137} was 12.3 %.

Seven known lines in In^{114}, Na^{22}, Cs^{137} and Zn^{65} were used for the energy calibration of the single channel analyzer. The window of this analyzer was adjusted to the photopeak of the isomeric transition. Each irradiated sample was treated chemically as described above before counting. The decay was then followed for at least 40 minutes in each measurement with two Flip-Flop scaling down units and a E1T scaler. One of the obtained decay curves is shown in fig. 2.

Taking into account the cross section of photoreaction and the observed gamma-ray spectra in energy measurements, the long component in these decay curves was easily identified to be due to the decay of 2.42-h Nd^{141} ground state. This state was produced by the (γ, n) reaction on Nd^{142} which was the competing reaction to produce Nd^{141m}.

From the weighted mean of seven independent determinations, the half life and its error were determined as

$$T_{\frac{1}{2}} = 61 \pm 2 \text{ sec.}$$

In order to see if the observed decay is due to the M4 transition, the internal

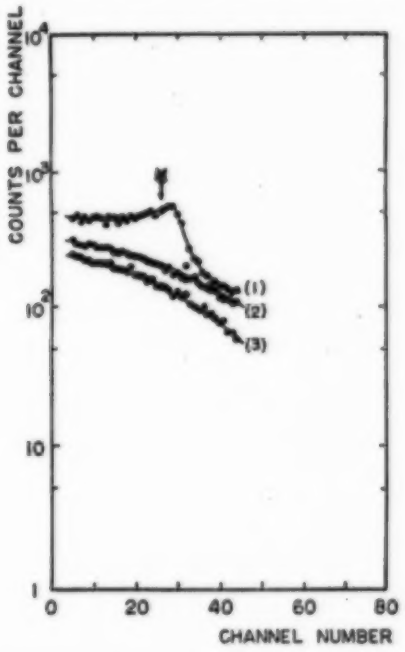

Fig. 3. Internal conversion electron spectrum of the isomeric gamma ray of Nd^{141m} measured with an anthracene scintillator. Curves (1), (2) and (3) show each spectrum obtained at 2 min 25 sec, 15 min 10 sec and 43 min 50 sec after the irradiation, respectively. The arrow shows the position of the 0.624-MeV internal conversion line in Cs^{137}.

conversion electrons following the decay of Nd^{141m} were looked for with an anthracene scintillator. For preparing a beta-ray source as soon as possible, we bombarded 300 mg of $NdCl_3$ sample as the target. The irradiated sample was dissolved into 0.5 ml of distilled water containing a half drop of HCl. This solution was removed on a piece of aluminium foil placed on a glass plate and was dried. The plate was previously heated with an infra-red lamp to dry the sample quickly.

The anthracene crystal used was 12 mm in diameter and 7 mm in thickness. Its resolution for the 0.624-MeV internal conversion line of Cs^{137} was about 15 %. The observed spectra are shown in fig. 3. Curves (1), (2) and (3) show each spectrum obtained at 2 min 25 sec, 15 min 10 sec and 43 min 50 sec after the

irradiation, respectively. The arrow shows the position of 0.624-MeV internal conversion line of Cs^{137}.

From this result the internal conversion coefficient for Nd^{141m} decay was roughly calculated as

$$2\,\% < \alpha < 40\,\%.$$

This value of α is consistent with the value expected for the M4 transition.

2.2. Sm^{143m}

From the systematics of the four known isomers and the newly added Nd^{141m}, the half life and the isomeric transition energy of Sm^{143m} were expected

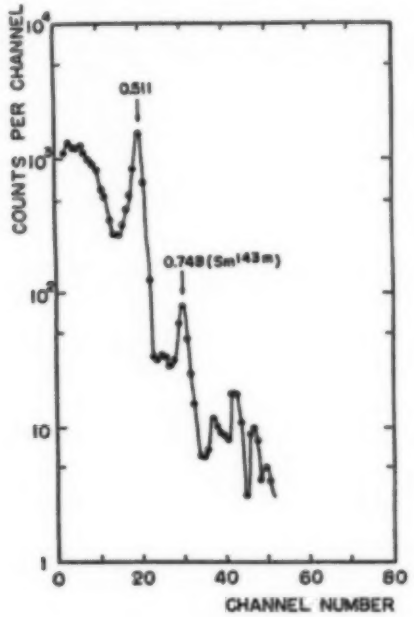

Fig. 4. Gamma-ray spectrum observed from photodisintegration of samarium at about 3 min after a 1-min irradiation.

to be about between 20 sec and 1 min, and between 0.7 MeV and 0.8 MeV, respectively.

Following the same procedure as the case of Nd^{141m}, a gamma ray at ≈ 0.75 MeV which decay with a half life of approximately 1 min was observed. In this case, however, the abundance of the target nucleide was $\frac{1}{10}$ compared with the case of Nd^{141m} and the positons from 8.8-min Sm^{143g} (see appendix) were unavoidable. One of the spectra obtained after removing O^{15} activity is shown in fig. 4.

The weighted average value of the energy determined as a result of five times measurements done with the same set-up as before was

$$E_\gamma = 0.748 \pm 0.003 \text{ MeV}.$$

The measurement of half life was more seriously disturbed by the 8.8-min activity of the Sm^{143g}. This is mostly because of the lower intensity of the gamma line and the existence of the 8.8-min ground state decay. Of the latter, no gamma ray was reported, but our preliminary observations soon revealed that there must be some high energy gamma rays. Any gamma ray higher than 0.75 MeV can cause some counts at the window we set for detecting Sm^{143m}. Also the high energy positons ($\approx$ 2.3 MeV) can cause counts in the window by annihilation in flight and the sum peak due to one annihilation gamma and one back scattered gamma.

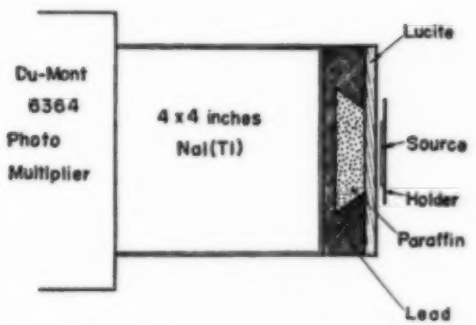

Fig. 5. Detailed picture of the slit used in the measurement of Sm^{143m} half life.

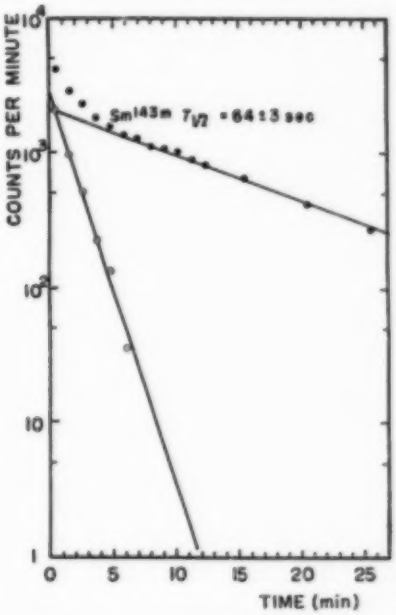

Fig. 6. Decay curve of the 0.748-MeV gamma ray. Long component is due to the 8.8-m Sm^{143g}.

In order to go around these difficulties, we first measured the decay characteristics of Sm^{143g} more precisely, especially its half life, since the exact value of the half life was needed for subtracting the unavoidable contributions of Sm^{143g} from the decay curve from which the half life of Sm^{143m} was obtained. The result of the measurement of the decay properties of Sm^{143g} is described in Appendix.

Secondly, an effort was made for minimizing the effects from positons. A slit whose picture is shown in fig. 5 was used in front of the $4'' \times 4''$ crystal. This reduced the Sm^{143g} contribution to the decay curve in proportion to Sm^{143m} by a factor of 2 to 3. We also tried to use some other types of absorber.

Finally, we performed some bombardments with decreased energy and dispensed with the chemistry, since in this case the time wasted for chemistry was more serious because of the influence of the longer component. One of the decay curves obtained under such conditions is shown in fig. 6.

With all these precautions we repeated the measurements fifteen times using various conditions for irradiation and counting. The weighted average value and the error of the half life of Sm^{143m} were thus determined as

$$T_{\frac{1}{2}} = 64 \pm 3 \text{ sec.}$$

2.3. Ce^{139m}

As seen in fig. 13, the matrix element of the decay of Ce^{139m} calculated from the previous data [6]) does not fall on a smooth line. Also the error in the previous measurement is larger than the errors in our measurements on Nd^{141m} and

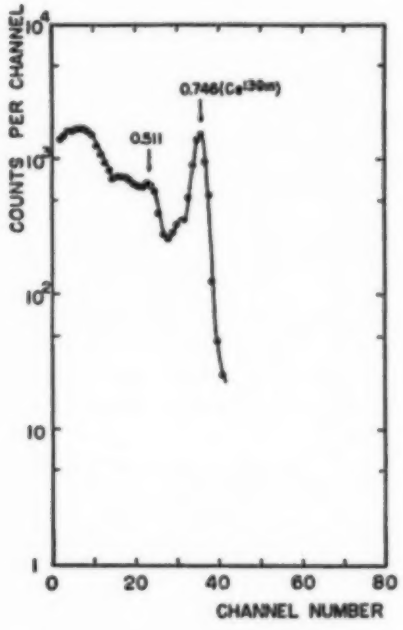

Fig. 7. Gamma-ray spectrum observed from photodisintegration of cerium at about 2 min after a 1.5-m irradiation.

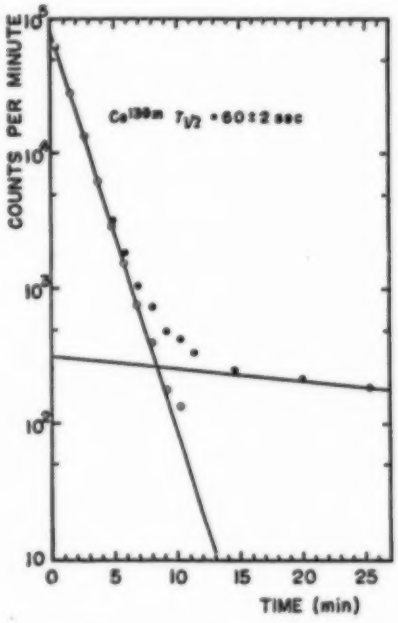

Fig. 8. Decay curve of the 0.746-MeV gamma ray

Sm^{143m}. Besides, the difficulties in the measurement of Ce^{139m} using the (γ, n) reaction should be less because of the high abundance of Ce^{140}(88.5 %) and the absence of any other confusing activity. Therefore, we tried to improve the data on Ce^{139m} by using the same method as employed for the measurements described above.

One difference in this case is the fact that CeO_2 does not dissolve in acid so readily as other oxides. But, since the amount of the Ce^{139m} activity produced is very enough, we bombarded CeO_2 for 1.5 min with 18-MeV bremsstrahlung.

The energy was thus determined from the weighted average value of eight measurements to be (see fig. 7)

$$E_\gamma = 0.746 \pm 0.002 \text{ MeV}$$

and the half life was determined from three measurements as (see fig. 8)

$$T_{\frac{1}{2}} = 60 \pm 2 \text{ sec.}$$

These values differ slightly from the previous determination [6]).

2.4. Xe^{135m}

In the estimation of the matrix elements from previous data (see fig. 13), the error in Te^{133m} is mostly caused by its large error in the beta-branching and the error in the Xe^{135m} measurement is mainly due to the error in its energy measurement. For the latter, it seemed to be possible to improve the results with similar measurements of energy and half life.

Xe^{135m}, however, was produced from the fission of uranium by slow neutron bombardment. A 100 mg uranium dioxide sample was irradiated in the JRR-1 reactor of Japan Atomic Energy Research Institute for one hour at the flux of 0.9×10^{12} neutrons/cm^2 · sec. After letting the short-lived activities die away, the irradiated UO_2 was dissolved into 10 ml of 6N HNO_3 and heated nearly to boiling. In order to remove effectively the long-lived fission gases which piled up from other fission products, helium scavenging gas was sent into the nitric acid solution for 10 minutes through a thin glass pipe at the rate of 5 ml/sec. After washing with the helium gas, the nitric acid sample solution was removed in a flask which was connected to a charcoal gas trap cooled with dry ice.

Ten minutes later, the 15-min Xe^{135m} which had been decaying from the 6.7-h I^{135} was milked on the charcoal. An iodine trap was used to prevent the active iodine to follow the gas before collecting the xenon on the charcoal. This charcoal trap containing Xe^{135} was mounted on the face of a 3″×3″ NaI(Tl) scintillation spectrometer and was cooled with dry ice during the measurement. The use of dry ice was essential, because at dry ice temperature krypton was scarcely collected on the charcoal. By this procedure, practically no other fission gas having strong activity but Xe^{135} was obtained.

The resolution of the spectrometer for 0.662-MeV gamma ray of Cs^{137} was 9.1 %. The pulse height spectrum was recorded on a RCL 256-channel analyzer. Ce^{144}, Au^{198}, Na^{22}, Cs^{137}, Mn^{54} and Zn^{65} sources were used to check the linearity and for the energy calibration. One of the spectra thus taken is shown in fig. 9.

As seen in this spectrum, a very strong line with an energy of ≈ 0.53 MeV was observed to decay with a half life of 15.6 min. This is definitely a peak due to Xe^{135m} from its energy and the half life, and also from the fission yield of I^{135} and the lapse of time before counting.

The isomeric transition energy of Xe^{135m} was determined from seven careful measurements. The weighted average value and the error were obtained as

$$E_\gamma = 0.528 \pm 0.003 \text{ MeV.}$$

The half life was determined from the observed decay curve of the 0.528-MeV

gamma-ray photopeak recorded by the multichannel analyzer. Since in this analyzer the dead time is automatically corrected, the data were directly plotted. Fig. 10 shows such a decay curve. The long component is due to the 9.2-h Xe^{135g}. The build up of this long component does not affect its subtraction because the channel was not taken to contain much of the contribution of the

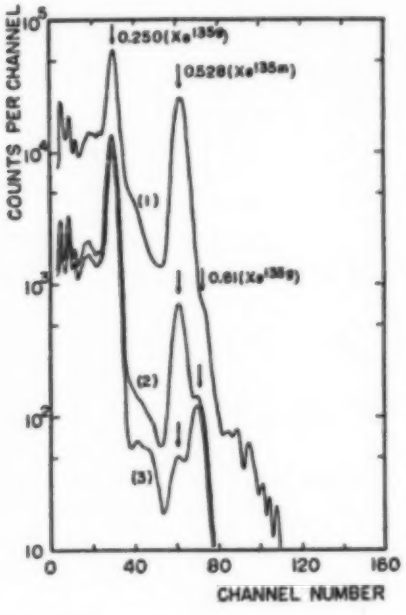

Fig 9. Gamma-ray spectrum observed from photodisintegration of xenon. Curves (1), (2) and (3) show each spectrum obtained at 15 min, 60 min and 120 min after the milking, respectively.

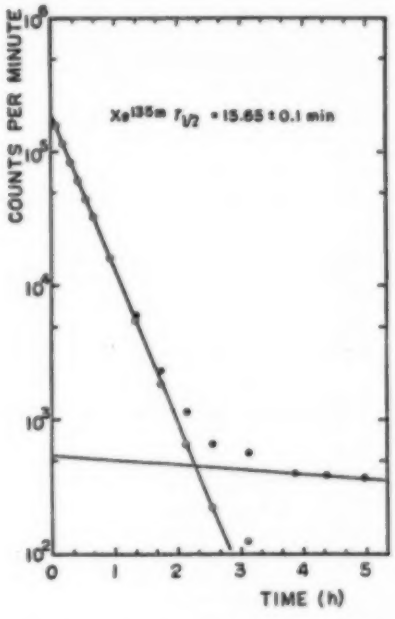

Fig. 10. Decay curve of the 0.528-MeV gamma ray. Long component is due to the 9.20-h Xe^{135g}.

0.61-MeV gamma ray and in the decay of Xe^{135g} the branching ratio to cause this 0.61-MeV gamma ray is only 3 %.

The half life thus obtained is

$$T_{\frac{1}{2}} = 15.65 \pm 0.1 \text{ min.}$$

3. Discussion

3.1. ENERGIES OF THE ISOMERIC STATES

Decay properties of the six isomers in $N = 81$ nuclei are summarized as a function of proton numbers in fig. 11. The values of the half lives are the partial half lives of the gamma transitions and the internal conversions, thus for Te^{133m} the half life is not the observed half life but was corrected for the beta-branching. In all other cases, the half lives are the observed half lives. Except for Te^{133m} and Ba^{137m} the values are taken from the present investigation.

Interesting points about the proton-number dependence of the isomeric

energy is its remarkably smooth rise and also its slight bend which makes the energy of Sm^{143m} lower than that of Nd^{141m}. This smooth rise is qualitatively explained from the shell model calculation by Bleuler and Terreaux [8]). Using

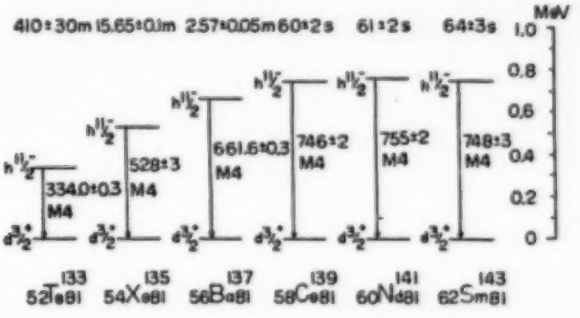

Fig. 11. Decay characteristics of the isomers in $N = 81$ nuclei. The values of half lives are the partial half lives for the gamma transitions and the internal conversions.

diffused well potentials, they calculate the binding energies of single nucleons in various shell model states as a function of A. A part of such a diagram is schematically shown in fig. 12. Since the height of the $h_{\frac{11}{2}}$ state above the $d_{\frac{3}{2}}$ ground state is the difference between these curves, the smooth rise is readily accounted for. The bend of the curve, however, seems to be much larger than

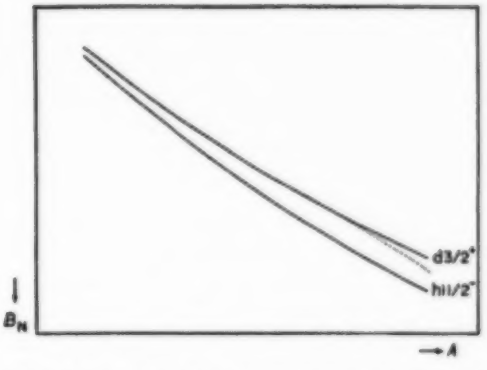

Fig. 12. Binding energies of the $h_{\frac{11}{2}}$- and the $d_{\frac{3}{2}}$+ neutrons in diffused potentials, schematically reproduced from ref. [8]).

expected from the results of such a calculation. Unfortunately, the errors in the measurements of the binding energies are not small enough to allow one to decide which of the $h_{\frac{11}{2}}$ and the $d_{\frac{3}{2}}$ states, is responsible for this bend. It would be extremely interesting to know which one is responsible.

One may, however, make some guess about the reason for this bend. As long as one considers a uniform potential, it may be difficult to expect such a large bend. The cause of the bend must be looked for in somewhere else, in some particular characteristic of this region, say, some shell effect in the proton shell. At this Z, protons are expected to fill, after the $Z = 50$ shell, from the $g_{\frac{7}{2}}$ state;

then later, the $d_{\frac{3}{2}}$ states should come in. When these states fill up two by two, it is not expected that the $g_{\frac{7}{2}}$ states first fill up completely and then the $d_{\frac{3}{2}}$ states come in, because of the possibility of configuration mixing. In the actual situation, it is thought that the amplitude of the $g_{\frac{7}{2}}$ states is at first higher, and then the $d_{\frac{3}{2}}$ states start to have larger amplitude as the proton number increases. This is suspected to be so since in the parallel case in even nuclei, the height of the 2^+ states usually changes rather smoothly. As to the value of the actual mixing ratio, this a question to which we do not have a definite answer.

However, such an effect probably causes some configuration mixing in the $d_{\frac{3}{2}}$ neutron-hole state. Let us consider qualitatively how this change of the mixing ratio affects the height of the $h_{\frac{11}{2}}$ and the $d_{\frac{3}{2}}$ neutron-hole states. Because of the difference of the angular part of the wave function, the change of the mixing ratio in the proton shell will not affect the height of the $h_{\frac{11}{2}}$ state so seriously. However, there must be more effect on the $d_{\frac{3}{2}}$ states since the $d_{\frac{3}{2}}$ proton state has almost exactly the same spatial wave function as the $d_{\frac{3}{2}}$ neutron state. Therefore, on addition of the $d_{\frac{3}{2}}$ protons, the $d_{\frac{3}{2}}$ neutron state should come down lower than expected from a single uniform potential, and when the $d_{\frac{3}{2}}$ protons start to fill, the neutron state should acquire additional binding energy. Such a shift of the single particle states is shown by dashed line in fig. 12. The bend of the energy-vs-proton number curve may be explained from such an effect. Since there are eight $g_{\frac{7}{2}}$ protons, it is expected that the bending starts around Ce^{139} and actually this is the case. If this view is correct, the order of the proton shell must be considered to be fairly well preserved inside the nuclei, that is, the paired proton states are not considerably mixed up.

Actually the magnetic moment of Ba^{137} ground state is 0.82 of the Schmidt value but at the Ce^{139} ground state the ratio becomes 0.74. This may also be explained from the fact that the mixing starts to be serious after around proton number eight.

3.2. TRANSITION MATRIX ELEMENTS

Fig. 13 shows the matrix elements for the gamma transition of these isomers. For correcting for the internal conversion, the conversion coefficients calculated by Rose [9]) were used. The values and the errors in previous measurements are drawn with closed circles and dashed lines. The new values give a smoother line. The ordinate is the ratio of the measured matrix elements and the single particle estimate. The latter is taken from Moszkowski's result [10]). Since the theoretical value depends very much on the nuclear radius or more precisely the way to take the radial wave functions, and since in this paper only a very rough estimate is made, the absolute scale does not mean much for the comparison.

The value for Sm^{143m} seems to be a little higher than the smoothly extrapolated line, but this could be due to some positon branchings in the decay. In

our measurement such small branchings, which could occur because of the high decay energy, could be ignored.

It may not be safe to draw any quantitative conclusion without calculation but it seems to be rather difficult to attribute such a large change in M4 matrix elements in $N = 81$ isomers only to the configuration mixing, especially since at Ba^{137} the value of magnetic moment is so close to the Schmidt value.

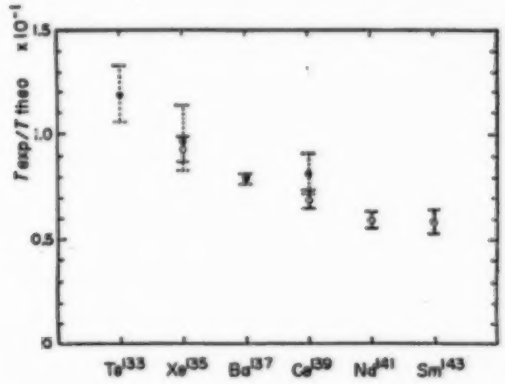

Fig. 13. Ratios of the observed gamma transition matrix elements to the single particle estimate for isomers in the $N = 81$ nuclei. Points with open circles are from present investigation and the closed circles are the weighted average values of previous data.

On the contrary, the radial matrix element, which can be calculated with a realistic potential, could cause such difference. Since the interaction for M4 transition includes r^5, the edge of the nucleus should have a decisive effect on the transition rates. The edge of the wave function, however, depends very much on the binding energy of the nucleon. Qualitatively speaking, the higher the

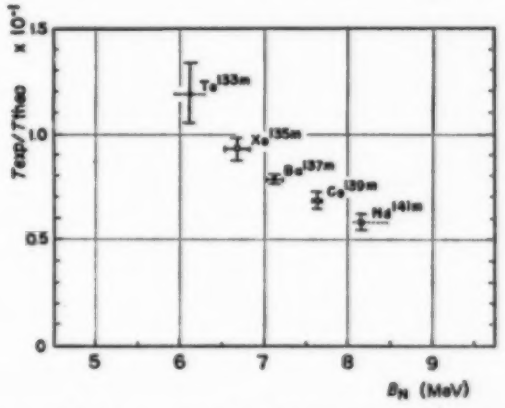

Fig. 14. Gamma transition matrix elements plotted against the binding energies of the $d_{\frac{1}{2}}$ neutrons (B_n) in the $N = 81$ nuclei.

binding energy, the smaller the edge of the wave function, thus the less the transition rate should be. Fig. 14 shows the plot of the transition rate against

the binding energy and the tendency is what is expected from such a simple consideration.

The authors wish to thank Dr. S. Ichiba for letting them use his equipment and for his kind help during the chemical procedure to prepare the Xe^{135m}.

Appendix

THE DECAY PROPERTIES OF Sm^{143g}

In order to observe the high energy gamma rays following the decay of Sm^{143g} and to obtain the precise half life of Sm^{143g} produced by the (γ, n) reaction on Sm^{144}, we irradiated 200 mg of high purity samarium oxide sample

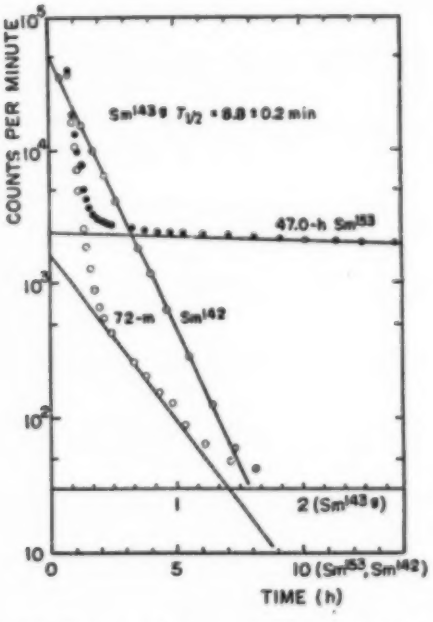

Fig. 15. Decay of the activities produced on samarium after a 8.5-min irradiation. Each long component is assigned to be due to 47.0-h Sm^{153} produced by the (γ, n) reaction on Sm^{154} and 72-m Sm^{142} produced by the $(\gamma, 2n)$ reaction on Sm^{144}, respectively.

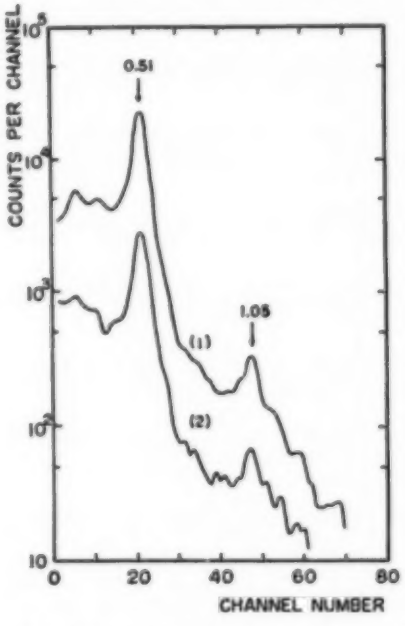

Fig. 16. Gamma ray spectrum observed from photo-disintegration of samarium. Curves (1) and (2) show each spectrum obtained 5.5 min and 52 min after the 8.5 min irradiation, respectively.

in the internal target [7]) for 8.5 minutes with the 25-MeV bremsstrahlung. The irradiated sample was inserted between a Geiger-Müller counter and the $4'' \times 4''$ NaI(Tl) scintillation spectrometer used in other measurements.

Because of the very high initial counting rate an accurate value of the dead time of the Geiger-Müller counter is indispensable for the precise correction of counting loss. The dead time of this counter for a certain voltage set at the center of the plateau was measured independently with the two source method and a synchro-scope to be 172 ± 5 sec. Fig. 15 shows a decay curve corrected with this value.

Taking into account the abundance ratio of samarium sample and the cross section of photoreaction, the longest component was assigned to be due to 47.0-h Sm^{153} produced by the (γ, n) reaction on Sm^{154} of which the abundance ratio is 22.5 %. As seen in fig. 15, the 72-m Sm^{142} produced by the $(\gamma, 2n)$ reaction on Sm^{144} was detected. After the subtraction of these two long components, using the least square fit, we obtained the half life of Sm^{143g} as

$$T_{\frac{1}{2}} = 8.8 \pm 0.2 \text{ min.}$$

The measurement of the half life was made four times changing the bombarding energy and using some lucite absorbers to avoid the effects from longer components. In each measurement the decay was followed at least 15 hours in order to subtract the long component precisely.

The gamma-ray spectrum obtained using the $4'' \times 4''$ NaI(Tl) scintillation spectrometer is shown in fig. 16. A weak gamma ray of 1.05 MeV with a half life of approximately 9 minutes and some other weaker high energy gamma rays were observed. This 1.05-MeV gamma ray is assigned to Sm^{143g} from its half life.

References

1) K. K. Gupta and R. D. Lawson, Phys. Rev. **114** (1959) 326
2) T. Alväger and G. Oelsner, Arkiv f. Fysik **12** (1957) 319
3) T. Alväger and G. Oelsner, Arkiv f. Fysik **12** (1957) 319
   A. C. Pappas, MIT Technical Report **63** (1953) 109; Phys. Rev. **87** (1952) 162; **81** (1951) 299A;
   P. H. Abelson, Phys. Rev. **56** (1939) 1
4) W. Riezler, Naturwiss. **31** (1943) 326;
   T. B. Novey and J. D. Knight, NNES **9** (1951) 1043;
   H. Götte, Naturwiss. **28** (1940) 449;
   C. S. Wu and E. Segrè, Phys. Rev. **67** (1945) 142;
   R. L. Heath and N. P. Alley, quoted by K. Way *et al.*, Nuclear Data Sheets (Nuclear Data Project, Washington, D. C. 1959);
   W. C. Peacock, A. R. Brosi, D. A. Bogard, Plutonium Project Mon N-432 (1947) 58; ORNL-176 (1948) 25; ORNL-65 (1948) 64
5) W. C. Peacock, quoted by K. Way *et al.*, Nuclear Data Sheets (Nuclear Data Project, Washington, D. C. 1959);
   A. C. G. Mitchell and C. L. Peacock, Phys. Rev. **75** (1949) 197;
   J. Townsend, M. Cleland and A. L. Hughes, Phys. Rev. **74** (1948) 499
   D. E. Muller, H. C. Hoyt, D. J. Klein and J. W. M. DuMond, Phys. Rev. **88** (1952) 775;
   G. Lindström, K. Siegbahn and A. H. Wapstra, Proc. Phys. Soc. B **66** (1953) 54;
   G. A. Graves, L. M. Langer and R. D. Moffat, Phys. Rev. **88** (1952) 344;
   S. K. Bhattacherjee and B. R. Brosi, Phys. Rev. **103** (1954) 190
6) B. H. Ketelle, H. Thomas and A. R. Brosi, Phys. Rev. **103** (1956) 190
7) H. Morinaga and T. Kuroyanagi, Nuclear Instruments **6** (1959) 66
8) K. Bleuler and Ch. Terreaux, Helv. Phys. Acta **30** (1957) 183
9) M. E. Rose, Internal Conversion Coefficients, (North-Holland Publishing Company, Amsterdam, 1958)
10) K. Siegbahn, Beta- and Gamma-ray Spectroscopy, (North-Holland Publishing Company, Amsterdam, 1955), Ch. XIII

1.D.1:5

Nuclear Physics **16** (1960) 246—263; © *North-Holland Publishing Co., Amsterdam*

Not to be reproduced by photoprint or microfilm without written permission from the publisher

SPECTRE α DU ^{214}Bi ET REMARQUES SUR QUELQUES ÉMETTEURS α DU Bi

R. J. WALEN et G. BASTIN-SCOFFIER

Laboratoire de l'Aimant Permanent, Centre National de la Recherche Scientifique, Paris

Reçu le 23 novembre 1959

Abstract: Alpha-spectrography of ^{214}Bi(RaC) shows, beside the 2 known groups, 4 other weak ones. Energies and intensities are, in MeV and 10^{-6} units: 5.512(82) — 5.448(116) — 5.268 (12.5) — 5.184(1.3) — 5.023(0.45) — 4.941(0.52). Systematics of hindrance factors of Bi α-emitters suggest a shell-model interpretation of the corresponding levels, which show, for the 208 and 210 isotopes of Tl, the same sequence of multiplets.

1. Introduction

Les développements théoriques concernant les mouvements collectifs nucléaires ont déplacé l'intérêt de la majorité des recherches récentes, sur les émissions α, vers les nucléides où de tels phénomènes se présentent à l'état le plus pur possible, c'est-à-dire loin des nombres Z et N dits magiques.

Par contre, le modèle en couches non compliqué de mouvements collectifs ne trouve plus son domaine d'application, pour les corps lourds, qu'à proximité immédiate du ^{208}Pb. Parmi les nucléides peu connus de cette région figure ^{210}Tl, dont les niveaux ne peuvent être atteints qu'à partir du faible embranchement α du ^{214}Bi.

De nombreux travaux récents ayant complété les connaissances des schémas de niveaux des nucléides de $Z = 81$, 82 et 83 et de N voisin de 126, nous avons repris la spectrographie α de ^{214}Bi(RaC) avec le spectrographe à aimant permanent du Centre National de la Recherche Scientifique.

1.1 HISTORIQUE

Le spectre α du ^{214}Bi a été établi par spectrographie magnétique par Rutherford *et al.* en 1933 [1]). Le spectre est difficile à étudier, l'embranchement α n'étant que de quelques 10^{-4}. On est donc très gêné par le fond qui, dans le dépôt actif du Radon, provient de ^{214}Po(RaC'), produit par l'embranchement β du ^{214}Bi. Les périodes relativement courtes ($\approx \frac{1}{2}$ heure) font que la source décroît rapidement durant les préparatifs d'une expérience soignée et qu'il faut des intensités initiales élevées. Ces faits expliquent que l'étude de ce spectre n'a pas été reprise sérieusement depuis sa première détermination.

2. Partie Expérimentale

2.1. SOURCE

Le dépôt actif est obtenu par activation sur une petite surface de platine dans un appareil permettant la récupération du Rn. La feuille de platine est ensuite chauffée dans le vide à 400° pour détruire les substances chimiques azotées co-déposées. Le dépôt actif est alors distillé, suivant une technique déjà décrite, sur une feuille mince de pyrex, couverte d'une légère couche d'Al pour diminuer les pertes par recul, enfin montée dans une capsule fermée par une deuxième feuille de pyrex. L'ensemble des opérations, de l'arrêt de l'activation jusqu'à la mise en route de la pose, exige 40 minutes.

2.2. ÉNERGIES

La source étant couverte, il est nécessaire de prendre certaines lignes sur la plaque nucléaire comme étalon d'énergie. Nous avons utilisé:

1) le ^{218}Po(RaA) qui, grâce au temps mort de 40 minutes, a une intensité qui en permet le dépouillement;

2) le ^{210}Po qui s'accumule à travers ^{210}Pb et ^{210}Bi(RaD et RaE) et pour lequel il faut poser de l'ordre d'une semaine, quelques semaines après la mort du dépôt actif rapide. Une légère correction est à apporter à l'énergie trouvée par suite du recul. Cette correction, calculée à partir de la quantité de Po qui quitte la source (mais reste dans la capsule), est inférieure à quelques keV.

2.3. INTENSITÉS

Nous avons beaucoup insisté sur la détermination absolue de l'intensité, par suite de la grande différence existant entre les résultats antérieurs et les nôtres (voir tableau 1).

Les sources obtenues par distillation ne permettent pas de mesurer d'une façon absolue l'intensité. La proportion Pb/Bi se modifie en effet durant la distillation et le mélange obtenu est équivalent à un dépôt actif de durée d'existence différente du dépôt actif initial. La grande intensité initiale de la source ($\approx$ 20 mc) et sa décroissance rapide ne permettent pas, avant la pose, d'identifier le rapport ^{214}Bi/^{214}Pb au moyen de la courbe d'intensité. Le RaC', enfin, donne évidemment sur les plaques une surexposition énorme empêchant toute lecture. D'autre part, après la pose, la source est trop près de son état d'équilibre pour qu'on puisse encore déterminer, d'après la décroissance, un rapport Bi/Pb assez précis pour pouvoir remonter au temps $t = 0$.

Nous avons utilisé trois méthodes, toutes sujettes à erreur, mais qui ont donné des indications concordantes:

1) On compare l'intensité de RaC à celle de la raie de structure fine du RaC'', que nous avons trouvée lors d'un travail précédent [2]) et dont l'intensité absolue, de même ordre de grandeur, est connue à ± 7 %.

2) On prépare une source témoin dans des conditions en tous points identiques à celles de la préparation de la source principale, et on suit au compteur α son évolution complète avant et après distillation. Les rapports Bi/Pb étant connus, on peut interpréter les mesures de la source principale, faites au compteur après la pose.

3) On utilise l'intensité de la raie du ^{210}Po obtenue en vue de l'étalonnage en énergie. A cet effet on calcule les quantités de RaD formées pendant l'activation et entre la fin de l'activation et la distillation, la quantité perdue pendant la distillation (d'après la modification, connue, du rapport Bi/Pb) et enfin, en valeur relative, celle qui correspond au RaC détruit durant la pose et après celle-ci. Ceci permet d'interpréter l'intensité de la ligne ^{210}Po, avec une certaine incertitude, car les calculs concernant l'évolution d'une filiation de 8 corps (Rn jusqu'à Po), avec modification en cours de route des proportions (rapports RaA/RaB/RaC et rapport RaD/RaE), sont très longs et nécessitent à plusieurs reprises des approximations. D'autres inconnues sont ici: perte de RaD par recul de RaC', gain de RaD détaché par recul des parois durant l'activation, forme chimique du RaD qui ne garantit pas une distillation strictement identique de RaB et RaD.

3. Résultats

Les trois méthodes citées dans le paragraphe précédent donnent pour l'embranchement α du RaC, respectivement: $2.2-2.05-2.05\times10^{-4}$. Nous avons adopté $(2.1\pm0.13)\times10^{-4}$.

La figure 1 montre le spectre α du ^{214}Bi avec, superposée, la raie du Po obtenue dans la pose longue. On y voit six raies dont les énergies et intensités sont précisées dans le tableau 1.

En vue de comparer les résultats obtenus avec d'autres isotopes de la famille du Bi, nous avons joint au tableau des données concernant le ^{212}Bi pour lequel des intensités plus précises ont été déterminées par une succession de poses décroissantes d'un dépôt actif à l'équilibre. Les énergies sont basées sur ^{210}Po et ^{218}Po et, pour le ^{212}Bi, sur la détermination absolue de Rytz [3]).

La pose avec ^{214}Bi précise certains points que nous n'avons pu fixer avec certitude lors d'un travail précédent sur la famille du Ra [2]):

1) La raie notée alors At_1 n'apparaît pas sur le spectre du dépôt actif et appartient donc bien à ^{218}At.

2) Une raie douteuse située derrière Rn (ref. [2]), p. 916) et non attribuée avec certitude n'a pas été retrouvée et est, par suite, explicable comme élargissement accidentel (recul, diffusion, etc. . . .) de la raie du Rn.

3) Par contre, sur cette même pose de Ra, nous avons recompté avec soin la région située dans la descente de ^{210}Po et on y trouve bien l'indication de la raie RaC_2.

TABLEAU 1

Groupe	Énergie (MeV)	ΔE_α	$h\nu$ (keV)	Intensité relative (%)	Intensité absolue	
^{214}Bi 0	5.512	0	0	39.2 $\pm$0.3	0.82×10^{-4}	Raies trouvées par Rutherford *et al.* [1]) avec des intensités respectives de 1.8×10^{-4} et 2.2×10^{-4}
1	5.448	63.8	65	53.9 $\pm$0.3	1.16×10^{-4}	
2	5.268	244 $\pm$0.5	249	5.8 $\pm$0.1	1.25×10^{-5}	$\pm$6 %. Énergie relative à $E_\alpha(^{210}\mathrm{Po}) = 5.304$ MeV
3	5.184	328 $\pm$1	336	0.61$\pm$0.06	1.3×10^{-6}	
4	5.023	489 $\pm$2	498	0.21$\pm$0.04	4.5×10^{-7}	
5	4.941	571 $\pm$2	581	0.25$\pm$0.05	5.2×10^{-7}	
^{212}Bi 0	6.086	0	0	27.1	9.1×10^{-3}	Énergie absolue de Rytz [3]).
1	6.047	39	39.8	69.7	2.35×10^{-1}	
2	5.764	322	328	1.78	6×10^{-3}	Différence d'énergie des niveaux 19.45$\pm$0.05 keV
3	5.622	464	473	0.165	5.5×10^{-4}	
4	5.603	483	492	1.19	4×10^{-3}	
5	5.477	609	621	0.014	4.7×10^{-5}	
6	5.341	745	759	10^{-3}	3.4×10^{-6}	
7	5.298$\pm$0.002	788	803	$1.1\times10^{-4}\pm10^{-5}$	3.7×10^{-7}	Vérifié par décroissance que non attribuable à ^{210}Po

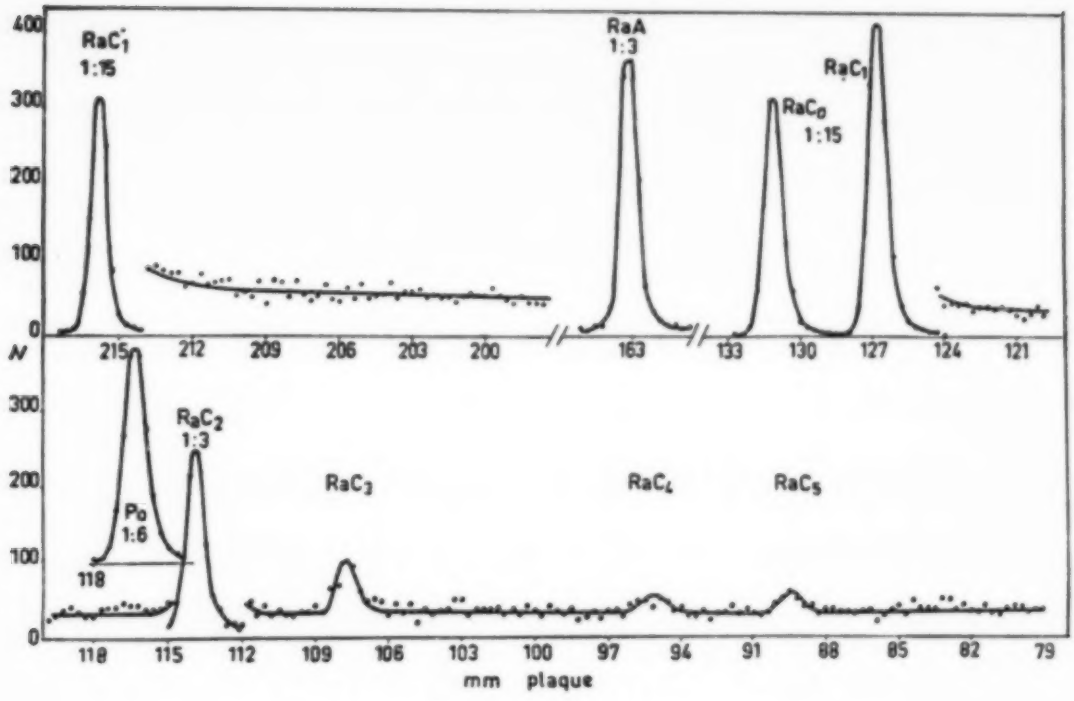

Fig. 1.

4. Discussion des émissions α des isotopes du Bi

Les isotopes du Bi pour lesquels nous avons récemment précisé des lignes de structure fine α (210, 212, 214) se trouvent placés dans le voisinage immédiat du ^{208}Pb. Dans cette région, le modèle en couches devrait permettre de classer un certain nombre de niveaux au moyen de configurations n'intéressant qu'un nombre très limité de nucléons. L'écart de la forme sphérique, très faible, et le nombre de nucléons participant à la formation de niveaux excités font que peuvent être négligés, pour les faibles excitations ($\approx$ 1 MeV) l'apparition de mouvements rotationnels ou de multiplets de Nilsson. Néanmoins, certains travaux théoriques récents montrent, dès que le nombre de nucléons (ou trous) „libres" excède 1, que les configurations ne sont plus pures. Des calculs poussés ont été effectués, par exemple sur le ^{208}Pb avec des hypothèses relativement différentes par Miss Kearsley [4]) et par True et Ford [5]): les mélanges de configurations sont importants, la configuration principale n'entre souvent que pour 50 % dans le mélange. Pour les isotopes de Bi et Tl, dont il est question ici, une configuration proposée ne peut donc être que la configuration dominante lorsque d'autres configurations de même spin peuvent exister.

Dans ce qui suit nous avons essayé d'utiliser sous sa forme simple le facteur d'empêchement † ($F = \log_{10}(T_e/T_c)$, T_e représente la période partielle expéri-

† Notre facteur F correspond approximativement à $-\log_{10} F$ de Fröman.

mentale relative à une raie α, et T_c la période calculée pour un noyau sphérique, en posant, comme d'autres auteurs l'ont déjà plus ou moins proposé, $F = F_c + F_s$, où F_c est le facteur centrifuge classique pour noyaux sphériques et où F_s est un facteur indiquant la difficulté de pré-formation de la particule α. Une indétermination évidente concerne le rayon nucléaire à adopter. En fait, celui-ci est inconnu et, pour le Bi, ne peut s'extrapoler à partir des émetteurs plus lourds: le cas du Tl est trop spécifique, ce noyau est situé dans une région à forte variation du rayon en fonction de Z et N. Le facteur F_s contient donc implicitement un terme inconnu qui devient une constante pour une structure fine donnée, et la comparaison des F_s relatifs à divers nucléides n'est pas instructive si aucune hypothèse plausible n'a été faite quant au rayon moyen. Ce genre de discussion n'est pas nouveau et fut déjà introduit il y a plus de 25 ans par Gamow, des contributions majeures étant dues ultérieurement à Feather, à Berthelot, à Nordström, à Perlman et Rasmussen et à Asaro [31]).

Les données expérimentales qui se sont accumulées les dernières années et le fait que ce n'est que très près du ^{208}Pb que les formules simples pour noyaux sphériques peuvent s'appliquer nous ont fait reprendre l'examen de cette région, afin d'utiliser les transitions α à l'établissement d'un schéma de niveaux là où d'autres types de rayonnements ne peuvent suffire à cela.

Nous avons adopté comme suite des niveaux pour particules impaires celle qui résulte surtout des études effectuées sur les noyaux qui ne diffèrent du ^{208}Pb que d'un seul nucléon, c'est-à-dire ^{207}Pb, ^{209}Pb, ^{207}Tl, ^{209}Bi, niveaux d'ailleurs confirmés en général par un certain nombre de noyaux différant du ^{208}Pb par un nucléon plus une ou plusieurs paires:

protons: $2d_{\frac{3}{2}}$, $2d_{\frac{5}{2}}$, $3s_{\frac{1}{2}}$ | $1h_{\frac{9}{2}}$, $2f_{\frac{7}{2}}$,

neutrons: $3p_{\frac{3}{2}}$, $2f_{\frac{5}{2}}$, $3p_{\frac{1}{2}}$ | $2g_{\frac{9}{2}}$, $1i_{\frac{13}{2}}$.

4.1. ^{210}Bi

Les données expérimentales des dernières années ont permis d'éclaircir beaucoup le schéma de ce nucléide et de ^{206}Tl. Elles sont les suivantes:

^{210}Bi(RaE) [5, 7]). Deux groupes α, par spectrographie magnétique:

groupe	E_α	I/désint.	T_α
1	4.686	0.5×10^{-6}	9×10^{11} sec
2	4.649	0.75×10^{-6}	6×10^{11} sec

S'il existe d'autres groupes: $T_\alpha > 6 \times 10^{13}$ sec.

Pas de transition fondamentale. Spins: RaE : 1^-, ^{206}Tl : 0^-.

^{210}Bi* [8–12]). La vie de cet isomère est calculée d'une façon très indirecte à partir de la section de capture ^{209}Bi(n, γ), dont le bilan est partagé entre les formations de RaE et ^{210}Bi*. Il en résulte [9]) $T = (8 \pm 2) \times 10^{13}$ sec. Comme nous

l'avons indiqué précédemment, cette valeur est une limite supérieure, d'autres processus pouvant exister pour expliquer une fraction de la section de capture, sans pour autant avoir été détectés dans les conditions expérimentales données.

TABLEAU 2

Rayonnements du $^{210}Bi^*$

N° du groupe α et niveau	E_α (MeV)	T_α (sec)	γ en coïncidence (keV)
(1)	5.13	$\approx 8 \times 10^{16}$	non mesuré
(2)	4.93	1.35×10^{14}	260
(3)	4.89	2.35×10^{14}	(260) – 300
(4)	4.59	1.6×10^{15}	260 – 300 (?) – 340 – 600
(5)	4.48	$\approx 1.6 \times 10^{16}$	non mesuré

Par mesures à la chambre d'ionisation (α) et au cristal (γ) Golenetskii *et al.* [11,12]) attribuent au $^{210}Bi^*$ les rayonnements du tableau 2.

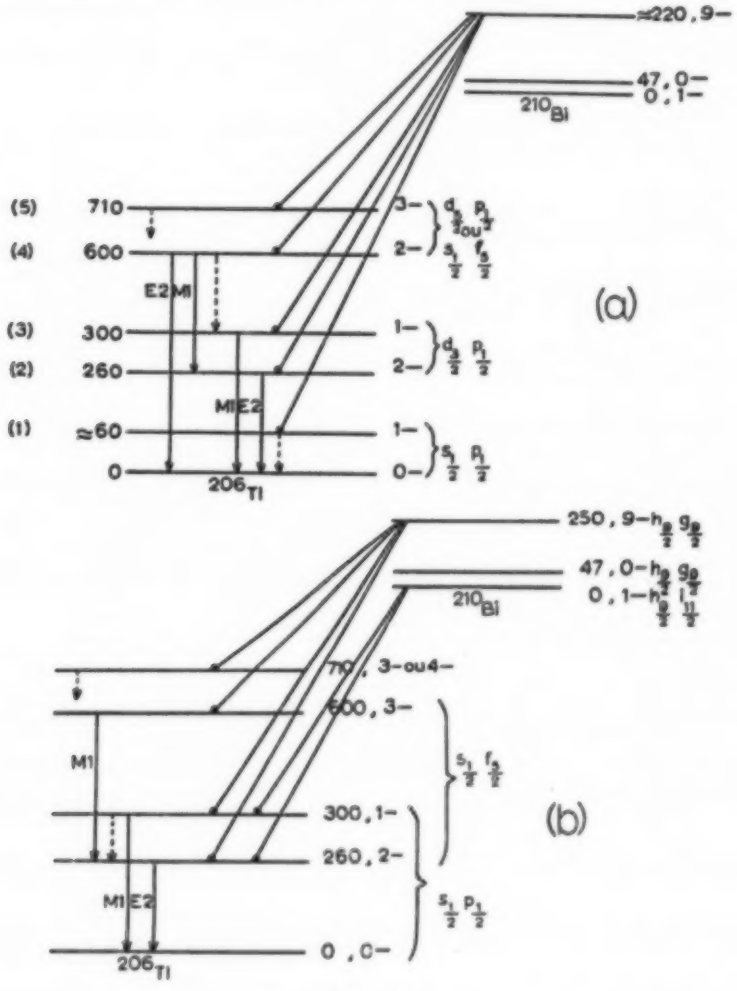

Fig. 2.

Tandis que Lévy et Perlman [8]) observent une accumulation de Po à partir de ^{210}Bi* avec une période partielle de 3.10^{16} sec, Golenetskii *et al.* [12]) n'observent pas le rayonnement α correspondant et donnent comme limite $T_\gamma > 3\times10^{17}$ sec. Le schéma proposé par ces auteurs [12]) est reproduit, en ce qui nous intéresse ici, figure 2a.

En réunissant les données concernant ^{210}Bi$_{1^-}$ et ^{210}Bi$_{9^-}$, on trouve un accord sur les points les plus importants, mais on peut suggérer quelques modifications dans les interprétations pour tenir compte des facteurs d'empêchement. Le ^{206}Tl étant un noyau pratiquement sphérique, un choix convenable des moments angulaires l_{min} et l'application du coefficient centrifuge sous sa forme simple $F_c = c'l(l+1)$ doivent conduire à une valeur à peu près constante pour tous les groupes α observés. Pour déterminer F et F_c nous avons utilisé des constantes que nous justifierons dans les conclusions. On trouve ainsi les résultats du tableau 3.

TABLEAU 3

Détermination des facteurs F pour ^{210}Bi

Niveau de ^{206}Tl	atteint par ^{210}Bi$_{9^-}$				atteint par ^{210}Bi$_{1^-}$				Choix du spin
	F	l_{min}	F_s	Spin	F	l_{min}	F_s	Spin	
(1)	10.5	≦8	>7.1	>0	>5.8				?
(2)	6.8	8	3.4	1$^-$ ou 2$^-$	2.8	2	2.5	2$^-$ ou 3$^-$	2$^-$
(3)	6.7	8	3.3	1$^-$ ou 2$^-$	2.4	0	2.4	1$^-$	1$^-$
(4)	5.4	6	3.4	3$^-$ ou 4$^-$	>2.8	>2	>2.4	>2$^-$	3$^-$
(5)	≈5.6	6	≈3.6	3$^-$ ou 4$^-$					3$^-$ ou 4$^-$

Les groupes α les plus intenses aboutissant aux niveaux (2) et (3) donnent des indications concordantes et fixent l'énergie du niveau 9$^-$ de ^{210}Bi* à ≈ 250 keV. Quant au niveau (1) proposé par Golenetskii *et al.* [12]), il possède des caractéristiques si peu communes qu'il est plus raisonnable d'attribuer le groupe α correspondant à autre chose que ^{210}Bi$_{9^-}$: ce groupe aurait un empêchement inexplicable d'au moins 3000($\Delta F_s > 3.5$) par rapport aux autres groupes. La transition ^{210}Bi$_{1^-} \xrightarrow{\alpha}$ (1) n'a pas été observée par nous quoiqu'elle eût dû présenter une intensité notable. Enfin, la transition (2) → (1), M1, serait inobservable à côté de (2) → (0), E2, ce qui est hautement improbable pour un noyau presque sphérique de masse paire.

Pour la même raison, la désexcitation de (4) proposée par Golenetskii *et al.* [12]), où des rayonnements E2 et M1 sont en concurrence, semble peu probable. Les noyaux impairs voisins de ^{208}Pb peuvent montrer des transitions multipolaires très anormales:

$f_{\frac{7}{2}} \rightarrow f_{\frac{5}{2}}$ dans ^{207}Pb : M1/E2 ≈ $\frac{1}{17}$ [13])

$[(p_{\frac{1}{2}})^2 f_{\frac{7}{2}}] \rightarrow [(p_{\frac{1}{2}})^2 f_{\frac{5}{2}}]$ dans ^{205}Pb : M1 ≪ E2 [14])

$d_{\frac{3}{2}} \rightarrow d_{\frac{5}{2}}$ dans ^{203}Tl : M1/E2 ≈ $\frac{1}{9}$ [15]),

qui permettent de concevoir une concurrence entre transitions $\Delta I = 1$, non et $\Delta I = 2$, non, partant du même niveau. Mais une étude comparative des noyaux pairs ($^{202, 204}$Pb et $^{202, 204}$Tl) [16]) dans la même région, montre que toutes les transitions y sont multipolaires simples, avec pas ou très peu de mélange. Il se peut que le pic observé à 600 keV, en coïncidence avec le groupe α allant vers (4), soit dû à un effet additif, dans le cristal, de deux γ en cascade (voir par exemple Girgis et van Lieshout [17]) qui ont étudié systématiquement le „pile up"). Cette hypothèse est renforcée, et par l'apparition d'un pic correspondant à deux fois l'énergie K_α du Tl, pic faible dans les coïncidences observées avec le groupe α le plus intense et attribuable dans ce cas aux photons secondaires Compton du γ260, et par la faible intensité γ qui a certainement motivé des mesures avec grand angle solide (d'après Golenetskii *et al.* [11]), sur le cristal, $\approx$ 1 photon/sec en coïncidence avec $E_\alpha = 4.59$ MeV).

Ces considérations nous font préférer le schéma b de la figure 2. Les configurations proposées ne sont que des possibilités, motivées parce que les séparations des doublets de la figure 2a (respectivement 60, 40 et 110 keV) semblent trop faibles pour l'interaction entre nucléons situés à l'intérieur des deux couches fermées. Dans les nucléides $^{202, 204}$Tl par exemple (fondamental $[s_{\frac{1}{2}} f_{\frac{5}{2}}]_{2^-}$, la séparation du doublet fondamental 2^- 3^- est supérieure à 490 keV pour 202, et à 410 keV pour 204, le niveau 3^- n'étant pas observé dans la cascade où il aurait été très apparent, car il aurait donné un rayonnement M1 en concurrence avec le E2 existant. Le premier niveau excité est 4^-, c'est-à-dire appartient au quadruplet $d_{\frac{5}{2}} f_{\frac{7}{2}}$, ce qui laisse supposer que l'état fondamental n'est *pas* $[s_{\frac{1}{2}} p_{\frac{3}{2}}]_{2^-}$ avec maintien d'un nombre pair de neutrons dans la couche $2f_{\frac{7}{2}}$.

Etant donné la faible excitation de $^{210}Bi_{9^-}$, F_s devrait avoir une valeur voisine du F_s de $^{210}Bi_{1^-}$(RaE), la préformation de la particule α ne devant pas présenter de différence notable. Une mesure plus directe de la période de $^{210}Bi_{9^-}$ serait souhaitable, au moyen par exemple de l'activité spécifique après plusieurs cycles de séparation isotopique. La période qui donnerait ici un bon accord serait de 4 à 6×10^5 ans.

La structure du RaE a été admise pendant longtemps comme étant $(f_{\frac{7}{2}p} g_{\frac{9}{2}n})_{1^-}$. Très récemment cependant, Newby et Konopinski [18]) ont montré qu'une interaction T entre proton $h_{\frac{9}{2}}$ et neutron $i_{\frac{13}{2}}$ pouvait déplacer de près de 0.8 MeV un des niveaux par rapport à l'autre et donner comme état fondamental $(h_{\frac{9}{2}p} i_{\frac{13}{2}n})_{1^-}$. Peut-être une fraction du ΔF_s entre les états 1^- et 9^- du ^{210}Bi (respectivement hi et hg prélevés extérieurement aux couches fermées) s'explique ainsi †.

† Les évaluations numériques n'ont porté que sur les niveaux 0^- et 1^-. Cependant Newby et Konopinski [18]) estiment, contrairement à Pryce [21]), que des niveaux de spin élevé ne peuvent intervenir que pour des énergies très élevées, ce qui laisse sans explication l'état isomérique.

4.2. ^{212}Bi

De préparation facile en sources intenses, ^{212}Pb(ThB) et ^{212}Bi(ThC) sont parmi les corps radioactifs les plus étudiés. Plusieurs recherches, dont surtout celles de Horton [19]), ont montré que l'état fondamental de ^{212}Bi est 1^- (distribution angulaire $\alpha-\gamma$) et que le fondamental et le premier niveau de ^{208}Tl ont des spins 5^+ et 4^+ (rayonnement γM1, vie de cet état excité, analyse du doublet α).

Les rayonnements β et γ de $^{212}\text{Pb} \xrightarrow{\beta} {}^{212}\text{Bi}$ ont été étudiés en dernier par Krisyouk *et al.* [20]) dont les résultats confirment ceux de Horton, les log *ft* et la multipolarité des γ s'accordant au mieux avec une suite de niveaux 1^-, 0^-, 1^-, 0^-. Aucun renseignement bien entendu n'existe sur l'emplacement des niveaux de spin plus élevé, niveaux qui sont possibles, mais qui ne peuvent être excités ici, car les transitions β se font de préférence vers les niveaux 1^- et 0^-, et les transitions γ mesurables sont toutes M1.

Krisyouk *et al.* ont proposé comme configuration de neutrons, pour les quatre premiers niveaux, $[(i_{\frac{13}{2}})^3]_{1^-}$, $[(i_{\frac{13}{2}})^2 g_{\frac{9}{2}}]_{0^-}$, $[(i_{\frac{13}{2}})(g_{\frac{9}{2}})^2]_{1^-}$, $[(g_{\frac{9}{2}})^3]_{0^-}$.

Etant donné l'ordre des niveaux pour un neutron isolé, cette inversion complète entre 1i et 2g est difficile à accepter. L'interaction entre un proton $h_{\frac{9}{2}}$ et un neutron $i_{\frac{13}{2}}$, telle qu'elle est calculée par Newby et Konopinski [18]), doit se saturer rapidement. Si on admet contrairement à Pryce [21]) que la configuration la plus stable du multiplet $[h_{\frac{9}{2}} g_{\frac{9}{2}}]$ n'est pas nécessairement 0^-, etcompte tenu de ce que l'énergie de formation d'une paire $i_{\frac{13}{2}}$ est plus élevée que celle d'une paire $g_{\frac{9}{2}}$, l'interaction spéciale entre $h_{\frac{9}{2}p}$ et $i_{\frac{13}{2}n}$ permet de proposer, pour les quatre premiers niveaux de ^{212}Bi, les deux configurations $[h_{\frac{9}{2}}(i_{\frac{13}{2}})^2 g_{\frac{9}{2}}]$ donnant 1^- puis 0^-, et $[h_{\frac{9}{2}}(g_{\frac{9}{2}})^3]$ donnant 1^- puis 0^-. Si, comme il est probable, il y a un certain mélange de configurations i^2g et g^3 dans les deux cas, on évite alors partiellement les difficultés signalées par Krisyouk *et al.* [20]) à propos de leur schéma: rayonnements γ à transitions de deux ou trois particules qui devraient être beaucoup plus freinés que ceux qui sont observés.

Cet ordre des niveaux peut paraître arbitraire. Nous avons raisonné comme suit. Les calculs de Pryce sur le ^{210}Bi utilisent l'approximation sans interaction et sans mélange de configurations où le fondamental est $[h_{\frac{9}{2}} g_{\frac{9}{2}}]_{0^-}$. D'après la position maintenant connue de $[h_{\frac{9}{2}} g_{\frac{9}{2}}]_{0^-}$ vis à vis du niveau 0^- (200 keV), on peut admettre pour $[h_{\frac{9}{2}} g_{\frac{9}{2}}]_{1^-}$, en première approximation, $\approx$ 100 keV. Le niveau 0^-, à configuration unique, reste le même en approximation supérieure. Mais de nombreuses configurations peuvent fournir un niveau de spin 1^-, et l'interaction de configuration repoussera le plus bas en énergie de ceux-ci d'une quantité pouvant atteindre aisément 200 ou 300 keV. Tout dépend ainsi de l'ordre dans lequel se classent les configurations 1^- en l'absence d'interaction. Nous avons admis, d'après les calculs de Newby et Konopinski, que $[h_{\frac{9}{2}} i_{\frac{13}{2}}]_{1^-}$ et $[h_{\frac{9}{2}} g_{\frac{9}{2}}]_{1^-}$ sont proches dans les Bi pairs, quoique évidemment écartés par l'effet de répulsion, et que le premier est le fondamental de ^{210}Bi (pour lequel le faible

Q_β de RaD ne permet pas de mettre en évidence le niveau 1^- suivant), tandis que le second est le fondamental de ^{212}Bi où le niveau 1i devient occupé par une paire. Dans ce dernier cas, le nombre plus important de configurations de spin 1^- augmente la répulsion et place donc encore plus haut le premier niveau 0^-. Pour ^{214}Bi, le nombre de nucléons atteignant 6, la complexité des mélanges doit déjà rendre très floue la notion de configuration dominante. En proposant ces configurations, notre but a été d'essayer de lier d'une façon simple le type de transition α et le facteur F_α, afin que ce dernier constitue à son tour un moyen d'interprétation.

L'interprétation possible des groupes α émis par ^{212}Bi se trouve résumée dans le tableau 4. La première interprétation théorique concernant les groupes 0 à 5 a été calculée par Pryce[21]) qui a prévu pour le doublet $[s_{\frac{1}{2}}^{-1}g_{\frac{9}{2}}]$ les spins 5 et 4, et pour le quadruplet $[d_{\frac{3}{2}}^{-1}g_{\frac{9}{2}}]$, par ordre croissant d'énergie: 3, 6, 4, 5. Cet ordre est incompatible avec l'ordre 4, 5, 3, 6 indiqué par l'expérience en se laissant conduire par les facteurs F et par les coefficients de conversion des rayonnements γ déterminés par Nielsen [22]). En particulier, l'emplacement du niveau 3^+ ne laisse pas de doute. Dans le tableau 4 nous avons indiqué, là où des valeurs de l sont possibles pour la transition α, les pourcentages du mélange qui donnent à F_c une valeur telle que F_α reste constant. Ces mélanges sont très élevés et ne coïncident pas avec les prévisions théoriques, en particulier pour le cas du doublet $[s_{\frac{1}{2}}g_{\frac{9}{2}}]$ où les mesures de distribution angulaire $\alpha-\gamma$ de Horton[19]) ont permis d'en évaluer la proportion ($\approx 80\ \%\ l_3 + 20\ \%\ l_5$). Aussi nous les présentons comme une donnée empirique sans chercher à les expliquer. On remarque que pour ^{212}Bi et ^{214}Bi, il en est ainsi pour toutes les transitions de ce type ($1^- \rightarrow 2n^+$). Les deux groupes 6 et 7 ne peuvent s'expliquer avec la même valeur 1.8 de F_α commune aux six premiers groupes. Deux niveaux $[s_{\frac{1}{2}}^{-1}i_{\frac{13}{2}}]$($5^+$, $l = 5$, et 6^+, $l = 5$ et 7) ne peuvent s'accorder avec la différence 0.8 entre les deux facteurs F. L'excitation du nucléide est encore trop faible pour admettre des états de parité —, aussi la seule possibilité qui nous est apparue est d'attribuer à ces deux niveaux la forme $[d_{\frac{3}{2}}^{-1}i_{\frac{13}{2}}]$, 6^+ et 7^+, l'augmentation de F_α pouvant s'expliquer au moyen de la formation de la particule α qui, au lieu d'utiliser une paire de neutrons extérieurs, prélève ceux-ci dans deux couches différentes (d'où un empêchement supplémentaire).

Une difficulté sérieuse de cette explication est l'absence expérimentale de $s_{\frac{1}{2}}^{-1}i_{\frac{13}{2}}$ et l'absence de toute autre raie α d'intensité supérieure à $\frac{1}{3}$ de la raie 7: il faut admettre une inversion entre le doublet et le quadruplet, c'est-à-dire une interaction très faible entre proton 3s et neutron 1i, et au contraire très forte entre proton 2d et neutron 1i. Par rapport aux multiplets formés avec le neutron 2g, l'énergie moyenne du doublet vis à vis du quadruplet s'est déplacée d'au moins 700 keV.

4.3 ^{214}Bi

L'interprétation de la structure fine du RaC nécessite avant tout la connaissance du niveau fondamental. De nombreuses propositions de spin se basant sur diverses systématiques ont été faites précédemment: 1^- par King [23]), 2^- par Wapstra [24]), 3^- par Feather [25]). La seule mesure directe a été effectuée par Demichelis et Radicati [26]) qui ont étudié la corrélation $(\beta_{2.6}/\gamma_{0.61})$ entre le spectre β qui aboutit au premier niveau excité de ^{214}Po et le γ qui succède. La corrélation trouvée permet d'éliminer à priori tous les états autres que 1^- et 2^-. Le choix de ces auteurs s'est porté sur 2^-, avec mélange T et S, car 1^- nécessiterait des termes d'interférence élevés et peu probables (0^- est de toutes façons éliminé à cause du spectre α qui présente nettement un doublet $s_{\frac{1}{2}}$).

Nous pensons néanmoins que les arguments pour 1^- restent très forts:

1) *Systématique des log ft.* En utilisant les intensités des embranchements β du ^{214}Bi déterminés par Ricci et Trivero [27]), on trouve:

$$
\begin{aligned}
^{210}\mathrm{Bi}_{1^-} &\rightarrow {}^{210}\mathrm{Po}_{0^+} &&: \approx 8\\
^{212}\mathrm{Bi}_{1^-} &\rightarrow {}^{212}\mathrm{Po}_{0^+} &&: \approx 7.64\\
^{212}\mathrm{Bi}_{1^-} &\rightarrow {}^{212}\mathrm{Po}_{2^+} &&: \approx 7.8\\
^{214}\mathrm{Bi} &\rightarrow {}^{214}\mathrm{Po}_{0^+} &&: \approx 8\\
^{214}\mathrm{Bi} &\rightarrow {}^{214}\mathrm{Po}_{2^+} &&: \approx 8\\
^{212}\mathrm{Pb}_{0^+} &\rightarrow {}^{212}\mathrm{Bi}_{1^-} &&: \approx 6.7\\
^{214}\mathrm{Pb}_{0^+} &\rightarrow {}^{214}\mathrm{Bi}_{\text{fondamental}} &&: \approx 6.5.
\end{aligned}
$$

Si 2^- était admis pour ^{214}Bi, on aurait des transitions β $\Delta I = 0$, oui et $\Delta I = 2$, oui, et on aurait dû trouver, en gros et respectivement, log $ft \approx 9$ et ≈ 7.5. Au point de vue systématique, on est tenté de donner à ^{214}Bi le même spin qu'à ^{210}Bi et ^{212}Bi.

2) *Structure fine de* ^{218}At. Nous avons montré [2]) qu'il y a deux groupes α, pour lesquels $F = 0.3$ et 1.3, et conduisant vers des niveaux distants de 45 ± 3 keV. Nous avons réexaminé ce spectre, et, malgré la statistique pauvre, il apparaît comme impossible d'identifier cette différence d'énergie avec celle du premier niveau excité du ^{214}Bi(53 keV). Cet intervalle de 53 keV n'apparaît donc pas dans le spectre α de ^{218}At et une transition α doit être interdite, soit vers le niveau fondamental, soit vers le niveau de 53 keV. Ce niveau est caractérisé par

(a) le rayonnement γ qui est M1,

(b) la proportion de rayonnement β qui l'atteint, bien plus faible que celle qui aboutit au niveau fondamental (rayonnement non détecté par coïncidence $\beta-\gamma$) [28, 29]).

Il faut donc pour le niveau 53 keV un spin supérieur d'une unité à celui du fondamental. Aucun de ces deux niveaux ne pouvant être 0^-, c'est ^{218}At qui doit avoir ce spin pour qu'une interdiction soit possible. Dans ce cas, il reste

comme schémas possibles des premiers niveaux et en tenant compte des valeurs de F, ceux de la figure 3.

Sur ces schémas nous avons fait figurer les plus intenses seulement des nombreuses transitions γ, mais qui sont ici particulièrement importantes: le niveau 295 alimente les niveaux 53 et 0, les deux transitions sont M1. Ce niveau 295 a donc le même spin que l'un des niveaux 53 ou 0. Or, le rayonnement β correspondant qui a un log $ft = 5.2$ ne peut être que $\Delta I = 0$, oui, ou, à la limite, $\Delta I = 1$, oui, mais en tous cas pas $\Delta I = 2$, oui, qui donnerait log $ft \geqq 7.5$. Donc le niveau 295 a un spin 0^- ou 1^-, ce qui élimine le schéma (b) où les transitions vers 53 et 0 seraient respectivement E2 et M1 (c'est-à-dire que la transition vers 53 serait très faible). Donc seul 1^- est possible pour le spin de ^{214}Bi. Le

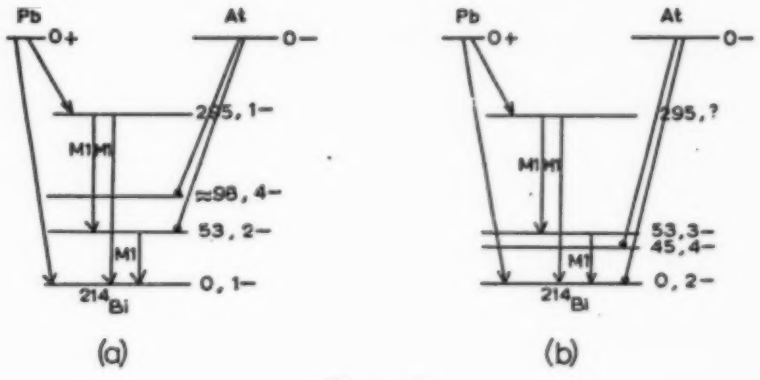

Figure 3.

cycle ^{218}Po ^{214}Pb ^{214}Bi ^{218}At ($Q_\alpha = 6.875$) donne dans ce cas pour ^{218}Po $\xrightarrow{\beta}$ ^{218}At: $E_\beta \approx 0.24$, log $ft = 6.2$, $\Delta I = 0$, oui. Cette valuer (6.2) est assez élevée en regard de la moyenne des spectres une fois défendus, favorisés, normaux, mais est acceptable à côté des très rares cas connus de la catégorie ($0^+ \rightarrow 0^-$). Les valeurs du facteur F des deux groupes α du schéma (a) donnent dans les deux cas $F_\alpha \approx 0$, ce qui peut signifier que les particules α sont formées par un prélèvement de deux paires, comme pour beaucoup de noyaux pairs et que les deux nucléons impairs restent dans la même configuration $[h_{\frac{9}{2}} g_{\frac{9}{2}}]$.

3) *Structure fine du* ^{214}Bi. Les deux raies les plus importantes forment un doublet très semblable à celui du ^{212}Bi: intensité inversée, différence entre les facteurs F presque identiques (^{212}Bi: $\Delta F = 0.5$, ^{214}Bi: $\Delta F = 0.6$). L'attribution à des transitions $1^- \rightarrow 5^+ (l = 5)$ et $1^- \rightarrow 4^+ (l = 3$ et $5)$ est presque inévitable: si le niveau de départ était 2^-, le doublet $[s_{\frac{1}{2}}^{-1} g_{\frac{9}{2}}]$ ne pourrait occasionner une inversion dans les intensités ($l_{min} = 3$ dans les deux cas) et il faudrait faire appel à $[s_{\frac{1}{2}}^{-1} i_{\frac{11}{2}}]$. Mais pour ^{206}Tl nous avons vu que le doublet $[s_{\frac{1}{2}}^{-1} i_{\frac{11}{2}}]$ est au moins 1 MeV plus haut que le doublet $[s_{\frac{1}{2}}^{-1} g_{\frac{9}{2}}]$. L'addition d'une paire de neutrons ne peut en aucun cas déplacer un doublet par rapport à l'autre d'une telle quantité. On peut alors admettre comme vraisemblable que ^{210}Tl a la structure $[s_{\frac{1}{2}}^{-1} g_{\frac{9}{2}}^{3}]$.

TABLEAU 4

Groupe	Énergie	Configuration initiale	Configuration finale	Formation particule α	l (moment angulaire α)	F	F_s	Remarques
^{210}Bi 2	4.685	$(hi)_{1}^{-}$	$(s^{-1}f^{-1})_{3}^{-}$	hi/sf	2	2.8	2.5	
3	4.647		$(s^{-1}p^{-1})_{1}^{-}$	hi/sp	0(100)2(0)	2.4	2.4	
Non obs. [4]	[4.35]		$(s^{-1}f^{-1})_{3}^{-}$	hi/sf	2−4	<2.8	2.4	F
^{210}Bi* 1	5.13	$(hg)_{9}^{-}$	—	—	—	10.5	?	
2	4.93		$(s^{-1}f^{-1})_{3}^{-}$	hg/sf	8−10	6.8	3.3	±0.3 (période incertaine)
3	4.89		$(s^{-1}p^{-1})_{1}^{-}$	hg/sp	8−10	6.7	3.4	Valeurs pour l_{min}, car pas
4	4.59		$(s^{-1}f^{-1})_{3}^{-}$	hg/sp	6−8	5.4	3.4	de terme de comparaison.
5	4.48		3^- ou 4^-		6−8	≈5.6	3.6	
^{211}Bi 0	6.618	$(hi^2)_{\frac{9}{2}}$	$(s^{-1})_{\frac{1}{2}}^{+}$	hi^2/s	5	3.1	1.7	
1	6.621		$(d^{-1})_{\frac{1}{2}}^{+}$	hi^2/d	3(≈90)5(≈10)	2.3	1.7	
^{212}Bi 0	6.086	$(hi^2g)_{1}^{-}$	$(s^{-1}g)_{5}^{+}$	hi^2/s	5	3.25	1.8	
1	6.047		$(s^{-1}g)_{4}^{+}$	hi^2/s	3 (45)5(55)	2.7	1.8	
2	5.764		$(d^{-1}g)_{4}^{+}$	hi^2/d	3 (30)5(70)	2.9	1.8	
3	5.622		$(d^{-1}g)_{5}^{+}$	hi^2/d	5	3.2	1.8	
4	5.603		$(d^{-1}g)_{3}^{+}$	hi^2/d	3	2.3	1.8	
5	5.477		$(d^{-1}g)_{6}^{+}$	hi^2/d	5 (50)7(50)	3.5	1.8	
6	5.341		$(d^{-1}i)_{6}^{+}$	hig/d	5 (50)7(50)	3.9	2.2	
7	5.298		$(d^{-1}i)_{7}^{+}$	hig/d	7	4.7±0.1	2.2	
Non obs.	<4.95		$(d^{-1}i)_{4}^{+}$	hig/d	3−5	≈3.1	Si2.2	Limite E_α calculée par le fond
^{213}Bi	5.86 ±0.03	$(hi^2g^2)_{\frac{9}{2}}^{-}$	$(s^{-1}g^2)_{\frac{1}{2}}^{+}$	hi^2/s	5	2.65±0.3	1.3±0.3	T et E_α très imprécis.
^{214}Bi 0	5.512	$(hi^2g^2)_{1}^{-}$	$(s^{-1}g^2)_{5}^{+}$	hi^2/s	5	2.95	1.5	
1	5.448		$(s^{-1}g^2)_{4}^{+}$	hi^2/s	3 (40)5(60)	2.5	1.5	
2	5.268		$(d^{-1}g^2)_{4}^{+}$	hi^2/d	3 (40)5(60)	2.5	1.5	
3	5.184		$(d^{-1}g^2)_{5}^{+}$	hi^2/d	5	3	1.5	
4	≈5.023		$(s^{-1}i^2g)_{4}^{+}$	hg^2/s	3 (40)5(60)	2.5 ±0.1	≈1.5	
5	≈4.941		$(d^{-1}g^2)_{3}^{+}$	hi^2/d	3	2.0 ±0.1	≈1.5	
Non obs.	<5.0		$(d^{-1}g^2)_{6}^{+}$	hi^2/d	5−7			Limite E_α calculée par le
Non obs.	<5.05		$(s^{-1}i^2g)_{5}^{+}$	hg^2/s	5			fond et pour $F_s = 1.5$.

Pour ces raisons, nous pensons que l'état fondamental de ^{214}Bi est décrit au mieux par $[h_{\frac{9}{2}}(i_{\frac{13}{2}})^2(g_{\frac{9}{2}})^3]_{1^-}$. A partir de là la structure fine α du ^{214}Bi s'explique comme celle du ^{212}Bi, mais on est très gêné cette fois-ci par la faiblesse de l'embranchement α, le fond provoqué par ^{214}Po ne permettant que de détecter les premières lignes du spectre jusqu'à quelques $^0/_{00}$ d'intensité relative. Trois niveaux de spins 4^+, 5^+, 3^+ (par ordre croissant d'énergie) peuvent être attribués au quadruplet $[d_{\frac{5}{2}}^{-1}(g_{\frac{9}{2}})^2 g_{\frac{9}{2}}]$, le terme 6^+ n'étant pas observé par défaut d'intensité.

Une raie (no 4 du tableau 1) pourrait correspondre à un terme du doublet $[s_{\frac{1}{2}}^{-1}(i_{\frac{13}{2}})^2 g_{\frac{9}{2}}]$, la ligne relative à l'autre terme n'étant plus détectée. Dans le tableau 4 nous avons indiqué la limite d'énergie des groupes α éventuels conduisant aux niveaux 6^+ et 5^+ manquant dans ce schéma, limites imposées par la précision statistique de l'expérience.

4.4. AUTRES ISOTOPES Bi

Pour obtenir une vue d'ensemble, nous avons joint au tableau 4 les isotopes de masse 211 et 213 (dont un seul est connu avec précision: ^{211}Bi) pour lesquels, par continuité de ce qui a été admis, on peut proposer les structures $[h_{\frac{9}{2}}(i_{\frac{13}{2}})^2]$ et $[h_{\frac{9}{2}}(i_{\frac{13}{2}})^2(g_{\frac{9}{2}})^2]$.

4.5. SYSTÉMATIQUE DES FACTEURS F_α

Le tableau 4 résume les diverses configurations principales proposées plus haut pour les isotopes émetteurs α du Bi de masse supérieure à 209, ainsi que les facteurs F et F_α qui s'en déduisent. Pour alléger l'écriture, les configurations n'y sont indiquées qu'au moyen des lettres s, p, d, f, h, g, i, sans indice, car il n'y a pas d'ambiguïté sur les niveaux et les nucléons ainsi désignés (par ex. s désigne $(s_{\frac{1}{2}})_p$, etc. . . .). La façon dont se constitue la particule α est indiquée avec la même convention, une barre verticale séparant les nucléons prélevés extérieurement aux deux niveaux magiques de ceux prélevés à l'intérieur. Dans toutes les transitions où plusieurs valeurs sont possibles pour le moment angulaire l emporté par la particule α, et où il existe un terme de comparaison sous forme d'une transition à valeur unique de l, on indique entre parenthèses le % du mélange qui donne un accord général entre groupes pour F_α. Comme nous l'avons signalé, il ne faut pas attacher de signification théorique précise à ces pourcentages.

Sur le tableau, nous avons ajouté quelques limites pour des raies non observées, mais qui pourraient raisonnablement exister, soit sous forme d'une valeur limite de F si l'énergie est prévue, soit sous forme d'une limite supérieure de E_α si F est prévu.

Les valeurs de F et F_c sont calculées au moyen d'une relation $\log_{10} T_c = A + B\, E_\alpha^{-\frac{1}{2}}$, et de la formule classique $F_c = \log_{10}[\exp(-cl(l+1)]$. Pour le Bi, nous avons adopté $B = 137.5$. Cette constante n'est pas celle

que l'on déduirait d'une extrapolation des familles de droites utilisées souvent pour déterminer les facteurs d'empêchement (voir par ex. Fröman [30])). Ces droites, empiriques, contiennent en effet implicitement un terme fonction du rayon R, donc de A, et ne peuvent s'appliquer aux différents groupes d'un même isotope. Mais par là même, les facteurs F_s que nous obtenons correspondent à la somme de plusieurs effets: difficulté de formation de la particule α, rayon qui diminue avec A, et aussi, choix entre nucléons susceptibles de former la particule α, choix qui diminue lorsqu'on se rapproche du ^{208}Pb. Pour des noyaux voisins des couches magiques, on ne peut s'attendre à une variation régulière† de R du type $r_0 A^{+\frac{1}{3}}$. Pour cette raison, nous ne cherchons pas à interpréter de près $F_s(A)$. Tout au plus peut-on remarquer que la variation rapide de F_s de ^{207}Tl à ^{206}Tl paraît être liée au fait que dans le premier cas la particule α est formée à partir d'une paire +2 nucléons solés, et dans le deuxième cas à partir de 4 nucléons prélevés dans des couches différentes. C'est ce qui nous a encouragés à attribuer aux groupes α no 6 et 7 du ^{212}Bi une provenance impliquant une formation à partir de 4 couches différentes avec une valeur de F_s plus élevée. Un effet du même genre paraît intervenir dans le cas de ^{211}Po et ^{211}Po^m où une forte variation de F_s est attribuée à un prélèvement à partir, respectivement, de 3 niveaux et de 4 niveaux.

La variation entre ^{208}Tl et ^{207}Tl est au contraire insignifiante, on peut en conclure que le neutron extérieur au niveau magique ne change pratiquement pas la distribution de charge des protons. La „préformation" α paraît donc être le phénomène prépondérant. On peut compléter ces remarques par quelques renseignements tirés de l'évolution des F_s des Po voisins du ^{208}Pb: pour les masses 218, 216, 214, $F_s \approx 0$. Pour 212, qui devrait être favorisé (α formé de deux paires), F_s atteint néanmoins 0.4. Cet empêchement peut être mis sur le compte du „choix unique", puisque ^{212}Po ne comporte que les composantes nécessaires à une particule α en dehors des deux couches fermées. Pour les autres nucléides Po, il y a au contraire un choix possible entre plusieurs paires de neutrons, et le manque de recouvrement des fonctions d'onde est compensé par les possibilités multiples qui s'offrent. Le ^{210}Po corrigé approximativement de la variation de rayon, a $F_s = 1.4$. Ceci fournit un ordre de grandeur pour l'empêchement qui résulte dans la préformation de la particule α du remplacement d'une paire de neutrons extérieurs ($g_{\frac{9}{2}}$ ou $i_{\frac{13}{2}}$) par une paire $p_{\frac{1}{2}}$ intérieure aux niveaux magiques, le choix unique subsistant: $\Delta F_s \approx 1$.

Mais la raie α correspondant à $^{210}Po_{0^+} \rightarrow {}^{206}Pb_{2^+}$ donne $F_s \approx 1.1$; ce groupe est favorisé par rapport au fondamental, malgré une formation α à partir d'une paire +deux nucléons de couches différentes. D'après [4, 5]), ce niveau 2^+ est un mélange dont les principales composantes sont $[p_{\frac{1}{2}} f_{\frac{5}{2}}]$, $[p_{\frac{3}{2}} f_{\frac{5}{2}}]$, $[p_{\frac{1}{2}} f_{\frac{7}{2}}]$, $(f_{\frac{5}{2}})^2$, $(p_{\frac{1}{2}})^2$. Peut-être s'agit-il d'une compensation due au choix très large possible: il suffit

† Si R varie régulièrement, on a comme ordre de grandeur $\Delta F = 0.02$ à 0.03 pour $\Delta A = 1$.

de prélever deux neutrons quelconques des trois premières couches qui en contiennent douze.

C'est dans le même sens d'ailleurs que l'on peut noter pour ^{214}Po que la transition α $0^+ \to 2^+$ est très défavorisée: $F_\alpha(0^+ \to 2_+) - F_\alpha(0_+ \to 0_+) = \Delta F_\alpha \approx 1.2$. En effet, $^{210}Pb_{2+}$ a une configuration dominante $(g_{\frac{9}{2}})^2_{2^+}$, non présente en première approximation dans la configuration de ^{214}Po: 3 paires de spin nul. Le ΔF_α est ainsi lié dans ^{214}Po à la présence d'une faible proportion de configurations du genre $[(h_{\frac{9}{2}})^2_{2^+}(g_{\frac{9}{2}})^2_{2^+}(i_{\frac{13}{2}})^2_{0^+}]_{0+}$. Dans ^{218}Po, le même facteur ΔF_α tombe à 0.6, par suite des possibilités multiples. En passant aux corps plus lourds (Ra ...), enfin, ΔF_α s'annule progressivement, car le modèle des particules, à caractère de plus en plus statistique, s'identifie peu à peu au modèle collectif.

La constante c qui détermine F_c a été choisie empiriquement en se basant sur les valeurs de F relatives aux transitions à l unique: $c=0.11$. D'après Fröman [30]) ceci correspondrait à $R = 6.3 \times 10^{-13}$, ce qui est très faible (pour ^{208}Pb, les données courantes indiquent 7.3×10^{-13}). Mais l'équation utilisée résulte de simplifications et d'approximations grandes, et, en tous cas, une valeur trop faible de c détruirait les régularités qui apparaissent pour les quatre isotopes du Bi.

5. Conclusions

Parmi les corps voisins des couches fermées, certains nucléons ne peuvent s'étudier que par spectrographie α, les conditions d'intensité et de filiation interdisant un recours à la spectrographie γ ou d'électrons de conversion.

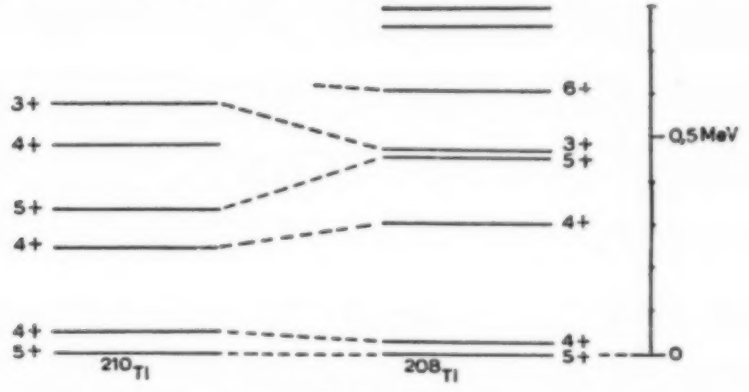

Figure 4.

^{210}Tl est parmi ceux-là. Nous avons cherché à exploiter au mieux les facteurs d'empêchement F que l'on déduit des intensités et des énergies des raies α faibles observées. La systématique montre que, dans la région du ^{208}Pb, les variations de F sont explicables avec quelques hypothèses simples et permettent bien d'établir des schémas nucléaires vraisemblables basés sur le modèle en couches. Toute extrapolation trop lointaine paraît cependant hasardeuse et des

règles empiriques sont d'autant plus approximatives qu'elles sont simples. Ainsi analysé, le spectre α du ^{214}Bi conduit à un schéma de niveaux du ^{210}Tl très comparable à celui du ^{208}Tl obtenu à partir du ^{212}Bi. Les multiplets présentent la même suite de spins, l'addition d'une paire de neutrons dilate les multiplets (de l'ordre de la moitié en plus), la distance des centres de gravité des multiplets reste grossièrement la même (fig. 4).

Peu de jours après l'achèvement de cet article, notre laboratoire a été frappé par la brusque disparition de son directeur, Mr. S. Rosenblum. Nous nous inclinons devant la mémoire de celui qui, durant de nombreuses années, a encouragé nos recherches et a été notre ami de tous les moments.

Bibliographie

1) Lord Rutherford, C. E. Wynn-Williams, W. B. Lewis et B. V. Bowden, Proc. Roy. Soc. A **139** (1933) 617;
W. B. Lewis et B. V. Bowden, Proc. Roy. Soc. A **145** (1934) 235
2) R. J. Walen et G. Bastin, C. R. Congrès Int. Phys. Nucl. Paris (1958) 910
3) A. Rytz, C. R. **233** (1951) 790
4) M. J. Kearsley, Nuclear Physics **4** (1957) 157
5) W. W. True et K. W. Ford, Phys. Rev. **109** (1958) 1675
6) R. J. Walen et G. Bastin, J. Phys. et Rad. **20** (1959) 589
7) E. Broda et N. Feather, Proc. Roy. Soc. A **1901** (1947) 20
8) H. B. Lévy et I. Perlman, Phys. Rev. **94** (1954) 152
9) D. J. Hughes et H. Palevsky, Phys. Rev. **92** (1953) 1206
10) N. Feather, Phil. Mag. **42** (1951) 568
11) S. V. Golenetskii, L. I. Rusinov et I. Filimonov, JETP **35** (1958) 1313
12) S. V. Golenetskii, L. I. Rusinov et I. Filimonov, JETP **37** (1959) 560
13) D. E. Alburger et A. W. Sunyar, Phys. Rev. **99** (1955) 695
14) M. Schmorak, R. Stockendal, J. A. McDonell, I. Bergström et I. Gerholm, Nuclear Physics **2** (1956) 193
15) J. Varma, Phys. Rev. **94** (1954) 1688
16) J. A. McDonell, R. Stockendal, C. J. Herrlander et I. Bergström, Nuclear Physics **3** (1957) 513
17) R. K. Girgis et R. van Lieshout, Nuclear Physics **12** (1959) 672
18) N. Newby et E. J. Konopinski, Phys. Rev. **115** (1959) 434
19) J. W. Horton, Phys. Rev. **101** (1956) 717
20) E. M. Krisyouk, A. G. Sergeyev, G. D. Latyshev et V. D. Vorobyov, Nuclear Physics **4** (1957) 579
21) M. H. L. Pryce, Proc. Phys. Soc. A **65** (1952) 772
22) O. B. Nielsen, Kgl. Danske Vid. Selsk. Mat. Fys. Medd. **30**, No 11(1955).
23) R. W. King, Rev. Mod. Phys. **26** (1954) 327
24) A. H. Wapstra, Thèse (1953) Amsterdam
25) N. Feather in Beta und gamma spectroscopy, ed. by K. Siegbahn (1955) p. 748
26) F. Demichelis et L. A. Radicati, Nuovo Cimento **3** (1956) 152
27) R. A. Ricci et G. Trivero, Nuovo Cimento **2** (1955) 745
28) K. O. Nielsen, O. B. Nielsen et M. A. Waggoner, Nuclear Physics **2** (1956) 476
29) H. Daniel, Z. Naturforsch. **11A** (1956) 759
30) P. O. Fröman, Kgl. Danske Vid. Selsk. Mat. Fys. Skr. **1**, No 3 (1957).
31) Voir notamment:
G. Gamow, Constitution of atomic nuclei and radioactivity (Clarendon Press 1931);
A. Berthelot, J. Phys. Radium **3** (1942) 17, 52;
I. Perlman, A. Ghiorso et G. T. Seaborg, Phys. Rev. **77** (1950) 26;
S. G. Nordström, Ark. Fys. **3** (1951) 547;
N. Feather, Nuclear stability rules (Cambridge University Press 1952);
F. Asaro, Thesis Berkeley (1953) ,UCRL 2180;
I. Perlman et O. Rasmussen, Handbuch der Physik, vol. **42** (1957)

1.E.3

Nuclear Physics **16** (1960) 264—277; © *North-Holland Publishing Co., Amsterdam*

Not to be reproduced by photoprint or microfilm without written permission from the publisher

NUCLEAR POLARIZATION OF Co^{55}

RUDOLF W. BAUER and MARTIN DEUTSCH

Department of Physics and Laboratory for Nuclear Science, Massachusetts Institute of Technology, Cambridge 39, Massachusetts †

Received 4 January 1960

Abstract: The angular distribution and linear polarization of the gamma rays emitted from 18-h Co^{55}, polarized at low temperatures in cerium-magnesium nitrate crystals, have been measured. The amplitude mixing ratios δ(E2/M1) of mixed multipole gamma transitions in Fe^{55} have been determined. With a spin of $\frac{7}{2}$ for Co^{55}, we find a spin sequence of $\frac{7}{2} \rightarrow \frac{5}{2} \rightarrow \frac{3}{2}$ in the main decay in Fe^{55}, and for the 0.935 MeV gamma ray a δ of $+0.36 \pm 0.11$. A possible spin sequence $\frac{5}{2} \rightarrow \frac{7}{2} \rightarrow \frac{3}{2}$ in Fe^{55} has been eliminated by our linear polarization measurements. The ratio of the nuclear g-values of Co^{58} and Co^{55} has been found from a simultaneous measurement of the angular distribution of the gamma rays from the two isotopes grown into the same crystals. The magnetic moment of Co^{55} is 5.3 ± 0.4 n.m., if the 1.03 MeV beta branch is predominantly a G.T. transition, or 4.6 ± 0.4 n.m., if a pure Fermi transition.

1. Introduction

The first successful nuclear polarization experiments at low temperatures using the magnetic h.f.s. polarization method were carried out by Ambler and coworkers [1]), using Co^{60} incorporated in the lattice of cerium-magnesium nitrate. With this technique and the same cooling salt, other long-lived Co isotopes have been polarized; for instance, Co^{58} by Ambler *et al.* [2]) and Co^{56} by Jastram *et al.* [3]), Diddens *et al.* [4]) and Ambler *et al.* [5]).

The purpose of the present work was to extend these polarization methods to the investigation of the relatively short-lived 18-h Co^{55}. A study of the spins of the levels and the multipolarity of the gamma rays was made, which also yielded information about the magnitude of the magnetic dipole moment of Co^{55}.

The nucleus ${}_{27}Co^{55}_{28}$ appeared to be of particular interest from the point of view of the shell model because of its proximity to the magic number 28. The beta and gamma spectra of Co^{55} had been investigated, but no spin measurements were available. To supplement these investigations we planned the nuclear polarization experiment.

† This work is supported in part through AEC Contract AT(30-1)-2098, by funds provided by the U. S. Atomic Energy Commission, the Office of Naval Research and the Air Force Office of Scientific Research.

Some of the research reported in this paper forms part of a Ph. D. thesis submitted by R. W. Bauer.

2. Decay Scheme

The principal features of the decay scheme of Co^{55} are established (see, for instance, Strominger *et al.*, Table of Isotopes [6]). Fig. 1a is based on this together with the intensities of the beta and gamma transitions measured by Deutsch and Hedgran [7]), Caird and Mitchell [8]), and recently by Mukerji *et al.* [9]). Some

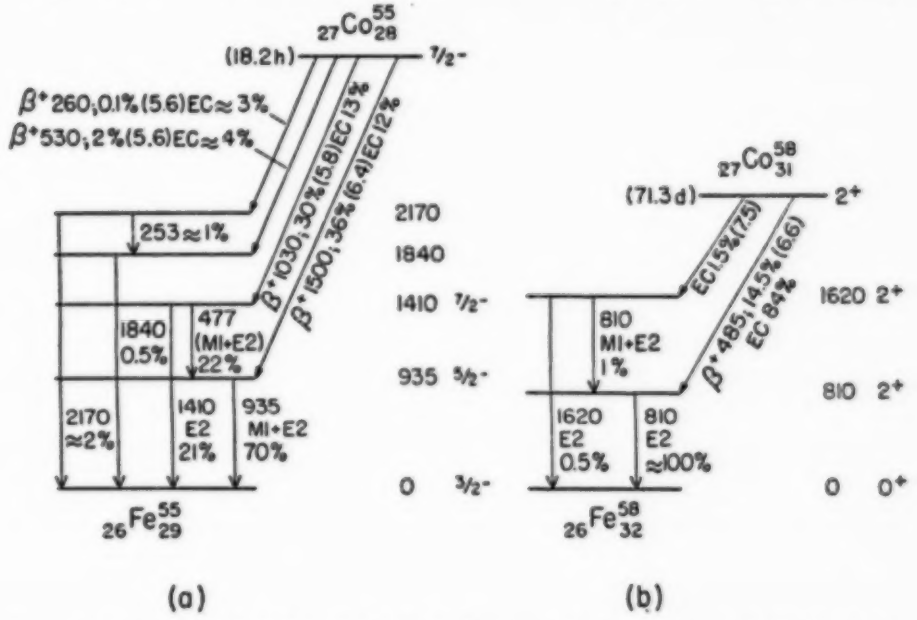

Fig. 1. Decay schemes of (a) Co^{55} and (b) Co^{58}. The energies are given in keV, the intensities in percent of disintegration. For the beta transitions the log *ft*-values are indicated.

discrepancies exist in the low intensity transitions both exciting and de-exciting the 1.84 and 2.17 MeV states of Fe^{55}. These levels can be left out of consideration since in our experiment only the three intense gamma rays were investigated.

The spin of Co^{55} is believed to be $\frac{7}{2}^-$. This assumption is based on shell model arguments, the nucleus being doubly magic with one proton missing from the $f_{\frac{7}{2}}$ shell. The ground state of Fe^{55}, beta unstable with a half-life of 2.9 y, decays by electron capture to Mn^{55} whose spin has been measured to be $\frac{5}{2}$. From the beta decay of $Fe^{55} \rightarrow Mn^{55}$, the properties of the beta decay $Co^{55} \rightarrow Fe^{55}$, and from shell model systematics (odd neutron in $p_{\frac{3}{2}}$ shell), the spin of the ground state of Fe^{55} is believed to be $\frac{3}{2}^-$.

The spin assignments of the 0.935 and 1.41 MeV excited states of Fe^{55} are not well established. No gamma-gamma angular correlation measurements are available. The log *ft*-values of the beta decay of Co^{55} are given in fig. 1a. The values of 5.8 and 6.4 for the two beta branches indicate allowed beta decay. The beta-gamma angular correlation experiments by Stevenson and Deutsch[10]) show that $\Delta J = 0, \pm 1$ in the beta decay, thus limiting the spins of the excited states under discussion to $\frac{5}{2}^-$, $\frac{7}{2}^-$, and $\frac{9}{2}^-$. The assignment of $\frac{9}{2}^-$ for either state

can be eliminated from the relative transition probabilities of the three intense gamma rays.

Several decay schemes published recently [6, 11] suggest $\frac{5}{2}^-$ for the 0.935 MeV, and $\frac{7}{2}^-$ for the 1.41 MeV excited states (i.e., a spin sequence $\frac{7}{2} \to \frac{5}{2} \to \frac{3}{2}$). The assignment of $\frac{5}{2}$ for the first excited state is largely based on shell model systematics ($f_{\frac{5}{2}}$ level is above $p_{\frac{3}{2}}$ level in this case). These spin assignments are given in fig. 1a. The opposite assignment, $\frac{7}{2}^-$ for the 0.935 MeV, and $\frac{5}{2}^-$ for the 1.41 MeV excited states (i.e., a spin sequence $\frac{5}{2} \to \frac{7}{2} \to \frac{3}{2}$) had not been ruled out by previous experiments. We shall interpret the results of our angular distribution experiments in terms of the two possible spin assignments and illustrate how our linear polarization measurements were used to eliminate the latter possible spin sequence and to decide between alternative amplitude mixing ratios of the gamma transitions in Fe^{55}.

3. Angular Distribution and Polarization Formalism

The expression for the angular distribution of a gamma ray with respect to the axis of orientation of an oriented spin system can be written as a series of even Legendre polynomials:

$$W(\theta) = 1 + \sum_{n=2,4\ldots} B_n U_n F_n(L) P_n(\cos\theta), \tag{1}$$

where $F_n(L)$ is a function of the angular momenta of the gamma transition, U_n is a similar function for any intermediate unobserved transition, and B_n is an orientation parameter. The character of the preceding beta transitions is contained in the terms U_n which can be written as

$$U_n = \lambda U_n^{\mathrm{F}} + (1-\lambda) U_n^{\mathrm{GT}}, \tag{2}$$

with $0 \leqq \lambda \leqq 1$ designating the amount of Fermi admixture; U_n^{F} and U_n^{GT} are the values appropriate for Fermi and Gamow-Teller transitions. For a definition of these quantities, see Blin-Stoyle and Grace [12]).

The anisotropy ε of the angular distribution of the gamma rays is defined by

$$\varepsilon = [W(\tfrac{1}{2}\pi) - W(0)]/W(\tfrac{1}{2}\pi). \tag{3}$$

This quantity is used in the evaluation of the amplitude mixing ratios of the gamma transitions in the Co^{55} decay and in the Co^{58}—Co^{55} comparison measurements.

The gamma radiation from an ensemble of oriented nuclei is in general partially polarized. Since a beam of partially polarized photons can be considered as an incoherent superposition of a beam of completely polarized photons and of a beam of unpolarized photons, we can characterize the degree of polarization by one single number P, defined by the ratio of the intensity of the polarized beam to the total intensity of the beam, where $0 \leqq P \leqq 1$.

Using the notation of eq. (1), the expression for the degree of polarization P of a gamma ray from a system of oriented nuclei with rotational symmetry can be written in the general form

$$P\xi = P_C\chi_C + P_L\chi_1, \tag{4}$$

where the polarization vectors of the gamma rays are the same as introduced by Tolhoek and Cox [13]). The degree of circular polarization P_C is

$$P_C = \frac{1}{W(\theta)} \sum_{n=1,3\ldots} B_n U_n F_n(L) P_n(\cos\theta) \tag{5}$$

and the degree of linear polarization P_L is

$$P_L = \pm \frac{1}{W(\theta)} \sum_{n=2,4\ldots} B_n U_n F_n(L) \frac{C(LLn, 11)}{C(LLn, 1-1)} \left[\frac{(n-2)!}{(n+2)!}\right]^{\frac{1}{2}} P_n^2(\cos\theta), \tag{6}$$

where the minus sign is for electric, the plus sign for magnetic transitions; $C(LLn, 11)$ are Clebsch-Gordan coefficients, P_n^2 $(\cos\theta)$ is the associated Legendre polynomial of order n.

Expressions (1), (5) and (6) can easily be expanded to cover mixed gamma transitions of multipole order L and $L+1$, using the amplitude mixing ratio δ, according to Biedenharn and Rose [14]) (for the second member of a gamma-gamma cascade), defined by

$$\delta = \pm\langle I_f||L+1||I_1\rangle / \langle I_f||L||I_1\rangle. \tag{7}$$

For a general treatment of mixed transitions, see for instance, the review by Blin-Stoyle and Grace [12]).

4. Apparatus and Experimental Procedure

In the experiments by Ambler *et al.* [1]) and Diddens *et al.* [4]), the successful use of cerium-magnesium nitrate $Ce_2Mg_3(NO_3)_{12} \cdot 24H_2O$ for nuclear polarization of Co isotopes has been reported. A discussion of the orientation mechanism has been presented by these authors. The reason for selecting this cooling salt for our experiment is that by adiabatic demagnetization with the facilities available a temperature of about 0.003° K can be reached, this giving rise to a high degree of nuclear polarization with an external field H_p of several hundred gauss.

Co^{55} was produced at the M.I.T. cyclotron by a (d, n) reaction on enriched Fe^{54}(81.1 %) obtained from the Union Carbide Nuclear Company, Oak Ridge, Tennessee. The radioactive cobalt was chemically separated. A deuteron bombardment of 60 μA-h on 20 mg of the separated isotope gave a yield of about 500 μc of Co^{55} and only about 10 μc of Co^{56}. The relative yield of Co^{55} as compared to Co^{56} from natural iron was too low for our experiment.

The source preparation was conventional; the activated cerium-magnesium nitrate crystals were grown from radioactive solutions. We allowed about one half-life for source preparation, mounting in the cryostat and cooling to 1°K. The assembled cryostat, the polarizing magnet and the counter geometry for the anisotropy measurements are shown in fig. 2.

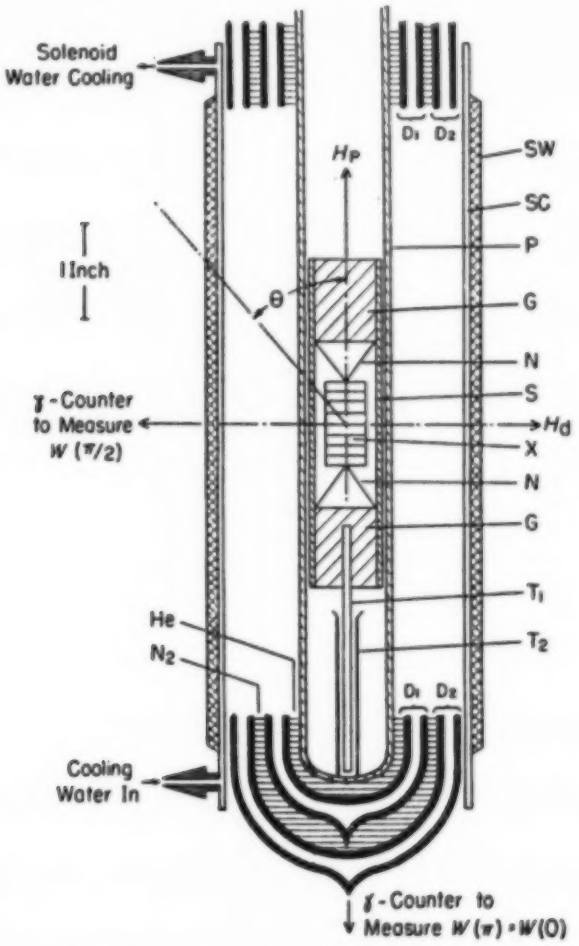

Fig. 2. Schematic diagram of the experimental arrangement for the measurement of the angular distribution of gamma rays. X are the Ce-Mg nitrate crystals containing the Co^{55} activity, suspended with nylon threads N from guard salts G (manganous ammonium sulfate). S supports of glass rod, T_1 and T_2 glass capillaries to support the sample in the pyrex salt chamber P. D_1 is the He dewar, D_2 nitrogen dewar. H_p is polarizing field produced by solenoid, SW solenoid windings, SC solenoid cooling jacket. The direction of the demagnetizing field H_d is indicated.

With 50—100 μc of Co^{55} at the beginning of the demagnetization experiments, the angular distribution of the 0.935 and 1.41 MeV gamma rays was observed as the crystals warmed up after each cooling cycle. The 0.477 MeV gamma ray could not be studied because of the intense annihilation radiation (see lower curve of fig. 3). Measurements were made with a polarizing field H_p of 450 gauss along the trigonal axis of the double nitrate crystals. Each of the two counters

consisted of a 2″×2″ NaI(Tl) crystal mounted on a DuMont 6392 photomultiplier tube (fig. 2).

The gamma spectra from both counters at successive time intervals after demagnetization were recorded in a multichannel pulse sorter at the Laboratory for Nuclear Science Data Center. The pulse height distribution of Co^{55} from the polar counter is given in the lower curve of fig. 3. The relative contributions of the 1.41 and 0.935 gamma rays were determined with the help of Na^{22} and Co^{58} in similar geometry.

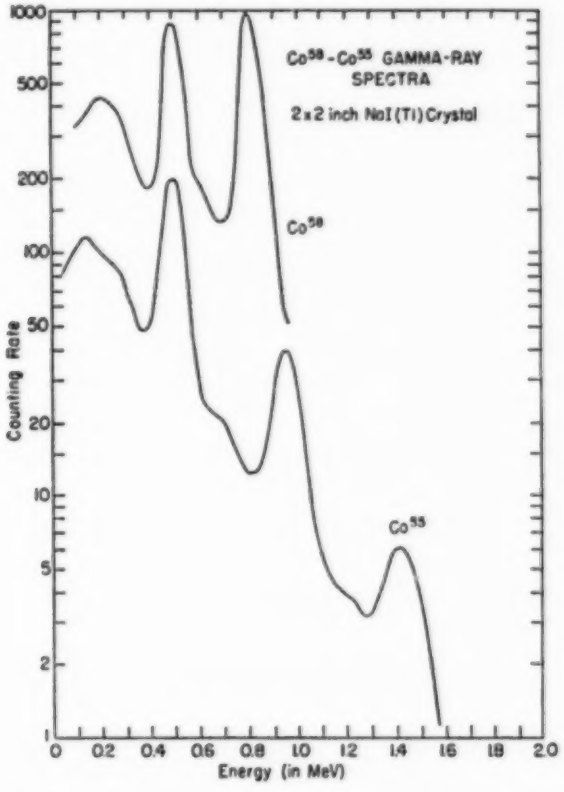

Fig. 3. Pulse height distribution of gamma rays from Co^{55} and Co^{58} using 2″×2″ NaI(Tl) scintillation spectrometer.

For the measurement of the ratio of the nuclear g-values of Co^{55} and Co^{58}, both isotopes were grown into the same cooling salt. About 60 μc of Co^{58} were used together with 10 μc of Co^{55}, so that the 0.81 MeV photopeak in Co^{58} was about ten times as intense compared to the 0.935 MeV photopeak in Co^{55}. Co^{58} was obtained from the Radioisotope Division of the Oak Ridge National Laboratory, Oak Ridge, Tennessee. The spectrum of Co^{58} is given in the upper curve of fig. 3. For the comparison measurements the angular distributions of the 0.81 MeV gamma ray of Co^{58} and of the 1.41 MeV gamma ray of Co^{55} were studied. The method of data accumulation was the same as above.

The decay scheme of Co^{58} with all the spin assignments is well established

(see, for instance, Strominger *et al.*, Table of Isotopes [6]); fig. 1b is based on this. The matrix elements of the predominant beta group exciting the 0.81 MeV state of Fe^{58} has been measured [15, 16]). Dagley *et al.* [16]) showed this transition to be of pure G.T. type. Recent paramagnetic resonance experiments [17]) showed the ground state of Co^{58} to have spin 2, and a magnetic dipole moment of 4.05 n.m. Thus Co^{58} seemed well suited as our "thermometric" isotope for the comparison type measurement of the magnetic dipole moment of Co^{55}.

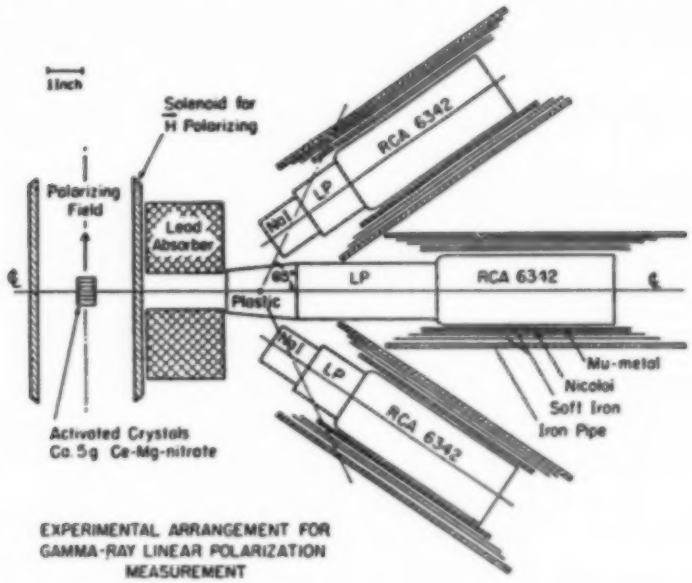

Fig. 4. Schematic diagram of the polarimeter. Four NaI scintillation counters are used, the two counters not shown are rotationally symmetric about the centre line CL in a plane perpendicular to the paper.

The experimental arrangement for the measurement of the linear polarization is given in fig. 4. Four NaI scintillation counters are used to increase to total coincidence rate. The associated electronic circuits are indicated in fig. 5. Using the method of linear addition of the pulses from the plastic scattering counter and the NaI counters, complex gamma-spectra can be investigated without sacrificing coincidence counting rate in favour of good angular resolution. A typical sum pulse height coincidence spectrum of the gamma radiation from Co^{55} is given in fig. 6. The 1.41 MeV and 0.935 MeV gamma rays are observed as peaks, the 0.477 MeV gamma rays and 0.511 MeV annihilation radiation are not resolved. Coincidence circuits with about 0.5 μsec resolving time are used, thus the chance coincidence rate was below 1 % of the total coincidence rate for sources of about 50 μc in the geometry shown in fig. 4.

For the analysis of the linear polarization, we observe the effect E defined by

$$E = \frac{N_\perp - N_\parallel}{N_\perp + N_\parallel} = P_L Q_L, \tag{8}$$

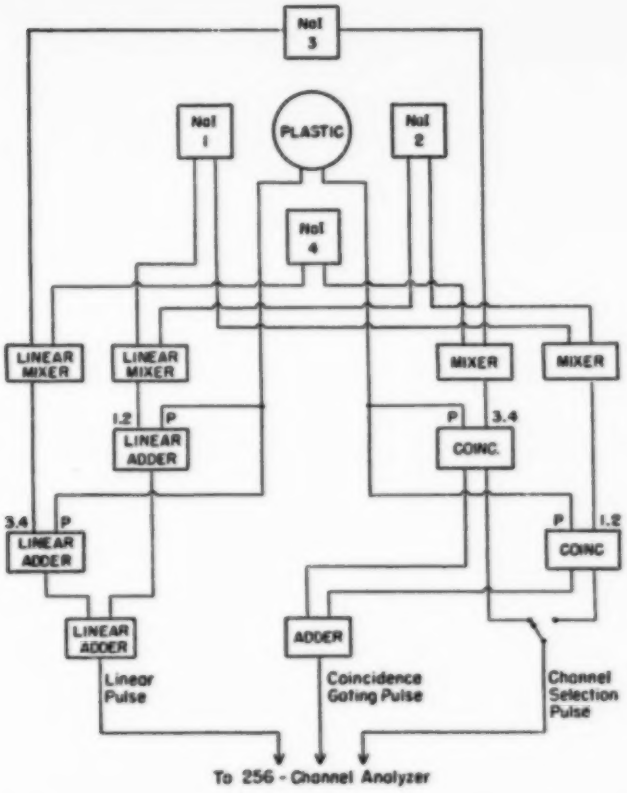

Fig. 5. Block diagram of the associated electronic circuitry for the polarimeter. Amplification and pulse-shaping units have been omitted.

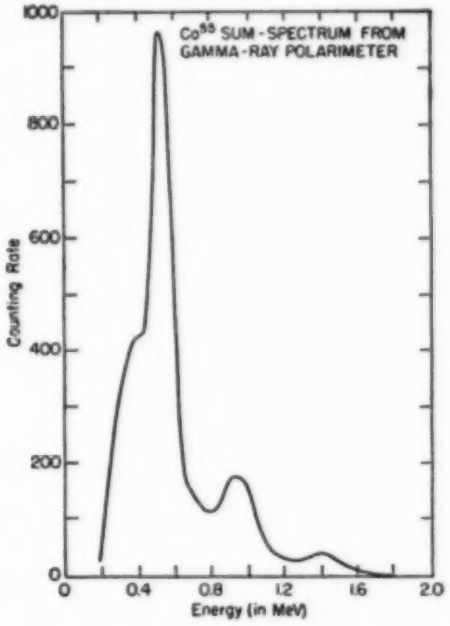

Fig. 6. Sum pulse-height sprectrum, gated by coincidences, of the gamma rays from Co^{55} as observed with the polarimeter in the geometry of fig. 4.

where $N_\parallel$ is the number of photons scattered by the plastic scintillator in the plane defined by the polarizing field and the direction of emission of the gamma rays, $N_\perp$ the number of photons scattered perpendicular to this plane. For electric gamma transitions $E < 0$, for magnetic radiations $E > 0$. The quantity Q_L is the ratio of the linear polarization-dependent part of the Compton cross section to the polarization-independent part. The degree of linear polarization P_L is defined in eq. (6). The polarimeter was tested on polarized Co^{60} and Co^{56}. Our results from these isotopes agree with those of Metzger and Deutsch [18]) and of Diddens [4]), the magnitude of the observed effects agree with the calculated efficiency of the polarimeter in the geometry of fig. 4.

5. Results

Two experiments were performed with sources containing Co^{55} alone, during which the anisotropies of the 0.935 MeV and 1.41 MeV gamma rays were observed. The results of the measurements performed with an external polarizing field of 450 gauss are given in fig. 7. It is seen that the anisotropy is positive

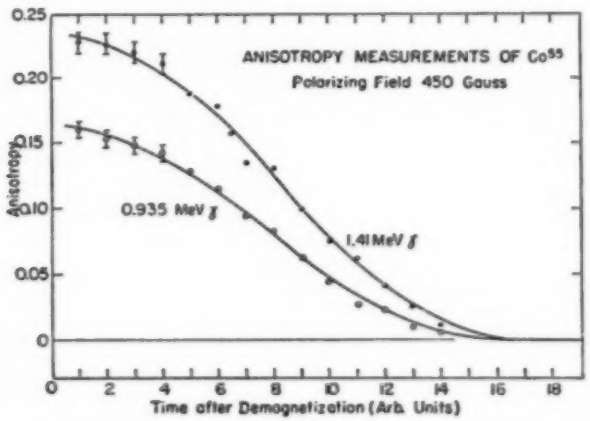

Fig. 7. The observed anisotropy ε of gamma rays from Co^{55} with a polarizing field of 450 gauss is plotted against warm-up time (arbitrary units). The curves are those calculated on the basis of certain spin assignments and mixing ratios (see text). Statistical errors are shown.

for the two gamma rays under investigation. The curves are those calculated on the basis of a spin of $\frac{7}{2}$ for Co^{55} and $\frac{3}{2}$ for the ground state of Fe^{55}, using the anisotropy of the E2 gamma transition as reference for the degree of orientation of the Co^{55} nuclei, having corrected for the disorientation due to the preceding transitions, and using the amplitude mixing ratios δ(E2/M1) for the other observed gamma transition, with the respective spin sequences of $(\frac{7}{2} \to \frac{5}{2} \to \frac{3}{2})$ and $\frac{5}{2} \to \frac{7}{2} \to \frac{3}{2})$ in Fe^{55}, as given in tables 1 and 2.

Both tables list two alternative values of δ(E2/M1) for the respective mixed gamma transitions. Measurements of the internal conversion coefficients by

TABLE 1

Alternative values of δ(E2/M1) for the 0.935 MeV γ-ray from angular distribution measurements of Co^{55}, values of the ratio of nuclear g-values of Co^{58} and Co^{55}, and of the nuclear magnetic dipole moment of Co^{55}, assuming a spin sequence ($\frac{7}{2} \rightarrow \frac{4}{2} \rightarrow \frac{2}{2}$) in Fe^{55}. In this case, the 1.50 MeV beta branch is pure GT, the 1.41 MeV γ-transition is pure E2. The sign of δ in this table is appropriate for the second member of a γ—γ cascade. P_L is the degree of linear polarization in the direction $\theta = \frac{1}{2}\pi$, calculated for a temperature where the observed angular distribution anisotropies are 0.22 and 0.15 for the 1.41 and 0.935 MeV γ-rays, respectively (see fig. 7).

	δ (0.935 MeV γ)	(g_{58}/g_{55})	μ_{55}	P_L (1.41 MeV γ)	P_L (0.935 MeV γ)
$\lambda_{1.03} = 0$ (pure GT) † see fig. 8		1.33 ± 0.10	5.35 ± 0.35		
$\lambda_{1.03} < 0.05$ (mostly GT)	$+0.37 \pm 0.07$	1.34 ± 0.11	5.30 ± 0.40	-0.22 ± 0.02	$+0.21 \pm 0.02$
$\delta_{0.47} < \lvert 0.10 \rvert$ (mostly M1) †	$+15 \quad \pm 6$			-0.22 ± 0.02	(-0.02 ± 0.02)
$0 \leqq \lambda_{1.03} \leqq 1$	$+0.37^{+0.10}_{-0.12}$	1.44 ± 0.21	4.95 ± 0.75	-0.22 ± 0.02	$+0.21 \pm 0.03$
$0 \leqq \lvert\delta_{0.47}\rvert \leqq \infty$	$+15^{-7}_{+15}$			-0.22 ± 0.02	(-0.02 ± 0.03)
$\lambda_{1.03} = 1$ (pure F) see fig. 9		1.55 ± 0.10	4.60 ± 0.40		

† $\lambda_{1.03}$ refers to the amount of Fermi-admixture in the 1.03 MeV beta branch, $\delta_{0.47}$ to the E2—M1 amplitude mixing ratio in the 0.475 MeV γ-transition. The values of (g_{58}/g_{55}) and μ_{55} are independent of $\delta_{0.47}$.

TABLE 2

Alternative values of δ(E2/M1) for the 1.41 MeV γ-ray from angular distribution measurements of Co^{55}, values of the ratio of nuclear g-values of Co^{58} and Co^{55}, and of the nuclear magnetic dipole moment of Co^{55}, assuming a spin sequence ($\frac{4}{2} \rightarrow \frac{7}{2} \rightarrow \frac{2}{2}$) in Fe^{55}. In this case, the 1.03 MeV beta branch is pure GT, the 0.935 MeV γ-transition is pure E2. The sign of δ in this table is appropriate for the second member of a γ—γ cascade. P_L is the degree of linear polarization in the direction $\theta = \frac{1}{2}\pi$, calculated for a temperature where the observed angular distribution anisotropies are 0.22 and 0.15 for the 1.41 and 0.935 MeV γ-rays, respectively (see fig. 7).

	δ (1.41 MeV γ)	(g_{58}/g_{55})	μ_{55}	P_L (1.41 MeV γ)	P_L (0.935 MeV γ)
$\lambda_{1.50} < 0.05$ (mostly GT) †	$+0.7 \pm 0.1$	1.80 ± 0.22	4.0 ± 0.5	$(+0.14 \pm 0.02)$	(-0.15 ± 0.02)
$\delta_{0.47} < \lvert 0.10 \rvert$ (mostly M1) †	$+3.0 \pm 0.5$			$(+0.02 \pm 0.02)$	(-0.15 ± 0.02)
$0 \leqq \lambda_{1.50} \leqq 1$	$+0.7^{+0.6}_{-0.3}$	1.80 ± 0.40	$4.0^{+1.0}_{-0.8}$	$(+0.14^{+0.05}_{-0.02})$	(-0.15 ± 0.02)
$0 \leqq \lvert\delta_{0.47}\rvert \leqq \infty$	$+3.0^{-2.0}_{+1.5}$			$(+0.02^{+0.08}_{-0.03})$	(-0.15 ± 0.02)

† $\lambda_{1.50}$ refers to the amount of Fermi-admixture in the 1.50 MeV beta branch, $\delta_{0.47}$ to the E2—M1 amplitude mixing ratio in the 0.475 MeV γ-transition. The values of (g_{58}/g_{55}) and μ_{55} depend upon $\delta_{0.47}$.

Mitchell [8]) do not allow a choice between the two alternative values of δ(E2/M1). In order to eliminate one of the two possible spin sequences and to decide between the values of δ(E2/M1), we performed the linear polarization measurements on the gamma rays emitted from polarized Co^{55}. The expected degrees of linear polarization P_L, calculated for a temperature where the observed angular distribution anisotropies are 0.22 and 0.15 for the 1.41 and 0.935 MeV gamma rays, respectively, are given in tables 1 and 2. The bracketed figures are shown to be incompatible with the linear polarization experiments.

Two experiments were carried out with sources containing both Co^{55} and Co^{58}, during which the anisotropies of the angular distribution of the gamma rays

from both isotopes were measured simultaneously. The experimental results are given in figs. 8 and 9. The families of curves represent the calculated anisotropies ε on the basis of the spin assignments given in fig. 1a, assuming a pure

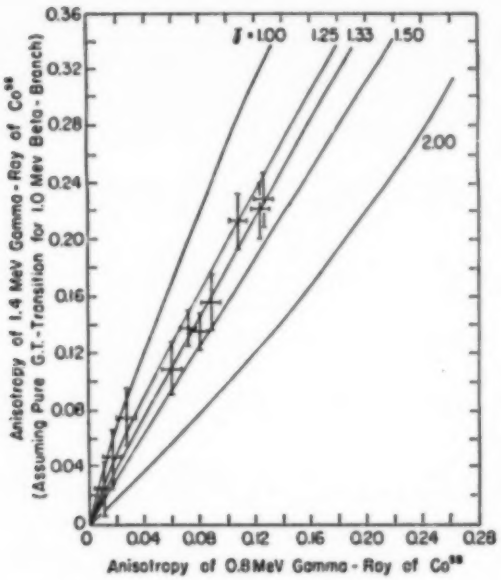

Fig. 8. The simultaneously observed anisotropies of gamma rays from Co^{55} and Co^{58}. The curves are those calculated for given ratios γ of the nuclear g-value of Co^{55} to that of Co^{58}, with a spin assignment as given in fig. 1, assuming a pure G. T. transition in the 1.03 MeV beta branch in Co^{55}. Statistical errors are shown.

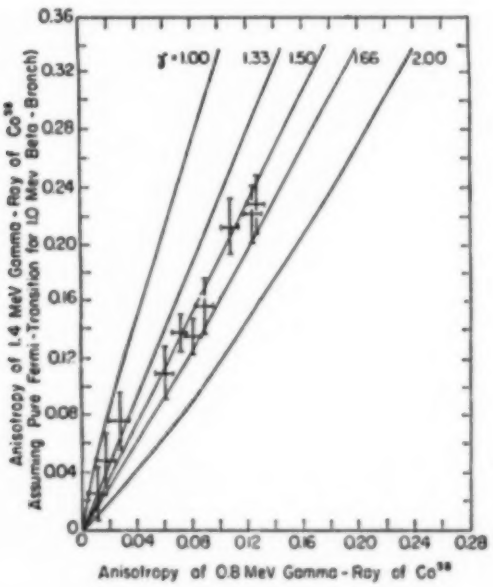

Fig. 9. The simultaneously observed anisotropies of gamma rays from Co^{55} and Co^{58}. The curves are those calculated for given ratios γ of the nuclear g-value of Co^{58} to that of Co^{55}, with a spin assignment as given in fig. 1, assuming a pure Fermi transition in the 1.03 MeV beta branch in Co^{55}. Statistical errors are shown.

G.T. transition (fig. 8) and a pure Fermi transition (fig. 9) in the 1.03 MeV beta branch. The parameter γ is the ratio of the nuclear g-value of Co^{58} to that of Co^{55}. The experimental points scatter around the theoretical curve of 1.33 ± 0.10 (for the G.T. case) and 1.55 ± 0.10 (for the Fermi case). The quoted errors, larger than those arising from statistics, include an estimate of errors arising from experimental uncertainties. Curves similar to figs. 8 and 9 can be drawn for the spin sequence $\frac{5}{2} \rightarrow \frac{7}{2} \rightarrow \frac{3}{2}$. The results for the various mixing ratios assumed and for the two possible spin sequences are given in tables 1 and 2, where the magnetic dipole moment of Co^{55} is calculated for the various cases using a nuclear g-value of 2.025 for Co^{58} and a spin of $\frac{7}{2}$ for Co^{55}. This method of measuring the magnetic moment is independent of the temperature, but it

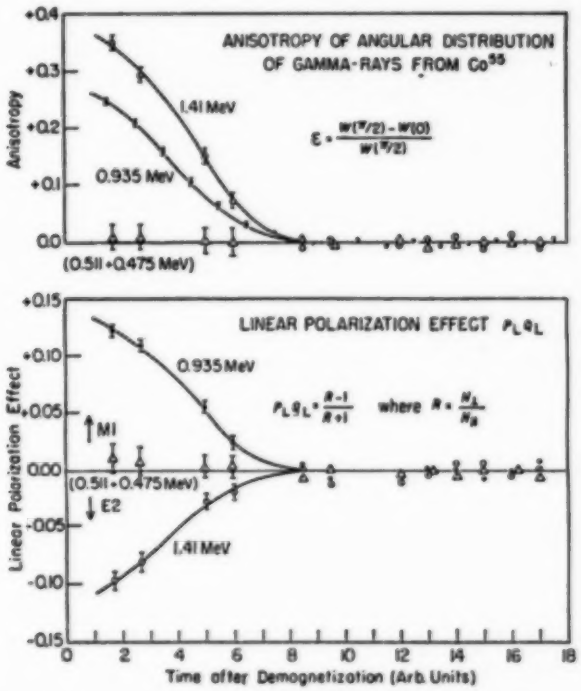

Fig. 10. The angular distribution anisotropy ε and the linear polarization effect $P_L Q_L$ of the gamma rays emitted from oriented Co^{55}, as a function of the warm-up time.

depends to a large degree on the assumption that no disturbances and reorientations of the relative populations of the magnetic substates of the intermediate levels of the decay take place.

One experiment was carried out with a source containing about 50 μc of Co^{55} alone, during which the linear polarization of the gamma rays was measured. The experimental results of the linear polarization effect $P_L Q_L$ and the simultaneously observed angular distribution anisotropy ε are given in fig. 10. The sign and the magnitude of the effect $P_L Q_L$ for the 0.935 MeV and the 1.410 MeV gamma ray determine the level sequence of Fe^{55} uniquely.

By comparing fig. 10 with tables 1 and 2, we get the following results: the 1.41 MeV gamma ray is pure E2; for the 0.935 MeV gamma ray the amplitude mixing ratio is $\delta(E2/M1) = +0.36 \pm 0.11$, i.e., about 12 % electric quadrupole admixture; thus the spin assignment for the 0.935 MeV state in Fe^{55} is $\frac{5}{2}^-$, for the 1.41 MeV state $\frac{7}{2}^-$; for the magnetic dipole moment of Co^{55} we find the alternative values of 5.3 ± 0.4 n.m., if the 1.03 MeV beta branch is predominantly a G.T. transition, 4.6 ± 0.4 n.m., if a pure Fermi transition. The possibility that the order of the spin assignments $\frac{5}{2}$ and $\frac{7}{2}$, respectively, for the first and second excited states of Fe^{55} should be reversed, has been eliminated by our linear polarization measurements. No statements can be made about the E2—M1 mixture of the 0.475 MeV gamma ray. Its anisotropy and polarization effects are being masked by the annihilation radiation.

For a unique determination of the magnetic moment of Co^{55}, the Fermi-G.T. mixture of the 1.03 MeV beta transition has to be measured. Assuming G.T. for this transition, the measured magnetic moment is $\mu \geqq 5$ n.m., while the Schmidt limit for this nucleus is +5.79 n.m. Comparing ${}_{27}Co^{55}_{28}$ with other spin $\frac{7}{2}$ nuclei having an odd number of protons in the $f_{\frac{7}{2}}$ shell and having 28 neutrons:

$${}_{25}Mn^{53}_{28} : \mu = 5.05 \text{ n.m.}$$
$${}_{23}V^{51}_{28} : \mu = 5.14 \text{ n.m.}$$

we see that all these cases have $\mu > 5$ n.m., thus favouring the above assumption of a G.T. transition. For a pure Fermi transition, however, the magnetic moment of Co^{55} would be $\mu \leqq 5.0$ n.m.

Acknowledgment is made to the U. S. Air Force for use of the Laboratory for Nuclear Science Data Center which was established with funds provided by the Air Force Office of Scientific Research under Contract No. AF49(638)-181.

We wish to express our appreciation to Professor W. M. Whitney for his advice during the course of our low temperature experiments; to Mr. Earle F. White for the cyclotron bombardments; to Mrs. Elizabeth W. Backofen for the chemical separations; and to Mr. D. Simons for his help during the latter stages of the polarization experiment.

References

1) E. Ambler, M. A. Grace, H. Halban, N. Kurti, H. Durand, C. E. Johnson and H. R. Lemmer, Phil. Mag. **44** (1953) 216
2) E. Ambler, R. W. Hayward, D. D. Hoppes, R. P. Hudson and C. S. Wu, Phys. Rev. **106** (1957) 1361
3) P. S. Jastram, C. M. Schroeder and R. C. Sapp, Bull. Am. Phys. Soc. **1** (1956) 91, 172
4) A. N. Diddens, W. J. Huiskamp, J. C. Severiens, A. R. Miedema and M. J. Steenland, Nuclear Physics **5** (1957) 58
5) E. Ambler, R. W. Hayward, D. D. Hoppes and R. P. Hudson, Phys. Rev. **108** (1957) 503
6) D. Strominger, J. M. Hollander and G. T. Seaborg, Revs. Mod. Phys. **30** (1958) 585

7) M. Deutsch and A. Hedgran, Phys. Rev. **75** (1949) 1443
8) R. S. Caird and A. C. G. Mitchell, Phys. Rev. **94** (1954) 412
9) A. Mukerji, V. S. Dubey and S. S. Malik, Bull. Am. Phys. Soc. **3** (1958) 62; Phys. Rev. (to be published)
10) D. T. Stevenson and M. Deutsch, Phys. Rev. **83** (1951) 1202
11) B. S. Dzelepow and L. K. Peker, Decay Schemes of Radioactive Nuclei (Acad. Science USSR Press, Moscow, 1958)
12) R. J. Blin-Stoyle and M. A. Grace, Handbuch der Physik **42** (1957) 555
13) H. A. Tolhoek and J. A. M. Cox, Physica **19** (1953) 101
14) L. C. Biedenharn and M. E. Rose, Revs. Mod. Phys. **25** (1953) 729
15) F. Boehm and A. H. Wapstra, Phys. Rev. **107** (1957) 1462
16) P. Dagley, M. A. Grace, J. S. Hill and C. V. Sowter, Phil. Mag. **3** (1958) 489
17) W. Dobrow and C. D. Jeffries, Phys. Rev. **108** (1957) 60
18) F. R. Metzger and M. Deutsch, Phys. Rev. **78** (1950) 551

1.C

Nuclear Physics **16** (1960) 278—303; © *North-Holland Publishing Co., Amsterdam*

Not to be reproduced by photoprint or microfilm without written permission from the publisher

INTRODUCTION OF MANY-PARTICLE VARIABLES FOR THE TREATMENT OF SPECIAL TRANSLATIONALLY INVARIANT MANY-BODY PROBLEMS

P. MÖBIUS

Physikalisches Institut, Technische Hochschule, Aachen †

Received 26 October 1959

Abstract: An attempt is made to treat special translationally invariant many-body problems by coordinate transformations introducing many-particle variables. These are adapted coordinates of such kind that the condition of translational invariance and the Pauli principle can be satisfied automatically. They are homogeneous functions of the particle coordinates obeying certain differential equations. The Schrödinger equation is transformed into these variables. There exist examples of systems of interacting particles which can be separated exactly in the many-particle variables but not in the particle coordinates.

1. Introduction

The time-independent behaviour of a quantal system of A particles is described by the eigenvalue problem

$$\mathscr{H}'(1 \ldots i \ldots A)\Psi'(1 \ldots i \ldots A) = E'\Psi'(1 \ldots i \ldots A) \tag{1}$$

where $\mathscr{H}'$ is the Hamilton operator of the system. The number i stands as an abbreviation for the space vector $\mathbf{r}'_i$, the spin variable σ_i and, if we also consider nuclear problems, for the isobaric spin variable τ_i of the i-th particle:

$$i = (\mathbf{r}'_i, \sigma_i, \tau_i).$$

Because of the general property of the Hamilton operator

$$\mathscr{H}'(\mathbf{r}'_1+\mathbf{a}, \mathbf{r}'_2+\mathbf{a}, \ldots \mathbf{r}'_A+\mathbf{a}) = \mathscr{H}'(\mathbf{r}'_1, \mathbf{r}'_2 \ldots \mathbf{r}'_A) \tag{2}$$

for an arbitrary vector $\mathbf{a}$, $\Psi'(1 \ldots A)$ must be an eigenfunction of the total linear momentum $\mathbf{P}$

$$\sum_1^A \frac{\hbar}{i} \frac{\partial}{\partial \mathbf{r}'_i} \Psi' = \mathbf{P}\Psi'. \tag{3}$$

If we consider only a system of Fermi-particles with equal masses $M_i = M$, the Pauli principle demands

$$\Psi'(1 \ldots i, k \ldots A) = -\Psi'(1 \ldots k, i \ldots A) \tag{4}$$

† Part of this work was performed at the Institute of Theoretical Physics, Göttingen.

which amounts to $\binom{A}{2}$ conditions for Ψ'. This means that only those eigenfunctions of (1) are physically meaningful which fulfil the $\binom{A}{2}+1$ subsidiary conditions (3) and (4).

The method which will be presented here consists in introducing "adapted coordinates" in such a way that the conditions (3) and (4) are satisfied automatically, and then transforming the Schrödinger equation (1) into those variables. The simplest way to fulfil the condition (3) is to split off the kinetic energy of the centre-of-mass motion in the Hamilton operator

$$\mathcal{H}' = \mathcal{H}_{\mathbf{R}} + \mathcal{H}.$$

This can be done by replacing the A position vectors $(\mathbf{r}'_1 \ldots \mathbf{r}'_A)$ of the particles by the centre-of-mass vector $\mathbf{R}$ and $(A-1)$ suitably chosen vectors $(\mathbf{r}_1 \ldots \mathbf{r}_{A-1})$, which will describe the internal motion. For this purpose we can use any linear transformation with an orthogonal matrix, where one of the new vectors represents just $\mathbf{R}$. Now, the $\binom{A}{2}$ permutations of (4) must be expressed in only $(A-1)$ available internal vectors $(\mathbf{r}_1 \ldots \mathbf{r}_{A-1})$ because the centre-of-mass vector is invariant under this process. Therefore, we have to choose an orthogonal matrix such that it also gives very simple expressions for the permutations in the internal vectors.

The next step is to construct a set of homogeneous functions of the $(3A-3)$ internal coordinates, which are invariant under the above permutations and obey certain differential equations. These functions are then introduced as independent variables in the Schrödinger equation. Because each of them contains several internal coordinates they are called "many-particle variables". The characteristic features of the many-particle variables are independent of the number of particles, therefore it is possible to get results containing A as a parameter which can have all values $A \geqq 3$.

The theory outlined here is developed in this paper only for a special type of translationally invariant many-body problem. The limitation is specified below. For convenience the method is demonstrated in detail for the very simple problem of A particles coupled together harmonically

$$\mathcal{H}' = \sum_1^A - \frac{\hbar^2}{2M} \frac{\partial^2}{\partial \mathbf{r}_i'^2} + \sum_{i>k=1}^A \tfrac{1}{2} c(\mathbf{r}'_i - \mathbf{r}'_k)^2. \tag{5}$$

Further examples treated in the paper are

$$\mathcal{H}' = \sum_1^3 - \frac{\hbar^2}{2M} \frac{\partial^2}{\partial \mathbf{r}_i'^2} + \sum_{i>k=1}^3 [c_2(\mathbf{r}'_i - \mathbf{r}'_k)^2 + c_4(\mathbf{r}'_i - \mathbf{r}'_k)^4] \tag{6}$$

and

$$\mathcal{H}' = \sum_1^A - \frac{\hbar^2}{2M} \frac{\partial^2}{\partial \mathbf{r}_i'^2} + \sum_{i>k=1}^A c_2(\mathbf{r}'_i - \mathbf{r}'_k)^2 + \sum_{\substack{i>k=1 \\ i>l=1}}^A c_\pi(\mathbf{r}'_i - \mathbf{r}'_k)^2(\mathbf{r}'_j - \mathbf{r}'_l)^2, \tag{7}$$

the last one containing many-body forces. For the problems (5)—(7) the Schrödinger equation can be separated exactly in the many-particle variables.

Only the totally antisymmetric and totally symmetric space functions and the corresponding eigenvalue spectrum are computed. The functions are obtained by solving a finite system of linear equations. An extension to intermediate symmetries is not a difficult problem.

2. Separation of the Centre-of-Mass Motion

As a starting point for our considerations we shall choose the very simple example of a system of A particles coupled together harmonically

$$\mathscr{H}' = \sum_1^A -\frac{\hbar^2}{2M}\frac{\partial^2}{\partial \mathbf{r}_i'^2} + \sum_{i>k=1}^A \tfrac{1}{2}c(\mathbf{r}'_i - \mathbf{r}'_k)^2. \tag{8}$$

To separate the centre-of-mass motion we can use any linear transformation with an orthogonal matrix where one new vector ($\mathbf{r}_A$) describes the centre of mass. The difficulty is not the separation but the fact that the eigenfunction of (8) has to obey the Pauli principle. This means it has to change sign for a permutation of two particles. The transformation introduces, instead of the A particle vectors ($\mathbf{r}'_1 \ldots \mathbf{r}'_A$), $(A-1)$ vectors describing the internal motion and $\mathbf{r}_A$ representing the centre-of-mass. Because $\mathbf{r}_A$ is invariant under an exchange of two particles there are only $(A-1)$ vectors available to express the $\binom{A}{2}$ permutations of the Pauli principle. The problem is now to choose such a matrix that the permutations look also very simple in the internal coordinates. One way is to demand that an exchange of two of the $(A-1)$ internal vectors $\mathbf{r}_i$ and $\mathbf{r}_k$ correspond to an exchange of two particle vectors $\mathbf{r}'_i$ and $\mathbf{r}'_k$.

A transformation having the three properties:

I. the matrix is orthogonal,

II. one vector represents the centre-of-mass,

III. a permutation of $\mathbf{r}_i$ and $\mathbf{r}_k$ corresponds a permutation of $\mathbf{r}'_i$ and $\mathbf{r}'_k$,

is

$$\mathbf{r}_i = \mathbf{r}'_i - \frac{\sqrt{A}}{\sqrt{A}-1}\mathbf{R} + \frac{1}{\sqrt{A}-1}\mathbf{r}'_A, \qquad (1 \leqq i \leqq A-1) \tag{9a}$$

$$\mathbf{r}_A = \sqrt{A}\mathbf{R}, \tag{9b}$$

where $\mathbf{R}$ is the centre-of-mass vector

$$\mathbf{R} = \frac{1}{A}\sum_1^A \mathbf{r}'_i.$$

For an infinite number of particles (9a) goes over into the transformation in the centre-of-mass system $\mathbf{r}_i = \mathbf{r}'_i - \mathbf{R}$.

Because the matrix (9) is orthogonal the momentum vectors transform like the space vectors. For (8) we get in the new variables

$$\mathcal{H}' = -\frac{\hbar^2}{2M}\frac{\partial^2}{\partial \mathbf{r}_A{}^2} + \sum_1^{A-1}\left[-\frac{\hbar^2}{2M}\frac{\partial^2}{\partial \mathbf{r}_i{}^2} + \tfrac{1}{2}Ac\mathbf{r}_i{}^2\right] \tag{10}$$

where the first term is the kinetic energy of the centre-of-mass motion. The subsidiary condition (3) is transformed into

$$\frac{\hbar}{i}\sqrt{A}\frac{\partial \Psi'}{\partial \mathbf{r}_A} = \mathbf{P}\Psi' \tag{3'}$$

and every solution of (10) satisfies automatically (3). In the new variables, Ψ' is a product of two functions

$$\Psi' = \chi(\mathbf{r}_A)\Psi(\mathbf{r}_1 \ldots \mathbf{r}_{A-1}) \tag{11}$$

where $\chi(\mathbf{r}_A)$ describes the centre-of-mass motion and cannot be made anti-symmetric. Therefore we split off this motion and investigate in the following only the problem of the internal motion,

$$\mathcal{H}\Psi(\mathbf{r}_1 \ldots \mathbf{r}_{A-1}) = E\Psi(\mathbf{r}_1 \ldots \mathbf{r}_{A-1}) \tag{12}$$

with

$$\mathcal{H} = \sum_1^{A-1}\left[-\frac{\hbar^2}{2M}\frac{\partial^2}{\partial \mathbf{r}_i{}^2} + \tfrac{1}{2}Ac\mathbf{r}_i{}^2\right] \tag{13}$$

The difficulty is now that the Pauli principle becomes more complicated in the $(A-1)$ internal coordinates $(\mathbf{r}_1 \ldots \mathbf{r}_{A-1})$ than in the A particle coordinates $(\mathbf{r}'_1 \ldots \mathbf{r}'_A)$.

3. Pauli Principle

To formulate the Pauli principle in the internal coordinates, we have to investigate how the $\binom{A}{2}$ subsidiary conditions (4) are transformed. For this purpose we introduce the auxiliary quantities $\bar{\mathbf{r}}_i$ which are obtained from the $\mathbf{r}_i(\mathbf{r}'_1 \ldots \mathbf{r}'_A)$ by interchanging two $\mathbf{r}'_k$. For the totally anti-symmetric and totally symmetric space functions, the Pauli principle then demands

$$\Psi(\mathbf{r}_1\mathbf{r}_2 \ldots \mathbf{r}_{A-1}) = \mp\Psi(\bar{\mathbf{r}}_1\bar{\mathbf{r}}_2 \ldots \bar{\mathbf{r}}_{A-1}). \tag{14}$$

According to (9) the following relations hold for the $\bar{\mathbf{r}}_i$, if $\mathbf{r}'_i$ and $\mathbf{r}'_k$ with $i, k \leqq A-1$ are permuted:

$$\bar{\mathbf{r}}_i = \mathbf{r}_k, \quad \bar{\mathbf{r}}_k = \mathbf{r}_i, \tag{15a}$$

$$\bar{\mathbf{r}}_l = \mathbf{r}_l \quad \text{for} \quad l \neq i, k.$$

These are $\binom{A-1}{2}$ conditions which (14) has to satisfy. They simply mean that

$\Psi(\mathbf{r}_1 \ldots \mathbf{r}_{A-1})$ has also to change sign if two of the internal coordinates are exchanged. But eqs. (15a) are not all the conditions. Because of

$$\binom{A}{2} = \binom{A-1}{2} + (A-1) \tag{16}$$

we have to add $(A-1)$ further conditions which are obtained by permuting $\mathbf{r}'_k$ with $\mathbf{r}'_A$. This gives for $\bar{\mathbf{r}}_k$,

$$\bar{\mathbf{r}}_k = \frac{1}{(\sqrt{A}-1)}\mathbf{r}_k + \frac{\sqrt{A}-2}{(\sqrt{A}-1)^2}\mathbf{y}, \quad \text{with} \quad \mathbf{y} = \sum_1^{A-1} \mathbf{r}_i \tag{15b}$$

and for all the $(A-2)$ other vectors $\bar{\mathbf{r}}_i$,

$$\bar{\mathbf{r}}_i = \mathbf{r}_i + \frac{1}{(\sqrt{A}-1)^2}[(\sqrt{A}-1)\mathbf{r}_k - \mathbf{y}] \qquad (i \neq k); \tag{15c}$$

k varies from 1 to $(A-1)$, and eqs. (15a—c) therefore contain all the conditions for (14). As examples, the $\bar{\mathbf{r}}_i$ will now be given for systems of 3 and 4 particles.

For 3 particles we have 3 conditions and two vectors $(\mathbf{r}_1, \mathbf{r}_2)$ describing the internal motion. Eqs. (15a) provides

$$1) \quad \bar{\mathbf{r}}_1 = \mathbf{r}_2, \qquad \bar{\mathbf{r}}_2 = \mathbf{r}_1 \tag{18a}$$

and (15b, c)

$$\begin{aligned} 2) \quad \bar{\mathbf{r}}_1 &= \tfrac{1}{2}\sqrt{3}\,\mathbf{r}_1 - \tfrac{1}{2}\mathbf{r}_2 & 3) \quad \bar{\mathbf{r}}_1 &= -\tfrac{1}{2}\sqrt{3}\,\mathbf{r}_1 - \tfrac{1}{2}\mathbf{r}_2 \\ \bar{\mathbf{r}}_2 &= -\tfrac{1}{2}\mathbf{r}_1 - \tfrac{1}{2}\sqrt{3}\,\mathbf{r}_2 & \bar{\mathbf{r}}_2 &= -\tfrac{1}{2}\mathbf{r}_1 + \tfrac{1}{2}\sqrt{3}\,\mathbf{r}_2. \end{aligned} \tag{18b, c}$$

For 4 particles there are three vectors $(\mathbf{r}_1\mathbf{r}_2\mathbf{r}_3)$ and 6 conditions. Eqs. (15a) provide 3 conditions:

$$\begin{aligned} 1) \quad \bar{\mathbf{r}}_1 &= \mathbf{r}_1 & 2) \quad \bar{\mathbf{r}}_1 &= \mathbf{r}_3 & 3) \quad \bar{\mathbf{r}}_1 &= \mathbf{r}_2 \\ \bar{\mathbf{r}}_2 &= \mathbf{r}_3 & \bar{\mathbf{r}}_2 &= \mathbf{r}_2 & \bar{\mathbf{r}}_2 &= \mathbf{r}_1 \\ \bar{\mathbf{r}}_3 &= \mathbf{r}_2 & \bar{\mathbf{r}}_3 &= \mathbf{r}_1 & \bar{\mathbf{r}}_3 &= \mathbf{r}_3 \end{aligned}$$

and (15b, c) the other 3:

$$\begin{aligned} 4) \quad \bar{\mathbf{r}}_1 &= \mathbf{r}_1 & 5) \quad \bar{\mathbf{r}}_1 &= -\mathbf{r}_3 & 6) \quad \bar{\mathbf{r}}_1 &= -\mathbf{r}_2 \\ \bar{\mathbf{r}}_2 &= -\mathbf{r}_3 & \bar{\mathbf{r}}_2 &= \mathbf{r}_2 & \bar{\mathbf{r}}_2 &= -\mathbf{r}_1 \\ \bar{\mathbf{r}}_3 &= -\mathbf{r}_2 & \bar{\mathbf{r}}_3 &= -\mathbf{r}_1 & \bar{\mathbf{r}}_3 &= \mathbf{r}_3. \end{aligned}$$

They are very simple in this case.

4. Definition of the Many-Particle Variables

The structure of the conditions (15a, b, c) requires us to look only for those eigenfunctions of (13) which can also be represented by homogeneous functions

of the internal coordinates. Therefore it is possible to introduce such homogeneous functions as independent variables instead of the internal coordinates. For our method we shall choose as a basic set the simplest homogeneous functions which are invariant under the substitutions (15a, b, c):

$$g(\mathbf{r}_1\mathbf{r}_2\ldots\mathbf{r}_{A-1}) = g(\bar{\mathbf{r}}_1\bar{\mathbf{r}}_2\ldots\bar{\mathbf{r}}_{A-1}). \tag{19}$$

Because the g depend in every case on $(A-1)$ or more of the $(3A-3)$ internal coordinates they are called many-particle variables (m.p.v.). The simplest one, a homogeneous function of first order, does not exist. The quantity

$$\xi = \sum_1^{A-1} x_i \tag{20}$$

is invariant under the substitutions (15a) but not under (15b, c). The same relation also holds for the sum of the y and z components. A m.p.v. of the second degree depending only on the x coordinates is

$$u(x_1\ldots x_{A-1}) = \sum_1^{A-1} x_i^2 \tag{21}$$

and one of the third degree

$$g_3(x_1\ldots x_{A-1}) = \sum_1^{A-1} x_i^3 - \frac{3}{\sqrt{A}(\sqrt{A}-1)}\,\xi\sum_1^{A-1} x_i^2 + \frac{1}{\sqrt{A}(\sqrt{A}-1)^2}\,\xi^3.$$

As will be shown later, we need for the construction of the eigenfunctions of an A-particle system all independent m.p.v. from degree 2 up to degree A. In the one-dimensional case there exists for every degree between 2 and A only one m.p.v., designated † by $u(x_1\ldots x_{A-1})$, $g_3(x_1\ldots x_{A-1}), \ldots, g_A(x_1\ldots x_{A-1})$ and introduced instead of the internal coordinates. In the three-dimensional case the situation is not so simple because the number of independent m.p.v. depends on the degree.

As examples, the m.p.v. are given for a one-dimensional system of 3 and 4 particles. In the case of 3 particles we have to construct the two m.p.v.

$$u(x_1x_2) = x_1^2+x_2^2, \tag{23a}$$

$$g_3(x_1x_2) = x_1^3+x_2^3-3x_1^2x_2-3x_1x_2^2; \tag{23b}$$

and in the case of 4 particles the following three m.p.v.:

$$u(x_1x_2x_3) = x_1^2+x_2^2+x_3^2,$$

$$g_3(x_1x_2x_3) = x_1x_2x_3,$$

$$g_4(x_1x_2x_3) = x_1^4+x_2^4+x_3^4-\alpha(x_1^2x_2^2+x_1^2x_3^2+x_2^2x_3^2),$$

† The m.p.v. u is not called g_2, because it obeys a differential equation different from those obeyed by all the other g_n.

where α is a factor determined by the differential equation which the g_n have to obey for $n \geqq 3$.

5. Construction of the Eigenfunctions in the One-Dimensional Case

The separation of the centre-of-mass motion changes the form of the subsidiary conditions we have to impose on Ψ to fulfil the Pauli principle. Though in the case of harmonically coupled particles the Hamilton operator (13) can be separated in the internal coordinates, it is in general no longer possible to write the total wave function in the form of a Slater determinant. This is due to the conditions (15b, c) which involve all coordinates. Therefore a new method must be developed. To get familiar with it, we shall first demonstrate the general lines of the method for a one-dimensional system of A harmonically coupled particles [1]).

The problem we are concerned with is in this case

$$\left\{\sum_1^{A-1}\left[-\frac{\hbar^2}{2M}\frac{\partial^2}{\partial x_i^2}+\tfrac{1}{2}Acx_i^2\right]\right\}\Psi(x_1\ldots x_{A-1})=E\Psi(x_1\ldots x_{A-1}), \quad (25)$$

Ψ having to obey the Pauli principle. Because the potential energy in (25) is, after introduction of the m.p.v., equal to

$$\sum_1^{A-1}\tfrac{1}{2}Acx_i^2=\tfrac{1}{2}Acu \quad (26)$$

we shall try for Ψ the following Ansatz:

$$\Psi(x_1\ldots x_{A-1})=\phi(x_1\ldots x_{A-1})f(u), \quad (27)$$

where both functions contain all coordinates. Instead of one unknown function, two such functions have now been introduced. Putting (27) into (25) we get

$$-\frac{\hbar^2}{2M}\left\{4u\frac{\mathrm{d}^2f}{\mathrm{d}u^2}\phi+\left[4\sum_1^{A-1}x_i\frac{\partial\phi}{\partial x_i}+2(A-1)\phi\right]\frac{\mathrm{d}f}{\mathrm{d}u}+f(u)\sum_1^{A-1}\frac{\partial^2\phi}{\partial x_i^2}\right\}$$
$$+[\tfrac{1}{2}Acu-E]f(u)\phi=0. \quad (28)$$

From (28) we obtain an equation for $f(u)$ alone if we impose on ϕ the following conditions †:

$$\sum_1^{A-1}\frac{\partial^2\phi}{\partial x_i^2}=0, \quad (29a)$$

$$\sum_1^{A-1}x_i\frac{\partial\phi}{\partial x_i}=k\phi, \quad (29b)$$

where k is a constant integer. With the substitutions

$$v=\alpha u, \qquad \alpha=\frac{1}{\hbar}(MAc)^{\frac{1}{4}}, \qquad \omega=\left(\frac{Ac}{M}\right)^{\frac{1}{2}}, \qquad e=\frac{2E}{\hbar\omega} \quad (30)$$

† That this Ansatz gives all admitted solutions is proved for the simple case of 3 particles.

and taking into account (29a, b), we get for $f(v)$ the differential equation

$$4v\frac{\mathrm{d}^2 f}{\mathrm{d}v^2}+2(2k+A-1)\frac{\mathrm{d}f}{\mathrm{d}v}+(e-v)f(v)=0. \tag{31}$$

The eigenfunctions of (31) are the so called "associated Laguerre functions"

$$f_{n,k}(v)=\mathrm{e}^{-\frac{1}{2}v}\sum_{\nu=0}^{n}a_\nu(n,k,A)v^\nu \tag{32}$$

with the coefficients

$$a_\nu=\frac{(-1)^\nu}{\nu!}\prod_{\mu=0}^{\nu}\frac{(n-\mu)}{(k+\mu+\frac{1}{2}(A-1))} \tag{33}$$

and the eigenvalues

$$e=4n+2k+A-1 \quad (n=0,1,2\ldots). \tag{34}$$

The energy of the system of A particles is

$$E=\hbar\omega[\tfrac{1}{2}(A-1)+2n_2+k] \quad (n_2=0,1,2\ldots). \tag{35}$$

The suffix 2 is added to n to indicate that this quantum number originates from u, the m.p.v. of the second degree. The functions $f_{n,k}(v)$ contain the number of particles A as a parameter. In order to get the selection rules for k we have to look for all functions $\phi_k(x_1\ldots x_{A-1})$ obeying (29a, b) and the Pauli principle. As indicated in the introduction we are only interested in the totally antisymmetric and totally symmetric space functions.

The problem is next to look for all homogeneous solutions of the $(A-1)$-dimensional Laplace equation satisfying the subsidiary conditions

$$\phi_k(x_1\ldots x_{A-1})=\mp\,\phi_k(x_1\ldots x_{A-1}). \tag{36}$$

This can be done very easily with the help of the many-particle variables. Let us first consider the totally antisymmetric space functions. The lowest admitted value of k is

$$k_0=\tfrac{1}{2}A(A-1) \tag{37}$$

and the corresponding function, designated by $\phi_{k0}\equiv\varphi$, is

$$\varphi(x_1\ldots x_{A-1})=\prod_{i>k=1}^{A-1}(x_i-x_k)\prod_{j=1}^{A-1}(\xi-(\sqrt{A}-1)x_j). \tag{38}$$

If we split off φ from ϕ_k, the remaining part must be symmetric under the transformation (15a—c). This is the case if it depends only on the m.p.v. For ϕ_k we try therefore the Ansatz

$$\phi_k(x_1\ldots x_{A-1})=\varphi(x_1\ldots x_{A-1})F_N(u,g_3\ldots g_A) \tag{39a}$$

with

$$k=\tfrac{1}{2}A(A-1)+N. \tag{40}$$

The condition (19) does not determine completely the m.p.v. It is still possible to impose upon them the following differential equation

$$\sum_1^{A-1} \frac{\partial^2}{\partial x_i^2}(\varphi g_n) = 0 \qquad (n = 3, 4 \ldots A). \tag{41a}$$

Putting (39a) into (29a), using the simplification due to (29b),

$$2u \frac{\partial F_N}{\partial u} + \sum_3^A n g_n \frac{\partial F_N}{\partial g_n} = N F_N \tag{42}$$

and because of (41a), we obtain for $F_N(u, g_3 \ldots g_A)$ the differential equation

$$(2N+A^2-5)\frac{\partial F_N}{\partial u} - 2u \frac{\partial^2 F_N}{\partial u^2} + \tfrac{1}{2}\sum_{n=3}^A \frac{\partial^2 F_N}{\partial g_n^2}\left[\sum_1^{A-1}\left(\frac{\partial g_n}{\partial x_i}\right)^2\right] + \sum_{n>l=3}^A \frac{\partial^2 F_N}{\partial g_n \partial g_l}\left[\sum_1^{A-1}\frac{\partial g_n}{\partial x_i}\frac{\partial g_l}{\partial x_i}\right] = 0, \tag{43a}$$

where the sums $\sum_1^{A-1}(\partial g_n/\partial x_i)(\partial g_l/\partial x_i)$ can always be expressed in terms of the m.p.v. The solutions of (31) and (43) contain the solution of the whole problem. The totally antisymmetric space functions are then given by

$$\Psi(x_1 \ldots x_{A-1}) = \varphi(x_1 \ldots x_{A-1}) f_{n_2 N}(u) F_N(u, g_3 \ldots g_A) \tag{44a}$$

and the corresponding energy eigenvalues are

$$E = \hbar\omega[\tfrac{1}{2}(A^2-1)+2n_2+N] \qquad (n_2 = 0, 1, 2 \ldots), \tag{45a}$$

where the values of N are determined by (43a). How this can be done, is demonstrated in detail for a system of 3 and $A \geqq 3$ particles. For the totally symmetric space function we make the Ansatz for ϕ_k

$$\phi_k(x_1 \ldots x_{A-1}) = F_k(u, g_3 \ldots g_A) \tag{39b}$$

and impose on the m.p.v. the differential equation

$$\sum_1^{A-1} \frac{\partial^2 g_n}{\partial x_i^2} = 0 \qquad (n = 3, 4 \ldots A) \tag{41b}$$

and obtain for $F_k(u, g_3 \ldots g_A)$ the equation

$$(2k+A-5)\frac{\partial F_k}{\partial u} - 2u \frac{\partial^2 F_k}{\partial u^2} + \tfrac{1}{2}\sum_{n=3}^A \frac{\partial^2 F_k}{\partial g_n^2}\left[\sum_1^{A-1}\left(\frac{\partial g_n}{\partial x_i}\right)^2\right] + \sum_{n>l=3}^A \frac{\partial^2 F_N}{\partial g_n \partial g_l}\left[\sum_1^{A-1}\frac{\partial g_n}{\partial x_i}\frac{\partial g_l}{\partial x_i}\right] = 0. \tag{43b}$$

The totally symmetric space functions are then given by

$$\Psi(x_1 \ldots x_{A-1}) = f_{n_2 N}(u) F_k(u, g_3 \ldots g_A) \tag{44b}$$

and the corresponding energy eigenvalues are

$$E = \hbar\omega[\tfrac{1}{2}(A-1)+2n_2+k]. \tag{45b}$$

The determination of k is completely analogous to that of N.

6. Application to a One-Dimensional System of Three Particles

6.1. THE METHOD

The 3-body problem is very simple. We consider only the totally antisymmetric space functions. The two m.p.v. are

$$u(x_1x_2) = x_1^2+x_2^2, \qquad g_3(x_1x_2) = x_1^3+x_2^3-3x_1^2x_2-3x_1x_2^2 \tag{23a, b}$$

and the function $\varphi(x_1x_2)$ is, according to (38),

$$\varphi(x_1x_2) = x_1^3-x_2^3+3x_1^2x_2-3x_1x_2^2. \tag{46}$$

The eigenfunctions are

$$\Psi_{n_2N}(x_1x_2) = \varphi(x_1x_2)f_{n_2N}(u)F_N(u, g_3), \tag{47}$$

where φ is given by (46) and $f_{n_2N}(u)$ by (32):

$$f_{n_2N}(u) = \mathrm{e}^{-\frac{1}{2}\alpha u}\sum_{\nu=0}^{n_2} a_\nu(n_2N)(\alpha u)^\nu \tag{48a}$$

with the coefficients

$$a_\nu = \frac{(-1)^\nu}{\nu!}\prod_{\mu=0}^{\nu}\frac{(n_2-\mu)}{(N+4+\mu)} \tag{48b}$$

and $F_N(u, g_3)$ must be determined by (43a). For three particles (43a) reduces to

$$(2N+4)\frac{\partial F_N}{\partial u} - 2u\frac{\partial^2 F_N}{\partial u^2} + \frac{1}{2}\frac{\partial^2 F_N}{\partial g_3^2}\left[\sum_1^2\left(\frac{\partial g_3}{\partial x_i}\right)^2\right] = 0. \tag{49}$$

From (23b) follows

$$\sum_1^2\left(\frac{\partial g_3}{\partial x_i}\right)^2 = 18(x_1^2+x_2^2)^2 = 18u^2;$$

putting this into (49) we obtain for $F_N(u, g_3)$ the differential equation

$$(2N+4)\frac{\partial F_N}{\partial u} - 2u\frac{\partial^2 F_N}{\partial u^2} + 9u^2\frac{\partial^2 F_N}{\partial g_3^2} = 0. \tag{50}$$

Because of the required homogeneity in the x_i, according to (29b), we can use as solutions only finite power series like

$$F_0 = 1, \qquad F_3 = g_3, \qquad F_6 = 2g_3^2-u^3, \qquad F_9 = g_3^3-g_3u^2. \tag{51}$$

It is convenient to distinguish between the two cases

$$N = 6N' \quad \text{and} \quad N = 6N'+3 \qquad \text{with} \quad N' = 0, 1, 2 \ldots . \tag{52}$$

The corresponding solutions are

$$F_{6N'} = \sum_{\nu=0}^{N'} (-2)^\nu \binom{N'+\nu}{2\nu} g_3^{2\nu} u^{3(N'-\nu)} \qquad (N' = 0, 1, 2 \ldots) \tag{53a}$$

and

$$F_{6N'+3} = \sum_{\nu=0}^{N'} (-2)^\nu \binom{N'+\nu+1}{2\nu+1} g_3^{2\nu+1} u^{3(N'-\nu)} \qquad (N' = 0, 1, 2 \ldots). \tag{53b}$$

The functions $F_N(u, g_3)$ are homogeneous functions in the x_i of degree N. Because we find one function corresponding to every power of g_3, the selection rule for N follows:

$$N = 3n_3 \quad \text{with} \quad n_3 = 0, 1, 2 \ldots . \tag{54}$$

Putting (54) in (53) and (45a) we get for the totally antisymmetric space function the expression

$$\Psi_{n_2 n_3}(x_1 x_2) = \varphi(x_1 x_2) f_{n_2 n_3}(u) F_{3n_3}(u, g_3) \tag{55}$$

where $F_{3n_3}(u, g_3)$ is given by (53a) for even $n_3 (n_3 = 2N')$ and by (53b) for odd $n_3 (n_3 = 2N'+1)$. For the corresponding eigenvalue spectrum one gets

$$E_{n_2 n_3} = \hbar\omega[4+2n_2+3n_3] \qquad (n_2, n_3 = 0, 1, 2 \ldots); \tag{56}$$

the quantum numbers n_2, n_3 may take on all non-negative integer numbers independently of each other.

Let us compare this excitation spectrum with that of a system of 3 independent harmonic oscillators having the eigenvalues

$$E_{\text{IPM}} = \hbar\omega[\tfrac{3}{2}+n_1+n_2+n_3] \tag{57}$$

with the condition $0 \leqq n_1 < n_2 < n_3$; eq. (57) can also be written in the form

$$E_{\text{IPM}} = \hbar\omega[\tfrac{3}{2}+3+1n_1+2n_2+3n_3] \quad \text{with} \quad n_1, n_2, n_3 = 0, 1, 2 \ldots . \tag{57a}$$

This comparison is done in table 1, where the degeneracy of the states according to (56) is written in the first column and that according to (57) in the second column. From the comparison one can conclude that (56) and (57) are entirely different problems. A completely formal connection is given by saying that the redundant states in (57) correspond to an excitation of the centre-of-mass motion [2]). This way of speaking is based on the identity

$$\sum_1^A \tfrac{1}{2} A c \mathbf{r}_i'^2 = \sum_{i>k=1}^{A} \tfrac{1}{2} c(\mathbf{r}'_i - \mathbf{r}'_k)^2 + \tfrac{1}{2} c(\sum_1^A \mathbf{r}'_i)^2 \tag{58}$$

which permits one to write for the Hamilton operator of A independent har-

monic oscillators

$$\mathscr{H}_{\text{IPM}} = \sum_1^A \left[-\frac{\hbar^2}{2M} \frac{\partial^2}{\partial \mathbf{r}_i'^2} + \tfrac{1}{2} Ac\, \mathbf{r}_i'^2 \right] \tag{59}$$

the relation

$$\mathscr{H}_{\text{IPM}} = -\frac{\hbar^2}{2M} \frac{\partial^2}{\partial \mathbf{r}_A{}^2} + \tfrac{1}{2} Ac\, \mathbf{r}_A{}^2 + \mathscr{H}(\mathbf{r}_1 \ldots \mathbf{r}_{A-1}) \tag{60}$$

where $\mathscr{H}$ is the Hamilton operator (13) describing the internal motion and $\mathbf{r}_A$ represents the centre-of-mass vector. Thus, (60) gives a harmonic oscillation for the centre-of-mass motion instead of a plane wave according to (10). This additional oscillator is responsible for the redundant states in (57). But this concept of connecting a translationally invariant Hamiltonian with a Hamiltonian of independent particles by the introduction of an external potential for the centre-of-mass is only useful for the example considered above and becomes rather complicated for other potentials [3]).

TABLE 1

Excitation spectra of the 3-particle and the 3-oscillator system

Excited quanta $\hbar\omega$		6	5	4	3	2	1	0
Degeneracy	3-particle	2	1	1	1	1	0	1
	3-oscill.	7	5	4	3	2	1	1

Because the Hamilton operator (13) can be separated in the internal coordinates it is also possible to write the eigenfunctions as linear combinations of Slater determinants. The eigenfunctions $\Psi_{n_2 n_3}(x_1 x_2)$ for the 4 lowest states are in this representation

$$\begin{aligned}
\Psi_{00} &= \left\{ \begin{vmatrix} H_0(x_1)H_0(x_2) \\ H_3(x_1)H_3(x_2) \end{vmatrix} + 3 \begin{vmatrix} H_1(x_1)H_1(x_2) \\ H_2(x_2)H_2(x_2) \end{vmatrix} \right\} e^{-\frac{1}{2}(x_1^2+x_2^2)}, \\
\Psi_{10} &= \left\{ \begin{vmatrix} H_0(x_1)H_0(x_2) \\ H_5(x_1)H_5(x_2) \end{vmatrix} + 3 \begin{vmatrix} H_1(x_1)H_1(x_2) \\ H_4(x_1)H_4(x_2) \end{vmatrix} - 2 \begin{vmatrix} H_2(x_1)H_2(x_2) \\ H_3(x_1)H_3(x_2) \end{vmatrix} \right\} e^{-\frac{1}{2}(x_1^2+x_2^2)}, \\
\Psi_{01} &= \left\{ \begin{vmatrix} H_0(x_1)H_0(x_2) \\ H_6(x_1)H_6(x_2) \end{vmatrix} - 15 \begin{vmatrix} H_2(x_1)H_2(x_2) \\ H_4(x_1)H_4(x_2) \end{vmatrix} \right\} e^{-\frac{1}{2}(x_1^2+x_2^2)}, \\
\Psi_{20} &= \left\{ \begin{vmatrix} H_0(x_1)H_0(x_2) \\ H_7(x_1)H_7(x_2) \end{vmatrix} + 3 \begin{vmatrix} H_1(x_1)H_1(x_2) \\ H_6(x_1)H_6(x_2) \end{vmatrix} - \begin{vmatrix} H_2(x_1)H_2(x_2) \\ H_5(x_1)H_5(x_2) \end{vmatrix} \right. \\
&\qquad \left. + 5 \begin{vmatrix} H_3(x_1)H_3(x_2) \\ H_4(x_1)H_4(x_2) \end{vmatrix} \right\} e^{-\frac{1}{2}(x_1^2+x_2^2)},
\end{aligned} \tag{61}$$

where $H_n(x)$ are the Hermite polynomials, normalization factors are omitted and $\alpha = 1$. Using m.p.v. they are

$$\begin{aligned}
\Psi_{00} &= \varphi e^{-\frac{1}{2}u}, \\
\Psi_{10} &= \varphi e^{-\frac{1}{2}u}(1-\tfrac{1}{4}u), \\
\Psi_{01} &= \varphi g_3 e^{-\frac{1}{2}u}, \\
\Psi_{20} &= \varphi e^{-\frac{1}{2}u}(1-\tfrac{1}{2}u+\tfrac{1}{4}u^2).
\end{aligned} \tag{62}$$

6.2. PROOF THAT THE METHOD PROVIDES ALL ADMITTED FUNCTIONS

In the case of 3 particles it is very easy to prove that the method provides all admitted eigenfunctions. Instead of x_1 and x_2, polar coordinates are introduced by

$$x_1 = r \sin \vartheta, \quad x_2 = r \cos \vartheta. \tag{63}$$

All solutions of (29a, b) have the form

$$\phi_k \propto r^k (a_k \cos k\vartheta + b_k \sin k\vartheta). \tag{64}$$

Now the Pauli principle requires according to (36)

$$\phi_k(\vartheta) = -\phi_k(\bar{\vartheta}) \tag{65}$$

because of $r = \bar{r}$. The 3 conditions (18) expressed in ϑ are

$$\bar{\vartheta}_1 = \frac{3\pi}{6} - \vartheta, \qquad \bar{\vartheta}_2 = \frac{7\pi}{6} - \vartheta, \qquad \bar{\vartheta}_3 = \frac{11\pi}{6} - \vartheta. \tag{66}$$

All functions of the form (64) obeying the conditions (65—66) are

$$\begin{aligned}
&r^{3+12\nu} \ [\cos(3+12\nu)\vartheta + \sin(3+12\nu)\vartheta], \\
&r^{6+12\nu} \ \cos(6+12\nu)\vartheta, \\
&r^{9+12\nu} \ [\cos(9+12\nu)\vartheta - \sin(9+12\nu)\vartheta], \\
&r^{12+12\nu} \sin(12+12\nu)\vartheta \qquad (\nu = 0, 1, 2 \ldots).
\end{aligned} \tag{67}$$

The functions (67) are identical with the solutions $F_N(u, g_3)$ of (50) multiplied by $\varphi(x_1 x_2)$ if both are expressed in the same coordinates. This justifies the Ansatz (39a). The justification of equation (27) is similar.

7. Application to a One-Dimensional System of A Particles

An extension of the above method to a system of A particles is straightforward. Out of the $(A-1)$ coordinates $(x_1 \ldots x_{A-1})$ we have to construct the $(A-1)$ m.p.v. $(u, g_3 \ldots g_A)$ according to (19) and (41). From the totally antisymmetric space function

$$\Psi(x_1 \ldots x_{A-1}) = \varphi(x_1 \cdots x_{A-1}) f_{n_3 N}(u) F_N(u, g_3 \ldots g_A) \tag{44a}$$

the first two functions are given by (38) and (32). It remains to look for all solutions $F_N(u, g_3 \ldots g_A)$ of (43). Because of the condition (29b) only finite

power series of the following form are admissible:

$$F_N(u, g_3 \dots g_A) = \sum_{(l_i)} \alpha_{l_A l_{A-1} \cdots l_3 l_2} g_A{}^{l_A} g_{A-1}^{l_{A-1}} \dots g_3{}^{l_3} u^{l_2}, \tag{68}$$

where the symbol (l_i) means a summation over all non-negative integer values of l_i obeing the subsidiary condition

$$N = Al_A + (A-1)l_{A-1} + \dots + 3l_3 + 2l_2. \tag{69}$$

Replacing l_2 by N with the help of (69) and putting (68) into (43) we get a $(A-2)$ dimensional recursion formula for the coefficients $\alpha_{l_A \dots l_3}(N, A)$. The solutions of this finite system of linear homogeneous equations for every permitted value of N gives then the functions $F_N(u, g_3 \dots g_A)$. Because of the structure of the differential equation (43) it is very easy to see, that e.g. the solutions for $0 \leqq N \leqq 8$ must have the form $(A \geqq 8)$

$N = 0$: $F_0 = 1$;

$N = 1, 2$: no solution;

$$\begin{aligned}
&N = 3: \quad F_3 = g_3; \\
&N = 4: \quad F_4 = g_4; \\
&N = 5: \quad F_5 = g_5; \\
&N = 6: \quad F_6^{(1)} = g_6, \quad F_6^{(2)} = \alpha_2 g_3{}^2 + \alpha_1 g_4 u + \alpha_0 u^3; \\
&N = 7: \quad F_7^{(1)} = g_7, \quad F_7^{(2)} = \beta_2 g_4 g_3 + \beta_1 g_5 u + \beta_0 g_3 u^2; \\
&N = 8: \quad F_8^{(1)} = g_8, \quad F_8^{(2)} = \gamma_4 g_4{}^2 + \gamma_3 g_6 u + \gamma_2 g_3{}^2 u + \gamma_1 g_4 u^2 + \gamma_0 u^4, \\
&\qquad\qquad\qquad F_8^{(3)} = \delta_4 g_5 g_3 + \delta_3 g_6 u + \delta_2 g_3{}^2 u + \delta_1 g_4 u^2 + \delta_0 u^4
\end{aligned} \tag{70}$$

where the coefficients are determined by (43). For every expression of the form

$$g_A{}^{l_A} g_{A-1}^{l_{A-1}} \dots g_3{}^{l_3} \tag{71}$$

there exists an independent solution. This degeneracy gives the selection rule for N:

$$N = 3n_3 + 4n_4 + \dots An_A, \qquad n_i = 0, 1, 2 \dots, \tag{72}$$

where the numbers n_i can take all non-negative integer values independently of each other. The eigenvalue spectrum (45a) is thereby determined †:

$$E = \hbar\omega[\tfrac{1}{2}(A^2-1) + 2n_2 + 3n_3 + 4n_4 + \dots An_A] \qquad (n_i = 0, 1, 2 \dots). \tag{73a}$$

The totally symmetric space function has, according to (45b), the spectrum

$$E = \hbar\omega[\tfrac{1}{2}(A-1) + 2n_2 + 3n_3 + 4n_4 + \dots An_A] \quad (n_i = 0, 1, 2 \dots). \tag{73b}$$

In either case there does not exist any state with only one excited quantum $\hbar\omega$.

† This result can also be obtained by methods of group theory. See e.g. M. Kretzschmar (to be published).

8. Construction of the Eigenfunctions in the Three-Dimensional case

In this section we shall extend the above method to a 3-dimensional system of A particles coupled harmonically. So we have to solve the eigenvalue problem according to (13),

$$\left\{\sum_1^{A-1}\left[-\frac{\hbar^2}{2M}\frac{\partial^2}{\partial \mathbf{r}_i^2}+\tfrac{1}{2}Ac\,\mathbf{r}_i^2\right]\right\}\Psi(\mathbf{r}_1\ldots\mathbf{r}_{A-1})=E\Psi(\mathbf{r}_1\ldots\mathbf{r}_{A-1}), \tag{74}$$

Ψ having to obey the Pauli principle in the form (15). An additional difficulty arises: we have to classify the eigenfunctions not only by the energy, but also by the total angular momentum and its z-component. The transformation (9a, b) gives for the total angular momentum

$$\mathbf{L}'=\sum_1^A \mathbf{r}'_i\times\mathbf{p}'_i \tag{75}$$

an expression

$$\mathbf{L}'=\mathbf{r}_A\times\mathbf{p}_A+\sum_1^{A-1}\mathbf{r}_i\times\mathbf{p}_i \tag{76}$$

where the first term represents the angular momentum of the centre-of-mass about a fixed point in space and the second term is the internal angular momentum,

$$\mathbf{L}=\sum_1^{A-1}\mathbf{r}_i\times\mathbf{p}_i. \tag{77}$$

Separating the centre-of-mass motion we have to classify Ψ by the eigenvalues of the operators

$$L^2\Psi(\mathbf{r}_1\ldots\mathbf{r}_{A-1})=\hbar^2L(L+1)\Psi(\mathbf{r}_1\ldots\mathbf{r}_{A-1}) \tag{78}$$

and

$$L_z\Psi(\mathbf{r}_1\ldots\mathbf{r}_{A-1})=\hbar M\Psi(\mathbf{r}_1\ldots\mathbf{r}_{A-1}), \tag{79}$$

with

$$L_z=\frac{\hbar}{i}\sum_1^{A-1}\left(x_i\frac{\partial}{\partial y_i}-y_i\frac{\partial}{\partial x_i}\right). \tag{80}$$

As a first step we introduce the 3 m.p.v.

$$u=\sum_1^{A-1}x_i^2,\quad v=\sum_1^{A-1}y_i^2,\quad w=\sum_1^{A-1}z_i^2, \tag{81}$$

so that the potential energy in (74) can be written as

$$\tfrac{1}{2}Ac(u+v+w). \tag{82}$$

As in the one-dimensional case, we try for Ψ the Ansatz

$$\Psi(\mathbf{r}_1\ldots\mathbf{r}_{A-1})=G(u,v,w)\phi(\mathbf{r}_1\ldots\mathbf{r}_{A-1}), \tag{83}$$

Putting (83) into (74) we can obtain an equation for $G(u, v, w)$ only if we impose upon $\phi(\mathbf{r}_1 \ldots \mathbf{r}_{A-1})$ the conditions

$$\sum_1^{A-1} \frac{\partial^2 \phi}{\partial \mathbf{r}_i^2} = 0 \tag{84a}$$

and

$$\sum_1^{A-1} x_i \frac{\partial \phi}{\partial x_i} = k_1 \phi, \qquad \sum_1^{A-1} y_i \frac{\partial \phi}{\partial y_i} = k_2 \phi, \qquad \sum_1^{A-1} z_i \frac{\partial \phi}{\partial z_i} = k_3 \phi. \tag{84b}$$

This gives for $G(u, v, w)$ the equation

$$\begin{aligned} 4\left[u\frac{\partial^2 G}{\partial u^2} + v\frac{\partial^2 G}{\partial v^2} + w\frac{\partial^2 G}{\partial w^2}\right] + [4k_1 + 2(A-1)]\frac{\partial G}{\partial u} + [4k_2 + 2(A-1)]\frac{\partial G}{\partial v} \\ + [4k_3 + 2(A-1)]\frac{\partial G}{\partial w} + \frac{2M}{\hbar^2}[E - \tfrac{1}{2}Ac(u+v+w)]G(u, v, w) = 0. \end{aligned} \tag{85}$$

For the angular momentum classification it is convenient to introduce new variables ρ, ξ, η given by

$$\rho = u+v+w, \qquad \xi = \frac{u}{u+v}, \qquad \eta = \frac{u+v}{u+v+w}. \tag{86}$$

The transformation of (85) gives now for $G(\rho, \xi, \eta)$ the differential equation

$$\begin{aligned} \left[\rho^2\frac{\partial^2 G}{\partial \rho^2} + \frac{\xi(1-\xi)}{\eta}\frac{\partial^2 G}{\partial \eta^2} + \eta(1-\eta)\frac{\partial^2 G}{\partial \eta^2}\right] + [k_1 + k_2 + k_3 + \tfrac{3}{2}(A-1)]\rho\frac{\partial G}{\partial \rho} \\ + \frac{1}{\eta}[k_1 + \tfrac{1}{2}(A-1) - (k_1 + k_2 + A - 1)\xi]\frac{\partial G}{\partial \xi} \\ + [k_1 + k_2 + A - 1 - (k_1 + k_2 + k_3 + \tfrac{3}{2}(A-1))\eta]\frac{\partial G}{\partial \eta} \\ + \frac{M}{2\hbar^2}\rho(E - \tfrac{1}{2}Ac\rho)G(\rho, \xi, \eta) = 0. \end{aligned} \tag{87}$$

Eq. (87) can be solved by standard methods. The result is

$$G_{n\lambda\mu}(\rho, \xi, \eta) = \rho^{(\lambda+\mu)} f_{n\lambda\mu}(\rho)\, \eta^{\mu} \vartheta_{\lambda,\mu}(\eta) \chi_{\mu}(\xi) \tag{88}$$

where $\chi_{\mu}(\xi)$ and $\vartheta_{\lambda,\mu}(\eta)$ are Jacobi polynomials obeying the differential equations

$$\begin{aligned} \xi(\xi-1)\frac{\mathrm{d}^2 \chi_{\mu}}{\mathrm{d}\xi^2} + [(k_1 + k_2 + A - 1)\xi - (k_1 + \tfrac{1}{2}(A-1))]\frac{\mathrm{d}\chi_{\mu}}{\mathrm{d}\xi} \\ - \mu(\mu + k_1 + k_2 + k_3 + A - 2)\chi_{\mu}(\xi) = 0 \qquad (\mu = 0, 1, 2 \ldots), \end{aligned} \tag{89}$$

$$\begin{aligned} \eta(\eta-1)\frac{\mathrm{d}^2 \vartheta_{\lambda,\mu}}{\mathrm{d}\eta^2} + [(2\mu + k_1 + k_2 + k_3 + \tfrac{3}{2}(A-1))\eta - (2\mu + k_1 + k_2 + A - 1)]\frac{\mathrm{d}\vartheta_{\lambda,\mu}}{\mathrm{d}\eta} \\ - \lambda(\lambda + 2\mu + k_1 + k_2 + k_3 + \tfrac{3}{2}A - \tfrac{5}{2})\vartheta_{\lambda,\mu}(\eta) = 0 \qquad (\lambda = 0, 1, 2 \ldots), \end{aligned} \tag{90}$$

and $f_{n\lambda\mu}(\rho)$ are Laguerre functions obyeing the differential equation

$$\rho \frac{\mathrm{d}^2 f_{n\lambda\mu}}{\mathrm{d}\rho^2} + [2(\lambda+\mu)+k_1+k_2+k_3+\tfrac{3}{2}(A-1)] \frac{\mathrm{d}f_{n\lambda\mu}}{\mathrm{d}\rho} + \frac{M}{2\hbar^2}[E_n - \tfrac{1}{2}Ac\rho] f_{n\lambda\mu}(\rho) = 0. \tag{91}$$

From (91) we get for the energy eigenvalues of our problem the relation

$$E_{n\lambda\mu} = \hbar\omega[\tfrac{3}{2}(A-1)+k_1+k_2+k_3+2(n+\lambda+\mu)] \qquad (n, \lambda, \mu = 0, 1, 2 \ldots), \tag{92}$$

where n, λ, μ can be all non-negative integers independently of each other. The selection rules for k_1, k_2, k_3 follow from the solutions of eq. (84a, b).

This involves the problem of looking for all solutions of the $(3A-3)$-dimensional Laplace equation which are homogeneous in the x_i as well as in the y_i and the z_i, and which obey the $\binom{A}{2}$ conditions

$$\phi_{k_1k_2k_3}(\mathbf{r}_1 \ldots \mathbf{r}_{A-1}) = \mp\phi_{k_1k_2k_3}(\bar{\mathbf{r}}_1 \ldots \bar{\mathbf{r}}_{A-1}). \tag{93a, b}$$

In the following we shall try to get the solutions with the help of the m.p.v. As mentioned above, the m.p.v. are homogeneous functions in x_i, y_i and z_i which are invariant under the substitutions (15)

$$g_{ijl}(x_1y_1z_1 \ldots x_{A-1}y_{A-1}z_{A-1}) = g_{ijl}(\bar{x}_1\bar{y}_1\bar{z}_1 \ldots \bar{x}_{A-1}\bar{y}_{A-1}\bar{z}_{A-1}). \tag{94}$$

The indices i, j, l are the degrees of homogeneity in x, y, and z.

No function with $i+j+l = 1$ exists. For $i+j+l = 2$, there are 6 functions. Because the 3 variables g_{200}, g_{020} and g_{002} satisfy other differential equations than all the other g_{ijl}, they are designated — similarly to the one-dimensional case — by u, v, w:

$$u = \sum_1^{A-1} x_i^2, \qquad v = \sum_1^{A-1} y_i^2, \qquad w = \sum_1^{A-1} z_i^2. \tag{81}$$

The other m.p.v. with $i+j+l = 2$ are

$$g_{110} = \sum_1^{A-1} x_i y_i, \qquad g_{101} = \sum_1^{A-1} x_i z_i, \qquad g_{011} = \sum_1^{A-1} y_i z_i. \tag{95}$$

In the case $i+j+l = 3$, there exist 10 m.p.v. which are designated by

$$g_{300}, g_{030}, g_{003}; \quad g_{210}, g_{120}, \quad g_{102}, g_{201}, \quad g_{012}, g_{021}; \quad g_{111}.$$

Considering a system of A particles we have to construct from the internal coordinates $(\mathbf{r}_1 \ldots \mathbf{r}_{A-1})$ all m.p.v. g_{ijl} which fulfil the condition

$$2 \leqq i+j+l \leqq A. \tag{96}$$

To get familiar with the procedure we shall give as an example the m.p.v. for a system of 3 particles. One only needs to compute the quantities:
for $i+j+l = 2$:

$$u = x_1^2+x_2^2, \quad g_{110} = x_1y_1+x_2y_2, \tag{97}$$

and for $i+j+l = 3$:

$$\begin{aligned}
g_{300} &= x_1^3+x_2^3-3(x_1^2x_2+x_1x_2^2),\\
g_{210} &= (x_1^2y_1+x_2^2y_2)-(2x_1x_2y_1+x_1^2y_2)-(2x_1x_2y_2+x_2^2y_1),\\
g_{111} &= (x_1y_1z_1+x_2y_2z_2)-(x_1y_2z_2+x_2y_1z_1)-(x_1y_1z_2+x_2y_2z_1)-(x_1y_2z_1+x_2y_1z_2),
\end{aligned} \tag{98}$$

because all the other g_{ijl} follow by cyclic permutation of x_i, y_i and z_i.

Because there are no such symmetries between the eigenvalues of the totally anti-symmetric and totally symmetric space functions as exist in the one-dimensional case, we shall treat the computation of these functions separately.

In the case of the totally symmetric function we try for $\phi_{k_1k_2k_3}$ the Ansatz

$$\phi_{k_1k_2k_3}(\mathbf{r}_1 \dots \mathbf{r}_{A-1}) = \phi_{k_1k_2k_3}(u, v, w; g_{ijl}), \tag{99}$$

which transforms (84a) after simple manipulations with the help of (84b) into the equation ($\phi_{k_1k_2k_3} \equiv \phi_k$)

$$\begin{aligned}
&[2k_1+A-5]\frac{\partial\phi_k}{\partial u}+[2k_2+A-5]\frac{\partial\phi_k}{\partial v}+[2k_3+A-5]\frac{\partial\phi_k}{\partial w}\\
&-2\left[u\frac{\partial^2\phi_k}{\partial u^2}+v\frac{\partial^2\phi_k}{\partial v^2}+w\frac{\partial^2\phi_k}{\partial w^2}\right]+\tfrac{1}{2}\sum_{g_{ijl}}\sum_{g'_{ijl}}\frac{\partial^2\phi_k}{\partial g_{ijl}\partial g'_{ijl}}\left[\sum_{\nu=1}^{A-1}\frac{\partial g_{ijl}}{\partial\mathbf{r}_\nu}\cdot\frac{\partial g'_{ijl}}{\partial\mathbf{r}_\nu}\right]=0,
\end{aligned} \tag{100}$$

if we impose on the g_{ijl} the condition

$$\sum_{\nu=1}^{A-1}\frac{\partial^2 g_{ijl}}{\partial\mathbf{r}_\nu^2}=0. \tag{101}$$

As solutions of (100) we need only finite power series obeying the homogeneity condition (84b). They are very easy to find for the lowest values of $\sum_1^3 k_i$. Therefore they will be given for the cases $0 \leqq \sum_1^3 k_i \leqq 4$ in which we need only to solve the equation

$$\begin{aligned}
&[2k_1+A-5]\frac{\partial\phi_k}{\partial u}+[2k_2+A-5]\frac{\partial\phi_k}{\partial v}+[2k_3+A-5]\frac{\partial\phi_k}{\partial w}\\
&\qquad -2\left[u\frac{\partial^2\phi_k}{\partial u^2}+v\frac{\partial^2\phi_k}{\partial v^2}+w\frac{\partial^2\phi_k}{\partial w^2}\right]\\
&+\tfrac{1}{2}\left[(u+v)\frac{\partial^2\phi_k}{\partial g_{110}^2}+(u+w)\frac{\partial^2\phi_k}{\partial g_{101}^2}+(v+w)\frac{\partial^2\phi_k}{\partial g_{011}^2}\right]\\
&\qquad +g_{011}\frac{\partial^2\phi_k}{\partial g_{110}\partial g_{101}}+g_{101}\frac{\partial^2\phi_k}{\partial g_{110}\partial g_{011}}+g_{110}\frac{\partial^2\phi_k}{\partial g_{101}\partial g_{011}}+\dots=0.
\end{aligned} \tag{102}$$

The solutions are

$$\sum_1^3 k_i = 0: \quad 1;$$

$$\sum_1^3 k_i = 1: \quad \text{no solution;}$$

$$\sum_1^3 k_i = 2: \quad g_{110},\ g_{101},\ g_{011};$$

$$\sum_1^3 k_i = 3: \quad \text{all } g_{ijl} \text{ with } i+j+l = 3; \tag{103}$$

$$\sum_1^6 k_i = 4: \quad \text{all } g_{ijl} \text{ with } i+j+l = 4 \text{ and}$$

$$\phi_{220} = g_{110}^2 - \frac{1}{A-1} uv, \quad \phi_{202} = g_{101}^2 - \frac{1}{A-1} uw, \quad \phi_{022} = g_{011}^2 - \frac{1}{A-1} vw,$$

$$\phi_{211} = g_{110}g_{101} - \frac{1}{A-1} ug_{011}, \quad \phi_{121} = g_{110}g_{011} - \frac{1}{A-1} vg_{101},$$

$$\phi_{112} = g_{101}g_{011} - \frac{1}{A-1} wg_{110}.$$

The excitation spectrum up to $3\hbar\omega$ of the totally symmetric space function is given in table 2 for an arbitrary number of particles $A \geqq 3$. For higher excited states the degeneracy depends on A.

TABLE 2

Totally symmetric states for A-particle system ($A \geqq 3$)

Excitation energy in $\hbar\omega$	Degeneracy	L
3	10	1,3
2	6	0,2
1	0	—
0	1	0

In the case of the totally antisymmetric functions $\phi_{k_1 k_2 k_3}$ we have to look first of all for all "irreducible antisymmetric factors". These are totally antisymmetric functions obeying the equations (84a, b) and (93) for the lowest possible values of $\sum_1^3 k_i$, and therefore they do not contain m.p.v. In the one-dimensional case there exists only one, given by (38). The situation is not so simple in the 3-dimensional case, because there exist, for a given A, several such factors. Let us call them $\varphi_{\alpha\beta\gamma}(\mathbf{r}_1 \ldots \mathbf{r}_{A-1})$. To have an example they are given for the case $A = 3$. The important ones are

$$\text{for } \sum_1^3 k_i = 2: \qquad \varphi_{110} = x_1 y_2 - x_2 y_1; \tag{104a}$$

$$\text{for } \sum_1^3 k_i = 3:$$

$$\begin{aligned} \varphi_{300} &= x_1^3 - x_2^3 + 3(x_1^2 x_2 - x_1 x_2^2), \\ \varphi_{210} &= (x_1^2 y_1 - x_2^2 y_2) + 2(x_1 x_2 y_1 - x_1 x_2 y_2) + (x_1^2 y_2 - x_2^2 y_1), \\ \varphi_{111} &= (x_1 y_1 z_1 - x_2 y_2 z_2) + (x_1 y_1 z_2 - x_2 y_2 z_1) + (x_1 y_2 z_1 - x_2 y_1 z_2) - (x_1 y_2 z_2 - x_2 y_1 z_1) \end{aligned} \tag{104b}$$

and all the others follow by cyclic permutation of x_i, y_i and z_i. The general totally antisymmetric functions $\phi_{k_1 k_2 k_3}$ can now be written in the form

$$\phi_{k_1 k_2 k_3} = \sum_{\alpha,\beta,\gamma} \varphi_{\alpha\beta\gamma} F^{(\alpha\beta\gamma)}_{N_1 N_2 N_3}(u, v, w;\ g_{ijl}) \tag{105}$$

with

$$\alpha + N_1 = k_1, \qquad \beta + N_2 = k_2, \qquad \gamma + N_3 = k_3. \tag{106}$$

We shall only demonstrate the computation for those $\phi_{k_1 k_2 k_3}$ for which the sum in (105) reduces to one term. The general case of (105) can be treated in a similar way. In the case considered here, we have next to single out from all the $g_{ijl}(2 \leqq i+j+l \leqq A)$ those obeying the condition

$$\sum_1^{A-1} \left[2 \frac{\partial \varphi_{\alpha\beta\gamma}}{\partial \mathfrak{r}_\nu} \cdot \frac{\partial g_{ijl}}{\partial \mathfrak{r}_\nu} + \varphi_{\alpha\beta\gamma} \frac{\partial^2 g_{ijl}}{\partial \mathfrak{r}_\nu^2} \right] = 0; \tag{107}$$

call these $g^{(\alpha\beta\gamma)}_{ijl}$. According to our assumption, $\phi_{k_1 k_2 k_3}$ is given by

$$\phi_{k_1 k_2 k_3}(\mathfrak{r}_1 \ldots \mathfrak{r}_{A-1}) = \varphi_{\alpha\beta\gamma}(\mathfrak{r}_1 \ldots \mathfrak{r}_{A-1}) F^{(\alpha\beta\gamma)}_{N_1 N_2 N_3}(u, v, w;\ g^{(\alpha\beta\gamma)}_{ijl}). \tag{108}$$

Eq. (108) transforms (84a) with the help of (84b) and (107) into a differential equation similar to (100) ($F^{(\alpha\beta\gamma)}_{N_1 N_2 N_3} \equiv F_N$, $g^{(\alpha\beta\gamma)}_{ijl} \equiv g_{ijl}$):

$$\begin{aligned} &[2(\alpha+N_1)+A-5] \frac{\partial F_N}{\partial u} + [2(\beta+N_2)+A-5] \frac{\partial F_N}{\partial v} + [2(\gamma+N_3)+A-5] \frac{\partial F_N}{\partial w} \\ &\qquad - 2 \left[u \frac{\partial^2 F_N}{\partial u^2} + v \frac{\partial^2 F_N}{\partial v^2} + w \frac{\partial^2 F_N}{\partial w^2} \right] \\ &\qquad + \tfrac{1}{2} \sum_{g_{ijl}} \sum_{g'_{ijl}} \frac{\partial^2 F_N}{\partial g_{ijl} \partial g'_{ijl}} \left[\sum_1^{A-1} \frac{\partial g_{ijl}}{\partial \mathfrak{r}_\nu} \cdot \frac{\partial g'_{ijl}}{\partial \mathfrak{r}_\nu} \right] = 0, \end{aligned} \tag{109}$$

where the relations between α, β, γ, k_i and N_i are given by (106).

To give an example we shall apply the above method to the case $\alpha = 1$, $\beta = 1$, $\gamma = 0$ for $A = 3$. This means that we have to look for all antisymmetric functions having the form

$$\phi_{k_1 k_2 k_3}(\mathfrak{r}_1 \mathfrak{r}_2) = \varphi_{110}(\mathfrak{r}_1 \mathfrak{r}_2) F^{(110)}_{N_1 N_2 N_3}(u, v, w;\ g^{(110)}_{ijl}), \tag{110}$$

where $\varphi_{110}(\mathbf{r}_1\mathbf{r}_2)$ is given by (104) and the $g_{ijl}^{(110)}$ are, according to (107),

$$g_{110} = x_1y_1+x_2y_2, \quad g_{003} = z_1^3+z_2^3-3(z_1^2z_2+z_1z_2^2). \tag{111}$$

For (109) we obtain

$$2N_1\frac{\partial F_N}{\partial u}+2N_2\frac{\partial F_N}{\partial v}+(2N_3-2)\frac{\partial F_N}{\partial w}-2\left[u\frac{\partial^2 F_N}{\partial u^2}+v\frac{\partial^2 F_N}{\partial v^2}+w\frac{\partial^2 F_N}{\partial w^2}\right]$$
$$+\tfrac{1}{2}(u+v)\frac{\partial^2 F_N}{\partial g_{110}^2}+9w^2\frac{\partial^2 F_N}{\partial g_{003}^2}=0. \tag{112}$$

The solutions to the lowest values of $\sum_1^3 N_i$ are easy to find:

$$\begin{aligned}
&\sum_1^3 N_i = 0: && 1;\\
&\sum_1^3 N_i = 1: && \text{no solution};\\
&\sum_1^3 N_i = 2: && g_{110};\\
&\sum_1^3 N_i = 3: && g_{003};\\
&\sum_1^3 N_i = 4: && g_{110}^2-\tfrac{1}{4}uv.
\end{aligned} \tag{113}$$

The degeneracy of the totally antisymmetric space functions for the ground state and the first two excited states for $A = 3$ is given in table 3.

TABLE 3

Totally antisymmetric states for system of 3 particles

Excitation energy in $\hbar\omega$	Degeneracy	L
2	15	1, 2, 3
1	10	1, 3
0	3	1

9. Classification of the Wave Functions

In this section we shall re-order the wave functions

$$\Psi_{n\lambda\mu,\,k_1k_2k_3} = \rho^{(\lambda+\mu)}f_{n,\,\lambda\mu}(\rho)\eta^{\mu}\vartheta_{\lambda,\,\mu}(\eta)\,\chi_{\mu}(\xi)\phi_{k_1k_2k_3} \tag{114}$$

in a representation containing the classification by 4 quantum numbers: energy E, total angular momentum L, its z-component M and a quantum number called n. The last one permits us to differentiate between degenerate

states having the same E, L, M. With the help of the relations

$$\mathbf{L}^2(\rho) \equiv 0, \qquad L_z(\rho) \equiv 0, \tag{115}$$

$$L_z(\eta) \equiv 0, \tag{116}$$

we can state the two rules:

I. If $\eta^\mu \vartheta(\eta)\chi_\mu(\xi)\phi_{k_1k_2k_3}$ is an eigenfunction of $\mathbf{L}^2$ and L_z every function

$$\rho^{(\lambda+\mu)} f_{n,\lambda\mu}(\rho)\eta^\mu \vartheta_{\lambda,\mu}(\eta)\,\chi_\mu(\xi)\phi_{k_1k_2k_3} \tag{117}$$

is automatically an eigenfunction of the same L and M, for arbitrary n.

II. If $\chi_\mu(\xi)\phi_{k_1k_2k_3}$ is an eigenfunction of L_z, every function

$$\rho^{(\lambda+\mu)} f_{n,\lambda\mu}(\rho)\eta^\mu \vartheta_{\lambda\ \mu}(\eta)\chi_\mu(\xi)\phi_{k_1k_2k_3} \tag{118}$$

is automatically an eigenfunction of the same M, for arbitrary values of n and λ.

The relevant step is the classification with respect to M. Because of rule II it is only necessary to assort the functions

$$\chi_\mu(\xi)\phi_{k_1k_2k_3} \equiv \psi_{\mu k_1k_2k_3} \tag{119}$$

as eigenfunctions of L_z. In order to do this we make the Ansatz

$$\psi_{E,M} = \sum_{k_1+k_2+k_3+2\mu=\text{const.}} c_{\mu k_1k_2k_3}\psi_{\mu k_1k_2k_3} \tag{120}$$

in the equation

$$L_z\psi_{E,M} - \hbar M\psi_{E,M} = 0, \tag{121}$$

which gives a finite homogeneous system of equations for the $c^{(M)}_{\mu k_1k_2k_3}$. The solutions then give the functions $\psi_{E,M}$.

As a simple example we shall treat the ground state of the totally antisymmetric space function for $A = 3$. Eq. (120) gives

$$\psi_{E_0,M} = \sum_{k_1+k_2+k_3=2} c_{k_1k_2k_3}\phi_{k_1k_2k_3} \equiv c_{110}\varphi_{110} + c_{101}\varphi_{101} + c_{011}\varphi_{011} \tag{122}$$

and from (121) follows

$$Mc_{110} = 0, \qquad -ic_{101} + Mc_{101} = 0, \qquad Mc_{011} + ic_{101} = 0, \tag{123}$$

which gives the 3 functions

$$\psi_{E_0,0} = \varphi_{110}, \qquad \psi_{E_0,1} = \varphi_{101} - i\varphi_{011}, \qquad \psi_{E_0,-1} = \varphi_{101} + i\varphi_{011}. \tag{124}$$

From the $\psi_{E,M}$ we can get, with the help of rule II, the total wave functions, if they are at the same time eigenfunctions of $\mathbf{L}^2$. If not, one has to repeat a similar procedure but only with functions of the same M. Using rule I then, one gets the total wave functions Ψ_{ELMn}. They are now classified by the four quantum numbers E, L, M, n. An easy calculation gives the angular momentum classification of the states in tables 2 and 3. In the 4th excited state of table 2, $L = 0$ occurs twice, differing now in the values of n which are $n = 0$ and $n = 4$.

10. Separation for the Centre-of-Mass Motion for Arbitrary Potentials $V(|\mathbf{r}'_i-\mathbf{r}'_k|)$

Now we shall separate the centre-of-mass motion of a system of A equal particles interacting by translationally invariant two-body forces with the potential $V(|\mathbf{r}'_i-\mathbf{r}'_k|)$. For this purpose we use again the transformation (9a, b), and everything already stated about this case can also be used here. The transformed differences are

$$\mathbf{r}'_i-\mathbf{r}'_k=\mathbf{r}_i-\mathbf{r}_k \quad \text{for} \quad i,k<A \tag{125a}$$

and

$$\mathbf{r}'_i-\mathbf{r}'_A=\frac{1}{(\sqrt{A}-1)}\,[(\sqrt{A}-1)\mathbf{r}_i-\mathbf{y}] \quad (1\leqq i<A) \quad \text{with} \quad \mathbf{y}=\sum_1^{A-1}\mathbf{r}_i. \tag{125b}$$

By this transformation the Hamilton operator

$$\mathscr{H}'=\sum_1^A-\frac{\hbar^2}{2M}\,\frac{\partial^2}{\partial\mathbf{r}_i'^2}+\sum_{i>k=1}^{A}V(|\mathbf{r}'_i-\mathbf{r}'_k|) \tag{126}$$

becomes after the separation of the centre-of-mass motion

$$\mathscr{H}=\sum_1^{A-1}-\frac{\hbar^2}{2M}\,\frac{\partial^2}{\partial\mathbf{r}_i^2}+\sum_{i>k=1}^{A-1}V(|\mathbf{r}_i-\mathbf{r}_k|)+\sum_1^{A-1}V\left(\frac{|(\sqrt{A}-1)\mathbf{r}_i-\mathbf{y})|}{\sqrt{A}-1}\right). \tag{127}$$

If it is possible to expand the potential energy into a power series of the type

$$\sum_{i>k=1}^{A}V(|\mathbf{r}'_i-\mathbf{r}'_k|)=V_0+\sum_{i>k=1}^{A}\Big[\sum_{\nu\geqq 2}c_\nu|\mathbf{r}'_i-\mathbf{r}'_k|^\nu\Big], \tag{128}$$

the transformation (9a, b) gives for it an expression

$$\sum_{i>k=1}^{A}V(|\mathbf{r}'_i-\mathbf{r}'_k|)\to V_0+\sum_1^{A-1}\left[Ac_2\mathbf{r}_i^2+\sum_{\nu\geqq 3}\frac{c_\nu}{(\sqrt{A}-1)^\nu}\,|(\sqrt{A}-1)\mathbf{r}_i-\mathbf{y}|^\nu\right]$$
$$+\sum_{i>k=1}^{A-1}\Big[\sum_{\nu\geqq 3}c_\nu|\mathbf{r}_i-\mathbf{r}_k|^\nu\Big]. \tag{129}$$

From this one can conclude that in most cases translationally invariant two-body forces are not transformed into two-body forces but into forces with potentials containing products of more than two internal coordinates. Exceptions are e.g. systems with $A=3$ and $A=4$. Here, the following relations are valid: for $A=3$:

$$\sum_{i>k=1}^{3}V(|\mathbf{r}'_i-\mathbf{r}'_k|)\to V(|\mathbf{r}_1-\mathbf{r}_2|)+V\left(\frac{1}{\sqrt{3}-1}\,|(2-\sqrt{3})\mathbf{r}_1+\mathbf{r}_2|\right)$$
$$+V\left(\frac{1}{\sqrt{3}-1}\,|\mathbf{r}_1+(2-\sqrt{3})\mathbf{r}_2|\right), \tag{130}$$

and for $A = 4$:

$$\sum_{i>k=1}^{4} V(|\mathbf{r}'_i-\mathbf{r}'_k|) \to \sum_{i>k=1}^{3} [V(|\mathbf{r}_i-\mathbf{r}_k|)+V(|\mathbf{r}_i+\mathbf{r}_k|)]. \tag{131}$$

An interesting application of (130) is the example

$$\sum_{i>k=1}^{3} c_2(\mathbf{r}'_i-\mathbf{r}'_k)^2+c_4(\mathbf{r}'_i-\mathbf{r}'_k)^4 \to 3c_2(\mathbf{r}_1^2+\mathbf{r}_2^2)+\tfrac{9}{2}c_4(\mathbf{r}_1^2+\mathbf{r}_2^2)^2 \tag{132}$$

which will be used later.

11. Treatment of Potentials V(u, v, w)

The above method for the computation of the eigenfunctions and the eigenvalue spectrum, which was only developed for the potential

$$V = \tfrac{1}{2}Ac(u+v+w), \tag{82}$$

can be extended easily to the cases of arbitrary $V(u, v, w)$. The only thing being altered is the differential equation for $G(u, v, w)$:

$$4\left[u\frac{\partial^2 G}{\partial u^2}+v\frac{\partial^2 G}{\partial v^2}+w\frac{\partial^2 G}{\partial w^2}\right]+[4k_1+2(A-1)]\frac{\partial G}{\partial u}+[4k_2+2(A-1)]\frac{\partial G}{\partial v}$$
$$+[4k_3+2(A-1)]\frac{\partial G}{\partial w}+\frac{2M}{\hbar^2}[E-V(u, v, w)]G(u, v, w) = 0. \tag{133}$$

For the total wave function

$$\Psi(\mathbf{r}_1 \ldots \mathbf{r}_{A-1}) = G(u, v, w)\phi(\mathbf{r}_1 \ldots \mathbf{r}_{A-1})$$

we can take everything we know about $\phi(\mathbf{r}_1 \ldots \mathbf{r}_{A-1})$ from the harmonic oscillator case. Some simple examples for $V(u, v, w)$ are, for two-body potentials,

$$\sum_{i>k=1}^{3} c_2(\mathbf{r}'_i-\mathbf{r}'_k)^2+c_4(\mathbf{r}'_i-\mathbf{r}'_k)^4 \to 3c_2(u+v+w)+\tfrac{9}{2}c_4(u+v+w)^2 \equiv 3c_2\rho+\tfrac{9}{2}c_4\rho^2, \tag{134}$$

for many-body potentials,

$$\sum_{i>k=1}^{A} c_2(\mathbf{r}'_i-\mathbf{r}'_k)^2+\sum_{i>k=1,j>l=1}^{A} c_\pi(\mathbf{r}'_i-\mathbf{r}'_k)^2\cdot(\mathbf{r}'_j-\mathbf{r}'_l)^2 \to Ac_2(u+v+w)$$
$$+A^2c_\pi(u+v+w)^2 \equiv Ac_2\rho+A^2c_\pi\rho^2, \tag{135}$$

for "deformed potentials",

$$\sum_{i>k=1}^{A} [a(x'_i-x'_k)^2+b(y'_i-y'_k)^2+c(z'_i-z'_k)^2] \to au+bv+cw. \tag{136}$$

Every potential of the type

$$V = V\left(\sum_{1}^{A}(\mathbf{r}'_i-\mathbf{r}'_k)^2\right) \tag{137}$$

is after the transformation only a function $V(\rho)$. In this case $G(\rho, \xi, \eta)$ is also given by (88) but $f_n(\rho)$ has now to obey the differential equation

$$\rho \frac{d^2 f_n}{d\rho^2} + [2(\lambda+\mu)+k_1+k_2+k_3+\tfrac{3}{2}(A-1)]\frac{df_n}{d\rho} + \frac{M}{2\hbar^2}(E_n - V(\rho))f_n(\rho) = 0. \quad (138)$$

Without going into details, we get already from (138) the degeneracy of the eigenvalues, because E_n is only a function of the two quantities

$$E_n = E_n(n, k_1+k_2+k_3+2(\lambda+\mu)). \quad (139)$$

In the case of small anharmonic terms in (134) and (135) we can use perturbation theory for a problem with one variable, getting the result

$$E_n = \hbar\omega[\tfrac{3}{2}(A-1)+k_1+k_2+k_3+2(\lambda+\mu)+p(n)] \qquad (n = 0, 1, 2 \ldots), \quad (140)$$

where $p(n)$ means a power series of n. Comparing this with the spectrum (92) we see that the degeneracy between states of the same energy, but with different values of n, is removed.

12. Concluding Remarks

The method developed here for the treatment of special many-body problems is not based on the sometimes rather doubtful "independent particle approximation". Thus, the antisymmetrized wave functions are given without using the concept of Slater determinants. It was only applied to potentials $V(u, v, w)$. The next step should be the extension to potentials V depending on all m.p.v. of the second degree $V(u, v, w, g_{110}, g_{101}, g_{011})$. To this class belongs the potential used by Elliott [4]) to obtain sequences of states which are similar to those of the collective model. It is, in the translationally invariant formulation,

$$V(\mathbf{r}'_1 \ldots \mathbf{r}'_A) \propto \sum_{i,k=1}^{A} \sum_{j,l=1}^{A} (\mathbf{r}'_i - \mathbf{r}'_k)^2 (\mathbf{r}'_j - \mathbf{r}'_l)^2 \mathscr{Y}_2^0\left(\frac{(\mathbf{r}'_i - \mathbf{r}'_k)\cdot(\mathbf{r}'_j - \mathbf{r}'_l)}{|\mathbf{r}'_i - \mathbf{r}'_k|\,|\mathbf{r}'_j - \mathbf{r}'_l|}\right), \quad (141a)$$

and after introduction of the internal coordinates,

$$V(\mathbf{r}_1 \ldots \mathbf{r}_{A-1}) \propto \sum_{i,j=1}^{A-1} \mathbf{r}_i^2 \mathbf{r}_j^2 \mathscr{Y}_2^0\left(\frac{\mathbf{r}_i \cdot \mathbf{r}_j}{|\mathbf{r}_i|\,|\mathbf{r}_j|}\right). \quad (141b)$$

Another extension should be to investigate how far the m.p.v. can be used for the description of the collective states. In the collective model they are described in terms of some variables called "collective coordinates" [5, 6]). In order to realize this concept, one has to make a coordinate transformation introducing a new set of variables instead of the internal coordinates $(\mathbf{r}_1 \ldots \mathbf{r}_{A-1})$ in such a way that the ground state and the low-lying excited states are represented by wave functions containing only the "collective coordinates" as

variables. For the higher excited states one then needs the remaining variables. A description by wave functions containing the internal coordinates as well as the "collective coordinates" as independent variables does not seem to be very convenient, because one has then to impose subsidiary conditions, which are certainly not easy to satisfy. However, because of the finite number of these states it may also be possible that this characteristic sequence of states is due to a definite increase of the number of m.p.v. necessary to represent the eigenfunctions. The problem would then be to look for a potential providing a non-degenerate ground state and non-degenerate low-lying excited states, for which one must introduce a definite number of additional m.p.v. when passing from one state to the next of increasing excitation. With the additional m.p.v. one must then connect the required increase of total angular momentum and energy.

I should like to thank Professor H. Steinwedel for discussions and criticism and Dr. G. Field for correcting my English.

References

1) P. Möbius, Preprint of the Institut für Theoretische Physik, Göttingen (1958)
2) J. P. Elliott and T. H. R. Skyrme, Proc. Roy. Soc. A **232** (1955) 561
3) H. J. Lipkin, Phys. Rev. **110** (1958) 1395
4) J. P. Elliott, Proc. Roy. Soc. A **245** (1958) 128, 562
5) A. Bohr and B. R. Mottelson, Dan. Mat. Fys. Medd. **27**, No. 16 (1953)
6) A. Bohr and B. R. Mottelson, Det Kongelige Norske Videnskabers Selskabs Forhandlinger **31**, No. 12 (1958); all further references are to be found in this paper

7.B

Nuclear Physics **16** (1960) 304—312; © *North-Holland Publishing Co., Amsterdam*

Not to be reproduced by photoprint or microfilm without written permission from the publisher

REGULARIZED VACUUM EXPECTATION VALUES IN QUANTUM FIELD THEORY

JOHN W. MOFFAT

RIAS, *Baltimore* 12, *Maryland*, U.S.A.

Received 4 January 1960

Abstract: A formal method of regularizing vacuum expectation values of Heisenberg current operators is introduced by imposing certain conditions on the spectral functions. The method is applied to Källén's calculation of the vacuum-polarization in an external electromagnetic field and leads to results which are explicitly gauge-invariant.

1. Introduction

In the relativistically invariant formalism of field theory there are still several problems of consistency left, which need clarification. Certain paradoxes occur due to the indeterminate nature of expressions which enter the calculations [1]). One of the more important problems arises in Källén's [2,3]) calculation of the resulting current due to the vacuum-polarization by an external electromagnetic field. The problem is formally connected with the occurrence of an expression which violates the gauge-invariance of the theory. Källén [2]) has shown that this current is given by †

$$\langle 0|j_\mu^{\text{ind}}(x)|0\rangle = -i\int_{-\infty}^{x}\langle 0|[j_\nu(x'), j_\mu(x)]|0\rangle A_\nu^{\text{ext}}(x')\mathrm{d}x' + \frac{L}{1-L}j_\mu^{\text{ext}}(x),$$

where $j_\mu^{\text{ind}}(x)$ is the induced current, and $A_\nu^{\text{ext}}(x)$ and $j_\nu^{\text{ext}}(x)$ are the vector potential and current of the external field. The condition for the gauge-invariance of $\langle 0|j_\mu^{\text{ind}}(x)|0\rangle$ is

$$\frac{\partial}{\partial x'_\nu}[\theta(x-x')\langle 0|[j_\nu(x'), j_\mu(x)]|0\rangle] = i\delta(x_0-x'_0)\langle 0|[j_4(x'), j_\mu(x)]|0\rangle = 0.$$

However, a simple calculation reveals that for equal times $x_0 = x'_0$,

$$\langle 0|[j_k(x), j_4(x')]|0\rangle = \frac{\partial}{\partial x_k}\delta(\mathbf{x}-\mathbf{x}')\int_0^\infty \prod(-a)\mathrm{d}a,$$

where $k = 1, 2, 3$. As the spectral function $\prod(-a) \geqq 0$, this expression can only vanish when $\prod(-a)$ is identically zero, which is only true in free-field electrodynamics! Therefore, it would appear that the calculation of the current due to the vacuum-polarization is not gauge-invariant.

† In this paper natural units $\hbar = c = 1$ are used throughout. The metric is $x^2 = \mathbf{x}^2 - x_0^2$, and $x_4 = ix_0 = it$.

A similar situation occurred in Schwinger's original calculation of the vacuum-polarization effect [4]) in perturbation theory. It was argued that the theory would yield gauge-invariant results in view of the fact that the time-component of the current commutes with $j_\nu(x)$ at all points on a space-like surface. However, Pauli and Villars [5]) pointed out that the specialization of the commutator to this case gives a result proportional to

$$\delta(\mathbf{x}-\mathbf{x}')(\partial\Delta^{(1)}/\partial x_\nu),$$

which is indeterminate on the light-cone. In order to overcome these difficulties within the framework of the interaction representation, Pauli and Villars [5]) applied a method of regularization of the free-field Δ-functions with the aid of auxiliary masses.

In the following, we shall introduce a method of regularization which is particularly suitable for application to calculations within the Heisenberg representation. By introducing an indefinite metric in Hilbert space the spectral function can be made to satisfy conditions which automatically remove the kinematical singularities in the vacuum expectation values. We adopt the formalistic attitude of Pauli and Villars [5, 6]), by treating the auxiliary spectrum of masses as an additional mathematical parameter in the theory. After the calculations have been performed the masses of the pathological particles are made infinitely heavy, so that they cannot appear in real physical processes.

An interesting feature of the method is that calculations in the Källén formalism, which involve doubtful interchanges of integration and other operations of a delicate nature, can be justified by carrying out the calculations within the regularized theory, and then finally passing to the limit of the non-regularized theory after the calculations have been performed. In view of this it would appear that Källén's [7]) proof that at least one of the renormalization constants in electrodynamics is infinite, becomes more convincing. The same is true of a recent proof that the pion mass renormalization constant δm^2 is infinite [8, 9]).

The application, in the final section of this paper, of the formal method of regularization to the problem of vacuum-polarization shows that within the Heisenberg representation the inconsistency mentioned above disappears; the calculation of the current due to the vacuum-polarization by an external field is gauge-invariant and self-consistent.

2. Regularized Vacuum Expectation Values

In the rigorous formulation of electrodynamics the vacuum expectation values of products of Heisenberg current operators play an essential role. We shall begin by studying these singular functions in the case of scalar fields (analogous results hold for fields with other transformation properties). If we

introduce a complete set of states as intermediate states in the vacuum expectation value of two scalar current operators, we can write it in the form

$$\langle 0|j(x)j(x')|0\rangle = \sum_{|n\rangle} \langle 0|j(0)|n\rangle\langle n|j(0)|0\rangle e^{i p_n(x-x')}, \tag{1}$$

where in view of translational invariance

$$\langle 0|j(x)|n\rangle = \langle 0|j(0)|n\rangle e^{i p_n x} \quad (p_n{}^0 \geqq 0). \tag{2}$$

We then obtain

$$\langle 0|j(x)j(x')|0\rangle = \frac{1}{(2\pi)^3}\int \mathrm{d}p e^{ip(x-x')} \Pi(p^2)\theta(p), \tag{3}$$

where

$$\begin{aligned} \theta(p) &= \tfrac{1}{2}[1+\varepsilon(p)], \quad \varepsilon(p) = \frac{p_0}{|p_0|}, \\ \Pi(p^2)\theta(p) &= V \sum_{p_n = p} \langle 0|j(0)|n\rangle\langle n|j(0)|0\rangle. \end{aligned} \tag{4}$$

(V = volume of periodicity).
In view of (3), we get the following expression for the vacuum expectation value:

$$\langle 0|j(x)j(x')|0\rangle = \int_0^\infty \Delta^{(+)}(x-x'; a)\Pi(-a)\mathrm{d}a, \tag{5}$$

where

$$\Delta^{(+)}(x) = \frac{1}{(2\pi)^3}\int \mathrm{d}p e^{ipx}\delta(p^2+a)\theta(p). \tag{6}$$

We derive in a similar fashion

$$\langle 0|[j(x), j(x')]|0\rangle = \int_0^\infty \Delta(x-x'; a)\Pi(-a)\mathrm{d}a, \tag{7}$$

where now

$$\Delta(x) = \frac{1}{(2\pi)^3}\int \mathrm{d}p e^{ipx}\varepsilon(p)\delta(p^2+a). \tag{8}$$

In order to exhibit clearly the singular behaviour of these functions, we give the development of $\Delta^{(+)}(x)$ and $\Delta(x)$ for small $\lambda(\lambda = -x^2)$:

$$\Delta^{(+)}(x) = \frac{1}{4\pi}\varepsilon(x^0)\delta(\lambda) + \frac{i}{4\pi^2\lambda} - \frac{ia}{8\pi^2}\ln\frac{\sqrt{a}|\lambda|^{\frac{1}{2}}}{2} - \frac{a}{16\pi}\varepsilon(x^0)\theta(\lambda) + O(\sqrt{|\lambda|}\ln|\lambda|), \tag{9}$$

$$\Delta(x) = \frac{1}{2\pi}\varepsilon(x^0)\delta(\lambda) - \frac{a}{8\pi}\varepsilon(x^0)\theta(\lambda) + O(\lambda). \tag{10}$$

There are four types of singularities in the expressions (9) and (10): a pole $1/\lambda$, a δ-function singularity, a pole $\ln|\lambda|$ and a discontinuity $\theta(\lambda)$. The factor $\varepsilon(x^0)$ does not introduce any additional singularities outside the light cone. Thus, as in the interaction representation, the vacuum expectation values of Heisenberg current operators are singular functions which have quite strong singularities on the light cone. The handling of these singular functions meets with certain difficulties, which are characterized by the occurrence of indeterminate expressions.

In view of the fact that $\Pi(p^2) \geqq 0$, we are forced to demand that the integral

$$\int^{\infty} \frac{\Pi(-a)}{a} \mathrm{d}a \tag{11}$$

should be *absolutely* convergent. This is a severe restriction on the theory as is borne out by Källén's [7]) proof that in electrodynamics (11) will not converge. Integrals of the type (11) appear in the definition of the vacuum expectation values. However, the integrals appearing in the renormalized operators (i.e., observable expressions in the theory) contain an a^2 in the denominator instead of a as in (11). Let us assume that the Hilbert space of state vectors $|\Psi\rangle$ has an indefinite metric. Then the spectral function is no longer positive definite and integrals of the type (11) can be made to converge. In view of the indefiniteness of the metric, we can write the spectral function as

$$\rho(-a) = \Pi(-a) + \sum(-a), \tag{12}$$

where $\Pi(-a) \geqq 0$, and $\sum(-a)$ is indefinite and describes the auxiliary mass spectrum associated with the intermediate states of negative norm.

From (9) and (10) it follows that the δ-function singularities and the first order poles $1/\lambda$ are independent of the mass, whereas the singularities in $\ln(\lambda)$ and $\theta(\lambda)$ appear with coefficients proportional to the square of the mass a. Since these are the only kinds of singularities which occur in the Δ-functions, we can regularize the vacuum expectation values of current operators by means of the conditions on the spectral functions

$$\int_0^{\infty} \rho(-a)\mathrm{d}a = 0, \tag{13}$$

$$\int_0^{\infty} a\rho(-a)\mathrm{d}a = 0. \tag{14}$$

We can make the vacuum expectation values continuous together with all their derivatives up to order $(n-1)$ inclusive by increasing the number of conditions to $(n+1)$. It is clear that with the above conditions the vacuum expectation value $\langle 0|[j(x), j(x')]|0\rangle$ vanishes for $(x-x')^2 = 0$. Furthermore, at $(x-x')^2 = 0$ we derive

$$\langle 0|j(x)j(x')|0\rangle = \frac{-i}{8\pi^2}\int_0^{\infty} \rho(-a)a \ln \sqrt{a}\mathrm{d}a, \tag{15}$$

as follows directly from (9). By means of the Laplace transform of the spectral function

$$R(s) = \int_0^\infty \rho(-a)\mathrm{e}^{-sa}\mathrm{d}a, \tag{16}$$

we can write the conditions (13) and (14) as

$$R(0) = 0 \quad \text{and} \quad \left[\frac{\partial R(s)}{\partial s}\right]_{s=0} = 0. \tag{17}$$

In the regularized theory, we have

$$\begin{aligned}\langle 0|[j(x), j(x')]|0\rangle &= \int_0^\infty \Delta(x-x'; a)\rho(-a)\mathrm{d}a \\ &= \int_0^\infty \Delta(x-x'; a)\,\Pi(-a)\mathrm{d}a + \int_0^\infty \Delta(x-x'; a)\sum(-a)\mathrm{d}a. \end{aligned} \tag{18}$$

According to the formalistic approach, adopted in the following, we impose the condition

$$\int_\kappa^\infty \frac{|\sum(-a)|}{a}\mathrm{d}a \to 0 \tag{19}$$

in the limit as the auxiliary masses approach infinity. (It would be sufficient to demand that $\int[\rho(-a)/a]\mathrm{d}a \to \int[\Pi(-a)/a]\mathrm{d}a$, which does not necessarily imply the decompositon in (12).) Here, κ is a lower bound obtained on the mass spectrum e.g. in pseudoscalar meson theory $\kappa = (3m)^2$, where m denotes an auxiliary mass parameter. Bogolyubov [6]) has proved that the compensating masses may be chosen in such a way that when their magnitudes are made to approach infinity in a prescribed manner the $\sum(-a)$ (or the coefficients c_i in the discrete case) remain finite. Therefore, we are at liberty to choose the auxiliary mass spectrum in such a manner that (19) is indeed satisfied. We then argue that *all* unphysical effects vanish in the limit as the auxiliary intermediate states involve infinitely heavy particles. Thus, only observable finite effects survive which take place via the physical intermediate states.

It can be shown that this method of regularizing the exact formulation of field theory within the framework of the Heisenberg representation can be extended to the case of 3-point functions and n-point functions. The conditions of regularity on the spectral function associated with the 3-point function have been derived by us using the results of Källén and Wightman [10]) on the analyticity properties of the 3-point function. However, we shall not present the details here as our results on the 2-point function will be sufficient for our study of the vacuum-polarization current and the gauge-invariance of electrodynamics.

3. Vacuum Polarization

We shall now consider the problem of calculating the vacuum-polarization effect in quantum electrodynamics using the method of regularization.

In the renormalized theory of electrodynamics the interaction energy due to the coupling between the external field A_μ^{ext} and the quantized field is given by [3])

$$\delta E = -\int \mathrm{d}^3x j'_\mu(x) A_\mu^{\text{ext}}(x), \tag{20}$$

where $j'_\mu(x)$ is the current of the quantized field. We shall therefore study a system with a weak external (c-number) electromagnetic field. We then have the following additional terms in the Lagrangian

$$\delta\mathscr{L} = \tfrac{1}{2}ieN^2[\bar{\psi}'(x), \gamma_\mu\psi'(x)]A_\mu^{\text{ext}}(x) + LA_\mu^{\text{ind}}(x) j_\mu^{\text{ext}}(x), \tag{21}$$

where the constants N and L are connected with the wave function and charge renormalization, $A_\mu^{\text{ext}}(x)$ is the external vector potential, $A_\mu^{\text{ind}}(x)$ is the induced vector potential and $j_\mu^{\text{ext}}(x)$ is the external current given by

$$j_\mu^{\text{ext}}(x) = -\left(\Box A_\mu^{\text{ext}}(x) - \frac{\partial^2 A_\nu^{\text{ext}}(x)}{\partial x_\mu \partial x_\nu}\right). \tag{22}$$

Operators ψ and A_μ are now defined as solutions of the Heisenberg equations of motion when $A_\mu^{\text{ext}} \equiv 0$. The operators ψ' and A_μ^{ind} are then expanded in a weak external (c-number) field $A_\mu^{\text{ext}}(x)$ to terms of second order [2, 3]).

In our regularized version of electrodynamics the spectral function will have the form

$$\begin{aligned}\rho(p^2) &= \frac{V}{-3p^2}\sum_{p_n=p}\langle 0|j_\mu(0)|n\rangle\langle n|j_\mu(0)|0\rangle \\ &= \Pi(p^2) + \sum(p^2),\end{aligned} \tag{23}$$

where $\Pi(p^2) \geqq 0$, and $\sum(p^2)$ contains the indefinite part of the norm in (23).

The important quantity to consider in the problem of vacuum-polarization is the vacuum expectation value of the induced current. This has been computed by Källén [2]):

$$\begin{aligned}\langle 0|j_\mu^{\text{ind}}(x)|0\rangle &= -\Box\langle 0|A_\mu^{\text{ind}}(x)|0\rangle \\ &= -i\int_{-\infty}^{x}\langle 0|[j_\nu(x'), j_\mu(x)]|0\rangle A_\nu^{\text{ext}}(x')\mathrm{d}x' + \frac{L}{1-L}j_\mu^{\text{ext}}(x).\end{aligned} \tag{24}$$

The integral on the right-hand side of (24) can be written

$$\begin{aligned}&-i\int_{-\infty}^{x}\langle 0|[j_\nu(x'), j_\mu(x)]|0\rangle A_\nu^{\text{ext}}(x')\mathrm{d}x' \\ &= -\tfrac{1}{2}i\int_{-\infty}^{\infty}[\varepsilon(x-x')\langle 0|[j_\nu(x'), j_\mu(x)]|0\rangle + \langle 0|[j_\nu(x'), j_\mu(x)]|0\rangle]A_\nu^{\text{ext}}(x')\mathrm{d}x'.\end{aligned} \tag{25}$$

The second term on the right-hand side of (25) vanishes, if no real transition is induced by the external field. We have

$$\langle 0|[j_\nu(x'), j_\mu(x)]|0\rangle = \frac{1}{(2\pi)^3}\int \mathrm{d}p\, \mathrm{e}^{ip(x'-x)}\varepsilon(p)[-p^2\delta_{\mu\nu} + p_\mu p_\nu]\rho(p^2). \tag{26}$$

A calculation of the first term in the integrand on the right-hand side of (25) gives

$$-\tfrac{1}{2}i\varepsilon(x-x')\langle 0|[j_\nu(x'), j_\mu(x)]|0\rangle$$
$$= \frac{1}{(2\pi)^4}\int \mathrm{d}p\, e^{ip(x'-x)}\left([-p^2\delta_{\mu\nu}+p_\mu p_\nu]\bar{\rho}(p^2)+[\delta_{\mu\nu}-\delta_{\mu 4}\delta_{\nu 4}]\int_0^\infty \rho(-a)\mathrm{d}a\right). \quad (27)$$

Here, $\bar{\rho}(p^2)$ denotes the expression

$$\bar{\rho}(p^2) = \int_0^\infty \frac{\mathrm{d}a\rho(-a)}{p^2+a}. \quad (28)$$

Let us write

$$K_{\mu\nu} = \theta(x-x')\langle 0|[j_\nu(x'), j_\mu(x)]|0\rangle, \quad (29)$$

where $K_{\mu\nu}$ occurs inside the bracket on the right-hand side of (25). Invariance of the induced current with respect to the gauge transformation $A_\mu \to A_\mu + (\partial\Phi/\partial x_\mu)$ yields

$$\int \mathrm{d}x' K_{\mu\nu}(x'-x)(\partial\Phi/\partial x'_\nu) = 0. \quad (30)$$

This requires that

$$\frac{\partial K_{\mu\nu}}{\partial x_\nu} = 0. \quad (31)$$

The integrated term vanishes because of the adiabatic removal of the coupling in the infinite past and future. The condition (31) clearly implies the charge conservation requirement $\partial K_{\mu\nu}/\partial x_\mu = 0$, as $K_{\mu\nu} = K_{\nu\mu}$. In momentum space (31) takes the form

$$K_{\mu\nu}p_\nu = 0. \quad (32)$$

Thus, (31) and (32) are evidently necessary in a gauge-invariant formalism. With the aid of $(\partial j_\nu(x)/\partial x_\nu) = 0$, we get

$$\frac{\partial}{\partial x'_\nu}[\theta(x-x')\langle 0|[j_\nu(x'), j_\mu(x)]|0\rangle] = i\delta(x_0-x'_0)\langle 0|[j_4(x'), j_\mu(x)]|0\rangle. \quad (33)$$

In view of gauge-invariance the vacuum expectation value of the equal time commutator in (33) must vanish. A calculation of this expression for $\mu = k$ and $x_0 = x'_0$ gives

$$\langle 0|[j_4(x'), j_k(x)]|0\rangle$$
$$= \frac{i}{(2\pi)^3}\int \mathrm{d}^3p\, e^{i\mathbf{p}\cdot(\mathbf{x}'-\mathbf{x})}p_k\int_{-\infty}^\infty \mathrm{d}p_0|p_0|\rho(\mathbf{p}^2-p_0^2) \quad (34)$$
$$= -\frac{\partial}{\partial x_k}\delta(\mathbf{x}'-\mathbf{x})\int_0^\infty \rho(-a)\mathrm{d}a.$$

Indeed, we see that this expression is zero in the *regularized* version of the theory, because our regularity condition (13) amounts to just this. But in

Källén's calculation $\rho(-a) \equiv \Pi(-a) \geqq 0$, and we must have

$$\int_0^\infty da\Pi(-a) \neq 0, \tag{35}$$

otherwise, $\Pi(p^2)$ would be identically zero. It would then appear that gauge-invariance and current conservation can only be satisfied by free-field electrodynamics. This inconsistency is removed in the regularized theory, since we can choose auxiliary masses such that

$$\int^\infty \Pi(-a)da + \int^\infty \Sigma(-a)da = 0 \tag{36}$$

remains zero as the auxiliary masses approach infinity, and condition (19) is satisfied.

In view of the regularity condition (13) it follows from (27) and (34) that we can safely conclude that

$$-\tfrac{1}{2}i\varepsilon(x'-x)\langle 0|[j_\mu(x), j_\nu(x')]|0\rangle = \frac{1}{(2\pi)^4}\int dp e^{ip(x'-x)}[-p^2\delta_{\mu\nu}+p_\mu p_\nu]\bar{\rho}(p^2), \tag{37}$$

since the last term in (27), which destroys gauge-invariance, now vanishes.

In renormalized electrodynamics, we know that

$$1+\bar{\rho}(0) = \frac{1}{1-L}, \tag{38}$$

where $\rho(p^2)$ is now the regularized spectral function. Introducing the functions $\rho(p^2)$ and $\bar{\rho}(p^2)$ into (24), and using (26) and (37), we get

$$\langle 0|j_\mu^{\text{ind}}(x)|0\rangle = \frac{1}{(2\pi)^4}\int dp e^{ipx}[-\bar{\rho}(p^2)+\bar{\rho}(0)-i\pi\varepsilon(p)\rho(p^2)]j_\mu^{\text{ext}}(p), \tag{39}$$

where we have gone over to momentum space with the aid of

$$\begin{aligned} j_\mu^{\text{ext}}(p) &= \int dx e^{-ipx} j_\mu^{\text{ext}}(x) \\ &= [p^2\delta_{\mu\nu}-p_\mu p_\nu]A_\nu^{\text{ext}}(p). \end{aligned} \tag{40}$$

In the limit as the auxiliary masses become infinite and condition (19) applies, we obtain the "dielectric constant" $\varepsilon(p^2)$ for the vacuum:

$$\varepsilon(p^2) = 1-\overline{\Pi}(p^2)+\overline{\Pi}(0)-i\pi\varepsilon(p)\Pi(p^2), \tag{41}$$

where $\varepsilon(p^2)$ is complex if $-p^2 \geqq 9\mu^2$. The imaginary part of $\varepsilon(p^2)$ is related to the expression for the creation of real particles by the external field. This is the result obtained by Källén [2,3].

We end this section by remarking, that in view of

$$\frac{1}{1-L} = 1+\int^\infty \frac{\Pi(-a)}{a}da + \int^\infty \frac{\Sigma(-a)}{a}da,$$

and by virtue of (19), we get in the limit of infinitely heavy auxiliary particles

$$\frac{1}{1-L} \to 1 + \int^{\infty} \frac{\Pi(-a)}{a} \mathrm{d}a. \tag{43}$$

According to Källén [7]), the integral in (43) is logarithmically divergent. Thus the renormalization constant $1/(1-L)$, which is finite in the regularized theory, is cut-off dependent and diverges in the limit as we pass to the non-regularized theory. The results obtained in this section prove that the requirement of gauge-invariance is a cut-off independent property of the exact formulation of electrodynamics.

4. Concluding Remarks

The results of the vacuum-polarization calculation show how cautious one should be when dealing with "gauge-invariant" indeterminate expressions. Indeed, the result of the calculation in the Heisenberg representation is by no means "gauge-invariant" unless the quantities involved are regularized in the above sense. Once the theory is regularized, all the expressions are gauge-invariant and one can proceed with the calculation without fear of internal contradictions. The interchanges of orders of integration can now be justified without the aid of a "subtraction formalism", because the oscillating part of $\rho(p^2)$ can be chosen to make the integrals over a converge, and the regularity conditions (13) and (14) are just those needed to make the Fourier integrals converge.

I am grateful to Dr. T. Fulton, Dr. P. Schwed and Professor F. Rohrlich for helpful criticism. I thank Professor A. Wightman for discussion.

References

1) J. Schwinger, Phys. Rev. Letters **3** (1959) 296; see also T. Gotô and T. Imamura, Prog. Theor. Phys. **14** (1955) 396
2) G. Källén, Helv. Phys. Acta **25** (1952) 417 (see especially p. 432)
3) G. Källén, Quantum Electrodynamics in Handbuch der Physik Vol. 5, part 1 (1958); see also G. Källén, CERN Report, Geneva (1956) and H. Lehmann, Nuovo Cimento **11** (1954) 342
4) J. Schwinger, Phys. Rev. **76** (1949) 790 (see appendix p. 814);
J. Schwinger Phys. Rev. **82** (1951) 664
5) W. Pauli and F. Villars, Revs. Mod. Phys. **21** (1949) 434; see also S. N. Gupta, Proc. Phys. Soc. A **66** (1953) 129
6) N. N. Boglyubov and D. V. Shirkov, Introduction to the Theory of Quantized Fields (Interscience Publ., New York 1959)
7) G. Källén, Mat. Fys. Medd. Dan. Vid. Selsk., **27**, No. 12 (1953)
8) J. W. Moffat, Nuclear Physics **13** (1959) 150
9) J. W. Moffat, Nuclear Physics **14** (1960) 682
10) G. Källén and A. Wightman, Mat. Fys. Medd. Dan. Vid. Selsk., **1**, No. 6 (1958)

2.A.1

Nuclear Physics **16** (1960) 313—317; © *North-Holland Publishing Co., Amsterdam*

Not to be reproduced by photoprint or microfilm without written permission from the publisher

NEUTRON TOTAL CROSS-SECTIONS IN THE 12 TO 21 MeV REGION

G. J. McCALLUM †, G. S. MANI †† and A. T. G. FERGUSON

Atomic Energy Research Establishment, Harwell, Berkshire

Received 28 January 1960

Abstract: Measurements have been made of the neutron total cross-sections of a number of elements at neutron energies between 12 and 21 MeV The results are discussed in terms of a simple optical model

1. Introduction

This note reports measurements of neutron total cross-sections of a number of elements for neutrons of energies between 12 MeV and 21 MeV. Measurements of a similar nature have been made for a wide range of elements by Bratenahl *et al.*[1]) and Coon *et al.*[2]) over the neutron energy range up to 14 MeV, and Cook and Bonner[3]) have data up to neutron energies of 18 MeV for some light elements. The measurement of the cross-sections at higher neutron energies would indicate to some extent the energy dependence of the real and imaginary part of the optical model potential.

2. Apparatus and Method

The source of neutrons was the H^3(d, n)He^4 reaction. Targets of Titanium Tritide were bombarded with deuterons of 2 MeV or 4 MeV from the Harwell Electrostatic Generator, and the various neutron energies obtained by varying the angle of observation. Fig. 1 shows the general arrangement of the apparatus. The neutron detector was a plastic scintillator. In order to compensate for gain changes in the system, proton recoils lying between an upper and lower amplitude limit were counted; the advantages of this system have been described by Bratenahl *et al.*[1]). In setting up the bias, the deuteron beam was pulsed and the time-of-flight spectrum observed. This showed γ-rays and neutrons from the (d, d) reaction in addition to the high energy neutrons. The bias levels were adjusted so that only the high energy neutron group appeared in the time-of-flight spectrum. The neutrons were continuously monitored by a second plastic scintillation detector set up in the same way as the first.

† Permanent address: Division of Nuclear Sciences, D S.I.R., New Zealand. Now at Atomic Energy of Canada Limited, Čhalk River, Ontario.

†† On leave from Atomic Energy Establishment, Trombay, India. Now at Rice Institute, Houston, Texas, U.S.A.

The samples were 2.5 cm in diameter and of a length chosen to give a transmission of about $\frac{1}{3}$. Some samples were in powder form contained in thin brass containers; in the final results correction was made for the effect of these containers. The samples and detector were aligned with the target by optical means.

A copper shadow bar 61 cm long was used to measure the number of neutrons reaching the detector by scattering, or from other sources. The results have also been corrected for in-scattering by the samples using the formula of Bratenahl *et al.*[1]). This correction was less than 5% in all cases.

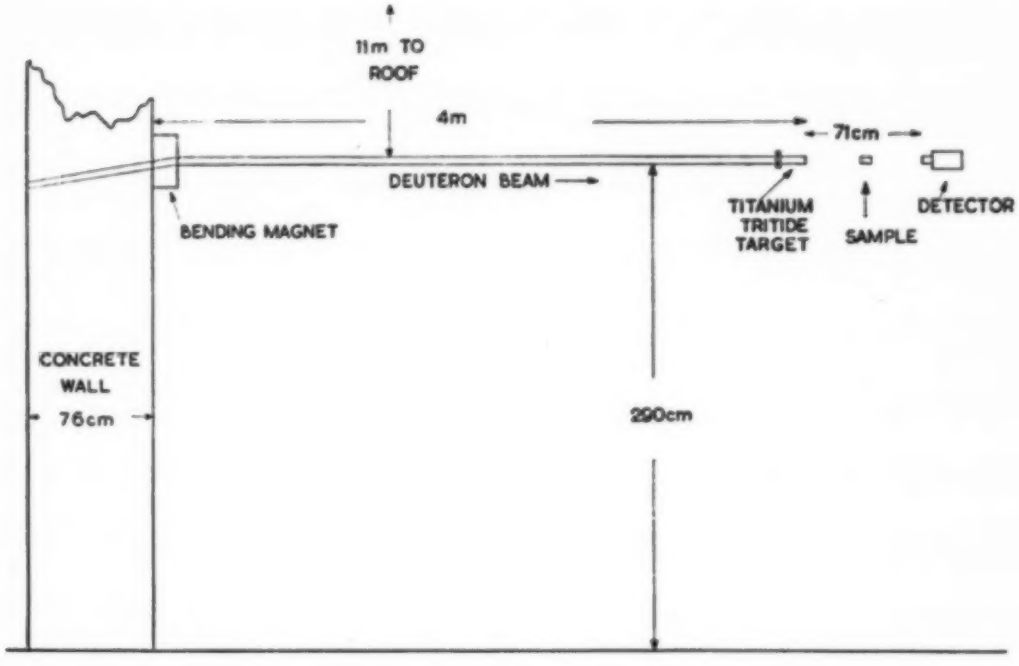

Fig. 1. The general arrangement of the apparatus.

3. Results

The results are shown in table 1 and fig. 2. It can be seen that they agree well with previous measurements below 14 MeV.

The cross-sections have been fitted to the formula

$$\sigma_t = 2\pi(r_0 A^{\frac{1}{3}} + \lambda\!\!\!^{-})^2 \qquad (1)$$

where A is the mass number and $\lambda\!\!\!^{-}$ the neutron wavelength divided by 2π. Fig. 3 is a plot of r_0 as a function of neutron energy for various elements. It can be seen that in most cases r_0 tends to a constant value at higher energies. The average value of r_0 above 18 MeV is plotted as a function of mass number A in fig. 4. The open circles in the figure are the measurements of Cook and Bonner[3]); their results are slightly lower than ours since their values have been averaged

over the energy range 13 to 18 MeV. The figure indicates that the simple relation given by (1), using one value of r_0, cannot be used to predict the total cross-section; however, the dip around mass number 45 can be explained by the optical model of Bjorklund and Fernbach [4]) which predicts maxima and minima in the value of r_0 obtained in total cross-section measurements.

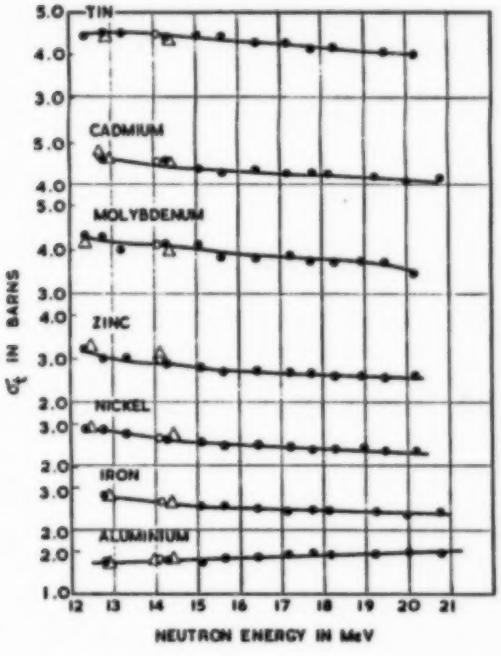

Fig. 2. The measured total cross-sections of a number of elements as a function of neutron energy.

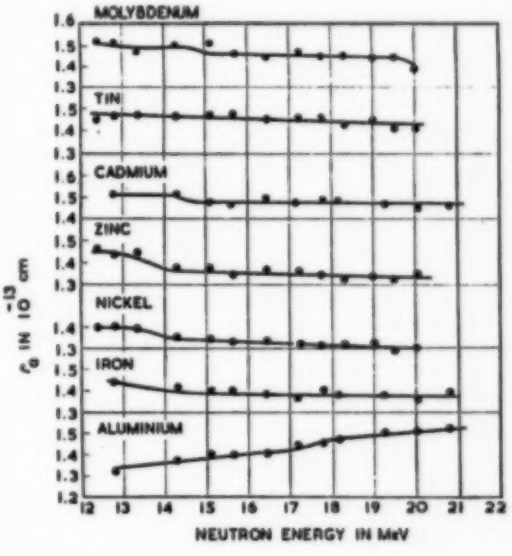

Fig. 3. The variation of r_0 as a function of neutron energy for a number of elements.

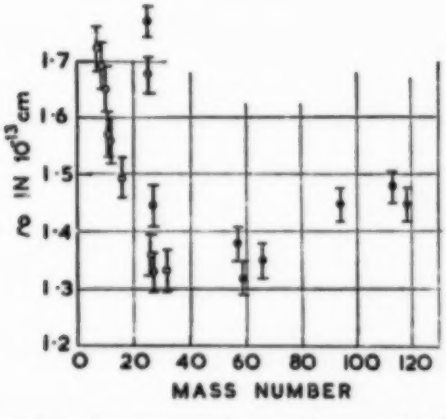

Fig. 4. The variation of the value of r_0 averaged over the energies 18—21 MeV as a function of mass number.

We wish to thank Dr. E. B. Paul for his keen interest in this work and to the operation staff of the accelerator for their unstinting co-operation in running

TABLE 1

Neutron total cross-sections and Fermi-radii of several elements

Energy (MeV)	Aluminium		Iron		Nickel		Zinc		Molybdenum		Cadmium		Tin	
	σ_t (b)	r_0 (10^{-13} cm)	σ_t (b)	r_0 (10^{-13} cm)	σ_t (b)	r_0 (10^{-13} cm)	σ_t (b)	r_0 (10^{-13} cm)	σ_t (b)	r_0 (10^{-13} cm)	σ_t (b)	r_0 (10^{-13} cm)	σ_t (b)	r_0 (10^{-13} cm)
20.8	1.95†	1.52	2.41	1.39							4.09	1.46		
20.20					2.32	1.30	2.57	1.34	3.43	1.39			3.96	1.41
20.02	1.94	1.51	2.35	1.36							4.05	1.45		
19.48					2.32	1.29	2.53	1.32	3.65	1.44			3.99	1.41
19.24	1.91	1.50	2.40	1.38							4.16	1.47		
18.97					2.40	1.32	2.57	1.33	3.68	1.44			4.13	1.44
18.30					2.37	1.31	2.57	1.32	3.72	1.45			4.09	1.43
18.15	1.89	1.47	2.45	1.38							4.23	1.48		
17.76	1.87	1.46	2.49	1.40	2.39	1.31	2.64	1.34	3.74	1.45	4.24	1.48	4.24	1.45
17.23					2.44	1.32	2.66	1.35	3.84	1.47			4.24	1.45
17.17	1.84	1.44	2.42	1.36							4.25	1.47		
16.45	1.81	1.41	2.51	1.38	2.47	1.33	2.73	1.36	3.79	1.45	4.29	1.48	4.26	1.45
15.64	1.81	1.50	2.55	1.40	2.49	1.33	2.70	1.34	3.85	1.46	4.28	1.47	4.37	1.47
15.09	1.75	1.40	2.56	1.39	2.56	1.34	2.80	1.37	4.10	1.51	4.38	1.48	4.41	1.47
14.29	1.78	1.37	2.63	1.41	2.61	1.35	2.90	1.37	4.12	1.50	4.55	1.51	4.40	1.46
13.35					2.76	1.39	3.00	1.44	4.01	1.47			4.50	1.47
12.79	1.75	1.37	2.81	1.44	2.84	1.40	3.03	1.43	4.22	1.51	4.63	1.51	4.51	1.47
12.37					2.85	1.40	3.22	1.46	4.29	1.52			4.46	1.45

† Errorxon all points is ±2 %

the machine. Two of us (G. J. M. and G. S. M) would like to express their thanks to A. E. R. E. Harwell and to all members of the Van de Graaff group for their hospitality and help.

References

1) A. Bratenahl, J. M. Peterson and J. P. Stoering, Phys. Rev. **110** (1958) 927
2) J. Coon, E. R. Graves and H. H. Barschall, Phys. Rev. **88** (1952) 562
3) C. F. Cook and T. W. Bonner, Phys. Rev. **94** (1954) 651
4) F. E. Bjorklund and S. Fernbach, Phys. Rev. **109** (1958) 1295

1.E.5

Nuclear Physics **16** (1960) 318—319; © *North-Holland Publishing Co., Amsterdam*

Not to be reproduced by photoprint or microfilm without written permission from the publisher

NUCLEAR RADII FROM NEUTRON SCATTERING

RICHARD WILSON

Cyclotron Laboratory, Harvard University, Cambridge, Mass. †

Received 15 December 1959

Abstract: It is shown how determinations of nuclear radii by neutron and electron scattering can be reconciled, with the exception of a possible anomaly for lithium.

The primary source of information on the radii of nuclei has come from electron scattering data [1]). The electron scattering data have been lacking in two respects. Firstly the cross sections have not been absolute, and secondly measurements have not been made at small momentum transfer q. It has not therefore been possible to obtain a value for the mean square radius in a model independent way. The values quoted are usually assuming plausible models, and therefore inherently involve other evidence.

This situation has been made most apparent in a recent paper [2]) which shows that the mean square radius is uncertain by as much as 10 %, and that it is not uniquely possible to put Li^6, Be^9 and C^{12}, for example, in order of increasing radii.

The purpose of this note is to show that, pending more precise electron scattering experiments to meet this need [3]), neutron or proton scattering experiments can give this information.

Some experiments on the scattering of 135 MeV neutrons by nuclei have been published [4]) and radii derived therefrom. These measurements were made at small momentum transfer and were statistically precise. The uncertainty due to inclusion of inelastically scattered protons is small at these momentum transfers. Recently, also, attempts have been made to discuss the scattering by light nuclei in terms of the impulse approximation [5]). It has been shown that the form factor appropriate to neutron scattering is the product of the nuclear form factor and the nucleon-nucleon scattering matrix,

$$F_N(q) = M(q)f(q), \tag{1}$$

just as the electron scattering form factor is the product of the nuclear form factor and the form factor of the proton:

$$F_E(q) = f_p(q)f(q). \tag{2}$$

These considerations are strictly correct only on Born approximation, but the

† Supported by the joint program of the Office of Naval Research and the U. S. Atomic Energy Commission.

deviations are negligible at small $q(qR \ll 1)$ and provided that only relative angular distributions are considered.

For helium this has been checked [6]) by a comparison of experiment and a calculation based on the Gammel-Thaler potential. The agreement for radii is fairly good even though the variations of $M(q)$ and $f(q)$ are about equal. For heavier nuclei, where the variation of $M(q)$ is less important, agreement should be better. The calculations in the table were made with an $M(q)$ given

TABLE 1

	Li^7	Be^9	C^{12}	N^{14}	O^{16}
apparent rms radius from neutron scattering	2.61 ±0.08	2.69 ±0.08	2.88 ±0.05	2.96 ±0.08	3.10 ±0.08
rms radius from neutron scattering corrected for nucleon-nucleon scattering matrix	1.85 ±0.07	1.96 ±0.07	2.21 ±0.04	2.32 ±0.07	2.50 ±0.07
rms radius from electron scattering corrected for proton size	2.70†	2.11	2.27	2.33	2.52

† Value for Li^6, not Li^7. A lower value comes from other models in ref.[2]).
All radii in units of 10^{-13} cm.

by $(1-3.4q^2/6)$, being an average of real and imaginary parts and taking no account of odd nucleons. The table shows the apparent radii of ref. [4]) and the true nuclear radii deduced therefrom. The errors are those of ref. [4]). Also shown are the radii from the models chosen by Hofstadter and collaborators as the most plausible, taken from ref. [2]), being the shapes suggested by the independent particle model. The agreement for C^{12}, N^{14} and O^{16} gives support to the choice for these nuclei. For Li and Be the disagreement suggests the choice is incorrect. The order of increasing r.m.s. radius is, from neutron experiments, unambiguous and independent of detailed assumptions about $M(q)$.

The same order is given, though less clearly, by 181 MeV proton scattering measurements [7]). A good energy for further measurements would be 350 MeV; here $M(q)$ is almost entirely imaginary and varies little with q. There is only a small Coulomb interference, and proton measurements could therefore also be used.

References

1) R. Hofstadter, Ann. Rev. Nucl. Sci. **7** (1957) 231;
D. G. Ravenhall, Revs. Mod. Phys. **30** (1958) 430
2) U. Meyer-Berkhout, K. W. Ford and A. E. S. Green, Annals of Phys. **8** (1959) 119
3) M. R. Yearian, J. Oeser and R. H. Helm, Bull. Am. Phys. Soc. **4** (1959) 61
4) C. P. Van Zyl, R. G. P. Voss and R. Wilson, Phil. Mag. **47** (1956) 1003;
R. Wilson, Phil. Mag. **47** (1956) 1013
5) H. McManus and R. M. Thaler, Phys. Rev. **110** (1958) 590;
A. F. Kerman, H. McManus and R. M. Thaler, Annals of Physics (in press)
6) A. M. Cormack, J. N. Palmieri, N. F. Ramsey and Richard Wilson, Phys. Rev. **115** (1959) 599
7) H. Tyrén and Th. A. J. Maris, Nuclear Physics **6** (1958) 82

1.B

Nuclear Physics **16** (1960) 320—330; © *North-Holland Publishing Co., Amsterdam*

Not to be reproduced by photoprint or microfilm without written permission from the publisher

PROTON-PROTON SCATTERING AT 98 AND 142 MeV

A. E. TAYLOR, E. WOOD and L. BIRD

Atomic Energy Research Establishment, Harwell, Berks.

Received 15 January 1960

Abstract: The differential cross section and the polarization in proton-proton scattering have been measured over the angular range 5° to 90° c.m. at 98 and 142 MeV. For angles greater than 37° c.m. the variation of the differential cross section can be expressed as $4.01\pm0.19(1-(0.02\pm0.045)\cos^2\theta)$ at 142 MeV and as $4.41\pm0.21(1+(0.02\pm0.07)\cos^2\theta)$ at 98 MeV, and the polarization cross section $P(d\sigma/d\omega)/\sin 2\theta$ can be expressed as $(0.806\pm0.021)+(0.339\pm0.063)\cos^2\theta$ and as $(0.54\pm0.05)-(0.04\pm0.12)\cos^2\theta$ at 142 and 98 MeV respectively.

1. Introduction

There has been a large amount of experimental data published on p—p and n—p scattering in the region of 40 to 300 MeV and various attempts have been made to interpret the nucleon-nucleon interaction in terms of phenomenological potentials. Little quantitative success has been obtained, although recent work by Signell and Marshak [1]) and Gammel and Thaler [2]) gives more reasonable agreement. The available information in the experimental data is therefore being extracted in the form of phase shifts, in the hope that when those are known as a function of energy any particular model may be more easily tested. Also a knowledge of the phase shifts may point to the required features of a model.

However, between 40 and 150 MeV there is not sufficient detailed experimental information for such a rigorous phase shift analysis as has been made at 310 MeV. Even at this higher energy, with all the data available from triple scattering experiments, no unique solution has yet been found; furthermore only those phase shifts which appear in the p—p interaction have been investigated. It is hoped that if sufficient data can be amassed at lower energies, where fewer partial waves are operative, it will be possible to arrive at a unique set of phase shifts. This might then also help in making a selection at the higher energy. The experiments described in this paper were measurements at 98 and 142 MeV of the differential cross section and of the polarization in p—p scattering over the angular range 5° to 90° c.m. The detailed shape of the curves in the region of interference between Coulomb and nuclear scattering is very sensitive to the choice of the phase shifts and is therefore a valuable region to study.

Descriptions of the method and apparatus will only be given where they have a bearing on the accuracy of the final results. Preliminary results were reported at the 1957 Rochester Conference. Some later measurements of the polarization at 142 MeV are included.

Previous measurements of the polarization in p—p scattering in the energy region 90—150 MeV have been made by Dickson and Salter [3]), Oxley, Cartwright and Rouvina [4]), Baskir, Tinlot and Spital [5]), Palmieri, Cormack, Ramsey and Wilson [6]), and measurements of the differential cross section in this same energy region have been made by Kruse, Teem and Ramsey [7]), Chamberlain, Segrè and Wiegand [8]), Marshall, Marshall and Nedzel [9]), Cassels [10]), Taylor and Wood [11]) and Palmieri, Cormack, Ramsey and Wilson [6]).

2. Method

The polarization and cross sections were determined from measurements of the number of protons scattered from the external polarized proton beam by a liquid hydrogen target, although for some of the measurements of differentia cross section at 142 MeV an unpolarized beam was used. A triple coincidence range telescope was used to detect the scattered protons and the telescope absorber was changed in order to maintain constant efficiency of detection for the different scattering angles. A calibrated, air filled, ionization chamber was used to monitor the incident beam, which had an energy of 149 MeV. For measurements at 98 MeV this beam was slowed down in polyethylene before entering the ionization chamber and hydrogen target. The counter telescope was mounted on an arm which could be swung from side to side of the beam direction and whose pivot was carefully set in the centre of the collimated beam.

Since measurements were required in the nucleon-Coulomb interference region, Coulomb scattering from the walls of the target would have been troublesome at the smallest angles at which measurements were to be made. The difficulty lies not only in the presence of a large background, but also in knowing the true background when the target is full, since the hydrogen not only reduces the energy of the emergent beam but also alters the effective angular resolution. Hence, the true background is not given by measurements with an evacuated target. It was therefore decided to build a telescope system which did not see the end windows of the target and this reduced the background to very small proportions. As a consequence the effective amount of hydrogen varied as $\operatorname{cosec}\theta$ where θ was the laboratory scattering angle. In order to achieve reasonable counting rates at the larger angles another telescope was used which had a wider geometrical angular resolution.

3. Apparatus

An external polarized proton beam, energy 149 MeV and polarization 0.46 ± 0.01, was obtained by scattering the internal proton beam of the

cyclotron from a carbon target at 6.3°. At this angle both the differential cross section and the polarization are relatively insensitive to variation in scattering angle, and inelastic scattering is only a small part of the total scattering. The absolute value of the polarization of the emergent beam can be obtained therefore with good accuracy from the asymmetry measured in a second scattering from carbon at 6.3°, though a small correction is still needed for the slight energy difference between the two scatterings. The energy and the energy spread of this external beam was estimated from the straggling curve to be 149 ± 2 MeV. Quadrupole focussing was used to increase the intensity in the experimental area where a beam of 10^6 protons/sec was collimated to an area of $2 \times \frac{1}{2}$ cm.

Two liquid hydrogen targets were used which had total surface densities of 1.31 and 1.11 g · cm^{-2}. The evaporation rate from the target was about 10 cm^3 of liquid hydrogen per hour when most of the ortho-parahydrogen conversion had taken place. With these evaporation rates there was little fear of bubbles

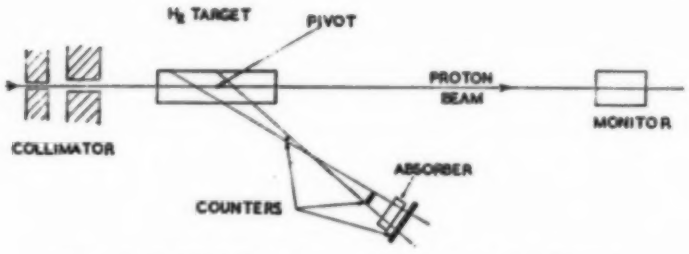

Fig. 1. Schematic diagram of geometrical layout.

in the beam appreciably reducing the surface density or of fluctuations in the surface density adding uncertainties to the polarization measurements.

The sizes of the plastic phosphors used in the triple coincidence telescope, and their distances from the target, were so chosen that the end windows of the target were not seen by the telescope (fig. 1). Several different sets of phosphors were used to cover different angular ranges. For instance, to cover the range 5 to 20° laboratory angles, the phosphors were 0.5×2 cm, 1.25×4 cm and 4×8 cm and were placed at 40, 63 and 86 cm respectively from the target. At all times the counters were set on plateaux of counting rate. Aluminium absorbers were placed between the second and third phosphors in order to reduce the background counts. However, at large scattering angles there were very few events other than the true hydrogen counts. The absorber thickness was chosen to give an efficiency of detection of about 0.85. This efficiency, defined as the ratio of triple counts to double coincidence counts, was measured by placing the telescope in the direct beam which had been reduced in intensity and whose energy was reduced to match the conditions at each scattering angle. The value of 0.85 was sufficiently above the knee of the straggling curve to be insensitive to small energy changes. To obtain the

true efficiency for any scattering angle a small correction was added to the measured value for those protons which were lost before being detected by the telescope. This correction was slightly energy sensitive amounting to 0.2 % at 10° and 0.6 % at 40° for the 98 MeV determination.

With a telescope designed to avoid seeing the target end windows the effective amount of hydrogen varied as cosec θ. The exact amount was determined both from a calculation and from a separate experiment. The hydrogen target was simulated by a stack of aluminium foils 0.005 cm thick, each separated by about 0.5 cm and occupying a total length equal to the length of the hydrogen target. These then provided about the same multiple Coulomb scattering as the hydrogen in the target. The ratio of the counting rates with this stack to the counting rate for an equal mass of aluminium at the pivot position was taken as the fraction of the target seen. This experiment was repeated for each of the sets of phosphors used to cover the different angular ranges and confirmed the cosec θ dependence. The constant of proportionality was determined to an accuracy of 1.8 %.

As the counter telescope was moved to different scattering angles, the apparent axis of rotation was found to displace slightly. This displacement was determined by observation with a theodolite mounted on the telescope arm of a plumb line suspended above the pivot. By careful shimming under the rollers on which the telescope arm moved, the displacement was reduced to less than 0.02 cm for all angles. The centre line of the phosphors was then aligned to pass through the axis of rotation using the same theodolite. Shadow photographs taken with X-ray films were used to set the pivot position in the centre of the beam and this was further checked in the course of accurately finding the beam direction.

With the scattering table and phosphors aligned as above, the direction of the beam was found by recording the single channel and coincidence rates as a function of the angle of the telescope arm as the phosphors were swept across the direct beam which had been greatly reduced in intensity. The scattering table and phosphors were assumed to be aligned when all rates peaked at the same angle, which would not have been the case if the pivot had not been in the centre of the beam. Angles could be read to 0.01° and the beam direction was determined to $\pm$ 0.02° at 142 MeV and slightly less accurately at 98 MeV.

The hydrogen target was placed over the pivot position with a possible uncertainty of $\pm$ 1 mm, which could lead to a slight uncertainty in the amount of hydrogen traversed by the recoil protons. As the area of the target was greater than the beam area, this uncertainty contributed only a small error to the measurements and was always less than the uncertainty from counting statistics.

4. Results

The differential cross section $d\sigma/d\omega$ was calculated from the formula

$$\frac{d\sigma}{d\omega} = \frac{C\,L}{cEM\,\delta\Omega\,N},$$

where C is the mean counts per monitor count, after allowance for background, L is the correction for counting losses, other than those measured in determining E,

c is the conversion factor from laboratory to barycentric coordinates,

E is the efficiency of detection,

M is the number of incident protons per monitor count,

$\delta\Omega$ is the solid angle which the telescope subtended at the target and

N is the effective surface density of hydrogen atoms determined from the separate experiment with the aluminium foil and by calculation.

All measurements of the scattered protons were made in repeated cycles of short duration and have been analysed for random variations outside those expected from counting statistics. There was a small and known systematic daily variation in the ionization chamber owing to pressure and temperature changes and account has been taken of these. However, as the measurements were made in cycles, this variation does not enter into the calculation of the polarization. Chi-squared tests were applied to all measurements and no significant departure from the expected was obtained. Backgrounds were measured with an evacuated target and, except for the results in column 2 of tables 1 and 2, fell from about 10 % to less than 1 % of the hydrogen counts within 4° of the smallest angle measured for each of the telescopes. The true background for the smallest angles was estimated from the angular variation of the measured background and the change in the angular resolution between a full and an evacuated target. This was necessary since the gaussian tails of the angular resolution function contribute significantly to the background in this region where the counting rate is varying rapidly with angle.

The error on the differential cross section can be divided into two parts; an absolute scale error, which depends on the accuracy with which M, $\delta\Omega$ and N are known, and a relative error which depends on the accuracy of the determination of C and E and on the possible deviation from the cosec θ dependence. From these terms the absolute scale was estimated to be accurate to $4\frac{1}{2}$ %. The errors quoted in the table are relative errors, and in the range 20° to 90°, for example, they were derived as follows: $\frac{1}{2}$ % counting errors, 1 % uncertainty in measurement of efficiency E, a possible 1 % deviation from the cosec θ dependence, 1 % fluctuation in the ionization chamber calibration and a 1 % uncertainty in the corrections applied to the measured efficiency E. Apart from the first two, the other estimates erred on the generous side. This then gave about 2 % total relative error.

In tables 1 and 2 of the differential cross section each column represents a separate absolute determination using different geometrical angular resolutions. The relative error between the absolute scales of the separate determinations is

TABLE 1

Differential cross-section (in mb/sr) for p—p scattering at 142 MeV

θ (c.m.)	Unpolarized beam		Polarized beam	
	Small angle telescope	Large angle telescope	Small angle telescope	Large angle telescope
5.19	69.24±2.6			
6.23	28.77±0.59			
7.27	12.96±0.43			
8.30	7.75±0.28			
8.82	5.76±0.30			
9.34	4.91±0.25			
10.38	4.37±0.21	4.32±0.14	4.27±0.04	
12.46		3.63±0.13	3.34±0.06	
14.53		3.77±0.14	3.28±0.05	
16.61		4.10±0.14	3.39±0.05	
20.76		3.74±0.13	3.63±0.05	3.44±0.07
25.95		3.83±0.16	3.62±0.06	3.77±0.07
31.06		3.60±0.16	3.62±0.06	3.90±0.07
37.2			3.95±0.06	
41.34			3.66±0.05	3.89±0.07
51.62				3.96±0.07
61.84				3.90±0.07
71.98				4.00±0.07
82.06				4.02±0.07
90.0				4.08±0.07

TABLE 2

p—p scattering at 98 MeV

θ (c.m.)	Cross section (mb/sr)		Polarization	
	Small angle telescope	Large angle telescope	Small angle telescope	Large angle telescope
10.2	12.40±0.30		0.029±0.031	
12.3	5.23±0.13		−0.004±0.033	
14.3	3.53±0.10		0.024±0.039	
16.4	3.28±0.08		0.085±0.035	
18.5	3.28±0.08		0.123±0.035	
20.5	3.62±0.15	3.71±0.10	0.052±0.059	0.117±0.020
22.6	3.86±0.09	3.72±0.10	0.143±0.033	0.088±0.021
25.6	3.93±0.12	4.05±0.10	0.128±0.037	0.110±0.016
30.7	4.27±0.13	3.97±0.10	0.113±0.040	0.127±0.014
40.9	4.21±0.19	4.47±0.10	0.123±0.062	0.121±0.010
51.1		4.46±0.10		0.105±0.010
61.3		4.45±0.10		0.107±0.015
71.4		4.46±0.10		0.073±0.012
81.4		4.39±0.10		0.043±0.011

about 3 % to 4 %. At 142 MeV the smallest angle measurements were made with an unpolarized beam. The agreement between the different determinations in the region of overlap is seen to be consistent with these errors except for two of the measurements at 142 MeV, namely at 16.6° and 20.8°. The agreement between the separate sets is improved if the results in the next to last column of table 1 are increased by 5 % and this has been done in fig. 2.

TABLE 3

Polarization in p—p scattering at 142 MeV

θ (c.m.)	Small angle telescope	Large angle telescope	Later measurements
5.19	-0.037 ± 0.034		
6.23	-0.027 ± 0.009		
8.30	$+0.031 \pm 0.024$		
9.34	$+0.089 \pm 0.023$		
10.38	$+0.153 \pm 0.035$		
10.38	0.107 ± 0.021		
12.46	0.130 ± 0.033		
14.53	0.180 ± 0.031		
16.61	0.155 ± 0.028		
20.76	0.181 ± 0.029	0.190 ± 0.009	
24.80	0.216 ± 0.037		
25.95		0.225 ± 0.011	
31.06	0.238 ± 0.028	0.241 ± 0.010	
37.20	0.283 ± 0.030		
41.34	0.250 ± 0.029	0.237 ± 0.011	
45.45			0.242 ± 0.005
49.55			0.240 ± 0.004
51.60	0.222 ± 0.011		0.232 ± 0.007
53.65			0.213 ± 0.004
57.70			0.205 ± 0.006
59.75			0.197 ± 0.005
61.80		0.196 ± 0.011	0.180 ± 0.005
65.90			0.170 ± 0.005
69.95			0.141 ± 0.005
72.00		0.113 ± 0.011	0.119 ± 0.006
74.05			0.097 ± 0.006
78.05			0.054 ± 0.007
82.10		0.066 ± 0.011	0.051 ± 0.015
90.0		0.010 ± 0.011	

The polarization in tables 2 and 3 were obtained from the measured asymmetries using the value 0.46 ± 0.01 for the incident beam polarization.

In the smallest angles region where the cross sections vary rapidly with decreasing angle, the measurements are seriously affected by the finite angular resolution. This is governed by the multiple Coulomb scattering in the liquid hydrogen, target wall, air and telescope and as a consequence the angular resolution can be represented by a gaussian with a standard deviation of 1.5° c.m.

5. Discussion of Results

The angular variation of the differential cross section at both 98 and 142 MeV is characterised by the constancy of the value for angles greater than 30° and by the presence of an interference minimum below 30° (figs. 2 and 3).

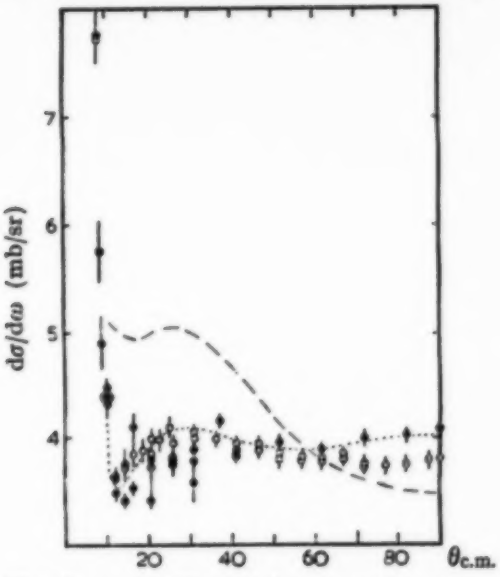

Fig. 2. p—p differential cross section at 142 MeV. The Harvard values are renormalised, as discussed in the text.

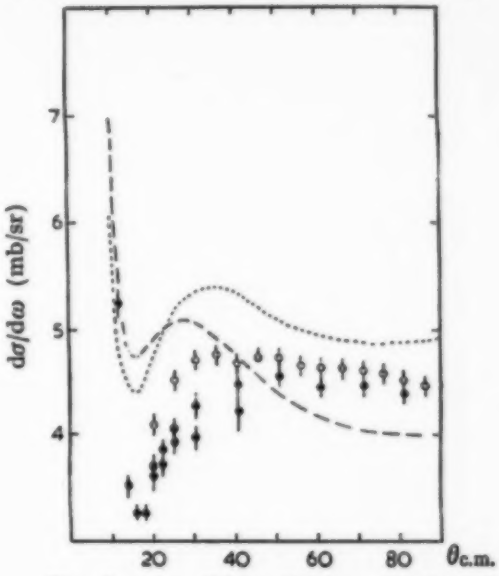

Fig. 3. p—p differential cross section at 98 MeV.

Legend for figs. 2—5: o data of Palmieri *et al.* [6]), • data of this paper, —— Gammel-Thaler model, ... Signell-Marshak model.

The angular variation for $\theta > 37°$ can be expressed at 142 MeV as

$$\frac{d\sigma}{d\omega} = (4.01 \pm 0.19)[1-(0.020 \pm 0.045)\cos^2\theta]\text{mb/sr},$$

and at 98 MeV as

$$\frac{d\sigma}{d\omega} = (4.41 \pm 0.21)[1+(0.02 \pm 0.07)\cos^2\theta]\text{mb/sr}.$$

In table 4 these results are compared with earlier and more recent Harvard

TABLE 4
Differential cross-section parameters

E_p (MeV)	A	a	Reference
142	4.01±0.19	−0.02±0.045	Present work
147	4.09±0.19	+0.05±0.02	Palmieri *et al.* [6])
98	4.41±0.21	+0.02±0.07	Present work
95	4.60±0.24	+0.12±0.05	Kruse *et al.* [7])
95.2	4.54±0.21	+0.08±0.03	Palmieri *et al.* [6])

The cross section from 37° to 90° (c.m.) is expressed as $d\sigma/d\omega = A(1+a\cos^2\theta)$mb/sr. The error on A also includes the error on the absolute scale for each determination.

data. The analysis was made by the authors of this paper. The value of the 90° differential cross section at 142 MeV agrees well with that of Palmieri *et al.*[6]) given in table 4, and with the value 4.05 ± 0.28 mb/sr obtained by Cassels [10]); it is not inconsistent with the value of 3.81 ± 0.13 mb/sr obtained by fitting the angular distribution to the measured total cross section [11]).

There appears to be a significant difference between the new Harvard date [6]) and the data presented here in the angular range 15° to 40°, where the Harvard values lie consistently higher both at 142 and 98 MeV. If however, the Harvard data at 147 MeV are normalized to their run H11 instead of H8, the difference is reduced considerably, as is shown in fig. 2 where this normalization has been used. However, there is perhaps still a slight difference in the overall shape as is shown in table 4 by the difference in the coefficient of $\cos^2\theta$. This might be attributed to a difference in technique. Whereas in the Harvard experiment

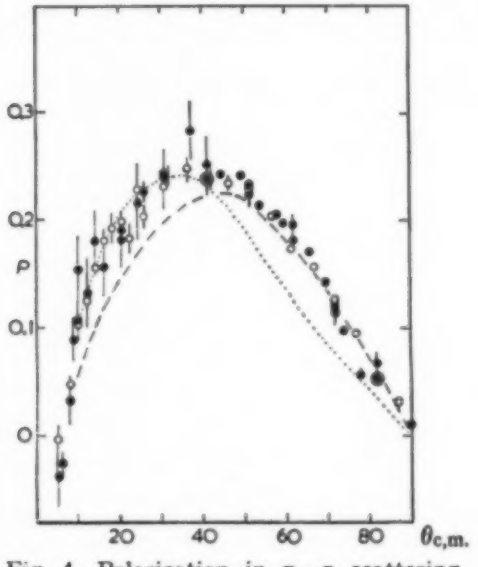

Fig. 4. Polarization in p—p scattering at 142 MeV.

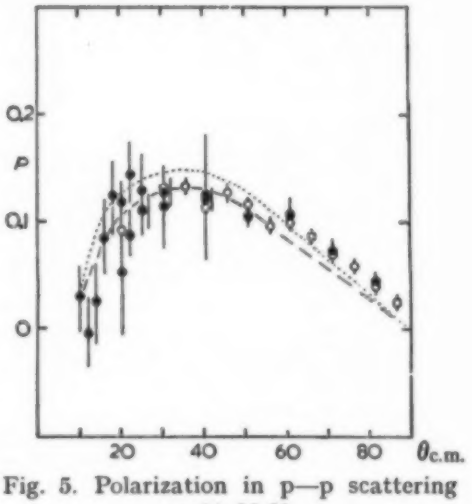

Fig. 5. Polarization in p—p scattering at 98 MeV.

all the target was seen at all angles, in this experiment the amount of hydrogen seen varied as cosec θ; this is a method which is well tried at low energies and was checked in this experiment. A further check is provided by the good agreement between the results determined in the different geometries. Another difference in the two experiments, which arises from the difference in method, is in the ratio of background to hydrogen counts. Apart from the smallest angles in each separate determination this ratio was less than 1 % in this experiment, whereas in the Harvard experiment this ratio decreased from about 20 % in the interference region to about 5 % at larger angles. In view of the overall good agreement and bearing in mind that the errors on the absolute scales are about 5 %, it is perhaps unnecessary to labour these small differences.

Analysis of the polarization results for $\theta > 37°$ gave for the angular variation at 142 MeV,

$$P\frac{d\sigma}{d\omega}/\sin 2\theta = (0.806\pm0.021)+(0.339\pm0.063)\cos^2\theta \text{ mb/sr},$$

and at 98 MeV,

$$P\frac{d\sigma}{d\omega}/\sin 2\theta = (0.541\pm0.050)+(0.040\pm0.12)\cos^2\theta \text{ mb/sr}.$$

There is good agreement between these results and those of Palmieri *et al.*[6]), as is shown in figs. 4 and 5.

6. Conclusion

The object of these experiments was to provide information for a phase shift analysis and for comparison with any proposed model of p—p scattering. If F waves contribute to the scattering, 9 phases have to be determined. The number of separate pieces of information contained in these results, which can be taken as the number of parameters by which the results can be expressed, is less than 9 and therefore the information is not sufficient for a phase shift analysis which includes F waves. However, it has been suggested that the phase shifts for F and higher order waves might be calculated from the one-pion exchange process [12]). Then this limited information may be sufficient to determine the lower order phase shifts.

Phillips [13]) has carried out an analysis, neglecting F waves, of this 98 MeV p—p data and the 95 MeV n—p data. He was able to find three different but equally good sets of phase shifts. One set was similar to that proposed by Feshback and Lomon [14]), and another set similar to that obtainable from the Signell and Marshak [1]) and Gammel and Thaler [2]) potentials. The prediction of these two models is shown in figs. 2, 3, 4 and 5.

For a proper phase shift analysis, or to distinguish between various phenomenological models, more data are required. This may mean more accurate determinations of the differential and polarized cross sections, in particular at small angles, as well as new data from triple scattering experiments.

References

1) P. S. Signell, R. Zinn and R. E. Marshak, Phys. Rev. Lett, **1** (1958) 416
2) J. L. Gammel and R. M. Thaler, Phys. Rev. **107** (1957) 291
3) J. M. Dickson and D. C. Salter, Nature **173** (1954) 946
4) C. L. Oxley, W. F. Cartwright and J. Rouvina, Phys. Rev. **93** (1954) 806
5) E. Baskir, J. Tinlot and S. Spital, Phys. Rev. **99** (1955) 639 (A)
6) J. N. Palmieri, A. M. Cormack, N. F. Ramsey and R. Wilson, Annals of Physics **5** (1958) 299

7) U. E. Kruse, J. H. Teem, and N. F. Ramsey, Phys. Rev. **101** (1956) 1079
8) O. Chamberlain, E. Segrè and C. Wiegand, Phys. Rev. **83** (1951) 923
9) J. Marshall, L. Marshall and V. A. Nedzel, Phys. Rev. **91** (1953) 767
10) J. M. Cassels, Proc. Phys. Soc. A **69** (1956) 495
11) A. E. Taylor and E. Wood, Proc. Phys. Soc. A **69** (1956) 645
12) P. Cziffa, M. H. MacGregor, M. J. Moravcsik and H. P. Stapp, Phys. Rev. **114** (1959) 880
13) R. J. N. Phillips, Proc. Phys. Soc. A **70** (1957) 721
14) H. Feshbach and E. Lomon, Phys. Rev. **102** (1956) 891

2.D

Nuclear Physics **16** (1960) 331—338; © *North-Holland Publishing Co., Amsterdam*

Not to be reproduced by photoprint or microfilm without written permission from the publisher

MODIFICATION OF THE FORM OF POTENTIAL IN AN EXCITED NUCLEUS AND ITS EFFECT ON THE BARRIER TRANSMISSION COEFFICIENT

J. NÉMETH

Central Research Institute for Physics, Budapest, Hungary, Nuclear Physics Laboratory

Received 20 November 1959

Abstract: The transmission coefficient of the nuclear potential barrier is calculated by taking into account the fact that the density distribution of an excited nucleus differs from that of one in the ground state. As an example the potential barrier of an excited nucleus of mass number 40 is determined on the basis of the statistical model and it is found that for 15 MeV excitation energy the transmission coefficient for protons emitted with 2 MeV energy is twice as large as that for a nucleus in the ground state.

1. Introduction

In studying the emission of charged particles it has been found by several authors [1]) that the shapes of proton spectra obtained in (n, p)-reactions do not quite agree with the evaporation theory. The agreement between theory and experiment becomes somewhat better if the fact is taken into account that part of the particles is ejected by instantaneous interactions and not by evaporation. However, the fact that the number of low-energy particles is much larger than is to be expected from calculations taking into account the presence of the Coulomb barrier, has still to be explained. According to this picture, particles of lower energy than the height of the Coulomb barrier can be emitted only by virtue of the tunnel effect. Assuming the density distribution of the nucleus to be round-edged, the result will be better than for a square-well potential [2]) and the introduction of a velocity-dependent potential [3]) also leads to a better agreement. On the other hand, the fact that the surface of the emitting nucleus oscillates also changes the shape of the energy spectra of emitted particles [4]), but even by taking into account all these effects, the agreement between theory and experiment cannot be considered as completely satisfactory.

There may be, however, an additional effect of appreciable importance which should be taken into account in the determination of the shape of proton spectra: the particles are evaporated by an excited nucleus, and potential and transmission coefficient of an excited nucleus differ from those of a nucleus in the ground state: for an excited nucleus expands, its one-particle potential

becomes more diffuse and the height and thickness of the Coulomb barrier decreases. The aim of the present paper is to determine the one-particle potential of a given excited nucleus and to calculate the modification of the transmission coefficient caused by this effect. Of course, rather rough approximations being used, we cannot expect exact numerical results, but rather informatory estimations as to the order of magnitude of the effect in question.

The potential of an excited nucleus is determined on the basis of the statistical model [5]). First, an approximation is given for the exact momentum distribution function and expressions $\rho = \sum_i |\psi_i|^2$ and $\tau = \sum_i |\nabla_i \psi_i|^2$ are determined as functions of the temperature $\theta = kT$ (sect. 2). In sect. 3 the binding energy is determined in terms of ρ and τ. In sect. 4 a form with two free parameters is postulated for the spatial density distribution. Determining now the free energy from its minimum condition we calculate these two parameters. In this way an expression is obtained for the density distribution, and making use of this expression in sect. 5 the one-particle potential is derived as a function of the coordinates and of the particle momentum for given excitation energy, i.e. for given temperature.

2. Determination of ϱ and τ in Terms of Temperature for an Infinite Nucleus

The wave function for an infinite nucleus is a Slater determinant of plane wave functions and thus ρ and τ are defined by

$$\rho = \frac{1}{V} \sum_i 1, \quad \tau = \frac{1}{V} \sum_i p_i^2, \quad (c = \hbar = 1). \tag{1a}$$

The summation can be replaced by an integration:

$$\rho = \frac{2}{\pi^2} \int p^2 \mathrm{d}p f(p), \quad \tau = \frac{2}{\pi^2} \int p^4 \mathrm{d}p f(p), \tag{1b}$$

where $f(p)$ is the Fermi momentum distribution function expressed as

$$f(p) = \frac{1}{e^{\left(\frac{p^2}{2m} - \zeta\right)/\theta} + 1}. \tag{2}$$

If the nucleus is in the ground state, i.e. $\theta = 0$, $f(p) = 1$ for $p^2/2m < \zeta$ and $f(p) = 0$ for $p^2/2m > \zeta$, so that in this case it is easy to evaluate expressions (1b). However, if the nucleus is in an excited state ($\theta \neq 0$), the above expressions cannot be used. It is not possible to determine the exact shape of function (2) in a simple analytical form and instead of (2) a reasonable approximation has to be found.

The function $f(p)$ can be expanded as follows:

$$\begin{aligned} f(p) &= 1 \quad \text{if} \quad \frac{\frac{p^2}{2m}-\zeta}{\theta} < -1, \\ f(p) &= 0 \quad \text{if} \quad \frac{\frac{p^2}{2m}-\zeta}{\theta} > 1, \\ f(p) &= \tfrac{1}{2}\left[1-\frac{\frac{p^2}{2m}-\zeta}{\theta}\right] = \frac{p_2^2-p^2}{p_2^2-p_1^2} \quad \text{if} \quad -1 < \frac{\frac{p^2}{2m}-\zeta}{\theta} < 1, \end{aligned} \tag{3}$$

where

$$\frac{p_1^2}{2m} = \zeta-\theta, \quad \frac{p_2^2}{2m} = \zeta+\theta. \tag{4}$$

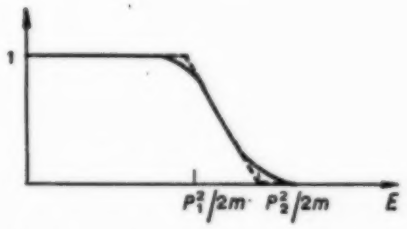

Fig. 1. Approximation used for the Fermi momentum distribution function. The solid line represents the real function, the dotted line its approximation.

The distribution function given above is shown in fig. 1. Substituting now (4) into (1b) and carrying out the integration, we obtain

$$\rho = \frac{2}{3\pi^2}\frac{2}{5}\frac{p_2^5-p_1^5}{p_2^2-p_1^2}, \quad \tau = \frac{2}{5\pi^2}\frac{2}{7}\frac{p_2^7-p_1^7}{p_2^2-p_1^2}. \tag{5}$$

A further approximation is required if we want to express τ in terms of ρ. If the condition $\theta/\zeta < 1$ is satisfied (i.e. if the temperature is not too high) the expressions p_1, p_2 given by (4) may be expanded in powers of θ/ζ. Substituting now the expansion into (5) and expressing ζ in terms of ρ, we have

$$\tau = \tfrac{3}{5}(\tfrac{3}{2}\pi^2)^{\frac{2}{3}}\rho^{\frac{5}{3}}\left(1+\frac{5}{12}\frac{\theta^2}{(\frac{3}{2}\pi^2\rho)^{\frac{2}{3}}}\right). \tag{6}$$

3. Determination of the Energy of a Finite Nucleus in Terms of ϱ and θ.

The determination of ρ and τ in the case of a finite nucleus is not so simple as above, since the model wave function to be applied now is not built up from

plane wave functions. Without knowing, however, the model wave function, τ may be obtained in terms of ρ by making use again of the Thomas-Fermi approximation, which assumes the validity of the above relation (6) for a finite nucleus also. Consequently, in the following treatment eq. (6) will be used also for finite nuclei.

Our further task is to determine the energy of a nucleus with density distribution ρ. We shall use here the method of Skyrme [6]). For an infinite nucleus we obtain the following effective one-particle velocity-dependent interaction

$$t(k) = t_0(\rho)+t_1(\rho)k^2, \tag{7}$$

where t_0 and t_1 are both functions of the density. With the help of eq. (7) the energy density of an infinite nucleus, neglecting the Coulomb energy, is given by

$$H = \left(\frac{1}{2m} + \rho t_1\right)\tau + \tfrac{1}{2}t_0\rho^2. \tag{8a}$$

In the energy expression for a finite nucleus an additional term, the surface energy, occurs, since the boundary conditions at the nuclear surface have to be satisfied by the wave function. Thus,

$$H = \left(\frac{1}{2m} + \rho t_1\right)\tau + \tfrac{1}{2}t_0\rho^2 + \tfrac{1}{2}B(\nabla\rho)^2. \tag{8b}$$

The nature of the dependence of t_0 and t_1 on the density is not known, we only know that the energy per particle in an infinite nucleus has to satisfy the following conditions (see ref. [6]):

$$E(\rho_0) = -E_0 = -15\ \text{MeV}, \quad \left(\frac{\mathrm{d}E}{\mathrm{d}\rho}\right)_{\rho=\rho_0} = 0, \quad \left(\rho^2\frac{\mathrm{d}^2E}{\mathrm{d}\rho^2}\right)_{\rho=\rho_0} = 30\ \text{MeV}. \tag{9}$$

The simplest shape of the energy satisfying the above conditions is

$$E = E_0\left[\left(\frac{\rho}{\rho_0}\right)^2 - 2\frac{\rho}{\rho_0}\right]. \tag{9a}$$

Introducing now, for simplicity, the assumption $t_1 = \text{const.}$, eqs. (9—9a) yield as a result for t_0 and t_1:

$$\rho_0 t_1 = \frac{0.5}{2m},$$

$$\tfrac{1}{2}t_0\rho^2 = \left[-15\left(\frac{\rho}{\rho_0}\right)^2 + 30\frac{\rho}{\rho_0} - \tfrac{3}{5}\left(\tfrac{3}{2}\pi^2\right)^{\frac{2}{3}}\frac{1}{2m}\rho^{\frac{5}{3}} - \tfrac{3}{5}\left(\tfrac{3}{2}\pi^2\right)^{\frac{2}{3}}\frac{0.5}{2m}\rho^{\frac{5}{3}}\right]\text{MeV}, \tag{10}$$

where

$$\rho_0 = \left(\tfrac{4}{3}\pi r_0^3\right)^{-1}, \quad r_0 = 1.2\times10^{-13}\ \text{cm}.$$

The coefficient B was calculated by Skyrme with the above assumptions and was found to be

$$\tfrac{1}{2}B = \frac{15\times 25}{64}\frac{r_0^2}{\rho_0}\,\text{MeV}. \tag{11}$$

Substituting now (10), (11) and (6) into (8b) and introducing the symbols

$$A\frac{35}{4}\frac{1}{(\frac{3}{2}\pi^2\rho_0)^{\frac{1}{3}}}\theta^2 = \alpha^2, \quad \frac{\rho}{\rho_0} = y,$$

where A is the mass number, the energy density of a finite nucleus is obtained as

$$\frac{H}{\rho_0} = \left[\frac{\alpha^2}{A}y^{\frac{1}{3}} + 0.5\frac{\alpha^2}{A}y^{\frac{4}{3}} - 15y^3 + 30y^2 + \frac{15\times 25}{64}r_0^2(\nabla y)^2\right]\text{MeV}. \tag{12}$$

4. Determination of Density as a Function of Position

In order to obtain an expression for the coordinate dependence of the density we assume a density function depending on two free parameters which will be determined from the minimum condition of the free energy. We postulate the following form of ρ:

$$\begin{aligned} &\frac{\rho}{\rho_0} = D^3 && \text{if} \quad r < a, \\ &\frac{\rho}{\rho_0} = D^3x^3 && \text{if} \quad a < r < b, \\ &\frac{\rho}{\rho_0} = 0 && \text{if} \quad r > b, \end{aligned} \tag{13}$$

where

$$x = \frac{b-r}{b-a} = \frac{b-r}{c}, \tag{14}$$

and a and $c = b-a$ are two free parameters representing the size of the nucleus and the thickness of the nuclear surface, respectively. The value of D^3 can be obtained from the normalization condition.

By substituting this shape of the density into (12) and integrating we obtain the total energy as a function of b, c, θ, A. Calculations can only be carried out numerically, and for this reason we have to choose a given nucleus. In what follows we are going to determine the energy of the Ca^{40} nucleus. Introducing the following symbols:

$$b = r_0A^{\frac{1}{3}}z, \quad d = c/b, \tag{15}$$

we have

$$\begin{aligned} E = \int H\mathrm{d}V = [&\alpha^2\delta_1(d)z^2 + \tfrac{1}{2}\alpha^2\delta_2(d)z^{-1} - 1200\delta_3(d)z^{-3} \\ &+ 600\delta_4(d)z^{-6} + 108.2\delta_5(d)z^{-5} + 105.26\delta_6(d)z^{-1}]\,\text{MeV}, \end{aligned} \tag{16}$$

where the last term represents the Coulomb energy which is thus also taken into account. The terms δ are third-order functions of d. Now the free energy is easy to calculate with the help of the energy function and the relation

$$E = F - T\frac{\mathrm{d}F}{\mathrm{d}T}. \tag{17}$$

It is obvious from eq. (16) that the energy may be written as

$$E = E_0 + T^2 E_1, \tag{18}$$

and we therefore obtain

$$F = E_0 - T^2 E_1 = [-\alpha^2\delta_1 z^2 - \tfrac{1}{2}\alpha^2\delta_2 z^{-1} - 1200\delta_3 z^{-3} + 600\delta_4 z^{-6} + 108.2\delta_5 z^{-5} + 105.26\delta_6 z^{-1}] \text{ MeV}. \tag{19}$$

The free energy has to be minimum with respect to d and z:

$$\frac{\partial F}{\partial z} = 0, \quad \frac{\partial F}{\partial d} = 0. \tag{20}$$

From eqs. (20) the value of d and z can be determined for a given α^2; i.e. for a given temperature. Substituting these values of d and z into (16) the relation between temperature and excitation energy can be determined.

The calculations are very tedious and only approximate solutions can be obtained. The following values of the parameters have been obtained:

(a) for the ground state:

$$D = 0.9473,\ z = 1.6248,\ a = 0.8352\, r_0 A^{\frac{1}{3}},\ c = 0.7896\, r_0 A^{\frac{1}{3}}; \tag{21a}$$

(b) for 15 MeV excitation energy:

$$D = 0.9455,\ z = 1.6517,\ a = 0.8319\, r_0 A^{\frac{1}{3}},\ c = 0.8258\, r_0 A^{\frac{1}{3}},\ \alpha^2 = 11.0655. \tag{21b}$$

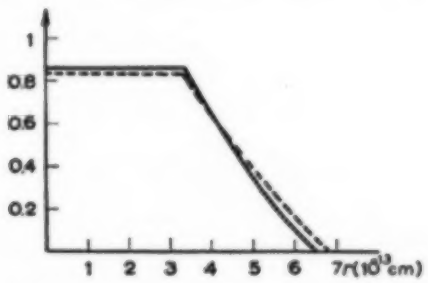

Fig. 2. Density of Ca^{40} as a function of the position. The full curve represents the density of the nucleus in the ground state, the dotted curve that for 15 MeV excitation energy.

It is easy to see that the inner radius a does not vary appreciably with the excitation energy. On the other hand, the variation of the surface thickness seems to be significant: it increases from 3.24×10^{-13} cm up to 3.39×10^{-13} cm. It has to be noted that surface thickness in the ground state does not depend

very sensitively on the mass number, e.g. for Pb^{208} it was found to be $c = 3.22 \times 10^{-13}$ cm. This result is in good agreement with that obtained by Skyrme. The modification of density with the excitation energy is shown in fig. 2.

5. Calculation of the Potential

The one-particle potential energy in terms of density can be obtained according to Skyrme [6]) and Moszkowski with the help of the following equation:

$$V_n(r, k) = t_0\rho + \tfrac{3}{5}t_1\tau + t_1\rho k^2 - B\nabla^2\rho. \tag{22}$$

Considering that $\varepsilon = (k^2/2m) + V(r, k)$ and substituting (10), (11), (13) into (22), the nuclear potential is obtained as

$$V_n = \frac{30D^6x^6 - 60D^3x^3 - 42D^2x^2 + (\alpha^2/80)Dx - 10.5D^5x^5 - 12.02(D^3/c^2)x + \frac{1}{2}D^3x^3\varepsilon}{1 + \frac{1}{2}D^3x^3} \text{ MeV}, \tag{23}$$

where ε is the total particle energy. The Coulomb potential, expressed as

$$V_c = \left[\frac{7.02}{r'} - \frac{0.7}{r'} D^3z^3d^2x^5\left(\tfrac{3}{2} - dx\right)\right] \text{MeV}, \tag{24}$$

where $r = r_0A^{\frac{1}{3}}r'$, has to be added to the nuclear potential. For calculating the transmission coefficient, it is sufficient to know the positive values of $V = V_n + V_c$ only. The positive parts of the potential in the ground state as well as in the excitation state for an excitation energy of 15 MeV can be seen in fig. 3.

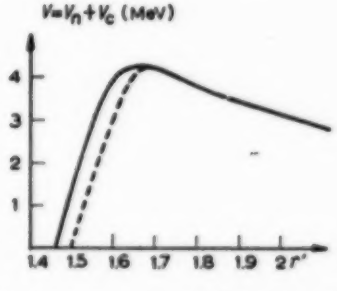

Fig. 3. Variation of the positive part of the one-particle potential of Ca^{40} for 15 MeV excitation energy. The full curve represents the nuclear potential in the ground state and the dotted one that in the excited state (excitation energy: 15 MeV). From $r' = 1.65$ both lines show the same trend.

It is obvious from this that in computing the transmission coefficient one has to take into account that the nucleus is in an excited state when emitting particles.

6. Conclusions

By means of the above procedure the transmission coefficient for an excited nucleus can be obtained. The calculations of proton spectra are, of course,

rather tedious, since the excitation energy of the residual nucleus differs for particles emitted with different energies and the shape of the potential has to be computed for each energy. We have calculated the transmission coefficient in the case of 15 MeV excitation energy for an emitted proton having an energy of 2 MeV and it was found to be

$$\frac{T_{\text{exc}}}{T_{\text{ground}}} \approx 1.9. \tag{25}$$

It is shown by this result that for protons emitted with 2 MeV energy the transmission coefficient increases to twice its initial value. With increasing energy of the emitted particles the above ratio decreases and finally will be reduced to 1. As a result of the above calculations the expected number of low-energy charged particles is higher than that predicted by the simple evaporation theory.

Of course, as mentioned above, numerically exact results cannot be expected from our approximate calculations. The most important sources of error are the following:

1) the approximation of the momentum distribution function;

2) the expansion of p_1 and p_2 in powers of θ/ζ (for a better approximation a term proportional to θ^3 would have to be included, therefore the approximation used here holds only for low excitation energies);

3) the Thomas-Fermi approximation;

4) the expression used for the effective interaction between the particles, in which terms proportional to k^4, k^6 have not been taken into account;

5) the assumption of the density dependence of t_0 and t_1;

6) the shape of the density function.

If only low excitation energies are considered the approximations 1), 2), 3) and 4) are rather good, but the applicability of 5) and 6) seems doubtful. These were used here only for the sake of simplicity, although it was assumed that they can be readily applied to get an estimation of the order of magnitude of this effect. Very great mathematical difficulties would have to be overcome to obtain more exact results.

The author is indebted to Prof. P. Gombás, Dr. G. Marx and Dr. G. Györgyi for the valuable discussions and advice in the course of this work.

References

1) Gugelot, Phys. Rev. **93** (1954) 425;
Cohen, Phys. Rev. **105** (1957) 1549
2) K. KiKucki, Progr. Theor. Phys. **17** (1957) 643
3) S. A. Moszkowski, Handbuch der Physik (1957) 416
4) J. Németh, Nuclear Physics **6** (1953) 686
5) P. Gombás, Acta Phys. Hung. **1** (1952) 329
6) T. H. R. Skyrme, Phil. Mag. **1** (1956) 1043

1.E.1:
3.A

Nuclear Physics **16** (1960) 339—350; © *North-Holland Publishing Co., Amsterdam*
Not to be reproduced by photoprint or microfilm without written permission from the publisher

ON THE DECAY OF ^{105}Ru

R. A. RICCI †, S. MONARO †† and R. VAN LIESHOUT
Instituut voor kernphysisch Onderzoek, Amsterdam

Received 18 January 1960

Abstract: The decay of 4.4 h ^{105}Ru was studied by means of scintillation techniques and with a double focusing spectrometer. Eight gamma rays were observed in addition to the isomeric transition from the 30 sec ^{105}Rh daughter. This last one was shown to be of E3 character. A decay scheme is proposed which shows similarities to those of neighbouring nucleides. The strong 725 keV gamma ray does not populate the isomeric state at 129 keV, but leads directly to the 35-h ground state.

1. Introduction

The 4.4 h ^{105}Ru was first reported in 1936 by Livingood [1]) in deuteron bombardment of ruthenium, but no mass assignment was made. In 1937 Pool, Cork and Thornton [2]) found the same activity in fast neutron bombardment of ruthenium, while De Vries and Veldkamp [3]) produced it by slow neutron capture in ruthenium; these last authors assigned the activity provisionally to mass 103. It was the first ruthenium isotope identified in fast neutron fission of uranium and thorium [4, 5]) and it has subsequently been found from thermal neutron fission [6]). A definite assignment to mass 105 was made by Sullivan, Sleight and Gladrow [6]).

However, despite its long history and the ease of production of ^{105}Ru, its decay scheme does not seem to be well established. The currently accepted decay scheme [7]) consists of a single negaton branch of 1.15 MeV, leading to a level in ^{105}Rh at 0.86 MeV, which deexcites by a 0.73 MeV gamma ray to the 30 sec ^{105}Rh isomeric state. This latter one in turn decays by an 0.13 MeV transition, which has been interpreted as E3, to the 35 hour ^{105}Rh ground state. In contrast to this, Heath [8]), in the "Scintillation Spectrometry Gamma-ray Spectrum Catalogue", shows a spectrum of ^{105}Ru, which consists of at least eight different gamma rays with energies between 0.27 and 0.96 MeV.

From a comparison with the level schemes of ^{103}Rh and with those of several odd mass Ag isotopes it would seem somewhat surprising if only one level in ^{105}Rh were populated from ^{105}Ru. It was therefore decided to study the decay of ^{105}Ru and to try to establish a level scheme for ^{105}Rh.

† On leave of absence from the Istituto Nazionale di Fisica Nucleare — Sottosezione di Napoli; Istituto di Fisica Superiore, Università di Napoli (Italia).

†† On leave of absence from the Istituto di Fisica dell' Università, Milano (Italia).

2. Production and Chemical Procedures

The sources were produced by 10 MeV deuteron bombardment of natural ruthenium. The irradiated target was left to decay for a few hours; it was thereafter dissolved in a boiling 6 *N* solution of sodium hydroxide to which sodium persulfate was added progressively. The solution was then made 6 *N* with sulfuric acid and the ruthenium tetroxide was distilled into a 4 *N* solution of sodium hydroxide. The ruthenium was precipitated by adding ethanol to the solution and by boiling it.

For a study of conversion line intensities in the double focusing beta ray spectrometer a source was prepared by electroplating at a current density of 100 mA/cm^2 from a 0.1 *N* solution of ruthenium chloride onto a gold foil. The electroplating process offers no special difficulties; sources, strong enough for the spectrometer work, were obtained in about five minutes. In order to obtain sufficiently high specific activity, a three hour bombardment (20 μAh) was performed on a target which had a thickness equal to the range of the 10 MeV deuterons. The sources prepared in this manner yielded satisfactory results.

3. Experimental Results

3.1. GAMMA RAY SCINTILLATION SPECTRUM

The direct gamma ray spectrum was measured with a NaI(Tl) crystal, 25 mm in diameter and 25 mm long, mounted on a DuMont type 6292 photomultiplier tube. A second crystal of the well-type (62 mm diameter, 62 mm long, diameter of the hole 9 mm and depth 31 mm), optically coupled to a DuMont type 6363 photomultiplier, was used to obtain some information about gamma-gamma coincidences by the summing technique. Coincidences were also performed with two 52 mm by 52 mm NaI(Tl) crystals; a single channel analyzer was used to select a photopeak which gated a coincidence circuit of the fast-slow type (resolving time: $2\tau = 20$ ns). All spectra were displayed on the RIDL 100 channel analyzer.

The direct spectrum as measured with the smaller crystal is shown in figs. 1 and 2 for two different energy regions. The gamma rays resolved from this spectrum and from the direct spectrum measured with the larger crystal by the usual procedure of successively peeling off the pulse height distributions due to the single gamma rays, are listed in table 1 with their relative intensities. For comparison, the energies of the gamma rays reported by Heath [7]) are also given; the agreement is very satisfactory.

All gamma rays listed decay with the same half-life, the best value of which is 4.44 ± 0.02 h, obtained as the average from a large number of measurements. The spectrum was not distorted to an appreciable extent by the gamma rays due to other ruthenium activities. Only the 0.22 MeV gamma ray [7]) due to

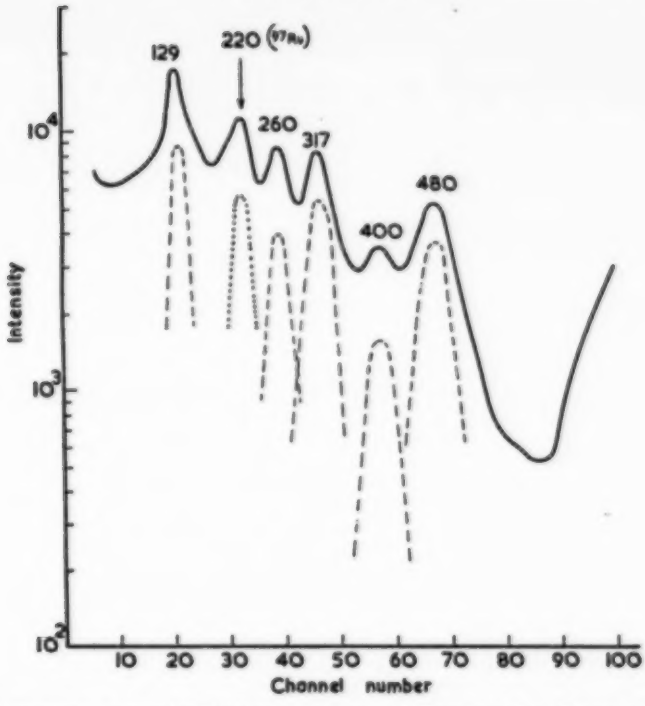

Fig. 1. The direct gamma ray scintillation spectrum following the decay of ^{105}Ru as measured with a 25 mm diameter by 25 mm high NaI(Tl) crystal. Low energy region. The various analyzed photopeaks are indicated.

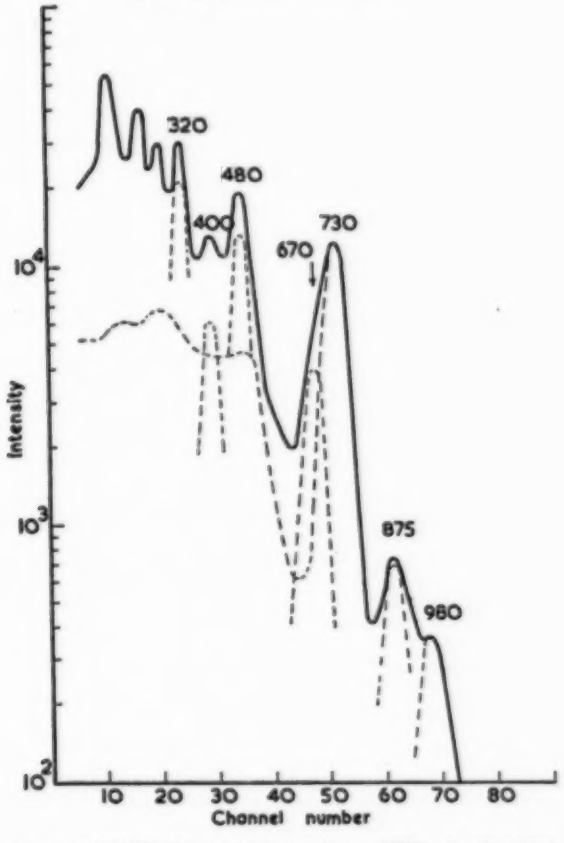

Fig. 2. The direct gamma ray scintillation spectrum from ^{105}Ru in the high energy region; see also the caption of fig. 1.

2.9 d ^{97}Ru showed up strongly (see fig. 1), whereas the much weaker 0.32 MeV gamma ray from this isotope became only visible towards the end of each series of measurements. The same was true for the 0.50 and 0.61 MeV gamma rays [7]) from 40 d ^{103}Ru. Owing to the much longer half-life of these two isotopes

TABLE 1

Energy and relative intensity values of the gamma rays from ^{105}Ru

^{105}Ru produced by $^{(104)}$Ru (10-MeV d, p) chem; $T_{\frac{1}{2}} = 4.44 \pm 0.02$ h		
Energy in keV		Relative intensity
Heath [7,8])	Present work	Present work
	130± 4	11±1
	210±10 †	10±4
265	260± 5	13±1
315	317± 5	26±3
400	400± 5	14±2
475	475± 7	42±3
670	670±10	26±7
720	725± 8	100
870	870±10	8±1
960	970±10	5±1

† Observed in coincidence only.

their contribution to the gamma ray spectrum was easily subtracted. The growth of ^{105}Rh as expected from the established genetic relationship [7]) was evident from the appearance of a 0.32 MeV gamma ray; its growth and decay was in agreement with the parent—daughter relation between the 4.4 h ^{105}Ru and the 35 h ^{105}Rh. In this case too, the contribution due to this gamma ray was only important in the last stages of each series of measurements and could easily be taken into account.

Gamma-gamma coincidences were first studied by means of the summing technique with the well-type crystal. Fig. 3 shows the spectrum of the source in three different geometries. A number of summing peaks is clearly visible, their energies and possible origin are listed in table 2. From their relative intensities in the various geometries it follows that there are no strong triple cascades involved.

Selected gamma-gamma coincidences were also performed. In these the photopeaks at 0.32, 0.40 and 0.48 MeV were selected successively as gating peaks. Figs. 4, 5 and 6 show the various coincidence results. In addition the 0.67 and 0.73 MeV peaks were selected as gating peaks; no coincident gamma ray transitions were observed. In the interpretation of these results contribu-

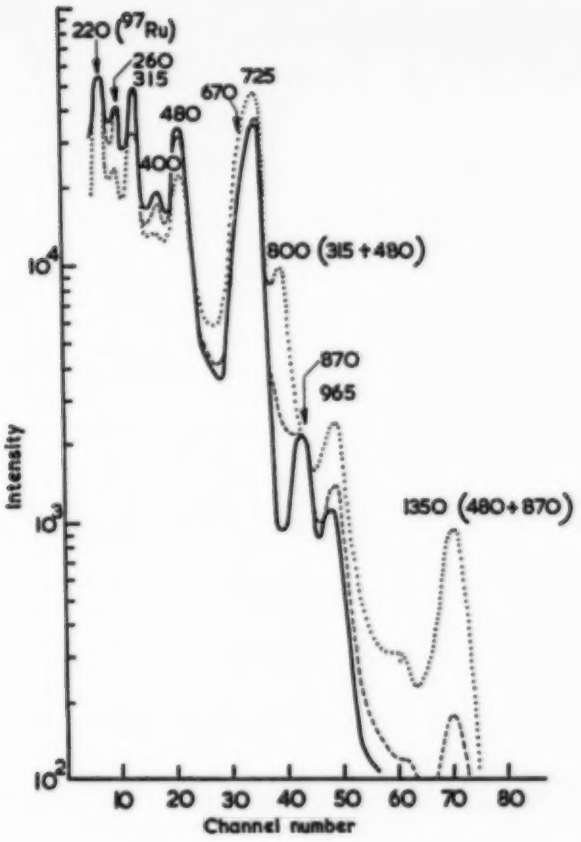

Fig. 3. The gamma ray scintillation spectrum of ^{103}Ru as measured with the 62 mm diameter by 62 mm high NaI(Tl) well-type crystal in different geometries

a) source at ≈ 12 cm from the crystal (full drawn curve);
b) source on the top of the crystal (dashed curve);
c) source in the well (dotted curve).

TABLE 2

Summing peaks and their interpretation

Energy in keV	Possible origin
1350	480+870
965?	–
800	315+480
670?	400+260?
No 880	–

tions due to coincidence with underlying Compton distributions, backscattering and accidental coincidences, were taken into account. The results of the measurements are collected in table 3.

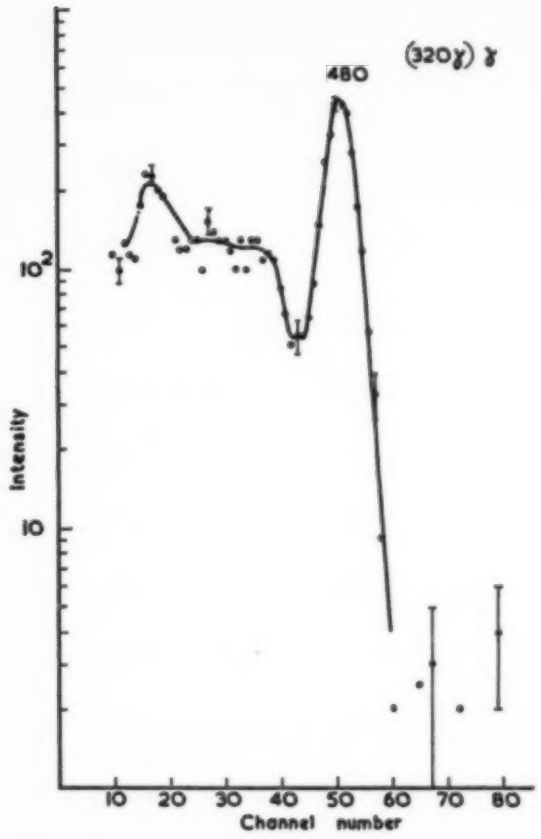

Fig. 4. Gamma ray scintillation spectrum in coincidence with the 315 keV gamma ray selected in the single channel analyzer as gating peak.

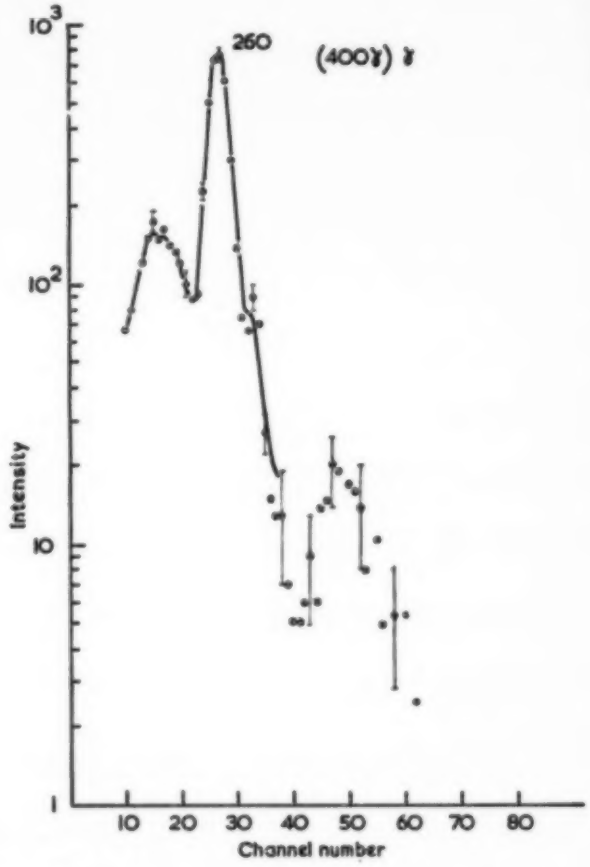

Fig. 5. Gamma ray scintillation spectrum in coincidence with the 400 keV gamma ray as gating peak.

TABLE 3

Gamma—gamma coincidence results

Coincident peak (keV)	Gating peak (keV)				
	315	400	475	670	725
210	—	—	Y	N	N
260	N	Y	N	N	N
315	N	N [a]	Y	N	N
400	N	N	? [b]	N	N
475	Y	? [b]	N [a]	N	N
670	N	N	N	N	N
725	N	N	N	N	N
870	N	N	Y	N	N
970	N	N	N [a]	N	N

Y: coincidences observed; N: coincidences not observed.

[a] The slight indications for coincidences at these energies are due to accidental coincidences

[b] Probably due to coincidences with Compton electrons of the 870 keV gamma ray.

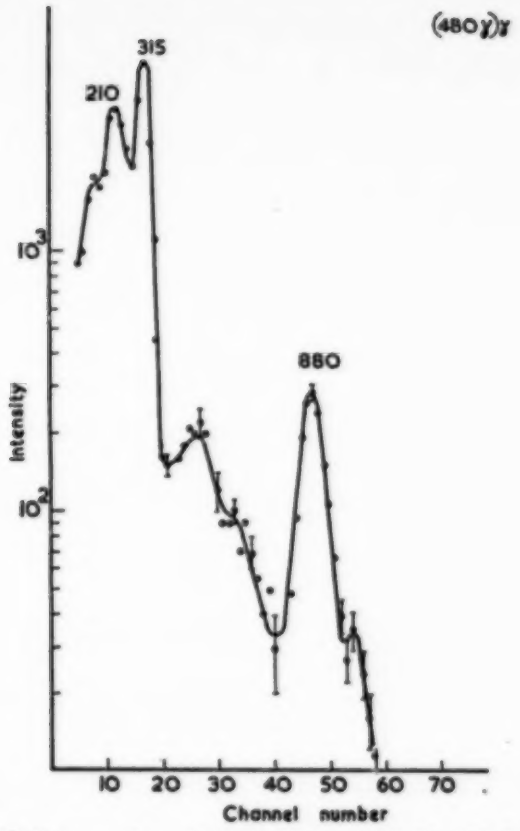

Fig. 6. Gamma ray scintillation spectrum in coincidence with the 475 keV gamma ray as gating peak.

3.2. BETA SCINTILLATION MEASUREMENT

The beta ray spectrum was measured with a stilbene crystal. In the energy region above ≈ 0.6 MeV only a 4.4 h period was present, whereas below this energy the growth of the 35 h ^{105}Rh activity could be observed; a small amount of the 40 d ^{103}Ru activity showed up towards the end of the measuring period

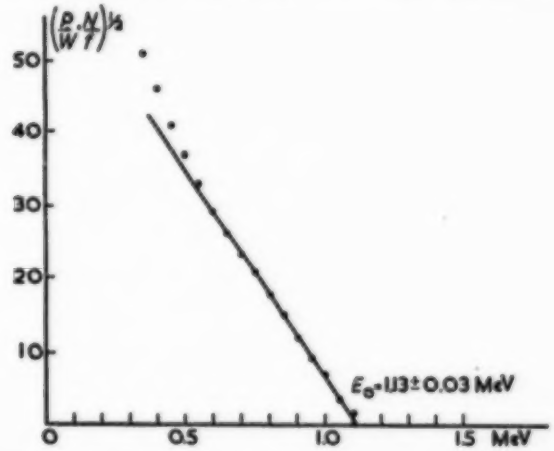

Fig. 7. Fermi—Kurie diagram of the ^{105}Ru beta ray spectrum measured with the scintillation spectrometer.

in the region below 0.2 MeV. A Fermi—Kurie analysis was made, which showed only one branch with a maximum energy of 1130±30 keV (fig. 7). This value is in good agreement with the more precise values of 1150±6 keV reported by Duffield and Langer [9]) and 1150±20 keV reported by Scoville, Fultz and Pool [10]) respectively, measured with magnetic spectrometers. Although scattering becomes important below ≈ 0.6 MeV, it can be concluded from the scintillation spectrum that there can be no branch with an energy as high as 0.6 MeV and with an intensity of more than 15 % of the main branch.

3.3. CONVERSION LINE MEASUREMENT

For a correct interpretation of the level scheme of ^{105}Rh it is indispensable to know the total intensity of the 0.13 MeV isomeric transition, which has been interpreted as E3 on the basis of life-time considerations [11]). The reported K/L

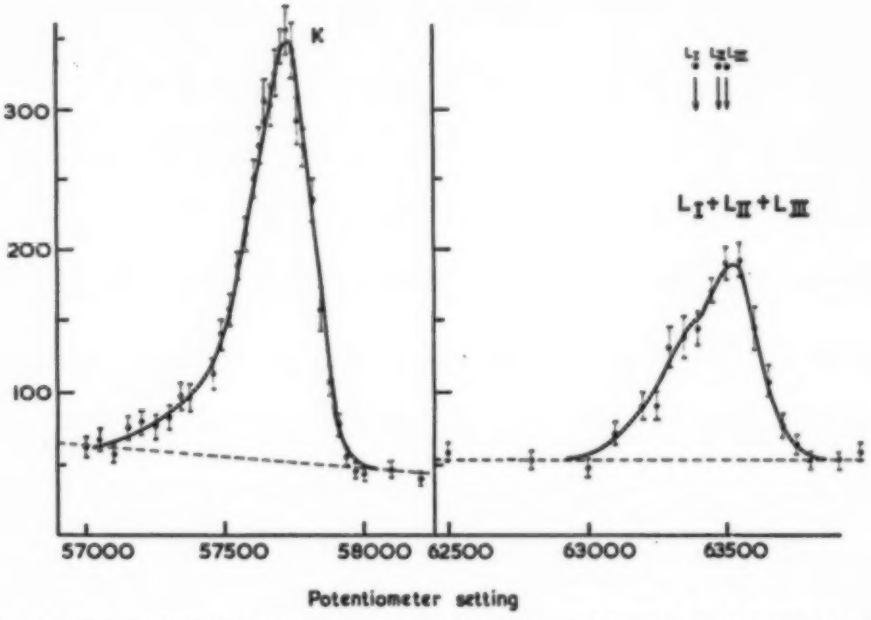

Fig. 8. K and L conversion lines corresponding to the 129.4±0.1 keV isomeric transition following the decay of ^{105}Ru as measured with the double focusing spectrometer. Resolution: 0.54 %, transmission: 1 %.

ratio [12]) of 1.4 is not in very good agreement with this assignment. It was therefore decided to remeasure this ratio with the new double focusing beta ray spectrometer [13]). An electroplated source was used but this could not be made very thin; the K-line showed a half-width of 0.54 % (fig. 8). This was sufficient to determine the energy of the transition to be 129.4±0.1 keV and the $K/\Sigma L$ ratio as 2.35±0.20. There is also an indication from the structure of the composite L-group that the transition is an electric one, since the L_I-peak seems to be weaker than L_{II}- and L_{III}-peaks.

4. Discussion

The 0.129 MeV isomeric transition from 30 sec ^{105}Rh can be identified as having octupole character from energy and life-time considerations. The experimental $K/\Sigma L$ ratio of 2.35 ± 0.20 allows only an interpretation as E3($K/\Sigma L = 2.10$) or perhaps M4($K/\Sigma L = 2.55$), so that a definite E3 assignment can now be made. Using the theoretical K- and L-conversion coefficients[14]) and assuming $MN/\Sigma L \approx \frac{1}{3}$, a total conversion coefficient of 4.2 is calculated. The total intensity of the isomeric transition becomes then 57 ± 5 units (see table 1; corrections for internal conversion for the other gamma rays should be negligible). Therefore it is impossible that the strong (100 units) 0.725 MeV gamma ray leads to this isomeric state as assumed hitherto. Instead it must be concluded that it goes directly to the 35 h ^{105}Rh ground state.

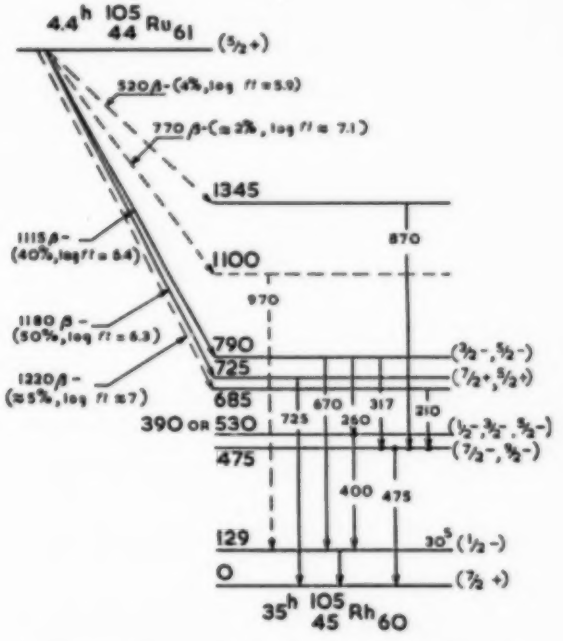

Fig. 9. Proposed decay scheme of ^{105}Ru.

The coincidence relations between the 260, 400 and 670 keV gamma rays show them to form a cascade and cross-over structure. This structure could be followed (or preceded) by the 475 keV transition as far as intensity considerations are concerned, but the absence of a coincidence between the 0.48 MeV gamma ray and any of the three others excludes this possibility.

The coincidences with the 475 keV transition suggest on the contrary that this is the lower member of a cascade, with the 210, 317 and 870 gamma rays feeding it in parallel.

Of these two independent structures of coincident gamma transitions only one can go to the isomeric level at 129 keV as follows from the intensity of the

transition deexciting it. If the first of the two structures (260, 400, 670 keV gamma rays) is supposed to feed the isomeric state, a level at 790 keV should be present. The cascade of the 315 and 475 keV gamma transitions can then be assumed to occur between this level and the ground state. This interpretation of the level structure in ^{105}Rh is therefore preferred. The other gamma rays can now be fitted into this level scheme according to coincidence relations (see fig. 9). The 210 keV gamma ray, seen only in the coincidence spectrum with the 475 keV peak, has been assumed to originate at a level at 395 keV. The 970 keV gamma ray has been placed on top of the isomeric state in order to improve the intensity balance of the transitions populating it (this balance is still not quite satisfactory). A level at 970 keV can, of course, not be completely excluded on these grounds.

TABLE 4

Energy and relative intensity values of the beta branches as deduced on basis of the proposed level scheme and the gamma ray intensities

Beta transition (MeV)	Intensity (%)	log *ft*
1.220	≈5	≈7
1.180	50	6.3
1.115	40	6.4
0.77?	≈2	≈7.1
0.52	4	5.9

The beta ray group of 1.15 MeV, which has been reported to be simple, should then in reality consist of two branches of approximately equal intensity, feeding the two levels at 725 and 790 keV. In addition there must be weak beta branches populating the levels at 685, 1100 and 1345 keV. The intensities of these various branches can be calculated from the gamma ray intensities on the basis of the decay scheme. (see table 4).

Again there is a slight discrepancy in the intensity balance, this time for transitions involving the level at 790 keV. Both these imperfections can be avoided if the intensity of the 670 keV gamma ray is readjusted (to 35 units). The intensity of this transition may have been underestimated since it must be resolved from the far stronger 725 keV peak.

A total decay energy of 1905±25 keV is derived for ^{105}Ru; this value is in good agreement with the one estimated according to the method of Way and Wood [15]).

The spins of the ground state and isomeric level of ^{105}Rh are almost certainly $\frac{7}{2}^+$ and $\frac{1}{2}^-$ respectively. The levels at 475 and 725 keV decay only to the $\frac{7}{2}^+$ ground state, which restricts their spins to $\frac{5}{2}^+$, $\frac{7}{2}$ or $\frac{9}{2}$. The levels at 530 and 790 keV do not decay to the ground state, but populate the isomeric $\frac{1}{2}^-$ level; therefore their spins are probably $\frac{1}{2}$, $\frac{3}{2}^-$ or $\frac{5}{2}^-$. Assuming the spin of ^{105}Ru to be

$\frac{5}{2}^+$, like that of other nucleides with 59 or 61 neutrons, it follows from the log ft-values of the two strong beta branches, that the spins of $\frac{9}{2}$ for the 725 keV level and of $\frac{1}{2}$ for the 790 keV level must be excluded. The relative intensities of the three gamma transitions depopulating the 790 keV level, suggest that all three final levels involved have the same parity. Finally, a spin $\frac{7}{2}^-$ for the 725 keV level can be excluded, since no gamma transition to the 475 keV level is observed.

The spins and parities derived on the basis of these arguments are shown on the decay scheme.

According to shell model predictions a spin $\frac{7}{2}^+$ or $\frac{3}{2}^+$ for the ^{105}Ru ground state could also be possible. The first choice would fix the spin of the 790 keV level as $\frac{5}{2}^-$ and allow a spin $\frac{9}{2}$ for the 725 keV level; the second choice would restrict the spin of the 725 keV level to $\frac{5}{2}^+$ and allow a spin $\frac{1}{2}$ for the 790 keV level; no further modifications would result.

A comparison of the level structure of ^{105}Rh with those of ^{103}Rh, ^{107}Ag, ^{109}Ag and ^{111}Ag shows some similarities [7, 16]). The level at 0.53 (or 0.39) MeV can well be the $\frac{3}{2}^-$ state belonging to the $K = \frac{1}{2}$ rotational band. The $\frac{5}{2}^-$ level of this band does not seem to be populated. Although the level at 0.79 MeV shows the correct decay characteristics to be identified with the $K = \frac{1}{2}$, $J = \frac{5}{2}^-$ level, the low log ft-value for the beta branch populating this level argues against an assignment of $K = \frac{1}{2}$. The absence of beta transitions to the levels at 0.53 (or 0.39) MeV and to the ground state is also observed in the decay of ^{103}Ru to similar levels and may be due to the same cause, viz. a pronounced difference of the nuclear configuration of initial and final states.

The authors would like to thank Prof. Dr. A. H. W. Aten Jr. and Prof. Dr. A. H. Wapstra for their interest in this work, Miss J. C. Kapteijn for performing the chemical separations and the personnel of the synchro-cyclotron for performing the irradiations. Thanks are also given to Mr. C. de Vries for his help in the conversion electron measurements and to R. K. Girgis and R. K. Gupta for interesting discussions.

This work was performed as part of the research program of the "Stichting voor Fundamenteel Onderzoek der Materie (F.O.M.)" which is financially supported by the "Nederlandse Organisatie voor Zuiver-Wetenschappelijk Onderzoek (Z.W.O.)".

References

1) J. J. Livingood, Phys. Rev. **50** (1936) 425
2) M. L. Pool, J. M. Cork and R. L. Thornton, Phys. Rev. **52** (1937) 239
3) H. de Vries and J. Veldkamp, Physica **5** (1938) 249
4) E. Segrè and G. T. Seaborg, Phys. Rev. **59** (1941) 212
5) Y. Nishina, T. Yasaki, K. Kimura and M. Ikawa, Phys. Rev. **59** (1941) 323, 677
6) N. R. Sleight, National Nuclear Energy Series **9** (1951) 805;
W. H. Sullivan, N. R. Sleight and E. M. Gladrow, N.N.E.S. **9** (1951) 808;

W. H. Sullivan, N. R. Sleight, E. M. Gladrow, N.N.E.S. **9** (1951) 817
7) Nuclear Data Sheets, National Research Council, Washington, D. C. Sheet NRC 58-11-55, 59
8) R. L. Heath, Scintillation Spectrometry Gamma-ray Spectrum Catalogue, A. E. C. Research and Development Report, IDO—16408 (1957)
9) R. B. Duffield and L. M. Langer, Phys. Rev. **81** (1951) 203
10) C. L. Scoville, S. C. Fultz and M. L. Pool, Phys. Rev. **85** (1952) 1046
11) M. Goldhaber and A. W. Sunyar, Phys. Rev. **83** (1951) 906
12) P. Axel and R. B. Duffield, priv. comm. reported in ref. [9])
13) C. de Vries, Thesis Amsterdam; to be published
14) M. E. Rose, Internal Conversion Coefficients (North-Holland Publishing Company, Amsterdam, 1958)
15) K. Way and M. Wood, Phys. Rev. **94** (1954) 119
16) S. F. Eccles, to be published

1.B

Nuclear Physics **16** (1960) 351—356; © *North-Holland Publishing Co., Amsterdam*

Not to be reproduced by photoprint or microfilm without written permission from the publisher

POLARIZATION OF 1.0-MeV NEUTRONS SCATTERED FROM DEUTERIUM

S. E. DARDEN, C. A. KELSEY and T. R. DONOGHUE

Physics Department, University of Notre Dame, Notre Dame, Indiana †

Received 18 January 1960

Abstract: Neutron polarization produced in the scattering of 1-MeV neutrons by deuterons has been measured. Asymmetry measurements were performed for c.m. scattering angles of 70°, 110° and 140° using the method of Levintov, Miller, and Shamshev. The polarization was found to be small and opposite in sign to that predicted by Delves and Brown. An asymmetry measurement was also carried out at a c.m. scattering angle of 110° for 2-MeV neutrons.

1. Introduction

In recent years interest in the few-nucleon problem has developed to the point where calculations [1–4]) on the scattering of neutrons and protons by deuterons have been undertaken in the hope that comparison with experiment would provide confirmation of present ideas concerning the nucleon-nucleon interaction and/or information on the forces involved when more than two nucleons are present. Delves and Brown [4]) have recently investigated theoretically the scattering of neutrons by deuterons for neutron energies below 3.5 MeV. In addition to total cross sections and angular distributions, the polarization produced in scattering has been calculated. Their results indicate the polarization should reach a value of about −13 % †† at neutron energies around 1-MeV and for c.m. scattering angles near 110°. Above 2 MeV the polarization is predicted to be quite small, in agreement with the measurements of Brüllmann *et al.*[5]), Cranberg [6]), and Bucher *et al.* [7]), and in disagreement with the results of White *et al.*[8]). Since no measurements had been made at neutron energies below 2.1 MeV it was decided to undertake a measurement of the polarization at 1.0 MeV. A measurement was also performed for one scattering angle at a neutron energy of 2.0 MeV.

2. Method

The method used by Levintov, Shamshev and Miller [9]) to investigate the polarization of neutrons from the D(d, n)He^3 reaction suggested itself for the

† Supported in part by the joint program of the office of Naval Research and the U. S. Atomic Energy Commission.

†† The positive direction of the polarization is taken to be in the direction of the vector $\mathbf{k} \times \mathbf{k}'$, where $\mathbf{k}$ and $\mathbf{k}'$ are the propogation vectors of the incident and scattered neutrons respectively.

present experiment since the scatterer is normally in the form of a gas and has a low atomic weight. Levintov *et al* used a group of long, thin recoil counters filled with helium to investigate the polarization of the D—D neutrons. By adjusting the helium pressure, the range of the helium recoils can be made sufficiently long compared to the diameter of the counter so that proper pulse height discrimination ensures that only pulses corresponding to the scattering of a neutron through a reasonably well-defined angle are recorded. In this way the variation of scattering cross section with azimuthal angle can be measured in a straight-forward manner.

A schematic diagram of the experimental arrangement used is given in fig. 1. The recoil detector, which was closely patterned after that of Levintov

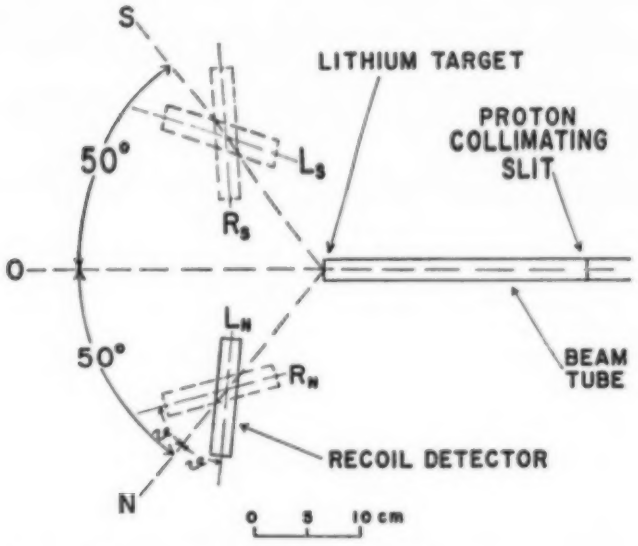

Fig. 1. Schematic top view of experimental arrangement.

et al., consisted of a group of seven brass proportional counters, each 11 cm long and 0.52 cm in diameter, placed in an outer brass tube which served as a container for the gas. The centre wires in the individual counters were of nickel 0.012 cm in diameter. Small Kovar-glass seals at either end insulated the centre wire from the counter wall. All of the centre wires were connected together inside the outer tube and also connected to a Kovar-glass lead-through in the stainless steel flange which formed the cap of the outer tube. In this way pulses from all seven counters could be fed to one preamplifier. The recoil detector was supported by a vertical arm attached to a turntable which could rotate the detector about a vertical axis passing through a point on the detector's longitudinal axis of asymmetry. This allows the angle ϑ, which the centre wires of the counters make with the incident neutron direction, to be set. The axis about which the detector was rotated was 14 cm from the neutron source. The detector turntable was itself mounted on a larger turntable which could be rotated about

a vertical axis passing through the neutron source. By properly setting this turntable, asymmetry measurements could be made in fluxes of neutrons having positive, negative or zero polarization. The distance from the detector's vertical axis of rotation to the beginning of the active volume of the counters varied with scattering angle and had an average value of about 4 cm.

Polarized 1.0-MeV neutrons emitted at a laboratory angle of 50° were produced by bombarding an evaporated lithium target with 2.9-MeV protons from the Notre Dame electrostatic accelerator. The energy spread of the neutrons was approximately 140 keV as determined from a measurement of the target thickness at threshold. For the measurement with 2.0-MeV neutrons, the proton energy was 4.0-MeV and the target thickness 110 keV. The position of the target spot was defined to within $\frac{1}{2}$ mm by a series of narrow collimating slits for the proton beam.

TABLE 1

Summary of data and results

Neutron energy (MeV)	Gas pressure (atm)	Recoil angle	c.m. scattering angle	Measured asymmetry L/R	$P(\theta)$
1.0	2.0 (D_2 +3 % C_3H_8)	20°	140°	1.034±0.023 (low bias) 1.021±0.028 (high bias)	0.107±0.050
1.0	2.0 (D_2 +3 % C_3H_8)	35°	110°	1.027±0.023 1.022±0.028	0.070±0.050
1.0	1.0 (D_2 +3 % C_3H_8)	55°	70°	1.145±0.030 1.182±0.035	0.092±0.050
2.0	2.0 (D_2 +3 % C_3H_8)	35°	110°	0.989±0.023 0.975±0.027	−0.080±0.060
1.0	0.25 (He +2 % CO_2)	40°	100°	1.228±0.020 1.268±0.020	0.32 ±0.05 (P_n) 0.30 ±0.05

For the azimuthal asymmetry measurements the counter was filled with purified deuterium to which had been added 3 % propane for stability. The pressures were chosen to give an average range [10]) of about 1.5 cm for deuterons having a recoil angle ϑ and are given in table 1. An asymmetry measurement was also performed with the counter filled with helium.

In carrying out the asymmetry measurements, the number of recoil pulses for a fixed amount of charge collected on the lithium target was recorded with the detector in a given position (e.g. position L_n in fig. 1). The detector was then rotated through the angle 2ϑ (position R_n) and the counts corresponding to an equal amount of charge collected were recorded. This procedure was repeated a number of times, after which the larger turntable was rotated about the neutron source to a position (S in fig. 1) subtending the same polar angle with the proton

beam direction as the initial position, but having an azimuthal angle differing by 180°. Counts were then recorded for the two positions of the counter turntable (positions L_s and R_s in fig. 1), again repeating the measurements a number of times. The apparatus was then realigned and the entire procedure repeated. Background was measured with the detector shielded from the source by 30 cm of paraffin and found to be less than 3 % of the counting rate in the direct beam. The measured asymmetry is given by

$$\frac{L}{R} = \frac{C(L_s)+C(R_n)}{C(L_n)+C(R_s)} \tag{1}$$

where $C(L_s)$ is the number of counts recorded in position L_s, etc. When the measurements are performed in this way, most of the experimental asymmetries introduced by errors in alignment and varying gas multiplication among the different counters in the detector are eliminated. That these effects were in any case small was attested to by the fact that asymmetries measured with the detector in a flux of unpolarized neutrons (position 0 in fig. 1) differed on the average from unity by only two percent.

Data with 1.0-MeV neutrons were taken at discriminator levels corresponding to approximately 65 % and 80 % of the pulse height for recoils making the angle ϑ with the incident neutron direction as given in table 1. For the 2.0-MeV measurement the discriminator levels were raised to 75 % and 85 % respectively, in order to discriminate against the lower energy group of neutrons from the $Li^7(p, n)Be^{7*}$ reaction. Pulse heights corresponding to these levels of discrimination were determined from a study of integral pulse height spectra for the recoil counter and the measured variation of counter efficiency with neutron bombarding energy. The estimated uncertainty in this pulse height calibration is about ± 15 %. However, the effect of this uncertainty on the values of $P(\theta)$ obtained from the measured deuteron asymmetries is small, since the asymmetries calculated using eq. (2) are relatively insensitive to the level of pulse height discrimination assumed. The overall angular resolution of the measurements was about $\pm 25°$ c.m.

For a given polarization $P(\theta)$ produced in the scattering, the measured asymmetry will be given by the expression

$$\frac{L}{R} = \frac{\int f' \bar{f} \left[\overline{\sigma(\theta)} + \overline{P_n P(\theta)\sigma(\theta)}\right] \frac{dV}{r^2}}{\int f' \bar{f} \left[\overline{\sigma(\theta)} - \overline{P_n P(\theta)\sigma(\theta)}\right] \frac{dV}{r^2}} \tag{2}$$

where the integral is taken over the active volume of the recoil counters. In this expression, $\sigma(\theta)$ is the n—d differential cross section [11]), f' is a measure of the yield of the $Li^7(p, n)Be^7$ reaction and r is the distance between the neutron

source and the volume element dV. The polarization of the incident neutrons is given by P_n. For each volume element dV, the cross sections and polarizations are averaged over the neutron energy spread and the c.m. solid angle corresponding to the angle of acceptance of the recoil counter. The factor f takes account of the variation of the gas multiplication near the ends of the counters, the effect of the level of pulse height discrimination used and the dependence of the c.m. solid angle of acceptance on the position of dV. Numerical integration was used in evaluating eq. (2). In order to determine the variation of gas multiplication near the ends of the counters, the detector was irradiated with a well collimated (0.6 cm) beam of neutrons incident at right angles to the longitudinal axis of asymmetry. For this measurement the energy of the neutrons was chosen to make the mean range of the recoil deuterons approximately 0.2 cm. Observation of the variation of counting rate with position of the portion of the counter being irradiated permitted a mapping of the gas multiplication of the counter. The value of $P(\theta)$ which, used in eq. (2), yields the measured value of L/R, is taken as the measured $P(\theta)$.

3. Results and Conclusions

Column five of table 1 contains the experimentally measured asymmetries at three scattering angles for 1.0-MeV neutrons and at one angle for 2.0-MeV neutrons. In addition, an asymmetry measurement was made with helium for 1.0-MeV neutrons for a c.m. scattering angle of 100°. Using the published data [12, 13, 14]) on n—α scattering, $P(\theta)$ and $\sigma(\theta)$ for helium could be calculated with a fair degree of confidence, and the measured L/R analyzed to give P_n. The value of 32 ± 5 % so obtained is in good agreement with the previously measured values of Striebel *et al.*[15]) and Austin [16]), and was used in analyzing the 1.0-MeV deuteron asymmetries. For the 2.0-MeV measurement, P_n was taken to be 37 % [6]). Values of $P(\theta)$ for n—d scattering are given in the last column of table 1. The quoted uncertainties include those arising from statistics (1.5 %), errors in alignment (2 %), and uncertainties in the factor f in eq. (1) (3 %). No significant bias effect was observed in any of the measurements, and the values of $P(\theta)$ given are averages for the two bias settings. The polarization of -8 ± 6 % found for 2.0-MeV neutrons is in fair agreement with the values of 2 ± 3 % found by Cranberg [6]) at 2.1 MeV, and -2 ± 7 % found by Bucher *et al.*[7]) at 2.3 MeV. The present result disagrees with the value of 48 ± 5 % obtained by White *et al.*[8]) for a neutron energy of 2.26 MeV.

At a neutron energy of 1.0 MeV the polarizations are seen to be small and positive. Although the uncertainties are of the order of 5 %, these results do not appear to be consistent with the predictions of Delves and Brown [4]). More precise measurements of the polarization in this energy region would undoubledly be of interest for comparison with theory.

The authors are indebted to Bro. Cosmas C. S. C. for the construction of the recoil detector.

References

1) R. A. Buckingham, S. J. Hubbard and H. S. W. Massey, Proc. Roy. Soc. A **211** (1952) 183
2) R. A. Christian and J. L. Gammel, Phys. Rev. **91** (1953) 100
3) B. H. Bransden, K. Smith and C. Tate, Proc. Roy. Soc. A **247** (1958) 73
4) L. M. Delves and D. Brown, Nuclear Physics **11** (1959) 432
5) M. Brüllmann, H. J. Gerber and D. Meier, Helv. Phys. Acta. **31** (1958) 318, 580
6) L. Cranberg, Phys. Rev. **114** (1959) 174
7) W. P. Bucher,.W. B. Beverly, G. C. Cobb and F. L. Hereford, Nuclear Physics **13** (1959) 164
8) R. E. White, A. Chisholm and D. Brown, Nuclear Physics **7** (1958) 233
9) I. I. Levintov, A. V. Miller, and V. N. Shamshev, Nuclear Physics **3** (1957) 221
10) C. J. Cook, E. Jones and T. Jorgensen, Phys. Rev. **91** (1953) 1417
11) R. K. Adair, A. Okazaki and M. Walt, Phys. Rev. **89** (1953) 1165
12) R. K. Adair, Phys. Rev. **86** (1952) 155
13) J. D. Seagrave, Phys. Rev. **92** (1953) 1222
14) H. R. Striebel and P. Huber, Helv. Phys. Acta **30** (1957) 67
15) H. R. Striebel, S. E. Darden and W. Haeberli, Nuclear Physics **6** (1958) 188
16) S. M. Austin, S. E. Darden, A. Okazaki, and Z. Wilhelmi, Bull. Am. Phys. Soc. **4** (1959) 403

4.E

Nuclear Physics **16** (1960) 357—359; © *North-Holland Publishing Co., Amsterdam*

Not to be reproduced by photoprint or microfilm without written permission from the publisher

NOTE ON THE DECAY OF THE NEW NUCLEIDE Cr^{56}

B. J. DROPESKY, A. W. SCHARDT and T. T. SHULL

Los Alamos Scientific Laboratory, University of California, Los Alamos, New Mexico †

Received 21 December 1959

Abstract: Cr^{56} has been identified and was found to decay with a 5.94 min half-life. A 1.5-MeV β-group and a 26-, 83-keV γ-ray cascade were observed in this decay.

Interest has been expressed by Kohman [1]) in the nucleide Cr^{56} because of the possibility that it might be sufficiently long-lived to be of geochemical significance. Jones [2]) searched for Cr^{56} in 350-MeV proton spallation products of Ni and Cu; on the basis of negative results he concluded that the half-life is either less than 1.3 h or longer than 210 years. Negative results were also obtained by Roy and Yaffe [3]) who tried to produce the isotope by double neutron capture on Cr^{54} in a reactor and concluded that the half-life of Cr^{56}, if long, is greater than $270 \times \sigma[Cr^{55}(n, \gamma)]$ years. This note reports the identification of Cr^{56}, which was made by the (t, p) reaction on Cr^{54} and was found to decay by an allowed β-transition with a half-life of only 5.94 min.

Normal Cr metal (2.4 % Cr^{54}) electroplated on a gold backing was bombarded with 2.7—2.9 MeV tritons. After irradiation and removal of the target the Cr was dissolved with a few drops of HCl. To remove the large amount of F^{18} produced on the oxide film of the Cr target HF and $HClO_4$ were added to the Cr solution, and then the HF was volatilized off by heating to fumes of $HClO_4$. The Mn activities were completely separated from the Cr by coprecipitation on $Fe(OH)_3$ from ammoniacal solution in which the Cr was oxidized to Cr^{+6}. The final purification step, which separated any V activity that was not carried out with the $Fe(OH)_3$, involved extraction of the Cr, as the peroxychromate, into ethyl acetate and back extraction into dilute NH_4OH. Sources for β-scintillation spectrometry were prepared by precipitating $BaCrO_4$ from this solution. Total elapsed time from end of bombardment to start of counting ranged from 11 to 17 minutes.

First evidence for the presence of Cr^{56} in the purified Cr sample came from the growth of 2.6-h Mn^{56} activity as identified by the 0.845, 1.81 and 2.13 MeV photopeaks observed with a 3×3-inch NaI(Tl) scintillator. The Cr^{56} half-life was estimated to be 6 min on the basis of the growth of the 0.845-MeV peak, but no intense γ-rays above 0.1 MeV were observed to decay with this half-life.

† Work performed under the auspices of the U. S. Atomic Energy Commission.

The low energy region of the γ-ray spectrum was examined with a $\frac{1}{2}$-inch thick NaI(Tl) crystal having a Be window plus a $\frac{3}{8}$-inch Be β-absorber. Gamma-rays of 26 ± 2 and 83 ± 3 keV were found (fig. 1), and it was established that they are in coincidence. A critical absorber for the 26-keV γ-ray removed the sum peak at 109 keV; any cross-over transition has an intensity of less than 2 % of the 83-keV γ-ray intensity. The β-spectrum in coincidence with these γ-rays was observed with a plastic scintillator and an end-point energy of 1.5 ± 0.15 MeV

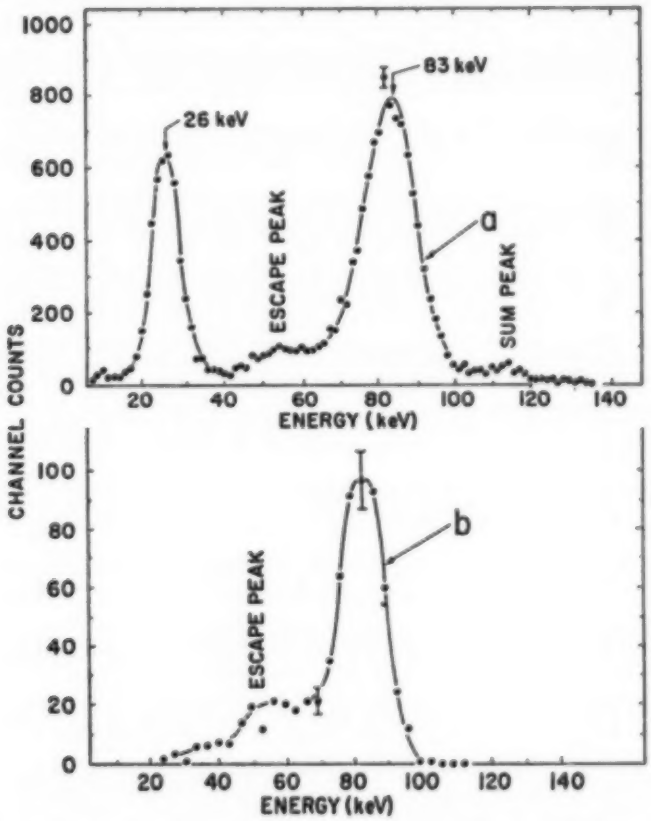

Fig. 1. Gamma-ray pulse-height spectrum from a Cr^{56} source.
Curve a: normal spectrum taken with Be window in front of crystal; the Mn^{56} contribution has been subtracted:
Curve b: gamma-rays in coincidence with the 26-keV photons.

was found. The ungated β-spectrum of Cr^{56} could not be measured since it was masked by 3.5-min Cr^{55}, which is a pure β-emitter having a 2.8 MeV end-point. The half-life of Cr^{56} is 5.94 ± 0.10 min, as determined by computer analysis of the data on the decay of the 83-keV photopeak as well as of β—γ coincidences (fig. 2).

The decay scheme of Cr^{56} (insert fig. 2) was constructed by assigning the observed γ-rays to transitions between the known levels [4]) of Mn^{56} at 108 ± 4, 25 ± 4 keV, and the ground state; this cascade accounts for all observed γ-rays. Since the Mn^{56} ground state is known to be 3+ (ref. [5]) a β-transition to it would be highly forbidden. Within the accuracy of our intensity measurements

(about 15 %) all Cr^{56} β-decays feed the 109 keV level in Mn^{56} with log $ft \approx 4.3$. Also, the upper limit on the conversion coefficient of the 83-keV γ-ray is consistent only with an E1 or M1 assignment, and the 26-keV transition is predominantly M1 on the basis of its conversion coefficient. Thus, the first and second excited states of Mn^{56} may be assigned uniquely as 2+ and 1+. For even nuclei in this region the first two neutron pairs past 28 neutrons are found in the $f_{\frac{7}{2}}$ subshell [6]). The low log ft value of the Cr^{56} decay may therefore be

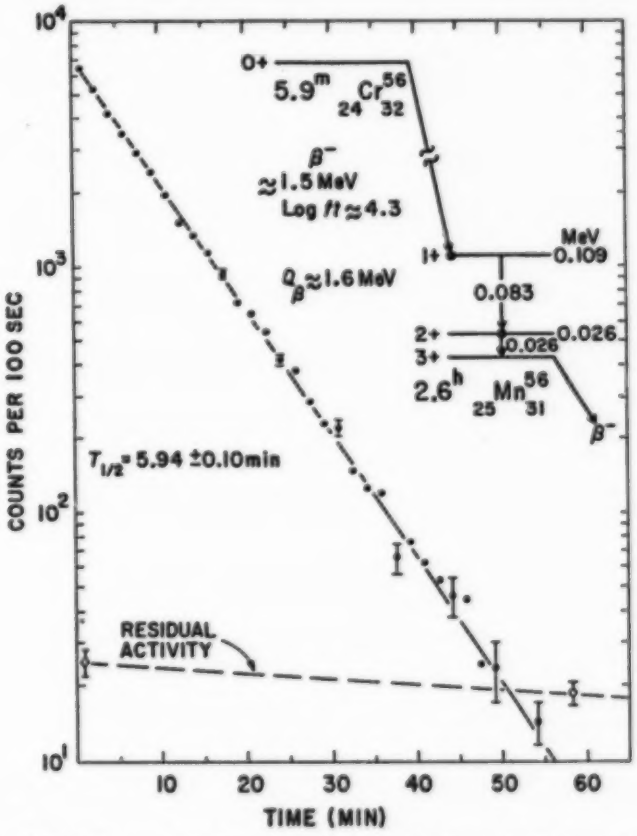

Fig. 2. Decay curve of Cr^{56} β—γ coincidences. The contribution of other activities, as determined during the next two hours, has been subtracted. The insert shows the proposed decay scheme of Cr^{56}.

explained on the basis of one $f_{\frac{7}{2}}$ neutron decaying into an $f_{\frac{1}{2}}$ proton which couples with the remaining odd $f_{\frac{7}{2}}$ neutron. The strong Nordheim rule predicts a 1+ spin for the lowest state of this configuration, which may be identified with the level at 109 keV.

References

1) T. P. Kohman, Ann. N. Y. Academy of Sci. **62** (1956) 503
2) J. W. Jones, U. S. Atomic Energy Commission Report, NYO-6627 (unpublished)
3) L. P. Roy and L. Yaffe, Can. J. Chem. **35** (1957) 176
4) Green, Smith, Buechner and Mazari, Phys. Rev. **108** (1957) 841
5) P. Kienle and R. E. Segel, Phys. Rev. **114** (1959) 1554
6) Schiffer, Lee and Zeidman, Phys. Rev. **115** (1959) 427

8.B

Nuclear Physics **16** (1960) 360—373; © *North-Holland Publishing Co., Amsterdam*

Not to be reproduced by photoprint or microfilm without written permission from the publisher

ELEMENTARY FIELDS AND IRREDUCIBLE REPRESENTATIONS OF THE LORENTZ GROUP

P. HILLION and J. P. VIGIER

Institut Henri Poincaré, Paris

Received 16 November 1959

Abstract: With the help of a new representation of the Lorentz group in terms of complex relativistic Euler angles we determine a specific set of finite-dimensional vector spaces irreducible under Lorentz transformations. If we further associate every elementary particle family with such a space we obtain a set of wave equations, among which an interesting new possibility for baryon waves.

1. Introduction

The idea of associating elementary field families with various irreducible representations of the Lorentz group has been developed by many authors, in particular by Dirac, Fierz and others [1]).

All these attempts, however, are difficult to interpret in terms of motions in Minkowski space for they utilize as a rule the general theory of group representation. In order to facilitate understanding and interpretation it is therefore tempting to start from a simple specific interpretation of that group and see whether any suggestive analogies can be derived from such a treatment. As we know, the Lorentz group can be described in many ways. One of the simplest has been developed only recently and consists in the four-dimensional extension of the classical three-dimensional Euler angle theory. This theory can be briefly summarized as follows.

We define a general frame in Minkowski space by four orthogonal unitary vectors $b_\mu{}^\xi (\xi = 1, 2, 3, 4)$ satisfying the orthonormality conditions

$$b_\mu{}^\xi b_\nu{}^\xi = \delta_{\mu\nu}, \quad b_\mu{}^\xi b_\mu{}^\eta = \delta^{\xi\eta}.$$

The time like vector is $ib_\mu{}^{(4)}$. (We have $x_4 = ix_0 = ict$.) If we start from a fixed reference frame $a_\mu{}^\xi$ the transition from this frame to any orientation of the moving frame $b_\mu{}^\xi$ is given by the expression

$$\begin{pmatrix} b_\mu^{(1)} \\ b_\mu^{(2)} \\ b_\mu^{(3)} \\ b_\mu^{(4)} \end{pmatrix} = \begin{vmatrix} \cos\frac{1}{2}\varphi^+ & \sin\frac{1}{2}\varphi^+ & 0 & 0 \\ -\sin\frac{1}{2}\varphi^+ & \cos\frac{1}{2}\varphi^+ & 0 & 0 \\ 0 & 0 & \cos\frac{1}{2}\varphi^+ & \sin\frac{1}{2}\varphi^+ \\ 0 & 0 & -\sin\frac{1}{2}\varphi^+ & \cos\frac{1}{2}\varphi^+ \end{vmatrix} \cdot \begin{vmatrix} \cos\frac{1}{2}\varphi^- & \sin\frac{1}{2}\varphi^- & 0 & 0 \\ -\sin\frac{1}{2}\varphi^- & \cos\frac{1}{2}\varphi^- & 0 & 0 \\ 0 & 0 & \cos\frac{1}{2}\varphi^- & -\sin\frac{1}{2}\varphi^- \\ 0 & 0 & \sin\frac{1}{2}\varphi^- & \cos\frac{1}{2}\varphi^- \end{vmatrix}$$

$$\times \begin{vmatrix} \cos\frac{1}{2}\theta^+ & 0 & -\sin\frac{1}{2}\theta^+ & 0 \\ 0 & \cos\frac{1}{2}\theta^+ & 0 & -\sin\frac{1}{2}\theta^+ \\ \sin\frac{1}{2}\theta^+ & 0 & \cos\frac{1}{2}\theta^+ & 0 \\ 0 & \sin\frac{1}{2}\theta^+ & 0 & \cos\frac{1}{2}\theta^+ \end{vmatrix} \cdot \begin{vmatrix} \cos\frac{1}{2}\theta^- & 0 & -\sin\frac{1}{2}\theta^- & 0 \\ 0 & \cos\frac{1}{2}\theta^- & 0 & \sin\frac{1}{2}\theta^- \\ \sin\frac{1}{2}\theta^- & 0 & \cos\frac{1}{2}\theta^- & 0 \\ 0 & -\sin\frac{1}{2}\theta^- & 0 & \cos\frac{1}{2}\theta^- \end{vmatrix}$$

$$\times \begin{vmatrix} \cos\frac{1}{2}\psi^+ & \sin\frac{1}{2}\psi^+ & 0 & 0 \\ -\sin\frac{1}{2}\psi^+ & \cos\frac{1}{2}\psi^+ & 0 & 0 \\ 0 & 0 & \cos\frac{1}{2}\psi^+ & \sin\frac{1}{2}\psi^+ \\ 0 & 0 & -\sin\frac{1}{2}\psi^+ & \cos\frac{1}{2}\psi^+ \end{vmatrix} \cdot \begin{vmatrix} \cos\frac{1}{2}\psi^- & \sin\frac{1}{2}\psi^- & 0 & 0 \\ -\sin\frac{1}{2}\psi^- & \cos\frac{1}{2}\psi^- & 0 & 0 \\ 0 & 0 & \cos\frac{1}{2}\psi^- & -\sin\frac{1}{2}\psi^- \\ 0 & 0 & \sin\frac{1}{2}\psi^- & \cos\frac{1}{2}\psi^- \end{vmatrix} \cdot \begin{pmatrix} a_\mu^{(1)} \\ a_\mu^{(2)} \\ a_\mu^{(3)} \\ a_\mu^{(4)} \end{pmatrix},$$

where the angles are defined by

$$\varphi^+ = \varphi_1 + i\varphi_2, \quad \varphi^- = \varphi_1 - i\varphi_2$$
$$\theta^+ = \theta_1 + i\theta_2, \quad \theta^- = \theta_1 - i\theta_2$$
$$\psi^+ = \psi_1 + i\psi_2, \quad \psi^- = \psi_1 - i\psi_2,$$

φ_1, θ_1, ψ_1 being the ordinary space Euler angles and $i\varphi_2$, $i\theta_2$, $i\psi_2$ hyperbolic angles describing pure Lorentz transforms [2]).

It can easily be shown that a set of self-dual bivectors built with the help of the b_μ^{ξ};

$$B_k^{r\pm} = b_k^r b_4^4 - b_4^r b_k^4 \pm \varepsilon_{ijk} b_i^r b_j^4 \quad i, j, k, r = 1, 2, 3$$

can be obtained from the corresponding expressions in a_μ^{ξ}:

$$A_k^{r\pm} = a_k^r a_4^4 - a_4^r a_k^4 \pm \varepsilon_{ijk} a_i^r a_j^4,$$

by the transformation

$$\begin{pmatrix} B_k^{(1)+} \\ B_k^{(2)+} \\ B_k^{(3)+} \end{pmatrix} = \begin{vmatrix} \cos\varphi^+\cos\theta^+\cos\psi^+ - \sin\varphi^+\sin\psi^+ & \cos\varphi^+\cos\theta^+\sin\psi^+ + \sin\varphi^+\cos\psi^+ & -\cos\varphi^+\sin\theta^+ \\ -\sin\varphi^+\cos\theta^+\cos\psi^+ - \cos\varphi^+\sin\psi^+ & -\sin\varphi^+\cos\theta^+\sin\psi^+ + \cos\varphi^+\cos\psi^+ & -\sin\varphi^+\sin\theta^+ \\ \sin\theta^+\cos\psi^+ & \sin\theta^+\sin\psi^+ & \cos\theta^+ \end{vmatrix} \cdot \begin{pmatrix} A_k^{(1)+} \\ A_k^{(2)+} \\ A_k^{(3)+} \end{pmatrix},$$

that is exactly the usual non-relativistic expression in Euler angles, where complex Euler angles $\omega^\pm = \{\varphi^\pm, \theta^\pm, \psi^\pm\}$ have replaced real ones; the transition from A_k^{r+} to B_k^{r+} is determined by the ω^+ only, the A_k^{r-}, B_k^{r-} by the ω^- only. This means, as Einstein and Meyer have noticed [3]), that we can represent any Lorentz transform by two complex-conjugate three-dimensional rotations. The explicit form of these representations can be obtained by writing the infinitesimal rotation operators corresponding to these complex rotations.

A short calculation [2]) gives for rotations around the bivectors $A_k{}^{r\pm}$:

$$\mathcal{J}_1{}^{\pm} = -\sin\varphi^{\pm} p_{\theta^{\pm}} - \operatorname{cotg}\theta^{\pm}\cos\varphi^{\pm} p_{\varphi^{\pm}} + \frac{\cos\varphi^{\pm}}{\sin\theta^{\pm}} p_{\psi^{\pm}}$$

$$\mathcal{J}_2{}^{\pm} = \cos\varphi^{\pm} p_{\theta^{\pm}} - \operatorname{cotg}\theta^{\pm}\sin\varphi^{\pm} p_{\varphi^{\pm}} + \frac{\sin\varphi^{\pm}}{\sin\theta^{\pm}} p_{\psi^{\pm}}$$

$$\mathcal{J}_3{}^{\pm} = p_{\varphi^{\pm}};$$

for rotations around the bivectors $B_k{}^{r\pm}$:

$$\mathcal{J}'^{\pm}_1 = \sin\psi^{\pm} p_{\theta^{\pm}} + \operatorname{cotg}\theta^{\pm}\cos\psi^{\pm} p_{\psi^{\pm}} - \frac{\cos\psi^{\pm}}{\sin\theta^{\pm}} p_{\varphi^{\pm}}$$

$$\mathcal{J}'^{\pm}_2 = \cos\psi^{\pm} p_{\theta^{\pm}} - \operatorname{cotg}\theta^{\pm}\sin\psi^{\pm} p_{\psi^{\pm}} + \frac{\sin\psi^{\pm}}{\sin\theta^{\pm}} p_{\varphi^{\pm}}$$

$$\mathcal{J}'^{\pm}_3 = p_{\psi^{\pm}};$$

here

$$p_{\theta^{\pm}} = -j\hbar\frac{\partial}{\partial\theta^{\pm}}, \quad p_{\varphi^{\pm}} = -j\hbar\frac{\partial}{\partial\varphi^{\pm}}, \quad p_{\psi^{\pm}} = -j\hbar\frac{\partial}{\partial\psi^{\pm}} \quad (j = \sqrt{-1}).$$

The difference between the two symbols i and j, both with squares equal to -1, has been introduced by Möller, Synge and others in order to avoid confusion [4]). It can be immediately noticed that the preceding operations which are not hermitian in the common sense of the word [5]) satisfy the commutation relations of the three dimensional rotation group:

$$[\mathcal{J}_k{}^{\pm}, \mathcal{J}_j{}^{\pm}] = -j\mathcal{J}_i{}^{\pm}, \quad [\mathcal{J}'^{\pm}_k, \mathcal{J}'^{\pm}_j] = -j\mathcal{J}'^{\pm}_i \qquad (i, j, k, \text{ is a circular permutation of } 1, 2, 3).$$

We also get the relations

$$[\mathcal{J}_k{}^{+}, \mathcal{J}_j{}^{-}] = 0, \quad [\mathcal{J}_k{}^{+}, \mathcal{J}'^{-}_j] = 0, \quad [\mathcal{J}'^{+}_k, \mathcal{J}'^{-}_j] = 0$$

which show that the $\mathcal{J}^{+}$ and $\mathcal{J}^{-}$ are independent.

Introducing further the two operators

$$(\mathcal{J}^{+})^2 = (\mathcal{J}'^{+})^2 \quad \text{and} \quad (\mathcal{J}^{-})^2 = (\mathcal{J}'^{-})^2,$$

we obtain

$$[\mathcal{J}_3{}^{+}, (\mathcal{J}^{+})^2] = 0, \quad [\mathcal{J}_3{}^{-}, (\mathcal{J}^{-})^2] = 0, \quad [\mathcal{J}'^{+}_3, (\mathcal{J}'^{+})^2] = 0,$$
$$[\mathcal{J}'^{-}_3, (\mathcal{J}'^{-})^2] = 0, \quad [(\mathcal{J}^{+})^2, (\mathcal{J}^{-})^2] = 0.$$

It is now clear that we can satisfy a Lorentz transform by the simultaneous eigenfunctions of three commuting operators among the preceding ones, namely

$$\mathcal{J}_3{}^{+}, \ \mathcal{J}'^{+}_3, \ (\mathcal{J}^{+})^2.$$

The explicit form for these eigenfunctions is given by expression

$$Y^{m^+,m'^+}_{j^+}(\omega^+) = (\sin\tfrac{1}{2}\theta^+)^{-m^++m'^+}(\cos\tfrac{1}{2}\theta^+)^{-m^+-m'^+}e^{i(m^+\varphi^++m'^+\psi^+)}$$
$$\times\frac{d^{j^+-m^+}}{d(\sin^2\tfrac{1}{2}\theta^+)^{j^+-m^+}}[(\sin\tfrac{1}{2}\theta^+)^{2j^+-2m'^+}(\cos\tfrac{1}{2}\theta^+)^{2j^++2m^+}] \equiv \Theta^{m^+,m'^+}_{j^+}(\theta^+)e^{i(m^+\varphi^++m'^+\psi^+)}$$

and we have shown in another paper [5]) that the number j^+ may take integer or half integer values, the corresponding values of m^+ and m'^+ being

$$-j^+,\ -j^++1,\ \ldots,\ j^+-1,\ j^+.$$

Obviously, the same results apply to angles ω^-.

Now, Miss Van Winter has shown [10]) that products of functions $Y^{m^+,m'^+}_{j^+}(\omega^+)\,Y^{m^-,m'^-}_{j^-}(\omega^-)$ transform under the $\mathcal{D}(j^+,j^-)$ representation of the proper Lorentz group. More precisely we can build functions which transform under the representation $\mathcal{D}(j^+,j^-)\oplus\mathcal{D}(j^-,j^+)$ of the full Lorentz group. To do this we use the eigenfunctions of the six commuting operators

$$(\mathcal{J}^+)^2,\ \mathcal{J}_3{}^+,\ (\mathcal{J}^-)^2,\ \mathcal{J}_3{}^-,\ S'^2,\ S'_3,$$

with

$$S'_k = \mathcal{J}'^+_k + \mathcal{J}'^-_k \qquad S'^2 = S'_kS'_k.$$

These eigenfunctions are series of linear products of the $Y^{m^+,m'^+}_{j^+}(\omega^+)\,Y^{m^-,m'^-}_{j^-}(\omega^-)$ eigenfunctions multiplied by suitable Clebsch-Gordan coefficients

$$Z^{m^+,m^-,m'}_{j^+,j^-,s'}(\omega^+,\omega^-) = \sum_{-m'^+,-m'^-}(j^+,j^-,-m'^+,-m'^-|j^+,j^-,s',-m')\,Y^{m^+,m'^+}_{j^+}(\omega^+)\,Y^{m^-,m'^-}_{j^-}(\omega^-) \tag{1}$$
$$(s' = j^++j^-,\ j^++j^--1,\ \ldots\ |j^+-j^-|,$$
$$m' = -s',\ -s'+1,\ \ldots,\ s'-1,\ s'),$$

and we have

$$(\mathcal{J}^\pm)^2 Z^{m^+,m^-,m'}_{j^+,j^-,s'}(\omega^+,\omega^-) = j^\pm(j^\pm+1)Z^{m^+,m^-,m'}_{j^+,j^-,s'}(\omega^+,\omega^-)$$
$$\mathcal{J}_3{}^\pm Z^{m^+,m^-,m'}_{j^+,j^-,s'}(\omega^+,\omega^-) = m^\pm Z^{m^+,m^-,m'}_{j^+,j^-,s'}(\omega^+,\omega^-)$$
$$S'^2 Z^{m^+,m^-,m'}_{j^+,j^-,s'}(\omega^+,\omega^-) = s'(s'+1)Z^{m^+,m^-,m'}_{j^+,j^-,s'}(\omega^+,\omega^-)$$
$$S'_3 Z^{m^+,m^-,m'}_{j^+,j^-,s'}(\omega^+,\omega^-) = m' Z^{m^+,m^-,m'}_{j^+,j^-,s'}(\omega^+,\omega^-).$$

Moreover [7]),

$$PZ^{m^+,m^-,m'}_{j^+,j^-,s'}(\omega^+,\omega^-) = (-1)^{j^++j^--s'}Z^{m^-,m^+,m'}_{j^-,j^+,s'}(\omega^+,\omega^-),$$
$$CZ^{m^+,m^-,m'}_{j^+,j^-,s'}(\omega^+,\omega^-) = (-1)^{|m^++m^--m'|}Z^{-m^+,-m^-,-m'}_{j^+,j^-,s'}(\omega^+,\omega^-), \tag{2}$$

P and C being respectively the parity and charge conjugation operators.

Now we can establish [5]) the following theorem: If in a set of functions $Z^{m^+,m^-,m'}_{j^+,j^-,s'}(\omega^+,\omega^-)$, we fix the values of j^+, j^-, s', m', the corresponding set

transforms like the representation $\mathscr{D}(j^+, j^-)\oplus\mathscr{D}(j^-, j^+)$ of the full Lorentz group. In other words, the functions of this set constitute the basic frame of a finite-dimensional vector space transforming into itself under the Lorentz group according to the corresponding representation. These spaces are of course subspaces of the general enumerably infinite dimensional Hilbert space containing all finite-dimensional representations of the full Lorentz group.

Starting from this result and generalizing Dirac's ideas [1]) we make two basic assumptions:

a. Every field is a vector Φ contained in one of these irreductible Hilbert subspaces. It is represented by its projections on the basic functions multiplied by the same scalar function $\rho^{\frac{1}{2}}$.

b. The wave field governing this Φ field takes a linear form, each component Φ_i satisfying the usual Klein-Gordon equation

$$(\Box-\chi^2)\Phi_i = 0$$

where χ^2 is the rest mass term.

Tentatively [6]), we propose the following correspondence:

$$\begin{array}{lll} \text{leptons} & \mathscr{D}(\frac{1}{2}, 0)\oplus\mathscr{D}(0, \frac{1}{2}), & s' = \frac{1}{2} \\ \pi\text{-mesons} & \mathscr{D}(1, 0)\oplus\mathscr{D}(0, 1), & s' = 1 \\ \text{K-mesons} & \mathscr{D}(\frac{1}{2}, \frac{1}{2}), & s' = 0 \\ \text{baryons} & \mathscr{D}(\frac{1}{2}, 1)\oplus\mathscr{D}(1, \frac{1}{2}), & s' = \frac{1}{2}. \end{array} \tag{3}$$

But before discussing this, it is useful to compare the preceding procedure with the usual spinor theory. In order to facilitate this comparison, we shall first summarize it in the next sections, using Van der Waerden's terminology and procedure. Only the photon does not fit into this theory.

2. Spinors and Representations of the Lorentz Group

If we consider the contravariant spinor $\varphi^s (s = 1, 2)$ with two components which transforms according to the representation $\mathscr{D}(\frac{1}{2}, 0)$ of the proper orthochronous Lorentz group, we can define in the usual way

a. the covariant spinor

$$\varphi_r = \varepsilon_{rs}\varphi^s \quad \text{with} \quad \varepsilon_{rs} = \begin{vmatrix} 0 & -1 \\ 1 & 0 \end{vmatrix}; \tag{4}$$

b. the covariant spinor $\varphi_{\dot{s}}$ which transforms according the representation $\mathscr{D}(0, \frac{1}{2})$ of the proper orthochronous group. We have

$$\varphi_{\dot{s}} = -P\varphi^r$$

where P is the parity operator.

c. the contravariant spinor $\varphi^{\dot{r}}$ which corresponds to $\varphi_{\dot{s}}$ according to

$$\varphi^{\dot{s}} = \varepsilon^{\dot{s}\dot{r}}\varphi_{\dot{r}} \quad \text{with} \quad \varepsilon^{\dot{r}\dot{s}} = \begin{vmatrix} 0 & 1 \\ -1 & 0 \end{vmatrix}. \tag{5}$$

To summarize, we get finally four two-components spinors, namely

$$\varphi^{s},\ \dot{\varphi}_{\dot{r}},\ \varphi^{\dot{s}},\ \varphi_{r}.$$

We know that starting from these spinors of rank 1 it is possible to build spinors of rank $2(j^+ + j^-)$ which transform according to the representation $\mathcal{D}(j^+, j^-)$ of the proper Lorentz group, and the components of these spinors are given by the relation

$$\Phi^{(j^+, j^-)}_{m^+, m^-} = \frac{(\varphi^1)^{j^+ + m^+}(\varphi^2)^{j^+ - m^+}}{\sqrt{(j^+ + m^+)!(j^+ - m^+)!}} \frac{(\varphi^{\dot{1}})^{j^- + m^-}(\varphi^{\dot{2}})^{j^- + m^-}}{\sqrt{(j^- + m^-)!(j^- - m^-)!}}, \tag{7}$$

where m^+ may take the values : $-j^+, -j^+ + 1, \ldots, j^+ - 1, j^+$, and m^- the values $-j^-, -j^- + 1, \ldots, j^- - 1, j^-$; the numbers j^+ and j^- are either integers or half-integers independently of each other.

With the help of eq. (7) we can build up spinors of rank $2(j^+ + j^-)$ according the representation $\mathcal{D}(j^+, j^-) \oplus \mathcal{D}(j^-, j^+)$ of the full Lorentz group. We shall here limit ourselves to two simple examples of this procedure, $\mathcal{D}(\frac{1}{2}, 0) \oplus \mathcal{D}(0, \frac{1}{2})$ and $\mathcal{D}(\frac{1}{2}, \frac{1}{2})$.

Representation $\mathcal{D}(\frac{1}{2}, 0) \oplus \mathcal{D}(0, \frac{1}{2})$.

With the four spinors (6) we can build up the following four Dirac spinors

$$\Phi_{\uparrow +} = \begin{pmatrix} \varphi_{r} \\ -\varphi^{\dot{s}} \end{pmatrix}, \quad \Phi_{\uparrow -} = \begin{pmatrix} \varphi^{\dot{s}} \\ \varphi_{r} \end{pmatrix}, \quad \Phi_{\downarrow +} = \begin{pmatrix} \varphi^{s} \\ -\varphi_{\dot{r}} \end{pmatrix}, \quad \Phi_{\downarrow -} = \begin{pmatrix} \varphi_{\dot{r}} \\ \varphi^{s} \end{pmatrix} \tag{8}$$

where

$$\Phi_{\uparrow -} = \gamma_4 \Phi_{\uparrow +} \quad \text{and} \quad \Phi_{\downarrow -} = \gamma_4 \Phi_{\downarrow +},$$

γ_4 being the matrix corresponding to the parity operator. This agrees with relations (4) and (5). We see, moreover, that $\Phi_{\uparrow +}$ and $\Phi_{\uparrow -}$ correspond to the spin $\frac{1}{2}\hbar$ and $\Phi_{\downarrow +}$, $\Phi_{\downarrow -}$ to the spin $-\frac{1}{2}\hbar$.

Representation $\mathcal{D}(\frac{1}{2}, \frac{1}{2})$.

In the same way, with the four spinors (6) we can build up four spinors of the second rank

$$\Phi^{r}_{\dot{s}},\ \Phi^{r\dot{s}},\ \Phi_{r}^{\ \dot{s}},\ \Phi_{r\dot{s}}, \tag{9}$$

with

$$\Phi^{r\dot{s}} = \varepsilon^{\dot{s}\dot{u}}\Phi^{r}_{\dot{u}}, \quad \Phi_{r\dot{s}} = \varepsilon_{rt}\Phi^{t}_{\dot{s}}, \quad \Phi_{r}^{\ \dot{s}} = \varepsilon_{rt}\varepsilon^{\dot{s}\dot{u}}\Phi^{t}_{\dot{u}}. \tag{10}$$

We shall now show that (6) and (7) do not yield all possible vector spaces which transform according to the representation $\mathcal{D}(j^+, j^-)$ of the proper Lorentz group.

3. Other Definitions of the Spinors

Let us consider the spinor ψ^s which transforms according the representation $\mathscr{D}(\frac{1}{2}, 0)$ of the proper Lorentz group and which is defined by the relation

$$\psi^s = \begin{vmatrix} 0 & 1 \\ -1 & 0 \end{vmatrix} (\varphi^{\dot{s}})^* \tag{11}$$

where $\varphi_{\dot{s}}$ is the spinor used in the preceding section, and the star denotes complex conjugation. Starting from ψ^s we can define in the same way as above the three spinors $\psi_{\dot{r}}$, $\psi^{\dot{s}}$, ψ_r which yields again four spinors

$$\psi^s,\ \psi_r,\ \psi^{\dot{s}},\ \psi_{\dot{r}}. \tag{12}$$

The definition of the components of the spinors $\Psi^{(j^+, j^-)}_{m^+, m^-}$ is analogous to that of the spinors $\Phi^{(j^+, j^-)}_{m^+, m^-}$:

$$\Psi^{(j^+, j^-)}_{m^+, m^-} = \frac{(\psi^1)^{j^+ + m^+}(\psi^2)^{j^+ - m^+}}{\sqrt{(j^+ + m^+)!(j^+ - m^+)!}} \cdot \frac{(\psi^{\dot{1}})^{j^- + m^-}(\psi^{\dot{2}})^{j^- - m^-}}{\sqrt{(j^- + m^-)!(j^- - m^-)!}}; \tag{13}$$

but one is also led to two other kinds of spinors of rank $2(j^+ + j^-)$:

$$X^{(j^+, j^-)}_{m^+, m^-} = \frac{(\psi^1)^{j^+ + m^+}(\psi^2)^{j^+ - m^+}}{\sqrt{(j^+ + m^+)!(j^+ - m^+)!}} \frac{(\varphi^{\dot{1}})^{j^- + m^-}(\varphi^{\dot{2}})^{j^- - m^-}}{\sqrt{(j^- + m^-)!(j^- - m^-)!}} + \frac{(\varphi^1)^{j^+ + m^+}(\varphi^2)^{j^+ - m^+}}{\sqrt{(j^+ + m^+)!(j^+ - m^+)!}} \frac{(\psi^{\dot{1}})^{j^- + m^-}(\psi^{\dot{2}})^{j^- - m^-}}{\sqrt{(j^- + m^-)!(j^- - m^-)!}}, \tag{14}$$

$$\Omega^{(j^+, j^-)}_{m^+, m^-} = \frac{(\psi^1)^{j^+ + m^+}(\psi^2)^{j^+ - m^+}}{\sqrt{(j^+ + m^+)!(j^+ - m^+)!}} \frac{(\varphi^{\dot{1}})^{j^- + m^-}(\varphi^{\dot{2}})^{j^- - m^-}}{\sqrt{(j^- + m^-)!(j^- - m^-)!}} - \frac{(\varphi^1)^{j^+ + m^+}(\varphi^2)^{j^+ - m^+}}{\sqrt{(j^+ + m^+)!(j^+ - m^+)!}} \frac{(\psi^{\dot{1}})^{j^- + m^-}(\psi^{\dot{2}})^{j^- - m^-}}{\sqrt{(j^- + m^-)!(j^- - m^-)!}}. \tag{15}$$

We shall call $X^{(j^+, j^-)}_{m^+, m^-}$ a mixed symmetrical spinor combination of rank $2(j^+ + j^-)$ and $\Omega^{(j^-, j^+)}_{m^+, m^-}$ a mixed skew-symmetrical spinor combination of rank $2(j^+ + j^-)$.

As an example let us consider the representations $\mathscr{D}(\frac{1}{2}, 0) \oplus \mathscr{D}(0, \frac{1}{2})$ and $\mathscr{D}(\frac{1}{2}, \frac{1}{2})$.

Representation $\mathscr{D}(\frac{1}{2}, 0) \oplus \mathscr{D}(0, \frac{1}{2})$

In a way similar to (8) we get the four Dirac spinors

$$\Psi_{\uparrow +} = \begin{pmatrix} \psi_r \\ -\psi^{\dot{s}} \end{pmatrix}, \quad \Psi_{\uparrow -} = \begin{pmatrix} \psi^{\dot{s}} \\ \psi_r \end{pmatrix}, \quad \Psi_{\downarrow +} = \begin{pmatrix} \psi^s \\ -\psi_{\dot{r}} \end{pmatrix}, \quad \Psi_{\downarrow -} = \begin{pmatrix} \psi_{\dot{r}} \\ \psi^s \end{pmatrix}. \tag{16}$$

From the definition (11) we can immediately deduce that these spinors Ψ are the charge conjugates of the spinors Φ given by the expressions (8). With the

aid of relations (14) and (15) we can build up the spinors

$$X_{\uparrow +}, X_{\uparrow -}, X_{\downarrow +}, X_{\downarrow -}; \quad \Omega_{\uparrow +}, \Omega_{\uparrow -}, \Omega_{\downarrow +}, \Omega_{\downarrow -}. \tag{17}$$

From the relations (14) and (15) it is obvious that the spinors (17) are those of Majorana, which are invariant under charge conjugation.

Representation $\mathscr{D}(\frac{1}{2}, \frac{1}{2})$

In a way similar to (9) we get the second rank spinors

$$\Psi_{\dot{s}}^{r}, \quad \Psi^{r\dot{s}}, \quad \Psi_{r}^{\dot{s}}, \quad \Psi_{r\dot{s}}. \tag{18}$$

The quantities (9) and (18) correspond to the components $+1$ and -1 of the triplet of spin 1. But we have also the spinors

$$X_{\dot{s}}^{r} = \varphi^{r}w_{\cdot} + \psi^{r}\varphi_{\dot{s}}, \quad X^{r\dot{s}}, \quad X_{r}^{\cdot r\dot{s}}, \quad X_{r\dot{s}}; \tag{19}$$

they correspond to the central component of the triplet of spin 1. Finally, we have the spinors

$$\Omega_{\dot{s}}^{r} = \varphi^{r}\psi_{\dot{s}} - \psi^{r}\varphi_{\dot{s}}, \quad \Omega^{r\dot{s}}, \quad \Omega_{r}^{\dot{s}}, \quad \Omega_{r\dot{s}}; \tag{20}$$

they are the elements of spin 0 of the representation $\mathscr{D}(\frac{1}{2}, \frac{1}{2})$.

Indeed, if we limit ourselves to the group of spatial rotations of the representation $\mathscr{D}(\frac{1}{2}, \frac{1}{2})$, the preceding spinors transform like

$$\Phi_{rs} = \varphi_{r}\varphi_{s}, \quad \Psi_{rs} = \psi_{r}\psi_{s}, \quad X_{rs} = \varphi_{s}\psi_{r} + \varphi_{r}\psi_{s}, \quad \Omega_{rs} = \varphi_{s}\psi_{r} - \psi_{s}\varphi_{r} \tag{21}$$

according to the representation $\mathscr{D}(\frac{1}{2}) \otimes \mathscr{D}(\frac{1}{2})$ of the rotation group. But $\mathscr{D}(\frac{1}{2}) \otimes \mathscr{D}(\frac{1}{2}) = \mathscr{D}(1) \oplus \mathscr{D}(0)$, and eqs. (21) show that Φ_{rs}, Ψ_{rs}, X_{rs} transform according to $\mathscr{D}(1)$ and Ω_{rs} according to $\mathscr{D}(0)$, which justifies our proposition.

4. Application to the Vector Spaces of the Functions $Z_{j^+, j^-, s'}^{m^+, m^-, m'}(\omega^+, \omega^-)$

Let us now return to the vector space of the functions (1), and construct with their help spinors of the types just discussed.

a. For the representation $\mathscr{D}(\frac{1}{2}, 0) \oplus \mathscr{D}(0, \frac{1}{2})$, we have to consider the following sets of indices:

$$\left.\begin{array}{ll} j^+ = 0, & j^- = \frac{1}{2} \\ j^+ = \frac{1}{2}, & j^- = 0 \end{array}\right\} \quad s' = \tfrac{1}{2}, \quad m' = \pm\tfrac{1}{2}.$$

According to the definitions (11) and (25) it appears that for $m' = \frac{1}{2}$ we have spinors of type φ and for $m' = -\frac{1}{2}$ spinors of type ψ; explicitly for $m' = \frac{1}{2}$:

$$\varphi^{\dot{s}}=\begin{pmatrix} Z^{0,\frac{1}{2},\frac{1}{2}}_{0,\frac{1}{2},\frac{1}{2}}(\omega^+,\omega^-) \\ Z^{0,-\frac{1}{2},\frac{1}{2}}_{0,\frac{1}{2},\frac{1}{2}}(\omega^+,\omega^-) \end{pmatrix} = \begin{pmatrix} Y^{\frac{1}{2},\frac{1}{2}}_{\frac{1}{2}}(\omega^-) \\ Y^{-\frac{1}{2},\frac{1}{2}}_{\frac{1}{2}}(\omega^-) \end{pmatrix}, \qquad \varphi^{\cdot}_{r}=\begin{pmatrix} -Z^{\frac{1}{2},0,\frac{1}{2}}_{\frac{1}{2},0,\frac{1}{2}}(\omega^+,\omega^-) \\ -Z^{-\frac{1}{2},0,\frac{1}{2}}_{\frac{1}{2},0,\frac{1}{2}}(\omega^+,\omega^-) \end{pmatrix} = \begin{pmatrix} -Y^{\frac{1}{2},\frac{1}{2}}_{\frac{1}{2}}(\omega^+) \\ -Y^{-\frac{1}{2},\frac{1}{2}}_{\frac{1}{2}}(\omega^+) \end{pmatrix},$$

$$\varphi_{r}=\begin{pmatrix} -Z^{0,-\frac{1}{2},\frac{1}{2}}_{0,\frac{1}{2},\frac{1}{2}}(\omega^+,\omega^-) \\ Z^{0,\frac{1}{2},\frac{1}{2}}_{0,\frac{1}{2},\frac{1}{2}}(\omega^+,\omega^-) \end{pmatrix} = \begin{pmatrix} -Y^{-\frac{1}{2},\frac{1}{2}}_{\frac{1}{2}}(\omega^-) \\ Y^{\frac{1}{2},\frac{1}{2}}_{\frac{1}{2}}(\omega^-) \end{pmatrix}, \qquad \varphi^{\dot{s}}=\begin{pmatrix} Z^{-\frac{1}{2},0,\frac{1}{2}}_{\frac{1}{2},0,\frac{1}{2}}(\omega^+,\omega^-) \\ -Z^{\frac{1}{2},0,\frac{1}{2}}_{\frac{1}{2},0,\frac{1}{2}}(\omega^+,\omega^-) \end{pmatrix} = \begin{pmatrix} Y^{-\frac{1}{2},\frac{1}{2}}_{\frac{1}{2}}(\omega^+) \\ -Y^{\frac{1}{2},\frac{1}{2}}_{\frac{1}{2}}(\omega^+) \end{pmatrix};$$

for $m' = -\frac{1}{2}$:

$$\psi^{\dot{s}}=\begin{pmatrix} -Z^{0,\frac{1}{2},-\frac{1}{2}}_{0,\frac{1}{2},\frac{1}{2}}(\omega^+,\omega^-) \\ -Z^{0,-\frac{1}{2},-\frac{1}{2}}_{0,\frac{1}{2},\frac{1}{2}}(\omega^+,\omega^-) \end{pmatrix} = \begin{pmatrix} -Y^{\frac{1}{2},-\frac{1}{2}}_{\frac{1}{2}}(\omega^-) \\ -Y^{-\frac{1}{2},-\frac{1}{2}}_{\frac{1}{2}}(\omega^-) \end{pmatrix}, \quad \psi^{\cdot}_{r}=\begin{pmatrix} Z^{\frac{1}{2},0,-\frac{1}{2}}_{\frac{1}{2},0,\frac{1}{2}}(\omega^+,\omega^-) \\ Z^{-\frac{1}{2},0,-\frac{1}{2}}_{\frac{1}{2},0,\frac{1}{2}}(\omega^+,\omega^-) \end{pmatrix} = \begin{pmatrix} Y^{\frac{1}{2},-\frac{1}{2}}_{\frac{1}{2}}(\omega^+) \\ Y^{-\frac{1}{2},-\frac{1}{2}}_{\frac{1}{2}}(\omega^+) \end{pmatrix}$$

$$\psi_{r}=\begin{pmatrix} Z^{0,-\frac{1}{2},-\frac{1}{2}}_{0,\frac{1}{2},\frac{1}{2}}(\omega^+,\omega^-) \\ -Z^{0,\frac{1}{2},-\frac{1}{2}}_{0,\frac{1}{2},\frac{1}{2}}(\omega^+,\omega^-) \end{pmatrix} = \begin{pmatrix} Y^{-\frac{1}{2},-\frac{1}{2}}_{\frac{1}{2}}(\omega^-) \\ -Y^{\frac{1}{2},-\frac{1}{2}}_{\frac{1}{2}}(\omega^-) \end{pmatrix}, \quad \psi^{\dot{s}}=\begin{pmatrix} -Z^{-\frac{1}{2},0,-\frac{1}{2}}_{\frac{1}{2},0,\frac{1}{2}}(\omega^+,\omega^-) \\ Z^{\frac{1}{2},0,-\frac{1}{2}}_{\frac{1}{2},0,\frac{1}{2}}(\omega^+,\omega^-) \end{pmatrix} = \begin{pmatrix} -Y^{-\frac{1}{2},-\frac{1}{2}}_{\frac{1}{2}}(\omega^+) \\ Y^{\frac{1}{2},-\frac{1}{2}}_{\frac{1}{2}}(\omega^+) \end{pmatrix}.$$

With the above spinors we can build up Dirac spinors according to eqs. (8) and (16), and Majorana spinors according to eq. (17).

b. For the representation $\mathscr{D}(\frac{1}{2},\frac{1}{2})$, the index s' takes the values 1 and 0, and we must therefore consider two different cases:

1. $s' = 1$

Here, $m' = \pm 1, 0$. There are accordingly three kinds of second rank spinors to consider, viz.

$$Z^{m^+,m^-,1}_{\frac{1}{2},\frac{1}{2},1}(\omega^+,\omega^-), \quad Z^{m^+,m^-,-1}_{\frac{1}{2},\frac{1}{2},1}(\omega^+,\omega^-), \quad Z^{m^+,m^-,0}_{\frac{1}{2},\frac{1}{2},1}(\omega^+,\omega^-); \tag{23}$$

the definition (1) yields, with the well-known values of the Clebsch-Gordan coefficients [8]),

$$Z^{m^+,m^-,1}_{\frac{1}{2},\frac{1}{2},1}(\omega^+,\omega^-) = \sqrt{\tfrac{2}{3}}\, Y^{m^+,\frac{1}{2}}_{\frac{1}{2}}(\omega^+) Y^{m^-,\frac{1}{2}}_{\frac{1}{2}}(\omega^-) = \sqrt{\tfrac{2}{3}}\, Z^{m^+,0,\frac{1}{2}}_{\frac{1}{2},0,\frac{1}{2}}(\omega^+,\omega^-) Z^{0,m^-,\frac{1}{2}}_{0,\frac{1}{2},\frac{1}{2}}(\omega^+,\omega^-),$$

$$Z^{m^+,m^-,-1}_{\frac{1}{2},\frac{1}{2},+1}(\omega^+,\omega^-) = \sqrt{\tfrac{2}{3}}\, Y^{m^+,-\frac{1}{2}}_{\frac{1}{2}}(\omega^+) Y^{m^-,-\frac{1}{2}}_{\frac{1}{2}}(\omega^-) = \sqrt{\tfrac{2}{3}}\, Z^{m^+,0,-\frac{1}{2}}_{\frac{1}{2},0,\frac{1}{2}}(\omega^+,\omega^-) Z^{0,m^-,-\frac{1}{2}}_{0,\frac{1}{2},\frac{1}{2}}(\omega^+,\omega^-),$$

$$Z^{m^+,m^-,0}_{\frac{1}{2},\frac{1}{2},1}(\omega^+,\omega^-) = \frac{1}{\sqrt{2}}\left(Y^{m^+,\frac{1}{2}}_{\frac{1}{2}}(\omega^+) Y^{m^-,-\frac{1}{2}}_{\frac{1}{2}}(\omega^-) + Y^{m^+,-\frac{1}{2}}_{\frac{1}{2}}(\omega^+) Y^{m^-,\frac{1}{2}}_{\frac{1}{2}}(\omega^-)\right)$$

$$= \frac{1}{\sqrt{2}}\left(Z^{m^+,0,\frac{1}{2}}_{\frac{1}{2},0,\frac{1}{2}}(\omega^+,\omega^-) Z^{0,m^-,-\frac{1}{2}}_{0,\frac{1}{2},\frac{1}{2}}(\omega^+,\omega^-) + Z^{m^+,0,-\frac{1}{2}}_{\frac{1}{2},0,\frac{1}{2}}(\omega^+,\omega^-) Z^{0,m^-,\frac{1}{2}}_{0,\frac{1}{2},\frac{1}{2}}(\omega^+,\omega^-)\right).$$

These expressions show that with the functions (23) we can build up second rank spinors of the respective types Φ, Ψ and X, thus checking the conclusions of the preceding section concerning the three states $m' = 1$, $m' = 0$, $m' = -1$ of the triplet with spin $s' = 1$.

2. $s' = 0$.

Here $m' = 0$, and we have the second rank spinors

$$Z^{m^+,m^-,0}_{\frac{1}{2},\frac{1}{2},0}(\omega^+,\omega^-) = \frac{1}{\sqrt{2}}\left(Y^{m^+,\frac{1}{2}}_{\frac{1}{2}}(\omega^+) Y^{m^-,-\frac{1}{2}}_{\frac{1}{2}}(\omega^-) - Y^{m^+,-\frac{1}{2}}_{\frac{1}{2}}(\omega^+) Y^{m^-,\frac{1}{2}}_{\frac{1}{2}}(\omega^-)\right)$$

$$= \frac{1}{\sqrt{2}}\left(Z^{m^+,0,\frac{1}{2}}_{\frac{1}{2},0,\frac{1}{2}}(\omega^+,\omega^-) Z^{0,m^-,-\frac{1}{2}}_{0,\frac{1}{2},\frac{1}{2}}(\omega^+,\omega^-) - Z^{m^+,0,-\frac{1}{2}}_{\frac{1}{2},0,\frac{1}{2}}(\omega^+,\omega^-) Z^{0,m^-,\frac{1}{2}}_{0,\frac{1}{2},\frac{1}{2}}(\omega^+,\omega^-)\right).$$

This shows that with the functions $Z^{m^+, m^-, 0}_{\frac{1}{2}, \frac{1}{2}, 0}(\omega^+, \omega^-)$ we can build second rank spinors of the type Ω, as established in section 3.

5. Four Vectors built up from Second Rank Spinors

It is well known that from second rank spinors one can build up several sets of four vectors. Let us consider the second rank spinors of each of the preceding types $\Phi_{\dot{s}}^{\ r}$, $\Psi_{\dot{s}}^{\ r}$, $X_{\dot{s}}^{\ r}$ and $\Omega_{\dot{s}}^{\ r}$. The corresponding four vectors can be defined as follows:

$$a_\mu^{(1)} = \tfrac{1}{2}\sigma^{\dot{s}}_{\mu,\,r}\Phi_{\dot{s}}^{\ r}, \quad a_\mu^{(0)} = \tfrac{1}{2}\sigma^{\dot{s}}_{\mu,\,r}X_{\dot{s}}^{\ r}, \quad a_\mu^{(-1)} = \tfrac{1}{2}\sigma^{\dot{s}}_{\mu,\,r}\Psi_{\dot{s}}^{\ r};$$

$$b_\mu^{(0)} = \tfrac{1}{2}\sigma^{\dot{s}}_{\mu,\,r}\Omega_{\dot{s}}^{\ r};$$

here the σ_μ's are the Pauli matrices and the 2×2 unit matrix, and the vectors are labelled with the aid of the values of the number $m' = 1,\ 0,\ -1$ which characterize the construction of the corresponding second rank spinors. Explicitly, we get, for instance, for $a_\mu^{(1)}$:

$$a_1^{(1)} = \tfrac{1}{2}(\Phi_{\dot{2}}^{\ 1}+\Phi_{\dot{1}}^{\ 2}) = \tfrac{1}{2}\left(Z^{-\frac{1}{2},\frac{1}{2},1}_{\frac{1}{2},\frac{1}{2},1}(\omega^+,\omega^-)+Z^{\frac{1}{2},-\frac{1}{2},1}_{\frac{1}{2},\frac{1}{2},1}(\omega^+,\omega^-)\right)$$

$$a_2^{(1)} = \frac{1}{2i}(\Phi_{\dot{2}}^{\ 1}-\Phi_{\dot{1}}^{\ 2}) = \tfrac{1}{2}i\left(Z^{-\frac{1}{2},\frac{1}{2},1}_{\frac{1}{2},\frac{1}{2},1}(\omega^+,\omega^-)-Z^{\frac{1}{2},-\frac{1}{2},1}_{\frac{1}{2},\frac{1}{2},1}(\omega^+,\omega^-)\right)$$

$$a_3^{(1)} = \tfrac{1}{2}(\Phi_{\dot{1}}^{\ 1}-\Phi_{\dot{2}}^{\ 2}) = \tfrac{1}{2}\left(Z^{\frac{1}{2},\frac{1}{2},1}_{\frac{1}{2},\frac{1}{2},1}(\omega^+,\omega^-)-Z^{-\frac{1}{2},-\frac{1}{2},1}_{\frac{1}{2},\frac{1}{2},1}(\omega^+,\omega^-)\right)$$

$$a_4^{(1)} = \frac{1}{2i}(\Phi_{\dot{1}}^{\ 1}+\Phi_{\dot{2}}^{\ 2}) = \tfrac{1}{2}i\left(Z^{\frac{1}{2},\frac{1}{2},1}_{\frac{1}{2},\frac{1}{2},1}(\omega^+,\omega^-)+Z^{-\frac{1}{2},-\frac{1}{2},1}_{\frac{1}{2},\frac{1}{2},1}(\omega^+,\omega^-)\right),$$

and obtain similar relations for $a_\mu^{(0)}$ and $a_\mu^{(-1)}$. For $b_\mu^{(0)}$ we get

$$b_1^{(0)} = \tfrac{1}{2}(\Omega_{\dot{2}}^{\ 1}+\Omega_{\dot{1}}^{\ 2}) = \tfrac{1}{2}\left(Z^{\frac{1}{2},\frac{1}{2},0}_{\frac{1}{2},\frac{1}{2},0}(\omega^+,\omega^-)+Z^{-\frac{1}{2},-\frac{1}{2},0}_{\frac{1}{2},\frac{1}{2},0}(\omega^+,\omega^-)\right),$$

$$b_2^{(0)} = \frac{1}{2i}(\Omega_{\dot{2}}^{\ 1}-\Omega_{\dot{1}}^{\ 2}) = \frac{1}{2i}\left(Z^{\frac{1}{2},\frac{1}{2},0}_{\frac{1}{2},\frac{1}{2},0}(\omega^+,\omega^-)-Z^{-\frac{1}{2},-\frac{1}{2},0}_{\frac{1}{2},\frac{1}{2},0}(\omega^+,\omega^-)\right),$$

$$b_3^{(0)} = \tfrac{1}{2}(\Omega_{\dot{1}}^{\ 1}-\Omega_{\dot{2}}^{\ 2}) = \tfrac{1}{2}\left(Z^{\frac{1}{2},-\frac{1}{2},0}_{\frac{1}{2},\frac{1}{2},0}(\omega^+,\omega^-)+Z^{-\frac{1}{2},\frac{1}{2},0}_{\frac{1}{2},\frac{1}{2},0}(\omega^+,\omega^-)\right),$$

$$b_4^{(0)} = \frac{1}{2i}(\Omega_{\dot{1}}^{\ 1}+\Omega_{\dot{2}}^{\ 2}) = \frac{1}{2i}\left(Z^{\frac{1}{2},-\frac{1}{2},0}_{\frac{1}{2},\frac{1}{2},0}(\omega^+,\omega^-)-Z^{-\frac{1}{2},\frac{1}{2},0}_{\frac{1}{2},\frac{1}{2},0}(\omega^+,\omega^-)\right).$$

Both in the general case — as a consequence of the definitions used for the spinors $\Phi_{\dot{s}}^{\ r}$, $\Psi_{\dot{s}}^{\ r}$, $X_{\dot{s}}^{\ r}$, $\Omega_{\dot{s}}^{\ r}$ — and in the particular case of the functions $Z^{m^+, m^-, m'}_{j^+, j^-, s'}(\omega^+, \omega^-)$ — because of the definition (2) used for the parity operator acting on these functions — it is easy to see that $a_\mu^{(1)}$, $a_\mu^{(0)}$, $a_\mu^{(-1)}$ are pseudo-vectors, while $b_\mu^{(0)}$ is a vector. We thus obtain the important result that four-vectors can be built up only with second rank mixed skew-symmetrical spinor combinations, while all other spinors yield pseudo-vectors.

It is easy to generalize these results to representations $\mathfrak{D}(j^+, j^-)\oplus\mathfrak{D}(j^-, j^+)$ of higher orders. In the case of representation $\mathfrak{D}(\frac{1}{2}, 1)\oplus\mathfrak{D}(1, \frac{1}{2})$, for instance, we get third rank spinors of two kinds:

1) those corresponding to the spin $\frac{3}{2}$:

$$\Phi^r\Phi_i^s,\quad \Phi^r\Psi_i^s,\quad \Phi^r X_i^s$$
$$\Psi^r\Phi_i^s,\quad \Psi^r\Psi_i^s,\quad \Psi^r X_i^s$$
$$X^r\Phi_i^s,\quad X^r\Psi_i^s,\quad X^r X_i^s$$

and similar spinors like $\Phi_r\Phi_i^s$, $\Phi_r\Phi_{\dot{s}}$, . . .;

2) those corresponding to the spin $\frac{1}{2}$:

$$\Phi^r\Omega_i^s,\quad X^r\Omega_i^s,\quad \Psi^r\Omega_i^s,\quad \Omega^r,\ \Omega_i^s,$$

and similar spinors like $\Phi_r\Omega_s^i$, $\Phi_r\Omega_{s\dot{r}}$, . . .

Likewise, in the case of the representation $\mathscr{D}(1, 1)$ we get fourth rank spinors of three different kinds:

1) corresponding to spin 2:

$$\Phi_s^r\Phi_u^t,\quad \Phi_s^r\Psi_u^t,\quad \Phi_s^r X_u^t,\quad \Psi_s^r X_u^t\ldots;$$

2) corresponding to spin 1:

$$\Phi_s^r\Omega_u^t,\quad X_s^r\Omega_u^t,\quad \Psi_s^r\Omega_u^t;$$

3) corresponding to spin 0:

$$\Omega_s^r\Omega_u^t.$$

We know further that these fourth rank spinors allow us to construct symmetrical traceless second order tensors, and it is clear that with the first and third kind of these fourth rank spinors we shall get tensors and with the second one pseudotensors. We can obviously generalize the latter result: for all the representations $\mathscr{D}(j^+, j^-)\oplus\mathscr{D}(j^-, j^+)$ with integer $j^+ + j^-$ we can construct tensors with spinors of rank $2(j^+ + j^-)$ corresponding to even values of the spin, and pseudotensors with spinors of rank $2(j^+ + j^-)$ corresponding to odd values of the spin. It appears further that if a spinor of rank $2(j^+ + j^-)$ is given, the corresponding spin is $j^+ + j^- - \eta$, η being the number of times we have used the mixed antisymmetrical combination of spinors Ω_u^t in the construction of the given spinor.

6. Classification of Elementary Fields

In the preceding sections we have defined new types of basic spinors Φ^r, Ψ^r, X^r and Ω^r which transform according to the representation $\mathscr{D}(\frac{1}{2}, 0)$ of the prope: Lorentz group and spinors $\Phi_{\dot{s}}$, $\Psi_{\dot{s}}$, $X_{\dot{s}}$, $\Omega_{\dot{s}}$ which transform according to the representation $\mathscr{D}(0, \frac{1}{2})$ of that group. With the help of matrices $\varepsilon_{r\dot{s}}$ and $\varepsilon^{\dot{r}s}$ we obtain immediately Φ_s, Ψ_s, X_s, Ω_s on the one hand and $\Phi^{\dot{r}}$, $\Psi^{\dot{r}}$, $X^{\dot{r}}$, $\Omega^{\dot{r}}$ on the other.

With these basic spinors we have constructed higher rank spinors corresponding to all possible values $j^+ + j^-, j^+ + j^- - 1, \ldots |j^+ - j^-|$ of the spin of the fields associated with the representation $\mathcal{D}(j^+, j^-) \oplus \mathcal{D}(j^-, j^+)$ of the full Lorentz group. We have given an explicit representation of these spinors with the help of the functions $Z^{m^+;m^-;m'}_{l^+,l^-,s'}(\omega^+, \omega^-)$ in the case of the group of complex conjugate 3-dimensional rotations isomorphic to the Lorentz group. We shall now drop this explicit representation to examine a consequence of the existence of this new type of spinors in the case of the full Lorentz group.

We propose to look for irreducible field equations corresponding the classification (3) proposed above, in the frame of the Fierz-Pauli and Rarita-Schwinger formalism.

As we know [9]), this formalism rests on two basic assumptions:

1) each spinor component satisfies separately the Klein-Gordon equation,

2) the field equations must be invariant under the full Lorentz group.

Moreover, we must distinguish two cases:

a. $j^+ + j^-$ is an integer: the fields are tensors of rank $j^+ + j^-$ and these tensors satisfy the Klein-Gordon equation.

b. $j^+ + j^-$ is half integer: the fields are spinors whose components are tensors of rank $2(j^+ + j^-) - 1$ and these spinors satisfy Dirac's equation.

The difference between the results obtained in the Rarita-Schwinger formalism and ours lies in the fact that until now one has always used one spinor type only, namely Φ^r (together with Φ_r, $\Phi^{\dot{s}}$ and $\Phi_{\dot{s}}$), which leads to the use of an auxiliary condition to enforce spin $j^+ + j^-$. The preceding analysis opens the possibility of using also Ψ, X and Ω to obtain all possible spin values contained in the representation $\mathcal{D}(j^+, j^-) \oplus \mathcal{D}(j^-, j^+)$ without any supplementary condition. Now, if one accepts our assumed classification, this implies that in order to fit it with experimental results (spin $\frac{1}{2}$ for fermions, 0 for mesons, 1 for photons) we must use the spinors for which the spin is equal to $|j^+ - j^-|$.

Before writing field equations we must therefore indicate the exact type of spinors we shall use for each representation $\mathcal{D}(j^+, j^-) \oplus \mathcal{D}(j^-, j^+)$. The results of the preceding sections lead immediately to the following prescriptions:

1) for the representation $\mathcal{D}(\frac{1}{2}, \frac{1}{2})$ we use the spinors $\Omega^r_{\dot{s}}$ and, of course, those we derive from the Ω with the help of the matrices ε_{rs} and $\varepsilon^{\dot{r}\dot{s}}$ (this will hold for all representations and will not be repeated);

2) for $\mathcal{D}(1, 0) \oplus \mathcal{D}(0, 1)$ the spinors Φ^{rs} and $\Phi_{\dot{r}\dot{s}}$, Ψ^{rs} and $\Psi_{\dot{r}\dot{s}}$, X^{rs} and $X_{\dot{r}\dot{s}}$, for here we have only one possible value (namely, 1) for the spin;

3) for $\mathcal{D}(1, 1)$ the spinors $\Omega^{rs}_{\dot{t}\dot{u}}$, which corresponds to spin 0;

4) for $\mathcal{D}(\frac{1}{2}, 0) \oplus \mathcal{D}(0, \frac{1}{2})$ the spinors Φ^r and $\Phi_{\dot{s}}$, Ψ^r and $\Psi_{\dot{s}}$, X^r and $X_{\dot{s}}$, Ω^r and $\Omega_{\dot{s}}$;

5) for $\mathcal{D}(\frac{1}{2}, 1) \oplus \mathcal{D}(1, \frac{1}{2})$, the spinors of the type $\Phi^r \Omega^s_{\dot{t}}$, $\Psi^r \Omega^s_{\dot{t}}$, $X^r \Omega^s_{\dot{t}}$. The corresponding field equations follow immediately:

a. The K mesons corresponding to $\mathcal{D}(\frac{1}{2}, \frac{1}{2})$, we get from the spinor $\Omega^r_{\dot{s}}$ the

four vector

$$A_\mu = \tfrac{1}{2}\sigma^{\dot{s}}_{\mu r}\Omega^{r}_{\dot{s}}$$

which obeys the equation

$$(\Box-\chi^2)A_\mu = 0.$$

b. If we assume π-mesons to be invariant under the representation $\mathscr{D}(1,0)\oplus\mathscr{D}(0,1)$, we can use the spinors Φ^{rs}, Ψ^{rs} or X^{rs} and form three corresponding self-dual antisymmetric tensors of the type

$$F_{\mu\nu} = \tfrac{1}{2}(\sigma^{\dot{r}}_{\mu s}\sigma_{\nu\dot{r}t}\Phi^{st}+\sigma^{\dot{s}}_{\mu r}\sigma_{\nu}{}^{ri}\Phi_{\dot{s}\dot{i}})$$

satisfying the wave equation

$$(\Box-\chi^2)F_{\mu\nu} = 0.$$

c. If we associate a field with the representation $\mathscr{D}(1,1)$ we must use the fourth rank spinor $\Omega^{rs}_{\dot{i}\dot{u}}$ to obtain spin 0 and build the traceless symmetric tensor

$$G_{\mu\nu} = \tfrac{1}{2}\sigma^{\dot{s}}_{\mu,r}\sigma^{\dot{u}}_{\nu,t}\Omega^{rs}_{\dot{i}\dot{u}}$$

obeying the equation

$$(\Box-\chi^2)G_{\mu\nu} = 0.$$

d. For leptons, invariant under $\mathscr{D}(\tfrac{1}{2},0)\oplus\mathscr{D}(0,\tfrac{1}{2})$, we can form the spinors

$$\begin{pmatrix}\varphi^r\\ \varphi_{\dot{s}}\end{pmatrix},\quad \begin{pmatrix}\psi^r\\ \psi_{\dot{s}}\end{pmatrix},\quad \begin{pmatrix}X^r\\ X_{\dot{s}}\end{pmatrix} \text{ and } \begin{pmatrix}\Omega^r\\ \Omega_{\dot{s}}\end{pmatrix}$$

each satisfying Dirac's equation.

e. Finally, the baryons assumed to correspond to $\mathscr{D}(\tfrac{1}{2},1)\oplus\mathscr{D}(1,\tfrac{1}{2})$ and spin $\tfrac{1}{2}$ will be described by spinors of the type $\Phi^r\Omega^s_{\dot{i}}$, $X^r\Omega^s_{\dot{i}}$ and $\Psi^r\Omega^s_{\dot{i}}$. With this starting point we define two-component spinors (each component being a four-vector)

$$\tfrac{1}{2}\sigma^{\dot{i}}_{us}\Phi^r\Omega^s_{\dot{i}} \quad\text{and}\quad \tfrac{1}{2}\sigma^{r}_{u\dot{i}}\Phi_{\dot{s}}\Omega^{\dot{i}}{}_{r},$$

and the corresponding expressions formed with $\chi^r\Omega^s_{\dot{i}}$ and $\Psi^r\Omega^s_{\dot{i}}$. The baryon equation becomes accordingly

$$(\gamma_\nu\partial_\nu+\chi)\begin{pmatrix}\tfrac{1}{2}\sigma^{\dot{i}}_{\mu s}\Phi^r\Omega^s_{\dot{i}}\\ \tfrac{1}{2}\sigma^{r}_{\mu\dot{i}}\Phi_{\dot{s}}\Omega_r{}^{\dot{i}}\end{pmatrix} = 0,$$

where the $\gamma\mu$'s are Dirac matrices. This wave equation is not equivalent to that of Rarita-Schwinger since its spin is necessarily $\tfrac{1}{2}$. In a subsequent paper we shall study possible covariant types of couplings and some consequences of our baryon equation. In fact, we have shown that the wave functions to be used for this representation are

$$\tfrac{1}{2}\begin{pmatrix}\sigma_{i\mu}{}^{\dot{s}}\sigma_i{}^{\mu\dot{i}}\Phi_{\dot{s}}\Omega^r_{\dot{i}}\\ \sigma_i{}^{\dot{\mu}}{}_r\sigma_i{}^{\dot{\mu}\dot{i}}\Phi^r\Omega^{\dot{s}}_{\dot{i}}\end{pmatrix} \qquad (i,j=1,2,3).$$

In conclusion we wish to express our deepest thanks to Professors Louis de Broglie and G. Petiau for many helpful suggestions and encouragement. Professor de Broglie's ideas on fusion theory combined with other studies of the Lorentz group have evidently been used as a starting point for this research.

References

1) P. A. M. Dirac, Proc. Roy. Soc. A **155** (1936) 447;
M. Fierz, Helvet. Phys. Acta **12** (1939) 3
2) F. Halbwachs, P. Hillion and J. P. Vigier, Ann. Inst. H. Poincaré **16** (1959) 115
3) A. Einstein and M. Mayer, Sitzber. Akad. Berlin (1932) 522;
see also E. Cartan, Leçons sur la théorie des spineurs (Hermann)
4) C. Möller, Ann. Inst. H. Poincaré **14** (1949) 251;
J. L. Synge, Relativity: the special theory (North Holland Publ. Co.)
5) P. Hillion and J. P. Vigier, Ann. Inst. H. Poincaré **16** (1959) 161
6) P. Hillion and J. P. Vigier, Cahiers de Physique (1959) 257;
D. Bohm, P. Hillion and J. P. Vigier, Progr. of Theor. Phys.
7) P. Hillion and J. P. Vigier, Ann. Inst. H. Poincaré **16** (1959) 217
8) J. M. Blatt and V. F. Weisskopf, Theoretical nuclear Physics, Appendix A
9) See for instance H. Umezawa, Quantum field theory (North Holland Publ. Co.)
10) C. van Winter, Thesis (Groningen 1957)

2.B

Nuclear Physics **16** (1960) 374—376; © *North-Holland Publishing Co., Amsterdam*
Not to be reproduced by photoprint or microfilm without written permission from the publisher

$Li^7(\alpha, p)Be^{10}$ AND $Li^6(\alpha, p)Be^9$ REACTIONS AT 30 MeV

P. R. KLEIN †, N. CINDRO ††, L. W. SWENSON and N. S. WALL

Department of Physics and Laboratory of Nuclear Science, Massachusetts Institute of Technology, Cambridge, Mass. †††

Received 25 January 1960

Abstract: Angular distributions for the $Li^7(\alpha, p)Be^{10}$ and $Li^6(\alpha, p)Be^9$ reactions were obtained for the ground state of the residual nucleus, using 30 MeV α particles. In the case of the Li^7 reaction an angular distribution was obtained leaving the residual nucleus in the first excited state. Of particular interest in all three of these angular distributions is the sharp increase in differential cross section at back angles. It is shown that the present theories of direct reactions are inadequate to account for this structure.

Recently several (α, p) ground state angular distributions using alpha particles in the neighborhood of 30 MeV have been found to exhibit an increase in differential cross section in the vicinity of 180° [1–4]). In order to help to determine the generality of this effect, the (α, p) reactions on Li^6 and Li^7, using enriched targets, were studied.

The ground state distribution of the $Li^7(\alpha, p)Be^{10}$ reaction is shown in fig. 1 together with typical statistical errors. Fig. 2 shows the distribution correspond-

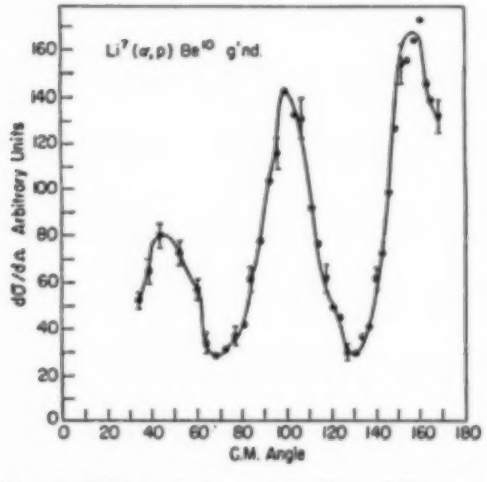

Fig. 1. Differential cross section of the reaction $Li^7(\alpha, p)Be^{10}$ for 30 MeV alpha particles.

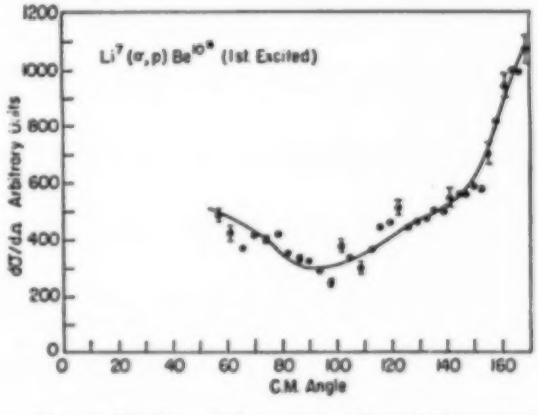

Fig. 2. Differential cross section of the reaction $Li^7(\alpha, p)Be^{10*}$ (1st excited state) for 30 MeV alpha particles.

† Now at Nuclear-Chicago, Des Plains, Illinois.

†† On leave of absence from Institu Ruder Bošković, Zagreb, Yugoslavia.

††† This work is supported in part through AEC Contract (AT-(30-1)-2098), by funds provided by the U. S. Atomic Energy Commission, the Office of Naval Research and the Air Force office of Scientific Research.

ing to the first excited state of this reaction. Shown in fig. 3 is the ground state angular distribution for the reaction $Li^6(\alpha, p)Be^9$. All the distributions were measured using 30 MeV alpha particles from, the MIT cyclotron. A scintillation counter using a NaI(Tl) crystal was used for particle detection in conjunction with a 20 channel pulse-height analyzer. The crystals were cut thick enough to stop the ground state proton group in all cases, and an aluminium absorber was used to stop the elastic alpha particles [5]).

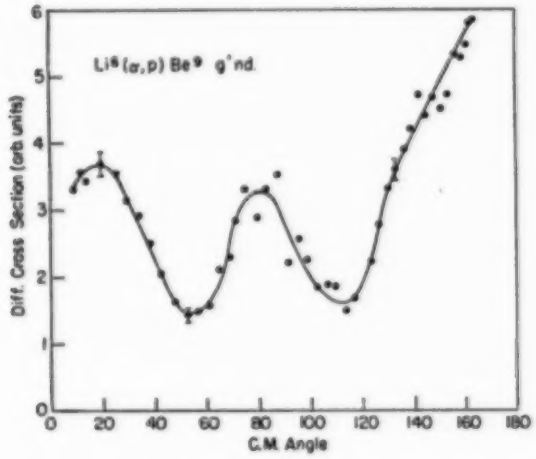

Fig. 3. Differential cross section of the reaction $Li^6(\alpha, p)Be^9$ for 30 MeV alpha particles.

All the distributions show an increase in cross section at the backward angles. As is well known, the approximate forms of the surface reaction theory [6]) have a forward peaking form factor. These simple forms of the direct reaction theory seem to fit various other (α, p) reactions at about 30 MeV adequately [5]).

A heavy particle stripping calculation [7]) on the $Li^7(\alpha, p)Be^{10}$ ground state reaction indicated that the momentum transfer involved was not high enough to match the oscillation period observed †. The first excited state of this reaction however, very likely could be fitted by heavy particle stripping, since it shows no rapid oscillation. A fit was not attempted due to the incompleteness of this distribution.

Neither could the semi-classical concept of reflection off the rear surface of the nucleus [9]) account for the appearance of a backward peaking which was unaccompanied by a more intense forward peak, even assuming a sharp discontinuity of refractive index at the nuclear surface. We thus feel that there is no adequate explanation for angular distributions of the type displayed here.

† A combination of heavy particle stripping, stripping and a "knock-out" process could not account for the results in the C^{13} reaction [8]).

References

1) R. Sherr and M. Rickey, Bull. Amer. Phys. Soc. **2** (1957) 29
2) C. E. Hunting, Ph. D., Thesis, Mass. Inst. of Tech., (Jan., 1958)
3) I. Nonaka, H. Yamaguchi and T. Mikomo, J. Phys. Soc. Japan, to be published
4) J. R. Priest, D. J. Tendam and E. Bleuler, Bull. Amer. Phys. Soc. **4** (1959) 17
5) C. E. Hunting and N. S. Wall, Phys. Rev. **115** (1959) 956
6) S. T. Butler, Phys. Rev. **106** (1957) 272
7) L. Madansky and G. F. Owen, Phys. Rev. **99** (1955) 1608
8) R. Sherr, private communication to N. S. Wall
9) Butler, Austern and Pearson, Phys. Rev. **112** (1958) 1227

10.A *Nuclear Physics* **16** (1960) 377—380; © *North-Holland Publishing Co., Amsterdam*

NEWS ITEMS

TENTH ANNUAL INTERNATIONAL CONFERENCE ON HIGH ENERGY PHYSICS, UNIVERSITY OF ROCHESTER

(August 25 — September 1, 1960)

The Tenth Annual International Conference on High Energy Physics will be held at the University of Rochester from August 25 to September 1, 1960. The aim of this annual conference is to assemble a group of active workers in high energy and particle physics for an informal and comprehensive discussion of the experimental results and theoretical developments during the previous year.

The Conference officially opens on Thursday, August 25, the first of two days of simultaneous sessions devoted to invited and contributed papers on the subjects indicated. Every Conference participant desiring to present a contributed paper at any of these four simultaneous sessions is requested to send a brief summary (2—3 pages) of his contribution directly to the chairman of the appropriate session (Dr. Cassels, Dr. Oppenheimer, Dr. Steinberger or Dr. Yang) not later than *June 1*. (*Two* copies of each summary should be sent as well to Dr. W. A. Jamison, Executive Secretary of the Conference). These summaries will enable the chairmen of the simultaneous sessions to organize their programs in a coherent fashion. The corrected 2—3 page summaries of all contributed papers, whether selected by the chairmen for presentation at the conference or not, will be inserted into the published Proceedings of the Conference. Some of the contributed papers, for which longer allocations of time are indicated, will no doubt be converted into invited papers by the chairmen of the simultaneous sessions.

The two days of simultaneous sessions will be followed (after a free week-end) by two types of plenary sessions. The four mornings of August 29 through September 1 will be devoted to plenary sessions of the rapporteur type and will provide an opportunity for rapporteurs to summarize the highlights of the material presented during the first two days of simultaneous sessions. The three afternoons of August 29, August 30 and September 1 will be devoted to plenary sessions of invited papers where the subjects do not appear to justify coverage by rapporteurs but rather by individual invited papers. Ample time for discussion will be provided at all plenary sessions.

The list of topics and speakers for the invited papers at both the simultaneous sessions and the afternoon plenary sessions will be announced after *June 15*. Suggestions with regard to the invited papers will be welcome before *June 1*. Suggestions may be sent to the chairman of the appropriate session or to the Chairman of the Conference. (It is important that copies of all such correspondence be sent to the Executive Secretary of the Conference.)

The organization of the scientific program for the Tenth Annual Conference is intended to strike a reasonable balance between rapporteur reports and individual presentations. As a result of this organization, it is possible to reduce the duration of the Conference to eight days and to close on September 1.

Notification of intended attendance to the Executive Secretary, Dr. Jamison, University of Rochester, Rochester 20, N.Y.

PRELIMINARY PROGRAM

Thursday, August 25, 1960

S1. Strong Interactions of Pions and Nucleons (Experimental)
Chairman: J. M. Cassels, Laboratory of Nuclear Studies, Cornell University, Ithaca, New York

S2. Strong Interactions of Pions and Nucleons (Theoretical)
Chairman: J. R. Oppenheimer, Institute for Advanced Study, Princeton, New Jersey

S3. Strong Interactions of Strange Particles
Chairman: J. Steinberger, Department of Physics, Columbia University, New York, New York

S4. Weak Interactions
Chairman: C. N. Yang, Institute for Advanced Study, Princeton, New Jersey

Friday, August 26, 1960

S1. Strong Interactions of Pions and Nucleons (Experimental)
Chairman: J. M. Cassels

S2. Strong Interactions of Pions and Nucleons (Theoretical)
Chairman: J. R. Oppenheimer

S3. Strong Interactions of Strange Particles
Chairman: J. Steinberger

S4. Weak Interactions
Chairman: C. N. Yang

Monday, August 29, 1960 (Morning)

R1. Strong Interactions of Pions and Nucleons I (photoproduction, pion scattering, pion production)
Chairman: H. Yukawa, Research Institute for Fundamental Physics, Kyoto University, Kyoto, Japan
Rapporteurs: (Experimental) J. Ashkin, Department of Physics, Carnegie Institute of Technology, Pittsburgh, 13, Pennsylvania;
(Theoretical) G. C. Wick, Brookhaven National Laboratory, Upton, Long Island, New York

Monday, August 29, 1960 (Afternoon)

P1. Structure of Elementary Particles: Invited papers on electron-nucleon scattering, electromagnetic structure of muon, etc.
Chairman: I. E. Tamm, Lebedev Institute, Academy of Sciences, Moscow, USSR

Tuesday, August 30, 1960 (Morning)

R2. Strong Interactions of Pions and Nucleons II (nucleon and antinucleon processes)
Chairman: E. Amaldi, Istituto di Fisica, Universita degli Studi, Rome, Italy
Rapporteurs: (Experimental) O. Chamberlain, Department of Physics, University of California, Berkeley 4, California;
(Theoretical) M. M. Lévy, Service de Physique Théorique, B. P. No. 12, Orsay (S. et O.), France
(Theoretical: general analytical techniques) K. Symanzik, Institute for Advanced Study, Princeton, New Jersey

Tuesday, August 30, 1960 (Afternoon)

P2. New Results at Superhigh Energies: Invited papers from Dubna, CERN and cosmic ray groups.
Chairman: C. J. Bakker, CERN, Geneva 23, Switzerland

Wednesday, August 31, 1960 (Morning)

R3. Strong Interactions of Strange Particles (production and interaction)
Chairman: L. Alvarez, Radiation Laboratory, University of California, Berkeley, California
Rapporteurs: (Experimental) R. K. Adair, Department of Physics, Yale University, New Haven, Connecticut;
(Theoretical) P. T. Matthews, Imperial College of Science and Technology, London, S. W. 7, England

Thursday, September 1, 1960 (Morning)

R4. Weak Interactions (ordinary and strange particles)
Chairman: A. I. Alikhanov, Institute for Theoretical and Experimental Physics, Academy of Sciences, Moscow, USSR
Rapporteurs: (Experimental: ordinary particles) V. L. Telegdi, Institute for Nuclear Studies, University of Chicago, Chicago 37, Illinois;
(Experimental: strange particles) M. Schwartz, Nevis Cyclotron Laboratories Columbia University, Irvington-on-Hudson, New York;
(Theoretical) L. B. Okun, Institute for Theoretical and Experimental Physics, Academy of Sciences, Moscow, USSR

Thursday, September 1, 1960 (Afternoon)

P3. Theories of Elementary Particles: Invited papers on invariance principles and models of elementary particles
Chairman: W. Heisenberg, Max-Planck-Institut für Physik und Astrophysik, Aumeisterstrasse, München 23, Germany.

SECOND REPORT OF THE EUROPEAN NUCLEAR ENERGY AGENCY

The European Nuclear Energy Agency of the O.E.E.C. has published its second report to the Council of Europe. In contrast to the first report, published in September 1958 and covering the first months of ENEA's existence, this new document is largely devoted to recording work done rather than proposals under consideration.

The 18-month period now reviewed has seen the setting up of the first three joint research undertakings sponsored by the Agency, and the start of their operations. It has also seen progress in work on questions of health and safety, information and training, and third party liability in cases of nuclear incidents.

The International Company EUROCHEMIC, created by the Convention of 20th December, 1957, was constituted in July, 1959. A Study and Research Office of some 50 people, established in 1958 within the framework of ENEA, is engaged on working out the pre-project for the plant and laboratories to be built at Mol in Belgium. Discussions are going on with the firms in participating countries which will be responsible for executing the project. Work on the site has begun and the safety problems arising out of the operation of the plant are the subject of special study.

The boiling heavy water reactor at Halden, Norway, which has been the subject of joint operation since the Agreement signed at Oslo on 11th June, 1958, has been functioning since June, 1959; at present it is being used to carry out a programme of low-power experiments relating to the physics and control of the reactor. The staff of the Project is about 100 and nearly half the scientific staff come from countries other than Norway.

On 23rd March, 1959, an Agreement was signed for the joint construction and operation of a high-temperature gas-cooled reactor (DRAGON) at the Winfrith Establishment in the United Kingdom; the research programme has been approved by the Board of Management of the project and is being carried out by an international team which already amounts to more than 100, half of the scientific staff coming from the Continent. The research work as well as the construction of Dragon, although based on the earlier work of the United Kingdom Atomic Energy Authority, will be carried out with the co-operation of all participating countries on the basis of international invitations to tender which are already under way.

These three joint undertakings represent a financial commitment of nearly 70 million dollars over a period of five years and the total staff will be about 700.

As part of its task of co-ordinating research, ENEA set up in June, 1959, with the Euratom Commission, the United States and Canada, a joint European-American Committee to direct the work of O.E.E.C. Member and Associate countries on the study and measurement of the nuclear properties of materials, and to circulate the results of measurements made.

In the special field of the utilization of radioisotopes, the Agency, in conjunction with the European Productivity Agency, is studying the possibility of developing practical methods of

preserving food by radiation under conditions which will enable local experiments to be conducted in different countries.

ENEA is also continuing to keep a watch on the problems raised in Europe by the training of specialists in nuclear science and techniques and is arranging yearly international courses in English and French given in national centres for University teachers and senior technical industrial executives from the European countries.

In October, 1959, the Steering Committee of the Agency approved arrangements made in liaison with Euratom for the regular and co-ordinated exchange of information on environmental radioactivity, thus making it possible to centralise and circulate measurements of airborne radioactive material at ground level and to warn the responsible authorities at the earliest possible moment in the event of any substantial increase in radioactivity being found in any O.E.E.C. country.

Uniform radiation norms for health protection measures in the O.E.E.C. countries have been elaborated by ENEA in cooperation with the Euratom Commission and were approved by the Council on 12th June, 1959. These norms cover general safety measures as well as maximum permissible doses for persons occupationally exposed, permissible concentrations of radioisotopes in water and air, and, finally, the maximum permissible doese for the population as a whole.

ENEA has also continued its work in elaborating a Convention on third party liability and insurance of operators of nuclear installations. The conclusion of this Convention is linked with measures to be taken by a number of European countries to intervene in the event of an incident causing damage in excess of the limit laid down.

The O.E.E.C. Security Control Convention, signed on 20th December, 1957, came into force on 22nd July, 1959. It will apply in the first place to ENEA's joint undertakings in order to ensure that operation cannot further any military purpose.

Finally, ENEA is following the execution of national programmes and is studying the place of nuclear power in Europe's energy production. The Stresa Conference in May, 1959, which assembled the leaders of the main industrial concerns interested in the development and application of nuclear energy, was the occasion for drawing up a general balance-sheet for the atomic industry in Europe. The purpose of the Conference was to examine the economic prospects of nuclear energy, the means of financing national and international programmes, the markets open to the producers of special nuclear materials, equipment, and instruments, and the legal system governing their activities.

Annexed to the ENEA Report are the texts of a number of Decisions, Progress Reports and other working documents relating to the Agency's current activities, together with a summary of national nuclear energy programmes, estimates of production up to 1965 and a forecast for the following decade.

The Report is to be debated during the April Session of the Consultative Assembly at Strasbourg.

2.I

Nuclear Physics **16** (1960) 381—401; © *North-Holland Publishing Co., Amsterdam*

Not to be reproduced by photoprint or microfilm without written permission form the publisher

PHOTOPROTONS FROM MEDIUM AND HEAVY ELEMENTS

W. C. BARBER and V. J. VANHUYSE †

High-Energy Physics Laboratory, Stanford University, Stanford, California ††

Received 26 January 1960

Abstract: Energy and angular distributions of protons produced by electron bombardment of targets of Nb, In, Ta, and Au were measured. Yield curves as a function of electron energy up to 40 MeV were measured for Nb, In, and Ta. The angular distributions are strongly forward for Ta and Au, less so for Nb, and slightly backward for In. The energy distributions are fairly smooth functions except in the case of Ta where two peaks are observed at about 9.5 and 11.5 MeV.

The yields were analyzed by means of a calculated number of photons (real and virtual) accompanying the electron through the target, and the following photoproton cross sections integrated over photon energy were obtained: Nb, 230 MeV · mb; In, 90 MeV · mb; Ta, 60 MeV · mb; and Au, 75 MeV · mb; the results have an estimated accuracy of ±25 %.

1. Introduction

The observation of photoprotons in numbers much greater than could be explained by the theory of the compound nucleus was the first evidence for a direct photoeffect on the separate nucleons in the nucleus [1,2]). In the meantime, an independent particle model [3]) ("IPM") has been successful in explaining many features of the giant resonance region of the nuclear photoeffect. There has been considerable discussion of the relation of this model to the older collective model of Migdal [4]), and Goldhaber and Teller [5]). The review article by Wilkinson [6]) gives a concise summary of the present state of photonuclear theories and experiments. These will not be discussed further here, except as they relate to the problem under consideration, photoproton emission from medium and heavy nuclei. For this problem the collective model is inadequate because it provides no mechanism for concentrating so much energy into one particle. The IPM pictures the photonuclear process as absorption of a γ-ray by a single particle in a transition from a shell-model ground state to an excited one. The particle either escapes directly from the nucleus or interacts with it to form a compound nucleus. In medium and heavy nuclei the IPM predicts that the chief contribution to the giant resonance should come from transitions between states of high orbital angular momentum. The direct emission of protons is inhibited by both the Coulomb and angular-

† Permanent address: University of Ghent, Belgian Interuniversity Institute for Nuclear Science.

†† Supported by the Office of Naval Research, the U. S. Atomic Energy Commission, and the Air Force Office of Scientific Research.

momentum barriers, and formation of a compound nucleus is a more likely process. Single-particle transitions can be found to final states of high energy and low orbital angular momentum which favour the direct emission of protons. The IPM thus predicts that there is not necessarily a close relation between the giant resonance and the emission of photoprotons. We shall be interested in another prediction of the model; that, because of the importance of many final states separated in energy, the cross sections and the proton energy distributions should not always be smooth functions.

The elements studied in our work have all been investigated to some extent in previous photoproton experiments [7–11]). De Sabbata [12]) has reviewed photoproton and photoneutron work and summarized most of the results. We have repeated and extended the measurements because our apparatus permits study in more detail and with greater statistical accuracy than the old measurements, which were usually done with nuclear emulsions.

The experiments were done with the electron beam from the Stanford Mark II accelerator. In all cases the electron beam traversed the target so that protons were produced by the direct interaction of the electrons as well as by the bremsstrahlung accompanying the electrons. This experimental method has the advantages of providing a high yield and simple means of monitoring the beam. The disadvantage that the interpretation of the experiments is more complicated is not as great as might be expected. The analysis can be carried out using virtual photon spectra which are continuous and not unlike bremsstrahlung spectra [13]). The fact that the virtual photon spectrum depends on the multipole order of the transition being excited can have an important influence on the angular distribution of the emitted protons. These problems will be considered in more detail in the discussion section below.

2. Apparatus

The configuration of the apparatus used in the experiment is shown in plan view in fig. 1. The electrons from the accelerator were energy-analyzed and

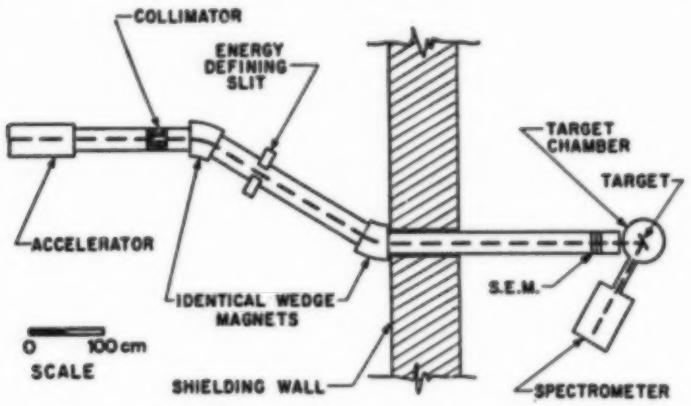

Fig. 1. Block diagram of experimental arrangement.

focused on the target by the two 30° wedge magnets. The number of incident electrons was monitored by the secondary-emission monitor ("SEM"). The X-rays produced by bremsstrahlung of the electrons in the foils of the SEM, the aluminium windows, and the air between the SEM and the target chamber, were also incident on the target. In some experiments a radiator was placed in the beam so that additional X-rays were produced. In all cases the number of radiation lengths of material in the beam was kept small so that more than 99 % of the bremsstrahlen traversed the target. The proton spectrometer was mounted to rotate about the intersection of the beam and the target so that the angle θ between the incident beam and the detected proton could be varied. The angle φ between the incident beam and a horizontal line in the plane of the target could be varied independently.

The evaluation of the important physical parameters affecting the experimental results was done as follows:

(1) The primary electron energy was determined by selection of the current through the wedge magnets. This magnetic system [14]) was previously calibrated to an estimated accuracy of 2 % by observation of the thresholds for the (γ, n) reactions on deuterium, Cu^{63}, O^{16}, and C^{12}.

(2) The SEM [15]), containing three aluminium foils, was calibrated at the beginning of the experiment against a Faraday cup that was placed in the position of the target chamber. This calibration revealed that the response of the SEM was affected by the condition of the aluminium surfaces. (At one time a change of 30 % was observed after the pressure was raised to permit a glow discharge between the high voltage and collector foils.) After the SEM had been in use for several days, its response relative to the Faraday cup became constant and was not changed by letting the system down to air (with high voltage off) and then re-evacuating. The ratio of the charge collected by the Faraday cup to the charge collected by the SEM was then measured at five different energies between 15 and 37 MeV and found to be 28.3 ± 0.4 independent of energy within the error of $\pm$ 1.5 %. The Faraday cup was studied in a previous experiment [16]), and its absolute accuracy is believed to be correct to 2 %. It is not certain that the SEM calibration did not change slowly over the period of several months during which measurements were taken. However, energy and angular distributions of protons from a given target were taken over relatively short periods of time, and measurements were reproducible within the statistical uncertainties which were often less than 2 %.

(3) The proton spectrometer consisted of a double-focusing wedge magnet with eight thin KI(Tl) scintillation counters located in the image focal plane of the magnet for simultaneous detection of eight proton momentum channels. The counters were shielded by approximately 5 cm of steel, 10 cm of lead, and 51 cm of paraffin. The magnet was a 120° wedge with tapered pole pieces to give a field index $n = \frac{1}{2}$. The mean radius of curvature was 46 cm and the

magnet gap was 5.7 cm at the centre of the pole pieces which were 17.1 cm wide. The vacuum chamber was made by welding stainless-steel sides to the pole pieces themselves so that the usable area of the magnet gap was 91 cm².

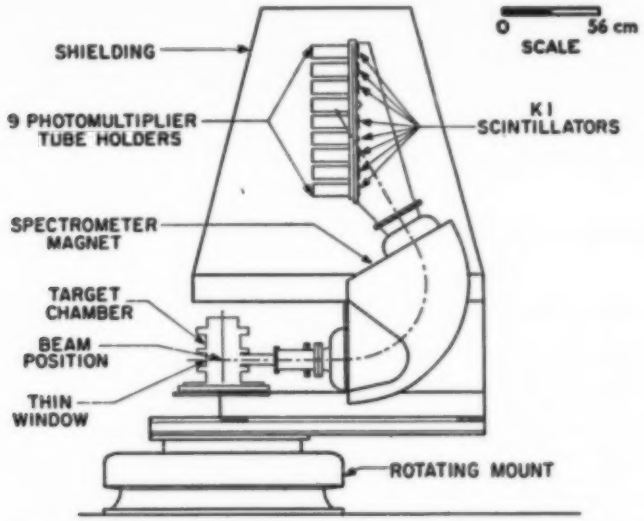

Fig. 2. Schematic side view of the proton spectrometer.

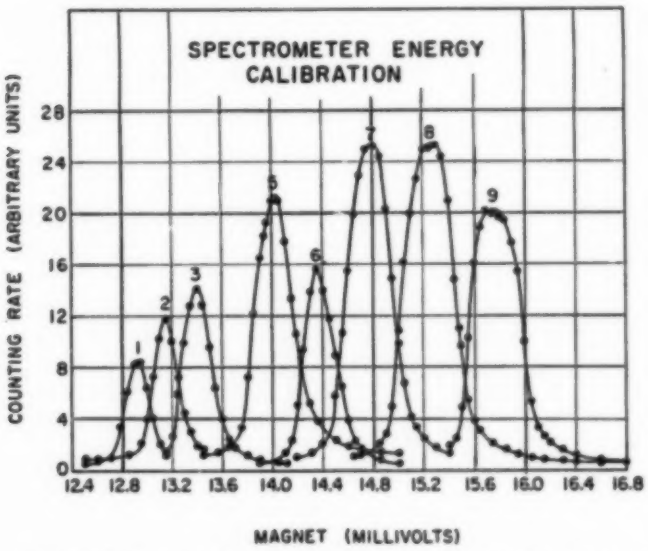

Fig. 3. Spectrometer resolution curves for the different counters, taken using the Cm^{244} α-particle source.

The magnet was placed 69 cm from the target so that the object and image distances were approximately equal for the central-momentum particles.

The first-order theory of the focusing of this type of magnet has been described by Judd [17]). From this theory the acceptance solid angle of the magnet was calculated to be 0.0102 sr. The counters were placed in the vertical plane as shown in fig. 2, whereas the first-order theory predicts a focal plane ap-

proximately 10° different from this. Measurements made by scanning the primary electron beam across the aperture of the magnet and testing the focal plane by means of photographic emulsions, indicated that the vertical focal plane was probably slightly better than the calculated one. In any event, the actual resolution of the different spectrometer channels is shown by the curves in fig 3, which were taken using a Cm^{244} source of 5.80 MeV α-particles at the position of the target. The source† when freshly prepared was measured to be less than 50 keV thick. However, the curves of fig. 3 were taken when the source was over a year old and an average α-energy of 5.75 MeV was assumed in making the momentum calibration of the spectrometer. The source height of 0.63 cm gave a computed spread of only 0.35 % to the momentum resolution of the spectrometer. The scintillators number from 1 through 9 beginning at the top, and were 7.0 cm high and 6.35 cm wide with the exceptions of 4 (an electron counter not used during these measurements) and 6, which was 3.8 cm high and 6.35 cm wide. The crystals were made thin (0.038 cm for numbers 6, 7, 8, and 9, and 0.051 cm for the others) in order to maximize the ratio of energy loss of protons to that of electrons. The thicknesses chosen were just sufficient to stop protons of about 15 MeV incident at the oblique angles shown in fig. 2. Protons of 25 MeV suffered energy losses of about 3 MeV, which was not much larger than the background caused by pile-up of electron pulses during operation with the most intense electron beams. The crystals were mounted on glass plates inside the vacuum chamber of the spectrometer. The crystals in positions 1 through 7 were covered with 0.0006 cm aluminium foils. Those in positions 8 and 9 were left uncovered. Lucite light pipes were used behind the glass plates in air to bring the light to the surface of RCA-6810 photomultiplier tubes. The output pulses of a few volts were amplified about ten times and counted after integral discrimination by scalers that were gated on by the gun pulse of the primary electron beam.

The calibration of the solid angle and energy acceptance of the spectrometer was checked by studying protons from the photodisintegration of the deuteron. The yield of protons was measured as a function of energy and angle from targets of CH_2 and CD_2, both with and without lead radiators in front of them. Suitable subtractions gave the yield due to the disintegration of the deuteron by real photons produced in the radiator only. The number of detected protons N_p per unit monitor response V can be written as

$$\frac{N_p}{V} = [\Delta E_p \times \Delta\Omega \times C] n_t \csc\varphi \int_0^{E_0} \frac{d^2\sigma(\theta, k, E_p)}{d\Omega\, dE_p} n(E_0, k, t)\, dk, \qquad (1)$$

where ΔE_p is the proton energy spread detected by the counter; $\Delta\Omega$ is the solid angle the counter; C is the number of electrons required to produce unit

† Supplied through the courtesy of the U. S. Atomic Energy Commission and Dr. I. Perlman of the University of California, Berkeley.

monitor response; n_t is the number of target nuclei per cm^2; φ is the target angle; $d^2\sigma/d\Omega dE_p$ is a differential cross section to produce a proton at an angle θ and energy E_p by photons of energy k; and $n(E_0, k, t)$ is the number of photons per unit energy interval (real and virtual) effective when one electron of energy E_0 traverses the target characterized by t. If eq. (1) is divided by E_p and rearranged so that only experimental quantities appear on one side, we obtain a quantity Y given by

$$Y \equiv \int_0^{E_0} \frac{d^2\sigma(\theta, k, E_p)}{d\Omega dE_p} n(E_0, k, t)dk = \frac{N_p \sin\varphi}{V E_p n_t} \left[\frac{\Delta E_p}{E_p} \Delta\Omega C\right]^{-1}. \quad (2)$$

In the special case of the deuteron, k and E_p are related by

$$k_1 = 2E_p + 2.23 \text{ (MeV)}, \quad (3)$$

and eq. (2) reduces to

$$2n(E_0, k_1, t) \frac{d\sigma}{d\Omega}(\theta, k_1) = \frac{N_p \sin\varphi}{V E_p n_t} \left[\frac{\Delta E_p}{E_p} \Delta\Omega C\right]^{-1}. \quad (4)$$

In eqs. (2) and (4) the quantities on the right-hand side are subject to experimental determination. Those in the first factor depend on the target and the observation made with it. Those in the square brackets are constants of the spectrometer and the monitor. For the deuteron calibration, $d\sigma/d\Omega$ was taken from the work of Whetstone and Halpern [18]), and $n(E_0, k, t)$ was calculated from the Bethe-Heitler formula. The quantities in the first factor were measured, and eq. (4) was used to obtain the value

$$\left[\frac{\Delta E_p}{E_p} \Delta\Omega C\right] = [9.52 \pm 1.4] \times 10^9 \quad (5)$$

of the square bracket for counter 7.

Independent evaluations of the quantities inside the sqaure brackets gave for counter 7: $\Delta E_p/E_p = 0.052$, $\Delta\Omega = 0.0102$, $C = 1.84 \times 10^{13}$, yielding a product of 9.75×10^9. The agreement is fortuitously too good. In analysing all the data for counter 7 we have used the value 9.52×10^9. The values of the quantity $(\Delta E_p/E_p)\Delta\Omega$ for the other counters relative to that of counter 7 were obtained by studying the same flat portion of a proton energy distribution with each counter in turn.

3. Results

The proton energy distributions, angular distributions, and excitation functions are shown in figs. 4—16. In each of these the quantity Y, defined

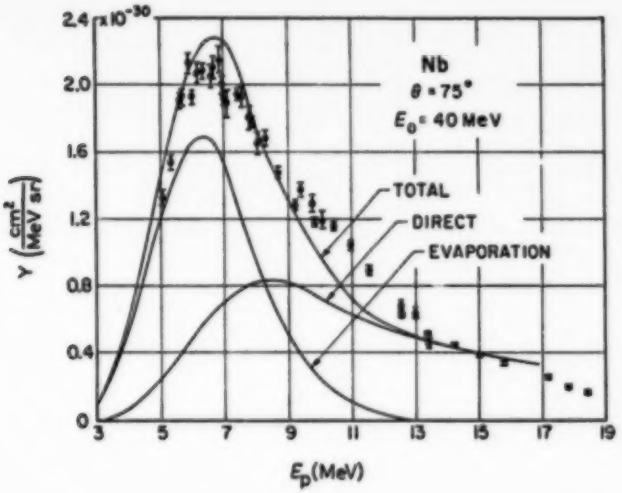

Fig. 4. Energy distribution of protons from Nb. The curves are calculated distributions arbitrarily normalized.

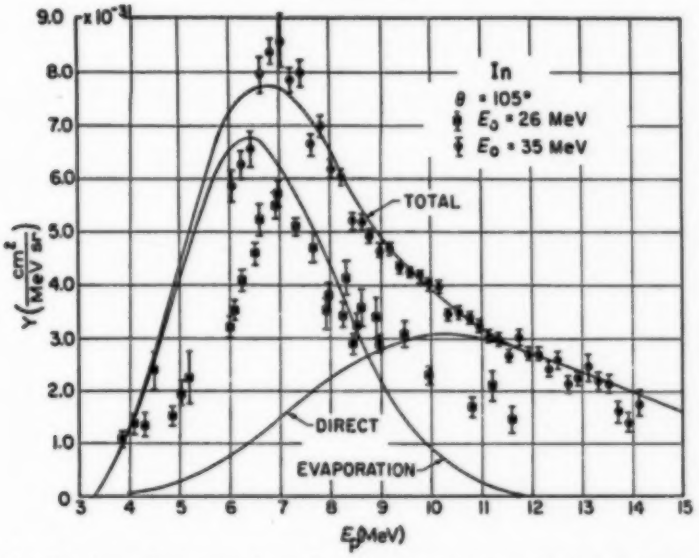

Fig. 5. Energy distribution of protons from In. The curves are calculated distributions arbitrarily normalized.

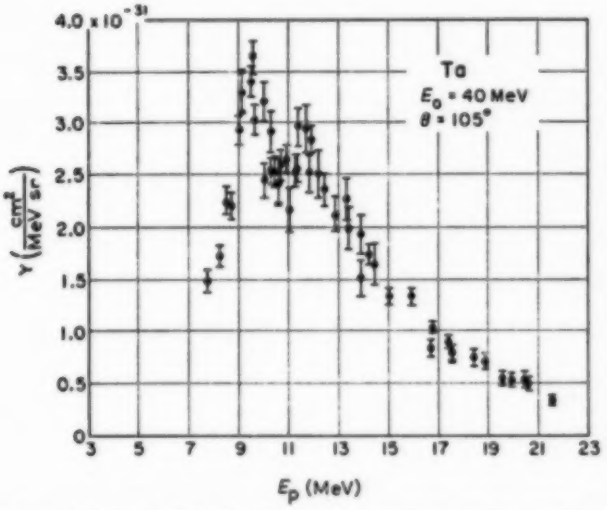

Fig. 6. Energy distribution of protons from Ta at 105°.

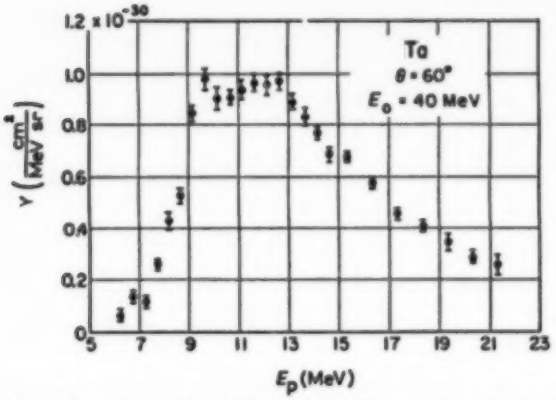

Fig. 7. Energy distribution of protons from Ta at 60°. The scales of abscissae on this figure and fig. 6 are not directly comparable because in the 60° measurements an additional radiator of 5.08×10^{-3} radiation length was in the primary beam upstream from the target.

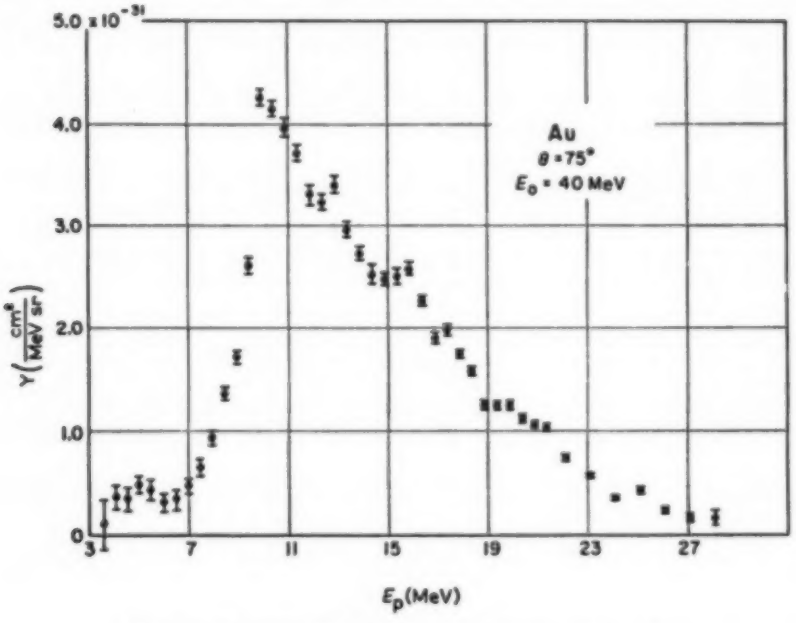

Fig. 8. Energy distribution of protons from Au.

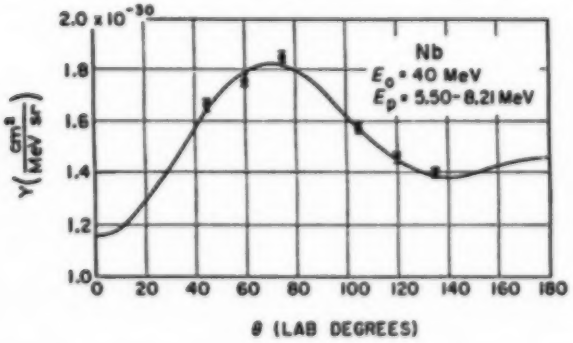

Fig. 9. Angular distribution of protons from Nb. The curve is a plot of the expression $(1.31 - 0.15 \cos\theta + 0.41 \sin^2\theta + 0.65 \cos\theta \sin^2\theta) \times 10^{-30}$, which is a four-parameter least-squares fit to the data.

by eq. (2), is plotted as a function of one of the quantities E_p, θ, or E_0. The values of the two quantities held constant are shown on the figures. All figures include data from several counters. The angular distributions and excitation functions represent combinations of data from several counters covering a band

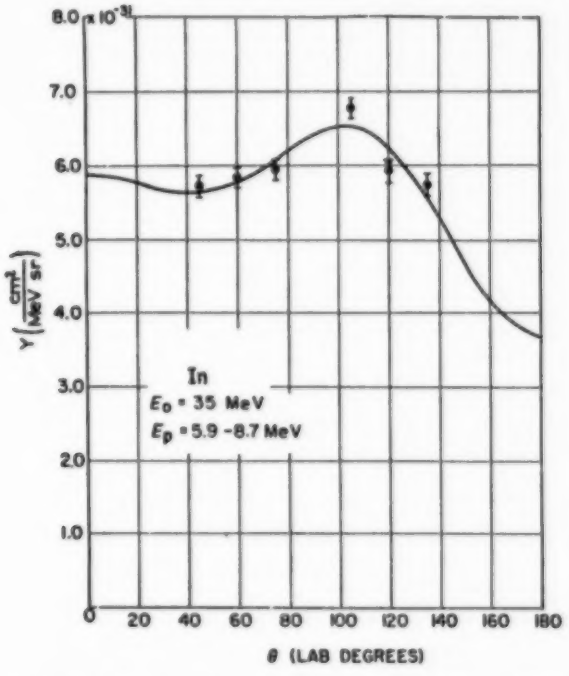

Fig. 10. Angular distribution of protons from In. The curve is a plot of $(4.76+1.08\cos\theta+1.64\sin^2\theta-2.04\cos\theta\sin^2\theta)\times10^{-31}$.

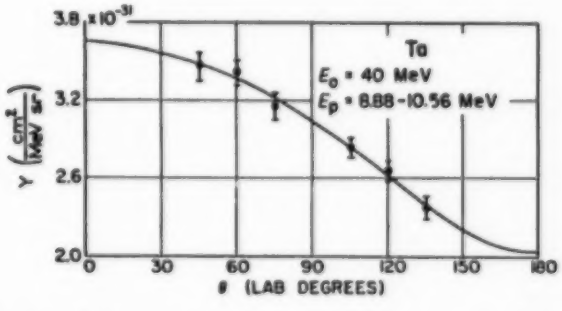

Fig. 11. Angular distribution of those protons from Ta which have energies near the first maximum in the energy distribution. The curve is a plot of $(2.83+0.80\cos\theta+0.21\sin^2\theta-0.07\cos\theta\sin^2\theta)\times10^{-31}$.

of proton energies. The indicated errors are standard deviations determined from counting statistics.

Table 1 gives data on the targets and radiators that were used. In all experiments the angle between the normal to the target and the line from the target to the spectrometer entrance was kept at 20° so that corrections for

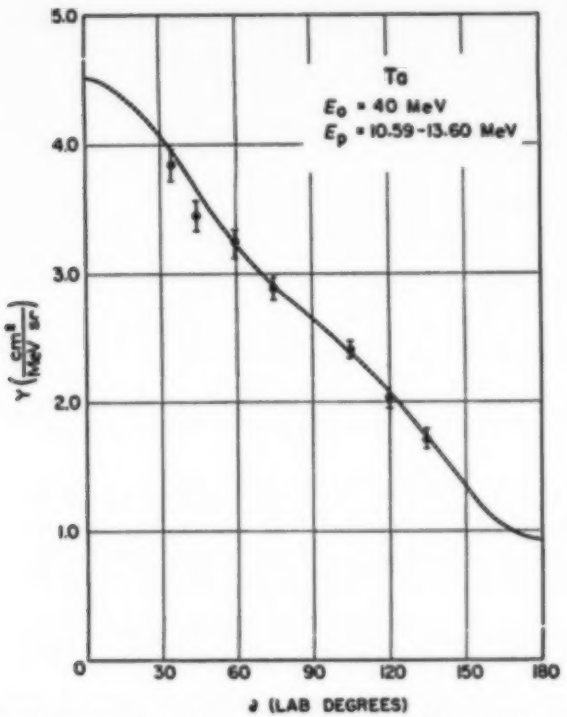

Fig. 12. Angular distribution of protons from Ta having energies near the second maximum in the energy distribution. The curve is a plot of $(2.72+1.80\cos\theta-0.09\sin^2\theta-0.84\cos\theta\sin^2\theta)\times10^{-31}$.

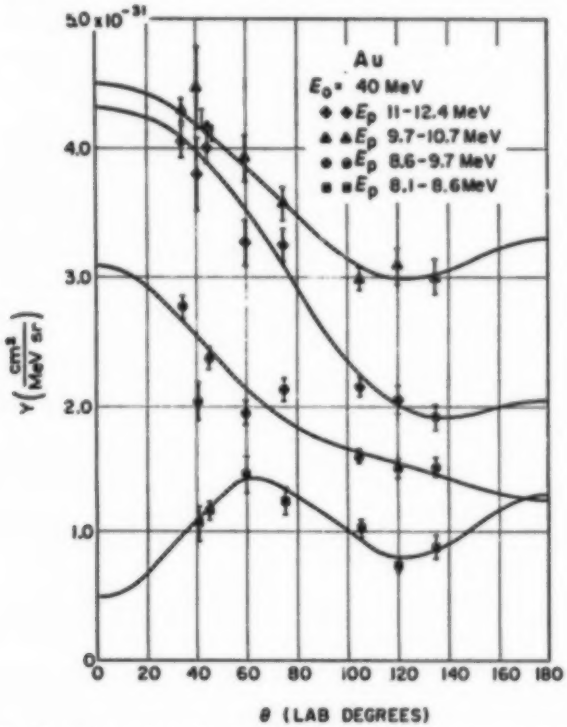

Fig. 13. Angular distribution of protons from Au. The curves represent the following least-squares fit to the data:

diamonds: $(3.2\ +1.15\cos\theta-0.58\sin^2\theta+0.51\cos\theta\sin^2\theta)\times10^{-31}$;
triangles: $(3.9\ +0.62\cos\theta-0.62\sin^2\theta+0.39\cos\theta\sin^2\theta)\times10^{-31}$;
circles: $(2.17+0.91\cos\theta-0.43\sin^2\theta-0.43\cos\theta\sin^2\theta)\times10^{-31}$;
squares: $(0.91-0.41\cos\theta+0.26\sin^2\theta+1.28\cos\theta\sin^2\theta)\times10^{-31}$.

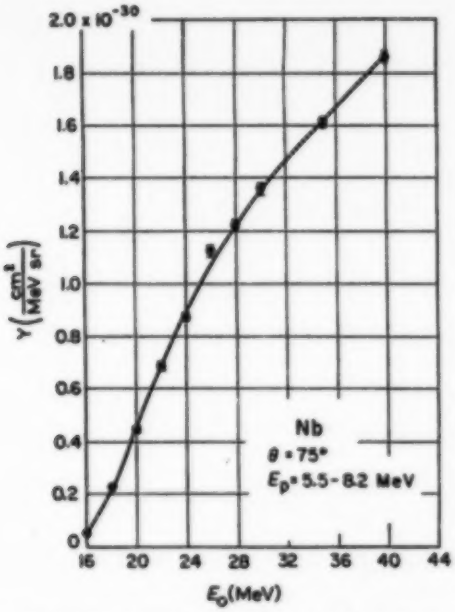

Fig. 14. Excitation of a group of protons from Nb as a function of primary electron energy. The curve was drawn arbitrarily.

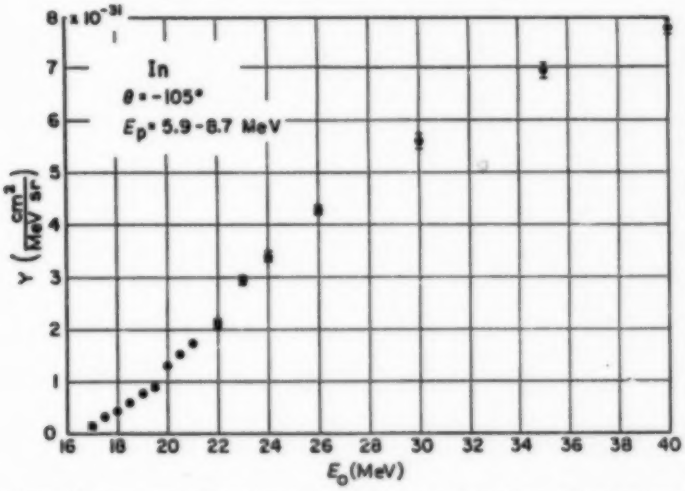

Fig. 15. Excitation of a group of protons from In as a function of primary electron energy

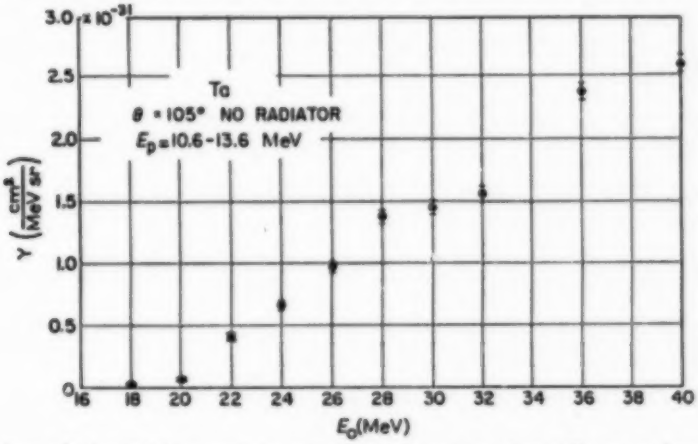

Fig. 16. Excitation of the higher-energy group of protons from Ta as a function of primary electron energy

proton energy loss in the target were independent of spectrometer angle. This correction has been made to the data assuming that all protons traversed one half the effective target thickness before emerging. The maximum correction was about 0.5 MeV. Because the target nuclei are heavy, the corrections for the motion of the centre of mass are small, and none has been made. All angles are in the laboratory system.

TABLE 1

Description of targets and radiators

Material	Thickness		Comments
	mg/cm²	radiation length $\times 10^3$	
Nb	21.8	0.233	Target for all Nb experiments
In	11.8	0.137	Target for all In experiments
Ta	29.43	0.46	Target for all Ta experiments except 60° energy distribution
Ta	16.60	0.26	Target for Ta energy distribution measured at 60°
Au	17.81	0.30	Target for all Au experiments
Al		0.30	Windows and SEM foils which were a source of bremsstrahlen in all experiments
Ta		3.12	Radiator used in Ta excitation functions
Ta+Au+Rh		5.08	Radiator used in Ta energy distribution measured at 60°
Electrodisintegration equivalent radiation length		1.46	Electric dipole for $E_0 = 40$ MeV, $k = 22$ MeV
		1.83	Electric quadrupole for $E_0 = 40$ MeV, $k = 22$ MeV

The proton energy distributions, figs. 4—8, are of similar shape for all the elements. The most remarkable features are perhaps the evidence for a double peak in the Ta distributions and the low-energy protons (3.5 to 7 MeV) from Au. These low-energy protons are especially surprising in view of the steep rise in the Au distribution from 7 to 10 MeV, which is presumably due to the Coulomb and angular-momentum barriers. The possibility that the low-energy protons are not produced from the Au but are due to some instrumental effect cannot be ruled out entirely. At low energies the proton pulses are not very large, and the background begins to be important. The correction for background was made by alternating runs with and without target and subtracting. The low-energy points with the Au target were observed under conditions where the counting rate with target in was about twice the rate with no target. We do not see how the small effect of the Au target on the 40 MeV electron beam (the rms multiple-scattering angle was about 0.03 radian) could increase the background by a large amount, but we were not

able to find a satisfactory method of proving this experimentally. We made a calculation to evaluate the number of low-energy protons which could result from higher-energy protons that lost energy as they travelled in the plane of the target and were then scattered at a large angle to enter the spectrometer. The contribution of this mechanism to the number of protons in the 3—6 MeV region was negligible.

The angular distributions, figs. 9—13, required a small correction becauses of a change in the number of real photons produced in the target itself as the target angle φ was changed. The correction, which never exceeded 5 %, was made on the basis of the change in the equivalent number of radiation lengths in the target relative to the other sources of photons. The angular resolution of the spectrometer was approximately $\pm 1.8°$.

The excitation functions, figs. 14—16, were taken with a fixed spectrometer angle and magnetic field. In the case of Ta two different spectrometer settings were employed, and altogether four excitation functions were measured, two with and two without an additional Ta radiator upstream from the target. For these runs, the background was evaluated by removing the target and not the radiator. Only one of the four Ta excitation functions is shown (fig. 16). No Au excitation function was measured.

Approximate cross sections, figs 17—20, were obtained from the excitation functions by photon-difference analyses. The effective photon spectrum was taken to be the sum of the bremsstrahlung spectrum (produced in the windows, in radiators when present, and in half of the target itself) plus the electric-dipole virtual-photon spectrum. The use of only the electric-dipole virtual-photon spectrum is an approximation because the large amount of forward

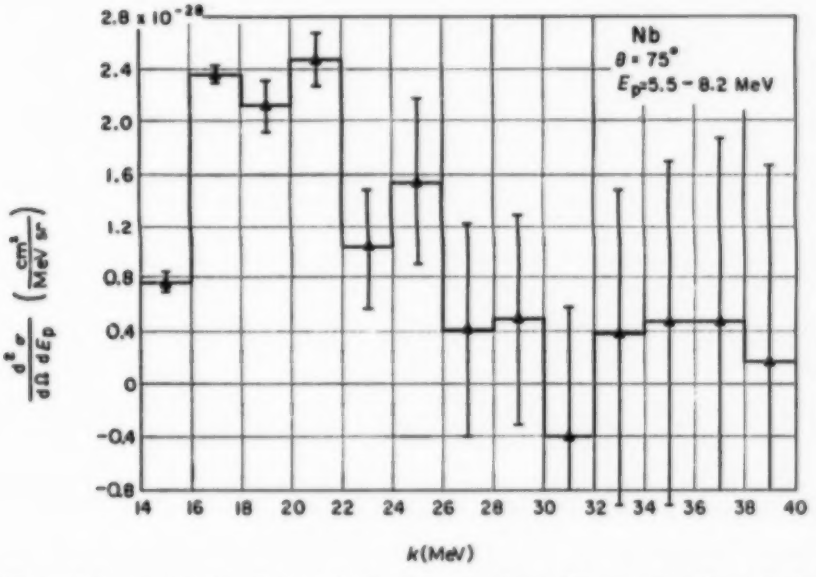

Fig. 17. Differential cross section for producing protons from Nb as a function of photon energy The histogram was drived by a photon-difference analysis of fig. 14.

asymmetry indicates the importance of other types of transitions. To illustrate the possible errors involved, the electric-dipole and electric-quadrupole virtual-photon intensity spectra for primary electrons of 40 MeV are shown

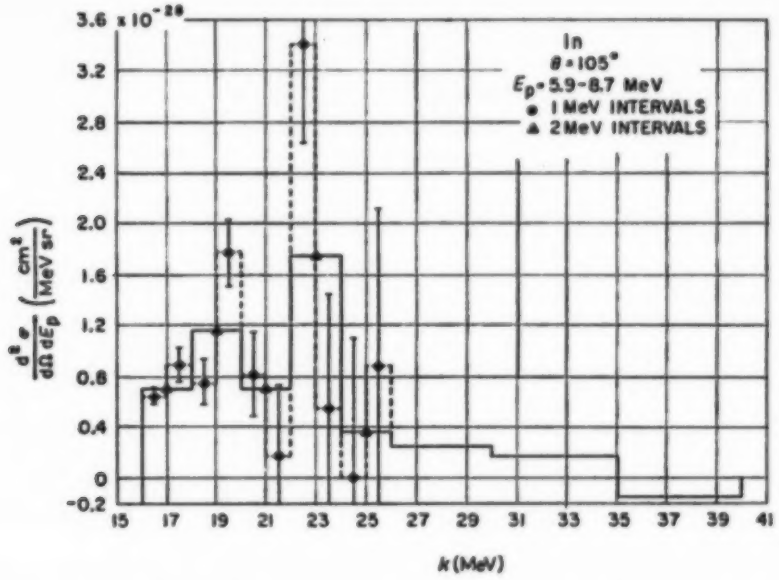

Fig. 18. Differential cross section for producing protons from In as a function of photon energy. The dashed and the solid histograms were derived by photon-difference analyses of fig. 15 using 1 and 2 MeV differences, respectively. The extent to which the two histograms agree indicates the reliability of the method.

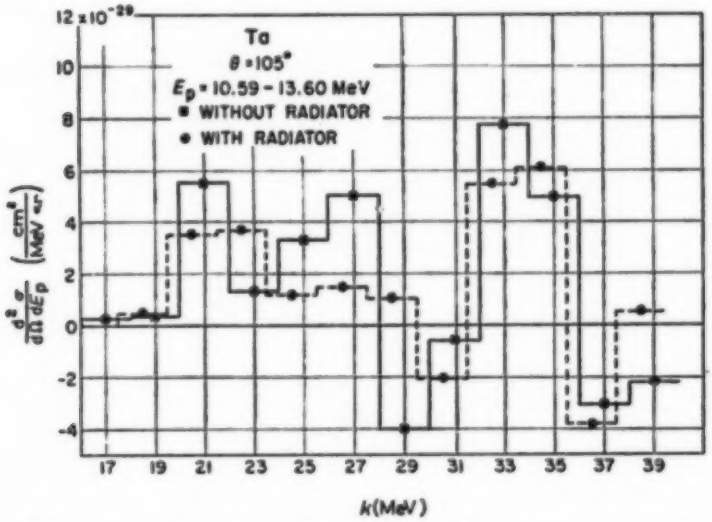

Fig. 19. Differential cross section for producing the higher-energy group of protons from Ta. The solid histogram was derived from a photon-difference analysis of fig. 16. The dashed histogram was similarly derived from an excitation function (not shown) taken with an additional radiator of 3.12×10^{-2} radiation length of Ta in the primary electron beam upstream from the target. The degree of reliability of the results can be judged from the agreement of the two histograms.

in fig. 21. The bremsstrahlung intensity spectrum from a radiator of 10^{-2} radiation length is shown for comparison. In view of the errors and approximations involved in determining the cross-section curves, their detailed structure

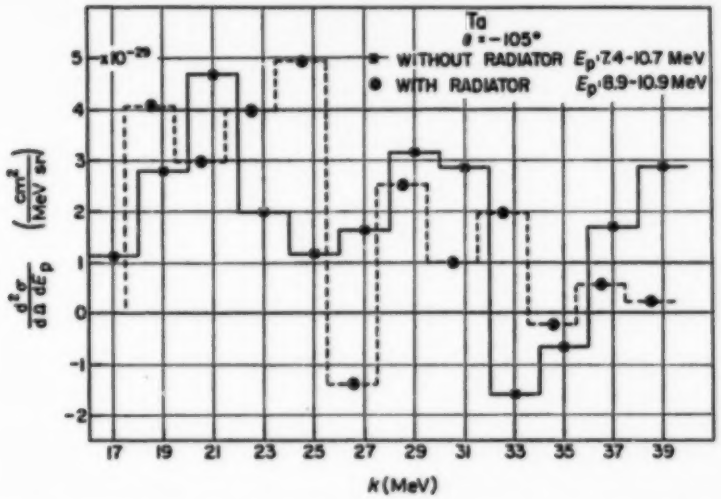

Fig. 20. Differential cross section for producing the lower-energy group of protons from Ta. The two histograms were derived by photon-difference analyses of two excitation functions (not shown) taken with and without the additional Ta radiator of 3.12×10^{-2} radiation length in the primary electron beam. Although the proton energy groups were not exactly the same in the two cases, they are close enough that the cross sections are expected to be nearly the same.

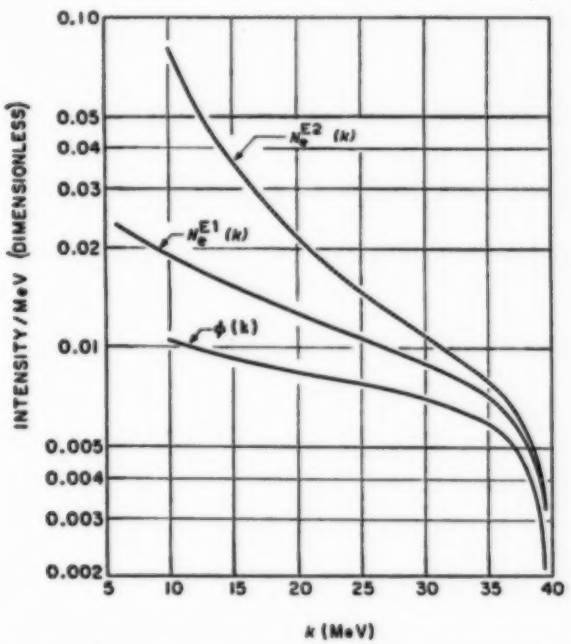

Fig. 21. Photon intensity distributions produced by electrons of 40 MeV: $\varphi(k)$ is the "thin-target" bremsstrahlung spectrum for a copper radiator of 0.01 radiation length; N_e^{E1} and N_e^{E2} are the virtual-photon spectra effective for producing electric-dipole and electric-quadrupole transitions, respectively.

is not significant. General features, such as the mean energy, the width, and the gross structure, are important and reveal, for example, that the main contribution to photoproton emission comes from photon energies 5 to 10 MeV higher than the giant resonance.

The proton spectrometer is not well suited for the determination of total cross sections because excitation functions covering the entire range of proton energies and angles would be required. Since reliable total cross sections are not available from other sources, we present the following estimates of the total cross sections integrated over photon energy to 40 MeV, based on extrapolations of the limited data available: Nb, 230 MeV · mb; In, 90 MeV · mb; Ta, 60 MeV · mb; Au, 75 MeV · mb. Our extrapolation probably introduces an uncertainty of about 25 % in these results.

4. Discussion

4.1. ENERGY DISTRIBUTIONS

The observed distributions from Nb and In can be formed by suitable combinations of calculated "direct" and "evaporation" energy distributions. The possibility of such fitting has been pointed out in previous photoproton studies [8, 11]). For illustration we have used the formulas given by Dawson [11])

$$I_e(E_p) = KE_p\sigma_c(E_p)\exp(-E_p/T)\int_{E_p+B_p}^{E_0} n(E_0, k, t)\sigma_{\gamma,n}(k)\,dk, \qquad (6)$$

for the evaporation distribution; and

$$I_d(E_p) = K'F(E_p)\int_{E_p+B_p}^{E_0} \frac{n(E_0, k, t)dk}{k^3}, \qquad (7)$$

for the direct distribution. The new symbols in eqs. (6) and (7) are: $I(E_p)$, the energy distribution function; K and K', arbitrary constants; $\sigma_c(E_p)$, the capture cross section for protons of energy E_p on the residual nucleus; T, the nuclear temperature; B_p, the proton binding energy; $F(E_p)$, the barrier penetrability for protons of energy E_p. The penetrability was calculated assuming a nuclear radius of $1.3 \times 10^{-13} A^{\frac{1}{3}}$ cm, and the nuclear temperature was assumed independent of excitation energy as $(100/A)^{\frac{1}{2}}$ MeV. The constants K and K' were chosen arbitrarily to give the best fit to the magnitude and shape of the observed energy distributions. The results, shown on figs. 4 and 5, indicate that the percentage of evaporation protons is 62 % in the case of Nb and 50 % in the case of In. The integrated evaporation cross sections are then 140 MeV · mb for Nb and 45 MeV · mb for In. These values are about two times larger than predicted by the calculations of Weinstock and Halpern [19]). In view of the approximations in the calculations and the crudeness

of the method of separating evaporation and direct protons, the agreement is satisfactory.

The proton energy distribution given by eq. (7) is an approximation to that predicted by the theory of Courant [2]) which did not consider the shell structure of the initial or final nuclear states. Calculations of photonuclear absorption based on the IPM have been made by Rand [20]) for a number of elements which have only one stable isotope, including Nb, Ta, and Au. Rand's calculations do not extend to the problem of the decay of the excited nuclear state. We have made estimates of the direct emission of protons using the Wilkinson picture that the excited IPM state decays either by direct particle emission (width Γ) or by compound nucleus formation, and that the relative probability of these processes is given by $\Gamma/2W$, where W is the imaginary part of the nuclear potential. Table 2 summarizes these estimates for Nb based on the

TABLE 2

Expected yield of photoprotons from Nb based on Rand's [20]) calculations

Transition	Transition energy (MeV)	E_p (MeV)	$\int\sigma_{abs}\,dk$ (MeV · b)	Γ (MeV)	$\int\sigma_{(\gamma,p)}\,dk$ (MeV · b)
$1g_{\frac{9}{2}} - 2f_{\frac{7}{2}}$	37.6	25	0.012	16.5	0.010
$1p_{\frac{1}{2}} - 2d_{\frac{3}{2}}$	19.9	9.7	0.102	3.7	0.056
$1f_{\frac{5}{2}} - 2d_{\frac{3}{2}}$	28.3	9.7	0.068	3.7	0.037
$2p_{\frac{1}{2}} - 3s_{\frac{1}{2}}$	24	11.0	0.109	7.3	0.075
$1f_{\frac{7}{2}} - 2d_{\frac{5}{2}}$	29.7	5	0.096	10^{-3}	0
					$\Sigma = 0.18$

assumption that $W = 1.5$ MeV and $\Gamma = 2k_p F\hbar^2/M_p R$, where $k_p = (2M_p E_p)^{\frac{1}{2}}/\hbar$, R is the nuclear radius, and F is the barrier penetration probability.

The general features of fig. 4 are in good agreement with table 2. The energy distribution shows a slight excess of protons over the predictions of eqs. (6) and (7) at 11 MeV where the shell transitions cluster. The agreement of the absolute yields is certainly within the expected accuracy of the IPM calculation.

The shell-model picture of In is the same as that for Nb except for the $g_{\frac{9}{2}}$ shell, where in In there are 9 protons and in Nb only one. We should expect the proton energy distribution for In to show an increased number of high-energy protons as a result of the increased strength of the first transition listed in table 2. The other transitions should be relatively decreased in intensity because of the increase of the Coulomb barrier. The decrease due to the barrier is apparent in comparing figs. 4 and 5; the predicted increase in the high-energy protons is difficult to detect because the transition energy is near the end point of our spectrum and the large value of Γ gives a large spread in energy for the resulting protons.

The Coulomb barriers of the Ta and Au nuclei are so high that the number of predicted evaporation protons is a small fraction of the observed number. The estimated yields based on Rand's calculations for Au are shown in table 3.

TABLE 3

Expected yield of photoprotons from Au based on Rand's [20]) calculations

Transition	Transition energy (MeV)	E_p (MeV)	$\int\sigma_{abs}\,dk$ (MeV · b)	Γ (MeV)	$\int\sigma_{(\gamma,p)}\,dk$ (MeV · b)
I: $2d_{\frac{3}{2}}-3p_{\frac{1}{2}}$	14.6	8.7	0.08	0.22	0.005
II: $1h_{\frac{11}{2}}-2g_{\frac{7}{2}}$	26.3	16	0.17	3.1	0.087
III: $2d_{\frac{3}{2}}-3p_{\frac{1}{2}}$	17.2	8.7	0.18	0.22	0.012
IV: $1g_{\frac{7}{2}}-2f_{\frac{5}{2}}$	22.5	8.7	0.95	0.045	0.014
V: $2d_{\frac{3}{2}}-2f_{\frac{5}{2}}$	14.6	8.7	0.20	0.045	0.003
					$\Sigma = 0.12$

The proton energies were assigned on the basis of extrapolations of curves given by Rand, and they are not expected to be accurate. The result that the h to g transition predicts more protons than are observed would be rectified if the proton energy were slightly lower. The observed proton energy distribution from Au, fig. 8, is in fair agreement with table 3. The rapid rise in number of protons between 8 and 10 MeV can be explained by the effect of the barrier on the p- and f-wave protons of about 9 MeV. The small bump observed at 16 MeV may be the result of the high-energy g-wave protons whose barrier cutoff is about 15 MeV. Protons below 7 MeV should be completely eliminated by the Coulomb barrier, and their presence is a puzzling feature of the distribution. It is possible that they are the result of some background effect, but we believe this is unlikely. Dawson[11]) also observed a statistically significant number of photoprotons from Au in this energy region.

Rand's calculations for Ta predict that transitions II, III, and IV of table 3 should be the important ones, and therefore the energy distribution would be expected to be similar to that of Au. The calculations did not take the deformation of the Ta nucleus into account, however. Nilsson [21]) showed that the deformation causes a splitting of the shell model state, which in a spherical nucleus had total spin J, into $(J+\frac{1}{2})$ levels. These levels are ordered in energy according to the magnitude of the projection Ω of their angular momentum on the symmetry axis of the nucleus. It was shown by Wilkinson[22]) that this results in a widening or a splitting of the giant resonance for deformed nuclei such that transitions involving states of higher Ω give rise to the higher-energy part of the resonance. In a similar way, the splitting of the states involved in transitions II, III and IV of table 3, which are most important in proton emission, will cause a broadening or a splitting of the proton energy

distributions. The higher-energy protons come from final states of high Ω The percentage splitting predicted by the Nilsson diagrams is somewhat higher than the experimental splitting (figs. 6 and 7), but the Coulomb barrier reduces the number of low-energy protons and narrows the distribution. In addition, the Nilsson model does not contain refinements, such as an energy-dependent nuclear potential, that would affect the amount of splitting.

4.2. ANGULAR DISTRIBUTIONS

The angular distributions were measured under conditions where approximately $\frac{2}{3}$ of the total yield resulted from the direct effect of electrons and $\frac{1}{3}$ from real photons accompanying the electrons. The angular distributions of the reaction products of these two interactions are not expected to be the same, but they are not very different. Bosco and Fubini [23]) have calculated the relation between the photo- and electrodisintegration distributions for electric-dipole transitions. Small-angle scattering gives rise to most of the transitions produced by electrons, and in the case of forward scattering the distribution of products will be the same as for photon-induced transitions. The scattering at finite angles is azimuthally symmetric and has the effect of smoothing the distribution of reaction products toward isotropy. The measurements of Barber, Dodge, and Vanhuyse [24]) of protons produced from C by electrons and photons indicate that in this case the angular distributions are about the same. In producing electric-quadrupole transitions, large-angle electron scatterings give a relatively larger contribution, so that the resulting angular distributions may differ considerably from the corresponding photon-induced distributions.

The large amount of isotropy in the Nb and In angular distributions can be attributed to the evaporation protons, and the importance of the s-wave final state of the direct protons listed in table 2. The Nb protons are distributed slightly forward and the In ones slightly backward. In^{115} possesses a large quadrupole moment, and the mechanism proposed by Sawicki [25]) for photon absorption in distorted nuclei produces a backward angular distribution.

The striking characteristic of the Au and Ta angular distributions is the strong forward asymmetry. The asymmetry cannot be caused by the electrodisintegration. Checks at a few angles showed it was increased when the real photon component of the primary beam was increased by placing radiators upstream from the target. The fore-aft asymmetry can result only from interference between final states of opposite parity. Mixing of electric-dipole and electric-quadrupole transitions is usually assumed to be the cause of this. On the shell-model picture there are many single-particle quadrupole transitions that give protons in the same final state as the dipole transitions we have shown to be important. The protons in the higher-energy peak of the Ta energy distribution are more forward than those in the lower-energy peak, and this

is correlated with a greater number of possible E2 transitions predicted by the Rand-Nilsson model.

The measurements of Toms and Stephens [9]), employing a maximum bremsstrahlung energy of 23 MeV, showed that the photoprotons from Ta were emitted almost isotropically, whereas those from Pb^{208} were just as strongly forward as our Ta and Au distributions. They remarked that this strong dependence on atomic number suggests a nuclear shell-structure effect. With this interpretation, the change in the Ta distribution with bremsstrahlung energy (isotropic at 23 MeV and strongly forward at 40 MeV) could be the result of different shell's coming into importance as the available excitation energy is increased.

4.3. CROSS SECTIONS

On the IPM the cross sections should be large at the transition energies corresponding with the proton energies observed in the cross-section determinations. In the case of Nb, fig. 17, protons in the energy range 5.5 to 8.2 MeV were observed. Reference to table 2 indicates that these should result from transitions in the neighbourhood of 20, 24, and 28 MeV. When the expected broadening of the transition energy is taken into account, the predicted cross section is in fair agreement with the observed one. Unfortunately the errors in the experimental cross sections are about the same as the large uncertainty in the IPM calculations. In this situation a significant disagreement is almost impossible. All of the measured cross sections show, however, that the protons result from transition energies significantly greater than the peak of the giant resonance. The cross sections are spread over a range of 10 MeV or more, and, especially in the case of Ta (figs. 19 and 20), their structure is more bumpy than would be expected from a smooth resonance curve.

We should like to thank Mr. W. R. Dodge for his help in constructing and operating the experimental equipment; and we gratefully acknowledge a grant from the Research Corporation that made possible the construction of the magnetic spectrometer. One of us (V.J.V.) is indebted to the Belgian Interuniversity Institute for Nuclear Science for a grant which made a stay at Stanford possible.

References

1) O. Hirzel and H. Wäffler, Helv. Phys. Acta **20** (1947) 373
2) E. D. Courant, Phys. Rev. **82** (1951) 703
3) D. H. Wilkinson, Physica **22** (1956) 1039
4) A. Migdal, J. Phys. USSR **8** (1944) 331
5) M. Goldhaber and E. Teller, Phys. Rev. **74** (1948) 1046
6) D. H. Wilkinson, Ann. Rev. Nuc. Sci. **9** (1959) 1
7) J. Halpern and A. K. Mann, Phys. Rev. **83** (1951) 370

8) M. E. Toms and W. E. Stephens, Phys. Rev. **92** (1953) 362
9) M. E. Toms and W. E. Stephens, Phys. Rev. **98** (1955) 626
10) M. M. Hoffmann and A. G. W. Cameron, Phys. Rev. **92** (1953) 1184
11) W. K. Dawson, Can. J. Phys. **34** (1956) 1480
12) V. De Sabbata, Nuovo Cimento **11**, supp. 2 (1959) 225
13) R. H. Dalitz and D. R. Yennie, Phys. Rev. **105** (1957) 1598
14) K. L. Brown, Rev. Sci. Instr. **27** (1956) 959
15) G. W. Tautfest and H. R. Fechter, Rev. Sci. Instr. **26** (1955) 229
16) W. C. Barber, Phys. Rev. **97** (1955) 1071
17) D. L. Judd, Rev. Sci. Instr. **21** (1950) 213
18) A. Whetstone and J. Halpern, Phys. Rev. **109** (1958) 2072
19) E. V. Weinstock and J. Halpern, Phys. Rev. **94** (1954) 1651
20) S. Rand, Phys. Rev. **107** (1957) 208; dissertation, University of California, Berkeley
21) S. G. Nilsson, Mat. Fys. Medd. Dan. Vid. Selsk. **29**, No. 16 (1955)
22) D. H. Wilkinson, Phil. Mag. **3** (1958) 567
23) B. Bosco and S. Fubini, Nuovo Cimento **9** (1958) 350
24) Barber, Dodge, and Vanhuyse, Bull. Am. Phys. Soc. **113** (1958) 173
25) J. Sawicki, Nuclear Physics **6** (1958) 525

7.C

Nuclear Physics **16** (1960) 402—404; © *North-Holland Publishing Co., Amsterdam*

Not to be reproduced by photoprint or microfilm without written permission from the publisher

THE PION-NUCLEON COUPLING CONSTANT

T. D. SPEARMAN
St John's College, Cambridge

Received 18 January 1960

Abstract: Using the sum rule obtained by taking the limit of infinite energy in the π—p forward scattering dispersion relation, a value for the renormalized coupling constant

$$f^2 = 0.078 \pm 0.008$$

is obtained, which is in good agreement with the values obtained from other methods.

1. Introduction

A sum rule, relating the s-wave scattering lengths for π—p scattering to the coupling constant and an integral over the total cross-section, can be obtained from the dispersion relations for π—p forward scattering [1, 2]). Investigation of this sum rule is encouraged by the fact that the discrepancy observed by Puppi and Stanghellini [3]) has been resolved and the dispersion relations for π—p forward scattering have now been shown to give agreement with experiment [4]). This agreement affords support to the assumption of constant cross-sections at high energies. Various arguments have been advanced [5]) which indicate that if the total cross-sections σ^+, σ^-, both approach constant limits, these limiting values must be equal. This suggests the validity of a cut-off procedure in evaluating the integral which occurs in the sum rule. Using the most recent data for the total cross-sections [6]), this sum rule is found to give excellent agreement with the values of the s-wave scattering lengths obtained by Hamilton and Woolcock [7]), for a value of the renormalized coupling constant

$$f^2 = 0.082 \pm 0.008.$$

2. Sum Rule for π—p Scattering

It has been shown that a sum rule for π—p scattering may be derived by taking the limit of the dispersion relation at infinite energy. The relation thus obtained may be written in the form

$$\frac{1}{\mu}\{D_{(-)}(\mu) - D_{(+)}(\mu)\} - \lim_{\omega\to\infty} \frac{1}{\omega}\{D_{(-)}(\omega) - D_{(+)}(\omega)\} = \frac{4f^2}{\mu^2} + \frac{1}{2\pi^2}\int_\mu^\infty \frac{d\omega}{k}[\sigma_-(\omega) - \sigma_+(\omega)], \quad (1)$$

where $D^{(\pm)}(\omega)$ are the real parts of the forward scattering amplitudes for $\pi^{\pm}$—p scattering in the laboratory system; $\sigma^{\pm}(\omega)$ are the total cross-sections; $k = (\omega^2-\mu^2)^{\frac{1}{2}}$; and f^2 is the renormalized coupling constant. It is not unreasonable to assume that

$$\lim_{\omega\to\infty} \frac{1}{\omega} \{D_{(-)}(\omega)-D_{(+)}(\omega)\} = 0,$$

although this has not yet been proved. If, as we should expect, the cross-sections become constant at high energies [5, 8]), this relation must hold.

We may use the relations

$$D_{(-)}(\mu) = (\tfrac{2}{3}a_1+\tfrac{1}{3}a_3)\left(1+\frac{\mu}{M}\right), \qquad D_{(+)}(\mu) = a_3\left(1+\frac{\mu}{M}\right)$$

to replace the first term in (1) by

$$\frac{2}{3\mu}(a_1-a_3)\left(1+\frac{\mu}{M}\right),$$

where a_1 and a_3 are the s-wave scattering lengths. This gives

$$\frac{2}{3\mu}\left(1+\frac{\mu}{M}\right)(a_1-a_3) = \frac{4f^2}{\mu^2}+I \tag{2}$$

where I denotes the integral

$$I = \frac{1}{2\pi^2}\int_{\mu}^{\infty}\frac{d\omega}{k}[\sigma_-(\omega)-\sigma_+(\omega)].$$

3. Cross-Section Integral

The integral I is evaluated using recent values for the total cross-sections [6]). The cross-sections $\sigma_+(\omega)$ and $\sigma_-(\omega)$ are assumed to be equal for energies greater than 2 GeV [5, 8]) and a cut-off is inserted at this energy. In terms of nuclear units $\hbar = \mu = c = 1$, the following value is obtained

$$I = 0.127\pm0.025.$$

4. The Scattering Lengths a_1, a_3

Hamilton and Woolcock [7]) have recently used a new method for analysing scattering data and obtained values for the s-wave scattering lengths

$$a_1 = 0.178, \qquad a_3 = -0.087,$$

in reasonable agreement with the Panofsky ratio data. Using a dispersion relation connecting the s and p-wave phase shifts at low energy †, these authors

† A similar procedure has been used by Geffen [9]).

have been able to modify appreciably the sets of phase shifts of Chiu and Lomon [10]) and Barnes *et al.*[11]).

5. The Renormalized Coupling Constant f^2

We may consider (2) as an equation for the renormalized coupling constant f^2 in terms of I, a_1 and a_3. The values obtained, using different sets of values for the scattering lengths, are given in the following table:

	a_1	a_3	f^2
Hamilton and Woolcock	0.178	−0.087	0.082 ± 0.008 †
Chiu and Lomon	0.160	−0.130	0.087 ± 0.008
Barnes *et al.*	0.205	−0.114	0.092 ± 0.008

The result obtained using the scattering lengths of Hamilton and Woolcock gives excellent agreement with the value

$$f^2 = 0.080 \pm 0.005,$$

obtained independently from the dispersion relations by the method of Puppi and Stanghellini [4]).

References

1) M. L. Goldberger, H. Miyazawa and R. Oehme, Phys. Rev. **99** (1955) 986
2) J. M. Cassels, Proceedings of the 1957 Rochester Conference (Interscience, New York)
3) G. Puppi and A. Stanghellini, Nuovo Cimento **5** (1957) 1305
4) T. D. Spearman, Nuovo Cimento **15** (1960) 147
5) I. Ia. Pomeranchuk, JETP **34** (1958) 725;
H. Miyazawa, Proceedings of the 1958 CERN Conference, p. 102;
see also S. Z. Belen'kii, JETP **6** (1958) 960;
L. B. Okun and Ia. Pomeranchuk JETP **3** (1956) 306
6) H. L. Anderson and N. Metropolis, Proceedings of the 1956 Rochester Conference (Interscience, New York);
H. C. Burrowes *et al.*, Phys. Rev. Lett. **2** (1959) 119;
S. M. Korenchenko and V. G. Zinov, JETP **6** (1958) 1006;
J. C. Brisson *et al.*, Phys. Rev. Lett. **3** (1959) 561;
U. E. Kruse and R. G. Arnold, University of Chicago Preprint;
S. W. Barnes *et al.*, to be published in Phys. Rev.;
H. L. Anderson *et al.*, Phys. Rev. **104** (1956) 339;
O. Cool *et al.*, Phys. Rev. **103** (1956) 1082
7) J. Hamilton and W. S. Woolcock, to be published
8) M. J. Longo *et al.*, Phys. Rev. Lett. **3** (1959) 568;
O. Cool *et al.*, Phys. Rev. **103** (1956) 1082
9) D. A. Geffen, Phys. Rev. **112** (1958) 1370
10) H. Y. Chiu and E. Lomon, Ann. of Phys. **6** (1959) 50
11) S. W. Barnes *et al.*, to be published in Phys. Rev.

† *Note added in proof:* It has been suggested to me by Mr. W. S. Woolcock that the values used for a_1 and a_3 should be those obtained after the so-called 'inner Coulomb contribution' has been removed. These 'strictly mesonic' scattering lengths give the rather lower value $f^2 = 0.078 \pm 0.008$.

1.B

Nuclear Physics **16** (1960) 405—422; © *North-Holland Publishing Co., Amsterdam*

Not to be reproduced by photoprint or microfilm without written permission from the publisher

KINETIC AND POTENTIAL ENERGY MATRIX ELEMENTS FOR THE TRITON

G. H. DERRICK †

The F.B.S. Falkiner Nuclear Research and Adolph Basser Computing Laboratories, School of Physics, The University of Sydney ††

Received 10 November 1959

Abstract: The matrix elements of the kinetic energy operator and of the common potential energy operators are calculated for the total angular momentum and isobaric spin functions of the triton. The conditions necessary for the convergence of the kinetic energy integrals are investigated.

1. Introduction

In a previous paper [1]) ††† a classification from the point of view of group theory was made of the possible total angular momentum and isobaric spin functions of the triton ground state. The triton wave function was shown to be a linear superposition of ten "states", each of which has a definite value of the orbital angular momentum L and of the total spin S, and a well defined behaviour under permutations of particles. These properties are summarized in table 1 of ref. [1]). Let us number the states from 1 to 10 in the order in which they appear in this table. Then the wave function of the triton is given by

$$\begin{aligned}\Psi = {} & f_1\mathscr{Y}_1+f_2\mathscr{Y}_2+2^{-\frac{1}{2}}(-f_{3,2}\mathscr{Y}_{3,1}+f_{3,1}\mathscr{Y}_{3,2})+f_4\mathscr{Y}_4+f_5\mathscr{Y}_5+2^{-\frac{1}{2}}(-f_{6,2}\mathscr{Y}_{6,1} \\ & +f_{6,1}\mathscr{Y}_{6,2})+2^{-\frac{1}{2}}(-f_{7,2}\mathscr{Y}_{7,1}+f_{7,1}\mathscr{Y}_{7,2})+2^{-\frac{1}{2}}(-f_{8,2}\mathscr{Y}_{8,1}+f_{8,1}\mathscr{Y}_{8,2}) \qquad (1) \\ & +2^{-\frac{1}{2}}(-f_{9,2}\mathscr{Y}_{9,1}+f_{9,1}\mathscr{Y}_{9,2})+2^{-\frac{1}{2}}(-f_{10,2}\mathscr{Y}_{10,1}+f_{10,1}\mathscr{Y}_{10,2}).\end{aligned}$$

The radial functions f depend only on the three interparticle distances r_{23}, r_{31} and r_{12}; f_1 and f_4 are symmetric in these variables, f_2 and f_5 antisymmetric, while

$$\begin{pmatrix}f_{3,1}\\f_{3,2}\end{pmatrix}, \quad \begin{pmatrix}f_{6,1}\\f_{6,2}\end{pmatrix}, \quad \begin{pmatrix}f_{7,1}\\f_{7,2}\end{pmatrix}, \quad \begin{pmatrix}f_{8,1}\\f_{8,2}\end{pmatrix}, \quad \begin{pmatrix}f_{9,1}\\f_{9,2}\end{pmatrix}, \quad \begin{pmatrix}f_{10,1}\\f_{10,2}\end{pmatrix}$$

belong to the two rows of the mixed representation [1]); the second subscript (1 or 2) indicates the row to which the function belongs.

The functions $\mathscr{Y}$ are eigenfunctions of the total angular momentum and of the total isobaric spin. They are functions of the three Euler angles α, β, γ,

† Now at the School of Mathematics, Institute for Advanced Study, Princeton, N.J.

†† Also supported by the Nuclear Research Foundation within the University of Sydney.

††† In eq. (7) of ref. [1]), the exponent of i should be $2\kappa+\mu-M_L$, *not* $2\kappa+\mu+M_L$.

introduced in ref. [1]) †, and of the spin and isobaric spin coordinates. $\mathscr{Y}_1$ and $\mathscr{Y}_4$ are antisymmetric under permutations of these variables, $\mathscr{Y}_2$ and $\mathscr{Y}_5$ symmetric, while the remaining pairs

$$\begin{pmatrix}\mathscr{Y}_{3,1}\\ \mathscr{Y}_{3,2}\end{pmatrix}, \quad \begin{pmatrix}\mathscr{Y}_{6,1}\\ \mathscr{Y}_{6,2}\end{pmatrix} \cdots \begin{pmatrix}\mathscr{Y}_{10,1}\\ \mathscr{Y}_{10,2}\end{pmatrix}$$

belong to the rows of the mixed representation. The explicit forms of these eigenfunctions are given in ref. [1]).

In the present paper we evaluate the matrix elements of the Hamiltonian H between the total angular momentum and isobaric spin functions $\mathscr{Y}$. These elements are given by

$$(\mathscr{Y}_\chi, H\mathscr{Y}_{\chi'}) = \sum_{\substack{\text{spin}\\ \text{iso-spin}}} \int_{-\pi}^{\pi} \mathrm{d}\alpha \int_0^{\pi} \sin\beta \, \mathrm{d}\beta \int_{-\pi}^{\pi} \mathrm{d}\gamma \mathscr{Y}_\chi^+ H \mathscr{Y}_{\chi'}.$$

In writing down the matrix elements we take the sixteen functions $\mathscr{Y}$ in the following order:

$$\begin{aligned}&\mathscr{Y}_1, \ \mathscr{Y}_2, \ \mathscr{Y}_{3,1}, \ \mathscr{Y}_{3,2}, \ \mathscr{Y}_4, \ \mathscr{Y}_5, \ \mathscr{Y}_{6,1}, \ \mathscr{Y}_{6,2},\\ &\mathscr{Y}_{7,1}, \ \mathscr{Y}_{7,2}, \ \mathscr{Y}_{8,1}, \ \mathscr{Y}_{8,2}, \ \mathscr{Y}_{9,1}, \ \mathscr{Y}_{9,2}, \ \mathscr{Y}_{10,1}, \ \mathscr{Y}_{10,2}.\end{aligned}$$

For convenience the elements corresponding to pairs of mixed symmetry states (such as $\mathscr{Y}_{3,1}$ and $\mathscr{Y}_{3,2}$) will be grouped together into sub-matrices. It will be understood that the matrix $(\mathscr{Y}_\chi, H\mathscr{Y}_{\chi'})$ is to operate on the column vector whose sixteen components are the coefficients of the sixteen functions $\mathscr{Y}$ in the total wave function Ψ in eq. (1), i.e. the radial wave functions

$$\begin{aligned}&f_1, \ f_2, \ -2^{-\frac{1}{2}}f_{3,2}, \ 2^{-\frac{1}{2}}f_{3,1}, \ f_4, \ f_5, \ -2^{-\frac{1}{2}}f_{6,2}, \ 2^{-\frac{1}{2}}f_{6,1}, \ -2^{-\frac{1}{2}}f_{7,2}, \ 2^{-\frac{1}{2}}f_{7,1},\\ &-2^{-\frac{1}{2}}f_{8,2}, \ 2^{-\frac{1}{2}}f_{8,1}, \ -2^{-\frac{1}{2}}f_{9,2}, \ 2^{-\frac{1}{2}}f_{9,1}, \ -2^{-\frac{1}{2}}f_{10,2}, \ 2^{-\frac{1}{2}}f_{10,1}\end{aligned}$$

taken in this order. Only an outline of the derivation of the matrix elements is given in the present paper. The details have been published elsewhere [3]).

2. The Kinetic Energy

In this section we calculate the matrix elements of the kinetic energy operator $-(\hbar^2/2M)(\nabla_1^2+\nabla_2^2+\nabla_3^2)$, M being the nucleon mass. First the operator is expressed in terms of our Euler angle and triangle coordinates, and then this transformed form of the operator used to derive the matrix elements.

2.1. THE KINETIC ENERGY OPERATOR IN EULER ANGLE AND TRIANGLE COORDINATES

If we change coordinates from the three position vectors $\mathbf{r}_1$, $\mathbf{r}_2$, $\mathbf{r}_3$ to an arbitrary set $X^1, X^2, \ldots X^9$, we have from the theory of tensors [4])

† We have adopted the convention of Goldstein [2]), where we identify (α, β, γ) with Goldstein's angles (ψ, θ, ϕ).

$$-(\nabla_1^2+\nabla_2^2+\nabla_3^2) = -\sum_{i,k=1}^{9} g^{-\frac{1}{2}} \frac{\partial}{\partial X^i}\left(g^{\frac{1}{2}} g^{ik} \frac{\partial}{\partial X^k}\right) \tag{2}$$

where

$$g^{ik} = \sum_{p=1}^{3} \nabla_p X^i \cdot \nabla_p X^k \qquad (i, k = 1, 2, \ldots 9)$$

and

$$g = \frac{1}{|g^{ik}|}.$$

We shall take $X^1 = r_{23}$, $X^2 = r_{31}$, $X^3 = r_{12}$, $X^4 = \alpha$, $X^5 = \beta$, $X^6 = \gamma$, and $(X^7, X^8, X^9) = \mathbf{r}_G$, the position vector of the centre of mass.

The details of the calculation of g^{ik} are given in ref. [3]). Using matrix notation, the result is

$$(g^{ik}) = (\mathfrak{S}^+ M \mathfrak{S}), \quad g^{\frac{1}{2}} = r_{23} r_{31} r_{12} \sin\beta$$

where the 9×9 matrix $(\mathfrak{S}^{ik})$ is a function of α, β and γ only, while the 9×9 matrix (M^{ik}) is a function of r_{23}, r_{31} and r_{12} only. To write down these matrices we need the following quantities:

θ_1, θ_2, θ_3, the angles included at the vertices of the triangle, i.e.

$$\cos\theta_1 = \frac{r_{31}^2+r_{12}^2-r_{23}^2}{2r_{31}r_{12}}, \text{ etc.};$$

$$R^2 = r_{23}^2+r_{31}^2+r_{12}^2;$$

$$\begin{aligned}
&\Delta = \text{area of triangle} = \tfrac{1}{2}|\mathbf{r}_{31}\times\mathbf{r}_{12}| \\
&\quad = \tfrac{1}{4}\sqrt{(r_{23}+r_{31}+r_{12})(-r_{23}+r_{31}+r_{12})(r_{23}-r_{31}+r_{12})(r_{23}+r_{31}-r_{12})}, \\
&\lambda_x = \tfrac{1}{2}(R^2+\sqrt{R^4-48\Delta^2}), \qquad \lambda_x\lambda_y = 12\Delta^2, \\
&\lambda_y = \tfrac{1}{2}(R^2-\sqrt{R^4-48\Delta^2}), \qquad \lambda_x+\lambda_y = R^2, \\
&\Lambda = \lambda_x-\lambda_y = \sqrt{R^4-48\Delta^2} \\
&\quad = \sqrt{2(r_{23}^2-r_{31}^2)^2+2(r_{31}^2-r_{12}^2)^2+2(r_{12}^2-r_{23}^2)^2};
\end{aligned} \tag{3}$$

$\frac{1}{3}\lambda_x$ and $\frac{1}{3}\lambda_y$ are the moments of inertia per unit mass about the major and minor principal axes of inertia respectively, i.e. about the body-X and body-Y axes.

The matrices $\mathfrak{S}$ and M are given by

$$\mathfrak{S} = \begin{array}{c} \begin{matrix} 123 & 456 & 789 \end{matrix} \\ \begin{pmatrix} I & . & . \\ . & S & . \\ . & . & I \end{pmatrix} \end{array} \begin{array}{l} 123 \\ 456 \\ 789 \end{array} \tag{4}$$

with

$$I = \begin{pmatrix} 1 & . & . \\ . & 1 & . \\ . & . & 1 \end{pmatrix},$$

$$S = \frac{1}{\sin\beta} \begin{array}{c} \begin{matrix} 4 & 5 & 6 \end{matrix} \\ \begin{pmatrix} -\sin\alpha\cos\beta & \cos\alpha\sin\beta & \sin\alpha \\ -\cos\alpha\cos\beta & -\sin\alpha\sin\beta & \cos\alpha \\ \sin\beta & & \end{pmatrix} \end{array} \begin{matrix} 4 \\ 5 \\ 6 \end{matrix}$$

and

$$(M^{ik}) = (M^{ki}) \quad \text{(writing the upper half only)}$$

$$= \begin{array}{c} \begin{matrix} 1 & 2 & 3 & 4 & 5 & 6 & 789 \end{matrix} \\ \begin{pmatrix} 2 & \cos\theta_3 & \cos\theta_2 & . & . & \dfrac{12\Delta(r_{31}^2-r_{12}^2)}{\Lambda^2 r_{23}} & . \\ & 2 & \cos\theta_1 & . & . & \dfrac{12\Delta(r_{12}^2-r_{23}^2)}{\Lambda^2 r_{31}} & . \\ & & 2 & . & . & \dfrac{12\Delta(r_{23}^2-r_{31}^2)}{\Lambda^2 r_{12}} & . \\ & & & \dfrac{3}{\lambda_x} & . & . & . \\ & & & & \dfrac{3}{\lambda_y} & . & . \\ & & & & & \dfrac{3R^2}{\Lambda^2} & . \\ & & & & & & \dfrac{I}{3} \end{pmatrix} \end{array} \begin{matrix} 1 \\ 2 \\ 3 \\ 4 \\ 5 \\ 6 \\ 789 \end{matrix}$$

A dot indicates one or more zero elements.

Substituting for g^{ik} in eq. (2) we have

$$-(\nabla_1^2+\nabla_2^2+\nabla_3^2)$$

$$= -\sum_{P,Q=1,2,3} \frac{1}{r_{23}r_{31}r_{12}} \frac{\partial}{\partial X^P}\left(r_{23}r_{31}r_{12}M^{PQ}\frac{\partial}{\partial X^Q}\right) - 2\frac{L_6}{(-i\hbar)}\sum_{P=1,2,3} M^{P6}\frac{\partial}{\partial X^P} \quad (5)$$

$$-\sum_{\kappa,\lambda=4,5,6} M^{\kappa\lambda}\frac{L_\kappa}{(-i\hbar)}\frac{L_\lambda}{(-i\hbar)} - \tfrac{1}{3}\left(\frac{\partial}{\partial \mathbf{r}_G}\right)^2,$$

where L_4, L_5 and L_6 are the components of orbital angular momentum referred to the body axes, i.e.

$$\begin{aligned}
\frac{L_4}{-i\hbar} &= -\sin\alpha\cot\beta\,\frac{\partial}{\partial\alpha} + \cos\alpha\,\frac{\partial}{\partial\beta} + \frac{\sin\alpha}{\sin\beta}\,\frac{\partial}{\partial\gamma} \\
\frac{L_5}{-i\hbar} &= -\cos\alpha\cot\beta\,\frac{\partial}{\partial\alpha} - \sin\alpha\,\frac{\partial}{\partial\beta} + \frac{\cos\alpha}{\sin\beta}\,\frac{\partial}{\partial\gamma} \\
\frac{L_6}{-i\hbar} &= \frac{\partial}{\partial\alpha};
\end{aligned} \tag{6}$$

L_4, L_5 and L_6 are hermitian operators with respect to the Euler angles, with the weight factor $\sin\beta$.

The first term on the right hand side of eq. (5) is the only non-zero one for S-state wave functions. We shall denote it by T_S. Alternative forms of this operator are

$$\begin{aligned}
T_S &= -\sum_{P,Q=1}^{3} \frac{1}{r_{23}r_{31}r_{12}}\,\frac{\partial}{\partial X^P}\left(r_{23}r_{31}r_{12}M^{PQ}\,\frac{\partial}{\partial X^Q}\right) \\
&= -2\sum_{\text{cyclic}}\left(\frac{\partial^2}{\partial r_{23}^2} + \frac{2}{r_{23}}\,\frac{\partial}{\partial r_{23}} + \frac{r_{31}^2+r_{12}^2-r_{23}^2}{2r_{31}r_{12}}\,\frac{\partial^2}{\partial r_{31}\,\partial r_{12}}\right);
\end{aligned} \tag{7}$$

T_S is hermitian with respect to r_{23}, r_{31} and r_{12}, with the weight factor $r_{23}r_{31}r_{12}$. On the other hand the operator

$$\sum_{P=1}^{3} M^{P6}\,\frac{\partial}{\partial X^P} = \sum_{\text{cyclic}} \frac{12\Delta(r_{31}^2-r_{12}^2)}{\Lambda^2 r_{23}}\,\frac{\partial}{\partial r_{23}}$$

is antihermitian in these coordinates.

2.2. THE KINETIC ENERGY MATRIX ELEMENTS

By direct application of the operators L_4, L_5 and L_6 to the representation coefficients $D^L_{\mu M_L}$ we find

$$\begin{aligned}
(L_4+iL_5)D^L_{\mu M_L} &= \hbar\sqrt{(L+\mu)(L-\mu+1)}\,D^L_{\mu-1M_L}, \\
(L_4-iL_5)D^L_{\mu M_L} &= \hbar\sqrt{(L-\mu)(L+\mu+1)}\,D^L_{\mu+1M_L}, \\
L_6\,D^L_{\mu M_L} &= \hbar\mu D^L_{\mu M_L}.
\end{aligned} \tag{8}$$

Using these relations we can find the matrix elements between the five basic Euler angle functions (eqs. (9), (10), (11), (12), (13), of ref. [1])), and hence the matrix elements between the total angular momentum and isobaric spin functions $\mathscr{Y}$. The final kinetic energy matrix has the form

$$\begin{array}{c} \\ \dfrac{\hbar^2}{2M} \end{array}
\begin{array}{c}
\begin{array}{ccc} 123 & 4567 & 8910 \end{array} \\
\begin{pmatrix} T_{SS} & . & . \\ . & T_{PP} & . \\ . & . & T_{DD} \end{pmatrix}
\end{array}
\begin{array}{c}
123 \\ 4567 \\ 8910
\end{array}$$

with no cross elements between states of different orbital angular momentum L. The matrices are

$$T_{SS} = \begin{array}{c} \begin{matrix} 1 & 2 & 3 \end{matrix} \\ \begin{pmatrix} 1 & . & . \\ . & 1 & . \\ . & . & e_0 \end{pmatrix} \end{array} T_S \quad \begin{matrix} 1 \\ 2 \\ 3 \end{matrix} \tag{9}$$

$$T_{PP} = \begin{array}{c} \begin{matrix} 4 & 5 & 6 & 7 \end{matrix} \\ \begin{pmatrix} 1 & . & . & . \\ . & 1 & . & . \\ . & . & e_0 & . \\ . & . & . & e_0 \end{pmatrix} \end{array} \left(T_S + \frac{R^2}{4\Delta^2}\right) \quad \begin{matrix} 4 \\ 5 \\ 6 \\ 7 \end{matrix}$$

$$T_{DD} = \begin{array}{c} \begin{matrix} 8 & 9 & 10 \end{matrix} \\ \begin{pmatrix} e_0\left(T_S + \frac{\frac{3}{4}R^2}{\Delta^2}\right) & \frac{3^{\frac{1}{2}} e_0 \Lambda}{4\Delta^2} & . \\ \frac{3^{\frac{1}{2}} e_0 \Lambda}{4\Delta^2} & e_0\left(T_S + \frac{R^6}{4\Delta^2\Lambda^2}\right) & 4e_2 \sum_{P=1}^{3} M^{P6} \frac{\partial}{\partial X^P} \\ . & 4e_2 \sum_{P=1}^{3} M^{P6} \frac{\partial}{\partial X^P} & e_0\left(T_S + \frac{R^6}{4\Delta^2\Lambda^2}\right) \end{pmatrix} \end{array} \begin{matrix} 8 \\ 9 \\ 10 \end{matrix}$$

where

$$e_0 = \begin{pmatrix} 1 & . \\ . & 1 \end{pmatrix} \quad \text{and} \quad e_2 = \begin{pmatrix} . & -1 \\ 1 & . \end{pmatrix}.$$

2.3. DISCUSSION

It will be seen that the kinetic energy is diagonal in the S-states and in the P-states, but couples together the three D-states. These D-state cross terms arise in two ways:

(i) The body-Z component of orbital angular momentum does not commute with the kinetic energy; states of different μ are coupled together.

(ii) The internal coordinates r_{23}, r_{31}, r_{12} are not completely orthogonal to the Euler angle coordinates α, β, γ since g^{16}, g^{26} and g^{36} are non-zero. It can be shown that no choice of body axes will lead to complete orthogonality.

If the triangle of the three particles degenerates to a straight line ($\Delta = 0$), or if the triangle is equilateral ($\Lambda = 0$), some P- and D-state matrix elements become singular. These singularities arise because our specification of the Euler angles fails at these triangle configurations. This point is discussed in section 4, where it is shown that the radial wave functions f must have definite asymptotic forms near the in- line and the equilateral positions.

3. The Potential Energy

We shall restrict ourselves to 2-body potentials, so that the potential operator may be written

$$V = V_{12}+V_{23}+V_{31}.$$

It will be sufficient to evaluate the matrix elements $(\mathscr{Y}_\chi, V_{12}\mathscr{Y}_{\chi'})$. If a variational method is used to calculate the binding energy, the matrix elements of V_{23} and V_{31} are not needed, since the expectation values of V_{12}, V_{23} and V_{31} are all equal by symmetry. The matrix elements of V_{23} and V_{31} can be readily obtained, if required, by using the identities

$$V_{23} = (13)\, V_{12}(13)^{-1}, \quad V_{31} = (23)\, V_{12}\,(23)^{-1},$$

where (13) and (23) are the permutations which interchange particles 1 and 3, and 2 and 3, respectively.

We shall calculate the matrix elements of the following operators:

$$\text{central} \begin{cases} \text{(even)} = \tfrac{1}{2}(1+P_{12}^M), & \text{(odd)} = \tfrac{1}{2}(1-P_{12}^M), \\ \text{(singlet)} = \tfrac{1}{4}(1-\boldsymbol{\sigma}_1\cdot\boldsymbol{\sigma}_2), & \text{(central triplet)} = \tfrac{1}{4}(3+\boldsymbol{\sigma}_1\cdot\boldsymbol{\sigma}_2), \\ \text{(Coulomb)} = \dfrac{e^2}{r_{12}}\,[\tfrac{1}{2}+\tfrac{1}{2}(\boldsymbol{\tau}_1)_\zeta]\,[\tfrac{1}{2}+\tfrac{1}{2}(\boldsymbol{\tau}_2)_\zeta], \end{cases}$$

$$\text{non-central} \begin{cases} S_{12} = \dfrac{3}{r_{12}^2}\,(\boldsymbol{\sigma}_1\cdot\mathbf{r}_{12})(\boldsymbol{\sigma}_2\cdot\mathbf{r}_{12})-\boldsymbol{\sigma}_1\cdot\boldsymbol{\sigma}_2, \\ \mathbf{L}_{12}\cdot(\mathbf{s}_1+\mathbf{s}_2) = \hbar^2\mathbf{r}_{12}\times[-\tfrac{1}{2}i\,(\boldsymbol{\nabla}_1-\boldsymbol{\nabla}_2)]\cdot\tfrac{1}{2}(\boldsymbol{\sigma}_1+\boldsymbol{\sigma}_2); \end{cases}$$

P_{12}^M is the space exchange (Majorana) operator for particles 1 and 2, $\mathbf{r}_{12} = \mathbf{r}_1-\mathbf{r}_2$, and $\boldsymbol{\sigma}$ and $\boldsymbol{\tau}$ denote the spin and isobaric spin vectors respectively. Combinations such as (singlet-even), (tensor-odd), and so on are readily obtained by multiplying together the appropriate matrices. It is understood that each of these operators, apart from the Coulomb operator, is to be multiplied by a function of r_{12}.

Many of the potential energy matrix elements must be zero because of the different symmetry properties of the two states. For example, states 1 and 5 are completely symmetric in all the space coordinates, while states 2 and 4 are completely antisymmetric in these variables. Since V_{12} is symmetric in the space coordinates of particles 1 and 2, its matrix elements 1—2, 1—4, 5—2, 5—4, all vanish. Further, the space exchange operator P_{12}^M has the eigenvalue $+1$ for the functions $f_1\mathscr{Y}_1$, $f_{3,1}\mathscr{Y}_{3,2}$, $f_5\mathscr{Y}_5$, $f_{6,2}\mathscr{Y}_{6,1}$, $f_{7,2}\mathscr{Y}_{7,1}$, $f_{8,1}\mathscr{Y}_{8,2}$, $f_{9,1}\mathscr{Y}_{9,2}$, $f_{10,2}\mathscr{Y}_{10,1}$, and the eigenvalue -1 for the functions $f_2\mathscr{Y}_2$, $f_{3,2}\mathscr{Y}_{3,1}$, $f_4\mathscr{Y}_4$, $f_{6,1}\mathscr{Y}_{6,2}$, $f_{7,1}\mathscr{Y}_{7,2}$, $f_{8,2}\mathscr{Y}_{8,1}$, $f_{9,2}\mathscr{Y}_{9,1}$, $f_{10,1}\mathscr{Y}_{10,2}$. It therefore follows that the

matrix elements of V_{12} from any member of one of these groups to any member of the other must vanish. (The corresponding elements of V_{23} and V_{31} need *not* be zero.)

Still other elements can be seen to vanish from the behaviour of the potential operators under separate rotations of the space and the spin coordinates. Thus all the central potentials are scalars with respect to both the space and the spin variables. Hence there are no central force cross terms between states of different orbital angular momentum L, or between doublet states and quartet states. Similar considerations hold for tensor and $\mathbf{L} \cdot \mathbf{S}$ forces, and these will be discussed in detail in sections 3.3 and 3.4.

For convenience the potential energy matrices will be partitioned into submatrices according to the value of the orbital angular momentum L. Thus each matrix will be written in the form

$$\begin{array}{c} \begin{matrix} 123 & 4567 & 8910 \end{matrix} \\ \begin{pmatrix} V_{SS} & V_{SP} & V_{SD} \\ V_{PS} & V_{PP} & V_{PD} \\ V_{DS} & V_{DP} & V_{DD} \end{pmatrix} \end{array} \begin{matrix} 123 \\ 4567 \\ 8910 \end{matrix}$$

3.1. THE CENTRAL FORCES

As was shown in the previous section, all central force matrix elements of the types S—P, P—D, D—S, doublet-quartet, are zero.

The matrix elements of the exchange operators follow immediately from the eigenfunctions of P_{12}^{M} listed in the previous section. They are

$$(\text{even})_{SS} = \begin{array}{c} \begin{matrix} 1 & 2 & 3 \end{matrix} \\ \begin{pmatrix} 1 & & \\ & \cdot & \\ & & \begin{matrix} \cdot & \cdot \\ \cdot & 1 \end{matrix} \end{pmatrix} \end{array} \qquad (\text{odd})_{SS} = \begin{array}{c} \begin{matrix} 1 & 2 & 3 \end{matrix} \\ \begin{pmatrix} \cdot & & \\ & 1 & \\ & & \begin{matrix} 1 & \cdot \\ \cdot & \cdot \end{matrix} \end{pmatrix} \end{array} \begin{matrix} 1 \\ 2 \\ 3 \end{matrix} \qquad (10)$$

$$(\text{even})_{PP} = \begin{array}{c} \begin{matrix} 4 & 5 & 6 & 7 \end{matrix} \\ \begin{pmatrix} \cdot & & & \\ & 1 & & \\ & & \begin{matrix} 1 & \cdot \\ \cdot & \cdot \end{matrix} & \\ & & & \begin{matrix} 1 & \cdot \\ \cdot & \cdot \end{matrix} \end{pmatrix} \end{array} \qquad (\text{odd})_{PP} = \begin{array}{c} \begin{matrix} 4 & 5 & 6 & 7 \end{matrix} \\ \begin{pmatrix} 1 & & & \\ & \cdot & & \\ & & \begin{matrix} \cdot & \cdot \\ \cdot & 1 \end{matrix} & \\ & & & \begin{matrix} \cdot & \cdot \\ \cdot & 1 \end{matrix} \end{pmatrix} \end{array} \begin{matrix} 4 \\ 5 \\ 6 \\ 7 \end{matrix}$$

$$(\text{even})_{DD} = \begin{array}{c} \begin{matrix} 8 & 9 & 10 \end{matrix} \\ \begin{pmatrix} \cdot\ \cdot & & \\ \cdot\ 1 & & \\ & \cdot\ \cdot & \\ & \cdot\ 1 & \\ & & 1\ \cdot \\ & & \cdot\ \cdot \end{pmatrix} \end{array} \qquad (\text{odd})_{DD} = \begin{array}{c} \begin{matrix} 8 & 9 & 10 \end{matrix} \\ \begin{pmatrix} 1\ \cdot & & \\ \cdot\ \cdot & & \\ & 1\ \cdot & \\ & \cdot\ \cdot & \\ & & \cdot\ \cdot \\ & & \cdot\ 1 \end{pmatrix} \end{array} \begin{matrix} 8 \\ 9 \\ 10 \end{matrix}$$

As with the kinetic energy matrices, elements corresponding to mixed representation states are grouped together into submatrices; a dot or a blank space indicates a zero element.

The spin states q_1 and q_3 are triplet in particles 1 and 2, while q_2 is singlet [1]). This leads to the following matrix elements for the operators (singlet)$=\frac{1}{4}(1-\boldsymbol{\sigma}_1 \cdot \boldsymbol{\sigma}_2)$ and

(central triplet) $= \frac{1}{4}(3+\boldsymbol{\sigma}_1 \cdot \boldsymbol{\sigma}_2)$:

$$(\text{singlet})_{SS} = \begin{array}{c} \begin{matrix} 1 & 2 & 3 \end{matrix} \\ \begin{pmatrix} \frac{1}{2} & \cdot & \cdot & \frac{1}{2} \\ \cdot & \frac{1}{2} & \frac{1}{2} & \cdot \\ \cdot & \frac{1}{2} & \frac{1}{2} & \cdot \\ \frac{1}{2} & \cdot & \cdot & \frac{1}{2} \end{pmatrix} \end{array} \begin{matrix} 1 \\ 2 \\ 3 \end{matrix} \tag{11}$$

$$\begin{matrix} (\text{central}) \\ (\text{triplet})_{SS} \end{matrix} = \begin{array}{c} \\ \begin{pmatrix} \frac{1}{2} & \cdot & \cdot & -\frac{1}{2} \\ \cdot & \frac{1}{2} & -\frac{1}{2} & \cdot \\ \cdot & -\frac{1}{2} & \frac{1}{2} & \cdot \\ -\frac{1}{2} & \cdot & \cdot & \frac{1}{2} \end{pmatrix} \end{array} \begin{matrix} 1 \\ 2 \\ 3 \end{matrix}$$

$$(\text{singlet})_{PP} = \begin{array}{c} \begin{matrix} 4 & 5 & 6 & 7 \end{matrix} \\ \begin{pmatrix} \frac{1}{2} & \cdot & \cdot & -\frac{1}{2} & \cdot & \cdot \\ \cdot & \frac{1}{2} & \frac{1}{2} & \cdot & \cdot & \cdot \\ \cdot & \frac{1}{2} & \frac{1}{2} & \cdot & \cdot & \cdot \\ -\frac{1}{2} & \cdot & \cdot & \frac{1}{2} & \cdot & \cdot \\ \cdot & \cdot & \cdot & \cdot & \cdot & \cdot \\ \cdot & \cdot & \cdot & \cdot & \cdot & \cdot \end{pmatrix} \end{array} \begin{matrix} 4 \\ 5 \\ 6 \\ \\ 7 \\ \end{matrix}$$

$$\begin{matrix} & 4 & 5 & & 6 & & 7 & \\ (\text{central}) & & & & & & & \\ (\text{triplet})_{PP} = & \begin{pmatrix} \frac{1}{2} & . & . & \frac{1}{2} & . & . \\ . & \frac{1}{2} & -\frac{1}{2} & . & . & . \\ . & -\frac{1}{2} & \frac{1}{2} & . & . & . \\ \frac{1}{2} & . & . & \frac{1}{2} & . & . \\ . & . & . & . & 1 & . \\ . & . & . & . & . & 1 \end{pmatrix} & \begin{matrix} 4 \\ 5 \\ 6 \\ \\ 7 \\ \end{matrix} \end{matrix}$$

$$(\text{singlet})_{DD} = 0 \qquad \begin{matrix} & 8 & 9 & 10 & \\ (\text{central}) & & & & \\ (\text{triplet})_{DD} = & \begin{pmatrix} 1 & . & & & \\ . & 1 & & & \\ & & 1 & . & \\ & & . & 1 & \\ & & & & 1 \quad . \\ & & & & . \quad 1 \end{pmatrix} & \begin{matrix} 8 \\ \\ 9 \\ \\ 10 \\ \end{matrix} \end{matrix}$$

The quartet P-state (number 7), and all three D-states are triplet in particles 1 and 2.

3.2. THE COULOMB ENERGY OF He^3

The operator

$$(\text{Coulomb}) = \frac{e^2}{r_{12}} [\tfrac{1}{2}+\tfrac{1}{2}(\tau_1)_\zeta][\tfrac{1}{2}+\tfrac{1}{2}(\tau_2)_\zeta]$$

gives the electrostatic interaction between particles 1 and 2. It vanishes unless both particles are protons. Though this operator is central, it does not commute with the total isobaric spin operator $(\tau_1+\tau_2+\tau_3)^2$. Consequently some $T = \frac{3}{2}$ states are mixed into the He^3 ground state, but these will be neglected.

For He^3, the probability that particles 1 and 2 are both protons is $\frac{2}{3}$ for the isobaric spin function v_1, and zero for the state v_2 [1]). This leads to the following matrix elements of the Coulomb energy between particles 1 and 2 in He^3:

$$(\text{Coulomb})_{SS} = \frac{e^2}{3r_{12}} \begin{matrix} & 1 & 2 & 3 & \\ & \begin{pmatrix} 1 & . & . & 1 \\ . & 1 & -1 & . \\ . & -1 & 1 & . \\ 1 & . & . & 1 \end{pmatrix} & \begin{matrix} 1 \\ 2 \\ \\ 3 \end{matrix} \end{matrix} \qquad (12)$$

$$(\text{Coulomb})_{PP} = \frac{e^2}{3r_{12}} \begin{array}{c} \begin{matrix} 4 & 5 & 6 & 7 \end{matrix} \\ \begin{pmatrix} 1 & . & . & 1 & . & . \\ . & 1 & 1 & . & . & . \\ . & 1 & 1 & . & . & . \\ 1 & . & . & 1 & . & . \\ . & . & . & . & . & . \\ . & . & . & . & . & 2 \end{pmatrix} \end{array} \begin{matrix} 4 \\ 5 \\ 6 \\ \\ 7 \end{matrix} \qquad (12)$$

$$(\text{Coulomb})_{DD} = \frac{e^2}{3r_{12}} \begin{array}{c} \begin{matrix} 8 & 9 & 10 \end{matrix} \\ \begin{pmatrix} 2 & . & & & & \\ . & . & & & & \\ & & 2 & . & & \\ & & . & . & & \\ & & & & . & . \\ & & & & . & 2 \end{pmatrix} \end{array} \begin{matrix} 8 \\ \\ 9 \\ \\ 10 \\ \end{matrix}$$

3.3. THE TENSOR FORCE

The tensor operator S_{12} may be written

$$S_{12} = \frac{3}{r_{12}^2}(\boldsymbol{\sigma}_1 \cdot \mathbf{r}_{12})(\boldsymbol{\sigma}_2 \cdot \mathbf{r}_{12}) - \boldsymbol{\sigma}_1 \cdot \boldsymbol{\sigma}_2 = \sum_{i,j=x,y,z} T_{ij} U_{ij} = \sum_{M=-2}^{2} (-1)^M T_M U_{-M}$$

where

$$T_{ij} = T_{ji} = \frac{3(\mathbf{r}_{12})_i (\mathbf{r}_{12})_j}{r_{12}^2} - \delta_{ij} \qquad i, j = x, y, z$$

$$U_{ij} = U_{ji} = \tfrac{1}{2}(\boldsymbol{\sigma}_1)_i (\boldsymbol{\sigma}_2)_j + \tfrac{1}{2}(\boldsymbol{\sigma}_1)_j (\boldsymbol{\sigma}_2)_i - \tfrac{1}{3}\delta_{ij}(\boldsymbol{\sigma}_1 \cdot \boldsymbol{\sigma}_2)$$

$$T_{\pm 2} = \tfrac{1}{2}(T_{xx} - T_{yy} \pm 2iT_{xy})$$

$$T_{\pm 1} = \mp T_{xz} - iT_{yz}$$

$$T_0 = 6^{-\frac{1}{2}}(2T_{zz} - T_{xx} - T_{yy}) = (\tfrac{3}{2})^{\frac{1}{2}} T_{zz},$$

with similar relations for the five components U_M.

Under rotations of space and spin coordinates respectively T_M and U_M transform as the covariant components of irreducible tensors belonging to the representation D^2 of the rotation group [5]). The $L = 0$ reduced part of T_{ij} vanishes because the trace of this tensor vanishes, while the symmetry under interchange of the indices i and j precludes any $L = 1$ part. Similarly, U_{ij} is a pure spin $S = 2$ operator.

Thus the tensor operator S_{12} is the "dot product" of the pure $L = 2$ space operator T_M with the pure $S = 2$ spin operator U_M. Hence the matrix elements

of S_{12} between a state of orbital angular L and total spin S, and a state with the values L' and S', will vanish unless

$$|L-L'| \leqq 2 \leqq L+L', \quad |S-S'| \leqq 2 \leqq S+S'.$$

These inequalities require that S-state to S-state, S-state to P-state, and doublet — doublet elements be zero. On the other hand the tensor operator will couple directly the predominant $^2S_{\frac{1}{2}}$ state to the $^4D_{\frac{1}{2}}$ states. The P-states will be connected with the S-states only to second order, via the D-states.

The detailed evaluation of the matrix elements of S_{12} by the techniques of Racah [6]) is given in ref. [3]). The elements involve the following quantities:

$$a = 3^{\frac{1}{2}} \cos 2\Theta = \frac{3^{\frac{1}{2}}}{\Delta}\left(\frac{16\Delta^2}{r_{12}^2} - R^2\right),$$

$$b = 3^{\frac{1}{2}} \sin 2\Theta = 3^{\frac{1}{2}} \frac{4\Delta}{\Delta r_{12}^2}\,(r_{23}^2 - r_{31}^2),$$

$$a^2 + b^2 = 3;$$

Θ is the angle between $\mathbf{r}_2 - \mathbf{r}_1$ and body-X axis, measured in a positive sense about the body-Z axis. Δ, Δ and R^2 were defined in section 2.1. The tensor force matrix elements are

(13)

	S			P				D					
	1	2	3	4	5	6	7	8	9	10			
1								.	−1	.	−a	b	.
2								1	.	a	.	.	b
3								−1	.	−a	.	.	−b
								.	1	.	a	−b	.
4				.	.	.	.	.	−1	.	.	−b	.	.	a
5					.	.	.	−1	.	.	.	.	b	a	.
6				.	.	.	.	1	.	.	.	.	−b	−a	.
7				.	.	.	.	.	−1	.	.	−b	.	.	a
				.	−1	1	.	1	.	.	.	.	b	a	.
				−1	.	.	−1	.	1	.	.	−b	.	.	a
8	.	1	−1	.	.	.	.	.	.	.	1	.	−a	.	.	−b
	−1	.	.	1	.	.	.	.	.	.	.	1	.	−a	b	.
9	.	a	−a	.	−b	.	.	−b	.	−b	−a	.	−1	.	.	.
	−a	.	.	a	.	b	−b	.	b	.	.	−a	.	−1	.	.
10	b	.	.	−b	.	a	−a	.	a	.	.	b	.	.	−1	.
	.	b	−b	.	a	.	.	a	.	a	−b	.	.	.	.	−1

S P D

As a check on the matrix elements of S_{12}, we note that the identity $S_{12}^2 = 2(3+\boldsymbol{\sigma}_1 \cdot \boldsymbol{\sigma}_2 - S_{12})$ is satisfied by the matrix given above.

3.4. THE $\mathbf{L} \cdot \mathbf{S}$ FORCE

In this section we consider the matrix elements of the operator $\mathbf{L}_{12} \cdot (\mathbf{s}_1+\mathbf{s}_2)$, where

$$\mathbf{L}_{12} = (\mathbf{r}_1-\mathbf{r}_2)\times\tfrac{1}{2}(\mathbf{p}_1-\mathbf{p}_2) = (\mathbf{r}_1-\mathbf{r}_2)\times -\tfrac{1}{2}i\hbar(\boldsymbol{\nabla}_1-\boldsymbol{\nabla}_2),$$
$$\mathbf{s}_1 = \tfrac{1}{2}\hbar\boldsymbol{\sigma}_1, \qquad \mathbf{s}_2 = \tfrac{1}{2}\hbar\boldsymbol{\sigma}_2.$$

The operator $\mathbf{L}_{12} \cdot (\mathbf{s}_1+\mathbf{s}_2)$ is the scalar product of the pure $L = 1$ space operator $\mathbf{L}_{12}$ with the pure $S = 1$ spin operator $(\mathbf{s}_1+\mathbf{s}_2)$. Hence the "selection rules" for non-vanishing matrix elements between two states with orbital and spin angular momenta L, S and L', S' respectively are

$$|L-L'| \leqq 1 \leqq L+L', \quad |S-S'| \leqq 1 \leqq S+S'.$$

Therefore S-state to S-state, and S-state to D-state matrix elements are zero. In contrast to the tensor force, the operator $\mathbf{L}_{12} \cdot (\mathbf{s}_1+\mathbf{s}_2)$ connects the P-states directly to the S-states.

In terms of a general set of coordinates, X^1, X^2, $-$, X^9, the differential operator $\mathbf{L}_{12}$ is given by

$$\mathbf{L}_{12} = \sum_{i=1}^{9} (\mathbf{L}_{12}X^i)\,\frac{\partial}{\partial X^i}.$$

Applying this result to our coordinates r_{23}, r_{31}, r_{12}, α, β, γ, $\mathbf{r}_G$, we obtain

$$\mathbf{L}_{12} = \hat{\mathbf{z}}\left[i\hbar\Delta\left(\frac{1}{r_{23}}\frac{\partial}{\partial r_{23}} - \frac{1}{r_{31}}\frac{\partial}{\partial r_{31}}\right) - \tfrac{3}{2}\frac{r_{12}^2}{\Lambda}\cos 2\Theta\, L_6\right]$$
$$+ \frac{\hat{\mathbf{x}}\sin\Theta+\hat{\mathbf{y}}\cos\Theta}{\sin\eta}\,[\cos(\eta-\Theta)\,L_4+\sin(\eta-\Theta)\,L_5];$$

$\hat{\mathbf{x}}$, $\hat{\mathbf{y}}$, $\hat{\mathbf{z}}$ are the unit vectors along the body axes, and L_4, L_5, and L_6 the body axes components of the total orbital angular momentum operator (see eq. (6)); Θ is the angle between $\mathbf{r}_2-\mathbf{r}_1$ and the body-X axis, and η the angle between $\mathbf{r}_2-\mathbf{r}_1$ and $\mathbf{r}_3-\frac{1}{2}(\mathbf{r}_1+\mathbf{r}_2)$; these angles are measured in a positive sense about the body-Z axis. We have the relations

$$\cos 2\Theta = \frac{1}{\Lambda}\left(\frac{16\Delta^2}{r_{12}^2} - R^2\right), \qquad \sin 2\Theta = \frac{4\Delta}{\Lambda r_{12}^2}(r_{23}^2-r_{31}^2),$$
$$\sin\eta = \frac{2\Delta}{\rho r_{12}}, \qquad \cos\eta = -\frac{(r_{23}^2-r_{31}^2)}{2\rho r_{12}},$$

where

$$\rho = |\mathbf{r}_3 - \tfrac{1}{2}(\mathbf{r}_1+\mathbf{r}_2)| = \tfrac{1}{2}(2r_{23}^2+2r_{31}^2-r_{12}^2)^{\frac{1}{2}}.$$

The detailed evaluation of the matrix elements of $\mathbf{L}_{12}\cdot(\mathbf{s}_1+\mathbf{s}_2)$ by the techniques of Racah [6]) is given in ref. [3]). It is convenient to introduce the following quantities:

$$B = \Delta\left(\frac{1}{r_{23}}\frac{\partial}{\partial r_{23}} - \frac{1}{r_{31}}\frac{\partial}{\partial r_{31}}\right),$$

$$C = B - \tfrac{1}{2}\cot\eta, \qquad E = B + \tfrac{1}{2}\cot\eta,$$

$$c = (\tfrac{3}{4})^{\frac{1}{2}}\frac{\cos(2\Theta-\eta)}{\sin\eta} = (\tfrac{3}{4})^{\frac{1}{2}}\frac{R^2}{4\Delta\Lambda}(r_{23}^2-r_{31}^2),$$

$$d = (\tfrac{3}{4})^{\frac{1}{2}}\frac{\sin(2\Theta-\eta)}{\sin\eta} = (\tfrac{3}{4})^{\frac{1}{2}}\frac{1}{\Lambda}(2r_{12}^2-r_{23}^2-r_{31}^2),$$

$$e = B\Theta - \tfrac{5}{4} \qquad = \tfrac{3}{2}\frac{r_{12}^2}{\Lambda}\cos 2\Theta - \tfrac{1}{4}.$$

The differential operator E is antihermitian.

In terms of the above quantities, the matrix elements are

$$\mathbf{L}_{12}\cdot(\mathbf{s}_1+\mathbf{s}_2)_{SS} = 0, \tag{14}$$

$$\mathbf{L}_{12}\cdot(\mathbf{s}_1+\mathbf{s}_2)_{PS} = \mathbf{L}_{12}\cdot(\mathbf{s}_1+\mathbf{s}_2)_{SP}^{+},$$

$$= \tfrac{1}{3}\hbar^2 B \begin{array}{c} \begin{array}{cccc} 1 & 2 & 3 & \end{array} \\ \begin{pmatrix} . & -1 & 1 & . \\ -1 & . & . & 1 \\ 1 & . & . & -1 \\ . & -1 & 1 & . \\ -1 & . & . & 1 \\ . & -1 & 1 & . \end{pmatrix} \end{array} \begin{array}{l} 4 \\ 5 \\ 6 \\ \\ 7 \\ \end{array}$$

$$\mathbf{L}_{12}\cdot(\mathbf{s}_1+\mathbf{s}_2)_{PP} = \tfrac{1}{6}\hbar^2 \begin{array}{c} \begin{array}{cccccc} 4 & 5 & 6 & & 7 & \end{array} \\ \begin{pmatrix} -2 & . & . & -2 & . & 1 \\ . & -2 & 2 & . & 1 & . \\ . & 2 & -2 & . & -1 & . \\ -2 & . & . & -2 & . & 1 \\ . & 1 & -1 & . & -5 & . \\ 1 & . & . & 1 & . & -5 \end{pmatrix} \end{array} \begin{array}{l} 4 \\ 5 \\ 6 \\ \\ 7 \\ \end{array}$$

$$\mathbf{L}_{12}\cdot(\mathbf{s}_1+\mathbf{s}_2)_{DS}=\mathbf{L}_{12}\cdot(\mathbf{s}_1+\mathbf{s}_2)^{+}_{SD}=0,$$

$$\mathbf{L}_{12}\cdot(\mathbf{s}_1+\mathbf{s}_2)_{DP}=\mathbf{L}_{12}\cdot(\mathbf{s}_1+\mathbf{s}_2)^{+}_{PD}$$

$$= \tfrac{1}{3}\hbar^2 \begin{array}{c} \begin{matrix} 4 & 5 & 6 & 7 \end{matrix} \\ \begin{pmatrix} -C & . & . & -C & . & -C \\ . & C & -C & . & C & . \\ -c & . & . & -c & . & -c \\ . & c & -c & . & c & . \\ . & -d & d & . & -d & . \\ -d & . & . & -d & . & -d \end{pmatrix} \end{array} \begin{matrix} \\ \\ 8 \\ \\ 9 \\ \\ 10 \end{matrix}$$

$$\mathbf{L}_{12}\cdot(\mathbf{s}_1+\mathbf{s}_2)_{DD}=\hbar^2 \begin{array}{c} \begin{matrix} 8 & 9 & 10 \end{matrix} \\ \begin{pmatrix} -\frac{3}{2} & . & d & . & . & -c \\ . & -\frac{3}{2} & . & d & c & . \\ d & . & 2e & . & . & -E \\ . & d & . & 2e & E & . \\ . & c & . & -E & 2e & . \\ -c & . & E & . & . & 2e \end{pmatrix} \end{array} \begin{matrix} \\ 8 \\ \\ 9 \\ \\ 10 \end{matrix}$$

3.5. DISCUSSION

The potentials of most importance in the triton ground state are those with non-zero matrix elements to the predominant S-state, number 1. These potentials, and the corresponding matrix elements, are listed below:

Potential	Matrix Elements
$\frac{1}{2}$(singlet-even)+$\frac{1}{2}$(central-triplet-even)	1–1
$\frac{1}{2}$(singlet-even)−$\frac{1}{2}$(central-triplet-even)	1–3
(tensor-even)	1–8, 1–9, 1–10
($\mathbf{L}\cdot\mathbf{S}$-even)	1–5, 1–6, 1–7

No odd potential can have matrix elements to S-state number 1, since this state is completely symmetric in all space coordinates. Thus the calculated binding energy of H^3 should not depend markedly on what assumptions are made about the ill-determined odd-state forces.

It will be noted that the matrix element 1–3 involves the difference of the (central) potentials in the singlet-even and the triplet-even states. This means that the mixed symmetry S-state number 3 will not be important if these two potentials are nearly equal. This is the case with the potentials discussed by Pease and Feshbach [7]). P-state number 5 is also unimportant, though $\mathbf{L}\cdot\mathbf{S}$

forces connect it directly to the main S-state. This P-state is completely antisymmetric in the internal coordinates r_{12}, r_{23}, r_{31}, and therefore has a very high kinetic energy [1]).

4. Asymptotic Behaviour near the In-Line and Equilateral Positions

When the three particles lie along a straight line the body-X and body-Z axes are undefined; according to how we approach the in-line position these axes may assume any pair of mutually perpendicular directions in the plane normal to the line of the particles (the body-Y axis). Similarly, when the three particles form an equilateral triangle the inertia ellipse degenerates to a circle, and the body-X and body-Y axes may take any pair of mutually perpendicular directions in the plane of the triangle. Unless special conditions are imposed on the radial wave functions f near these singular configurations the wave function will be discontinuous (in Cartesian coordinates) and the kinetic energy integrals diverge.

To derive these conditions it is convenient to replace the internal coordinates r_{23}, r_{31}, r_{12} by the following set:

$$\begin{aligned} \Delta &= \text{area of the triangle,} \\ F &= 3^{-\frac{1}{2}}(r_{23}^2+r_{31}^2-2r_{12}^2), \\ G &= r_{23}^2-r_{31}^2. \end{aligned}$$

We have the relations

$$\Delta^2 = 3(F^2+G^2), \qquad R^4 = 48\Delta^2+3(F^2+G^2);$$

Δ, F and G are orthogonal in the sense that the S-state kinetic energy operator T_S, eq. (7), involves no cross derivatives when expressed in these coordinates:

$$T_S = -4R^2\left[\frac{1}{16\Delta}\frac{\partial}{\partial\Delta}\left(\Delta\frac{\partial}{\partial\Delta}\right)+\frac{\partial^2}{\partial F^2}+\frac{\partial^2}{\partial G^2}\right].$$

In addition, the domains of variation are quite independent: $\Delta > 0$, F and G take all real values. In these coordinates the two singular configurations are

(i) in-line position, $\Delta = 0$: F and G arbitrary.

(ii) equilateral position, $F = 0$, $G = 0$: Δ arbitrary.

We shall assume that the potential and its derivatives are continuous everywhere, except possibly at the hard core (or if there be no core, except when two particles coincide).

4.1. THE IN-LINE POSITION, $\Delta = 0$

Let us attempt a formal solution of the Schrödinger equation in the neighbourhood of $\Delta = 0$, where each radial wave function has the form

$$f(r_{23}, r_{31}, r_{12}) = \Delta^c \sum_{s=0}^{\infty} A_s(F, G)\Delta^s,$$

with $A_0(F, G) \neq 0$. Direct substitution in the Schrödinger equation then gives the values of the constants c for the different radial wave functions f. In this way we obtain, as $\Delta \to 0$,

$$\begin{aligned} f_1, f_2, f_3, f_8, f_9 &\approx 1+O(\Delta^2, \Delta^4, -), \\ f_4, f_5, f_6, f_7, f_{10} &\approx \Delta+O(\Delta^3, \Delta^5, -), \\ 3^{\frac{1}{2}}f_8+f_9 &\approx \Delta^2+O(\Delta^4, \Delta^6, -). \end{aligned} \tag{15}$$

4.2. THE EQUILATERAL POSITION, $F = 0$, $G = 0$

If we attempt a formal power series expansion of the internal wave functions of the form

$$f(r_{23}, r_{31}, r_{12}) = \Lambda^c \sum_{s,t} A_{st}(\Delta) F^s G^t$$

we obtain †, as $F \to 0$ and $G \to 0$,

$$\begin{aligned} f_1, f_4 &\approx 1+O(F^2, FG, G^2), \\ f_2, f_5 &\approx 3F^2G-G^3+O(F^5, F^4G, F^3G^2, \ldots), \\ f_3, f_6, f_7, f_8 &\approx \left[\begin{pmatrix} F \\ G \end{pmatrix} + O(F^2, FG, G^2)\right], \\ f_9, f_{10} &\approx \frac{1}{\Lambda}\left[\begin{pmatrix} F \\ G \end{pmatrix} + O(F^2, FG, G^2)\right], \\ f_9-f_{10} &\approx \frac{1}{\Lambda}\left[\begin{pmatrix} G^2-F^2 \\ 2FG \end{pmatrix} + O(F^3, F^2G, FG^2, G^3)\right], \\ f_9+f_{10} &\approx \frac{1}{\Lambda}\left[\begin{pmatrix} F \\ G \end{pmatrix} + O(F^3, F^2G, FG^2, G^3)\right]. \end{aligned} \tag{16}$$

It should be noted that the expression for f_9-f_{10} contains no linear terms in F or G, while that for f_9+f_{10} has no quadratic terms.

The results eq. (15) and (eq. (16) are also obtained if we insist that the wave function should possess a Taylor expansion in Cartesian coordinates about every point where the potential is regular. This condition is stronger than is necessary to ensure that the kinetic energy operator be hermitian. However, the energy computed by the variation method would not be lowered by permitting the wave function discontinuities at a set of points of zero measure; such more general functions can be approached as closely as we please by a sequence of regular functions.

† By f_9 is meant the two-row matrix $\begin{pmatrix} f_{9,1} \\ f_{9,2} \end{pmatrix}$, with similar meanings for the other pairs of mixed representation functions f_6, f_7, f_8, f_9, f_{10}.

5. Summary

The matrix elements of the kinetic energy operator between the total angular momentum and isobaric spin states of the triton are given by eq. (9). There is no coupling between states of different orbital angular momentum L, or between different S-states, or between different P-states. On the other hand the kinetic energy operator couples together all three D-states. In order that the kinetic energy integrals converge, the radial wave functions must satisfy eq. (15) near the in-line position, and eq. (16) near the equilateral position.

Eqs. (10), (11), (12), (13) and (14) give the matrix elements of the common potential energy operators. Unlike the kinetic energy, the non-central tensor and $\mathbf{L} \cdot \mathbf{S}$ forces couple together states of different orbital angular momentum. The predominant S-state (number 1) is connected directly to the mixed symmetry S-state number 3 by spin-dependent forces, to P-states 5, 6, and 7 by $\mathbf{L} \cdot \mathbf{S}$ forces, and to D-states 8, 9 and 10 by tensor forces. Little information about odd-state forces can be expected from the triton ground state, since only even-state forces possess matrix elements to S-state number 1.

The author is greatly indebted to Professor J. M. Blatt for suggesting the problem and for his constant help and encouragement. He also wishes to thank the Australian Atomic Energy Commission and the University of Sydney Research Committee for research grants during 1958 and 1959 respectively.

Finally he has much pleasure in thanking Professor H. Messel for the excellent research facilities afforded him in the School of Physics, The University of Sydney.

References

1) G. Derrick and J. M. Blatt, Nuclear Physics **8** (1958) 310
2) H. Goldstein, Classical Mechanics (Addison-Wesley, Cambridge, Mass., 1950) Ch. 4
3) G. H. Derrick, Thesis, University of Sydney (1959)
4) P. G. Bergmann, Introduction to the Theory of Relativity (Prentice-Hall, New York, 1942) Ch. V
5) E. P. Wigner, Gruppentheorie (Vieweg, Braunschweig, 1931) Chs. XIV, XV
6) G. Racah, Phys. Rev. **62** (1942) 438
7) R. L. Pease, Thesis, M.I.T. (1950);
R. L. Pease and H. Feshbach, Phys. Rev. **81** (1951) 142L

1.D.1:
6.D

Nuclear Physics **16** (1960) 423—431; © *North-Holland Publishing Co., Amsterdam*
Not to be reproduced by photoprint or microfilm without written permission from the publisher

METHOD FOR SEPARATING THE RELATIVE MOTION OF TWO NUCLEONS IN OSCILLATOR POTENTIAL WELL

V. V. BALASHOV and V. A. ELTEKOV

Research Institute of Nuclear Physics of the Moscow University, Moscow

Received 29 August 1959

Abstract: Invariant coefficients independent of magnetic quantum numbers are introduced for separating the relative motion of two nucleons in an oscillator potential well ("generalized Talmi coefficients"). Tables of these coefficients are given for the first oscillator states including 3p and 3f shells.

1. Introduction

Oscillator wave functions have found wide application in shell model calculations. Their main advantage is that they allow one to separate in a simple way the variables of the relative and the centre-of-mass motions of two particles in a potential well. Application of the oscillator function to nuclear spectroscopy was treated in detail by Talmi [1]). In particular, he pointed out a method for separating the relative motion of two nucleons. However, the coefficients introduced by Talmi are rather inconvenient in practice. They depend on the magnetic quantum numbers which are not integrals of the motion and therefore the separation of variables in a state with definite integrals of motion requires cumbersome calculations involving Clebsch-Gordan coefficients.

We shall introduce new, generalized Talmi coefficients which do not depend on the magnetic quantum numbers and allow us to separate the centre-of-gravity motion of two nucleons from their relative motion directly in a state with a definite total angular momentum (sec. 2). The properties of these coefficients are treated in sec. 3. Sec. 4 deals with the calculation of matrix elements of the pair interaction operator of nucleons with the help of Talmi coefficients. Calculation of such matrix elements presents a topical problem which is usualli solved by the Slater method [2]). The latter is effective only in calculations connected with central forces and it becomes very much involved in calculating matrix elements of tensor and spin-orbit forces. Contrary to the Slater method, the Talmi method is equally valid for central and non-central forces since it reduces the task to evaluating matrix elements corresponding to the states of relative motion. It proves to be particularly valuable in investigating the properties of nucleon-nucleon interactions in a nucleus on the basis of the experimental values of nuclear levels [3]).

Apparently, the oscillator approximation holds only for light nuclei. Therefore, one may expect that the Talmi coefficients calculated below for the first oscillator states (up to 3p and 3f-shells) would cover the entire range of the oscillator model which is of practical interest.

2. Generalized Talmi Coefficients

Let us consider the Hamiltonian of two non-interacting nucleons moving in an oscillator potential well:

$$H = \frac{1}{2m}(p_1^2+m^2\omega^2 r_1^2)+\frac{1}{2m}(p_2^2+m^2\omega^2 r_2^2) = H_1+H_2. \tag{1}$$

Passing to the variables of the centre-of-gravity and the relative motion

$$\mathbf{R} = \tfrac{1}{2}(\mathbf{r}_1+\mathbf{r}_2), \qquad \mathbf{P} = \mathbf{p}_1+\mathbf{p}_2, \qquad \mathbf{r} = \mathbf{r}_2-\mathbf{r}_1, \qquad \mathbf{p} = \tfrac{1}{2}(\mathbf{p}_2-\mathbf{p}_1), \tag{2}$$

we obtain

$$H = \frac{1}{2M}(P^2+M^2\omega^2 R^2)+\frac{1}{2\mu}(p^2+\mu^2\omega^2 r^2) = H_{\mathrm{cg}}+H_{\mathrm{rel}}, \tag{3}$$

where

$$M = 2m, \quad \mu = \tfrac{1}{2}m.$$

Suppose $\Psi^{n_1}_{l_1m_1}(\mathbf{r}_1)$ and $\Psi^{n_2}_{l_2m_2}(\mathbf{r}_2)$ are the eigenfunctions of the Hamiltonians H_1 and H_2:

$$(H_1-E_{n_1})\Psi^{n_1}_{l_1m_1}(\mathbf{r}_1) = 0. \qquad (H_2-E_{n_2})\Psi^{n_2}_{l_2m_2}(\mathbf{r}_2) = 0. \tag{4}$$

Here l and m are the orbital moment of a nucleon and its z-component, n is the principal quantum number †: $E_n = \hbar\omega(n+\frac{3}{2})$.

The possibility of separating the variables of the relative and centre-of-gravity motion in (3) makes it possible to reduce the product of functions $\Psi^{n_1}_{l_1m_1}(\mathbf{r}_1)$ and $\Psi^{n_2}_{l_2m_2}(\mathbf{r}_2)$ to products of functions $\Psi^{N}_{\lambda M}(\mathbf{R})$ and $\Psi^{n}_{\Lambda m}(\mathbf{r})$ which are the eigenfunctions of operators H_{cg} and H_{rel}:

$$\Psi^{n_1}_{l_1m_1}(\mathbf{r}_1)\Psi^{n_2}_{l_2m_2}(\mathbf{r}_2) \to \Psi^{N}_{\lambda M}(\mathbf{R})\Psi^{n}_{\Lambda m}(\mathbf{r}). \tag{5}$$

It is to be noted that the $\Psi^{n}_{\Lambda m}(\mathbf{r})$ state is more "spread", while the $\Psi^{N}_{\lambda M}(\mathbf{R})$ state is more "concentrated", than a single-particle state: the parameter of well "width" r_0 which determines the rate of decrease of the radial functions $\exp(-r^2/2r_0^2)$ is equal to $(\hbar/m\omega)^{\frac{1}{2}}$ for single-particle functions, to $(2\hbar/m\omega)^{\frac{1}{2}}$ for functions of relative motion and to $(\hbar/2m\omega)^{\frac{1}{2}}$ for the centre-of-gravity functions.

The generalized Talmi coefficients $\langle {}^{n_1l_1}_{n_2l_2}|TSL|^{N\lambda}_{n\Lambda}\rangle$ are determined by the

† Our n is different from Talmi's [1]): $n = 2n_{\mathrm{Talmi}}+l$. In this connection we shall use the following spectroscopic notations for the sequence of oscillator states: 0s; 1p; 2s, 2d; 3p, 3f; 4s, 4d, 4g; 5o, 5f, 5h; 6s, 6d, 6g, 6i; ...

relation

$$|(n_1l_1)(n_2l_2) : TSL\mathscr{M}\rangle =$$

$$= \sum_{\substack{\Lambda\lambda M \\ n\Lambda m}} \left\langle \begin{matrix} n_1l_1 \\ n_2l_2 \end{matrix} \middle| TSL \middle| \begin{matrix} N\lambda \\ n\Lambda \end{matrix} \right\rangle \langle \lambda M, \Lambda m : L\mathscr{M}\rangle \Psi^N_{\lambda M}(\mathbf{R})\Psi^n_{\Lambda m}(\mathbf{r}). \quad (6)$$

Here $\langle \lambda M, \Lambda m : L\mathscr{M}\rangle$ is a Clebsch-Gordan coefficient, $|(n_1l_1)(n_2l_2) : TSL\mathscr{M}\rangle$ is the orbital function of a two-nucleon state in the (n_1l_1) and (n_2l_2) shells with a total orbital angular momentum L and its z-component $\mathscr{M}$, isobaric spin T and spin S; T and S indicate the parity of the orbital function: in accordance with the Pauli principle it is odd for even $T+S$ and even for odd $T+S$.

The coefficients $\left\langle \begin{matrix} n_1l_1 \\ n_2l_2 \end{matrix} \middle| TSL \middle| \begin{matrix} N\lambda \\ n\Lambda \end{matrix} \right\rangle$ are related to the transformation coefficients (5) introduced in ref. [1]) by the simple relation

$$\left\langle \begin{matrix} n_1l_1 \\ n_2l_2 \end{matrix} \middle| TSL \middle| \begin{matrix} N\lambda \\ n\Lambda \end{matrix} \right\rangle$$

$$= \sum_{\substack{m_1, m_2 \\ M, m}} \langle l_1m_1, l_2m_2 : L\mathscr{M}\rangle \langle \lambda M, \Lambda m : L\mathscr{M}\rangle \left\langle \begin{matrix} n_1l_1m_1 \\ n_2l_2m_2 \end{matrix} \middle| ST \middle| \begin{matrix} N\lambda M \\ n\Lambda m \end{matrix} \right\rangle. \quad (7)$$

Since the generalized Talmi coefficients are independent of $\mathscr{M}$, it is evidently unnecessary to calculate coefficients $\left\langle \begin{matrix} n_1l_1m_1 \\ n_2l_2m_2 \end{matrix} \middle| ST \middle| \begin{matrix} N\lambda M \\ n\Lambda m \end{matrix} \right\rangle$ with different values $m_1+m_2 = M+m = \mathscr{M}$.

With the help of eq. (6) it is easy to obtain the formula for expanding the relative motion in functions of the two nucleon states with definite total angular momentum J, these functions depending on all the space, spin and isospin variables:

$$|(n_1l_1)(n_2l_2) : {}^{2T+1,\,2S+1}L_{JM}\rangle$$

$$= \sum \langle \lambda\mu, J_0M_0 : JM\rangle U(\lambda\Lambda jS : LJ_0) \left\langle \begin{matrix} n_1l_1 \\ n_2l_2 \end{matrix} \middle| TSL \middle| \begin{matrix} N\lambda \\ n\Lambda \end{matrix} \right\rangle$$

$$\times |n\Lambda TSJ_0M_0(\mathbf{r})\rangle \cdot \Psi^N_{\lambda\mu}(\mathbf{R}). \quad (8)$$

Here $|n\Lambda TSJ_0M_0(\mathbf{r})\rangle$ is the function of the relative motion of two nucleons with total angular momentum J_0 and its Z-component M_0, principal quantum number n, orbital quantum number l, spin S, and isobaric spin T; $U(abcd : ef) = \sqrt{(2e+1)(2f+1)}W(abcd : ef)$ is the Racah coefficient [4]).

3. Properties of Generalized Talmi Coefficients

1) $$n_1+n_2 = N+n.$$

2) $$\sum_{N\lambda,\, n\Lambda} \left\langle \begin{matrix} n_1l_1 \\ n_2l_2 \end{matrix} \middle| TSL \middle| \begin{matrix} N\lambda \\ n\Lambda \end{matrix} \right\rangle^2 = 1.$$

3) $$\left\langle \begin{matrix} n_1l_1 \\ n_2l_2 \end{matrix} \middle| TSL \middle| \begin{matrix} N\lambda \\ n\Lambda \end{matrix} \right\rangle = 0, \quad \text{if} \quad T+S+\Lambda \text{ is even.}$$

TABLE 1. Tables of generalized Talmi coefficients

$S+T$ even $\quad n_1+n_2=2$

	$N\lambda, n\Lambda$ / n_1l_1, n_2l_2	1p 1p
$L=0$	2s 0s	1
$L=1$	1p 1p	1
$L=2$	2d 0s	1

$S+T$ odd $\quad n_1+n_2=2$

	$N\lambda, n\Lambda$ / n_1l_1, n_2l_2	2s 0s	0s 2s	2d 0s	0s 2d
$L=0$	2s 0s	$\frac{1}{\sqrt{2}}$	$\frac{1}{\sqrt{2}}$	–	–
	1p 1p	$\frac{1}{\sqrt{2}}$	$-\frac{1}{\sqrt{2}}$	–	–
$L=2$	2d 0s	–	–	$\frac{1}{\sqrt{2}}$	$\frac{1}{\sqrt{2}}$
	1p 1p	–	–	$\frac{1}{\sqrt{2}}$	$-\frac{1}{\sqrt{2}}$

$S+T$ odd $\quad n_1+n_2=3$

	$N\lambda, n\Lambda$ / n_1l_1, n_2l_2	1p 2s	3p 0s	1p 2d	3f 0s
$L=1$	2s 1p	$\frac{1}{6}$	$\frac{1}{2}\sqrt{\frac{5}{3}}$	$-\frac{\sqrt{5}}{3}$	–
	2d 1p	$-\frac{\sqrt{5}}{3}$	$\frac{1}{\sqrt{3}}$	$\frac{1}{3}$	–
	3p 0s	$\frac{1}{2}\sqrt{\frac{5}{3}}$	$\frac{1}{2}$	$\frac{1}{\sqrt{3}}$	–
$L=2$	2d 1p	–	–	1	–
$L=3$	2d 1p	–	–	$\frac{1}{2}$	$-\frac{\sqrt{3}}{2}$
	3f 0s	–	–	$\frac{\sqrt{3}}{2}$	$\frac{1}{2}$

$S+T$ even $\quad n_1+n_2=4$

	$N\lambda, n\Lambda$ / n_1l_1, n_2l_2	3p 1p	1p 3p	3f 1p	1p 3f
$L=0$	3p 1p	$-\frac{1}{\sqrt{2}}$	$\frac{1}{\sqrt{2}}$	–	–
$L=1$	3p 1p	$-\frac{1}{\sqrt{2}}$	$-\frac{1}{\sqrt{2}}$	–	–
	2d 2d	$\frac{1}{\sqrt{2}}$	$-\frac{1}{\sqrt{2}}$	–	–
$L=2$	3p 1p	$-\frac{\sqrt{2}}{5}$	$\frac{\sqrt{2}}{5}$	$-\frac{1}{5}\sqrt{\frac{21}{2}}$	$\frac{1}{5}\sqrt{\frac{21}{2}}$
	3f 1p	$-\frac{1}{5}\sqrt{\frac{21}{2}}$	$\frac{1}{5}\sqrt{\frac{21}{2}}$	$\frac{\sqrt{2}}{5}$	$-\frac{\sqrt{2}}{5}$
	2d 2s	$-\frac{1}{2}\sqrt{\frac{3}{5}}$	$-\frac{1}{2}\sqrt{\frac{3}{5}}$	$\frac{1}{2}\sqrt{\frac{7}{5}}$	$\frac{1}{2}\sqrt{\frac{7}{5}}$
$L=3$	3f 1p	–	–	$\frac{1}{\sqrt{2}}$	$\frac{1}{\sqrt{2}}$
	2d 2d	–	–	$\frac{1}{\sqrt{2}}$	$-\frac{1}{\sqrt{2}}$
$L=4$	3f 1p	–	–	$\frac{1}{\sqrt{2}}$	$-\frac{1}{\sqrt{2}}$

TABLE 1. (*continued*)

$S+T$ odd $\qquad n_1+n_2=4$

	$N\lambda, n\Lambda$ / n_1l_1, n_2l_2	2s 2s	4s 0s	0s 4s	2d 2d	2d 2s	2s 2d	4d 0s	0s 4d	4g 0s	0s 4g
$L=0$	2s 2s	$\frac{1}{6}$	$\frac{1}{2}\sqrt{\frac{5}{6}}$	$\frac{1}{2}\sqrt{\frac{5}{6}}$	$-\frac{\sqrt{5}}{3}$	–	–	–	–	–	–
	2d 2d	$-\frac{\sqrt{5}}{3}$	$\frac{1}{\sqrt{6}}$	$\frac{1}{\sqrt{6}}$	$\frac{1}{3}$	–	–	–	–	–	–
	3p 1p	–	$\frac{1}{\sqrt{2}}$	$-\frac{1}{\sqrt{2}}$	–	–	–	–	–	–	–
$L=1$	3p 1p	–	–	–	1	–	–	–	–	–	–
$L=2$	2d 2s	–	–	–	$-\frac{1}{3}\sqrt{\frac{7}{2}}$	$-\frac{1}{6\sqrt{2}}$	$-\frac{1}{6\sqrt{2}}$	$\frac{1}{2}\sqrt{\frac{7}{6}}$	$\frac{1}{2}\sqrt{\frac{7}{6}}$	–	–
	2d 2d	–	–	–	$\frac{2}{3}$	$-\frac{\sqrt{7}}{6}$	$-\frac{\sqrt{7}}{6}$	$\frac{1}{2\sqrt{3}}$	$\frac{1}{2\sqrt{3}}$	–	–
	3p 1p	–	–	–	–	$\frac{1}{2}\sqrt{\frac{3}{5}}$	$-\frac{1}{2}\sqrt{\frac{3}{5}}$	$\frac{1}{2}\sqrt{\frac{7}{5}}$	$-\frac{1}{2}\sqrt{\frac{7}{5}}$	–	–
	3f 1p	–	–	–	–	$-\frac{1}{2}\sqrt{\frac{7}{5}}$	$\frac{1}{2}\sqrt{\frac{7}{5}}$	$\frac{1}{2}\sqrt{\frac{3}{5}}$	$-\frac{1}{2}\sqrt{\frac{3}{5}}$	–	–
$L=3$	3f 1p	–	–	–	1	–	–	–	–	–	–
$L=4$	2d 2d	–	–	–	$-\frac{1}{2}$	–	–	–	–	$\frac{1}{2}\sqrt{\frac{3}{2}}$	$\frac{1}{2}\sqrt{\frac{3}{2}}$
	3f 1p	–	–	–	–	–	–	–	–	$\frac{1}{\sqrt{2}}$	$-\frac{1}{\sqrt{2}}$

TABLE 1. (*continued*)

$S+T$ odd $\qquad n_1+n_2=5$

	$N\lambda, n\Lambda$ / $n_1 l_1, n_2 l_2$	5p 0s	3p 2s	1p 4s	3p 2d	1p 4d	3f 2d	3f 2s	5f 0s	1p 4g	5h 0s
$L=1$	3p 2s	$\frac{1}{2}\sqrt{\frac{7}{6}}$	$\frac{1}{6}$	$\frac{1}{2\sqrt{2}}$	$-\frac{2}{3\sqrt{5}}$	–	$-\sqrt{\frac{7}{15}}$	–	–	–	–
	3p 2d	$\sqrt{\frac{7}{30}}$	$-\frac{2}{3\sqrt{5}}$	$-\frac{1}{\sqrt{10}}$	$-\frac{11}{30}$	$\frac{1}{2}\sqrt{\frac{7}{5}}$	$\frac{1}{5}\sqrt{\frac{7}{3}}$	–	–	–	–
	3f 2d	$\frac{1}{\sqrt{10}}$	$-\sqrt{\frac{7}{15}}$	$\sqrt{\frac{7}{30}}$	$\frac{1}{5}\sqrt{\frac{7}{3}}$	$-\frac{1}{\sqrt{15}}$	$\frac{1}{5}$	–	–	–	–
$L=2$	3p 2d	–	–	–	$\frac{3}{10}$	$\frac{1}{2}\sqrt{\frac{7}{5}}$	$-\frac{\sqrt{14}}{5}$	–	–	–	–
	3f 2d	–	–	–	$-\frac{\sqrt{14}}{5}$	$\sqrt{\frac{2}{5}}$	$\frac{1}{5}$	–	–	–	–
$L=3$	3f 2s	–	–	–	$\frac{1}{4\sqrt{5}}$	$\frac{5}{4\sqrt{7}}$	$-\sqrt{\frac{3}{10}}$	$-\frac{1}{4}$	$\frac{\sqrt{3}}{4}$	$-\sqrt{\frac{3}{14}}$	–
	3p 2d	–	–	–	$-\frac{9}{20}$	$-\frac{1}{4\sqrt{35}}$	$-\frac{1}{5}\sqrt{\frac{3}{2}}$	$\frac{1}{4\sqrt{5}}$	$\frac{3}{4}\sqrt{\frac{3}{5}}$	$3\sqrt{\frac{3}{70}}$	–
	3f 2d	–	–	–	$-\frac{1}{5}\sqrt{\frac{3}{2}}$	$\sqrt{\frac{3}{70}}$	$\frac{7}{10}$	$-\sqrt{\frac{3}{10}}$	$\frac{1}{\sqrt{10}}$	$-\frac{1}{2\sqrt{35}}$	–
$L=4$	3f 2d	–	–	–	–	–	$-\frac{1}{2}$	–	–	$\frac{\sqrt{3}}{2}$	–
$L=5$	3f 2d	–	–	–	–	–	$-\frac{1}{2}$	–	–	$\frac{1}{2\sqrt{2}}$	$\frac{1}{2}\sqrt{\frac{5}{2}}$

TABLE 1 (*continued*)

$S+T$ even $\qquad n_1+n_2=6$

	$N\lambda, n\Lambda$ / $n_1 l_1, n_2 l_2$	3p 3p	5p 1p	1p 5p	3f 3f	3f 3p	3p 3f	5f 1p	1p 5f	5h 1p	1p 5h
$L=1$	3p 3p	$\frac{3}{10}$	$\frac{1}{2}\sqrt{\frac{7}{10}}$	$\frac{1}{2}\sqrt{\frac{7}{10}}$	$-\frac{\sqrt{14}}{5}$	–	–	–	–	–	–
	3f 3f	$-\frac{\sqrt{14}}{5}$	$\frac{1}{\sqrt{5}}$	$\frac{1}{\sqrt{5}}$	$\frac{1}{5}$	–	–	–	–	–	–
$L=2$	3f 3p	–	$-\frac{1}{2}\sqrt{\frac{3}{5}}$	$\frac{1}{2}\sqrt{\frac{3}{5}}$	–	$-\frac{1}{2\sqrt{2}}$	$\frac{1}{2\sqrt{2}}$	$\frac{3}{2\sqrt{10}}$	$-\frac{3}{2\sqrt{10}}$	–	–
$L=3$	3f 3p	–	–	–	$-\frac{3}{5}\sqrt{\frac{3}{2}}$	$\frac{1}{10\sqrt{2}}$	$\frac{1}{10\sqrt{2}}$	$\frac{3}{2\sqrt{10}}$	$\frac{3}{2\sqrt{10}}$	–	–
	3f 3f	–	–	–	$\frac{2}{5}$	$-\frac{3\sqrt{3}}{10}$	$-\frac{3\sqrt{3}}{10}$	$\frac{1}{2}\sqrt{\frac{3}{5}}$	$\frac{1}{2}\sqrt{\frac{3}{5}}$	–	–
$L=4$	3f 3p	–	–	–	–	$-\frac{1}{2\sqrt{2}}$	$\frac{1}{2\sqrt{2}}$	$-\frac{1}{6}\sqrt{\frac{5}{2}}$	$\frac{1}{6}\sqrt{\frac{5}{2}}$	$\frac{\sqrt{11}}{6}$	$-\frac{\sqrt{11}}{6}$
$L=5$	3f 3f	–	–	–	$-\frac{1}{2}$	–	–	–	–	$\frac{1}{2}\sqrt{\frac{3}{2}}$	$\frac{1}{2}\sqrt{\frac{3}{2}}$

TABLE 1 (*continued*)

$S+T$ odd $\qquad n_1+n_2=6$

	$N\lambda, n\Lambda$ / $n_1 l_1, n_2 l_2$	4d 2d	2d 4d	4g 2d	2d 4g	4s 2s	4s 4s	6s 0s	0s 6s
$L=0$	3p 3p	$-\sqrt{\frac{7}{30}}$	$\sqrt{\frac{7}{30}}$	–	–	$-\frac{1}{4\sqrt{15}}$	$\frac{1}{4\sqrt{15}}$	$\frac{1}{4}\sqrt{\frac{21}{5}}$	$-\frac{1}{4}\sqrt{\frac{21}{5}}$
	3f 3f	$\frac{1}{\sqrt{10}}$	$-\frac{1}{\sqrt{10}}$	–	–	$-\frac{1}{2}\sqrt{\frac{7}{5}}$	$\frac{1}{2}\sqrt{\frac{7}{5}}$	$\frac{1}{2\sqrt{5}}$	$-\frac{1}{2\sqrt{5}}$

		4s 2d	2d 4s	4d 2s	2s 4d	6d 0s	0s 6d
$L=2$	3p 3p	$-\frac{23}{20\sqrt{15}}$	$\frac{23}{20\sqrt{15}}$	$\frac{1}{10}\sqrt{\frac{7}{6}}$	$-\frac{1}{10}\sqrt{\frac{7}{6}}$	$\frac{3\sqrt{7}}{20}$	$-\frac{3\sqrt{7}}{20}$
	3f 3p	$\frac{1}{10}\sqrt{\frac{7}{10}}$	$-\frac{1}{10}\sqrt{\frac{7}{10}}$	$-\frac{2}{5}$	$\frac{2}{5}$	$\frac{3}{10}\sqrt{\frac{3}{2}}$	$-\frac{3}{10}\sqrt{\frac{3}{2}}$
	3f 3f	$-\frac{1}{5}\sqrt{\frac{21}{10}}$	$\frac{1}{5}\sqrt{\frac{21}{10}}$	$-\frac{\sqrt{3}}{5}$	$\frac{\sqrt{3}}{5}$	$\frac{1}{5\sqrt{2}}$	$-\frac{1}{5\sqrt{2}}$

		4g 2s	2s 4g	6g 0s	0s 6g
$L=4$	3f 3p	$-\frac{1}{2\sqrt{30}}$	$\frac{1}{2\sqrt{30}}$	$\frac{1}{2}\sqrt{\frac{11}{10}}$	$-\frac{1}{2}\sqrt{\frac{11}{10}}$
	3f 3f	$-\frac{1}{4}\sqrt{\frac{11}{5}}$	$\frac{1}{4}\sqrt{\frac{11}{5}}$	$\frac{1}{4}\sqrt{\frac{3}{5}}$	$-\frac{1}{4}\sqrt{\frac{3}{5}}$

		6i 0s	0s 6i
$L=6$	3f 3f	$\frac{\sqrt{5}}{4}$	$-\frac{\sqrt{5}}{4}$

	$N\lambda, n\Lambda$ / $n_1 l_1, n_2 l_2$	4d 2d	2d 4d	4g 2d	2d 4g
$L=6$	3f 3f	–	–	$-\frac{\sqrt{3}}{4}$	$\frac{\sqrt{3}}{4}$

4) $$\left\langle \begin{matrix} n_1 l_1 \\ n_2 l_2 \end{matrix} \middle| TSL \middle| \begin{matrix} N\lambda \\ n\Lambda \end{matrix} \right\rangle = (-1)^{\Lambda} \left\langle \begin{matrix} n_2 l_2 \\ n_1 l_1 \end{matrix} \middle| TSL \middle| \begin{matrix} N\lambda \\ n\Lambda \end{matrix} \right\rangle .$$

5) If n_1+n_2 is even,

$$\left\langle \begin{matrix} n_1 l_1 \\ n_2 l_2 \end{matrix} \middle| TSL \middle| \begin{matrix} N\lambda \\ n\Lambda \end{matrix} \right\rangle = (-1)^{L-l_2} \left\langle \begin{matrix} n_1 l_1 \\ n_2 l_2 \end{matrix} \middle| TSL \middle| \begin{matrix} n\Lambda \\ N\lambda \end{matrix} \right\rangle$$

If n_1+n_2 is odd,

$$\left\langle \begin{matrix} n_1 l_1 \\ n_2 l_2 \end{matrix} \middle| TSL \middle| \begin{matrix} N\lambda \\ n\Lambda \end{matrix} \right\rangle = (-1)^{L-l_2} \left\langle \begin{matrix} n_1 l_1 \\ n_2 l_2 \end{matrix} \middle| T'S'L \middle| \begin{matrix} n\Lambda \\ N\lambda \end{matrix} \right\rangle ;$$

the numbers $T+S$ and $T'+S'$ have opposite parities.

4. Calculation of Matrix Elements of Two-Nucleon Potential

Suppose V_{12} is a potential of the arbitrary charge-independent invariant pair interaction of nucleons. Using eq. (8) we obtain a simple formula for calculating matrix elements of this potential:

$$\begin{aligned} &\langle (n_1 l_1)(n_2 l_2) : {}^{2T+1,2S+1}L_J | V_{12} | (n'_1 l'_1)(n'_2 l'_2) : {}^{2T+1,2S+1}L'_J \rangle \\ &\quad = \sum_{N\lambda, n\Lambda, n'\Lambda', J_0} U(\lambda\Lambda JS : LJ_0) U(\lambda\Lambda' JS : L'J_0) \left\langle \begin{matrix} n_1 l_1 \\ n_2 l_2 \end{matrix} \middle| TSL \middle| \begin{matrix} N\lambda \\ n\Lambda \end{matrix} \right\rangle \\ &\quad \cdot \left\langle \begin{matrix} n'_1 l'_1 \\ n'_2 l'_2 \end{matrix} \middle| TSL' \middle| \begin{matrix} N\lambda \\ n'\Lambda' \end{matrix} \right\rangle \langle n\Lambda TSJ_0 | V_{12} | n'\Lambda' TSJ_0 \rangle \end{aligned} \tag{9}$$

Owing to the scalar character of the V_{12} potential in ordinary and isobaric spaces, the matrix elements $\langle n\Lambda TSJ_0|V_{12}|n'\Lambda' TSJ_0\rangle$ are diagonal with respect to J, T, and the parity of $\pi = (-1)^{\Lambda}$, and, taking into account the Pauli principle, also with respect to the spin S.

In the particular case of central interaction, $V_{12} = V(r_{12})$,

$$\langle n\Lambda TSJ_0 | V_{12} | n'\Lambda' TSJ_0 \rangle = \delta_{\Lambda\Lambda'} \langle n\Lambda | V(r_{12}) | n'\Lambda \rangle ,$$

where

$$\langle n\Lambda | V(r_{12}) | n'\Lambda \rangle \equiv \int \Psi^{n*}_{\Lambda m}(\mathbf{r}_{12}) V(r_{12}) \Psi^{n'}_{\Lambda m}(\mathbf{r}_{12}) d\mathbf{r}_{12} .$$

Using a familiar relation for the Racah coefficients, we obtain finally

$$\begin{aligned} &\langle (n_1 l_1)(n_2 l_2) : {}^{2T+1,2S+1}L_J | V(r_{12}) | (n_1' l'_1)(n'_2 l'_2) : {}^{2T+1,2S+1}L'_J \rangle \\ &\quad = \delta_{LL'} \sum_{N\lambda, nn'\Lambda} \left\langle \begin{matrix} n_1 l_1 \\ n_2 l_2 \end{matrix} \middle| TSL \middle| \begin{matrix} N\lambda \\ n\Lambda \end{matrix} \right\rangle \left\langle \begin{matrix} n'_1 l'_1 \\ n'_2 l'_2 \end{matrix} \middle| TSL \middle| \begin{matrix} N\lambda \\ n\Lambda \end{matrix} \right\rangle \langle n\Lambda | V(r_{12}) | n'\Lambda \rangle . \end{aligned} \tag{10}$$

References

1) I. Talmi, Helv. Phys. Acta **25** (1952) 185
2) K. W. Ford and E. J. Konopinski, Nuclear Physics **9** (1958) 218
3) Y. M. Shirokov, V. V. Balashov and K. A. Tumanov, JETP **32** (1957) 1676
4) H. A. Jahn, Proc. Roy. Soc. A **205** (1950) 195

1.B:8.B

Nuclear Physics **16** (1960) 432—459; © *North-Holland Publishing Co., Amsterdam*

Not to be reproduced by photoprint or microfilm without written permission from the publisher

μ-HYDROGEN MOLECULAR ION AND COLLISIONS BETWEEN μ-HYDROGEN ATOM AND PROTON, DEUTERON AND H ATOM

TA-YOU WU, R. L. ROSENBERG † and H. SANDSTROM

Division of Pure Physics, National Research Council, Ottawa, Canada

Received 13 November 1959

Abstract: To the order μ/M, the ratio of meson and proton masses, the following quantities are calculated: (1) the energy of the ground state of the molecular ion $(p-\mu-p)^+$; (2) the square of the meson wave function at the position of a proton in $(p-\mu-p)^+$, (3) the "vibrational" level of $(p-\mu-p)^+$. The theory of direct and exchange collisions $(p-\mu)+d \rightarrow (p-\mu)+d$, $(p-\mu)+d \rightarrow (d-\mu)+p$ is given in terms of the coupling between the meson and nucleon motions. These cross-sections and that of the elastic scattering $(p-\mu)+p$ are calculated for energies corresponding to the temperature of liquid hydrogen. Also the cross-section of the $(p-\mu-p)^+$ formation process $(p-\mu)+H \rightarrow (p-\mu-p)^++e$ is calculated, leading to a value $\approx 1/18$ for the relative chance of a μ-meson being found in the atomic $(p-\mu)$ system and in the molecular system $(p-\mu-p)^+$ in liquid hydrogen. This, together with (2), leads to the relative probability of ≈ 6.3 of a μ-meson being captured by a proton in the molecular and the atomic state, if μ-capture in the hyperfine state $F = 0$ only (corresponding to an interaction V—A for the capture process) is assumed.

1. Introduction

The discovery [1]) of the nuclear fusion $p+d+\mu \rightarrow He^3+\mu$ by μ-catalysis has been the occasion for a number of studies [2,3]) of the cross-sections of some collision processes involving a μ-mesonic hydrogen atom and a proton, a deuteron or hydrogen atom, such as

$$\text{elastic collisions} \quad \begin{cases} (p-\mu)+p \rightarrow (p-\mu)+p, & (1) \\ (p-\mu)+d \rightarrow (p-\mu)+d, & (2) \end{cases}$$

$$\text{inelastic collisions} \quad \begin{cases} (p-\mu)+d \rightarrow (d-\mu)+p, & (3) \\ (p-\mu)+H \rightarrow (p-\mu-p)^++e. & (4) \end{cases}$$

While in principle such collision processes present no essentially new problems, in the actual calculation, they do present certain features arising from the considerable value of the ratio μ/M of the meson and the proton mass, which is negligible in the corresponding processes involving an electron in place of the μ. Also in some projected experiments of measuring the μ-capture $(\mu+p \rightarrow N+\nu)$ interaction constant in a hydrogen bubble chamber, it is necessary to know the relative chance of the μ being captured in the atomic $(p-\mu)$ and in the mole-

† Permanent address: Department of Mathematics, University of New Brunswick, N.B., Canada.

cular $(p-\mu-p)^+$ system. The purpose of the present work is to calculate to the order μ/M

i) the energy of the ground state of the molecular ion $(p-\mu-p)^+$,

ii) the value of the meson wave function at the position of a proton in $(p-\mu-p)^+$,

iii) the vibrational level of $(p-\mu-p)^+$,

and to study the processes (1)—(4) by going beyond the zeroth order Born-Oppenheimer approximation when necessary.

2. Hamiltonian of p—μ—d System

Let R be the distance p—d; ξ, η the elliptic coordinates of μ with respect to p—d; ϑ, φ the polar angles of the line p—d; and ψ the angle of μ around p—d. The Hamiltonian, after separating off the motion of the centre of mass of the system, is

$$H = H_0 + H_1^{S} + H_1^{A}, \tag{5}$$

$$H_0 = -\frac{4}{\rho^2(\xi^2-\eta^2)}\left\{X + \left(\frac{1}{\xi^2-1}+\frac{1}{1-\eta^2}\right)\frac{\partial^2}{\partial\psi^2} + 2\rho\xi - \tfrac{1}{2}\rho(\xi^2-\eta^2)\right\}, \tag{6}$$

$$\begin{aligned} H_1^{S} = -\frac{\bar{\mu}(M+D)}{MD}\Bigg[&\frac{\xi^2+\eta^2-2}{\rho^2(\xi^2-\eta^2)}\left\{X + \left(\frac{1}{\xi^2-1}+\frac{1}{1-\eta^2}\right)\frac{\partial^2}{\partial\psi^2}\right\} + \nabla_\rho^{\,2} \\ &- \frac{2}{\rho^2}Y\left(1+\rho\frac{\partial}{\partial\rho}\right) + \frac{1}{\rho^2}\left\{\frac{1}{\sin^2\vartheta}\frac{\partial^2}{\partial\psi^2} - 2\frac{\cot\vartheta}{\sin\vartheta}\frac{\partial^2}{\partial\varphi\partial\psi} - 2\frac{\partial^2}{\partial\psi^2}\right\} \\ &+ \frac{2\xi\eta}{\rho^2[(\xi^2-1)(1-\eta^2)]^{\frac{1}{2}}}\left\{\sin\psi\frac{\partial}{\partial\vartheta} - \frac{\cos\psi}{\sin\vartheta}\frac{\partial}{\partial\varphi} + \cot\vartheta\cos\psi\frac{\partial}{\partial\psi}\right\}\frac{\partial}{\partial\psi} \\ &- \frac{2[(\xi^2-1)(1-\eta^2)]^{\frac{1}{2}}}{\rho^2(\xi^2-\eta^2)}\left\{\cos\psi\frac{\partial}{\partial\vartheta} + \frac{\sin\psi}{\sin\vartheta}\frac{\partial}{\partial\varphi} - \cot\vartheta\sin\psi\frac{\partial}{\partial\psi}\right\}\left\{\eta\frac{\partial}{\partial\xi} - \xi\frac{\partial}{\partial\eta}\right\}\Bigg], \end{aligned} \tag{7}$$

$$\begin{aligned} H_1^{A} = -\frac{\bar{\mu}(D-M)}{MD}\Bigg[&-\frac{2\xi\eta}{\rho^2(\xi^2-\eta^2)}\left\{X + \left(\frac{1}{\xi^2-1}+\frac{1}{1-\eta^2}\right)\frac{\partial^2}{\partial\psi^2}\right\} + \frac{2}{\rho^2}Z\left(1+\rho\frac{\partial}{\partial\rho}\right) \\ &- \frac{2}{\rho^2[(\xi^2-1)(1-\eta^2)]^{\frac{1}{2}}}\left\{\sin\psi\frac{\partial}{\partial\vartheta} - \frac{\cos\psi}{\sin\vartheta}\frac{\partial}{\partial\varphi} + \cot\vartheta\cos\psi\frac{\partial}{\partial\psi}\right\}\frac{\partial}{\partial\psi} \\ &+ \frac{2[(\xi^2-1)(1-\eta^2)]^{\frac{1}{2}}}{\rho^2(\xi^2-\eta^2)}\left\{\cos\psi\frac{\partial}{\partial\vartheta} + \frac{\sin\psi}{\sin\vartheta}\frac{\partial}{\partial\varphi} - \cot\vartheta\sin\psi\frac{\partial}{\partial\psi}\right\}\left\{\xi\frac{\partial}{\partial\xi} - \eta\frac{\partial}{\partial\eta}\right\}\Bigg] \end{aligned} \tag{8}$$

where

$$\begin{aligned}
\nabla_\rho^2 &= \frac{\partial^2}{\partial\rho^2}+\frac{2}{\rho}\frac{\partial}{\partial\rho}+\frac{1}{\rho^2}\left(\frac{\partial^2}{\partial\vartheta^2}+\cot\vartheta\frac{\partial}{\partial\vartheta}+\frac{1}{\sin^2\vartheta}\frac{\partial^2}{\partial\varphi^2}\right),\\
X &= \frac{\partial}{\partial\xi}(\xi^2-1)\frac{\partial}{\partial\xi}+\frac{\partial}{\partial\eta}(1-\eta^2)\frac{\partial}{\partial\eta},\\
Y &= \frac{1}{\xi^2-\eta^2}\left\{\xi(\xi^2-1)\frac{\partial}{\partial\xi}+\eta(1-\eta^2)\frac{\partial}{\partial\eta}\right\},\\
Z &= \frac{1}{\xi^2-\eta^2}\left\{\eta(\xi^2-1)\frac{\partial}{\partial\xi}+\xi(1-\eta^2)\frac{\partial}{\partial\eta}\right\}.
\end{aligned} \tag{9}$$

In (6), (7), (8), energy and length are in units of

$$\varepsilon=\frac{\bar\mu}{m_e}\text{ rydberg},\qquad \bar a_\mu=\frac{m_e}{\bar\mu}a_B,\qquad \frac{1}{\bar\mu}=\frac{1}{\mu}+\frac{1}{2M}+\frac{1}{2D}. \tag{10}$$

Upon interchanging the two nuclei A, B, the coordinates transform as

$$\xi\to\xi,\qquad \eta\to-\eta,\qquad \vartheta\to\pi-\vartheta,\qquad \varphi\to\pi+\varphi,\qquad \psi\to-\psi,$$

and it is seen that $H_1^{\,S}$ is symmetric and $H_1^{\,A}$ is antisymmetric with respect to the interchange of the two nuclei.

For states of zero total angular momentum, it can be shown that $\partial/\partial\vartheta=\partial/\partial\varphi=\partial/\partial\psi=0$.

In general, only the total energy and the total angular momentum are constants of motion of the system.

3. Lowest Mesonic States of $(p-\mu-p)^+$

We shall first consider the symmetric system $(p-\mu-p)^+$ and the states of zero total angular momentum. The Hamiltonian $H=H_0+H_1^{\,S}$ is given by (6), (7) in which $D=M$ and $\partial/\partial\vartheta=\partial/\partial\varphi=\partial/\partial\psi=0$.

To the zeroth order in μ/M, the Schrödinger equation

$$[H_0-V(\rho)]\psi(\xi,\eta;\rho)=0 \tag{11}$$

has been solved by a number of authors for the hydrogenic molecular ion H_2^+. The two lowest states $1s\sigma g$, $2p\sigma u$ have wave functions ψ_g, ψ_u which are symmetric and antisymmetric with respect to the centre of p−p,

$$\begin{aligned}
&\left[-\frac{4}{\rho^2(\xi^2-\eta^2)}\{X+2\rho\xi-\tfrac{1}{2}\rho(\xi^2-\eta^2)\}-V_g(\rho)\right]\psi_g(\xi,\eta;\rho)=0,\\
&\left[-\frac{4}{\rho^2(\xi^2-\eta^2)}\{X+2\rho\xi-\tfrac{1}{2}\rho(\xi^2-\eta^2)\}-V_u(\rho)\right]\psi_u(\xi,\eta;\rho)=0.
\end{aligned} \tag{12}$$

In the present work $V_g(\rho)$, $V_u(\rho)$ refer to the asymptotic state $\rho\to\infty$ as zero

level, i.e.,

$$V_g(\infty) = V_u(\infty) = 0.$$

The exact eigenvalues $V(\rho)$ and eigenfunctions ψ have been tabulated by Bates *et al.* [4]) †. For the $(p-\mu-p)^+$ system, we have only to substitute the units (10) for the rydberg and the Bohr radius r_B in the case of H_2^+. We shall refer to Bates *et al.* [4]) for these and other excited states of (11).

To the next order in μ/M, we have

$$[H_0+H_1^S-E]\Psi(r_\mu, \rho) = 0. \tag{13}$$

We follow Born in expanding

$$\Psi(r_\mu, \rho) = \sum_n \psi_n(\xi, \eta, \varphi; \rho)\Phi_n(\rho) \tag{14}$$

where ψ_n are the solutions of (11). On putting (14) in (13), multiplying by $\psi_g(\xi, \eta; \rho)d\tau_\mu$, $(d\tau_\mu = \frac{1}{8}\rho^3(\xi^2-\eta^2)d\xi d\eta)$ and integration over ξ, η, one obtains

$$\left[-\frac{2\bar{\mu}}{M}\nabla_\rho^2+\mathfrak{V}_g(\rho)\right]\Phi_g(\rho) = E\Phi_g(\rho), \tag{15}$$

where

$$\mathfrak{V}_g(\rho) = V(\rho)+\langle g|\bar{H}_1^S|g\rangle+\frac{2\bar{\mu}}{M}\int\left(\frac{\partial\psi_g}{\partial\rho}\right)^2 d\tau_\mu \equiv V_g(\rho)+\Delta_g(\rho), \tag{16}$$

$$\langle g|\bar{H}_1^S|g\rangle = \frac{2\bar{\mu}}{M\rho^2}\int\frac{\xi^2+\eta^2-2}{\xi^2-\eta^2}\left[(\xi^2-1)\left(\frac{\partial\psi_g}{\partial\xi}\right)^2+(1-\eta^2)\left(\frac{\partial\psi_g}{\partial\eta}\right)^2\right]d\tau_\mu$$
$$-\frac{4\bar{\mu}}{M\rho}\int\frac{\partial\psi_g}{\partial\rho}Y\psi_\rho d\tau_\mu. \tag{17}$$

Calculation of $\Delta_g(\rho)$ from the exact wave function $\psi_g(\xi, \eta; \rho)$ has been carried out by Dalgarno and McCarroll [5]) by a numerical evaluation of the integrals in (16) and (17). In an earlier work, Wu and Bhatia [6]) have calculated $\Delta E_g(\rho)$ with the approximate wave function of Guillemin-Zener. Unfortunately there are some errors in the $\Delta E_g(\rho)$ given. The correct expression and the numerical values of $\Delta E_g(\rho)$ are given below ††.

† The energy $E(\rho)$ in the paper of Bates *et al.* [4]) does not include the Coulomb energy between the two nuclei. The relation between the $E(\rho)$ there and the $V(\rho)$ in the present work is

$$V(\rho) = E(\rho)+\frac{2}{\rho}+1.$$

†† In the work of Wu and Bhatia [6]) and also in Dalgarno and McCarroll [5]), the unit of energy is μ/m_e rydberg instead of the $\bar{\mu}/m_e$ rydberg in (10), corresponding to a slightly different arrangement of H_0 and H_1^S in which, instead of (6),

$$H_1^S = -\frac{\mu(M+D)}{MD}\left[\frac{\xi^2+\eta^2}{\rho^2(\xi^2-\eta^2)}\{X+\ldots\}\right].$$

In their choice of writing H_0 and H_1^S, (16) (17) would have become

With the wave function of Guillemin-Zener

$$\psi_g(r_\mu;\rho)=N[\exp\{-\tfrac{1}{2}(\alpha+\beta)r_{\mu A}-\tfrac{1}{2}(\alpha-\beta)r_{\mu B}\}+\exp\{-\tfrac{1}{2}(\alpha+\beta)r_{\mu B}-\tfrac{1}{2}(\alpha-\beta)r_{\mu A}\}]$$
$$= N\exp(-\tfrac{1}{2}\lambda\xi)[\exp(\tfrac{1}{2}\nu\eta)+\exp(-\tfrac{1}{2}\nu\eta)],$$

where $\alpha(\rho)$, $\beta(\rho)$ are functions of ρ, and

$$\lambda(\rho)=\alpha\rho, \quad \nu(\alpha)=\beta\rho, \tag{18}$$

the energy correction $\Delta E_g(\rho)$ is, in the notation of Wu and Bhatia [6]),

$$\Delta E_g(\rho)\approx\frac{\mu}{M}\Bigg[\frac{\alpha^2+\beta^2}{2}-\frac{\beta^2}{Q}(1+\lambda+\tfrac{1}{3}\lambda^2)-\frac{\alpha^2}{18Q^2}\left\{\lambda+\lambda^2+\frac{3}{2}\left(\frac{\alpha^2}{\beta^2}-1\right)\left(1+\frac{\beta^2}{\alpha\nu}\right)\left(S-\frac{D}{\nu}\right)\right\}^2$$
$$+\frac{1}{\lambda}\frac{\mathrm{d}\alpha}{\mathrm{d}\rho}\left\{1+\lambda-\frac{1}{Q}\left[2\lambda+\tfrac{1}{2}\lambda S+\frac{\alpha}{2\beta}D+\left(1+\frac{D}{2\nu}\right)(1+\tfrac{3}{2}\lambda^2)\right]\right. \tag{19}$$
$$\left.+\frac{1}{6Q^2}\left[\lambda+\tfrac{2}{3}\lambda+\frac{\alpha}{2\beta}D+\frac{\alpha^2}{\beta^2}\left(S-\frac{D}{\nu}\right)\right]\left[3\lambda+\lambda^2-\lambda^3+\tfrac{3}{2}\lambda S+\frac{3}{2}\left(S-\frac{D}{\nu}\right)\left(1-\frac{\alpha^2}{\beta^2}\right)(\lambda+2)\right]\right\}$$
$$-\frac{1}{\alpha^2}\left(\frac{\mathrm{d}\alpha}{\mathrm{d}\rho}\right)^2\left\{\frac{1}{2}+\frac{1}{Q}\left[3+\lambda+\frac{\alpha}{2\beta}D+\frac{3}{2\nu}D\right]-\frac{1}{2Q^2}\left[\left(1+\frac{D}{2\nu}\right)(\lambda+2)\right]^2\right\}\Bigg],$$

where

$$S=\mathrm{e}^{\nu}+\mathrm{e}^{-\nu}, \quad D=\mathrm{e}^{\nu}-\mathrm{e}^{-\nu},$$

$$Q=\frac{1}{2}\left(\frac{\alpha}{\beta}\right)^2\left[S-\frac{D}{\nu}+\frac{\beta}{\alpha}\left(1+\frac{\beta}{\alpha\nu}\right)D\right]+1+\lambda+\tfrac{1}{3}\lambda^2.$$

In (19), (20), (21) energy is in units of μ/m_e rydberg. The $\approx$ sign in (19) indicates that the much smaller terms containing $\mathrm{d}\beta/\mathrm{d}\rho(\ll \mathrm{d}\alpha/\mathrm{d}\rho)$ have been neglected. In the calculation of $\Delta E_g(\rho)$, the $\alpha(\rho)$, $\beta(\rho)$ are first determined, for each ρ, by a variational calculation of the energy $E(\rho)$ in the usual Born-Oppenheimer approximation. The following table gives the value $(M/\mu)\Delta E_g(\rho)$, i.e., the expression within the heavy brackets in (19).

$$\mathfrak{V}_g(\rho)=V_g(\rho)+\langle g|\bar{H}_1^s|g\rangle+\frac{2\mu}{M}\int\left(\frac{\partial\psi_g}{\partial\rho}\right)^2\mathrm{d}\tau_\mu\equiv V_g(\rho)+\Delta E_g(\rho),$$

where

$$\langle g|\bar{H}_1^s|g\rangle=\frac{2\mu}{M\rho^2}\int\frac{\xi^2+\eta^2}{\xi^2-\eta^2}\left[(\xi^2-1)\left(\frac{\partial\psi_g}{\partial\xi}\right)^2+(1-\eta^2)\left(\frac{\partial\psi_g}{\partial\eta}\right)^2\right]\mathrm{d}\tau_\mu-\frac{4\mu}{M}\int\frac{\partial\psi_g}{\partial\rho}Y\psi_g\,\mathrm{d}\tau_\mu,$$

now in units of μ/m_e rydberg. The $\Delta E_g(\rho)$ in (19), (20), (21) are in this notation.

With the choice made in (6), (7), (10), instead of the asymptotic value (20), we now have asymptotically in (16)

$$\Delta_g(\rho)\to 0,$$

and

$$\mathfrak{V}_g(\rho)\to V_g(\rho)\to 0.$$

Thus the choice (6), (7), (10) absorbs the asymptotic correction $\Delta_g(\infty)$ into $\mathfrak{V}_g(\rho)$ in (16), to the order μ/M. It is for this reason that the choice (6), (7), (10) has been made.

When this is taken into account, (16) is in agreement with the result of Dalgarno and McCarroll[8]).

It is seen that in the limiting cases

i) $\rho \to \infty$, where $\alpha = \beta \to 1$,

$$\Delta E_g(\infty) = \mu/M \text{ (in units of } \mu/m_e \text{ rydberg)}, \tag{20}$$

ii) $\rho \to 0$, where $\alpha = 2$, $\beta = 1$,

$$\Delta E_g(0) = 2\mu/M. \tag{21}$$

These values are the expected "relative motion" corrections for one (p—μ) atom and one mesic helium atomic ion of mass 2, respectively. If we refer the energy to that of the separated atoms as zero, then instead of $\Delta E_g(\rho)$ we use

$$\Delta E_g(\rho) - \Delta E_g(\infty). \tag{22}$$

This corresponds to subtracting 1.000 from the values of the bracket expression in table 1. It is seen that the effect of this correction to $V_g(\rho)$ for the coupling

TABLE 1

Value of [ ] in (19). The correction $\Delta E_g(\rho)$ in units of μ/m_e rydberg is given by μ/M [ ]

ρ	[ ]	ρ	[ ]	ρ	[ ]	ρ	[ ]
0.01	2.00	1.01	1.07	2.8	0.779	5.0	0.846
0.05	1.96	1.21	0.995	3.0	0.777	5.5	0.881
0.11	1.88	1.41	0.936	3.2	0.778	6.0	0.904
0.21	1.72	1.61	0.888	3.4	0.781	6.5	0.925
0.31	1.58	1.81	0.848	3.6	0.787	7.0	0.941
0.41	1.46	1.91	0.832	3.8	0.792	7.5	0.955
0.51	1.37	2.01	0.820	4.0	0.796		
0.61	1.29	2.11	0.811	4.2	0.801		
0.71	1.22	2.21	0.803	4.4	0.811		
0.81	1.16	2.41	0.792	4.6	0.821		
0.91	1.11	2.60	0.783	4.8	0.830	∞	1.00

between the motions of the μ and the M's is a slight deepening of the potential in the valley and a rise of μ/M (relative to the asymptote $\rho \to \infty$) at $\rho = 0$. In this connection it may be noted that Dalgarno and McCarroll [5]) give in their fig. 2 the value $\Delta E(0) - \Delta E(\infty) = \frac{3}{2}\mu/M$ instead of the correct value μ/M given by (20), (21) in our work. The reason for their $\frac{3}{2}\mu/M$ is not clear.

4. The Wave Function of μ at the Position of the Proton in $(p—\mu—p)^+$ ion

In order to determine the interaction constant governing the μ-capture process

$$\mu^- + p \to N + \nu$$

in a hydrogen bubble chamber, two informations are pertinent, namely, i) the relative chance r of the μ being captured by a proton from the 1S state of the μ-hydrogen atom (p—μ) and from the ground state $1s\sigma g$ of the molec-

ular ion $(p-\mu-p)^+$, and ii) the values of $\psi^2(0)$ in the atom, and $\psi_g^2(\xi = 1, \eta = \pm 1; \rho_e)$ in the molecular ion. In (119) below, r will be calculated. In the present Section, we shall calculate the ratio R of the probability of finding a meson at a proton in the ground state in $(p-\mu-p)^+$ to that in the atom $(p-\mu)$,

$$R = \frac{|\psi_g(1, 1; 2)|^2 + |\psi_g(1, -1; 2)|^2}{|\psi(0)|^2}. \tag{23}$$

In the zeroth (Born-Oppenheimer) approximation, R can be calculated from the exact wave function $\psi_g(\xi, \eta; \rho)$[4]). It is found that

$$R = 1.317\,35 \tag{24}$$

(which is for infinite M).

To the order μ/M, treating H_1^S in (1) as a perturbation, the wave function of the ground state is, up to μ/M,

$$\psi_g(\xi, \eta; \rho) = \psi_g^0(\xi, \eta; \rho) + \sum_n \frac{\langle ng|H_1^S|g\rangle}{E_g^0 - E_{ng}^0} \psi_{ng}^0(\xi, \eta; \rho) \tag{25}$$

where ψ_{ng}^0 are the solutions of (11). The summation extends over all excited states of zero total angular momentum and even parity. From (7) and (12), one obtains

$$\frac{M}{2\mu}\langle ng|H_1^S|g\rangle = \int \psi_{ng}^0 \left(E_g + \frac{8\xi}{\rho(\xi^2-\eta^2)}\right)(\xi^2+\eta^2-2)\psi_g^0 \mathrm{d}\tau_\mu$$

$$+ \frac{2}{\rho^2}\int \psi_{ng}^0 Y \psi_g^0 \mathrm{d}\tau_\mu + \frac{2}{\rho}\int \psi_{ng}^0 Y \frac{\partial \psi_g^0}{\partial \rho}\mathrm{d}\tau_\mu - \int \psi_{ng}^0 \left(\frac{\partial^2}{\partial \rho^2} + \frac{2}{\rho}\frac{\partial}{\partial \rho}\right)\psi_g^0 \mathrm{d}\tau_\mu. \tag{26}$$

While in principle the exact solutions ψ_{ng}^0 can be found and $\langle ng|H_1^S|g\rangle$ calculated, such a calculation is obviously too laborious. One expects the coefficients $\langle ng|H_1^S|g\rangle/(E_g^0 - E_{ng}^0)$ to decrease with n in the series $2s\sigma g$, $3s\sigma g$, $4s\sigma g \ldots$ Also reference to figs. 1, 2, 3 in the paper of Bates *et al.* [4]) shows that the value of ψ_{ng}^0 at $\xi = 1$, $\eta = \pm 1$, $\rho = 2$ also decreases with n,

$$\psi_g^0(1, \pm 1; 2) : \psi_{2g}^0(1, \pm 1; 2) : \psi_{3g}^0(1, \pm 1; 2) \approx 4.4 : 2 : 1. \tag{27}$$

Thus we shall only calculate the effect of $2s\sigma g$ in (25). After a somewhat lengthy calculation of (26) with the exact wave functions of $\psi_{1s\sigma g}^0$ and $\psi_{2s\sigma g}^0$, the ratio R comes out to be

$$R = 1.421\,78 \tag{28}$$

which differs from the zeroth approximation (24) by an amount of the expected order μ/M. The inclusion of higher states ng presumably will not change the second figure after the decimal by more than a few units.

5. The Vibrational State of 1sσg of $(p-\mu-p)^+$

From the corrected "potential" $\mathfrak{V}_g(\rho)$ of the $(p-\mu-p)^+$ ion given by (16), (17) and table 1, it is possible to calculate the vibrational energy and wave function of the 1sσg state by solving the equation (15). For this purpose, we have employed an improved method of the WKB type due to Miller and Good [7]†, which is free from the appearance of singular (classical turning) points and which has been found to give very accurate values for both the eigenvalues and eigenfunctions in a few test cases. For $(p-\mu-d)^+$ which is of interest in the nuclear fusion process, one replaces $2\mu/M$ in (15), (16), (19) by $\mu(M+D)/MD$. The lowest vibrational level is

$$\begin{aligned}(p-\mu-p)^+ &: E_{v=0} = -0.1017 \\ (p-\mu-d)^+ &: E_{v=0} = -0.1092\end{aligned} \quad \text{in } \mu/m_e \text{ rydberg}, \tag{29}$$

which are measured from the respective asymptotic ($p \to \infty$) state as zero. The normalized "vibrational" wave function of $(p-\mu-p)^+$ is given in table 2.

A search has been made for an excited vibrational state $v = 1$ in $(p-\mu-p)^+$

TABLE 2

Normalized vibrational wave function of $(p-\mu-p)^+$ (see (116))

ρ	$\rho\Phi_0(\rho)$	ρ	$\rho\Phi_0(\rho)$
0	0		
0.2	0.0119	4.2	0.4334
0.4	0.0373	4.4	0.3982
0.6	0.0783	4.6	0.3591
0.8	0.1317	4.8	0.3325
1.0	0.1972	5.0	0.3013
1.2	0.2565	5.5	0.2323
1.4	0.3304	6.0	0.1752
1.6	0.3978	6.5	0.1311
1.8	0.4618	7.0	0.0982
2.0	0.5104	7.5	0.0714
2.2	0.5523	8.0	0.0509
2.4	0.5789	8.5	0.0379
2.6	0.5930	9.0	0.0271
2.8	0.5983	9.5	0.0194
3.0	0.5910	10	0.0141
3.2	0.5768	11	0.0073
3.4	0.5533	12	0.0037
3.6	0.5302	13	0.0018
3.8	0.5006	14	0.0009
4.0	0.4695	15	0.0004

† The authors are grateful to Dr. M. E. Rose for calling our attention to this paper.

by using the quantum condition

$$\int_{\rho_1}^{\rho_2}\left[\frac{M}{2\mu}(E-\mathfrak{V}_g)\right]d\rho = (v+\tfrac{1}{2})\pi. \tag{30}$$

A value $E \approx -0.0005$ (in the same scale as (32)) seems almost to satisfy the above condition. In $(d-\mu-d)^+$, mainly because M in (30) is replaced by $2M$ and, to a small extent, because the correction $\Delta E_g(\rho)-\Delta E_g(\infty)$ is half that for $(p-\mu-p)^+$ thereby making the potential trough $\mathfrak{V}_g(\rho)$ slightly deeper, an excited vibrational state $v = 1$ is stable. The existence of a real (or "virtual" in the sense of the ^1S state of the deuteron) state will only manifest itself in the scattering of $p-\mu$ by p at very low energies.

6. The $(p-\mu-d)^+$ ion

For the unsymmetric system $(p-\mu-d)^+$, the term H_1^A in (5) destroys the symmetry and the μ-meson wave functions no longer have the g and u property. The ψ_g and ψ_u in this case are now mixed. In principle, if the quantum numbers of the solutions of (11), (12) are denoted collectively by n, the energy levels of the mesonic state are given by

$$|\langle n|H_0+H_1^S+H_1^A|m\rangle - V(\rho)\delta_{mn}| = 0. \tag{31}$$

We shall, in the problem of slow collisions, make the approximation of considering only the two lowest states (that correspond to ψ_g, ψ_u in $(p-\mu-p)^+$. Then for any value ρ, the energies of these two levels are given by the roots of

$$\begin{vmatrix} \langle g|H_0+H_1^S|g\rangle - V(\rho) & \langle g|H_1^A|u\rangle \\ \langle u|H_1^A|g\rangle & \langle u|H_0+H_1^S|u\rangle - V(\rho) \end{vmatrix} = 0, \tag{32}$$

where

$$\langle g|H_0+H_1^S|g\rangle = V_g(\rho)+\langle g|\bar{H}_1^S|g\rangle+\frac{\bar{\mu}(M+D)}{MD}\int\left(\frac{\partial\psi_g}{\partial\rho}\right)^2 d\tau_\mu \equiv \mathfrak{V}_g(\rho), \tag{33a}$$

$$\langle u|H_0+H_1^S|u\rangle = V_u(\rho)+\langle u|\bar{H}_1^S|u\rangle+\frac{\bar{\mu}(M+D)}{MD}\int\left(\frac{\partial\psi_u}{\partial\rho}\right)^2 d\tau_\mu \equiv \mathfrak{V}_u(\rho), \tag{33b}$$

and $\langle g|\bar{H}_1^S|g\rangle$ is given, as in (17), by

$$\frac{MD}{\bar{\mu}(M+D)}\langle g|\bar{H}_1^S|g\rangle = \frac{1}{\rho^2}\int\frac{\xi^2+\eta^2-2}{\xi^2-\eta^2}\left[(\xi^2-1)\left(\frac{\partial\psi_g}{\partial\xi}\right)^2+(1-\eta^2)\left(\frac{\partial\psi_g}{\partial\eta}\right)^2\right]d\tau_\mu$$
$$-\frac{2}{\rho}\int\frac{\partial\psi_g}{\partial\rho}Y\psi_g d\tau_\mu, \tag{34a}$$

$$\frac{MD}{\bar{\mu}(D-M)}\langle g|H_1^{A}|u\rangle = -\frac{1}{\rho^2}\int\frac{2\xi\eta}{\xi^2-\eta^2}\left[(\xi^2-1)\frac{\partial\psi_g}{\partial\xi}\frac{\partial\psi_u}{\partial\xi}+(1-\eta^2)\frac{\partial\psi_g}{\partial\eta}\frac{\partial\psi_u}{\partial\eta}\right]d\tau_\mu$$
$$-\frac{4}{\rho^2}\langle g|Z|u\rangle-\frac{2}{\rho}\int\psi_g Z\frac{\partial\psi_u}{\partial\rho}d\tau_\mu, \quad (35a)$$

with similar expressions (34b) (35b) for $\langle u|\bar{H}_1^{S}|u\rangle$, $\langle u|H_1^{A}|g\rangle$ obtainable from these by interchanging all g and u. It is seen that

$$\langle g|H_1^{A}|u\rangle \neq \langle u|H_1^{A}|g\rangle, \quad (36)$$

$$\langle g|Z|u\rangle = -\langle u|Z|g\rangle. \quad (37)$$

[We may remark that (36) is not inconsistent with the hermitian property of H_1^{A}. In fact the two matrix elements in (36) are equal if the integration extends not only to τ_μ but also to ρ.]

Let the roots of (32) be denoted by $V_L(\rho)$, $V_U(\rho)$ and the eigenfunctions by $\psi_L(\xi,\eta;\rho)$, $\psi_U(\xi,\eta;\rho)$, the subscripts L and U meaning "lower" and "upper" respectively. Then

$$\begin{aligned}\int\psi_L(H_0+H_1^{S}+H_1^{A})\psi_L d\tau_\mu &= V_L(\rho),\\ \int\psi_U(H_0+H_1^{S}+H_1^{A})\psi_U d\tau_\mu &= V_U(\rho),\end{aligned} \quad (38)$$

and

$$\int\psi_L\psi_U d\tau_\mu = 0. \quad (39)$$

We may write

$$\begin{aligned}V_L(\rho) &= \mathfrak{V}_g(\rho)+w_L(\rho),\\ V_U(\rho) &= \mathfrak{V}_u(\rho)+w_U(\rho),\end{aligned} \quad (40)$$

$$\begin{aligned}\psi_L(\xi,\eta;\rho) &= [1+\zeta^2(\rho)]^{-\frac{1}{2}}[\psi_g(\xi,\eta;\rho)+\zeta(\rho)\psi_u(\xi,\eta;\rho)],\\ \psi_U(\xi,\eta;\rho) &= [1-\zeta^2(\rho)]^{-\frac{1}{2}}[\psi_u(\xi,\eta;\rho)-\zeta(\rho)\psi_g(\xi,\eta;\rho)],\end{aligned} \quad (41)$$

where $w_L(\rho)$, $w_U(\rho)$ are functions of ρ and are of order $2\bar{\mu}(D-M)/MD$, and so is $\zeta(\rho)$ except for large ρ (see (44), (32), (33), (47)).

The asymptotic behaviour of $V_L(\rho)$, $V_U(\rho)$, ψ_L, ψ_U can be found from a study of $\mathfrak{V}_g(\rho)$, $\mathfrak{V}_u(\rho)$, $w_L(\rho)$, $w_U(\rho)$. The difference $\Delta_g(\rho)$ in (33a)

$$\Delta_g(\rho) \equiv \mathfrak{V}_g(\rho)-V_g(\rho) = \langle g|\bar{H}_1^{S}|g\rangle+\frac{\bar{\mu}(M+D)}{MD}\int\left(\frac{\partial\psi_g}{\partial\rho}\right)^2 d\tau_\mu \quad (42)$$

has been discussed in sec. 3 above. One has only to multiply the Δ_g of sec. 3 (for the p$-\mu-$p system) by the factor $(M+D)/2D = \frac{3}{4}$ for the system p$-\mu-$d. Similarly for $\Delta_u(\rho)$ which is given by (42) with g replaced by u. One gets

$$\Delta_g(\infty) = \Delta_u(\infty) = 0. \quad (43)$$

Also

$$V_g(\infty) = V_u(\infty) = 0.$$

Hence asymptotically for large ρ,

$$\mathfrak{V}_g(\rho) = \mathfrak{V}_u(\rho) \to 0. \tag{44}$$

Asymptotically for $\rho \to 0$, $\Delta_g(\rho)$ is finite as shown in (21) and table 1. $\Delta_u(\rho)$ can be found by putting in a $\psi_u(\xi, \eta; \rho)$ similar to (18) the asymptotic relations $\xi \to 2r/\rho$, $\eta \to \cos\vartheta$ where r, ϑ are the polar coordinates of the μ meson, namely, for $\rho \to 0$,

$$\psi_u(\xi, \eta; \rho) \to \sqrt{2}\, r e^{-r} \cos\vartheta; \qquad \frac{\partial \psi_u}{\partial \rho} \to \sqrt{2}\,\frac{r}{\rho}(1-r)e^{-r}\cos\vartheta$$

and

$$\Delta_u(\rho) \to \frac{\bar{\mu}(M+D)}{MD}\,\frac{2}{\rho^2}. \tag{43a}$$

Again with a Guillemin-Zener type wave function (18), one obtains, asymptotically for large ρ

$$\langle g|H_1^{\wedge}|u\rangle \to \langle u|H_1^{\wedge}|g\rangle \to -\frac{\bar{\mu}(D-M)}{2MD} \equiv -\tfrac{1}{2}\Delta_0, \tag{45}$$

and asymptotically for $\rho \to 0$,

$$\begin{aligned} &\langle g|H_1^{\wedge}|u\rangle \to -\frac{\bar{\mu}(D-M)}{MD}\,\frac{64\sqrt{2}}{81\rho}, \\ &\langle u|H_1^{\wedge}|g\rangle \to \text{finite}. \end{aligned} \tag{45a}$$

From (32), (40) and (45), one obtains, as $\rho \to \infty$,

$$w_U(\rho) \to \tfrac{1}{2}\Delta_0, \quad w_L(\rho) \to -\tfrac{1}{2}\Delta_0, \tag{46}$$

where Δ_0 is the asymptotic separation $V_U - V_L$ †. Asymptotically,

$$\begin{aligned} \psi_U(\xi, \eta; \rho) &\to \frac{1}{\sqrt{2}}[\psi_u(\xi, \eta; \rho) - \psi_g(\xi, \eta; \rho)] \to \psi_0(r_{\mu p}), \\ \psi_L(\xi, \eta; \rho) &\to \frac{1}{\sqrt{2}}[\psi_g(\xi, \eta; \rho) + \psi_u(\xi, \eta; \rho)] \to \psi_0(r_{\mu d}), \end{aligned} \tag{47}$$

where $\psi_0(r_{\mu p})$ is the hydrogenic wave function of μ in the 1s state centred at the

† In units of μ/m_e rydberg, Δ_0 in (45) is

$$\Delta_0 = \frac{\mu}{2M\left(1+\frac{3\mu}{4M}\right)^2}.$$

The exact difference between the 1s state energy of $(p-\mu)$ and $(d-\mu)$, is, in the same units,

$$\Delta_0 = \frac{\mu}{2M\left(1+\frac{\mu}{M}\right)\left(1+\frac{\mu}{2M}\right)} \quad (\approx 135\text{ eV}).$$

proton, etc.

$$\psi_0(r_{\mu p}) = \sqrt{\frac{\alpha^3}{\pi}} e^{-\alpha r_{\mu p}} . \tag{48}$$

The asymptotic behaviour (47) is the result of the removal of the degeneracy of the system $H_0+H_1^S$ as $\rho \to \infty$ (as shown by (44)) by the term H_1^A. From (32), (44), (45), (46), it is seen that the eigenvalues of $H_0+H_1^S+H_1^A$ have the asymptotic values $V_L \to -\frac{1}{2}\Delta_0$, $V_U \to \frac{1}{2}\Delta_0$, and the eigenfunctions the asymptotic form (47).

Thus in passing from the symmetric $(p-u-p)^+$ to the unsymmetric $(p-u-d)^+$, the "potential curves" $V_{2p\sigma u}(\rho)$, $V_{1s\sigma g}(\rho)$ pass into $V_U(\rho)$, $V_L(\rho)$ respectively, which asymptotically for large ρ are separated by Δ_0 and correspond to the two states $(p-u)+d$ and $(d-u)+p$ respectively. This result, also given in a qualitative discussion by Marshall and Schmidt [8]), seems rather natural at first thought, but is in fact only approximate and somewhat misleading. The $V_U(\rho)$, $V_L(\rho)$ result from treating the distance ρ as a parameter and not as a variable in the Schrödinger equation of the system, and as a consequence have a meaning only in the "static nuclei" picture. Since the asymptotic separation Δ_0 of $V_U(\rho)$, $V_L(\rho)$ has its origin in the relative motion between the meson and the nuclei, strictly speaking it is not correct to have the dynamical effect represented by Δ_0 in the static nuclei picture of potential curves.

7. Deviation from the Franck-Condon Rule due to the Coupling Correction

We shall for a moment consider the more general molecular system in which the ordinary electrons are replaced by μ mesons ($p-\mu-\mu-p$ hydrogen molecule, for example). To a first approximation the spectrum of the μ-molecule will resemble that of the e-molecule except that the energy scale is changed by a factor $\approx \mu/m_e$. To the next approximation in μ/M, in addition to small changes in energies, there may be a change in the intensity distribution of bands in a mesonic ("electronic") transition. Consider a mesonic transition $A \to X$. If the state A is "perturbed", through the coupling $H_1(\mu/M)$, by another state B with a very different equilibrium separation r_e from that of A, the result is that the transitions $A \to X$ will seem to give rise to "non-vertical" transition, i.e., to a deviation from the usual Franck-Condon principle. We shall not go into this since μ-molecules are rare and short-lived, and their spectra, lying in the X-ray region, are not easily measurable with the accuracy of ordinary spectroscopy.

8. Scattering Process

For the scattering problem (of very low energies so that one may neglect the effect of excited mesonic states), we make the Ansatz that the wave function of

the system is expressible in the form †

$$\Psi(\xi, \eta; \rho, \vartheta) = \frac{1}{\sqrt{2}}[\psi_L(\xi, \eta; \rho)\Phi_L(\rho) + \psi_U(\xi, \eta; \rho)\Phi_U(\rho)]. \tag{49}$$

On putting this into the Schrödinger equation

$$(H_0 + H_1^S + H_1^A - E)\Psi(\xi, \eta; \rho, \vartheta) = 0,$$

multiplying by $\psi_L d\tau_\mu$, $\psi_U d\tau_\mu$ successively and integrating over ξ, η, one obtains the coupled equations for $\Phi_L(\rho)$, $\Phi_U(\rho)$ ††

$$\begin{aligned}\left[\frac{\tilde{\mu}(M+D)}{MD}\nabla_\rho^2 - V_L(\rho) + E\right]\Phi_L(\rho) &= -\Lambda(\rho)\Phi_U(\rho),\\ \left[\frac{\tilde{\mu}(M+M)}{MD}\nabla_\rho^2 - V_U(\rho) + E\right]\Phi_U(\rho) &= \Lambda(\rho)\Phi_L(\rho),\end{aligned} \tag{50}$$

where

$$\Lambda(\rho) = \frac{2\tilde{\mu}(D-M)}{MD}\langle\psi_L|Z|\psi_U\rangle\frac{1}{\rho}\frac{\partial}{\partial\rho}. \tag{51}$$

Thus the H_1^A, the interaction between the μ and the p, d motions, couples the Φ_L and Φ_U, the wave functions "associated" with the μ being in the ψ_L, ψ_U state respectively.

The problem of various scattering processes involving p, d and μ is now one of finding solutions of (50) that satisfy various asymptotic conditions corresponding to the scattering problem.

9. Elastic Scattering $(p-\mu)+p \to (p-\mu)+p$

For the elastic scattering in the process above, we use the results of the preceding section, first with some simplifications arising from the vanishing of H_1^A and then with a proper account of the Pauli principle.

With $H_1^A = 0$, one has $w_L(\rho) = w_U(\rho) = \zeta(\rho) = \Delta_0 = 0$ in (40), (41), (45), (46), which now become

$$\begin{aligned}V_L(\rho) &= \mathfrak{V}_g(\rho) \to 0 \text{ asymptotically},\\ V_U(\rho) &= \mathfrak{V}_u(\rho) \to 0 \text{ asymptotically},\end{aligned} \tag{40A}$$

† We might emphasize that although the $\psi_U(r_\mu; \rho)$, $\psi_L(r_\mu; \rho)$ and the $V_U(\rho)$, $V_L(\rho)$ are subject to the limitation of the "static nuclei" approximation pointed out at the end of section 6, the following Ansatz (49) and also the alternative Ansatz (82) are not subject to this limitation, since the functions $\Phi_U(\rho)$, $\Phi_L(\rho)$ in (49) and $\Phi_u(\rho)$, $\Phi_g(\rho)$ in (82) are still to be determined by the Schrödinger equation itself.

†† We must make it clear that if we assume eq. (49), the results from (50), (50A), (69) are valid for all l waves.

$$\psi_L = \psi_g(\xi, \eta; \rho) \to \frac{1}{\sqrt{2}}[\psi_0(r_{\mu A}) + \psi_0(r_{\mu B})] \text{ asymptotically,}$$
$$\psi_U = \psi_u(\xi, \eta; \rho) \to \frac{1}{\sqrt{2}}[\psi_0(r_{\mu A}) - \psi_0(r_{\mu B})] \text{ asymptotically,} \quad (41A)(47A)$$

we have

$$(H_0 + H_1^S)\psi_g = \mathfrak{V}_g(\rho)\psi_g,$$
$$(H_0 + H_1^S)\psi_u = \mathfrak{V}_u(\rho)\psi_u, \quad (38A)$$

and

$$\Psi(\xi, \eta; \rho, \vartheta) = \frac{1}{\sqrt{2}}[\psi_g \Phi_g + \psi_u \Phi_u]. \quad (49A)$$

The equations for $\Phi_g(\rho)$, $\Phi_u(\rho)$ are now

$$\left[\nabla_\rho^2 + \frac{M}{2\bar{\mu}}(E - \mathfrak{V}_g(\rho))\right]\Phi_g(\rho) = 0,$$
$$\left[\nabla_\rho^2 + \frac{M}{2\bar{\mu}}(E - \mathfrak{V}_u(\rho))\right]\Phi_u(\rho) = 0, \quad (50A)$$

which are not coupled, since $\{{g \atop u}\}$ is an exact symmetry property.

Consider the collision of a proton and a $(p-\mu)$ atom in the 1S state. The total wave function of the system can be written, in the same approximation as (47A), in one of the following forms

$$\chi_s(\sigma_A, \sigma_B, \sigma_\mu) \cdot \begin{cases} \psi_g(r_\mu; \rho)\Phi_{go}(\rho), \\ \psi_u(r_\mu; \rho)\Phi_{ue}(\rho) \end{cases}$$
$$\chi_a(\sigma_A, \sigma_B, \sigma_\mu) \cdot \begin{cases} \psi_g(r_\mu; \rho)\Phi_{ge}(\rho) \\ \psi_u(r_\mu; \rho)\Phi_{uo}(\rho) \end{cases} \quad (52)$$

where χ_s, χ_a are the spin wave functions symmetric and antisymmetric in the spins σ_A, σ_B of the two protons; Φ_{ge}, Φ_{go} are the even-wave and odd-wave solutions, respectively, and similarly for Φ_{ue}, Φ_{uo}, of (50A). We see solutions of (50A) which asymptotically for large ρ, behave as

$$\Phi_g(\rho) \to e^{i\gamma K\rho} + \frac{e^{i\gamma K\rho}}{\rho} f_g(\vartheta),$$
$$\Phi_u(\rho) \to e^{i\gamma K\rho} + \frac{e^{i\gamma K\rho}}{\rho} f_u(\vartheta), \quad (53)$$
$$\gamma^2 = \frac{M}{2\bar{\mu}}, \qquad K^2 = E,$$

where the amplitude f_g, f_u are given by

$$f_g(\vartheta) = \frac{1}{2i\gamma K}\sum (2l+1)[e^{2i\delta_l(g)}-1]P_l(\cos\vartheta),$$
$$f_u(\vartheta) = \frac{1}{2i\gamma K}\sum (2l+1)[e^{2i\delta_l(u)}-1]P_l(\cos\vartheta), \tag{54}$$

$\delta_l(g)$, $\delta_l(u)$ being the phase shifts in the field $\mathfrak{V}_g(\rho)$, $\mathfrak{V}_u(\rho)$, of R_l

$$\left[\frac{d^2}{d\rho^2}+\gamma^2K^2-\gamma^2\mathfrak{V}_g-\frac{l(l+1)}{\rho^2}\right]R_{gl}(\rho)=0,$$
$$\left[\frac{d^2}{d\rho^2}+\gamma^2K^2-\gamma^2\mathfrak{V}_u-\frac{l(l+1)}{\rho^2}\right]R_{ul}(\rho)=0, \tag{55}$$

$R_{gl}(\rho)$ being the radial part of Φ_g, etc. See (72). With (53), the function (49A) is, asymptotically,

$$\Psi(\xi,\eta;\rho,\vartheta)\to e^{i\gamma K\rho}\psi_0(r_{\mu A})+\frac{e^{i\gamma K\rho}}{\rho}[\tfrac{1}{2}(f_g+f_u)\psi_0(r_{\mu A})+\tfrac{1}{2}(f_g-f_u)\psi_0(r_{\mu B})], \tag{56}$$

which describes a scattering process in which the μ meson is initially bound with the proton A, and is, after collision, associated with A and B with the amplitude $\frac{1}{2}(f_g+f_u)$, $\frac{1}{2}(f_g-f_u)$ respectively. We now take account of the Pauli principle for χ_s by including only the $l=\{^{\text{odd}}_{\text{even}}$ waves in $\{^{\phi_g}_{\phi_u}$ in (53). The corresponding result for (56) gives the cross section for the χ_s state scattering (1) for the "direct" scattering

$$(p_A-\mu)+p_B\to(p_A-\mu)+p_B,$$
$$d\sigma_D=\frac{2\pi}{4}|f_g(l\text{ odd})+f_u(l\text{ even})|^2\,d\cos\vartheta, \tag{57}$$

and for the "exchange" scattering,

$$(p_A-\mu)+p_B\to(p_B-\mu)+p_A,$$
$$d\sigma_{Ex}=\frac{2\pi}{4}|f_g(l\text{ odd})-f_u(l\text{ even})|^2\,d\cos\vartheta. \tag{58}$$

Since the cross terms in both (57) and (58) vanish on integration over ϑ on account of parity considerations, it is seen that σ_D and σ_{Ex} are the same. The total χ_s state scattering is hence

$$d\sigma_s=\pi[|f_g(l\text{ odd})|^2-|f_u(l\text{ even})|^2]d\cos\vartheta. \tag{59}$$

For the χ_a state scattering, entirely similar argument gives

$$d\sigma_a=\pi[|f_g(l\text{ even})|^2+|f_u(l\text{ odd})|^2]d\cos\vartheta. \tag{60}$$

From a consideration of the spin wave function $\chi(\sigma_A,\sigma_B,\sigma_\mu)$ it can be shown that for both the initial hyperfine states $F=0$, 1 of the mesonic atom, the

cross-section of (1) is given by

$$d\sigma = \tfrac{1}{4}[3d\sigma_s + d\sigma_a]. \tag{61}$$

In terms of the phase shifts in (54), we have from (54), (59), (60), (61),

$$\sigma = \frac{4\pi}{\gamma^2 K^2}\Big[\tfrac{3}{8}\sum_{\text{odd}}(2l+1)\sin^2\delta_l(g) + \tfrac{3}{8}\sum_{\text{even}}(2l+1)\sin^2\delta_l(u) + \tfrac{1}{8}\sum_{\text{even}}(2l+1)\sin^2\delta_l(g) + \tfrac{1}{8}\sum_{\text{odd}}(2l+1)\sin^2\delta_l(u)\Big]. \tag{62}$$

To calculate the phase shifts $\delta_l(g)$, $\delta_l(u)$ from (55), we note that for $\rho \leqq 9$, $V_g(\rho)$, $V_u(\rho)$ are available from the exact solution of (12) [4]. For large $\rho(\rho > 10)$, $V_g(\rho)$, $V_u(\rho)$ are essentially the Van der Waals interaction between a proton and the induced dipole of the $(p-\mu)$ atom,

$$V_g(\rho) \approx V_u(\rho) \to -\frac{9}{2\rho^4}. \tag{63}$$

From the values of the exact $V_g(\rho)$, $V_u(\rho)$, it is found that for $\rho > 7$, the following relations are beginning to be valid

$$V_g(\rho) + V_u(\rho) \approx -\frac{9}{\rho^4}, \tag{64}$$

$V_u(\rho) - V_g(\rho)$ exponentially decreasing.

Calculations with the exact V_g, V_u of ref. [4]) and extrapolated according to (63) give the phases in table 3.

TABLE 3

Scattering phases of $(p-\mu)+p$ for $1s\sigma g$ and $2p\sigma u$ states

K^2	Scattering by $V_{1s\sigma g}$			Scattering by $V_{2p\sigma u}$		
	δ_0	δ_1	δ_2	δ_0	δ_1	δ_2
10^{-7}	$\pi+0.004\,76$			$-0.002\,47$		
10^{-6}	$\pi+0.014\,98$					
10^{-4}	$\pi+0.016\,8$			$-0.079\,4$		
10^{-3}	$\pi+0.017\,0$			$-0.273\,2$		
10^{-2}	$\pi-0.330\,0$	$\pi-0.2375$		$-0.916\,9$	-0.1823	
10^{-1}	$1.562\,8$	1.2666	1.5325	$-2.423\,4$	-1.3298	-0.6454

We may remark here that, on the basis of sec. 3 and (43), the replacement of $\mathfrak{V}_g$ in (55) by V_g is not a bad approximation. For $\mathfrak{V}_u$, however, in view of (43a), the use of $\mathfrak{V}_u$ instead of V_u will tend to impart some p wave (but only for $\rho \approx 0$) character to $\delta_0(u)$ and hence to make $\delta_0(u)$ smaller (in absolute value) than the values given in table 3. For the lowest energy $K^2 = 10^{-7}$, however, the σ given in (65) will be slightly too large by a factor certainly not exceeding 2.

For $K^2 = 10^{-7}$, corresponding to a temperature of a few degrees Kelvin, the scattering cross-section of the process (1) is

$$\sigma \approx 1.7 \times 10^{-18}\ \text{cm}^2. \tag{65}$$

For $K^2 = 10^{-4}$ (≈ 0.28 eV), $\sigma = 0.92 \times 10^{-18}$ cm^2.

10. Direct and Exchange Scattering of (p—μ)+d

In the following we shall call (2) the direct, and (3) the exchange scattering, and use the subscripts D, Ex. According to section 8, we make the Ansatz (49), which asymptotically for large ρ, by virtue of (47), gives

$$\Psi(\xi, \eta; \rho, \vartheta) \to \frac{1}{\sqrt{2}} [\psi_0(r_{\mu d})\Phi_L(\rho) + \psi_0(r_{\mu p})\Phi_U(\rho)]. \tag{66}$$

Thus $\Phi_L(\rho)$ is "associated" with the meson being bound with the deuteron, etc. The hydrogenic wave functions $\psi_0(r_{\mu d})$, $\psi_0(r_{\mu p})$ are given in (48).

Let the deuteron be incident on (p—μ) with (relative) kinetic energy k_d^2, and let the kinetic energy of the proton scattered in the exchange process be k_p^2. Then, by (46),

$$k_p^2 = k_d^2 + \Delta_0. \tag{67}$$

By (40), (44), (46), the asymptotic values of $V_L(\rho)$, $V_U(\rho)$ are

$$V_L(\rho) \to -\tfrac{1}{2}\Delta_0, \qquad V_U(\rho) \to \tfrac{1}{2}\Delta_0. \tag{68}$$

The equations (50) are then, up to the order $\bar{\mu}(D-M)/MD$,

$$\begin{aligned} [\nabla_\rho^2 + \gamma^2(k_p^2 - V_L(\rho) - \tfrac{1}{2}\Delta_0)]\Phi_L(\rho) &= -\gamma^2 \Lambda(\rho)\Phi_U(\rho), \\ [\nabla_\rho^2 + \gamma^2(k_d^2 - V_U(\rho) + \tfrac{1}{2}\Delta_0)]\Phi_U(\rho) &= \gamma^2 \Lambda(\rho)\Phi_L(\rho). \end{aligned} \tag{69}$$

where

$$\gamma^2 = \frac{MD}{\bar{\mu}(M+D)}. \tag{70}$$

We seek solutions which asymptotically for large ρ behave as

$$\begin{aligned} \Phi_U(\rho) &\to e^{i\gamma \mathbf{k}_d \cdot \rho} + \frac{e^{i\gamma k_d \rho}}{\rho} f_D(\vartheta), \\ \Phi_L(\rho) &\to \frac{e^{i\gamma k_p \rho}}{\rho} f_{Ex}(\vartheta), \end{aligned} \tag{71}$$

where $f_D(\vartheta)$, $f_{Ex}(\vartheta)$ are the amplitudes of the direct and exchange scattering

(2), (3) respectively. We shall expand $\Phi_L(\rho)$, $\Phi_U(\rho)$, etc. in the form

$$\Phi_L(\rho) = \sum c_l \frac{1}{\rho} R_{Ll}(\rho) P_l(\cos\vartheta),$$
$$\Phi_U(\rho) = \sum c_l \frac{1}{\rho} R_{Ul}(\rho) P_l(\cos\vartheta). \tag{72}$$

so that (69) gives

$$\left[\frac{d^2}{d\rho^2} - \frac{l(l+1)}{\rho^2} + \gamma^2(k_p^2 - V_L - \tfrac{1}{2}\Delta_0)\right] R_{Ll} = -\gamma^2 \Lambda(\rho) R_{Ul},$$
$$\left[\frac{d^2}{d\rho^2} - \frac{l(l+1)}{\rho^2} + \gamma^2(k_d^2 - V_U + \tfrac{1}{2}\Delta_0)\right] R_{Ul} = \gamma^2 \Lambda(\rho) R_{Ll}. \tag{73}$$

We proceed to solve these equations by iteration. Let $R^{(1)}_{Ll}(\rho)$, $R^{(2)}_{Ll}(\rho)$ be the solutions of the homogeneous equations obtained by replacing the righthand side of (73) by zero, whose asymptotic behaviours are given by

$$R^{(1)}_{Ll}(\rho) \to \sin(\gamma k_p \rho - \tfrac{1}{2} l\pi + \delta_l(L)),$$
$$R^{(2)}_{Ll}(\rho) \to \frac{1}{k_p} \exp i(\gamma k_p \rho - \tfrac{1}{2} l\pi + \delta_l(L)). \tag{74}$$

Similarly, for $R^{(1)}_{Ul}(\rho)$, $R^{(2)}_{Ul}(\rho)$. Then the solutions of (73) which vanish at $\rho = 0$ and satisfy the asymptotical condition (71) are [9])

$$R_{Ll}(\rho) = \gamma R^{(2)}_{Ll}(\rho) \int_0^\rho R^{(1)}_{Ll}(\rho) \Lambda(\rho) R_{Ul}(\rho)\, d\rho, \tag{75a}$$

$$R_{Ul}(\rho) = R^{(1)}_{Ul}(\rho) - \gamma R^{(2)}_{Ul}(\rho) \int_0^\rho R^{(1)}_{Ul}(\rho) \Lambda(\rho) R_{Ll}(\rho) d\rho. \tag{75b}$$

Since, as we shall see, the integrals in (75) are very small compared with unity, we shall start the iteration by taking $R_{Ul}(\rho) \approx R^{(1)}_{Ul}(\rho)$ in (75a), thus finding $R^*_{Ll}(\rho)$ which is substituted into (75b) to give $R_{Ul}(\rho)$. The asymptotic forms of these solutions are then

$$R_{Ll}(\rho) \to \frac{\gamma A_l(L)}{k_p} \exp i(\gamma k_p \rho - \tfrac{1}{2} l\pi + \delta_l(L)),$$
$$R_{Ul}(\rho) \to \sin(\gamma k_d \rho - \tfrac{1}{2} l\pi + \delta_l(U)) - \frac{\gamma A_l(U)}{k_d} \exp i(\gamma k_d \rho - \tfrac{1}{2} l\pi + \delta_l(U)), \tag{76}$$

where

$$A_l(L) = \int_0^\infty R^{(1)}_{Ll}(\rho) \Lambda(\rho) R^{(1)}_{Ul}(\rho) d\rho,$$
$$A_l(U) = \int_0^\infty R^{(1)}_{Ul}(\rho) \Lambda(\rho) R^*_{Ll}(\rho) d\rho. \tag{77}$$

On comparing (72), (76) with (71), we obtain

$$f_{\mathrm{D}}(\vartheta) = \frac{i}{2\gamma k_{\mathrm{d}}} \sum (2l+1) \left[1 - \left(1 - \frac{2i\gamma A_l(\mathrm{U})}{k_{\mathrm{d}}} \right) e^{2i\delta_l(\mathrm{U})} \right] P_l(\cos\vartheta),$$

$$f_{\mathrm{Ex}}(\vartheta) = -\frac{1}{k_{\mathrm{d}} k_{\mathrm{p}}} \sum (2l+1) A_l(\mathrm{L}) e^{i(\delta_l(\mathrm{L})+\delta_l(\mathrm{U}))} P_l(\cos\vartheta). \tag{78}$$

On writing

$$A_l(\mathrm{U}) = a_l(\mathrm{U}) + i b_l(\mathrm{U}),$$

the cross-sections are, from (78),

$$\sigma(\mathrm{D}) = \frac{4\pi}{\gamma^2 k_{\mathrm{d}}^2} \sum (2l+1) \left[\left(1 + \frac{2\gamma b_l}{k_{\mathrm{d}}} \right) \sin^2\delta_l(\mathrm{U}) - \frac{\gamma a_l}{k_{\mathrm{d}}} \sin 2\delta_l(\mathrm{U}) + \frac{\gamma^2 |A_l(\mathrm{U})|^2}{k_{\mathrm{d}}^2} \right] \tag{79}$$

$$\sigma(\mathrm{Ex}) = \frac{4\pi}{(k_{\mathrm{d}} k_{\mathrm{p}})^2} \sum (2l+1) |A_l(\mathrm{L})|^2, \tag{80}$$

in units of $\bar{a}_\mu^{\,2}$ of (10).

In an actual calculation one may replace the complicated $\Lambda(\rho)$ defined in (51) by

$$\Lambda_0(\rho) = \frac{2\bar{\mu}(D-M)}{MD} \langle \mathrm{g}|Z|\mathrm{u}\rangle \frac{1}{\rho} \frac{\partial}{\partial\rho} \tag{81}$$

where $\langle \mathrm{g}|Z|\mathrm{u}\rangle$ is the matrix element of Z in (9) with respect to the exact eigenfunctions of H_0 in (12). This approximation may be justified by noting that for the region of ρ which is relevant, ψ_{L}, ψ_{U} differ from ψ_{g}, ψ_{u} only by quantities of $O(2\bar{\mu}(D-M)/MD)$. Even with this approximation, the evaluation of $\Lambda_0(\rho)$ and of $A_l(\mathrm{U})$, $A_l(\mathrm{L})$ would be a lengthy one, especially since the exact functions ψ_{u}, ψ_{g} are not available for $\rho > 9$ [4]).

11. Direct and Exchange Scattering Processes of (p—μ)+d: an Alternative Treatment

While the method of section 3 is a natural one from the physical point of view of "potential curves", an equivalent alternative method is possible. This will be briefly sketched below.

In place of the Ansatz (49), we shall use the equivalent one †

$$\Psi(\xi, \eta; \rho, \vartheta) = \frac{1}{\sqrt{2}} [\psi_{\mathrm{g}}(\xi, \eta; \rho)\Phi_{\mathrm{g}}(\rho) + \psi_{\mathrm{u}}\Phi_{\mathrm{u}}]. \tag{82}$$

The Φ_{g}, Φ_{u} satisfy the coupled equations ††

† See footnote † of section 8.
†† See footnote †† of section 8.

$$\left[-\frac{\bar{\mu}(M+D)}{MD}\nabla_\rho^2+\mathfrak{V}_g(\rho)-E\right]\Phi_g(\rho) = -[\langle g|H_1^A|u\rangle-A_0(\rho)]\Phi_u(\rho),$$
$$\left[-\frac{\bar{\mu}(M+D)}{MD}\nabla_\rho^2+\mathfrak{V}_u(\rho)-E\right]\Phi_u(\rho) = -[\langle u|H_1^A|g\rangle+A_0(\rho)]\Phi_g(\rho), \tag{83}$$

where the $\mathfrak{V}(\rho)$, $A_0(\rho)$ are defined in (33)—(35), (81).

On introducing

$$\chi_D = \Phi_g(\rho)-\Phi_u(\rho), \quad \chi_{Ex} = \Phi_g(\rho)+\Phi_u(\rho), \tag{84}$$

eq. (82) becomes

$$\Psi(\xi,\eta;\rho,\vartheta) = \tfrac{1}{2\sqrt{2}}[(\psi_g-\psi_u)\chi_D+(\psi_g+\psi_u)\chi_{Ex}] \tag{85}$$

which asymptotically

$$\to\tfrac{1}{\sqrt{2}}[\psi_0(r_{\mu p})\chi_D+\psi_0(r_{\mu d})\chi_{Ex}]. \tag{85a}$$

On comparing this with (66), it is seen that $\chi_D(\rho)$ is like $\Phi_U(\rho)$ in being associated with the meson being bound with the proton for $\rho\to\infty$, etc. The χ's satisfy the coupled equations

$$\left[-\frac{\bar{\mu}(M+D)}{MD}\nabla_\rho^2+V_D(\rho)-E\right]\chi_D(\rho) = -[\tfrac{1}{2}(\mathfrak{V}_g-\mathfrak{V}_u)+v(\rho)]\chi_{Ex},$$
$$\left[-\frac{\bar{\mu}(M+D)}{MD}\nabla_\rho^2+V_{Ex}(\rho)-E\right]\chi_{Ex}(\rho) = -[\tfrac{1}{2}(\mathfrak{V}_g-\mathfrak{V}_u)-v(\rho)]\chi_D, \tag{86}$$

where

$$v(\rho) = \tfrac{1}{2}[\langle g|H_1^A|u\rangle-\langle u|H_1^A|g\rangle]-A_0(\rho), \tag{87}$$

and

$$\left.\begin{matrix}V_D(\rho)\\V_{Ex}(\rho)\end{matrix}\right\} = \tfrac{1}{2}(\mathfrak{V}_g+\mathfrak{V}_u)\mp\tfrac{1}{2}[\langle g|H_1^A|u\rangle+\langle u|H_1^A|g\rangle]$$
$$\to\begin{cases}\tfrac{1}{2}A_0\\-\tfrac{1}{2}A_0\end{cases}, \tag{88}$$

by (44)—(46).On using k_p^2, k_d^2 as in (67)—(69), one obtains for (86)

$$[\nabla_\rho^2+\gamma^2(k_d^2-V_D+\tfrac{1}{2}A_0)]\chi_D = \gamma^2[\tfrac{1}{2}(\mathfrak{V}_g-\mathfrak{V}_u)+v]\chi_{Ex},$$
$$[\nabla_\rho^2+\gamma^2(k_p^2-V_{Ex}-\tfrac{1}{2}A_0)]\chi_{Ex} = \gamma^2[\tfrac{1}{2}(\mathfrak{V}_g-\mathfrak{V}_u)-v]\chi_D, \tag{89}$$

where $\gamma^2 = MD/(M+D)\bar{\mu}$. These two equations correspond to those in (69) in the method of section 9. The calculation of the cross-sections from (89) proceeds exactly as in (69)—(80). The cross-sections are then given by

$$\sigma_{\mathrm{D}}=\frac{4\pi}{\gamma^2 k_{\mathrm{d}}{}^2}\sum(2l+1)\left[\left(1+\frac{2\gamma b_l(\mathrm{D})}{k_{\mathrm{d}}}\right)\sin^2\delta_l(\mathrm{D})-\frac{\gamma a_l(\mathrm{D})}{k_{\mathrm{d}}}\sin 2\delta_l(\mathrm{D})+\frac{\gamma^2|A_l(\mathrm{D})|^2}{k_{\mathrm{d}}{}^2}\right] \tag{90a}$$

$$\sigma_{\mathrm{Ex}}=\frac{4\pi}{(k_{\mathrm{d}}k_{\mathrm{p}})^2}\sum(2l+1)|A_l(\mathrm{Ex})|^2, \tag{90b}$$

in units of $\bar{a}_\mu{}^2$ of (10). Here

$$\begin{aligned}A_l(\mathrm{Ex}) &= \int_0^\infty R_l^{(1)}(\mathrm{Ex})[\tfrac{1}{2}(\mathfrak{V}_{\mathrm{g}}-\mathfrak{V}_{\mathrm{u}})-v]R_l^{(1)}(\mathrm{D})\mathrm{d}\rho,\\ A_l(\mathrm{D}) &= \int_0^\infty R_l^{(1)}(\mathrm{D})[\tfrac{1}{2}(\mathfrak{V}_{\mathrm{g}}-\mathfrak{V}_{\mathrm{u}})+v]R_l{}^*(\mathrm{Ex})\mathrm{d}\rho,\end{aligned} \tag{91}$$

and $R_l^{(1)}(\mathrm{D})$, $R_l^{(2)}(\mathrm{D})$, $R_l^{(1)}(\mathrm{Ex})$, $R_l^{(2)}(\mathrm{Ex})$ have the same meaning as $R_{\mathrm{U}l}^{(1)}$, $R_{\mathrm{U}l}^{(2)}$, $R_{\mathrm{L}l}^{(1)}$, $R_{\mathrm{L}l}^{(2)}$ in (73), (74), but with respect to the homogeneous equations

$$\begin{aligned}\left[\frac{\mathrm{d}^2}{\mathrm{d}\rho^2}-\frac{l(l+1)}{\rho^2}+\gamma^2(k_{\mathrm{d}}{}^2-V_{\mathrm{D}}+\tfrac{1}{2}\Delta_0)\right]R_l(\mathrm{D})=0,\\ \left[\frac{\mathrm{d}^2}{\mathrm{d}\rho^2}-\frac{l(l+1)}{\rho^2}+\gamma^2(k_{\mathrm{p}}{}^2-V_{\mathrm{Ex}}-\tfrac{1}{2}\Delta_0)\right]R_l(\mathrm{Ex})=0,\end{aligned} \tag{92}$$

and $R_l{}^*(\mathrm{Ex})$ is to be calculated as described in connection with $R_{\mathrm{L}l}^*$ in (75a), (75b).

For $k_{\mathrm{d}}{}^2=5\times10^{-7}$ and $k_{\mathrm{p}}{}^2=\Delta_0+k_{\mathrm{d}}{}^2=0.050\,66$, corresponding to the collision of a $(\mathrm{p}-\mu)$ atom with a deuteron at the temperature of liquid hydrogen, numerical integration of (92), with the approximation of neglecting the small terms in $H_1{}^{\wedge}$ in (88) †, gives

$$\begin{aligned}\delta_0(\mathrm{D})&=0.031\,78,\\ \delta_0(\mathrm{Ex})=-1.196\,3,\quad \delta_1(\mathrm{Ex})&=-0.313\,71,\quad \delta_2(\mathrm{Ex})=0.020\,83.\end{aligned} \tag{93}$$

An evaluation of the effect of the term v in (91) by means of (35a), (37), (81) and the solutions $R_l^{(1)}(\mathrm{Ex})$, $R_l^{(1)}(\mathrm{D})$ shows that

$$\int_0^\infty R_0^{(1)}(\mathrm{Ex})vR_0^{(1)}(\mathrm{D})\mathrm{d}\rho\approx-0.64\times10^{-4},$$

and on neglecting this, we have

$$\begin{aligned}A_0(\mathrm{Ex})&=-1.250\times10^{-3},\\ |A_1(\mathrm{Ex})|&\ll|A_0(\mathrm{Ex})|.\end{aligned} \tag{94a}$$

† i.e., setting $V_{\mathrm{Ex}}+\frac{1}{2}\Delta_0=V_{\mathrm{D}}-\frac{1}{2}\Delta_0=\frac{1}{2}(V_{\mathrm{g}}+V_{\mathrm{u}})$ in (92). Considerations show that the effect of not making this approximation is to make $\delta_0(\mathrm{D})$ smaller than the value 0.03178 given in (93), but is not important on the iteration procedure or on the $A_0(\mathrm{Ex})$, $A_0(\mathrm{D})$. From the magnitudes of the three terms in (90a), we find that using the $V_{\mathrm{Ex}}(\rho)$, $V_{\mathrm{D}}(\rho)$ as given in (88) without the approximation here would not have lowered the order of magnitude of $\sigma(\mathrm{D})$ in (95).

Similarly, the contribution of v to $A_0(\mathrm{D})$ in (91) can also be neglected, and we obtain

$$A_0(\mathrm{D}) = (2.408-8.876\,i)\times 10^{-6}. \tag{94b}$$

With these values of $A_0(\mathrm{D})$, $A_0(\mathrm{Ex})$ and neglecting the contribution from the higher angular momenta, we find

$$\begin{aligned}\sigma(\mathrm{D}) &= 7.49\times 10^{3}\tilde{a}_{\mu}^{\,2} = 5.0\times 10^{-18}\ \mathrm{cm}^2,\\ \sigma(\mathrm{Ex}) &= 7.75\times 10^{2}\tilde{a}_{\mu}^{\,2} = 5.17\times 10^{-19}\ \mathrm{cm}^2.\end{aligned} \tag{95}$$

With this $\sigma(\mathrm{Ex})$ for $(\mathrm{p}-\mu)+\mathrm{d}\rightarrow(\mathrm{d}-\mu)+\mathrm{p}$, one readily obtains for the exchange rate in liquid deuterium

$$R_{\mathrm{Ex}} = Nv\sigma(\mathrm{Ex}) = 1.1\times 10^{9}\ \mathrm{sec}^{-1}, \tag{96}$$

which is one order of magnitude smaller than the value $R_{\mathrm{Ex}} = 1.15\times 10^{10}\ \mathrm{sec}^{-1}$ reported by Cohen *et al.* [3]). We cannot discuss this discrepancy except to remark that their R_{Ex} corresponds to a $\sigma(\mathrm{Ex}) = 5\times 10^{-18}\ \mathrm{cm}^2$, which is as large as the $\sigma(\mathrm{D})$ we calculate here and seems a bit too large.

12. Scattering of $(\mathrm{d}-\mu)+\mathrm{p}$

For the processes

$$\begin{aligned}&\text{direct:} && (\mathrm{d}-\mu)+\mathrm{p}\rightarrow(\mathrm{d}-\mu)+\mathrm{p},\\ &\text{exchange:} && (\mathrm{d}-\mu)+\mathrm{p}\rightarrow(\mathrm{p}-\mu)+\mathrm{d},\end{aligned} \tag{97}$$

the general theory of section 8 is valid, while in sec. 10 the roles of p, d, and U, L have to be interchanged. Thus in (71), (76), (78)—(80), we interchange the subscripts U and L, and p and d. Thus, for

$$k_{\mathrm{p}}^{\,2} > \Delta_0$$

the cross sections of (97) are given by

$$\sigma(\mathrm{D}) = \frac{4\pi}{(\gamma k_{\mathrm{p}})^2}\sum(2l+1)\left[\left(1+\frac{2\gamma b_l(\mathrm{L})}{k_{\mathrm{p}}}\right)\sin^2\delta_l(\mathrm{L})-\frac{\gamma a_l(\mathrm{L})}{k_{\mathrm{p}}}\sin 2\delta_l(\mathrm{L})+\frac{\gamma^2}{k_{\mathrm{p}}^{\,2}}|A_l(\mathrm{L})|^2\right],$$

$$\sigma(\mathrm{Ex}) = \frac{4\pi}{(k_{\mathrm{d}}k_{\mathrm{p}})^2}\sum(2l+1)|A_l(\mathrm{U})|^2,$$

corresponding to the (79) (80) in sec. 10. Similarly, in sec. 11 we interchange the role of p and d thereby changing the sign of v, $H_1^{\wedge}$, Δ_0 in (87)—(89) and converting V_{D} into V_{Ex} and vice versa in (89). Eqs. (89) now become

$$\begin{aligned}[\nabla_\rho^{\,2}+\gamma^2(k_{\mathrm{p}}^{\,2}-V_{\mathrm{Ex}}-\tfrac{1}{2}\Delta_0)]\chi_{\mathrm{D}} &= \gamma^2[\tfrac{1}{2}(\mathfrak{V}_{\mathrm{g}}-\mathfrak{V}_{\mathrm{u}})-v]\chi_{\mathrm{Ex}},\\ [\nabla_\rho^{\,2}+\gamma^2(k_{\mathrm{d}}^{\,2}-V_{\mathrm{D}}+\tfrac{1}{2}\Delta_0)]\chi_{\mathrm{Ex}} &= \gamma^2[\tfrac{1}{2}(\mathfrak{V}_{\mathrm{g}}-\mathfrak{V}_{\mathrm{u}})+v]\chi_{\mathrm{D}},\end{aligned}$$

where V_{Ex}, V_D, v, Δ_0 have the same meaning as in (87)—(88). The cross-sections are then given by

$$\sigma(\mathrm{D}) = \frac{4\pi}{(\gamma k_p)^2}\sum(2l+1)\left[\left(1+\frac{2\gamma b_l(\mathrm{Ex})}{k_p}\right)\sin^2\delta_l(\mathrm{Ex}) - \frac{\gamma a_l(\mathrm{Ex})}{k_p}\sin 2\delta_l(\mathrm{Ex}) + \frac{\gamma^2}{k_p^2}|A_l(\mathrm{Ex})|^2\right],$$

$$\sigma(\mathrm{Ex}) = \frac{4\pi}{(k_d k_p)^2}\sum(2l+1)|A_l(\mathrm{D})|^2,$$

where $\delta_l(\mathrm{Ex})$ are the phase shifts of the solutions of

$$\left[\frac{\mathrm{d}^2}{\mathrm{d}\rho^2} - \frac{l(l+1)}{\rho^2} + \gamma^2(k_d^2 - V_D(\rho) - \tfrac{1}{2}\Delta_0)\right] R_l^{(1)}(\mathrm{Ex}) = 0$$

and are hence the $\delta_l(\mathrm{D})$ in sec. 11. Thus, now $\delta_0(\mathrm{Ex}) = 0.031\,78$ by (93).

For liquid hydrogen temperature, $k_p^2 = 5\times10^{-7}$ so that the exchange (or excitation) process in (97) is energetically not possible. In this case, $R_{Ex}(\rho)$ is an exponentially decreasing function of ρ instead of an oscillatory one as in sec. 11, and this makes the $A_l(\mathrm{Ex})$ very small. Thus $\sigma(\mathrm{Ex}) = 0$ and

$$\begin{aligned}\sigma(\mathrm{D}) &\approx \frac{4\pi}{(\gamma k_p)^2}\sum(2l+1)\sin^2\delta_l(\mathrm{Ex}) \\ &\approx \frac{4\pi}{(\gamma k_p)^2}\sin^2\delta_0(\mathrm{Ex}) = 5.0\times10^{-18}\ \mathrm{cm}^2.\end{aligned} \tag{98}$$

This value does not seem to indicate a "Ramsauer" effect at this energy (i.e., $\sigma(\mathrm{D}) \to 0$ as $k_p^2 \to 0$) reported by Cohen *et al.* [3]) We must point out, however, that the value $\delta_0(\mathrm{Ex}) = 0.031\,78$ (see (93)) has been calculated with the approximation noted in the footnote to (93). For such low energies a much more accurate calculation may be necessary to settle this question of "Ramsauer effect" for the elastic scattering in (97).

13. Formation of $(p—\mu—p)^+$ by Process (4)

The observation of the nuclear fusion by μ-catalysis indicates the presence of the molecular systems $(p—\mu—p)^+$, $(p—\mu—d)^+$. We shall consider the process (4)

$$(p—\mu)+H \to (p—\mu—p)^+ + e + 250. \tag{99}$$

The value of $V\sigma$ corresponding to liquid hydrogen temperature has been calculated by Jackson [2]) and by Cohen [3]). The former obtains, in a Born approximation, the value

$$V\sigma = 2.1\times10^{-14}\ \mathrm{cm}^3/\mathrm{sec}, \tag{100}$$

where the latter give

$$V\sigma = 1.8\times 10^{-16}\ \text{cm}^3/\text{sec}, \tag{100a}$$

These rather widely divergent results make a further examination of the problem desirable.

Since the result of a perturbation calculation depends on the choice of the approximate wave functions for the initial and the final states, we shall avoid choices for which the use of plane waves is a bad approximation. Now, for the ejected electron with an energy of about 250 eV, a plane wave is a reasonably fair approximation. On the other hand, for the relative motion of the mesic atom and H at the low energies of liquid hydrogen, a plane wave is an unjustified approximation. We shall represent the final state Ψ_f as a $(p-\mu-p)^+$ ion in the ground state $1s\sigma g$ plus a free electron, i.e.

$$\Psi_f(r_\mu, r_e, R) = \psi_g(\xi, \eta; R)\Phi_0(R)\frac{1}{\sqrt{\Omega}}e^{ikr_e} \tag{101}$$

where Ω is a volume. These functions satisfy the following equations (all quantities in c.g.s. units)

$$\left[-\frac{\hbar^2}{2\mu}\nabla_\mu^2 - \frac{e^2}{r_{\mu A}} - \frac{e^2}{r_{\mu B}} + \frac{e^2}{R}\right]\psi_g = V_g(R)\psi_g, \tag{102}$$

$$\left[-\frac{\hbar^2}{M}\nabla_R^2 + V_g(R)\right]\Phi_0(R) = \left[E + w_0 - \frac{\hbar^2 k^2}{2m}\right]\Phi_0 \tag{103}$$

$$-\frac{\hbar^2}{2m}\nabla_e^2 e^{ikr_e} = \frac{\hbar^2 k^2}{2m}e^{ikr_e}; \tag{104}$$

E is the kinetic energy of relative motion of $(p-\mu)$ and H at infinite separation; w_0 is the energy of the H atom in the (initial) ground state ($w_0 = -1$ rydberg). At the low temperature of liquid hydrogen, the rotational states of the $(p-\mu-p)^+$ system are not excited on account of the small moment of inertia. Thus, by the Pauli principle, the $(p-\mu-p)^+$ must be left in a para-state, i.e., antisymmetric in the spins of the two protons. Eq. (103) gives for $\Phi_0(R)$ the lowest vibration-rotational state, i.e. k^2 of the ejected electron is such that

$$E + w_0 - \frac{\hbar^2 k^2}{2m} = -0.1017\frac{e^2}{2a_\mu} \tag{105}$$

where $-0.1017\ e^2/2a_\mu$ is the energy of lowest vibrational state of $(p-\mu-p)^+$ measured from the asymptote $R \to \infty$ as zero.

The Hamiltonian of the system can be put in the form

$$H = H_f^0 + H_f^1, \tag{106}$$

where

$$H_f^0 = -\frac{\hbar^2}{2\mu}\nabla_\mu^2 - \frac{e^2}{r_{\mu A}} - \frac{e^2}{r_{\mu B}} + \frac{e^2}{R} - \frac{\hbar^2}{M}\nabla_R^2 - \frac{\hbar^2}{2m}\nabla_e^2, \tag{107}$$

$$H_f^1 = -\frac{e^2}{r_{eA}} - \frac{e^2}{r_{eB}} + \frac{e^2}{r_{e\mu}}. \tag{107a}$$

The initial state, in the same Born-Oppenheimer approximation, can be described by

$$\Psi_i(r_\mu; r_e; R) = \psi_0(r_{\mu A})\Phi_1(R)\zeta(r_{eB}), \tag{108}$$

where $\psi_0(r_{\mu A})$, as in (48), is the wave function of the meson localized around proton A, $\zeta(r_{eB}) = \sqrt{\beta^3/\pi}e^{-\beta r_{eB}}$ is the electron hydrogenic wave function in the 1s state around proton B, and $\Phi_1(R)$ is a solution of (50A) for positive energy E. Instead of (108), we shall write, using (47a),

$$\Psi_i = \frac{1}{\sqrt{2}}[\psi_g(r_\mu; R)\Phi_{1g}(R) + \psi_u(r_\mu; R)\Phi_{1u}(R)]\zeta(r_{eB}). \tag{109}$$

The transition probability for the process i $\rightarrow$ f is proportional to the square of the matrix element

$$\int \Psi_f^* H_f^1 \Psi d\tau \approx \int \Psi_f^* H_f^1 \Psi_i d\tau, \tag{110}$$

where Ψ is the exact wave function. On account of the symmetry of H'_f and Ψ_f in (101), this reduces to

$$\langle f|H'_f|i\rangle = \frac{1}{\sqrt{2}}\int \Psi_f^* H'_f \psi_g(r_\mu; R)\Phi_{1g}(R)\zeta(r_{eB})d\tau. \tag{111}$$

At this point the use of a plane wave for $\Phi_1(R)$ would be a bad approximation. However, instead of the plane wave

$$\frac{1}{\sqrt{\Omega}}e^{iKR} = \frac{1}{2\pi\sqrt{\Omega}}\sum (2l+1)i^l\sqrt{\tfrac{1}{2}\pi KR}\,J_{l+\frac{1}{2}}(KR)P_l(\cos\vartheta),$$

we may use

$$R\Phi_1(R) = \frac{1}{2\pi\sqrt{\Omega}}\sum (2l+1)F_l(KR)P_l(\cos\vartheta) \equiv \frac{1}{\sqrt{\Omega}}R\varphi(R) \tag{112}$$

where $F_l(KR)$ is the solution of (55) for a (small) positive energy E which asymptotically for large R behaves as

$$F_l(KR) \rightarrow \frac{1}{K}\sin(KR - \tfrac{1}{2}l\pi + \delta_l). \tag{112a}$$

Thus $\Phi_1(R)$ and $\Phi_0(R)$, being both solutions of (50A) or (103), are orthogonal.

In the integration over the electron coordinate of the term $1/r_{eA}$ in (111)

with $\zeta(r_{eB}) = \sqrt{\beta^3/\pi}e^{-\beta r_{eB}}$, it is convenient to expand $\zeta(r_{eB})$ in terms of the hydrogenic wave functions $\zeta(r_{eA})$ with centre at the proton A.

$$e^{-\beta r_{eB}} = \sum_n C_n(R)\zeta_n(r_{eA}), \qquad R = r_B - r_A.$$

Since the contributions to (111) come mainly from the values of R near the equilibrium value R_e of $V_g(\rho)$, i.e., $R_e = 2a_\mu (a_\mu = \frac{1}{210}a_B)$, it is sufficient to take the 1s term $\zeta_{1s}(r_{eA})$ in the above expansion, and then it can be shown

$$C_{1s}(R) \approx 1 - \tfrac{1}{6}(\beta R)^2.$$

Similarly, in integrating over r_e of the term $1/r_{e\mu}$ in (111), we expand

$$e^{-\beta r_{eB}} = \sum_n C_n(r_{\mu B})\zeta_n(r_{e\mu})$$

and the same approximation of taking the $\zeta_{1s}(r_{e\mu})$ leads to

$$C_{1s}(r_{\mu B}) \approx 1 - \tfrac{1}{6}(\beta r_{\mu B})^2, \qquad r_{\mu B} = \tfrac{1}{2}R(\xi - \eta).$$

With these approximations, on recalling that $\psi_g(r_\mu; R)$ is normalized to unity for any R, (111) reduces to

$$-\frac{e^2}{\Omega}\sqrt{\frac{\beta^3}{2\pi}}\frac{4\pi}{\beta^2+k^2}\int d\mathbf{R}\Phi_0(R)\varphi^*(R)\left[e^{iKR}C(R) - \int e^{-ik r_{\mu B}}C(r_{\mu B})\psi_g^2(r_\mu; R)dr_\mu\right].$$

For energy 250 eV of the electron, we have

$$ka_\mu \approx 1.8\times 10^{-2}; \quad \beta a_\mu = 5\times 10^{-3}. \tag{113}$$

On expanding the exponential functions, we obtain

$$\langle f|H_f^1|i\rangle = \frac{e^2}{2\Omega}\sqrt{\frac{\beta^3}{2\pi}}\frac{4\pi}{\beta^2+k^2}\cdot$$

$$\int d\mathbf{R}\Phi_0(R)\varphi^*(R)\left[(\mathbf{k}\cdot\mathbf{R})^2 + \tfrac{1}{3}(\beta R)^2 - \int dr_\mu \psi_g^2(r_\mu; R)\{(\mathbf{k}\cdot\mathbf{r}_{\mu B})^2 + \tfrac{1}{3}(\beta r_{\mu B})^2\}\right]. \tag{114}$$

It is seen that $\langle f|H_f^1|i\rangle$ is the difference of two terms of the same general order To simplify the integrals, let us replace $(\mathbf{k}\cdot\mathbf{R})^2$, $(\mathbf{k}\cdot\mathbf{r}_{\mu B})^2$ by the averages $\frac{2}{3}(kR)^2$, $\frac{2}{3}(kr_{\mu B})^2$. Using (105), we have for the integral in (114)

$$\approx 4\pi k^2 \times 0.8 \int R^2 dR R^2 \Phi_0(R)\varphi(R)\left[1 - \tfrac{1}{4}\int dr_\mu (\xi-\eta)^2\psi_g^2\right].$$

The cross-section of (97) is, on changing to the units (10),

$$\sigma = \frac{v}{V}\frac{(4\pi a)^2}{(207)^5}\left(\frac{k^2}{\beta^2+k^2}\right)^2\frac{1}{K^2}\left|\int_0^\infty d\rho\rho^4\varphi(\rho)\Phi_0(\rho)\left[1 - \tfrac{1}{4}\int dr_\mu(\xi-\eta)^2\psi_g^2\right]\right|^2 \tag{115}$$

where the $\Phi_0(\rho)$, $\varphi(\rho)$ are now the radial wave functions and are normalized according to

$$\int_0^\infty \Phi_0^2(\rho)\rho^2 d\rho = 1; \qquad \rho\varphi(\rho) \to \sin(K\rho+\delta_0), \tag{116}$$

and $(K\hbar)^2 = MEa_\mu^2$, E = kinetic energy of $(p-\mu)$ in ergs, and v, V are the velocities of the ejected electron and the $(p-\mu)$ atom. Using (113), one obtains

$$V\sigma \approx 7\times 10^{-18}\left|\int_0^\infty \ldots d\rho\right|^2. \tag{117}$$

The wave function $\Phi_0(\rho)$ of the ground vibrational state of $(p-\mu-p)^+$ has been given in table 2, and the function $\varphi(\rho)$ is obtained by numerical integration of (55) for $l = 0$. Only S-waves contribute in our case. For $K^2 = 10^{-7}$ corresponding to $T \approx 5°$K, calculation gives

$$V\sigma = 2.1\times 10^{-16}\ \text{cm}^3/\text{sec}. \tag{118}$$

This value is in good agreement with the value (100a) obtained by Cohen [3]).

In liquid hydrogen, the rate of formation of $(p-\mu-p)^+$ by the process (99) is

$$\lambda = N_0 V\sigma \approx 9\times 10^6\ \text{sec}^{-1}.$$

The mean relative chance r of the μ meson existing in the atomic system $(p-\mu)$ and its existing in the molecular system $(p-\mu-p)^+$ in a hydrogen bubble chamber during its lifetime $\tau = 2\times 10^{-6}$ sec can be estimated at †

$$r = \frac{\int_0^\infty e^{-(\lambda+1/\tau)t}dt}{\int_0^\infty [e^{-t/\tau}-e^{-(\lambda+1/\tau)t}]dt} \approx \frac{1}{18}. \tag{119}$$

The value $\lambda = 9\times 10^6\ \text{sec}^{-1}$ here is to be compared with the value $\lambda = 1.5\times 10^6\ \text{sec}^{-1}$ recently obtained by Zel'dovich and Gershstein [10]) for a different mechanism for the formation of $(p-\mu-p)^+$, namely, a dipole transition from the initial state $(p-\mu)+d$ to an excited rotational excited state of $1s\sigma g$, accompanied by an energy transfer to an electron.

From the value R in (28) for the ratio of the square of the wave function of the μ meson at a proton in the molecular ion $(p-\mu-p)^+$ to $\psi^2(0)$ in the atom $(p-\mu)$, and the ratio r in (119), it is possible to calculate the relative probability g of a μ meson being captured

$$\mu+p \to N+\nu$$

by a proton in the molecular and the atomic state in a liquid hydrogen bubble chamber. We must, however, also consider the effect of the μ meson and proton spin. For liquid hydrogen temperature, the molecular ion $(p-\mu-p)^+$ is in the lowest rotational state of the $1s\sigma g$ state so that the system is anti-symmetric in the spins of the protons. The μ-hydrogen atom $(p-\mu)$ is in the hyperfine state

† The authors are grateful to Dr. H. Primakoff for a comment on the expression (119).

$F=0$. It can easily be shown that this spin wave function of $(p-\mu-p)^+$,

$$(\alpha_1\beta_2-\beta_1\alpha_2)\alpha_\mu \quad \text{or} \quad (\alpha_1\beta_2-\beta_1\alpha_2)\beta_\mu,$$

corresponds to the relative probabilities 1 : 3 for the system being in a singlet and a triplet state for the meson and one of the two protons. Thus if μ-capture can take place only in the singlet state of the $p-\mu$ system, the relative probability g is

$$g=\tfrac{1}{4}R/r\approx 6.3. \tag{120}$$

The effect of the hyperfine structure of $p-\mu$ on the μ-capture has been discussed by Bernstein *et al.* [11]).

The authors wish to thank Mr. I. T. Wang who undertook the calculation of the expression (19) and the table 1 in 1957-8. One of the authors (Wu) wishes to express his appreciation to Dr. C. N. Yang of the Institute of Advanced Study, Princeton, for many discussions, and to Dr. J. R. Oppenheimer for the hospitality shown him at the Institute where part of the present work was done.

References

1) L. W. Alvarez *et al.*, Phys. Rev. **105** (1957) 1127
2) J. D. Jackson, Phys. Rev. **106** (1957) 330
3) S. Cohen, D. L. Judd and R. J. Riddell, Phys. Rev. **110** (1958) 1471
4) D. R. Bates, K. Ladsham and A. L. Stewart, Phil. Trans. Roy Soc. A **246** (1953) 215; R. F. Wallis and M. Hulbert, Jr., J. Chem. Phys. **22** (1954) 774
5) A. Dalgarno and R. McCarroll, Proc. Roy. Soc A **237** (1956) 383
6) T. Y. Wu and A. B. Bhatia, J. Chem. Phys. **24** (1956) 48
7) S. C. Miller and R. H. Good, Jr., Phys. Rev. **91** (1953) 174
8) H. Marshall and Th. Schmidt, Z.f. Physik **150** (1958) 293
9) C. F. Mott-Massey, Theory of Atomic Collisions 2nd ed. (Oxford Univ. Press 1949), Ch. VI
10) Ia. B. Zel'dovich and S. S. Gershstein, J. Exp. Theor. Phys. U.S.S.R. **35** (8), no. 3 (1959)
11) Bernstein, Lee, Yang and Primakoff, Phys. Rev. **111** (1958) 313

1.D.2

Nuclear Physics **16** (1960) 460—473; © *North-Holland Publishing Co., Amsterdam*

Not to be reproduced by photoprint or microfilm without written permission from the publisher

COMMENTS ON DAVYDOV AND FILLIPPOV'S THEORY OF THE PROPERTIES OF EVEN NUCLEI

T. TAMURA and T. UDAGAWA

Department of Physics, Tokyo University of Education

Received 19 November 1959

Abstract: It is shown that all the experimental data on even nuclei, which the theory of Davydov and Filippov explains, can as well be explained by more conventional theories. It is further shown that there exist several experimental data in which the theory of Davydov and Filippov may meet with difficulty, but which could be explained by the conventional theory.

1. Introduction

In a recent paper Davydov and Filippov [1]† proposed a model in an attempt to explain systematically the properties of lower levels of even nuclei. The basic idea of their model is to consider each of these nuclei to have a definite ellipsoidally deformed shape and to perform rotational motions. The shape of this deformation is characterized by the two parameters β and γ of Bohr and Mottelson [2, 3]), and is kept fixed during the rotation.

In the usually considered spheroidal nuclei, i.e. nuclei which have $\gamma = 0°$, the only possible mode of rotation is around an axis which goes through the centre of mass and is perpendicular to the symmetry axis. Therefore, if no internal motion is considered, i.e. if the deformation is considered to be kept fixed as in DF, one expects to have only a single band of rotational states with spins †† $I = 0, 2, 4, \ldots$ and with energies proportional to $I(I+1)$.

On the other hand, in DF, γ is not necessarily restricted to 0°, but is allowed to take any value from 0° to 30°. Therefore other modes of rotational motion become possible and consequently some new rotational states can appear, even if the deformation is kept fixed. In the limit in which γ is quite close to 0°, the spectra thus obtained have, of course, properties which are expected to appear for axially symmetric deformations in the above conventional theory. In the other limit of γ tending to 30°, the spectra are quite different from the above type of rotational band structure, and look very much like those observed in the so-called vibrational region of Scharff-Goldhaber and Weneser [4]). In between these two extreme values of γ the spectra change smoothly and embody fairly well the properties of the observed spectra in the

† This paper will be referred to as DF in the following.

†† Throughout this paper we consider exclusively even parity states, therefore, the parity will not be specified.

transitional region. DF thus claim that their theory can explain experimental date of even-nuclei which lie in all the regions of the periodic table in which the collective motions play a dominant role.

The purpose of the present paper is to show that almost all the experimental data which are explained by DF can as well be explained by the more conventional, and thus probably more natural theories.

For this purpose we shall first enumerate in sec. 2 the items which are predicted by DF and are stated to be in agreement with experiment. The explanation of these items in terms of the more conventional theories will be given in sec. 3, while sec. 4 will be devoted to the evaluation of the moments of inertia and the mass parameter for the γ-vibration, as these quantities are required for the discussion in sec. 3. There are some other experimental data, which could be explained by the conventional theories but seem to be unsatisfactorily predicted by DF. These items will be discussed in sec. 5, together with other concluding remarks.

2. Brief Summary of the Predictions of DF

As was explained in the introduction, we shall begin this section with the enumeration of the items which are predicted by DF.

(i) The energy ratio † $\varepsilon_2(2)/\varepsilon_1(2)$, which will henceforth be denoted by ρ, is much larger than two if γ is close to 0°, decreases smoothly with increasing γ and is reduced to two when γ approaches 30°. This allows one to associate the theoretical spectra with those of nuclei which belong, respectively, to the rotational, transitional and vibrational regions.

(ii) In the limit of γ tending to 0°, the energies of the lowest $I=0, 2, 4, 6, \ldots$ states are approximately proportional to $I(I+1)$, and this is in agreement with experiment.

(iii) There exists a relation

$$\varepsilon_1(2)+\varepsilon_2(2)=\varepsilon_1(3). \tag{1}$$

Experimentally this relation is satisfied fairly well all over the regions of the periodic table in which the collective motion plays a dominant role.

(iv) The ratio of the reduced transition probabilities ††
$b(\mathrm{E2};\ 22\rightarrow 0)/b(\mathrm{E2};\ 21\rightarrow 0)$, which we henceforth call R_1, is given by

$$R_1=\frac{\sqrt{9-8\sin^2(3\gamma)}-3+2\sin^2(3\gamma)}{\sqrt{9-8\sin^2(3\gamma)}+3-2\sin^2(3\gamma)}. \tag{2}$$

† $\varepsilon_n(I)$ is the energy of a state with spin I, above the ground state, n-th lowest among all the spin I states.

†† The notation $b(\mathrm{E2};\ 22\rightarrow 21)$, e.g., means the reduced transition probability of the E2 γ-rays from the second excited to the first excited spin 2 states. Other b's are to be understood similarly.

Since this ratio R_1 and the energy ratio $\varepsilon_2(2)/\varepsilon_1(2)$ are in DF both one-valued functions of a single variable γ, it is possible to express (2) as a function of $\not{p}$. This relation is shown in fig. 1 as a solid curve [5]). In this figure experimental values of the ratio R_1 are also plotted [5]), and the agreement is very good,

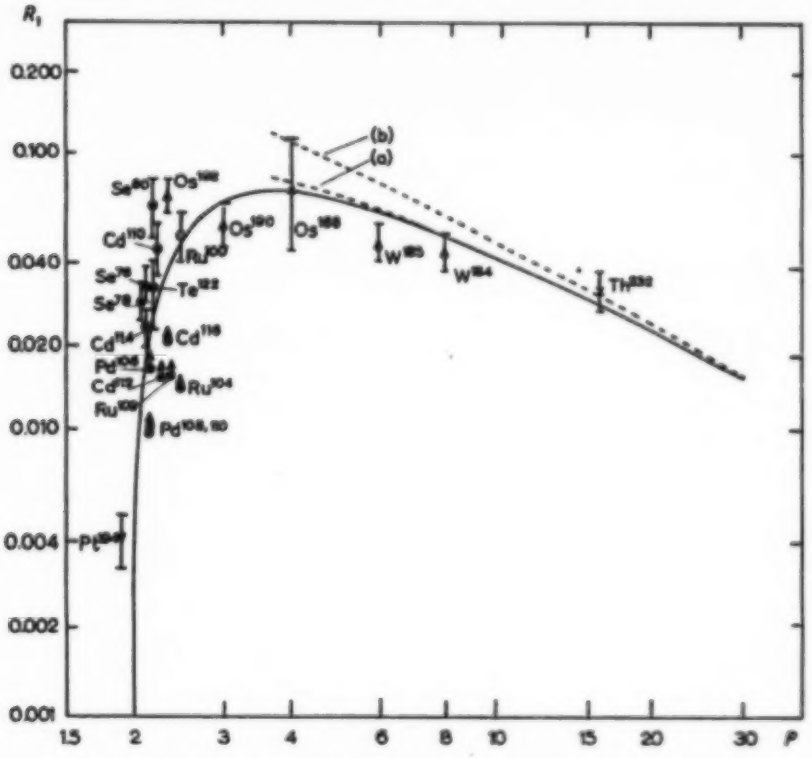

Fig. 1. Ratio $b(E2; 22 \to 0)/b(E2; 21 \to 0)$ plotted as a function of the energy ratio $\varepsilon_2(2)/\varepsilon_1(2)$. Curves (a) and (b)† are our theoretical results, respectively, for $a = 11/8$ and $a = 1$. Other parts of the figure are taken from ref. [5]).

although it becomes somewhat poorer in the extreme vibrational region in the sense that DF does not explain the big fluctuation in the experimental values.

(v) The similar ratio $b(E2; 22 \to 21)/b(E2; 22 \to 0)$, which will henceforth be called R_2, is given by

$$R_2 = \frac{20}{7} \frac{\sin^2(3\gamma)}{9 - 8\sin^2(3\gamma) - [3 - 2\sin^2(3\gamma)]\sqrt{9 - 8\sin^2(3\gamma)}}, \qquad (3)$$

and is shown in the same way in fig. 2 by a solid curve, together with experiments [5]). Again the agreement is pretty good.

(vi) The ratio $b(M1; 22 \to 21)/b(E2; 22 \to 21)$ is also given as a function of γ and thus of $\not{p}$. For several cases in which experimental data are available DF claims very good agreement. On this point, however, there seems to exist some doubtful treatment in DF and this point has already been discussed [6]).

† By an oversight, kindly pointed out to us by Dr. J. Wesener, curve (b) was incorrectly drawn in the figure. Its true position is just half-way between the curves marked (a) and (b).

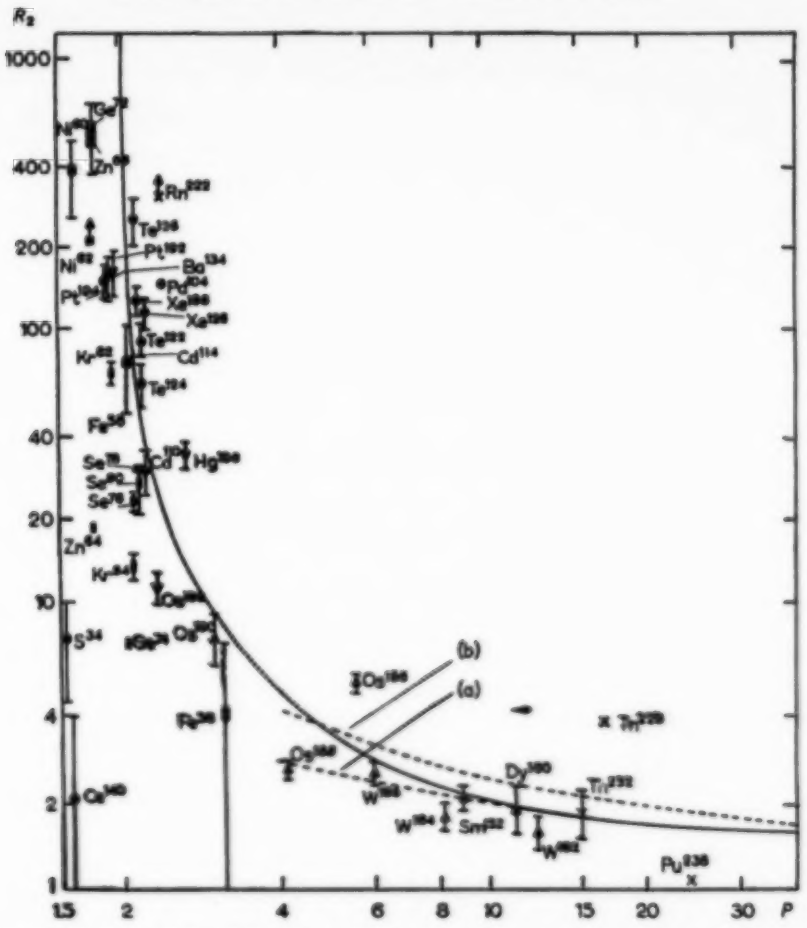

Fig. 2. Ratio $b(E2; 22 \to 21)/b(E2; 22 \to 0)$. Explanations are the same as in fig. 1, except that curves (a) and (b) † correspond, respectively, to $a = 1$ and $a = 11/8$.

3. Explanation in Terms of the Conventional Theories

In this section it will be shown how each of the items enumerated in Sec. 2 can be explained in terms of the conventional theories.

(i') In the ordinary rotational model of the strongly deformed spheroidal nuclei, the second excited spin 2 state is interpreted as the γ-vibrational state. The magnitude of $\varepsilon_2(2)$ will be equal to $\hbar\sqrt{C_\gamma/B_\gamma}$, where B_γ is the mass parameter and C_γ the rigidity associated with this vibrational motion ††. The more the deformation develops, the more this deformed shape will be stabilized, and concequently C_γ will become larger. Thus $\varepsilon_2(2)$ will increase with increased deformation, unless B_γ increases more rapidly than C_γ does. On the other hand $\varepsilon_1(2)$ is inversely proportional to the moment of inertia $\mathcal{I}$ associated with the ground rotational band. This moment of inertia $\mathcal{I}$ increases, and thus $\varepsilon_1(2)$ decreases with increased deformation. It is thus quite easy to understand that the ratio p gets larger values in the strongly deformed nuclei,

† The true position of curve (b) is slightly lower than that drawn in the figure.

†† This statement does not hold rigorously. The equality of $\varepsilon_2(2)$ and $\hbar\sqrt{C_\gamma/B_\gamma}$ holds, however, approximately. See the discussion below under (iv').

so long as B_γ does not increase very rapidly with increased deformation. It will be shown in (iv') below that to a good approximation B_γ is proportional to $\mathscr{I}$. Thus p is proportional to $\sqrt{C_\gamma \mathscr{I}}$, which certainly increases with increased deformation, and thus the large magnitude of p in the strongly deformed region can be explained.

In the limit of pure surface vibration of Bohr and Mottelson [2,3]), p is exactly equal to two. For the explanation of the deviation of p from two, two different explanations have been proposed; one by Scharff-Goldhaber and Weneser [4]) and the other by Wilets and Jean [7]). Neither of these theories seems, however, to explain all the known experimental data on the vibrational nuclear states, if the properties of states with spins other than 2 are included. In a recent paper by Komai and one of the present authors [6]) (T.T.) it has been shown that, if one adds a slightly γ-dependent term of the form

$$\sum_n k_n(\beta-\beta_n)^n \cos^n(3\gamma)$$

to the γ-independent potential $\frac{1}{2}C(\beta-\beta_0)^2$ of Wilets and Jean, it is possible to explain almost all the properties of the known lower states of Cd^{114}, which is considered as a characteristic example of the vibrational nuclei, including, of course, the magnitude of p. Thus we may believe that DF's claim (i) can be explained by the conventional theory also in the vibrational region.

(ii') As will be discussed somewhat in detail in (iv') below, the conventional rotational model (with rotation-vibration interaction) and DF seem to be essentially equivalent to each other in the strongly deformed region. Thus both theories explain experiment concerning the level structure at least of the ground band.

(iii') This rule (1) is satisfied exactly in the pure surface excitation model [2]), because $\varepsilon_1(2)$, $\varepsilon_2(2)$ and $\varepsilon_1(3)$ are equal to $\hbar\omega$, $2\hbar\omega$ and $3\hbar\omega$, respectively, where $\hbar\omega$ is the energy of one phonon excitation. Even in the region where p deviates slightly from two, this rule (1) can be explained to hold, as is seen [6]) in the example of Cd^{114}.

In the strongly deformed region $\varepsilon_1(2)$ is equal to $3\hbar^2/\mathscr{I}$. On the other hand the first excited spin 3 state may be interpreted as the second member of the $K=2$ (γ-vibrational) rotational band, and it is easy to see that $\varepsilon_1(3)=3\hbar^2/\mathscr{I}'+\varepsilon_2(2)$ where $\mathscr{I}'$ is the moment of inertia associated with this rotational band. The rule (1) is thus satisfied also in the strongly deformed region if a relation $\mathscr{I} \approx \mathscr{I}'$ is proved.

Now, it is well known that the magnitude of the moment of inertia can very well be evaluated by using the cranking formula [8]), and the physical meaning of this formula would be the following. Nucleons in a nucleus are supposed to be contained in a box which is cranked by some outer forces. The nucleons are forced to follow the change of the orientation of this box and, for this,

some energy is needed, which is observed as the energy of rotation. It is thus easy to see that the magnitude of this energy of rotation is determined by the nature of the intrinsic motion of the nucleons, in addition to the shape of the cranked box. As the moment of inertia is inversely proportional to this energy of rotation, its magnitude is also determined by the nature of the intrinsic motion. In going from the ground state to the γ-vibrational states, it is expected that there happens essentially no change in the nature of the internal motion, although the shape of the cranked box may be changed slightly. Thus it would be quite natural to suppose that the relation $\mathcal{I} \approx \mathcal{I}'$ is correct and this verifies that the relation (1) holds also in the strongly deformed region.

We thus have shown that the rule (1) can be explained at least in the two extreme regions. It would not then be a very dangerous guess to expect that this rule can also be explained in the transitional region, as an insertion between these two extremes.

(iv′) As for nuclei which lie in the vibrational region, it has been shown for the particular case of Cd^{114} that the conventional theory gives a value for the ratio R_1 which agrees with experiment [6]). Although the conventional theory does not give this ratio as an analytic function of one or a set of parameters, as is the case in DF, it may be believed that the same procedure which has been applied successfully to Cd^{114} could as well be applied to other cases and explains the experiments. Therefore there may exist no serious difficulties in this region concerning the ratio R_1.

In the strongly deformed region, R_1 may be evaluated in the conventional theory as follows. As has been mentioned above in (i′) the second excited spin 2 state is interpreted as the γ-vibrational state. Therefore, as is seen from the well known property of any vibrational motion in quantum mechanics, and as will be shown below somewhat in detail, the reduced transition probability $b(\mathrm{E2};\ 22 \to 0)$ is approximately proportional to $1/\sqrt{B_\gamma C_\gamma}$, and the proportionality factor is a known constant. On the other hand, once the equilibrium value β_0 of the deformation parameter β is fixed, it is easy to evaluate $b(\mathrm{E2};\ 21 \to 0)$. Thus, once B_γ and C_γ are known, the desired evaluation of the ratio R_1 is straightforward.

For the evaluation of B_γ and C_γ we first note that the part of the Hamiltonian which describes the γ-vibration is given by

$$H_\gamma = -\frac{\hbar^2}{2B_\gamma}\frac{\partial^2}{\partial\gamma^2} + \tfrac{1}{2}C_\gamma\gamma^2. \tag{4}$$

Then the mass parameter B_γ could be evaluated by using the well-known Inglis formula [8])

$$B_\gamma = 2\hbar^2 \sum_n \frac{|\langle n|\partial/\partial\gamma|\mathrm{i}\rangle|^2}{E_{n1}}. \tag{5}$$

The details of the evaluation of this expression is given in sec. 4. There also the moment of inertia $\mathscr{I}$ for the ground band is evaluated by using the cranking formula [9])

$$\mathscr{I} = 2\hbar^2 \sum_n \frac{|\langle n|J_x|\mathrm{i}\rangle|^2}{E_{n1}}, \tag{6}$$

and it is found that, at least for the examples considered, there exists the following simple relation †.

$$\mathscr{I} \approx 3B_\gamma. \tag{7}$$

As was mentioned above, $\varepsilon_1(2)$ is equal to $3\hbar^2/\mathscr{I}$, and thus (7) leads to the relation

$$B_\gamma = \frac{\hbar^2}{\varepsilon_1(2)}. \tag{8}$$

It is easy to see from (4), and from the assumption that the magnitudes of the moments of inertia are the same for the ground and the γ-vibrational bands, that $\varepsilon_2(2)$ is given by

$$\varepsilon_2(2) = \hbar\sqrt{\frac{C_\gamma}{B_\gamma}} + \tfrac{1}{3}\varepsilon_1(2). \tag{9}$$

Inserting (8) into (9), and then solving the latter for C_γ, we get

$$C_\gamma = \frac{(\varepsilon_2(2)-\varepsilon_1(2))^2}{\varepsilon_1(2)} \approx \varepsilon_2(2)p\left(1-\frac{2}{3p}\right) \tag{10}$$

to first order in $1/p$. From (8) and (10) we already know that $b(\mathrm{E2};\ 22 \to 0)$ which is proportional to $1/\sqrt{B_\gamma C_\gamma}$ is just inversely proportional to p, in the lowest order in $1/p$.

For a more precise evaluation of R_1, we first note that the reduced transition probability of any γ-ray is, in general, given by

$$b(\mathrm{E\ or\ M}L;\ \mathrm{i} \to \mathrm{f}) = \sum_{\mu M1} |\langle \mathrm{f}|\mathscr{M}_\mu|\mathrm{i}\rangle|^2, \tag{11}$$

where i and f specify, respectively, the initial and final states concerned, and the operator $\mathscr{M}_\mu$ is given, for the E2 transition probability in the strongly deformed nuclei, by

$$\mathscr{M}_\mu = \frac{3}{4\pi} ZeR_0^2\beta\left[\cos\gamma D^{(2)}_{\mu,0}(\theta_1) + \sin\gamma\left(\frac{D^{(2)}_{\mu,2}(\theta_1)+D^{(2)}_{\mu,-2}(\theta_1)}{\sqrt{2}}\right)\right]. \tag{12}$$

The reduced transition probability $b(\mathrm{E2};\ 21 \to 0)$ has a very simple ex-

† It may be of some interest to mention that if $\mathscr{I}$ and B_γ are both evaluated as in the original paper of Bohr (ref. [2])), the equality of $\mathscr{I}$ and $3B_\gamma$ is exact, although in that case the Hamiltonian for the γ-vibration is not the same as (4).

pression [10]):

$$b(\mathrm{E2};\ 21 \to 0) = (eQ_0)^2. \tag{13}$$

For the evaluation of $b(\mathrm{E2};\ 22 \to 0)$, we first mention that the explicit form of the wave functions of the initial and the final states are given by

$$|\mathrm{i}\rangle_m = \psi_m(2_2^+) = \sqrt{\frac{5}{16\pi^2}}\,(D^{(2)}_{m,2}(\theta_1) + D^{(2)}_{m,-2}(\theta_1))\left(\frac{2\alpha}{\sqrt{\pi}}\right)^{\frac{1}{2}} \alpha\gamma e^{-\frac{1}{2}\alpha^2\gamma^2}, \tag{14a}$$

and

$$|\mathrm{f}\rangle = \psi(0^+) = \sqrt{\frac{1}{8\pi^2}}\,D^{(0)}_{0,0}\left(\frac{\alpha}{\sqrt{\pi}}\right)^{\frac{1}{2}} e^{-\frac{1}{2}\alpha^2\gamma^2}, \tag{14b}$$

with

$$\alpha = \left(\frac{B_\gamma C_\gamma}{\hbar^2}\right)^{\frac{1}{4}}.$$

Then by using (11) and (12), the following result can be easily obtained:

$$\begin{aligned} b(\mathrm{E2};\ 22 \to 0) &= (eQ_0)^2 \frac{\hbar}{2\sqrt{B_\gamma C_\gamma}} \\ &= (eQ_0)^2 \frac{1}{2p}\left(1 + \frac{1}{3p}\right). \end{aligned} \tag{15}$$

From (13) and (15) the ratio R_1, in our case, is given by

$$R_1^{\mathrm{TU}} = \frac{1}{2p}\left(1 + \frac{1}{3p}\right). \tag{16}$$

It would be worthwhile to mention that (16) is inversely proportional to p, in the lowest order of $1/p$, which is just what DF gives in the extreme rotational region, as is seen from fig. 1.

To make clearer the comparison of our result (16) with that of DF, i.e. with (2), we make the following limiting evaluation. First we note that p is given in DF as

$$p = \frac{3 + \sqrt{9 - 8\sin^2(3\gamma)}}{3 - \sqrt{9 - 8\sin^2(3\gamma)}}. \tag{17}$$

It is easy to solve this equation for $\sin^2(3\gamma)$ as a function of p. Then this is inserted into (2) so that R_1 is expressed as a function of p. As we are dealing with the case in which $p \gg 1$, we may expand this function in a power series of $1/p$. Then R_1 in DF is given, to the first order in, $1/p$, as

$$R_1^{\mathrm{DF}} = \frac{1}{2p}\left(1 - \frac{3}{2p}\right). \tag{18}$$

It is seen that (16) and (18) coincide to the lowest order in $1/p$, and this fact shows that the conventional theory also explains experimental data in the very strongly deformed region.

To obtain a better agreement with experiment, and thus with DF, for p not very much larger than unity, it would be appropriate to take into account the so called rotation-vibration interaction. As we are, however, still considering values of p fairly larger, though not very much larger, than unity we may treat this interaction as a perturbation.

The interaction Hamiltonian may be described as

$$H' = -\frac{\hbar^2}{\sqrt{3}\,\mathscr{I}} a[I_1^2 - I_2^2]\gamma \tag{19}$$

with obvious notations. This H' is the same as the one given in eq. (96) of ref. [2]), if the factor a is put equal to unity. It is not clear whether the same expression can also be used here, but the correct form will not differ very much from this, and to take into account a possible deviation we inserted a factor a, which will have a value of the order of unity.

By using (19) it is seen that the state $|\mathrm{i}\rangle_m$ which appeared in (14a) is to be replaced by

$$|2_2^+\rangle_m \equiv |\mathrm{i}\rangle_m = \psi_m(2_2^+) - \tfrac{1}{3}\sqrt{2}\, a \frac{1}{p\sqrt{p}} \psi_m(2_1^+) \tag{20}$$

to the lowest order in $1/p$; $\psi_m(2_2^+)$ was given in (14a), while $\psi_m(2_1^+)$ is given by

$$\psi_m(2_1^+) = \sqrt{\frac{5}{8\pi^2}}\, D^{(2)}_{m,0}(\theta_1) \left(\frac{\alpha}{\sqrt{\pi}}\right)^{\frac{1}{2}} \mathrm{e}^{-\frac{1}{2}\alpha^2\gamma^2}. \tag{21}$$

Using (14b) and (20), $b(\mathrm{E2};\ 22 \to 0)$ is re-evaluated and the refined value of R_1^{TU} is given by

$$R_1^{\mathrm{TU}} = \frac{1}{2p}\left[1 - (4a-1)\frac{1}{3p}\right]. \tag{22}$$

If in (22) a is put equal to $\frac{11}{8}$, R_1^{TU} coincides exactly with R_1^{DF} of eq. (18), and this is illustrated by the curve (a) in fig. 1. If a is put equal to unity R_1^{TU} becomes slightly too large for p not very much larger than unity, as is seen from the curve (b) in fig. 1.

Although there exists some ambiguity concerning the magnitude of a, it is thus shown that the conventional theory for the deformed nuclei, with inclusion of the rotation-vibration interaction, explains pretty well the experimental ratio R_1, and the agreement holds even in the transitional region to a fairly large extent. It would be possible to obtain a better agreement in this region by further taking into account the β-vibration, and by calculating the effect of the rotation-vibration interactions to higher orders.

In closing this subsection, it might be of value to mention the following remark. We have not calculated C_γ from first principles, as we intended to derive a result which is as simple as possible, and as close to the result of DF as possible. It is, however, not difficult to perform this sort of calculation, once the Nilsson type of single-particle orbits are obtained for non-zero γ's. In such a case we can evaluate R_1, e.g., without resort to the relations like (10) and this would give a larger flexibility to the theory.

The importance of this sort of flexibility seems to be more important in the vibrational region. This is seen from fig. 1 where in the vibrational region the experimental values show rather big fluctuations, while the theoretical value of DF is a unique function of γ. Although detailed calculations have not yet been performed, it is expected that the conventional theory [6]) would find no serious difficulty in explaining these fluctuating experimental values.

(v') It has also been shown [6]) that the experimental value of the ratio $R_2 = b(\mathrm{E2};\ 22 \to 21)/b(\mathrm{E2};\ 22 \to 0)$ can well be explained for the vibrational nuclei. For the case of very deformed nuclei a discussion similar to that explained in (iv') can also be applied here and, corresponding to (22), we get

$$R_2^{\mathrm{TU}} = \tfrac{10}{7}\left(1+\frac{4a}{p}\right). \tag{23}$$

For the evaluation of $b(\mathrm{E2};\ 22 \to 21)$ which is needed in obtaining (23), the wave function given in (20) is used to describe the initial state, while the final (i.e. the first excited spin 2) state wave function is described as

$$|2_1^+\rangle_m \equiv |\mathrm{f}\rangle_m = \psi_m(2_1^+)+\tfrac{1}{3}\sqrt{2}\,a\frac{1}{p\sqrt{p}}\psi_m(2_2^+). \tag{24}$$

Corresponding to (18) the R_2 in DF is given by

$$R_2^{\mathrm{DF}} = \tfrac{10}{7}\left(1+\frac{4}{p}\right). \tag{25}$$

Comparison of (23) and (25) shows that they coincide if $a = 1$ and the corresponding result is given in fig. 2 as curve (a). If a is put equal to $\frac{11}{8}$, as in (iv'), we get the curve (b) in fig. 2 and it is seen that both curves can explain the experiments fairly well.

4. Evaluation of the Mass Parameter and the Moment of Inertia

In this section the values of the moment of inertia $\mathscr{I}$ and the mass parameter B_γ will be evaluated for the strongly deformed even-nuclei. For this purpose the prescription proposed by Inglis [8]) will be followed; i.e. these quantities will be calculated by using (6) and (5).

For the description of the intrinsic motions which is needed in this calcula-

tion, the best would be to take the Nilsson model[11]) as the starting point. As we are considering, however, only very deformed nuclei, it will be a good approximation to characterize the single particle states by the asymptotic quantum numbers $[Nn_z\Lambda] \equiv \alpha$ as well as $\Omega = \Lambda+\Sigma$, the component of the total angular momentum along the symmetry axis. Correspondingly, in the calculation of the matrix elements which appear in the numerator of the Inglis formula (5) and (6), the asymptotic wave functions may be used in place of the exact Nilsson wave functions.

It is well known that if only the idealized single particle motions are assumed for the intrinsic motion, eq. (6) yields the rigid values for $\mathcal{I}$, which are too large compared with experiment. This fact has first been pointed out by Bohr and Mottelson [9]) and the necessity of taking into account the residual interaction was invoked. Probably the same conclusion will be true for the evaluation of B_γ. In a recent paper by Belyaev [12]) the effect of the residual pair interaction was discussed fairly in detail, and here the main line of our calculation will follow his method.

In the ground state of an even-nucleus the nucleons occupy the Nilsson orbits pairwise, and the interaction between these paired nucleons is especially strong. In order to obtain an excited intrinsic state, at least one of these pairs must be broken up and a sizable amount of energy is required. Thus if the energy gap is denoted by Δ, and if in one of the excited states $|n\rangle$ a pair in the orbit $[\alpha\Omega] \equiv \nu$ is broken up and one of the paired nucleons is excited up to another orbit $[\alpha'\Omega'] \equiv \nu'$, the energy denominator which appears in (5) and (6) is to be expressed as

$$E_{n1} = E_\nu + E_{\nu'} \quad \text{with} \quad E_\nu = [(\varepsilon_\nu - \lambda)^2 + \Delta^2]^{\frac{1}{2}}, \tag{26}$$

where λ is the Fermi energy in the sense of Belyaev, while ε_ν is the energy of the orbit ν. It is clear that (26) is much larger than $\varepsilon_{\nu'} - \varepsilon_\nu$ which is to be used for the energy denominator in (5) and (6) if no pair interaction is considered, and this fact certainly reduces the magnitudes of $\mathcal{I}$ and B_γ.

In addition to the change in the denominator, the pair interaction gives rise to some change also in the numerator; i.e. it has to be taken into account that both the ground and the excited states do not have any pure configuration in the sense of the Nilsson model. A very convenient way of taking this fact into account was given by Belyaev, and it is, after replacing $\langle n|J_x|\mathrm{i}\rangle$ and $\langle n|\partial/\partial\gamma|\mathrm{i}\rangle$ by $\langle\nu'|j_x|\nu\rangle$ and $\langle\nu'|\partial/\partial\gamma|\nu\rangle$, to multiply them by a factor

$$(u_{\nu'}v_\nu - u_\nu v_{\nu'}), \tag{27}$$

where u and v are defined in ref. [12]). Summarizing, eqs. (6) and (5) are now rewritten, respectively, as

$$\mathcal{I} = 2\hbar^2 \sum_{\nu\nu'} \frac{|\langle\nu'|j_x|\nu\rangle|^2}{E_\nu + E_{\nu'}} (u_{\nu'}v_\nu - u_\nu v_{\nu'})^2, \tag{28}$$

and

$$B_\gamma = 2\hbar^2 \sum_{\nu\nu'} \frac{|\langle \nu'|\partial/\partial\gamma|\nu\rangle|^2}{E_\nu + E_{\nu'}} (u_{\nu'}v_\nu - u_\nu v_{\nu'})^2. \tag{29}$$

In (28) the evaluation of the matrix element $\langle \nu'|j_x|\nu\rangle$ is well known and we mention here only that the selection rules which are required for obtaining non-vanishing matrix elements are, noting that $j_x = l_x + s_x$,

$$\begin{aligned} &N' = \begin{matrix} N \\ N\pm 2 \end{matrix}, \quad n'_x = n_x \pm 1, \quad \Lambda' = \Lambda \pm 1, \quad \Sigma' = \Sigma \qquad \text{for } l_x; \\ &N' = N, \quad n'_x = n_x, \qquad \Lambda' = \Lambda, \qquad \Sigma' = \Sigma \pm 1 \quad \text{for } s_x. \end{aligned} \tag{30}$$

On the other hand, for the evaluation of (29) we first assume that the (time-dependent) perturbation to the single particle motion, due to the deviation of the one-body potential from cylindrical symmetry, is given by

$$\begin{aligned} H' &= \sum_\nu -\tfrac{1}{2} M\omega_0^2 \sqrt{\frac{15}{4\pi}} \beta\gamma (x_\nu^2 - y_\nu^2) = \sum_\nu -\frac{\hbar\omega_0}{\sqrt{3}} \varepsilon\gamma (\xi_\nu^2 - \eta_\nu^2); \\ \xi^2 &= \frac{M\omega_x}{\hbar} x^2, \qquad \eta^2 = \frac{M\omega_y}{\hbar} y^2, \end{aligned} \tag{31}$$

In the derivation of this perturbation term we used a method which is similar to that used by Nilsson in deriving the non-spherically-symmetric term in his Hamiltonian. By using (31) and following the procedure employed by Inglis [8]), it is easy to see that $\langle \nu'|\partial/\partial\gamma|\nu\rangle$ is replaced by

$$\frac{\hbar\omega_0}{\sqrt{3}} \varepsilon \left(\frac{1}{\varepsilon_{\nu'} - \varepsilon_\nu}\right) \langle \nu'|\xi^2 - \eta^2|\nu\rangle. \tag{32}$$

In this case the selection rules, which correspond to (30), are given by

$$N' = \begin{matrix} N \\ N\pm 2 \end{matrix}, \qquad n'_x = n_x, \qquad \Lambda' = \Lambda \pm 2, \qquad \Sigma' = \Sigma. \tag{33}$$

After these preparations we can now proceed to the evaluation of $\mathcal{I}$ and B_γ. For the actual calculation we take $\Delta = 1$ MeV, following the remrak of Bohr, Mottelson and Pines [13]). The parameter λ is fixed so that the total numbers of protons and neutrons, in the sense of Belyaev, coincide with the actual numbers of these nucleons in the particular nucleus for which we intend to calculate $\mathcal{I}$ and B_γ. Finally the energies ε_ν are taken from the tables prepared by Nilsson and Mottelson [11, 14]) †.

The actual calculation is performed for the two arbitrarily chosen nuclei

† As was mentioned above, the asymptotic quantum numbers and wave function are used in the evaluation of the matrix elements in (28) and (29). In evaluating the denominator, however, more precise energies obtained by Nilsson and Mottelson are used.

Er^{164} and Yb^{170} and the results are given in table I †. It is seen that the agreement between the experimental and the theoretical moments of inertia is rather good. It is also seen from this table that the rule $\mathcal{I} \approx 3B_\gamma$ holds pretty well

TABLE 1

Results of the calculation of B_γ and $\mathcal{I}$.

	$\hbar^2/B_\gamma$ (theor.)	$3\hbar^2/\mathcal{I}$ (theor.)	$3\hbar^2/\mathcal{I}$ (experim.)
Er^{164}	95	82	90
Yb^{170}	103	86	84

The first and the second columns give, respectively, the theoretical values of $\hbar^2/B_\gamma$ and $3\hbar^2/\mathcal{I}$. These are calculated by assuming that the equilibrium value of β is equal to 0.3. Column 3 gives the experimental value of $3\hbar^2/\mathcal{I}$, taken from ref. [19]). All values in keV.

and this result will support our argument given in sec. 3 (iv′) and (v′). Although the actual calculation has been performed only for the above two cases, it may be expected that this relation will hold quite generally.

5. Concluding Remarks

It is shown that all the experimental data with which the predictions of DF agree can as well be explained by the conventional theories, although some more detailed calculations remain to be performed for each nucleus.

In the rotational region, it is further possible to show that not only both theories give results which agree equally well with experiments, but also the wave functions derived in these theories look very much alike. Thus, the wave function of the second excited spin 2 state, in the conventional theory is, if the rotation-vibration interaction is taken into account,

$$|2_2^+\rangle_m = \psi_m(2_2^+) - \tfrac{1}{3}\sqrt{2}\,\frac{1}{p\sqrt{p}}\,\psi_m(2_1^+) \qquad (34)$$

in the lowest order expansion in p^{-1} as is seen from (20) if we put $a = 1$. On the other hand the corresponding wave function in DF is, to the same order in p^{-1},

$$|2_2^+\rangle_m = \text{const}\left[\left(\frac{D^{(2)}_{m,2}(\theta_1)+D^{(2)}_{m,-2}(\theta_1)}{\sqrt{2}}\right) - \tfrac{1}{3}\sqrt{2}\,\frac{1}{p\sqrt{p}}\,D^{(2)}_{m,0}(\theta_1)\right]. \qquad (35)$$

The similarity between (34) and (35) is clearly seen by noting that $\psi_m(2_2^+)$ and $\psi_m(2_1^+)$ are proportional, respectively, to $\frac{1}{\sqrt{2}}[D^{(2)}_{m,2}(\theta_1)+D^{(2)}_{m,-2}(\theta_1)]$ and $D^{(2)}_{m,0}(\theta_1)$.

Such a result seems to be quite natural, because in both models the nucleus

† After completion of the manuscript, we learned that Griffin and Rich performed a very similar calculation of the moments of inertia of even rare earth nuclei (see ref. [18])).

is considered to have a stable shape with a non-vanishing $\beta = \beta_0$ and $\gamma = 0°$. It should, however, still be mentioned that the basic idea of these two models is not the same, because in DF the nuclear shape is considered to be kept fixed, while in the conventional theory the nucleus is allowed to change its shape.

The difference between these two models becomes more apparent if we come to the so-called vibrational region, and here there seems to exist several experimental data which would be difficult to fit with DF. In a recent article Mallmann [15]) summarized experimental data concerning the energies of various states of even nuclei. In particular he found that the ratio $\varepsilon_1(6)/\varepsilon_1(2)$ varies from 3 to 7 as $\varepsilon_1(4)/\varepsilon_1(2)$ varies from 2 to $\frac{10}{3}$. The minimum possible value of $\varepsilon_1(6)/\varepsilon_1(2)$ in DF is, however, 5 and it might be one of the difficulties in this theory. A similar difficulty may appear also for $\varepsilon_1(4)$. Further in DF there can appear no excited 0^+ state, as has been pointed out in our previous paper [6]). It should be mentioned that such difficulties do not appear in the conventional model. Thus it might be concluded that, in spite of the surprising success of DF concerning two $I = 2$ states, this model has some intrinsic difficulty in itself.

References

1) A. S. Davydov and G. F. Filippov, Nuclear Physics **8** (1958) 237
2) A. Bohr, Mat. Fys. Medd. Dan. Vid. Selsk. **26**, No. 14 (1952)
3) A. Bohr and B. R. Mottelson, Mat. Fys. Medd. Dan. Vid. Selsk. **27**, No. 16 (1953)
4) G. Scharff-Goldhaber and J. Weneser, Phys. Rev. **98** (1955) 212; see also J. Raz, Phys. Rev. **114** (1959) 1116
5) D. M. van Patter, Nuclear Physics **14** (1959) 42
6) T. Tamura and L. G. Komai, Phys. Rev. Letters **3** (1959) 344
7) L. Wilets and M. Jean, Phys. Rev. **102** (1956) 788
8) D. R. Inglis, Phys. Rev. **96** (1954) 1059; **97** (1955) 701
9) A. Bohr and B. R. Mottelson, Mat. Fys. Medd. Dan. Vid. Selsk. **30**, No. 1 (1955); Norske Vidensk. Selsk. Forhand. **31**, No. 12 (1958)
10) See e.g. Alder, Bohr, Huns, Mottelson and Winther, Revs. Mod. Phys. **28** (1956) 432
11) S. G. Nilsson, Mat. Fys. Medd. Dan. Vid. Selsk. **29**, No. 16 (1955)
12) S. T. Belyaev, Mat. Fys. Medd. Dan. Vid. Selsk., **31**, No. 11 (1959)
13) A. Bohr, B. R. Mottelson and D. Pines, Phys. Rev. **110** (1958) 936
14) B. R. Mottelson and S. G. Nilsson, Mat. Fys. Skr. Dan. Vid. Selsk. **1**, No. 8 (1959)
15) C. A. Mallmann, Phys. Rev. Letters **2** (1959) 507
16) J. J. Griffin and M. Rich, Phys. Rev. Letters **3** (1959) 342

5

Nuclear Physics **16** (1960) 474—491; © *North-Holland Publishing Co., Amsterdam*

Not to be reproduced by photoprint or microfilm without written permission from the publisher

SYSTEMATICS OF ALPHA-RADIOACTIVITY IN THE RARE EARTH REGION

KENNETH S. TOTH † and JOHN O. RASMUSSEN

Lawrence Radiation Laboratory

and

Department of Chemistry, University of California, Berkeley, California ††

Received 29 December 1959

Abstract: Alpha decay energy data in the rare earth region are extended by means of closed decay energy cycle calculations and are then correlated for each element as a function of neutron number. The marked effect of the closed shell at 82 neutrons on the alpha decay energies is discussed. Evidence is presented for a sharp drop at 90 neutrons in the normal alpha-decay energy versus neutron number trend, as well as for a proton subshell at 64 protons. Half-lives are calculated using a formula derived from simple barrier-penetration theory. The calculated values are compared with experimental half-lives and discrepancies are discussed. Reduced level widths δ^2 are determined for rare earth alpha emitters using barrier penetration factors calculated from the real potential derived by optical model analysis of alpha elastic scattering data. The reduced widths are in turn used to propose hindrance factors for odd-mass alpha emitters.

1. Introduction

From the observation of the slope of the mass-defect curve it has been noted that most isotopes whose mass numbers are greater than 150 are unstable with respect to alpha-particle emission. Radioactive decay by this means is commonly observed in both natural and artificial isotopes of elements whose atomic numbers are greater than 82. In marked contrast, alpha emission for isotopes of elements with $Z < 83$ is rather unusual. Prior to 1949 only one alpha-emitting isotope was known in the medium-heavy region, i.e. the alpha-emitting nucleide in natural samarium discovered by Hevesy and Pahl in 1932 [1]). The lack of alpha-emitters in this region can be well accounted for by the fact that alpha-decay rates depend on the decay energies in a very sensitive exponential manner, as shown by the formulae developed independently by Gamow [2]) and by Condon and Gurney [3]). Naturally-occurring isotopes in the medium-heavy element region might be unstable toward alpha-particle emission by as much as 2 MeV and still have half-lives too long to be readily observed.

Kohman made an analysis of alpha-particle binding energies in the same

† Present address: Electronuclear Research Division, Oak Ridge National Laboratory.

†† This work was carried out mainly under the auspices of the U. S. Atomic Energy Commission.

region based on the semi-empirical equation of Bohr and Wheeler and on the experimental mass-defect curve [4]). He predicted that sufficiently neutron-deficient isotopes of the medium-heavy elements might exhibit alpha decay. Such a prediction can also be made on the basis of alpha-decay energy systematics in the heavy elements where the trend (with two inversions which will be discussed later) is that of increasing alpha-decay energies with decreasing neutron numbers for a given atomic number. The electron-capture or positon decay energies also generally increase with decreasing neutron numbers. Thus, whether or not alpha emission could be detected in the medium-heavy elements as neutrons were removed before the total half-lives became inconveniently short had to be tested experimentally. In 1949 Thompson and co-workers reported positive results obtained in a survey in which targets of various elements of interest were subjected to high-energy particle bombardments [5]). They discovered alpha-radioactivity in neutron-deficient isotopes of gold and mercury and some rare-earth elements. Since that time other alpha emitters with $Z < 83$ have been reported in both naturally occurring and artificially produced isotopes. The majority of the latter were reported by Rasmussen, Thompson and Ghiorso in 1953 [6]). In addition, Dunlavey and Seaborg produced Sm^{146} also in 1953 [7]), while Toth and Rasmussen discovered and reported two new dysprosium alpha emitters in 1958 [8]). The discovery of naturally occurring alpha emitters in the region below bismuth has been carried out chiefly by two groups (1) Kauw, Porschen and Riezler who have used nuclear emulsions to detect the alpha radioactivity [9–13]) and (2) Macfarlane and Kohman who have used an ionization chamber as the detector [14]). As a result there are known at present eighteen alpha emitters with $Z < 83$ whose mass numbers are fairly certain.

The present study is limited to the rare earths because fifteen of these alpha emitters have atomic numbers between 60 (neodymium) and 66 (dysprosium). The clustering of alpha radioactivity in the 82-neutron region allows correlation of alpha-energy and decay-rate data in a manner similar to that used in studies of alpha systematics in the heavy elements. In this paper alpha decay data have been correlated and possible conclusions as well as predictions derived on the basis of such correlations.

2. Summary of Information

The information on rare earth alpha emitters is summarized in table 1.

3. Alpha Decay Energy Systematics

Decay energy information is most conveniently summarized in a diagram where alpha-decay energies are plotted as a function of neutron (or mass) number. Compilations of similar data in the heavy elements have shown that

TABLE 1. Summary of information

Alpha emitter	Total half-life	Other decay modes observed	Alpha energy (MeV)	Method of detection	Alpha half-life	Method of $T_{\frac{1}{2}\alpha}$ determination	Reference
Dy^{154}	13 ±2 h [a])	none observed	3.35±0.05 [a])	ionization chamber			[9])
Dy^{153}	5 ±0.5 h	indirect evidence for E.C. decay	3.48±0.05	ionization chamber	≈13.4 y	estimated from reaction yield	[6, 15])
Dy^{152}	2.3±0.2 h	E.C. and β^+	3.66±0.05	ionization chamber	≈1.45 y	estimated from reaction yield	[6, 8, 15, 16])
Dy^{151}	19 ±4 min	E. C. and β^+	4.06±0.04	ionization chamber			[6, 8, 16])
Dy^{150}	7 ±2 min	E.C. and β^+	4.21±0.06	ionization chamber			[6, 8, 16])
Tb^{151}	19 ±1 h	E.C.	3.44±0.1	ionization chamber	≈7.4 ×10³ y	$\frac{\text{X ray}}{\alpha}$ ratio	[6, 8, 15])
Tb^{149}	4.1±0.2 h	E.C.	3.95±0.02	alpha spectrograph	36 ±7 h	$\frac{\text{total}}{\alpha}$ ratio	[6, 16, 17])
Gd^{152}		natural β stable isotope	2.15±0.03	ionization chamber	1.13×10¹⁴±0.08 y	decay rate of known number of atoms	[14])
Gd^{150}	10^6 y	β-stable	2.70±0.15	ionization chamber	≈3×10⁶ y	decay rate of known numbers of atoms	[6, 15])
Gd^{149}	9.0±1 d	E.C.	3.00±0.15	ionization chamber	≈4×10³ y	$\frac{\text{X ray}}{\alpha}$ ratio	[6])
Gd^{148}		β-stable (?)	3.16±0.10	ionization chamber	≈1.3×10⁸ y	estimated from reaction yield	[6, 15])
Eu^{147}	24 ±2 d	E.C.	2.88±0.10	ionization chamber	≈4.4×10⁸ y	$\frac{\text{X ray}}{\alpha}$ ratio	[6, 15])
Sm^{147}		natural β-stable isotope	2.18±0.02	ionization chamber	≈1.3×10¹¹ y	decay rate of known number of atoms	[1, 18, 19])
			2.24±0.02	ionization chamber	1.18±0.05×10¹¹ y	decay rate of known number of atoms	[14])
Sm^{148}		β-stable	2.55±0.05	nuclear emulsion	≈5×10⁷ y	estimated from reaction yield	[7])
Nd^{144}		natural β-stable isotope	1.90±0.1	nuclear emulsion	≈1.5×10¹⁵ y	decay rate of known numbers of atoms	[20])
		natural β-stable isotope	1.84±0.02	ionization chamber	2.36±0.29×10¹⁵ y	decay rate of known number of atoms	[14])

[a]) In recent preliminary results, R. D. Macfarlane in Berkeley finds a long-lived dysprosium activity of about 2.9 MeV decay energy. If this newer activity indeed represents the ground state decay of Dy^{154}, the 3.35 MeV activity belonging to an isomer, some of the discussion of this paper regarding an α-energy discontinuity between 88 and 90 neutrons would be altered.

in such a plot the points for a given element lie on an approximately straight line. As mentioned briefly in the introduction alpha-decay energies for a given Z number increase with decreasing neutron number. Discontinuities in this monotonic trend appear in two places in the heavy element region. The first, an extremely pronounced one appears at 128 neutrons as a consequence of the closed shell at 126 neutrons. As a result of the major closed shell the maximum alpha-decay energy for a given element is reached at 128 neutrons owing to the abnormally low neutron binding energies just beyond the closed shell. Alpha-decay energies are abnormally low for isotopes with 126 neutrons. The normal trend is found to resume in isotopes with less than 125 neutrons. A similar but much less pronounced effect takes place at 154 neutrons, presumably as a consequence of a neutron subshell at 152 neutrons [21]).

Information in the rare earth region ($60 \leqq Z \leqq 66$) is much more fragmentary, but the basic structure of increasing alpha-decay energy with decreasing neutron number is unmistakable. The influence of the closed shell at 82 neutrons is also similar to that of the shell at 126 neutrons. The maximum in alpha-decay energies is reached at 84 neutrons for a particular Z number. A discontinuity in the normal trend is presumably present at this point, since no isotopes with neutron number less than 84 have been found to emit alpha-particles despite the fact that several such isotopes with reasonable half-lives are known in this region. At a later point in this section additional evidence is presented to support the idea of a discontinuity at 84 neutrons.

The alpha-decay energy data shown in table 1 can be supplemented by means of closed energy cycles. The method consists of predicting decay energies by the construction of a system of energy-balance cycles from existing alpha- and beta-energies in which an individual closed cycle is made up of two alpha- and two beta-decay energies. Then, if 3 of the 4 pieces of information that constitute a cycle are known, the fourth can be calculated. The method has been highly successful in the heavy element region [22]). The application of a similar method in the 82-neutron region is limited for a number of reasons, the chief of which is scarcity of experimentally known alpha energies. This can be at least partially overcome through the interpolation and extrapolation of the family of curves showing alpha-decay energy versus neutron number. Another reason for the limited applicability of the closed-cycle method is that alpha emitters in this region decay by electron-capture, a process for which it is generally not possible to make a direct experimental measurement of the decay energy. A systematic study of closed energy cycles in a limited region, however, has been carried out because new information does come to light. The cycles are divided into 4 sets since they connect only nucleides differing in mass number by four, and these sets are labelled $4n$, $4n+1$, $4n+2$ and $4n+3$ respectively. The notation can be illustrated thus: "$4n+2$" means that the mass numbers of nucleides of this type when divided by four have a

remainder of 2 and so on. The cycles are shown in figs. 1—4. The beta-decay energies and lower limits of these numbers used in the cycles have been taken chiefly from a compilation by King [23], and a later one by Lidofsky [24]) and from the new Table of Isotopes [25]). The three exceptions are: (1) Pm^{144} E.C.

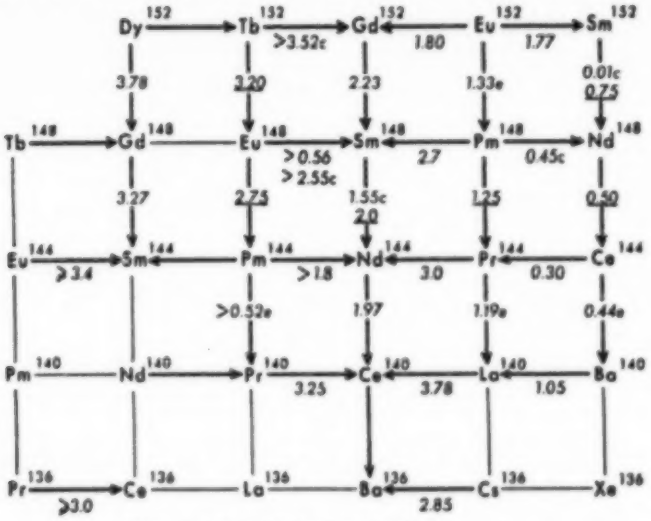

Fig. 1. Closed decay cycle $4n$.

In figs. 1—4,
a number indicates an experimental value;
an underlined number indicates a value estimated from fig. 5;
a number followed by e indicates a value calculated using only experimental energies;
a number followed by c indicates a value calculated using energies estimated from fig. 5.

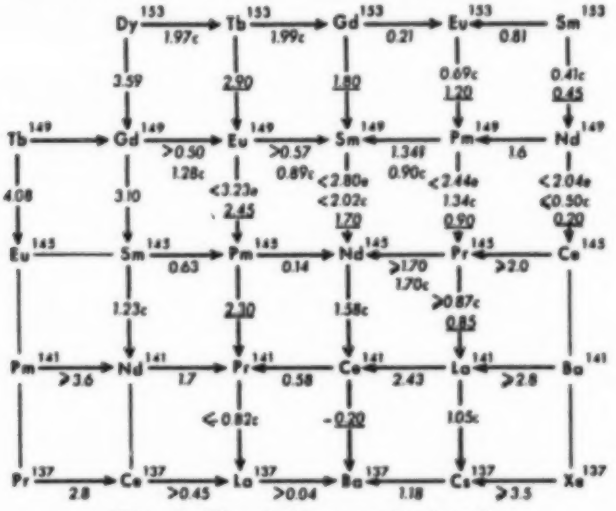

Fig. 2. Closed decay cycle $4n+1$.

decay energy > 1.8 MeV, obtained from some recent work by Toth and Nielsen [26]); (2) Eu^{146} and Gd^{146} E.C. decay energies, 3.30 and 2.15 MeV respectively, taken from a publication by Gorodinski *et al.* [27]); and (3) Nd^{151} $Q_{\beta^-}=2.4$ MeV, and Sm^{155} $Q_{\beta^-}=1.8$ MeV, taken from two recent publications of Schmid and Burson [28,29]). The Q_{α}'s (alpha-decay energies) used throughout

the cycle calculations are known as the effective decay energies and consist of the total alpha disintegration energies of the bare nuclei. These Q_{eff}'s are equal to the alpha particle energies in the laboratory system plus the recoil energy plus the orbital electron screening correction $\Delta E_{s.c.}$, where

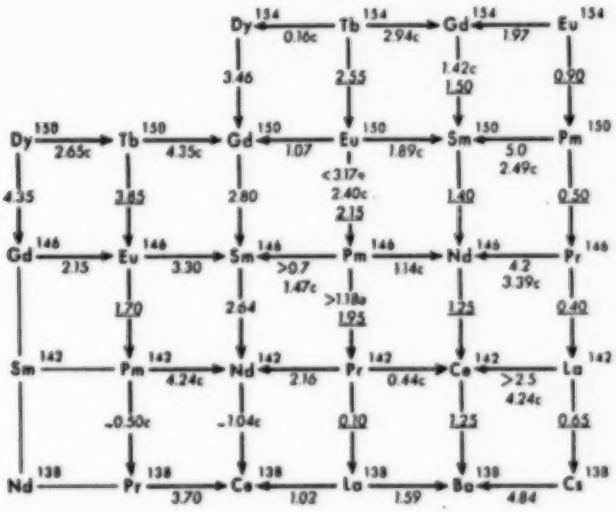

Fig. 3. Closed decay cycle $4n+2$.

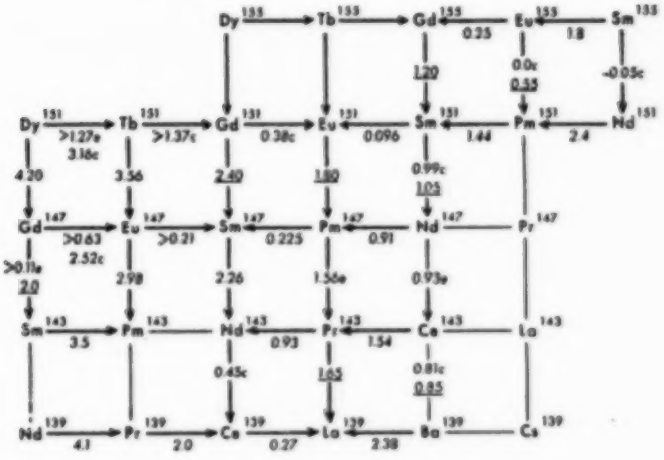

Fig. 4. Closed decay cycle $4n+3$.

$\Delta E_{s.c.}=65.3\ (Z+2)^{\frac{7}{3}}-80\ (Z+2)^{\frac{2}{3}}$ eV, and is approximately equal to 20 keV for the rare earth nucleides.

Using only experimental Q_{eff}'s the following decay energies can be calculated by the method of closed cycles:

(a) $4n$ cycle

Eu^{152}	$Q_{eff}=1.33$ MeV
Pm^{144}	$Q_{eff}>0.52$ MeV
Pr^{144}	$Q_{eff}=1.19$ MeV
Ce^{144}	$Q_{eff}=0.44$ MeV

(b) $4n+1$ cycle Eu^{149} $Q_{eff} < 3.23$ MeV
Sm^{149} $Q_{eff} < 2.80$ MeV
Pm^{149} $Q_{eff} < 2.44$ MeV
Nd^{149} $Q_{eff} < 2.04$ MeV

(c) $4n+2$ cycle Eu^{150} $Q_{eff} < 3.17$ MeV
Pm^{146} $Q_{eff} > 1.18$ MeV

(d) $4n+3$ cycle Dy^{151} $Q_{E.C.} > 1.27$ MeV
Gd^{147} $Q_{eff} > 0.11$ MeV
Pm^{147} $Q_{eff} = 1.56$ MeV
Nd^{147} $Q_{eff} = 0.93$ MeV.

The calculated values for Eu^{152}, Pm^{147}, Nd^{147}, Pr^{144} and Ce^{144} were added to the experimentally determined ones, bringing the total of known alpha decay energies to 20. The 20 numbers were then used to draw fig. 5 in which they were plotted against neutron numbers. The points for particular elements have

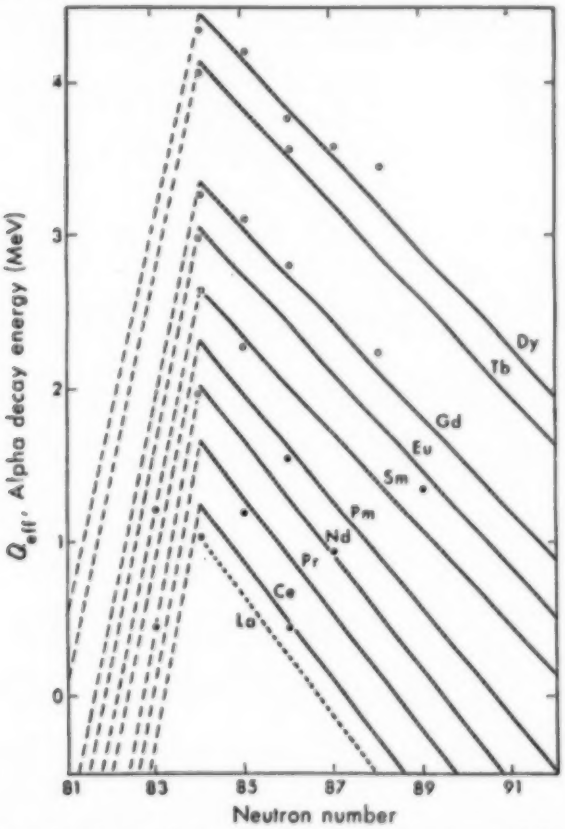

Fig. 5. Plot of Q_{eff} versus neutron number. ○ indicates an experimental decay energy. • indicates a decay energy calculated from closed decay cycles using only experimentally determined decay energies.

The Nd^{143} and Sm^{145} points have been calculated from decay cycles using Pr^{143} and Pm^{145} energies estimated from the full lines in the figure. Dashed lines have been drawn for all the elements shown with the Nd^{143} and Sm^{145} points serving as guides, to show the discontinuity occurring at 84 neutrons. The lanthanum line is drawn parallel to the cerium line and through the La^{141} point calculated from a closed decay cycle.

been joined in an idealized fashion by drawing straight lines through them. It is these lines that were used in estimating unknown alpha-decay energies by means of either interpolation or extrapolation. The fact that the points should in reality be joined by a series of roughly parallel zigzagging lines rather than straight lines introduces an error into any Q_{ett} that is read off these lines However, under the circumstances (for some elements only one point is known) such straight-line extrapolations and interpolations are the best that can be made.

We will now illustrate by two examples the manner in which the remainder of the cycles were constructed. In the first case 1.65 MeV is read off the praseodymium line for the Q_{ett} of Pr^{143}, and the Q_{ett}'s for Ce^{143} and Nd^{143} are calculated to be 0.81 and 0.45 MeV, respectively. The Ce^{143} value thus determined is in good agreement with the Q_{ett} estimated from fig. 5. The second case represents a less straightforward calculation. The Q_{ett} for Pm^{146} was found to be > 1.18 MeV using the experimentally determined Sm^{146} alpha-decay energy. The lower limit agrees with the value of 1.95 MeV estimated from the promethium line. Using this approximate Q_{ett} for Pm^{146} one calculates the Q_{β^-} for Pm^{146} to be about 1.47 MeV. In turn, using this Q_{β^-}, the Eu^{150} Q_{ett} is found to be about 2.4 MeV in good agreement with the approximate value of 2.15 MeV read off the europium curve in fig. 5. The numbers shown in the closed cycles are labelled as to how they have been determined. Rather than go through each cycle individually, only those of special interest will be discussed.

The Q_{ett}'s for Sm^{145} and Nd^{143} have been calculated to be 1.25 and 0.45 MeV respectively. The two isotopes each have 83 neutrons and their Q_{ett}'s are to be compared with the experimental alpha-decay energies of Sm^{146} and Nd^{144}. In both cases there are decreases of approximately 1.4 MeV for the Q_{ett}'s in going from 84- to 83-neutron isotopes. This is evidence that the 82-neutron closed shell does indeed exert the same influence on alpha-decay energies as does the 126-neutron shell in the heavy elements. The Sm^{145} and Nd^{143} points have been placed in fig. 5 and two lines drawn connecting these points to those of Sm^{146} and Nd^{144}, respectively. Similar lines have been drawn for the other elements parallel to the first two. The calculated limits for the Q_{ett}'s of Gd^{147} and Pm^{144} (also 83-neutron isotopes) of > 0.11 and > 0.51 MeV, respectively, are seen to be in agreement with the values read off the gadolinium and promethium lines. Additional evidence concerning the influence of the 82-neutron shell may be obtained in the following manner. The Q_{ett}'s for the 83-neutron isotopes Pr^{142} and Ce^{141} can be estimated to be 0.10 and -0.20 MeV, respectively. Using these Q_{ett}'s the alpha-decay energies of the 82-neutron nucleides Nd^{142} and Pr^{141} are found to be negative. The negative alpha-decay energies not only for the two 82-neutron isotopes but also for Ce^{141} indicate that the three nucleides are stable with respect to emission of alpha particles.

In general the closed-cycle calculations are internally consistent indicating that the accuracy of the curves in fig. 5 is fair considering the idealized straight-line extrapolations. Some discrepancies do arise. Beta-decay energies taken from King's compilation seem almost certainly to be in error in two instances. These are: (a) Pm^{149} $Q_{\beta^-}=1.34$ MeV, and (b) Pm^{148} $Q_{\beta^-}=2.7$ MeV. The first value is listed in King's compilation with a questionmark after it, indicating that the number is uncertain. Considering the uncertainty we should like to propose a Q_{β^-} of 0.90 MeV for Pm^{149}, thus removing the inconsistency. The Q_{β^-} of Pm^{148} is employed in two cycle calculations. In one, the Q_{ett} of Eu^{152} used in Fig. 5 is calculated. In the second, using 1.25 MeV for the Pm^{148} Q_{ett}, that of Sm^{148} is found to be 1.55 MeV, while the number estimated from fig. 5 is 2.0 MeV. If the Pm^{148} Q_{β^-} is decreased by, say, 0.25 MeV, the calculated Sm^{148} Q_{ett} is in essential agreement with the Fig. 5 value. The Eu^{152} Q_{ett} becomes 1.58 MeV, a number that is as much above the europium line in fig. 5 as the 1.33 MeV value is below that line. We would therefore propose that the correct Pm^{148} Q_{β^-} is less than 2.7 MeV and is closer to 2.45 MeV. Another inconsistency is apparent in the Gd^{155}, Eu^{155}, Sm^{151} and Pm^{151} closed cycle. Here the calculated Eu^{155} Q_{ett} is approximately 0.55 MeV less than the fig. 5 value. The Eu^{155} Q_{β^-} is probably correct. That of Pm^{151} is less certain. Perhaps the Pm^{151} Q_{β^-} is in error. A more striking inconsistency appears in connection with the following two beta-decay energies: Pm^{150} Q_{β^-} (5.0 MeV) and Pr^{146} Q_{β^-} (4.2 MeV). Because the Q_{ett} of Sm^{150} must be $>$ the Q_{ett} of Pm^{150}, the Q_{β^-} of Pr^{146} should be $>$ the Q_{β^-} of Pm^{150}. Another indication that the Pm^{150} Q_{β^-} is too large is found if the Q_{ett} of Eu^{154} is estimated to be 0.90 MeV. Then the calculated Gd^{154} Q_{ett} is almost 2.5 MeV larger than that expected from fig. 5. The alpha decay energy of La^{141} has been calculated to be approximately 1.05 MeV. Starting with this point, a line may be drawn parallel to the cerium line in fig. 5. From the lanthanum line the Q_{ett} of La^{142} can be estimated to be 0.65 MeV. Working backwards, the two beta-decay energies are found to be: (a) Pr^{146} $Q_{\beta^-}=3.39$ MeV and (b) Pm^{150} $Q_{\beta^-}=2.49$ MeV. Now, using the above-estimated Eu^{154} Q_{ett}, that of Gd^{154} is found to be 1.42 MeV, in agreement with the value of 1.50 MeV obtained from fig. 5.

The discrepancies in the two other instances seem to be due to rather sharp drops in the alpha-decay energy versus neutron number curves somewhere between 88 and 90 neutrons. There is experimental evidence in the case of the dysprosium alpha emitters of such an abrupt decrease. Dy^{154} has been found to have an energy of 3.46 MeV [8]), a number somewhat higher than would be expected, but not in serious disagreement with the straight line drawn through the other four dysprosium decay energies. Recently Riezler and Kauw have searched for alpha activity in Dy^{156} using dysprosium enriched in Dy^{156} [12]). They report that they were unable to see any alpha tracks attributable to Dy^{156} and set a lower limit of 10^{18} years for the isotope's alpha half-life by

alpha decay of energy exceeding 2.2 MeV. The expected energy for Dy^{156}, according to the line in fig. 5, should be about 2.7 MeV, so that there seems to be a sharp decrease in energy of at least half an MeV. There are rather abrupt nuclear-structure changes between 88 and 90 neutrons in neighbouring rare-earth nucleides, as reflected in first-excited-state energies and spectroscopic isotope shifts of even nuclei and in quadrupole and magnetic moments in

TABLE 2

Beta decay energies calculated using closed cycles

Cycle series	Isotope	Beta decay energy (MeV)	Previoulsly known beta decay energy (MeV)
$4n$	Tb^{153}	>3.52 (E.C.)	
	Eu^{148}	>2.55 (E.C.)	>0.56
	Pm^{148}	0.45 (E.C.)	
$4n+1$	Dy^{153}	1.97 (E.C.)	
	Tb^{153}	1.99 (E.C.)	
	Gd^{149}	1.28 (E.C.)	>0.50
	Eu^{149}	0.89 (E.C.)	>0.57
	Pm^{149}	0.90 ($\beta-$)	1.34
	Pr^{145}	1.70 ($\beta-$)	≧1.70
$4n+2$	Tb^{154}	0.16 ($\beta-$)	
	Tb^{154}	2.94 (E.C.)	
	Dy^{150}	2.65 (E.C.)	
	Tb^{150}	4.35 (E.C.)	
	Eu^{150}	1.89 (E.C.)	
	Pm^{150}	2.49 ($\beta-$)	5.0
	Pm^{146}	1.47 ($\beta-$)	>0.7
	Pm^{146}	1.14 (E.C.)	
	Pr^{146}	3.39 ($\beta-$)	4.2
	Pm^{142}	4.24 (E.C.)	
	Pr^{142}	0.44 (E.C.)	
	La^{142}	4.24 ($\beta-$)	>2.5
$4n+3$	Dy^{151}	3.16 (E.C.)	
	Tb^{151}	>1.37 (E.C.)	
	Gd^{151}	0.38 (E.C.)	
	Gd^{147}	2.52 (E.C.)	>0.63

Eu^{151} and Eu^{153}. Perhaps the discontinuity is related to these sudden changes in isotopes having 88 and 90 neutrons. The sharp decrease could account for the following discrepancies that arise in our cycle calculations. If the Q_{ett} of Eu^{152} (89n) is taken to be 1.50 MeV, that of Sm^{152} (90n) is found to be about 0.23 MeV, while from fig. 5 one would predict a Q_{ett} of 0.75 MeV. A similar instance exists in the cycle involving the Q_{ett}'s of Gd^{153} (89n) and Eu^{153} (90n). There the calculated Q_{ett} for Eu^{153} is 0.69 MeV while the estimated one is

1.20 MeV. One notes that using the 1.20 MeV Q_{eff} for Eu^{153}, that for Sm^{153} is calculated to be 0.41 MeV, a value in good agreement with that of 0.45 MeV obtained from the samarium line. It therefore seems that the discrepancy occurs only when the two isotopes involved in the cycle happen to have 89 and 90 neutrons, respectively. This would indicate that the sharp decrease takes place between 89 and 90 neutrons and that the lines past 90 neutrons continue approximately parallel to the original slope. Since only differences between Q_{eff}'s are used, it does not matter if both of the alpha-decay energies used in a calculation have been decreased from their original values (estimated from fig. 5) by approximately the same amount. With the available data these seem to be the only such checks on our proposal of a discontinuity.

Examining the alpha-energy trends with atomic number for 84-neutron nuclei in fig. 5, one notes that the large break between gadolinium (64p) and terbium (65p) is outstanding, suggesting a proton subshell at 64. From the differences in alpha energies of the 84-neutron nuclei it would seem that the 65^{th} proton is less tightly bound than the general average in the region. The "break" was noted for the first time by Rasmussen, Thompson and Ghiorso [6]) who proposed that a splitting between the $2d_{\frac{3}{2}}$ and $2d_{\frac{5}{2}}$ levels in the Mayer nuclear shell model could account for a slight extra stabilization of the 64-proton configuration. The single-particle states for odd-Z nuclei in the region $50 < Z < 82$ come in the following order: $g_{\frac{7}{2}}$, $d_{\frac{3}{2}}$, $h_{\frac{11}{2}}$, $d_{\frac{5}{2}}$ and $s_{\frac{1}{2}}$ [30]). There does occur a substantial splitting between the $d_{\frac{3}{2}}$ and $h_{\frac{11}{2}}$ states which might account for a proton subshell at Z equal to 64.

In summary, then, (1) the curves in fig. 5 can be used with fair accuracy in obtaining extrapolated and interpolated alpha-decay energies at least up to 89 neutrons, (2) good evidence exists that 83- and 82-neutron isotopes have alpha-decay energies much less than those of 84-neutron nucleides for a given element, (3) some evidence is available indicating a sharp decrease in the normal alpha-decay energy versus neutron number trend in going from 89 to 90 neutrons, and (4) a proton subshell may exist at 64 protons. Table 2 lists beta decay energies calculated using closed cycles.

4. Alpha-Decay Rate Correlations

Half-lives for alpha-decay transitions proceeding from even nuclei to ground levels in the daughter nuclei in the heavy element region have been found to agree well with those calculated from simple Coulomb barrier penetration theory [31]). Most decay rate correlations have been made using a semi-empirical treatment rather than employing equations that arise from the penetration theory. The treatment is based on the fact that if experimental alpha half-lives for even ground state transitions are plotted against $Q_{eff}^{-\frac{1}{2}}$ a series of parallel straight lines are obtained, one for each element. The equation of these

lines may be represented as

$$\log t_{\frac{1}{2}} = \frac{A}{(Q_{\text{eff}})^{\frac{1}{2}}} + B.$$

The constants A and B are evaluated for even-Z elements from the known experimental data, and a least squares fit to the values for A and B is obtained yielding equations for A and B, respectively, valid in the heavy element region. In this way similar lines are then drawn for odd-Z elements. Transitions other than ground state transitions from even nuclei exhibit rates that are slower than those predicted from simple theory [31]), that is, those calculated from the above equation using the appropriate constants A and B. The slower transitions include in addition to those proceeding from odd-mass nuclei the non-ground-state transitions of even nuclei. Hindrance factors are then defined for the slower transitions, taking these to be the ratios of the experimental half-lives to the half-lives calculated from the above equation.

A similar treatment in the rare earth region is not possible owing to the lack of accurately known alpha half-lives. Instead we have calculated half-lives using equations directly from the barrier penetration theory and compared them with the experimentally determined ones. In the simple theory the barrier is pictured as a potential made up of a Coulomb potential $V=2Ze^2/r$, with a sharp cut-off at a certain radius termed the effective nuclear radius R. The alpha particle confined within the barrier makes frequent collisions with the wall and has a probability for penetrating the barrier. The decay constant $\lambda = fP$, where f is the frequency factor expressed as collisions per second with the wall, and P is the quantal penetrability factor. From the WKB approximation the penetration factor is

$$P \approx \exp\left\{\frac{-2}{\hbar}\int_R^{\frac{2Ze^2}{E}} \sqrt{2M\left(\frac{2Ze^2}{r} - E\right)}\,\mathrm{d}r\right\},$$

where Z is the charge of the recoil nucleus and M is the reduced mass of the system. The integral has been evaluated analytically, and using Bethe's notation [32]), $P \approx \exp\left[-2g(Z, R)\gamma(x)\right]$ where $x=E/B$ (B being the barrier height $2Ze^2/R$), $g(Z,R)=(2e/\hbar)\sqrt{MZR}$, and $\gamma(x)=x^{-\frac{1}{2}}$ arc cos $(x^{\frac{1}{2}})-(1-x)^{\frac{1}{2}}$. For the pre-exponential factor f, different expressions have been used by various authors. Rasmussen, Thompson and Ghiorso calculated alpha half-lives in the rare earth region using 5 different formulae for f and found that the calculated half-lives for particular isotopes differed very little [6]). The formulae used in the calculations presumably give the same rate dependence on decay energy. For our purposes we have chosen formula (3) in that paper, which is an approximation to the decay rate formula derived by Preston [33]).

The expression derived by Preston is

$$\lambda = \frac{2^{\frac{1}{2}}}{M^{\frac{1}{2}}R}\,\frac{(E-U)(B-E)^{\frac{1}{2}}}{(E-U)+(B-E)}\,P, \tag{1}$$

where U is the internal potential energy of the alpha particle within the nucleus. Kaplan, in his correlation of even alpha-emitter data [34]), also used the formula and was able to show from his correlations that

$$E-U \approx \pi^2\hbar^2/2MR^2. \tag{2}$$

For the heavy element alpha-emitters correlated by Kaplan, $E-U$ is about 0.52 MeV, small enough to be neglected with respect to $(B-E)$ in the denominator of the expression (1) for λ. Substituting for $E-U$ from (2), expression (1) becomes

$$\lambda = \frac{2^{\frac{1}{2}}\pi^2\hbar^2}{M^{\frac{1}{2}}R^3(B-E)^{\frac{1}{2}}}\,P. \tag{3}$$

This, then, is the formula used in our calculations.

Before λ can be determined, the effective nuclear radius R must be known. Using the decay rate data for Gd^{148} and Ra^{224}, the R values (for the recoil nuclei Sm^{144} and Em^{220}) in the two regions were found by Rasmussen *et al.* to be 8.00 and 9.25×10^{-13} cm respectively [6]). From these R values the

TABLE 3

Comparison of theoretical and experimental alpha half-lives

Isotope	Q_{eff} (MeV)	Theor. half-life	Exper. half-life	Ratio (exp./theor.)
(a) Dy^{153}	3.59	9.57 y	13.4 y	1.4
Dy^{152}	3.78	0.38 y	1.45 y	3.8
Tb^{151}	3.56	4.08 y	5.8×10^{2} y	1.4×10^{2}
Tb^{149}	4.08	8.4 h	36 h	4.3
Gd^{152}	2.23	2.11×10^{14} y	1.13×10^{14} y	$(1.9)^{-1}$
Gd^{150}	2.80	8.37×10^{6} y	3×10^{6} y	$(2.8 \times 10^{1})^{-1}$
Gd^{149}	3.10	6.92×10^{3} y	4×10^{3} y	$(1.7)^{-1}$
Eu^{147}	2.98	2.09×10^{4} y	5×10^{3} y	$(4.2)^{-1}$
Eu^{147}	3.06	4.06×10^{3} y	5×10^{3} y	1.2
Sm^{147}	2.26	1.63×10^{12} y	1.3×10^{11} y	$(1.25 \times 10^{1})^{-1}$
Sm^{147}	2.32	2.00×10^{11} y	1.18×10^{11} y	$(1.7)^{-1}$
Sm^{148}	2.64	1.78×10^{7} y	5×10^{7} y	2.8
Nd^{144}	1.97	1.37×10^{15} y	1.5×10^{15} y	1.1
Nd^{144}	1.92	1.14×10^{16} y	2.36×10^{15} y	$(4.8)^{-1}$
(b) Dy^{156}	2.60	4.40×10^{10} y	$> 10^{18}$ y	
Dy^{156}	2.20	1.16×10^{16} y	$> 10^{18}$ y	
Dy^{154}	3.46	1.04×10^{3} y		
Dy^{151}	4.20	6.2 h	> 19 min	
Dy^{150}	4.35	53 min	> 7 min	
Tb^{151}	3.20	3.95×10^{3} y	$> 2.2 \times 10^{4}$ y	

constants a and b used in an effective nuclear radius formula of the type $R=(aA^{\frac{1}{3}}+b) \times 10^{-13}$ cm were determined, and found to be 1.58 and -0.30 respectively. We have calculated the alpha half-lives of the isotopes listed in table 1 using the above radius formula and expression (3) for the decay constant λ. Table 3 compares the experimental half-lives with the theoretical ones. A plot of the logarithm of the half-life versus the inverse of the square root of the decay energy is shown in fig. 6. Both the theoretical and the experimental half-lives have been included in the diagram. As mentioned previously the points for a given element in such a plot for even nuclei fall

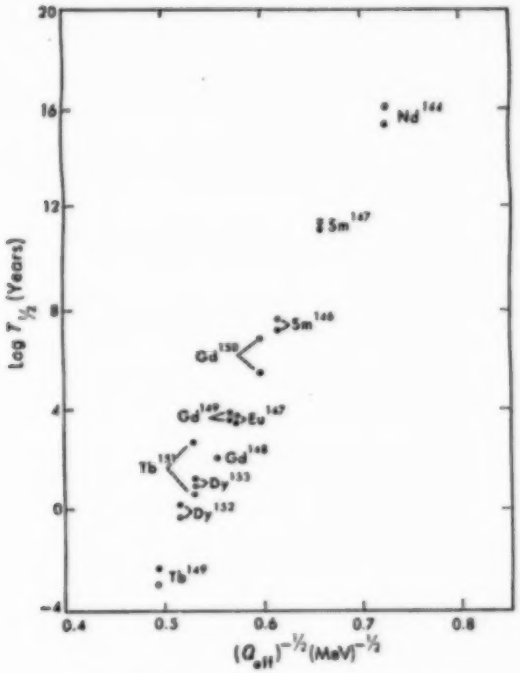

Fig. 6. Plot of $T_{\frac{1}{2}}$ versus $(Q_{eff})^{-\frac{1}{2}}$.
• indicates an experimental half-life.
○ indicates a calculated half-life.

on a straight line. This can be readily seen if the function $\gamma(x)$ is expanded in a Taylor series about $x = 0$. Then the expression for P becomes

$$\log P = \frac{(2MBR)^{\frac{1}{2}}}{\hbar}\left[\frac{\pi B^{\frac{1}{2}}}{E^{\frac{1}{2}}} - 4 + \frac{E}{B} - \frac{3E^2}{4B^2} + \dots\right]$$

where it is indeed observed that the main energy dependence of log P is an inverse square root dependence.

Bearing in mind the sensitive dependence of half-lives on decay energies let us consider the results of table 3 (a). Excepting for Gd^{150} the theoretical and experimental half-lives of all the even isotopes are in agreement within a factor of 5. Deviations of such magnitudes are not surprising if errors involved

in the determinations of experimental half-lives and decay energies are considered. A change of 70 keV in a Q_{eff} is sufficient to account for a difference of a factor of 10 in the calculated half-life. The discrepancy in the Gd^{150} case is much greater (a factor of 28). Here again the deviation is probably due to errors in the half-life and decay energy measurements. The decay energy is correct to only ± 0.15 MeV while the experimental half-life is accurate to only a factor of 2.

From heavy element data it is known that odd-mass alpha emitters have half-lives longer than those calculated from theory. For Dy^{153} and Gd^{149} the theoretical and experimental half-lives do not deviate by large amounts. Errors in the experimental data preclude any conclusions as to whether or not the discrepancies are significant. The Eu^{147} decay energy is based on the experimental Sm^{147} value. Using the two older decay energies of Eu^{147} and Sm^{147} the half-lives calculated are found to be greater than the experimental ones. The deviation is particularly large for Sm^{147}. A more recent measurement of the Sm^{147} decay energy has been made by Macfarlane [14]). (The remeasurement affects some of the artificial alpha emitters where Sm^{147} was used as a standard.) This number together with the consequent new Eu^{147} decay energy yields theoretical half-lives in essential agreement with the experimental ones. Larger deviations for all four of the above odd-mass isotopes are not excluded by the experimental data. It is not possible to state with certainty if any of the four nucleides exhibit hindered alpha decay rates. According to table 3 (a) the 2 remaining odd-mass isotopes, Tb^{149} and Tb^{151}, seem to have hindered decays. Taking into consideration the experimental limits of error the two half-lives still appear to be greater than the calculated ones. Thus the alpha decay rates of Tb^{149} and Tb^{151} seem to be indeed hindered.

In table 3, part (b), half-lives have been claculated for Dy^{151}, Dy^{150} and Tb^{152} and are compared with the experimental half-life limits for the same nucleides. The experimental values for Dy^{151} and Dy^{150} have been taken as being greater than the total half-lives of these isotopes. The Tb^{152} limit is much more significant since it indicates that the half-life is greater than the theoretically calculated one showing that the odd-mass isotope has a hindered alpha-decay rate. The Tb^{152} half-life limit has been determined from an α/E.C. branching ratio limit of $< 10^{-7}$ set by Toth, Faler and Rasmussen [35]). Theoretical alpha-decay rates have been calculated for Dy^{156} using two decay energies, 2.6 and 2.2 MeV. The first is taken from the extrapolated dysprosium line in fig. 5, while the second is the upper limit set by Riezler and Kauw [12]). Their experimental alpha half-life limit of $> 10^{18}$ years for Dy^{156} shows that even 2.2 MeV for the Q_{eff} is still somewhat large. Thus there seems to be indeed a sharp drop from the expected decay energy of approximately 0.5 MeV at 90 neutrons at least for the dysprosium alpha emitters. The calculated Dy^{154} half-life has been included for comparison.

The Coulomb potential with a sharp cut-off at some effective nuclear radius is not a realistic nuclear potential. Hoping to obtain a more significant treatment of alpha decay data, Rasmussen has calculated barrier penetrabilities for even and odd-mass alpha emitters using a potential derived from alpha-scattering information[36,37]). The potential used was deduced by Igo from optical-model analyses of alpha-scattering data[38]). The $V(r)$ consists of an exponential expression for the real part of the nuclear potential valid in the surface region for $|V| \lesssim 10$ MeV:

$$V(r) = -1100 \exp\left\{-\left[\frac{r-1.17\,A^{\frac{1}{3}}}{0.574}\right]\right\} \text{MeV},$$

where r is in 10^{-13} cm and A is the mass number. Rasmussen has calculated the penetration factors P using the above $V(r)$ and then determined the reduced alpha emission widths δ^2 from the expression $\lambda = \delta^2 P/h$, where "λ" is the decay constant and h is Planck's constant. Hindrance factors F were then determined for odd-mass isotopes as well as for non-ground-state transitions in even nucleides. The factor F for odd-mass isotopes was defined as $F = (\delta_1^2 + \delta_2^2)/2\delta_{\text{odd}}^2$, where δ_1^2 and δ_2^2 are reduced widths for ground-state transitions of nearest or next nearest even nuclei and δ_{odd}^2 is the reduced width for the odd-mass isotope in question. We have taken the δ^2 values for Sm^{146}, Gd^{148}, Tb^{149} and Tb^{151} from the two publications of Rasmussen[36,37]). In addition, employing the same IBM-650 program the δ^2 values for Nd^{144}, Sm^{147}, Eu^{147} (using the newer experimental data for these three isotopes [14]), Gd^{150}, Gd^{152}, Dy^{152} and Dy^{153} have been calculated. The information together with hindrance factors for odd-mass isotopes is summarized in table 4. Also

TABLE 4

Reduced widths and hindrance factors

Nucleide	$(E_\alpha + E_{se})$*	Exper. $T_{\frac{1}{2}\alpha}$ (sec)	Reduced width δ^2 (MeV)	Hindrance factor F	Even nucleides used to calculate F
Nd^{144}	1.86	7.45×10^{22}	0.223		
Sm^{146}	2.57	1.58×10^{15}	0.0152		
Sm^{147}	2.26	3.72×10^{18}	0.0750	2.03×10^{-1}	Sm^{146}
Eu^{147}	3.00	2.07×10^{11}	0.0167	3.01	Sm^{146}, Gd^{148}
Gd^{148}	3.18	4.47×10^{9}	0.0852		
Gd^{149}	3.02	1.15×10^{11}	0.0954	8.20×10^{-1}	Gd^{148}, Gd^{150}
Gd^{150}	2.72	2.08×10^{14}	0.0713		
Gd^{152}	2.17	3.56×10^{11}	0.0952		
Tb^{149}	3.97	1.48×10^{5}	0.0115	6.83	Gd^{148}, Gd^{150}
Tb^{151}	3.42	2.40×10^{10}	6.13×10^{-4}	1.36×10^{2}	Gd^{150}, Gd^{152}
Dy^{152}	3.68	1.55×10^{7}	0.0425		
Dy^{153}	3.50	1.93×10^{8}	0.0785	5.41×10^{-1}	Dy^{152}

* Does not include alpha particle recoil energy.

shown in the table are the even isotopes used to determine F for any given odd-mass nucleide.

The reduced widths in principle should be constant for even (ground-state transitions) and favoured alpha decay. The experimental data for Dy^{152} and Dy^{153} are so uncertain that it is difficult to state whether or not the Dy^{153} decay rate is indeed favoured. The Tb^{149}, Tb^{151} and Eu^{147} decay rates are seen to be hindered even taking into account experimental limits of error. Gd^{149} is presumably favoured in its alpha decay. Here the data are again uncertain enough to make any conclusion very doubtful. Sm^{147} seems to exhibit a favoured alpha decay rate. This is dependent on the δ^2 of Sm^{146} which seems to be a little low compared to the reduced widths of the other even nucleides. However, even if its δ^2 is increased to a value closer in magnitude to that of the other even reduced widths the Sm^{147} decay rate would still tend to be favoured. The Sm^{147} decay energy and experimental half-life are known sufficiently well so that its calculated δ^2 must be quite accurate. The spins of Sm^{147} [39,40]) and of its alpha-decay daughter, Nd^{143} [41,42]), have been both found to be $\frac{7}{2}$. The wave functions of the odd nucleon in parent and daughter should be very similar, thus leading to a large overlap integral between initial and final odd-nucleon wave functions. Perhaps this explanation can account for the enhanced Sm^{147} alpha-decay rate.

5. Conclusion

Before our knowledge of alpha systematics in the 82-neutron region can be extended any further, more data are certainly needed. Some of the already known alpha half-lives will have to be redetermined more accurately. A number of alpha emitters are known whose partial alpha half-lives have not yet been determined. New alpha emitters will have to be discovered and their decay energies and half-lives found. It is certain that alpha emitters, undiscovered as yet, do exist with measurable half-lives. Unknown alpha emitters above dysprosium must exist, as indicated by the holmium alpha activity reported by Rasmussen *et al.* [6]), and also by the following experiment carried out by the authors. Natural dysprosium containing 0.05 % Dy^{156} and 0.09 % Dy^{158} was bombarded with 48-MeV helium ions. Presumably erbium isotopes were produced with mass numbers 156 or greater, since (α, 5n) reactions are not energetically possible at the bombarding energy, at least not with any appreciable cross sections. Chemical separations were not attempted. The samples were counted in alpha counters, and half-lives of reasonable duration (hours) were observed. These alpha emitters were either erbium or holmium isotopes, but were definitely not dysprosium nucleides, since the dysprosium daughters would have mass numbers 156 or greater and these are known not to emit alpha radiation.

References

1) G. Hevesy and M. Pahl, Nature **130** (1932) 846
2) G. Gamow, Z. Physik **52** (1929) 510
3) E. U. Condon and R. W. Gurney, Phys. Rev. **33** (1929) 127
4) T. P. Kohman, Phys. Rev. **76** (1949) 448
5) Thompson, Ghiorso, Rasmussen and Seaborg, Phys. Rev. **76** (1949) 1406
6) Rasmussen, Thompson and Ghiorso, Phys. Rev. **89** (1953) 33
7) D. C. Dunlavey and G. T. Seaborg, Phys. Rev. **92** (1953) 206
8) K. S. Toth and J. O. Rasmussen, Phys. Rev. **109** (1958) 121
9) W. Porschen and W. Riezler, Z. Naturforsch. **9a** (1954) 701
10) W. Porschen and W. Riezler, Z. Naturforsch. **11a** (1956) 143
11) W. Riezler and G. Kauw, Z. Naturforsch. **12a** (1957) 665
12) W. Riezler and G. Kauw, Z. Naturforsch. **13a** (1958) 904
13) W. Riezler and G. Kauw, Z. Naturforsch. **14a** (1959) 196
14) R. D. Macfarlane, Natural Alpha Radioactivity in Medium-Heavy Elements (Thesis) Department of Chemistry, Carnegie Institute of Technology, NYO-7687, May 1959
15) Rasmussen, Rollier and Toth, to be published
16) K. S. Toth and J. O. Rasmussen, J. Inorg. Nucl. Chem. **10** (1959) 198
17) L. Winsberg UCRL-3958; also Bull. Am. Phys. Soc. **3** (1958) 406
18) W. P. Jesse and J. Sadauskis, Phys. Rev. **78** (1950) 1
19) G. Beard and M. L. Wiedenbeck, Phys. Rev. **95** (1954) 1245
20) E. C. Waldron, V. A. Schultz and T. P. Kohman, Phys. Rev. **93** (1954) 254
21) Ghiorso, Thompson, Higgins, Harvey and Seaborg, Phys. Rev. **95** (1954) 293
22) Glass, Thompson and Seaborg, J. Inorg. Nucl. Chem. **1** (1955) 3; and B. M. Foreman and G. T. Seaborg, J. Inorg. Nucl. Chem. **7** (1958) 305
23) R. W. King, Revs. Mod. Phys. **26** (1954) 327
24) L. J. Lidofsky, Revs. Mod. Phys. **29** (1957) 773
25) Strominger, Hollander and Seaborg, Revs. Mod. Phys. **30** (1958) 585
26) K. S. Toth and O. B. Nielsen, Phys. Rev. **115** (1959) 1004
27) Gorodinski, Murin and Pokrovsky, Izvestia Akad. Nauk S.S.S.R., Ser. Fiz. **22** (1958) 811
28) L. C. Schmid and S. B. Burson, Phys. Rev. **115** (1959) 178
29) L. C. Schmid and S. B. Burson, Phys. Rev. **115** (1959) 447
30) B. R. Mottelson and S. G. Nilsson, Mat. Fys. Skr. Dan. Vid. Selsk. **1**, (1959) No. 8
31) I. Perlman and J. O. Rasmussen, Handbuch der Physik, S. Flügge, ed., Vol. 42, (Springer Verlag, Berlin, **1957**) p. 143
32) H. A. Bethe, Revs. Mod. Phys. **9** (1937) 69
33) M. A. Preston, Phys. Rev. **71** (1947) 865
34) I. Kaplan, Phys. Rev. **81** (1951) 962
35) Toth, Faler and Rasmussen, Phys. Rev. **115** (1959) 158
36) J. O. Rasmussen, Phys. Rev. **113** (1959) 1593
37) J. O. Rasmussen, Phys. Rev., to be published
38) G. Igo, Phys. Rev. Letters **1** (1958) 72
39) G. S. Bogle and H. E. D. Scovil, Proc. Phys. Soc. A **65** (1952) 360
40) K. Murakawa, Phys. Rev. **93** (1954) 1232
41) B. Bleaney and H. E. D. Scovil, Proc. Phys. Soc. A **63** (1950) 1369
42) K. Murakawa and J. S. Ross, Phys. Rev. **82** (1951) 967

1.E.1:
4.E

Nuclear Physics **16** (1960) 492—501; © *North-Holland Publishing Co., Amsterdam*
Not to be reproduced by photoprint or microfilm without written permission from the publisher

ON THE DECAY OF $^{106}Rh^{m}$

O. J. SEGAERT and J. L. DEMUYNCK
Natuurkundig Laboratorium, Rijksuniversiteit, Ghent, Belgium

Received 5 December 1959

Abstract: The $^{106}Rh^{m}$ isotope was produced by irradiating Pd with 25 MeV deuterons. The beta and gamma radiations following the decay of 133 ± 4 min $^{106}Rh^{m}$ were investigated with scintillation spectrometers. The $^{106}Rh^{m}$ was found to decay mainly by 790, 950, 1180 and 1620 keV beta transitions. Gamma rays of 220, 407, 450, 512, 620, 735, 820, 1055, 1140, 1225, 1560, 1740, 1860, 2120, and 2280 keV were assigned with certainty. Relative intensities of the beta and gamma rays are reported (tables 1 and 2). A tentative level scheme is proposed.

1. Introduction

In 1955, G. B. Baró *et al.* [1]) revealed the existence of an isomer of $^{106}Rh^{m}$. The $^{106}Rh^{m}$ isotope was formed by (n, p), (n, α) and (d, α) reactions, but not as a normal fission product or as a daughter of ^{106}Ru. An activity with a half life of 117 min was reported. The maximum energy of the negatons emitted was determined, from absorption curves with aluminium, as 0.7 MeV. The newly found $^{106}Rh^{m}$ appeared not to disintegrate by gamma emission (< 1 %) to the 30 sec state of ^{106}Rh. A total disintegration energy Q of about 3.6 MeV was reported. Some of the gamma rays known from the decay of ^{106}Rh and from ^{106}Ag as well as additional ones were observed.

W. Nervik *et al.* [2]) found a period of 138 min and a maximum energy for the negatons of ≈ 1 MeV. Their measurements have revealed nine gamma rays. (table 2). Several gamma rays together with their relative intensities were reported by S. Mayo *et al.* (refs. [3]) and [4])).

Due to the complexity of the spectrum it is difficult to construct a decay scheme which can accommodate all gamma rays. With the aim of establishing a level scheme, the beta and gamma radiation was examined. The decay was followed for 20 hours under the same experimental conditions. A detailed analysis of the pulse height distribution was performed by comparison with spectra of samples emitting essentially single gamma rays.

2. Source Preparation and Chemical Procedure

Sources of $^{106}Rh^{m}$ were prepared by irradiating Pd with the deuteron beam of the synchrocyclotron of the Instituut voor kernphysisch Onderzoek in Amsterdam. A deuteron beam with an energy of 25 MeV was used. The bombardment

lasted for 20 minutes in order to reduce the amount of ^{105}Rh produced. (Some ^{105}Rh was always present, its contribution was subtracted.) The irradiated target was allowed to decay for one hour before chemical separations were performed. In order to reduce the amount of 23 min ^{107}Rh, the measurements were started two hours after irradiation. The chemical procedure to separate the Rh fraction, as described below, was the same in all cases.

The targets of Pd powder were dissolved in $HCl+HNO_3$. Ruthenium carrier was added before distillation with $6N$ H_2SO_4. Trivalent ferric and monovalent silver holdback carriers were added. Rh and Fe were coprecipitated by the addition of ammonia. The filtrate was dissolved in a small quantity of HCl. Holdback carriers of Pd- and Ag-ions were added to this solution. A specific precipitate of rhodium as $K_3Rh(NO_2)_6$ was obtained with KCl, CH_3COOH and KNO_2. Finally the precipitate was dried with alcohol and ether.

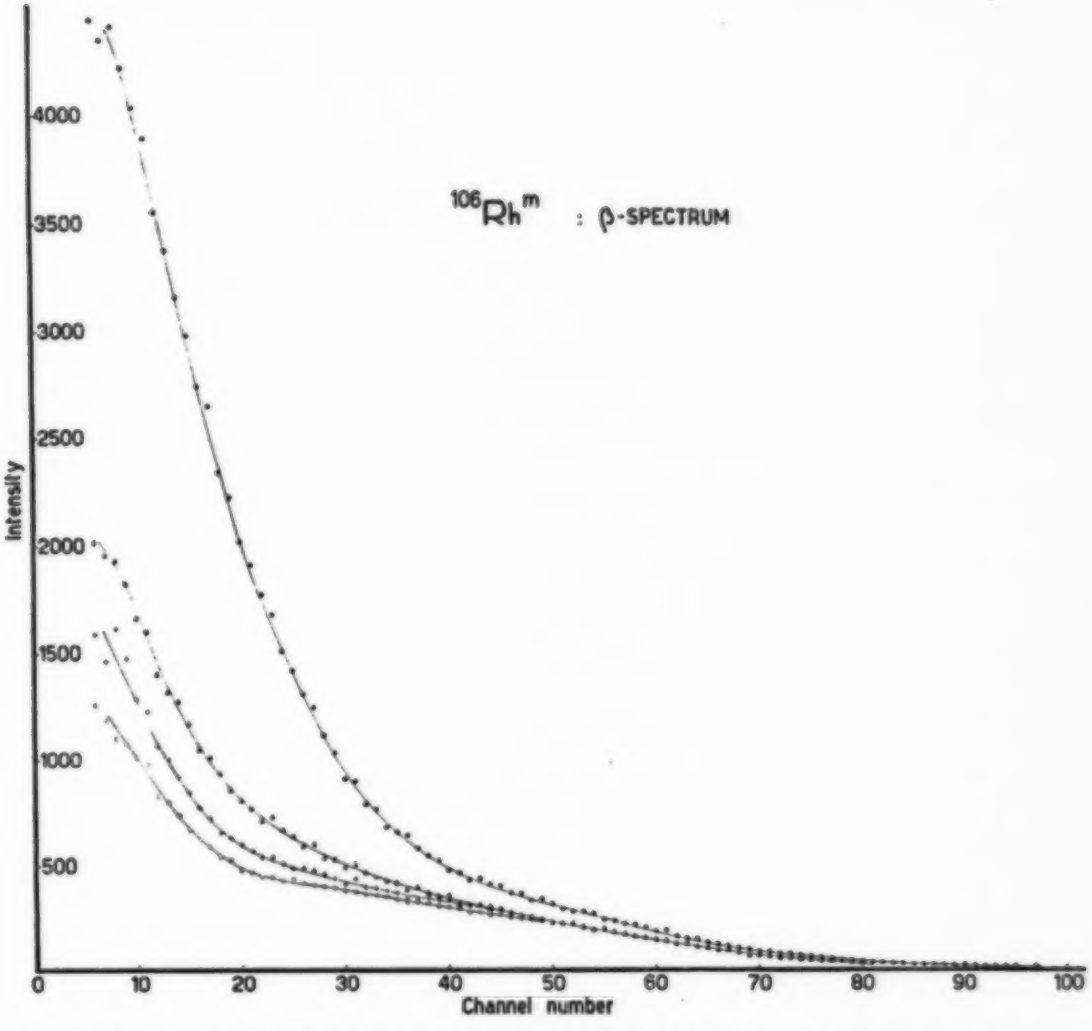

Fig. 1. The decay of the $^{106}Rh^{m}$ beta spectrum respectively 4 h, 9 h, 13.3 h and 20 h after irradiation.

3. Measurements and Results

The gamma-ray spectrum of $^{106}Rh^{m}$ was studied using a cylindrical NaI(Tl) crystal of 2.5×2.5 cm coupled to a 6292 Dumont photomultiplier, and with a cylindrical well-type NaI(Tl) crystal of 6.2×6.2 cm external size having a hole

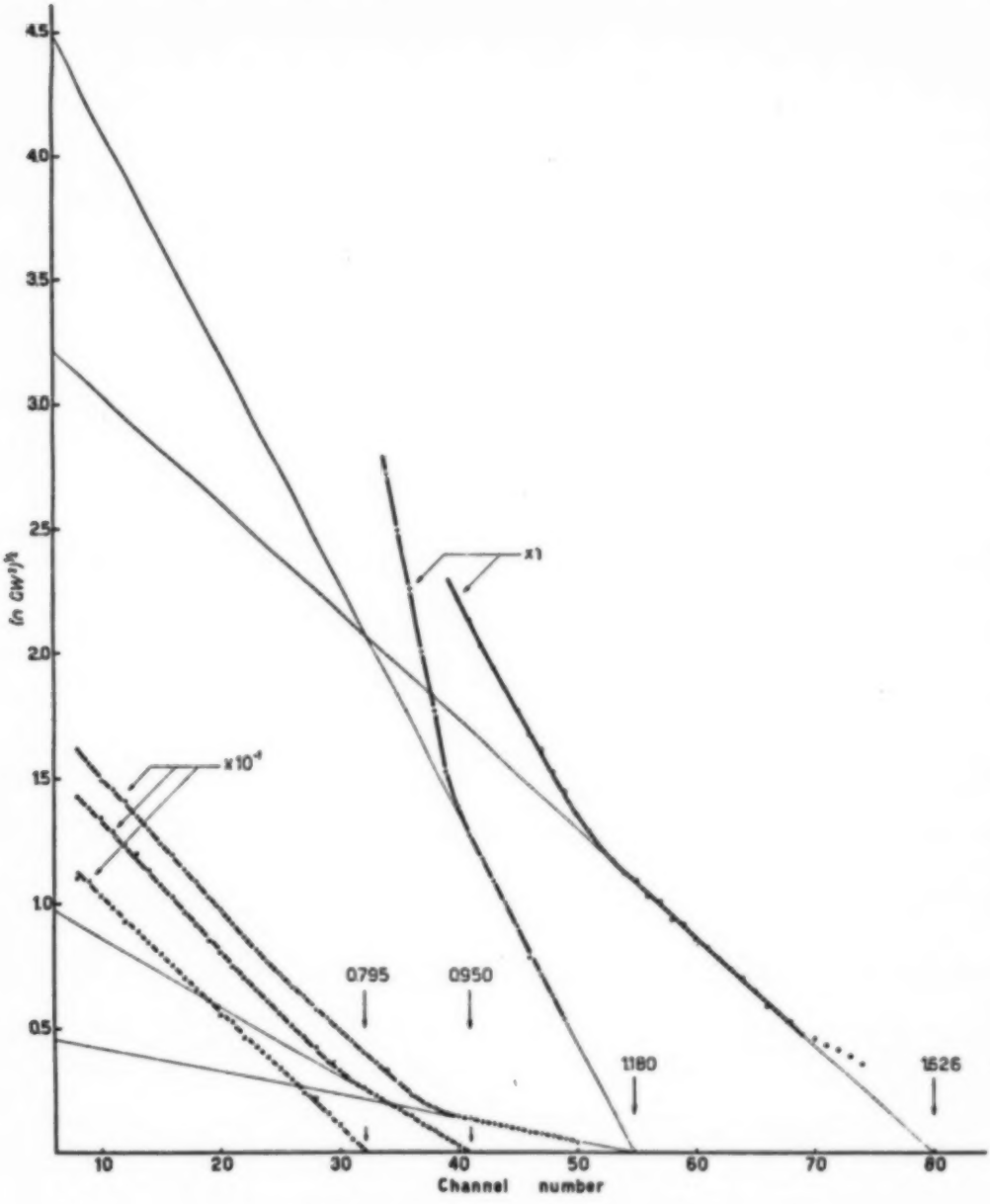

Fig. 2. The Fermi plot of the $^{106}Rh^{m}$ beta spectrum.

of 9 mm diameter and 31 mm depth, used for direct and summing studies. The beta decay was measured with an anthracene crystal spectrometer (crystal diameter 3.8 cm, height 1 cm). The spectra were displayed on a RIDL 100 channel analyser.

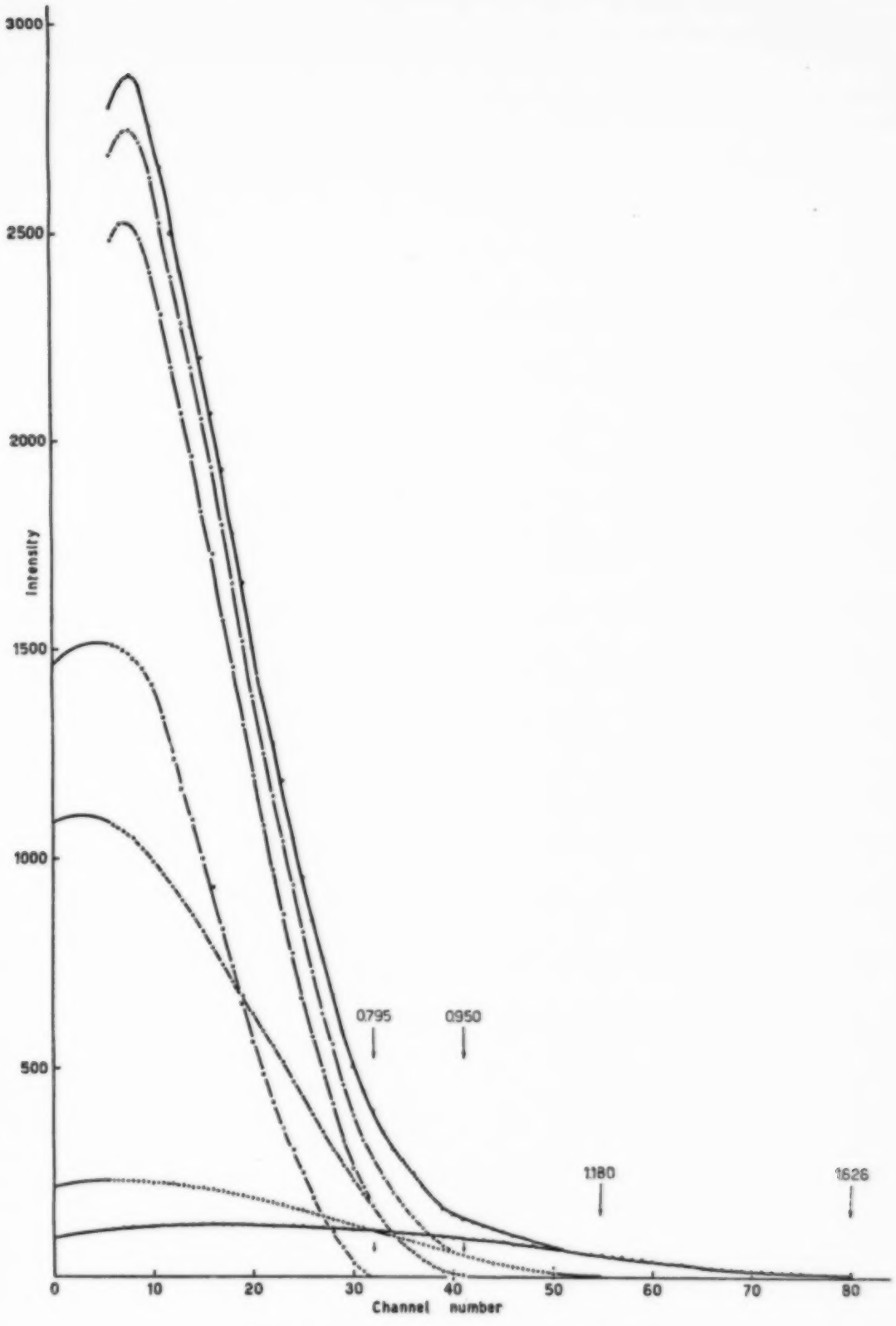

Fig. 3. The analysed beta spectrum of $^{106}Rh^{m}$.

3.1. THE BETA SPECTRUM

The beta spectra were recorded 4 h, 9 h, 13.3 h and 20 h after irradiation. The pulse height distributions were corrected for background, and for contributions due to gamma-ray detection (fig. 1). At the moment the last spectrum was measured all $^{106}Rh^{m}$ activity had decayed. From the third and the last pulse height distribution, the presence of a 560 keV component with half life 33 ± 3 h was established. Other higher energy components decayed with half lifes $\geqq 7$ days. The gamma-ray spectrum showed a very intense peak at 315 keV (half life 34 ± 2 h). From this, one of the contaminations could be identified as ^{105}Rh, produced by the $^{108}Pd(d,\alpha n)$ reaction. The pulse height distributions due to the contaminating activities were subtracted from the original spectrum, after correction for their respective decay periods. From a Fermi analysis of the remaining $^{106}Rh^{m}$ spectrum, beta transitions of the allowed type were found at 1.62 ± 0.02, 1.18 ± 0.02, 0.950 ± 0.03 and 0.795 ± 0.40 MeV. Figs. 2, 3, and table 1 summarize the results of the analysis. The energy determination of higher components was not attempted because of the relatively large statistical error involved. Their total intensity is about 1 % of the total disintegration rate.

TABLE 1

Intensities and log ft values for the various beta branches from $^{106}Rh^{m}$.

E_β (MeV)	E_β (MeV)	E_β (MeV)	Intensity (%)	log ft
0.7	≈ 1	0.79 ± 0.04	40 ± 4	5.3
0.95	(formerly assigned to ^{107}Rh)	0.95 ± 0.03	38 ± 4	5.6
		1.18 ± 0.03	11 ± 2	6.5
		1.62 ± 0.02	10 ± 2	7.1
Baro *et al.* [1])	Nervik and Seaborg [2])	present work		

3.2. THE DIRECT GAMMA SPECTRUM

During the examination of the direct gamma spectra, care was taken to suppress summing effects, by placing the source at a distance of 8 cm (1 inch crystal) or at a distance of 12 cm (2.5 inch crystal). The beta rays were absorbed with a 1 cm thick carbon absorber. The results obtained in the analysis of the $^{106}Rh^{m}$ spectra are summarized in table 2 together with a review of all previous investigations [2, 3, 4]). The analysed pulse height distribution were obtained by subtraction of two spectra taken at intervals of 2 hours (half-life of $^{106}Rh^{m}$). The energies and intensities reported in column 3 of table 2, are the mean values obtained from the 1 inch crystal spectrometer measurements, and from measurements done with the source outside the well-type crystal (2.5 inch diameter); cf. figs. 4 and 5. For isolated peaks the relative intensities have

TABLE 2

Energies and relative intensities of the gamma rays from $^{106}Rh^{m}$ (133 min) as reported by different groups

Nervik and Seaborg [2])	Mayo *et al.* [4])		Present investigation (accepted averages)			
energy (MeV)	energy (MeV)	rel. intensity	energy (MeV)	rel. intensity†	summing peaks energy (MeV)	possible origin
0.195					1.14	0.513±0.620
0.225	0.220	18	0.220 ±0.005	20 ±4	1.36	0.735±0.620
			0.407 ±0.005	20 ±4		0.513±0.820
	0.435	43	0.450 ±0.005	35 ±5	1.44	0.620±0.820
0.510	0.515	100	0.512 ±0.005	100	1.56	0.513±1.050
0.630	0.610	26	0.620 ±0.005	33 ±5		0.735±0.820
0.715	0.735	36	0.735 ±0.005	47 ±8	1.65	—
	0.820	45	0.820 ±0.01	40 ±6	1.74	0.513+1.225
	0.940	?	0.950?±0.01	3.5±1	(1.86)	(0.735+1.140)
1.06	1.070	40	1.055 ±0.010	29 ±4	1.96	0.820±1.140
			1.140 ±0.010	14 ±2	2.06	0.513+1.56
					(2.1)	—
1.20	1.225	23	1.225 ±0.010	19 ±3	2.28	0.735±1.56
1.26	1.38	?				1.050+1.225
1.50	1.555	23	1.56 ±0.01	21 ±3	2.31	—
	1.760	7	1.74 ±0.02	2 ±0.4	2.44	—
	1.860	8	1.86 ±0.02	2 ±0.4	2.68	—
	2.090	1	2.12 ±0.02	1 ±0.2	2.79	—
	2.260	1	2.28 ±0.02	0.5±0.1	—	—

† The 512 keV transition has been normalized to 100.

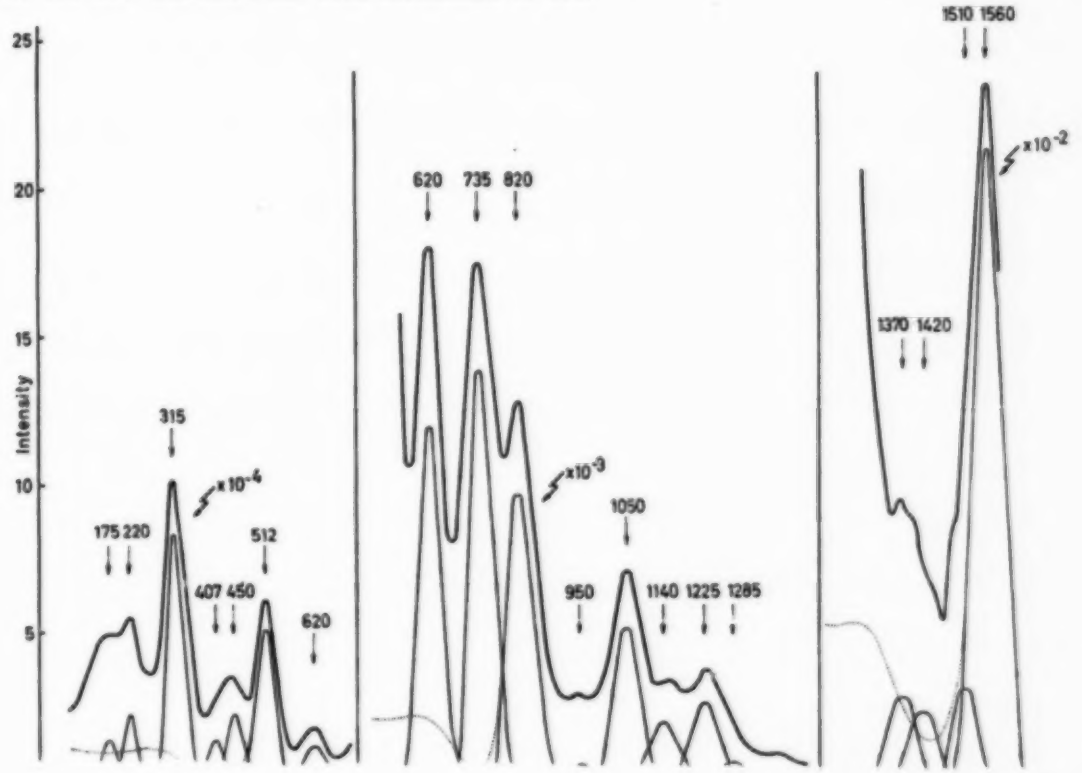

been determined with ≈ 15 % accuracy. For weak peaks lying on a high Compton distribution, for peaks in the immediate vicinity of pair peaks, or for those pairs of peaks having a great difference in intensity, the accuracy is somewhat less. The spectra for the source outside the well were examined several times

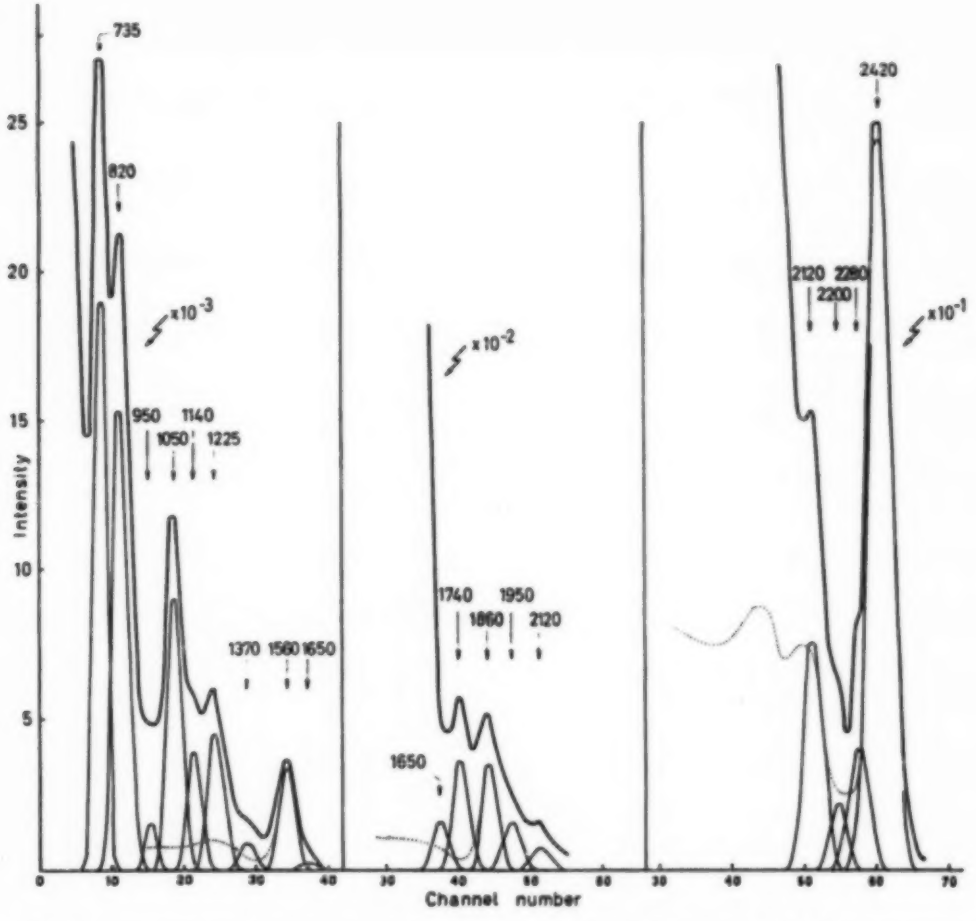

Fig. 5. $^{106}Rh^{m}$ gamma spectrum with 1 cm carbon and with 2.5 inch crystal, higher energy region.

over a period of about 20 h, in order to identify the gamma-ray lines decaying with the correct half life. The gamma transitions with energies 220, 407, 450, 512, 620, 735, 820, 1055, 1140, 1225, 1560, 1760, 1860, 2120, and 2280 MeV showed the same half life. (The average value of the half life found from all runs is 133 ± 4 min).

3.3. THE SUMMING SPECTRA

The summing spectra taken in the 100—1600 keV and in the 600—3000 keV regions were followed over a period of 20 hours. The pulse height distribution obtained by subtraction of two spectra, taken at 4 hour intervals, were analysed. Comparison with the direct spectra allowed sum peaks to be identified at ener-

gies of 1.35, 1.44, 1.56, 1.65, 1.76, 1.96, 2.06, 2.28, 2.44, 2.68, and 2.79 MeV, which decayed with the correct half life. A level at 2.79 MeV must therefore exist, together with levels at 2.44 and 2.68 MeV.

Additional peaks were found at 1.86 and 2.1 MeV corresponding to gamma-ray transition energies, revealed in the direct spectra. It could not be deduced with complete certainty whether their intensities increased due to summing. The various summing peaks, together with their possible origin, are mentioned in column 4 of table 2.

4. Discussion

The foregoing results are summarized in an energy level diagram for ^{106}Pd, given in fig. 6. This decay scheme should be considered only as purely tentative,

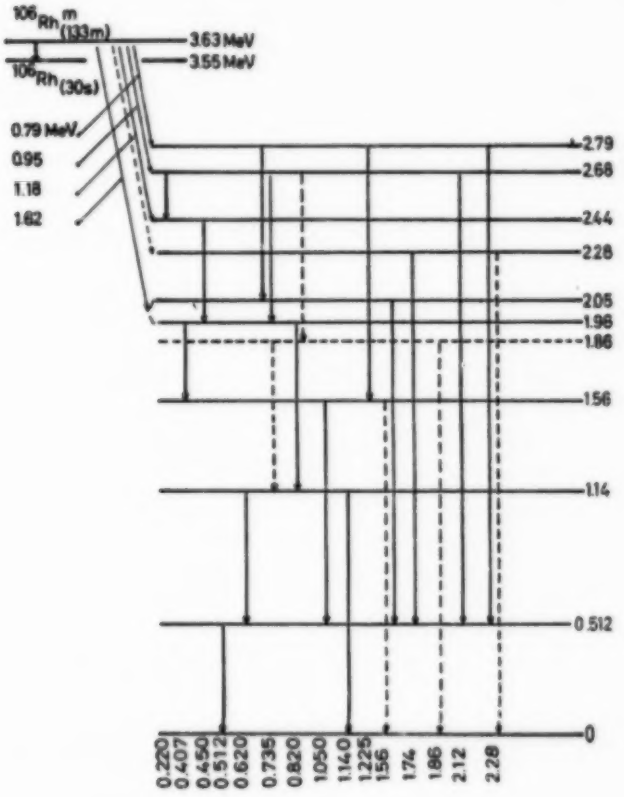

Fig. 6. Tentative decay scheme of $^{106}Rh^{m}$.

since it has not been possible to establish all the positions of the transitions by experiment. In order to fit the gamma-ray energies, levels at 512, 1140, 1560, (1860), 1960, 2050, 2280, 2440, 2680, and 2790 keV were accepted. The energy values of the beta transitions suggest the isomeric state to occur at 3.63 ± 0.03 MeV above the ^{106}Pd ground state. This is in agreement with the value of the total disintegration energy Q of about 3.6 MeV reported by G. Baró *et al.* [1]).

Since most of the beta transitions proceed to the highest energy states, and since $^{106}Rh^{m}$ appears not to disintegrate by gamma emission ($< 1\ \%$) [1]) to the 30 sec state of ^{106}Rh, the 90 ± 40 keV gamma transition should be at least E4 and/or M3, requiring $\Delta J \geqq 3$, without parity change. On the basis of energy matching the 1.62 MeV beta transition can proceed to the 2.05 MeV and/or to the 1.96 MeV level(s).

The branching ratio of cascade to cross over gamma rays from the second level is 2.35 ± 0.30. This agrees well with the value 2.3 ± 0.3 reported by R. L. Robinson *et al.* [5]), in the case of 8.3 d ^{106}Ag and ^{106}Rh. The first excited state must occur at 0.513 MeV since it explains the strongest gamma-ray following the decay of ^{106}Pd, in agreement with the observations in ^{106}Rh (30 sec) and ^{106}Ag. The summing measurements suggest levels at 1.14 MeV and 1.56 MeV, which are the origin of gamma transitions of 0.620 MeV, 1.14 MeV, 1.56, and 1.05 MeV. A spin of 2^+ can be assigned to the first state since its energy fits with the value found in the ^{106}Rh (30 sec) decay. A spin of 2^+ can also be assigned to the level at 1.14 MeV since it has been excited in Coulomb excitation experiments. The presence of a crossover transition to the ground state, (its energy being ≈ 2.2 times that of the first excited state) and the branching ratio of cascade to cross over, fit with the general trend for even mass nucleides in the medium weight range [5, 6, 7]).

Relative intensity considerations, energy matching and the results from the beta and the sum spectra support the existence of levels at 1.96 and 2.05 MeV. The existence of the 2.28 MeV level has been postulated in order to accommodate the 1.74 MeV transition, proceeding to the first excited state. The very low intensity of the 1.74 MeV gamma-ray suggests that a low intensity beta branch goes to this level.

A decay scheme can be constructed accepting the levels mentioned above. This possibility is illustrated with full lines. In this case the 0.735 MeV gamma-ray intensity is subdivided into approximately equal parts situated between the 2.79—2.05 MeV levels and the 2.68—1.96 MeV levels. In this case, the 1.86 MeV gamma-ray cannot be fitted. One can solve this difficulty by accepting a supplementary level at 1.86 MeV. This possibility is illustrated with dashed lines. In this case, the 0.735 MeV gamma-ray intensity has to be subdivided into equal parts respectively between the 2.79—2.05 MeV levels and the 1.86—1.14 MeV levels; the 0.820 MeV gamma-ray intensity should be subdivided into equal components between the 2.68—1.86 MeV levels and 1.96—1.14 MeV levels.

5. Conclusions

Levels in ^{106}Pd can be populated by the beta decay of four different nucleides: ^{106}Rh (30 sec, $J = 1^+$), $^{106}Rh^{m}$ (133 min, $J \geqq 4$), ^{106}Ag (24 min, $J = 1^+$) and ^{106}Ag (8.3 d, $J = 6$). As already pointed out (Nuclear Data sheets NRC 58-5-37)

there is a striking similarity between the gamma ray spectra from 8.3 d ^{106}Ag and from 133 min $^{106}Rh^{m}$. The energies of most of the gamma rays are the same, and both spectra show strong gamma transitions up to 1.56 MeV. This is in good agreement with the postulated high spin value of the two nucleides and it may suggest that the spin of $^{106}Rh^{m}$ is also 6.

The structure of the gamma-ray spectrum of 30 sec ^{106}Rh is completely different; strong gamma rays occur only up to energies of 620 keV. The relative intensities of the 1.14 and 0.62 MeV gamma transitions show that they probably originate at a single level in the case of $^{106}Rh^{m}$ and 8.3 d ^{106}Ag. In the decay of 30 sec ^{106}Rh, however, there must be an additional transition from the 0^+ level at 1.137 MeV as can be expected from the 1^+ spin assignment.

The authors wish to thank Prof. Dr. J. L. Verhaeghe and Prof. Dr. P. M. Endt for their interest in this work. One of the authors (O. J. S.) is indebted to Prof. Dr. P. C. Gugelot for extending to him the facilities of the "Instituut voor kernphysisch Onderzoek, Amsterdam", and to Dr. R. van Lieshout and Dr. H. van den Bold for valuable discussions. He would like to thank Mrs. A. Funke-Klopper for performing the many chemical separations, and the personnel of the synchro-cyclotron for the irradiations.

References

1) G. B. Baró, W. Seelmann-Eggebert and I. E. Zabala, Zeitschrift für Naturforschung **1** (1955) 80
2) W. E. Nervik and G. T. Seaborg, Phys. Rev. **97** (1955) 1092
3) S. Mayo and S. J. Nassiff, Publ. Comm. Nucl. Energia Atomica (Buenos Aires) Ser. Fis. **1** no. 12 (1957)
4) S. Mayo and S. J. Nassiff, Phys. Rev. **111** (1958) 1140
5) R. L. Robinson, F. K. McGowan and W. G. Smith, Bull. Am. Phys. Soc. **4** (1959) 279
6) K. Way, D. N. Kundu, C. L. McGinnis and R. van Lieshout, Ann. Rev. Nucl. Sc. **6** (1956) 129
7) F. K. McGowan and P. H. Stelson, Comptes Rendus du Congrès International de Physique Nucléaire, Paris (1958) 756

1.C

Nuclear Physics **16** (1960) 502—517; © *North-Holland Publishing Co., Amsterdam*

Not to be reproduced by photoprint or microfilm without written permission from the publisher

SUR LA FONCTION DE GREEN À UNE PARTICULE EN MÉCANIQUE STATISTIQUE QUANTIQUE

ROGER BALIAN et CYRANO DE DOMINICIS

Service de Physique Mathématique, Centre d'Études Nucléaires de Saclay, Gif-sur-Yvette (S & O)

Reçu le 30 novembre 1959

Abstract: Some analytical properties of the mass operator are examined in perturbation theory, and a simple form of the one particle Green's function for a grand canonical ensemble is obtained by analytical continuation. An approximation is then considered, which neglects terms where energy denominators are accidentally vanishing or equal. In this approximation, all quantities of interest can be diagrammatically built up like the corresponding ones for the ground state of a system of N particles; only the statistical factors for each state are no longer step functions in momentum space. The resulting expressions for "local" virial coefficients are examined, also the energy of the system fits in with the form Landau has assumed for his theory of Fermi liquids. In spite of difficulties arising from the use of a discrete spectrum of energies, this approximation is suggestive of what a more exact treatment could be.

1. Introduction

Divers auteurs[1–6]) ont considéré récemment l'utilisation du formalisme des fonctions de Green pour un ensemble grand canonique. Les valeurs moyennes des observables du système sont alors représentées paramétriquement en fonction de α et β (c'est-à-dire de l'activité chimique $z = e^{\alpha}$ et de la température $1/k\beta$). Il serait souhaitable, en particulier pour l'étude des transitions du système, de disposer d'une représentation plus directe — si elle existe — du type du développement du viriel, ou plus exactement en fonction d'une densité locale.

Dans ce but, nous examinons dans une première partie quelques propriétés analytiques de l'opérateur de masse, valables en théorie des perturbations, et nous en déduisons une représentation commode, en intégrale de Fourier, de la fonction de Green $G_k(it)$ prolongée sur l'échelle des vrais temps t (par opposition aux „temps" u mesurés sur l'échelle des températures, entre 0 et β). Cette représentation permet, contrairement à ce qui se passe pour $G_k(u)$ dans le calcul de valeurs moyennes, de se débarrasser des contributions des bornes (0, β). Elle rend donc plus facile une séparation entre ce qui doit dépendre de α, β (statistique) et ce qui n'en dépend pas (dynamique). Etant obtenue par prolongement analytique de $G_k(u)$, elle garde certains des avantages de $G_k(u)$ en ce qui concerne la simplicité de l'opérateur de masse et sa relation à la fonction de Green.

La deuxième partie se place dans le cadre d'une certaine approximation. Dans un développement en perturbation, les sources de difficultés et de complications résident dans l'existence de dénominateurs d'énergie nuls ou égaux entre eux. Il y a d'abord les dénominateurs que nous appellerons identiquement nuls ou égaux parce qu'ils le sont en vertu de la conservation de l'impulsion. Les dénominateurs peuvent ensuite devenir accidentellement nuls ou égaux lorsqu'on fait varier de toutes les façons possibles les diverses impulsions indépendantes. Cette annulation ou égalité accidentelle de dénominateurs d'énergie est en général loin d'être négligeable, puisqu'elle est tenue pour responsable du phénomène de Cooper[7]) pour les fermions. Nous ferons néanmoins, dans cette deuxième partie, l'approximation qui consiste à laisser de côté des contributions de ce genre, et qui implique l'emploi d'un spectre discret d'énergies d'excitation. Nous verrons dans la discussion (au dernier paragraphe) comment l'utilisation de ce spectre discret restreint la portée des résultats. Les regroupements que l'on est amené à faire sont cependant indicatifs de ce qui pourrait être fait en dehors de cette approximation. En particulier, la représentation diagrammatique qui s'introduit alors pour un ensemble grand canonique devient la même que celle qui correspond à un système de N particules dans son état fondamental.

Dans cette approximation, le logarithme de la grande fonction de partition $\log Z$ et l'énergie moyenne $\bar{E}$ du système deviennent des fonctionnelles d'une densité „locale" (dans l'espace des impulsions $\mathbf{k}$, normées à $\hbar=1$) $n(k)$, *qui contient toute la dépendance en* α *et* β. La densité moyenne du système est la moyenne de la densité „locale". Les coefficients des puissances de n dans $\log Z$ fournissent, dans ce cas, un analogue quantique particulièrement simple des coefficients locaux du viriel de J. Yvon[8]). Enfin, la dérivée fonctionnelle de l'énergie moyenne $\bar{E}$ par rapport à $n(k)$ s'interprète comme une énergie de quasi-particule, $n(k)$ s'identifiant à la fonction de Fermi des quasi-particules libres. Ces derniers résultats coïncident avec l'hypothèse faite par Landau [9]) dans sa théorie des liquides de Fermi.

PREMIÈRE PARTIE

PROPRIÉTÉS DE LA FONCTION DE GREEN ET DE L'OPÉRATEUR DE MASSE

1. Représentation du propagateur en série de Fourier

Considérons le propagateur

$$G_k(u-v) = \frac{\mathrm{Tr}\,\{\mathrm{T}e^{-\beta H+\alpha N}\hat{\eta}_k(u)\hat{\eta}_k^+(v)\}}{\mathrm{Tr}\,e^{-\beta H+\alpha N}}, \tag{1.1}$$

où T désigne le T-produit, où $0 < u < \beta$, $0 < v < \beta$, et

$$\hat{\eta}_k(u) = e^{uH}\eta_k e^{-uH},$$
$$\hat{\eta}_k^+(v) = e^{vH}\eta_k^+ e^{-vH}.$$

Il s'exprime en théorie des perturbations comme la somme des contributions des diagrammes connexes ouverts, partant de v et arrivant à u, les „temps" de chaque interaction étant compris entre 0 et β. Le contribution de chaque diagramme se calcule suivant des règles qui ont été énoncées en détail à propos du développement du potential de Gibbs (B.D. § 4)†.

La fonction G_k possède une représentation simple en série de Fourier[1-6]). Pour des fermions,

$$G_k(\omega) = \int_{-0}^{\beta} du\, e^{\omega u} G_k(u),$$
$$G_k(u) = \frac{1}{\beta} \sum_{\omega} e^{-\omega u} G_k(\omega) \qquad \left(\omega = (2n+1)\frac{i\pi}{\beta} + \frac{\alpha}{\beta}\right). \tag{1.2}$$

Dans cette représentation, le propagateur libre s'écrit

$$G_k^{(0)}(\omega) = \frac{1}{\varepsilon_k - \omega} \tag{1.3}$$

(où ε_k est l'énergie de l'état d'impulsion $\mathbf{k}$), et le propagateur complet prend la forme

$$G_k(\omega) = \frac{1}{\varepsilon_k - \omega - \Sigma_k^*(\omega)}; \tag{1.4}$$

$\Sigma_k^*(\omega)$ est la représentation en série de Fourier de l'opérateur de masse, qui s'exprime en théorie des perturbations comme la somme des contributions de tous les diagrammes propres. L'équation (1.4) traduit le fait que G_k s'exprime en théorie des perturbations comme l'itération de Σ_k^*:

$$G_k(u-v) = G_k^{(0)}(u-v) + \int_0^{\beta} du_1 \int_0^{\beta} dv_1\, G_k^{(0)}(u-v_1)\Sigma_k^*(v_1-u_1)G_k(u_1-v).$$

2. L'opérateur de masse

Nous allons examiner quelques propriétés de l'opérateur de masse en analysant une contribution typique. Soit un diagramme d'ordre p contribuant à $\Sigma_k^*(u-v)$ pour $u > v$, et comprenant $q-1$ interactions à l'extérieur de l'intervalle (v, u) et $p-q-1$ interactions à l'intérieur (fig. 1). Considérons la famille des q diagrammes obtenus en laissant u et v fixes, et en faisant tourner sur le cercle des „temps" (B.D., fig. 2) les interactions extérieures à l'intervalle (v, u) (fig. 1). Par suite de l'invariance cyclique (B.D. § 5), la

† Nous désignerons dans la suite la référence [10]) par B.D.

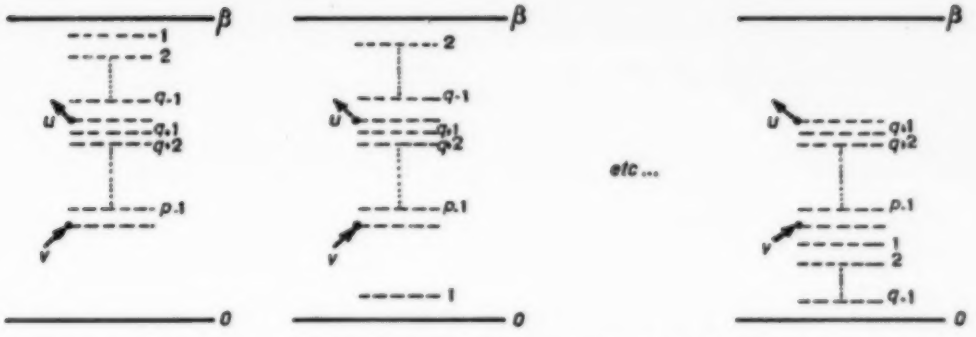

Fig. 1. Une famille de diagrammes contribuant à $\Sigma_k^*(u-v)$, déduits les uns de autres par „rotation" sur le cercle des temps, u et v restant fixes.

somme de leurs contributions ne dépend que de la différence $u-v$, et est égale à celle d'un diagramme unique dont l'entrée serait à l'origine des „temps" (fig. 2).

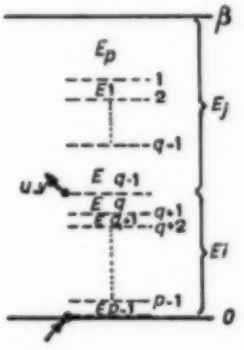

Fig. 2. Le diagramme dont la contribution est égale à celle de la famille représentée fig. 1.

L'invariance cyclique entraîne également

$$\Sigma_k^*(x-\beta)=-e^{\alpha}\Sigma_k^*(x) \qquad (\text{pour } \beta > x > 0),$$

relation sur laquelle repose l'existence de la transformée en série de Fourier $\Sigma_k^*(\omega)$.

La contribution correspondante à $\Sigma_k^*(\omega)$ peut se calculer à partir du diagramme de la fig. 2 où $E_1, E_2, \ldots E_p$ désignent les énergies entre les interactions, E_i les énergies intérieures et E_j les énergies extérieures à l'intervalle $(0, u-v)$ $(i=q, \ldots, p-1$; et $j=p, 1, 2, \ldots q-1)$. L'intégration sur les „temps" donne alors

$$\sum_{ij} \frac{-e^{-\beta(E_j-E_p)}}{\prod_{i'\neq i}\prod_{j'\neq j}(E_{i'}-E_i)(E_{j'}-E_j)} \frac{1-e^{\beta(\omega-E_i+E_j)}}{\omega-E_i+E_j}, \tag{1.5}$$

ou, en remplaçant $e^{\beta\omega}$ par $-e^{\alpha}$, puisque $\omega=(2n+1)(i\pi/\beta)+(\alpha/\beta)$,

$$\sum_j \frac{e^{-\beta(E_j-E_p)}}{\prod_{j'\neq j}(E_{j'}-E_j)\prod_i(E_i-\omega-E_j)} + \sum_i \frac{-e^{\alpha-\beta(E_i-E_p)}}{\prod_{i'\neq i}(E_{i'}-E_i)\prod_j(E_j+\omega-E_i)}, \quad (1.6)$$

c'est-à-dire

$$\sum_{ij} \frac{-e^{-\beta(E_j-E_p)}}{\prod_{i'\neq i}\prod_{j'\neq j}(E_{i'}-E_i)(E_{j'}-E_j)} \left\{\frac{1}{\omega-E_i+E_j} + \frac{e^{\alpha-\beta(E_i-E_j)}}{\omega-E_i+E_j}\right\}. \quad (1.7)$$

L'expression (1.6) s'interprète en diagrammes de la façon habituelle dans la représentation indépendante du temps:

a) à chaque terme de $\sum_j$ correspond un diagramme du type de la fig. 1. Le dénominateur est le produit des énergies d'excitation lues sur le diagramme que l'on aurait fictivement refermé sur lui-même, ε_k étant remplacé par ω. Le facteur $\exp\{-\beta(E_j-E_p)\}$, associé aux facteurs statistiques du diagramme original (fig. 2) rétablit les facteurs statistiques lus sur le diagramme considéré (B.D. § 5);

b) à chaque terme de $\sum_i$ correspond de même un diagramme déduit de la fig. 2 par une rotation sur le cercle des „temps" telle que l'entrée soit au-dessus de la sortie.

Nous écrirons $\Sigma_k^*(\omega) = \sigma_k^+(\omega)+\sigma_k^-(\omega)$, où $\sigma_k^+(\omega)$ et $\sigma_k^-(\omega)$ désignent la somme des contributions des types (a) et (b) respectivement. On remarquera que chacun des deux termes de (1.6) conserve un sens si un certain nombre d'énergies sont égales entre elles†.

Jusqu'ici, $\Sigma_k^*(\omega)$ n'a été considéré que pour les valeurs $\omega = (2n+1)(i\pi/\beta)+(\alpha/\beta)$. Le prolongement dans le plan complexe de la variable ω comporte un arbitraire. Par exemple, (1.5) définit $\Sigma_k^*(\omega)$ comme une somme de fonctions entières, se comportant à l'infini comme $e^{\beta\omega}$. Par contre (1.6) ou (1.7) définit $\Sigma_k^*(\omega)$, $\sigma_k^+(\omega)$ et $\sigma_k^-(\omega)$ comme une somme de fonctions nulles à l'infini, holomorphes dans le demi-plan supérieur et le demi-plan inférieur. Avec ce dernier choix, que nous conserverons par la suite, on a, pour ω infiniment voisin de l'axe réel,

$$\operatorname{Im}\sigma_k^+(\omega) = \operatorname{Im} e^{-\alpha+\beta\omega}\sigma_k^-(\omega) = \operatorname{Im}\frac{1}{1+e^{\alpha-\beta\omega}}\Sigma_k^*(\omega). \quad (1.8)$$

3. Représentation du propagateur par une intégrale de contour

On peut remplacer une série de Fourier par une intégrale de contour[4,6] lorsque $F(\omega)$ est une fonction analytique:

† La fonction $\Sigma_k^*(\omega)$ contient de plus un terme réel, indépendant de ω, σ_k^0, représenté par l'ensemble des diagrammes dont le temps d'entrée et le temps de sortie sont confondus (par exemple celui du premier ordre dans l'interaction). Pour soulager l'écriture, nous avons laissé ce terme de côté, ce qui ne modifie pas les résultats.

$$\frac{1}{\beta}\sum_{\omega} F(\omega) = \frac{1}{2\pi i}\int_C d\omega \frac{F(\omega)}{1+e^{-\alpha+\beta\omega}} = -\frac{1}{2\pi i}\int_C d\omega \frac{F(\omega)}{1+e^{\alpha-\beta\omega}}. \quad (1.9)$$

Le contour C est donné par la fig. 3; il n'entoure aucune singularité de $F(\omega)$.

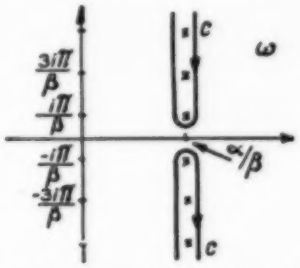

Fig. 3. Le contour C, correspondant a $G_k(u)$ pour $-\beta < u < \beta$.

Dans le cas du propagateur,

$$G_k(u) = -\frac{1}{2\pi i}\int_C d\omega \frac{f^+(\omega)e^{-\omega u}}{\varepsilon_k-\omega-\Sigma_k^*(\omega)} \quad (1.10)$$

$$= \frac{1}{2\pi i}\int_C d\omega \frac{f^-(\omega)e^{-\omega u}}{\varepsilon_k-\omega-\Sigma_k^*(\omega)}, \quad (1.11)$$

où on a posé

$$f^{\pm}(\omega) = \frac{1}{1+e^{\pm(\alpha-\beta\omega)}}.$$

On peut utiliser les propriétés analytiques des divers termes du développement de $\Sigma_k^*(\omega)$ en perturbation (absence de singularité hors de l'axe réel, caractère borné à l'infini) pour déformer le contour C en le contour C' de la figure 4. Cette opération peut s'effectuer sur la forme (1.10) lorsque $0 < u < \beta$,

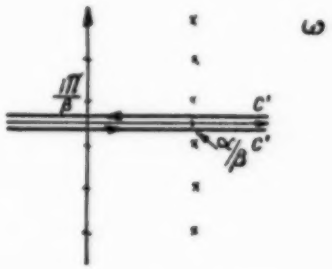

Fig. 4. Le contour C', permettant le prolongement analytique de $G_k(u)$.

ou (1.11) lorsque $-\beta < u < 0$, conduisant à

$$-\frac{1}{2\pi i}\int_{C'} d\omega \frac{f^+(\omega)e^{-\omega u}}{\varepsilon_k-\omega-\Sigma_k^*(\omega)} \quad (0 < u < \beta) \quad (1.12)$$

et à

$$\frac{1}{2\pi i}\int_{C'} d\omega \, \frac{f^-(\omega)e^{-\omega u}}{\varepsilon_k-\omega-\Sigma_k^*(\omega)} \quad (-\beta < u < 0). \quad (1.13)$$

La forme (1,12) permet de prolonger analytiquement $G_k(u)$ dans le plan complexe de la variable u lorsque $0 < \mathrm{Re}\, u < \beta$, en particulier pour $G_k(it)$ et $t > 0$. De même la forme (1.13) permet de définir $G_k(it)$ pour $t < 0$, par prolongement analytique à travers le troisième quadrant.

On peut alors rassembler (1.12) et (1.13) sous forme d'une intégrale de Fourier, valable pour $t \gtrless 0$:

$$G_k(it) = \frac{1}{2\pi i}\int_{-\infty}^{+\infty} d\omega \, e^{-i\omega t}\left[\frac{f^+(\omega)}{\varepsilon_k-\omega-i\varepsilon-\Sigma_k^*(\omega+i\varepsilon)} + \frac{f^-(\omega)}{\varepsilon_k-\omega+i\varepsilon-\Sigma_k^*(\omega-i\varepsilon)}\right]. \quad (1.14)$$

On notera qu'avec les conventions adoptées $G_k(it)$ est aussi donné par (1.1), où maintenant le T-produit porte sur de vrais temps.

La méthode indiquée au début de ce paragraphe pour calculer $G_k(it)$ est la même que celle des références[4,6]). Les résultats obtenus sont cependant différents, car nous sommes partis de la forme (1.4) pour $G_k(\omega)$ que nous avons prolongée grâce aux propriétés analytiques de Σ_k^* établies en théorie des perturbations, au lieu d'utiliser une représentation spectrale.

On pourrait formellement effectuer le même calcul dans le cas de bosons. La seule différence proviendrait alors de ce que, dans le spectre des valeurs de $\omega = 2n(i\pi/\beta) + (\alpha/\beta)$, figure une valeur réelle $\omega = \alpha/\beta$ que l'on doit isoler avant de faire la transformation (1.9). Un tel résultat n'est toutefois pas susceptible d'applications aussi immédiates que pour les fermions, en raison de phénomènes de condensation propres aux bosons.

DEUXIÈME PARTIE

L'APPROXIMATION DES DÉNOMINATEURS NON ACCIDENTELLEMENT ÉGAUX

1. Une fonction de Green modèle

Nous considérons maintenant la fonction

$$\mathcal{G}_k(t) = \frac{1}{2\pi i}\int_{-\infty}^{+\infty} d\omega \, e^{-i\omega t}\left[\frac{F_k^+}{\varepsilon_k-\omega-i\varepsilon-S_k(\omega)} + \frac{F_k^-}{\varepsilon_k-\omega+i\varepsilon-S_k(\omega)}\right], \quad (2.1)$$

où

$$S_k(\omega) = \sigma_k^+(\omega+i\varepsilon) + \sigma_k^-(\omega-i\varepsilon), \quad (2.2)$$

et où les F_k^+ sont des quantités indépendantes de ω, telles que $F_k^+ + F_k^- = 1$.

Cette fonction de Green modèle s'interprète aisément en diagrammes.

Si on se place dans la représentation dépendant du temps ($-\infty < t < +\infty$), la transformée $\sigma_k^+(t)$ en intégrale de Fourier de $\sigma_k^+(\omega+i\varepsilon)$ est nulle pour $t<0$, et s'interprète comme l'ensemble des diagrammes propres pour $t > 0$ ($\sigma^+(\omega)$ est en effet une somme de fonctions holomorphes dans le demi-plan supérieur et bornées à l'infini). De même $\sigma_k^-(t)$ est nulle pour $t > 0$ et correspond aux diagrammes propres pour $t < 0$. Il en résulte que dans chacun des diagrammes qui contribuent à $\mathcal{G}_k(t)$ les lignes k sont toujours de même sens. A un ensemble de lignes k toutes montantes, correspond un seul facteur F_k^+; de même à un ensemble de lignes k toutes descendantes correspond un seul facteur F_k^-. Ces diagrammes sont les mêmes que ceux qui s'introduisent dans les problèmes relatifs au calcul de l'énergie de l'état fondamental; $F_k^\pm$ est alors remplacé par 1 si $k \gtrless k_F$ et 0 si $k \lessgtr k_F$ (k_F est l'impulsion de Fermi).

2. Calcul du propagateur dans l'approximation des dénominateurs non accidentellement égaux

Nous allons comparer les expressions de $G_k(it)$ et $\mathcal{G}_k(t)$ dans l'approximation suivante: nous développons d'abord en puissances de Σ_k^* et S_k, et nous exprimons σ_k^+ et σ_k^- à l'aide de l'équation (1.7) ou des équations analogues qui s'introduisent lorsque diverses énergies d'excitation sont identiquement égales. Nous supposons alors le spectre des énergies d'excitation discret, et nous négligeons chacune des contributions qui proviennent d'une égalité accidentelle de ces énergies. (Dans l'interprétation en diagrammes de $\mathcal{G}_k(t)$, cela revient à négliger chacune des contributions de diagrammes ayant des dénominateurs accidentellement égaux ou nuls).

L'expression (1,7) de $\sigma_k^+(\omega)+\sigma_k^-(\omega)=\Sigma_k^*(\omega)$ est, lorsqu'il n'y a pas d'énergies d'excitation accidentellement ni identiquement égales, de la forme

$$\sigma_k^\pm(\omega) = \int \mathrm{d}\mathscr{E}\, \frac{\varphi_k^\pm(\mathscr{E})}{\omega-\mathscr{E}}\,. \tag{2.3}$$

S'il y a des dénominateurs identiquement égaux, l'expression (1.7) contient des termes de la forme

$$\int \mathrm{d}\mathscr{E}\, \frac{\varphi_k(\mathscr{E})}{(\omega-\mathscr{E})^a}$$

qu'il est facile, par intégration par parties, de remettre sous la forme (2.3) (les contributions des bornes sont nulles).

D'après nos hypothèses, et en négligeant les dénominateurs accidentellement égaux, nous prendrons

$$\sigma_k^\pm(\omega) = \sum_m \frac{\varphi_k^\pm(\mathscr{E}_m)}{\omega-\mathscr{E}_m}\,. \tag{2.4}$$

Pour $t > 0$, l'intégration sur ω donne immédiatement

$$G_k(it) = \sum_{n=0}^{\infty} \left\{ \frac{(-)^n}{n!} \frac{\partial^n}{\partial \varepsilon_k{}^n} [f^+(\varepsilon_k) e^{-i\varepsilon_k t} [\Sigma_k{}^*(\varepsilon_k)]^n] \right.$$
$$\left. + (-)^n n \sum_m e^{-i\mathscr{E}_m t} \frac{\varphi_k{}^+(\mathscr{E}_m)}{(\mathscr{E}_m - \varepsilon_k)^{n+1}} [\Sigma_k{}^*(\mathscr{E}_m)']^{n-1} \right\}, \tag{2.5}$$

$$\mathscr{G}_k(t) = \sum_{n=0}^{\infty} \left\{ \frac{(-)^n}{n!} F_k{}^+ \frac{\partial^n}{\partial \varepsilon_k{}^n} [e^{-i\varepsilon_k t} [S_k(\varepsilon_k)]^n] \right.$$
$$\left. + (-)^n n \sum_m e^{-i\mathscr{E}_m t} \frac{\varphi_k{}^+(\mathscr{E}_m)}{(\mathscr{E}_m - \varepsilon_k)^{n+1}} [S_k(\mathscr{E}_m)']^{n-1} \right\}. \tag{2.6}$$

Dans (2.5) nous avons utilisé la relation

$$f^+(\omega)[\varphi_k{}^+(\omega) + \varphi_k{}^-(\omega)] = \varphi_k{}^+(\omega),$$

conséquence de (1.8). L'approximation que nous avons faite a permis d'une part d'évaluer l'intégrale (1.14) ou (2.1) comme une somme de résidus par rapport aux pôles ε_k et $\mathscr{E}_m$, d'autre part de négliger les pôles $\mathscr{E}_m$ accidentellement multiples dans le produit $(\Sigma_k{}^*(\omega))^n$ ou $(S_k(\omega))^n$, de sorte que les derniers termes de (2.5) ou (2.6) s'écrivent en fonction de $\Sigma_k{}^*(\mathscr{E}_m)'$ ou $S_k(\mathscr{E}_m)'$, sommes de termes de la forme $1/(\mathscr{E}_m - \mathscr{E}_{m'})$ où $\mathscr{E}_{m'} \neq \mathscr{E}_m$. Enfin, dans l'approximation considérée, ε_k n'est pas un pôle de $\sigma_k{}^{\pm}(\omega)$ et on a les égalités entre quantités réelles $\Sigma_k{}^*(\varepsilon_k) = S_k(\varepsilon_k)$ et $\Sigma_k{}^*(\mathscr{E}_m)' = S_k(\mathscr{E}_m)'$. Les termes en $\exp[-i\mathscr{E}_m t]$ de (2.5) et (2.6) s'identifient alors immédiatement. Les termes en $\exp[-i\varepsilon_k t]$ se réarrangent en vertu de la formule suivante, qui dérive de celle de Lagrange:

$$\int d\omega\, F(\omega) \sum_{n=0}^{\infty} \frac{(-)^n}{n!} \delta^{(n)}(\omega - \varepsilon_k) [\Sigma_k{}^*(\omega)]^n = \left. \frac{F(\omega_0)}{1 + \dfrac{\partial \Sigma_k{}^*(\omega_0)}{\partial \omega_0}} \right|_{\omega_0 = \varepsilon_k + \Sigma_k{}^*(\omega_0)} \tag{2.7}$$

et que l'on peut appliquer successivement pour $F(\omega) = f^+(\omega) e^{-i\omega t}$ et $F(\omega) = F_k{}^+ e^{-i\omega t}$.

Les termes en $e^{-i\varepsilon_k t}$ de (2.5) et (2.6) s'identifient donc, avec le choix

$$F_k{}^+ = \frac{1}{1 + e^{\alpha - \beta(\varepsilon_k + W_k)}}, \tag{2.8}$$

où W_k est tel que

$$W_k = -\Sigma_k{}^*(\varepsilon_k + W_k) = -S_k(\varepsilon_k + W_k). \tag{2.9}$$

L'équation (2,9) se résoud par la formule de Lagrange [11]:

$$W_k = \sum_{n=1}^{\infty} \frac{(-)^n}{n!} \frac{\partial^{n-1}}{\partial \varepsilon_k^{n-1}} [S_k(\varepsilon_k)]^n, \tag{2.10}$$

ce qui s'écrit encore, dans le cadre de notre approximation,

$$W_k = \sum_{n=1}^{\infty} - \frac{1}{2\pi i n} \int_{-\infty}^{+\infty} d\omega \left\{ \left[\frac{S_k(\omega)}{\varepsilon_k - \omega - i\varepsilon} \right]^n - \left[\frac{S_k(\omega)}{\varepsilon_k - \omega + i\varepsilon} \right]^n \right\}. \qquad (2,11)$$

La formule (2,11) montre que W_k s'interprète en diagrammes vide-vide analogues à ceux que donnent Hugenholtz et Van Hove[12]) pour l'énergie de Fermi relative à l'état fondamental d'un système.

Un résultat analogue pour $t < 0$ permet de même l'identification de $G_k(it)$ et $\mathcal{G}_k(t)$ pour $t < 0$.

Il en résulte que, dans l'approximation où l'on considère comme négligeable chacune des contributions à dénominateurs accidentellement nuls ou égaux, on peut écrire la fonction de Green sous une forme compacte (2,1) dont la représentation en diagrammes diffère de la représentation habituelle (pour un ensemble grand canonique) sur trois points:

a) dans chaque diagramme, seules existent des lignes toujours montantes ou toujours descendantes pour un état donné: par exemple il n'y a plus de diagrammes du type de la fig. 5 dans la représentation de log Z;

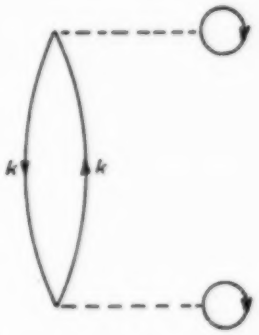

Fig. 5. Un diagramme contribuant à log Z dans la formulation B.D., n'y contribuant plus dans la nouvelle formulation, puisque le même état k figure dans une ligne montante et une ligne descendante.

b) pour chaque état, il y a un seul facteur de Fermi $F_k^{\pm}$, même si cet état apparaît plusieurs fois comme dans la fig. 6;

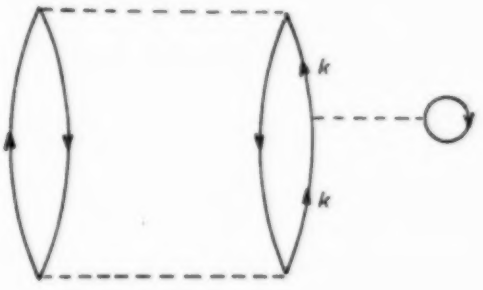

Fig. 6. Un diagramme avec une ligne k montante répétée: on n'introduit qu'un facteur F_k^+.

c) les facteurs de Fermi $F_k^{\pm}$ sont alors donnés par (2.8) et (2.11), dont nous avons donné l'interprétation en diagrammes.

Ces règles présentent une analogie étroite avec celles concernant les diagrammes relatifs à un système de N particules dans son état fondamental.

3. Expression du nombre moyen de particules et de la densité „locale"

Le nombre moyen de particules du système grand canonique est donné par

$$\bar{N} = -\sum_k G_k(-0) = -\sum_k \mathcal{G}_k(-0).$$

Le seul diagramme qui donne une contribution non nulle est celui d'ordre zéro en S_k. En effet, tous les autres diagrammes s'annulent deux à deux, de la même façon que les diagrammes analogues qui interviennent dans le calcul de

$$N = -\sum_k G_k^{\mathrm{F}}(-0) = -\sum_k G_k^{(0)\mathrm{F}}(-0) = \sum_{k<k_F} 1,$$

pour l'état fondamental du système.

On peut donc interpréter F_k^-, que nous noterons désormais $n(k)$, comme une densité „locale" dans l'espace des impulsions, c'est-à-dire comme le nombre de particules moyen dont l'impulsion est $\mathbf{k}$, puisque

$$\bar{N} = \sum_k n(k). \tag{2.12}$$

Considérons maintenant l'ensemble des diagrammes fermés vide-vide, connexes, construits avec les règles ci-dessus. Si nous remplaçons F_k^- par $n(k)$ et F_k^+ par $1-n(k)$, et si nous sommons sur tous les états, nous obtenons une quantité

$$\mathcal{F}\{n\} = \sum_{p=2}^{\infty}\Big[\sum_{k_1 k_2 \cdots k_p} A_p(k_1, k_2, \ldots k_p) n(k_1) n(k_2) \ldots n(k_p)\Big], \tag{2.13}$$

fonctionnelle de n, *où les* A_p *sont indépendants de* α *et* β.

L'interprétation en diagrammes de W_k se traduit par

$$W_k = \frac{\delta}{\delta n(k)} \mathcal{F}\{n\}, \tag{2.14}$$

soit

$$W_k = \sum_{p=1}^{\infty}\Big[\sum_{k_1 k_2 \cdots k_p} B_p(k, k_1, k_2, \ldots k_p) n(k_1) n(k_2) \ldots n(k_p)\Big] \tag{2.15}$$

où B_p s'obtient en fixant successivement à k chaque impulsion dans A_{p+1}, et où

$$n(k) = \frac{1}{1+\mathrm{e}^{-\alpha+\beta(\varepsilon_k+W_k)}}. \tag{2.16}$$

4. Expression de la Grande Fonction de Partition Z

On obtient $\log Z$ par intégration sur $z=e^{\alpha}$ de l'expression (2,12) et (2,16) de $\bar{N}$, soit

$$\log Z = \sum_k \int_0^z \frac{dz}{z} \frac{z e^{-\beta(\varepsilon_k+W_k)}}{1+z e^{-\beta(\varepsilon_k+W_k)}}$$

$$= \sum_k \left[-\log [1-n(k)] + \beta W_k n(k) - \beta \int_0^z dz\, W_k \frac{\partial n(k)}{\partial z} \right].$$

Puisque

$$\sum_k \int_0^z dz\, W_k \frac{\partial n(k)}{\partial z} = \mathscr{F}\{n\} = \sum_k \int W_k \delta n(k),$$

ceci peut encore s'écrire

$$\log Z = -\sum_k [\log [1-n(k)] - \beta W_k n(k)] - \beta \mathscr{F}\{n\} \tag{2.17}$$

$$= -\sum_k \log [1-n(k)] - \beta \sum_{p=1} \frac{p}{p+1} \sum_{k k_1 \cdots k_p} B_p(k, k_1, \ldots k_p) n(k) n(k_1) \ldots n(k_p). \tag{2.18}$$

La forme (2.17) rappelle l'expression B.D. (41).

Sur la forme (2.18), on lit directement un analogue quantique des $\beta_p(x x_1 \ldots x_p)$ classiques introduits par J. Yvon[8]). On notera cependant que les B_p sont indépendants de la température, contrairement aux β_p; toute la dépendance en β est passée dans les densités „locales".

L'expression $\mathscr{F}\{n\}$, en tant que fonctionelle de n, et par suite les B_p, s'interprètent facilement, puisqu'il suffit de remplacer dans les diagrammes vide-vide connexes, représentant $\mathscr{F}$, chaque ligne montante k par $1-n(k)$, chaque ligne descendante k' par $n(k')$, et de regrouper les termes en n^{p+1}. Dans l'exemple simple de la fig. 7, cette opération se traduit en „ouvrant" les lignes; on

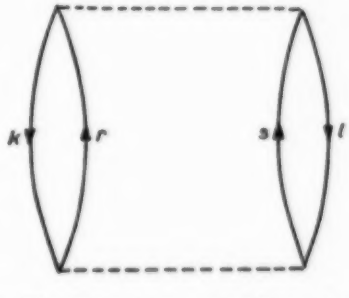

Fig. 7. Un diagramme contribuant a $\mathscr{F}\{n\}$.

passe ainsi aux diagrammes de la fig. 8 tracés sur un cylindre, où les états des lignes coupant la génératrice origine portent le poids n, les autres le poids 1,

et où les dénominateurs sont égaux à la différence entre l'énergie entre les interactions et l'énergie sur la génératrice origine. Le diagramme (8a) contribue à B_1, (8b) et (8c) à B_2 et (8d) à B_3. Il existe donc, à cause de la statistique,

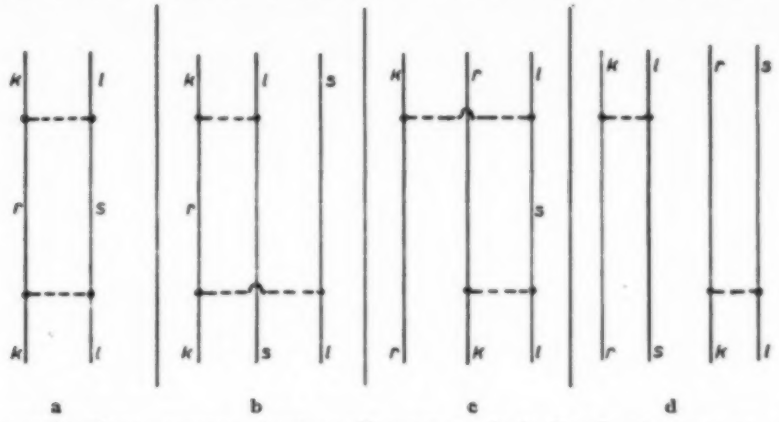

Fig. 8. Les contributions correspondant au diagramme de la fig. 7, obtenues en „ouvrant" les lignes: a contribue à B_1 (ou A_2), b et c à B_2 (ou A_3), d à B_3 (ou A_4).

une contribution à B_2 du deuxième ordre dans l'interaction, alors que classiquement, le diagramme correspondant $\prec$ est réductible et ne contribue pas à β_2 [13]).

On pourrait donner une règle générale pour une construction directe des diagrammes „ouverts" contribuant à chaque A_{p+1} ou B_p; en fait, il est plus simple de prendre tous les diagrammes vide-vide connexes et de les „ouvrir" en prenant soin, lorsqu'il y a pour un état donné des lignes montantes répétées, de n'en ouvrir aucune ou de les ouvrir toutes. Plusieurs lignes correspondant au même état peuvent alors couper la génératrice origine; on doit leur affecter un seul facteur n.

5. Expression de l'énergie moyenne $\bar{E}$

Il suffit d'écrire

$$\bar{E} = -\frac{\partial}{\partial\beta}\log Z$$

$$= \sum_k \left[\varepsilon_k + W_k + \beta\frac{\partial W_k}{\partial\beta}\right] n(k) - \left[\sum_k W_k n(k) - \mathscr{F}\{n\}\right] - \beta\frac{\partial}{\partial\beta}\left[\sum_k W_k n(k) - \mathscr{F}\{n\}\right].$$

Or on a

$$\sum_{k k_1 \cdots k_p} B_p(k, k_1, \ldots k_p) n(k_1) \ldots n(k_p) \frac{\partial n(k)}{\partial\beta}$$

$$= \frac{1}{p+1} \sum_{k k_1 \cdots k_p} B_p(k, k_1, \ldots k_p) \frac{\partial}{\partial\beta}\left[n(k) n(k_1) \ldots n(k_p)\right]$$

$$= \frac{\partial}{\partial\beta} \sum_{k k_1 \cdots k_p} A_{p+1}(k, k_1, \ldots k_p) n(k) n(k_1) \ldots n(k_p),$$

c'est-à-dire

$$\sum_k W_k \frac{\partial n(k)}{\partial \beta} = \frac{\partial}{\partial \beta} \mathscr{F}\{n\},$$

d'où on tire pour l'énergie moyenne

$$\bar{E} = \sum_k \varepsilon_k n(k) + \mathscr{F}\{n\} \tag{2.19}$$

$$= \sum_k \varepsilon_k n(k) + \sum_k \int W_k \delta n(k). \tag{2.20}$$

La formule (2.19) est l'analogue de l'expression de Goldstone[14, 15, 16]) pour l'énergie de l'état fondamental d'un système. La formule (2.20) conduit par dérivation fonctionelle à

$$\frac{\delta \bar{E}}{\delta n(k)} = \varepsilon_k + W_k. \tag{2.21}$$

Cette équation coïncide avec l'hypothèse de Landau[9]) pour les liquides de Fermi; on peut interpréter $\varepsilon_k + W_k$ comme une énergie de quasi-particule ne dépendant de α et β que par l'intermédiaire de n; $n(k)$ a la forme du facteur de Fermi pour une quasi-particle d'impulsion k.

6. Discussion

L'approximation qui a conduit aux résultats du paragraphe précédent, et qui consiste à négliger les contributions des diagrammes dont les énergies intermédiaires sont accidentellement nulles ou égales, manque évidemment de réalisme. On a dû substituer dans la démonstration du paragraphe II, 2, un spectre discret $\mathscr{E}_m$ au spectre continu des énergies d'excitation $\mathscr{E}$. L'équation (2.7), qui permet de démontrer que $G_k(it) = \mathscr{G}_k(t)$, et la série de Lagrange (2.10) qui définit W_k ont alors un rayon de convergence de l'ordre de la distance des $\mathscr{E}_m$. Elles conduisent, en toute rigueur, parmi l'infinité des racines de l'équation (2,9) (infinité due à la nature discrète du spectre), à la racine la plus proche de ε_k. Ceci restreint donc la portée des résultats établis: leur valeur reste seulement indicative tant qu'un retour du spectre discret au continu ne peut être effectué.

On remarquera cependant que, si on se place dans l'approximation considérée, la contribution au second coefficient du viriel B_1 (diagrammes en échelle) prend une forme non triviale qui reconstitue[17]) le résultat exact (déphasages). Il n'en serait pas de même si l'on avait essayé de faire — de façon moins cohérente — une approximation minimum pour passer de (1.14) à (2.5). D'une manière tout à fait générale, les expressions que l'on a à sommer sur les différents états d'impulsion ne présentent, avant regroupement, aucune

singularité pour des énergies d'excitation devenant égales ou nulles. Nous avons vu par exemple au § I, 2 que c'est le cas pour l'opérateur de masse. On pourrait donc séparer, a priori, tous les termes qui comportent des dénominateurs accidentellement égaux ou nuls; ces termes ne contribuent qu'à un ordre plus bas dans le volume Ω puisqu'il n'y a pas de singularités au départ. *Négliger systématiquement tous les termes à dénominateurs d'énergie accidentellement nuls ou égaux, conduirait donc au résultat asymptotiquement exact (en $1/\Omega$).* En fait, nous avons, dans des termes qui pris ensemble se comportaient de façon régulière, séparé diverses composantes sans procéder aux mêmes opérations d'élimination sur chacune d'entre elles. Ainsi, afin de reconstituer des facteurs statistiques du type (2.8), nous n'avons pas, dans les termes en $[\Sigma_k^*(\varepsilon_k)]^n$ de (2.5), éliminé partout les dénominateurs accidentellement égaux. Pour B_1, le calcul peut cependant être mené de façon cohérente, ce qui explique le résultat.

On remarquera que si on redéveloppe les facteurs $F^{\pm}$ de (2.17) en puissances de $f^{\pm}$ il redevient possible d'éliminer tous les dénominateurs accidentellement égaux ou nuls et (2.17) redevient asymptotiquement exact. On peut alors repasser à un spectre continu; la relation (2.17) ainsi développée constitue le résultat exact, les termes individuels qui la composent n'ayant cependant un sens que s'ils sont proprement regroupés. Si on imagine un processus qui redonne un sens à chaque terme individuel (en prenant par exemple des parties principales pour les intégrales divergentes), le resommation en (2.17) redevient possible, cela naturellement au prix de termes supplémentaires.

Indiquons brièvement un autre exemple du genre de regroupements qui pourraient être effectués pour un spectre $\mathscr{E}$ continu. Si nous retournons à l'expression exacte (1.14) de G_k dans laquelle les $\Sigma_k^*(\omega \pm i\varepsilon)$ sont maintenant des fonctions continues de ω sur l'axe réel, nous trouvons que, (pour $t > 0$)

$$G_k(it) = \sum_{n=0}^{\infty} \frac{(-)^n}{n!} \frac{\partial^n}{\partial \omega^n} \{f^+(\omega) e^{-i\omega t} [\Sigma_k^*(\omega - i\varepsilon)]^n\}\big|_{\omega=\varepsilon_k} - \frac{1}{i\pi} \sum_{n=1}^{\infty} (-)^n \int_{-\infty}^{+\infty} d\omega \frac{f^+(\omega) e^{-i\omega t}}{(\omega - \varepsilon_k + i\varepsilon)^{n+1}} \operatorname{Im} \{[\Sigma_k^*(\omega + i\varepsilon)]^n\}. \tag{2.22}$$

Le premier terme peut s'exprimer comme précédemment à l'aide du développement de Lagrange (qui n'offre plus de difficulté de convergence) en fonction d'un nouveau potentiel $\mathfrak{W}_k$, analogue à W_k, mais complexe. L'équation analogue à (2.9) construite à l'aide de $\Sigma_k^*(\omega)$ pour $\operatorname{Im} \omega < 0$ et de son prolongement analytique à travers l'axe réel peut alors avoir une racine unique dont la valeur

$$\mathfrak{W}_k = \sum_{n=1}^{\infty} \frac{(-)^n}{n!} \frac{\partial^{n-1}}{\partial \omega^{n-1}} [\Sigma_k^*(\omega - i\varepsilon)]^n\big|_{\omega=\varepsilon_k} \tag{2.23}$$

sera cette fois de l'ordre de grandeur de ε_k. Mais l'interprétation en diagrammes du deuxième terme n'est plus aussi simple.

Les auteurs tiennent à remercier le Professeur C. Bloch, Monsieur J. Lascoux et le Professeur J. Yvon pour d'intéressantes et utiles discussions.

Note ajoutée sur épreuves: On a pu, pour un volume infini, établir *rigoureusement* les équations (2.12) à (2.21), en redéfinissant de façon adéquate la fonctionnelle $\mathcal{F}$. Ceci fera l'objet d'une prochaine publication.

Bibliographie

1) T. Matsubara, Progr. Theor. Phys. **14** (1955) 351
2) E. Montroll et J. Ward, Phys. of Fluids **1** (1958) 55
3) L. Landau, J.E.T.P. **34** (1958) 262
4) P. C. Martin et J. Schwinger, Bull. Am. Phys. Soc. **3** (1958) no. 3
5) A. Abrikosov, L. Gorkov et I. Dzyaloshinsky, J.E.T.P. **36** (1959) 900
6) E. Fradkin, J.E.T.P. **36** (1959) 1286
7) L. Cooper, Phys. Rev. **104** (1956) 1189
8) J. Yvon, Act. Sc. Ind. **203** (1935)
9) L. Landau, J.E.T.P. **30** (1956) 1058
10) C. Bloch et C. De Dominicis, Nuclear Physics **7** (1958) 459
11) A. Klein et R. Prange, Phys. Rev. **112** (1958) 994
12) N. Hugenholtz et L. Van Hove, Physica **24** (1958) 363
13) J. Mayer et M. Mayer, Statistical Mechanics (New York, Wiley 1940)
14) J. Goldstone, Proc. Roy. Soc. A **239** (1957) 267
15) N. Hugenholtz, Physica **23** (1957) 481
16) C. Bloch, Nuclear Physics **7** (1958) 451
17) M. Cohen, prépublication

1.D.2:
2.H

Nuclear Physics **16** (1969) 518—528; © *North-Holland Publishing Co., Amsterdam*
Not to be reproduced by photoprint or microfilm without written permission from the publisher

COULOMB EXCITATION OF BETA- AND GAMMA-VIBRATIONAL STATES IN Sm^{152}

R. K. SHELINE and H. L. NIELSEN †

Chemistry Department, Florida State University, Tallahassee, Florida

and

A. SPERDUTO

Laboratory of Nuclear Science, Massachusetts Institute of Technology, Cambridge, Massachusetts

Received 6 January 1960

Abstract: A Sm^{152}-target made by electromagnetic isotope separation has been bombarded with 7.5—8.5 MeV deuterons and 8.6 MeV protons. Inelastic scattered groups corresponding to Coulomb excitation of the level at 122 keV have been observed in every case, and in one run with 8.5 MeV deuterons Coulomb excitation of levels at 807 keV and 1079 keV has been seen. The reduced transition probabilities to these states are measured as 4.1 ± 0.1, 0.07 ± 0.02 and 0.12 ± 0.02 respectively, in units of $e^2 \times 10^{-48}$ cm^4. The reduced transition probabilities for the two highest excited states are several times the single particle values. This is a strong indication of the collective nature of both these states. Accordingly, these levels are interpreted as beta- and gamma-vibrational states. The partial lifetime and the nuclear strength parameter for the E0-transition between the 807 keV and the 122 keV levels have been calculated from the experimental data and are found to be in poor agreement with the theoretical values.

1. Introduction

The measurement of inelastic scattered projectiles is an important and direct method to obtain Coulomb excitation cross sections for levels in the target nucleus. A study of the regions of deformed nuclei by this method has been made previously and has provided information on the ground state rotational bands in even nuclei and rotational bands built up on the ground state as well as intrinsic states in odd-mass nuclei. In the case of even nuclei it is expected that also quadrupole vibrations other than the ground state band must be strongly excited. High cross sections are predicted by the unified model [1]) for the E2 Coulomb excitation of the members with spin-parity 2^+ of the beta-vibration with $K = 0$, $n_\beta = 1$, $n_\gamma = 0$ and the gamma-vibration with $K = 2$, $n_\beta = 0$, $n_\gamma = 1$.

Coulomb excitation of gamma-vibrations in five even nuclei has been reported by McGowan and Stelson [2]). Their results obtained by bombardment with 4—5 MeV protons and measurement of gamma-ray yield are listed in table 1. Earlier results for Coulomb excitation of gamma-vibrations in Os^{190} and Os^{192} were published by Barloutaud *et al.* [3]).

† Now at Institute for Theoretical Physics, University of Copenhagen, Copenhagen, Denmark.

A 2^+ level at 760 keV in Th^{232} has been reached in Coulomb excitation with 5 MeV protons [4]). The reduced transition probability is measured as 4.3 times the single particle value [5]) and the level is supposed to be a member of a beta-vibration [1,4,6]).

The present experimental data on beta- and gamma-vibrational bands are scarce and any further knowledge on this subject would be of theoretical interest.

TABLE 1

Coulomb excitation of gamma-vibrational states in 5 even nuclei (McGowan and Stelson, ref. [2]))

Nucleus	Excited 2^+ level (keV)	B(E2) in independent particle units (Weisskopf)
W^{184}	891±9	5.5±1.6
W^{186}	730±7	5.5±1.0
Os^{188}	633±6	6.3±1.9
Os^{190}	557±6	4.3±1.0
Os^{192}	489±5	4.6±1.0

In this work vibrational states in the deformed nucleus Sm^{152} have been studied by measurement of inelastic scattered particles. The vibrational level-energies are expected to be about one MeV in this region. This indicates that high bombarding energies of the order of the Coulomb barrier must be applied. Another experimental condition to be stressed is extreme purity of target material as well as supporting foils. The region of interest on the spectrogram of elastic and inelastic scattered particles is located from the Sm^{152} elastic peak and about one MeV upwards in excitation energy. Any impurity, especially of elements with high mass number, present in target and foils will give rise to an elastic peak and eventually a number of inelastic peaks obscuring parts of this region. The way the requirements outlined above have been met and a discussion of the implication they might have on the validity of the results are described in the following section.

2. Target Preparations

The Sm^{152} targets were prepared using the isotope separator of the Institute for Theoretical Physics in Copenhagen. Three or four double thicknesses (total thickness $\approx 120\mu g$) of formvar cast on water were collected on a thin aluminium target holder approximately rectangular in shape with a rectangular hole in the middle for the target. Aluminium (50—200μg) was evaporated onto the formvar. This was necessary for the conduction of heat and consequent stability of the target both in isotope separation and Van de Graaff bombardment. Then Sm^{152} was deposited on the formvar-aluminium film by the isotope separator. This was accomplished by charging the ion source of the separator

with waterfree $SmCl_3$. The separator was operated in the normal way except that just before collection of the Sm^{152} on the target a 49 to 49.5 keV decelerating potential was used to decelerate the Sm ions from 50 keV to very low energies. In this way the isotope separator beam did not destroy the targets. Target areas of approximately rectangular shape, $\frac{3}{4}-1$ mm wide and ≈ 4 mm long, were produced. Sm^{152} purity greater than 99.9 % was achieved. Three targets were prepared with integrated target currents varying from 60 000 to 100 000 μC.

Final thicknesses as estimated from the inelastic scattering varied from 20 μg to 50 μg and dit not seem to depend solely on the initial target current used. Targets prepared in this way can stand repeated prolonged bombardments at least up to 0.3 μA of 7—8.5 MeV protons or deuterons. A complete description of the experimental technique used in depositing the separated Sm^{152} is given in ref. [19]).

3. Experimental Procedure

The Sm^{152}-target was bombarded with 7.5, 8.0, and 8.5 MeV deuterons and 8.6 MeV protons from the MIT-ONR Van de Graaff accelerator. The outcoming beam was deflected 90° in the field of a magnet which, together with a slit system, defined the energy. The slit setting used in the experiments gave a beam of dimensions about 1×6 mm. The position of the target was arranged with respect to the incident beam so that the incoming and the outcoming beams were symmetrical about a plane vertical to the target. The outcoming beam, taken out at a deflecting angle θ_{lab} to the incident beam, was analysed in a broad range magnetic spectrograph. This apparatus has been described in detail in previous papers [7, 8]). The spectrograph, which can be rotated about a vertical axis, resolves the outcoming particle-groups with respect to their momentum in a 90°, 50 cm radius magnet and collects them on a set of nuclear track-plates with 50 μm thick Eastman NTA emulsion. In order to reduce the elastic peak of Sm^{152} in magnitude in relation to the inelastic peaks, it is advantageous to work at backward angles. Measurements were here carried out at $\theta_{lab} = 90°$ and 130°. The plates were counted in strips of 0.5 mm width by means of a low power microscope. From the separation of a group from the elastic scattering peak the Q-value of the inelastic scattering reaction and then the excitation-energy of the corresponding level in the target nucleus were calculated. The intensity of a peak was evaluated from the total number of tracks in the peak corrected for background and for solid angle variation along the plate (see ref. [7]), fig. 8).

The beam current averaged 0.05 μA through the experiments. The unscattered part of it was measured in a beam integrator; exposures were made in the range 800—2250 μC total charge. Three exposures of different length were made on each set of plates, the plate system being translated between each exposure. This was of importance since a long exposure, necessary with regard to weak

inelastic groups, gave an extremely intense elastic peak for Sm^{152}. A short exposure, however, resulted in a countable peak. From the ratio of values for the integrated beam current in the two exposures, the true ratio of intensities of elastic and inelastic peaks was determined.

The range of energies 7.5—8.5 MeV deuterons and 8.6 MeV protons chosen for the bombardment of Sm^{152} in this work is in the vicinity of the Coulomb barrier at about 11—12 MeV, and a considerable penetration of the barrier must be expected. The cross sections for formation of compound nuclei are found [9]) to be of the order of 100 mb for 8.6 MeV protons. The total Coulomb excitation cross section for E2 excitation of the 122 keV level in Sm^{152}, calculated from ref. [1]) (p. 458), is about 30 mb for protons and about 60 mb for deuterons. However, the decay of the compound nucleus can be assumed to occur mainly through other channels than the inelastic channels corresponding to the 122 keV level and other levels in Sm^{152}. Any contribution from a compound nucleus formation will introduce a strong bombarding energy dependence for the measured reduced transition probabilities. No systematic variation of this kind was observed (see table 2), so that the conditions on which the calculation of Coulomb excitation cross sections are based seem to be fulfilled within the limits of the experiments.

4. Calculations

The calculations of the Coulomb excitation cross sections follow the method described by Elbek and Bockelman in an earlier paper [10]).

The differential cross section for Rutherford scattering is given by

$$\frac{d\sigma_R}{d\Omega} = 4980 \frac{1}{E^2} \frac{1}{\sin^4 \frac{1}{2}\theta} \text{ mb/sr}$$

for scattering of deuterons or protons of energy E on Sm^{152} through the angle θ. Both E (in MeV) and θ are for centre-of-mass system. If pure Rutherford scattering is assumed for the Sm^{152} elastic peak, the ratio of intensities of an inelastic peak and the elastic peak multiplied by the Rutherford differential cross section gives directly the differential cross section for the inelastic scattered group. The theoretical Coulomb excitation cross sections in classical approximation are given in ref. [1]). For E2 excitation one obtains

$$\frac{d\sigma_C}{d\Omega} = 4819 \left(1+\frac{A_1}{A_2}\right)^{-2} \frac{A_1}{Z_2^2} (E_{MeV} - \Delta E') B(E2) \frac{df_{E2}(\xi, \theta)}{d\Omega} \text{ mb/sr},$$

where Z and A are atomic numbers and mass numbers and subscripts 1 and 2 refer to projectile and target nucleus, respectively; E_{MeV} is the bombarding energy in the laboratory system and

$$\Delta E' = \left(1+\frac{A_1}{A_2}\right) \Delta E,$$

where ΔE is the excitation energy in MeV. The quantity $df_{E2}/d\Omega$ is tabulated in ref. [1]) as function of centre-of-mass angle θ and

$$\xi = \frac{Z_1 Z_2 A_1^{\frac{1}{3}} \Delta E'}{12.65(E_{\mathrm{MeV}} - \frac{1}{2}\Delta E')^{\frac{1}{3}}} \left[1 + \tfrac{5}{32}\left(\frac{\Delta E'}{E}\right)^2\right].$$

Thus, an experimental value for the reduced transition probability $B(\mathrm{E2}, 0^+ \rightarrow 2^+)$ can be calculated on the basis of the measured differential cross sections.

In the region of deformed nuclei, $B(\mathrm{E2})$ is usually compared to the single particle reduced transition probability, defined in ref. [1]) by

$$B(\mathrm{E2}, 0+ \rightarrow 2+)_{sp} = 2 \times 10^{-5} A_2^{4/3} e^2 \times 10^{-48}\ \mathrm{cm}^4$$

or $B(\mathrm{E2})_{sp} = 0.024$ for Sm^{152}.

The electric quadrupole moment Q_0 and the quadrupole deformation parameter β are calculated from the formulae

$$B(\mathrm{E2}, 0+ \rightarrow 2+) = \frac{5}{16\pi} e^2\, Q_0^2,$$

$$Q_0 = \frac{3}{(5\pi)^{\frac{1}{2}}} Z_2 R_0^2 \beta(1+0.16\beta),$$

with

$$R_0 = 1.2\, A_2^{\frac{1}{3}} \times 10^{-13}\ \mathrm{cm}.$$

5. Results

Fig. 1 gives part of a spectrogram obtained in one of the experiments with highest bombarding energy (8.5 MeV deuterons). One sees the elastic peak of Sm^{152} in two different exposures, the Coulomb excited 122 keV level and elastic peaks of Cl^{37}, Cl^{35} and Al^{27}. Chlorine is a contaminant originating from the target preparation. Aluminium is present in the backing material. A small but significant peak falls about 10 keV to the left of the place where the S^{32} elastic peak was expected, if sulphur were present in the target. However, a sulphur contamination has not been observed in any of the other 6 runs, so that there are strong reasons to assume that the small peak is due solely to a Coulomb excited level in Sm^{152} with energy calculated to be 807 keV. Another minor peak is seen to the left of the Al^{27} peak; it can only originate from a Coulomb excited level in 1079 keV in Sm^{152}. The excitation energy for the 122 keV level, calculated for the 7 runs, gives 122 ± 3 keV, where the error quoted is the standard deviation. The accuracy in the energy determination for the two higher levels is much poorer because of the poorer statistics in the small peaks. It is estimated as ± 10 keV.

It is of great importance to be reasonably certain that the inelastic deuteron peaks observed in fig. 1 originate from Coulomb excitation rather than any other mode of excitation. Probably, the best evidence is the absence of excitation of other levels of Sm^{152} which are known to exist from decay scheme work (see fig. 2) but would have very small Coulomb excitation cross-sections because of the nature of the level. There is a slight indication of a very weak peak at 65.92 cm. This corresponds to an energy of 361 keV, well within the experimental error of the 4+ state in Sm^{152} at 366 keV, and a cross-section not outside that expected for double Coulomb excitation. The fact that the cross-sections

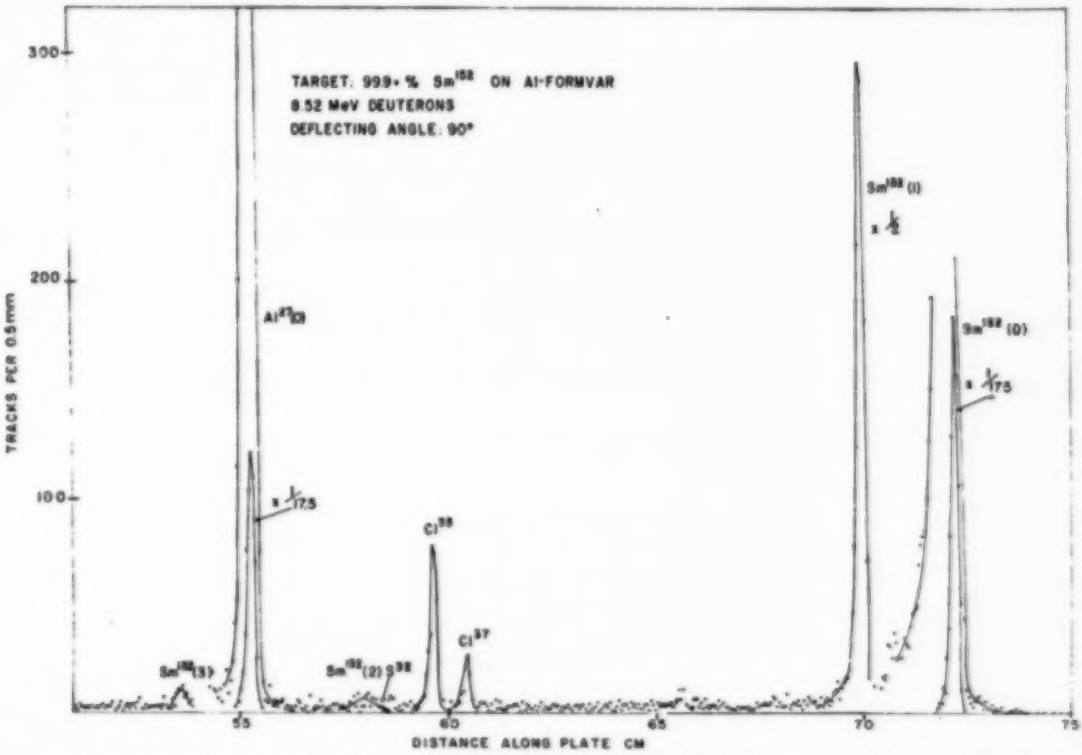

Fig. 1. Elastic and inelastic scattered deuteron-groups from a Sm^{152} target on aluminized Formvar backing. The esposures were 1750 and 10 μC. The incident deuteron energy was 8.5 MeV. The arrow the theoretical postion of the S^{32} elastic scattering peak if sulphur were present in the target. Cl^{35} and Cl^{37} are the only contaminants detected besides carbon, nitrogen, oxygen and aluminium from the backing material.

for the levels at 122, 807 and 1079 keV are not out of line with previous data on similar levels, the independence of reduced probabilities on bombarding energy together with the absence of other peaks gives credibility to the suggestion that there is no important nuclear interaction contributing to the excitation.

Table 2 lists the experimental results for the Coulomb excitation cross sections and the reduced transition probabilities $B(E2, 0+ \rightarrow 2+)$ for the 122 keV level. The weighted average of $B(E2)$ is $(4.1 \pm 0.1)e^2 \times 10^{-48}$ cm^4, corresponding to a nuclear quadrupole moment $Q_0 = 6.4 \times 10^{-24}$ cm^2 and a deformation parameter $\beta = 0.31$. This $B(E2)$ is about 170 times the single particle value.

TABLE 2

Coulomb excitation cross sections and reduced transition probabilities for the 122 keV level in Sm^{152}

Incident energy (MeV)	Projectile	Deflecting angle (degrees)	Differential cross section (mb/sr)	Reduced transition probability $B(E2, 0+2\rightarrow 2^+)$ ($e^2\times 10^{-48}$ cm^4)
8.551	d	90°	5.5	4.2±0.1 †
8.522	d	90°	5.0	3.8±0.1
8.018	d	130°	5.3	4.4±0.5
7.520	d	130°	4.1	4.1±0.2
7.514	d	130°	5.9	5.9±0.8
7.512	d	130°	4.5	4.4±0.1
8.623	p	90°	2.0	3.0±0.2

† The errors quoted are estimated from the error in determining the background.

The cross sections for the Coulomb excitation of the higher levels in Sm^{152} were carefully calculated giving each point in the small peaks equal weight and subtracting the background determined from the neighbouring regions where again each point was given equal weight. These cross sections and the corresponding reduced transition probabilities in units of $e^2\times 10^{-48}$ cm^4 as well as in single particle units are presented in table 3.

TABLE 3

Coulomb excitation cross sections and reduced transition probabilities for the 807 keV beta-vibrational and 1079 keV gamma-vibrational levels in Sm^{152}

Excitation energy (keV)	Incident energy (MeV)	Projectile	Deflecting angle (degrees)	Differential cross section (mb/sr)	Reduced transition probability $B(E2, 0+ \rightarrow 2+)$	
					($e^2\times 10^{-48}$ cm^4)	(single particle units)
807	8.522	d	90°	0.06	0.07±0.02	3±1
1079	8.522	d	90 °	0.08	0.12±0.02	5±1

6. Discussion

6.1. LEVEL AT 122 keV

Coulomb excitation of the first excited state at 122 keV in Sm^{152} has been measured in several cases. Heydenburg and Temmer [11]) report the reduced transition probability 3.1 $e^2\times 10^{-48}$ cm^4, measured by the gamma-radiation produced by excitation with 6 MeV alpha-particles. Sharp and Buechner [12]) used essentially the same method as we have applied in the present work; they obtain for $B(E2)$ a weighted average of 3.20±0.36, calculated on the

basis of 2.96±0.40 measured at 130° deflection and 4.10±0.80 for 90° deflection. 7-MeV protons were used in the bombardments.

Thus the reduced transition probability measured from gamma-ray yield deviates appreciably from our value, which leads to a deformation parameter somewhat higher than expected for Sm^{152}, located at the very beginning of the region of strongly deformed nuclei.

6.2. BETA- AND GAMMA-VIBRATIONAL STATES

Further discussion is illustrated with the level scheme for Sm^{152} in fig. 2 which is based mainly on data by Nathan and Hultberg [13]), Grodzins [14]), Cork *et al.* [15]) and our own results.

Our level at 807 keV shown in fig. 2 is identified (not inconsistently with the experimental error in our determination) with the 2+ level at 811 keV, discussed in detail by Nathan and Hultberg, who in agreement with their experimental results propose an assignment 2+ to this level and interpret it as

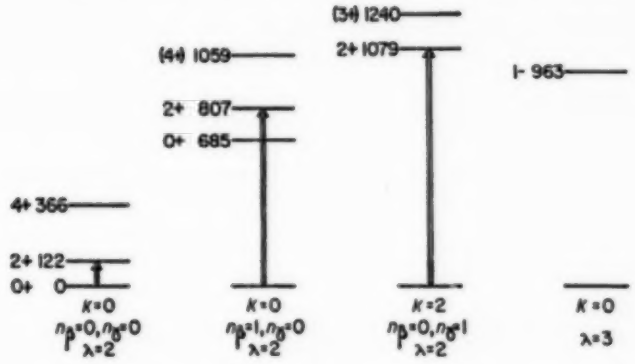

Fig. 2. Level scheme for Sm^{152}. The bands are from left to right: Groundstate rotational band, beta-vibrational band, gamma-vibrational band and an octupole vibrational state.

the second member of a beta-vibrational band. The first member of this sequence, the 0+ level at 685 keV, has been observed by Marklund *et al.* [16]).

The energy difference between the 2+ and 0+ states in the beta-vibrational band is 126 keV (on the basis of the spectroscopic results [13, 16]) compared with 122 keV for the corresponding difference in the ground state rotational band. For the latter band the excitation energy ratio E_4/E_2 for the 4+ and the 2+ state is 3.00, whereas the theory of the unified model predicts 3.33 for strongly deformed nuclei. The deviation is consistent with the already mentioned location of Sm^{152} at the border of the region of strong deformations. If, as a rough estimate, we apply the same E_4/E_2 ratio for the beta-vibration, E_4 and E_2 now being the energy separations of the 4+ and the 2+ (811 keV) level from the 0+ level at 685 keV, we can expect a 4+ level at about 1063 keV. The existence of a level at 1059 keV in Sm^{152} has been reported by Cork *et al.* [15]) but is not well established. However, for the reasons stated above, we consider this level as the 4+ member of the beta-vibrational band, as indicated in fig. 2.

The level observed at 1079±10 keV in this work is identified with the 1082 keV, 2+ level reported by Nathan and Waggoner [17]) and interpreted together with the 3+ level at 1226 keV as members of a gamma-vibrational sequence. Nathan and Hultberg later measured these energies as 1087 and 1240 keV.

6.3. THE 2+ → 2+ TRANSITION

The work of Nathan and Hultberg together with our experimental value of $B(\mathrm{E2}, 0+ \rightarrow 2+)$ for the excitation of the 807 keV, 2+ level makes it possible to calculate the lifetime for the electric monopole transition between this state and the first excited state at 122 keV. The de-excitation of the 2+ beta-vibrational state takes place by E2 gamma-emission to the 4+ and the 0+ states in the ground state rotational band and by mixed E2 and E0 to the 2+ state of the latter band. The E0-transition occurs through emission of conversion electrons. The theoretical branching ratio for E2 transitions to the 0+ and 2+ levels is

$$\frac{B(\mathrm{E2}, 2+ \rightarrow 0+)}{B(\mathrm{E2}, 2+ \rightarrow 2+)} = 0.7 \qquad (1)$$

In the equation

$$B(\mathrm{E2}, I_i \rightarrow I_f) = \frac{2I_f+1}{2I_i+1} B(\mathrm{E2}, I_f \rightarrow I_i)$$

we put $I_i = 2$, $I_f = 0$, and using $B(\mathrm{E2}, 0+ \rightarrow 2+) = 0.07 \pm 0.02$ from table 3 we obtain

$$B(\mathrm{E2}, 2+ \rightarrow 0+) = \tfrac{1}{5}0.07 = 0.014,$$

and then from (1),

$$B(\mathrm{E2}, 2+ \rightarrow 2+) = \frac{0.014}{0.7} = 0.02.$$

The transition probability for this transition is calculated from ref. [1]), page 500:

$$T_\gamma = 1.23 \times 10^{-2} \times 689^5 \times B(\mathrm{E2}) = 3.8 \times 10^{10}\ \mathrm{sec}^{-1}. \qquad (2)$$

Nathan and Hultberg's estimate for the ratio of E0 K-conversion rate to the E2 gamma-ray rate is

$$\frac{I_{e,\mathrm{K},\mathrm{E0}}}{I_{\gamma,\mathrm{E2}}} = 0.07.$$

This gives directly the transition probability for the E0 K-conversion

$$W = T_\gamma \frac{I_{e,\mathrm{K},\mathrm{E0}}}{I_{\gamma,\mathrm{E2}}} = (2.7 \pm 0.8) \times 10^9\ \mathrm{sec}^{-1} \qquad (3)$$

or the partial lifetime

$$\tau = (0.37 \pm 0.11) \times 10^{-9}\ \mathrm{sec}.$$

This is to be compared to the theoretical lifetime 3.0×10^{-9} sec calculated by Reiner [6]) †. It is worthwhile to point out that even if the branching ratio (1) deviates considerably from the theoretical value 0.7 for strongly deformed nuclei, the expression (3) is only slightly changed. $T_\gamma(2)$ as well as $I_{\gamma,E2}$ are inversely proportional to the branching ratio, so that W is only dependent on the branching ratio through $I_{e,K,E0}$, which varies very slowly with this ratio (see Nathan and Hultberg [13])).

The so-called nuclear "strength parameter" ρ can now be evaluated from the graph given by Church and Weneser [18]), showing for different nuclei the relation between the E0 transition probability divided by ρ^2, and the energy of the transition. For $Z = 62$ and transition energy 689 keV we obtain $W/\rho^2 = 23\times10^{10}\,\mathrm{sec}^{-1}$, and hence

$$\rho = 0.34\pm0.05.$$

The theoretical value is 0.10 as calculated by Reiner [6]).

The agreement between experimental and theoretical values of the lifetime and nuclear strength parameter for this E0 transition is not satisfactory. Reiner [6]) used the value $\beta_0^2 = 0.084$ in calculating ρ, whereas β_0^2 was determined in these experiments as 0.096. This alters the calculated values slightly in the experimental direction. There is also the possibility that the assumption that the $2+ \rightarrow 2+$ transition consists only of E0 and E2 components is in error. However, it is unlikely that either of these explanations is sufficient to explain the magnitude of the discrepancies. It seems more probable that the hydrodynamical model is not a sufficiently good description of this nuclear vibration It should also be remembered that Sm^{152} is not a very good example of a deformed nucleus.

On the other hand the accumulation of large Coulomb excitation cross sections and reduced transition probabilities (several times single particle) to high lying levels in even nuclei (see tables 1 and 3) is strong evidence for the fact that these states have considerable collective nature.

This project provides evidence for the necessity of cooperation in nuclear research. The problem was conceived in Copenhagen. Thanks are due Professor A. Bohr and Professor B. R. Mottelson in the initial discussions. Special thanks are due for the targets which were prepared by O. Skilbreid and M. C. Olesen. The excellence of the targets made possible the difficult investigation. The bombardments were done at The Massachusetts Institute of Technology. We are especially indebted to Professor W. W. Buechner for his hospitality and to Mr. W. A. Tripp, whose careful counting of the plates was so vital to this project. The work at The Massachusetts Institute of Technology was supported in

† The electronic matrix element given by Reiner, based on interpolations, differs significantly from the calculated one. This results in a change for the lifetime from 1.6×10^{-9} sec to 3.0×10^{-9} sec.

part through funds provided by Contract No. AEC AT(30—1)-2098 with the United States Atomic Energy Commission, the Office of Naval Research, and the Air Force Office of Scientific Research. Finally, the work was analyzed and the paper written at Florida State University. Contract DA-01-009-ORD-705 with the Office of Ordnance Research, Contract AT-(40-1)-2434 with the Atomic Energy Commission, and Contract AF 49(638)-427 with the Air Force Office of Scientific Research are gratefully acknowledged.

References

1) K. Alder, A. Bohr, T. Huus, B. Mottelson and A. Winther, Revs. Mod. Phys. **28** (1956) 432
2) F. K. McGowan and P. H. Stelson, Bull. Am. Phys. Soc. **3** (1958) 228
3) R. Barloutaud, P. Lehmann and A. Lévêque, Compt. rend. **245** (1957) 523
4) P. H. Stelson and F. K. McGowan, Phys. Rev. **99** (1955) 112
5) F. K. McGowan, Report on the Paris Conference 1958
6) A. S. Reiner, Structure Effects in the Interaction Between Nuclei and Atomic Electrons Thesis (1958) p. 102; and private communication (1959)
7) C. P. Browne and W. W. Buechner, Rev. Sci. Instr. **27** (1956) 899
8) W. W. Buechner, M. Mazari and A. Sperduto, Phys. Rev. **101** (1956) 188
9) J. M. Blatt and V. F. Weisskopf, Theoretical Nuclear Physics (J. Wiley & Sons, 1952)
10) B. Elbek and C. K. Bockelman, Phys. Rev. **105** (1957) 657
11) N. P. Heydenburg and G. M. Temmer, Phys. Rev. **100** (1955) 150
12) R. D. Sharp and W. W. Buechner, Phys. Rev. **109** (1958) 1698
13) O. Nathan and S. Hultberg, Nuclear Physics **15** (1960)
14) L. Grodzins, Phys. Rev. **109** (1958) 1014
15) J. M. Cork, M. K. Brice, R. G. Helmer and D. E. Sarason, Phys. Rev. **107** (1957) 1621
16) I. Marklund, O. Nathan and G. Wood, to be published
17) O. Nathan and M. A. Waggoner, Nuclear Physics **2** (1956) 548
18) E. L. Church and J. Weneser, Phys. Rev. **103** (1956) 1035
19) B. Elbek, M. C. Olesen and O. Skilbreid, Nuclear Physics **10** (1959) 294

5

Nuclear Physics **16** (1960) 529—533; © *North-Holland Publishing Co., Amsterdam*

Not to be reproduced by photoprint or microfilm without written permission from the publisher

MEASUREMENT OF THE ENERGY OF THE WEAK GROUP IN THE α-SPECTRUM OF Po^{210}

T. FÉNYES

Institute for Experimental Physics, Debrecen, Hungary

Received 7 December 1959

Abstract: The nuclear spectrum of Po^{210} was examined by a scintillation $\alpha-\gamma$ coincidence equipment combined with an electromagnetic α-spectrometer. Accepting 5.3054 ± 0.0010 MeV (absolute V) as the value [1]) for the kinetic energy of the main group, that of the weak group was found to be 4.525 ± 0.005 MeV.

1. Introduction

As is well known, Po^{210} emits mostly α-particles of 5.3 MeV kinetic energy, but it has also some γ-radiation of very low intensity. The γ-spectrum has been investigated by a number of authors. The measurements have revealed that the γ-radiation of Po^{210} consists of a single line of about 800 keV. No other lines have been observed, at any rate not in the interval between 25 keV and 2.5 MeV [2]).

In 1952, De Benedetti and Minton [3]) succeeded in directly disclosing the existence of the weak α-group pertaining to γ-radiation of about 800 keV by means of scintillation spectrometers and by applying the $\alpha-\gamma$ coincidence method.

In 1958, Bastin-Scoffier and Walen [4]) measured the ratio of intensity of the weak group to the main group accurately by using a magnetic α-spectrometer.

The aim of this investigation was the precise determination of the energy ratio between the weak and main α-groups through direct α-spectroscopy (by an electromagnetic spectrometer).

2. Experimental Details

At the Institute for Experimental Physics of the L. Kossuth University of Debrecen, an electromagnetic α-spectrometer of semicircular type was constructed on the plans of Prof. A. Szalay and the author [5]). This spectrometer was completed with accessory devices such as an electronic magnetic field stabilizer, a vacuum equipment and scintillation counters.

Along a semicircle of 44.3 cm radius, in a 3.2 cm wide and 0.46 cm high band, the electromagnet of the spectrometer produces a homogeneous magnetic field vertical to the path of the α-particles. The electromagnet is fed by a dynamo. A current of 16—18 A at 100 V dynamo terminal voltage passes through the spectrometer coils. The iron core of the spectrometer was cut out of the wheel of a railway carriage.

At a constant magnetizing current, the inhomogeneity of the magnetic field of the spectrometer was not significant, at least on the part where the

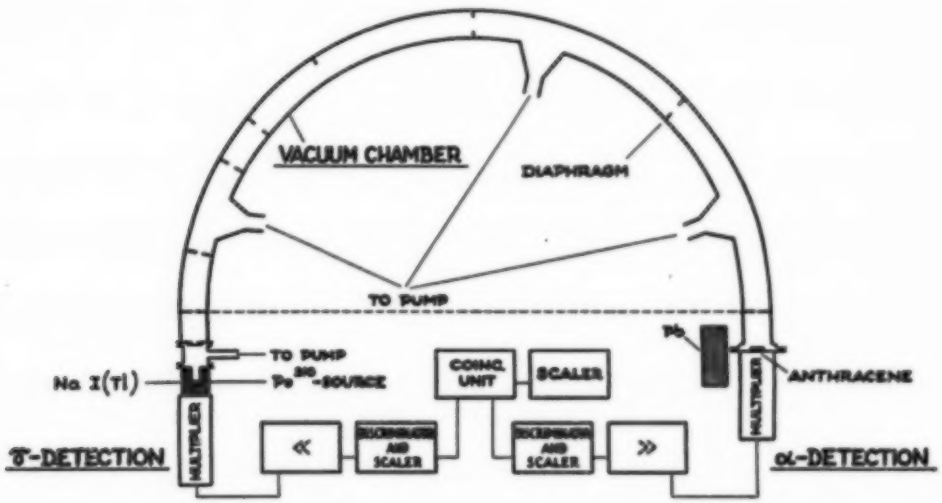

Fig. 1. Semicircular focussing magnetic α-spectrometer combined with $\alpha-\gamma$ coincidence equipment for measurement of the exact energy of the weak α-group of Po^{210}.

α-particles were moving. The resulting effective inhomogeneity of the magnetic field strength (which was calculated after the method of Hartree [6]) proved to be a few times 0.1 ‰ and remained of the same order of magnitude when it was examined at different time intervals, temperatures and magnetic field strengths.

The fluctuation of direct current arising from the collector-slices of the dynamo is filtered by an LC circuit connected parallel with the spectrometer coil, shunting the A.C. component at the given frequency. The principle of compensating the slow irregular field strength fluctuation is to introduce a well defined resistance into the main circuit and — after amplifying the appearing voltage fluctuation signal — to let a current pass through a second coil fitted to the spectrometer, which will just compensate the change. At stabilization, the temporal fluctuation of the magnetic field strength is $\leqq \pm 1‰$ in the air-gap of the spectrometer.

The vacuum is maintained by an oil diffusion pump. When measuring spectra, the vacuum is generally a few times 10^{-5} mm Hg, but better than 10^{-3} mm Hg in every case. The vacuum chamber is made of brass with numerous

hard aluminium slits placed in it in order to avoid or at least minimize the Rutherford-scattering of α-particles on the chamber walls. The chamber constitutes a unit independent of the magnet-pole-faces, and the scintillation counter-heads for measuring α- or γ-rays can be fitted to its both ends (fig. 1).

After semicircular focussing, the α-particles were detected by an anthracene crystal scintillation counter. The diameter of the crystal was 12 mm and its thickness 5 mm. As anthracene evaporates in the vacuum to a small extent, the front surface was coated with zapon lacquer of a few $\mu g/cm^2$ thickness and covered with an Al foil in order to decrease loss of light. The Al foil, being 0.42 mg/cm^2 thick, did not slow down considerably the α-particles (the zapon lacquer did so even less). The light pulses were transformed by an electron multiplier into electric ones which then were counted by a decade counter tube system consisting of five units.

The γ-photons were counted by an instrument similar to the former scintillation counter but fitted with a well type NaI(Tl) crystal. The shape of the crystal was a cylinder of 44 mm height, with a base plate of 35 mm diameter. In order to improve the counting efficiency of γ-photons, a hole $\approx$ 21 mm in diameter and $\approx$ 22 mm deep was bored into the crystal along its axis, in which was sunk the cylindrically shaped forepart of the vacuum chamber containing the Po-source.

With proper precautions, the effect of the magnetic field of the spectrometer upon the electron multiplier could be reduced to a minimum.

The resolving time of the coincidence apparatus was $(1.69 \times 10^{-7} \pm 5\ \%)$ sec.

The Po-source was prepared by Professor A. Szalay after his reported method [7]). The method is based on the volatilisation and concentration of Po in hydrogen stream. In this way very pure, homogeneous and highly concentrated sources are obtainable. A screw consisting of $\approx$ 85 % Pt and 15 % Ir served as a base for the source. The Po was placed on the circular front face of the screw 3 mm in diameter and carefully polished beforehand. In order to avoid the disturbing effect of α-particles emitted from Po eventually deposited on the side of the screw, its head was shaped cone-like.

Measurement of the magnetic field strength was made by a precision fluxmeter of high sensitivity and a measuring coil. The latter was specifically thin that it might just get into the air-gap of the spectrometer beside the vacuum chamber.

During the examination of Po^{210} the transmission of the spectrometer (the fraction of all monokinetic α-particles leaving the source which is actually counted in the detector) was 2 to 3×10^{-6}, at $\delta(H\rho)/H\rho = 3.5\ \%$ resolving power.

To avoid contamination of the vacuum chamber of the spectrometer by Po, the space about the source was separately evacuated and isolated from the other parts of the vacuum chamber by means of a few $\mu g/cm^2$ thick zapon

lacquer layer. During a short-lasting measurement it was determined, where the place of the main group was on the const. $\times H\rho$ axis with respectively without the entrance zapon lacquer layer. The replacement of the main group was 1 (counted in the unit used for the abscissa of the fig. 2). The effect was taken into account when calculating the energy of the weak group.

To avoid the impact of photons Compton-scattered in the NaI/Tl/ crystal upon the anthracene crystal, a thick lead absorber was placed between the two counters.

3. Results

When measuring $\alpha-\gamma$ coincidence spectra, the discriminator voltage of the γ-counter was set to register as many photons of 800 keV (not only those

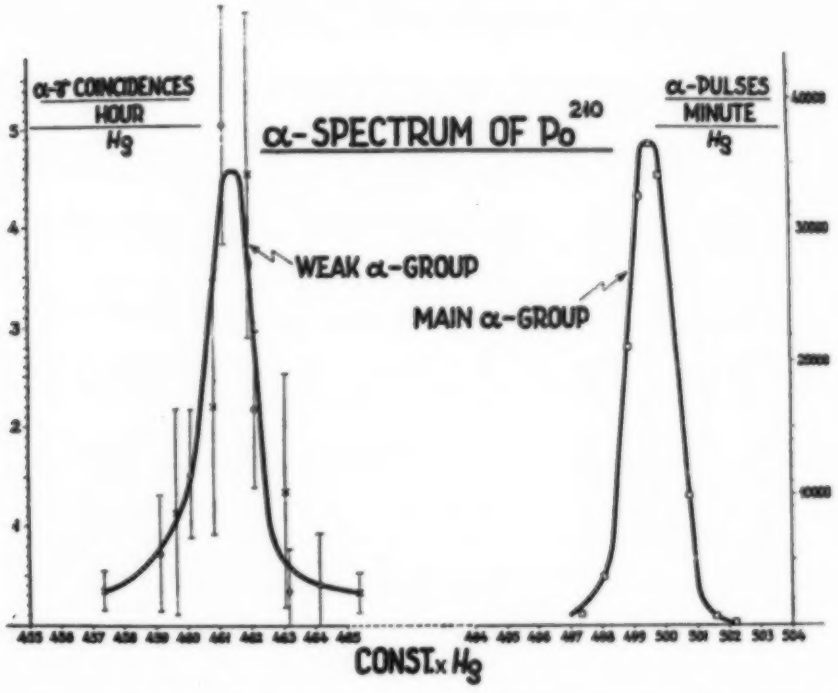

Fig. 2. α-spectrum of Po^{210}. Abscissa: const. $\times H\rho$, ordinate left: number of $\alpha-\gamma$ coincidences per hour per $H\rho$, ordinate right: number of α-pulses per minute per $H\rho$ (H: magnetic field strength, ρ: radius of curvature).

absorbed by the photo- but also by the Compton-effect) as possible. Care was taken, however, that it should not detect at all the X-rays arising from Migdal-effect and conversion.

The results obtained by Po^{210} of 6.2 mc strength are shown in fig. 2.

The points of measurements marked by dots are results of the first and those marked by crosses are the results of the second series of measurements. The curve of the main group (squares) was measured several times in both

series of measurements (altogether 15 times). The plotted curve of the main group represents the mean value of the measurements.

As follows from the above, the kinetic energy of the weak group is

$$E = 4.525 \pm 0.005 \text{ MeV}$$

if the 5.3054 ± 0.0010 MeV value is accepted for the energy of the main group[1]). The energy of the γ-photon

$$E_\gamma = 795.6 \pm 5 \text{ keV}.$$

The (weak group/main group) intensity ratio could not be calculated precisely, but it roughly agrees with the published[4]) value 1.07×10^{-5}.

A detailed description of the equipment and the measurements is given in ref. [8]).

I am greatly indebted to Professor A. Szalay, not only for preparing the sources, but also for his continuous, helpful support. Acknowledgement is due to Miss I. Szabó for her help with the preparation of the source as well as to my colleagues Dr. D. Berényi, G. Máthé and T. Schárbert for making the coincidence equipment available.

References

1) F. A. White, F. M. Rourke, J. C. Sheffield, R. P. Schuman and J. R. Huizenga, Phys. Rev. **109** (1958) 437
2) W. C. Barber and R. H. Helm, Phys. Rev. **86** (1952) 275;
D. E. Alburger and M. H. L. Pryce, Phys. Rev. **95** (1954) 1482 (see these papers for a more extensive list of references)
3) S. De Benedetti and G. H. Minton, Phys. Rev. **85** (1952) 944
4) G. Bastin-Scoffier and R. J. Walen, Comptes rendus **247** (1958) 2333
5) A. Szalay and T. Fényes, Fizikai Szemle **2** (1952) 98
6) D. R. Hartree, Proc. Camb. Phil. Soc. **21** (1923) 746
7) A. Szalay, Zeitschrift f. Phys. **112** (1939) 29
8) T. Fényes, Kandidátusi disszertáció (1958)

6.A:9.B

Nuclear Physics **16** (1960) 534—544; © *North-Holland Publishing Co., Amsterdam*

Not to be reproduced by photoprint or microfilm without written permission from the publisher

CHARACTERISTICS OF HEAVY ION TRACKS IN NUCLEAR EMULSIONS

P. G. ROLL † and F. E. STEIGERT

Sloane Physics Laboratory, Yale University, New Haven, Connecticut ††

Received 13 January 1960

Abstract: Ilford G-5 nuclear emulsion plates have been exposed in vacuum to beams of He^4, B^{10}, B^{11}, C^{12}, N^{14}, O^{16}, F^{19}, and Ne^{20} ions. The ions were accelerated to about 10 MeV per amu, degraded to the desired energy by a variable thickness of metal foil or gas, and analyzed magnetically. Range-energy relations for these ions in dessicated G-5 emulsions have been determined in this manner with an estimated accuracy of ± 1 %. Because the range-energy relations are intended for use in nuclear reaction experiments with machine-accelerated particles, no corrections have been made for emulsion density. Comparison with similarly-exposed Ilford emulsions of various different grain sizes and sensitivities indicates no significant dependence of the range-energy relation on emulsion type. The track width was also measured in detail as a function of residual range for all ion species used.

1. Introduction

In order to properly utilize beams of accelerated heavy ions which are currently available at several laboratories, it is necessary to have information concerning the range-energy relations for heavy ions in various materials. A series of measurements of these relations in several stopping media has been carried out using beams from the Yale Heavy Ion Linear Accelerator. The present paper is a report of the results of these measurements in nuclear emulsion.

In performing nuclear reaction experiments with heavy ions, it is necessary both to measure the energy of the charged particles involved and to identify the species of ion. The energy of a heavy ion of known identity may be determined by measuring the length of the track it produces in nuclear emulsion and using the appropriate range-energy relation. To this end, range-energy relations for He^4, B^{10}, B^{11}, C^{12}, N^{14}, O^{16}, F^{19}, and Ne^{20} ions in dessicated Ilford G-5 emulsion have been obtained for energies up to 10 MeV per atomic mass unit (amu). In the more sensitive emulsions, heavy ion tracks possess a peculiar tapering shape. The amount of taper is a function of nuclear charge Z, and hence can be used as a means of identifying heavy ion species. Detailed measurements of track width vs. residual range have been carried out to investigate this phenomenon over the range $5 \leqq Z \leqq 10$.

† General Electric Edwin W. Rice Fellow, 1958—59.

†† This work was supported by the Office of Naval Research and the U. S. Atomic Energy Commission. Preliminary reports can be found in ref. [1]).

Previous to the recent availability of reasonably intense monochromatic heavy ion beams from linear accelerators, the small body of experimental range-energy information for heavy ions had been obtained either indirectly from nuclear reactions [2,3]) or by using in some manner the continuous energy spectrum produced by a cyclotron [4,5,6]). Neither of these general methods has resulted in high precision. Heckman *et al* [7]) have recently reported some accurate range-energy measurements for C^{12}, N^{14}, O^{16}, Ne^{20}, and A^{40} accelerated in the Berkeley Heavy Ion Linear Accelerator and analyzed by a 180° magnetic spectrometer.

Theoretically, the earliest attempt to compute range-energy relations for heavy ions was undertaken by Longchamp [8]), who used calculations given by Knipp and Teller [9]) for the ratio Z^*/Z of effective charge to nuclear charge. This quantity was then used in the standard Bethe-Bloch specific energy loss equation to compute the range-energy relations. Later, Papineau [10]) improved on this method by collecting the available experimental data concerning the effective charge Z^*. These data indicated that the nuclear charge was partially neutralized by captured electrons to considerably higher velocities than those assumed by Longchamp. The resulting range-energy relations agreed reasonably well with the data available at the time. Because the function Z^*/Z had to be extrapolated, however, the calculations were uncertain in the high-energy region. Livesey [11]) has also computed heavy ion range-energy relations for low energies, using a more complicated semi-empirical method to estimate Z^*.

The first impetus toward studying the width and taper properties of heavy ion tracks in nuclear emulsion came from the discovery of a heavy primary component in cosmic rays. Freier *et al.*[12]) observed this taper and calculated a "taper length", assuming that track width is proportional to specific energy loss $-\mathrm{d}E/\mathrm{d}x$, and that the thinning down is caused by capture of electrons as the ion slows down. Longchamp[13]) assumed, on the other hand, that track width is caused by δ rays produced along the path of the heavy ion. Some simple assumptions concerning this mechanism, together with his range-energy calculations [8]), enabled him to compute "taper lengths" which were in good agreement with the few pieces of experimental evidence available at the time. Recently, Skjeggestad [14]) and Bizetti and Della Corte [15]) have devised more elaborate semi-empirical theories based on Longchamp's δ ray assumption. Using automatic photometric measuring machines, both these groups have obtained experimental data concerning track width as a function of residual range for a few heavy ion species. Their theories result in a good quantitative fit to these data. Lozhkin [16]) has made similar measurements and obtained similar results. In addition, Lozhkin and Perfilov [17]), and Ostroumov and Yakovlev [18]) have applied these methods to actual identification of heavy ion species produced in reactions induced by high-energy protons.

2. Apparatus and Procedure

A schematic diagram of the apparatus used is shown in fig. 1. The analyzed beam from the heavy ion accelerator is first scattered at a small angle from a thin foil of gold or nickel to reduce the beam intensity. To vary the energy, foils or gas could be inserted in the beam path via either the foil changer or a gas range cell. Following this, the ions passed through two 0.005-inch collimating slits, which were mounted at either end of a laminated iron tube. The second of these slits was positioned near the edge of the flat-field region of the magnet, so that the ions were effectively shielded by the tube from most of the fringing field. To be detected, the ions must follow a circular trajectory of known radius and pass through a 0.006-inch detector slit located inside the flat-field region of the magnet. After passing out of the magnetic field, the ions were detected in a scintillation crystal spectrometer or in a nuclear emulsion plate from the plate magazine.

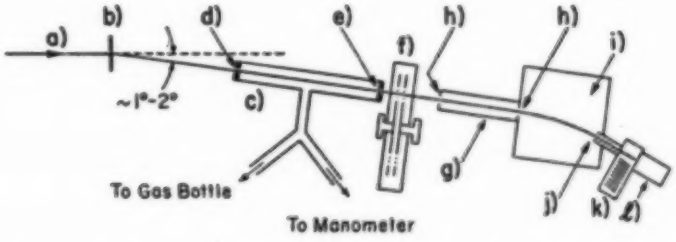

Fig. 1. Schematic diagram of apparatus. a) Analyzed heavy ion beam; b) thin scattering foil; c) gas range cell; d) 0.2 mil nickel foil window; e) 0.1 mil nickel foil window; f) foil changer; g) laminated iron magnetic shield; h) 5 mil collimating slits; i) magnet pole face; j) 6 mil exit slit; k) nuclear emulsion plate magazine; l) scintillation counter.

The procedure followed was to adjust the magnetic field to maximize the counting rate in the scintillation counter. This was accomplished with a counting rate meter and by observation of the pulse rate on an oscilloscope. One of the 16 emulsion plates in the magazine was then positioned in the path of the ions and exposed. From the counting rate observed, an exposure could be estimated which gave a density of tracks convenient for scanning.

The magnetic field was measured both with a commercial Nuclear Magnetic Resonance Gaussmeter and by measuring the voltage across a calibrated series resistance in the magnet circuit. In this manner, the field could be regulated and measured to an accuracy of a few tenths of a per cent. The radius of curvature ρ of the trajectory followed by ions passing through the centers of the collimating and detector slits was measured optically. Two independent methods of measurement were used. Furthermore, each time ρ was measured, two persons made a minimum of twelve independent observations to randomize measurement errors. The resulting random (statistical) standard deviation was in all cases 0.3 % or less. To guard against variations in ρ due

to accidental disalignment, etc., periodic measurements were made throughout the time span of the experiment. Each measurement of ρ was made either immediately before or after a run. The residual fringing field mentioned above results in a perturbation of the ion trajectories equivalent to an increase in this measured ρ of the order of 0.1 %. Several different charge states of the heavy ions could be observed as the magnetic field strength was varied. At higher energies, the maximum charge state was by far the most intense and could be easily identified. As the energy decreased to the point at which electron capture in the absorbing foils or ga became more important and range straggling more serious (about 3 or 4 MeV per amu), identification of charge state became more difficult, especially for the heavier ions. However, it was possible to identify and follow each of the various charge states by varying the magnetic field and referring to magnet calibration curves. In addition, requiring the range-energy relation to be continuous always made unambiguous determination of charge state possible. In a few instances for ions heavier than O^{16}, two or three charge states could come through the detector slit simultaneously. In this case, the different states appeared as clearly-defined range groups in the emulsion.

The emulsions used were all 50 μm thick on 1″ × 3″ glass plates, and were so oriented that the ions entered at a mean grazing angle of 5° to the emulsion surface. Most of the plates were electron-sensitive Ilford G-5 emulsions and came from several different emulsion batches. However, several of each of the other Ilford emulsions types were exposed for purposes of comparison. Because the emulsions were relatively thin, were exposed in vacuum, and were pumped on continuously through a liquid nitrogen cold trap for two to twelve hours prior to exposure, it is felt that they were close to completely dessicated at the time of exposure. Hence, the ranges measured correspond to an emulsion density of about 4.00 g/cm^3 [7, 19, 20].

The emulsions were processed within an hour or two after removal from the evacuated plate magazine. Processing consisted of 5 min in fresh, full-strength D-19 developer at 20° C and with continuous agitation, a 30—60 sec rinse in tap water, three fixation baths of 15, 30, and 60 min in fresh Kodak acid fixer, followed by a 2 to 6 hour wash in running tap water. Plates were processed in 4″ × $3\frac{1}{4}$″ × $2\frac{3}{4}$″ horizontal glass staining dishes, generally containing 16 to 18 plates each.

3. Range Measurements

The plates were scanned and ranges measured using microprojectors[21] at 200×, 500× and 1000× magnification, depending on the track lengths involved. At the beginning of each day's scanning, the magnifications of the projectors were calibrated with a Leitz stage micrometer. Magnifications over

the fields of view were uniform and could be reset to an accuracy of better than $\pm 0.3\,\%$. Six persons including the authors were engaged in scanning plates, so that data for any given range-energy curve was obtained by at least three persons, and about half of the plates were scanned twice by different persons. By this means, systematic bias of any of the scanners could be detected and eliminated. Tracks which underwent obvious nuclear scatters or reactions were excluded. Measurements were made from the beginning to the end of the photographic image of the track, as judged by the scanners. Since the object of this work was to obtain range-energy relations which can be used most directly in nuclear reaction studies with emulsions, no corrections have been made to the measured ranges for such effects as finite grain size, emulsion density, etc. (However, a 0.4 % correction for the 5° dip angle was made). To obtain the range-energy relations for the eight heavy ions, about 225 plates were scanned and some 100 000 tracks measured.

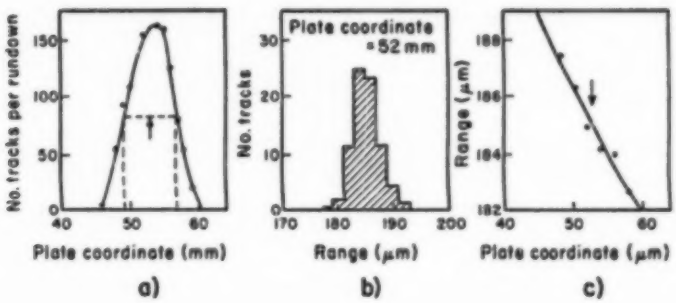

Fig. 2. Steps in determining the range corresponding to the mean radius of curvature.
a) Track density distribution along the horizontal dimension of the plate.
b) Range spectrum of a typical rundown. The resolution (full width at half maximum) has a representative value of 3 %.
c) Typical range gradient along the horizontal plate dimension. The coordinate of the center of the track density distribution (fig. 2a) is the coordinate of the range corresponding to the mean radius of curvature.

Because the finite-width detector slit accepts particles following trajectories having a small range of radii of curvature, there will be an energy gradient across the slit. This appears as a range gradient across the length of the plate. Hence, the following procedure was followed to find the range corresponding to the mean radius of curvature ρ. A track density distribution (number of tracks per vertical traverse or "rundown" on the microprojector stage) was obtained over the horizontal plate dimension (fig. 2a). The centre of this distribution was defined as the midpoint of the full width at half maximum. Tracks were then measured in 6 rundowns of width 0.6 mm or less, obtaining about 50 to 100 tracks in each rundown. The range spectrum of a typical rundown is shown in fig. 2b. From these, range is plotted as a function of horizontal plate coordinate, displaying the range gradient over the length of

the plate (fig. 2c). Assuming that the centre of the track density distribution corresponds to the measured radius of curvature, the appropriate range may be selected from this curve. Such a procedure was followed for all but a few plates corresponding to lower energies. The track density on these plates was too low; a range spectrum of all tracks on the plate was therefore taken, and the centre of this spectrum selected as the appropriate range. This method was checked on more dense plates and found to give essentially identical results.

4. Range-Energy Results

The final range-energy relations for the eight heavy ions are displayed in fig. 3. In order to show all the data on approximately the same scale, the

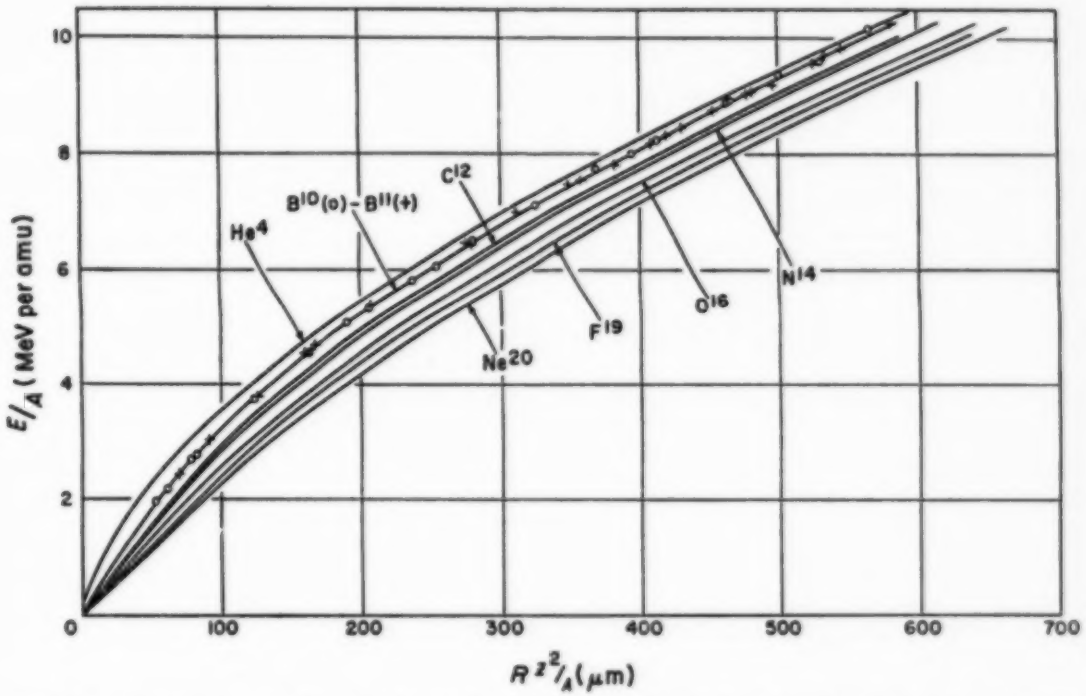

Fig. 3. Range-energy relations for heavy ions in dessicated Ilford G-5 emulsion. As a typical case, experimental points are shown for B^{10}(○) and B^{11}(+) ions.

ranges have been multiplied by Z^2/A for the ion. If it were not for the fact that the effective ion charge Z^* is less than the nuclear charge Z over much of the range of all ions except He^4, the curves would all coincide. Experimental points are shown for B^{10}—B^{11} and the best fits to the data for all ions are given by the solid curves. The scatter of experimental points appears about the same for the ions other than B^{10}—B^{11}, but these have been omitted from fig. 3 to avoid confusion. In table 1 are compiled range-energy values taken from the smooth curves of fig. 3. Exposures of Ilford K-5, C-2, E-1, G-0, K-0, K minus 1, and K minus 2 emulsions to higher-energy ions of several

species gave results which did not differ significantly from those for G-5 emulsion.

TABLE 1

Range-energy relations for heavy ions in dessicated Ilford G-5 emulsion. Values taken from smooth curves through experimental points.

E/A (MeV per amu)	Range (μm)							
	He^4	B^{10}	B^{11}	C^{12}	N^{14}	O^{16}	F^{19}	Ne^{20}
0	0	0	0	0	0	0	0	0
0.5	6.7	5.0	5.5	5.4	4.7	4.8	5.4	4.9
1.0	15.3	10.2	11.3	10.5	9.3	9.5	9.9	9.2
1.5	26.9	15.9	17.5	15.6	14.1	14.2	14.1	13.4
2.0	40.9	21.7	23.9	21.2	19.1	19.2	18.8	17.6
2.5	57.5	28.6	31.4	27.2	24.5	24.5	23.9	22.2
3.0	76.6	36.5	40.2	33.9	30.6	30.2	29.3	27.0
3.5	98.3	45.0	49.5	41.4	37.2	36.0	35.1	32.3
4.0	122.2	54.1	59.5	49.6	44.5	42.4	41.5	37.8
4.5	147.0	64.0	70.4	58.3	52.2	49.2	48.4	43.8
5.0	174.9	74.8	82.3	67.5	60.4	56.7	55.8	50.1
5.5	204.3	86.6	95.3	77.7	68.9	64.5	63.6	56.7
6.0	235.1	99.3	109.3	88.4	78.0	72.6	71.5	63.5
6.5	267.9	112.8	124.1	99.7	87.7	81.2	79.6	70.6
7.0	302.6	126.7	139.3	111.5	98.1	90.2	88.0	77.9
7.5	339.3	141.3	155.5	123.7	108.9	99.7	96.7	85.7
8.0	377.8	156.8	172.5	136.8	119.9	109.5	106.0	93.8
8.5	418.4	173.1	190.4	150.6	131.3	120.0	115.9	102.1
9.0	461.4	189.9	208.9	164.7	143.0	131.2	126.5	110.9
9.5	506.0	206.6	227.3	179.1	155.4	142.8	137.5	120.0
10.0	552.6	223.9	246.3	194.0	168.3	154.8	148.7	129.4

Estimated errors in measuring ρ and the magnetic field strength are both about 0.3 %. Ranges greater than 50—60 μm could be determined with a precision of ± 0.5 % or better. However, due to possible fluctuations in the composition and density of the emulsions [19]), it is felt that an accuracy of ± 1 % should be more realistically assigned to the ranges. Overall accuracy of the smoothed range-energy relations is then estimated to be ± 1 % in both energy and range. In the region below about 2 MeV per amu, the errors could become somewhat larger than this, due to the very short tracks and the low track densities on the plates involved.

The ranges calculated by Papineau [10]) for Ilford C-2 emulsion of unspecified density are systematically a few per cent greater than those in table 1. In a later calculation, Papineau [22]) made a new extrapolation of the effective charge data, which resulted in ranges slightly less than those reported here. These deviations, although systematic, appear with one exception to lie just within the combination of our experimental error and that estimated for the α and proton range-energy relations on which Papineau's calculations are based. The exception is O^{16}, where the deviation is just slightly greater than the estimated combination of experimental errors.

As would be expected, a comparison with the recent results of Heckman *et al.*[7]) for emulsion of density 3.815 g/cm^3 indicates that at the higher energies, ranges in the less dense emulsion are in general systematically somewhat greater. In the case of the range-energy relation for He^4 ions, accurate data for dessicated emulsion is available for comparison. Below 5 MeV per amu, the data of Steigert, Toops and Sampson in Kodak NTA emulsion [23]) and Rotblat in Ilford C-2 emulsion [24]) agree to well within the estimated experimental error. Rotblat's smoothed curve has been used to fit our data in this region. For higher energies, Rotblat's proton range-energy curve [24]) is almost exactly parallel to the best fit of the present experimental data for He^4.

5. Track Width Measurements

Tracks on a number of range-energy plates were examined in further detail to obtain information on the variation of track width with residual range or energy. Two techniques were employed to perform the width measurements. A high-resolution microprojector was used at 2540× magnification and width measured as a function of residual range at 5μm intervals along the tracks. As in the range measurements, the magnification was calibrated before each use with a stage micrometer. These measurements were repeated using a binocular microscope equipped with two special filar eyepieces oriented at right angles, and a high-resolution oil-immersion objective (n.a. 1.40). The magnification achieved by this means was about 1400× and the resolution was considerably improved. As in the range measurements, magnification over the field of view of the microprojector was uniform. In the case of the binocular microscope, width measurements were carried out only in the central region of the field of view, where the magnification was found to be uniform.

Because of the relatively large grain size of G-5 emulsion and the copious production of δ rays along heavy ion tracks, the track profile is rather irregular, with many protrusions and indentations in the generally tapering shape. The scanners were instructed for these measurements to determine the exact width of the track at 5μm intervals. With the microprojector, this could be done to a precision of about 0.2μm and with the binocular microscope to about 0.06μm. The results of width measurements on a large number of tracks of the same species were then averaged to smooth out these irregularities in the track profile.

6. Track Width Results

Simple qualitative observations of heavy ion tracks in emulsions of various sensitivity and grain size confirmed the conclusions reached similarly by others [7, 16]). Track width seems to be dependent almost entirely on production of a solid core of δ rays along the ion path. It is only for the extremely electron-

insensitive emulsions (e.g., K-0, K minus 1, and K minus 2) that the tracks appear to approach a constant width. Only for the least sensitive emulsions (e.g., K minus 2) can individual grains be counted in a heavy ion track, and here the grain density tends to be qualitatively proportional to specific energy loss $-\mathrm{d}E/\mathrm{d}x$.

Results of the track width measurements are shown in figs. 4 and 5 as a function of residual range. Fig. 4 gives the best fits to data for ions between He^4 and Ne^{20} inclusive, in G-5 emulsion. The typical scatter of experimental points is shown for the case of N^{14} ions in fig. 5. This figure also indicates the difference in the width-residual range relations for G-5 and K-5 emulsions.

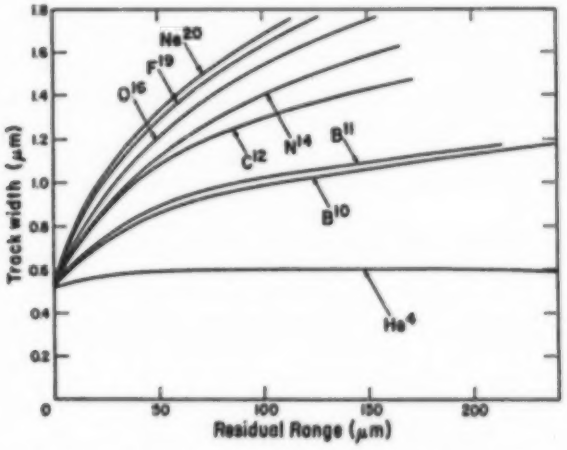

Fig. 4. Track width as a function of residual range for various heavy ions in dessicated Ilford G-5 emulsion. Curves shown are best fits to the experimental data.

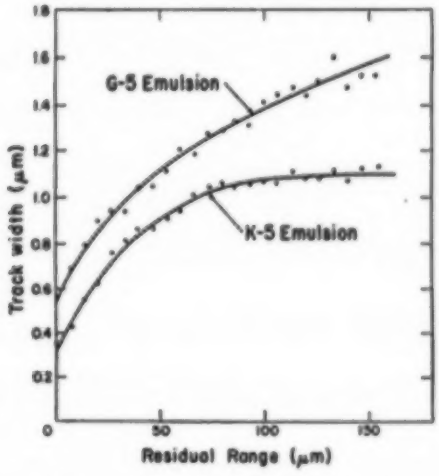

Fig. 5. Track width as a function of residual range for N^{14} ions in dessicated G-5 and K-5 emulsion. Experimental points are shown.

Each of the curves of fig. 4 is based on measurements of a minimum of 50 tracks. To eliminate possible systematic errors introduced by the plate scanners or by differences in composition of emulsion batches, measurements were made

on a total of 240 O^{16} tracks of about the same range. These tracks were distributed on four separate plates from two different emulsion batches and were scanned by five persons. Similarly, about 50 N^{14} tracks in plates from two other emulsion batches were measured and compared. No significant or noticable differences in the results appeared due to either scanner bias or emulsion batch composition. In addition, the possible effects of non-uniform development through the thickness of the emulsion were investigated by measuring about 300 C^{12} tracks of various ranges on different emulsion plates. The longest-range C^{12} tracks (about 200μm) will penetrate the emulsion to a considerable depth, whereas short tracks will lie close to the surface over their entire range. If non-uniform development effects were significant, the end of a long track should be less strongly developed and therefore thinner than the end of a short track. No such effects could be detected in this group of measurements. It was expected that the relatively thin emulsions used and the harsh development procedure would eliminate this source of error.

It may be noted on fig. 4 that there is apparently a small mass effect causing a separation of the B^{10} and B^{11} width vs. residual range curves. Although this difference may not be experimentally significant, it is systematic. However, when track width is graphed as a function of ion velocity (either MeV per amu or β), the B^{10} and B^{11} curves become indistinguishable.

The results reported here are in qualitative agreement with the experimental measurements and semi-empirical models of both Skjeggestad [14]) and Bizetti and Della Corte [15]). The operational definition of track width used by both of these groups differs somewhat from that of the present work. They have both employed photometric measuring machines, which effectively average the track width over cells of length 10μm or so.

The emulsion exposures involved in this work were made possible by the efforts and cooperation of the operators and staff of the Yale Heavy Ion Linear Accelerator. Their efforts in obtaining usable intensities of the more difficult ion beams were especially appreciated. The cooperation of Mr. E. Newman, Jr. was invaluable in carrying out the experimental work. We are grateful to Dr. L. C. Northcliffe for many valuable discussions, as well as participation in early phases of the work and construction of some of the equipment used. For bearing the brunt of the tedious job of plate scanning, we are greatly indebted to our staff of plate scanners.

References

1) P. Roll and F. E. Steigert, Bull. Am. Phys. Soc. **4** (1959) 109;
P. G. Roll and F. E. Steigert, Bull. Am. Phys. Soc. **4** (1959) 51;
P. G. Roll, F. E. Steigert and A. M. Smith, Bull. Am. Phys. Soc. **4** (1959) 270
2) P. Cuer and J. P. Longchamp, Comptes rend. **232** (1951) 1824
3) W. H. Barkas, Phys. Rev. **89** (1953) 1019

4) H. L. Reynolds and A. Zucker, Phys. Rev. **96** (1954) 393
5) R. Chaminade, M. Crut, H. Faraggi, A. Garin-Bonnet, J. Olkowsky and A. Papineau, Comptes rend. **242** (1956) 105
6) D. M. Parfanovitch, N. V. Rabin and A. M. Semchinova, Sov. Phys. JETP **4** (1957) 99
7) H. H. Heckman, B. L. Perkins, W. G. Simon, F. M. Smith and W. H. Barkas, University of California Radiation Laboratory Report UCRL-8763 (1959)
8) J. P. Longchamp, J. Phys. Rad. **14** (1953) 89
9) J. K. Knipp and E. Teller, Phys. Rev. **59** (1941) 659
10) A. Papineau, Comptes rend. **242** (1956) 2933
11) D. L. Livesey, Can. J. Phys. **34** (1956) 203
12) P. Freier, E. J. Lofgren, E. P. Ney, F. Oppenheimer, H. L. Bradt and B. Peters, Phys. Rev. **74** (1948) 1818
13) J. P. Longchamp, J. Phys. Rad. **14** (1953) 433
14) O. Skjeggestad, Nuovo Cimento **8** (1958) 927
15) P. G. Bizetti and M. Della Corte, Nuovo Cimento **11** (1959) 317
16) O. V. Lozhkin, Sov. Phys. JETP **5** (1957) 293
17) O. V. Lozhkin and N. A. Perfilov, Sov. Phys. JETP **4** (1957) 790
18) V. I. Ostroumov and Yu. G. Yakovlev, JETP **35** (1958) 1358
19) W. H. Barkas, P. H. Barrett, P. Cuer, H. H. Heckman, F. M. Smith and H. K. Ticho, Nuovo Cimento **8** (1958) 185
20) W. H. Barkas, Nuovo Cimento **8** (1958) 201
21) H. S. Plendl and F. E. Steigert, Rev. Sci. Inst. **27** (1956) 239
22) A. Papineau, Private Communication
23) F. E. Steigert, E. C. Toops and M. B. Sampson, Phys. Rev. **83** (1951) 474
24) J. Rotblat, Nature **167** (1951) 550

1.B:1.C

Nuclear Physics **16** (1960) 545—567; © *North-Holland Publishing Co., Amsterdam*

Not to be reproduced by photoprint or microfilm without written permission from the publisher

NUCLEAR SHELL MODEL: HARTREE-FOCK APPROXIMATION WITH GAMMEL-THALER TWO-NUCLEON POTENTIAL

G. E. TAUBER †

Department of Physics, Western Reserve University, Cleveland, Ohio

and

TA-YOU WU

Division of Pure Physics, National Research Council, Ottawa, Canada

Received 25 November 1959

Abstract: To investigate how good or bad the Hartree-Fock approximation is for the atomic nuclei, a calculation has been carried out with the phenomenological two-nucleon potential $V(\mathbf{r}_i-\mathbf{r}_j)$ of Gammel-Thaler containing a repulsive core, a central, a tensor and an $\mathbf{L}\cdot\mathbf{S}$ interaction. Harmonic oscillator wave functions are used for the one-nucleon wave functions. The parameters in the wave functions and a multiplicative parameter in $V(\mathbf{r}_i-\mathbf{r}_j)$ are determined from O^{16} by the variational principle and the empirical total energy. These (now fixed) parameters are then used to calculate the energy of the configuration $(1s)_p^2\,(1p)_p^5\,(1s)_n^2\,(1p)_n^6$ of O^{15}. It is found that the $\mathbf{L}\cdot\mathbf{S}$ term in $V(\mathbf{r}_i-\mathbf{r}_j)$ gives rise to a doublet $E(J=\frac{3}{2})-E(J=\frac{1}{2})=+31.6$ MeV. The total binding energy is $E(J=\frac{1}{2})=-114.8$ MeV compared with the empirical value -111.97 MeV. The sign of this doublet corresponds, on the picture of the individual nucleon moving in an effective central field and possessing an $\mathbf{l}_i\cdot\mathbf{s}_i$ interaction, to a sign of $\mathbf{l}_i\cdot\mathbf{s}_i$ opposite to that of the electron, and is in agreement with the fundamental hypothesis of the nuclear shell model of Mayer and of Jensen *et al.* The magnitude of the doublet, however, is too large, by a factor of about 5. These results are discussed.

1. Introduction

Considerable work has recently appeared on the problem of nuclear models. Brueckner and others [1]) have suggested and developed a general scheme of treating the many-nucleon system starting with two-nucleon interactions. Actual calculations for a finite nucleus seem, however, very lengthy, if not difficult [2]). The familiar and much simpler Hartree-Fock method may be regarded as a first approximation to this general scheme. Hence it is of interest to investigate, by actual calculations for specific nuclei, how satisfactory or otherwise the Hartree-Fock method is.

In a previous work, the present authors [3]) have employed the Hartree-Fock method, using a nucleon-nucleon potential $V(|\mathbf{r}_i-\mathbf{r}_j|)$ containing only central fields and no repulsive core. The procedure employed is i) to adjust the

† This work was supported in part by the Air Force Office of Scientific Research, Contract AF 18 (603)—61.

"strength" parameter V_0 in $V(r_{ij})$ and the parameters in the (harmonic oscillator type) one-nucleon wave functions by the empirical total binding energy of O^{16} and the (Ritz) variational method, and ii) to use the parameters so determined to calculate the total binding energies of O^{15}, O^{17}. The agreement is not very satisfactory. One obvious objection to that procedure is that the two-nucleon potential $V(r_{ij})$ employed does not have the repulsive core, tensor and $\mathbf{L}\cdot\mathbf{S}$ components that have been found necessary to account for the two-nucleon scattering and polarization data. In view of this, the result of the previous work does not furnish a critical test of the Hartree-Fock approximation.

More recently, phenomenological two-nucleon potentials to account for all the available data on the two-nucleon have been available [4]). These potentials contain a repulsive core, a central field, a tensor field and an $\mathbf{L}\cdot\mathbf{S}$ term, all depending on the spin and the isobaric spin of the state. The presence of an $\mathbf{L}\cdot\mathbf{S}$ interaction in $V(\mathbf{r}_i-\mathbf{r}_j)$ is of special interest. It has been found by Kisslinger [5]) and by Nigam and Sundaresan [6]) that the spin-orbit interaction in a nucleus arising from tensor forces in the two-nucleon potential comes out to be too small according to the theory of Brueckner. More recently Nigam and Sundaresan [7]) † found that with an $\mathbf{L}\cdot\mathbf{S}$ interaction of the Signell-Marshak potential in the Brueckner theory, there results a spin-orbit splitting of the nuclear energy levels of the correct sign, although the splitting is small compared with what is needed in the shell model of Mayer, Jensen *et al.* Since the Hartree-Fock approximation may be regarded as a first approximation in the scheme of Brueckner, one may expect to obtain a corresponding spin-orbit splitting of the nuclear energy, and hence to support the fundamental hypothesis of the nuclear shell model that the individual nucleon has a spin-orbit interaction in addition to an effective central potential.

Thus the purpose of the present work is to extend the previous work on the Hartree-Fock method to the case where the two-nucleon potential is the most recent one of Gammel-Thaler [4]). Actual calculations are carried out for the O^{16}, O^{15} nuclei, to see how satisfactory or otherwise the Hartree-Fock approximation is, and to find out the contribution of $\mathbf{L}\cdot\mathbf{S}$ in $V(\mathbf{r}_i-\mathbf{r}_j)$ to the "spin-orbit" interaction in $V(r_i)$ that is assumed and is so important in the shell model.

The Hamiltonian of the nuclear system is

$$H=\sum H_0(i)+\sum_{i\neq j}V_{ij}+\sum_{i\neq j}\frac{e^2}{r_{ij}} \tag{1.1}$$

where $H_0(i)$ is the one-particle Hamiltonian and represents the kinetic energy

$$H_0(i)=-\frac{\hbar^2}{2M}\nabla_i^2, \tag{1.2}$$

† These authors inform the writers that their eq. (11) and the figures in their table 1 should be multiplied by a factor 4.

V_{ij} the nucleon-nucleon interaction and e^2/r_{ij} the Coulomb interaction between protons. The two-body potential V_{ij} is infinite if $r(r = r_{ij})$ is less than r_0, the size of the core, and is a linear sum of central, tensor and spin-orbit interaction if $r > r_0$. Thus, we have

$$V_{ij} = \infty, \quad \text{for} \quad r_{ij} \leqq r_0,$$
$$V_{ij} = V_{ij}^{C}+V_{ij}^{T}+V_{ij}^{LS}, \quad r_{ij} \geqq r_0. \tag{1.3}$$

The central potential is taken to be a linear sum of the various spin dependent interactions and given by

$$V_{ij}^{C} = [a_0+a_\sigma(\boldsymbol{\sigma}_i \cdot \boldsymbol{\sigma}_j)+a_\tau(\boldsymbol{\tau}_i \cdot \boldsymbol{\tau}_j)+a_{\sigma\tau}(\boldsymbol{\sigma}_i \cdot \boldsymbol{\sigma}_j)(\boldsymbol{\tau}_i \cdot \boldsymbol{\tau}_j)]J^{C}(r_{ij}) \tag{1.4}$$

where $\boldsymbol{\sigma}$ and $\boldsymbol{\tau}$ indicate the spin and isobaric spin operators respectively, and a_0 etc. are the strengths of the various interactions to be determined from the two-nucleon data. $J^{C}(r)$ represents the central potential for which we take the Yukawa type

$$J^{C}(r) = \frac{r_C}{r} \exp\left(-\frac{r}{r_C}\right) \tag{1.4a}$$

where r_C is the range of the central force.

The corresponding form for the tensor potential V_{ij}^{T} is given by

$$V_{ij}^{T} = [b_0+b_\tau(\boldsymbol{\tau}_1 \cdot \boldsymbol{\tau}_2)]J^{T}(r)S_{ij} \tag{1.5}$$

where S_{ij} is the tensor operator

$$S_{ij} = \frac{3}{r^2}(\boldsymbol{\sigma}_i \cdot \mathbf{r})(\boldsymbol{\sigma}_j \cdot \mathbf{r})-(\boldsymbol{\sigma}_i \cdot \boldsymbol{\sigma}_j), \tag{1.6}$$

and the radial dependence $J^{T}(r)$ is again given by an expression of the form (1.4a) with r_C replaced by r_T, the range of the tensor force. In (1.5) the operator $(\boldsymbol{\sigma}_i \cdot \boldsymbol{\sigma}_j)$ does not appear, since it is known that $PS_{ij} = S_{ij}P = S_{ij}$ where $P = \frac{1}{2}[1+(\boldsymbol{\sigma}_i \cdot \boldsymbol{\sigma}_j)]$. The b's again are found from the two nucleon data.

Finally for the spin orbit interaction V_{ij}^{LS} we take

$$V_{ij}^{LS} = [c_0+c_\tau(\boldsymbol{\tau}_i \cdot \boldsymbol{\tau}_j)]J^{LS}(r)\mathbf{L} \cdot \mathbf{S} \tag{1.7}$$

where $\mathbf{L} \cdot \mathbf{S}$ is the spin-orbit operator

$$\mathbf{L} \cdot \mathbf{S} = \tfrac{1}{2}[(\mathbf{r}_i-\mathbf{r}_j) \times (\mathbf{p}_i-\mathbf{p}_j)] \cdot (\boldsymbol{\sigma}_i+\boldsymbol{\sigma}_j), \tag{1.8}$$

and $J^{LS}(r_{ij})$ again of the Yukawa type (1.4a) with r_C replaced by r_{LS}, the corresponding range for the spin-orbit interaction. As $(\boldsymbol{\sigma}_i \cdot \boldsymbol{\sigma}_j)(\boldsymbol{\sigma}_i+\boldsymbol{\sigma}_j) = \boldsymbol{\sigma}_i+\boldsymbol{\sigma}_j$, only c_0 and c_τ appear in (1.7), to be determined by the two-nucleon data.

The total binding energy E is then given by

$$E = \int \Psi^* H \Psi \mathrm{d}\tau \tag{1.9}$$

where, in the case of a closed shell configuration (such as O^{16}), Ψ is a Slater determinantal wave function Φ multiplied by a correlation function F:

$$\Psi = \Phi F = \Phi \prod_{i \neq j} f(r_{ij}). \tag{1.10}$$

The determinant Φ is formed of the single-nucleon central-field wave functions which are in turn a product of a space part $\phi_{nlm}(r_i)$, a spin part α_i or β_i, and an isospin part ν_i or π_i (for neutron and proton state respectively). We shall take, following Dąbrowski [8]),

$$f(r) = \begin{cases} 0 & , \quad r \leqq r_0, \\ 1-\exp[-\beta\{(r-r_0)^2-1\}], & r \geqq r_0. \end{cases} \tag{1.11}$$

For an unclosed shell (such as O^{15}) Ψ in (1.9) is a linear combination of (six) Slater determinants Φ_A each corresponding to one (m_{li}, m_{si}) state of the missing nucleon from the otherwise closed shell,

$$\Psi = \sum c_A \Psi_A = \sum_A c_A \Phi_A \prod_{i \neq j} f(r_{ij}). \tag{1.12}$$

The energies are given by the roots of

$$|H_{AB} - E\delta_{AB}| = 0 \tag{1.13}$$

where

$$H_{AB} = \int \Psi_A^* H \Psi_B \mathrm{d}\tau. \tag{1.14}$$

The effect of the introduction of F in (1.10) has been studied by a number of authors [9]). Applying (1.2) on (1.10), one gets three terms

$$-\frac{\hbar^2}{2M}\langle(\Phi^*\nabla_i^2\Phi)F^2\rangle + \frac{\hbar^2}{2M}\langle\Phi^*\Phi(\nabla_i F)^2\rangle - \frac{\hbar^2}{2M}(\Phi^*\Phi\nabla F \cdot \mathrm{d}\mathbf{S}). \tag{1.15}$$

If one now applies the cluster development of Ursell in statistical mechanics, the first order approximation leads to an expression for the energy of the form

$$E = T_0 + \langle\Phi\left|\frac{\hbar^2}{2M}\left(\frac{\mathrm{d}f}{\mathrm{d}r_{ij}}\right)^2\right|\Phi\rangle + \bar{V} + \bar{C} \tag{1.16}$$

+ higher order terms in the ratio of total excluded volume to total volume of nuclei, where T_0 is the kinetic energy calculated with the help of the Slater determinant function Φ; the second term in (1.16), which will be denoted by $\bar{K}$ in sections 3, 4 contains the increase of the kinetic energy due to the curvature of the correlation function, while the third term is the effective potential energy (neglecting the non-orthogonality produced by the correlation function)

$$\bar{V} = \langle\Phi|\sum f^2(r_{ij})V(r_{ij})|\Phi\rangle;$$

$\bar{C}$ is the Coulomb interaction (1.17)

$$\bar{C} = \langle\Phi|\sum f^2(r_{ij})\frac{e^2}{r_{ij}}|\Phi\rangle.$$

The constants a_0 etc. entering in the expressions for the central, tensor and spin-orbit interaction are to be determined from the two-nucleon data. Gammel and Thaler [4]) have used a general two-body interaction of the form (1.3) and obtained values for the constants summarized in table 1. From (1.4) one finds for the various states the potential

$$\begin{aligned} &\text{Triplet even} \quad a_0+a_\sigma-3a_\tau-3a_{\sigma\tau},\\ &\text{Triplet odd} \quad a_0+a_\sigma+a_\tau+a_{\sigma\tau},\\ &\text{Singlet even} \quad a_0-3a_\sigma+a_\tau-3a_{\sigma\tau},\\ &\text{Singlet odd} \quad a_0-3a_\sigma-3a_\tau+9a_{\sigma\tau}. \end{aligned} \tag{1.18}$$

If we assume that the ranges are the same in the central potential for singlet, triplet, even and odd states, we can solve these equations and the corresponding ones for the tensor and spin-orbit interaction in terms of the constants listed in

TABLE 1

Constants for two-body interactions of Gammel-Thaler

	Potential constants in MeV			
	Triplet even	Triplet odd	Singlet even	Singlet odd
Central potential	− 100.7	0	−425.5	100
Tensor potential	− 257	22		
Spin-orbit potential	−5000	−7317.5		
Core r_0 in 10^{-13} cm	0.4	0.41	0.4	0.5
	Reciprocal ranges $1/r$ in 10^{13} cm^{-1}			
Central potential	1.23	−	1.45	1.0
Tensor potential	1.203	0.8		
Spin orbit potential	3.7	3.7		

TABLE 2

Constants for two-body interactions in (1.4), (1.5), (1.7) employed in the present work

	Potential in MeV; Core radius $r_0 = 0.4\times10^{-13}$ cm	Inverse range in 10^{13} cm^{-1}
Central potential	$a_0 = -92.41$, $a_\sigma = 67.24$, $a_\tau = -13.96$, $a_{\sigma\tau} = 39.14$	1.25
Tensor potential	$b_0 = -48$ $\quad b_\tau = 70$	1
Spin-orbit potential	$c_0 = -6738$ $\quad c_\tau = -579.4$	3.7

table 1. The result is shown in table 2 together with the chosen values of the various ranges. The only parameters still to be determined are the range of the radial wave function and the constant entering in the correlation function f.

These are to be determined by the variational principle.

$$\delta E = \delta \int \Psi^* H \Psi d\tau = 0. \tag{1.19}$$

In the present work, we use harmonic oscillator wave functions and determine the parameter in these functions by (1.19). Furthermore we shall assume a common multiplicative factor for all the potential constants in table 2, and determine this factor by the requirement that the total energy E of the nucleus be equal to the empirical value E_0 of the binding energy of the nucleus O^{16}

$$\int \Psi^* H \Psi d\tau = E_0 \quad \text{for} \quad O^{16}. \tag{1.19a}$$

The parameters so determined are applied to O^{15} as a test of the Hartree-Fock approximation [3]).

In Section 2 of this paper we develop the general expressions for the matrix elements H_{ij} involving central, tensor and spin-orbit interaction, kinetic energy and Coulomb energy. In Section 3, we apply these results to O^{16} and the parameters in the wave function are determined by the variational principle. In Section 4, these parameters are applied to O^{15}. From the secular equation, of order 6×6, corresponding to the six wave functions of the $(1s)_\nu^2(1p)_\nu^5$ $(1s)_\pi^2\,(1p)_\pi^6$ configuration of the O^{15} nucleus, the binding energy and the $^2P_{\frac{3}{2}}-{}^2P_{\frac{1}{2}}$ separation are obtained. The results are discussed. In the appendices, the relevant integrals for the various potentials are given explicitly.

To obtain the average central potential and effective spin-orbit interaction for a single nucleon, one would write down the Hartree-Fock equations for the various nucleon states as in our previous work [3]), and instead of solving these integral differential equations we shall calculate the approximate effective potentials for the various states by means of the harmonic oscillator wave functions determined above. This will be reported in a subsequent paper.

2. Matrix Elements

For the general interaction given by (1.1) we shall now calculate the matrix elements. For O^{15}, we have six wave functions Φ_A in (1.12), each being a 15×15 determinant multiplied by the correlation function F of (1.10). These six wave functions are given in (4.1) below. The diagonal element of the potential energy V of state Ψ_A is

$$\langle A|V|A\rangle = \tfrac{1}{2}\sum_{n\neq k}\int\int \psi_n^*(1)\psi_k^*(2)V_{12}[\psi_n(1)\psi_k(2)-\psi_n(2)\psi_k(1)]d\tau_1 d\tau_2 \tag{2.1}$$

where $\psi_n(1)$ represents the one-particle wave function and includes the spatial wave function $\phi_{nlm}(r_1)$ the spin α_1 or β_1 and isospin ν_1 or π_1 wave function.

Here n stands for the totality of all the quantum numbers. The non-diagonal matrix elements are given by

$$\langle A|V|B\rangle = \sum_n \int\int \psi_n^*(1)\psi_k^*(2)V_{12}[\psi_n(1)\psi_p(2)-\psi_n(2)\psi_p(1)]d\tau_1 d\tau_2. \quad (2.2)$$

In (2.2) k, p stand for the totality of the quantum numbers of the missing neutron in state B and A respectively. Thus for $\langle A|V|B\rangle$: $k = \beta$, p0 and $p = \beta$, p$\bar{1}$. See (4.1).

We shall now consider the various types of interactions, central, tensor and spin-orbit interactions (see section 1) separately.

2.1. CENTRAL INTERACTION

As the central interaction V^C is diagonal in both $M_l = \sum m_{li}$ and $M_s = \sum m_{si}$, it follows that V^C has no non-diagonal elements with respect to the six wave-functions in (4.1). For diagonal elements, summation over the isospin coordinate permits one to separate the matrix element into three parts, corresponding to neutron-neutron (ν, ν), neutron-proton (ν, π) and proton-proton (π, π) energies according to

$$\bar{V}^C = \bar{V}^C_{\nu\nu} + \bar{V}^C_{\nu\pi} + \bar{V}^C_{\pi\pi} \quad (2.3)$$

for which the various contributions are given by

$$\bar{V}^C_{\nu\nu} = \tfrac{1}{2}\sum_n^\nu \sum_{\substack{m \\ n\neq m}}^\nu \int\int \chi_n^*(1)\chi_m^*(2)V^C_{\nu\nu}(1,2)[\chi_n(1)\chi_m(2)-\chi_n(2)\chi_m(1)]d\tau_1 d\tau_2, \quad (2.4a)$$

a similar expression for $\bar{V}^C_{\pi\pi}$ obtained from (2.4a) by replacing ν by π, and

$$\begin{aligned}\bar{V}^C_{\nu\pi} = {} & \textstyle\sum_n^\nu \sum_m^\nu \int\int \chi_n^*(1)\chi_m^*(2)V^C_{\nu\pi}(1,2)\chi_n(1)\chi_m(2)d\tau_1 d\tau_2 \\ & - \textstyle\sum_n^\nu \sum_m^\nu \int\int \chi_n^*(1)\chi_m^*(2)\bar{V}^C_{\nu\pi}(1,2)\chi_n(2)\chi_m(1)d\tau_1 d\tau_2.\end{aligned} \quad (2.4b)$$

Here χ represents the product of the space and spin part of the wave function and the symbol $\sum^\nu$, $\sum^\pi$ represents summations extending over the occupied neutron and proton states respectively. The effective potential operators in (2.4) are given by

$$V^C_{\nu\nu}(1,2) = V^C_{\pi\pi}(1,2) = [a_0 + a_\tau + (a_\sigma + a_{\sigma\tau})(\boldsymbol{\sigma}_1 \cdot \boldsymbol{\sigma}_2)]J^C(r_{12}), \quad (2.5a)$$

$$V^C_{\nu\pi}(1,2) = [a_0 - a_\tau + (a_\sigma - a_{\sigma\tau})(\boldsymbol{\sigma}_1 \cdot \boldsymbol{\sigma}_2)]J^C(r_{12}), \quad (2.5b)$$

$$\bar{V}^C_{\nu\pi}(1,2) = 2[a_\tau + a_{\sigma\tau}(\boldsymbol{\sigma}_1 \cdot \boldsymbol{\sigma}_2)]J^C(r_{12}). \quad (2.5c)$$

One finds after carrying out the summations over spin coordinate

$$\begin{aligned}\bar{V}^C_{\nu\nu} = {} & \tfrac{1}{2}[(\nu\alpha|J^C|\nu\alpha)_0 + (\nu\beta|J^C|\nu\beta)_0 - (\nu\alpha|J^C|\nu\alpha)_e - (\nu\beta|J^C|\nu\beta)_e](a_0 + a_\sigma + a_\tau + a_{\sigma\tau}) \\ & + (\nu\alpha|J^C|\nu\beta)_0(a_\sigma + a_\tau - a_\sigma - a_{\sigma\tau}) - 2(\nu\alpha|J^C|\nu\beta)_e(a_\sigma + a_{\sigma\tau}),\end{aligned} \quad (2.6a)$$

a similar expression for $V^C_{\pi\pi}$ on replacing ν's by π's in (2.6a), and

$$\begin{aligned} V^C_{\nu\pi} = {} & [(\nu\alpha|J^C|\pi\alpha)_o + (\nu\beta|J^C|\pi\beta)_o](a_0 - a_\tau + a_\sigma - a_{\sigma\tau}) \\ & + [(\nu\alpha|J^C|\pi\beta)_o + (\nu\beta|J^C|\pi\alpha)_o](a_0 - a_\tau - a_\sigma + a_{\sigma\tau}) \\ & - [(\nu\alpha|J^C|\pi\alpha)_e + (\nu\beta|J^C|\pi\beta)_e]2(a_\tau + a_{\sigma\tau}) - [(\nu\alpha|J^C|\pi\beta)_e + (\nu\beta|J^C|\pi\alpha)_e]4a_{\sigma\tau}. \end{aligned} \tag{2.6b}$$

Here and in the following, the subscripts o, e denote the ordinary and the exchange integrals respectively. Thus,

$$\begin{aligned} (\nu\alpha|J^C|\nu\alpha)_o = {} & \int\int \rho_{\nu\alpha}(1) J^C(r_{12}) \rho_{\nu\alpha}(2) d\tau_1 d\tau_2 \\ & - \sum_k^\nu \int\int \phi_k^*(1)\phi_k(1) J^C(r_{12}) \phi_k^*(2)\phi_k(2) d\tau_1 d\tau_2 \end{aligned} \tag{2.7a}$$

$$\begin{aligned} (\nu\alpha|J^C|\nu\alpha)_e = {} & \int\int \rho_{\nu\alpha}(1,2) J^C(r_{12}) \rho_{\nu\alpha}(2,1) d\tau_1 d\tau_2 \\ & - \sum_k^\nu \int\int \phi_k^*(1)\phi_k(1) J^C(r_{12}) \phi_k^*(2)\phi_k(2) d\tau_1 d\tau_2 \end{aligned} \tag{2.7b}$$

$$(\nu\alpha|J^C|\pi\alpha)_o = \int\int \rho_{\nu\alpha}(1) J^C(r_{12}) \rho_{\pi\alpha}(2) d\tau_1 d\tau_2,$$

$$(\nu\alpha|J^C|\pi\alpha)_e = \int\int \rho_{\nu\alpha}(1,2) J^C(r_{12}) \rho_{\pi\alpha}(2,1) d\tau_1 d\tau_2,$$

where k is the totality of the *spatial* quantum numbers n, l, m, and

$$\rho_{\nu\alpha}(1) = \sum_k^{\nu,\alpha} \phi_k^*(1)\phi_k(1), \quad \rho_{\nu\alpha}(1,2) = \sum_k^{\nu,\alpha} \phi_k^*(1)\phi_k(2), \tag{2.8}$$

and similarly $\rho_{\nu\beta}$, $\rho_{\pi\alpha}$, $\rho_{\pi\beta}$. The indices ν, α in the summation in (2.8) indicate a summation over all occupied states of neutrons with spin α, etc.

2.2 TENSOR INTERACTION

For the tensor interaction V^T in (1.5), summation over the isobaric spin coordinate permits one to separate the matrix element into three parts corresponding to n—n, n—p, and p—p interactions according to

$$V^T = V^T_{\nu\nu} + V^T_{\nu\pi} + V^T_{\pi\pi}, \tag{2.9}$$

where $V^T_{\nu\nu}$, etc. are given by expressions similar to (2.4), in which

$$\begin{aligned} V^T_{\nu\nu}(1,2) = V^T_{\pi\pi}(1,2) &= (b_0 + b_\tau) S_{12} J^T(r_{12}), \\ V^T_{\nu\pi}(1,2) &= (b_0 - b_\tau) S_{12} J^T(r_{12}), \\ V^T_{\nu\pi}(1,2) &= 2b_\tau S_{12} J^T(r_{12}). \end{aligned} \tag{2.9a}$$

a) *Diagonal matrix elements*

Carrying out the summation over the spin variables in (2.1) with the help of the properties of the tensor operator S_{ij} ((A.1) in Appendix A), one obtains for the various contributions in (2.9)

$$ {}_{\mathrm{D}}V^{\mathrm{T}}_{\nu\nu} = [\tfrac{1}{2}(\nu\alpha|T|\nu\alpha)_{\mathrm{o}}+\tfrac{1}{2}(\nu\beta|T|\nu\beta)_{\mathrm{o}}-(\nu\alpha|T|\nu\beta)_{\mathrm{o}}](b_0+b_\tau) $$
$$ -[\tfrac{1}{2}(\nu\alpha|T|\nu\alpha)_{\mathrm{e}}+\tfrac{1}{2}(\nu\beta|T|\nu\beta)_{\mathrm{e}}-(\nu\alpha|T|\nu\beta)_{\mathrm{e}}](b_0+b_\tau), \quad (2.10a) $$

a similar expression for ${}_{\mathrm{D}}V^{\mathrm{T}}_{\pi\pi}$ on replacing ν by π, and

$$ {}_{\mathrm{D}}V^{\mathrm{T}}_{\nu\pi} = [(\nu\alpha|T|\pi\alpha)_{\mathrm{o}}+(\nu\beta|T|\pi\beta)_{\mathrm{o}}-(\nu\alpha|T|\pi\beta)_{\mathrm{o}}-(\nu\beta|T|\pi\alpha)_{\mathrm{o}}](b_0-b_\tau) $$
$$ -[(\nu\alpha|T|\pi\alpha)_{\mathrm{e}}+(\nu\beta|T|\pi\beta)_{\mathrm{e}}-(\nu\alpha|T|\pi\beta)_{\mathrm{e}}-(\nu\beta|T|\pi\alpha)_{\mathrm{e}}]2b_\tau. \quad (2.10b) $$

The expressions $(\nu\alpha|T|\nu\alpha)_{\mathrm{e}}$, etc. have the meaning of (2.7a, 7.b), etc. Here and in the following

$$ T = 2Y_{2,0} = 3\cos^2\vartheta-1, \quad T_\pm = Y_{2,\pm1} = 3\sin\vartheta\cos\vartheta\,\mathrm{e}^{\pm i\psi}. \quad (2.11) $$

b) *Non-diagonal matrix elements*

The non-diagonal matrix elements, say $(A|V^{\mathrm{T}}|B)$ in (2.2), can again be separated into three contributions corresponding to n—n, n—p and p—p interactions. Depending on the various spin states of k and p in (2.2), reference to (A.1) in Appendix A leads to the following results (see (2.16) below):

i) $k(\alpha)$, $p(\alpha)$

$$ {}_{\mathrm{N}}V^{\mathrm{T}}_{\nu\nu} = [(\nu\alpha|T|\nu\alpha\alpha)_{\mathrm{o}}-(\nu\beta|T|\nu\alpha\alpha)_{\mathrm{o}}-(\nu\alpha|T|\nu\alpha\alpha)_{\mathrm{e}}+(\nu\beta|T|\nu\alpha\alpha)_{\mathrm{e}}](b_0+b_\tau), \quad (2.12a) $$

$$ {}_{\mathrm{N}}V^{\mathrm{T}}_{\nu\pi} = [(\pi\alpha|T|\nu\alpha\alpha)_{\mathrm{o}}-(\pi\beta|T|\nu\alpha\alpha)_{\mathrm{o}}](b_0-b_\tau) $$
$$ -[(\pi\alpha|T|\nu\alpha\alpha)_{\mathrm{e}}-(\pi\beta|T|\nu\alpha\alpha)_{\mathrm{e}}]2b_\tau. \quad (2.12b) $$

ii) $k(\beta)$, $p(\beta)$

One replaces α by β in (2.12a) and (2.12b). (2.13a, b)

iii) $k(\alpha)$, $p(\beta)$

$$ {}_{\mathrm{N}}V^{\mathrm{T}}_{\nu\nu} = [(\nu\alpha|T_-|\nu\alpha\beta)_{\mathrm{o}}-(\nu\beta|T_-|\nu\alpha\beta)_{\mathrm{o}}-(\nu\alpha|T_-|\nu\alpha\beta)_{\mathrm{e}}+(\nu\beta|T_-|\nu\alpha\beta)_{\mathrm{e}}](b_0+b_\tau) \quad (2.14a) $$

$$ {}_{\mathrm{N}}V^{\mathrm{T}}_{\nu\pi} = [(\pi\alpha|T_-|\nu\alpha\beta)_{\mathrm{o}}-(\pi\beta|T_-|\nu\alpha\beta)_{\mathrm{o}}](b_0-b_\tau) $$
$$ -[(\pi\alpha|T_-|\nu\alpha\beta)_{\mathrm{e}}-(\pi\beta|T_-|\nu\alpha\beta)_{\mathrm{e}}]2b_\tau. \quad (2.14b) $$

iv) $k(\beta)$, $p(\alpha)$

$$ {}_{\mathrm{N}}V^{\mathrm{T}}_{\nu\nu} = [(\nu\alpha|T_+|\nu\beta\alpha)_{\mathrm{o}}-(\nu\beta|T_+|\nu\beta\alpha)_{\mathrm{o}} $$
$$ -(\nu\alpha|T_+|\nu\beta\alpha)_{\mathrm{e}}+(\nu\beta|T_+|\nu\beta\alpha)_{\mathrm{e}}](b_0+b_\tau), \quad (2.15a) $$

$$ {}_{\mathrm{N}}V^{\mathrm{T}}_{\nu\pi} = [(\pi\alpha|T_+|\nu\beta\alpha)_{\mathrm{o}}-(\pi\beta|T_+|\nu\beta\alpha)_{\mathrm{o}}](b_0-b_\tau) $$
$$ -[(\pi\alpha|T_+|\nu\beta\alpha)_{\mathrm{e}}-(\pi\beta|T_+|\nu\beta\alpha)_{\mathrm{e}}]2b_\tau. \quad (2.15b) $$

The corresponding expressions for $V^{\mathrm{T}}_{\pi\pi}$ are obtained from the appropriate $V^{\mathrm{T}}_{\nu\nu}$ by replacing ν by π in (2.12a), (2. 13a), (2.14a), (2. 15a). The appropriate energy integrals in (2.12—15) are given by

$$ (\nu\beta|T|\nu\alpha\alpha)_{\mathrm{o}} = \int\int \rho_{\nu\beta}(1)J^{\mathrm{T}}(r_{12})(3\cos^2\vartheta-1)\dot{\phi}^{\nu}_{k\alpha}(2)\phi^{\nu}_{p\alpha}(2)\mathrm{d}\tau_1\mathrm{d}\tau_2 \quad (2.16a) $$

$$(\nu\beta|T|\nu\alpha)_e = \int\int \rho_{\nu\beta}(1,2)J^T(r_{12})(3\cos^2\vartheta - 1)\dot{\phi}^{\nu}_{k\alpha}(2)\phi^{\nu}_{p\alpha}(1)d\tau_1 d\tau_2$$

$$(\nu\alpha|T_-|\nu\alpha\beta)_o = \int\int \rho_{\nu\alpha}(1)J^T(r_{12})3\sin\vartheta\cos\vartheta\, e^{-i\psi}\dot{\phi}^{\nu}_{k\alpha}(2)\phi^{\nu}_{p\beta}(2)d\tau_1 d\tau_2 \qquad (2.16b)$$

$$(\nu\alpha|T_+|\nu\beta\alpha)_e = \int\int \rho_{\nu\alpha}(1,2)J^T(r_{12})\,3\sin\vartheta\cos\vartheta\, e^{i\psi}\dot{\phi}^{\nu}_{k\beta}(2)\phi^{\nu}_{p\alpha}(1)d\tau_1 d\tau_2.$$

2.3. SPIN-ORBIT INTERACTION

For the spin-orbit interaction the potential V^{LS} is given by (1.7). It is again possible to separate the matrix element into its n—n, n—p and p—p components by summation over the isospin coordinates

$$V^{LS} = V^{LS}_{\nu\nu} + V^{LS}_{\nu\pi} + V^{LS}_{\pi\pi}, \qquad (2.17)$$

for which the effective potentials are given by

$$V^{LS}_{\nu\nu} = V^{LS}_{\pi\pi} = (c_0 + c_\tau)J^{LS}(r_{12})\mathbf{L}\cdot\mathbf{S}, \qquad (2.17a)$$

$$V^{LS}_{\nu\pi} = (c_0 - c_\tau)J^{LS}(r_{12})\mathbf{L}\cdot\mathbf{S}, \qquad (2.17b)$$

$$\bar{V}^{LS}_{\nu\pi} = 2c_\tau J^{LS}(r_{12})\mathbf{L}\cdot\mathbf{S}. \qquad (2.17c)$$

a) *Diagonal matrix elements*

Summation over the spin variables in (2.1) with the help of (A.2) in Appendix A yields for the various contributions in (2.17)

$${}_D V^{LS}_{\nu\nu} = \tfrac{1}{2}[(\nu\alpha|L_z|\nu\alpha)_o - (\nu\beta|L_z|\nu\beta)_o - (\nu\alpha|L_z|\nu\alpha)_e + (\nu\beta|L_z|\nu\beta)_e](c_0 + c_\tau), \qquad (2.18a)$$

a similar expression for ${}_D V^{LS}_{\pi\pi}$ on replacing ν by π, and

$${}_D V^{LS}_{\nu\pi} = [(\nu\alpha|L_z|\pi\alpha)_o - (\nu\beta|L_z|\pi\beta)_o](c_0 - c_\tau) - [(\nu\alpha|L_z|\pi\alpha)_e - (\nu\beta|L_z|\pi\beta)_e]2c_\tau. \qquad (2.18b)$$

The meaning of $(\nu\alpha|L_z|\nu\alpha)$, etc. is that of (2.7a, 7b). In the following, (2.20—24),

$$L_\pm = L_x \pm iL_y. \qquad (2.19)$$

b) *Non-diagonal matrix elements*

For the non-diagonal matrix elements depending on the spin state of k and p, we have the following contributions for the different cases (see (A.2) in Appendix A):

i) $k(\alpha)$, $p(\alpha)$

$${}_N V^{LS}_{\nu\nu} = [(\nu\alpha|L_z|\nu\alpha\alpha)_o - (\nu\alpha|L_z|\nu\alpha\alpha)_e](c_0 + c_\tau), \qquad (2.20a)$$

$${}_N V^{LS}_{\nu\pi} = (\pi\alpha|L_z|\nu\alpha\alpha)_o(c_0 - c_\tau) - (\pi\alpha|L_z|\nu\alpha\alpha)_e 2c_\tau. \qquad (2.20b)$$

ii) $k(\beta)$, $p(\beta)$

$$ {}_{\mathrm{N}}\bar{V}^{\mathrm{LS}}_{\nu\nu} = -[(\nu\beta|L_z|\nu\beta\beta)_{\mathrm{o}} - (\nu\beta|L_z|\nu\beta\beta)](c_0+c_\tau), \tag{2.21a} $$

$$ {}_{\mathrm{N}}\bar{V}^{\mathrm{LS}}_{\nu\pi} = -(\pi\beta|L_z|\nu\beta\beta)_{\mathrm{o}}(c_0-c_\tau) + (\pi\beta|L_z|\nu\beta\beta)_{\mathrm{e}}\,2c_\tau. \tag{2.21b} $$

iii) $k(\alpha)$, $p(\beta)$

$$ {}_{\mathrm{N}}\bar{V}^{\mathrm{LS}}_{\nu\nu} = \tfrac{1}{2}[(\nu\alpha|L_-|\nu\alpha\beta)_{\mathrm{o}} + (\nu\beta|L_-|\nu\alpha\beta)_{\mathrm{o}} - (\nu\alpha|L_-|\nu\alpha\beta)_{\mathrm{e}} - (\nu\beta|L_-|\nu\alpha\beta)_{\mathrm{e}}](c_0+c_\tau), \tag{2.22a} $$

$$ {}_{\mathrm{N}}\bar{V}^{\mathrm{LS}}_{\nu\pi} = \tfrac{1}{2}[(\pi\alpha|L_-|\nu\alpha\beta)_{\mathrm{o}} + (\pi\beta|L_-|\nu\alpha\beta)_{\mathrm{o}}](c_0-c_\tau) - \tfrac{1}{2}[(\pi\alpha|L_-|\nu\alpha\beta)_{\mathrm{e}} + (\pi\beta|L_-|\nu\alpha\beta)_{\mathrm{e}}]2c_\tau. \tag{2.22b} $$

iv) $k(\beta)$, $p(\alpha)$

$$ {}_{\mathrm{N}}\bar{V}^{\mathrm{LS}}_{\nu\nu} = \tfrac{1}{2}[(\nu\alpha|L_+|\nu\beta\alpha)_{\mathrm{o}} + (\nu\beta|L_+|\nu\beta\alpha)_{\mathrm{o}} - (\nu\alpha|L_+|\nu\beta\alpha)_{\mathrm{e}} - (\nu\beta|L_+|\nu\beta\alpha)_{\mathrm{e}}](c_0+c_\tau), \tag{2.23a} $$

$$ {}_{\mathrm{N}}\bar{V}^{\mathrm{LS}}_{\nu\pi} = \tfrac{1}{2}[(\pi\alpha|L_+|\nu\beta\alpha)_{\mathrm{o}} + (\pi\beta|L_+|\nu\beta\alpha)_{\mathrm{o}}](c_0-c_\tau) - \tfrac{1}{2}[(\pi\alpha|L_+|\nu\beta\alpha)_{\mathrm{e}} + (\pi\beta|L_+|\nu\beta\alpha)_{\mathrm{e}}]2c_\tau. \tag{2.23b} $$

The corresponding expressions for ${}_{\mathrm{N}}\bar{V}^{\mathrm{LS}}_{\pi\pi}$ are obtained from the appropriate ${}_{\mathrm{N}}\bar{V}^{\mathrm{LS}}_{\nu\nu}$ by replacing ν by π. The energy integrals are given by

$$ (\nu\alpha|L_-|\nu\alpha\beta)_{\mathrm{o}} = \iint \rho_{\nu\alpha}(1) J^{\mathrm{LS}}(r_{12}) L_- \dot{\phi}^{\nu}_{k,\alpha}(2)\phi^{\nu}_{p,\beta}(2)\mathrm{d}\tau_1\mathrm{d}\tau_2, $$

$$ (\nu\alpha|L_+|\nu\beta\alpha)_{\mathrm{e}} = \iint \rho_{\nu\alpha}(1,2) J^{\mathrm{LS}}(r_{12}) L_+ \dot{\phi}^{\nu}_{k,\beta}(2)\phi^{\nu}_{p,\alpha}(1)\mathrm{d}\tau_1\mathrm{d}\tau_2. \tag{2.24} $$

2.4. COULOMB INTERACTION AND KINETIC ENERGY

As the Coulomb interaction only affects protons, only $V_{\pi\pi}$ is different from zero, Moreover, no spin-dependent terms enter, and hence one obtains from (2.6a)

$$ \bar{C} = \bar{C}_{\pi\pi} = \tfrac{1}{2}[(\pi\alpha|C|\pi\alpha)_{\mathrm{o}} + (\pi\beta|C|\pi\beta)_{\mathrm{o}}] + (\pi\alpha|C|\pi\beta)_{\mathrm{o}} - \tfrac{1}{2}[(\pi\alpha|C|\pi\alpha)_{\mathrm{e}} + (\pi\beta|C|\pi\beta)_{\mathrm{e}}], \tag{2.25} $$

where we have defined

$$ (\pi\alpha|C|\pi\alpha)_{\mathrm{o}} = \iint \rho_{\pi\alpha}(1)\,\frac{e^2}{r_{12}}\,\rho_{\pi\alpha}(2)\mathrm{d}\tau_1\mathrm{d}\tau_2, $$

$$ (\pi\alpha|C|\pi\alpha)_{\mathrm{e}} = \iint \rho_{\pi\sigma}(1,2)\,\frac{e^2}{r_{12}}\,\rho_{\pi\alpha}(2,1)\mathrm{d}\tau_1\mathrm{d}\tau_2. \tag{2.26} $$

The contribution to the kinetic energy arises from two sources. In (1.16) there is the zeroth order contribution T_0 and then there is the correlation energy arising from the finite slope of the correlation function f. For the space part of

the individual particle wave function we take

$$\phi_{nlm}(\mathbf{r}_i) = \frac{1}{r_i} R_{nl}(r_i) Y_{l,m}(\vartheta_i, \varphi_i) \tag{2.27}$$

where R_{nl} is the radial function of the three dimensional harmonic oscillator [10])

$$R_{nl}(r) = N_{nl} r^{l+1} \exp\left(-\tfrac{1}{2}\nu_{nl} r^2\right) L^{l+\frac{1}{2}}_{n+l+\frac{1}{2}}(\nu_{nl} r^2),$$
$$N^2_{nl} = \frac{2^{l-n+2}(2l+2n+1)!!}{\sqrt{\pi} n![(2l+1)!!]^2}, \tag{2.28}$$

where n and l are the radial and azimuthal quantum numbers respectively, L is the associated Laguerre polynomial and ν_{nl} a parameteric constant to be determined from the variational principle. With the wave function given by (2.28) the matrix elements of the one-particle Hamiltonian $H_0(i)$ are then simply given by

$$\langle nl|H_0|nl\rangle = (\tfrac{3}{2}+2n+l)\frac{\hbar^2}{2M}\nu_{nl}. \tag{2.29}$$

The total contribution from (2.29) to T_0 is then obtained by summing over the appropriate values of n and l for the particular nucleus in question.

The correlation energy can be obtained from the corresponding expressions for the central interaction by noting that no spin-dependent interactions appear. We thus obtain for the mean correlation energy K

$$\bar{K} = \bar{K}_{\nu\nu} + \bar{K}_{\nu\pi} + \bar{K}_{\pi\pi} \tag{2.30}$$

which we have again separated into contributions corresponding to neutron-neutron, neutron-proton and proton-proton interactions. From (2.6) we obtain for these

$$\bar{K}_{\nu\nu} = \tfrac{1}{2}[(\nu\alpha|K|\nu\alpha)_0 + (\nu\beta|K|\nu\beta)_0] + (\nu\alpha|K|\nu\beta)_0 - \tfrac{1}{2}[(\nu\alpha|K|\nu\alpha)_e + (\nu\beta|K|\nu\beta)_e], \tag{2.31a}$$

a corresponding expression for $\bar{K}_{\pi\pi}$ by replacing ν by π in (2.31a), and

$$\bar{K}_{\nu\pi} = (\nu\alpha|K|\pi\alpha)_0 + (\nu\beta|K|\pi\beta)_0 + (\nu\alpha|K|\pi\beta)_0 + (\nu\beta|K|\pi\alpha)_0 \tag{2.31b}$$

where

$$(\nu\alpha|K|\nu\alpha)_0 = \sum^{\nu,a}_{n\neq m}\sum^{\nu,a}\int\int \dot{\phi}_n(1)\phi_n(1)K\dot{\phi}_m(2)\phi_m(2)\mathrm{d}\tau_1\mathrm{d}\tau_2 \tag{2.32a}$$

$$(\nu\alpha|K|\pi\alpha)_e = \int\int \rho_{\nu\alpha}(1,2)K\rho_{\pi\alpha}(2,1)\mathrm{d}\tau_1\mathrm{d}\tau_2 \tag{2.32b}$$

$$K = \frac{\hbar^2}{2M}\left(\frac{\mathrm{d}f(r)}{\mathrm{d}r}\right)^2, \quad r = r_{12}. \tag{2.32c}$$

This, then, completes the general calculations of the various matrix-elements entering in the Hamiltonian (1.1), and in the next sections we shall apply our results to the nuclei O^{16} and O^{15}.

3. The Nucleus O^{16}: $(1s)_\nu^2(1p)_\nu^6(1s)_\pi^2(1p)_\pi^6$

For the closed shells of O^{16}, the wave function Ψ is one single 16×16 determinant. The energy is given by (1.16)

$$E = T_0+\bar{K}+\bar{V}^C+\bar{C} \tag{3.1}$$

where T_0 can be readily calculated from (2.29) [3] †

$$T_0 = (6\nu_s+30\,\nu_p)\,\frac{\hbar^2}{2M}. \tag{3.2}$$

To evaluate the matrix elements of K (the correlation energy) and $V(\mathbf{r}_i-\mathbf{r}_j)$ by means of the various expressions in § 2, it is most convenient to perform a transformation of the coordinates $\mathbf{r}_i$, $\mathbf{r}_j$ of the two particles to

$$\mathbf{R} = \tfrac{1}{2}(\mathbf{r}_i+\mathbf{r}_j), \quad \mathbf{r} = \mathbf{r}_j-\mathbf{r}_i. \tag{3.3}$$

A most convenient property of the harmonic oscillator wave functions $\phi_{nlm}(\mathbf{r}_i)$ in (2.27) is that the product

$$\phi_{n_1 l_1 m_1}(\mathbf{r}_i)\phi_{n_2 l_2 m_2}(\mathbf{r}_j)$$

transforms, under (3.3), into a combination of the harmonic oscillator wave functions in $\mathbf{R}$ and $\mathbf{r}$, viz. [10])

$$\phi_{n_1 l_1 m_1}(\mathbf{r}_i)\phi_{n_2 l_2 m_2}(\mathbf{r}_j) = \sum a_{N,n}^{n_1,n_2}\phi_{NLM}(\mathbf{R})\phi_{n\lambda m}(\mathbf{r}) \tag{3.4}$$

where the indices n_1, n_2, N, n in the coefficient a stand for n_1, l_1, m_1; n_2, l_2, m_2; etc., and the summation extends over all values of N, L, M, n, λ, m such that the two sides of (3.4) have i) the same angular momentum $m_1+m_2 = M+m$, ii) the same energy $2n_1+l_1+2n_2+l_2 = 2N+L+2n+l$, iii) the same symmetry with respect to inversion of $\mathbf{r}_i$, of $\mathbf{r}_j$, and of both $\mathbf{r}_i$ and $\mathbf{r}_j$, iv) the same symmetry with respect to the interchange of i and j. These considerations, together with an explicit calculation of the relation (3.4) for the simple case of $\varphi_1 = \varphi_2 = \phi = \varphi$ enable one to determine the coefficients a. In the present work, only $\phi_{1s}(\mathbf{r}_i)$, $\phi_{1pm}(\mathbf{r}_j)$ are involved, and the transformation relations (3.4) for various products $\phi_{n_1 l_1 m_1}(\mathbf{r}_i)\phi_{n_2 l_2 m_2}(\mathbf{r}_j)$ are given in the appendix in Talmi's [10]) paper.

In terms of the functions $\phi_N(\mathbf{R})$, $\phi_n(\mathbf{r})$, all the integrals in the various matrix elements of K, $V(\mathbf{r}_i-\mathbf{r}_j)$ become one-particle integrals, and the evaluation of all the expressions (2.6)—(2.32) is reduced to a matter of simple counting. Omitting all the details, we give the following result for O^{16}:

$$\bar{K} = \tfrac{3}{2}(31K_s+34K_p+15K_d), \tag{3.5}$$

† It must be noted that in using the transformation (3.3)—(3.4) it is necessary to set $\nu_s = \nu_p$ for the 1s and 1p states.

where

$$\left.\begin{matrix} K_s \\ K_p \\ K_d \end{matrix}\right\} = \frac{\hbar^2}{2M}\int_{r_0}^{\infty} \left.\begin{matrix} R_{1s}^2(r) \\ R_{1p}^2(r) \\ R_{1d}^2(r) \end{matrix}\right\} \left(\frac{df(r)}{dr}\right)^2 dr, \tag{3.6}$$

$$\begin{aligned} \bar{V}^C &= \tfrac{3}{2}(a_0 - a_\tau - a_\sigma - 3a_{\sigma\tau})(31J_s - 30J_p + 15J_d) + 96a_0 J_p, \\ \bar{C} &= \tfrac{31}{4}C_s + \tfrac{33}{2}C_p + \tfrac{15}{4}C_d, \end{aligned} \tag{3.7}$$

where J_l are the central-field integrals

$$\left.\begin{matrix} J_s \\ J_p \\ J_d \end{matrix}\right\} = \int_{r_0}^{\infty} \left.\begin{matrix} R_{1s}^2(r) \\ R_{1p}^2(r) \\ R_{1d}^2(r) \end{matrix}\right\} f^2(r) J^C(r) dr, \tag{3.8}$$

and the C_l the Coulomb integrals

$$\left.\begin{matrix} C_s \\ C_p \\ C_d \end{matrix}\right\} = e^2 \int_0^{\infty} \left.\begin{matrix} R_{1s}^2(r) \\ R_{1p}^2(r) \\ R_{1d}^2(r) \end{matrix}\right\} f^2(r) \frac{1}{r} dr. \tag{3.9}$$

It is to be noted that the tensor and $\mathbf{L}\cdot\mathbf{S}$ interactions contribute nothing to the energy of closed-shell configurations.

These integrals K_l, J_l, C_l depend on the parameter ν in the function R_{nl}, and the parameter β in $f(r)$. They are given in Appendix B. One could have calculated the total energy E in (3.1) by determining the ν and β by

$$\frac{\partial E}{\partial \nu} = 0, \quad \frac{\partial E}{\partial \beta} = 0. \tag{3.10}$$

We have adopted the procedure of our previous work [3]), namely, of introducing a multiplicative parameter ξ in all the two-nucleon potentials V^C, V^T, V^{LS}. This leads to

$$E = E(\nu, \beta, \xi) = T_0 + \bar{K} + \xi \bar{V}^C + \bar{C} \tag{3.11}$$

instead of (3.1). The parameters ξ, ν, β are then determined by (3.10) and the requirement that E be equal to the empirical binding energy of O^{16},

$$T_0 + \bar{K} + \xi \bar{V}^C + \bar{C} = E_0 = -127.56 \text{ MeV}. \tag{3.12}$$

The solution of these three somewhat complicated equations follows the same procedure as in a previous work [3]). The result is

$$\lambda \equiv \nu r_C^2 = 0.3719, \quad \beta = 1.14, \quad \xi = 1.023. \tag{3.13}$$

This value of ν in the wave function (2.28) leads to a value 1.96×10^{-13} cm for the root-mean-square radius of the O^{16} nucleus.

The idea of introducing the parameter ξ in this manner [3]) is to allow for a possible deviation of the two-nucleon potential *in* a nucleus (such as O^{16}, O^{15})

from the Gammel-Thaler potential for two "free" nucleons. It is true that from O^{16} alone, the procedure adopted here does not furnish a test of the Hartree-Fock approximation. The deviation of ξ from unity may be due to either or both of the causes: (1) deviation of $V(\mathbf{r}_i-\mathbf{r}_j)$ in a complex nucleus from the $V(\mathbf{r}_i-\mathbf{r}_j)$ for two "free" nucleons, (2) insufficiency of the Hartree-Fock approximation. A test of the latter is furnished, however, by calculating the total energy E of O^{15} with the constants (3.13) determined from O^{16}. This is done in the following section.

4. Energy Matrix for O^{15}

For O^{15} the configuration is $(1s)_\nu^2\ (1p)_\nu^5\ (1s)_\pi^2\ (1p)_\pi^6$. Hence we have six different Slater determinants depending on the state of the missing 1p-neutron. The various wave functions are then given by (15×15) determinants formed of the following one-particle wave functions where s and p denote the two possible values of the angular quantum number $l = 0$, 1, and 1, 0, $\bar{1}$ the possible values of the magnetic quantum number $m_l = 1, 0, -1$:

W.F.	Neutrons		Protons	
M	α (spin up)	β (spin down)	α (spin up)	β (spin down)
$A\ \ \frac{3}{2}$	s p1 p0 p$\bar{1}$	s p1 p0	s p1 p0 p$\bar{1}$	s p1 p0 p$\bar{1}$
$B\ \ \frac{1}{2}$	s p1 p0 p$\bar{1}$	s p1 p$\bar{1}$	s p1 p0 p$\bar{1}$	s p1 p0 p$\bar{1}$
$C\ -\frac{1}{2}$	s p1 p0 p$\bar{1}$	s p0 p$\bar{1}$	s p1 p0 p$\bar{1}$	s p1 p0 p$\bar{1}$
$D\ \ \frac{1}{2}$	s p1 p0	s p1 p0 p$\bar{1}$	s p1 p0 p$\bar{1}$	s p1 p0 p$\bar{1}$
$E\ -\frac{1}{2}$	s p1 p$\bar{1}$	s p1 p0 p$\bar{1}$	s p1 p0 p$\bar{1}$	s p1 p0 p$\bar{1}$
$F\ -\frac{3}{2}$	s p0 p$\bar{1}$	s p1 p0 p$\bar{1}$	s p1 p0 p$\bar{1}$	s p1 p0 p$\bar{1}$

(4.1)

We have to calculate all possible matrix elements for central, tensor and spin-orbit interaction arising from the various wave functions and obtain the energy levels by diagonalizing the resulting (6×6) matrix.

To calculate all the matrix elements (2.7), (2.16), (2.24), it is again convenient to use the transformation (3.3)—(3.4). Thus one obtains for the central interaction V^C,

$$\begin{aligned}\bar{V}^C &= \langle A|V^C|A\rangle = \langle B|V^C|B\rangle = \ldots = \langle F|V^C|F\rangle \\ &= \tfrac{15}{4}(a_0-a_\tau-a_\sigma-3a_{\sigma\tau})(11J_s-\tfrac{52}{5}J_p+5J_d)+84a_0J_p \qquad (4.2)\end{aligned}$$

where the J_l are defined in (3.8) and given in Appendix B.

For the tensor interaction V^T, it follows from (2.10a), (2.10b) that all the diagonal elements are zero. For the non-diagonal elements, it follows from the fact that V^T is diagonal with respect to the total M that all elements vanish except

$$\langle B|V^T|D\rangle, \quad \langle C|V^T|E\rangle.$$

A direct calculation of (2.12)—(2.15) shows, however, that

$$\langle B|V^{\mathrm{T}}|D\rangle = \langle C|V^{\mathrm{T}}|E\rangle = 0. \tag{4.3}$$

Hence the tensor interaction V^{T} has no contribution to O^{15} in the lowest configuration.

For the $\mathbf{L}\cdot\mathbf{S}$ interaction V^{LS}, an essential simplification is achieved by the transformation (3.3), (3.4). Here

$$\mathbf{L} = 2[\mathbf{r}\times\nabla_r]. \tag{4.4}$$

With the transformation relations (3.4), the evaluation of all the expressions (2.18)—(2.24) is again reduced to a matter of counting. One obtains the following non-vanishing elements, all others vanishing:

$$\begin{aligned}\bar{V}^{\mathrm{LS}} &= \langle A|V^{\mathrm{LS}}|A\rangle = \langle F|V^{\mathrm{LS}}|F\rangle = -\langle C|V^{\mathrm{LS}}|C\rangle = -\langle D|V^{\mathrm{LS}}|D\rangle \\ &= -\tfrac{3}{2}(c_0+c_\tau)I_{\mathrm{p}} - \tfrac{5}{2}(c_0-3c_\tau)I_{\mathrm{d}}, \end{aligned} \tag{4.5}$$

$$\begin{aligned}{}_{\mathrm{N}}\bar{V}^{\mathrm{LS}} &= \langle B|V^{\mathrm{LS}}|D\rangle = \langle D|V^{\mathrm{LS}}|B\rangle = \langle C|V^{\mathrm{LS}}|E\rangle = \langle E|V^{\mathrm{LS}}|C\rangle \\ &= -\frac{9}{\sqrt{2}}(c_0+c_\tau)I_{\mathrm{p}} - \frac{5}{\sqrt{2}}(c_0-3c_\tau)I_{\mathrm{d}} \\ &= \sqrt{2}\ \bar{V}^{\mathrm{LS}}, \end{aligned} \tag{4.6}$$

where

$$\left.\begin{matrix} I_{\mathrm{p}} \\ I_{\mathrm{d}} \end{matrix}\right\} = \int_{r_0}^{\infty} \left\{\begin{matrix} R_{1\mathrm{p}}^2(r) \\ R_{1\mathrm{d}}^2(r) \end{matrix}\right\} f^2(r) J^{\mathrm{LS}}(r)\,\mathrm{d}r. \tag{4.7}$$

The integrals I_t are given in Appendix B.

For the Coulomb interaction between protons, one obtains of course the same expression as for O^{16}, namely

$$\begin{aligned}\bar{C} &= \langle A|\sum\frac{e^2}{r_{ij}}|A\rangle = \ldots = \langle F|\sum\frac{e^2}{r_{ij}}|F\rangle \\ &= \tfrac{31}{4}C_{\mathrm{s}} + \tfrac{33}{2}C_{\mathrm{p}} + \tfrac{15}{4}C_{\mathrm{d}}, \end{aligned} \tag{4.8}$$

where C_t is defined in (3.9) and given in Appendix B.

The kinetic energy T_0 in (1.16) is obtained by summing in (2.29) over all the nucleons:

$$T_0(\mathrm{O}^{15}) = (6\nu_{\mathrm{s}} + \tfrac{55}{2}\nu_{\mathrm{p}})\frac{\hbar^2}{2M}. \tag{4.9}$$

(See footnote to (3.2) concerning $\nu_{\mathrm{s}} = \nu_{\mathrm{p}}$).

Finally the "correlation energy" $\bar{K}$ represented by the second term in (1.16) is given by the diagonal elements $\langle A|K|A\rangle = \ldots \langle F|K|F\rangle$:

$$\bar{K} = \tfrac{165}{4}K_{\mathrm{s}} + 45K_{\mathrm{p}} + \tfrac{75}{4}K_{\mathrm{d}} \tag{4.10}$$

where K_t is defined in (3.6) and given in Appendix B.

The energy levels of the configuration $(1s)_\nu^2(1p)_\nu^5(1s)_\pi^2(1p)_\pi^6$ of O^{15} are given by the roots of the matrix

$$\begin{vmatrix} \overline{\mathcal{H}}+\xi\mathcal{V}^{LS}-E & 0 & 0 & 0 & 0 & 0 \\ 0 & \overline{\mathcal{H}}-E & 0 & \xi\sqrt{2}\mathcal{V}^{LS} & 0 & 0 \\ 0 & 0 & \overline{\mathcal{H}}-\xi\mathcal{V}^{LS}-E & 0 & \xi\sqrt{2}\mathcal{V}^{LS} & 0 \\ 0 & \xi\sqrt{2}\mathcal{V}^{LS} & 0 & \overline{\mathcal{H}}-\xi\mathcal{V}^{LS}-E & 0 & 0 \\ 0 & 0 & \xi\sqrt{2}\mathcal{V}^{LS} & 0 & \overline{\mathcal{H}}-E & 0 \\ 0 & 0 & 0 & 0 & 0 & \overline{\mathcal{H}}+\xi\mathcal{V}^{LS}-E \end{vmatrix} \tag{4.11}$$

where

$$\overline{\mathcal{H}} = T_0+\bar{K}+\xi\mathcal{V}^{C}+\bar{C}, \tag{4.12}$$

$T_0, \bar{K}, \bar{C}, \mathcal{V}^{C}, \mathcal{V}^{LS}$ being given by (4.9), (4.10), (4.8), (4. 2) and (4.5) respectively. It can be seen that (4.11) has two distinct roots one of which is doubly degenerate and one four-fold degenerate, namely,

$$E = \begin{cases} \overline{\mathcal{H}} + \xi\mathcal{V}^{LS} & \text{(double)}, \quad M = \pm\frac{3}{2}, \\ \overline{\mathcal{H}} + \xi\mathcal{V}^{LS} & \text{(double)}, \quad M = \pm\frac{1}{2}, \\ \overline{\mathcal{H}} - 2\xi\mathcal{V}^{LS} & \text{(double)}, \quad M = \pm\frac{1}{2}. \end{cases} \tag{4.13}$$

The root $E = \overline{\mathcal{H}}+\xi\mathcal{V}^{LS}$ corresponds to the state $J = \frac{3}{2}$, and the other to $J = \frac{1}{2}$.

With the parameters $\nu = \lambda/r_C^2$ for the radial wave functions, β for the correlation function and ξ for the two-nucleon potential as determined from O^{16} and given in (3.13), we now calculate for O^{15} the energy $\overline{\mathcal{H}}$ in (4.12) and also the matrix element in (4.5). We find

$$\overline{\mathcal{H}} = T_0+\bar{K}+\bar{C}+\xi\mathcal{V}^{C} = -93.7 \text{ MeV}, \tag{4.14}$$

$$\mathcal{V}^{LS} = \langle A|V^{LS}|A\rangle = 10.3 \text{ MeV}. \tag{4.15}$$

These lead to a doublet separation

$$^2P_{\frac{3}{2}}-{}^2P_{\frac{1}{2}} = 3\xi\mathcal{V}^{LS} = 31.6 \text{ MeV} \tag{4.16}$$

and

$$E(^2P_{\frac{1}{2}}, O^{15}) = \overline{\mathcal{H}}-2\xi\mathcal{V}^{LS} = -114.8 \text{ MeV}. \tag{4.17}$$

This last value is to be compared with the empirical value $E(O^{15}) = -111.9$ MeV, and the value -88.1 MeV obtained previously with the Hartree-Fock method and the same harmonic oscillator wave functions, but with a purely central two-nucleon potential without a repulsive core. It is seen that the improvement of the present work (Hartree-Fock, harmonic oscillator wave function, Gammel-Thaler two-nucleon potential) over the previous work is considerable. The good agreement, however, between the calculated E in

(4.17) with the empirical value is only apparent and is somewhat fortuitous, on the following considerations.

Let us consider first the sign of the doublet separation in (4.16). From the empirical values in table 2 of the constants c_0 and c_τ for the $\mathbf{L}\cdot\mathbf{S}$ potential, it is seen from (4.5) that $\bar{V}^{LS}$ is positive. Thus the level $J=\frac{3}{2}$ lies above that for $J=\frac{1}{2}$. Now in atomic spectra, the electron spin-orbit interaction (with $E_{j=l+\frac{1}{2}} > E_{j=l-\frac{1}{2}}$) leads to an inverted doublet ($E_{j=l-\frac{1}{2}} > E_{j=l+\frac{1}{2}}$) for the "closed shell minus one" configuration. In our nuclear case (4.13), the $O^{15}(1p)_p^5$ doublet is "normal", and if one thinks in terms of an average effective central field for the individual nucleons, this situation (4.13) would correspond to a "spin-orbit" interaction of the individual nucleon which has a splitting of the opposite sign (i.e., $E_{j=l-\frac{1}{2}} > E_{j=l+\frac{1}{2}}$) to that of the electron in the atom. It may be recalled that this "anomalous" sign is exactly what is postulated in the shell model of Mayer, Jensen *et al.* to account for the shell structure and the magic numbers of the nuclei. Thus in a qualitative way, a two-nucleon potential containing an $\mathbf{L}\cdot\mathbf{S}$ interaction leads to a result consistent with the shell model of Mayer, [11]) Jensen *et al.* [12]) even in the Hartree-Fock approximation.

Consider next, however, the magnitude of the $^2P_{\frac{3}{2}}-{}^2P_{\frac{1}{2}}$ in (4.16). The value ≈ 31 MeV is probably too large † by a factor ≈ 5. Now the values of the matrix element $\bar{V}^{LS}=\langle A|V^{LS}|A\rangle$ in (4.5) depends on the amplitude of V^{LS} through the coefficients c_0, c_τ (tables 1, 2) and on the range r_{LS} through the integrals I_p, I_d in (4.7) and (B.4) in Appendix B. It is found that changing the value of $1/r_{LS}$ from 3.7×10^{13} to 4×10^{13} alone (without changing the parameters ν, r_0, β) reduces the value of I_p by about 30 percent (I_d being very small compared with I_p). This suggests that the large value found for $\bar{V}^{LS}$ in (4.15) may be due to an insufficiently accurate V^{LS} in the Gammel-Thaler potential.

With a view to examining the Gammel-Thaler potential (table 1) with special reference to the low energy properties of the two-nucleon system, we consider the ground state of the deuteron. We write the Schrödinger equation for the wave functions u, w of the $^3S+{}^3D$ states of the deuteron in the form

$$\begin{aligned}
&\frac{d^2u}{d\rho^2}-\left[1-A\frac{e^{-a\rho}}{\rho}\right]u=-\sqrt{8}B\frac{e^{-b\rho}}{\rho}w,\\
&\frac{d^2w}{d\rho^2}-\left[1+\frac{6}{\rho^2}-A\frac{e^{-a\rho}}{\rho}+2B\frac{e^{-b\rho}}{\rho}+3C\frac{e^{-c\rho}}{\rho}\right]w=-\sqrt{8}B\frac{e^{-b\rho}}{\rho}u,
\end{aligned}\tag{4.18}$$

where

$$\rho=\alpha r,$$
$$\alpha^2=\frac{M}{\hbar^2}|E|,\quad E=\text{binding energy}=-2.226\ \text{MeV}$$

† The $^2P_{\frac{3}{2}}$ in O^{15} is not known, but may tentatively be identified with a level at ≈ 6.15 MeV marked as odd and $J\leq\frac{1}{2}$ in the diagram of the recent article by Ajzenberg-Selove and Lauritsen [13]).

and the coefficients a, b, c, A, B, C are related to the ranges and amplitudes of the central V^{C}, the tensor V^{T} and $\mathbf{L}\cdot\mathbf{S}$ V^{LS} potential respectively:

$$a=\frac{1}{\alpha r_{C}}, \qquad b=\frac{1}{\alpha r_{T}}, \qquad c=\frac{1}{\alpha r_{LS}}, \tag{4.19}$$
$$Aa|E|=V_{C}, \quad Bb|E|=V_{T}, \quad Cc|E|=V_{LS},$$

V_{C}, V_{T}, V_{LS} being the absolute values of the coefficients under the column "triplet-even" in table 1.

We shall put into (4.18) the known binding energy E, and the values of $r_{C}, r_{T}, r_{LS}, V_{C}=100.7$ MeV, $V_{LS}=5000$ MeV from tables 1,2 and solve (4.18) for the eigenvalue of B (i.e., of V_{T}), subject to the boundary conditions

$$u(\rho)=w(\rho)=0, \quad \text{at} \quad \rho=\alpha r_{0}=0.09264,$$
$$u(\rho)\to e^{-\rho}, \quad w(\rho)\to e^{-\rho}\left(1+\frac{3}{\rho}+\frac{3}{\rho^{2}}\right), \quad \text{as} \quad \rho\to\infty.$$

It is found that $V_{T}\approx 285.4$ MeV, compared with the value $V_{T}=257$ MeV in table 1 given by Gammel and Thaler. This means that in order to have the observed binding energy of the deuteron, it is necessary to have a stronger tensor interaction than that given by Gammel and Thaler, or, equivalently, their potential for the triplet even states in table 1 probably gives no stable deuteron state. Thus it is not too surprising that the $\mathbf{L}\cdot\mathbf{S}$ interaction of Gammel-Thaler, while representing the high energy scattering and polarization data very well, may not give the separation $^{2}P_{\frac{3}{2}}-{}^{3}P_{\frac{1}{2}}$ of O^{15} correctly. Considering this uncertainty in the $\mathbf{L}\cdot\mathbf{S}$ potential, we can conclude, from the present work, that is is possible to obtain a correct spin-orbit separation from an appropriate $\mathbf{L}\cdot\mathbf{S}$ term in the two-nucleon potential — a situation quite different from the tensor interaction, which gives too small a spin-orbit separation [5,6].

Now, if the good, apparent agreement between the calculated E in (4.17) and the empirical value is only a fortuitous result of the inaccurate $V^{LS}(r_{ij})$, it means that a V^{LS} giving a correct and hence much smaller value for $\bar{V}^{LS}$ in (4.15) would lead to too small a binding energy for O^{15}. There will then be a difference between the binding energy calculated, (4.17) and the empirical value. This may be due partly to the Hartree-Fock approximation itself which gives no contribution from the tensor interaction to E (unless one goes beyond the usual Hartree-Fock approximation by including some configuration mixing), and partly to the many further approximations made, namely, (i) the neglect of terms in the cluster development in dealing with the correlation function, (1.15), (1.16) and (ii) the use of harmonic oscillator functions, (2.28). To go beyond the present approximation regarding the cluster expansion would involve difficult calculations; but it would be comparably easy to improve on the use of harmonic oscillator wave functions. Since the $R_{nl}(r)$ for each l, in (2.28), form a complete set, one may expand the true (in the sense of Hartree-

Fock) $R^0_{1s}(r)$, say, in terms of the $R_{ns}(r)$ of (2.28), and in practice one may take a few terms

$$\begin{aligned} R^0_{1s}(r) &= \alpha_{11}R_{1s}(r)+\alpha_{12}R_{2s}(r)+\dots \\ R^0_{1p}(r) &= \alpha_{21}R_{1p}(r)+\alpha_{22}R_{2p}(r)+\dots \end{aligned} \tag{4.18}$$

where the α's are determined by the Ritz variational method (and by normalization). With these $R^0_{nl}(r)$, all integrals in $\bar{K}$, $\bar{C}$, $\bar{V}^C$, $\bar{V}^{LS}$ become sums of integrals involving harmonic oscillator wave functions, which can be evaluated with the aid of the transformation (3.3)—(3.4). This will free the investigation of the Hartree-Fock approximation of the restriction to harmonic oscillator wave functions. Such studies are necessary before one can properly assess the degree of validity of the Hartree-Fock approximation. This will be attempted in the near future.

The authors would like to express their appreciation to Messrs. Ferate, Ogata and Yeh for their help in the work and Mrs. M. Ratner for numerical computations.

Appendix A

The calculation of the matrix elements of the tensor interaction operator S_{ij} (1.6) for various spin states of i and j is facilitated by the following table of matrix elements of S_{ij}.

	$\alpha_i\alpha_j$	$\alpha_i\beta_j, \beta_i\alpha_j$	$\beta_i\beta_j$
$\alpha_i\alpha_j$	${}^2Y_{2,0}$	$Y_{2,-1}$	$Y_{2,-2}$
$\alpha_i\beta_j, \beta_i\alpha_j$	$Y_{2,1}$	$-2Y_{2,0}$	$-Y_{2,-1}$
$\beta_i\beta_j$	$Y_{2,2}$	$-Y_{2,1}$	${}^2Y_{2,0}$

(A.1)

${}^2Y_{2,0} = 3\cos^2\vartheta_{ij}-1$, $Y_{2,\pm1} = 3\sin\vartheta_{ij}\cos\vartheta_{ij}\,e^{\pm i\psi_{ij}}$, $Y_{2,\pm2} = 3\sin^2\vartheta_{ij}e^{\pm 2i\psi_{ij}}$, ϑ_{ij}, ψ_{ij} being the spherical polar angles between $\mathbf{r}_i$ and $\mathbf{r}_j$.

The matrix elements of $\mathbf{L}\cdot\mathbf{S}$ (1.8) for various spin states of i, j are given in the following table:

	$\alpha_i\alpha_j$	$\alpha_i\beta_j, \beta_i\alpha_j$	$\beta_i\beta_j$
$\alpha_i\alpha_j$	L_z	$\frac{1}{2}L_-$	0
$\alpha_i\beta_j, \beta_i\alpha_j$	$\frac{1}{2}L_+$	0	$\frac{1}{2}L_-$
$\beta_i\beta_j$	0	$\frac{1}{2}L_+$	$-L_z$

(A.2)

where

$$L_\pm = L_x \pm iL_y.$$

Appendix B

The integrals C_l (3.9) for the Coulomb energy, K_l (3.5) for the "correlation" energy, J_l (3.8) for the central field, and I_l (4.7) for the $\mathbf{L}\cdot\mathbf{S}$ interaction are given explicitly below.

$$R_{1l}(r) = N_{1l} r^{l+1} \exp(\tfrac{1}{4}\nu r^2), \quad r = r_{12};$$
$$N_{1s}^4 = 2\nu^3/\pi, \quad N_{1p}^4 = 2\nu^5/3^2\pi, \quad N_{1d}^4 = 2\nu^7/15^2\pi, \; N_{1f}^4 = 2\nu^9/105^2\pi; \tag{B.1}$$
$$R_{2s}^2(r) = \tfrac{3}{2}R_{1s}^2 - 3R_{1p}^2 + \tfrac{5}{2}R_{1d}^2.$$

$$C_s = \frac{1}{\zeta\eta}\mathscr{C},$$

$$C_p = \frac{2}{3(\zeta\eta)^2}\mathscr{C}[x\eta(3+\zeta)+2\beta^2], \tag{B.2}$$

$$C_d = \frac{4}{15(\zeta\eta)^3}\mathscr{C}[x^2\eta^2(12+6\zeta+\zeta^2)+2\beta^2 x\eta(9+2\zeta)+8\beta^4],$$

where

$$x = \tfrac{1}{2}\nu r_0^2, \quad \zeta = x+\beta, \quad \eta = x+2\beta, \quad \mathscr{C} = \frac{4e^2}{r_0}\left(\frac{x}{\pi}\right)^{\frac{1}{2}}\beta^2 e^{-x},$$

and r_0 is the radius of the repulsive core of the potential $V(r_{12})$.

$$K_s = \mathscr{K}[(\tfrac{3}{2}+\eta)e^{-x} + \tfrac{3}{4}Q]$$

$$K_p = \frac{2x}{3\eta}\mathscr{K}[(\tfrac{15}{4}+\tfrac{5}{3}\eta+\eta^2)e^{-x} + \tfrac{15}{8}Q] \tag{B.3}$$

$$K_d = \frac{4x^2}{15\eta^2}\mathscr{K}[(\tfrac{105}{8}+\tfrac{35}{4}\eta+\tfrac{7}{2}\eta^2+\eta^3)e^{-x} + \tfrac{105}{16}Q]$$

$$K_f = \frac{8x^3}{105\eta^3}\mathscr{K}[(\tfrac{945}{16}+\tfrac{315}{8}\eta+\tfrac{63}{4}\eta^2+\tfrac{9}{2}\eta^3+\eta^4)e^{-x} + \tfrac{945}{32}Q]$$

where

$$\mathscr{K} = \frac{4\hbar^2}{Mr_0^2}\left(\frac{x^3}{\pi}\right)^{\frac{1}{2}}\left(\frac{\beta}{\eta}\right)^2, \quad Q = \left(\frac{\pi}{\eta}\right)^{\frac{1}{2}} e^{2\beta}(1-E_2(\sqrt{\eta})),$$

and $E_2(t)$ is the error function

$$E_2(t) = \frac{2}{\sqrt{\pi}}\int_0^t e^{-t^2}dt.$$

For J_l, on using (1.4a), we obtain the following (dimensionless) integrals

$$J_s = 2\frac{r_C}{r_0}\left(\frac{x^3}{\pi}\right)^{\frac{1}{2}}(J_{s0}-2J_{s1}+J_{s2}),$$

$$(x+n\beta)J_{sn} = \exp\left(-x-\frac{r_0}{r_C}\right)-T_n,$$

$$J_p = \tfrac{4}{3}\frac{r_C}{r_0}\left(\frac{x^5}{\pi}\right)^{\frac{1}{2}}(J_{p0}-2J_{p1}+J_{p2}), \tag{B.4}$$

$$(x+n\beta)^2 J_{pn} = (1+z_n^2+3y_n-3z_n\sqrt{y_n})\exp\left(-x-\frac{r_0}{r_C}\right)-(\tfrac{3}{2}+y_n)T_n,$$

$$J_d = \tfrac{8}{15}\frac{r_C}{r_0}\left(\frac{x^7}{\pi}\right)^{\frac{1}{2}}(J_{d0}-2J_{d1}+J_{d2}),$$

$$(x+n\beta)^3 J_{dn} = [2(1+z_n^2+\tfrac{1}{2}z_n^4)+10y_n(1+z_n^2)+5y_n^2-5\sqrt{y_n}z_n(\tfrac{3}{2}+2y_n+z_n^2)]$$
$$\cdot\exp\left(-x-\frac{r_0}{r_C}\right)-(\tfrac{15}{4}+5y_n+y_n^2)T_n,$$

$$J_f = \tfrac{16}{105}\frac{r_C}{r_0}\left(\frac{x^7}{\pi}\right)^{\frac{1}{2}}(J_{f0}-2J_{f1}+J_{f2}),$$

$$(x+n\beta)^4 J_{fn} = [6(1+z_n^2+\tfrac{1}{2}z_n^4+\tfrac{1}{6}z_n^6)+42y_n(1+z_n^2+\tfrac{1}{2}z_n^4)+35y_n^2(1+z_n^2)+7y_n^3$$
$$-7\sqrt{y_n}z_n\{\tfrac{15}{4}+\tfrac{5}{2}z_n^2+z_n^4+\tfrac{5}{2}y_n(3+2z_n^2)+3y_n^2\}]\exp\left(-x-\frac{r_0}{r_C}\right)$$
$$-(\tfrac{105}{8}+\tfrac{105}{4}y_n+\tfrac{21}{2}y_n^2+y_n^3)T_n,$$

where

$$y_n = \left(\frac{r_0}{2r_C}\right)^2\cdot\frac{1}{x+n\beta}, \qquad z_n = \sqrt{x+n\beta}+\sqrt{y_n}, \qquad n = 0, 1, 2,$$

$$T_n = (\pi y_n)^{\frac{1}{2}}e^{n\beta+y_n}(1-E_2(z_n)).$$

For I_l in (4.7), one simply replaces r_C in (B.4) by $r_{LS} = \frac{1}{3.7}\times 10^{-13}$ cm. See table 2.

References

1) K. A. Brueckner, Phys. Rev. **97** (1955) 1353;
K. A. Brueckner and C. A. Levinson, Phys. Rev. **97** (1955) 1344;
R. J. Eden, Phys. Rev. **99** (1955) 1418; Proc. Roy. Soc. A **235** (1956) 408
H. A. Bethe, Phys. Rev. **103** (1956) 1353, and references given in the last paper
2) K. A. Brueckner, J. L. Gammel and H. Weitzner, Phys. Rev. **110** (1958) 431
3) G. E. Tauber and T. Y. Wu, Phys. Rev. **105** (1957) 1772

4) Gammel, Christian and Thaler, Phys. Rev. **105** (1957) 311;
Gammel and R. M. Thaler, Phys. Rev. **107** (1957) 291, 1337
5) L. Kisslinger, Phys. Rev. **104** (1956) 1077
6) B. P. Nigam and M. K. Sundaresan, Can. J. Phys. **36** (1958) 571
7) B. P. Nigam and M. K. Sundaresan, Phys. Rev. **111** (1958) 284
8) J. Dąbrowski, Proc. Phys. Soc. A **71** (1958) 658
9) R. Jastrow, Phys. Rev. **98** (1955) 1479;
F. Iwamoto and M. Yamada, Prog. Theor. Phys. **17** (1957) 543;
T. Ohmura, M. Morita and M. Yamada, Prog. Theor. Phys. **17** (1957) 326
10) I. Talmi, Helv. Phys. Acta **25** (1952) 185
11) M. Goeppert Mayer, Phys. Rev. **75** (1949) 1969; **78** (1950) 16, 22
12) Haxel, Jensen and Suess, Phys. Rev. **75** (1949) 1766
13) F. Ajzenberg-Selove and T. Lauritsen, Nuclear Physics **11** (1959) 195

1.E.4:
2.H

Nuclear Physics **16** (1960) 568—590; © *North-Holland Publishing Co., Amsterdam*
Not to be reproduced by photoprint or microfilm without written permission from the publisher

PARTIAL GAMMA RAY WIDTHS FOR LOW LYING LEVELS IN ALUMINIUM AND MAGNESIUM

F. R. METZGER, C. P. SWANN and V. K. RASMUSSEN

Bartol Research Foundation of the Franklin Institute, Swarthmore, Pennsylvania †

Received 25 January 1960

Abstract: The gamma rays resulting from the bombardment of Al and Mg with protons of 3.3 to 4.2 MeV energy were used to excite low lying levels in Al^{27}, Mg^{24}, and Mg^{25}. Combining the results of self absorption and resonance scattering studies with measured branching ratios, the following partial widths Γ_0 for the ground state transitions were obtained:

(1.01 MeV, $\frac{3}{2}+$) level in Al^{27} : $\Gamma_0 = 0.98\,\Gamma = (3.9\pm1.6) \times 10^{-4}$ eV

2.21 MeV level in Al^{27} : $\Gamma_0 = 0.98\,\Gamma = (g_1/g_2)(2.4\pm0.3) \times 10^{-3}$ eV

(1.37 MeV, 2+) level in Mg^{24} : $\Gamma_0 = \Gamma = (4.2\pm1.5) \times 10^{-4}$ eV

(1.61 MeV, $\frac{7}{2}+$) level in Mg^{25} : $\Gamma_0 = \Gamma = (3.0\pm1.5) \times 10^{-3}$ eV

The angular distribution of the 1.01 MeV resonance radiation was found to be of the form $W(\theta) = 1+(0.02\pm0.13)P_2(\cos\theta)$, that of the 2.21-MeV radiation $W(\theta) = 1+(0.23\pm0.03)P_2(\cos\theta)$.

1. Introduction

The studies of Mg^{25}, Al^{25}, and Si^{29} by the Chalk River group [1–4]) have suggested the existence of strong collective phenomena in these nuclei, and have enhanced the interest in the dynamical properties of these and other nuclei in this region of the periodic table. Al^{27} appeared to be especially well suited for measurements of level widths with the resonance fluorescence method which makes use of the gamma rays from inelastic proton scattering [5, 6, 7]) because it is the only stable isotope of aluminium and has a high (p, n) threshold ($E_p = 5.79$ MeV [8]). Recently, Coulomb excitation of the (0.84 MeV, $\frac{1}{2}+$) and the (1.01 MeV, $\frac{3}{2}+$) levels has been observed [9]), and the partial E2 widths [$\Gamma_{0.84}(E2) = 1.8\times10^{-5}$ eV; $\Gamma_{1.01}(E2) = 3.9\times10^{-5}$ eV] were found to be considerably larger than the Weisskopf unit, indicating collective phenomena in Al^{27}. Little is known about the third excited state at 2.21 MeV. The total angular momentum is most likely $\frac{3}{2}$ [10]). In two recent papers [11, 12]) a negative parity has been favoured.

A first survey using Al+p at $E_p = 4.1$ MeV showed strong resonance scattering from the 2.21 MeV level and considerably less scattering from the 1.01 MeV

† Assisted by the Joint Program of the U. S. Office of Naval Research and the U. S. Atomic Energy Commission. Reproduction in whole or in part is permitted for any purpose of the United States Government.

level. No appreciable resonance scattering from the 0.84 MeV level was expected in view of the long lifetime [9]) for this pure E2 transition.

When magnesium was used as a comparison scatterer, resonance scattering from the 1.37 MeV level in Mg^{24} was observed and was attributed to the presence of 1.37 MeV radiation from the reaction $Al^{27}(p, \alpha)Mg^{24}$. Since mean lives ranging from 3×10^{-11} s [13]) to 2.6×10^{-13} s [14]) have been reported for the first excited 2+ state in Mg^{24}, it was decided to carry out another determination of its width with the resonance fluorescence technique. In the course of this study it was found more convenient to use the 1.37 MeV gamma rays from $Mg^{24}(p, p')$ rather than those from $Al^{27}(p, \alpha)$ because of the smaller intensity of the competing transitions of higher energy in the former reaction. The use of a natural magnesium target and scatterer introduced gamma rays and resonance scattering from excited states in Mg^{25} and Mg^{26}. Since future studies of these isotopes with enriched targets were planned, only the most obvious effects were included in the present study and the results are to be considered as preliminary.

All the experiments were carried out in a new target room constructed of concrete which had been selected for its low radioactivity content [15]). The background in the energy region of interest was found to be approximately six times smaller than the background in the old target room. Since, for the 1.01 MeV transition, the room background in the new room was of the same order of magnitude as the sum of the resonance effect and the leakage through the direct-beam attenuator, the study of the 1.01 MeV transition would have been very difficult under the previous background conditions. As the "natural" background was reduced, one became more conscious of the background caused by neutrons through capture in the detector, the scatterer and the surrounding materials. With a target of virgin pig aluminium ($\approx$ 99.7 percent Al) at a bombarding energy of 4.15 MeV, the neutron contribution to the background became appreciable, and 99.99 percent pure aluminium had to be used.

The experiments emphasized anew the importance of self absorption experiments and the caution with which scattering results are to be used for lifetime determinations. It was found that for these targets with higher Z and higher density than those used in previous experiments, the scattering and slowing down of the excited recoil nuclei in the target material can no longer be neglected even for a transition with a lifetime as short as a few times 10^{-14} s. Since it is difficult to estimate the magnitude of these effects, the evaluation of $N(E_\tau)$, the number of gamma rays per unit energy interval at the resonance energy, is uncertain in such cases and the widths obtained from a scattering experiment alone are not very reliable. Whenever possible, the scattering experiments were supplemented with self absorption studies which are independent of the momentum distribution of the recoil nuclei.

The situation becomes really serious for the long-lived excited states ($\approx 10^{-12}$ s) for which the slowing-down process has almost reached its final

stage, thermalization. In a previous experiment [7]) with Na^{23}, for example, the slowing down of the recoil nuclei during the lifetime of the 440 keV level ($\approx 2\times10^{-12}$ s) resulted in $N_{exp}(E_r) \approx 6.5\times N_0(E_r)$, i.e. in a 6.5-fold increase of the actual intensity of resonant gamma rays over the intensity $N_0(E_r)$ estimated on the basis of the kinematics of the reaction, neglecting slowing down. On the other hand, in the case of the 1.37 MeV level in Mg^{24} with approximately the same lifetime, $N_{exp}(E_r)$ was found to be approximately $0.7\,N_0(E_r)$. The large difference may be shown to follow from the higher atomic number and the higher density, and from the difference in the ratio of the initial momentum to the momentum necessary to compensate for the gamma recoil energy losses.

2. The Gamma Ray Sources

2.1. $Al^{27}+p$

Thick water-cooled targets of 99.99 percent pure aluminium, bombarded with a 10μA proton current from the Bartol-ONR generator, provided the exciting gamma radiation. The bombarding energies ranged from 3.3 to 4.2 MeV. In this range of bombarding energies, the gamma rays from Al+p have recently been studied [11]) with the aid of an intermediate-image spectrometer. At $E_p = 3$ MeV, gamma rays of 0.84, 1.01 and 1.37 MeV energy were observed, the first two being attributed to $Al^{27}(p, p')$, the third to $Al^{27}(p, \alpha)Mg^{24}$. At higher bombarding energies additional gamma rays with energies of 1.72, 2.21, 2.74 and 3 MeV were excited, the 2.21 MeV radiation being by far the most intense of the four. With the possible exception of the 2.74 MeV radiation which could, at least partially, be produced by $Al(p, \alpha)$, these more energetic gamma rays were attributed to the inelastic scattering process. Since the 0.84, 1.01, 2.21, 2.74 and 3 MeV gamma rays are ground state transitions in Al^{27} they all could give rise to resonance fluorescence in this element. However, at the bombarding energies used, the 0.84, 2.74 and 3 MeV levels were not appreciably resonance excited either because their widths are small, the branching unfavourable, the intensities $N(E_r)$ in the exciting beam small, or because of a combination of these factors. Of the two remaining levels at 1.01 and 2.21 MeV, the 2.21 MeV level can be studied conveniently at a bombarding energy of 4.155 MeV where the yield of 2.21 MeV gamma rays is high, the neutron background still tolerable, and the intensity of the higher energy gamma rays in the direct beam small. A typical pulse height distribution of the gamma radiation from Al+p at this bombarding energy is shown in fig. 1. The yield of 2.21 MeV gamma rays was found to be $\approx 6\times10^{7}\,\mu C^{-1}$.

The 1.01 MeV transition was studied at bombarding energies of 3.55, 3.33, and 3.30 MeV. At $E_p = 3.30$ MeV, the thick target yield of 1.01 MeV gamma rays was measured as $\approx 8\times10^{7}\,\mu C^{-1}$, and the ratio of the peak counting rates

in the full energy lines was approximately 200 : 1 in favour of the 1.01 MeV over the 2.21 MeV radiation. Considering the relative probability of producing resonance scattering, and the relative magnitude of the 2.21 MeV pulse height distribution at the position of the 1.01 MeV peak and at the full energy peak, this meant that the contribution of the resonance scattering from the 2.21 MeV level at the position of the 1.01 MeV line would be smaller than 5 % of the 1.01 MeV line.

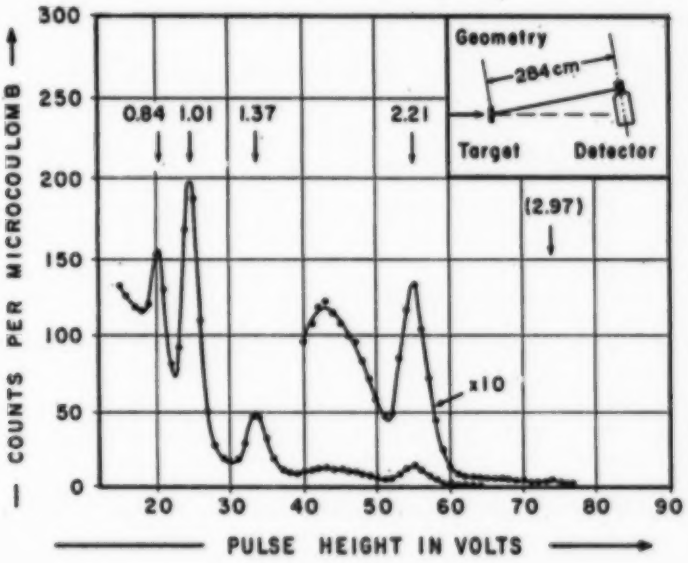

Fig. 1. Pulse height distribution of the gamma radiation from $Al^{27}+p$ at $E_p = 4.155$ MeV (thick target). A NaI(Tl) crystal of 4.4 cm diameter and 5.1 cm length, shielded with 0.32 cm of Pb, was used in the geometry indicated in the insert.

The use of a low bombarding energy also eliminated the possibility that cascade decay from the 2.21 MeV level through the 1.01 MeV level might simulate 1.01 MeV resonance scattering. Although it was thus possible to eliminate this effect of the 2.21 MeV level branching, its direct effect on the evaluation of the 2.21 MeV scattering experiment made a study of the intensities of possible 1.37—0.84 MeV and 1.20—1.01 MeV cascades with coincidence techniques desirable. Sodium iodide detectors of 3.8 cm × 3.8 cm and 4.4 cm × 5.1 cm were connected in a conventional fast-slow coincidence circuit with a resolving time of 10^{-8} s and placed close to the aluminium target. The efficiency of the arrangement was determined with a Co^{60} source of known strength placed at the position of the target. When the Al+p radiation was studied with this coincidence arrangement at $E_p = 4.155$ MeV, it soon became apparent that the intensities of the 1.20—1.01 MeV and 1.37—0.84 MeV cascades were smaller than 10 % of the 2.21 MeV intensity, and that the presence of 1.72—1.01 MeV coincidences from the decay of the 2.74 MeV level interfered with the determination of the small branching ratios. Typical pulse height

distributions are shown in fig. 2. The coincidence peaks at 1.01 and 1.72 MeV can be fully accounted for by a 1.72—1.01 MeV cascade involving approximately 2 % of the 1.01 MeV transitions. From the absence of a peak at 1.20 MeV, the

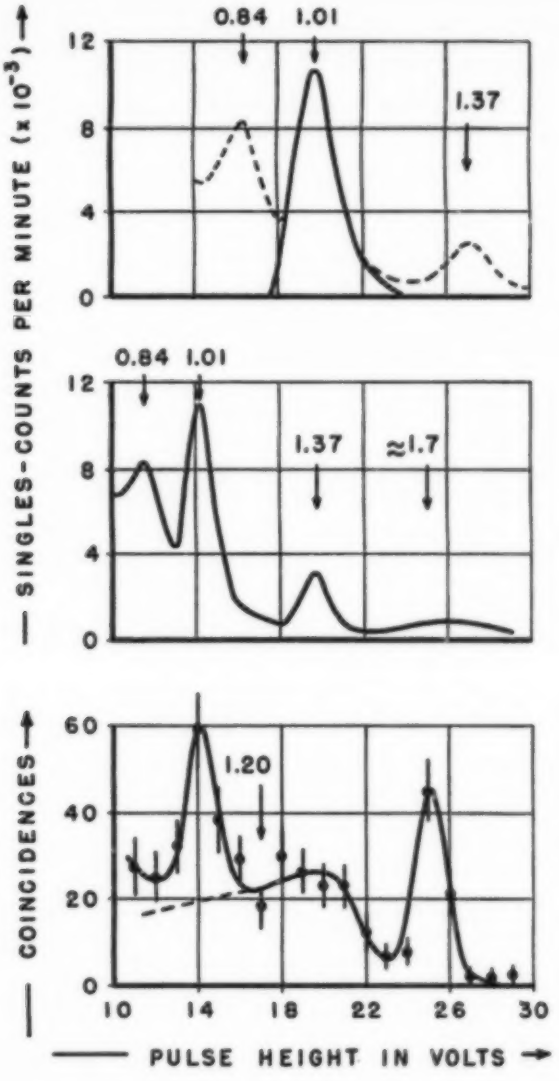

Fig. 2. Pulse height distributions observed in the search for 1.2 MeV transitions from the 2.21 MeV level to the 1.01 MeV level. The figure in the middle represents the pulse height distribution of the singles counts from counter B. The bottom curve gives the pulse height distribution of those pulses from B which are in coincidence with the selected group of pulses from counter A indicated by the heavily drawn curve in the top figure. The dashed curve in this top figure represents the singles pulse height distribution in counter A.

intensity of a possible 1.20—1.01 MeV cascade was estimated to be less than 2 % of the intensity of the 2.21 MeV ground state transition.

From similar data with the gate on the 0.84 MeV line, the 1.37—0.84 MeV cascade was estimated to account for 1.3 ± 1.3 percent of the deexcitations of

the 2.21 MeV level. For the following, a value $\Gamma_0/\Gamma = 0.98 \pm 0.02$ was used for the ratio of the partial width Γ_0 of the ground state transition and the total width Γ of the 2.21 MeV level.

The angular distribution of the 0.84 and the 1.01 MeV gamma radiations with respect to the proton beam was measured at $E_p = 3.55$ MeV and found to be isotropic. The angular distribution of the 1.37 MeV radiation at the same bombarding energy showed a small anisotropy ($\approx$ 8 percent). The distribution of the 2.21 MeV radiation, measured at $E_p = 4.155$ MeV, was found to be approximately of the form $W(\beta) = 1+0.16 \cos^2\beta$, where β is the angle with respect to the direction of the proton beam.

For the evaluation of the scattering experiments it is necessary to know, for the range of emission angles β subtended by the scatterers, $N(E_r, \beta) = F(E_r, \beta)N_{\text{total}}$, the number of gamma rays per unit energy interval at the resonance energy E_r. While the calculation of the actual fraction $F(E_r, \beta)$ when the excited nuclei lose appreciable energy by collision is virtually impossible, it is a simple matter to calculate, on the basis of the excitation function and the kinematics of the reaction, the fraction $F_0(E_r, \beta)$ relating to the collision-free case with isotropic distributions and correlations of the reaction products. For the emission angles used in the experiments, the calculated values were

$$F_0(1.01 \text{ MeV}) = 3.2 \times 10^{-4} \text{ eV}^{-1} \text{ for } E_p = 3.30 \text{ MeV},$$
$$F_0(1.37 \text{ MeV}) = 5.2 \times 10^{-5} \text{ eV}^{-1} \text{ for } E_p = 4.155 \text{ MeV},$$
$$F_0(2.21 \text{ MeV}) = 1.08 \times 10^{-4} \text{ eV}^{-1} \text{ for } E_p = 4.155 \text{ MeV}.$$

2.2 Mg+p

A water-cooled magnesium target of 99.95 percent purity was bombarded with protons in the energy range of 3 to 4 MeV in the hope of obtaining a more favourable source of 1.37 MeV gamma rays than the reaction $Al^{27}(p, \alpha)$. It was found that the thick target yield of the 1.37 MeV radiation from the magnesium target increased by a factor of ten when the bombarding energy was raised from 3 to 4 MeV. Since the neutron background at $E_p = 4$ MeV was still tolerable, this energy was chosen for the experiments. A pulse height distribution of the gamma radiation at this bombarding energy is reproduced in fig. 3. From this figure it may be seen that, aside from the 1.37 MeV gamma ray, the 1.61 MeV radiation from $Mg^{25}(p, p')$ and the 1.83 MeV transition from the first excited state of Mg^{26} were also present. In addition, an indication of 1.96 MeV gamma radiation, attributed to $Mg^{25}(p, p')$, was found. Since the 1.96 MeV level decays in 50 percent of the disintegrations to the 0.58 MeV level in Mg^{25} [2]), the corresponding 1.38 MeV gamma ray must be part of the main 1.37 MeV peak, accounting for approximately 7 percent of the peak height. Whether this cascade gamma ray will contribute to the resonance excitation of the 1.37 MeV

level in Mg^{24} depends on the lifetime of the 1.96 MeV level and on the precise energies of the levels. Since the 1.96 MeV transition is presumably M1, and the 1.96 MeV level is therefore expected to be short lived, it is likely that the contribution of the 1.38 MeV cascade gamma ray will be that corresponding to the collision-free approximation. In calculating the fraction of 1.37 MeV gamma rays per unit energy interval at the resonance energy for Mg+p, the weighted average $F_0(1.37\ \text{MeV}) = 1.33\times10^{-4}\ \text{eV}^{-1}$ of the contributions from $Mg^{24}(p, p')$ and $Mg^{25}(p, p')$ was used.

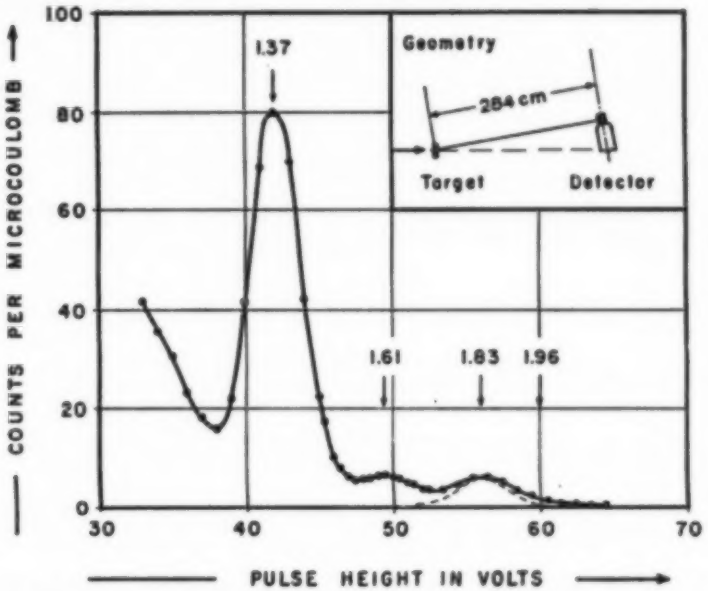

Fig. 3. Pulse height distribution of the gamma radiation from Mg+p at $E_p = 4$ MeV (thick target) A NaI(Tl) crystal of 4.4 cm diameter and 5.1 cm length, shielded with 0.32 cm of Pb, was used in the geometry indicated in the insert.

The thick target yield of 1.37 MeV radiation at the bombarding energy $E_p = 4$ MeV, $\approx 18\times10^7\ \mu C^{-1}$, was more than twice that of the reaction $Al^{27}(p, \alpha)$ at $E_p = 4.155$ MeV. Since, in addition, $F_0(1.37\ \text{MeV})$ for Mg(p, p') is approximately twice that of the $Al^{27}(p, \alpha)$ reaction, the use of Mg(p, p') promised to be considerably more favourable.

The thick target yield for the 1.61 MeV transition at $E_p = 4$ MeV was estimated to be $1.4\times10^7\ \mu C^{-1}$. The fraction of 1.61 MeV gamma rays per eV at resonance was calculated for an effective proton energy of 3.8 MeV as $F_0(1.61\ \text{MeV}) = 1.2\times10^{-4}\ \text{eV}^{-1}$.

3. The 2.21 MeV Level in Al^{27}

3.1. SCATTERING, ANGULAR DISTRIBUTION

Most of the experiments with the 2.21 MeV radiation were carried out in a ring geometry (fig. 4) using aluminium, magnesium (Dow metal †) and SiO_2

† A typical analysis of the alloy used for the scatterer was: 95.7 % Mg, 3 % Al, 0.3 % Mn, and 1.0 % Zn.

scatterers. The aluminium scatterer had an inside diameter of 34.5 cm, an outside diameter of 40.0 cm, and was 10.1 cm wide; it had an average density of 1.9 g/cm^3 because the individual 0.32 cm thick sheets making up the scatterer

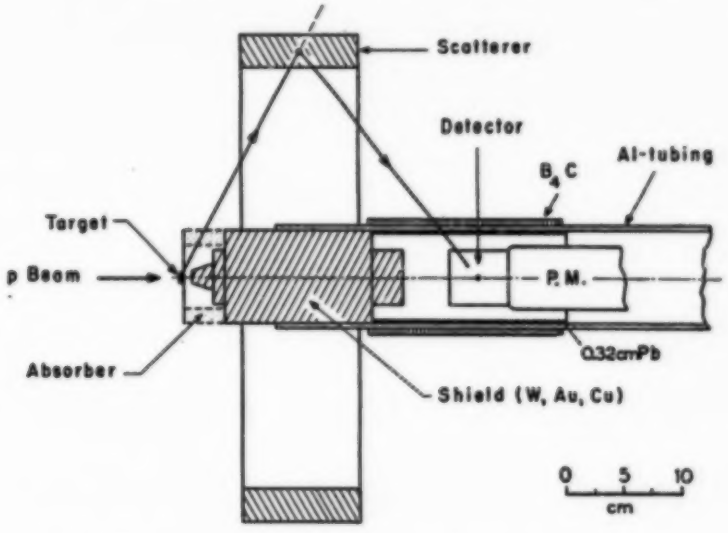

Fig. 4. Geometry used for the self absorption experiments.

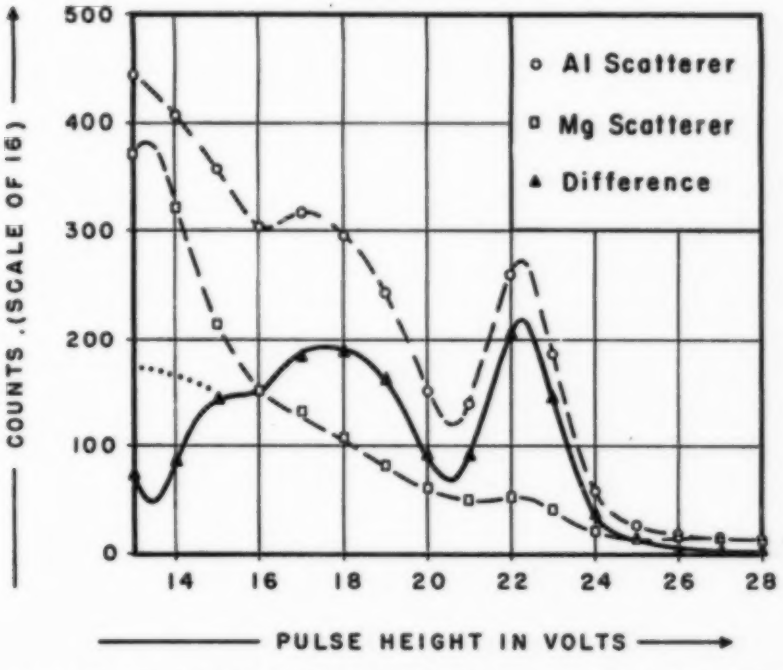

Fig. 5. Pulse height distributions of the $Al^{27}+p$ radiation scattered from Al and Mg scatterers in the geometry of fig. 4. $E_p = 4.155$ MeV. The difference curve representing the resonance scattered radiation is heavily drawn and has the shape expected for a 2.21 MeV gamma ray at pulse heights 15 to 26. Below pulse height 15 the curve dips (the expected shape is indicated by the dotted line) because of the presence of 1.37 MeV resonance scattering from the Mg comparison scatterer.

were spaced apart in order to reduce the density approximately to that of the comparison scatterers, Mg and SiO_2, and thus to match the scatterers with respect to the number of electrons.

The pulse height distributions observed in a typical scattering experiment, using the gamma radiation from $Al^{27}+p$ at 4.155 MeV, are shown in fig. 5. The difference curve exhibits the shape expected for a 2.21 MeV gamma ray. The deviation below pulse height 15 is a consequence of resonance fluorescence from the first excited state of Mg^{24} excited in the magnesium scatterer by the 1.37 MeV gamma radiation from $Al^{27}(p, \alpha)Mg^{24}$. Approximately 80 percent of the counting rate with the magnesium scatterer at pulse heights above 1.5 MeV is attributed to leakage through the direct beam attenuator. Of the remaining counting rate, the major portion was caused by the aluminium present in the Dow metal of the "magnesium" comparison scatterer. Thus the actual background scattering from the comparison scatterer amounted to less than one percent of the Al—Mg difference. Resonance scattering from the higher energy levels was observed to be of the order of two percent of the scattering from the 2.21 MeV level. Because of the weakness of this scattering from the higher levels no effort was made to study it in more detail. In correcting for this contribution, it was assumed that the 3 MeV level (doublet) was responsible for all the resonance scattering above 2.21 MeV. The appropriate shape of the 3 MeV line was deduced from pulse height distributions of the 2.61 MeV gamma ray in Pb^{208} and the 3.11 MeV radiation in C^{13}.

It has been pointed out earlier [5, 6]) that the resonant gamma rays from inelastic scattering are restricted to a limited conical zone around approximately 90° to the proton beam provided the lifetime of the level is so short that no collisions of the recoiling nuclei take place before the emission of the gamma radiation. In the absence of collisions the distribution of the resonant gamma rays within the conical zone, $F_0(E_\gamma, \beta)$, where β is the angle with the proton beam, depends upon the angular distribution of the excited Al^{27} nuclei and upon the distribution of the gamma radiation with respect to the Al^{27*} velocity. One way of obtaining the shape of the distribution $F(E_\gamma, \beta)$ experimentally consists in measuring the resonance scattering from a small scatterer placed at different angles β relative to the proton beam. For the 2.21 MeV radiation of Al^{27} at a bombarding energy of 4.155 MeV one expects the conical zone of the resonant gamma rays to extend from 46° to 130°. The first measurements with a 2.54 cm wide scatterer in a ring geometry of the type shown in fig. 4 indicated a rapid falling off of $F(E_\gamma, \beta)$ for $\beta \leqq 50°$. However, even at an angle $\beta = 30°$ an appreciable resonance effect was observed. The measurements at angles smaller than 30° became very awkward with the ring geometry. It was therefore decided to use a "point" geometry for measurements down to $\beta = 0°$. When the two sets of measurements were combined, the "cone" shape shown in fig. 6 was obtained. From this figure it is evident that collision effects are already present

for the very short-lived 2.21 MeV state and that therefore the effective $F(E_r, \beta)$ is only approximately known.

For a geometry of the type shown in fig. 4, the resonance scattering counting rate may be expressed in the form

$$N_{\text{scatt}} = n_r \frac{g_2}{g_1} \frac{\lambda^2}{4} \frac{\Gamma_0^2}{\Gamma} \sum_\nu \left\{ \frac{N(E_r, \beta_\nu) \Delta V_\nu \mu_\nu \varepsilon_\nu f(\theta_\nu) \, e^{-n(\sigma_T l_{i\nu} + \sigma_T' l_{o\nu})}}{4\pi d_{i\nu}^2 d_{o\nu}^2} \right\} \qquad (1)$$

where the summation extends over all the volume elements ΔV_ν of the scatterer. Whenever there occurs appreciable branching from the level, the factor Γ_0^2/Γ replaces the usual width Γ, Γ_0 being the partial gamma width for the ground state transition and Γ the total width of the level. In eq. (1), n_r is the

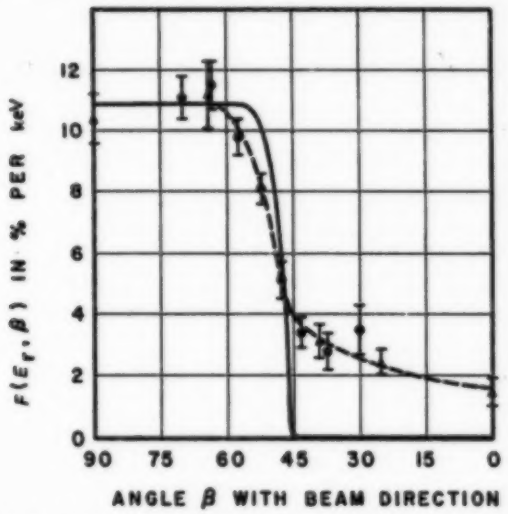

Fig. 6. Comparison of the calculated and the measured shapes of the effective cone of emission of resonant 2.21 MeV gamma rays for a thick Al target bombarded with protons of 4.155 MeV energy. The average of the experimental points at 90°, 70°, 65° and 64° was normalized to the value of the "plateau" of the calculated curve.

number of resonant nuclei per cm^3, g_2 and g_1 are the statistical weights of excited state and ground state, respectively; $\lambda = 1.24 \times 10^{-10}/E_\gamma$ is the wavelength of the gamma radiation in cm if the gamma ray energy E_γ is expressed in MeV, σ_T and σ'_T are the total cross sections for electronic absorption of the incoming and outgoing radiation, σ'_T being somewhat smaller than σ_T because of the possibility of scattering-in; n is the total number of nuclei per cm^3, $l_{i\nu}$ and $l_{o\nu}$ are the incoming and outgoing scatterer path lengths traversed by the radiation in reaching the center of ΔV_ν, and in leaving it on the way to the detector; $d_{i\nu}$ and $d_{o\nu}$ are the distances from the volume elements to the source and the detector, respectively;

$$\mu_\nu = \sum_{m=0}^{\infty} \frac{(-1)^m (n_r K l_{i\nu})^m}{m!(m+1)^{\frac{1}{2}}}$$

is the resonance attenuation for the incoming path length $l_{1\nu}$, K being the effective peak absorption cross section $K = (g_2\lambda^2\Gamma_0)/(4g_1\pi^{\frac{1}{2}}\Delta)$ containing the Doppler width $\Delta = (E_\gamma/c)(2kT/M)^{\frac{1}{2}}$; $f(\theta_\nu)$ is the value of the normalized angular distribution function for the scattering angle θ_ν; ε_ν the ratio of the detection efficiencies with oblique and with normal incidence for a given distance from the detector. Since the incident and the resonance scattered radiation have the same energy, it is not necessary to know the energy dependence of the detection efficiency, nor is a determination of the effective area of the crystal necessary as long as the measurement of the direct beam intensity is carried out with the same detector. As written in eq. (1), $N(E_r, \beta)$ is given by

$$N(E_r, \beta) = N_{DB}(\beta)D^2F(E_r, \beta) \tag{2}$$

where $N_{DB}(\beta)$ is the counting rate in a direct beam measurement with normal incidence of the gamma radiation on the detector placed at a distance D from the target.

Because of the uncertainties as to the slowing-down process, the actual fractions $F(E_r, \beta)$ appearing in eq. (2) were replaced for the evaluation of the scattering experiments by the "collision free" fractions $F_0(E_r)$ given in sections 2.1 and 2.2.

As may be seen from eq. (1), the evaluation of the scattering experiments in terms of line widths requires a knowledge of the angular distribution of the resonance radiation. Such a knowledge might enable one to determine, in addition, the mixing ratio of competing multipoles in the transition and might provides clues as to the spin of the excited state. For the angular distribution

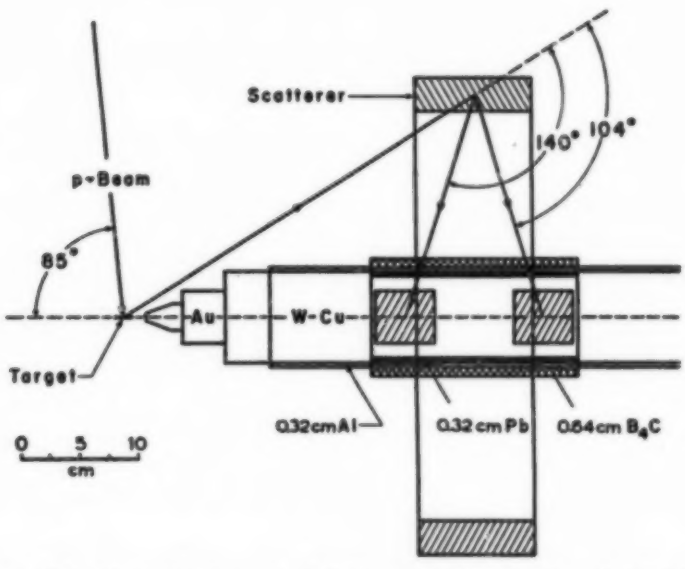

Fig 7. Geometry used for the measurement of the angular distribution of the 2.21 MeV resonance radiation. Note that the axis of the detection system is tilted relative to the beam direction.

measurements, the geometry of fig. 7 was used. The relative position of source and scatterer remained the same during the whole experiment, the scattering angle being changed by moving the detector. The main advantage of this procedure is that of being independent of an accurate knowledge of the cone shape $F(E_\gamma, \beta)$. It should be pointed out that in this experiment the axis of the detection system was tilted relative to the beam direction because of the particular cone shape for the 2.21 MeV radiation (fig. 6) and the restrictions of the ring geometry. With the usual positioning of the detection system (fig. 4), the angle β would have had to be $\approx 30°$ and the resonance effect would have been low. By swinging the detection system by $\approx 90°$ the scatterers were at more favourable angles (60°—120°) and the angular distribution could be measured with some degree of accuracy. Measurements were taken with 10.2 cm wide scatterers as well as with 2.54 cm wide scatterers at mean scattering angles of 100°, 104°, 140° and 144°. The products of relative detection efficiency and solid angle of the scintillation counter in these positions were empirically determined using the 2.19 MeV gamma rays from a point source of Pr^{144} (Ce^{144}).

3.2. SELF ABSORPTION EXPERIMENT

The self absorption experiment was carried out in the geometry of fig. 4 with ring absorbers of 7.6 cm outside diameter placed between target and shield. The aluminium absorber had an inside diameter of 5.1 cm, the inside diameter of the magnesium absorber was adjusted to give that absorber the electronic attenuation of the aluminium absorber. The two absorbers were compared in a good geometry transmission experiment using Co^{60} gamma rays and the matching was found to be good to within 3 percent. It should be mentioned that, while the magnesium scatterer was actually Dow metal, the magnesium absorber was machined from magnesium which had an aluminium contamination of only 0.003 percent.

TABLE 1

2.21 MeV level in Al^{27}. $E_p = 4.155$ MeV. Total counts (scale of 16) in a typical self absorption experiment in the geometry of fig. 4 using nominal 1.27 cm absorbers. The actual counting time for each scatterer-absorber combination was 6400 seconds.

Scatterer	Absorber	Counts in peak	Differences
Al	Al	563.0±5.9	$Al_{Al} - Mg_{Al} = 399.9 \pm 6.7$
Mg	Al	163.1±3.2	
Al	Mg	644.7±6.3	
Mg	Mg	163.9±3.2	$Al_{Mg} - Mg_{Mg} = 480.8 \pm 7.1$

The counting rates of a typical run are given in table 1. The time required for this run was 10 hours. From the differences given in table 1, the self absorption

for this particular run is obtained as

$$R = \frac{(\mathrm{Al_{Mg}} - \mathrm{Mg_{Mg}}) - (\mathrm{Al_{Al}} - \mathrm{Mg_{Al}})}{\mathrm{Al_{Mg}} - \mathrm{Mg_{Mg}}} = 0.168 \pm 0.021.$$

Here $\mathrm{Al_{Mg}}$ stands for the counting rate with the Al scatterer and the Mg absorber, i.e., the suffix refers to the absorber. The values of R expected for different widths Γ_0 may be calculated using eq. (1) and adding the path lengths in the absorber to the incoming path lengths $l_{1\nu}$.

3.3. RESULTS

The angular distribution data were analyzed under the assumption that $W(\theta) = A_0 + A_2 P_2(\cos\theta)$. The experiments with the 10.2 cm scatterers led to a value $A_2/A_0 = 0.23 \pm 0.03$, while those performed with the 2.54 cm scatterers yielded $A_2/A_0 = 0.25 \pm 0.07$. The average value is

$$A_2/A_0 = 0.23 \pm 0.03.$$

The scattering experiment was evaluated by inserting into eq. (1) the result of the angular distribution measurements, and the "collision-free" value $F_0(2.21) = 1.08 \times 10^{-4}\ \mathrm{eV}^{-1}$ from section 2.1. The information provided by the self absorption study was not used. A value for $(g_2/g_1)\Gamma_0$ was first calculated neglecting the self absorption within the scatterer. Then the self absorption corresponding to this first width was taken into account and a second value for $(g_2/g_1)\Gamma_0$ was obtained. The self absorption correction corresponding to this new width was then applied, etc. This iteration process converges rapidly to a "self consistent" value for $(g_2/g_1)\Gamma_0$. For one of the runs of $3\frac{1}{2}$ hours duration, the total counts were

$$N_{\mathrm{scatt}} = 7552, \quad N_{\mathrm{DB}}(60°) = 2.32 \times 10^6 \text{ at } D = 289\ \mathrm{cm}.$$

Using $n_r = 4.24 \times 10^{22}\ \mathrm{cm}^{-3}$, $\lambda^2 = 3.15 \times 10^{-21}\ \mathrm{cm}^2$, and writing for the sum in eq. (1) $\sum = N(E_r) \sum' = 1.08 \times 10^{-4}\ N_{\mathrm{DB}} D^2 \sum'$, with $\sum' = 5.53 \times 10^{-4}$ for $\mu_\nu = 1$, one arrives at the relation

$$7552 = 33.4 \frac{g_2}{g_1} \frac{\Gamma_0^2}{\Gamma} \times 11.2 \times 10^3.$$

According to 2.1, the branching for the 2.21 MeV level is $\Gamma_0/\Gamma = 0.98$. With this one obtained as a first approximation a value $(g_2/g_1)\Gamma_0 = 2.06 \times 10^{-2}$ eV. Using the iteration process described above, the consecutive values for $(g_2/g_1)\Gamma_0$ were, in units of 10^{-2} eV, 2.06, 2.39, 2.45, 2.47, 2.47, ... A similar, but somewhat shorter run gave a self-consistent $(g_2/g_1)\Gamma_0$ of 2.54×10^{-2} eV in good agreement with the first run. When the directly measured self absorption from section 3.2 was used to correct the scattering data for resonance attenuation in the scatterer, a value $(g_2/g_1)\Gamma_0 = 2.44 \times 10^{-2}$ eV was calculated for the first

run. It is felt that, in spite of the good statistical accuracy, the "scattering value" for the width, $(g_2/g_1)\Gamma_0 = 2.5\times10^{-2}$ eV, is only reliable to within a factor two because of the uncertainty in $N(E_r)$ introduced by the collisions. In calculating the Doppler width Δ appearing in the expression μ_ν for the resonance attenuation within the scatterer, an effective temperature of 326° K was used. The difference between this value and the actual temperature of 300° K represents the effect of the crystalline binding [16]) in Al, assuming a Debye temperature [17]) of $\theta = 394°$.

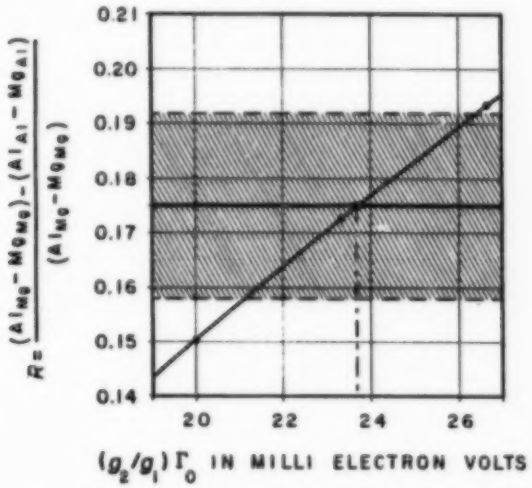

Fig. 8. Comparison of the calculated self absorption with the range of experimental values.

In the self absorption study (sect. 3.2), the final ratio R was found to have the value $R = 0.175\pm0.017$ for a nominal 1.27 cm Al absorber. Using eq. (1), modified for the use of an absorber, the numerator and denominator in the expression for R were calculated for three different values of $(g_2/g_1)\Gamma_0$. The relationship of R and $(g_2/g_1)\Gamma_0$ obtained in this way is indicated in fig. 8 in which the experimental information is also incorporated. From fig. 8 one reads off

$$\frac{g_2}{g_1}\Gamma_0 = (2.36\pm0.30)\times10^{-2}\,\text{eV}.$$

The close agreement with the result of the scattering experiment indicates that in the case of the 2.21 MeV level the modification of $N(E_r)$ by collisions was small.

4. The 1.01 MeV Level

4.1. SCATTERING, ANGULAR DISTRIBUTION

Since preliminary experiments had indicated that the lifetime of the 1.01 MeV level in Al^{27} was much longer than that of the 2.21 MeV level, collision effects were expected to be large for the 1.01 MeV radiation, and scattering experiments

were considered of not much help in determining the width of the level. Consequently, no specific scattering experiments were performed. However, scattering information is available from both the angular distribution and the self absorption experiments.

The angular distribution of the 1.01 MeV resonance radiation was determined by measurements at two scattering angles, 104° and 140°. A slight modification of the geometry of fig. 7 was used. The Mg comparison scatterer was replaced by a SiO_2 scatterer in order to avoid interference from the 1.37 MeV level in Mg^{24}. Moreover, the axis of the detection system was not tilted, but coincided with the beam direction. This was possible because, even in the absence of collisions, the conical zone containing the resonant 1.01 MeV gamma rays was considerably larger than it had been for the 2.21 MeV radiation. In addition, large collision effects were expected to produce a more or less isotropic distribution of the quanta capable of exciting the 1.01 MeV level. Because of the smallness of the resonance effect, no attempt was made to use 2.54 cm scatterers. The angular dependence of the product of relative detection efficiency and solid angle was determined with a point source of Sc^{46} which has an average gamma ray energy of 1.01 MeV.

4.2. SELF ABSORPTION

The geometry was that of fig. 4, the only change being the use of an absorber path length of 2.54 cm. Since it was found that the absorber material could not be made bigger than the 7.62 cm diameter heavy metal shield without interference from stray radiation, the magnesium in the comparison absorber was combined with copper to match the electronic absorption of the 7.62 cm o.d., 2.54 cm i.d. aluminium absorber.

A first self absorption experiment was carried out at $E_p = 3.55$ MeV with sulfur as the comparison scatterer. This sulfur scatterer had also been matched with the other 10.2 cm wide scatterers as far as the total number of electrons was concerned. However, an appreciable mis-match with respect to the non-resonant elastic (Rayleigh) scattering was observed. In addition, at $E_p = 3.55$ MeV, the contribution of the 2.21 MeV resonance scattering in the pulse height region of 1.01 MeV was very considerable. Since the self absorption of the 2.21 MeV resonance radiation is much larger than that of the 1.01 MeV radiation, the 2.21 MeV contribution in the 1.01 MeV pulse height region is strongly attenuated and simulates a larger 1.01 MeV self absorption. In order to reduce these possible sources of error and uncertainty, the bombarding energy was reduced to 3.30 MeV and the sulfur scatterer replaced by a SiO_2 scatterer for which the matching with respect to the non-resonant elastic scattering was at least 2.5 times better. Since the self absorption was very small, 50 hours of actual running time were necessary to obtain the still somewhat unsatisfactory result given in sect. 4.3.

4.3. RESULTS

Assuming the form $W(\theta) = A_0 + A_2 P_2(\cos\theta)$, the ratio A_2/A_0 for the 1.01 MeV resonance radiation was found to have the value $A_2/A_0 = 0.02 \pm 0.13$.

With this, and assuming the collision-free value for the fraction of 1.01 MeV gamma rays per eV at the resonance energy as given in sect. 2.1, the scattering information was evaluated using eq. (1). With $n_r = 4.24 \times 10^{22}$ cm^{-3}; $g_2/g_1 = \frac{2}{3}$; $\lambda^2 = 1.51 \times 10^{-20}$ cm^2 and $\mu_r = 1$, the angular distribution experiment at 140° ($E_p = 3.33$ MeV) led to $\Gamma_0^2/\Gamma = 3.2 \times 10^{-4}$ eV, while the scattering in the self absorption experiment ($E_p = 3.30$ MeV) gave $\Gamma_0^2/\Gamma = 3.1 \times 10^{-4}$ eV. According to Lyons and Lazar [18]) and the Chalk River group [19]), Γ_0/Γ for the 1.01 MeV state is 0.98. With this, and correcting for ≈ 1.5 percent self absorption, the naive interpretation of the scattering information led to $\Gamma_0 = 3.3 \times 10^{-4}$ eV. A more meaningful interpretation of the scattering data in the light of the experience with the 1.37 MeV level in Mg^{24} will be given in section 7.2.

After correcting for the contribution of the 2.21 MeV level, the self absorption measured at $E_p = 3.55$ MeV using a sulfur comparison scatterer was $R = 0.08 \pm 0.06$. The self absorption measured at $E_p = 3.30$ MeV, using a SiO_2 comparison scatterer, was $R = 0.016 \pm 0.032$. A value $R = 0.03 \pm 0.03$ is considered to give a fair representation of the experimental results. From a plot of R versus Γ_0 similar to that given in fig. 8, the width Γ_0 was found to be

$$\Gamma_0 = 2.6^{+2.6}_{-2.6} \times 10^{-4} \text{ eV}.$$

5. The 1.37 MeV Level in Mg^{24}

The 1.37 MeV level in Mg^{24} is known to be a 2+ state. The angular distribution of the resonance radiation was therefore not measured, but assumed to be that for a 0—2—0 spin sequence, namely $f(\theta) = 1.25 - 3.75\cos^2\theta + 5\cos^4\theta$.

Since the self absorption could not be measured with sufficient accuracy when the reaction $Al^{27}(p, \alpha)$ was used as the gamma ray source, further studies were carried out with the gamma rays from Mg+p at $E_p = 4$ MeV. The pulse height distributions of the direct Mg+p radiation and of the Mg+p radiation scattered from Al and Mg scatterers in the geometry of fig. 4 were measured in an exploratory one-half hour run preceding the actual experiments with the 1.37 MeV radiation. The results of this short study are summarized in fig. 9 where the pulse height distribution of the resonance scattered radiation is compared with that of the direct beam. It was clear from this comparison that the 1.61 MeV transition in the 10.1 percent abundant isotope Mg^{25} is much more effective in producing resonance fluorescence than the 1.37 and the 1.83 MeV transitions, and that the contribution from this line had to be taken into account in the analysis of the 1.37 MeV data. Consequently, the twenty-channel analyzer was adjusted to accept both the 1.37 and 1.61 MeV lines during the 1.37 MeV self absorption experiments. The data thus collected were used for the determination of the partial widths of both transitions.

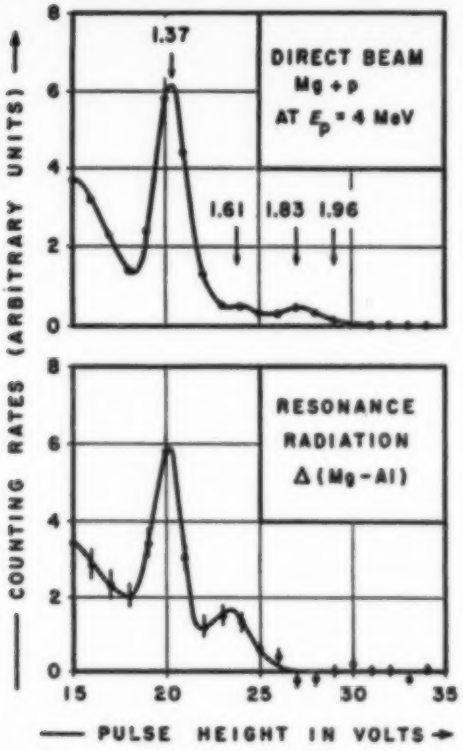

Fig. 9. Pulse height distributions of the direct beam (top) and of the resonance scattered radiation (bottom) for Mg. The resonance scattering from the (1.83 MeV, 2+) level in Mg^{26} is seen to be at least one order of magnitude smaller than the scattering from the 1.61 MeV level in Mg^{25}.

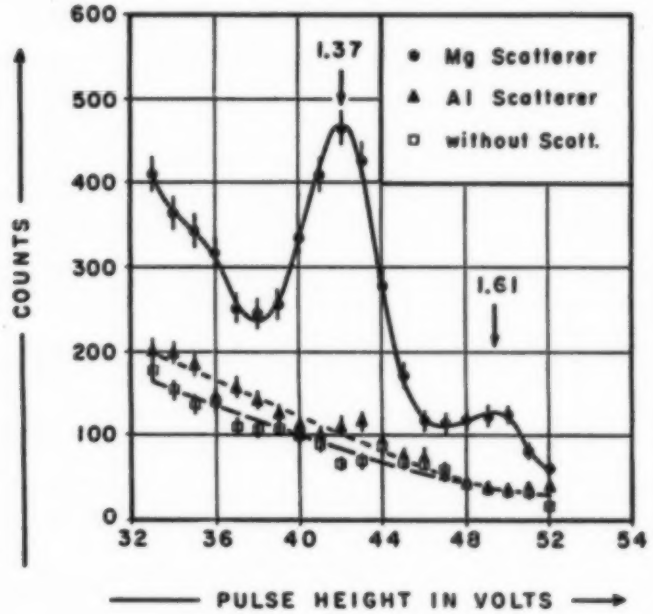

Fig. 10. Pulse height distributions of the Mg + p radiation scattered from Mg and from Al and of the background radiation observed without scatterer. $E_p = 4.0$ MeV.

For the actual self absorption experiments, magnesium and aluminium scatterers of 10.2 cm width were used in the geometry of fig. 4. Typical pulse height distributions are shown in fig. 10. With a magnesium absorber of 7.62 cm outside diameter and 3.84 cm inside diameter, the self absorption of the 1.37 MeV resonance radiation was measured as $R = 0.058 \pm 0.019$. This value has already been corrected for a small contribution from the 1.61 MeV level. With $\Gamma = \Gamma_0$ for the 1.37 MeV level, the self absorption was found to lead to a width $\Gamma(1.37) = (4.2 \pm 1.5) \times 10^{-4}$ eV corresponding to a mean life $\tau_\gamma = (1.6^{+0.8}_{-0.5}) \times 10^{-12}$ s for this pure E2 transition.

Since the experimental lifetime was close to that of the 1.01 MeV transition in Al^{27}, for which one should like to have some way of estimating the slowing-down effects, it seemed to be of interest to calculate for the reactions Mg^{24} (p, p') and Al^{27}(p, α) the actual fractions $F(1.37)$ of 1.37 MeV gamma rays per eV interval at the resonance energy from the experimental data, and to compare them with the "collision-free" values $F_0(1.37)$. Using the "collision-free" values F_0 from sections 2.1 and 2.2, widths of 2.9×10^{-4} eV and 3.8×10^{-4} eV were obtained from the magnitude of the resonance scattering in the self absorption experiments with the reactions Mg(p, p') and Al(p, α), respectively. Comparison with the width obtained from the self absorption yields the ratios $F/F_0 = 0.7 \pm 0.3$ for the reaction Mg(p, p') and $F/F_0 = 0.9 \pm 0.4$ for the reaction Al(p, α) and the actual fractions $F_{pp'} = 9.2 \times 10^{-5}$ eV^{-1} and $F_{p,\alpha} = 4.7 \times 10^{-5}$ eV^{-1}. The large uncertainties in the ratios reflect mainly the error in the self absorption width of the 1.37 MeV transition.

6. The 1.61 MeV Level in Mg^{25}

Using the information gathered on the 1.61 MeV line in the course of the 1.37 MeV self absorption studies, a preliminary estimate for the width of the 1.61 MeV level was obtained.

From the self absorption $R = 0.05 \pm 0.04$ of the 1.61 MeV resonance scattering by a 7.62 cm o.d., 3.84 cm i.d. magnesium absorber, a width $\Gamma_0 = (1.7 \pm 1.4) \times 10^{-2}$ eV was calculated. For this calculation the most probable spin value [2]) of $\frac{7}{2}$ was used. With the same spin value, and using the collision-free value $F_0 = 1.2 \times 10^{-4}$ eV^{-1} from section 2.2, the analysis of the resonance scattering led to a width $\Gamma_0 = (5 \pm 2) \times 10^{-4}$ eV, assuming $\Gamma_0 = \Gamma$. Based on these two measurements, a preliminary value $\Gamma = (3 \pm 1.5) \times 10^{-2}$ eV was adopted for the total width of the 1.61 MeV level in Mg^{25}.

7. Discussion

7.1. THE 2.21 MeV LEVEL IN Al^{27}

In quoting the partial width Γ_0 of the 2.21 MeV ground state transition, the statistical factor was incorporated because there still exists some uncertainty concerning spin and parity of the 2.21 MeV excited state in Al^{27}. The observa-

tion of an anisotropic distribution of the 2.21 MeV gamma rays from Al(p, p′) (section 2.1) immediately rules out spin $\frac{1}{2}$. Spin $\frac{7}{2}$ and higher spins are ruled out by the observation [10]) in the capture reaction $Mg^{26}(p, \gamma)$ of strong transitions from resonance levels with spins $\frac{1}{2}$ and $\frac{3}{2}$ to the 2.21 MeV state. This same observation favours the value $\frac{3}{2}$ among the remaining possibilities of $\frac{3}{2}$ and $\frac{5}{2}$. Studies [12]) of the angular distribution of the inelastically scattered protons in the reaction $Al^{27}(p, p')$ at $E_p = 5$ MeV favour a large momentum transfer ($l = 3$) and suggest $\frac{1}{2}-$ and $\frac{9}{2}-$ assignments. Since, however, these spins have

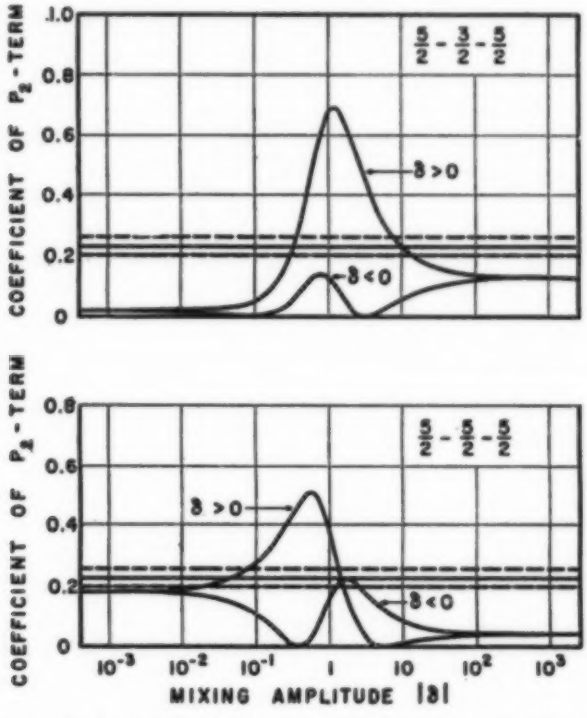

Fig. 11. Theoretical coefficients [20]) of the P_2-terms in the angular distribution function $W(\theta) = 1 + A_2 P_2(\cos\theta)$ for mixed dipole-quadrupole resonance radiation. The upper figure applies to an excited state with spin $\frac{3}{2}$, the lower figure to an excited state with spin $\frac{5}{2}$. The range of the experimental coefficient for the 2.21 MeV level is indicated.

already been ruled out and since one would expect considerable $l = 1$ contributions for spins $\frac{3}{2}$ and $\frac{5}{2}$, the conclusion concerning the parity drawn from these experiments must be viewed with caution.

Of the remaining four possible assignments: $\frac{3}{2}\pm$ and $\frac{5}{2}\pm$, at least one is made unlikely by the observed angular distribution of the resonance radiation (3.3). In fig. 11, the observed coefficient of $P_2(\cos\theta)$ in the angular distribution of the 2.21 MeV resonance radiation is compared with the predicted coefficients [20]) for different mixing amplitudes $\delta = (I_{\text{quadr.}}/I_{\text{dipole}})^{\frac{1}{2}}$ and the two possible spin values. The assumption is made that the incident gamma beam was unpolarized. From fig. 11 one finds that for spin $\frac{3}{2}$ the smallest value of $|\delta|$

permitted by the experiment is 0.3. With a Γ_0 of 3.6×10^{-2} eV this would mean that the partial quadrupole width $\Gamma(2)$ must be larger than 3×10^{-3} eV. With $R = 1.2\times10^{-13}\,A^{\frac{1}{3}}$ cm, the single particle estimates of Blatt and Weisskopf [21]) for the partial quadrupole widths are $\Gamma(E2) = 2.1\times10^{-4}$ and $\Gamma(M2) = 2.6\times10^{-5}$. Thus, with the spin value $\frac{3}{2}$, the E2 transition probability would be enhanced by at least a factor 14, the M2 transition probability by a factor of at least 115. While a factor 14 is not uncommon for collective E2 transitions, an enhancement of an M2 transition by more than two orders of magnitude would be extremely unusual. On this basis the $\frac{3}{2}-$ assignment is eliminated or at least appears to be very unlikely. For the spin value $\frac{5}{2}$ a similar conclusion cannot be drawn, i.e., both parity assignments are possible.

In table 2 the widths Γ_0, the mixing ratios and the enhancement factors derived from the resonance fluorescence experiments are summarized for the three possible assignments of spins and parities to the 2.21 MeV level in Al^{27}.

TABLE 2

2.21 MeV level in Al^{27}. Mixing ratios and widths for different spin and parity assignments.

J	Parity	Γ_0 (10^{-3} eV)	δ	δ^2	$\Gamma_{exp}(2)$ (10^{-3} eV)	$\frac{\Gamma_{exp}(2)}{\Gamma_{sp}(2)}$
$\frac{5}{2}$	+	36 ± 5	0.3 -0.37	$0.11^{+0.03}_{-0.02}$	$3.6^{+1.4}_{-1.1}$	17^{+7}_{-5}
$\frac{3}{2}$	+	24 ± 3	0.02$-$0.08	$(2.7^{+3.7}_{-2.3})\cdot10^{-3}$	$0.07^{+0.10}_{-0.06}$	$0.3^{+0.5}_{-0.25}$
$\frac{3}{2}$	−					2.5^{+4}_{-2}

The last column lists the ratio of the observed partial quadrupole width to that expected on the basis of the independent particle model [21]).

Table 2 shows that, as long as one depends on the angular distribution of the resonance radiation for the determination of the mixing in the 2.21 MeV transition, the experimental value for the enhancement of the E2 transition probability depends strongly on the spin assignment. A discussion of the applicability of the rotational model to Al^{27} is, therefore, premature as long as the spin and parity of the 2.21 MeV level are not known. A study of the polarization of the resonance radiation, a detailed analysis or the correlations of the cascades leading to the 2.21 MeV level, or Coulomb excitation of the level with heavy ions should solve this problem.

For all the assignments of table 2 the small branching from the 2.21 MeV level to the 1.01 MeV level is somewhat surprising and will have to be explained by more detailed considerations of the two states involved (K-forbiddenness?). The small branching of the 0.84 MeV level is expected for the $\frac{5}{2}+$ assignment, but for the two other assignments it poses the same problem as the branching to the 1.01 MeV level. It certainly would be of considerable help if not just a

limit for the branching were available, but if the actual branching were determined. An improvement by a factor of ten over our limit should be possible. It should probably be mentioned that a spin assignment of $\frac{7}{2}$ to the 2.21 MeV level would explain the small branching and would make the 2.21 MeV level the possible analogue of the 1.61 MeV $\frac{7}{2}+$ states in Al^{25} and Mg^{25}. However, as was pointed out earlier, such an assignment is in conflict with some of the observations [10]) on the capture radiation from $Mg^{26}(p, \gamma)$.

7.2. THE 1.01 MeV LEVEL IN Al^{27}

The self absorption experiment with the 1.01 MeV transition in Al^{27} was compatible with a rather large range of widths. Since some information on the slowing down in Al and Mg was available from the experiments with the 1.37 MeV level in Mg^{24}, an attempt was made to use this information for an estimate of the slowing down in the Al(p, p′) reaction involving the 1.01 MeV state of Al^{27}. The pertinent information for the three reactions involved in this comparison is collected in table 3.

TABLE 3

Information used for the slowing-down calculations.

Reaction	E_p (MeV)	E_γ (MeV)	$v_{initial}$ ($10^{-3}c$)	v_{min} ($10^{-3}c$)	$10^{12} \times \tau_{level}$ (s)	$10^5 \times F_{obs}$	$10^5 \times F_0$	$\frac{F_{obs}}{F_0}$
Mg(p, p′)	4.00	1.37	0.82 – 6.38	6.1	$1.6^{+0.8}_{-0.5}$	9.2	13.3	0.7 ± 0.3
Al(p, α)	4.155	1.37	3.85 – 10.21	6.1	$1.6^{+0.8}_{-0.5}$	4.7	5.2	0.9 ± 0.4
Al(p, p′)	3.30	1.01	0.57 – 5.07	4.0	>1.2	–	22	–

$v_{initial}$ and v_{min} are recoil velocities of the excited nuclei, v_{min} being the lowest velocity capable of providing compensation for the gamma recoil energy losses. v_{min} is obtained from the relation $(v_{min}/c)E_\gamma = E_\gamma^2/Mc^2$. The "collision-free" F_0 values were taken from sections 2.1 and 2.2, the observed F values and the ratios F/F_0 from section 5

The similarity in the recoil velocity distributions for the two inelastic scattering reactions and the small difference in atomic number between Al and Mg made it reasonable to assume that the slowing-down for Mg(p, p′) was almost identical to that for Al^{27}(p, p′) except for a density correction. Rudimentary range-velocity curves for nitrogen, oxygen and argon recoils are available [22]) and do not differ too much. Since Mg and Al were expected to fall somewhere between the oxygen and nitrogen curves on one side and the argon curve on the other, a range-velocity curve intermediate between the two sets was drawn and used to calculate the slowing down of Al and Mg recoils from the initial velocities given in table 3 to the minimum velocities at which resonant gamma rays can be emitted. Noting that the fraction of gamma rays per unit energy interval increases as v_{init}/v, and folding-in the exponential decay, the

curves of fig. 12 were obtained. The portions of the curves covering the ranges of lifetimes determined experimentally in the self absorption studies are drawn more heavily. The F/F_0 values for Mg(p, p') are seen to range from 1.35 to 0.92, those for Al(p, α) from 1.9 to 1.3. Comparison with table 3 shows that in both cases the curves of fig. 12 give high estimates of F/F_0. It may then be inferred that for the reaction Al(p, p') $F/F_0 < 1.2$. Combined with the information obtained in section 4.3. from the scattering data, this leads to a lower limit for the partial width of the 1.01 MeV gamma transition: $\Gamma_0 > 2.3\times10^{-4}$ eV.

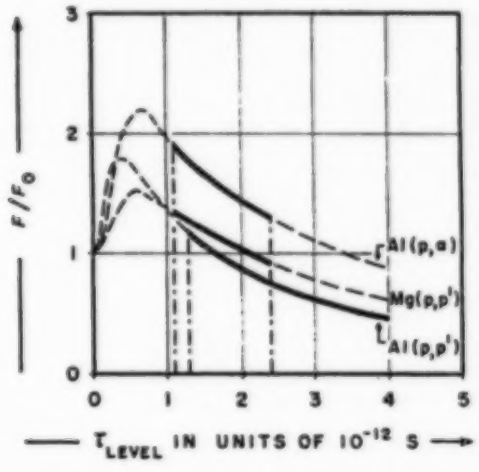

Fig. 12. Effect of collisions on the fraction of gamma rays per unit energy interval at the resonance energy E_r. The fraction F is plotted in units of the "collision-free" fraction F_0 for different values of the mean life of the excited state and for the bombarding conditions given in table 3. The regions allowed by the self absorption studies are heavily drawn.

Thus the scattering data and the self absorption study restrict the width $\Gamma_0(1.01)$ to a narrow range of energies which may be summarized by quoting $\Gamma_0 = (3.8\pm1.6)\times10^{-4}$ eV.

From Coulomb excitation experiments with heavy ions [9]) the partial E2 width of the 1.01 MeV level is known to be $\Gamma(E2) = 3.9\times10^{-5}$ eV. The E2/M1 mixing ratio δ^2 in the 1.01 MeV transition is thus $\delta^2 = 0.1\pm0.05$. A comparison of the experimental value $A_2 = 0.02\pm0.13$ from section 4.3. with the theoretical coefficients A_2 which may be read off from fig. 11 (top) for this range of $|\delta|$ values strongly favours a negative mixing amplitude δ.

7.3. THE 1.37 MeV LEVEL IN Mg^{24}

Our value for the lifetime of this level is in line with the recently accumulating evidence [23–27]) which indicates that the extreme values reported earlier [13,14]) must be in error. The average value of all the measurements, omitting the two extremes, is $\Gamma = (3.9\pm0.4)\times10^{-4}$ eV. This is approximately 21 times larger than the single particle width [21]) calculated with $R = 1.2\times A^{\frac{1}{3}}\times10^{-13}$ cm for an E2 transition.

References

1) Litherland, Paul, Bartholomew and Gove, Phys. Rev. **102** (1956) 208
2) Gove, Bartholomew, Paul and Litherland, Nuclear Physics **2** (1956/57) 132
3) Bromley, Gove and Litherland, Can. Journ. Phys. **35** (1957) 1057
4) Litherland, McManus, Paul, Bromley and Gove, Can. Journ. Phys. **36** (1958) 378
5) Metzger, Swann and Rasmussen, Phys. Rev. **110** (1958) 906
6) Swann, Rasmussen and Metzger, Phys. Rev. **114** (1959) 862
7) Rasmussen, Metzger and Swann, Nuclear Physics **13** (1959) 95
8) Kington, Bair, Cohn and Willard, Phys. Rev. **99** (1955) 1393
9) Alkhazov, Grinberg, Gusinskii, Erokhina and Lemberg, JETP **35** (1958) 1055 [translation: Soviet Phys. JETP **35** (1959) 736]
10) Van der Leun, Endt, Kluyver and Vrenken, Physica **22** (1956) 1223
11) Ranken, Bonner, Castillo-Bahena, Harlow and Rabson, Phys. Rev. **112** (1958) 239
12) De S. Barros, Forsyth, Jaffe and Taylor, Proc. Phys. Soc. A **73** (1959) 793
13) C. F. Coleman, Phil. Mag. **46** (1955) 1135
14) N. A. Burgov and Iu. V. Terekhov, JETP **35** (1958) 932 [translation: Soviet Phys. JETP **35** (1959) 651]
15) Swann, Rasmussen and Albrecht, Journ. Franklin Inst. **268** (1959) 226
16) W. E. Lamb, Phys. Rev. **55** (1939) 190
17) J. deLaunay, in Solid State Physics, edited by F. Seitz and D. Turnbull (Academic Press, New York, 1956) Vol. **2**, p. 233
18) W. S. Lyon and N. H. Lazar, Phys. Rev. **101** (1956) 1524
19) Almqvist, Bromley, Gove and Litherland, Bull. Am. Phys. Soc. **2** (1957) 178
20) L. C. Biedenharn and M. E. Rose, Revs. Mod. Phys. **25** (1953) 729
21) J. M. Blatt and V. F. Weisskopf, Theoretical Nuclear Physics (John Wiley and Sons, New York, 1952), Ch. XII
22) P. M. S. Blackett and D. S. Lees, Proc. Roy. Soc. A **134** (1931/32) 658
23) Richard H. Helm, Phys. Rev. **104** (1956) 1466
24) N. Deliagin and V. Shipnel, Bull. Acad. Sci. U.S.S.R. **22** (1958) 861
25) Alkhazov, Grinberg, Gusinskii, Erokhina and Lemberg, JETP **35** (1958) 1056 [translation: Soviet Phys. JETP **35** (1959) 737]
26) Arns, Sund and Wiedenbeck, Phys. Rev. Letters **2** (1959) 50
27) S. Ofer and A. Schwarzschild, Phys. Rev. Letters **3** (1959) 384

5

Nuclear Physics **16** (1960) 591—596; © *North-Holland Publishing Co., Amsterdam*

Not to be reproduced by photoprint or microfilm without written permission from the publisher

SEARCH FOR THE NATURAL ALPHA ACTIVITY OF TUNGSTEN†

G. B. BEARD and W. H. KELLY

Department of Physics and Astronomy, Michigan State University, East Lansing, Michigan

Received 26 January 1960

Abstract: Scintillation properties of $CdWO_4$ and $CaWO_4$ crystals have been studied and the crystals used in the search for natural alpha activity in tungsten. The relative scintillation efficiencies for gammas were found to be nearly the same for the two crystals and equal to approximately 0.1 that of NaI(Tl). An external source of 5.3 MeV alpha particles produces approximately the same size pulses as 1.7 MeV gammas. The scintillation decay times were found to be 3.3μs and 3.9μs for $CaWO_4$ and $CdWO_4$, respectively.

Background measurements were made with a 3.8 cm diameter × 0.64 cm NaI(Tl) crystal. No indication of an alpha activity of tungsten was seen. It is concluded that any tungsten alpha activity present corresponds to a half-life of greater than $8\,K\times10^{17}$ y where K is the relative isotopic abundance of the isotope undergoing decay. This is in disagreement with the previously reported half-life of $2.2\,K\times10^{17}$ y.

1. Introduction

A naturally occurring alpha radioactivity associated with tungsten has been reported [1,2]) with an energy of 3.0 MeV and a half-life of $2.2\,K \times 10^{17}$ years, where K is the relative abundance of the isotope undergoing decay. According to standard alpha decay theory this activity should be attributed to a rare, and as yet undiscovered, tungsten isotope [1,2]).

These results were obtained using nuclear emulsion techniques. This method has the advantage that accurate energy determinations can be made with the disadvantage that specific activities are difficult to measure accurately. Therefore, the tungsten alpha activity has been reinvestigated using a different technique to obtain a more accurate measurement of the specific activity.

Considering the very low specific activity and short range of the alpha particles (i.e. a few microns), one could best observe the decay by a device in which the tungsten forms part of the detector. Fortunately this condition can be fulfilled using cadmium or calcium tungstate crystals, both of which have been known to be good scintillators for some time [3]). With them relatively large amounts of tungsten can be used without the otherwise overwhelming problem of self-absorption.

† This research was supported in part by the United States Air Force under contract No. AF49(638)-10 monitored by the Air Force Office of Scientific Research of the Air Research and Development Command.

2. Scintillation Properties of $CdWO_4$ and $CaWO_4$ Crystals

Large, clear crystals of either $CdWO_4$ or $CaWO_4$ are relatively rare. They can be grown artificially with some difficulty and only $CaWO_4$ (scheelite) crystals are found in nature. Along with various smaller specimens, one large $CdWO_4$ and a somewhat smaller scheelite crystal were obtained. After polishing the $CdWO_4$ crystal weighed 20.9 g and was roughly 4.5 cm long by 1.3 cm wide and 0.5 cm thick with fairly flat surfaces top and bottom. The $CaWO_4$ crystal weighed 9.85 g after polishing and had a more compact, though irregular, shape. Neither crystal was completely transparent throughout.

For the study of the scintillation response and for the counting experiments, the crystals were mounted on a 6363 photomultiplier. A long time constant (≈ 50 μs) at the photomultiplier anode was used because of the long scintillation decay times of the crystals. At the output of a cathode follower preamplifier, the relative pulse heights due to Cs^{137} gamma rays from the two large crystals were approximately the same and equal to about one-tenth of the pulse heights from a NaI(Tl) crystal. The rise time of the scheelite crystal pulses was about 7.5 μs while the pulses from the large $CdWO_4$ crystal had a rise time of about 10 μs. Well defined photo peaks were obtained for various gamma ray energies. The resolution for 0.662 MeV gammas was 24 % for the scheelite and 31 % for the $CdWO_4$ crystal. Most of the difference in resolution between the crystals is attributed to the much poorer geometry of the $CdWO_4$ crystal for the detection of gamma rays. Good linearity for gamma response was obtained for both crystals in the energy range from 30 keV to 1.28 MeV.

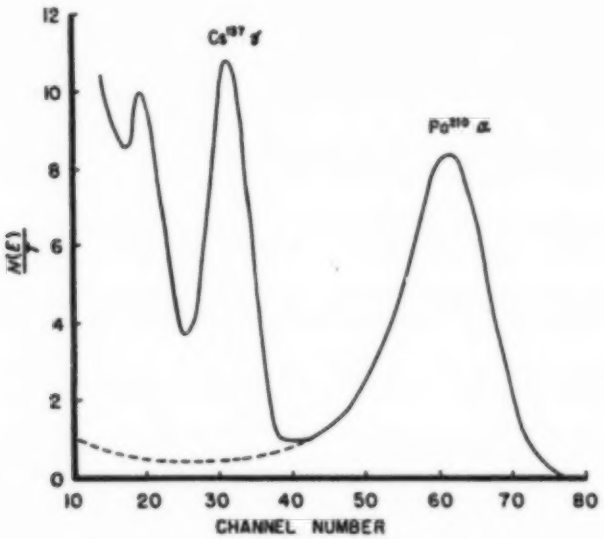

Fig. 1. Spectrum of the Po^{210} 5.3 MeV alphas and the 0.662 MeV gammas of Cs^{137} obtained using a thin $CdWO_4$ crystal weighing 0.50 g. The dashed line shows the low energy region with no gammas present.

To measure the response to alpha particles a small amount of Po^{210} in the form of polonium chloride was applied directly to the surfaces of small $CaWO_4$ and $CdWO_4$ crystals. The work of der Mateosian and Yuan [4]) with Po^{210} applied on the surface of NaI(Tl) crystals has shown that, at least for NaI(Tl), one may expect fairly good agreement with results from an internal alpha source.

Fig. 1. shows the Po^{210} 5.3 MeV alpha peak along with the response to Cs^{137} 0.662 MeV gammas obtained using a thin $CdWO_4$ crystal weighing 0.50 g. Similar results were obtained using a small artificial $CaWO_4$ crystal, although the relative heights of the gamma and alpha peaks were somewhat different in the two cases. This may have been partially due to different surface conditions on the two crystals; one was quite smooth and the other rough. The 5.3 MeV alpha particles produced approximately the same size pulses as 1.7 MeV gammas. The rise times for the output pulses produced by gamma rays and alpha particles were the same. No Po^{210} was added to the large $CdWO_4$ and scheelite crystals used in the search for the tungsten alpha activity because such contamination could impair their usefulness in future experiments.

As a further check on the response of these crystals to alpha particles and to establish a lower limit for the position of the anticipated tungsten 3.0 MeV alpha peak, a thin layer of $SmCl_3$ was evaporated in a vacuum onto the top face of the large $CdWO_4$ crystal. The resulting increase in counting rate due to the 2.2 MeV alphas of Sm^{147} is shown by the crosses in the top curve of fig. 2. The amount of $SmCl_3$ added to the crystal was unknown although it did amount to a readily visible layer. Comparing the response of the two $CdWO_4$ crystals to the Po^{210} and Sm^{147} alphas relative to the Cs^{137} gamma peak, it appears that $CdWO_4$ may be nonlinear for low energy alpha particles. Because of the difference in crystals and surface layers involved, nothing quantitative can be inferred. However, it does set upper and lower boundaries for the position of the 3.0 MeV tungsten alpha activity and one can therefore specify the region where the tungsten alpha peak should appear if present.

3. Low Level Counting Experiments

An RIDL Model A-61 amplifier and 256 channel pulse height analyzer were used with the previously described detector and preamplifier to record the counts. The photomultiplier assembly including preamplifier was placed horizontally in a cubical container made of iron 15 cm thick on four sides and 7.6 cm thick on the ends. The iron container was surrounded by 7.6 cm of lead on all sides. An additional 7.6 cm of lead were used on the top shielding against cosmic rays. A background anti-coincidence counter was not used because of space limitations in the shielded housing.

Runs were made with both the large $CdWO_4$ and scheelite crystals. In the case of the $CdWO_4$ the total counting time was 193 hours, approximately

$\frac{2}{3}$ before and $\frac{1}{3}$ after the addition of the $SmCl_3$. The counting time for the scheelite crystal was 120 hours. A 3.8 cm diameter × 0.64 cm NaI(Tl) crystal was used to determine the background which was counted for a total of 112 hours. In all three cases, the photo peak of the Cs^{137} 0.662 MeV gamma ray was used for periodic gain checks.

4. Results

The top curve of fig. 2 shows the results obtained using the $CdWO_4$ crystal both with and without $SmCl_3$. Also plotted on the same figure is the spectrum

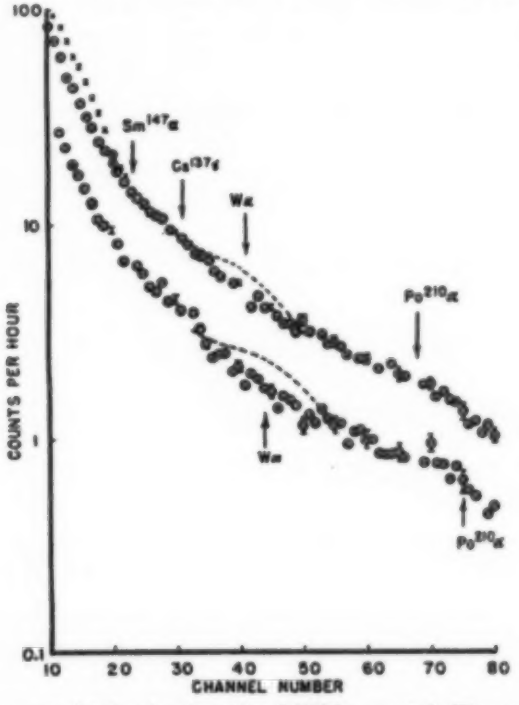

Fig. 2. The top spectrum was obtained using the $CdWO_4$ crystal. The crosses show the increased counting rate after $SmCl_3$ was added. The bottom spectrum was obtained using the $CaWO_4$ crystal. The dashed curves show the peaks to be expected for a tungsten alpha activity corresponding to a half-life of $2.2\,K \times 10^{17}$ y, centered on the most likely channel in each case. The error flags show the statistical standard deviations for the various sections of the spectra and the arrows designate the regions of interest.

obtained later with the $CaWO_4$ crystal. For each spectrum the most likely channel for the center of a tungsten alpha peak is indicated. The small bump at about channel 30 that appears on the $CaWO_4$ spectrum was also present in some of the last background runs obtained with the NaI(Tl) crystal. It coincides with the Cs^{137} calibration peak and results from an accidental contamination that occurred after the $CdWO_4$ spectrum was obtained. The contamination corresponded to an effective source strength of about 0.1×10^{-12} c at the crystal and did not interfere with the region of interest where the background remained unchanged.

The dashed curves on the spectra show the peaks to be expected for an alpha activity corresponding to a half-life of $2.2K \times 10^{17}$ years centered on the most likely channel in each case. A triangular distribution with a resolution of 25 % was assumed. This resolution is consistent with the relative responses of the $CdWO_4$ crystal to gamma rays and alpha particles. Since the $CaWO_4$ crystal had better resolution, this figure is somewhat conservative for the $CaWO_4$. The peaks found for the high energy Po^{210} alphas had around 24 % resolution. However, considerably better resolution should be expected for internal alpha sources of the same energy [4]).

Fig. 3 shows the difference between each tungstate crystal spectrum and the NaI(Tl) background spectrum. In each case the background spectrum was

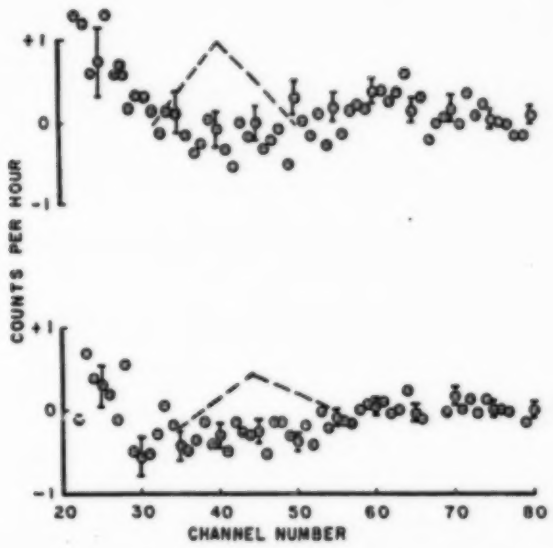

Fig. 3. The top plot shows the difference between the $CdWO_4$ crystal spectrum and the NaI(Tl) background spectrum normalized at channel 55. The bottom plot shows the difference between the $CaWO_4$ crystal spectrum and the NaI(Tl) background spectrum normalized at channel 60. The dashed curves show the expected shapes of the difference plots for a tungsten alpha activity corresponding to a half-life of $2.2K \times 10^{17}$ y.

normalized at channels just above the region of the tungsten alpha peak. The dashed curves show the expected shapes of the difference plots for the conditions given in the previous paragraph. Below channel 30 the counting rates become relatively high and small percentage variations give rather large difference counts.

From fig. 2 it can be seen that the spectra from the $CdWO_4$ and $CaWO_4$ crystals fail to show the expected peaks. This result is corroborated by the lack of any significant deviations from the normalized background spectrum as shown in fig. 3. Since this background was measured using a NaI(Tl) crystal having different scintillation characteristics from the tungstate crystals, it probably does not represent the true background for them. However, it is

reasonable to assume that after normalization it should represent a good approximation for the relatively small energy region involved. Assuming a peak whose height is two standard deviations above background should be seen, it is concluded that any tungsten alpha activity present corresponds to a half-life of greater than $8K \times 10^{17}$ years.

The authors wish to thank Mr. Paul E. Desautels of the Smithsonian Institution for giving them the scheelite crystal and Dr. Richard Kebler of the Linde Company for the large $CdWO_4$ crystal as well as smaller specimens. They also acknowledge the assistance of Mr. Howard Covington and Mr. Ralph A. Peters in the early stages of the problem.

References

1) W. Porschen and W. Riezler, Z. Naturforsch. **8a** (1953) 503
2) W. Porschen and W. Riezler, Z. Naturforsch. **11a** (1956) 143
3) J. A. Birks, Scintillation Counters (McGraw-Hill, New York, 1953), Ch. 5
4) E. der Mateosian and L. C. L. Yuan, Phys. Rev. **90** (1953) 868

1.D.2

Nuclear Physics **16** (1960) 597—607; © *North-Holland Publishing Co., Amsterdam*

Not to be reproduced by photoprint or microfilm without written permission from the publisher

COUPLING OF NUCLEAR ROTATION AND MOTION OF THE OUTER NUCLEON

A. S. DAVYDOV

P. N. Lebedyev Physical Institute, USSR Academy of Sciences, Moscow

Received 4 November 1959

Abstract: A theory of rotational states of odd mass nuclei is developed for the case when additional coupling between nuclear rotation and motion of the outer nucleon is introduced. The reduced probabilities for E2 and M1 transitions between the rotational states are computed. It is shown that the relative reduced probabilities are uniquely defined by the positions energy levels of the nucleus.

1. Introduction

In a number of even mass nuclei the one-nucleon excitation energy is much greater than the energy of rotation and hence in a first approximation the adiabatic approximation can be employed to describe rotational states of such nuclei. In odd mass nuclei the energy of one-nucleon excitations is frequently comparable with the rotational energy and hence the question of applicability of the adiabatic approximation requires special consideration.

Non-adiabatic conditions arise as a result of interaction between rotation of the nucleus and the motion of the outer nucleon and oscillations of the nuclear surface. For odd mass nuclei interactions of the first type are apparently the most important. Interactions of this type may significantly modify the structure of the rotational spectrum of the nucleus. In this paper the case of weak coupling between the external nucleon and the non-spherical part of the potential is investigated, when there is a large coupling between rotation and single particle motion.

2. Case of Weak Coupling in an Axially Symmetric Nucleus

As a model of an odd mass nucleus we consider a system consisting of a nuclear core which, to a certain approximation, is assumed to be axially symmetrical, and of a single nucleon. The energy spectrum of low excited states of such a system depends on the coupling between the angular momentum **j** of the nucleon and the rotational angular momentum **R**. Coupling between these angular momenta depends on the relative role of the interaction between the nucleon, and the non-spherical part of the potential well, on the one hand, and between the nucleon and rotation of the nucleus, on the other. The role of the

rotation of the nucleus is determined by the distance between neighbouring rotational levels. If the energy of the first of these interactions is large compared with the difference of the rotational levels one can speak of the strong coupling case. An inequality of opposite sign signifies weak coupling. Intermediate cases between these two extremes are, of course, also possible. It should also be kept in mind that the distances between neighbouring rotational levels increase with increase of the rotational angular momentum **R** and for some values of they may exceed the binding energy, between the nucleon and the non-spherical part of the potential. Thus strong coupling may change into weak coupling in one and the same nucleus.

In the case of strong coupling in an axially symmetrical nucleus the projection of the angular momentum of the nucleon Ω on the nuclear axis is an integral of motion. Generally speaking, the total angular momentum of the nucleon is not an integral of motion. This case has been considered by Bohr and Mottelson [1, 2]). In the case of weak coupling the projection of the angular momentum on the nuclear axis does not have a definite value, whereas the total angular momentum may have a definite value.

Assume (as is ordinarily done) that the interaction between a nucleon and an axially symmetrical core can be described by the operator

$$H_{\text{int}} = V_{\text{p}}(r)+\beta T(3j_{\xi}^{2}-\mathbf{j}^{2}), \tag{1.1}$$

where $V_{\text{p}}(r)$ is a spherical potential well. The second term in (1.1) determines the interaction between the nucleon and the non-spherical part of the potential, which we briefly shall call the "nucleon-axis" interaction. The parameter β specifies the deviation of the nucleus from spherical symmetry.

The operator (1.1) commutes with the operator $\mathbf{j}^2$ and therefore in our system the angular momentum of the outer electron is an integral of motion. For $j = \frac{1}{2}$ the nucleon-axis coupling vanishes, that is, we have here the extreme case of weak coupling. Of course, in reality the operator (1.1) does not exactly characterize the interaction between the nucleon and the core and in the general case j is not a good quantum number. However, it may be assumed that in some cases when the admixture of $j \neq \frac{1}{2}$ states is small, weak coupling will be realized in the nucleus even when β is not a very small quantity. For small values of β weak coupling may occur in states with $j \neq \frac{1}{2}$.

Ordinarily, investigation of one-nucleon states is performed under the assumption that the nucleus does not rotate. If the nucleus does rotate the rotational and nucleon motion mutually influence each other. Suppose that this influence can be described by an operator proportional to the scalar product of the angular momenta. Then in the case of weak coupling, in a first approximation, the nucleon-axis coupling can be neglected and the Hamiltonian can be written as

$$H = A\mathbf{R}^2+W\mathbf{R}\cdot\mathbf{j}+H_0, \tag{1.2}$$

where A is a parameter specified by the moment of inertia of the nucleus; H_0 is the Hamiltonian for a motionless core and a nucleon moving in a centrally symmetrical potential; W is a parameter characterizing the magnitude of the additional coupling between the outer nucleon and the rotational angular momentum. In molecular theory an analogous interaction between rotational and electron motions leads to various coupling schemes for the corresponding angular momenta (coupling case b of Hund).

It should be mentioned that Zaretsky and Shutko[3]) have previously attempted to introduce an additional interaction between the nucleon spin and the rotation of the nucleus. The operator for this interaction ("quasi-magnetic interaction") between nucleon spin and rotation was chosen, in analogy with the case of diatomic molecules, in the form $\gamma(\mathbf{R}+\mathbf{L})\cdot\mathbf{S}$, where $\mathbf{L}$ is the nucleon orbital angular momentum and $\mathbf{S}$ is the nucleon spin.

This expression derived from the theory of free spin molecules (case b after Hund) for which the sum of the rotational and orbital angular momentum of the electron is conserved, cannot, in our opinion, be applied to the theory of rotational states with sufficient justification since the spin-orbit interaction is large in medium and heavy nuclei.

If the total nuclear angular momentum operator $\mathbf{I}=\mathbf{R}+\mathbf{j}$ is introduced, the Hamiltonian (1.2) assumes the form

$$H = A\mathbf{I}^2+(W-2A)\mathbf{I}\cdot\mathbf{j}+H_0+(A-W)\mathbf{j}^2. \tag{1.3}$$

For $j=\frac{1}{2}$ the wave function satisfying the requisite symmetry conditions [1, 2]) and corresponding to a state with a total angular momentum I has the form

$$\psi^m_{IK} = \frac{\sqrt{2I+1}}{4\pi}\{D^I_{mK}\varphi^{\frac{1}{2}}_{\frac{1}{2}}+(-1)^{I-\frac{1}{2}}D^I_{m,\,-K}\varphi^{\frac{1}{2}}_{-\frac{1}{2}}\}. \tag{1.4}$$

The operator $\mathbf{I}$ acts only on the function D^I_{mK} which depends on the Eulerian angles specifying the orientation of the nucleus in space. The operator $\mathbf{j}$ acts on the function φ which specifies the state of the nucleon and the intrinsic state of the core.

Choose the quantization axis ζ along the symmetry axis of the nucleus. Then from the condition of rotation about an axis perpendicular to axis ζ it follows that the function (1.4) should satisfy the condition $R_\zeta\psi_{IK}=(I_\zeta-j_\zeta)\psi_{IK}=0$, which yields $K=\frac{1}{2}$.

By introducing the abridged notation

$$|ImK\Omega\rangle = \sqrt{\frac{2I+1}{8\pi^2}}\,D^I_{mK}\varphi_{\Omega}^{\frac{1}{2}} \tag{1.5}$$

and employing the matrix elements

$$\langle Im\,K\Omega|I_\zeta j_\zeta|Im\,K\Omega\rangle = K\Omega,$$

$$\langle Im\,K\Omega|I_\xi j_\xi+I_\eta j_\eta|Im\,,K-1,\,\Omega-1\rangle = \tfrac{1}{2}[(I+K)(I-K+1)(j+\Omega)(j-\Omega+1)]^{\frac{1}{2}}$$

we get

$$E = (\psi_{I\frac{1}{2}}|H|\psi_{I\frac{1}{2}}) = A\{I(I+1)+a(-1)^{I+\frac{1}{2}}(I+\tfrac{1}{2})\}+E_0, \tag{1.6}$$

where

$$a = 1-\frac{W}{2A}. \tag{1.7}$$

The form of formula (1.6) is exactly the same as that of the Bohr-Mottelson formula [2]) for strong coupling with $K = \frac{1}{2}$. However, the physical meaning of the constant a is now different. The parameter a of Bohr and Mottelson has the value

$$a^{\mathrm{BM}} = \sum(-1)^{j-\frac{1}{2}}(j+\tfrac{1}{2})|C_j|^2,$$

where $|C_j|^2$ is the probability that in the given state the nucleon has an angular momentum j. In deriving this expression account was taken of the decoupling

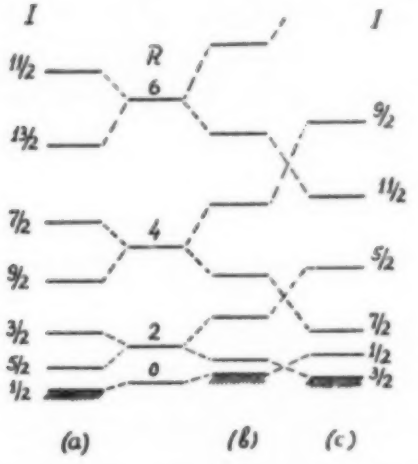

Fig. 1. Spacing of rotational levels of an odd-mass axially symmetric nucleus (a) $-4 < W/A < 0$, (b) $0 < W/A < 4$, (c) $4 < W/A < 8$.

operator $\mathbf{I}\cdot\mathbf{j}$ which enters into the rotational kinetic energy operator and relates states differing by 1 in quantum number K. In order to still regard K as a good quantum number, matrix elements with $K = \pm\frac{3}{2}$ must be rejected. In a state with a definite angular momentum $j = \frac{1}{2}$ one has $a^{\mathrm{BM}} = 1$. In order to obtain agreement with the experimental data ($a = -0.58$ for Pu^{239}; $a = 2.3$ for F^{19}) one is compelled to assume that admixtures of states with $j \neq \frac{1}{2}$ are quite significant.

Formula (1.7) can be deduced in an elementary way. Since $\mathbf{R}\cdot\mathbf{j} = \frac{1}{2}(\mathbf{I}^2-\mathbf{R}^2-\mathbf{j}^2)$ we find that the mean value of the operator (1.2) in a state with definite values of I, R and $j = \frac{1}{2}$ is

$$E = AR(R+1)+\tfrac{1}{2}W\{I(I+1)-R(R+1)\}+E'_0. \tag{1.8}$$

The quantum number R which corresponds to rotation of an even nuclear core assumes only even values and hence

$$R = I + \tfrac{1}{2}(-1)^{I+\frac{1}{2}}. \tag{1.9}$$

Inserting (1.9) into (1.8) we obtain (1.6).

Thus in the absence of nucleon-axis interaction, the nucleon-rotation interaction leads to a shift and splitting of the rotational levels of the nuclear core. The dependence of the rotational spectrum of such a nucleus on the dimensionless parameter W/A is schematically represented in fig. 1. For $W/A < 4$ the ground state of the nucleus corresponds to a stationary core and possesses a spin of $\frac{1}{2}$. If the spin of the ground state of the nucleus is $I = \frac{3}{2}$ (when $W/A > 4$) the nuclear core rotates in the ground state and in the first excited state $I = \frac{1}{2}$ the nuclear core does not rotate.

3. Case of Weak Coupling in a Non-Axial Nucleus

If the shape of the nuclear core is that of a tri-axial ellipsoid the Hamiltonian of a system consisting of the core and a single nucleon can, in the case of weak coupling ($j = \frac{1}{2}$), be written as

$$H = \frac{\hbar^2}{B\beta^2}\left\{\tfrac{1}{8}\sum \frac{I_l - j_l}{\sin^2(\gamma - \frac{2}{3}\pi l)} + \lambda \mathbf{I}\cdot\mathbf{j}\right\} + H_0. \tag{3.1}$$

The solution of the Schroedinger equation with operator (3.1) can be sought in the form

$$\Psi(I) = \sum b_K \psi_{IK}, \quad I = \tfrac{1}{2}, \tfrac{3}{2}, \ldots \tag{3.2}$$

where the ψ_{IK} are defined in (1.4) For non-axial nuclei the condition $K = \frac{1}{2}$ should be replaced by a more general one

$$K - \tfrac{1}{2} = 2\nu, \quad \nu = 0, \pm 1, \pm 2, \pm \ldots. \tag{3.3}$$

The state of a spin $\frac{1}{2}$ nucleus can be described by the function

$$\Psi(\tfrac{1}{2}) = \psi_{\frac{1}{2}\frac{1}{2}}. \tag{3.4}$$

The energy of this state (in $\hbar^2/(B\beta^2)$ units) with respect to the value $\langle \varphi_{\frac{1}{2}} | H_0 | \varphi_{\frac{1}{2}} \rangle$ will equal $\varepsilon_{\frac{1}{2}}^{(\lambda)} = \frac{3}{4}\lambda$.

According to (3.2) and (3.3) the wave functions of the first excited states have the form

$$\begin{aligned}
\Psi_i(\tfrac{3}{2}) &= a_i\psi_{\frac{1}{2}\frac{1}{2}} + b_i\psi_{\frac{1}{2}-\frac{1}{2}}, \quad i = 1, 2,\\
\Psi_i(\tfrac{5}{2}) &= c_i\psi_{\frac{1}{2}\frac{1}{2}} + d_i\psi_{\frac{1}{2}-\frac{1}{2}} + e_i\psi_{\frac{1}{2}\frac{1}{2}}, \quad i = 1, 2, 3,\\
\Psi_i(\tfrac{7}{2}) &= A_i\psi_{\frac{1}{2}\frac{1}{2}} + B_i\psi_{\frac{1}{2}-\frac{1}{2}} + G_i\psi_{\frac{1}{2}\frac{1}{2}} + D_i\psi_{\frac{1}{2}-\frac{1}{2}}, \quad i = 1, 2, 3, 4,\\
\Psi_i(\tfrac{9}{2}) &= \alpha_i\psi_{\frac{1}{2}\frac{1}{2}} + \beta_i\psi_{\frac{1}{2}-\frac{1}{2}} + \gamma_i\psi_{\frac{1}{2}\frac{1}{2}} + \delta_i\psi_{\frac{1}{2}-\frac{1}{2}} + \nu_i\psi_{\frac{1}{2}\frac{1}{2}}, \quad i = 1, 2, 3, 4, 5.
\end{aligned} \tag{3.5}$$

The energy of the two spin $\frac{3}{2}$ levels are defined by the formula

$$\varepsilon_i^{(\lambda)}(\tfrac{3}{2}) = \frac{9[1+(-1)^i\sqrt{1-\frac{8}{9}\sin^2(3\gamma)}]}{4\sin^2(3\gamma)} - \tfrac{3}{4}\lambda, \quad i = 1, 2. \tag{3.6}$$

The dependence of a_i and b_i on γ is expressed by formulas which are identical to those derived by Davydov and Filippov [4]) (formula (2.4)) for coefficients a_i and b_i of the wave functions of spin 2 states of even nuclei.

The energies of other excited states cannot be expressed by simple analytical functions of γ and λ. They can be found by numerical solution (for each value of γ and λ) of the sets of algebraic equations obtained by inserting (3.5) into the Schroedinger equation.

For $j \geqq \frac{5}{2}$ and small values of λ (see condition (3.9)) the interaction between rotation and the one-nucleon motion can be taken into account by perturbation theory methods. In the zero approximation ($\lambda = 0$) all excited states are two-fold degenerate †. For example

$$\varepsilon_i^0(\tfrac{3}{2}) = \varepsilon_i^0(\tfrac{5}{2}) = \frac{9[1+(-1)^i\sqrt{1-\frac{8}{9}\sin^2(3\gamma)}]}{4\sin^2(3\gamma)}, \quad i = 1, 2,$$

$$\varepsilon_i^0(\tfrac{5}{2}) = \varepsilon_2(\tfrac{7}{2}) = \frac{9}{2\sin^2(3\gamma)}.$$

The energies of other excited states (in the zero approximation) are indicated in table 1 for four values of γ. The values of coefficients c_i, d_i, ... ν_i of wave functions (3.5) in the zero approximation are presented in table 2.

TABLE 1

Energy (in $\hbar^2/(\beta B^2)$ units) of excited odd-mass nuclear levels (zero approximation)

γ^0	0	10	20	30
$\varepsilon_1(\frac{3}{2}) = \varepsilon_1(\frac{1}{2})$	0	1.063	1.265	1.5
$\varepsilon_1(\frac{7}{2}) = \varepsilon_1(\frac{5}{2})$	3.333	3.531	3.954	4.0
$\varepsilon_2(\frac{3}{2}) = \varepsilon_2(\frac{1}{2})$	∞	16.93	4.732	3.0
$\varepsilon_1(\frac{11}{2}) = \varepsilon_1(\frac{9}{2})$	7	7.378	7.695	7.5
$\varepsilon_2(\frac{5}{2}) = \varepsilon_2(\frac{7}{2})$	∞	18.03	6.0	5.5

In a first approximation the energy of rotational states with $I \geqq \frac{5}{2}$ is defined by the formula

$$\varepsilon_i^{(\lambda)}(I) = \varepsilon_i^0(I) + \Delta\varepsilon_i(I), \tag{3.7}$$

where the

$$\Delta\varepsilon_i(I) = \lambda\langle\Psi_i(I)|\mathbf{I}\cdot\mathbf{j}|\Psi_i(I)\rangle \tag{3.8}$$

yield the corrections to the energy levels of the zero approximation if the inequality

$$|\Delta\varepsilon_i(I)| < |\varepsilon_i(I) - \varepsilon_{i+1}(I)| \tag{3.9}$$

† With an accuracy to a factor of 4 connected with a different choice of energy units these values coincide with the rotational energy of non-axial even nuclei [4]).

holds. The shifts of spin $\frac{5}{2}$ and $\frac{7}{2}$ levels computed according to (38) can be expressed in terms of the coefficients of the zero approximation functions

TABLE 2

Values of coefficients defining rotational state wave functions (zero approximation)

$\varepsilon_i(I)$	γ°	0	10	20	30
$\varepsilon_1(\frac{1}{2})$	c_1 $e_1 = \sqrt{5}d_2$	1 0	1 0.002	0.992 0.115	0.850 0.518
$\varepsilon_2(\frac{1}{2})$	c_2 $e_2 = \sqrt{5}d_2$	0 0.912	−0.0062 0.912	−0.077 0.910	−0.116 0.908
$\varepsilon_3(\frac{1}{2})$	c_3 $d_3 = -\sqrt{5}e_3$	0 $\sqrt{5/6}$	0 $\sqrt{5/6}$	0 $\sqrt{5/6}$	0 $\sqrt{5/6}$
$\varepsilon_1(\frac{7}{2})$	A_1 $B_1 = \sqrt{3}G_1$ D_1	1 0 0	0.999 0.0262 0.0001	0.955 0.256 0.0175	0.739 0.573 0.125
$\varepsilon_2(\frac{7}{2})$	$A_2 = D_2$ $B_2 = -3^{-\frac{1}{2}}G_2$	0 0.5	0 0.5	0 0.5	0 0.5
$\varepsilon_1(\frac{9}{2})$	α_1 β_1 γ_1 δ_1 ν_1	1 0 0 0 0	0.999 0.0165 0.0253 0.001 0.0001	0.952 0.216 0.210 0.009 0.0139	0.699 0.382 0.497 0.175 0.293

(table 2) with the aid of the formulas

$$\Delta\varepsilon_i(\tfrac{5}{2}) = [1.75c_i^2+2.1e_i^2]\lambda, \qquad i = 1, 2.$$
$$\Delta\varepsilon_3(\tfrac{5}{2}) = -1.25\lambda,$$
$$\Delta\varepsilon_i(\tfrac{7}{2}) = -\{1.75(A_i^2+D_i^2)+\tfrac{7}{3}B_i^2\}\lambda, \quad i = 1, 3, 4,$$
$$\Delta\varepsilon_2(\tfrac{7}{2}) = 2.25\lambda.$$

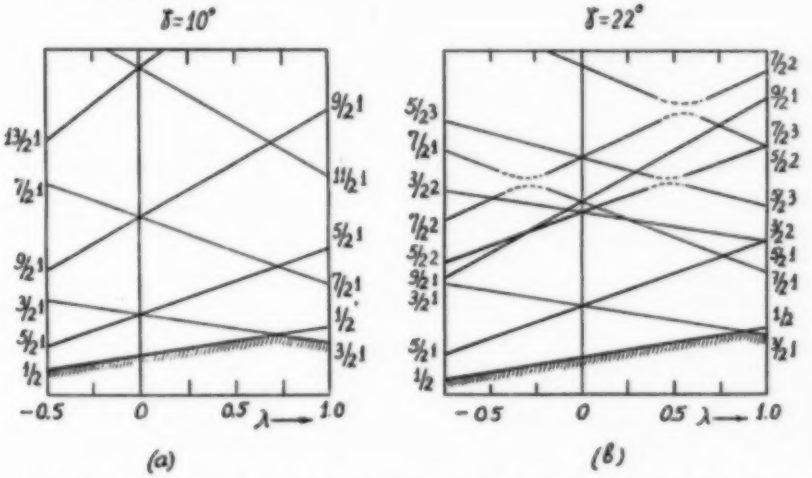

Fig. 2. Spacing of energy levels of odd-mass non-axial nucleus depending on parameter γ: (a) $\gamma = 10°$, (b) $\gamma = 22°$.

Energy level schemes computed for nuclei with values of γ equal to 10 and 22° are presented in fig. 2. The dotted lines denote those places at which the level positions should be computed without making use of perturbation theory. Perturbation theory can be employed to compute the rotational states of nuclei with $\gamma < 18°$.

4. Electric Quadrupole Transitions between Rotational States

All levels of the rotational band possess the same parity and therefore E2 transitions are electric quadrupole transitions of the lowest possible multipolarity. The reduced probabilities for electric quadrupole transitions between rotational states described by functions (3.4) and (3.5) can easily be calculated by taking into account that the E2 transition operator has the form

$$Q_{2\mu} = eQ_0 \left\{ D^2_{\mu 0} \cos\gamma + \frac{1}{\sqrt{2}} (D^2_{\mu 2} + D^2_{\mu -2}) \sin\gamma \right\},$$

where Q_0 is the intrinsic electric quadrupole moment of the nucleus. Thus the reduced E2 transition probability (in $e^2Q_0^2/16\pi$ units) is defined by the expression

$$b(\mathrm{E2};\, I\mathrm{i} \to I'\mathrm{f}) = \frac{5}{2I+1} \sum_{m\mu m'} |(\Psi_{\mathrm{f}m'}(I') | Q_{2\mu} | \Psi_{\mathrm{i}m}(I))|^2. \tag{4.1}$$

Inserting (3.5) into (4.1) we find that the reduced probabilities for E2 transitions from two levels of spin $\frac{3}{2}$ to levels of spin $\frac{1}{2}$ are given by the formula

$$b(\mathrm{E2};\, \tfrac{3}{2} i \to \tfrac{1}{2}) = \tfrac{1}{2} \left[1 - (-1)^i \frac{3 - 2\sin^2(3\gamma)}{\sqrt{9 - 8\sin^2(3\gamma)}} \right], \quad i = 1, 2.$$

The reduced probability for transition between two levels of spin $\frac{3}{2}$ is

$$b(\mathrm{E2};\, \tfrac{3}{2} 2 \to \tfrac{3}{2} 1) = \tfrac{10}{7} \frac{\sin^2(3\gamma)}{9 - 8\sin^2(3\gamma)}$$

The reduced probabilities for E2 transitions from spin $\frac{5}{2}$ levels to a spin $\frac{1}{2}$ level are defined by the expression

$$b(\mathrm{E2};\, \tfrac{5}{2} i \to \tfrac{1}{2}) = \left(c_i \cos\gamma + \frac{d_i + \sqrt{5}\, e_i}{\sqrt{6}} \sin\gamma \right)^2, \quad i = 1, 2, 3.$$

If values of the coefficients of the zero approximation wave functions (table 2) are employed we find $b(\mathrm{E2};\, \frac{5}{2} 3 \to \frac{1}{2}) = 0$. Thus, in Coulomb excitation of a nucleus in a spin $\frac{1}{2}$ state, only two of the three spin $\frac{5}{2}$ levels can be excited.

The reduced E2 transition probabilities between other levels can be expressed in terms of the coefficients of wave functions (3.5) by the formulas

$$b(\mathrm{E2};\tfrac{5}{2}i\to\tfrac{3}{2}f)=\tfrac{2}{7}\{(\sqrt{6}\,d_ib_f-c_ia_f)\cos\gamma+[c_ib_f-\sqrt{\tfrac{2}{3}}(2d_i-\sqrt{5}\,e_i)a_f]\sin\gamma\}^2,$$

$$b(\mathrm{E2};\tfrac{5}{2}i\rightleftarrows\tfrac{5}{2}f)$$
$$=\tfrac{1}{14}\{(5e_ie_f-4c_ic_f-d_id_f)\cos\gamma+\sqrt{\tfrac{3}{2}}[3(c_id_f+c_fd_i)+\sqrt{5}(c_ie_f+c_fe_i)]\sin\gamma\}^2,$$

$$b(\mathrm{E2};\tfrac{7}{2}i\to\tfrac{5}{2}f)=\tfrac{5}{42}\{(3d_fB_i-\sqrt{\tfrac{6}{5}}\,a_fA_i-\sqrt{15}\,e_fD_i)\cos\gamma$$
$$+(2a_fG_i+\tfrac{2}{\sqrt{5}}d_fA_i-\sqrt{3}\,a_fB_i-e_fA_i-\sqrt{7}\,d_fD_i)\sin\gamma\}^2.$$

The formulas thus obtained permit one to calculate the ratio of the reduced probabilities for E2 transitions between rotational states of the nucleus. The ratios are expressed in terms of coefficients which determine the wave functions. In the zero approximation these coefficients uniquely depend on the parameter γ (see table 2) which characterizes the deviation from axial symmetry. In the exact solution part of the coefficients of wave functions pertaining to states with spins exceeding or equal to $\frac{5}{2}$ will also depend on parameter λ which takes into account coupling between rotational and one-nucleon motion. However, even in the case of an exact solution the ratio of the reduced transition probabilities will be determined only by the relative position of the nuclear rotational levels. Reduced probability values in $e^2Q_0^2/16\pi$ unit for some E2 transitions computed with the zero approximation wave functions are represented in fig. 3.

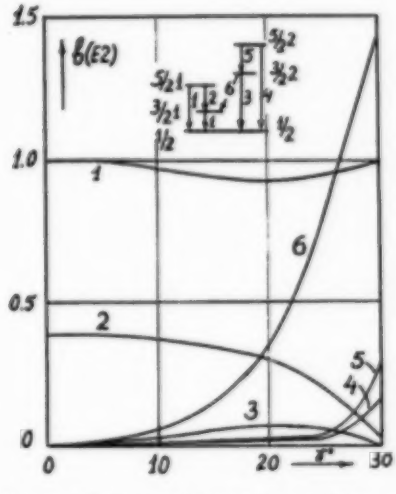

Fig. 3. Reduced probabilities of some E2 transitions in an odd mass nucleus (in $\hbar^2/(B\beta^2)$ units) for various values of the non-axiality parameter γ.

It should be noted that in the case of strong coupling and $K=\frac{1}{2}$ the wave functions of the rotational states of axially symmetrical nuclei are linear combinations of wave functions with definite angular momenta $\varphi_{\frac{1}{2}}=\sum C_j\varphi_{j\frac{1}{2}}$. The relative position of the rotational levels defines only $a=\sum(-1)^{j-\frac{1}{2}}(j+\frac{1}{2})|C_j|^2$ and does not permit one to determine the C_j separately. Thus, in this case, data on the position of rotational levels are by themselves insufficient to yield information on the relative probabilities of E2 transitions between them.

5. Magnetic Dipole Transitions between Rotational States

In the laboratory coordinate system the dipole magnetic transition operator in an odd mass nucleus can be written down as follows:

$$\mathfrak{M}(1\nu) = \mathfrak{M}_R(1\nu)+\mathfrak{M}_j(1\nu), \tag{5.1}$$

where

$$\mathfrak{M}_R(1\nu) = \mu_0 g_R \int \mathbf{R}(\mathbf{r}) \cdot \nabla(rY_{1\nu})d\tau$$

is the collective motion operator, μ_0 is the Bohr magneton, g_R the collective motion gyromagnetic ratio, $\mathbf{R} = \int \mathbf{R}(\mathbf{r})d\tau$ the rotational angular momentum operator, $\mathfrak{M}_j(1\nu) = \mu_0 g_j \nu \cdot \nabla(rY_{1\nu})$ is the nucleon dipole magnetic transition operator and g_j the corresponding gyromagnetic ratio.

Taking into account that $\mathbf{R} = \mathbf{I}-\mathbf{j}$ and $\nabla(rY_{1\nu}) = (-1)^\nu \sqrt{\frac{3}{4\pi}}\,\mathbf{e}_\nu$, where $\mathbf{e}_\nu$ are unit vectors satisfying the relations $(-1)^\nu \mathbf{e}_\nu \cdot \mathbf{e}_{\nu'} = \delta_{\nu\nu'}$, $\nu = 0,\ 1,\ -1$, and neglecting the term containing the total angular momentum operator (which does not lead to transitions) we transform (5.1) to

$$\mathfrak{M}(1\nu) = \sqrt{\frac{3}{4\pi}}\,\mu_0(g_j-g_R)j_\nu.$$

Since in (1.4) the internal motion functions are defined with respect to a coordinate system fixed to the nucleus, operator $\mathfrak{M}(1\nu)$ must be transformed in the same coordinate system

$$\mathfrak{M}(1\nu) = \sqrt{\frac{3}{4\pi}}\,\mu_0(g_j-g_R)\sum_\mu D^1_{\nu\mu} j_\mu. \tag{5.2}$$

The operator j_μ acts only on the internal motion wave functions, in which case

$$j_\mu \varphi_\Omega^j = (-1)^\mu \sqrt{j(j+1)}\,(j1\Omega+\mu,\ -\mu|j\Omega)\varphi^j_{\Omega+\mu},$$

where $(j_1 j_2 m_1 m_2|jm)$ are vector summation coefficients.

The matrix elements of the operator (5.2) for the wave functions (1.5) have the form

$$\langle I'm'K'\Omega'|\mathfrak{M}(1\nu)|Im\,K\Omega\rangle = \frac{3\mu_0(g_j-g_R)}{4\sqrt{\pi}}\sqrt{\frac{2I+1}{2I'+1}}$$
$$\times (I1m\nu|I'\nu')\sum_\mu (-1)^\mu (\tfrac{1}{2}1\Omega+\mu,\ -\mu|\tfrac{1}{2}\Omega)(I1K\mu|I'K')\delta_{\Omega',\Omega+\mu}. \tag{5.3}$$

The reduced probability for M1 transitions is defined by the formula

$$B(\mathrm{M1};\, I\mathrm{i} \to I'\mathrm{f}) = \frac{1}{2I+1}\sum_{m\nu m'} |(\Psi_{\mathrm{f}m'}(I')|\mathfrak{M}(1\nu)|\Psi_{\mathrm{i}m}(I))|^2.$$

By employing the functions (3.5) we can find the values of the reduced M1 transition probabilities expressed in units of $3\mu_0^2(g_j-g_R)^2(20\pi)^{-1}$:

$$b(\mathrm{M1};\tfrac{3}{2}i \to \tfrac{1}{2}) = 0, \quad i = 1, 2; \quad b(\mathrm{M1};\tfrac{3}{2}2 \to \tfrac{3}{2}1) = 0;$$

$$b(\mathrm{M1};\tfrac{5}{2}i \to \tfrac{3}{2}f) = \tfrac{1}{3}\{\sqrt{6}\, a_f c_i + b_f[d_i + \sqrt{5}\, e_i]\}^2, \quad i = 1, 2, 3, \quad f = 1, 2;$$

$$b(\mathrm{M1};\tfrac{5}{2}i \rightleftarrows \tfrac{5}{2}f) = \tfrac{1}{28}\{7c_i c_f - 3d_i d_f + 5e_i e_f + 2\sqrt{5}\,[d_i e_f + d_f e_i]\}^2, \quad i, f = 1, 2, 3,$$

$$b(\mathrm{M1};\tfrac{7}{2}i \to \tfrac{5}{2}f) = \tfrac{5}{64}(B_i - \sqrt{3}\, C_i)^2 (e_f - \sqrt{5}\, d_f)^2.$$

Thus the relative probabilities for M1 transitions between rotational levels, just as the relative probabilities for E2 transitions, are uniquely defined by the spacing of the levels. In the strong coupling theory [5]) the ratio of reduced M1 transition probabilities depends on the auxiliary parameter b_0 which must be determined from experiment.

The theory of rotational states of odd mass atomic nuclei possessing weak coupling, developed above, permits one in a broad way to compare the theory with the experimental data on the position of the rotational levels and the transition probabilities between them.

References

1) A. Bohr, Mat. Fys. Medd. Dan. Vid. Selsk. **28**, No. 14 (1952)
2) A. Bohr and B. Mottelson, Mat. Fys. Medd. Dan. Vid. Selsk **28**, No. 16 (1933)
3) D. F. Zaretsky and A. V. Shutko, JETP **32** (1957) 370
4) A. S. Davydov and G. F. Filippov, Nuclear Physics **10** (1958) 440
5) S. G. Nilsson, Mat. Fys. Medd. Dan. Vid. Selsk. **29**, No. 16 (1955)

7.B

Nuclear Physics **16** (1960) 608—618; © *North-Holland Publishing Co., Amsterdam*

Not to be reproduced by photoprint or microfilm without written permission from the publisher

APPLICATION OF DISPERSION RELATIONS FOR TESTING QUANTUM ELECTRODYNAMICS AT SMALL DISTANCES

P. S. ISAEV and I. S. ZLATEV

Joint Institute for Nuclear Research, Dubna

Received 7 October 1959

Abstract: Corrections to the Bethe-Heitler bremsstrahlung formula in the lowest approximation in e are calculated using the method of dispersion relations. The problem of the limit of applicability of quantum electrodynamics at small distances is considered.

1. Introduction

Recently a number of papers by Drell [1]) have extensively discussed one of the variants of modification of quantum electrodynamics and pointed out experimental possibilities for checking it at small distances.

In ref. [2]), for example, consideration is given to the pair production (e^+, e^-) by γ-quanta on nucleons, which under certain conditions allows of testing the electron propagator at distances $\geqq 0.7\times 10^{-13}$ cm. The limitations in the process of pair production to energies of γ-quanta $\lesssim$ 140 MeV [2]) were partly due to theoretical difficulties in considering dynamic corrections caused by the proton current (see graphs 2a and 2b), as well as to difficulties in considering the interference terms of the type 1a+2a, etc.

In ref. [3]) we suggest the use of the method of dispersionr elations for calculating the generalized graphs 3a and 3b. Thus there arises a possibility of calculating the processes of bremsstrahlung and pair production (taking account of the meson cloud of the nucleon) up to rather high energies until the corrections of the highest orders in e become essential.

In the present paper we are concerned with calculating the one-nucleon term in dispersion relations for bremsstrahlung and the interference term (one-nucleon approximation+graphs of the Bethe-Heitler type calculated earlier [4])), as well as with an approximate estimate of the one-pion state contribution.

The calculation of one-nucleon and interference contributions up to energies $\approx$ 500 to 600 MeV, taking account of form factors, has proved possible because the well-known Hofstadter form factors may be strictly introduced in the one-nucleon term on the basis of the method of dispersion relations [3]).

We calculate the one-nucleon term without taking into account the anomalous magnetic moment; in the interference contribution we keep the terms propor-

tional to the first degree anomalous magnetic moment. The estimates of the inaccuracies arising therefrom are discussed in the corresponding sections.

Graph 1a

Graph 1b

Graph 2a

Graph 2b

Graph 3a

Graph 3b

The exact calculation of π-meson contributions to the process of bremsstrahlung with the aid of the method under discussion is a complicated and laborious task. Yet in our dispersion relations it is possible to obtain an approximate estimate of the one-π-meson contribution when the square of the 4-momentum of the virtual photon is close to zero (a case close to the real Compton effect). The paper also contains estimates of the contributions of the highest order in e and the process of multiple bremsstrahlung. These estimates warrant the conclusion that in the process of bremsstrahlung with the energy of the incident electron ≈ 500 MeV there is a possibility of checking quantum electrodynamics up to distances $\geqq 3\times 10^{-14}$ cm.

It is interesting to note that at $\varphi = 0$ and large angles θ, θ_0 ($\theta \approx \theta_0$) the one-nucleon and interference terms have a rather sharp and high maximum, sometimes exceeding by several orders the Bethe-Heitler cross section.

2. One-Nucleon Contribution

In the laboratory system of coordinates the matrix element of bremsstrahlung in one-nucleon approximation (see ref. [3]) coincides with the matrix element corresponding to the sum of the graphs (2a+2b) with the only difference that in the one-nucleon approximation there are the known Hofstadter form factors $F_i((\kappa^2, M^2, M^2)$ instead of the unknown form factor functions $\Phi_i(\kappa^2, p'^2, M^2)$.

Thus the matrix element of one-nucleon approximation is of the form

$$\cdot\langle \mathrm{f}|S|\mathrm{i}\rangle = ie^3 \frac{Mm}{(2\pi)^4} \frac{l_n g_{ml}}{\sqrt{2k_0 E E_0 \mathscr{E}\mathscr{E}_0}} \frac{\delta(p-p_0+q-q_0+k)}{(q-q_0)^2}$$

$$\bar{u}(\mathbf{q},\sigma)\gamma^m u(\mathbf{q}_0,\sigma_0)\overline{W}(\mathbf{p},S)\left\{\left(\gamma^n - \frac{\mu}{2M}\tfrac{1}{2}[\hat{k},\gamma^n]\right)\frac{\hat{k}+\hat{p}+M}{(k+p)^2-M^2}\right.$$

$$\left(F_1(|q-q_0|^2)\gamma^l + F_2(|q-q_0|^2)\frac{\mu}{2M}\tfrac{1}{2}[\hat{\kappa},\gamma^l]\right) \qquad (2.1)$$

$$+\left(F_1(|q-q_0|^2)\gamma^l + F_2(|q-q_0|^2)\frac{\mu}{2M}\tfrac{1}{2}[\hat{\kappa},\gamma^l]\right)$$

$$\left.\cdot\frac{\hat{p}_0-\hat{k}+M}{(p_0-k)^2-M^2}\left(\gamma^n - \frac{\mu}{2M}\tfrac{1}{2}[\hat{k},\gamma^n]\right)\right\} W(\mathbf{p}_0,S_0).$$

Here M is the mass of the nucleon, m the mass of the electron, l_n is the free photon polarization vector,

$$g_{ml} = \begin{pmatrix} 1 & 0 & 0 & 0 \\ 0 & -1 & 0 & 0 \\ 0 & 0 & -1 & 0 \\ 0 & 0 & 0 & -1 \end{pmatrix},$$

$p_0(E_0, \mathbf{p}_0)$, $p(E, \mathbf{p})$, $q_0(\mathscr{E}_0, \mathbf{q}_0)$, $q(\mathscr{E}, \mathbf{q})$ and $k(k_0, \mathbf{k})$ are the four-momenta of the initial and final states of the nucleon, the initial and final states of the electron, and of the photon respectively, $u(\mathbf{q}, \sigma)$ is the spinor describing an electron in the state $(\mathbf{q}, \sigma)$, $W(\mathbf{p}, S)$ is the spinor describing nucleons in the state $(\mathbf{p}, S)$, and γ^n are the Dirac matrices satisfying the condition

$$\gamma^m\gamma^n + \gamma^n\gamma^m = 2g^{mn}I \quad (I = \text{unit matrix}).$$

Further,

$$\hat{k} = \gamma\cdot k = \gamma_0 k_0 - \boldsymbol{\gamma}\cdot\mathbf{k}, \quad \kappa = q_0 - q,$$

μ is the anomalous magnetic moment of a nucleon, equal to 1.79 nuclear magnetons, and $\mathscr{F}_1(|q_0-q|^2)$ and $\mathscr{F}_2(|q_0-q|^2)$ are the nucleon form factors.

From (2.1) it is clear that the cross section $\mathrm{d}\sigma_N$, corresponding to the square of the matrix element $|\langle \mathrm{f}|S|\mathrm{i}\rangle|^2$ may be written in the form

$$\mathrm{d}\sigma_N = A_0 + A_1\mu + A_2\mu^2 + A_3\mu^3 + A_4\mu^4$$

and μ is always accompanied by the factors $k/2M$ or $\kappa/2M$. These factors characterize the magnitudes of the corresponding contributions. For example for $\mathscr{E} = 0.54$ and $k_0 = 0.25$ (in units $\hbar = c = M = 1$ where M is the mass of the nucleon), the quantity $k/2M = \frac{1}{8}$, and $\kappa/2M < \frac{1}{4}$ and therefore for angles $\lesssim 90°$ the contribution $\sum_{i=1}^{4} A_i\mu^i$ turns out to be small if compared with the contribution of A_0. The differential cross section of A_0 has the form

$$A_0 = \frac{e^6}{8(2\pi)^5}\frac{|\mathbf{q}_0||\mathbf{q}|^3}{\mathcal{E}_0^2\mathcal{E}}\frac{k_0\,dk_0\,d\Omega_k\,d\Omega_q}{(M+\mathcal{E}_0-k_0)|\mathbf{q}|-\mathcal{E}|\mathbf{q}_0|(\cos\theta\cos\theta_0+\sin\theta\sin\theta_0\cos\varphi)+\mathcal{E}k\cos\theta}\frac{F^2(\kappa^2)}{|q_0-q|^4}$$

$$\left\{\frac{\mathbf{q}_0^2\sin^2\theta_0-2|\mathbf{q}||\mathbf{q}_0|\sin\theta\sin\theta_0\cos\varphi+\mathbf{q}^2\sin^2\theta}{(pk)^2}[4M^2\mathcal{E}\mathcal{E}_0+(q-q_0)^2(M^2+m^2-M\mathcal{E}_0+M\mathcal{E})]\right.$$

$$+\frac{\mathbf{q}^2\sin^2\theta_0}{pk}[(q-q_0)^2-4M\mathcal{E}]+\frac{\mathbf{q}^2\sin^2\theta}{pk}[(q-q_0)^2+4M\mathcal{E}_0]-\frac{Mk_0(q-q_0)^2}{pk}-(q-q_0)^2$$

$$+\frac{4(\mathcal{E}_0-\mathcal{E})(\mathcal{E}_0-|\mathbf{q}_0|\cos\theta_0)(\mathcal{E}-|\mathbf{q}|\cos\theta)}{pk}+\frac{2m^2k_0(\mathcal{E}_0-|\mathbf{q}_0|\cos\theta-\mathcal{E}+|\mathbf{q}|\cos\theta)}{pk} \qquad (2.2)$$

$$-\frac{4}{M}[m^2(\mathcal{E}_0-|\mathbf{q}_0|\cos\theta_0-\mathcal{E}+|\mathbf{q}|\cos\theta)+k_0(\mathcal{E}_0-|\mathbf{q}_0|\cos\theta_0)(\mathcal{E}-|\mathbf{q}|\cos\theta)]$$

$$\left.+\frac{2}{M}[\mathcal{E}\mathcal{E}_0-|\mathbf{q}||\mathbf{q}_0|(\cos\theta\cos\theta_0+\sin\theta\sin\theta_0\cos\varphi)](\mathcal{E}_0-|\mathbf{q}_0|\cos\theta_0-\mathcal{E}+|\mathbf{q}|\cos\theta).\right.$$

Here θ_0 is the angle between the vectors $\mathbf{q}_0$ and $\mathbf{k}$, θ the angle between the vectors $\mathbf{q}$ and $\mathbf{k}$, φ the angle between the vectors $\mathbf{k}\times\mathbf{q}_0$ and $\mathbf{k}\times\mathbf{q}$, and $d\Omega_{q_0}d\Omega_k = \sin\theta_0 d\theta_0 \sin\theta d\theta d\varphi_0 d\varphi$.

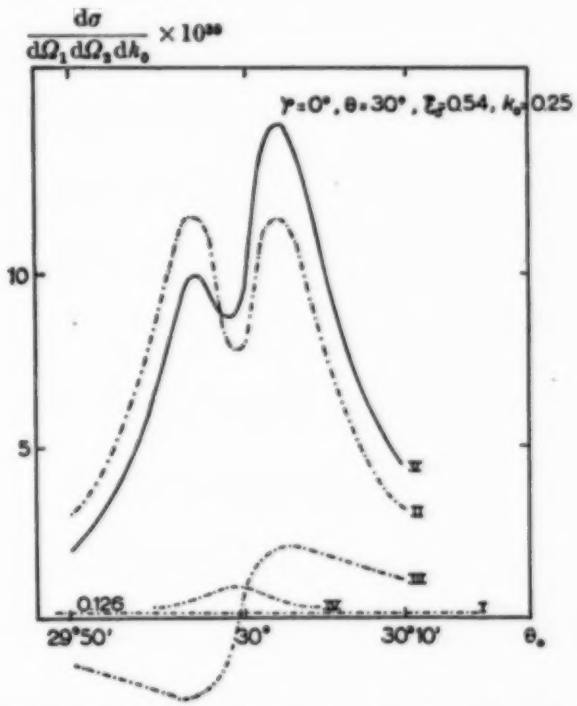

Fig. 1. I – Bethe-Heitler cross-section; II – One-nucleon maximum; III – Interference term $B_1\mu$; IV – Interference term B_0; V – Resulting curve.

The expression $|q-q_0|^4$ is a swiftly variable function of angles, which leads to the sharp maximum. A detailed study of the latter shows that in the region $\varphi = 0, \theta \approx \theta_0$ it consists of two maxima (see fig. 1). For the considered values of

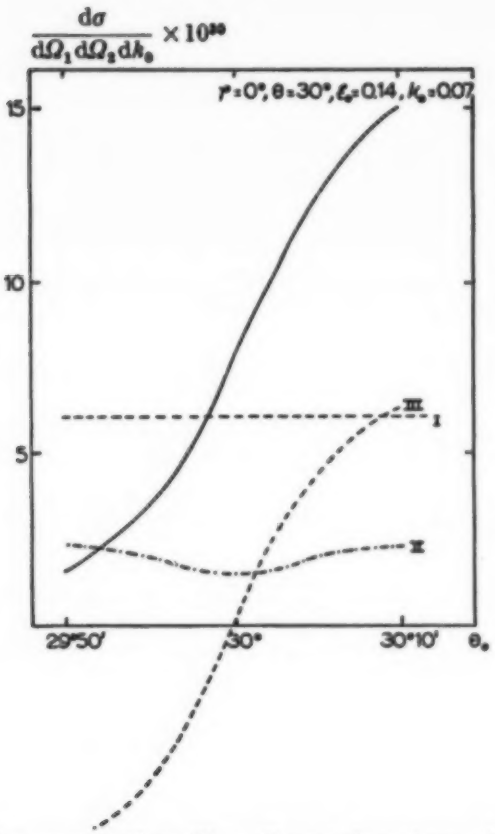

Fig. 2. I — Bethe-Heitler cross-section; II — One-nucleon term; III — Interference term; IV — Resulting curve.

TABLE 1

Relative contributions of one-nucleon term to differential cross-section

	θ / θ_e	30°	90°	150°
$\varphi = 0$	6°	0.36×10^{-4}	0.14×10^{-3}	0.11×10^{-3}
	30°	62	0.28×10^{-2}	0.23×10^{-2}
	60°	0.018	0.042	0.016
	90°	0.014	$0.16 \times 10^{+3}$	0.19
	120°	0.030	1.4	3.2
	150°	0.066	1.4	0.69×10^{3}
$\varphi = 90°$	6°	0.56×10^{-4}	0.15×10^{-4}	0.12×10^{-3}
	30°	0.24×10^{-2}	0.47×10^{-2}	0.30×10^{-4}
	60°	0.69×10^{-2}	0.027	0.019
	90°	0.91×10^{-2}	0.085	0.12
	120°	0.022	0.26	0.70
	150°	0.053	0.77	5.4
$\varphi = 150°$	6°	0.63×10^{-4}	0.16×10^{-3}	0.12×10^{-3}
	30°	0.17×10^{-2}	0.40×10^{-2}	0.33×10^{-2}
	60°	0.41×10^{-2}	0.014	0.017
	90°	0.62×10^{-2}	0.036	0.081
	120°	0.018	0.14	0.37
	150°	0.048	0.49	2.9

the incident electron and photon energies the maximum considerably exceeds the Bethe-Heitler cross section. If φ increases, the maximum decreases rather rapidly. If the energy of the initial electron decreases, it is natural to expect that the relative contribution of the one-nucleon term will also decrease. The relative height of the maximum is to decrease as well. Indeed, when $\mathscr{E}_0 = 0.14$, $k_0 = 0.07$ and $\varphi = 0$, $\theta_0 \approx \theta = 30°$ the width of the maximum increases and its relative height decreases (see fig. 2). With the energy of γ-quantum diminishing (for example, $k_0 = 0.25, 0.15, 0.05$) the height of the maximum first decreases (for $k_0 = 0.15$) and then begins to increase. In general at any energy the maximum is symmetrical with respect to $\theta = \theta_0$. The appearance of the maximum may be represented graphically if the electron and nucleon lines are interchanged in the Bethe-Heitler graphs, the two Bethe-Heitler maxima (one in the region $0 \leqq \theta_0 \leqq \pi$ and the other in $-\pi \leqq \theta_0 \leqq 0$) being removed into the region $\theta \approx \theta_0$ in the one-nucleon term.

For a detailed study of the contribution of (2.2) we have obtained the curves of differential cross sections for the initial electron energy $\mathscr{E}_0 = 0.54$ and for the γ-quantum energy $k_0 = 0.25$. As might be expected, the contribution of (2.2) proved to be inessential in the region of small angles and comparable with the Bethe-Heitler cross section in the region of large angles $\theta_1\theta_0 \geqq 90°$. Table 1 represents the ratios between differential cross section (2.2) and the Bethe-Heitler cross section (eq. (3) of ref. [4])). It will be noted that the points $\theta = \theta_0$ are not strictly the points of the maximum (see fig. 1) and therefore the ratio between the contributions of the one-nucleon term and the Bethe-Heitler cross section in the points of the maximum will be even greater than the ratio in table 1. We have also calculated the term $A_4\mu^4$ and compared it with the contribution of A_0. It turned out that in the region of angles $\leqq 90°$, the most interesting one at present, where the cross section of the process remains still comparatively large, the contribution of $A_4\mu^4$ is inessential.

Thus, confining ourselves to the region of angles $\leqq 90°$ and considering only the contribution of A_0 in the one-nucleon term, we make an error $\leqq 2\ \%$ in the differential cross section of bremsstrahlung. In the maximum for $\theta \approx \theta_0$ this evaluation of the error is not suitable; it will arise mainly from an inaccuracy in determining the one-nucleon contribution proper.

As follows from table 1 and the ratio $\kappa/2M < \frac{1}{4}$, the general contribution of the terms $A_1\mu + A_2\mu^2 + A_3\mu^3 + A_4\mu^4$ in the region of angles $\gtrsim 90°$ becomes considerable and cannot be neglected. Yet the calculation of these contributions within the framework of the usual perturbation method is extremely cumbersome. In the maximum ($\theta \approx \theta_0$) the contribution of the terms $A_1\mu$, $A_2\mu^2$, $A_3\mu^3$, $A_4\mu^4$ is at least by order less than the contribution of A_0 since $|q-q_0|/2M \approx m/M$ and the factor $k/2M = \frac{1}{8}$ in the region of the energies under consideration.

3. Contribution of Interference Term

The matrix elements corresponding to graphs (1a+1b) and the one-nucleon term were written down earlier (see ref. [4]) and eq. (2.1)). Just as in the one-nucleon term, the interference contribution may be expanded into a sum of terms

$$d\sigma'_I = B_0+B_1\mu+B_2\mu^2+B_3\mu^3.$$

Because of the large values of the cross sections obtained from the Bethe-Heitler graphs we cannot confine ourselves to the contribution of B_0, but have to consider the term $B_1\mu$. Such an approximation is close to that used in ref. [5]). In calculations we discarded the terms $\approx m^2$ in the numerator, which is equivalent to the substitution $\mathscr{E}\leftrightarrow|q|$ and $\mathscr{E}_0\leftrightarrow|q_0|$. The final expression for $d\sigma_I = B_0+B_1\mu$ has the form (in the laboratory system)

$$d\sigma_I = \frac{e^6}{8(2\pi)^5}\frac{\mathscr{E}k_0}{\mathscr{E}_0 ME}\frac{dk_0 d\Omega_k d\Omega_q}{\left|\frac{df}{d\mathscr{E}}\right|}\frac{1}{(q_0-q)^2}\frac{1}{(p_0-p)^2}F(|q_0-q|^2)F(|p_0-p|^2)$$

$$\cdot\left\{\frac{\mathscr{E}_0^2\sin^2\theta_0}{(pk)(q_0k)}[\Phi+2M\mathscr{E}(q_0-q)^2-4M^2\mathscr{E}(\mathscr{E}_0+\mathscr{E}-k_0)]\right.$$

$$+\frac{\mathscr{E}^2\sin^2\theta}{(pk)(qk)}[\Phi-2M\mathscr{E}_0(q_0-q)^2-4M^2\mathscr{E}_0(\mathscr{E}_0+\mathscr{E}+k_0)]$$

$$-\frac{\mathscr{E}\mathscr{E}_0\sin\hat{v}\sin\theta_0\cos\varphi}{pk}\left[\Phi\left(\frac{1}{qk}+\frac{1}{q_0k}\right)+\frac{2}{qk}(M(\mathscr{E}+k_0)(q_0-q)^2-2M^2\mathscr{E}(\mathscr{E}_0+\mathscr{E}+k_0))\right.$$

$$\left.-\frac{2}{q_0k}(M(\mathscr{E}_0-k_0)(q_0-q)^2+2M^2\mathscr{E}_0(\mathscr{E}_0+\mathscr{E}-k))\right]$$

$$+(2p_0k+q_0k-qk)(qk+q_0k)\left[\frac{(p_0-p)^2}{(p_0k)(pk)}+\frac{(q_0-q)^2}{(qk)(q_0k)}\right]-4q_0p_0-4p_0q+2q_0k+2qk$$

$$+\frac{2(p_0q)(q_0k)(pk)}{(p_0k)(qk)}+\frac{2(pq)(q_0k)(p_0k)}{(pk)(qk)}-\frac{2(p_0q_0)(qk)(pk)}{(p_0k)(q_0k)}-\frac{2(pq_0)(p_0k)(qk)}{(pk)(q_0k)}$$

$$+\mu\left[\frac{\mathscr{E}_0^2\sin^2\theta_0}{(pk)(q_0k)}\left(W+U+2(qk)^2+\frac{(q_0k)^2(qk)}{p_0k}-\frac{(qk)^3}{p_0k}\right)\right.$$

$$+\frac{\mathscr{E}^2\sin^2\theta}{(pk)(qk)}\left(W+U+2(q_0k)^2-\frac{(qk)^2(q_0k)}{p_0k}+\frac{(q_0k)^3}{p_0k}\right)$$

$$+\frac{\mathscr{E}\mathscr{E}_0\sin\theta\sin\theta_0\cos\varphi}{pk}\left(-(U+W)\left(\frac{1}{qk}+\frac{1}{q_0k}\right)-2(qk+q_0k)+\frac{2(qk)^2}{p_0k}-\frac{2(q_0k)^2}{p_0k}\right)$$

$$+\frac{(q-q_0)^2}{pk}\left(\frac{(qk+q_0k)^3}{(qk)(q_0k)}+2\frac{(q_0k)^2-(qk)^2}{p_0k}\right)+\frac{(qk-q_0k)^3}{(pk)(p_0k)}\left(\frac{p_0q_0}{q_0k}-\frac{p_0q}{qk}\right)$$

$$+2(qk-q_0k)\left(\frac{q_0k}{pk}\left(\frac{pq}{pk}-\frac{p_0q}{p_0k}\right)+\frac{qk}{q_0k}\left(\frac{pq_0}{pk}-\frac{p_0q_0}{p_0k}\right)\right.$$

$$\left.+\left((qk^2)-(q_0k)^2\right)\left(\frac{1}{pk}+\frac{3}{p_0k}+\frac{qk-q_0k}{(pk)(p_0k)}\left(\frac{p_0q}{qk}+\frac{p_0q_0}{q_0k}\right)\right)\right]\Bigg\},$$

where

$$f(\mathcal{E}) = E(\mathcal{E})+\mathcal{E}+k_0-M-\mathcal{E}_0,$$

$$\Phi = -2(p_0q_0-p_0q-p_0k)(q_0-q)^2+2(M^2+m^2)(p_0q+p_0k-p_0q_0+(q_0-q)^2),$$

$$U = 2(q_0-q)^2(p_0q_0-p_0q-p_0k)-(q_0-q)^4$$
$$+2(q_0q)(-\tfrac{1}{2}(q-q_0)^2+p_0q_0-p_0q-p_0k)+(p_0k)(q_0k)-(p_0k)(qk)$$
$$+(p_0q_0)(qk)+(p_0q)(q_0k)-(qk)(q_0k)+(qk)^2+(q_0k)^2$$
$$-(p_0q_0)(q_0k)-(p_0q)(qk),$$

$$W = 2(qk-q_0k)^2-\tfrac{1}{2}(q-q_0)^4+(q_0k)(qk)$$
$$+(m^2+qq_0+2p_0q+2p_0k-2p_0q_0)(p_0q_0-p_0q-p_0k-\tfrac{1}{2}(q-q_0)^2), \text{ and}$$

$$\mu = 1.79.$$

Table 2 gives the ratios between the differential cross-sections of the inter-

TABLE 2

Relative contributions of interference terms to differential cross-section

	θ_0 \ θ	30°		90°		150°	
		$B_0/d\sigma_{BH}$	$\mu B_1/d\sigma_{BH}$	$B_0/d\sigma_{BH}$	$\mu B_1/d\sigma_{BH}$	$\mu B_1/d\sigma_{BH}$	$\mu B_1/d\sigma_{BH}$
$\varphi = 0°$	6°	0.011	0.14 $\times 10^{-4}$	0.014	0.11 $\times 10^{-3}$	0.34 $\times 10^{-3}$	0.62 $\times 10^{-3}$
	30°	−0.013	5.7	0.046	0.13 $\times 10^{-2}$	−0.044	−0.011
	60°	0.20	0.94 $\times 10^{-2}$	−0.44	−0.045	−0.22	−0.050
	90°	0.13	0.026	0.12	0.83 $\times 10^{4}$	−0.64	−0.13
	120°	0.099	0.037	0.57	0.48	−1.24	−0.070
	150°	0.059	0.031	0.23	0.23	−0.047	−0.6 $\times 10^{4}$
$\varphi = 90°$	6°	−0.74 $\times 10^{-3}$	−0.19 $\times 10^{-4}$	−0.39 $\times 10^{-2}$	−0.38 $\times 10^{-3}$	−0.30 $\times 10^{-3}$	−0.77 $\times 10^{-3}$
	30°	−0.071	−0.11 $\times 10^{-3}$	−0.080	−0.85 $\times 10^{-3}$	−0.066	−0.016
	60°	−0.065	−0.46 $\times 10^{-2}$	−0.20	−0.027	−0.22	−0.051
	90°	−0.033	−0.50 $\times 10^{-2}$	−0.26	−0.045	−0.44	−0.096
	120°	−0.023	−0.34 $\times 10^{-2}$	−0.23	−0.033	−0.61	−0.090
	150°	−0.92 $\times 10^{-2}$	+0.19 $\times 10^{-3}$	−0.12	+0.031	−0.62	+0.028
$\varphi = 150°$	6°	−0.013	−0.68 $\times 10^{-4}$	−0.014	−0.14 $\times 10^{-2}$	−0.78 $\times 10^{-3}$	−0.19 $\times 10^{-3}$
	30°	−0.056	−0.21 $\times 10^{-2}$	−0.074	−0.012	−0.074	−0.020
	60°	−0.071	−0.90 $\times 10^{-2}$	−0.14	−0.031	−0.19	−0.052
	90°	−0.076	−0.019	−0.20	−0.052	−0.35	−0.089
	120°	−0.076	−0.024	−0.25	−0.066	−0.46	−0.095
	150°	−0.054	−0.018	−0.21	−0.033	−0.57	+0.052

ference terms B_0 and $B_1\mu$ and the Bethe-Heitler differential cross-section.

The interference contributions of $d\sigma_I$, generally speaking, proves to be considerable and, for examhle, reaches 20 % of $d\sigma_{B\text{-}H}$ when $\varphi = 0$, $\theta = 30°$ and $\theta_0 = 60°$. The contribution of $B_1\mu$ is approximately by order less than the contribution of B_0 (with the exception of the points of the maximum). These contributions become comparable only at large angles. Thus, the interference term is calculated with a sufficiently high degree of accuracy and the error in the differential cross-section of bremsstrahlung for the energies under consideration proves to be < 1 % (except for the points of maximum and large angles, of course).

The calculations for $\mathscr{E}_0 = 0.54$ and $k_0 = 0.25$ and other values of $\mathscr{E}_0$ and k_0 were carried out with the Ural computer. The curve in the maximum ($\varphi = 0$, $\theta_0 \approx \theta$) was plotted with respect to θ_0 with a step of 30'' and an accuracy to the seventh significant figure. In a number of cases the step of 30'' proved to be insufficient for an accurate determination of the maximum. Fig. 1 represents curves III and IV corresponding to the interference term when $\mathscr{E}_0 = 0.54$ and $k_0 = 0.25$.

4. Evaluation of One-Pion Contribution

Dispersion relations (see ref. [3])) connect the Hermitian and anti-Hermitian parts of the bremsstrahlung amplitude. If the unitarity condition $S^+S = 1$ is written in one-meson approximation, the anti-Hermitian part of the virtual Compton effect may be expressed in terms of the amplitude of real and virtual π-meson photoproduction. The amplitude of virtual π-meson photoproduction was found in refs. [6, 7]) and of real photoproduction it may be taken from experimental data. Thus, it is possible in principle to calculate the one-pion contribution accurately. Now an approximate evaluation of the contribution which may be obtained within the limits of small values of κ^2 is sufficient for us. In this case the virtual Compton effect may be regarded as close to the real one and the results of refs. [8–11]) may be used. In the experimental data [8]) available today the Compton effect was measured at angles $\gtrsim 50°$. For energies $\lesssim 100$ MeV the experimental curve is in good agreement with the Powell cross-section.

For energies > 150 MeV, meson corrections begin to have a considerable effect. Gell-Mann and Mathews [10]) compared the dispersion relations obtained by them with experimental data on the Compton effect on nucleons for the scattering angle $\theta = 90°$. Calculations were carried out by means of dispersion relations in the one-meson static approximation with account of the $(\frac{3}{2}, \frac{3}{2})$ resonance. The authors obtained a satisfactory agreement with experiment up to the energies of γ-quanta ≈ 250 MeV.

Capps [9]) and Aniba and Sato [11]) obtained results similar to those of ref. [10]). Certain discrepancies in the results of these papers are inessential for us since we are concerned with an approximate evaluation of the one-pion state contribution.

Thus, in the case $\kappa^2 \approx 0$ under consideration, the amplitude of T^C (see ref. [3])) is close to the amplitude of the real Compton effect.

We can now obtain the required evaluation by comparing the value of the cross section of one-nucleon contribution when $\theta = \theta_0$ ($\varphi = 0$) and the values of the cross section of Compton scattering at the same angles taken from refs. [9–11]).

For the angle $\theta_0 = \theta = 30°$ the energy of the γ-quantum is ≈ 250 MeV. The contribution of the one-pion state proves to be smaller than that of the one-nucleon term.

For the angles $\theta_0 = \theta = 60°$ and the energy of γ-quantum ≈ 270 MeV the contribution of the one-pion state is approximately five or six times as large as that of one-nucleon state. At the energy of the incident γ-quantum ≈ 300 MeV (the angle $= 90°$), the contribution of one-pion state is approximately fifteen times as great as that of the one-nucleon term.

The obtained estimates related to the Compton effect are believed to be valid for the virtual Compton effect as well when $|\theta - \theta_0| \leqq 5°$ (then κ^2 is rather small).

5. Corrections of the Highest Order in e

Corrections of the highest order in e are found in the papers of Fomin [12]) and Mitra, Napayanaswamy and Pande [13]). We are using the evaluations obtained by Fomin.

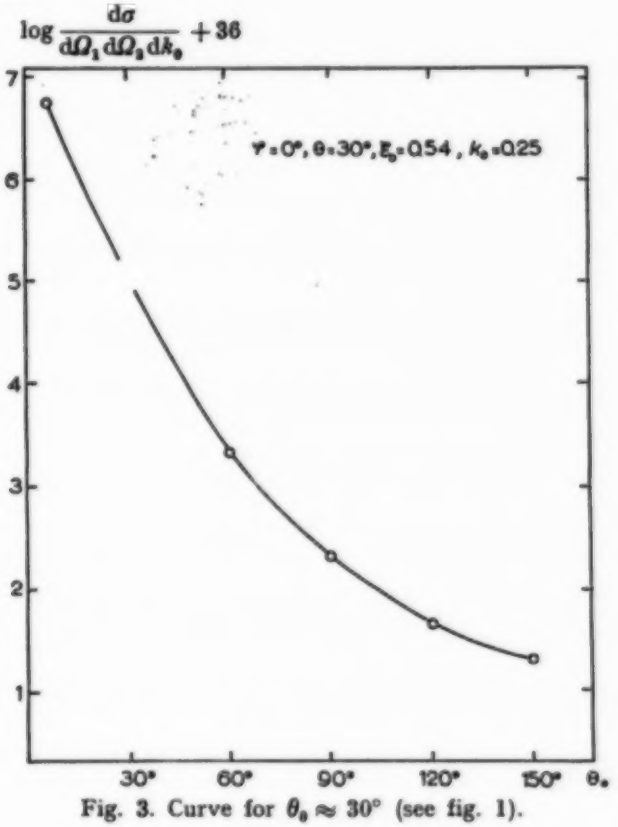

Fig. 3. Curve for $\theta_0 \approx 30°$ (see fig. 1).

In the ultra-relativistic case and for not too small angles the total contribution of radiative corrections and corrections for double bremsstrahlung does not exceed several per cent. This evaluation was obtained without taking into account the nucleon recoil. The nucleon recoil effect, however, does not introduce any essential changes.

6. Conclusion

Using the calculations of the corrections obtained in the present paper (secs. 2—4) we may obtain the cross section of bremsstrahlung in the lowest order in e with a definite degree of accuracy.

Thus, for example, when $\varphi = 0$, $\theta = 30°$, the curve with respect to θ_0 up to angles $\approx 40°$ is plotted within an accuracy up to 5 per cent (see fig. 3). Radiative corrections and double bremsstrahlung corrections do not exceed a few per cent.

Assuming that in checking the cross section of bremsstrahlung the experimental error is 10 per cent, we find that quantum electrodynamics is checked up to distances $\geqq 3\times 10^{-14}$ cm for angles θ, $\theta_0 \approx 30°$, the energy of the incident electron $= 0.54$ and the energy of γ-quantum $= 0.25$. (In all above discussions the region of the maximum is excluded.)

The exact calculation of the one-π-meson state allows us to test quantum electrodynamics down to still smaller distances.

In conclusion we express our deep gratitude to Acad. N. N. Bogolyubov and A. A. Logunov for the proposed subject of the paper and valuable advice, and D. V. Shirkov and A. N. Tavkhelidse for useful discussions. The authors are also indebted to N. I. Polumordvinova for making calculations on the Ural Computer.

References

1) S. D. Drell, Annals of Physics **4** (1958) 75 (additional references to papers devoted to the problems of testing quantum electrodynamics at small distances and to the problems of quantum electrodynamics modification are given in this paper)
2) J. D. Bjorken, S. D. Drell and S. C. Frautschi, Phys. Rev. **112** (1958) 1409
3) P. S. Isaev and I. S. Zlatev, JETP **37** (1959) 728
4) P. S. Isaev and I. S. Zlatev, Nuovo Cimento **13** (1959) 1
5) R. A. Berg and C. N. Lindner, Phys. Rev. **112** (1958) 2072
6) Fubini, Nambu and Watagin, Phys. Rev. **111** (1958) 329
7) L. D. Soloviev (private communication)
8) C. L. Oxley and V. L. Telegdi, Phys. Rev. **110** (1958) 733; **100** (1955) 435;
C. S. Janes, R. Gomes, C. Pugh and D. K. Frisch, Phys. Rev. **100** (1955) 1245
9) R. K. Capps, Phys. Rev. **108** (1957) 1032 (other references to the theoretical work on the Compton effect may be found in this paper)
10) Chew, Report at Annual Conference on High Energy Physics, CERN, 1958
11) T. Akiba and I. Sato, Progr. Theor. Phys. **19** (1958) 93
12) P. I. Fomin, JETP **35** (1958) 707
13) A. N. Mitra, P. Napayanaswamy and L. K. Pande, Nuclear Physics **10** (1959) 629

1.E.1:
3.A

Nuclear Physics **16** (1960) 619—624; © *North-Holland Publishing Co., Amsterdam*
Not to be reproduced by photoprint or microfilm without written permission from the publisher

DECAY OF Ba^{133}

M. K. RAMASWAMY, W. L. SKEEL and P. S. JASTRAM
Department of Physics, Ohio State University, Columbus, Ohio †

Received 25 January 1960

Abstract: The gamma-rays following the electron-capture decay of 7.5 year Ba^{133} have been studied by means of a coincidence scintillation spectrometer. Gamma rays at 79, 79, 274, 302, 358 and 381 keV have been observed. In addition, the presence of a 56 keV gamma ray was confirmed. The resulting decay scheme with levels at 79, 158, 381 and 437 keV is in excellent agreement with previous work. Spin and parity assignments are made for these levels.

1. Introduction

Prior to 1957 the work of Hayward *et al.*[1]) and Langevin [2]) on the decay of Ba^{133} had produced somewhat inconsistent results. The decay scheme was recently re-examined by Crasemann *et al.* [3]) using magnetic-lens and scintillation spectrometers. Gamma rays of 79, 302 and 355 keV and conversion electrons corresponding to 158 and 276 keV transitions were observed. On the basis of gamma-gamma coincidence experiments, a level scheme for Cs^{133} was proposed with levels at 79, 158, 381 and 434 keV. The 57 keV gamma ray reported by Hayward *et al.*[1]) was not observed, and an upper limit of 5 % (as compared with the 79 keV gamma ray) was set. The difficulty of identifying a gamma ray of 57 keV arises from the proximity to the iodine escape peak from the 79 keV photon, which occurs at about the same energy. Further, no gamma rays with energy greater than 355 keV were detected by Crasemann *et al.*[3]).

More recently, the decay of Ba^{133} has been studied by Stewart *et al.*[4]), Koicki *et al.*[5]) and Gupta *et al.*[6]). A gamma ray of about 56 keV is reported by these groups, but unfortunately its intensity was not given [4, 5]). Additional gamma rays at 220 and 382 keV were also reported by Stewart *et al.*[4]). The 220 keV gamma ray was not observed by Koicki *et al.*[5]), while the 381 keV gamma ray was not seen by Gupta *et al.*[6]). The present investigation was undertaken in order to re-examine the gamma rays and their relative intensities; in particular, attention was focussed on the 56 keV transition.

2. Experimental Procedure

The Ba^{133} source used in the present investigation was obtained from the Oak Ridge National Laboratory. The gamma rays were examined in a scintilla-

† Supported by the U. S. Atomic Energy Commission.

tion spectrometer using a 3.8 cm diameter by 5.1 cm thick NaI(Tl) crystal and an EMI 9536B photomultiplier. For the gamma-gamma coincidence experiments two such detectors were employed and connected to a coincidence circuit of resolving time $2\tau = 2\ \mu s$. With this resolving time and the source strength employed the chance coincidence rate never exceeded 7 % of the true coincidence rate. The coincidence spectrum was measured by means of an automatic scanning system developed by Mr. W. L. Skeel of this laboratory.

3. Experimental Results

The gamma ray spectrum measured in the 3.8 cm × 5.1 cm NaI counter is shown in fig. 1. A source-to-detector distance of 4 cm was used. In addition to

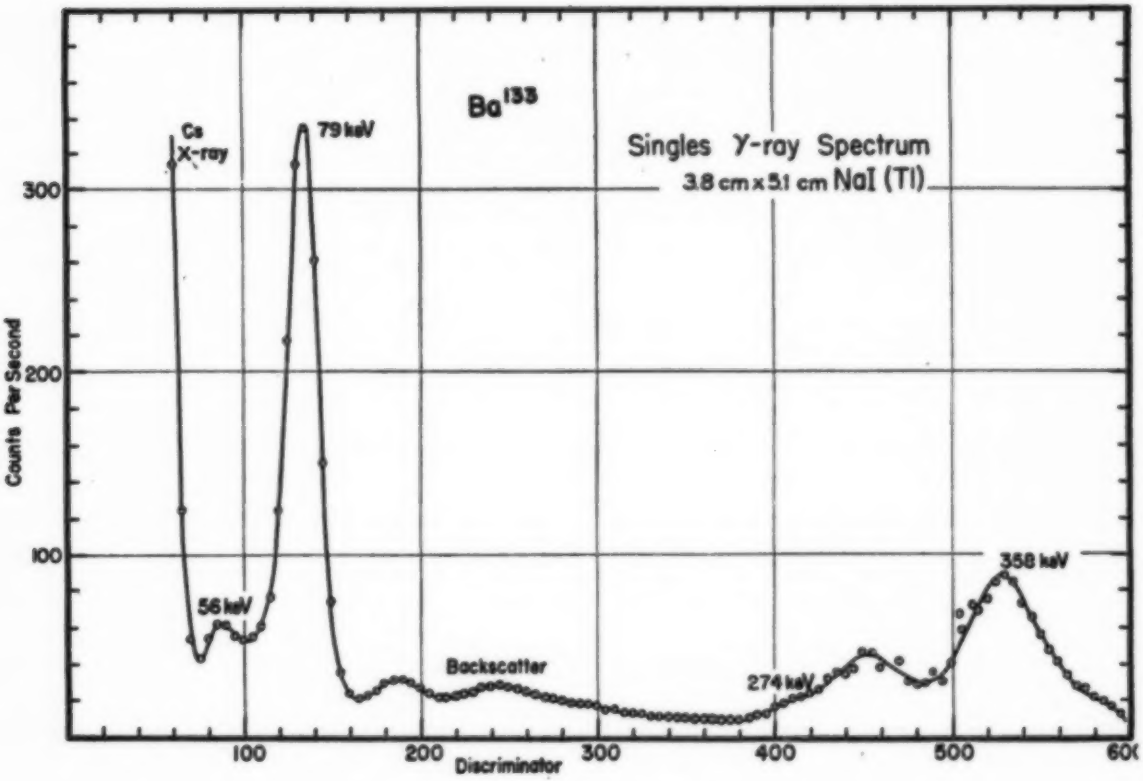

Fig. 1. Gamma-ray spectrum measured in the 3.8 cm × 5.1 cm NaI counter. Source-to-detector distance 4 cm. Gamma-rays are present at 79, 302, 358 and 381 keV and possibly at 274 keV. The region marked "backscatter" is caused by the backscattering effects due to higher energy gamma rays.

the 31 keV Cs K X-ray, gamma-rays are found at 79, 302, 358 and 381 keV. There is some evidence for a gamma ray at 274 keV, corresponding to the 276 keV gamma ray observed by Gupta, [6]) Stewart *et al.*[4]) and Koicki *et al.*[5]). The humps that appear in the region marked "Backscatter" are presumably due to backscattering of the 302, 358 and 381 keV gamma rays. There appears to be

no evidence for a gamma ray at 220 keV. The backscattering peaks mask the presence of any weak 158 keV gamma ray that may be present. The peak that appears at 56 keV is partly due to the iodine escape resulting from the 79 keV gamma-ray and partly to a 56 keV gamma-ray, as is demonstrated by the γ—γ coincidence experiments. In table 1 are listed the various gamma rays and their relative intensities after taking into account the variation of efficiency with energy [7]). The relative intensity of the 56 keV gamma ray was deduced from the coincidence experiments described below.

TABLE 1

Gamma rays of Ba^{133}

Energy (keV)	56	79_1	79_2	274	302	358	381
Rel. Intensity	2.4	35	7	2	38	100	14

For the gamma-gamma coincidence measurements the discriminator of one counter channel was adjusted to accept a particular gamma ray, while the other counter, placed on the opposite side of the source, scanned the coincidence spectrum. Fig. 2 shows the spectrum coincident with the 79 keV gamma ray. In addition to the Cs X-ray, gamma rays of 79, 302 and 358 keV appear. The

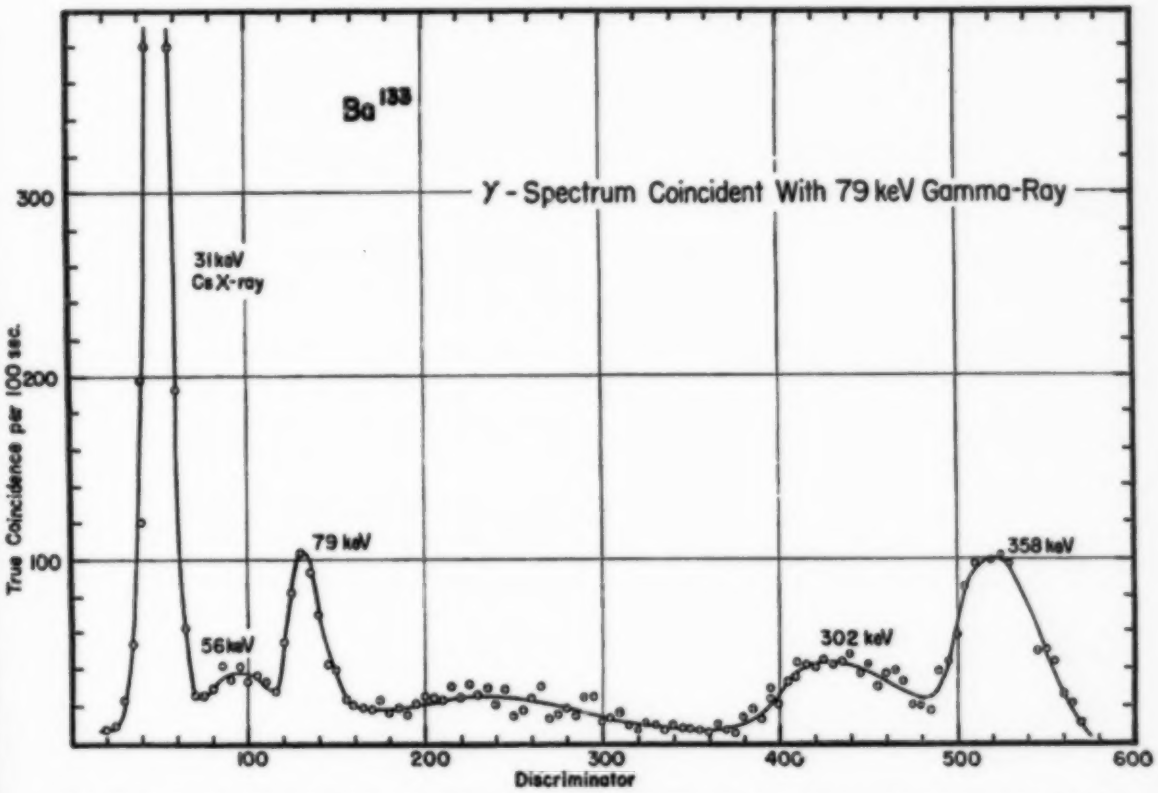

Fig. 2. Gamma-ray spectrum coincident with 79 keV gamma ray. Gamma rays are present at 56, 79, 302 and 358 keV. The 274 keV gamma ray indicated in fig. 1 is still not resolved.

274 keV gamma ray indicated in the singles spectrum is not resolved from the 302 keV peak. A peak appears again at 56 keV. Figs. 3a, 3b and 3c show the spectra coincident with the 302, 358 and 381 keV gamma-rays respectively. If we assume, in agreement with the coincidence-spectra results, that the 56 keV gamma ray occurs in a transition from the 437 keV to the 381 keV level (fig. 4), and that these are the parent levels respectively of the 358 keV and the 302 keV photons, then the fraction of 79 keV transitions that appear in the escape peak at 56 keV can be obtained from the ratio of the intensity of the 56 keV peak to that of the 79 keV photon in the spectrum coincident with the 358 keV transition. This fraction turns out to be approximately 9.4 %. The spectrum

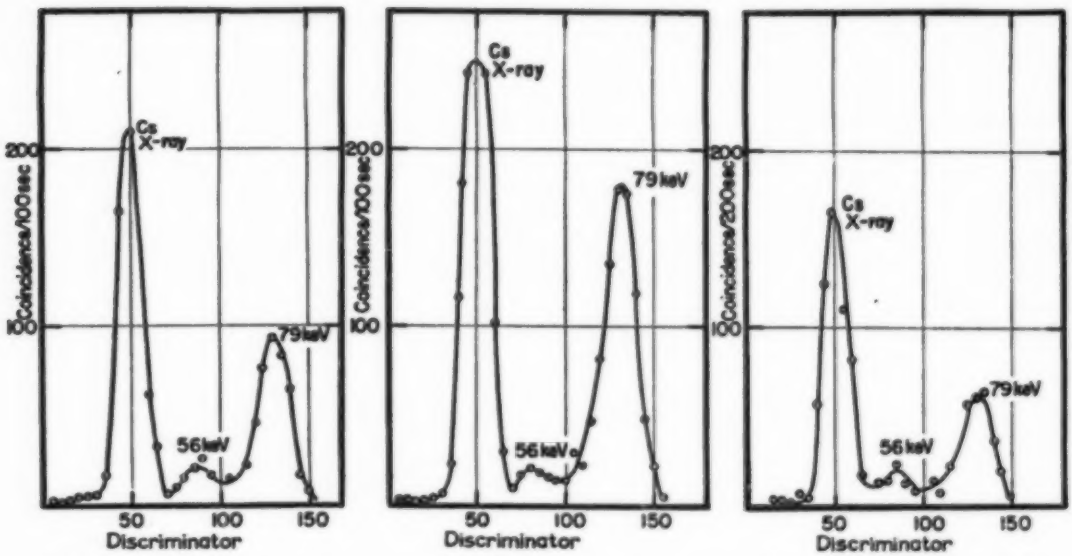

Fig. 3a Gamma-spectrum coincident with 302 keV gamma ray.

Fig. 3b. Gamma-spectrum coincident with 358 keV gamma ray.

Fig. 3c. Gamma-spectrum coincident with 382 keV gamma ray.

coincident with the 302 keV gamma ray, which admits a coincident 56 keV transition, yields for the same ratio a value estimated to be 15 %. The difference of 5.6 % has therefore to be attributed to the presence of a 56 keV gamma ray. This transition is confirmed by the spectrum coincident with the 382 keV gamma ray. The appearance of some 79 keV intensity in the spectrum is due to the fact that the discriminator, set at the 382 keV peak, necessarily accepted pulses from the incompletely resolved 358 keV gamma ray.

4. Discussion

The level scheme shown in fig. 4 is constructed on the basis of the present singles and coincidence spectrum measurements. This scheme † is in excellent

† Our scheme is slightly different from that of Gupta [6]), who postulates 100 % electron capture to the 437 keV level.

agreement with previous work [4, 5, 6]). The dotted line indicates the 158 keV transition reported by Crasemann *et al.*[3]) from conversion-electron spectrum measurements, which is presumably hidden by the pulse-height distributions of higher-energy gamma rays in the scintillation-counter spectrum.

The spin and parity assignment for Cs^{133} is $\frac{7}{2}+$ [8]), and that for the ground state of Ba^{133} is presumably $\frac{1}{2}+$ [9]) from systematics of the isomerism of this isotope. The measured K-conversion coefficient [3]) of the 79 keV gamma ray is consistent with this transition being M1 and the 79 keV level is then $\frac{5}{2}+$. The recent measurement of the lifetime of this level [4]) indicates that this is probably a $d_{\frac{5}{2}}$ level. The 158-keV level is observed in Coulomb excitation [10]) and is weakly fed by beta-decay from Xe^{133} [11]). Hence the spin assignment is either $\frac{3}{2}+$ or $\frac{5}{2}+$. However, the absence of electron capture from the ground state

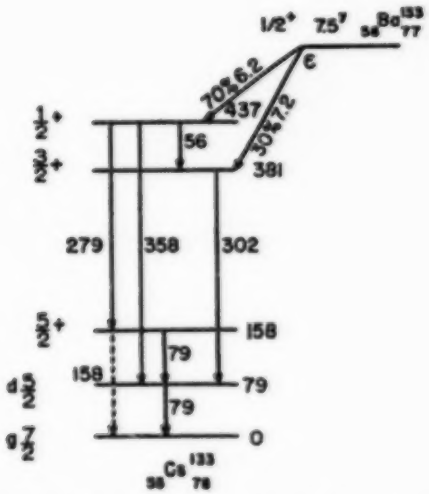

Fig. 4. Proposed decay scheme for Ba^{133}. The dotted transition is due to Crasemann [3]).

of Ba^{133} (spin $\frac{1}{2}+$) makes the $\frac{5}{2}+$ assignment the more likely. The measured conversion coefficients of the 302 and 358 keV gamma rays yield assignments of $\frac{3}{2}+$ for the 381 keV level, and $\frac{1}{2}+$ for the 438 keV level. The electron-capture decays to these levels would then be allowed. The energy available for the Ba^{133}—Cs^{133} decay is expected to be approximately 700 keV, from beta-decay systematics of Way and Wood [12]). On the basis of the observed gamma ray intensities, the amount of electron capture is estimated to be about 70 % to the 437 keV level and 30 % to the 381 keV level. From these and the half-life of 7.5 years [13]) for Ba^{133}, the log *ft* values are calculated to be at least 8. This appears rather large for allowed transitions. Recently, Gupta *et al.*[6]) have measured the L/K ratio, and estimate the energy available for the Ba^{133}—Cs^{133} decay to be about 500 keV. Thus the energy available for capture to the 437 keV level is about 60 keV and that to the 381 keV level about 115 keV. The corresponding log *ft* values are about 6.3 and 7.2 respectively, in a more reason-

able range for allowed transitions. It would, however, be of interest to determine the decay energy more directly. A suitable method would be to measure the end-point of the inner bremsstrahlung spectrum coincident with the 358+79 sum peak, or by the use of the coincidence summing technique [6]).

References

1) Hayward, Hoppes and Earnst, Phys. Rev. **93** (1954) 916A
2) M. Langevin, Compt. Rend. **238** (1954) 1310; **240** (1955) 289; Ann. Phys. **1** (1956) 57
3) Crasemann, Pengra and Lindstrom, Phys. Rev. **108** (1957) 1500
4) Stewart, Lu and Clikeman, Bull. Am. Phys. Soc. **3** (1958) 208
5) Koicki, Mijatovic and Simic, Bull. Inst. Nucl. Sci. Boris Kidrich (Belgrade) **8** (1958) 1
6) Gupta, Jha, Joshi and Madan, Nuovo Cimento **8** (1958) 48
7) P. R. Bell in Beta and Gamma-Ray Spectroscopy (North-Holland Publishing Company Amsterdam, 1955) Ch. 5
8) P. F. A. Klinkenberg, Revs. Mod. Phys. **24** (1952) 63
9) M. Goldhaber and R. D. Hill, Revs. Mod. Phys. **24** (1952) 217
10) L. W. Fagg, Bull. Am. Phys. Soc. **2** (1957) 207
11) F. Pleasonton, Oak Ridge National Laboratory Report-2430 (1958) p. 46
12) K. Way and M. Wood, Phys. Rev. **94** (1954) 119; revised
13) S. Katcoff; quoted by Beggs, Robinson and Fink, Phys. Rev. **101** (1956) 149

1.D.2

Nuclear Physics **16** (1960) 625—644; © *North-Holland Publishing Co., Amsterdam*

Not to be reproduced by photoprint or microfilm without written permission from the publisher

ON THE COUPLING OF A $j = \frac{3}{2}$ PARTICLE TO NUCLEAR QUADRUPOLE SURFACE OSCILLATIONS

B. F. BAYMAN and L. SILVERBERG †

Institute for Theoretical Physics, University of Copenhagen,
and
NORDITA (*Nordisk Institut for Teoretisk Atomfysik*), *Copenhagen*

Received 5 November 1959

Abstract: An intermediate coupling calculation is performed for a nucleon confined to move in a $j = \frac{3}{2}$ orbit and coupled to a nuclear surface capable of performing quadrupole oscillations. It is shown that each term in the hamiltonian commutes with a symplectic group of transformations. This feature is used to define a representation in which the hamiltonian matrix takes an especially simple form. It is possible to follow the transition from weak to strong coupling, at which there appear sets of rotational bands built on equidistant vibrational excitations. These rotational bands have some special features due to the γ-instability of the problem.

1. Introduction

A simple model which exhibits some of the features of the interplay between particle and collective degrees of freedom in heavy nuclei consists of a particle which moves in a j-shell and is coupled to a surface capable of performing quadrupole vibrations [1, 2]). The behaviour of this system is determined by the comparative magnitudes of the coupling strength and the phonon excitation energy.

It would be interesting to be able to follow the transition from the weak-coupling limit, where the particle and surface are independent, to the strong-coupling limit, where the surface acquires a large stable deformation which is then capable of low-energy rotational excitations. The most straightforward approach would appear to be the diagonalization of the matrix of the particle-surface interaction with respect to the states of the uncoupled motion [3, 4, 5]). But for high phonon numbers there occur many states with the same angular momentum, and the calculation and subsequent diagonalization of the matrix become very difficult. Hence this method is usually restricted to weak coupling when only the first few phonons contribute to the ground state. However, if the particle moves in a $j = \frac{3}{2}$ shell, the problem has a simplifying feature ††. In section 2 it is shown that the hamiltonian then commutes with a group of

† On leave from the Institute for Theoretical Physics, Lund, Sweden.

†† The $j = \frac{1}{2}$ case has been treated in detail in ref. [3]) for weak and intermediate coupling.

transformations isomorphic with the group of 4×4 symplectic matrices. This is related to the γ-instability of the problem, and facilitates the classification of the states (section 3) and the construction of the entire interaction matrix (section 4). The resulting matrix is sufficiently simple to enable us to follow the transition from weak to strong coupling, at which there occurs a level structure describable in terms of rotational bands built upon vibrational excitations (section 5). Moreover, this description is supported by the $B(\mathrm{E2})$ values and multipole moments.

2. The Symmetry of the Hamiltonian

The surface is characterized by five coefficients α_μ, defined by [1]),

$$R(\vartheta,\varphi) = R_0[1+\sum_\mu \alpha_\mu Y_\mu{}^2(\vartheta,\varphi)]. \tag{1}$$

For small oscillations around equilibrium, the surface hamiltonian is approximately harmonic:

$$H_s = \frac{1}{2B}\sum_\mu \pi_\mu{}^*\pi_\mu + \tfrac{1}{2}C\sum_\mu \alpha_\mu{}^*\alpha_\mu, \tag{2}$$

where the π_μ are the momenta canonically conjugate to the α_μ, B is a mass parameter and C the surface deformability †. The particle hamiltonian H_p is that of a single particle moving in a central field with spin-orbit coupling. The particle-surface coupling is taken to be

$$H_{\mathrm{int}} = -k\sum_\mu \alpha_\mu Y_\mu{}^2(\vartheta_p,\varphi_p), \tag{3}$$

where (ϑ_p,φ_p) are the polar coordinates of the particle and k is the coupling strength. The total hamiltonian of the system can then be written

$$H = H_s+H_p+H_{\mathrm{int}}. \tag{4}$$

We attempt to find the eigenvectors of (4) as linear combinations of those of the uncoupled system, H_s+H_p. These basis eigenvectors can be labelled

$$|j;N(\alpha)R;IM\rangle. \tag{5}$$

Here j is the single-particle angular momentum, N is the number of quanta (phonons) of surface oscillation, and R is the surface angular momentum. The additional label α is needed for $N>3$ when several states with the same N and R occur. The particle and surface angular momenta are vector coupled to a total angular momentum I with z-component M. In the following we will restrict our attention to the states arising from the coupling of arbitrarily many phonons to a single particle with $j=\frac{3}{2}$. Our problem is then to construct the matrix of the hamiltonian (4) with respect to these states and to diagonalize

† The notation is that of refs. [1]) and [3]).

it. The part of this hamiltonian referring to states with $j = \frac{3}{2}$ commutes with a symplectic group, and this simplifies our task considerably.

Suppose the single-particle states $\psi_\alpha^{\frac{1}{2}}$ are subjected to the symplectic transformation

$$\psi_\alpha^{\frac{1}{2}} \to \sum_\gamma (S_{p_4})_{\gamma\alpha} \psi_\gamma^{\frac{1}{2}}. \tag{6}$$

This is defined to be the most general linear unitary transformation leaving invariant the quadratic form

$$\sum_{\alpha=-\frac{1}{2}}^{\frac{1}{2}} (-1)^\alpha \psi_\alpha^{\frac{1}{2}}(1) \psi_{-\alpha}^{\frac{1}{2}}(2). \tag{7}$$

This quadratic form is essentially the vector coupling of $\psi^{\frac{1}{2}}(1)$ and $\psi^{\frac{1}{2}}(2)$ to an angular momentum zero. Hence (7) remains invariant if ψ undergoes the unitary transformation

$$\psi_\alpha^{\frac{1}{2}} \to \sum_\gamma D^{\frac{1}{2}}_{\gamma\alpha}(R) \psi_\gamma^{\frac{1}{2}}. \tag{8}$$

Thus the 3-dimensional rotations (8) are a subgroup of the symplectic group. The well-known relation

$$D^{\frac{1}{2}*}_{\alpha\beta} = (-1)^{\alpha-\beta} D^{\frac{1}{2}}_{-\alpha,-\beta}$$

can easily be shown to follow from the unitarity of the $D^{\frac{1}{2}}$ and the invariance of (7), and hence it applies to all matrices of the symplectic group

$$(S_{p_4})^*_{\alpha\beta} = (-1)^{\alpha-\beta} (S_{p_4})_{-\alpha,-\beta}. \tag{9}$$

When the single-particle *states* undergo the transformation (6), the single-particle *operator* $Y_\mu{}^2(\vartheta_p, \varphi_p)$ transforms into $S_{p_4} Y_\mu{}^2(\vartheta_p, \varphi_p) S^{-1}_{p_4}$, whose matrix elements are given by

$$\begin{aligned}(\psi_\alpha^{\frac{1}{2}} | S_{p_4} Y_\mu{}^2 S^{-1}_{p_4} | \psi_\beta^{\frac{1}{2}}) &= \sum_{\gamma,\delta} (S_{p_4})^*_{\beta\gamma} (S_{p_4})_{\alpha\delta} (\tfrac{3}{2} 2\gamma\mu | \tfrac{3}{2}\delta) (\tfrac{3}{2} || Y^2 || \tfrac{3}{2}) \\ &= \sum_{\gamma,\delta} (-1)^{\gamma-\beta} (S_{p_4})_{-\beta,-\gamma} (S_{p_4})_{\alpha\delta} (\tfrac{3}{2} 2\gamma\mu | \tfrac{3}{2}\delta) (\tfrac{3}{2} || Y^2 || \tfrac{3}{2}).\end{aligned} \tag{10}$$

To evaluate this sum we recall that the $(j+1)(2j-1)$ 2-particle states $\psi(j^2 IM)$, where $I = 2,4 \ldots, 2j-1$, spread out the irreducible representation (1,1) of the symplectic group [6]). If $j = \frac{3}{2}$, the five states $\psi((\frac{3}{2})^2 2M)$ themselves spread out this representation. Thus,

$$\begin{aligned}S_{p_4}[\sum_{\kappa,\lambda} (\tfrac{3}{2}\tfrac{3}{2}\kappa\lambda | 2M) \psi_\kappa^{\frac{1}{2}} \psi_\lambda^{\frac{1}{2}}] &= \sum_{M'} U^{(1,1)}_{M'M}(S_{p_4}) [\sum_{\pi\rho} (\tfrac{3}{2}\tfrac{3}{2}\pi\rho | 2M') \psi_\pi^{\frac{1}{2}} \psi_\rho^{\frac{1}{2}}] \\ &= \sum_{\substack{\kappa,\pi \\ \lambda\rho}} (\tfrac{3}{2}\tfrac{3}{2}\kappa\lambda | 2M) (S_{p_4})_{\pi\kappa} (S_{p_4})_{\rho\lambda} \psi_\pi^{\frac{1}{2}} \psi_\rho^{\frac{1}{2}}, \\ \sum_{\kappa,\lambda} (\tfrac{3}{2}\tfrac{3}{2}\kappa\lambda | 2M) (S_{p_4})_{\pi\kappa} (S_{p_4})_{\rho\lambda} &= \sum_{M'} U^{(1,1)}_{M'M}(S_{p_4}) (\tfrac{3}{2}\tfrac{3}{2}\pi\rho | 2M'), \\ \sum_{\kappa,\lambda} (-1)^{\lambda-\rho} (\tfrac{3}{2} 2 - \lambda M | \tfrac{3}{2}\kappa) (S_{p_4})_{\pi\kappa} (S_{p_4})_{\rho\lambda} &= \sum_{M'} U^{(1,1)}_{M'M}(S_{p_4}) (\tfrac{3}{2} 2 - \rho M' | \tfrac{3}{2}\pi).\end{aligned} \tag{11}$$

This sum (11) is precisely what we need in (10). Hence the latter becomes

$$(\psi_\alpha^{\frac{1}{2}}|S_{p_4} Y_\mu^2 S_{p_4}^{-1}|\psi_\beta^{\frac{1}{2}}) = \sum_{\mu'} U^{(1,1)}_{\mu'\mu}(S_{p_4})(\tfrac{3}{2}2\beta\mu'|\tfrac{3}{2}\alpha)(\tfrac{3}{2}||Y^2||\tfrac{3}{2})$$
$$= \sum_{\mu'} U^{(1,1)}_{\mu'\mu}(S_{p_4})(\psi_\alpha^{\frac{1}{2}}|Y^2_{\mu'}|\psi_\beta^{\frac{1}{2}}). \tag{12}$$

Thus, if we consider only its matrix elements within the shell $j = \frac{3}{2}$, the operator $Y_\mu^2(\vartheta_p\varphi_p)$ undergoes the transformation

$$Y_\mu^2(\vartheta_p\varphi_p) \to \sum_{\mu'} U^{(1,1)}_{\mu'\mu}(S_{p_4}) Y^2_{\mu'}(\vartheta_p\varphi_p) \tag{13}$$

when the states $\psi_\alpha^{\frac{1}{2}}$ undergo the transformation (6). Therefore, if with the transformation (6) we associate the transformation

$$\alpha_\mu \to \sum_{\mu'} U^{(1,1)*}_{\mu'\mu}(S_{p_4})\,\alpha_{\mu'}$$
$$\pi_\mu \to \sum_{\mu'} U^{(1,1)*}_{\mu'\mu}(S_{p_4})\pi_{\mu'}, \tag{14}$$

then

$$\sum_\mu \alpha_\mu Y_\mu^2 \to \sum_{\mu'\mu''} U^{(1,1)*}_{\mu'\mu}(S_{p_4}) U^{(1,1)}_{\mu''\mu}(S_{p_4})\alpha_{\mu'} Y^2_{\mu''} = \sum_{\mu'} \alpha_{\mu'} Y^2_{\mu'}, \tag{15}$$

demonstrating the invariance of H_{int} under the joint transformation (6) and (14). Moreover, the transformation (6) evidently commutes with H_p, since it mixes eigenstates corresponding to the same single-particle eigenvalue. And the unitarity of the matrices $U^{(1,1)}$ guarantees the invariance of H_s under the transformation (14). Thus it follows that *each term of the hamiltonian* (4) *is invariant under transformations of the symplectic group defined as in* (6) *and* (14). The rotational invariance of (4) is of course a special application of this result.

In addition to being unitary, the representation matrices $U^{(1,1)}$ are orthogonal. This follows from the branching law †

$$\underset{2}{I} = \underset{2}{(1,1)} \times \underset{2}{(1,1)} = \underset{0}{(0,0)} \dot{+} \underset{1,3}{(2,0)} \dot{+} \underset{2,4.}{(2,2)} \tag{16}$$

Hence the state obtained by vector coupling of $\psi_{1,2}((\frac{3}{2})^2 2M)$ and $\psi_{3,4}((\frac{3}{2})^2 2M)$ to a total angular momentum of zero is a symplectic scalar. Thus the bilinear form

$$\sum_{M=-2}^{2} (-1)^M \psi_M \psi_{-M} \tag{17}$$

is invariant under the transformation

$$\psi_M \to \sum U^{(1,1)}_{M'M} \psi_{M'}.$$

† Such branching laws for S_{p_4} may easily be determined from the branching law [7]) for representations of U_4 together with the rule [6]) for the decomposition of representations of U_4 into representations of S_{p_4}.

This is the defining property of the orthogonal group R_5. The phonon transformations (14) induced by the symplectic transformations (6) are thus precisely the transformations used by Rakavy [8]) to obtain additional quantum numbers for the characterization of the phonon states. These are the most general transformations leaving invariant the linear form

$$\beta^2 = \sum_\mu \alpha_\mu^* \alpha_\mu \tag{18}$$

and at the same time preserving the reality conditions

$$\alpha_\mu^* = (-1)^\mu \alpha_{-\mu}.$$

Those transformations (14) which are not merely rotations without change of shape must therefore change the "γ" of the surface [1]), since they certainly cannot change β. Since the hamiltonian (4) is invariant with respect to these transformations, the system we are considering is unstable with respect to 'γ-vibrations'. †

We could just as well treat the problem of two $j = \frac{3}{2}$ particles coupled to a quadrupole surface. Moreover we could allow them to interact with any Wigner-Heisenberg force without destroying the invariance of the hamiltonian under S_{p_4}, since any such 2-particle force can be expressed in terms of the Casimir operator for S_{p_4}. But the additional degree of freedom associated with the second particle increases considerably the complexity of the energy matrices.

If we were dealing with a particle in a shell with $j > \frac{3}{2}$, the five $Y_\mu^2(\vartheta_p \varphi_p)$ would not by themselves carry a representation of $S_{p_{2j+1}}$, but would become mixed with the $Y_\mu^4(\vartheta_p \varphi_p), \ldots, Y_\mu^{2j-1}(\vartheta_p \varphi_p)$. In order to construct an invariant hamiltonian we should thus need to bring in $2^4, \ldots, 2^{2j-1}$-pole deformations, all with the same frequency as the quadrupole deformation. This is far removed from the actual situation in nuclei.

3. Classification of the States

In the previous section we found a group of transformations S_{p_4} (eqs. (6) and (14)), more general than R_3, under which the entire hamiltonian (4) as well as its uncoupled part, $H_s + H_p$, are invariant. To utilize this additional symmetry, we will choose our basis eigenvectors (5) to carry irreducible representations of S_{p_4}.

We must first decide which irreducible representations occur for each phonon number. It is convenient to introduce [1]) the phonon creation operators defined by

$$b_\mu^+ = \sqrt{\frac{B\omega}{2\hbar}}\, \alpha_\mu^+ - i \sqrt{\frac{1}{2\hbar B\omega}}\, \pi_\mu^+, \qquad \omega = \sqrt{\frac{C}{B}}, \tag{19}$$

† This is discussed from a somewhat different viewpoint in ref. [2]), App. III.

which satisfy the usual boson commutation rules

$$[b_\mu, b_\nu^+] = \delta_{\mu,\nu}, \tag{20}$$

and in terms of which the surface hamiltonian (2) can be written

$$H_s = \hbar\omega \sum_\mu (b_\mu^+ b_\mu + \tfrac{1}{2}). \tag{2'}$$

The eigenvalues equal $\hbar\omega(N+\frac{5}{2})$, where $N = 0, 1, 2, \ldots$

According to (19), the b_μ^+ transform under S_{p_4} in the same manner as the α_μ^+ and π_μ^+ (14),

$$b_\mu^+ \to \sum U^{(1,1)}_{\mu',\mu}(S_{p_4}) b_{\mu'}^+. \tag{21}$$

The five states of one phonon thus spread out the representation (1,1). The fifteen states of two phonons spread out the symmetrized Kronecker product $(1,1)\times(1,1)$. From (16) we see that this decomposes into $(0, 0)$, $I = 0$ and $(2,2)$, $I = 2,4$. Proceeding in a similar manner, we can convince ourselves that the states of N phonons carry the representation

$$(N, N) \dot{+} (N-2, N-2) \dot{+} \ldots \dot{+} \begin{cases} (1,1) \\ (0,0) \end{cases} \tag{22}$$

of S_{p_4}. If we would use the conventional notation [7]) for the labelling of irreducible representations of R_5, this sum would be

$$(N, 0) \dot{+} (N-2, 0) \dot{+} \ldots \dot{+} \begin{cases} (1, 0) \\ (0, 0) \end{cases}. \tag{22'}$$

The 4×4 matrices S_{p_4} are of course a representation of themselves. This representation is designated (1,0) and is evidently the one that the four single-particle states $\psi_m^{\frac{3}{2}}$ carry. The particle-phonon states thus carry the representation given by the product of (1,0) and the sum (22). From the rule (see footnote, p. 628)

$$(N, N) \times (1, 0) = (N+1, N) \dot{+} (N, N-1) \tag{23}$$

we calculate that the states of N phonons and one particle carry the representation

$$(N+1, N) \dot{+} (N, N-1) \dot{+} (N-1, N-2) \dot{+} \ldots \dot{+} (2, 1) \dot{+} (1, 0). \tag{24}$$

By means of a chain calculation such as that described by Flowers [6]) we infer the following rule for the angular momenta contained in $(\sigma+1, \sigma)$:

$$I = \sigma+S+\tfrac{3}{2},\ \ \sigma+S-\tfrac{3}{2},\ \ \sigma+S-\tfrac{9}{2}, \ldots \sigma-S+ \begin{cases} \frac{1}{2} \\ \frac{3}{2}, \\ \frac{5}{2} \end{cases} \tag{24'}$$

where $S = 0, 1, 2, \ldots, \sigma$. This rule is consistent with the dimension formula [6])

$$N_{\sigma+1,\sigma} = \tfrac{2}{3}(\sigma+1)(\sigma+2)(\sigma+3),$$

and we have verified it up to $\sigma = 5$, but have not succeeded in proving it generally.

4. Construction of the Matrices

Since H commutes with S_{p_4}, it has no matrix elements between states with inequivalent irreducible transformation properties. Moreover, it will not lift the degeneracy of states spreading out a given irreducible representation of S_{p_4}. Therefore, for each representation it is sufficient to calculate and diagonalize the matrix referring to a single angular momentum. This is conveniently chosen to be the largest angular momentum possible.

Consider the representation $(\sigma+1, \sigma)$. Reference to (23) and (24) shows that it occurs once and only once for every phonon number greater than or equal to σ. Moreover it arises in the phonon-particle products

$$\begin{aligned}(\sigma,\sigma)\times(1,0) &= (\sigma+1,\sigma)\dot{+}(\sigma,\sigma-1) \quad \text{for} \quad \sigma, \sigma+2, \sigma+4 \ldots \text{ phonons} \\ (\sigma+1,\sigma+1)\times(1,0) &= (\sigma+2,\sigma+1)\dot{+}(\sigma+1,\sigma) \qquad (25) \\ &\qquad\qquad \text{for} \quad \sigma+1, \sigma+3, \sigma+5 \ldots \text{ phonons.}\end{aligned}$$

There is one σ-phonon state with $R_z = 2\sigma$, viz. $(b_2^+)^\sigma|0\rangle$, and this is clearly the highest R_z obtainable with σ phonons. There is also one state with $R_z = 2\sigma-1$, viz. $(b_2^+)^{\sigma-1}b_1^+|0\rangle$, but two states with $R_z = 2\sigma-2$, viz.

$$(b_2^+)^{\sigma-1}b_0^+|0\rangle \quad \text{and} \quad (b_2^+)^{\sigma-2}b_1{}^+b_1^+|0\rangle.$$

Thus the highest σ-phonon angular momentum is $R = 2\sigma$, and it occurs only once. Since $R = 2\sigma$ does not occur for $\sigma-2$ phonons, it must occur in the representation (σ, σ) (see (22)). Furthermore there exists no σ-phonon state with $R = 2\sigma-1$, since only one $R_z = 2\sigma-1$ is available and that one belongs to the $R = 2\sigma$ set. But there is one σ-phonon state with $R = 2\sigma-2$, and since it cannot occur for $\sigma-2$ phonons, it must also occur in (σ, σ). Hence the highest phonon angular momenta occurring in the representation (σ, σ) are $R = 2\sigma$ and $2\sigma-2$, each occurring once. Then (24) and (25) tell us that the highest particle-phonon angular momentum in $(\sigma+1, \sigma)$ is $I = 2\sigma+\frac{3}{2}$. For $N = \sigma+2\nu$, phonons it occurs only once: $|\frac{3}{2}; \sigma+2\nu, (\sigma, \sigma), 2\sigma; 2\sigma+\frac{3}{2}, M\rangle$. Since $I = 2\sigma+\frac{3}{2}$ does not occur in $(\sigma, \sigma-1)$, it follows that this state automatically has the symplectic transformation properties $(\sigma+1, \sigma)$. However, for $\sigma+2\nu+1$ phonons, $I = 2\sigma+\frac{3}{2}$ can be achieved in two ways:

$$|\tfrac{3}{2}; \sigma+2\nu+1, (\sigma+1, \sigma+1), 2\sigma+2; 2\sigma+\tfrac{3}{2}, M\rangle$$

$$\text{and} \quad |\tfrac{3}{2}; \sigma+2\nu+1, (\sigma+1, \sigma+1)2\sigma; 2\sigma+\tfrac{3}{2}, M\rangle.$$

One linear combination of these states belongs to the representation $(\sigma+1, \sigma)$,

and the orthogonal partner to $(\sigma+2, \sigma+1)$. This latter can be determined by the requirement that it be orthogonal to $H_{\text{int}}|\frac{3}{2}; \sigma+2\nu, (\sigma, \sigma), 2\sigma; 2\sigma+\frac{3}{2}, M\rangle$, which definitely belongs to $(\sigma+1, \sigma)$. Hence we need the four matrix elements

$$\langle\tfrac{3}{2}; \sigma+2\nu, (\sigma, \sigma), 2\sigma; 2\sigma+\tfrac{3}{2}, M|H_{\text{int}}|\tfrac{3}{2}; \sigma+2\nu+1, (\sigma+1, \sigma+1), \begin{matrix}2\sigma+2\\2\sigma\end{matrix}; 2\sigma+\tfrac{3}{2}, M\rangle,$$
$$\langle\tfrac{3}{2}; \sigma+2\nu+1, (\sigma+1, \sigma+1), \begin{matrix}2\sigma+2\\2\sigma\end{matrix}; 2\sigma+\tfrac{3}{2}, M|H_{\text{int}}|\tfrac{3}{2}; \sigma+2\nu+2, (\sigma, \sigma), 2\sigma; 2\sigma+\tfrac{3}{2}, M\rangle. \tag{26}$$

To calculate these one uses the formula [3])

$$\langle\tfrac{3}{2}; N(\alpha)R; IM|H_{\text{int}}|\tfrac{3}{2}; N'(\alpha')R'; IM\rangle$$
$$= (-1)^{R+I+\frac{1}{2}} 2y\hbar\omega \sqrt{5(2R'+1)}\, W(R'R\tfrac{3}{2}\tfrac{3}{2}; 2I)\langle N(\alpha)R||b||N'(\alpha')R'\rangle, \tag{27}$$

where y is a dimensionless coupling parameter †

$$y = \frac{k}{\sqrt{40\pi\hbar\omega C}} \tag{28}$$

and the reduced matrix element $\langle N(\alpha)R||b||N'(\alpha')R'\rangle$ is defined by

$$\langle N(\alpha)RR_s|b_\mu|N'(\alpha')R'R'_s\rangle = (R2R_s\mu|R'R'_s)\langle N(\alpha)R||b||N'(\alpha')R'\rangle. \tag{29}$$

To calculate it we must construct the states $|N(\alpha)RR_s\rangle$. This is easily done for the states we need. First of all, we can write immediately that

$$|\sigma(\sigma, \sigma), 2\sigma, 2\sigma\rangle \propto (b_2^+)^\sigma|0\rangle. \tag{30}$$

There are two $(\sigma+1)$-phonon states with $R_s = 2\sigma$. We can determine the linear combination of these two states which has $R = 2\sigma$ from the condition that it be annihilated by

$$R_+ = \sum_{\mu=-2}^{2} \sqrt{(2-\mu)(2+\mu+1)}\, b_{\mu+1}^+ b_\mu.$$

We find

$$|\sigma+1, (\sigma+1, \sigma+1), 2\sigma, 2\sigma\rangle \propto 2b_2^{+\sigma} b_0^+|0\rangle - \sqrt{\tfrac{3}{2}}\, b_2^{+\sigma-1} b_1^{+2}|0\rangle. \tag{31}$$

We can now construct the states of $\sigma+2\nu$ and $\sigma+2\nu+1$ phonons with the same symplectic transformation properties as (30) and (31) by multiplying by the ν-th power of the symplectic scalar

$$\{b^+b^+\} \equiv \sum_\mu (22\mu-\mu|00) b_\mu^+ b_{-\mu}^+. \tag{32}$$

Hence

$$|\sigma+2\nu, (\sigma, \sigma), 2\sigma, 2\sigma\rangle \propto \{b^+b^+\}^\nu b_2^{+\sigma}|0\rangle \tag{30'}$$

† The coupling parameter y is related to x of refs. [2]) and [3]) by

$$y = \tfrac{1}{5}\sqrt{3}\, x.$$

$$|\sigma+2\nu+1,\ (\sigma+1,\sigma+1)\ 2\sigma,\ 2\sigma\rangle \propto 2\{b^+b^+\}^\nu b_2^{+\sigma} b_0^+|0\rangle - \sqrt{\tfrac{3}{2}}\{b^+b^+\}^\nu b_2^{+\sigma-1} b_1^{+2}|0\rangle. \tag{31'}$$

To calculate the normalization factors we need the commutation relations

$$\{bb\}\{b^+b^+\} - \{b^+b^+\}\{bb\} = \tfrac{4}{5}N+2 \tag{33a}$$

$$\{bb\}b_\mu^+ - b_\mu^+\{bb\} = (-1)^\mu \frac{2}{\sqrt{5}}\, b_{-\mu}, \tag{33b}$$

from which we readily obtain

$$C_\sigma^{\ \nu} \equiv \langle b_2^\sigma \{bb\}^\nu \{b^+b^+\}^\nu b_2^{+\sigma}\rangle = \frac{\sigma!\,\nu!}{5^\nu}\prod_{\alpha=1}^{\nu}(4\alpha+4\sigma+6), \tag{34a}$$

$$\begin{aligned} D_\sigma^{\ \nu} = \langle b_2^\sigma b_0 \{bb\}^\nu \{b^+b^+\}^\nu b_0^+ b_2^{+\sigma}\rangle &= \tfrac{1}{2}\sigma\langle b_2^{\sigma-1} b_1^{\,2}\{bb\}^\nu\{b^+b^+\}^\nu b_1^{+2} b_2^{+\sigma-1}\rangle \\ &= \frac{\sigma!\,\nu!}{5^\nu}\prod_{\alpha=1}^{\nu}(4\alpha+4\sigma+10). \end{aligned} \tag{34b}$$

The normalized states are thus

$$|\sigma+2\nu,\ (\sigma,\sigma),\ 2\sigma,\ 2\sigma\rangle = \frac{1}{\sqrt{C_\sigma^{\ \nu}}}\{b^+b^+\}^\nu b_2^{+\sigma}|0\rangle, \tag{30''}$$

$$\begin{aligned} &|\sigma+2\nu+1,\ (\sigma+1,\sigma+1),\ 2\sigma,\ 2\sigma\rangle \\ &\quad = \sqrt{\frac{\sigma}{(4\sigma+3)D_\sigma^{\ \nu}}}\,[2\{b^+b^+\}^\nu b_2^+ b_0^{+\sigma}|0\rangle - \sqrt{\tfrac{3}{2}}\{b^+b^+\}^\nu b_1^{+\sigma-1} b_2^{+2}|0\rangle]. \end{aligned} \tag{31''}$$

We are now able to calculate all the reduced phonon matrix elements we need. For example, according to (29),

$$\begin{aligned} &\langle \sigma+2\nu,\ (\sigma,\sigma),\ 2\sigma,\ 2\sigma|b_2|\sigma+2\nu+1,\ (\sigma+1,\sigma+1),\ 2\sigma+2,\ 2\sigma+2\rangle \\ &\quad = (2\sigma\ 2\ 2\sigma\ 2|2\sigma+2\ 2\sigma+2)\langle \sigma+2\nu,\ (\sigma,\sigma),\ 2\sigma||b||\sigma+2\nu+1,\ (\sigma+1,\sigma+1),\ 2\sigma+2\rangle \\ &= \frac{1}{\sqrt{C_\sigma^{\ \nu} C_{\sigma+1}^{\ \nu}}}\langle \{bb\}^\nu b_2^\sigma b_2 b_2^{+\sigma+1}\{b^+b^+\}^\nu\rangle = \sqrt{\frac{C_{\sigma+1}^{\ \nu}}{C_\sigma^{\ \nu}}} = \sqrt{(\sigma+1)\,\frac{2\sigma+2\nu+5}{2\sigma+5}}. \end{aligned}$$

Hence

$$\langle \sigma+2\nu,\ (\sigma,\sigma),\ 2\sigma||b||\sigma+2\nu+1,\ (\sigma+1,\sigma+1),\ 2\sigma+2\rangle = \sqrt{(\sigma+1)\,\frac{2\sigma+2\nu+5}{2\sigma+5}}. \tag{35a}$$

In the same way we calculate

$$\langle \sigma+2\nu,\ (\sigma,\sigma),\ 2\sigma||b||\sigma+2\nu+1,\ (\sigma+1,\sigma+1),\ 2\sigma\rangle = \sqrt{\frac{2(2\sigma+1)(2\sigma+2\nu+5)}{(4\sigma-1)(2\sigma+5)}}, \tag{35b}$$

$$\langle \sigma+2\nu+1,\ (\sigma+1,\sigma+1),\ 2\sigma+2||b||\sigma+2\nu+2,\ (\sigma,\sigma),\ 2\sigma\rangle = \sqrt{\frac{(2\sigma+2)(4\sigma+5)}{(4\sigma+1)(2\sigma+5)}}\,(\nu+1), \tag{35c}$$

$$\langle \sigma+2\nu+1,\ (\sigma+1,\sigma+1),\ 2\sigma||b||\sigma+2\nu+2,\ (\sigma,\sigma),\ 2\sigma\rangle = \sqrt{\frac{4(2\sigma+1)}{(4\sigma-1)(2\sigma+5)}}\,(\nu+1), \tag{35d}$$

$$\langle \sigma+2\nu+1,\ (\sigma+1,\sigma+1),\ 2\sigma||b||\sigma+2\nu+2,\ (\sigma+2,\sigma+2),\ 2\sigma+2\rangle = \sqrt{\frac{\sigma(4\sigma+7)(2\nu+2\sigma+7)}{(4\sigma+3)(2\sigma+7)}}, \tag{35e}$$

$$\langle \sigma+2\nu+1,\ (\sigma+1,\sigma+1),\ 2\sigma||b||\sigma+2\nu+2,\ (\sigma,\sigma),\ 2\sigma-2\rangle = \sqrt{\frac{(2\sigma-2)(4\sigma+1)(4\sigma+3)}{(2\sigma+5)(4\sigma-3)(4\sigma-1)}}, \tag{35f}$$

of which (35 e and f) will be needed in section 6.

Substituting (35a) and (35b) in (27) together with the algebraic expression for the Racah coefficient occurring there, we get

$$\begin{aligned}\langle \tfrac{3}{2};\ \sigma+2\nu,\ (\sigma,\sigma),\ 2\sigma;\ 2\sigma+\tfrac{3}{2},\ M|H_{\text{int}}|\tfrac{3}{2};\ \sigma+2\nu+1,\ (\sigma+1,\sigma+1),\ 2\sigma+2;\ 2\sigma+\tfrac{3}{2},\ M\rangle \\ = y\sqrt{\frac{(4\sigma+5)(4\sigma+6)}{2(4\sigma+3)(2\sigma+5)}}\,(2\sigma+2\nu+5), \\ \langle \tfrac{3}{2};\ \sigma+2\nu,\ (\sigma,\sigma),\ 2\sigma;\ 2\sigma+\tfrac{3}{2},\ M|H_{\text{int}}|\tfrac{3}{2};\ \sigma+2\nu+1,\ (\sigma+1,\sigma+1),\ 2\sigma;\ 2\sigma+\tfrac{3}{2},\ M\rangle \\ = y\sqrt{\frac{4\sigma(2\sigma+2\nu+5)}{(4\sigma+3)(2\sigma+5)}}.\end{aligned} \tag{36}$$

Then the linear combination of the $\sigma+2\nu+1$-phonon states receiving the full strength of H_{int}, and therefore transforming according to $(\sigma+1,\sigma)$, is

$$\begin{aligned}&|\sigma+2\nu+1;\ (\sigma+1,\sigma);\ I=2\sigma+\tfrac{3}{2},\ M\rangle \\ &\quad=\sqrt{\frac{8\sigma}{(4\sigma+3)(4\sigma+10)}}\,|\tfrac{3}{2};\ \sigma+2\nu+1,\ (\sigma+1,\sigma+1),\ 2\sigma;\ 2\sigma+\tfrac{3}{2},\ M\rangle \\ &\quad+\sqrt{\frac{(4\sigma+5)(4\sigma+6)}{(4\sigma+3)(4\sigma+10)}}\,|\tfrac{3}{2};\ \sigma+2\nu+1,\ (\sigma+1,\sigma+1),\ 2\sigma+2;\ 2\sigma+\tfrac{3}{2},\ M\rangle,\end{aligned} \tag{37}$$

and the matrix element is

$$\langle \sigma+2\nu;\ (\sigma+1,\sigma);\ I=2\sigma+\tfrac{3}{2}|H_{\text{int}}|\sigma+2\nu+1;\ (\sigma+1,\sigma);\ I=2\sigma+\tfrac{3}{2}\rangle = y\sqrt{2\sigma+2\nu+5}. \tag{38}$$

Furthermore (35c), (35d) and (27) imply that

$$\begin{aligned}\langle\sigma+2\nu+1,\,(\sigma+1,\sigma+1),\,2\sigma+2;\,2\sigma+\tfrac{3}{2},\,M|H_{\text{int}}|\sigma+2\nu+2,\,(\sigma,\sigma),\,2\sigma;\,2\sigma+\tfrac{3}{2},\,M\rangle \\ = y\sqrt{\frac{(4\sigma+6)(4\sigma+5)}{(4\sigma+3)(2\sigma+5)}}\,(\nu+1), \\ \langle\sigma+2\nu+1,\,(\sigma+1,\sigma+1),\,2\sigma;\,2\sigma+\tfrac{3}{2},\,M|H_{\text{int}}|\sigma+2\nu+2,\,(\sigma,\sigma),\,2\sigma;\,2\sigma+\tfrac{3}{2},\,M\rangle \\ = y\sqrt{\frac{8\sigma}{(4\sigma+3)(2\sigma+5)}}\,(\nu+1),\end{aligned} \tag{39}$$

from which we can calculate

$$\begin{aligned}\langle\sigma+2\nu+1;\,(\sigma+1,\sigma);I=2\sigma+\tfrac{3}{2}|H_{\text{int}}|\sigma+2\nu+2;\,(\sigma+1,\sigma);I=2\sigma+\tfrac{3}{2}\rangle \\ = y\sqrt{2\nu+2}.\end{aligned} \tag{40}$$

Eqs. (2′), (38) and (40) now enable us to construct the entire matrix of H for the representation $(\sigma+1,\sigma)$. In units of $\hbar\omega$ it is

$$\begin{bmatrix}
\sigma+\frac{1}{2} & y\sqrt{2\sigma+5} & & & & & & & & \\
y\sqrt{2\sigma+5} & \sigma+\frac{7}{2} & y\sqrt{2} & & & & & & & \\
 & y\sqrt{2} & \sigma+\frac{9}{2} & y\sqrt{2\sigma+7} & & & & & & \\
 & & y\sqrt{2\sigma+7} & \sigma+\frac{11}{2} & y\sqrt{4} & & & & & \\
 & & & y\sqrt{4} & \sigma+\frac{13}{2} & \cdot & & & & \\
 & & & & \cdot & & y\sqrt{2\nu} & & & \\
 & & & & & y\sqrt{2\nu} & \sigma+2\nu+\frac{1}{2} & y\sqrt{2\sigma+2\nu+5} & & \\
 & & & & & & y\sqrt{2\sigma+2\nu+5} & \sigma+2\nu+\frac{7}{2} & y\sqrt{2\nu+2} & \\
 & & & & & & & y\sqrt{2\nu+2} & \sigma+2\nu+\frac{9}{2}\cdots
\end{bmatrix} \tag{41}$$

Such a matrix occurs for $\sigma = 0, 1, 2, \ldots$ All other matrix elements vanish. This matrix has been calculated for $I = 2\sigma+\frac{3}{2}$. However, the fact that H is a symplectic scalar guarantees that the level positions will be the same for all the angular momenta contained in $(\sigma+1,\sigma)$ (see (24′)).

5. Eigenvalues and Eigenvectors

The eigenvectors of the coupled hamiltonian (4) can be labelled $|r;\,(\sigma+1,\sigma)\beta IM\rangle$. This state transforms under S_{p_4} as the β, I, M row of the irreducible representation $(\sigma+1,\sigma)$. The label β is required if I occurs more than once in $(\sigma+1,\sigma)$, and $r = 0, 1, 2, \ldots$ is a 'principal' quantum number indicating that this is the $(r+1)^{\text{st}}$-lowest state with these symplectic transformation properties. We seek an expansion of this state in terms of eigenvectors of the uncoupled motion

$$|r;\,(\sigma+1,\sigma)\beta IM\rangle = \sum_n a^{\sigma}_{rn}(y)|N=n;\,(\sigma+1,\sigma)\beta IM\rangle. \tag{42}$$

According to (41), the $a^{\sigma}_{rn}(y)$ are to be determined from the eigenvalue condition

$$y\sqrt{n+2-(-1)^{n-\sigma}(\sigma+2)}\,a^{\sigma}_{r,n-1}(y)+(n+\tfrac{5}{2}-E_r{}^{\sigma}(y))a^{\sigma}_{rn}(y)$$
$$+y\sqrt{n+3+(-1)^{n-\sigma}(\sigma+2)}\,a^{\sigma}_{r,n+1}(y)=0 \qquad n=\sigma,\sigma+1,\sigma+2\ldots \tag{43}$$

For small values of the coupling parameter, y, we can approximate $E_r{}^{\sigma}(y)$ and $a^{\sigma}_{rn}(y)$ by means of the first few terms in a perturbation expansion based on the uncoupled motion, $E_r{}^{\sigma}(0)=\sigma+r+\frac{5}{2}$, $a^{\sigma}_{nr}(0)=\delta_{n,r+\sigma}$. We find

$$E_r{}^{\sigma}(y)=\sigma+r+\tfrac{5}{2}-y^2[1+(-)^r\,2(\sigma+2)]$$
$$+y^4[(-)^r\,2(\sigma+2)(2r+2\sigma+5)]\ldots \tag{44a}$$

$$a^{\sigma}_{rn}(y)=\delta_{n,r+\sigma}+y[\delta_{n,r+\sigma-1}f_{r-1}-\delta_{n,r+\sigma+1}f_r]+\tfrac{1}{2}y^2[\delta_{n,r+\sigma-2}f_{r-2}f_{r-1}-\delta_{n,r+\sigma}(f_r{}^2+f^2_{r-1})$$
$$+\delta_{n,r+\sigma+2}f_rf_{r+1}]+\tfrac{1}{6}y^3\{\delta_{n,r+\sigma-3}f_{r-3}f_{r-2}f_{r-1}+3\delta_{n,r+\sigma-1}f_{r-1}[f^2_{r-2}-3f^2_{r-1}+f_r{}^2]$$
$$-3\delta_{n,r+\sigma+1}f_r[f^2_{r-1}-3f_r{}^2+f^2_{r+1}]-\delta_{n,r+\sigma+3}[f_rf_{r+1}f_{r+2}]\}, \tag{44b}$$

where we have used the abbreviation

$$f_r=\sqrt{r+\sigma+3+(-)^r(\sigma+2)}.$$

As y increases from 0, $E_r{}^{\sigma}(y)$ thus starts out horizontally, but $E_{\sigma}{}^{0}(y)\ldots$ curve downwards whereas $E_{\sigma}{}^{1}(y)$, $E_{\sigma}{}^{3}(y),\ldots$ curve upwards. This behaviour is illustrated in fig. 1.

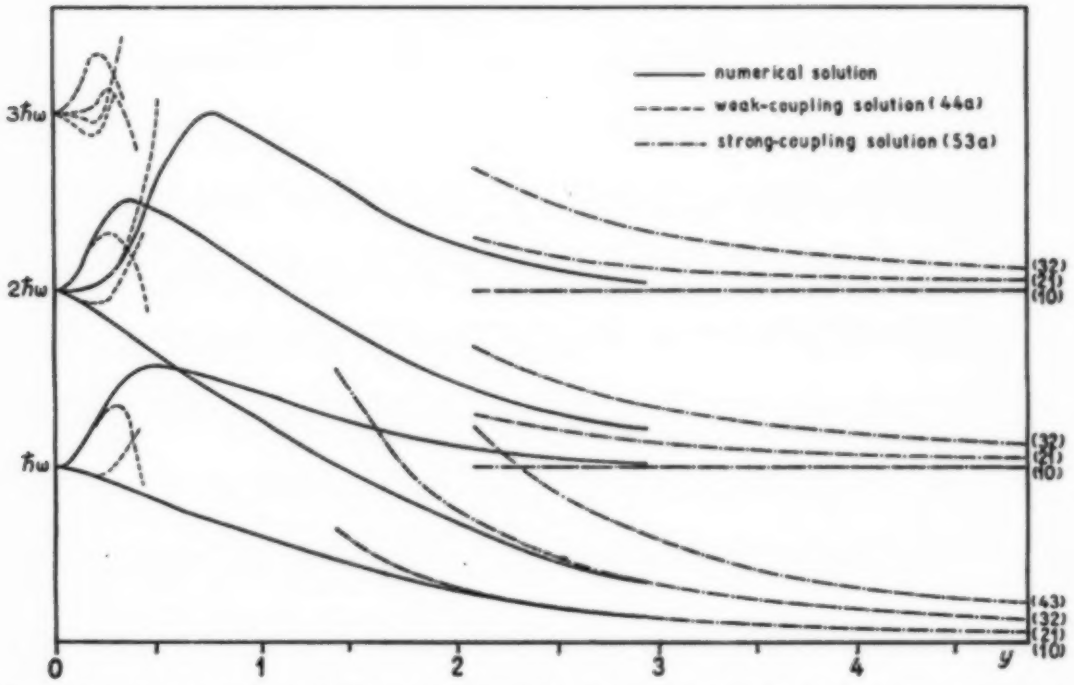

Fig. 1. Low-lying levels as a function of the coupling strength y. The angular momenta associated with each representation $(\sigma+1,\sigma)$ are given in fig. 2.

For very large y, we expect the high phonon states to make the greatest contribution to the low levels. For the corresponding rows of the matrix, the

alternating terms in (43) become of negligible importance. If we further modify (43) by extending it upwards so that its first diagonal element is $\frac{1}{2}$ rather than $\sigma+\frac{5}{2}$, we arrive at the equation

$$y\sqrt{n+2}\,\alpha_{r,n+1}+(n+\tfrac{5}{2}-\varepsilon^{(r)})\alpha_{r,n+2}+y\sqrt{n+3}\,\alpha_{r,n+3}=0 \qquad (45)$$
$$(n=-2,-1,0,1,2,\ldots).$$

But this is just the eigenvalue problem for the matrix of a displaced harmonic oscillator hamiltonian

$$H_0=-\tfrac{1}{2}\frac{\mathrm{d}^2}{\mathrm{d}q^2}+\tfrac{1}{2}q^2+\sqrt{2}\,yq=-\tfrac{1}{2}\frac{\mathrm{d}^2}{\mathrm{d}q^2}+\tfrac{1}{2}(q+\sqrt{2}\,y)^2-y^2 \qquad (46)$$

constructed with respect to the states $\psi_n(q)$ of the undisplaced oscillator. From (46) we see that the eigenvalues of this matrix are

$$\varepsilon^r=r+\tfrac{1}{2}-y^2 \qquad (47a)$$

and that the corresponding eigenvector can be obtained from an expansion of the displaced eigenstates in terms of the undisplaced ones:

$$\psi_r(q+\sqrt{2}\,y)=\sum_n \alpha_{rn}(y)\psi_n(q),$$

from which we calculate

$$\alpha_{rn}(y)=(-)^n\mathrm{e}^{-\frac{1}{2}y^2}\sqrt{n!r!}\,y^{n+r}\sum_m\frac{(-)^m y^{-2m}}{m!(n-m)!(r-m)!}. \qquad (47b)$$

Eq. (47b) indicates that for large y and small r and σ, the function $\psi_r(q+\sqrt{2}y)$ contains only small contributions from $\psi_0(q),\ldots,\psi_{\sigma+1}(q)$. Thus we might expect that the $\sigma+2$ 'spurious states' introduced in going from (43) to (45) will have little effect on the eigenvalues and eigenvectors of the low levels of (43). Hence

$$E_r^{\sigma}(y)\to\varepsilon^r=r+\tfrac{1}{2}-y^2 \qquad (r=0\,1\,2\ldots,\sigma=0\,1\,2\ldots), \qquad (48a)$$

$$a^{\sigma}_{rn}(y)\to\alpha_{r,n-2}(y)=(-)^n\mathrm{e}^{-\frac{1}{2}y^2}\sqrt{(n+2)!r!}\,y^{n+r}\sum_m\frac{(-)^m y^{-2m}}{m!(n+2-m)!(r-m)!} \qquad (48b)$$
$$(n=\sigma,\sigma+1\ldots).$$

Notice that the energies in (48a) depend only on the principal quantum number r. Thus, as $y\to\infty$, we see the appearance of equidistant groups (labelled by $r=0,1,2,\ldots$) of many close-lying levels (labelled by $\sigma=0,1,2$). These groups will be interpreted below as superpositions (due to the γ-instability of the problem) of rotational bands built upon equidistant vibrational excitations.

In order to investigate the approach to the strong-coupling limit (48), we

might perform on (43) the similarity transformation (defined by the $\alpha_{rn}(y)$ of (47b)) which exactly diagonalizes (45). For large y, the result would be an almost diagonal matrix, which could then be treated by perturbation theory. However, this similarity transformation is much easier to perform if we modify (43) by the addition of the $\sigma+2$ 'spurious' rows. We designate this modified matrix by H'; it has the element

$$H'_{nn} = n+\tfrac{1}{2}, \tag{49a}$$

$$H'_{n,n+1} = H'_{n+1,n} = y\sqrt{n+1+(-)^{n-\sigma}(\sigma+2)}, \quad (n = 0, 1, 2 \ldots). \tag{49b}$$

Our perturbation theory then exhibits only the effect of dropping the alternating terms in going from (43) to (45).

The first-order correction to the energy (48a) is given by the diagonal element of the transformed matrix:

$$\begin{aligned} \tilde{H}'_{rr} = \sum_{i,j=0}^{\infty} \alpha_{ri}\alpha_{rj}H'_{ij} &= \sum_{n=0}^{\infty} (\alpha_{rn}\alpha_{r,n+1}H'_{n,n+1}+\alpha_{rn}^2 H'_{nn}+\alpha_{r,n+1}\alpha_{rn}H'_{n+1,n}) \\ &= \sum_{n=0}^{\infty} (\alpha_{rn}^2 H'_{nn}+2\alpha_{rn}\alpha_{r,n+1}H'_{n,n+1}). \end{aligned} \tag{50}$$

For large y and small σ and r, the principal contribution to the n-sums of (50) will be from terms with $n \gg \sigma$, so that we can use a binomial expansion on (49b):

$$H'_{n,n+1} = y\left[\sqrt{n+1}+(-)^{n-\sigma}\frac{\sigma+2}{2\sqrt{n+1}} - \frac{(\sigma+2)^2}{8(n+1)^{\frac{3}{2}}}+\ldots\right]. \tag{51}$$

The leading term in (51) is the off-diagonal element of the matrix of the displaced harmonic oscillator. Hence the corresponding n-sum, together with the contribution from the diagonal element H'_{nn}, equals the oscillator eigenvalue (48a). The alternating factor in the second term of (50) gives rise to a term proportional to e^{-y^2}. For large y this factor is negligible compared with the contribution from the third term of (51), which gives the principal deviation of (50) from (48a). We must therefore calculate

$$\begin{aligned} &\sum_{n=0}^{\infty} \frac{\alpha_{rn}\alpha_{r,n+1}}{(n+1)^{\frac{3}{2}}} \\ &= \frac{e^{-y^2}y^{2r}}{r!}\sum_{mm'}(-)^{m+m'}\binom{r}{m}\binom{r}{m'}(y^2)^{-m-m'}\sum_{n}\frac{(y^2)^{n+1}(n+1)!}{(n+1-m)!(n-m')!(n+1)^2}. \end{aligned} \tag{52}$$

Since the n-sum in (52) is also dominated by the large n-terms, we can replace $(n+1)^2$ by $n(n+1)$ with little error. This sum is thus approximately equal to

$$\sum_{n}(y^2)^{n+1}\frac{(n-1)(n-2)\ldots(n-1-m')}{(n+1-m)!},$$

which, for $m' > 0$, is equal to

$$\frac{\partial^{m'-1}}{\partial z^{m'-1}} (y^2)^m z^{m-2} e^{y^2 z}|_{z=1}.$$

Differentiating by means of the Leibnitz formula, we obtain a sum of terms whose m-dependence is of the form $(y^2)^m m^t$ with $t \leqq m-1$. The m-sum in (52) thus becomes $\sum_m (-)^m \binom{r}{m} m^t$, which vanishes for $t < m$. Thus we only get a contribution to (52) if $m' = 0$. The n-sum is then approximately

$$\sum_n \frac{(y^2)^{n+1}}{(n+1-m)!(n+1)} = (y^2)^m \int_0^1 z^m e^{z y^2} dz,$$

and the entire expression (52) is

$$\frac{(y^2)^r}{r!} e^{-y^2} \int_0^1 \sum_m (-)^m \binom{r}{m} z^m e^{z y^2} dz = \frac{1}{r!} \int_0^1 [y^2(1-z)]^r e^{-y^2(1-z)} dz$$

$$= \frac{1}{y^2 r!} \int_0^{y^2} u^r e^{-u} du \to \frac{1}{y^2} \qquad \text{for large } y.$$

Substituting this result in (51) and (50), we find

$$E_r(y) = r + \tfrac{1}{2} - y^2 + \frac{(\sigma+2)^2}{4y^2} + \ldots \qquad (r = 0, 1, 2 \ldots;\ \sigma = 0, 1, 2 \ldots). \quad (53a)$$

The last term gives the rotational splitting between the levels of each band. Fig. 2 illustrates the structure of the spectra implied by (53a) (for a particular r). It may be noted that for the (S, K) band we have $I = K + \sigma - S$ and thus $(\sigma+2)^2 = I(I+2[2-K+S]) + (2-K+S)^2$. For the band built upon the ground state $(S = 0,\ K = \frac{3}{2})$ we thus find the familiar $I(I+1)$ rotational-energy splittings. The other bands are somewhat distorted, and as we shall see in the next section, all the bands are considerably mixed.

A similar, but lengthier, calculation shows that for small n

$$a_n{}^r(y) = \alpha_{n+2}^r(y) \left[1 - \frac{(\sigma+2)^2}{8y^2} \log \frac{y^2}{e} + \ldots \right]. \quad (53b)$$

Eqs. (44) and (53) give the solution to our problem in the limits of weak and strong coupling. Between these limits we must use numerical methods. One considers the submatrix of (41) consisting of its first N rows and columns. A trial eigenvalue E_1 is substituted in the first $N-1$ equations (43), and the N^{th} equation then determines an eigenvalue E_2. The true eigenvalue of the $N \times N$ submatrix lies between E_1 and E_2, so a new trial value of $E_3 = \frac{1}{2}(E_1 + E_2)$ is used and the procedure is iterated until the desired accuracy is attained. This can be rapidly done on a digital computer †, and the simple form of (41)

† Smil, the electronic digital computer in Lund, was used.

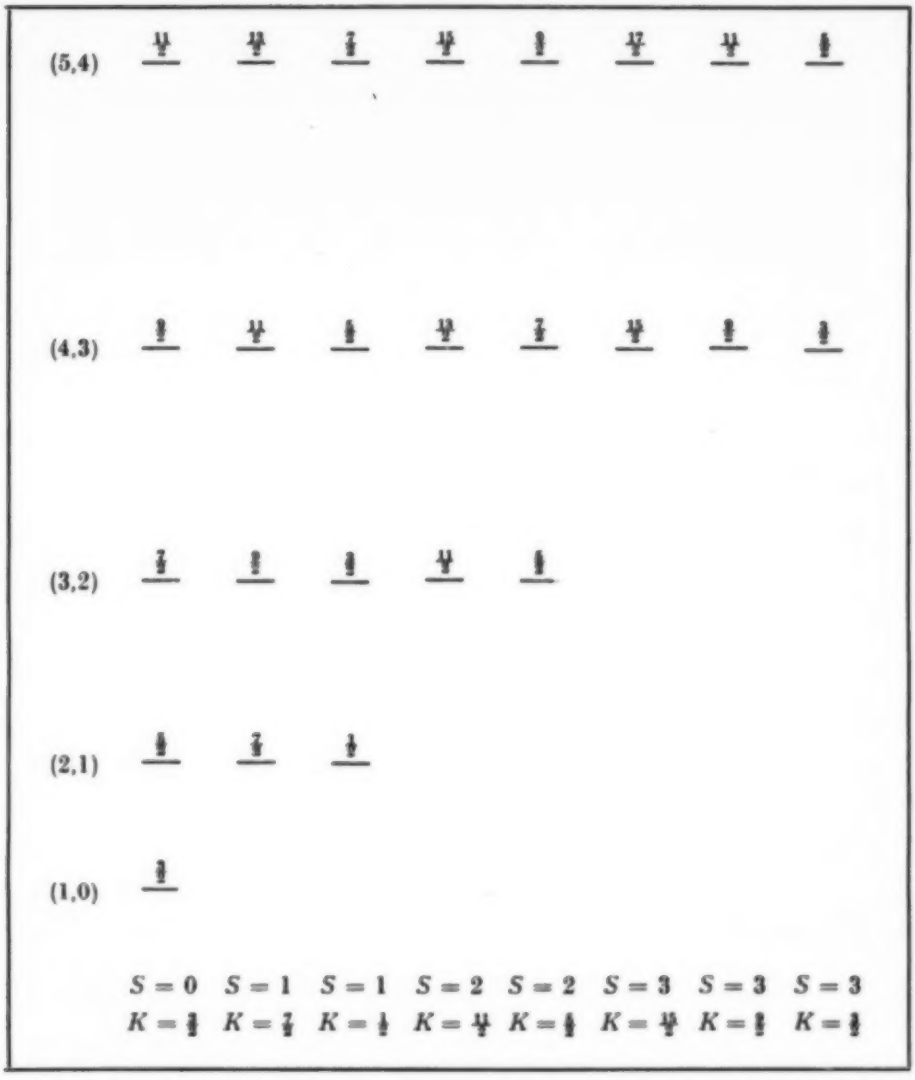

Fig. 2. Structure of rotational bands in the strong-coupling limit. The band labelled by K, S has its lowest level ($I = K$) for $\sigma = S$. The quantum numbers K and S are related by

$$K = 2S+\tfrac{1}{2},\ 2S-\tfrac{1}{2},\ \ldots\ \begin{matrix}\tfrac{1}{2}\\ \tfrac{3}{2}\end{matrix}\ \text{(cf. (24'))}.$$

makes it possible to handle matrices whose size is independent of the size of the computer store. To calculate the curves shown in fig. 1, N was chosen sufficiently great to ensure the accuracy of the 4^{th} decimal place of $E^{(\tau)}$. For $y = 3$ this required $N = 30$.

6. E2 Transition Probabilities and Multipole Moments

We shall now determine the extent to which the E2 transition probabilities and quadrupole moments support our rotational interpretation of the spectrum derived in the last section.

The B-value for an E2 transition between eigenstates of the coupled system can be written [2])

$$B(\mathrm{E2})_{\tau,\sigma,\beta,I\to s,\sigma',\beta',I'} = \left(\frac{3ZeR_0^2}{4\pi}\right)^2 \sum_{\mu,M'} |\langle \tau;\ (\sigma+1,\sigma)\beta I M|\alpha_\mu^+|s;\ (\sigma'+1,\sigma')\beta' I' M'\rangle|^2. \tag{54}$$

According to (14), α_μ^+ transforms under S_{p_4} as the 2, μ component of the representation (1,1). Thus the branching law †

$$(11)\times(\sigma'+1,\sigma') = (\sigma'+2,\sigma'+1)+(\sigma'+1,\sigma')+(\sigma',\sigma'-1)+(\sigma'+2,\sigma'-1) \tag{55}$$

implies the E2 selection rule

$$\Delta\sigma = 0.\quad \pm 1. \tag{55'}$$

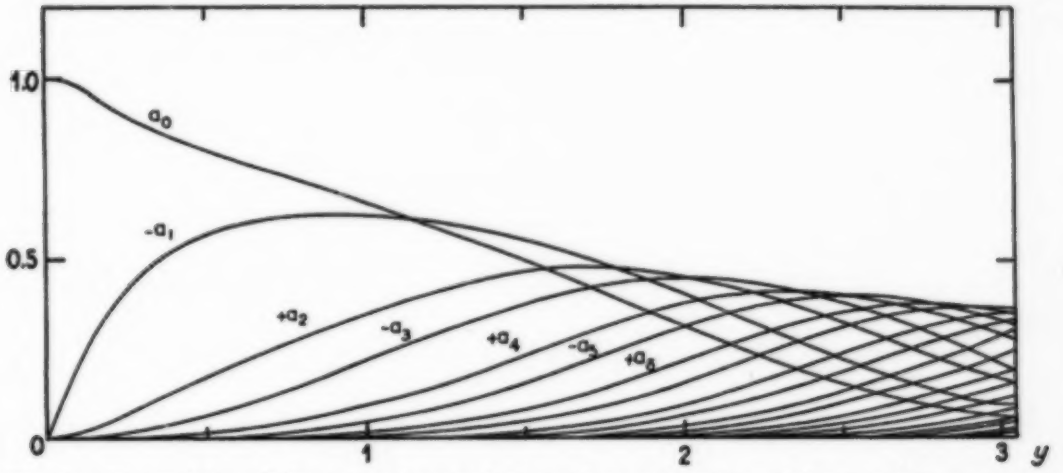

Fig. 3a. Composition of the ground state ($a_{0n}^2 = a_n$) as a function of the coupling strength y (cf. fig. 4, ref. [2])).

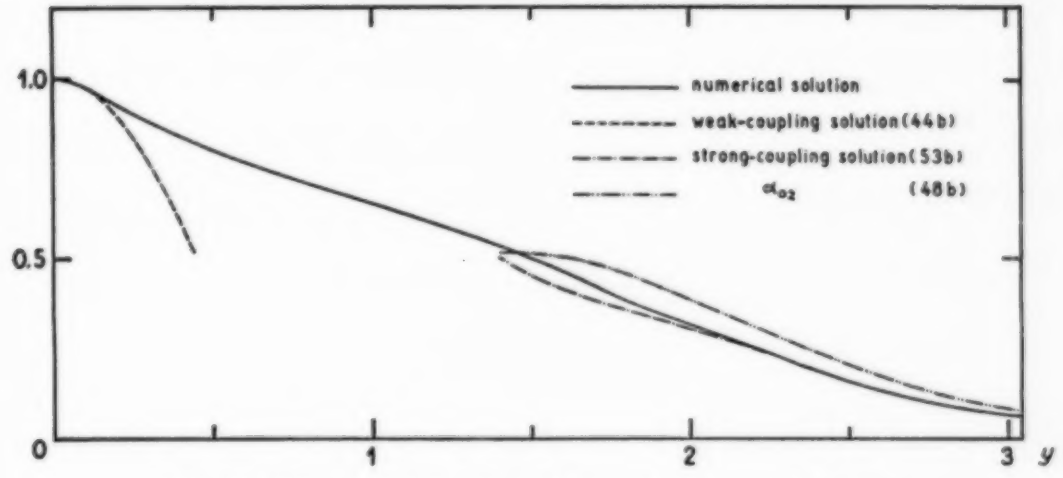

Fig. 3b. Comparison of exact and approximate wave functions.

† See footnote, page 628. The index β can now be interpreted as the labels (K, S) of fig. 2.

Furthermore, a two-fold application of the Wigner-Eckart theorem enables us to factorize the matrix element in (54) as follows:

$$\langle r;\,(\sigma+1,\,\sigma)\beta I M|\alpha_\mu{}^+|s;\,(\sigma'+1,\,\sigma')\beta' I' M'\rangle$$
$$= (2I'\mu M'|IM)\big((1,1)(\sigma'+1,\,\sigma')2\beta' I'|(\sigma+1,\,\sigma)\beta I\big)\big(r;\,(\sigma+1,\,\sigma)||\alpha^+||s;\,(\sigma'+1,\,\sigma')\big). \tag{56}$$

The second factor is a Clebsch-Gordan coefficient for S_{p_4}. The first two factors are determined entirely by group theory and so are independent of the coupling strength y. The entire dependence of (56) on y is contained in the reduced matrix element. Since the latter is independent of β and I, we can determine it by calculating (56) in the relatively simple case in which I and I' assume their maximum values. Then, according to (54), we must calculate

$$\langle r;\,(\sigma+1,\,\sigma),\,2\sigma+\tfrac{3}{2},\,M|\alpha_\mu{}^+|s;\,(\sigma'+1,\,\sigma'),\,2\sigma'+\tfrac{3}{2},\,M\rangle$$
$$=\sum a^\sigma_{rn}(y)a^{\sigma'}_{rm}(y)\langle N=n;\,(\sigma+1,\,\sigma),\,2\sigma+\tfrac{3}{2},\,M|\alpha_\mu{}^+|N=m;\,(\sigma'+1,\,\sigma'),\,2\sigma'+\tfrac{3}{2},\,M'\rangle. \tag{57}$$

We use the relation

$$\alpha^+_\mu = \sqrt{\frac{\hbar}{2B\omega}}\,(b^+_\mu+(-1)^\mu b_{-\mu}) \tag{19'}$$

and the methods of section 4 to calculate the matrix elements of b^+_μ and $b_{-\mu}$. We find

$$\begin{aligned}
&\langle r,\,(\sigma+1,\,\sigma),\,2\sigma+\tfrac{3}{2},\,M|\alpha_\mu{}^+|s,\,(\sigma+1,\,\sigma),\,2\sigma+\tfrac{3}{2},\,M'\rangle\\
&\quad= \frac{(2\;2\sigma+\frac{3}{2}\;\mu M'|2\sigma+\frac{3}{2}\;M)}{2\sigma+5}\sqrt{\frac{(4\sigma+5)(4\sigma+6)}{(4\sigma+2)(4\sigma+3)}\,\frac{\hbar}{2B\omega}}\\
&\quad\times\sum_{\nu=0}^{\infty}[(a^\sigma_{r,\,\sigma+2\nu+1}\,a^\sigma_{s,\,\sigma+2\nu}+a^\sigma_{s,\,\sigma+2\nu+1}a^\sigma_{r,\,\sigma+2\nu})\sqrt{2\sigma+2\nu+5}\\
&\quad+(a^\sigma_{r,\sigma+2\nu+2}a^\sigma_{s,\,\sigma+2\nu+1}+a^\sigma_{s,\sigma+2\nu+2}\,a^\sigma_{r,\sigma+2\nu+1})\sqrt{2\nu+2}]\\
&\quad=(2\;2\sigma+\tfrac{3}{2}\,\mu M'|2\sigma+\tfrac{3}{2}\,M)\big((1,1)(\sigma+1,\,\sigma)2,\,2\sigma+\tfrac{3}{2}|(\sigma+1,\,\sigma),\,2\sigma+\tfrac{3}{2}\big)\\
&\quad\cdot\langle r;\,(\sigma+1,\,\sigma)||\alpha^+||s;\,(\sigma+1,\,\sigma)\rangle
\end{aligned} \tag{58a}$$

and similarly

$$\begin{aligned}
&\langle r,\,(\sigma+2,\,\sigma+1),\,2\sigma+\tfrac{7}{2},\,M|\alpha^+_\mu|s,\,(\sigma+1,\,\sigma)2\sigma+\tfrac{3}{2},\,M'\rangle\\
&\quad=(2\;2\sigma+\tfrac{3}{2}\;\mu M'|2\sigma+\tfrac{3}{2}\;M)\sqrt{\frac{\sigma+1}{2\sigma+5}\,\frac{\hbar}{2B\omega}}\\
&\quad\times\sum_{\nu=0}^{\infty}[a^{\sigma+1}_{r,\,\sigma+2\nu+1}\,a^\sigma_{s,\,\sigma+2\nu}\sqrt{2\sigma+2\nu+5}+a^{\sigma+1}_{r,\,\sigma+2\nu+2}a^\sigma_{s,\,\sigma+2\nu+1}\sqrt{2\sigma+2\nu+7}\\
&\quad+a^{\sigma+1}_{r,\,\sigma+2\nu+1}a^\sigma_{s,\,\sigma+2\nu+2}\sqrt{2\nu+2}+a^{\sigma+1}_{r,\,\sigma+2\nu+2}a^\sigma_{s,\,\sigma+2\nu+3}\sqrt{2\nu+2}]\\
&\quad=(2\;2\sigma+\tfrac{3}{2}\;\mu M'|2\sigma+\tfrac{7}{2}\;M)\big((11)(\sigma+1,\,\sigma)2,\,2\sigma+\tfrac{3}{2}|(\sigma+2,\,\sigma+1),\,2\sigma+\tfrac{7}{2}\big)\\
&\quad\cdot\langle r;\,(\sigma+2,\,\sigma+1)||\alpha^+||s;\,(\sigma+1,\,\sigma)\rangle.
\end{aligned} \tag{58b}$$

For large y, we can use the approximation (48b) and then the methods of section 5 to approximate the sums in (58a) and (58b). Using

$$\sum_r \alpha_{rn}\alpha_{s,n+1}\sqrt{n+1} = -y\delta_{rs}+\sqrt{r+1}\,\delta_{r,s+1}, \tag{59}$$

which follows from (47b), we finally get

$$B(\mathrm{E2})_{r\sigma\beta I\to s\sigma'\beta' I'} \overset{y\to\infty}{\to} \left(\frac{3ZeR_0^2}{4\pi}\right)^2 \frac{2I'+1}{2I+1}\,\frac{((1,1)(\sigma+1,\sigma)2\beta I|(\sigma+1,\sigma)\beta' I')^2}{((1,1)(\sigma+1,\sigma)2,\,2\sigma+\tfrac{3}{2}|(\sigma+1,\sigma),\,2\sigma+\tfrac{3}{2})^2}$$
$$\cdot\,\frac{(4\sigma+5)(4\sigma+6)}{(2\sigma+5)^2(4\sigma+2)(4\sigma+3)}\,\frac{\hbar}{2B\omega}\times[|2y\delta_{r,s}+\delta_{r+1,s}\sqrt{r+1}+\delta_{s+1,r}\sqrt{s+1}|^2], \tag{60a}$$

$$B(\mathrm{E2})_{r,\sigma+1,\beta I\to s\sigma'\beta' I'} \overset{y\to\infty}{\to} \left(\frac{3ZeR_0^2}{4\pi}\right)^2 \frac{2I'+1}{2I+1}\,\frac{((1,1)(\sigma+1,\sigma)2\beta' I'|(\sigma+2,\sigma+1)\beta I)^2}{((1,1)(\sigma+1,\sigma)2,\,2\sigma+\tfrac{3}{2}|(\sigma+2,\sigma+1),\,2\sigma+\tfrac{7}{2})^2}$$
$$\cdot\,\frac{\sigma+1}{2\sigma+5}\,\frac{\hbar}{2B\omega}\times|2y\delta_{r,s}+\delta_{r+1,s}\sqrt{r+1}+\delta_{s+1,r}\sqrt{s+1}|^2. \tag{60b}$$

Eqs. (60 a and b) show the dominance, in the strong-coupling limit, of E2 transitions within a single group of rotational bands ($r=s$) over those connecting different groups ($r\neq s$).

It is easy to spot certain S_{p_4} Clebsch-Gordan coefficients whose value is unity. For example, the fact that $I=2\sigma+\frac{3}{2}$ occurs only once in $(1,1)\times(\sigma+1,\sigma)$ implies that $((1,1)(\sigma+1,\sigma)2,\,2\sigma+\frac{3}{2}|(\sigma+2,\sigma+1),\,2\sigma+\frac{7}{2})=1$. Furthermore, if $\sigma=0$, (55) reduces to

$$\begin{array}{ccccccc} (1,1) & \times & (1,0) & = & (2,1) & + & (1,0) \\ 2 & & \frac{3}{2} & & \frac{1}{2} & & \frac{3}{2} \\ & & & & \frac{5}{2} & & \\ & & & & \frac{7}{2}. & & \end{array}$$

Again, since each I on the right-hand side occurs only once, we can be certain that

$$((1,1)(1,0)2\tfrac{3}{2}|(2,1)I) = ((1,1)(1,0)2\tfrac{3}{2}|(1,0)\tfrac{3}{2}) = 1.$$

According to (60b) this has the consequence that $B(\mathrm{E2})_{r(1,0)\frac{1}{2}\to s(2,1)I}$ is proportional to $2I+1$, independently of y.

If the columns in fig. 2 really described rotational bands, we should expect a much stronger transition to the $(2,1)$, $I=\frac{5}{2}$ level than to either $(2,1)$, $I=\frac{1}{2}$ or $\frac{7}{2}$. Hence, although we have found something like a rotational spectrum, the bands are extensively mixed.

The reduced matrix elements determined by (58a) enable us to calculate the static surface quadrupole moment [2]):

$$Q^{\sigma}_{r;\sigma\beta I} = \frac{3ZR_0^2}{\sqrt{5\pi}} \langle r;\,(\sigma+1,\,\sigma)\beta I I\,|\alpha_0|\,r;\,(\sigma+1,\,\sigma)\beta I I\rangle \to \frac{3ZR_0^2}{\sqrt{5\pi}}\,\frac{1}{2\sigma+5}$$

$$\cdot\, 2y \sqrt{\frac{(4\sigma+5)(4\sigma+6)I(2I-1)}{(4\sigma+2)(4\sigma+3)(I+1)(2I+3)}}\;\frac{((1,1)(\sigma+1,\sigma)2\beta I|(\sigma+1,\sigma)\beta I)}{((1,1)(\sigma+1,\sigma)2,\,2\sigma+\tfrac{3}{2}|(\sigma+1,\sigma),\,2\sigma+\tfrac{3}{2})}. \tag{61}$$

For the ground state, for which $\sigma = 0$ and $I = \frac{3}{2}$, this reduces to the "normal" strong-coupling limit given in ref. [2]). A similar calculation leads to the "normal" strong-coupling limit for the expectation value of† R_s of $I/(I+1) = \frac{3}{5}$. It has been conjectured [2]) that the special features associated with $j = \frac{3}{2}$ would lead to somewhat higher limits for these two quantities.

We see then that, although the γ-instability associated with a $j = \frac{3}{2}$ particle has a marked effect on the dynamical properties of the strong-coupling limit, the static properties are unaffected.

We are indebted to Professors T. Gustafson, A. Bohr and B. R. Mottelson for many valuable suggestions.

† R_s is an irreducible tensor with respect to S_{p_4}, transforming as the 1, 2 row of (20).

References

1) A. Bohr, Mat. Fys. Medd. Dan. Vid. Selsk. **26**, no. 14 (1952)
2) A. Bohr and B. R. Mottelson, Mat. Fys. Medd. Dan. Vid. Selsk. **27**, no. 16 (1953)
3) D. C. Choudhury, Mat. Fys. Medd. Dan. Vid. Selsk. **28**, no. 4 (1954)
4) K. W. Ford and C. Levinson, Phys. Rev. **100** (1955) 3
5) B. J. Raz, Preprint Argonne National Laboratory (1957)
6) B. H. Flowers, Proc. Roy. Soc. A **212** (1952) 248
7) H. A. Jahn, Proc. Roy. Soc. A **201** (1950) 516
8) G. Rakavy, Nuclear Physics **4** (1957) 289

2.D

Nuclear Physics **16** (1960) 645—656; © *North-Holland Publishing Co., Amsterdam*

Not to be reproduced by photoprint or microfilm without written permission from the publisher

SPECTRA OF γ-RAYS FROM NEUTRON CAPTURE BY HEAVY NUCLEI (I)

L. V. GROSHEV, A. M. DEMIDOV and V. I. PELEKHOV

Atomic Energy Institute of Academy of Sciences, Moscow, USSR

Received 23 October 1959

Abstract: Comparison is drawn between the experimentally measured and calculated γ-spectra from the thermal neutron reaction (n, γ) for the two forms of energy dependence of the level density $\rho(u) = \rho_0 e^{u/\tau}$ and $\rho(u) = \rho_0 e^{\sqrt{au}}$ where τ and a are constants. The effect of the energy gap in the level density of even † nuclei on the spectrum of γ-rays in the range 0.8 to 4 MeV is discussed. The energy gap results in an essential difference between the spectra of odd nuclei and those of even nuclei.

1. Introduction

For several years we have measured the spectra of the γ-rays from thermal neutron capture for a large number of elements. Measurements have been carried out with a magnetic Compton spectrometer having a resolution of 2 %. The results thus obtained were collected in an atlas [1]) published in 1958 as well as in a number of subsequent papers [2, 3]).

In the present paper we consider some features of the γ-spectra of heavy elements (A = 100—200) not too close to the magic nuclei. With a resolution of 2 %, the main part of γ-transitions in the spectra of these elements falls to the unresolved part whose form is our primary concern in the present paper. To obtain the general form of the spectrum, measurements with a magnetic Compton spectrometer are rather convenient since this instrument makes it possible to measure, under uniform conditions, almost the whole spectrum of the γ-rays from the reaction (n, γ), or to be more specific, in the energy interval from 0.3 to 12 MeV.

The question of the shape of the unresolved part of the γ-spectrum for heavy elements was discussed in our paper at the Second Geneva Conference [4]). We compared the unresolved spectrum parts for heavy nuclei with different parity of the numbers of protons and neutrons, and established the effect of nucleon pairing on the form of the γ-spectrum in its upper part. The effect of nucleon pairing is manifested in that the upper limit of the unresolved part in even nuclei lies approximately by 1.5 MeV lower than the neutron binding

† In accordance with the convention adopted in this journal, odd stands for odd-odd and even for even-even.

energy, whereas these two quantities practically coincide in odd nuclei. This fact distinctly indicates an energy gap near the ground state of even nuclei.

The present paper resumes the problem of the general shape of the spectrum and its dependence on the distribution of density levels in heavy nuclei. The

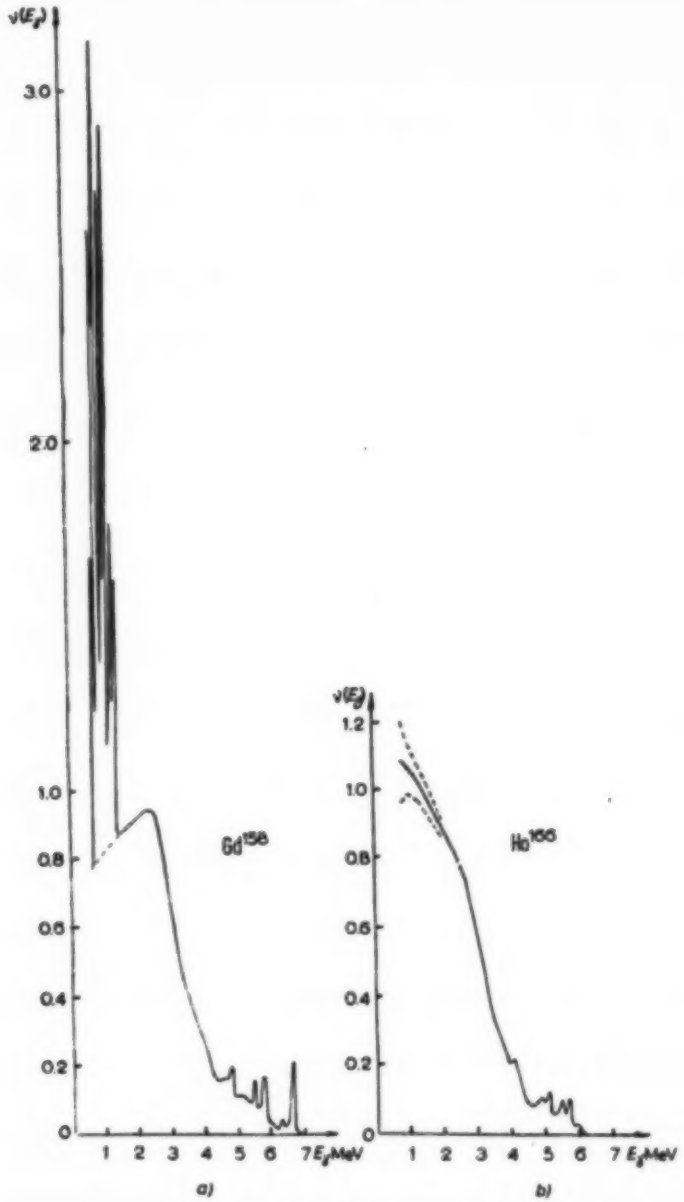

Fig. 1. Spectra of γ-rays of Gd^{158} and Ho^{166}.

reason is twofold: the completion of the calculation of the spectrum by a computor [5]), on the one hand, and some additional inferences on the form of the spectrum of various nuclei at low energies, on the other.

To bring out the peculiarities in the region of small energies which are of

interest to us, it is convenient, in representing the spectrum, to mark off the quantity $\nu(E_\gamma)$, the number of photons per unit energy interval for one captured neutron on the axis of the ordinates instead of $\nu(E_\gamma)H\rho$, as was done in the previous papers [1, 4]). Absolute values of $\nu(E_\gamma)$ mostly obtained by normalising the energies radiated by the nuclei to the neutron binding energy.

Fig. 1 exemplifies the γ-spectra of the even nucleus Gd^{158} and the odd nucleus Ho^{166}. As is clear from it, in the case of Gd^{158}, separate peaks corresponding to

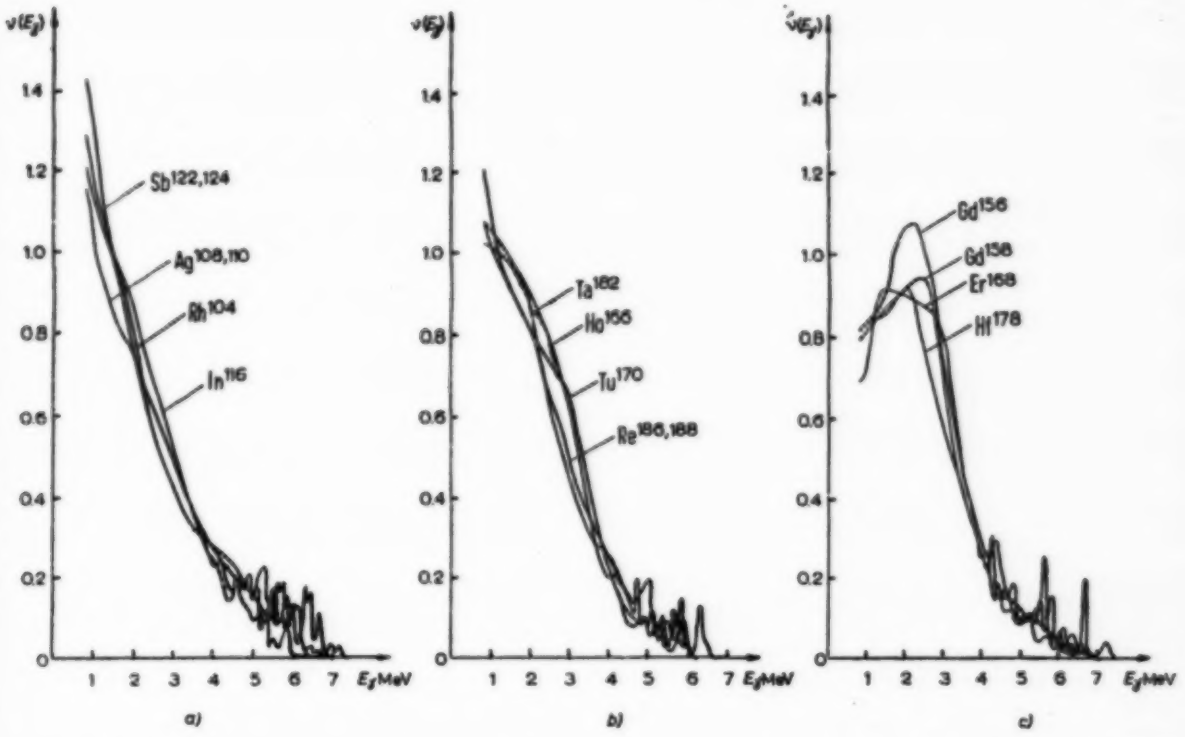

Fig. 2. Experimental spectra of γ-rays of odd nuclei with $A \approx 110$ (fig. 2a), odd nuclei with $A \approx 175$ (fig. 2b) and even non-spherical nuclei (fig. 2c).

the monochromatic lines are seen against the background of the unresolved part in the lower and upper regions. A similar picture is characteristic of other even nuclei. For odd nuclei such peaks are observed only in the upper part of the spectrum.

In this paper we consider the γ-spectra of even and odd nuclei with $100 < A < 200$ only.

With the exception of gadolinium, all spectra are obtained with natural admixtures of isotopes. In the notations of this paper we shall indicate the isotope (or isotopes) responsible for the main contribution to the spectrum under consideration.

The atomic weights and atomic numbers of isotopes in all cases refer to the radiating nuclei formed after the neutron capture.

For odd nuclei we have the spectra of Rh^{104}, $Ag^{108, 110}$, In^{116}, $Sb^{122, 124}$, La^{140}, Eu^{152}, Ho^{166}, Tu^{170}, Ta^{182}, $Re^{186, 188}$, $Ir^{192, 194}$ and Au^{198}. Fig. 2a represents spectra of Rh, Ag, In and Sb, while fig. 2b those of Ho, Tu, Ta and Re. The nuclei of the first group have an atomic weight $A \approx 110$ and are all spherical. For the second group of nuclei $A \approx 175$ and all of them belong to the category of deformed nuclei.

For even nuclei we have the spectra of Mo^{96}, Cd^{114}, $Sn^{116; 118; 120}$, Nd^{144}, Sm^{150}, Gd^{156}, Gd^{158}, Er^{168}, Hf^{178}, Pt^{196} and Hg^{200}.

Fig. 2c represents the spectra of four deformed nuclei Gd^{156}, Gd^{158}, Er^{168} and Hf^{178}. These spectra have been obtained from the experimentally measured ones by cutting off the peaks with energy less than 2 MeV. For Gd^{158} (see fig. 1) this cutting off is shown by a dotted line. Lines in the region of small energies are discarded for the convenience of comparing the spectra of various nuclei.

In figs. 1b, 7, 8b a dotted line shows experimental errors in the measurement of the spectrum. Since errors increase as the photon energy decreases, all experimental spectra are plotted for energies $\geqq 0.8$ MeV.

As is clear from fig. 2, within each of the three groups, the spectra may be well represented by an averaged curve. The averaged spectra thus obtained are given separately in fig. 3. This graph shows that the spectra for two groups of odd nuclei (curve I and II) do not differ essentially. Therefore, an average spectrum for all eight odd isotopes may be taken as we did at first. Yet a more detailed analysis reveals one singularity repeated in all spectra of the nuclei with $A \approx 175$, but absent in the nuclei with $A \approx 110$. What is meant is the small protuberance in curve II in the region of energies from 2 to 3 MeV. This distinction appears in theoretical calculations as well. (For details see ref. [5]).

The division of the spectra of odd nuclei into two groups proves to be reasonable also because the neutron binding energy B_n for the nuclei with $A \approx 110$ on the average turns out to be somewhat higher than for the nuclei with $A \approx 175$, as is clear from table 1.

For even isotopes indicated in fig. 2c the neutron binding energies are equal to 8.46, 7.87, 7.76 and 7.55 MeV respectively. These numbers show that the neutron binding energies do not differ very much from each other within each group of nuclei. For this reason we have not reduced the spectra to the same value of the binding energy.

The mean experimental spectra represented in fig. 3 may be compared with the spectra calculated theoretically (see ref. [5]). These calculations are carried out for a neutron binding energy equal to 6.4 MeV in odd nuclei and 7.6 MeV in even nuclei for the two laws of the excitation energy dependence on the level density: $\rho(u) = \rho_0 e^{\sqrt{au}}$ and $\rho(u) = \rho_0 e^{u/\tau}$, a and τ being constants. In the case of even nuclei it was assumed that these laws apply beginning from the energy Δ, representing the energy gap at the ground state.

For even nuclei the main calculations were carried out with $\Delta = 1.2$ MeV, approximately equal to the difference of the neutron binding energies in even and odd nuclei adopted in the calculation. For that reason the effective energy of excitation in even nuclei — the energy calculated from the upper edge of the

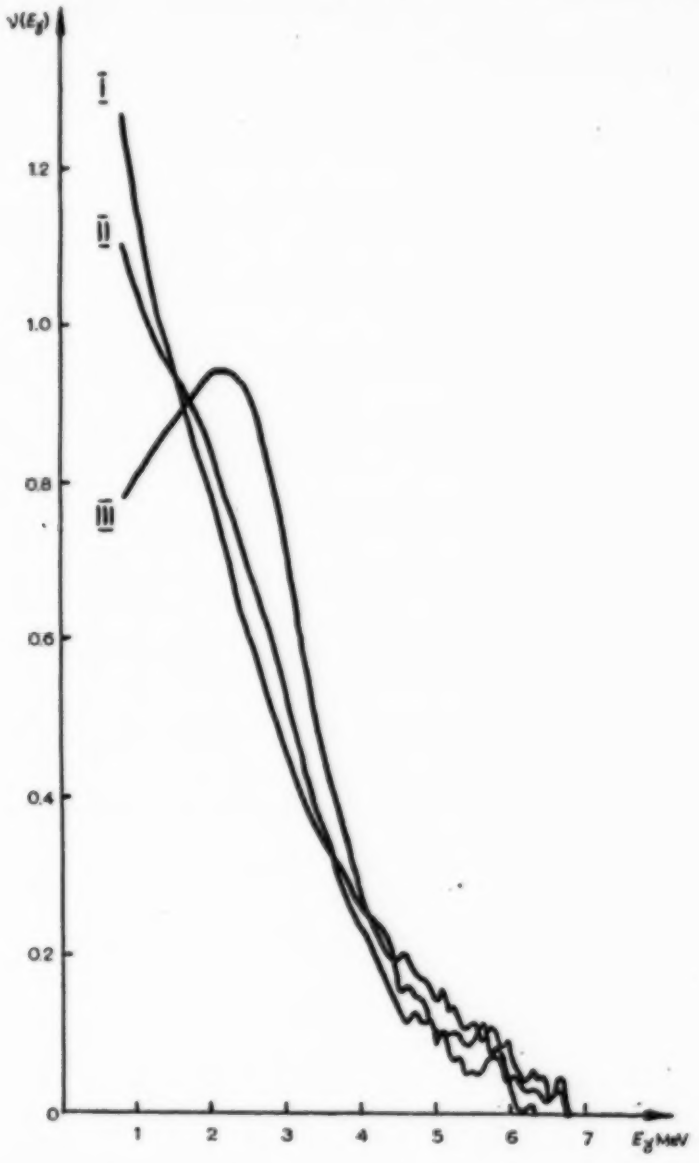

Fig. 3. Mean experimental spectra for odd nuclei with $A \approx 110$ (I) odd nuclei with $A \approx 175$ (II) and even non-sperical nuclei (III).

gap — is 6.4 MeV, and consequently the calculations are conducted in the same energy range for both categories of nuclei.

For the law $\rho = \rho_0 e^{\sqrt{au}}$ theoretical calculations are carried out for the values of a lying in the interval from 5 to 60 MeV^{-1}, while for the law $\rho = \rho_0 e^{u/\tau}$ the values of τ changing by 0.1 MeV between 0.4 and 1 MeV as well as $\tau = 1.2$

MeV are taken. In the case of even nuclei the calculations were carried out for different values of the parameter $\alpha = (1/\rho_0)(\bar{M}_b^2/\bar{M}_a^2)$ where M_b and M_a represent the matrix elements of parallel transitions to the ground state through the gap and into the states lying above the gap (for details see ref. [5])).

The comparison between the average experimental spectra and the theoretically computed curves makes it possible to choose values of the parameter a, if $\rho = \rho_0 e^{\sqrt{au}}$, or of the parameter τ, if $\rho = \rho_0 e^{u/\tau}$.

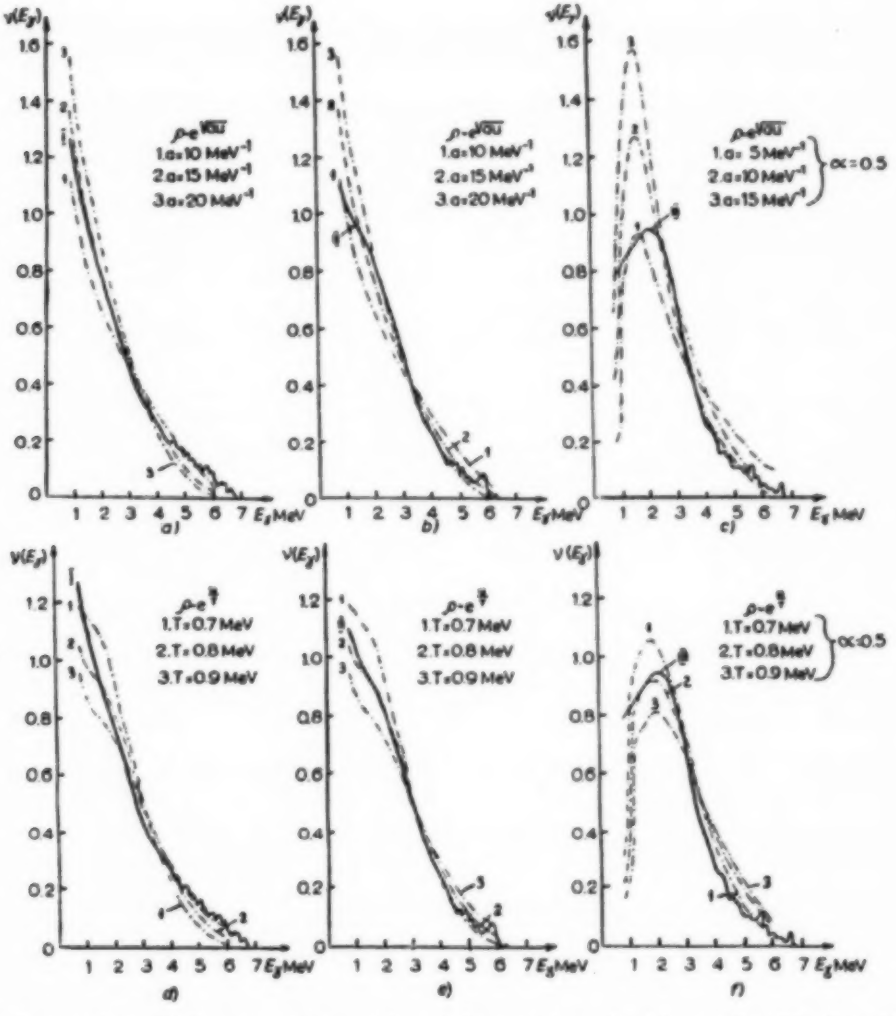

Fig. 4. Comparison of the average experimental γ-spectra of odd nuclei with $A \approx 110$ (figs. a and d) odd nuclei with $A \approx 175$ (figs. b and e) and even non-spherical nuclei (figs. c and f) with the spectra calculated theoretically for the two laws of the energy dependence of the level density $\rho = \rho_0\sqrt{au}$ and $\rho = \rho_0 e^{u/\tau}$. The theoretical spectra are represented by a dash- and-dot line.

This comparison is shown in fig. 4 which represents three theoretical curves alongside the average experimental spectra of the different categories of nuclei. The curves are calculated for the law $\rho = \rho_0 e^{\sqrt{au}}$ (the upper part of fig. 4) and for the law $\rho = \rho_0 e^{u/\tau}$ (the lower part of fig. 4). The theoretical curves are

plotted in all cases for three values of a or τ (see caption to fig. 4) chosen so that these curves, with intermediary values of a and τ, approximate the experimental spectra most closely (with exception of fig. 4c).

It is clear from fig. 4 that in the case of odd nuclei the calculated curves prove to be sufficiently close to the experimental spectra for both laws of energy dependence of level density provided the parameters are properly selected.

Yet a more detailed comparison of the curves of fig. 4 shows (see fig. 4a and d) that for $A \approx 110$ and for the law $\rho = \rho_0 e^{\sqrt{au}}$ with $a = 15$ MeV^{-1} in the case of spherical nuclei there is a somewhat better agreement between experimental and theoretical spectra than for the exponential level density.

The opposite is true for deformed nuclei with $A \approx 175$. In this case the experimental spectrum agrees best of all with the theoretical curve calculated for the exponential law $\rho = \rho_0 e^{u/\tau}$ with $\tau = 0.8$ MeV. A small difference in the spectra of the odd nuclei with $A \approx 110$ and those with $A \approx 175$ may be accounted for by the difference in the level densities in spherical and deformed nuclei (see part II). It is worthwhile to mention once again that the difference in the spectra for the two categories of odd nuclei under consideration is not very essential and is manifested only in the details of the curves.

In the case of even nuclei the agreement between experimental and theoretical spectra is not so good as for odd nuclei (see figs. 4c and f). Yet under the law $\rho = \rho_0 e^{u/\tau}$ the smallest discrepancy between these two types of curves is obtained at the same value of $\tau = 0.8$ MeV as for the deformed odd nuclei $A \approx 175$.

The theoretical curves are in a considerably worse agreement with experimental spectra under the laws $\rho = \rho_0 e^{\sqrt{au}}$ and $\alpha = 0.5$. With $a = 15$ MeV^{-1} obtained from the comparison of the spectra for odd nuclei, the theoretical curve sharply differs from the experimental spectrum. For smaller values of a the discrepancy somewhat decreases yet it is still considerably larger than that of the curve 2 of fig. 4f.

Another essential circumstance will be pointed out: the above comparison involves the absolute values of $\nu(E_\gamma)$, apart from the shape of the spectra.

Let us now compare the average experimental spectra of odd and even nuclei shown in fig. 3. It is clear from fig. 3 that there is an essential difference in the low energy ends of these spectra, viz., the number of photons with energies $E < 1.5$ MeV in the unresolved part of spectra of even nuclei is essentially smaller than in that of odd nuclei, while the number of photons with energies from 2 to 4 MeV greater.

This difference in the spectrum of the even nucleus can be accounted for by the existence of an energy gap in the spectrum of nuclear levels caused by nucleon pairing. Qualitatively, this reduces to the following. In the process of the de-excitation of an even nucleus, apart from the γ-transitions gradually bringing the nucleus to the upper limits of the gap (type a transitions), parallel transitions (of b type) appear, bringing the nucleus through the gap into the

ground state or into near lying states corresponding to collective excitations. In the case of an odd nucleus the a type transitions only take place. The photons emitted in the b type transitions are generally more energetic if compared with the a transitions and originate from the exclusion of the latter. This outflow of the b type photons decreases as the energy of the nucleus excitation increases.

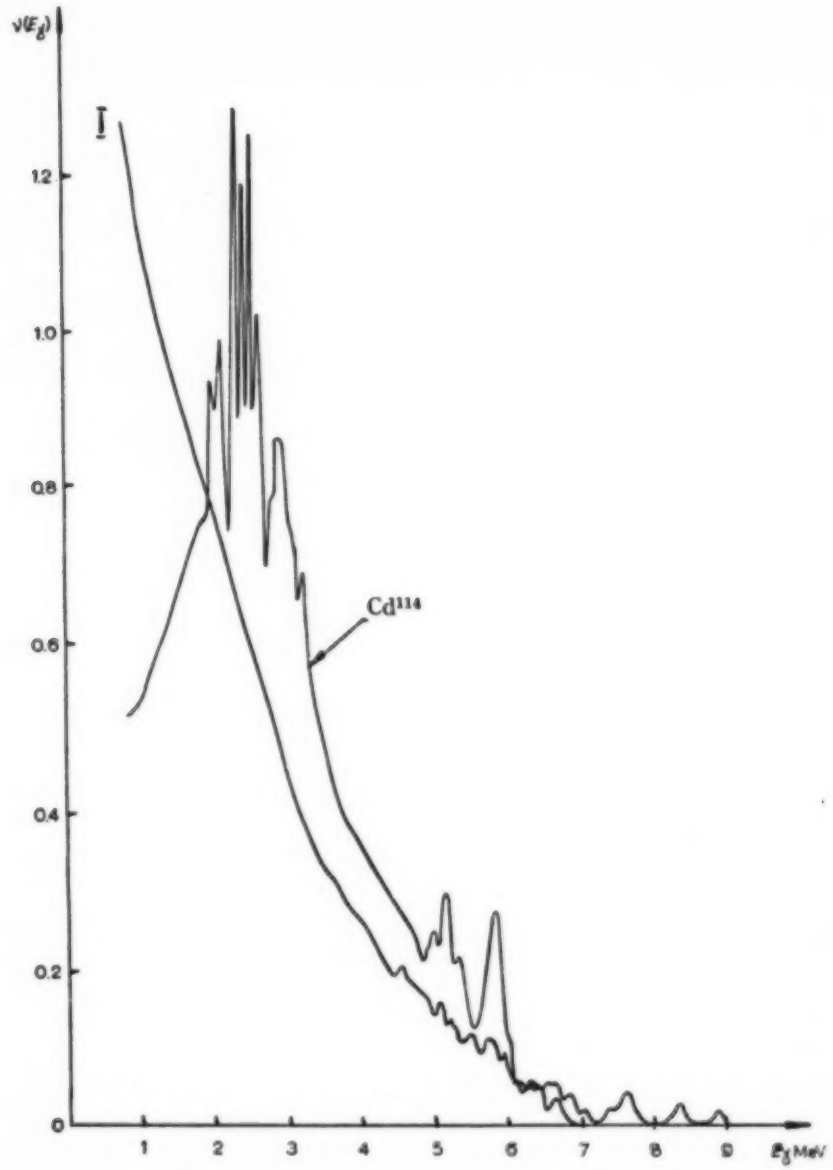

Fig. 5. Comparison of the spectrum of Cd^{114} with the average experimental spectrum for odd nuclei with $A \approx 110$ (I).

On the other hand, if the energy of excitation approaches 1.5—2.0 MeV, these transitions may prove to be prohibited, though the de-excitation into the ground state would be more advantageous as far as energy is concerned. The usual spin forbiddenness will act here for spherical nuclei, while the forbidden-

ness with respect to the quantum number K will come into play for deformed nuclei. These types of forbiddenness result in an intense population of the levels in the neighbourhood of 1 MeV, which is seen especially clearly in non-spherical nuclei. A group of intense lines of such energy (see, for example, fig. 1) appears in

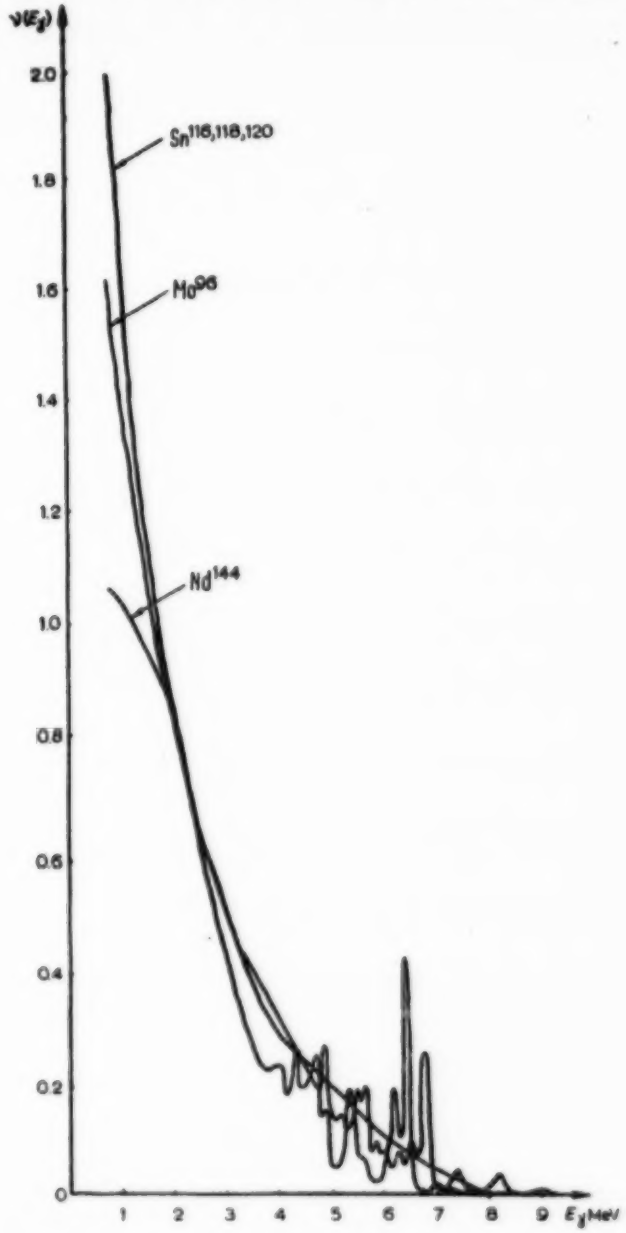

Fig. 6. Spectra of γ-rays of Mo^{96}, $Sn^{116,118,120}$ and Nd^{144}.

the spectra of these nuclei, as was shown before in ref. [6]). It follows from experimental data that the de-excitation of the non-spherical even nuclei passes through the levels situated at the gap energy in approximately 50 per cent of cases and through the type b transitions coming from higher excited states in the same number of cases.

Let us consider now γ-spectra of other nuclei. Alongside the average spectrum for spherical odd nuclei, fig. 5 represents an experimental spectrum for Cd^{114} (as in other even nuclei, the lines with energy less than 2 MeV are cut off here). There is qualitatively the same type of difference between the spectra of Cd^{114}

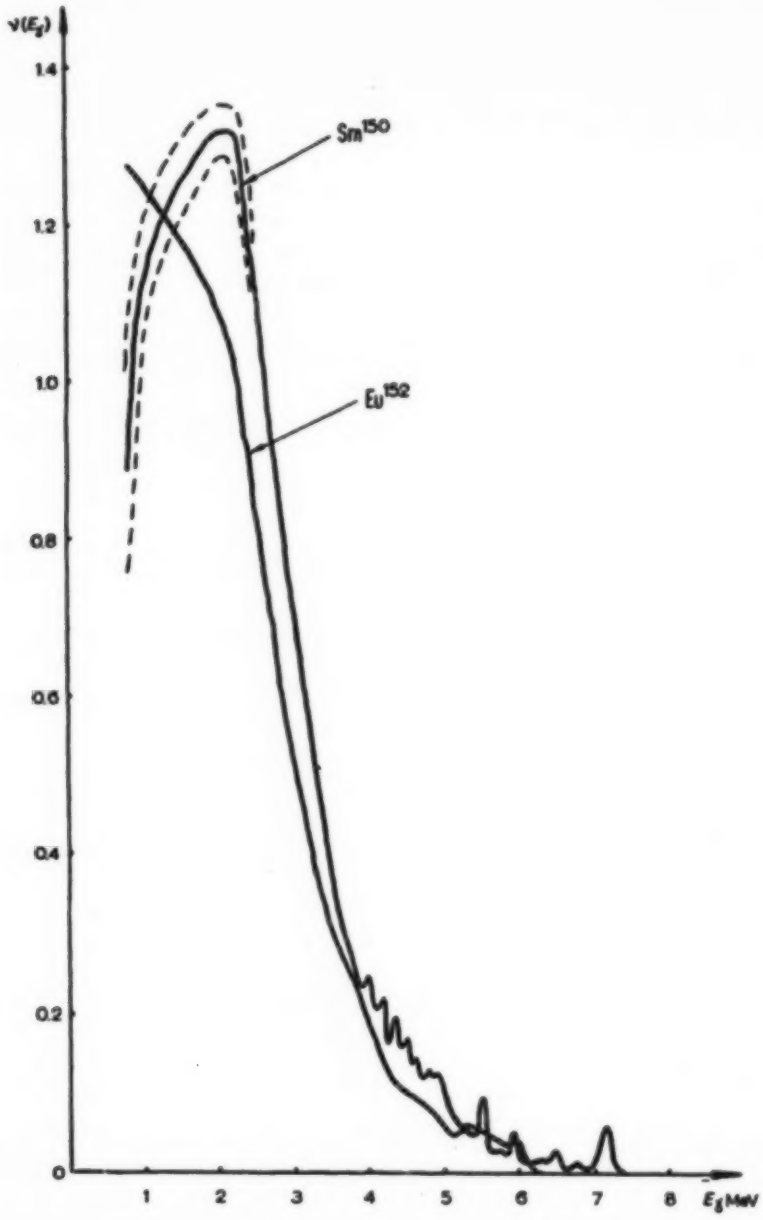

Fig. 7. Comparison of the γ-ray spectra of Sm^{150} and Eu^{152}.

and odd nuclei as that considered above. The spectrum Cd^{114} was not averaged with other even nuclei since this isotope has a considerably higher neutron binding energy equal to 9 MeV.

Fig. 6 represents the spectra of the following even nuclei: Mo^{96}, $Sn^{116, 118, 120}$

and Nd^{144}. The shape of the unresolved parts of these spectra is rather close to those of odd nuclei. This result may well be understood if the b type transitions, i.e., those causing the outflow into the ground state, are considered in detail. The fact is that this outflow may pass not only into the ground state but also into the lowest excited states. Whereas the excited levels in non-spherical even nuclei to which an effective outflow is possible are situated at low excitation energies (170—300 keV), the first excited level in spherical nuclei, particularly in Mo^{98}, Sn^{118} and Nd^{144}, is situated at 0.78, 1.2 and 0.7 MeV respectively,

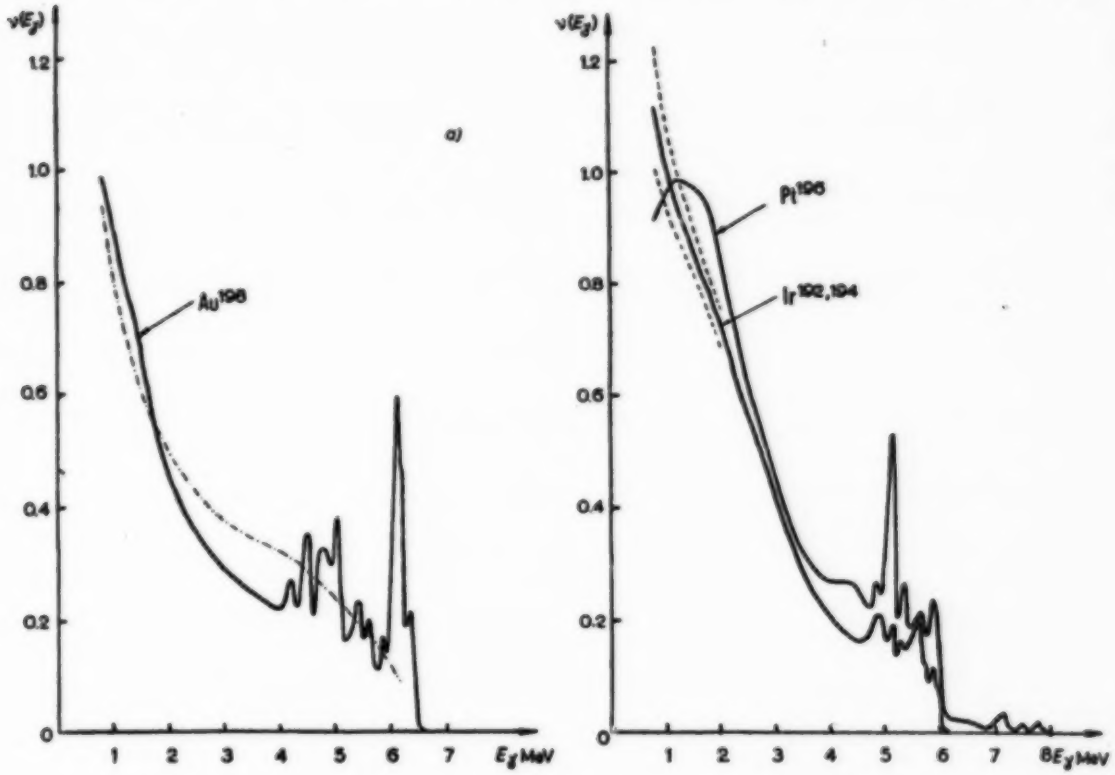

Fig. 8. Spectrum of γ-rays of nuclei close to $Z = 82$ and $N = 126$.
a) Comparison of the experimental spectrum of Au^{198} and the theoretical spectrum for $\rho = \rho_0 e^{\sqrt{aU}}$ and $a = 5\ \mathrm{MeV}^{-1}$ (dash-and-dot curve),
b) Comparison of spectra of $Ir^{192, 194}$ and Pt^{196}.

absorbing up to 90 % of all cascades. Since the energy of nucleon pairing in these nuclei is equal to 1.5 to 2 MeV, a noticeable outflow not into the ground state but to the low excited levels perceptibly decreases the effective width of the energy gap in these nuclei. Thus, in the nuclei under consideration the energy of b transitions differs from that of a transitions not by 1.5 to 2 MeV but by a smaller value equal to the effective width of the energy gap, which leads to a considerable smoothing down of the differences in the γ-spectra of the indicated even and odd nuclei.

In the case of Cd^{114} we also observe a larger population of the first level with

an energy of 0.56 MeV. Yet evidently the effective energy gap in this case will still be large enough since it has an essential effect on the form of the spectrum of Cd^{114}.

Let us turn now to the two neighbouring nuclei Eu^{152} and Sm^{150}. The spectra of these nuclei markedly differ from the mean spectra given above. For Sm^{150} this difference lies in a larger height of the maximum of the spectrum and for Eu^{152} it lies in exceeding the spectrum in the region of small energies if compared with other odd nuclei.

It is noteworthy, however, that in comparing the spectra of Sm^{150} and Eu^{152} (see fig. 7) qualitatively the same pattern is observed as established above in comparing the spectra of even and odd nuclei (see fig. 3).

As was mentioned earlier [4, 7]), in the elements lying near the twice magic nucleus Pb^{208} the spectra of γ-rays considerably differ in their shape from the above discussed spectra of heavy elements far from the magic ones. As an example, the spectrum of Au^{198} is given in fig. 8a. The same figure represents a theoretical spectrum calculated under the assumption that the density of levels is given by the formula $\rho = \rho_0 e^{\sqrt{au}}$ with $a = 5$ MeV^{-1}. Both curves are quite close to each other. It should be noted, however, that such a sharp decrease in the value of a for Au^{198} was not confirmed by other experiments [4]) and another reason was pointed out for such a substantial change in the form of the spectrum Au^{198} as compared with the spectra of the nuclei not close to the magic ones.

It will be noted that the effect of the energy gap on the spectra of γ-rays is observed quite distinctly in this region as well. Fig. 8b represents experimental spectra for the neighbouring nucleus of the odd $Ir^{192, 194}$ and for the even Pt^{196}. It is clear from the figure that if we abstract ourselves from the change in the form in the upper part of the spectrum connected with approaching $Z = 82$ and $N = 126$ (see ref. [4])), the same qualitative difference in the spectra of odd and even nuclei is observed as that illustrated in fig. 3.

References

1) L. V. Groshev, A. M. Demidov, V. N. Lutsenko and V. I. Pelekhov, Atlas of Thermal Neutron Capture γ-Rays Spectra (Atomizdat, 1958)
2) L. V. Groshev, B. I. Gavrilov and A. M. Demidov, Atomic Energy **6** (1959) 281
3) L. V. Groshev, A. M. Demidov and V. I. Pelekhov, Atomic Energy (in print)
4) L. V. Groshev, A. M. Demidov, V. N. Lutsenko and V. I. Pelekhov, Reports of Soviet Scientists at the 2nd International Conference for Peaceful Use of Atomic Energy, vol. 1, Nuclear Physics (Atomizdat, 1959) p. 281
5) V. M. Strutinski, L. V. Groshev and M. K. Akimova, Nuclear Physics **16** (1960) 657
6) L. V. Groshev, A. M. Demidov, V. N. Lutsenko and V. I. Pelekhov, Atomic Energy **4** (1958) 5
7) G. A. Bartholomew, P. J. Campion, J. W. Knowles and G. Manning, Report at the Colombia Conference (September 1957)

2.D

Nuclear Physics **16** (1960) 657—673; © *North-Holland Publishing Co., Amsterdam*

Not to be reproduced by photoprint or microfilm without written permission from the publisher

SPECTRA OF γ-RAYS FROM NEUTRON CAPTURE BY HEAVY NUCLEI (II)

V. M. STRUTINSKI, L. V. GROSHEV and M. K. AKIMOVA

Atomic Energy Institute of the USSR Academy of Sciences, Moscow

Received 23 October 1959

Abstract: The spectra of γ-rays accompanying thermal neutron capture are calculated for dipole γ-radiation for two variants of the dependence of nuclear level density on energy. Parameters for the formula of nuclear level density are determined from comparison with experimental spectra. The results thus obtained for nuclear level density are compared with the data derived from other experiments.

1. General Theory

The capture of thermal neutron by nucleus results in the formation of a comparatively strongly excited nucleus with an excitation energy from 6 to 8 MeV. In the heavy nuclei with an atomic weight $A > 100$ transition from an excited state arising from thermal neutron capture may occur in many different ways because of a high density of levels. Therefore, the part of the spectrum unresolved with the present-day measuring technique accounts for an overwhelming portion of γ-transitions in such elements. In light nuclei as well as in the heavy nuclei close to the magic ones the spectrum of γ-rays is practically linear because of a low level density [1]). The present paper is concerned with the continuous spectra only.

As is shown by experimental data, the form of the spectrum of γ-quanta in heavy nuclei is sufficiently definite and changes from nucleus to nucleus comparatively little. It may be supposed, therefore, that the spectrum of the emitted quanta is largely determined by the general properties of the distribution of nuclear levels and the multipolarity of radiation transitions and relatively weakly depends on the specific properties of the latter's matrix elements.

In accordance with the statistical theory we assume that the relative probability of the emission of a γ-quantum with an energy E by the nucleus in a state with the energy u is represented by the formula [2])

$$w(u, E) = E^{\kappa}\rho(u-E)/n(u) \qquad (1)$$

where $\rho(u-E)$ is the density of the final states of the nucleus. It is assumed that the distribution (1) is only determined by the energies of the initial and final states of the nucleus. This is justified to some extent by the fact that the probability $w(u, E)$ may be interpreted as a relative probability of the transition

averaged with respect to a sufficiently large number of initial and final states of the nucleus. The distribution (1) is normalised to the total probability of disintegration equal to unity. Hence, the normalisation factor $n(u)$ is determined as

$$n(u) = \int_0^u E^\kappa \rho(u-E)\mathrm{d}E. \tag{2}$$

The average matrix element of the transition which we consider as a constant does not enter eq. (1). The constant κ is equal to $2l+1$, where 2^l is the multipolarity of the radiation.

To calculate the total spectrum of the γ-radiation of the nucleus it is necessary to sum the spectra of all stages of the cascade. The problem is solved in the simplest way if the energy of emitted quanta may be considered small as compared with the excitation of the nucleus. The calculation of the spectrum in this approximation was carried out by V. G. Nosov and one of the authors of the present paper (V. S.) [1]. The emission of a large number of quanta is characteristic for this case. Considering the number of quanta as a continuous quantity, the following expression may be obtained for the spectrum of γ-quanta:

$$\nu(E)\mathrm{d}E = \mathrm{d}E \int_E^{u_0} w(u, E) \frac{\mathrm{d}u}{\bar{E}(u)} \tag{3}$$

where $\nu(E)\mathrm{d}E$ is the number of emitted quanta with the energy in the interval E, $E+\mathrm{d}E$, u_0 is the initial energy of excitation and $\bar{E}(u)$ is an average energy of γ-quanta emitted by the nucleus with an energy u:

$$\bar{E}(u) = \int_0^u E w(u, E)\mathrm{d}E. \tag{4}$$

The complete number of quanta $\nu(u_0)$ is in this approximation equal to

$$\int_0^{u_0} \nu(E)\mathrm{d}E = \int_0^{u_0} \bar{E}^{-1}(u)\mathrm{d}u. \tag{5}$$

Putting in eq. (1) $\rho \approx \rho_0 \exp\{s(u)\}$, where $s(u)$ is the entropy of the nucleus, we obtain

$$\bar{E}(u) \approx (\kappa+1)T(u), \tag{6}$$

$$\bar{\nu}(u_0) = \int_0^{u_0} \frac{\mathrm{d}u}{(\kappa+1)T(u)} = (\kappa+1)^{-1} s(u_0). \tag{7}$$

The average quadratic fluctuation of the number of quanta is equal to

$$\sqrt{\overline{\nu^2} - \bar{\nu}^2} = \sqrt{\frac{s(u_0)}{\kappa+1}}. \tag{8}$$

In eqs. (6) and (7) $T(u)$ is the nuclear temperature.

$$T^{-1}(u) = \mathrm{d}s/\mathrm{d}u.$$

The experimental data on the spectra of γ-rays accompanying the thermal neutron capture and the results of calculations according to eqs. (3)—(7) were compared in ref. [1]). These equations yield a fairly good qualitative approximation. Yet when applied to a thermal neutron capture this accuracy is insufficient since the number of the emitted quanta proves to be rather small ($\approx$ from 3 to 4 quanta per capture). The average energy of quanta approximately equals 1.5 to 2 MeV, i.e., by no means small if compared with the nuclear excitation energy.

A more accurate calculation of the spectrum of emitted quanta may be carried out if one discards the assumption underlying the evaluation of eqs. (3)—(7), viz., that the variation of the energy of the nucleus due to the emission of the γ-quantum is small, and its corollary: replacing the summation of various chains of disintegration by an integration over stages characterized by average values of excitation energy.

The calculation may be carried out on the basis of the kinetic equation describing the multistage process of the γ-radiation of the nucleus [3]). In the present case, when the radiation of quanta is the only process at work, this equation has the following form:

$$\frac{\partial y_k(u, t)}{\partial t} = \int_u^{u_0} y_{k-1}(u', t)\Gamma(u')w(u', u'-u)\mathrm{d}u' - \Gamma(u)y_k(u, t) \tag{9}$$

where $y_k(u, t)$ is the probability to find k quanta and the nucleus in the state with the energy u at time t in the system nucleus $+\gamma$-quanta. In eq. (9) $\Gamma(u)$ is the probability of disintegration per unit time of the nucleus of energy u, multiplied by $\hbar$.

At the initial instant $t = 0$ the following equation holds:

$$y_k(u_0, 0) = \delta_{k0}\delta(u-u_0) \tag{10}$$

(δ_{ab} is the δ-symbol and $\delta(x)$ is the δ-function), since there were no quanta in the system at $t = 0$ and the nucleus was in the initial state. A simpler equation may be obtained from eq. (9) for a quantity directly connected with the spectrum of γ-quanta of interest to us. To obtain this equation let us introduce a function $N(u, t)$, the probability that there is a nucleus with an energy u and any number of quanta at time t:

$$N(u, t) = \sum_{k=0}^{\infty} y_k(u, t). \tag{11}$$

The function $y_0(u, t)$ satisfies the following differential equation (see eq. (9)):

$$\frac{\partial y_0(u, t)}{\partial t} = -\Gamma(u)y_0(u, t). \tag{12}$$

This considered, the following equation is obtained for the function $N(u, t)$ by

summing both parts of eq. (9) over k:

$$\frac{\partial N(u,t)}{\partial t} = \int_0^{u_0} \Gamma(u')w(u', u'-u)N(u', t)\mathrm{d}u' - \Gamma(u)N(u, t). \tag{13}$$

In a similar way eq. (10) can yield as a boundary condition

$$N(u, 0) = \delta(u-u_0). \tag{14}$$

Let $\nu(E, t)$ be the number of quanta with an energy E in the system at a moment t. For the function $\nu(E, t)$ the following equation holds:

$$\frac{\partial \nu(E,t)}{\partial t} = \int_E^{u_0} N(u', t)\Gamma(u')w(u', E)\mathrm{d}u', \tag{15}$$

whose solution satisfying the boundary condition $\nu(E, 0) = 0$ is the function

$$\nu(E, t) = \int_E^{u_0} w(u', E)\mathrm{d}u' \int_0^t \Gamma(u')N(u', t)\mathrm{d}t'. \tag{16}$$

The function $\nu(E, t)$ when $t = \infty$ gives the number of quanta with the energy E emitted by the nucleus in the process of decay:

$$\nu(E) \equiv \nu(E, t = \infty) = \int_E^{u_0} w(u', E)\mathrm{d}u' \int_0^{\infty} \Gamma(u')N(u', t)\mathrm{d}t'. \tag{17}$$

Let us now find an equation for the function

$$Z(u) = \int_0^{\infty} \Gamma(u')N(u', t')\mathrm{d}t'.$$

For this both parts of eq. (13) should be integrated over t:

$$N(u, \infty) - N(u, 0) = \int_u^{u_0} Z(u')w(u', u'-u)\mathrm{d}u' - Z(u). \tag{18}$$

This relation is the wanted integral equation for the function $Z(u)$. Indeed, using eq. (14) and noticing that $N(u, \infty) = 0$ for all $u > 0$, one obtains

$$Z(u) = \int_u^{u_0} w(u', u'-u)Z(u')\mathrm{d}u' + \delta(u-u_0). \tag{19}$$

The function $\nu(E)$ may then be written as

$$\nu(E) = \int_E^{u_0} w(u', E)Z(u')\mathrm{d}u'. \tag{20}$$

The function $Z(u)$ gives the probability that in the process of the radiation of γ-quanta the nucleus will pass through the state with the energy u. Eqs. (3) and (20) for the spectrum of γ-quanta formally coincide inasmuch as the function $Z(u)$ is equal to $[\bar{E}(u)]^{-1}$.

For the following, it is better to put eqs. (19) and (20) into a somewhat different form by introducing a new function $\zeta(u) = Z(u) - \delta(u-u_0)$. Eqs. (19)

and (20) then become

$$\zeta(u) = \int_u^{u_0} w(u', u'-u)\zeta(u')\mathrm{d}u' + w(u_0, u_0-u) \tag{21}$$

and

$$\nu(E) = w(u_0, E) + \int_E^{u_0} w(u', E)\zeta(u')\mathrm{d}u'. \tag{22}$$

The first term in eq. (22) corresponds to the γ-quanta emitted from the initial states of the nuclei and the second represents the spectrum of the subsequent quanta.

Using the method of successive approximations to solve the integral eq. (21) one gets the well-known expression for the spectrum of the γ-rays:

$$\nu(E) = w(u_0, E) + \int_0^{u_0-E} w(u_0, E')w(u_0-E', E)\mathrm{d}E' + \ldots \tag{23}$$

where the successive terms of the series represent the probability of the emission of a quantum with an energy E as the first, the second and so on the chain. The effective number of terms in this series depends on E. When $E \lesssim 1$—2 MeV this number proves to be too large and eq. (23) cannot be used for actual calculation of the spectrum since it involves the evaluation of integrals of high multiplicity.

In the important case when the function $w(u, E)$ is represented by eq. (1), the integral eq. (21) may be reduced to a differential equation. To do so, we substitute eq. (1) into eq. (21) for the function $w(u, E)$, divide both parts of the equation by $\rho(u)$ and differentiate them $\kappa+1$ times over u. As a result we obtain the differential equation of the $\kappa+1$-th order for the function $\zeta(u)$

$$\frac{\mathrm{d}^{\kappa+1} f(u)}{\mathrm{d}u^{\kappa+1}} = (-1)^{\kappa+1}\kappa!\frac{\rho(u)}{n(u)}f(u) \tag{24}$$

where $f(u) = \zeta(u)/\rho(u)$, and the boundary condition at the point $u = u_0$

$$\left(\frac{\mathrm{d}^\lambda f(u)}{\mathrm{d}u^\lambda}\right)_{u=u_0} = \begin{cases} 0 & \text{if } \lambda = 0, \ldots, \kappa-1 \\ \dfrac{(-1)^\kappa \kappa!}{n(u_0)} & \text{if } \lambda = \kappa. \end{cases} \tag{25}$$

In certain simple cases eq. (24) makes it possible to determine the function $\zeta(u)$ at once. To determine the qualitative properties of the function $\zeta(u)$, one notices that the function $n(u)$ is equal to $\kappa!T^{\kappa+1}\rho(u)$ when u is large ($u \gg \kappa T$) and equals $(\kappa+1)^{-1}u^{\kappa+1}$ when $u \to 0$ (we assume here that the level density is a continuous function down to $u = 0$). Taking this into account, we may find with the help of eq. (24) that $\zeta(u)$ behaves like

$$w(u_0, u_0-u) \approx (u_0-u)^\kappa \rho(u)/\kappa!T(u)$$

when

$$u_0 - \bar{E}(u) \approx u_0 - (\kappa+1)T(u_0) \lesssim u \leqq u_0,$$

like c/u, where c is a constant, when $u \to 0$, and like $\{(\kappa+1)T(u)\}^{-1}$ in the intermediary region where $u \gg T(u)$.

These properties are obvious from the viewpoint of the above-mentioned physical meaning of the function $Z(u)$ (cf. eqs. (3), (6)). Practically, the region of energies in which $\zeta(u)$ may be represented by $\{(\kappa+1)T\}^{-1}$ is small, which leads to an inaccuracy in eq. (3). A graph of the function $\zeta(u)$ is given in fig. 1 (curve 1). The divergence of the function $\zeta(u)$ when $u \to 0$ means that nuclei with a low energy of excitation are accumulated in the process of emission of

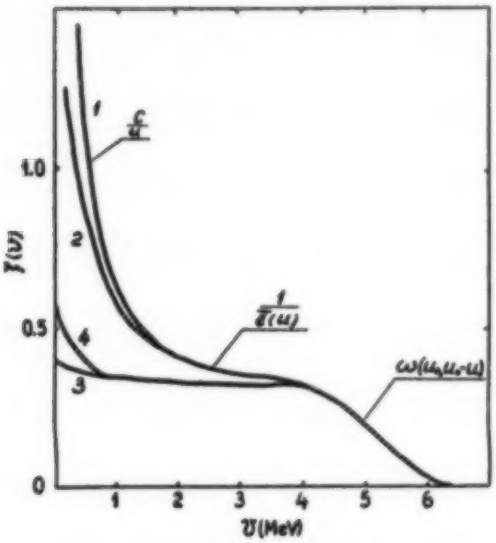

Fig. 1. Graph of the function $\zeta(v)$ calculated for version I of level density for the following values of parameters:
1) $\alpha = 0$ (odd nucleus), $u = v$; 2) $\alpha = 1/400$ MeV; 3) $\alpha = 0.5$ MeV;
4) α function of energy (curve 1, fig. 7), $\alpha_1 = 1/400$ MeV; $\alpha_2 = 0.5$ MeV, $v^* = 0.4$ MeV, $\tau = 0.8$ MeV.

quanta. As a consequence, the spectrum of γ-rays emitted by the nuclei will also diverge as $1/E$ when $E \to 0$. This is common to all cases when the density of nuclear levels may be considered as a continuous function starting with small energy values. It may be expected that this situation corresponds closer than any other to the case of odd heavy nuclei where, as a consequence of the presence of the two odd unpaired particles, the density of levels increases more or less uniformly, straight from the ground state of the nucleus. In even nuclei the pairing of particles leads to a gap between the ground and the first excited state. For nuclei of average atomic weight this quantity Δ equals 1.0 to 1.2 MeV. For the sake of simplicity we may assume that in an even nucleus, below the energy Δ there are no levels at all, while above this energy the level density is determined by the same law as in odd nuclei. In other words we take $\rho_{\text{even}}(u)$ as

$$\rho_{\text{even}}(u-\Delta) = \begin{cases} 0 & \text{if} \quad u < \Delta \\ \rho_0 \rho(v) & \text{if} \quad u \geqq \Delta, \end{cases} \tag{26}$$

where v is the energy of the excitation of an even nucleus minus the gap energy. The universal function $\rho(v)$ is normalised in a way that $\rho(0) = 1$.

If there is a gap in the spectrum of nuclear levels the radiation transitions in even nuclei may be divided into two groups since there may be a high energy transition into the ground state ($E = u$) from any excited state of an even nucleus alongside the transitions into excited states with the excitation energy $u \geqq \Delta$ ($E < u-\Delta$). The transitions of the former type will be called a transitions and the ground state transitions b transitions (see fig. 2).

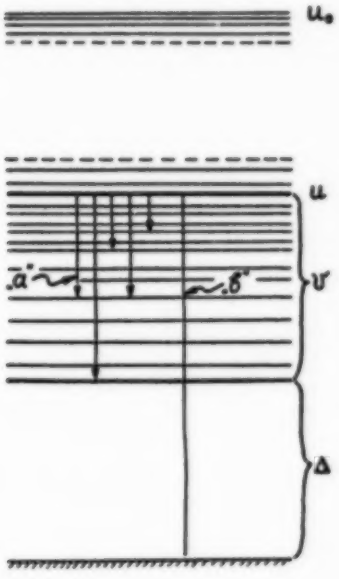

Fig. 2. Qualitative graph of transitions in an even nucleus.

The function $w(u, E)$ in the case of an even nucleus may be written as

$$w_{\text{even}}(u, E) = w_a + w_b \tag{27}$$

where

$$w_a = \frac{E^3 \rho(u-E-\Delta)}{n^*(u)}, \tag{28}$$

$$w_b = \frac{\alpha E^3 \delta(u-E)}{n^*(u)}. \tag{29}$$

The normalisation factor

$$n^*(u) = \int_0^u \{E^3 \rho(u-E-\Delta) + \alpha\delta(u-E)\} dE = \alpha(\Delta+v)^3 + \int_0^v E^3 \rho(v-E) dE. \tag{30}$$

The constant $\alpha = (\overline{M_b^2}/\overline{M_a^2})\rho_0^{-1}$ where M_b and M_a are the matrix elements for b and a transitions.

We assume here that the a and b transitions are both of the dipole type.

Besides, as was assumed above, the average square of the matrix element for a transitions does not depend on energy.

If the function $\zeta(v) = \zeta(u = \Delta+v)$ is substituted for the function $\zeta(u)$, it is easy to show that eq. (21) and differential eqs. (24) and (25) are valid for the function $\zeta(v)$, if only the function $w(u, E)$ is replaced by $w_a(u, E)$, with $u = \Delta+v$ in the latter and the function $n(u)$ is replaced by the function

$$n^*(v) = \alpha(\Delta+v)^3+n(v), \tag{31}$$

where $n(v)$ is represented by eq. (2):

$$\zeta(v) = \int_v^{v_0} w_a(v', v'-v)\zeta(v')dv'+w_a(v_0, v_0-v). \tag{32}$$

The spectrum of γ-quanta of the even nucleus may be written as

$$\nu_{even}(E) = w_a(u_0, E)+\nu_a(E)+\nu_b(E) \tag{33}$$

where $w_a(u_0, E)$ is the spectrum of γ-quanta emitted by the nucleus in the initial state (direct transitions from the initial state of the nucleus into the ground state may be neglected in this term),

$$\nu_b(E) = \alpha E^3\left(\zeta(v)/n^*(v)\right)_{v=E-\Delta} \tag{34}$$

is the spectrum of quanta of the b transitions, while

$$\nu_a(E) = \int_E^{v_0} \{E^3\rho(v-E)\zeta(v)\}/\{n^*(v)\}dv, \qquad v_0 = u_0-\Delta \tag{35}$$

is the spectrum of quanta of the a transitions. The term $\nu_b(E)$ in eq. (33) is to be considered when $E \geqq \Delta$. Since it is assumed that the density of levels in the even nucleus at the energies $u \geqq \Delta$ and the density of levels in the odd nucleus coincide apart from an unessential constant factor, and the initial energy in the former is greater by exactly Δ † than in the latter, the solution of eq. (21), the function $\zeta(u)$ and the spectrum of γ-quanta (22) for the odd nucleus are obtained as particular cases of eqs. (33) and (35) when $\alpha = 0$; the variable v should be regarded as the energy of excitation of the odd nucleus calculated from the ground state ($\Delta = 0$).

The effect of the b transitions in the nucleus with a gap may easily be traced qualitatively. Indeed, the presence of the b transitions results first of all in the accumulation of nuclei with energy close to Δ being weakened: the function $\zeta(v)$ remains finite when $v \to 0$ if $\alpha \neq 0$. Consequently, the function $\nu_a(E)$ vanishes when $E \to 0$. This decrease in the number of low energy quanta is compensated by a respective increase in the number of transitions with energy

† Actually, the difference of neutron binding energies in the even and odd nuclei somewhat exceeds Δ, defined as the magnitude of the energy gap in the spectrum of levels of the even nucleus. This fact is not essential since the spectrum of γ-quanta depends relatively weakly on the initial energy of excitation.

$E > \Delta$. The function $\zeta(v)$ for several values of α and the function $\zeta(u)$ for the odd nucleus ($\alpha = 0$) are represented in fig. 1.

The parameter α may be roughly estimated from the width δ of the energy range $0 < v < \delta$, in which the b transitions are more probable. This evidently takes place when the first term in the expression for $n^*(v)$ (31) exceeds the second. Making them equal each other, one obtains the following relation between the parameters α and δ:

$$\alpha = \frac{n(\delta)}{(\Delta+\delta)^3}. \tag{36}$$

According to eq. (36) $\delta \approx 1$ MeV corresponds to $\alpha \approx 1$ MeV, while $\delta \approx 0.2$ MeV corresponds to $\alpha \approx \frac{1}{1000}$ MeV.

The function $n(v)$ is a sharply increasing function of v. Therefore, when $v \gtrsim \delta$ the first term in eq. (31) is negligibly small if compared with the second. As a result, the spectrum of the even nucleus essentially differs from that of the odd one only in the interval $0 < E < \delta$ where the spectrum of the even nucleus is characterised by a fewer number of quanta and in the interval $\Delta < E \lesssim \Delta+\delta$ where the spectrum of the even nucleus has an additional contribution of the b transitions.

2. Results of Numerical Computations

Now let us proceed to the results of the calculation and its comparison with experimental data. To calculate the spectrum of γ-quanta, eqs. (24) and (32) were numerically integrated with the Strela electronic computor of the Moscow State University.

Two expressions for the function $\rho(v)$ were used:

$$\rho(v) = \exp(v/\tau) \qquad \tau = \text{const} \qquad \text{(version 1)} \tag{37}$$

and

$$\rho(v) = \exp(\sqrt{av}), \quad a = \text{const} \qquad \text{(version 2)}. \tag{38}$$

At the earlier stages of the calculations, the differential equation (24—25) was used to find the function $\zeta(v)$. They were solved according to the standard programme drawn by the Runge-Kutta method with an automatic choice of the magnitude of step ensuring an accuracy no less than 0.1 %. After the programme had been made for solving integral eq. (33) by the method of Euler's broken lines, all calculations were carried out with the integral equation. The step was chosen constant and equal to 0.2 MeV as the comparison of the solutions of the integral equation and those of the differential equation obtained before showed that this step ensured the wanted accuracy of an order of 0.1 %. Integral (35) and the functions $w(v_0, E)$ and $n_b(E)$ were calculated simultaneously with the solution of the integral equation. These functions, together with

the functions $\zeta(v)$ and $n(v)$ were taken out of the computor at points from 0.2 to 6.4 MeV in steps of 0.2 MeV. In all cases the parameter v_0 was taken the same and equal to 6.4 MeV which roughly corresponds to the average binding energy of the neutron in the odd nuclei.

For Δ the value 1.2 MeV was taken in most cases, which roughly corresponds to the position of the peak in the experimental spectra of even nuclei (see below). For the parameter τ in eq. (37) values were taken in the interval from 0.4 to 2.5 MeV and for the parameter a (eq. (38)) in the interval from 2 MeV^{-1} to 60 MeV^{-1}. The constant α was taken to be equal to 0, $\frac{1}{1000}$, $\frac{1}{400}$, $\frac{1}{32}$, 0.2, 0.5 and 2 MeV.

Fig. 3 represents a series of spectra of odd nuclei ($\alpha = 0$) calculated for version 1 of the level density for some values of the parameter τ.

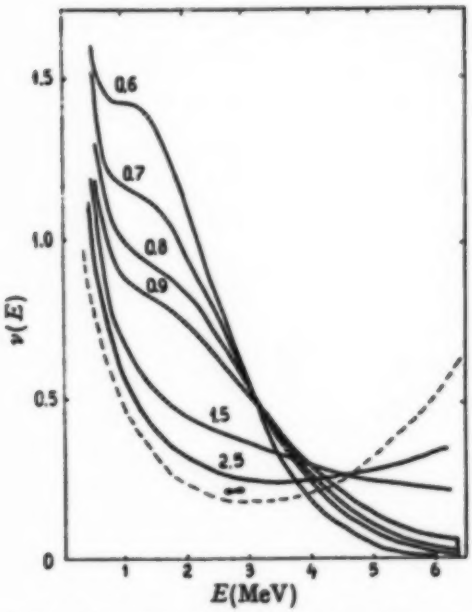

Fig. 3. Spectra of γ-rays calculated for version 1 of level density. Values of the parameter τ (in MeV) are indicated ($\alpha = 0$).

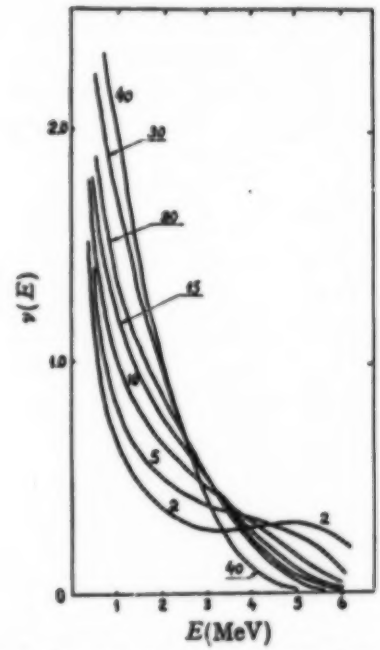

Fig. 4. Spectra of γ-rays calculated for version 2 of level density. Values of parameter a (in MeV^{-1}) are indicated ($\alpha = 0$).

Fig. 4 also represents several theoretical spectra of odd nuclei calculated for the level density (38) (version 2). A dotted line in fig. 3 represents a spectrum of γ-rays for $\tau = \infty$ (or $a = 0$). This spectrum was obtained as a result of an analytical solution of differential equation (24) and the integral $\nu_a(E)$ (eq. (35)) which are possible when $\rho = \text{const}$. As is shown in the previous paper [4]), the best agreement with experiment can be obtained when $\tau = 0.8$ MeV (version 1) or $a = 15$ MeV^{-1} (version 2; the initial temperature of the nucleus $T_0 = (4u_0/a)^{\frac{1}{2}} \approx 1.3$ MeV corresponds to this value of a). This relation between "equivalent" values of the parameters τ and a is quite natural if it is taken into account that the *average*

temperatures are expected to be close to each other. In the same way, the curves $\nu(E)$ for versions 1 and 2 may be made close to each other for other values of τ, if the parameter a is chosen properly. There is a small qualitative difference between the spectra represented in figs. 3 and 4, however. The spectra calculated for exponential density (version 1) have a characteristic bend in the region $E \approx 1$ to 2 MeV. There is no such bend in the curves represented in fig. 4 (version 2). The bend arises because the first term in eq. (33) is a bell-shaped curve (see fig. 5). The second term $\nu_a(E)$ is a uniformly decreasing

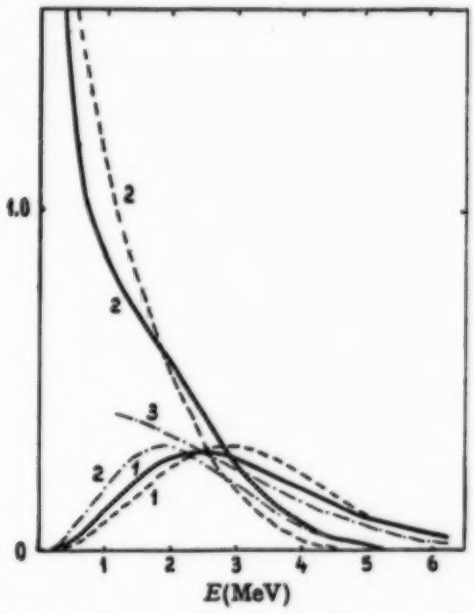

Fig. 5. Composite parts of the total spectrum of γ-rays (see eq. (33)). Solid lines correspond to $\alpha = 0$ for version 1 of level density ($\tau = 0.8$ MeV). Dotted line is the same for version 2 ($a = 15$ MeV^{-1}) and dash-and-dot line corresponds to $\alpha = 0.5$ MeV, $\tau = 0.8$ MeV. Curves marked 1 are the functions $w(u_0, E)$, the function $\nu_a(E)$ is marked 2 and the function $\nu_b(E)$ is marked 3.

function. In the case 2 the spectrum $\nu_a(E)$ proves to be rich in soft quanta and the maximum of the function $w(u_0, E)$ has no explicit effect on the form of the total spectrum as a result of a more sharp dependence of level density (38) on energy at $u \lesssim 1$ MeV.

The presence of a bend at $E \approx 1$ to 2 MeV in the spectra of all studied deformed odd nuclei [4]) shows that the level density at low energies ($\lesssim 1$ MeV) decreases more smoothly than exp $(\sqrt{au})$. It is noteworthy that no bend is observed in the spectra of spherical nuclei.

As is clear from the comparison of curves represented in fig. 5 the contribution of the function $\nu_a(E)$ to the total spectrum is rather small (< 10 %) for the γ-ray energy $E \gtrsim 5$ MeV. The radiation transitions with such energy are almost exclusively those from the initial state. Their average intensity is approximately equal to

$$w(u_0, u_0) \approx \frac{u_0^3 \rho(0)}{n(u_0)} \approx \frac{u_0^3}{6\tau^4 \rho(u_0)} \approx 0.5\ \%, \tag{39}$$

which does not differ much from the experimental value (≈ 0.5 to $3\ \%$).

Fig. 6 represents γ-spectra calculated according to eqs. (31—35)for $\alpha \neq 0$ (even nuclei) and for $\tau = 0.8$ MeV (version 1).

The experimental spectra of deformed even nuclei is characterised, as compared with odd nuclei, by a greater number of quanta of relatively higher energy (≈ 2 to 4 MeV) while there are comparatively fewer soft quanta ($E \lesssim 1.5$ MeV)

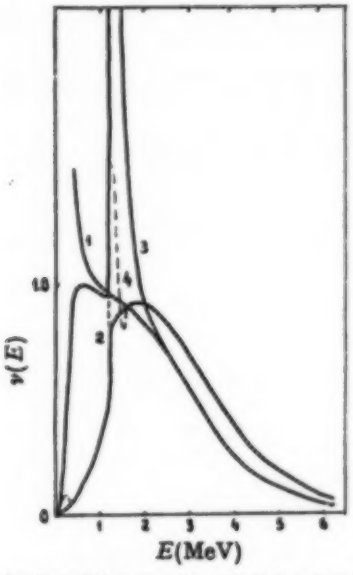

Fig. 6. Spectra of even nuclei calculated for version 1 of density levels for $\tau = 0.8$ MeV for various values of α. Curve 1 corresponds to $\alpha = 0$, curve 2 corresponds to $\alpha = 0.5$ MeV, curve 3 corresponds to $\alpha = 1/400$ MeV; for curve 4, α is taken as a step curve (curve 1 in fig. 7), $\alpha_1 = 1/400$ MeV, $\alpha_2 = 0.5$ MeV and $v^* = 0.4$ MeV.

in their spectra and, besides, there is a sharp peak with a width $\lesssim 0.5$ MeV at $E \approx 1$ MeV [4]). The first two peculiarities impel one to choose a comparatively large value of α. For exponential density (version 1) the best agreement for even nuclei is obtained when $\alpha = 0.5$ and $\tau = 0.8$ MeV [4]), i.e., for the same value of τ as for odd nuclei lying in this region.

The above-mentioned peculiarity of the density (38) leads to a considerable difference of spectra calculated for versions 1 and 2 in the case of even nuclei.

In version 2 the spectrum of γ-quanta is characterised by a far larger value of $\nu(E)$ in the region $E \lesssim 1$ MeV and decreases with the growth of E more steeply than the spectrum calculated for exponential level density (version 1).

Therefore, $a \approx 5$ MeV^{-1} has to be taken to ajust the theoretical spectrum calculated for version 2 to the experimental spectra of even deformed nuclei. Such a small value of this parameter ($T_0 \approx 2.3$ MeV) seems rather improbable, especially if one takes into account that a proves to be equal to 15 MeV^{-1} for

odd nuclei. Therefore, it may be concluded that the shape of the spectrum of the even nuclei testifies to a weak dependence of the temperature of deformed even nuclei on the energy above the gap, at least if compared with eq. (38).

Let us now turn to the third peculiarity of the spectra of even deformed nuclei, i.e., a sharp peak at $E \approx 1$ MeV. In principle, such a peak appears when a small value of α is taken, ranging from $\frac{1}{400}$ to $\frac{1}{1000}$ MeV^{-1} (see fig. 6). Yet with such α the theoretical spectrum does not practically differ from the spectrum for $\alpha = 0$ (i.e., the spectrum of the odd nucleus) anywhere, except in the region of the peak and the corresponding region of $E \lesssim 0.5$ MeV (cf. curve 1 and curve 3 on fig. 6). On the otherhand, no sharp maximum arises at all when α is of order unity, though the general form of the theoretical spectrum in this case is in good agreement with the experimental one for the deformed even nuclei. It is natural to try to solve this contradiction by considering the dependence of α on the energy of nuclear excitation. Indeed, all three peculiarities of the spectrum of deformed even nuclei may be accounted for qualitatively

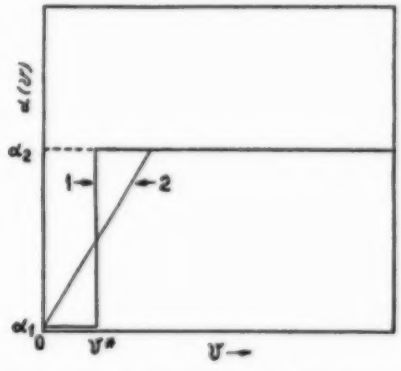

Fig. 7. Two versions of the dependence of α on v for which the spectra of γ-rays were calculated.

if it is assumed that the parameter α depends on energy, just as is represented in fig. 7 (curve 1), taking $v^* \approx 0.4$ MeV. With this α the spectrum of γ-quanta will coincide with that calculated for $\alpha = 0.5$ in the range of the energy of γ-quanta $v^* \lesssim E < \Delta$ and $E > \Delta + v^*$, while in the region $\Delta < E \lesssim \Delta + v^*$ the spectrum will have a sharp maximum as when α is small. This may easily be traced by considering the dependence of $\nu_b(E)$ on α: $\nu_b/\Delta = \zeta(v = 0)$ irrespective of α. The spectrum of γ-quanta was also calculated for a non-constant α, having the form of a step (curve 1 in fig. 7) and a smoothed curve (curve 2) for the following values of the parameters α_1, α_2 and v^*: $\alpha_2 = \alpha_1 + 0.5$ MeV, $\alpha_1 = \frac{1}{400}$; $v^* = 0.4$, 0.8, $\tau = 0.7$, 0.8, 0.9 MeV. The parameter Δ was assumed to equal 0.8 and 1.2 MeV. The level density was used in the form (37).

As an example, fig. 6 also represents a spectrum calculated for the function $\alpha(v)$ taken as a step function. The discontinuity is to be attributed to the sharp jump in α and of course will be smoothed down if the region of the jump in α is somewhat spread over. The spectra calculated for curve 2 in fig. 7 do not

practically differ from the spectra with the constant $\alpha = \alpha_2$. The spectrum represented in fig. 6 for the variable α possesses all features of the experimental spectra of even nuclei, which warrants the conclusion that in the region ≈ 0.5 MeV over the gap the value of α is very small if compared with the remaining region of energy. Neither the specific value of the parameter α near the gap (α_1), nor the assumptions on the multipolarity of transitions through the gap are important for the essential peculiarities of the shape of the spectrum.

So far the structure of levels of the deformed even nuclei above the gap has been investigated quite inadequately and sheer guesses may only be made as to the origin of forbiddenness for the transitions through the gap when the excitation of the nucleus is not too high. The formation of nuclei with large spins towards the end of the process of emission of γ-qaunta might be one of the causes of such forbiddenness. This, however, can hardly be so, since near the ground state of even deformed nuclei there are always closely located rotational levels with sufficiently large spins to which the radiation transition could be possible. Selection of transitions by parity cannot lead to a sharp change of α either, since the selection of transitions into the ground state by parity also holds for the transitions from the strongly excited states. An additional selection rule connected with the conservation of the projection of the momentum on the axis of the nucleus in deformed nuclei (quantum number K) is a possible explanation of the dependence of α on energy, similar to that represented in fig. 7. The ground state is characterised by $K = 0$. The selection rule with respect to K, $\Delta K = 0, 1$ would select only those excited states for which $|K| = 0, 1$ in the case of dipole transitions. If we assume that there are no states with such K near the gap, with the exception probably of the lowest state, the dipole transitions would prove impossible, while the radiation transitions through the gap less probable. This is borne out by the well studied schemes of the decay of W^{182} [6]) and a number of other deformed even nuclei [7]). The quantum number K, on the other hand, is only an approximate adiabatic integral of motion and it may well be supposed that the forbiddenness connected with K is not essential if it concerns the transition into the ground state from the strongly excited states of the nucleus: the wave function of such states is evidently a superposition of states with various values of K, including such for which the transition into $K = 0$ is allowed. This makes it possible to suppose that the ratio of the matrix elements $\overline{M_b^2}/\overline{M_a^2}$ is in general close to the unity. The pre-exponential factor in eq. (26) then coincides with α^{-1} from which the average distance between the levels of nucleus at the binding energy may be estimated by using the values of the parameters α and τ, determined from γ-spectra. By order of magnitude this value should coincide with the average distance between the neutron resonances (changing of a nuclear spin in the process of deexcitation is not large and may be neglected). This actually takes place, as may be checked. Reversing this argument, an inference may be drawn

on the approximate equality of the matrix elements on the basis of the obtained value of α ($\alpha \approx 0.5$ MeV). It will be emphasized, however, that only a rough estimate is aimed at in this discussion.

The calculation of the spectrum of γ-quanta was also carried out for certain values of the parameter under the assumption that the radiation transitions through the gap (of the b type) are quadrupole. In all cases the shape of the calculated spectrum sharply differs from the experimental one.

It is noteworthy to compare the data on the distribution of nuclear levels with the results obtained by other methods. The most direct method is a direct calculation of the number of levels below certain energy. This method was recently used by T. Erikson [8]) to determine the energy dependence of level density below the neutron binding energy for certain nuclei with $A < 60$. The distribution of levels agrees with eq. (37), the parameter τ being equal to 1.0 to 1.2 MeV. This result agrees with the determination of level densities by the spectrum of secondary particles in the reaction (α, α') in the same region of nuclei [9]). A somewhat better agreement with eq. (38) is indicated for the reaction (p, p') [10]). All these results unfortunately refer to lighter nuclei, which probably accounts for the discrepancy between the value of τ obtained from γ-spectra (0.8 MeV) and directly by the count of levels (1.0 to 1.2 MeV). Incidentally, the results of the analysis of γ-spectra point to the fact that there is no strong dependence of the parameters characterising the dependence of level density on energy when A changes within the range of 100 to 200 [4]). The absence of any perceptible dependence of temperature on atomic weight was also indicated in ref. [10]).

The spectra of nuclei close to the magic ones, on the other hand, are characterized by relatively higher values of τ (or respectively smaller values of a). Thus, for gold the best agreement with the experimental spectrum is obtained when $a \approx 3$ to 5 MeV^{-1}. It will also be noted that the average distribution of intensity in the spectra of light odd nuclei [5]) qualitatively agrees with the theoretical one calculated under the assumption that $\rho = \text{const.}$ (fig. 3), which does not contradict other data on the level densities of these nuclei.

The temperature of the nucleus at the neutron binding energy may also be determined by the density of neutron resonances, the value of the initial temperature of nuclei in the region of rare earth elements obtained being equal to 0.6 to 0.7 MeV, which corresponds to the value of the parameter $a = 40$ to 60 MeV^{-1}. This value considerably differs from the above-mentioned value of $a = 15$ MeV^{-1} obtained from γ-spectra. This difference decreases considerably if one takes into account that the expression for level densities with given momentum for a Fermi-gas contains a pre-exponential factor decreasing with energy approximately as u^{-2}. If, on the other hand, one tries to approximate the function $u^{-2} \exp(\sqrt{au})$ by the expression of the $\exp(\sqrt{a^* u}+c)$ type, choosing the constants a^* and c so as to fit the points, say $u = 2$ MeV and

$u = 6.5$ MeV, a somewhat smaller value will be obtained for the constant a^*. Thus if $a = 30$ MeV^{-1} or 60 MeV^{-1}, the constant a^* is equal to 20 MeV^{-1} and 35 MeV^{-1} respectively. It is just these values of the "effective" constant a^* which should be compared with the value of a obtained from γ-spectra or in other similar cases if the level density is represented by an expression of type (38).

Similarly, if the function $u^{-2}\exp(\sqrt{au})$ is approximately represented as $\exp((u/\tau)+c)$ the constant τ will be equal to 0.7 MeV for $T_0 = 0.6$ MeV, determined from neutron resonances, i.e., a value not too different from the value 0.8 MeV obtained from γ-spectra †.

As for a possibility of choosing between distributions (37) and (38), both forms of the distribution of levels lead to rather similar results, as was mentioned above. Some features of the shape of spectra of odd deformed nuclei in the region $E \approx 1$ to 2 MeV as well as the comparison of the theoretical spectra and those of even deformed nuclei compel us, however, to give preference to exponential formulae (37) or at any rate to draw the conclusion that the dependence of the level densities on the energy near the gap is weaker than that given by eqs. (26) and (38). This result agrees with what is obtained if nuclear pairing is taken into consideration. In deformed nuclei pairing of particles leads to a difference of the dispersion of elementary excitations from the dispersion of free particles. The energy of excitation is given by the expression [11])

$$E_\nu = \sqrt{\varepsilon_\nu^2 + (\tfrac{1}{2}\Delta)^2} \tag{40}$$

where ε_ν is the energy of a free particle calculated from the Fermi level. The level density of elementary excitation, $\mathrm{d}\nu/\mathrm{d}E_\nu$, decreases with energy. This leads to an almost constant level density at lower excitations in odd nuclei and at the energy u in the region $\Delta < u \lesssim 2\Delta$ in even nuclei when there are only two quasi-particles. As the energy of excitation and hence the number of destroyed pairs increases, the level density begins to increase rapidly, which increase is described closely by an exponential law [12]). In other words, given the finite energy necessary to free the particles, the temperature of the system depends on energy more weakly than for free particles. At sufficiently large energies the pairing effect vanishes and the level density is described by an expression of type (38).

The result of an analysis of γ-spectra of deformed nuclei agrees very well with the pattern described above. Unfortunately, in spherical nuclei the grouping of levels in shells and subshells greatly interferes even with a qualitative description of the energy dependence of the level density. The fact that the level density of odd spherical nuclei in the range of energy $u \lesssim 1$ MeV increases more rapidly may be accounted for either by the pairing energy being small or

† These results were obtained in cooperation with Y. V. Adamchuk.

generally by the particle dispersion law differing from eq. (40). For two free odd particles the level density grows as u^2.

The authors are indebted to Prof. A. N. Tikhonov and Docent A. V. Lukyanov whose courtesy made it possible to carry out calculations with the electronic computor of the Moscow State University.

Note added in proof: Data on the shape of the γ-spectra of even deformed nuclei as a function of energy may also be obtained if it is assumed that there are no nuclear levels in the region between $u = 1$ to 1.2 MeV (Δ in our notation) and $u = \Delta + v^* \approx \Delta + 0.5$ MeV. This may occur if the levels at 1 MeV are collective ones, such as γ-vibrational and connected rotational levels. The energy $\Delta + v^*$ must then be identified as a gap energy. Unfortunately, at the present time there are not enough experimental data to support strongly either of the two indicated assumptions on the level structure of real deformed even nuclei in the MeV region.

References

1) L. V. Groshev, A. M. Demidov, V. N. Lutsenko and V. I. Pelekhov, Proc. of the Second International Conference on Peaceful Uses of Atomic Energy, vol. **15**, p. 138, P/2029
2) J. Blatt and V. Weisskopf, Theoretical Nuclear Physics, chapter XII
3) Nuclear Physics, edited by Segrè, vol. II, chapter I
4) L. V. Groshev, A. M. Demidov and V. I. Pelekhov, Nuclear Physics **16** (1960) 645
5) L. V. Groshev, B. P. Adyasevich and A. M. Demidov, Reports of the Soviet Delegation at the International Conference for Peaceful Uses of Atomic Energy, Physical Research, p. 252 (USSR Academy of Sciences, 1955)
6) J. J. Murray, F. Boehm, P. Marmier and J. DuMond, Phys. Rev. **97** (1955) 1007;
G. Alaga, K. Adler, A. Bohr and B. Mottelson, Mat. Fys. Medd. Dan. Vid. Selsk. **29**, No. 9 (1959);
C. J. Gallagher, J. O. Newton and V. S. Shirley, Phys. Rev. **113** (1959) 1298;
C. J. Gallagher and J. O. Rasmussen, Phys. Rev. **112** (1958) 1730
7) B. F. Dzhelepov and L. K. Peker, Disintegration Schemes of Radioactive Isotopes (USSR Academy of Sciences, Moscow, 1958)
8) T. Erikson, Nuclear Physiscs **11** (1959) 481
9) H. W. Fullbright, N. O. Lassen and N. O. Roy Poulsen, Mat. Fys. Medd. Dan. Vid. Selsk. **31**, No. 10 (1959)
10) B. L. Cohen and A. G. Rubin, Phys. Rev. **111** (1959) 1958
11) S. Belyaev, Mat. Fys. Medd. Dan. Vid. Selsk. **31** No. 11 (1959)
12) V. Strutinski, Congr. Int. Phys. Nucl. Paris, 1958

2.B:2.G:
2.L.

Nuclear Physics **16** (1960) 674—682; © *North-Holland Publishing Co., Amsterdam*
Not to be reproduced by photoprint or microfilm without written permission from the publisher

CIRCULARLY POLARIZED GAMMA RAYS FROM DIRECT NUCLEAR REACTIONS

G. R. SATCHLER

Oak Ridge National Laboratory, Oak Ridge, Tennessee

Received 18 January 1960

Abstract: The residual nuclei following a reaction are left in a polarized state in general. One way of measuring this polarization is to observe any γ-rays the residual nucleus emits. Their angular distribution reveals the even moments of the polarization while their circular polarization depends upon the odd moments. Following a general discussion of circular polarization, and the predictions of the direct interaction picture of nuclear reactions, simple cases of stripping reactions and inelastic scattering are considered. Valuable information can be obtained concerning both the reaction mechanism and the reduced widths and nuclear spins involved.

1. Introduction

Measurement of the angular distribution of γ-rays following a nuclear reaction A(a, b)B, in coincidence with the outgoing particles b, has proved a valuable test of whether the reaction is "direct" [1, 2]). It also yields more information on the reduced widths (or transition amplitudes) and the nuclear spins involved [3]) and can be used for more detailed tests of theories of the reaction mechanism [4, 5, 6]). The purpose of this note is to point out that additional information of this nature can be obtained by studying the circular polarization of these γ-rays †. It has been suggested that this is a possible alternative to measuring the polarization of the particles b, say in a deuteron stripping reaction [7]), but it can yield additional information which supplements that from the particle polarization. This is readily understandable, since the γ-ray emission depends upon the polarization state of the recoiling residual nucleus B. In general this will depend upon a different combination of reduced widths from that determining the polarization of b. Further, if the nucleus B, before the γ-emission, has a spin J_B greater than the spin S_b of the emitted particle b, higher spin multipole moments (or statistical tensors [8])) will be required to describe the polarization state of B than of b, so that more parameters can be extracted from the γ-ray measurement. For example, if b is a nucleon of spin $S_b = \frac{1}{2}$, it can only have vector polarization, or a spin dipole moment, while if $J_B > \frac{1}{2}$ its orientation state may include 2^k-pole spin moments up to $k = 2J_B$.

† Measurement of their linear polarization does not yield new information on the reaction mechanism, although of course it can give the parity change in the γ-transition.

A preliminary study of circularly polarized γ-rays from deuteron stripping reactions was given earlier in a privately circulated manuscript [9]). This is extended here to other direct reactions, but rather than considering the general formulae in detail we take simple illustrative examples of stripping reactions and inelastic scattering.

Since the phenomenon under study is essentially the polarization of the residual nucleus B, the discussion also applies to the emission of other radiation. In particular the observation of an up-down asymmetry in the emission of β-particles [10]), or of the polarization of internal conversion electrons [11]), depends upon the same nuclear polarization moments as the circular polarization of γ-rays. All these measurements have to be made in coincidence with particles b emitted in a definite direction, and the choice between them is one of practical expedience; in most cases the γ-ray would seem easiest to measure.

2. General Theory

The angular distribution of circularly polarized photons from the reaction A(a, b)B(γ)C, measured in coincidence with particles b emitted in some definite direction, has the form

$$W_\sigma = \sum_{kq} (-\sigma)^k a_{kq} C_{kq}(\theta\phi), \tag{1}$$

independently of any assumption about the reaction mechanism. The C_{kq} is a renormalized spherical harmonic, $C_{kq}(\theta\phi) = (4\pi/2k+1)^{\frac{1}{2}} Y_k^q(\theta\phi)$, so that $C_{00} = 1$ and C_{k0} is the Legendre polynomial $P_k(\cos\theta)$. The polarization index $\sigma = \pm 1$ is the projection of the photon spin along its direction of motion; the usual optical convention is to call $\sigma = -1$ right hand and $\sigma = +1$ left hand, although some authors use the opposite convention. Photons of a plane wave travelling along the positive z-axis have electric vectors proportional to $(\mathbf{e}_x + i\sigma\mathbf{e}_y) \exp i(kz - \omega t)$, if $\mathbf{e}_x$, $\mathbf{e}_y$ are unit vectors along the x- and y-axes of a right handed system. The degree of circular polarization is then given by

$$C = \frac{W_- - W_+}{W_- + W_+} = \frac{\sum_{k\,\mathrm{odd},\,q} a_{kq} C_{kq}(\theta\phi)}{\sum_{k\,\mathrm{even},\,q} a_{kq} C_{kq}(\theta\phi)}. \tag{2}$$

The denominator of eq. (2) is proportional to the γ-ray distribution seen by a polarization-insensitive counter [4, 5]). Additional information can be obtained from the polarization measurement because of the odd k values appearing in the numerator of eq. (2). If the z-axis is chosen along the γ-ray direction, and using $C_{kq}(00) = \delta_{q0}$, eq. (2) reduces to

$$C = \Big(\sum_{k\,\mathrm{odd}} a_{k0}\Big) \Big/ \Big(\sum_{k\,\mathrm{even}} a_{k0}\Big). \tag{3}$$

The coefficients a_{kq} have the form

$$a_{kq} = \rho_{kq}(J_B J_B) \sum_{LL'} F_k(LL' J_C J_B) C_L C_{L'}, \tag{4}$$

where J_B, J_C are the spins of nuclear states B and C respectively, and C_L^2 is the relative intensity of 2^L-pole γ-ray in the transition B to C. The F_k are the well-known γ-ray correlation coefficients; numerical tables are available both for even [8]) and odd [12]) values of k. All information on the reaction A(a, b)B is contained in the statistical tensors $\rho_{kq}(J_B J_B)$ which, of course, depend upon the direction of emission of particle b. They are the spin moments mentioned in the Introduction, which describe the state of orientation of the spin J_B of the nucleus before it emits the γ-ray. The ρ_{kq} behave like the spherical harmonic Y_k^{q*} under rotations of the coordinate axes, so that eq. (1) has the proper scalar product form. As usual, k is limited to $k \leqq 2J_B$, with $-k \leqq q \leqq k$; the appearance of odd k means C need not vanish even when $J_B = \frac{1}{2}$ and the unpolarized γ-distribution is isotropic. (The γ-parameter F_k further limits $k \leqq L+L'$). Since W is real, ρ_{kq} (and thus also a_{kq}) has the symmetry $\rho_{kq} = (-)^q \rho^*_{k-q}$, so that ρ_{k0} and a_{k0} are real.

If the z-axis were chosen in the reaction plane containing particles a and b, we have the further property that the ρ_{kq} and a_{kq} are real for even k, imaginary for odd k; hence the a_{k0} vanish for odd k and, from eq. (3), γ-rays emitted in the reaction plane have zero circular polarization. This could be anticipated on general grounds. C is the expectation value of an axial vector (the photon spin) which is directed along the photon direction of motion because of the transverse nature of its vibrations. The only other axial vector in the problem is $\mathbf{k}_a \times \mathbf{k}_b$, where $\mathbf{k}_a$, $\mathbf{k}_b$ are the wave vectors of particles a and b. So the observed circular polarization must be proportional to the scalar product of these two axial vectors. This is zero for γ-rays in the reaction plane and a maximum for γ-rays perpendicular to the plane (however, C itself need not be a maximum for γ-rays along $\mathbf{k}_a \times \mathbf{k}_b$). This is reflected in eq. (2) if the z-axis is chosen along $\mathbf{k}_a \times \mathbf{k}_b$, so that θ is the angle between the γ-ray and $\mathbf{k}_a \times \mathbf{k}_b$. With these axes ρ_{kq} only exist for even q, so the numerator of eq. (2) is a series of *odd* powers of $\cos\theta$. Thus C also changes sign upon reflection through the reaction plane, so that it vanishes if averaged over the directions in azimuth of particle b. The evenness of q gives rise to the additional symmetry $C(\theta\phi) = C(\theta, \pi+\phi)$ in these axes.

So far we have made no assumption about the reaction mechanism †. If the reaction amplitude for a transition from a state with spin components M_A, m_a to one with M_B, m_b is $\langle \mathbf{k}_b, J_B M_B, s_b m_b | T | \mathbf{k}_a, J_A M_A, s_a m_a \rangle$, the ρ_{kq} are given by

$$\rho_{kq}(J_B J_B) = \sum \langle J_B M_B, J_B q - M_B | kq \rangle (-)^{J_B - M_B + q} \times \langle \mathbf{k}_b, J_B M_B, s_b m_b | T | \mathbf{k}_a, J_A M_A, s_a m_a \rangle \times \langle \mathbf{k}_b, J_B M_B - q, s_b m_b | T | \mathbf{k}_a, J_A M_A, s_a m_a \rangle^*, \quad (5)$$

summed over M_A, m_a, M_B and m_b; $\langle a\alpha, b\beta | c\gamma \rangle$ is a Clebsch-Gordan coefficient

† Thus, the discussion applies equally to any triple correlation experiment in which the third transition emits a γ-ray whose circular polarization is observed.

for the addition of angular momenta. The differential cross-section for particles b is proportional to $\rho_{00}(J_B J_B) = (2J_B+1)^{-\frac{1}{2}} \sum |\langle T \rangle|^2$. If we assume the reaction to be "direct", we may calculate the reaction amplitudes, for example in a distorted-wave Born approximation where T is replaced by V, the interaction assumed responsible for the reaction [1, 4, 5]). It is convenient to express $\langle T \rangle$ in terms of amplitudes $A_m(jls)$ for the transfer of definite total angular momentum j, made up from the change l in relative orbital motion and s the change of spin between a and b; m is the z-component of l. According to the vector equations

$$\mathbf{J}_B = \mathbf{J}_A + \mathbf{j}, \qquad \mathbf{j} = \mathbf{l} + \mathbf{s}, \qquad \mathbf{s} = \mathbf{s}_a - \mathbf{s}_b, \tag{6}$$

we can write

$$\begin{aligned}\langle \mathbf{k}_b, J_B M_B, s_b m_b | T | \mathbf{k}_a, J_A M_A, s_a m_a \rangle = \sum_{jls} & \langle J_A M_A, jM_B - M_A | J_B M_B \rangle \\ & \times \langle lm, sm_a - m_b | jM_B - M_A \rangle \langle s_a m_a, s_b - m_b | sm_a - m_b \rangle \\ & \times (-)^{s_b - m_b} (2l+1)^{\frac{1}{2}} A_m(jls).\end{aligned} \tag{7}$$

The A_m also depend on $\mathbf{k}_a$ and $\mathbf{k}_b$, but we will not indicate this explicitly. We describe the A_m for a few simple cases below; a more detailed discussion of angular momentum in direct reactions will be given elsewhere. For purposes of orientation, however, consider the simplest model of a *surface* direct reaction in Born approximation, in which the particles a and b are described by plane waves and T is replaced by a spin-independent contact interaction [2]). Then the A_m become

$$A_m(jls) = a(jls) C_{lm}(\theta\phi)^* j_l(QR), \tag{8}$$

where $a(jls)$ plays the role of a reduced width and R is the nuclear radius. The recoil momentum $\mathbf{Q} = \mathbf{k}_a - \mathbf{k}_b$ (the target is assumed infinitely heavy), and $(\theta\phi)$ are the polar angles of $\mathbf{Q}$. Eq. (8) exhibits the general property of the A_m, that they transform under coordinate rotations like the spherical harmonic C^*_{lm}.

With eq. (7), the statistical tensors (5) become

$$\begin{aligned}\rho_{kq}(J_B J_B) = \sum_{jj'll's} & [(2l+1)(2l'+1)(2j+1)(2j'+1)]^{\frac{1}{2}} (2J_B+1)(-)^{J_A - J_B - s + l'} \\ & \times W(jj' J_B J_B; kJ_A) W(ll' jj'; ks) \rho_{kq}(jls, j'l's),\end{aligned} \tag{9}$$

where the W's are Racah coefficients and

$$\rho_{kq}(jls, j'l's) = \sum_m A_m(jls) A_{m-q}(j'l's)^* (-)^{l'+q-m} \langle lm, l'q-m | kq \rangle,$$

so

$$\rho_{00}(J_B J_B) = (2J_B+1)^{\frac{1}{2}} \sum_{jlsm} |A_m(jls)|^2. \tag{10}$$

In particular, if the A_m are hermitian in the sense that $A_m = (-)^m A^*_{-m}$ (as they are in the approximation (8)), it soon follows from eqs. (9) and (10) that $\rho_{kq}(J_B J_B)$ vanishes when k is odd. Hence in these cases the circular polarization

C is also zero; in particular this is the prediction of the statistical theory of compound nucleus reactions.

Other qualitative predictions can be made if the distorted wave Born approximation is used, because the initial and final state distortions have opposing effects in some ways. For example it was argued on semi-classical grounds [2]) that in a stripping reaction the two distortions tended to produce polarizations of opposite sign for the outgoing particles b, and this may be demonstrated analytically when k_a and k_b have similar magnitudes, and a zero range interaction is used. Under similar circumstances one may also show for any direct reaction that interchanging the initial and final state distorted waves (neglecting spin-orbit coupling) has the effect of replacing the tensors ρ_{kq} in eq. (4) by $\rho'_{kq} = (-)^k \rho_{k-q}$, when the z-axis is chosen along $\mathbf{k}_a \times \mathbf{k}_b$ and the x-axis along $\mathbf{k}_a - \mathbf{k}_b$. This corresponds to a rotation by π about $\mathbf{k}_a - \mathbf{k}_b$. The circular polarization then becomes $C'(\theta\phi) = -C(\theta, -\phi)$. Thus if the distorted waves for a and b were the same, we would also have $C' = C$. This does not lead to complete extinction of the polarization; rather, $C = 0$ in the (x, y), (y, z) and (x, z) planes. In particular, C vanishes along $\pm \mathbf{k}_a \times \mathbf{k}_b$, unless the total intensity itself vanishes in this direction.

3. Special Cases †

3.1. STRIPPING REACTIONS

If particle a is a complex which may be regarded as made up of b and another particle x, the reaction may proceed by the stripping of a, x being captured by the target and b being released. This is the basis of the deuteron stripping reaction [2]). If b and x are in an s-state of relative motion when they form particle a, the spin transfer s is just the spin of particle x, while j and l are the total and orbital angular momentum with which x is captured by the target. The amplitude A_m then becomes

$$A_m(jls) = \theta_{jl}(2s_a+1)^{\frac{1}{2}}(2s+1)^{-\frac{1}{2}} B_{lm}, \tag{11}$$

where θ_{jl} is the "reduced width" for the capture and B_{lm} is the stripping integral. Eq. (10) may then be written

$$\rho_{kq}(jls, j'l's) = (2s_a+1)(2s+1)^{-1}\theta_{jl}\theta_{j'l'}\rho_{kq}(ll'). \tag{12}$$

With deuteron stripping, x is a nucleon and we have $s_a = 1$, $s_b = s = \frac{1}{2}$, while the B_{lm} and $\rho_{kq}(ll')$ have been discussed in detail in ref. [5]).

If there is only one l value, using eq. (12) we may write $\rho_{kq}(J_B J_B) = c_k(l)\rho_{kq}(ll)$. Further, if $l = 1$, we have $\rho_{20}(11) = (\frac{1}{2})^{\frac{1}{2}}\rho_{00}(11)$ if the z-axis is chosen along $\mathbf{k}_a \times \mathbf{k}_b$ [5]), and the polarization (3) for γ-rays in this

† In these, it is assumed that the effect of spin-orbit coupling on the distorted waves for a and b may be neglected.

direction becomes

$$C = \frac{(3)^{\frac{1}{2}} c_1 F_1 \langle m \rangle}{(2)^{\frac{1}{2}} c_0 + c_2 F_2}, \tag{13}$$

where $\langle m \rangle$ is the mean value of the projection of l on the z-axis:

$$\langle m \rangle = \sum_m m |B_{lm}|^2 / \sum_m |B_{lm}|^2. \tag{14}$$

The vector polarization of particles b is also proportional to $\langle m \rangle$, hence it varies with the angle of b in the same way as eq. (13). The observation of this similarity would provide evidence for the distorted wave theory of the reaction. The polarization of b, however, depends on a different combination of reduced widths θ_{jl}. In a (d, p) stripping, the proton polarization for $l = 1$ is given by [5])

$$P = \tfrac{1}{3}\langle m \rangle (\tfrac{1}{2}\theta_{\frac{1}{2}}^2 - \theta_{\frac{1}{2}}^2)(\theta_{\frac{1}{2}}^2 + \theta_{\frac{1}{2}}^2)^{-1},$$

while, as an example for comparison, a transition with $J_A = 1$, $J_B = \frac{1}{2}$, $L = 1$, $J_C = \frac{3}{2}$ would give from eq. (13)

$$C = \tfrac{1}{6}\langle m \rangle (\tfrac{5}{2}\theta_{\frac{1}{2}}^2 + (8)^{\frac{1}{2}}\theta_{\frac{1}{2}}\theta_{\frac{3}{2}} - \theta_{\frac{3}{2}}^2)(\theta_{\frac{1}{2}}^2 + \theta_{\frac{3}{2}}^2)^{-1}.$$

The most notable difference is that cross terms between different j occur in C but not in P. Further, while the proton polarization P from a (d, p) stripping reaction is limited to $\leqq \frac{1}{3}$, there is no such restriction on the γ-ray polarization C. For example, capture with $l = 1$ by a spin zero target followed by dipole emission to $J_C = \frac{1}{2}$ gives (along $\mathbf{k}_d \times \mathbf{k}_p$), $C = -\langle m \rangle$ whether $J_B = j = \frac{1}{2}$ or $\frac{3}{2}$; experimentally $\langle m \rangle$ often approaches its maximum value of one.

3.2. INELASTIC SCATTERING

If the scattering interaction is spin independent (and exchange is ignored) only $s = 0$ (and thus $j = l$) transfers contribute to eqs. (7) or (9). This, of course, is always true when the scattered particles are spinless, and is usually assumed when the scattering excites collective oscillations in the target [2, 6, 13]). The $s \neq 0$ terms correspond to "spin flip", and must be taken into account in a more detailed description of, say, nucleon scattering [4]). They are also necessary to give non-zero polarization of the outgoing particles b, but we shall assume them negligible here, and write

$$A_m(jls) = \delta_{s0}\delta_{jl}(2s_a+1)^{\frac{1}{2}} B_{lm}. \tag{15}$$

The statistical tensor (9) becomes

$$\rho_{kq}(J_B J_B) = \sum_{ll'} [(2l+1)(2l'+1)]^{\frac{1}{2}} (2s_a+1)(2J_B+1)(-)^{J_A - J_B + k - 1} W(ll' J_B J_B; k J_A) \rho_{kq}(ll'), \tag{16}$$

where, as in the stripping case,

$$\rho_{kq}(ll') = \sum_m B_{lm} B^*_{l'm-q}(-)^{l'+q-m}\langle lm, l'q-m|kq\rangle \tag{17}$$

and

$$\rho_{00}(ll') = \delta_{ll'}(2l+1)^{-\frac{1}{2}} \sum_m |B_{lm}|^2.$$

The recently proposed diffraction model of inelastic scattering, in the form discussed so far [6]), leads to $B_{lm} = (-)^m B^*_{l-m}$ and hence, as pointed out by Blair, zero circular polarization. The distorted wave Born approximation will, in general, predict a non-zero polarization so that its measurement is of some interest [14]). Ignoring spin, the scattering interaction may be expanded in multipoles of the coordinates $(r\theta\phi)$ of the scattered particle,

$$V(\mathbf{r}, \xi) = \sum_{\lambda\mu} v_{\lambda\mu}(r, \xi) C_{\lambda\mu}(\theta\phi), \tag{18}$$

where ξ represents the internal coordinates of the target. Then in Born approximation we replace T by V in expressions (7) and soon find

$$(2l+1)^{\frac{1}{2}} B_{lm} = \langle \mathbf{k}_b | V_{lm} | \mathbf{k}_a \rangle \tag{19}$$

where

$$V_{lm}(r\theta\phi) = C^*_{lm}(\theta\phi)\langle J_B || v_l^* || J_A\rangle$$

and the reduced nuclear matrix element is defined by

$$\langle J_B M_B | v^*_{lm}(r, \xi) | J_A M_A\rangle = \langle J_B || v_l^* || J_A\rangle \langle J_A M_A, lm | J_B M_B\rangle.$$

In the approximation of a collective surface coupling the reduced matrix element is proportional to $\delta(r-R)$, where R is the nuclear radius [2]). The states $|\mathbf{k}\rangle$ in eq. (19) are the usual distorted waves with appropriate boundary conditions [2]); only when the distortion is neglected so the $|\mathbf{k}\rangle$ become plane waves does the amplitude (19) have the symmetry $B_{lm} = (-)^m B^*_{l-m}$ which makes C vanish. Blair's treatment of the diffraction model [6]) is essentially an approximation for small scattering angles θ_b, and comparison with the Born approximation should therefore be made in this region. If the z-axis is chosen along $\mathbf{k}_a$ and the y-axis along $\mathbf{k}_a \times \mathbf{k}_b$, the ρ_{kq} (if they exist) are proportional to $(\theta_b)^q$ at small angles. So in general the Born theory still predicts a circular polarization C of order θ_b at small scattering angles.

A case of particular interest is inelastic scattering from spin-zero even nuclei, especially quadrupole ($l = 2$) excitation of the first 2^+ state. These transitions have one important property. If spin-flip is neglected (so $s = 0$ only) and there is no change of parity, the intensity of γ-rays de-exciting back to the ground state vanishes perpendicular to the reaction plane. This is always true for spinless particles since s must be zero for them. This result is seen most easily without recourse to the above formalism, if we take a quantization axis along $\mathbf{k}_a \times \mathbf{k}_b$. The target and final nuclear spins are zero, the excited nucleus has spin

l. Further, the photon must carry away the same z-component of angular momentum as transferred in the scattering, namely m. But photons emitted along the quantization axis can only carry a component ± 1; hence only $m = \pm 1$ can contribute to these. Now m is the difference in z-components of the orbital momenta of the incident and scattered particle. Each partial wave is characterized by a spherical harmonic $Y_L^M(\mathbf{k})$, where $\mathbf{k}$ is the particle wave number; with a z-axis perpendicular to $\mathbf{k}$ only the harmonics with $(L-M)$ even do not vanish. The parity change in the transition is given by $(-)^{L_a-L_b}$; if this is *even* then so is the corresponding $M_b-M_a = m$. Then $m = \pm 1$ is strictly forbidden and no ground-state γ-rays can be emitted along $\mathbf{k}_a \times \mathbf{k}_b$. Of course, if the scattered particle has spin, and the $s \neq 0$ terms are not neglible, the z-component of the excited nuclear spin may differ from m owing to an additional spin-flip contribution, and to this extent the γ-emission becomes allowed.

This result is relevant to the circular polarization measurement because detection perpendicular to the reaction plane is the easiest experimental arrangement [11]). So it is of interest to study the polarization for photons emitted at a small angle θ to $\pm(\mathbf{k}_a \times \mathbf{k}_b)$. We find for $l = 2$ and $s = 0$,

$$W(\theta\phi)C(\theta\phi) = \pm[(\tfrac{15}{2})^{\frac{1}{2}}|\rho_{32}|\rho_{00}^{-1} \cos 2(\phi-\phi_2)+\tfrac{1}{4}\langle m\rangle]\theta^2, \qquad (20)$$

where $\rho_{32} = |\rho_{32}| \exp(-2i\phi_2)$, $\langle m\rangle$ is defined by eq. (14), and we have made use of the general relations [5]) for $l = 2$ that, with $\mathbf{k}_a \times \mathbf{k}_b$ as z-axis, $\rho_{30}(22) = \frac{1}{2}\rho_{10}(22)$ and $\rho_{42}(22) = (\frac{3}{4})^{\frac{1}{2}}\rho_{22}(22)$. The γ-ray intensity $W(\theta\phi)$ is normalized to 4π total intensity and for small θ varies as θ^2; for example in the Born approximation with plane waves [3, 4]) we would have $W = \frac{15}{8}\sin^2 2\theta \approx \frac{15}{2}\theta^2$, when ϕ coincides with the direction of the recoil momentum $\mathbf{k}_a - \mathbf{k}_b$. Thus C is a constant for small θ. It is less easy to estimate the right side of eq. (20); of course both ρ_{32} and $\langle m\rangle$ vanish in the plane wave approximation. It has a maximum value of about $3\theta^2$, but seems unlikely to achieve this in practice; more detailed predictions must await the results of numerical calculations of the distorted wave type.

A general property of the distorted wave theory was described at the end of section 2. This holds for inelastic scattering if exchange is neglected, or with exchange if a zero-range interaction is used. For inelastic scattering the condition $k_a \approx k_b$ is the adiabatic approximation, appropriate when the energy loss is small compared to the incident energy. Under these circumstances the two distorted waves will be very similar, and again we have $W(\theta\phi) \approx W(\theta, -\phi)$ and $C(\theta\phi) \approx -C(\theta, -\phi)$ if the z-axis is along $\mathbf{k}_a \times \mathbf{k}_b$ and the x-axis along $\mathbf{k}_a - \mathbf{k}_b$. In particular this is reflected in eq. (20), for then $\langle m\rangle$ vanishes and ρ_{32} becomes pure imaginary, so that $\phi_2 = \pm\frac{1}{4}\pi$. Then eq. (20) also represents the singular case where the total intensity W goes to zero at $\theta = 0$, but the ratio C remains finite (although still varying as $\sin 2\phi$). These results are still true when spin-

orbit coupling is included in the distorted waves, provided we can neglect the spin dependence of the interaction V responsible for the inelastic scattering.

References

1) R. Sherr, Proceedings of Conference on Nuclear Structure, University of Pittsburgh (1957).
2) N. Austern, Chap. VD of Fast Neutron Physics, edited by J. B. Marion and J. L. Fowler (Interscience Publishers Inc., New York, to be published)
3) G. R. Satchler, Proc. Phys. Soc. A **66** (1953) 1081; *ibid.* A **68** (1955) 1037
4) C. A. Levinson and M. K. Banerjee, Annals of Physics **3** (1958) 67
5) R. Huby, M. Y. Refai and G. R. Satchler, Nuclear Physics **9** (1958) 94;
W. Tobocman and G. R. Satchler, Phys. Rev. (to be published)
6) J. S. Blair, Phys. Rev. **115** (1959) 928
7) D. H. Wilkinson (private communication)
8) L. C. Biedenharn and M. E. Rose, Revs. Mod. Phys. **25** (1953) 729
9) G. R. Satchler, Analysis of Deuteron Stripping Reactions (1958) (unpublished)
10) L. F. Chase and G. Igo, Phys. Rev. **116** (1959) 170
11) R. L. Becker and M. E. Rose, Nuovo Cimento **13** (1959) 1182
12) K. Alder, B. Stech and A. Winther, Phys. Rev. **107** (1957) 728
13) J. S. Blair and E. M. Henley, Phys. Rev. **112** (1958) 2029
14) J. B. Gerhart and F. H. Schmidt, Cyclotron Research, University of Washington, Annual Progress Report (1959)

4.D

Nuclear Physics **16** (1960) 683—689; © *North-Holland Publishing Co., Amsterdam*

Not to be reproduced by photoprint or microfilm without written permission from the publisher

BRANCHING RATIOS OF K CAPTURE TO POSITON EMISSION IN NON-UNIQUE FIRST FORBIDDEN $2^- \rightarrow 2^+$ BETA TRANSITIONS

J. KONIJN, B. VAN NOOIJEN and A. H. WAPSTRA

Laboratorium voor Technische Fysika der Technische Hogeschool, Delft

Received 15 February 1960

Abstract: The ratio of K capture to positon emission in $2^- \rightarrow 2^+$ transitions cannot always be explained by admixture of unique forbidden transitions in transitions having essentially an allowed K/β^+ ratio. On the other hand, the normal theory for transitions with $|\Delta J| = 1$ gives values for ^{74}As, ^{84}Rb, ^{126}I and ^{200}Tl which do not depend heavily on the actual values of matrix elements and which nearly agree with the experimental ones.

1. Introduction

According to Brysk and Rose [1]) branching ratios of K capture to positon emission in non-unique first forbidden transitions should not differ much from those in allowed transitions. However, experimental data on $2^- \rightarrow 2^+$ transitions in the decays of ^{74}As [2,3]), ^{84}Rb [4,5]) and ^{126}I [6]) have shown the existence of deviations of the order of 30 % to 60 % from the allowed values [6–8]).

Perlman *et al.* [7]) give an explanation of these differences based on the assumption that in the part of the transitions in which the spin change $|\Delta J|$ is 0 or 1, the K/β^+ ratio is nearly equal to that for allowed transitions, but that, in all three cases in question, an appreciable part occurs with a spin change $|\Delta J| = 2$. This interpretation gives a reasonable agreement with the observed ratios in ^{74}As and ^{126}I but not in ^{84}Rb. Furthermore, Perlman *et al.* notice that the agreement in the ^{74}As and ^{126}I cases is only obtained by accepting a somewhat higher value for the intensity of the $|\Delta J| = 2$ part in these transitions than is compatible with the known comparative half-lives of unique first forbidden transitions.

Recently, Van Nooijen *et al.* [9]) measured the K/β^+ ratio in the $2^- \rightarrow 2^+$ transition occurring in the decay of ^{200}Tl. This ratio is reported to have a value of 110 ± 10, which is considerably higher than the theoretical value † of 65 ± 4 computed using the procedure proposed by Perlman *et al.* [6,7]) (according to Perlman's procedure the percentage of $|\Delta J| = 2$ transitions should decrease with increasing mass number).

† The theoretical value for allowed transitions is 57 ± 2 [6,10]).

Since now only two out of four cases agree with the theory as applied by Perlman *et al.*, it was decided to try a different procedure. In the following it will be shown that the use of matrix elements belonging to $|\Delta \mathbf{J}| = 1$ transitions alone already gives an easy explanation.

2. Theoretical Computation

Using the notation of Perlman *et al.* [7]) rewritten for V—A interaction, the K/β^+ ratio for these transitions is

$$\left(\frac{K}{\beta^+}\right)_{2^-\to 2^+} \Big/ \left(\frac{K}{\beta^+}\right)_{\text{allowed}} \tag{1}$$

$$= \frac{\frac{G_A^2}{G_V^2}\, t^2 C_{1K}^D(\mathrm{A}) + C_{1K}^A(\mathrm{V}) + \Lambda^2\kappa^2 C_{1K}^B(\mathrm{T}) + 2\Lambda\kappa C_{1K}^D(\mathrm{T}) - 2\,\frac{G_A}{G_V}\, t\,[C_{1K}^A(\mathrm{ST}) + \Lambda\kappa C_{1K}^B(\mathrm{ST})]}{\frac{G_A^2}{G_V^2}\, t^2 C_1^D(\mathrm{A}) + C_1^A(\mathrm{V}) + \Lambda^2\kappa^2 C_1^B(\mathrm{T}) + 2\Lambda\kappa C_1^D(\mathrm{T}) - 2\,\frac{G_A}{G_V}\, t\,[C_1^A(\mathrm{ST}) + \Lambda\kappa C_1^B(\mathrm{ST})]}.$$

The ratio of the interaction constants G_A^2/G_V^2 is taken equal to [11]) 1.3 ± 0.1. The various C factors will be recomputed from the formulas in table 1 of the paper of Perlman *et al.* [7]) using the more modern value [1]) $R = 0.426\ \alpha A^{\frac{1}{3}}$ in computing $\kappa = \alpha Z/2R$; the results are given in table 1.

TABLE 1

$C_1^Z(\mathrm{XY})$ factors for positon emission and K capture

	^{74}As $W_0 = 2.81$		^{84}Rb $W_0 = 2.54$		^{126}I $W_0 = 1.90$		^{200}Tl $W_0 = 3.06$	
	β^+	K	β^+	K	β^+	K	β^+	K
$C_1^D(\mathrm{A})$	78.85	112.46	92.41	126.95	151.80	191.88	279.53	377.78
$C_1^A(\mathrm{V})$	69.03	67.12	83.17	80.83	144.52	141.61	256.57	273.83
$C_1^B(\mathrm{T})$	1	1	1	1	1	1	1	1
$C_1^D(\mathrm{T})$	−8.30	−7.99	−9.16	−8.83	−12.29	−11.83	−16.79	−16.42
$C_1^A(\mathrm{ST})$	−72.97	−86.06	−87.05	−100.6	−147.7	−164.5	−266.84	−320.9
$C_1^B(\mathrm{ST})$	8.91	10.57	9.68	11.23	12.55	13.84	17.55	19.41
κ^2	80.01	83.55	93.11	96.76	148.2	152.2	257.8	262.3

The ratios of $(K/\beta^+)_{2^-\to 2^+}$ to $(K/\beta^+)_{\text{allowed}}$ have been computed from eq. (1) for $t = +1$ and $\Lambda = 1$ as well as for $t = -1$ and $\Lambda = 1$; the results are shown in table 2. The influence of a variation in Λ and t on these ratios has been examined in all the four transitions in question. According to King and Peaslee [14]) Λ and the absolute value of t should be about 1. All the ratios show about the same weak dependence on Λ and t in the neighbourhood of the two possible combinations. The results obtained for ^{84}Rb and ^{200}Tl are given in fig. 1a and 1b explicitly.

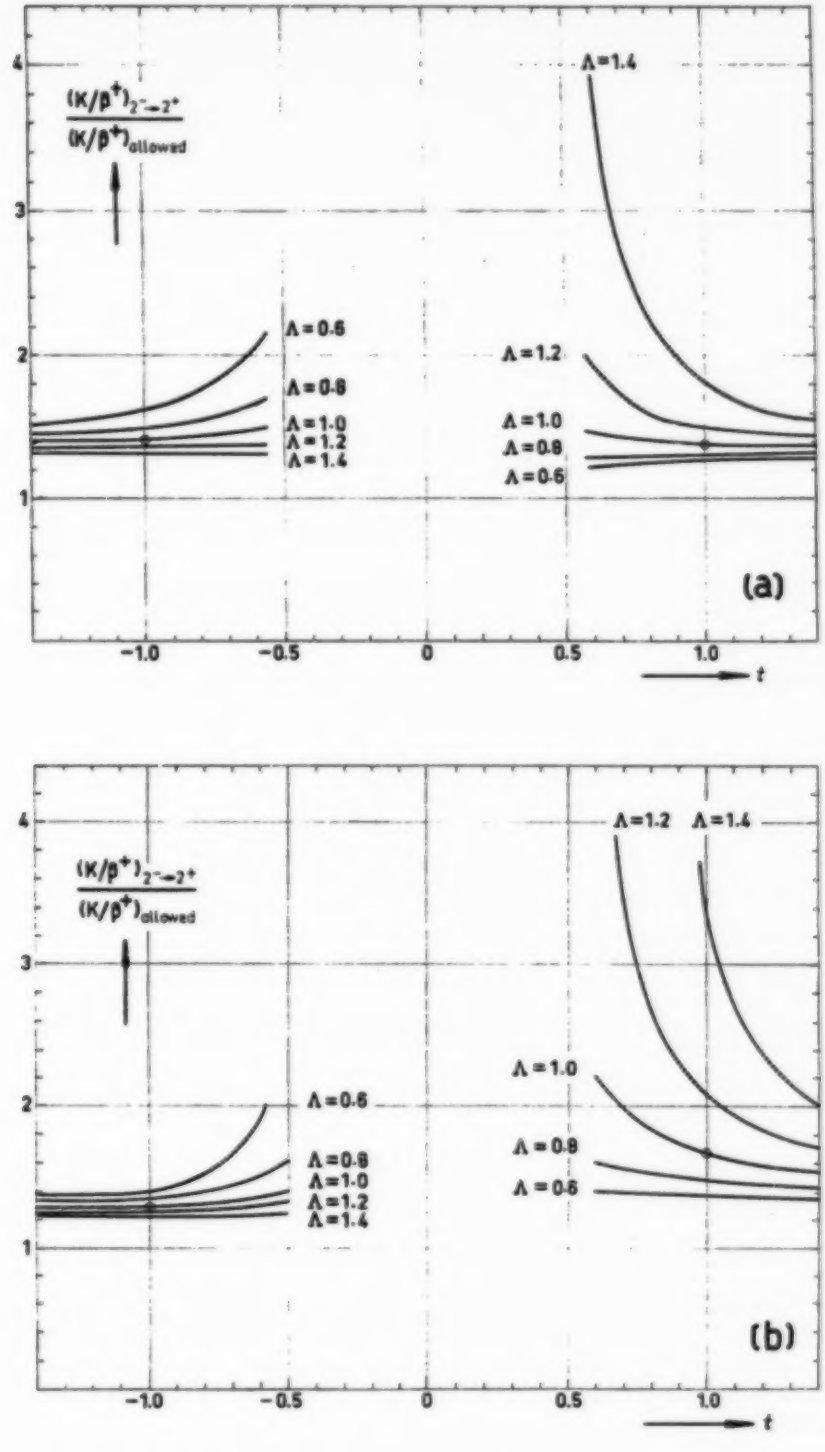

Fig. 1. The ratio $(K/\beta^+)_{2^- \to 2^+}$ to $(K/\beta^+)_{\text{allowed}}$ as a function of t and with Λ as a parameter for ^{84}Rb (fig. 1a) and for ^{200}Tl (fig. 1b).

TABLE 2

Observed and calculated K/β^+ ratios for the $2^- \rightarrow 2^+$ transitions occurring in the decays of ^{74}As, ^{84}Rb, ^{128}I and ^{200}Tl

Nucleus	End point of the positon distribution (keV)	K/β^+ ratios experimental values	Theoretical values of K/β^+ ratios for allowed transitions	The ratio of $(K/\beta^+)_{2^- \rightarrow 2^+}$ to $(K/\beta^+)_{\text{allowed}}$			
				Experimental values (ratio of columns 3 and 4)	Values according to ref. [6])	Values according to this paper	
						$t = +1$	$t = -1$
1	2	3	4	5	6	7	8
^{74}As	920±10 [2])	1.50±0.16 †	1.16±0.03	1.3±0.2	1.23	1.46	1.48
^{84}Rb	782±12 [5,6])	5.1 ±0.4 [4]) 5.12±0.11 [5])	3.4 ±0.3	1.5±0.2	1.23	1.39	1.43
^{128}I	459± 7 [6])	145 ±4 [6])	125 ±7	1.2±0.1	1.11	1.31	1.30
^{200}Tl	1068±7 [9,12])	110 ±10 ††	57 ±2	1.9±0.3 ††	1.11	1.68	1.29

† Mean value from refs. [2,3]).

†† Preliminary result.

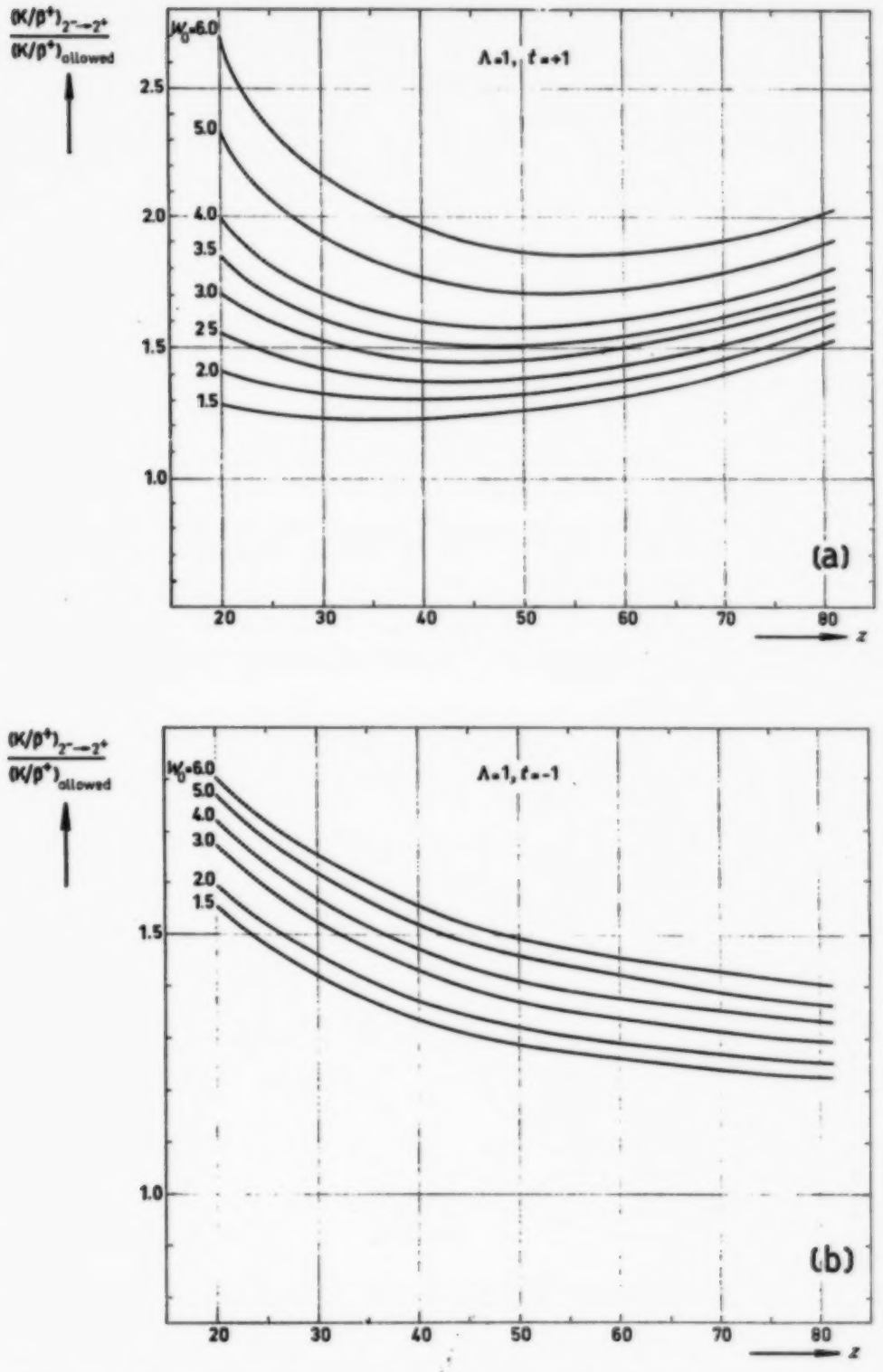

Fig. 2. The ratio of $(K/\beta^+)_{2^-\to 2^+}$ to $(K/\beta^+)_{\text{allowed}}$ as a function of Z (charge of the daughter nucleus), with the maximum energy release W_0 (in units of m_0c^2 including rest mass) as a parameter. Separate drawings are presented for $\Lambda = 1$, $t = +1$ (fig. 2a) and for $\Lambda = 1$, $t = -1$ (fig. 2b).

In fig. 2a and 2b the ratios of $(K/\beta^+)_{2^-\to 2^+}$ to $(K/\beta^+)_{\text{allowed}}$ are shown as a function of Z (charge of the daughter nucleus) with the maximum positon energy release W_0 (in units of m_0c^2 including rest mass) as a parameter; in the underlying calculations an average value for the mass number A was adopted at each Z value.

3. Discussion

Table 2 shows that, especially for $t \approx +1$, the result of our computation follows the trend of the experimental data better than that obtained by Perlman *et al.* [6,7]) from the assumption that the $|\Delta \mathbf{J}| = 2$ matrix elements would play a significant role.

It is seen from fig. 1a and 1b that the ratio of $(K/\beta^+)_{2^-\to 2^+}$ to $(K/\beta^+)_{\text{allowed}}$ does not strongly depend on Λ and t in the environment of the point $\Lambda = 1$, $t = +1$ and even less in that of the point $\Lambda = 1$, $t = -1$. This result supports the computation as outlined in section 2. It is estimated that the ratios of $(K/\beta^+)_{2^-\to 2^+}$ to $(K/\beta^+)_{\text{allowed}}$ computed according to the procedure given in the preceding section leads to values which agree within about 10 % with experiment. A rapid estimate of the ratio of $(K/\beta^+)_{2^-\to 2^+}$ to $(K/\beta^+)_{\text{allowed}}$ may be obtained from the curves presented in fig. 2a and 2b.

From the above it appears that it is not necessary to assume a somewhat uncommonly high transition probability for the $|\Delta \mathbf{J}| = 2$ part in the $2^- \to 2^+$ transitions in order to explain the K/β^+ ratios.

The above results were obtained neglecting the effect of the finite size of the nucleus. This effect has been discussed for K capture by Brysk and Rose [1]) and for positon emission by Rose and Holmes [13]). The results of the calculations by Rose and Holmes, carried out for $Z = 60$ and $Z = 96$ only, do not allow reliable interpolations for intermediate Z values. A rough estimate of the influence of the finite-size correction in the case of ^{200}Tl, leads to an increase of about 10 % for the ratio of $(K/\beta^+)_{2^-\to 2^+}$ to $(K/\beta^+)_{\text{allowed}}$.

The K/β^+ ratios for first forbidden transitions with $|\Delta \mathbf{J}| = 0$ tend to be somewhat lower than for allowed transitions. This may point to the fact that in $2^- \to 2^+$ transitions only the contribution of a combination of matrix elements leading to a spin change of $|\Delta \mathbf{J}| = 1$ is of importance.

References

1) H. Brysk and M. E. Rose, Revs. Mod. Phys. **30** (1958) 1169 and Oak Ridge National Laboratory Report ORNL-1830 (1955), unpublished
2) S. Johansson, Y. Cauchois and K. Siegbahn, Phys. Rev. **82** (1951) 275
3) J. Scobie, Nuclear Physics **3** (1957) 465
4) J. P. Welker and M. L. Perlman, Phys. Rev. **100** (1955) 783
5) J. Konijn, H. L. Hagedoorn, H. van Krugten and J. Slobben, Physica **24** (1958) 931
6) D. S. Harmer and M. L. Perlman, Phys. Rev. **114** (1959) 1133

7) M. L. Perlman, J. P. Welker and M. Wolfsberg, Phys. Rev. **110** (1958) 381
8) J. Konijn, B. van Nooijen, H. L. Hagedoorn and A. H. Wapstra, Nuclear Physics **9** (1958) 296
9) B. van Nooijen, H. van Krugten and A. H. Wapstra, Nuclear Physics, to be published
10) P. F. Zweifel, Phys. Rev. **107** (1957) 329
11) A. Winther and O. Kofoed-Hansen, ref. [13]) in R. P. Feynman and M. Gell-Mann, Phys. Rev. **109** (1958) 193
12) C. J. Herrlander and T. R. Gerholm, Nuclear Physics **3** (1957) 161
13) M. E. Rose and D. K. Holmes, Oak Ridge National Laboratory Report ORNL-1022 (1951), unpublished
14) R. W. King and D. C. Peaslee, Phys. Rev. **94** (1954) 1284

1.E.5:
2.D.

Nuclear Physics **16** (1960) 690—697; © *North-Holland Publishing Co., Amsterdam*
Not to be reproduced by photoprint or microfilm without written permission from the publisher

THE NUCLEAR SURFACE IN AN EXCITED NUCLEUS

A. M. LANE
Atomic Energy Research Establishment, Harwell
and
K. PARKER
Atomic Weapons Research Establishment, Aldermaston

Received 15 January 1960

Abstract: Measurements of the alpha spectra from (p, α) reactions in medium weight nuclei have suggested that the Coulomb barrier against alpha particle emission is considerably lower for the excited nucleus than for the ground state. In an attempt to confirm this suggestion theoretically the variation of surface diffuseness with excitation energy has been studied by considering a Fermi gas of nucleons in a semi-infinite potential with a diffuse edge. It is found that the calculated particle density shows very little variation with nuclear temperature. This suggests that the barrier penetrability should remain roughly constant up to 30 MeV. The variation of kinetic energy density in the nuclear surface has been obtained as a by-product of the calculations.

1. Introduction

The study of the nuclear surface reported in this paper has been motivated by the apparent conflict between conventional ideas about the surface and recent experimental results on (p, α) reactions. Using 23 MeV protons, Fulmer and Cohen [1]) measured the spectra of alpha particles from various elements. Since the angular distributions of the alphas are fairly isotropic, they assume that the compound nucleus mechanism is responsible for the reaction. In this case the spectrum of alphas should be

$$N(E_\alpha) = \text{constant} \cdot E_\alpha \sigma_c(E_\alpha; E_p+Q-E_\alpha)\omega(E_p+Q-E_\alpha), \qquad (1)$$

where E_α, E_p are the alpha and proton energies, Q is the Q-value, $\sigma_c(E_\alpha; E^*)$ is the "compound nucleus" or "absorption" cross section for alphas of energy E_α incident on the residual nucleus of excitation energy E^*, and $\omega(E^*)$ is the level density of the latter nucleus. Such a spectrum has a peak at the energy where the rate of increase of σ_c is just balanced by the rate of decrease of ω. The variation of σ_c is determined predominantly by the radius R at which the Coulomb barrier is cut off; that of ω is determined by the nuclear temperature T.

Fulmer and Cohen [1]) report that the observed peak position is an MeV or so less than the value one would estimate using (1) and "reasonable values" for T and R. In other words, there is an excess of low energy alphas. The value used for $R(1.5\, A^{\frac{1}{3}} \times 10^{-13}$ cm) gives agreement with observed alpha absorption

cross sections into ground states. Since it is conventionally assumed that $\sigma_c(E_a; E^*)$ does not depend on E^*, in the first instance one attributes the discrepancy to a mis-estimate of T rather than R. However, Fulmer and Cohen[1]) find that if T is reduced to fit the observed peak position new disagreements appear (in the absolute (p, α) cross section, for example). Therefore one must conclude that if (1) is at all applicable the discrepancy must be understood in terms of a dependence of the absorption cross section σ_c on the energy E^* of the residual nucleus. If one uses R as a parameter, fitting the observed peak leads to values of R which are, for Ni and Rh, 17 % and 40 % respectively, larger than $1.5A^{\frac{1}{3}} \times 10^{-13}$ cm. Since the peak energy corresponds to E^* about 15 MeV, this poses the theoretical problem: why does the effective barrier radius of the nucleus increase by the order of 25 % when the nucleus is excited to 15 MeV?

The first explanation to suggest itself is that the nucleus undergoes a volume expansion with increasing energy. LeCouteur [2]) estimated the nuclear thermal expansion coefficient (which is related to the nuclear compressibility). He found that the radius increases by 10 % in a nucleus of mass 100 for an excitation of 400 MeV. This value, whose smallness is a reflection of the near-incompressibility of nuclear matter, means that this effect is not the one we are looking for.

Another possible explanation is that the increase in barrier radius is a *surface* rather than a *volume* effect. Bagge [3]) and Yamaguchi [4]) computed the increase with temperature of the RMS radius of an incompressible liquid drop of uniform density but variable shape. Using simple thermodynamic theory and representing excited states as quantised surface oscillations, Bagge found an increase of 5 % for Br at 15 MeV excitation. Although larger than the volume effect, this is still too small.

The problem of estimating the increase in surface thickness can also be treated on the basis of the independent particle model, and it is the purpose of the present paper to describe this. One sees that, for a nucleus with all particle levels filled up to a certain "Fermi level" the surface thickness or diffuseness increases with temperature because higher levels are populated as the temperature rises. The wave functions of these levels have their turning points at larger radii than those of the filled levels because of the diffuseness of the potential and their exponential tails reach out further because of the lighter binding. One can make estimates of the effect with the Thomas-Fermi model but their accuracy is uncertain and a proper computation is needed if any quantitatively reliable results are to be obtained.

2. The Model of the Nuclear Surface

Our model of the nuclear surface is similar to those used by Swiatecki [5, 6]) in his investigations of the nuclear surface energy. A Fermi gas of particles is considered to occupy the semi-infinite volume $x < 0$ and to be confined by a

potential change in the x direction near $x = 0$. The constant (zero) potential in the region $x < 0$ corresponds to the interior of the nucleus, the constant (positive) potential in the region $x > 0$ corresponds to the exterior of the nucleus and the region of increasing potential about $x = 0$ corresponds to the nuclear surface. The fact that the system is bounded by a plane surface means that we neglect any effects of curvature in the nuclear surface. The form of the potential is somewhat arbitrary but we have chosen to use the Saxon-Woods form

$$V(x) = \frac{V_0 \exp[\alpha(x-a)]}{1+\exp[\alpha(x-a)]}, \tag{2}$$

where V_0 is the well depth, a is the nuclear (potential) radius and α is a diffuseness parameter.

In the detailed calculation we consider a nucleus with $A = 100$. No distinction is made between neutrons and protons. The parameters α, a and V_0 are chosen to accord roughly with those used by Ross, Mark and Lawson [7]) in their investigation of nucleon energy levels in a static Saxon-Woods potential. In the region of $A = 100$ they found $V_0 \approx 51$ MeV for the proton well and $V_0 \approx 43$ MeV for the neutron well; we have taken $V_0 \approx 47$ MeV as a mean value. We choose $a = 1.2A^{\frac{1}{3}} \times 10^{-13}$ cm since Ross, Mark and Lawson [7]) suggest that their chosen value of $1.3A^{\frac{1}{3}} \times 10^{-13}$ cm is approximately 8 % too large. Similarly, we take $\alpha = 1.16 \times 10^{13}$ cm^{-1}, again smaller than the value used by Ross, Mark and Lawson [7]). The results of the calculations are insensitive to small variations in the values of these parameters.

The particle density can now be calculated from this potential using standard statistical methods.

The wave function of a particle of mass m, with components of momentum (p_x, p_y, p_z) moving in the potential $V(x)$ can be written

$$\Psi = \left(\frac{2}{L^3}\right)^{\frac{1}{2}} q(x) \exp\left(\frac{iyp_y}{n}\right) \exp\left(\frac{izp_z}{n}\right), \tag{3}$$

normalised in a large cube of side L.

If E is the total energy of the particle and p is the x-component of momentum for large negative $x (V(x) = 0)$, then

$$2mE = p^2+p_y^2+p_z^2 = p_x^2+2mV(x)+p_y^2+p_z^2 \tag{4}$$

and the equation for $q(x)$ can be written

$$q''(x)+\frac{2m}{\hbar^2}\left[\frac{p^2}{2m} - V(x)\right] q(x) = 0 \tag{5}$$

with boundary conditions

$$\begin{aligned} q(x, p) &\sim \sin\left[\frac{px}{\hbar}+\Delta(p)\right] \quad \text{as } x \to -\infty \\ q(x, p) &\sim b \exp(-\kappa x) \qquad \text{as } x \to +\infty, \end{aligned} \tag{6}$$

where $\kappa^2\hbar^2 = 2mV_0 - p^2$ and b is a constant. We consider only bounded solutions for $q(x, p)$.

The particle density in an excited nucleus at temperature τ can now be written (using standard properties of a Fermi gas) as

$$n(x, \tau) = \frac{16}{h^3}\iiint \frac{|q(x, p)|^2}{1+\exp[\beta(E-\lambda)]}\,dp\,dp_y\,dp_z, \tag{7}$$

where $\beta = 1/\tau$ and λ is the chemical potential. For small values of τ, λ differs from the Fermi energy, E_F, by a small term in τ^2. The multiplying factor includes a factor 4 since each level can hold two neutrons and two protons.

After evaluating the p_y and p_z integrals we find

$$n(x, \tau) = 32\frac{m\pi\tau}{h^3}\int_0^\infty |q(x, p)|^2 \ln\left\{1+\exp\left(\frac{p_\lambda^2-p^2}{2m\tau}\right)\right\} dp, \tag{8}$$

where

$$p_\lambda^2 = 2m\lambda. \tag{9}$$

In the ground state

$$n(x, 0) = \operatorname*{Lt}_{\tau\to 0} n(x, \tau) = \left(\frac{16\pi}{h^3}\right)\int_0^{p_F} |q(x, p)|^2 (p_F^2-p^2)dp, \tag{10}$$

where p_F is the Fermi momentum.

Now $n(x, \tau)-n(x, 0)$ can be written as a rapidly convergent power series in τ^2 (as, for example, is done in the theory of metals) but since we have to evaluate the wave functions numerically it is just as easy to evaluate (8) exactly as to use the power series.

Eq. (5) was solved numerically on the DEUCE computer at A.W.R.E., Aldermaston, for values of p giving bound solutions and (8) and (10) evaluated for $\tau = 0$, 1, 2, 4 MeV. (The restriction to bound states means that in (8) the effective upper limit of the integration corresponds to $p^2/2m = 47$ MeV.) The Fermi energy was taken as 39 MeV corresponding to a binding energy of 8 MeV for the last nucleon.

3. Result and Discussion

The calculated particle density was found to vary very little with τ and, indeed, on any reasonable scale density profiles coincide. Fig. 1 shows the nuclear potential and the particle density. The potential radius is a. The mass

radius is taken to be given by the half maximum density point. We have also calculated the particle density given by the simple Thomas-Fermi formula $n(x) = \text{constant}\ [E-V(x)]^{\frac{3}{2}}$ and confirmed Swiatecki's [6]) conclusion that this

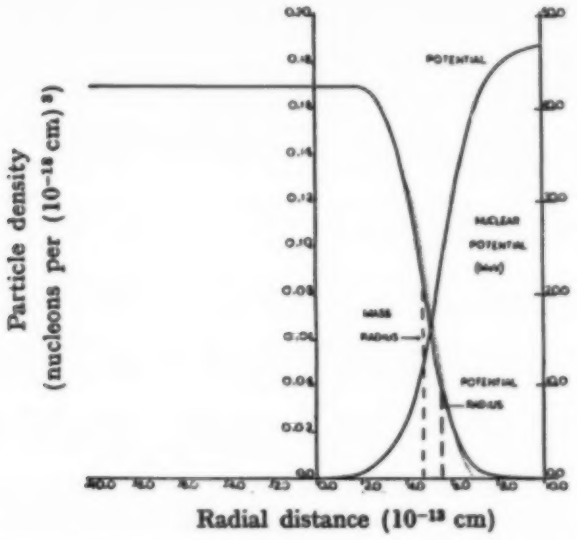

Fig. 1. The nuclear potential and particle density in a nucleus with $A = 100$. Exact density ——; Thomas-Fermi value of density ·····

gives an excellent approximation to the exact density. In fig. 2 we have plotted the density for $\tau = 0$ and $\tau = 4$ MeV on an enlarged scale in the region of the surface where they differ. The maximum difference in particle density occurs

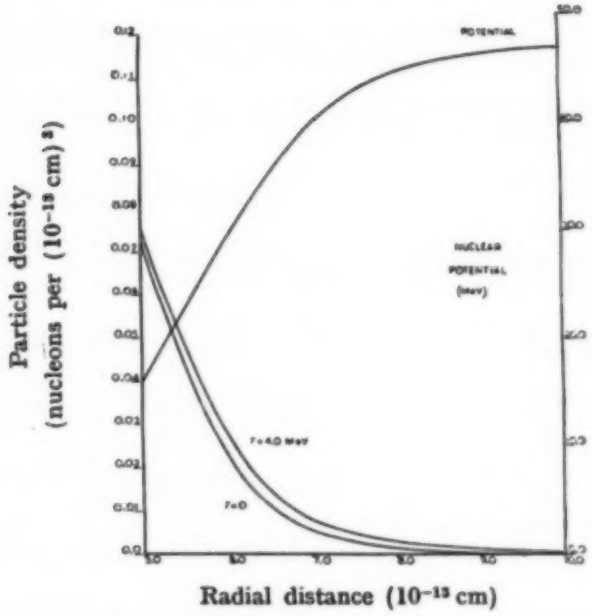

Fig. 2. The variation of particle density with temperature in a nucleus with $A = 100$.

outside both the mass and potential radii. Although the difference is as much as 25 % relatively the absolute increase in density is exceedingly small ($\approx$ 3 % of the central value).

The temperature of a nucleus at excitation energy E^* may be obtained from the Fermi gas equation of state, $\tau \approx 10E^*/A$. For $A = 100$ and $E^* = 15$ MeV and 150 MeV, τ is about 1.5 MeV and 4 MeV respectively. From fig. 1 it follows that there is very little decrease in barrier height for energies up to 100 MeV. The decrease can be roughly estimated as the difference in nuclear potential for radial points having the same particle density. We find a decrease of 1—2 MeV for $\tau = 4$ MeV.

It is true that we have not differentiated between neutrons and protons or taken into account Coulomb forces; neither is our calculation self-consistent in that any change in density will modify the potential. The introduction of such refinements are unlikely to invalidate the conclusion that for excitation energies up to 30 MeV the Coulomb barrier (and penetration factors) are virtually constant.

The smallness of the effect must be understood in the following terms. Of the single particle levels in the potential well, those with highest energy will have wave functions extending furthest into the negative energy region. In the excited nucleus particles from below the Fermi energy are excited into higher levels. Initially only particles just below the Fermi level will be excited so that the average extension of the wave function into the negative energy region is almost unaltered. It is only at very high excitation energies that particles from low lying levels will be excited to any appreciable extent with consequent marked increase in nuclear radius.

It appears that an alternative explanation must be sought for the results of Fulmer and Cohen [1]) and for similar results, on (p, α) reactions for protons of energies 9.5—23 MeV, of Fulmer and Goodman [8]). Possibilities include a breakdown in the independence assumption or a different form of level density law. It is also worth noting that if optical model calculations of compound nucleus formation cross sections for alpha particles due to Igo [9]) are used instead of those based on a square well model as given by Blatt and Weisskopf [10]) there is better though not complete agreement between theory and experiment.

Since this work was begun details have become available of two other experiments involving emission of alpha particles from the compound nucleus in the same range of excitation energy Brady [11]) has investigated (p, α) reactions using 17 MeV protons and finds alpha particle spectra which disagree with those of Fulmer and Goodman [8]) and are in agreement with continuum theory using reasonable compound nucleus cross sections and level densities. Fulbright, Lassen and Paulsen [12]) have measured the spectra of inelastically scattered alpha particles using 20 MeV incident alpha particles. Their spectra can be

fitted by continuum theory calculations using either a constant (reasonable) nuclear temperature or a temperature proportional to the square root of the excitation energy. The results of these two experiments support our general conclusion that lowering of the Coulomb barrier in excited nuclei is unimportant for excitations up to a few tens of MeV.

4. The Kinetic Energy Density

There are two possible definitions of the kinetic energy density in the nucleus, namely

$$t_1 = \sum_k \Psi_k^* \left(\frac{p^2}{2m}\right) \Psi_k = -\left(\frac{L}{\pi}\right)^3 \left(\frac{\hbar^2}{2m}\right) \int_{\mathbf{k}} \Psi_k^* \nabla^2 \Psi_k \, \mathrm{d}\mathbf{k} \tag{11}$$

and

$$t_2 = \frac{1}{2m} \sum_k |\mathbf{p}\Psi_k|^2 = \left(\frac{L}{\pi}\right)^3 \left(\frac{\hbar^2}{2m}\right) \int_{\mathbf{k}} \mathrm{grad}\ \Psi_k^*,\ \mathrm{grad}\ \Psi_k \, \mathrm{d}\mathbf{k} \tag{12}$$

where the integration is over all wave vectors $\mathbf{k}$.

If t_1 and t_2 are integrated over all space they give the same value for the total kinetic energy in the nucleus.

With our model these expressions give, in the ground state of the nucleus,

$$t_1 = \left(\frac{1}{2m\pi^2\hbar^3}\right) \int_0^{p_F} |q(x,p)|^2 (p_F^4 - p^4)\mathrm{d}p - \left(\frac{2}{\pi^2\hbar^3}\right) \int_0^{p_F} |q(x,p)|^2 V(x)(p_F^2 - p^2)\mathrm{d}p \tag{13}$$

and

$$t_2 = \left(\frac{1}{m\pi^2\hbar}\right) \int_0^{p_F} |q'(x,p)|^2 (p_F^2 - p^2)\mathrm{d}p + \left(\frac{1}{2m\pi^2\hbar^3}\right) \int_0^{p_F} |q(x,p)|^2 (p_F^2 - p^2)^2 \, \mathrm{d}p \tag{14}$$

where $q'(x,p)$ is the partial differential of q with respect to x.

Eqs. (13) and (14) were evaluated numerically and the resulting kinetic energy densities are plotted in fig. 3 together with the value given by the Thomas-Fermi formula, in which the kinetic energy density is proportional to the $\frac{5}{3}$- power of the local particle density. In fact, once t_1 has been computed, t_2 can be found by using the formula

$$t_2 - t_1 = \frac{\hbar^2}{4m} \frac{\mathrm{d}^2}{\mathrm{d}x^2} [n(x,0)]. \tag{15}$$

The expression t_2 and the Thomas-Fermi value are both positive definite, but t_1 can take on negative values. There is little difference between the three values for the kinetic energy density; but the fact that the Thomas-Fermi approxima-

tion agrees more closely with t_1 than t_2 throws doubt on the validity of this approximation, as used, for example, by Skyrme [13]) in calculations of the nuclear surface energy.

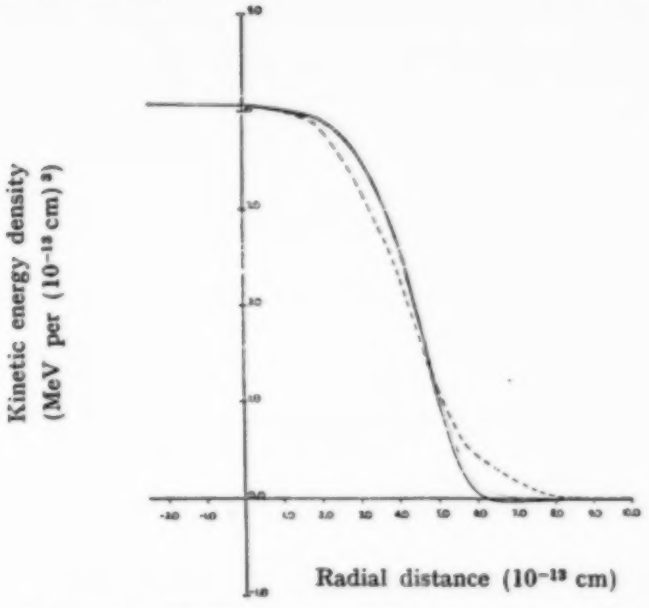

Fig. 3. The kinetic energy density in a nucleus with $A = 100$.
—— t_1 ---- t_2 ..... t_3 Thomas-Fermi value

The numerical calculations in this work were carried out by Mr. R. Hinves.

We would like to thank Dr. G. Igo, Dr. C. B. Fulmer and Dr. C. D. Goodman for sending details of their work in advance of publication, Dr. A. A. Ross for details of preliminary calculations with the Thomas-Fermi model and Professor R. Scherr for a discussion of the work of F. L. Brady.

References

1) C. B. Fulmer and B. L. Cohen, Phys. Rev. **112** (1958) 1672
2) K. J. LeCouteur, Proc. Phys. Soc. A **63** (1950) 259
3) E. Bagge, Annalen der Physik **33** (1938) 389
4) Y. Yamaguchi, Prog. Theor. Phys. **5** (1950) 501
5) W. J. Swiatecki, Proc. Phys. Soc. A **64** (1951) 226
6) W. J. Swiatecki, Proc. Phys. Soc. A **68** (1955) 285
7) A. A. Ross, H. Mark and R. D. Lawson, Phys. Rev. **102** (1956) 1613
8) C. B. Fulmer and C. D. Goodman,Private communication
9) G. Igo, Phys. Rev. **115** (1959) 1665
10) J. M. Blatt and V. F. Weisskopf, Theoretical Nuclear Physics (John Wiley and Sons, New York, 1952) p. 353
11) F. L. Brady, unpublished work
12) H. W. Fulbright, R. O. Lassen and N. O. Roy Poulsen, Mat. Fys. Medd. Dan. Vid. Selsk. **31** No. 10 (1959)
13) T. H. R. Skyrme, Phil. Mag. **1** (1956) 1043

10.D *Nuclear Physics* **16** (1960) 698; © *North-Holland Publishing Co., Amsterdam*

BOOK REVIEWS

Directory of nuclear reactors, Vol. II: Research, test and experimental reactors (International Atomic Energy Agency, Vienna 1959. 348 p. $ 3.50)

The first volume of the Directory was reviewed in this journal (**14** (1959/60) 176). The second volume is of special importance to those who are interested in the didactic and research utilization of reactors: they have here an excellent guide, up to date, complete and authoritative. The typographical outlay is of high standard as regards both the tables and the diagrams. It is regrettable, however, that an international agency of such importance should ignore the recommendations of the SUN commission of the IUPAP in the matter of symbols and units.

L. R.

Multilateral agreements (Legal series No. 1) (International Atomic Energy Agency, Vienna 1959. 258 p. $ 2.50)

With this useful compilation, the IAEA inaugurates a new series in its programme of collecting and publishing information on all aspects of atomic energy. In the present volume one finds the complete texts of ten official documents establishing the statutes of various international organizations such as CERN, the Joint Institute at Dubna and EURATOM, or embodying the conventions regulating several projects and mutual relations.

L. R.

D. BERSHADER (Editor), *The magnetodynamics of conducting fluids* (Stanford University Press, 1959. 145 pages. $ 4.50).

This is the third volume to be published in the series of proceedings of the yearly Lockheed-sponsored symposia on magnetohydrodynamics (MH) held at Palo Alto.

In this volume a trend has been continued, which was already apparent in the preceding volume, towards dealing mainly with the problems of MH-*flow*. Out of the seven contributions five deal with theory and experiments on MH-flow or magneto*aero*dynamic flow, as it could more properly be termed in the setting of the aircraft and missile industry, while the remaining two deal with the subject of magnetohydrodynamic waves.

The first contribution by A. Busemann discusses in a largely qualitative manner the problems of flow existence and stability. The next two articles, by J. D. Cole and H. Grad respectively, both deal with the propagation of magnetohydrodynamic waves. Although they contain some unavoidable duplication both articles are very instructive; especially the one by Grad is written with admirable clarity, which is also needed in the complex jungle of different wave types in MH.

An analysis of the flow characteristics for magnetically driven plasmas in the non-steady one-dimensional and the steady two-dimensional cases is given by M. Mitchner in the fourth paper. This paper, and the following contribution by F. Fishman *et al.*, constitute the only attempts at analyzing experimental data in terms of MH flow theory. It is to be hoped that the experimental results which are forthcoming all over the world will be of a quality that justifies the highly developed theoretical work in this field. The article by Fishman *et al.* describes experiments most relevant to the question of utilizing MH devices to produce lift and drag in high-speed flight; it is a beautiful account of the effect of a magnetized solenoid on a supersonic crosswise flow.

The last two contributions are theoretical studies into the importance of MH effects on some simple flow configurations involving adjacent rigid objects. The one by E. L. Resler, Jr. and J. E. McCune is a parameter study of the flow along a "wavy wall" and around "airfoils". The other by G. F. Carrier and H. P. Greenspan treats the problem of an electrically conducting fluid flowing along a semi-infinite plane with a magnetic field parallel to the plane; even this simple-looking problem gives rise to interesting conclusions when the interaction between fluid and magnetic field is introduced.

As an account of the complications introduced into ordinary hydrodynamic *flow* by inclusion of strong electromagnetic interactions this book is highly recommended.

Carl F. Wandel

AUTHOR INDEX

AKIMOVA, M. K. *see* V. M. STRUTINSKI
BALASHOV, V. V. and V. A. ELTEKOV, Method for separating the relative motion of two nucleons in oscillator potential well 423
BALIAN, ROGER et CYRANO DE DOMINICIS, Sur la fonction de Green à une particule en mécanique statistique quantique 502
BARBER, W. C. and V. J. VANHUYSE, Photoprotons from medium and heavy elements 381
BASHANDY, E., *see* J. LINDSKOG
BASTIN-SCOFFIER, G., *see* R. J. WALEN
BATCHELOR, R., A. J. FERGUSON, H. E. GOVE and A. E. LITHERLAND, Gamma rays from the 4.24 MeV state in magnesium-24 38
BAUER, RUDOLF W. and MARTIN DEUTSCH, Nuclear polarization of Co^{55} . 264
BAYMAN, B. F. and L. SILVERBERG, On the coupling of a $j = \frac{3}{2}$ particle to nuclear quadrupole surface oscillations 625
BEARD, G. B. and W. H. KELLY, Search for the natural alpha activity of tungsten. 591
BIRD, L., *see* A. E. TAYLOR
CINDRO, N., *see* P. R. KLEIN
DARDEN, S. E., C. A. KELSEY and T. R. DONOGHUE, Polarization of 1.0-MeV neutrons scattered from deuterium 351
DAVYDOV, A. S., Coupling of nuclear rotation and motion of the outer nucleon 597
DE DOMINICIS, CYRANO *see* ROGER BALIAN
DEMIDOV, A. M., *see* L. V. GROSHEV
DEMUYNCK, J. L., *see* O. J. SEGAERT
DERRICK, G. H., Kinetic and potential energy matrix elements for the triton 405
DEUTCH, B. I., F. R. METZGER and F. J. WILHELM, Nuclear resonance fluorescence with the 105-keV E1 transition of Gd^{155} using an ultra-centrifuge 81
DEUTSCH, MARTIN, *see* RUDOLF W. BAUER
DONOGHUE, T. R., *see* S. E. DARDEN
DRAPER, J. E., and T. E. SPRINGER, Multiplicity of resonance neutron capture gamma rays 27
DROPESKY, B. J., A. W. SCHARDT and T. T. SHULL, Note on the decay of the new nucleide Cr^{56} 357

ELTEKOV, V. A., *see* V.V. BALASHOV
EL-WAHAB, M. A., *see* A. S. MELIGY
ENGLAND, J. B. A., R. MCKEAGUE and P. E. HODGSON, The elastic scattering of 19 MeV deuterons by krypton and xenon 52
ESTULIN, I. V., A. S. MELIORANSKY and L. F. KALINKIN, Low-lying energy levels of Cs^{134} 168
EWAN, G. T., *see* J. S. GEIGER
FÉNYES, T., Measurement of the energy of the weak group in the α-spectrum of Po^{210} 529
FERGUSON, A. T. G., *see* G. J. MCCALLUM
GALLAGHER, C. J., Classification of beta- and gamma-ray transitions between intrinsic states in deformed even-mass nuclei 215
GEIGER, J. S., R. L. GRAHAM and G. T. EWAN, Conversion electron spectrum from Ce^{144} decay. 1
GERHOLM, T. R., *see* J. LINDSKOG
GOVE, H. E., *see* R. BATCHELOR
GRAHAM, R. L., *see* J. S. GEIGER
GROSHEV, L. V., A. M. DEMIDOV and V. I. PELEKHOV, Spectra of γ-rays from neutron capture by heavy nuclei (I) 645
GROSHEV, L. V., *see* V. M. STRUTINSKI
HALBERT, M. L. and A. ZUCKER, Nitrogen-aluminium elastic scattering 158
HILLION, P. and J. P. VIGIER, Elementary fields and irreducible representations of the Lorentz group 360
HODGSON, P. E., *see* J. B. A. ENGLAND
HOOGENBOOM, A. M., *see* O. J. SEGAERT
HORVAT, P., J. PAHOR and M. VAKSEIJ, The photonuclear reactions (γ, d) and (γ, np) on K^{39} 90
ISAEV, P. S. and I. S. ZLATEV, Application of dispersion relations for testing quantum electrodynamics at small distances 608
JASTRAM, P. S., *see* M. K. RAMASWAMY
KALINKIN, L. F., *see* I. V. ESTULIN
KELLY, W. H., *see* G. B. BEARD
KELSEY, C. A., *see* S. E. DARDEN
KERMAN, A. K., *see* C. A. MALLMANN
KLEIN, P. R., N. CINDRO, L. W. SWENSON and N. S. WALL, Li^7 (α, p) Be^{10} and Li^6 (α, p) Be^9 reactions at 30 MeV 374
KONIJN, J. B., VAN NOOIJEN and A. H. WAPSTRA, Branching ratios of K capture to positon emission in non-unique first forbidden $2^- \rightarrow 2^+$ beta transitions 683
KOTAJIMA, K. and H. MORINAGA, Isomers in N = 81 nuclei 231
LANE, A. M. and K. PARKER, The nuclear surface in an excited nucleus 690
LINDSKOG, J., E. BASHANDY and T. R. GERHOLM, Determination of a

7×10^{-11} sec half-life for the first excited state in thallium 201 . . . 175
LITHERLAND, A. E., *see* R. BATCHELOR
MALLMANN, C. A. and A. K. KERMAN, Comparison of asymmetric quadrupole rotor energy level predictions for even nuclei with experimental results 105
MANI, G. S., *see* G. J. MCCALLUM
MCCALLUM, G. J., G. S. MANI and A. T. G. FERGUSON, Neutron total cross-sections in the 12 to 21 MeV region 313
MCGOWAN, F. K., *see* P. H. STELSON
MCKEAGUE, R., *see* J. B. A. ENGLAND
MELIGY, A. S., S. TADROS and M. A. EL-WAHAB, Isotope shift and nuclear deformations 99
MELIORANSKY, A. S., *see* I. V. ESTULIN
METZGER, F. R., C. P. SWANN and V. K. RASMUSSEN, Partial gamma ray widths for low lying levels in aluminium and magnesium 568
METZGER, F. R., *see* B. I. DEUTCH
MÖBIUS, P., Introduction of many-particle variables for the treatment of special translationally invariant many-body problems 278
MOFFAT, JOHN W., Regularized vacuum expectation values in quantum field theory 304
MONARO, S., *see* R. A. RICCI
MORINAGA, H., *see* K. KOTAJIMA
MORINAGA, H., *see* H. YUTA
MOUTON, W. L. and P. B. SMITH, Resonant absorption of the gamma radiation from the Ne^{22} (p, γ) Na^{23} reaction 206
NAGAI, HIROYUKI, *see* HAJIME NARUMI
NARUMI, HAJIME and HIROYUKI NAGAI, Electric and magnetic moments of odd-neutron nuclei on the single configuration model 193
NÉMETH, J., Modification of the form of potential in an excited nucleus and its effect on the barrier transmission coefficient 331
NIELSEN, H. L., *see* R. K. SHELINE
ONEDA, S., *see* B. SAKITA
PAHOR, J., *see* P. HORVAT
PARKER, K., *see* A. M. LANE
PELEKHOV, V. I., *see* L. V. GROSHEV
RAMASWAMY, M. K. and P. S. JASTRAM, Angular correlation of the 1.07—1.24 MeV gamma cascade in the decay of Ga^{68} 113
RAMASWAMY M. K., W. L. SKEEL and P. S. JASTRAM, Decay of Ba^{133} 619
RASMUSSEN, JOHN O., *see* KENNETH S. TOTH
RASMUSSEN, V. K., *see* F. R. METZGER
RICCI, R. A., S. MONARO and R. VAN LIESHOUT, On the decay of ^{105}Ru 339
ROLL, P. G. and F. E. STEIGERT, Characteristics of heavy ion tracks in

nuclear emulsions 534
ROSENBERG, R. L., *see* TA-YOU WU
SAKITA, B. and S. ONEDA, On the decay interaction of strange particles 72
SANDSTROM, H., *see* TA-YOU WU
SATCHLER, G. R., Circularly polarized gamma rays from direct nuclear reactions 674
SCHARDT, A. W., *see* B. J. DROPESKY
SEGAERT, O. J., J. DEMUYNCK, A. M. HOOGENBOOM and H. VAN DEN BOLD, On the decay of ^{106}Rh 138
SEGAERT, O. J. and J. L. DEMUYNCK, On the decay of ^{106}Rh^{m} 492
SHELINE, R. K. and H. L. NIELSEN and A. SPERDUTO, Coulomb excitation of beta- and gamma-vibrational states in Sm^{152} 518
SHULL, T. T., *see* B. J. DROPESKY
SILVERBERG, L., *see* B. F. BAYMAN
SKEEL, W. L., *see* M. K. RAMASWAMY
SMITH, P. B., *see* W. L. MOUTON
SPEARMAN, T. D., The pion-nucleon coupling constant 402
SPERDUTO, A., *see* R. K. SHELINE
SPRINGER, T. E., *see* J. E. DRAPER
STEIGERT, F. E., *see* P. G. ROLL
STELSON, P. H. and F. K. MCGOWAN, Coulomb excitation of Li^{7}, F^{19} and Na^{23} by Ne^{20} ions. 92
STRUTINSKI, V. M., L. V. GROSHEV and M. K. AKIMOVA, Spectra of γ-rays from neutron capture by heavy nuclei (II) 657
SWANN, C. P., *see* F. R. METZGER
SWENSON, L. W., *see* P. R. KLEIN
TADROS, S., *see* A. S. MELIGY
TALMI, IGAL, Symplectic invariance and the pairing property of nuclear interactions. 153
TAMURA, T. and T. UDAGAWA, Comments on Davydov and Fillippov's theory of the properties of even nuclei 460
TAUBER, G. E. and TA-YOU WU, Nuclear shell model: Hartree-Fock approximation with Gammel-Thaler two-nucleon potential 545
TAYLOR, A. E., E. WOOD and L. BIRD, Proton-proton scattering at 98 and 142 MeV 320
TOTH, KENNETH S. and JOHN O. RASMUSSEN, Systematics of alpha-radioactivity in the rare earth region 474
UDAGAWA, T., *see* T. TAMURA
VAKSEIJ, M., *see* P. HORVAT
VAN DEN BOLD, H., *see* O. J. SEGAERT
VANHUYSE, V. J., *see* W. C. BARBER
VAN LIESHOUT, R., *see* R. A. RICCI

VAN NOOIJEN, B., *see* J. KONIJN
VIGIER, J. P., *see* P. HILLION
WALEN, R. J. et G. BASTIN-SCOFFIER, Spectre α du ^{214}Bi et remarques sur quelques émetteurs α du Bi 246
WALL, N. S., *see* P. R. KLEIN
WAPSTRA, A. H., *see* J. KONIJN
WERNTZ, CARL, Meson capture in He^3 59
WILHELM, F. J., *see* B. I. DEUTCH
WILSON, RICHARD, Nuclear radii from neutron scattering 318
WOOD, E., *see* A. E. TAYLOR
WU, TA-YOU, R. L. ROSENBERG and H. SANDSTROM, μ-Hydrogen molecular ion and collisions between μ-hydrogen atom and proton, deuteron and H atom 432
WU, TA-YOU, *see* G. E. TAUBER
YUTA, H. and H. MORINAGA, Study of heavy odd-mass indium isotopes from the (γ, p) reaction on tin 119
ZIATEV, I. S., *see* P. S. ISAEV
ZUCKER, A., *see* M. L. HALBERT

SUBJECT INDEX

1. Nuclear Structure

1.B *Two- and three-body problems*

Meson capture in He^3, Carl Werntz 59
Proton-proton scattering at 98 and 142 MeV, A. E. Taylor, E. Wood and L. Bird 320
Polarization of 1.0-MeV neutrons scattered from deuterium, S. E. Darden, C. A. Kelsey and T. R. Donoghue 351
Kinetic and potential energy matrix elements for the triton, G. H. Derrick . 405
μ-Hydrogen molecular ion and collisions between μ-hydrogen atom and proton, deuteron and H atom, Ta-You Wu, R. L. Rosenberg and H. Sandstrom 432
Nuclear shell model: Hartree-Fock approximation with Gammel-Thaler two-nucleon potential, G. E. Tauber and Ta-You Wu 545

1.C *Many-particle systems*

Introduction of many-particle variables for the treatment of special translationally invariant many-body problems, P. Möbius 278
Sur la fonction de Green à une particule en mécanique statistique quantique, Roger Balian et Cyrano de Dominicis 502
Nuclear shell model: Hartree-Fock approximation with Gammel-Thaler two-nucleon potential, G. E. Tauber and Ta-You Wu 545

1.D *Nuclear models*

1.D.1 *Shell model*

Electric and magnetic moments of odd-neutron nuclei on the single configuration model, Hajime Narumi nd Hiroyuki Nagai. 193
Isomers in N = 81 nuclei, K. Kotajima and H. Morinaga 231
Method for separating the relative motion of two nucleons in oscillator potential well, V. V. Balashov and V. A. Eltekov 423
Spectre α du ^{214}Bi et remarques sur quelques émetteurs α du Bi, R. J. Walen et G. Bastin-Scoffier 246

1.D.2 *Collective model*

Conversion electron spectrum from Ce^{144} decay, J. S. Geiger, R. L. Graham and G. T. Ewan 1
Gamma rays from the 4.24 MeV state in magnesium-24, R. Batchelor, A. J. Ferguson, H. E. Gove and A. E. Litherland 38
Nuclear resonance fluorescence with the 105-keV E1 transition of Gd^{155} using an ultracentrifuge, B. I. Deutch, F. R. Metzger and F. J. Wilhelm 81
Classification of beta- and gamma-ray transitions between intrinsic states in deformed even-mass nuclei, C. J. Gallagher 215
Comments on Davydov and Fillippov's theory of the properties of even nuclei, T. Tamura and T. Udagawa 460
Coulomb excitation of beta- and gamma-vibrational states in Sm^{152}, R. K. Sheline, H. L. Nielsen and A. Sperduto 518
Coupling of nuclear rotation and motion of the outer nucleon, A. S. Davydov 597
On the coupling of a $j = \frac{3}{2}$ particle to nuclear quadrupole surface oscillations, B. F. Bayman and L. Silverberg 625

1.E *Properties of nuclei*

1.E.1 *Energy levels*

Conversion electron spectrum from Ce^{144} decay, J. S. Geiger, R. L. Graham and G. T. Ewan 21
On the decay of ^{103}Ru, R. A. Ricci, S. Monaro and R. van Lieshout . . 339
On the decay of $^{106}Rh^{m}$, O. J. Segaert and J. L. Demuynck 492
Decay of Ba^{133}, M. K. Ramaswamy, W. L. Skeel and P. S. Jastram . . 619

1.E.3 *Electric and magnetic moments*

Electric and magnetic moments of odd-neutron nuclei on the single configuration model, Hajime Narumi and Hiroyuki Nagai 193
Nuclear polarization of Co^{56}, Rudolf W. Bauer and Martin Deutsch . . 264

1.E.4 *Transition probabilities; cross sections*

Gamma rays from the 4.24 MeV state in magnesium-24, R. Batchelor, A. J. Ferguson, H. E. Gove and A. E. Litherland 38
Nuclear resonance fluorescence with the 105-keV E1 transition of Gd^{155} using an ultracentrifuge, B. I. Deutch, F. R. Metzger and F. J. Wilhelm 81
Partial gamma ray widths for low lying levels in aluminium and magnesium, F. R. Metzger, C. P. Swann and V. K. Rasmussen . . . 568

1.E.5 *Nuclear radii; matter distributions*

Isotope shift and nuclear deformations, A. S. Meligy, S. Tadros and M. A. El-Wahab 99
Nuclear radii from neutron scattering, Richard Wilson 318
The nuclear surface in an excited nucleus, A. M. Lane and K. Parker . 690

2. Nuclear Reactions

2.A *General properties*

2.A.1 *Cross-sections, energy relations*

Multiplicity of resonance neutron capture gamma rays, J. E. Draper and T. E. Springer 27
Neutron total cross-sections in the 12 to 21 MeV region, G. J. McCallum, G. S. Mani and A. T. G. Ferguson 313

2.B *Angular distributions; correlations; polarization*

$Li^{7}(\alpha, p)Be^{10}$ and $Li^{6}(\alpha, p)Be^{9}$ reactions at 30 MeV, P. R. Klein, N. Cindro, L. W. Swenson and N. S. Wall 374
Circularly polarized gamma rays from direct nuclear reactions 674

2.C *Resonance reactions; R-matrix theory*

Resonant absorption of the gamma radiation from the $Ne^{22}(p, \gamma)Na^{23}$ reaction, W. L. Mouton and P. B. Smith. 206

2.D *Statistical model*

Modification of the form of potential in an excited nucleus and its effect on the barrier transmission coefficient, J. Németh 331
Spectra of γ-rays from neutron capture by heavy nuclei (I), L. V. Groshev, A. M. Demidov and V. I. Pelekhov 645
Spectra of γ-rays from neutron capture by heavy nuclei (II), V. M. Strutinski, L. V. Groshev and M. K. Akimova 657
The nuclear surface in an excited nucleus, A. M. Lane and K. Parker 690

2.E *Optical model*

The elastic scattering of 19 MeV deuterons by krypton and xenon, J. B. A. England, R. McKeague and P. E. Hodgson 52

2.G *Stripping and pick-up*

Circularly polarized gamma rays from direct nuclear reactions 674

2.H *Coulomb excitation*

Coulomb excitation of Li^{7}, F^{19} and Na^{23} by Ne^{20} ions, P. H. Stelson and F. K. McGowan 92
Coulomb excitation of beta- and gamma-vibrational states in Sm^{152}, R. K. Sheline, H. L. Nielsen and A. Sperduto 518
Partial gamma ray widths for low lying levels in aluminium and magnesium, F. R. Metzger, C. P. Swann and V. K. Rasmussen 568

2.I *Photonuclear processes*

The photonuclear reactions (γ, d) and (γ, np) on K^{39}, P. Horvat, J. Pahor and M. Vakselj 90
Photoprotons from medium and heavy elements, W. C. Barber and V. J. Vanhuyse 381

2.L *Scattering processes (except two-nucleon system and meson-scattering)*

The elastic scattering of 19 MeV deuterons by krypton and xenon, J. B. A. England, R. McKeague and P. E. Hodgson 52
Circularly polarized gamma rays from direct nuclear reactions 674

3. Electromagnetic Radiation

3.A *Gamma radiation*

Gamma rays from the 4.24 MeV state in magnesium-24, R. Batchelor, A. J. Ferguson, H. E. Gove and A. E. Litherland 38
Isomers in N = 81 nuclei, K. Kotajima and H. Morinaga 231
On the decay of ^{105}Ru, R. A. Ricci, S. Monaro and R. van Lieshout 339
Decay of Ba^{133}, M. K. Ramaswamy, W. L. Skeel and P. S. Jastram 619

3.B *Internal conversion*

Conversion electron spectrum from Ce^{144} decay, J. S. Geiger, R. L. Graham and G. T. Ewan 31

3.C *Extranuclear effects*

Nuclear resonance fluorescence with the 105-keV E1 transition of Gd^{155} using an ultracentrifuge, B. I. Deutch, F. R. Metzger and F. J. Wilhelm 81

4. Beta Decay; Parity

4.D *K-Capture*

Branching ratios of K capture to position emission in non-unique first forbidden $2^{-} \rightarrow 2^{+}$ beta transitions, J. Konijn, B. van Nooijen and A. H. Wapstra . . . 683

4.E *Analysis of data*

Note on the decay of the new nucleide Cr^{48}, B. J. Dropesky, A. W. Schardt and T. T. Shull 357
On the decay of $^{103}Rh^{m}$, O. J. Segaert and J. L. Demuynck 492

5. Alpha Decay

Spectre α du ^{214}Bi et remarques sur quelques émetteurs α du Bi, J. R. Walen et G. Bastin-Scoffier 246
Systematics of alpha-radioactivity in the rare earth region, Kenneth S. Toth and John O. Rasmussen 474
Measurement of the energy of the weak group in the α-spectrum of Po^{210}, T. Fényes 529
Search for the natural alpha activity of tungsten, G. B. Beard and W. H. Kelly 591

6. Methods and Instruments

6.A *Experimental*

Characteristics of heavy ion tracks in nuclear emulsions, P. G. Roll and F. E. Steigert 534

6.D *Tables and computational aids*

Method for separating the relative motion of two nucleons in oscillator potential well, V. V. Balashov and V. A. Eltekov 423

7. Quantum Field Theory

7.B *Quantum electrodynamics*

Regularized vacuum expectation values in quantum field theory, John W. Moffat 304
Application of dispersion relations for testing quantum electro-dynamics at small distance, P. S. Isaev and I. S. Zlatev 608

7.C *π-meson field (scattering and nuclear forces)*

The pion-nucleon coupling constant, T. D. Spearman 402

8. Elementary Particles

8.B *Theory, interactions, transformation properties*

Meson capture in He^{3}, Carl Werntz 59
On the decay interaction of strange particles, B. Sakita and S. Oneda 72
Elementary fields and irreducible representations of the Lorentz group, P. Hillion and J. P. Vigier 360
μ-Hydrogen molecular ion and collisions between μ-hydrogen atom and proton, deuteron and H atom, Ta-You Wu, R. L. Rosenberg and H. Sandstrom . . 432

9. Cosmic Radiation

9.B *Passage of particles through matter*

Characteristics of heavy ion tracks in nuclear emulsions, P. G. Roll and F. E. Steigert 534

10. News Items

10.B *Reports on conferences and congresses*

International conference on nuclear structure (Ontario, August 29—September 3 1960) 190
Tenth annual international conference on high energy physics, University of Rochester (August 25—September 1 1960) 377

10.D *Book reviews*

Kowarski, L. (Editor), Proceedings of the International Conference on high-energy accelerators and instrumentation — CERN 1959 (L. R.) . . . 188
Kopfermann, H., Nuclear moments (L. R.) 188
Schindewolf, Ulrich, Physikalische Kernchemie (Ove Nathan) 188
McConnell, J., Quantum particle dynamics, 2nd revised edition (L. R.) . . 189
Roman, P., Theory of elementary particles (L. R.) 189
Oeec, Towards a new energy pattern in Europe, (L. R.) 189
Directory of nuclear reactors, Vol. II: Research, test and experimental reactors (L.R.) 798
Multilateral agreements (L.R.) 798
Bershader D. (Editor), The magnetodynamics of conducting fluids (Carl F. Wandel) 798

10.E *Erratum*

Balian, R., Densité de niveaux d'un système de Nucléons en interaction dans une couche 192